Number 7 Volume 24 1960

BULLETIN

of the

ACADEMY OF SCIENCES OF THE USSR

— PHYSICAL SERIES —

(Izvestiya Akademii Nauk SSSR)
(Seriya fizicheskaya)

Reproduction rights reserved
by
Columbia Technical Translations
5 Vermont Avenue
White Plains, New York

Single Issues
$20

Annual Subscription
$215

Lithoprinted in U.S.A.
EDWARDS BROTHERS, INC.
Ann Arbor, Michigan

Transactions

of the

Tenth All-Union Conference on Nuclear Spectroscopy

(Moscow, 19-27 January 1960)

(Continued from Vol.24, No.3;
to be continued in Vol.24, Nos.9 & 12 and Vol.25, No.1)

FORMATION OF Eu^{145} IN SPALLATION OF TANTALUM

- A.A.Bashilov, O.V.Larionov, M.K.Nikitin & V.B.Smirnov

The purpose of the present work was to investigate the formation of Eu^{145} as a result of spallation of tantalum bombarded with 660 Mev protons in the Joint Institute for Nuclear Research Synchrocyclotron. The radioactive europium isotopes forming in the reaction were investigated by observing the γ-radiation.

Six hours after bombardment the rare earths were first separated chemically from the tantalum target; then the individual rare earth elements were separated from the integral fraction. The europium fraction was subjected to chromatographic purification, after which it was dissolved in 0.1 N HNO_3 solution containing La^{3+} as hold-back carrier to prevent adsorption. Appropriate aliquots were then taken and the europium and samarium activities were deposited on lanthanum hydroxide; the rare earth hydroxides were dissolved in 0.05 N HNO_3, and the solution was passed through a chromatographic column (length 10 cm, diameter 2 mm, resin Dowex-50x-12, grain size 10-15 μ). Finally, the europium and samarium were eluted with 0.3 M ammonium lactate (pH = 5.6). Chromatograms were recorded by means of a scintillation counter; clear separation of the europium and samarium peaks was obtained for all the aliquots (Fig.1).

The γ-radiation was investigated by means of an NaI scintillation counter with a resolution of 8% for the Cs^{137} 660 kev line.

In the spectrum of the europium fraction we observed the known γ-lines of Eu^{146} (Ref.1), Eu^{147} (Ref.2) and Eu^{149} (Ref.3). In addition, we detected γ-rays of energies 0.89, 1.66, 1.86 and 2.0 Mev (Fig.2). The intensity of these new lines fell off with a period T = = 5.5 days. Even from a superficial examination of the tabular data on known neutron-deficient europium isotopes it was apparent

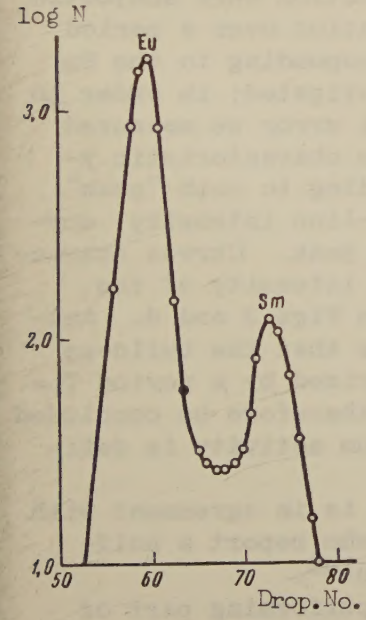

Fig.1. Europium and samarium chromatogram.

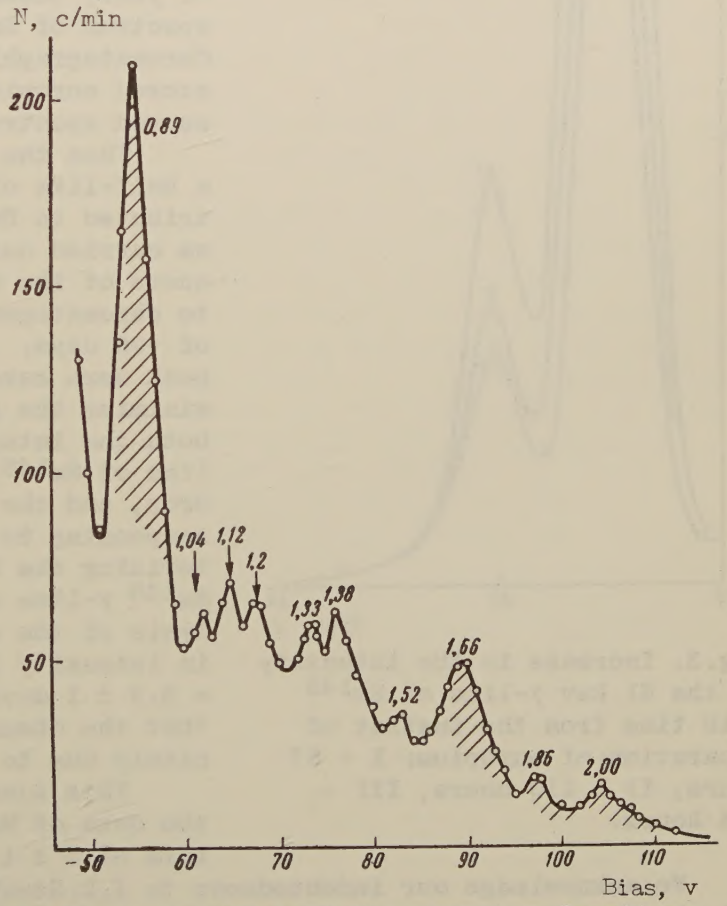

Fig.2. Gamma-spectrum of the europium fraction; the γ-lines of Eu^{145} are hatched.

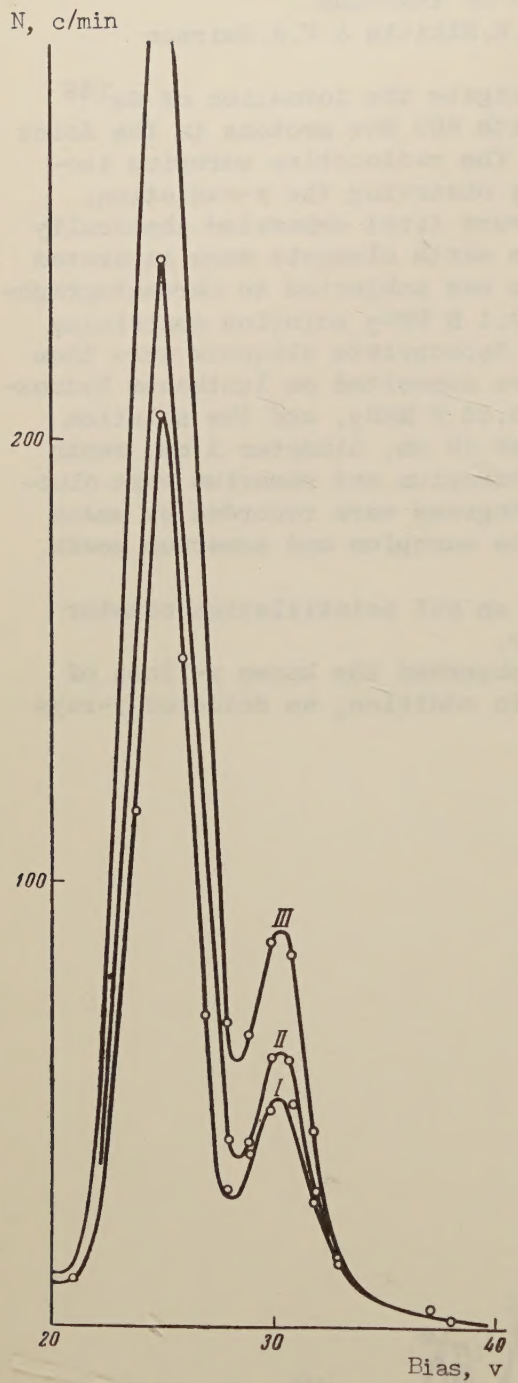

Fig.3. Increase in the intensity of the 61 kev γ-line of Sm^{145} with time from the instant of separation of europium: I - 87 hours, II - 110 hours, III - 254 hours.

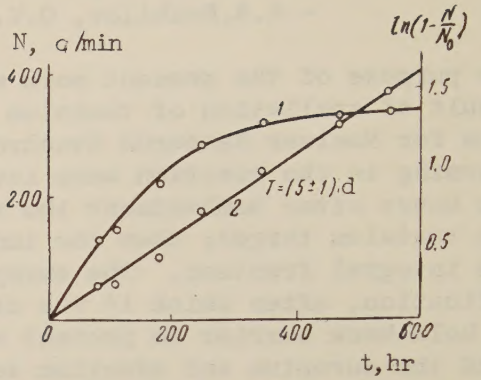

Fig.4. Increase in the integral γ-radiation from Sm^{145}: 1 - plot referred to the left-hand scale, 2 - right hand scale.

that the observed activity was due either to Eu^{145} or Eu^{144}. A more definitive identification of this activity was made by studying the daughter products. First, we investigated the γ-spectrum of europium samples held for ~1 year; these exhibited the characteristic spectrum of Sm^{145}: x-rays and 61 kev γ-rays. Chromatographic separation of Sm from the stored europium samples showed that the observed spectrum really belonged to samarium.

Thus the observed europium activity with a half-life of 5.5 days could clearly be attributed to Eu^{145}. To confirm this further we carried out the following experiment. Aliquots of the europium fraction were subjected to chromatographic separation over a period of ~25 days. Drops corresponding to the Sm peak were carefully investigated; in order to minimize the experimental error we measured both the intensity of the characteristic γ-line of Sm^{145}, corresponding to each "peak" drop, and the integral γ-line intensity, corresponding to the entire peak. Curves characterizing the build-up in intensity of the Sm^{145} γ-line are shown in Figs.3 and 4. Analysis of the curves shows that the build-up in intensity is characterized by a period T = = 5.5 ± 1 days. It may therefore be concluded that the observed europium activity is definitely due to Eu^{145}.

This identification is in agreement with the data of Hoff et al[4] who report a half-life of 5 ± 1 days for Eu^{145}.

We acknowledge our indebtedness to I.B.Stankevich for performing part of the chemical operations and V.B.Savichev for assistance in carrying out the measurements.

References

1. N.M.Anton'eva, A.A.Bashilov & B.S.Dzhelepov. Program of the Tenth All-Union Conference on Nuclear Spectroscopy, M.-L., 1960.
2. N.M.Anton'eva, A.A.Bashilov, B.S.Dzhelepov & B.K.Preobrazhenskii, Izv. AN SSSR, Ser.fiz., 22, 906 (1958). (Trans.Bulletin, 22, 899.)
3. N.M.Anton'eva, A.A.Bashilov, B.S.Dzhelepov, V.V.Il'in & B.K.Preobrazhenskii, Ibid., 23, 204 (1959). (Trans.Bulletin, 23, 196.)
4. R.W.Hoff, J.O.Rasmussen & S.G.Thompson, Phys.Rev., 83, 1068 (1951).

MAGNETIC GAMMA-SPECTROMETER WITH HIGH RESOLUTION

- L.V.Groshev, A.M.Demidov, V.N.Lutsenko & A.F.Malov

For several years we have employed a magnetic Compton spectrometer with a resolution of 2% for investigating the spectrum of thermal neutron capture γ-rays in the energy range from 0.3 to 12 Mev. These measurements yielded much new data on the γ-rays from the (n,γ) reaction[1], but at the same time they showed that the resolution of our instrument was inadequate for complete separation of the spectrum into individual lines even in the case of light nuclei. In the case of heavy nuclei it was feasible to investigate only the general shape of the spectrum, since only an insignificant part of it could be obtained in the form of discrete γ-lines. It became obvious that for more detalied investigation of the γ-spectra from the (n,γ) reaction it was essential to have a spectrometer with an appreciably higher resolution.

Below we describe the new magnetic Compton spectrometer by means of which one can investigate γ-ray spectra in the same energy interval with a resolution of 0.3% in the range above 2 Mev. At lower energies the resolution of the instrument is poorer, but is still superior to that of the old spectrometer.

Principle of the Spectrometer

Fig.1 shows a diagram of the experiment in which the new spectrometer is used for observing the spectrum of γ-rays accompanying thermal neutron capture. The investigated sample is placed in the tangential channel of the IRT reactor[2] close to the active zone. The channel diameter is 150 mm; the diameter of the sample 110 mm. The γ-ray beam is collimated by a series of lead and iron inserts, the neutrons being stopped by a 10 cm layer of paraffin loaded with B_4C. The right-hand end of the channel is stoppered with a lead plug. At the location of the converter the dimensions of the beam are 45 x 65 mm; the divergence of the beam does not exceed 36'.

The new instrument operates on the same principle as the old spectrometer, namely, energy analysis of the Compton electrons ejected from the large area converter in the direction of the incident γ-rays. The main difference between the two instruments is the following. In the old spectrometer collection of the electrons and their subsequent energy analysis were realized by different parts of a single magnetic field. It can be shown that under these conditions with optimum dimensions of the spectrometer slits the momentum spread of the collected electrons is appreciably smaller than the momentum spread permissible on the basis of the final resolution of the analyzing section of the spectrometer. Consequently, in this instrument the collecting and analyzing sections are poorly matched. If we could enhance the resolving power of the analyzing section of the spectrometer without changing the collection section, we would improve the resolution with no sacrifice in the overall efficiency of the instrument. However, in an instrument with a single magnetic field one can obtain improvement of the resolution only by decreasing the width of the slits or by increasing the radius of the instrument, which leads to decrease of the angle of electron collection and thus reduces the luminosity of the instrument. Hence in the new instrument two different magnetic fields are utilized for collecting the electrons from the converter and for their energy analysis. This makes it possible to specify the most advantageous field configuration for each function.

The new spectrometer is diagramed in Fig.2. The Compton electrons ejected from the converter within a small angle in the direction of the γ-rays are collected in the axially symmetric magnetic field and directed first on the horizontal slit S_1 and then on the vertical slit S_2. We call this part of the spec-

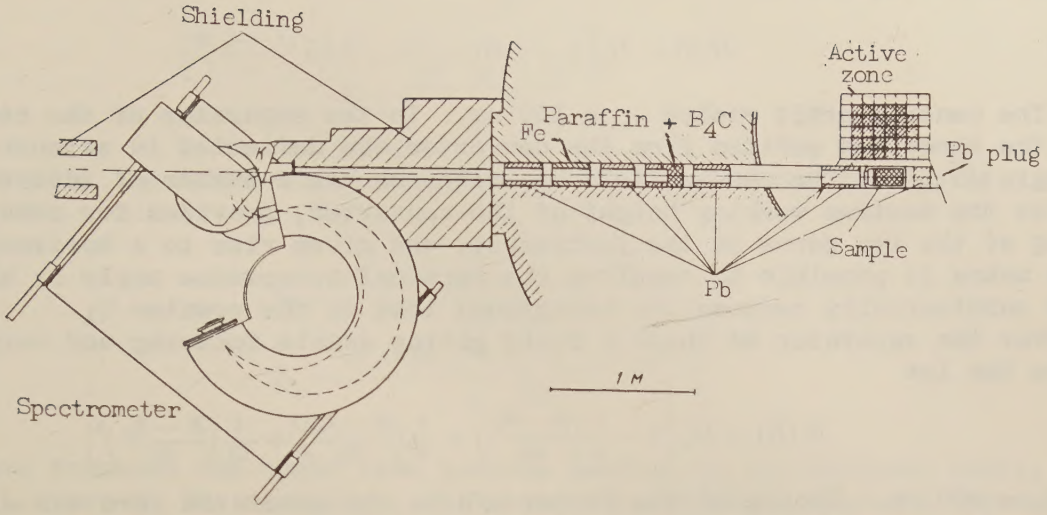

Fig.1. Diagram of the experiment. K - converter.

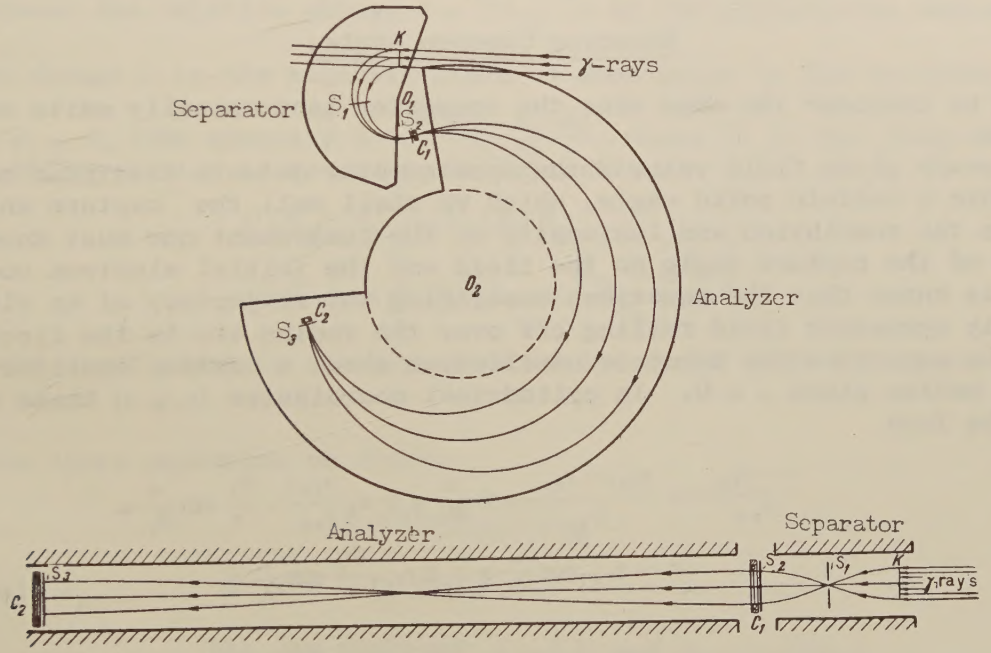

Fig.2. Magnetic Compton spectrometer. Above - projection of the electron trajectories on the median plane of the instrument. Below - projection of the trajectories on the vertical plane passing through the optical axis of the instrument. K - converter; S_1, S_2 & S_3 - slits; C_1 & C_2 - Geiger-Müller counters.

trometer the separator. The electrons passing through slit 2 enter the magnetic analyzer, which is essentially a $\sqrt{2}\ \pi$ focusing β-spectrometer. Geiger-Müller counters C_1 and C_2 with thin windows are located behind slits S_2 and S_3. In the illustrated experiment one measures the variation in the number of coincidences of pulses from counters C_1 and C_2 as a function of the analyzer field, as this is varied simultaneously with the separator field.

For the separator we chose a field focusing the electrons in the radial direction at an angle of $\sqrt{5}\ \pi$, and in the vertical direction at $\sqrt{5}\ \pi/2$. Such focus-

ing is obtained with variation of the magnetic field over the radius according to the following law

$$H(r) = H_0\left[1 - 0.80\,\frac{r - r_0}{r_0} + 0.65\left(\frac{r - r_0}{r_0}\right)^2\right]. \qquad (1)$$

The central orbit radius r_0 = 150 mm. In the separator of the new instrument the electrons emitted from the converter are deflected in azimuth through an angle $\sqrt{5}\ \pi/2$. The chosen field distribution has a number of advantages: it insures the maximum working height of the converter, provides for convenient combining of the two parts of the instrument, and gives rise to a horizontal focus, which makes it possible to regulate the vertical acceptance angle by the slit S_1, which substantially reduces the background load on the counter C_1.

For the separator we chose a field giving double focusing and varying according to the law

$$H(R) = H_0\left[1 - \frac{1}{2}\left(\frac{R - R_0}{R_0}\right) + \frac{1}{8}\left(\frac{R - R_0}{R_0}\right)^2 + \frac{1}{16}\left(\frac{R - R_0}{R_0}\right)^3\right] \qquad (2)$$

for R_0 = 600 mm. Choice of the factor 1/8 in the quadratic term was dictated by the consideration that the horizontal divergence of the electron beam in the analyzer is appreciably greater than the vertical divergence.

Electron Capture Angles

Let us consider the case when the converter isotropically emits monoenergetic electrons.

At every given field value H the spectrometer detects electrons emitted forward within a certain solid angle, which we shall call the "capture angle". To calculate the resolution and luminosity of the instrument one must know the dependence of the capture angle on the field and the initial electron coordinates.

It is known that the equations describing the trajectory of an electron in an axially symmetric field falling off over the radius are in the first approximation the equations for harmonic oscillation about a certain equilibrium radius r_{eq} and median plane $z = 0$. In cylindrical coordinates (r, φ, z) these equations are of the form

$$\frac{r - r_{eq}}{r_{eq}} = \frac{r_{ini} - r_{eq}}{r_{eq}}\cos\frac{\pi}{\Phi_r}\varphi + \alpha_0\frac{r_{ini}}{r_{eq}}\cdot\frac{\Phi_r}{\pi}\sin\frac{\pi}{\Phi_r}\varphi, \qquad (3)$$

$$z = z_{ini}\cos\frac{\pi}{\Phi_z}\varphi + \beta_0 r_{ini}\frac{\Phi_z}{\pi}\sin\frac{\pi}{\Phi_r}\varphi, \qquad (4)$$

where

$$r_{eq} = \frac{pc}{H(r_{eq})e}, \qquad (5)$$

p is the electron momentum, r_{ini}, z_{ini}, α_0 and β_0 are, respectively, the coordinates and angles of the electron at the initial point. Applying these equations to the separator, we obtain the initial conditions for the analyzer. By means of analogous equations we can find the coordinates of the electron after deflection through the $\sqrt{2}\ \pi$ angle in the analyzer.

For an electron ejected from the converter to pass through slit S_2 of width d, its initial horizontal angle of emission α_0 must lie between the limit angles

$$\left.\begin{aligned}\alpha_1 &= \frac{r_0 - r_{eq} + d/2}{r_{ini}\sqrt{5}}\\ \text{and}\qquad \alpha_2 &= \frac{r_0 - r_{eq} - d/2}{r_{ini}\sqrt{5}}.\end{aligned}\right\} \tag{6}$$

Analogously, the limit angles for passage of the electron through slit S_3 of width d are

$$\left.\begin{aligned}\alpha_3 &= \frac{2R_0 - 2R_{eq} + r_0 - r_{eq} + d/2}{r_{ini}\sqrt{5}},\\ \text{and}\qquad \alpha_4 &= \frac{2R_0 - 2R_{eq} + r_0 - r_{eq} - d/2}{r_{ini}\sqrt{5}}.\end{aligned}\right\} \tag{7}$$

In these formulas the upper case letters pertain to the analyzer radii; the lower case letters to the separator. To obtain the explicit relationship between the limit angles and the strength of the magnetic field one must establish the relation between the relative change $\delta = \frac{R_{eq} - R_0}{R_0}$ of the equilibrium radius and the relative change Δ in the magnetic field at some point in the analyzer, for example, at $R = R_0$ (the quantity $\Delta = \frac{H(R_0) - H_0(R_0)}{H_0(R_0)}$, where H_0 is the field for which $R_{eq} = R_0$). This relation is given by the expressions

$$\left.\begin{aligned}&H(R_{eq})\,R_{eq} = H_0(R_0)\,R_0\\ \text{and}\qquad &H(R_{eq}) \approx H(R_0)\left(1 - A\frac{R_{eq} - R_0}{R_0}\right),\end{aligned}\right\} \tag{8}$$

where A is the coefficient in the expansion of the field shape in powers of $\frac{R - R_0}{R_0}$.

From the above equations we obtain

$$\Delta = \delta\frac{A\delta + A - 1}{(\delta + 1)(1 - A\delta)}. \tag{9}$$

For small δ,

$$\Delta \approx \delta(A - 1);$$

$$\left.\begin{aligned}&\text{for the analyzer } A = 0.5 \text{ and } \Delta_a = -0.5\delta_a,\\ &\text{for the separator } A = 0.8 \text{ and } \Delta_s = -0.2\delta_s.\end{aligned}\right\} \tag{10}$$

As noted above, the analyzer and separator magnetic fields are varied in unison, hence

$$\Delta_a = \Delta_s = \Delta. \tag{11}$$

Utilizing (10) and (11), we can rewrite (6) and (7) in the following form

$$\left.\begin{aligned}\alpha_{1;2} &= \frac{5\Delta r_0 \pm d/2}{r_{ini}\sqrt{5}},\\ \text{and}\qquad \alpha_{3;4} &= \frac{(4R_0 + 5r_0)\,\Delta \pm d/2}{r_{ini}\sqrt{5}}.\end{aligned}\right\} \tag{12}$$

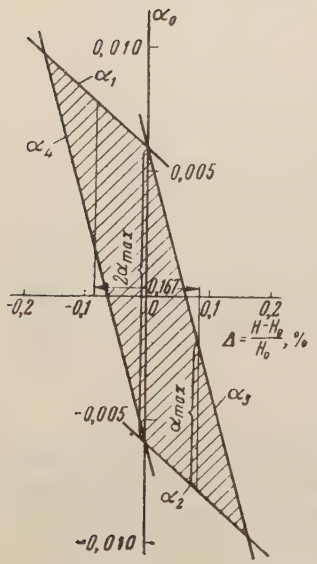

Fig.3. Variation of the vertical capture angle with the relative change in the magnetic field.

Fig.3 shows the variation of these angles with Δ for the case R_0 = 600 mm, $r_{ini} = r_0$ = 150 mm and d = 4 mm. Thus the hatched area in Fig.3 gives the emission angles for which the electrons are detected by the spectrometer. At Δ = 0, the instrument utilizes the maximum angle interval $2\alpha_{0max}$ = 0.012. This corresponds to the top of the peak. It will also be evident from Fig.3 that the width of the peak (width at half height) is 0.167%. We note that this is the effective value of the analyzer peak calculated without taking aberration into account, and is equal to $d/4R_0$.

The vertical capture angle does not depend on the strength of the magnetic field and is determined by the width h of the slit S_1:

$$2\beta_{0max} = \frac{2h}{r_{ini}\sqrt{5}}. \qquad (13)$$

With h = 5 mm, β_{0max} = 0.015.

It will be evident from (12) and (13) that the capture angles are inversely proportional to r_{ini}. Within the limits of the converter this gives a factor of two variation of the solid capture angle $\Omega = 2\alpha_{0max} \cdot 2\beta_{0max}$.

In the above calculations we have neglected aberrations distorting the shape of the trajectories in the section between the separator and the analyzer and electron scattering in the counter windows.

Resolution of the Spectrometer

In the spectrometer under consideration the line width for monochromatic γ-rays is determined primarily by the following factors: 1) the geometry of the instrument, 2) the natural width of the Compton line, 3) the dependence of the Compton electron energy on the angle of emission and divergence of the γ-ray beam, and 4) multiple scattering of electrons in the converter and the windows and gas of the first counter. Let us evaluate the contribution of each of these factors.

1. The geometric peak width does not depend on the energy of the γ-rays in the case when the converter is replaced by a source of monoenergetic electrons. The above calculation of the capture angles, which gave a value of $d/4R_0$ for the peak width, and direct experiments with Cs^{137} sources showed that the geometric part of the line width is determined wholly by the analyzer. In addition to the $d/4R_0$ term, the expression for the peak width must include a term characterizing the diffusion of the line in the analyzer owing to aberration.

In order to determine the aberration of the analyzer, we carried out a series of measurements of the peak width for the 624 kev conversion electron line of Cs^{137}. Cs^{137} sources of different widths were mounted in the position of slit S_2. By way of illustration in Fig.4 we reproduce the conversion electron spectrum for the case when $d_1 = d_2$ = 1 mm, where d_1 and d_2 are the widths of the source and receiving slit, respectively. On the basis of the experimental data we obtained the following formula

$$\frac{\Delta H_\rho}{H_\rho} = \frac{d_1 + d_2}{8R_0} + 3 \cdot 10^{-4}. \qquad (14)$$

The constant term in this formula gives the smearing out of the line owing

to aberration.*

Thus the total geometric line width for the spectrometer is

$$\left(\frac{\Delta H\rho}{H\rho}\right)_{geom} = \frac{d_1 + d_2}{8R_0} + 3\cdot 10^{-4}.$$

For $d_1 = d_2$ = 4 mm, the geometric width equals 0.2%.

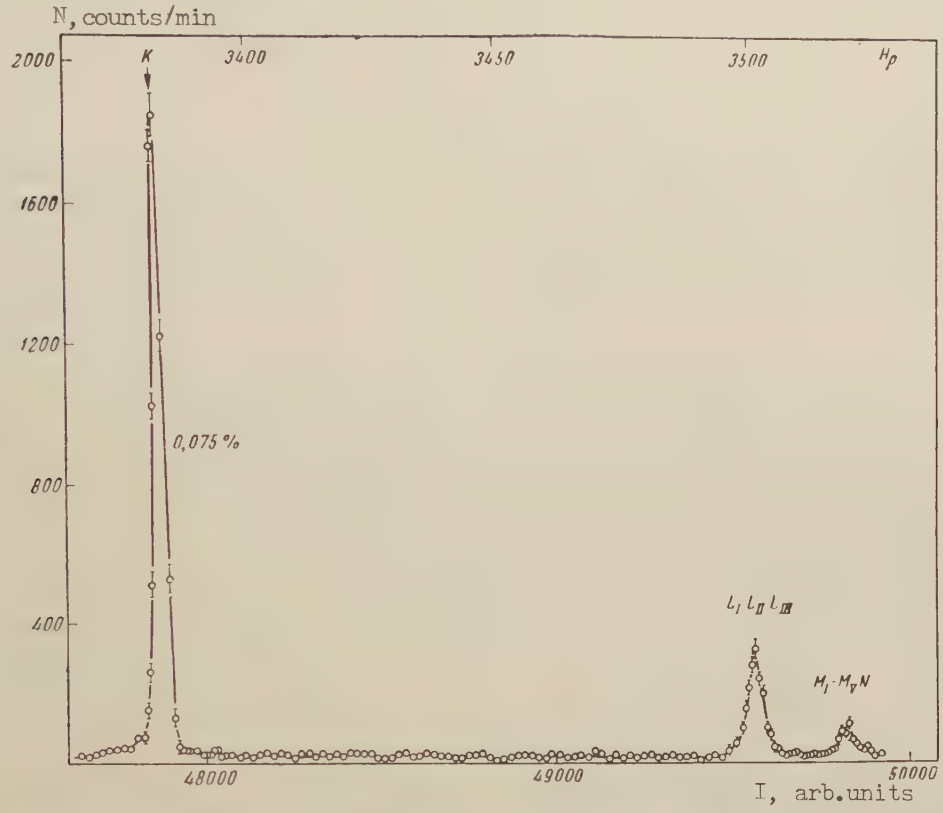

Fig.4. Spectrum of Ba^{137} internal conversion electrons obtained with the analyzer of the spectrometer. Source - 1 x 25 mm; slit - 1 x 50 mm; relative solid angle utilized - 0.2%.

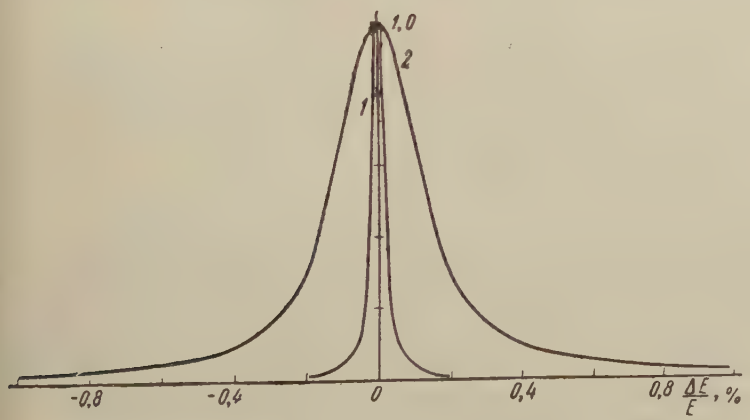

←Fig.5. Natural shape of the Compton electron line for a converter of polystyrene: 1 - for $h\nu$ = 6.13 Mev, 2 - for $h\nu$ = 1.02 Mev.

2. The natural Compton line width, connected with electron motion in the atom, makes a substantial contribution to the peak width in the range of γ-ray energies under 2 Mev. The Compton effect on bound electrons was first treated by Dzhelepov[3]. We calculated the dependence of the

---

*In measurements with Compton electrons the aberration of the analyzer may be somewhat smaller inasmuch as the vertical divergence angle of the electron beam in this case is smaller than in working with conversion electrons from Ba^{137}.

natural line width on the γ-ray energy for a polystyrene - $[CH]_x$ - converter. In these calculations we used the electron velocity distribution in a carbon atom given by DuMond[4]. We obtained the following expression:

$$\left(\frac{\Delta h\nu}{h\nu}\right)_{\text{natural}} = 92\,\frac{K+1}{K(2K+1)}\cdot 10^{-4}, \tag{15}$$

where

$$K = \frac{h\nu}{mc^2}.$$

The natural shape of Compton electron lines calculated for $h\nu$ = 1.02 and 6.13 Mev is shown in Fig.5.

3. The width due to the dependence of the Compton electron energy on the angle of emission and divergence of the γ-ray beam increases with increase of the photon energy. Approximate calculations show that the contribution of this effect to the total line width is given by

$$\left(\frac{\Delta h\nu}{h\nu}\right)_{\text{ang}} \approx \frac{(1+K)^2}{1+2K}\cdot 10^{-4}. \tag{16}$$

4. The principal contribution to the peak width associated with electron scattering in the converter and the windows and gas of the pass-through counter C_1 and in the residual gas in the spectrometer chamber is made by multiple scattering in the converter. The contribution of this factor was evaluated experimentally (see below).

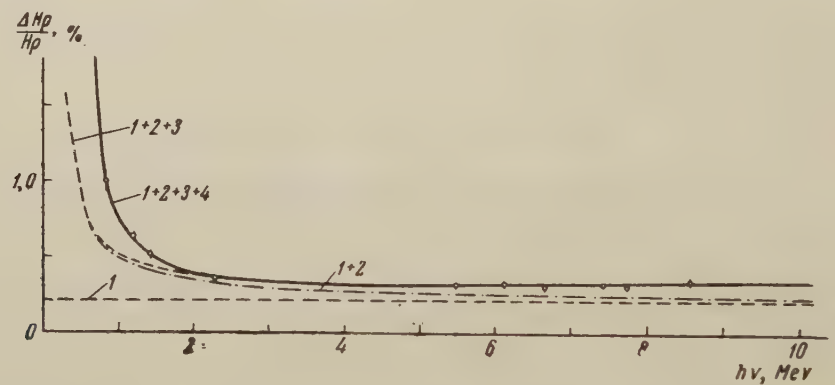

Fig.6. Variation of the peak width with γ-ray energy. The figures at the curves identify the width components comprised in the given curve: 1 - geometric width, 2 - natural width, 3 - angular width, 4 - width due to electron scattering. The points give the experimental values of the peak widths in the spectrum of the γ-rays from the $Cl^{35}(n,\gamma)Cl^{36}$ reaction.

Fig.6 shows the variation of the different components contributing to the peak width as a function of the γ-ray energy for the case when slits S_2 and S_3 are equal to 4 mm, slit S_1 to 5 mm and the polystyrene converter has a thickness of 20 μ. The contributing factors taken into account in plotting the curves are identified by the numerals at the curves. The figure also shows the experimental values of the peak widths found in measuring the spectrum of γ-rays emitted in thermal neutron capture by chlorine-35. The difference between the experimental width values and the total width due to factors 1,2 and 3 is attributable mainly to broadening owing to multiple electron scattering. It will be evident from the figure in the case of a 20 μ polystyrene converter appreciable line broadening owing to multiple electron scattering is evinced only in the range of energies below 1.5 Mev. It must be noted that our arithmetic addition of the contributions

from the different factors must be regarded as an approximate procedure inasmuch as strictly speaking these contributions are not fully additive.

In addition to the γ-ray dependence of the line width, we also determined the variation of the peak width with the converter thickness and the slit width. For polystyrene converters the optimum thickness was found to be 20 μ. By reducing the width of slit S_1 to 3 mm and of slits S_2 and S_3 to 2 mm, one can obtain a resolution of 0.23% for energies above 2 Mev. At the same time, however, the peak height is reduced by a factor of 3.5.

Spectral Response

For determining the spectral response ε of the instrument one must calculate the energy dependence of the area under the peak per photon incident on the converter and per unit $H\rho$ interval. The sensitivity was calculated on the assumption that all the electrons ejected from the converter within the solid capture angle have the same energy; multiple scattering in the converter and counter C_1 was neglected.

It can readily be shown that the area under the peak due to electrons ejected from 1 cm^2 of the converter is equal to the integral

$$S(h\nu) = N \int_0^{\infty} dH \int_{-\beta_{0\max}}^{\beta_{0\max}} \int_{\alpha_1(H)}^{\alpha_2(H)} f(h\nu, \alpha, \beta)\, d\alpha\, d\beta, \qquad (17)$$

where N is the number of electrons per 1 cm^2 converter, and $f(h\nu, \alpha, \beta)$ is the differential Compton effect cross section calculated for recoil electrons. The magnetic field dependence of the limits of integration as regards angle α was determined above in the section on "Electron Capture Angles". Integrating (17) over α, β and H, we obtain

$$S(h\nu) = H\rho \cdot \varepsilon(h\nu).$$

The function $\varepsilon(h\nu)$ calculated for the central part of the converter is shown in Fig.7. Inasmuch as $f(h\nu, \alpha, \beta)$ is only weakly dependent on α and β, $\varepsilon(h\nu)$ calculated for the center of the converter, can be applied to the entire converter area. Variation of the Compton electron energy with the angle of ejection and multiple scattering of the electrons in the converter should not within the range of moderate values significantly affect the peak area inasmuch as they do not change the total number of electrons ejected within the limits of the small capture angle (see, for example, Dzhelepov[5]).

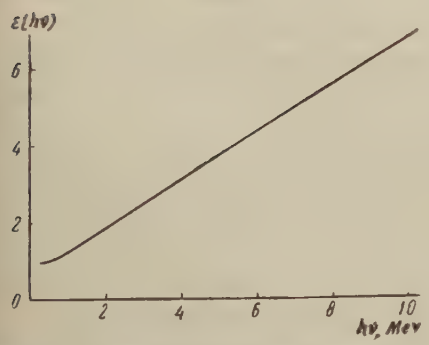

Fig.7. Spectral response of the instrument.

In measuring relative γ-ray intensities one must, in addition to the spectral response of the spectrometer, also take into account γ-ray absorption in the sample and along the path from the sample to the converter and also the electron loss owing to scattering in counter C_1.

Another parameter of interest is the absolute efficiency of the spectrometer, i.e., the number of counts at the line peak per photon emitted from the source located at a distance, say, of 5 meters. Calculations yielded an efficiency for 5 Mev γ-rays of $1 \cdot 10^{-12}$ counts per photon; the experimental value is $0.7 \cdot 10^{-12}$ counts per photon. We recall that for the old spectrometer the efficiency was $0.7 \cdot 10^{-11}$ counts per photon. The lower efficiency of the new spectrometer is due to the fact that we reduced the converter thickness from 80 to 20 μ and also

decreased the effective electron capture angles somewhat.

Measurements of the spectrum of γ-rays emitted in thermal neutron capture by chlorine show that the efficiency of the new spectrometer is high enough for investigation of such spectra with good statistics.[6]

Design of the Spectrometer

The analyzer and separator magnets are independent magnets, each weighing about 3.5 tons. The magnet assembly of the analyzer is designed in the form of a "double mushroom". The outside diameter of the magnet is 1700 mm; the width of the magnetic path is 500 mm; the width of the gap at R_0 = 600 mm is 100 mm. The magnet windings, consisting of four sections of 1000 turns each, with a current of 1.2 amp provide a 600 oersted field, corresponding to an electron energy of ~10 Mev.

The separator magnet is C-shaped and has a gap width of 110 mm at r_0 = 150 mm; the windings, which consist of 8 sections of 1140 turns each, provide working fields in the range from 80 to 2400 oersted (i up to 10 amp). The magnet mounting provides for relative adjustment of the magnet positions.

The profiles of the magnet pole pieces were calculated so that their surfaces would be equipotential surfaces of the induced field. The tolerance in machining the profiles was 0.05 mm.

Investigation of the magnetic field configuration showed that azimuthal symmetry in both magnets was realized within 0.2% if the investigated points are at least one gap width removed from the radial cross section of the pole piece. The actual field distribution over the radius for the separator differs by less than 0.1% from the design value. In the analyzer magnet this agreement obtains only for H > 500 oersted, i.e., only at the high end of the working field range. At lower field values there is some variation in the field distribution over the radius owing to nonlinear iron effects. However, the resultant astigmatism does not lead to impairment of the resolution of the analyzer, inasmuch as the design of the vacuum chamber provides for displacement of the C_2 counter assembly in the process of measurement to adjust for displacement of the radial focus. As was noted above the focusing characteristics of the analyzer were investigated with reference to the 624 kev Cs^{137} line. Although the astigmatism at this energy is appreciable, the effective resolution proved to be fully equal to the calculated value for the field (2).

Inasmuch as the vertical angles of the electrons entering the analyzer do not exceed 0.015 radians, the loss in intensity connected with noncoincidence of the radial and vertical focuses is negligibly small. This was substantiated by tests.

In order to minimize the influence of the prehistory of the magnet iron on the configuration of the magnetic field, both magnets are fully demagnetized prior to each experiment by means of an automatic circuit.

The magnet power supply circuit provides for current regulation to within 1 in $5 \cdot 10^5$. The magnetic field meter, which utilizes the principle of a permalloy transformer, indicates the magnetic field with an accuracy of 1 part in $5 \cdot 10^5$.

During experiments a vacuum of $\sim 10^{-2}$ mm Hg is maintained in the spectrometer chamber. The counters C_1 and C_2 have 5 μ thick terelene windows.

Adjustment of the Spectrometer

Adjustment of the spectrometer consists primarily of determining the positions of the analyzer and separator focuses at different γ-rays energies, adjustment of positions of the converters, slits and relative location of the magnets and finding the optimum analyzer-separator field intensity ratio.

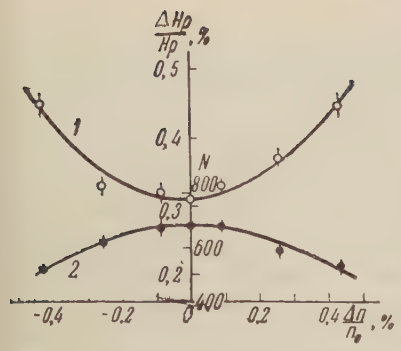

Fig.8. Variation of the peak height and width (7.79 Mev Cl^{36} line) with $\Delta n/n_o$, where $n = H_a/H_s$; n_o = optimum field ratio.

Regarding the last point we note that inasmuch as the field meters are not located on the central orbits and the field intensity distribution in the analyzer changes with variation of the field, the ratio of the analyzer and separator fields must be determined experimentally. Fig.8 shows the variation of the peak height and width with the field ratio for the 7.79 Mev line of Cl^{36}. It will be evident from Fig.8 that the ratio $n = H_a/H_s$ must be maintained within 0.1% of the optimum value. The variation of the analyzer-separator field ratio with the field intensity was obtained from diagrams similar to that shown in Fig.8.

Determination of γ-Ray Energies

For determining the γ-ray energies we plotted a calibration curve on the basis of the reference points listed in the accompanying table.

γ-Lines used in plotting the calibration curve

Reaction yielding the emitting isotope	, Mev	Method of energy determination and References
$B^{10}(n,\alpha)Li^7$	0.4773 ± 0.0004	Diffraction spectrometer (7)
$Na^{24}(\beta^-)Mg^{24}$	1.3679 ± 0.001	Magnetic spectrometer (8)
$H(n,\gamma)D$	2.2228 ± 0.0011	From nuclear mass measurements (9)
$Na^{24}(\beta^-)Mg^{24}$	2.7533 ± 0.0016	Magnetic spectrometer (8 & 10)
$C^{12}(n,\gamma)C^{13}$	4.944 ± 0.003	From the (d,p) reaction (11) and nuclear mass measurements (9)
$Cl^{35}(n,\gamma)Cl^{36}$	8.573 ± 0.004	Nuclear mass measurements (12)

In the future we plan to increase the number of reference points. In the energy range under 3 Mev there is available a sufficient number of γ-lines with well known energy (these are mainly γ-rays from different radioactive isotopes). In this energy region uncertainty in energy determinations on our spectrometer is evaluated to be 1-2 kev. In the energy region above 3 Mev for the reference points one must depend on data obtained from nuclear mass measurements and the (d,p) reaction. The error in energy determinations in this region depends primarily on the accuracy of the reference points and amounts to about 5 kev.

We desire to acknowledge our gratitude to D.V.Pavlov for design calculations of the magnetic system of the spectrometer, I.M.Kamyshev for preparing the engineering drawings and supervising the construction of the instrument and A.S.Volkov for constructing the electronic equipment, and the personnel of the IRT reactor for assistance in carrying out the measurements.

References

1. L.V.Groshev, A.M.Demidov, V.N.Lutsenko & V.I.Pelekhov, Atlas spektrov -luchei radiatsionnogo zakhvata teplovykh neitronov (Atlas of thermal neutron capture γ-ray spectra), Atomizdat, M., 1958.

2. V.V.Goncharov, E.N.Babulevich, Yu.G.Nikolaev & Yu.F.Chernilin, Report No.2185 presented at the Second International Conference on Peaceful Uses of Atomic Energy, Geneva, 1958.

3. B.S.Dzhelepov, Doklady AN SSSR, 101, 825 (1955). (Trans.Sov.Phys. - Doklady).
4. J.W.M.DuMond, Revs.Mod.Phys., 5, 1 (1933).
5. B.S.Dzhelepov, Izv.AN SSSR, Ser.fiz., 18, 95 (1954).
6. L.V.Groshev, A.M.Demidov & V.N.Lutsenko, Present issue of the Bulletin, p.834.
7. J.W.M.DuMond, Ann.Phys., 2, 283 (1957).
8. A.Hedgran & D.Lind, Arkiv Fys., 5, 177 (1952).
9. V.A.Kravtsov, Usp.fiz.nauk, 65, 452 (1958).
10. H.T.Motz, R.E.Carter & P.C.Fisher, Bull.Amer.Phys.Soc., II, 4, 477 (1959).
11. D.M.Van Patter & W.Whaling, Revs.Mod.Phys., 29, 757 (1957).
12. C.T.Giese & J.L.Benson, Phys.Rev., 110, 712 (1958).

CONVERSION ELECTRON SPECTRUM OF NEUTRON-DEFICIENT LUTETIUM ISOTOPES IN THE 1000 TO 3500 kev REGION

- B.S.Dzhelepov, I.F.Uchevatkin & S.A.Shestopalova

As is known[1-4], the conversion electron spectrum of the lutetium fraction in the spallation products of tantalum is very complicated. At the time this study was undertaken there had been reported approximately 100 γ-transitions belonging to Lu^{169}, Lu^{170}, Lu^{171} and Lu^{172}. However, only one γ-line with an energy exceeding 1600 kev was known (E = 2040 ± 40 kev, T = 2.2 ± 0.7 days)[5], although on the basis of β-systematics (according to Cameron) one might expect γ-transitions with energies up to 3.5 Mev in the lutetium fraction.

In view of this, we undertook a search for conversion lines with energies exceeding 1 Mev. The lutetium fraction separated from a proton-bombarded tantalum target was investigated by means of a triple focusing β-spectrometer operating under the conditions described in Ref.6. The low coincidence background (1-2 coinc/hr) in this instrument makes it possible to measure extremely weak lines.

$Lu^{171+172}$

The experimental results are given in Fig.1 and Table 1.

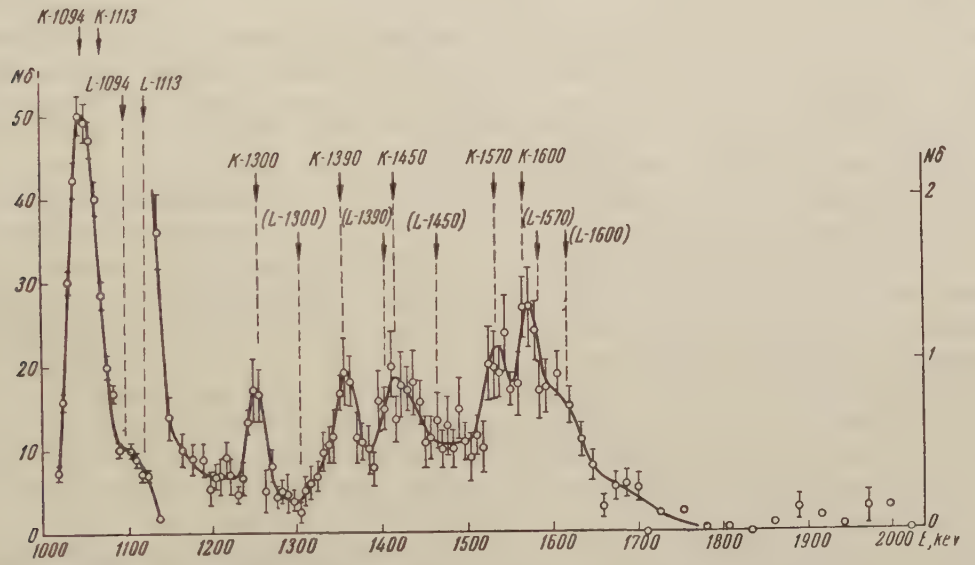

Fig.1. Spectrum of Lu^{172} conversion electrons with energies above 1000 kev.

Measurements in the 1000 to 1200 kev region of the spectrum were started 7 days after separation of the lutetium fraction. Our instrument recorded ~200 coinc/min at the well-known K-1094 line. We followed the decay in intensity of this line for 52 days and found that its decay period is 6.5 ± 0.2 days; this value is close to the period of Lu^{172}. In the work of Refs.4 and 7 there was detected a transition of 1103 kev energy in Lu^{171} (T ≈ 8 days). Apparently, the corresponding conversion line is appreciably weaker than the K-1094 line, inasmuch as even the points for the last two series of measurements fall on the same ln I vs time straight line corresponding to a period of 6.5 days. According to the data of Turkevich et al[8], there exists yet another line, approximately 14 times weaker than the K-1094 line, corresponding to a 1113 kev transition. These lines were not resolved in our experiments. No lines in the higher energy region have been reported hitherto.

Table 1

Lu^{172} conversion electrons with energies > 1000 kev

No.	Conversion electron energy, kev	Relative intensity	Transition energy, kev	Half-life, days
1*	1033	1**	1094	6,5±0,2
2	1240±10	$1 \cdot 10^{-2}$	1300±10	6,3±1,5
3	1330±15		1390±15	5,7±1,5
4	1390±15	$1 \cdot 10^{-1}$	1450±15	6,5±1,5
5	1510±20		1570±20	6,0±1,5
6	1540±20		1600±20	6,2±1,5

*The listed electron energy was taken from Ref. 4 as the most accurate value.

**The unit intensity was taken as the integral area under the conversion lines corresponding to the 1094 and 1113 kev transitions.

We detected five new lines in the 1200 to 1700 kev interval. Measurements in this region of the spectrum were started 22 days after separation of the fraction; presumably by this time very little Lu^{169} and Lu^{170} remained in the fraction. Among the newly detected lines the smallest number of coincidences was recorded at the peak of the K-1300 line; the actual count in the first series of measurements was 0.6 coinc/min, which is still approximately 25 times higher than the background due to chance and cosmic coincidences. Hence we could follow the decrease in intensity of the new lines for 18-20 days.

As will be evident from Table 1, these lines are characterized by a period of about 6 days; they probably belong to Lu^{172}. As will be seen in Fig.1, with the resolution of our instrument ($\Delta H\rho/H\rho$ = 3.5%) the last two lines - K-1570 and K-1600 - are barely resolved. In the vicinity of 1600 kev on the high energy side of the E_e = 1540 kev line there is a hump, which presumably may be attributed to a group of unresolved lines.

The K-1450 line of Lu^{172} is close in energy to the well-known Lu^{170} K-1454 line. This conversion line of Lu^{170} is very intense, and we initially measured it 7 days after separation of the fraction; 24 days after separation this line should have fallen off ~300 times in intensity (T ≈ 2 days) and should have yielded 0.4 coinc/min; actually, however, we observed 1.1 ± 0.1 coinc/min.

Thus the contribution from both lines at the beginning of measurement of the $L^{171+172}$ activity was approximately the same, and then the contribution of the Lu^{170} K-1454 line fell off rapidly. In the last series of measurements the intensity of the line with T = 2 days amounted to approximately 6% the intensity of the line with T = 6 days. This fact was taken into account in processing the results shown in Fig.1. We followed the decrease in intensity of the 678 kev conversion line, corresponding to a 739 kev transition in Lu^{171} (Refs.4 & 7) for 50 days. We determined the period on the basis of 12 series of measurements and obtained a value of 8.3 ± 0.2 days.

$Lu^{169+170}$

In the 1060 to 1350 kev region of the spectrum there are unresolved conversion electron lines, the intensity of which falls off with a period of ~2 days. The results of investigation of this section of the spectrum are shown in Fig.2; these measurements were carried out on the 7th through 11th days after separation

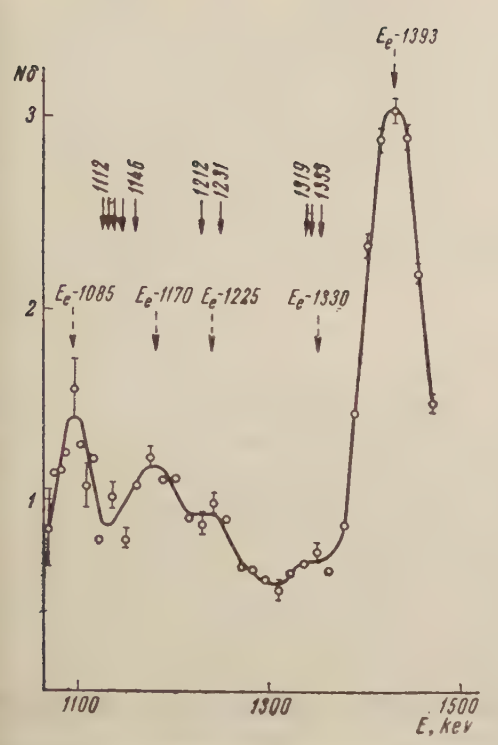

Fig.2. Conversion electron spectrum of $Lu^{169+170}$ in the 1060 to 1400 kev interval. The period was evaluated for the regions identified by the dashed line arrows (T ≈ 2 days). The solid line arrows indicate the conversion lines of Lu^{169} observed by Harmatz et al[9].

of the fraction. In the first series of measurements the lines with T = 6 days amounted to 50% in the 1085 kev region and 7% in the 1200-1300 kev region; in the last series of measurements the corresponding values were 70 and 13%, respectively. As will be evident from Fig.2 the conversion lines in this region are not resolved. We followed the decrease in intensity in the regions of the incipient peaks (see dashed arrows in Fig.2) and evaluated the corresponding period. The results are given in Table 2. The solid line arrows in Fig.2 indicate the positions of the conversion lines of Lu^{169} detected by Harmatz et al[9].

In Fig.3 we give the results of investigation of the conversion spectrum of the lutetium fraction in the energy range from 1350 to 3500 kev. These measurements were started a few hours after separation of the fraction. The high peak at ~1400 kev is due to overlapping of two lines (the relatively strong K-1454 line and the weaker K-1481 line, both of which have been attributed to Lu^{170} by Turkevich's group.[4,8]

We followed the decrease in intensity of this double line for about a month and found T = 2.1 ± 0.1 days. It follows from the work of Turkevich et al[8] that Lu^{170} has another weak line corresponding to a transition of 1567 kev energy. Harmatz et al[9] report observing a conversion line corresponding to a 1592.6 kev transition in Lu^{169}. In Fig.3 this line is evinced in the form of a jump on the high energy side of the K-(1454-1481) line. If this line is inscribed in the spectrum with the maximum possible height, it will be evident from Fig.3 that in the 1550 to 1860 kev interval there still persists an excess of conversion electrons, which may be attributed to two or more unresolved lines. We followed the decrease in intensity in the region of the incipient peaks (K-1690 and K-1810) and found T ≈ 2 days.

We investigated the section of the spectrum above 1800 kev with particular care (this section is plotted to an enlarged scale in Fig.3). In this region there are no lines of Lu^{171} and Lu^{172}, which have a period of 6-8 days. The initial coincidence rate at the peak of the weakest line - K-2360 - was 28 coinc/min, which is approximately 1000 times greater than the background due to cosmic and chance coincidences. As will be evident from the figure there are conversion electrons up to an energy of 3300 kev, but most of the lines remain unresolved. We followed the decay of the most intense lines carefully for 16 days (~8 periods). The values of the period are listed in column 7 of Table 2; on the basis of this data it may be asserted that all these hard lines belong to Lu^{170}.

The positron spectrum was investigated in the range of energies above 450 kev. We detected two components. The intensity of the component with end-point energy 2445 ± 20 kev decreases with a period of 48 ± 3 hours; accordingly, this spectrum belongs to Lu^{170}. The intensity of the spectrum with end-point energy 1250 ± 30

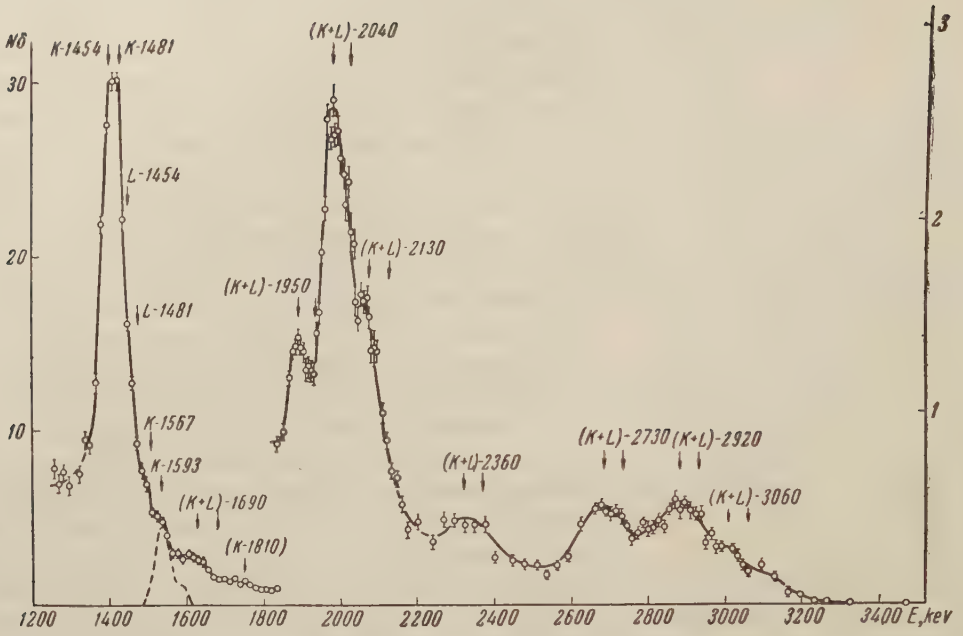

Fig.3. Conversion electron spectrum of the lutetium fraction in the 1350 to 3500 kev range.

Table 2

Spectrum of $Lu^{169+170}$ conversion electrons with energies above 1000 kev

No.	Conversion electron lines		γ-transition energy			T, hr.	Assign-ment
	energy, kev	relat. intens.	Our data*	Ref.8	Ref.9		
1	2	3	4	5	6	7	8
1	1085±10	1,1	1145±10			48±10	—
2	1170					45±5	(Lu^{170})?
3	1225					44±6	—
4	1330					50±10	(Lu^{170})?
5**	1393	1	1454	1454	—	48±2	Lu^{170}
6	1490÷1850	~0,4	—	1567			—
7	1890±20	0,2	1950±20			48±2	Lu^{170}
8***	1980±10		2040±10		2040±40	46±3	Lu^{170}
9	2070±20		2130±20			47±3	Lu^{170}
10	2300±20	0,1	2360±20			53±6	Lu^{170}
11	2670±20		2730±20			49±5	Lu^{170}
12	2860±20		2920±20			49±5	Lu^{170}
13	(3000±30)		(3060±30)			~48	Lu^{170}

---

*We assume that all lines listed in column 2 are K-lines.

**The indicated energy value has been taken from Ref.8 as the most accurate value.

***Note added in proof: More recent measurements of the spectrum of Lu^{170} by means of a spectrometer with a resolution of 1.4% yielded a value of E_e = 1992 ± 4 kev; the corresponding transition energy is 2053 ± 4 kev.

kev decreases with a period of 34 ± 4 hours; this spectrum belongs to Lu^{169}. These results are in good agreement with the data of Ref.10. In separating the components we assumed that the spectra have the Fermi shape. The intensity ratio S_{1250}/S_{2445}, referred to the time of separation of the fraction, equals 3.6 ± 1.5.

We take this opportunity to thank A.I.Medvedev, who participated in the measurements of the Lu^{170} spectrum, and M.K.Nikitin for chromatographic separation of the lutetium fraction.

"D.I.Mendeleev" All-Union Scientific Research Metrology Institute

References

1. Yu.G.Bobrov, K.Ya.Gromov, B.S.Dzhelepov & B.K.Preobrazhenskii, Izv.AN SSSR, Ser.fiz., 21, 940 (1957). (Trans.Bulletin, 21, 942.)

2. K.Ya.Gromov, B.S.Dzhelepov, A.G.Dmitriev & B.K.Preobrazhenskii, Ibid., 21, 1573 (1957). (Trans. Bulletin, 21, 1562.)

3. G.M.Gorodinskii, A.N.Murin, V.N.Pokrovskii & B.K.Preobrazhenskii, Ibid., 21, 1004 (1957). (Trans.Bulletin, 21, 1005.)

4. V.M.Kel'man, R.Ya.Metskhvarishvili, B.K.Preobrazhenskii, V.A.Romanov & V.V.Tuchkevich, Zhur.eksp.i teor.fiz., 35, 1309 (1958). (Trans.Soviet Physics - JETP.)

5. L.Dillman, R.Henry, N.Gove & R.Becker, Phys.Rev. Letters, 2, 27 (1959); Phys.Rev., 113, 635 (1959).

6. B.S.Dzhelepov, I.F.Uchevatkin & S.A.Shestopalova, Zhur.eksp.i teor.fiz., 37, 857 (1959). (Trans.Soviet Physics - JETP.)

7. M.Iodko, V.Romanov & V.Tuchkevich, Transactions of the Tenth All-Union Conference on Nuclear Spectroscopy, Moscow, Jan., 1960.

8. V.Tuchkevich, V.Romanov & M.Iodko, Ibid.

9. B.Harmatz, T.H.Handley & J.W.Mihelich, Phys.Rev., 114, 1082 (1959).

10. B.S.Dzhelepov, O.E.Kraft & E.B.Kreshtofova, Izv.AN SSSR, Ser.fiz., 23, 1431 (1959). (Trans.Bulletin, 23, 1422.)

CONVERSION ELECTRON SPECTRUM OF Lu^{167} + Yb^{167}

- A.S.Basina, B.S.Dzhelepov & V.A.Chikhladze

The lutetium fraction obtained by chromatographic separation from the rare earth products of spallation of tantalum was investigated on a lens spectrometer with a resolution of ~2%. The tantalum targets were bombarded 15 to 30 min with fast protons in the Joint Institute for Nuclear Research synchrophasotron. The fraction was separated from the target 1 hr 50 min after irradiation; investigation of the conversion spectrum was started 50 min later. The sources were prepared by evaporation of lutetium lactate on a 5 μ thick aluminum backing; the source diameter did not exceed 4 mm. The counter windows passed > 30 kev electrons.

At present the following neutron-deficient lutetium isotopes are known:[1-5]

$$Lu^{174} \xrightarrow[160\ d]{EC} Yb^{174}$$

$$Lu^{173} \xrightarrow[160\text{-}500\ d]{EC} Yb^{173}$$

$$Lu^{172} \xrightarrow[6.5\ d]{EC} Yb^{172}$$

$$Lu^{171} \xrightarrow[8.5\ d]{EC} Yb^{171}$$

$$Lu^{170} \xrightarrow[2.0\ d]{EC} Yb^{170}$$

$$Lu^{169} \xrightarrow[1.3\ d]{EC} Yb^{169} \xrightarrow[30.6\ d]{EC} Tm^{169}$$

$$Lu^{167} \xrightarrow[55\ min]{EC} Yb^{167} \xrightarrow[19\ min]{EC} Tm^{167} \xrightarrow[9.6\ d]{EC} Er^{167}.$$

(The end nuclides in the above chains are all stable.)

One could expect our sources to contain activities due to lutetium isotopes with A = 167, 169, 170, 171 and 172. Inasmuch as lutetium 173 and 174 have a long period, their activity in our sources was low. On the other hand, lutetium isotopes with a half-life appreciably shorter than that of Lu^{167} would decay to a negligible level during the 2-hour period required for chemical and chromatographic separation.

The purpose of the present work was to investigate the conversion electron spectrum of Lu^{167} + Yb^{167} in the energy interval from 30 to 340 kev. In the energy range above 340 kev we observed no lines, the intensity of which fell off with a period of about 1 hour.

In the 30 to 340 energy interval, in addition to the lines appearing in the decay series $Lu^{167} \rightarrow Yb^{167} \rightarrow Tm^{167} \rightarrow Er^{167}$, there appeared lines of Lu^{169}, Yb^{169}, Lu^{170}, Lu^{171} and Lu^{172}. These lines constituted a background: they were investigated after the decay of Lu^{167} and Yb^{167}, normalized according to their periods to the time of start of measurements and subtracted. The experimental spectrum of Lu^{167} and Yb^{167} reduced in this manner to 1 hour after separation of the fraction is shown in the accompanying figure.

$Lutetium^{167}$ was detected in the products of spallation of tantalum by Aron et al[4] by means of a scintillation spectrometer. These authors observed the disintegration of Lu^{167} (T = 55 ± 3 min) and the formation of Yb^{167} (T = 18 min). In the spectrum of Lu^{167} they observed γ-rays with an energy of about 240 kev; in the spectrum of the daughter Yb^{167} - γ-rays with energies of ~100 and 170 kev.

In the conversion electron spectrum of our sample, one to six hours after separation we observed a number of extremely bright lines, the intensity of which fell off with a period of 55 ± 5 min. After effacement of the lines of the short

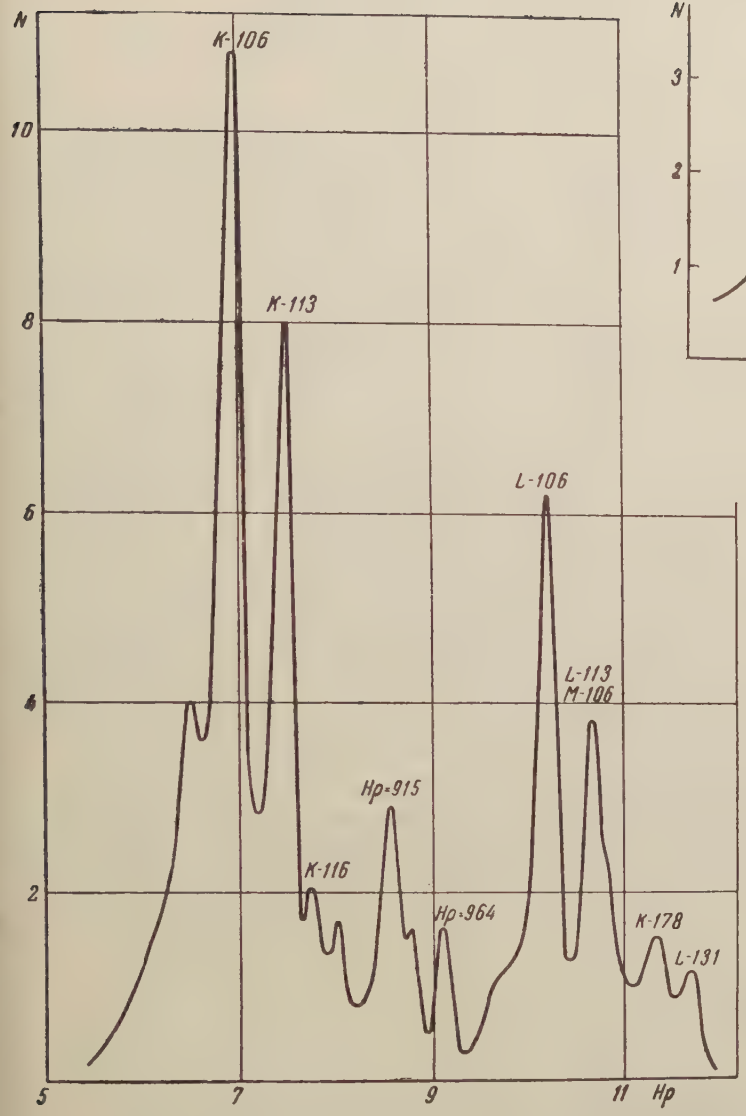

a

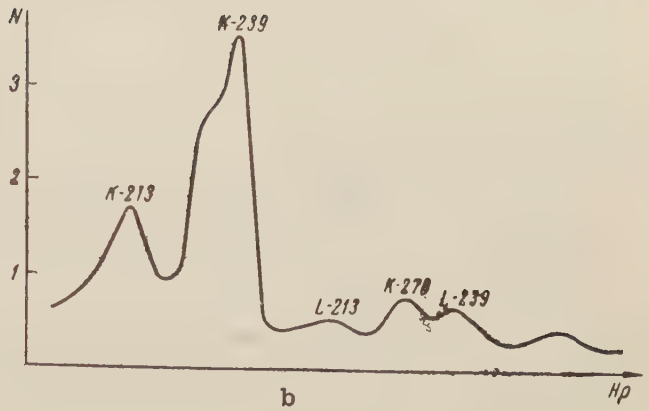

b

period activity, there were clearly evinced in the spectrum of our source conversion lines associated with the 208 kev γ-transition occurring in Tm^{167} (Ref.6).

Clearly, we were dealing with the conversion electron spectrum of Lu^{167} and Yb^{167} in equilibrium with it.

Recently, Harmatz et al[7] investigated separated Lu^{167} and Yb^{167}. Hence in Tables 1 and 2 we list the energies and relative intensities of the conversion lines separately for Lu^{167} and Yb^{167} (the separation is based on the data of Harmatz et al[7]). For comparison purposes, in addition to our own data, we also give the relative line intensities taken from Harmatz et al. Considering the experimental accuracy of our measurements, the agreement is satisfactory.

Table 1

Conversion electrons emitted in the decay $Lu^{167} \rightarrow Yb^{167}$

E_{e^-}, kev	E_γ, kev	T, min	Intensity		Identification
			Our data	Ref.7	
151,6	212,9	58±5	42±6	46	*K*-213
176,6	238	56±5	100	100	*K*-239
216,4	277,7	65±15	19±5	16	*K*-278
228	238	65±15	17±4	19	*L*-239
339,5	400,8	56±5	10±2	10	*K*-401

Table 2

Conversion electrons emitted in the decay $Yb^{167} \rightarrow Tm^{167}$

E_{e^-}, kev	E_γ, kev	T, min	Intensity		Identification
			Our data	Ref.7	
46,7	106,0	56±5	340±70	370	*K*-106
53,5	112,8	55±5	190±40	155	*K*-113
57,6	116,9	—	25±5	22	*K*-116
60,8	63	—	19±6	24	*M*-62*
95,7	105,8	55±5	100	100	*L*-106
103,6	105,9	56±5	58±9	50	*M*-106 и *L*-113
108	117	—	16±7	23	*L*-116
116,5	175,6	53±5	16±5	11	*K*-176
122,3	131,4	55±5	14±5	13	*L*-132

*Includes K-122 electrons of Lu^{167}.

Table 3

Unidentified Lu^{167} + Yb^{167} electrons, not reported in Ref.7

E_{e^-}, kev	T, min	Intensity (our data)
68,9	56±15	50±10
76,0	100±40	30±15
169,0	60±15	30±15

It would be of interest to carry out a comparison of the relative intensities of the transitions involved in the disintegration of Lu^{167} and Yb^{167}. Unfortunately, the relative intensities of the Lu^{167} K-239 and Yb^{167} L-106 lines could not be determined with sufficient accuracy: according to our evaluations the intensity of the Lu^{167} K-239 line amounts to from 35 to 55% the intensity of the Yb^{167} L-106 line. The 60 to 80 kev interval of the spectrum, wherein there were detected lines with energies 68.9 and 76 kev (not reported in Ref. 7), was investigated in an auxiliary series of experiments by Gromov & Dneprovskii[8] on an instrument with high resolution. Their data substantiate the existence of lines due to short period activities in this energy interval.

Scientific Research Physical Institute,
"A.A.Zhdanov" Leningrad State University &
Joint Institute for Nuclear Research

References

1. B.S.Dzhelepov & L.K.Peker, Skhemy raspada radioaktivnykh yader (Decay schemes of radioactive nuclei), M.-L., 1958.

2. D.Strominger, J.M.Hollander & G.T.Seaborg, Tables of Isotopes, Revs.Mod. Phys., 30, 585 (1958).

3. Yu.G.Bobrov, K.Ya.Gromov, B.S.Dzhelepov & B.K.Preobrazhenskii, Izv.AN SSSR, Ser.fiz., 21, 940 (1957). (Trans.Bulletin, 21, 942.)

4. P.M.Aron, A.V.Kalyamin, A.N.Murin & V.A.Yakovlev, Ibid., 22, 817 (1958). (Trans.Bulletin, 22, 811.)

5. K.Ya.Gromov, B.S.Dzhelepov & B.K.Preobrazhenskii, Ibid., 22, 775 (1958). (Trans.Bulletin, 22, 770.)

6. K.Ya.Gromov, B.S.Dzhelepov & B.K.Preobrazhenskii, Ibid., 21, 918 (1957). (Trans.Bulletin, 21, 920.)

7. B.Harmatz, T.H.Handley & J.W.Mihelich, Phys.Rev., 114, 1082 (1959).

8. K.Ya.Gromov & I.S.Dneprovskii, Trudy II Ezhegodnogo soveshchaniya po neitrono-defitsitnym izotopam (Transactions of the Second Annual Conference on Neutron-Deficient Isotopes), Dubna, 1959.

CONVERSION ELECTRON SPECTRUM OF THE DYSPROSIUM FRACTION FROM SPALLATION OF TANTALUM

- A.S.Basina, K.Ya.Gromov & B.S.Dzhelepov

1. Experimental conditions

We investigated the conversion electron spectrum of the dysprosium fraction, obtained by chromatographic separation from the rare earths formed in the spallation of tantalum, on a magnetic lens β-spectrometer with a resolution of ~1.9%. The tantalum target was bombarded with fast protons for 15-20 min. The separation of the fraction was carried out 2 hours after bombardment. Measurement of the spectrum began about 1 hour after separation of the fraction.

The sources were prepared by preliminary evaporation of dysprosium lactate with subsequent transfer of the activity onto an aluminum foil by means of a weak acetic acid solution. This procedure allows of preparing thin sources and substantially shortens the preparation time, which is important in working with short-lived isotopes. We used sources in the form of a circular spot 3 mm in diameter. The counter window transmitted $\geqslant 20$ kev electrons.

2. Composition of the source

According to the data in the literature[1,2], there exist the following neutron-deficient dysprosium isotopes with a period greater than 1 hour:

$$Dy^{159} \xrightarrow[140\ d]{EC} Tb^{159}$$

$$Dy^{157} \xrightarrow[8.2\ hr]{EC} Tb^{157} \xrightarrow{EC} Gd^{157}$$

$$Dy^{155} \xrightarrow[10.5\ hr]{EC} Tb^{155} \xrightarrow[5.6\ d]{EC} Gd^{155}$$

$$Dy^{154} \xrightarrow[13\ hr]{\alpha} Gd^{150}$$

$$Dy^{153} \xrightarrow[5\ hr]{\alpha} Gd^{150}$$

$$Dy^{152} \xrightarrow[2.3\ hr]{\alpha} Gd^{148}$$

In working with our sources we observed radiation from Dy^{152}, Dy^{153}, Dy^{155} and Dy^{157}; no radiation from Dy^{154} and Dy^{159} was observed.

Initially, we studied the conversion electron spectrum continuously over a period of ~30 hours. Then, to follow the decay of the terbium daughter isotopes, we observed the same part of the spectrum every 24 hours for as long as the activity permitted good detection.

In the spectrum of the dysprosium fraction we observed lines the intensities of which fell off with the following periods: ~6 hr, 8-11 hr, ~20 hr and several days (more precise determination of the decay period of these lines of the longer-lived isotopes was impossible owing to the low level of activity of the source). In addition, we noted that the intensity of a number of lines at first increased with a period of 2.5 hours and then decreased with a period of ~20 hours.

On the basis of the data in the literature we attributed the 8-11 hr activity to Dy^{155} and Dy^{157}, and the longer periods to terbium daughter activities. The assignments for the ~6 hr, ~2.5 hr and 20 hr periods will be discussed below.

3. Dy^{157} and Dy^{155}

The conversion electron spectra of Dy^{157} and Dy^{155} were investigated by Mihelich, Harmatz & Handley[3] and Toth & Rasmussen[4].

There are many conversion lines in the spectra of these isotopes in the region below 300 kev. This together with the relatively low resolution of our instrument greatly hampered analysis of the experimental spectra. In this energy region we could not in a number of cases differentiate on the basis of the decay period between the lines of 8 hr Dy^{157} and 10 hr Dy^{155} and the lines of ~5 hr Dy^{153}.

In the spectra of our sources we clearly discerned conversion lines of the 227 and 271.4 kev transitions in Dy^{155} (Ref.4) and the 326 kev transition in Dy^{157} (Ref.3). Also clearly discernible were the conversion lines of a γ-transition with an energy of 82 kev. A transition with a close energy - 82.9 kev - was detected by Mihelich et al[3] in the spectrum of Dy^{157}. However, the relative intensity of the conversion lines associated with the 82 and 326 kev transitions according to our measurements is appreciably higher than the intensity according to the measurements of Mihelich et al. Thus according to our data L-82:M-82:K--326 = 270:100:100, whereas according to Mihelich et al L-82.9:M-82.9LK-326.6 = = 15:4:100.

In view of this it may be asserted that a major part of the intensity of the L-82 and M-82 conversion lines arises in the decay of some other isotope (not Dy^{157}). We are inclined to assign this line to the decay of Dy^{153} in the Dy^{157} source used by Mihelich et al).

The daughter nuclide forming in the decay of Dy^{155} is Tb^{155}, the spectrum of which has been thoroughly studied[5,3]. The lines appearing in the decay of Tb^{155} (T = 5.6 days) to Gd^{155}, and associated with transitions of 87, 101, 105, 148, 162, 180 and 263 kev energy, were evinced in the spectrum of our source some 50-80 hours after irradiation, i.e., after the lines due to the decay of the dysprosium isotope had faded.

The dysprosium isotope with mass number 154 was discovered by Toth & Rasmussen[6], who found that it is an α-emitter and has a period of 13 hours. According to Cameron's tables, the mass difference between Dy^{154} and neighboring Tb^{154} is 529 kev. Electron capture by Dy^{154} with the formation of Tb^{154} as the daughter nucleus is energetically possible. In the spectrum of our source, however, we observed no lines that could be assigned to Dy^{154} or lines of Tb^{154}, the spectrum of which is known from two independent studies[3,5].

4. Dy^{153}

The existence of the isotope Dy^{153} with a period of 5 ± 0.5 hours was established by Toth & Rasmussen[6] by observation of α-decay.

The mass spectrometric experiments of Dobronravova et al[7] showed that Dy^{153} is present in the products of spallation of tantalum. In this investigation it was found by means of a scintillation spectrometer that γ-rays of ~80 kev energy are emitted in the decay of Dy^{153}. As noted above, we observed in the conversion spectrum of our source a group of lines the intensity of which fell off with a period of ~6 hr. In the spectrum of the source some 50-60 hours after separation, when the lines of the short-lived dysprosium isotopes had disappeared, there were clearly evinced conversion lines associated with the 41.5, 109, 212 and 250 kev γ-transitions in Tb^{153}, the spectrum of which is well known[3,5]. Thus there can be no doubt that Dy^{153} was present in our sources.

In Table 1 we have listed the energies, relative intensities and evaluated

Table 1

Conversion electrons of Dy^{153}

E_{e^-}, kev	E_γ, kev	T, hr	Relative intensity (exp.)	Identification
28,8	80,8	7±2		*K*-81
47,4	99,4	7,5±1,0	200±60	*K*-99
72,8	81,1	8,5±1,5	200±60	*L*-81
79,9	81,9	8,5±1,5	70±20	*M*-81
90,7	99,4	8±2	50±15	*L*-99
95,7	97,7	8±2	40±10	*M*-99 & *K*-147?
138,4	147	6±1	25±6	*L*-147?
191,9	244	6±1	40±6	*K*-244
203,1	255	5±1	100	*K*-255
237,4	245	6±2	4±2	*L*-244
246,8	255	6±1	13±3	*L*-255

periods of the conversion lines that we feel justified in assigning to the decay of Dy^{153}.

The 99.4 kev γ-transition was observed earlier in the dysprosium fraction from the spallation of tantalum by Dzhelepov et al[8], and was tentatively attributed to Dy^{155} or Dy^{157}. However, no transition of this energy was observed in the investigations of Mihelich et al[3] and Toth & Rasmussen[4] devoted to these isotopes. Hence we feel justified in attributing this 99.4 kev transition to the decay of Dy^{153}. Our anomalously high value for the half-life can readily be explained: the spectrum of our source was extremely rich in conversion lines in this region, while the resolution of our instrument was relatively low.

We identified the 138.4 kev conversion line as the L-147 line on the basis of the data of Zvol'skii[9], who observed a transition of this energy in the dysprosium fraction; the K line of this transition is superposed on the M line of the 99.4 kev transition.

We observed no other intense conversion lines with a period close to 6 hours in the energy interval from 20 to 1100 kev.

$$5.\ Dy^{152} \xrightarrow[2.5\ hr]{EC} Tb^{152} \xrightarrow[20\ hr]{EC} Gd^{152}$$

Prior to 1959 only one neutron deficient isotope with mass number 152 was known, namely, Dy^{152} (2.3 hr), which was discovered in a survey for α-activity by Rasmussen, Thompson & Ghiorso[10].

As noted above, in studying the conversion electron spectrum of our dysprosium fraction we observed that the intensity of a number of lines at first increased with a period of 2-2.5 hours and then fell off with a period of 19-20 hours. A typical intensity vs time curve for one of these lines is shown in Fig.1.

The fact that among these lines there proved to be lines associated with the 344 kev transition, which was observed earlier in β^--decay of Eu^{152} (Refs.11 & 12), and the fact that the build-up period of these lines agrees with the decay period of Dy^{152} gives reason to infer that we are dealing here with the conversion lines of transitions involved in the chain

$$Dy^{152} \xrightarrow[2.5\ hr]{EC} Tb^{152} \xrightarrow[20\ hr]{EC} Gd^{152}.$$

This establishes the existence of electron capture in Dy^{152} with the formation of Tb^{152} as the daughter nucleus. We did not observe any conversion lines appearing in the decay of Dy^{152} (T = 2.3 hr). In July 1959, Toth, Faler & Ras-

Table 2

Conversion electrons of Tb^{152}

E_{e^-}	E_γ	Relative intensity (exp.)	Identification
293,7	344	100	*K*-344*
336,2	344	30±3	*L*-344*
362	412	4±2	*K*-412
382	432	23±5	*K*-432*
404	412	very weak	*L*-412
425	433	4±2	*L*-432
536	586	8±2	*K*-586*
565	615	40±5	*K*-615*
609	617	7±2	*L*-615
1000	1050	very weak	*K*-1050?

---

*Growth and decay curves were recorded for these lines.

mussen[13] reported their discovery of a new terbium isotope, Tb^{152} ($T = 18.5 \pm 0.3$ hr; $E_\gamma = 344$ kev).

Thus it has now been reliably established that there exist three terbium isotopes with half-lives of about 18 hours: Tb^{151}, Tb^{152} and Tb^{154}. The terbium isotope with mass number 151 was not present in our source owing to the short decay period of the parent Dy^{151} ($T = 19$ min, according to Toth & Rasmussen[6]).

In view of this we feel justified in assuming that all the observed conversion lines with $T \approx 20$ hr can be assigned to the decay of Tb^{152}. The energies and relative intensities of these lines are listed in Table 2. The conversion electron spectrum of Tb^{152} is shown in Fig.2.

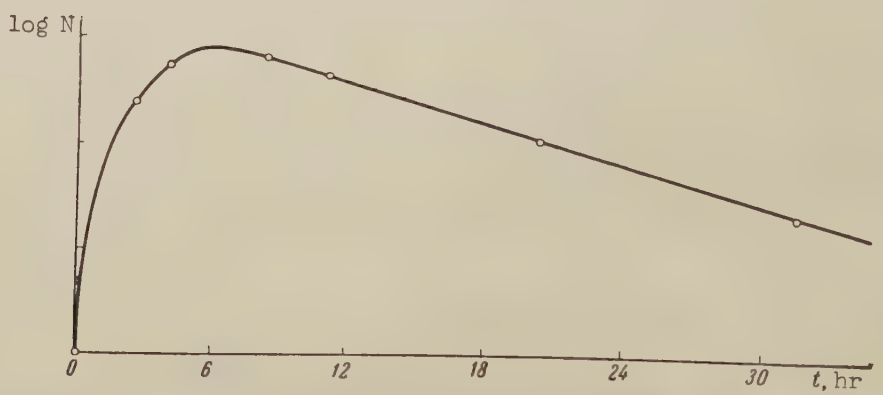

Fig.1. Typical intensity vs time curve for a number of conversion lines.

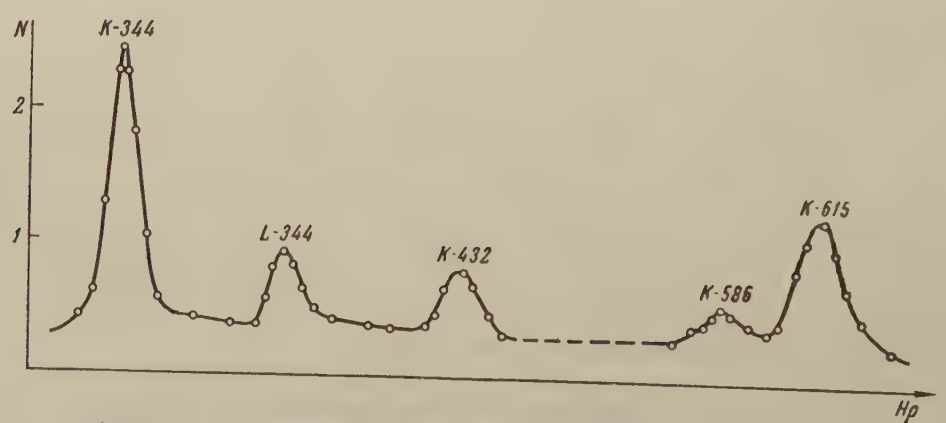

Fig.2. Conversion electron spectrum of Tb^{152}.

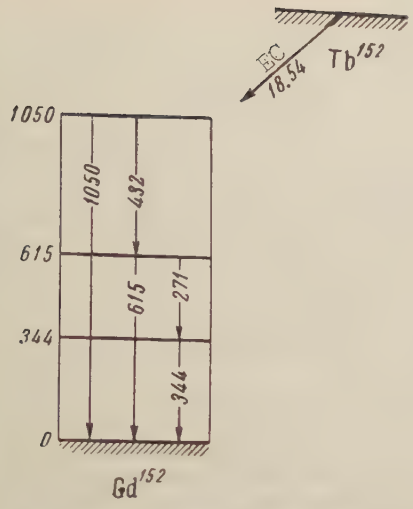

Fig.3. Decay scheme for Tb^{152}.

The 615 and 432 kev γ-transitions cannot be in cascade with the 344 kev transition from the first excited level to the ground state, inasmuch as the relative intensities of these transitions proved to be too high for any reasonable multiple order assignments (from E1 to M3).

A tentative decay scheme for Tb^{152} is shown in Fig.3. If we hypothesize a level at 615 kev, we should expect to observe a transition of 271 kev energy to the 344 kev level of Gd^{152}. No such transition has been observed in the decay of Eu^{152}, but a transition of this energy was detected by Anton'eva et al[5] in the spectrum of the terbium fraction (possibly the same γ-rays were observed by Toth, Faler and Rasmussen[13], who evaluated their energy as 265 kev). We were unable to observe lines associated with the 271 kev transition (if it exists) inasmuch as at the same energy there is an intense line of Dy^{155}.

We observed conversion electrons of very low intensity from a transition of 1050 kev energy. Unfortunately, we were unable to evaluate the decay period of the K line more accurately than ~1 day. Anton'eva et al report a period of 18 hours for this transition. If one introduces a level at 1050 kev in Gd^{152}, the 432 kev transition can readily be accomodated in the decay scheme.

In the energy range from 400 to 1100 kev we detected a large number of very weak electron lines (E_{e^-} = 433, 448, 455, 492, 532, 543, 570, 652, 664, 765, 780, 953, 864, 873, 894, 927, 950 and 1050 kev), for which we cannot give a reasonable close evaluation of the periods. Some of these lines (432.1 and 455.9 kev), according to the data of Toth & Rasmussen[4], may be assigned to the decay of Dy^{155} or Dy^{157}, but the origin of most of these lines is still unclear, and their assignments must await further investigation.

We desire to express our gratitude to V.A.Morozov and G.A.Mironov for assistance in carrying out the measurements and I.A.Yutlandov and V.A.Khalkin for carrying out the chemical separations.

Scientific Research Physical Institute at
"A.A.Zhdanov" Leningrad State University,
&
Joint Institute for Nuclear Research

Note added in proof: Invoking the new data reported by Abdurazakov et al[14] and Bonch-Osmolovskaya et al[15] one can adduce additional arguments in favor of the proposed decay scheme for Tb^{152}. Abdurazakov et al showed that the radiation of the dysprosium fraction comprises γ-rays of 272.0 kev energy, which may be attributed to Tb^{152}. The corresponding γ-transition is located between the 615 and 344 kev levels in the decay scheme (Fig.3). Bonch-Osmolovskaya et al in investigating the β^+-spectrum of Tb^{152} discovered components with end-point energies 1.65 and 2.7 Mev, the difference between which corresponds to the energy of the hypothesized 1050 kev level.

References

1. B.S.Dzhelepov & L.K.Peker, Skhemy raspada radioaktivnykh yader (Decay schemes of radioactive nuclei), M.-L., 1958.

2. D.Strominger, J.M.Hollander & G.T.Seaborg, Table of Isotopes, Revs.Mod. Phys., 30, 585 (1958).

3. J.W.Mihelich, B.Harmatz & T.H.Handley, Phys.Rev., 108, 989 (1957).

4. K.S.Toth & J.O.Rasmussen, Ibid., 115, 150 (1959).

5. N.M.Anton'eva, A.A.Bashilov, B.S.Dzhelepov & B.K.Preobrazhenskii, Doklady AN SSSR, 119, 241 (1958). (Trans.Soviet Physics - Doklady.)

6. K.S.Toth & J.O.Rasmussen, Phys.Rev., 109, 121 (1958).

7. A.N.Dobronravova, L.M.Kruzhanskii, A.N.Murin & V.N.Pokrovskii, Izv.AN SSSR, Ser.fiz., 22, 815 (1958). (Trans.Bulletin, 22, 809.)

8. B.S.Dzhelepov, B.K.Preobrazhenskii, I.N.Rogachev & P.A.Tishkin, Ibid., 22, 126 (1958). (Trans.Bulletin, 22, 125.)

9. I.Zvol'skii, Spektr konversionnykh elektronov disprozievoi fraktsii. (Conversion electron spectrum of a dysprosium fraction) Program of the Tenth All-Union Conference on Nuclear Spectroscopy, M.-L., 1960.

10. J.O.Rasmussen, S.G.Thompson & A.Ghiorso, Phys.Rev., 89, 33 (1953).

11. B.S.Dzhelepov, V.G.Nedovesov, N.N.Zhukovskii & G.E.Shukin, Izv.AN SSSR, Ser.fiz., 21, 966 (1957). (Trans.Bulletin, 21, 968.)

12. B.V.Bobykin & K.M.Novik, Ibid., 21, 1556 (1957). (Trans.Bulletin, 21, 1546.)

13. K.S.Toth, K.T.Faler & J.O.Rasmussen, Phys.Rev., 115, 158 (1959).

14. A.A.Abdurazakov, K.Ya.Gromov, and others, Izv.AN SSSR, Ser.fiz., 24, 278 (1960). (Trans.Bulletin, 24, 266.)

15. N.N.Bonch-Osmolovskaya, B.S.Dzhelepov & O.E.Kraft, Ibid., 24, 283 (1960). (Trans.Bulletin, 24, 270.)

ON THE 106 kev TRANSITION IN Tm^{167}

- A.S.Basina & V.A.Morozov

We felt it would be of interest, using the recent data of Harmatz, Handley & Mihelich[1] on the multipole order of the transitions in Tm^{167}, to determine experimentally the intensity of the transitions in percent per disintegration. Specifically, we carried out such a determination for the 106 kev transition (E2 + + M1) from the 5/2+ to the 3/2+ level. The lutetium fraction separated chromatographically from the rare earth products of spallation of tantalum was subjected to a second separation to isolate the daughter ytterbium.

The conversion electron spectrum of the source obtained in this manner was investigated on a magnetic lens β-spectrometer with a resolution of 1.9%. The counter window passed $\geqslant$ 20 kev electrons.

The second separation was carried out one hour after the initial separation of the lutetium fraction (i.e., three hours after proton bombardment of the tantalum target). Hence our source contained primarily Yb^{167} (T = 19 ± 0.5 min according to our measurements) formed in the decay of Lu^{167} (T = 55 min according to Aron et al[2]).

The conversion spectrum of Yb^{167} comprises an intense L line associated with the 106 kev transition.[3]

We measured the relative intensities of the Yb^{167} L-106 and Tm^{167} K-208 lines. Using the data furnished by K.Ya.Gromov regarding the 208 kev transition in Er^{167} (29% per disintegration) we calculated the intensity in percent per disintegration for the 106 kev transition in Yb^{167}. The calculations were carried out on the assumption that this transition is pure M1 and yielded a value of ~59%.

It may be noted that the intensity of the analogous 109 kev transition (5/2+→3/2+) in Tm^{169}, the level scheme[5] for which is similar to that for Tm^{167}, amounts to 58% per disintegration.

We are sincerely grateful to K.Ya.Gromov for making available the decay data and to I.A.Yutlandov and B.A.Khalkin for the chemical part of the work.

"V.G.Khlopin" Radium Institute,
Academy of Sciences of the USSR

References

1. B.Harmatz, T.H.Handley & J.W.Mihelich, Phys.Rev., 114, 1082 (1959).

2. P.M.Aron, A.V.Kalyamin, A.N.Murin & V.A.Yakovlev, Izv.AN SSSR, Ser.fiz., 22, 817 (1958). (Trans.Bulletin, 22, 811.)

3. A.S.Basina, B.S.Dzhelepov & A.M.Chikhladze, Present issue of the Bulletin, p.810.

4. K.Ya.Gromov, B.S.Dzhelepov & B.K.Preobrazhenskii, Izv.AN SSSR, Ser.fiz., 21, 918 (1957).

5. K.Ya.Gromov, B.S.Dzhelepov & B.K.Preobrazhenskii, Ibid., 22, 775 (1958). (Trans.Bulletin, 22, 770.)

THE (n,2n) AND (γ,n) REACTIONS ON Au^{197}

- M.A.Bak, K.A.Petrzhak & Chen' Tya-Mei

Reactions of the (n,2n) and (γ,n) type are distinguished by the fact that in both the same initial nucleus is converted to the same next lighter isotope. We felt it would be of interest to investigate these reactions in cases when the neutron and γ-energies are close. Hence we undertook an investigation of the interaction of neutrons having an energy of ~14 Mev and γ-rays of the continuous spectrum having an end-point energy close to ~14 Mev with Au^{197} nuclei. It can be shown that at the indicated neutron and gamma energies in the case of Au^{197} there occur only the (n,2n) and (γ,n) reactions, respectively. The cross section for the (n,2n) reaction at the given neutron energy was found to be approximately 1800 ± 500 mb (Ref.1), while the cross section for the (γ,n) reaction at E_γ = 17.5 Mev is 460 ± 50 mb (Ref.2). The product of both reactions is Au^{196}.

McMillan et al[3] bombarded gold with fast neutrons from a (Li + D) source and detected two activities with period of 13.0 hr and 5.5 days. Similar results were obtained by Wilkinson[4,5], who gives the short period as 14.0 ± 0.3 hr. The appearance of activities with two periods in this case is due to the Au^{197}(n,2n)-Au^{196} reaction, and hence the above mentioned authors hypothesize the existence of an isomeric state. Further work in this direction, however, was not undertaken inasmuch as in a number of investigations in which the reaction product was Au^{196} no activity with the short period was detected. As for the photoneutron reaction, it was found that in the case of irradiation of Au^{197} with ~17 Mev γ-rays from the (Li + p) reaction there resulted only the activity with the long (5.5 day) period.

It will be apparent therefore that the nature of the short period activity in the decay of Au^{196} has not yet been clarified. It is interesting to note that Seaborg in his "Table of Isotopes" included an isomeric state of this nucleus with a period of 14 hours, while in the tables compiled by Dzhelepov & Peker this isomeric state is omitted.

In the present experiments the ~14 Mev neutrons were obtained from a H^3(d,n)He^4 type neutron generator, and the γ-rays from a betatron with a tungsten target. The gold targets were foils 14 mm in diameter with a superficial density of 12-14 mg/cm^2. In the neutron bombardment experiments particular attention was paid to shielding the target against slow neutrons. This shielding was realized by a 12 mm thick layer of boron carbide (superficial density - 1.4 g/cm^2) and a 1 mm thick layer of cadmium. This shielding insured virtually complete elimination of thermal and resonance neutrons at the location of the gold target, as is proved by the fact that there was no noticeable activity with a period of 2.7 days due to the (n,γ) reaction on the Au^{197}.

After irradiation or bombardment the gold targets were mounted at a distance of 1.5 cm from the end window of a BFL-25 counter. The duration of each counting period was chosen so that the statistical uncertainty would not exceed 1-2%. The measurements were carried out under the same conditions periodically for 10 to 15 days.

Investigation of the β-activity of the Au^{197} samples showed that in the case of neutron bombardment there form activities falling off with two periods, namely, a short period of 9.7 ± 0.3 hours and a long period of 5.6 ± 0.1 days, while in the case of γ-irradiation there is formed only the long period activity. Possibly the short period activity might appear in the case of irradiation with higher energy γ-rays.

Experiments with aluminum absorbers yielded a rough evaluation of the upper bound of the beta energy spectrum: $E_\beta \leqslant 250$ kev.

Recently there appeared the report of Van Lieshout et al[6], who also found that Au^{196}, in addition to a period of 5.5 days, exhibits an activity of 10.0 ± ± 0.5 hours if the Au^{197} target is bombarded with neutrons of appropriate energy. Van Lieshout et al, however, do not give a definitive decay scheme for this 10 hr isomer.

We hope in the near future to establish the decay scheme for the Au^{196} isomer by investigating its γ-spectrum.

"V.G.Khlopin" Radium Institute,
Academy of Sciences of the USSR

References

1. E.B.Paul & R.L.Clarke, Canad.J.Phys., 31, 267 (1953).
2. H.Wäffler & O.Hirzel, Helv.Phys.Acta, 21, 200 (1948).
3. E.McMillan, M.Karen & S.Ruben, Phys.Rev., 52, 375 (1937).
4. G.Wilkinson, Phys. Rev., 73, 252 (1948).
5. G.Wilkinson, Phys.Rev., 75, 1019 (1949).
6. R.Van Lieshout, R.K.Girgis, R.A.Ricci, A.H.Wapsta & C.Ythier, Physica, 25, 8, 703 (1959).

ROTATIONAL ENERGY OF EVEN-EVEN AND ODD NUCLEI

- A.S.Davydov

Introduction

In a report[1] presented at the Ninth All-Union Conference on Nuclear Spectroscopy we gave a review of investigations devoted to rotational states of even-even nuclei. It was shown that the hypothesis regarding the nonaxial shape of atomic nuclei, developed in the work of Davydov & Filippov[2] and Davydov & Rostovskii[3], makes it possible to identify a number of low-lying states in even-even nuclei as rotational excited states even in case of violation of the interval rule 1:3.3:7:12:...., which has long been regarded as a necessary condition for classification of excited states as rotational ones.

Rotation of axially symmetric nuclei is possible only about an axis perpendicular to the nuclear symmetry axis. Such rotation is associated (in the adiabatic approximation) with one value of the moment of inertia of the nucleus. In even-even nuclei excited states corresponding to the first rotational band are characterized by the sequence of even quantum numbers $J = 0, 2, 4, \ldots$, defining the square of the angular momentum of the nucleus, and the quantum number $K = 0$, the projection of the total angular momentum on the nuclear symmetry axis. In addition, there may exist other rotational bands corresponding to the same character of rotation with different internal excitations of the nucleus. In particular, there was considered the band corresponding to γ-oscillations with $K = 2$. In excitations corresponding to γ-oscillations the root mean square deviation from axial symmetry is nonzero, i.e., $\bar{\gamma}^2 \neq 0$. Consequently, the presence of γ-oscillations (even oscillations corresponding to zero energy) automatically leads to the possibility of rotation of the nucleus about the symmetry axis with a moment of inertia differing from zero.

If we proceed from the assumption that the shape of the nucleus need not necessarily be axially symmetrical, the rotational excitations will correspond not to one but in general to three principal moments of inertia of the nucleus. The character of rotation of the nucleus becomes more complicated, and accordingly, the spectrum of the rotational states becomes richer even without taking into account internal excitations.

The theory of nonaxial nuclei developed in Refs.2 & 3 was based on the following three simplifying assumptions:

a) The internal state of the nucleus does not change incident to its rotation,

b) The three principal moments of inertia of the nucleus depend on a parameter determining the deviation of the nucleus from axial symmetry by means of the equations

$$I_i = A \sin^2\left(\gamma - \frac{2\pi}{3} i\right), \qquad i = 1, 2, 3. \tag{1}$$

c) In calculating the probability for electromagnetic transitions between rotational states it was assumed that the electric charge is uniformly distributed over the nuclear volume.

With these three simplifications the theory of rotational states of nonaxial even-even nuclei leads to simple results that can readily be compared with experiment. It was found that the first excited state always has spin 2. The spin sequence of the other excited states and the ratio of their energies to the energy of the first excited state is a unique function,

$$\xi = \frac{E_2(2)}{E_1(2)},$$

i.e., the ratio of the energy of the second excited state with spin 2 to the energy of the first excited state with the same spin.

The sequence of spins and energies of the rotational states of nonaxial nuclei is illustrated in Fig.1, in which these quantities are plotted as functions of the nonaxiality parameter γ. The relative probabilities for electromagnetic transitions between all rotational states are unique functions of the same parameter.

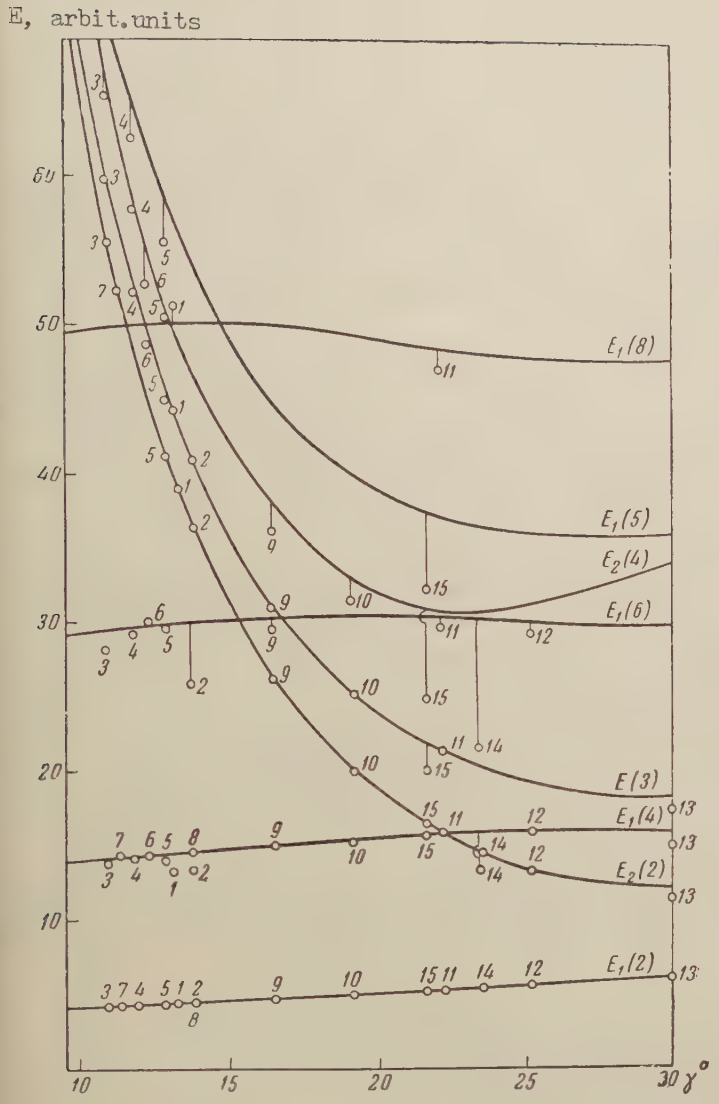

Fig.1. Variation of the energy of rotational states of even-even nuclei with the nonaxiality parameter γ. The points give the experimental values for the nuclei: 1) Sm^{152}, 2) Gd^{154}, 3) Gd^{156}, 4) Dy^{160}, 5) Er^{166}, 6) Er^{168}, 7) W^{182}, 8) W^{184}, 9) Os^{186}, 10) Os^{188}, 11) Os^{190}, 12) Os^{192}, 13) Pt^{192}, 14) Hg^{198}, 15) Mg^{24}.

I. Comparison of the results of the theory of rotational states of nonaxial nuclei with experiment

Since the publication in 1958 of Refs.2 & 3 there have appeared here and abroad a number of studies devoted to comparison of the results of the theory of rotational states of nonaxial nuclei with experimental data; there have also been attempts to develop this theory further. In the present section we shall review the results of such comparisons.

1. The Canadian physicists King & Johns[4] investigated the excited states of four osmium isotopes. They compared their results with the deductions from the theory of nonaxial nuclei[2,3] and with the inferences from earlier theories. Identifying the second excited state with spin 2 with γ-oscillations, these authors come to the conclusion that osmium nuclei have a low stability as regards change in shape, i.e., are "soft" nuclei. In connection with this they question the possibility of utilizing the concept of a stable nuclear shape.*

Despite this deduction, King & Johns conclude that the theory of Davydov &

---

*It must be noted that the theory of rotational states of nonaxial nuclei is not based on the assumption of a "rigid" nuclear shape as regards variation of γ. It is sufficient that the root mean square deviation $\overline{\gamma^2}$ be different from zero and not change appreciably incident to rotation of the nucleus.

Filippov is very attractive inasmuch as it leads to numerical prediction of the relative location of levels and transition probabilities for these nuclei. In contrast, the theory of Bohr & Mottelson, which utilizes β- and γ-oscillations, leads only to order of magnitude evaluations, so that it can jestingly be called the "soft" theory for "soft" nuclei.

2. In their work DeMille et al[5] repeated the calculations for the location of the rotational states having spins 2, 6 and 8. Their results agreed with those given in Ref.3. Further, DeMille et al compared the results of theory with the available experimental data and came to the conclusion that "the theory of Davydov & Filippov successfully explains a large number of nuclear energy levels. However, it cannot predict all the low-lying excited levels inasmuch as there exist other 0+ and 2+ levels, the presence of which is not connected with rotation of the asymmetrical solid."

3. The American physicists Malman & Kerman (Argonne National Laboratory, preprint, 1959) also carried out a comparison of the results of the theory of rotational states of nonaxial nuclei with experimental data. On the basis of this comparison, Malman & Kerman come to the conclusion that "the theory of an asymmetrical top agrees with the experimental data for a wider region of nuclei than the theory of a symmetrical top. In its present state, however, it does not fully explain the low-lying energy levels of even states with $E_1(4)/E_1(2) < 2.67$." These authors propose the following approximate formula for a correction to the position of the energy levels taking into account the interaction of the rotation with oscillations of the nuclear surface:

$$E_i(J) = E_i^0(J) - b\{E_i^0(J)\}^2, \qquad (2)$$

where $E_i^0(J)$ is the energy of the level with spin J in the adiabatic approximation. The authors note that the introduction of this correction improves the agreement of theory with experiment. By way of example, they give a comparison of the experimental values of the ratio of the energy of excited states of Os^{190} to the energy of the first excited state with the corresponding deductions from the theory of nonaxial nuclei and the theory of axial nuclei. This comparison is reproduced in the following table.

Values of the energy level ratio $\frac{E_i(J)}{E_1(2)}$ for Os^{190}

State		Experimental data	Theoretical data	
Spin & parity	Level No.		Nonaxial nuclei	Axial nuclei
2+	2	2,99	2,98	—
4+	1	2,94	2,96	3,05
6+	1	5,61	5,60	5,44
8+	1	8,90	8,89	7,11

4. Van Patter[6] carried out an extensive comparison of the experimental data with the theory of nonaxial nuclei as regards the probabilities for electric quadrupole transitions between rotational states. Fig.2, taken from the work of Van Patter, shows the theoretical curve for the ratio of the reduced probabilities of E2 transitions $\frac{B(E2;\ 2' \to 2)}{B(E2;\ 2' \to 0)}$ between two levels of spin 2 and directly from the second excited level to the ground state. The points in the figure give the experimental ratios for 45 nuclei. It must be borne in mind that there is a certain ambiguity in calculating the experimental ratios owing to the admixture of magnetic dipole 2'→2 transitions, which in a number of cases can only be evaluated

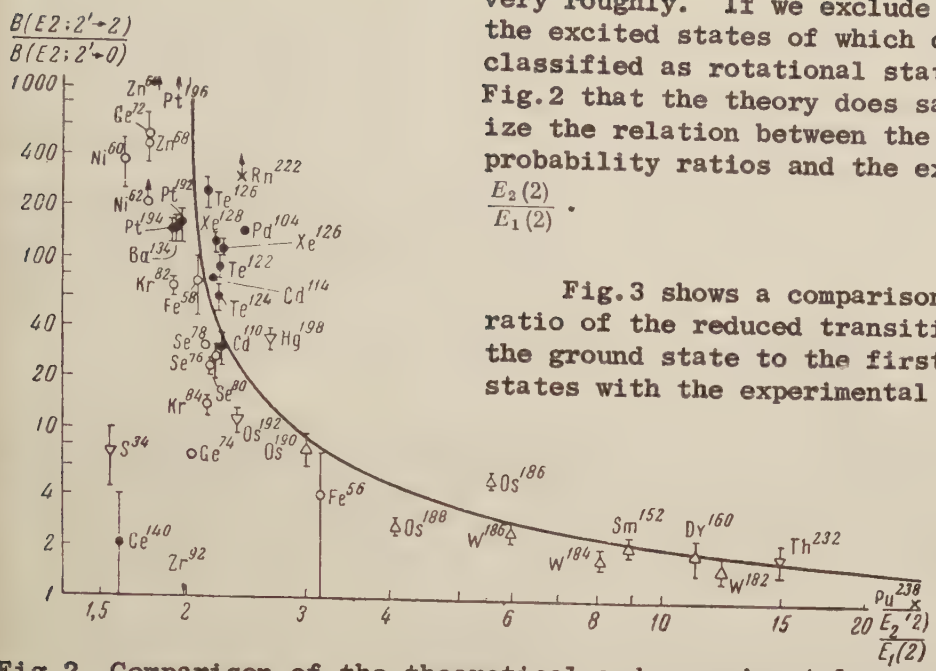

Fig.2. Comparison of the theoretical and experimental ratios of the reduced probabilities for E2 transitions between the two spin 2 levels and the second excited level in the ground state (2'→2 and 2'→0). The curve is calculated according to the theory of Davydov & Filippov.

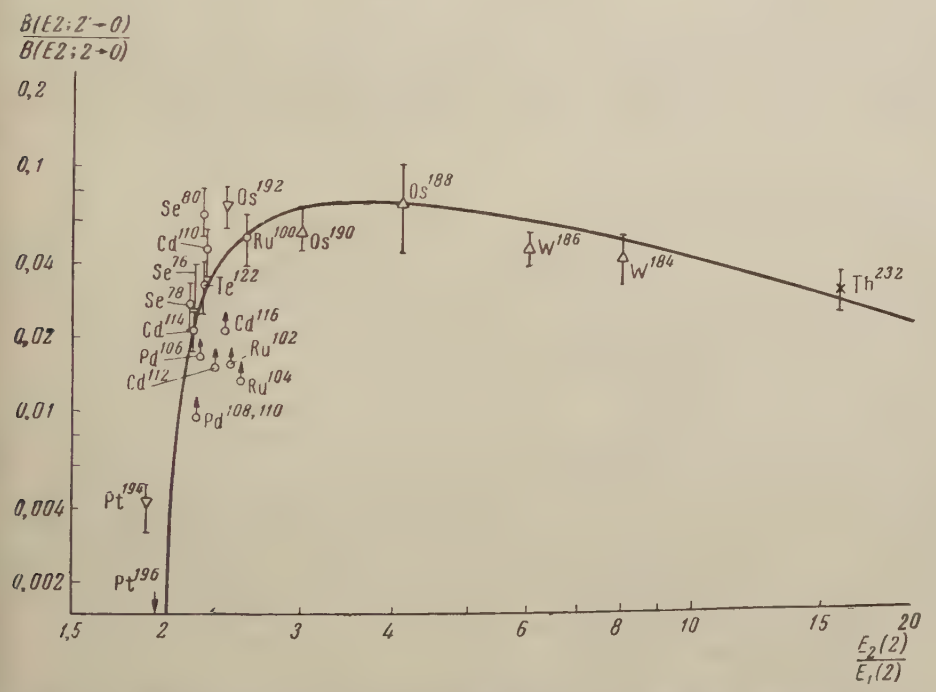

Fig.3. Comparison of the theoretical and experimental ratios of the reduced probabilities for E2 0→2' and 0→2 transitions. Curve based on the theory of Davydov & Filippov.

very roughly. If we exclude S^{34}, Ce^{140} and Zr^{92}, the excited states of which cannot be definitively classified as rotational states, it follows from Fig.2 that the theory does satisfactorily characterize the relation between the indicated transition probability ratios and the experimental ratios $\frac{E_2(2)}{E_1(2)}$.

Fig.3 shows a comparison of the theoretical ratio of the reduced transition probabilities from the ground state to the first two excited spin 2 states with the experimental values obtained for 20 nuclei from Coulomb excitation data (work of Barloutaud and his co-workers and Stelson & McGowan). Van Patter makes the following comment regarding this figure: "The agreement with the theory of Davydov & Filippov is really surprising particularly because no other theory yields quantitative values for this ratio."

5. An extensive comparison of the results of the theory of nonaxial nuclei with the experimental data was carried out by the Leningrad physicists Grigor'ev & Avotina[7]. The curve in Fig.1, which was taken from their work, shows the variation of the energy of the rotational levels with the nonaxiality parameter in the range $\gamma = 10$ to 30°. The points in the figure give the experimental values of the ratio of the energy levels and of their deviation from the theoretical curves

for 15 nuclei. It will be evident from this figure that the greatest deviation of the experimental values from the theoretical ones is observed for Mg^{24}, Gd^{154} and Hg^{198}. The deviation increases with increase of the rotational moment of the excited state of the nucleus. Grigor'ev & Avotina note that the corrections to the energy levels are poorly described by the term $-bJ^2(J+1)^2$, which is usually used in the theory of axial nuclei. They note further that fulfillment of the equality $\varepsilon(3) = \varepsilon_1(2) + \varepsilon_2(2)$, following from the adiabatic theory of nonaxial nuclei, cannot be regarded as a good criterion for applicability of the adiabatic approximation.

II. Further development of the theory of rotational states of nonaxial even-even nuclei

The above results of comparison of the experimental data with the theory of rotational states of nonaxial nuclei based on the simplifying assumptions set forth in the introduction show that in general the theory correctly describes the experimentally observed relationships. Upon more detailed comparison, however, it becomes evident that the agreement is not complete. The greatest deviations of the experimental data from the theoretical values are observed for nuclei in which the energy ratio $\frac{E_2(2)}{E_1(2)} < 3$. To discover the reasons for these divergences one must first elucidate how the results of the simple theory of rotational states of nonaxial nuclei will change if one renounces the above mentioned simplifications.

We first turned to investigations of the role of the choice of the explicit dependence of the principal moments of inertia on the parameters defining the nuclear shape. In view of the fact that the experimental values of the moments of inertia of nuclei occupy an intermediate position between the moments of inertia of a solid and the moments of inertia of the hydrodynamic model, MacDonald (Harwell preprint 1959) proposed the following expression for describing the moments of inertia of nuclei:

$$I_i = I_i^H \left[\left(\frac{I_i^H}{I_i^R} \right)^{1/2} + p \right]^{-2}, \qquad i = 1, 2, 3, \tag{3}$$

where the I_i^R are the moments of inertia of a solid ellipsoid, the I_i^H are the moments of inertia agreeing with (1) for $A = 4B\beta^2$, and p is a new parameter which is taken equal to 0.1 or 0.2. Equation (3) has the attribute that in the limit as $p \to 0$, $I_i \to I_i^R$. For $p \neq 0$ and as $\gamma \to 0$, the moment of inertia $I_3 \to 0$. For $p \neq 0$ and as $\beta \to 0$ all $I_i \to 0$.

Eq. (3) may be regarded as an empirical formula taking into account the deviation of the nuclear moments of inertia from their values given by the hydrodynamic model. MacDonald in his work investigated only rotational states having spin 2. In this case, as was shown in Ref. 8, one cannot establish which corrections are more significant: those for the nonadiabatic conditions or those for deviation of the moments of inertia from their hydrodynamic values. Hence, MacDonald's attempts to restrict the corrections only to choice of the value of the parameter p cannot be regarded as justified (see below).

Davydov, Rabotnov & Chaban[8] investigated rotational states of a nonaxial nucleus with three arbitrary principal moments of inertia. It was shown that if one expresses the energy of all the rotational states in dimensionless units $\varepsilon(J) = \frac{E(J)}{E_1(2)}$, where $E_1(2)$ is the energy of the first excited state, the energy of

rotational states with spins 3 and 5 will be directly determinable from the experimental ratio $\xi = \frac{E_2(2)}{E_1(2)}$ by means of the formulas

$$\varepsilon(3) = 1 + \xi, \quad \varepsilon_1(5) = 4 + \xi, \quad \varepsilon_2(5) = 1 + 4\xi$$

regardless of the specific values of the nuclear moments of inertia. The energy of rotational states with other spin values proves to depend not only on the parameter ξ, but also on another parameter η, which can vary in intervals defined in terms of ξ by means of the inequalities

$$\left.\begin{aligned} \xi^2(3-\xi) \leqslant 54\eta \leqslant 3\xi - 1, \quad \text{if} \quad 1 \leqslant \xi \leqslant 3, \\ 0 \leqslant 54\eta \leqslant 3\xi - 1, \quad \text{if} \quad \xi \geqslant 3. \end{aligned}\right\} \qquad (4)$$

The actual value of the parameter η depends on the motion of the nucleons, which determine the corresponding values of the moments of inertia of the nucleus. In particular, if the moments of inertia are characterized by Eqs.(1), the values of η are given by the expression

$$\eta = \eta_{\text{hyd}} = \frac{\xi^2}{18(1+\xi)}.$$

Fig.4 shows the ξ dependences of the energy ratios $\varepsilon_1(4)$ and $\varepsilon_2(4)$ for different values of η satisfying inequalities (4). The hatched region corresponds to values of η lying between η_{hyd} and η_{MD}, corresponding to moments of inertia determined by means of the MacDonald formula (3) taking $\beta = p = 0.2$.

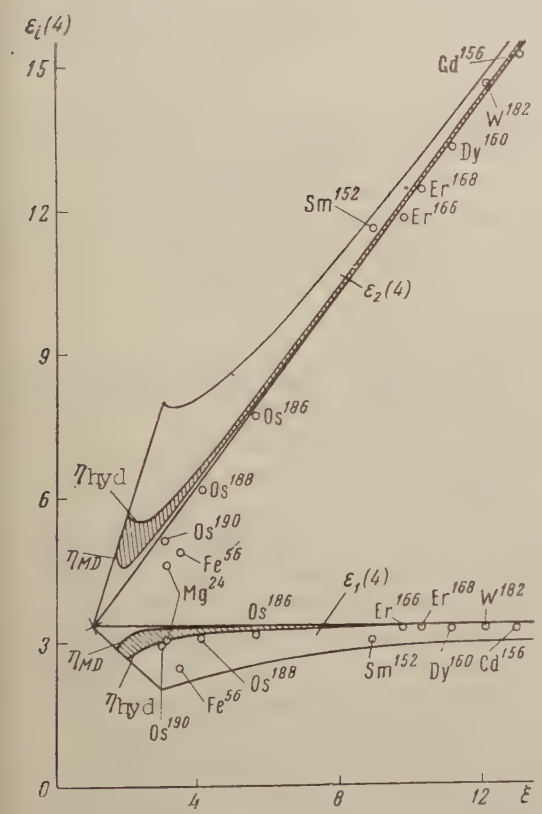

Fig.4. Variation of the energy ratio of two rotational levels with spin 4 with the value of the parameters ξ and η. (MD = value from the MacDonald formula.)

We note that the values of η, satisfying inequalities (4), correspond to all possible relationships between the principal moments of inertia and in particular to relationship which are not realized in a nucleus. For example, the case of rotation of a solid sphere ($I_1 = I_2 = I_3$; $\xi = 1$), is identified by the cross in Fig.4. The same thing may be said of cases for which η is close to zero.

At present it is commonly assumed that nuclear moments of inertia are intermediate between the values deriving from the hydrodynamic model and the model of a solid. The theoretical calculations of Migdal[9] lead to the same conclusion. Hence the actual relationships between nuclear moments of inertia apparently correspond to values of η for which the $\varepsilon_i(J)$ ratios are shifted from the hydrodynamic values in the direction of the regions identified by hatching in Fig.4. Taking this into account, we can readily show that the $\varepsilon_i(J)$ ratios change little with the variation of η allowable for nuclei. The variation of the energy ratio is particularly small for $\xi \geqslant 4$.

Most all the now available experimental ratios $\varepsilon_1(4)$ lie below the possible (in the adiabatic approximation) theoretical values given by the hatched area in Fig.4, while the experimental values of $\varepsilon_2(4)$ lie below the theoretical ratios for all values of η satisfying inequalities (4). This shows that agreement with experiment cannot be improved in going over from the hydrodynamic moments of inertia to the intermediate values (between the hydrodynamic and the solid body model). As will readily be apparent from Fig.4, if we formally choose a relationship between the three principal moments of inertia that is not realized in an actual nucleus but improves the agreement of the experimental values of the ratio $\varepsilon_1(4)$ we at the same time impair the agreement for the ratio $\varepsilon_2(4)$. Thus it can be asserted that the deviation between theory and experiment is due to use of the adiabatic approximation in performing the calculations.

The analysis carried out in Ref.8 gives reason to hope that investigation of the corrections to the adiabatic approximation can be based on the hydrodynamic approximation for the principal moments of inertia of nuclei.

A theory of collective excitations for nonaxial even-even nuclei taking into account the interaction of rotational and vibrational states was developed in the work of Chaban[10]. Chaban showed that the strength of the coupling between the rotation and β-oscillations of the nuclear surface depends on the magnitude of the dimensionless parameter $\delta = 2^{-1/2}\beta/\beta_{00}$, i.e., is proportional to the ratio of the parameter β, characterizing the deviation from spherical symmetry, to the amplitude β_{00} of the zero order oscillations of the nuclear surface. Separation of the rotational motion from the vibrational is possible only for values of $\delta > 2.5$. For smaller values of δ, coupling between the rotation and the oscillations is so strong that such separation becomes meaningless and one can speak only of collective excitations. At values of $\delta < 1$ the collective motions again reduce to one type, namely, to oscillations of the nuclear surface.

As was shown by Chaban[10], for $\delta > 3$ the correction to the vibrational energy owing to coupling with oscillations of the nuclear surface may be approximated by the formula (2), where $E_i^0(J)$ is the energy of the i-th rotational level having spin J, and b is a parameter characterizing the given nucleus. The magnitude of b depends on the height of the first excited level with spin 0, corresponding to β-oscillations. For $\delta < 3$ the corrections to the adiabatic approximation become large and are no longer given by the simple formula (2).

The nuclei Hg^{198}, Fe^{56}, Cd^{110} and Cd^{114} are characterized by values of $\delta < 2$. For these nuclei, therefore, the corrections to the adiabatic approximation are large. Values of $\delta > 3$ obtain for Os^{192}, Os^{190}, Os^{188}, Os^{186}, Er^{166}, Er^{168}, Dy^{160}, Gd^{156} and a number of other nuclei. The rotational states of these nuclei are fairly well described by adiabatic theory. Nuclei such as Gd^{154} and Sm^{152} occupy an intermediate position, i.e., for them δ lies between 2 and 3.

Chaban also showed that the relation $\varepsilon(3) = \varepsilon_1(2) + \varepsilon_2(2)$ of the theory of nonaxial nuclei is relatively insensitive to corrections for adiabaticity. Hence it cannot serve as a measure of the deviation from adiabatic behavior. This is in agreement with the deductions of Grigor'ev & Avotina based on analysis of the experimental data.

If we assume that the nuclear charge is uniformly distributed through the volume and that the principal moments of inertia are characterized by formula (1), we find that the relative probabilities for E2 transitions between rotational levels of a nonaxial nucleus, taking into account the corrections to the adiabatic approximation, are determined primarily by change in the value of the parameter γ attributed to the given nucleus. Taking into account the corrections to the adiabatic approximation as regards the height of the levels leads to a small (~5%) decrease in the value of γ calculated by the adiabatic approximation equations. Experimental determination of the probability for electromagnetic transi-

tions between excited nuclear states is still far from accurate (the errors involved are of the order of 20 to 40%). In fact, in some cases the data of different authors differ by up to an order of magnitude. Hence at present detailed comparison of theory with experiment is difficult.

III. Theory of rotational states of odd nuclei

In odd nuclei the energy of single nucleon excitations often only insignificantly exceeds the energy of rotation, hence in investigating rotational states one must bear in mind the possibility of nonfulfillment of adiabatic conditions as regards both oscillations of the nuclear surface and single nucleon excitations. In a number of cases, apparently, interaction of the rotation with the single nucleon motion may be significant. This interaction may greatly alter the structure of the rotational spectrum.

In investigating the rotational states of an odd nucleus we will proceed from the Hamiltonian proposed in the work of Bohr & Mottelson:

$$H = \frac{\hbar^2}{2}\sum_{i=1}^{3}\frac{(\hat{J}_i-\hat{j}_i)^2}{I_i} + H_p + T\beta\{\cos\gamma(3\hat{j}_3^2-\hat{\mathbf{j}}^2)+\sqrt{3}(\hat{j}_1^2-\hat{j}_2^2)\sin\gamma\}, \qquad (5)$$

where the I_i are the three principal moments of inertia of the nucleus, defined by Eq.(1), and the J_i and j_i are the three projections of the operators of the total angular momentum of the nucleus and the momentum of the outer nucleon, respectively. The first term in (5) corresponds to the operator of the energy of rotation of the nuclear core; H_p is the Hamiltonian of the outer nucleon, located in the central symmetrical part of the core field. The last term in (5) represents the operator of interaction of the outer nucleon with the nonspherical part of the core field.

Authors have generally investigated systems described by the Hamiltonian (5) with $\gamma = 0$, which corresponds to the model of an odd axially symmetrical nucleus. The energy spectrum of such a system depends on the coupling between the angular momentum J of the outer nucleon and the angular momentum of the rotation:

$$\mathbf{R} = \mathbf{J} - \mathbf{j}. \qquad (6)$$

The coupling between these momenta is determined by the relative roles of the interaction of the nucleon with the nonspherical part of the potential well, on the one hand, and of the rotation of the nucleus, on the other hand. The role of the latter is determined by the separation between neighboring rotational levels. If the energy of the first interaction is large compared to the energy difference between the rotational levels, we have a case of strong coupling; if the opposite inequality obtains - weak coupling. Obviously, there may be intermediate cases between the two extreme ones. One should also bear in mind that the energy differences between neighboring rotational levels increase with increase of R, and at certain values of R they may exceed the binding energy of the nucleus with the nonspherical part of the potential. Thus in one and the same nucleus a case of strong coupling may go over into a case of weak coupling.

In the case of strong coupling in an axially symmetric nucleus the integral of motion is the projection Ω of the angular momentum of the nucleon on the nuclear axis. It must be noted that the total angular momentum of the nucleon in general may not be an integral of motion. This case was considered in the work of Bohr & Mottelson. In the case of weak coupling the projection of the angular momentum of the outer nucleon on the nuclear axis does not have a definite value.

An attempt to extend the case of strong coupling to nonaxial odd nuclei was recently undertaken by Davidson (Rensselaer Polytechnic, Preprint 1959). Davidson

found the eigenvalues of the Hamiltonian obtained from (5) by discarding all terms except

$$H_0 = \frac{\hbar^2}{2} \sum_i \frac{\hat{J}_i^2}{I_i} .$$

Such extreme simplification of the problem is admissible (with some approximation) for axial odd nuclei, but is not justified for nonaxial odd nuclei. Davidson obtained an explicit expression for the energy of the states with spins $J = 1/2$ and $3/2$:

$$E_{1/2} = \frac{9}{8 \sin^2 (3\gamma)} ,$$

$$E_i\left(\frac{3}{2}\right) = \frac{45 - (-1)^i 12 \sqrt{9 - 8 \sin^2 (3\gamma)}}{8 \sin^2 (3\gamma)} , \quad i = 1, 2.$$

The energies of these states and of other states with spins $J \leqslant 9/2$, obtained by numerical calculations, are plotted in Fig.5 in $\hbar^2/4B\beta^2$ units. Virtually identical results were obtained earlier by Filippov (private communication). A shortcoming of this simplified model is that the energy of all levels (including the ground state) tends to infinity in going over to axial nuclei ($\gamma \to 0$). However, the level energy differences $E_1(J) - E_1(1/2)$ remain finite.

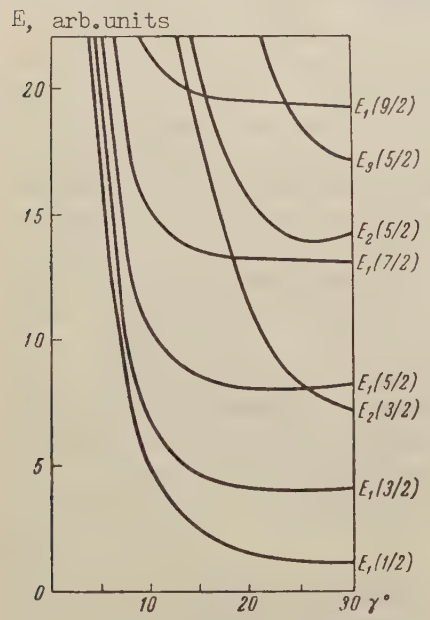

Fig.5. Energy E (in $\hbar^2/4B\beta^2$ units) of the rotational states of odd nuclei for the case of weak coupling (after Davidson).

With a view to investigating the influence of coupling of the nuclear rotation with the motion of the outer nucleon on the rotational states, we shall consider the case of weak coupling of the outer nucleon with the nonspherical part of the nuclear potential. The extreme case of weak coupling in a system described by the Hamiltonian (5) is realized when the outer nucleon is in states with quantum number $j = 1/2$. Obviously, the interaction of the outer nucleon with the nonspherical part of the core potential in an actual nucleus is not described precisely by the last term in (5), which is commutative with the operator $\hat{j}^2$. Because of this the total momentum of the nucleon is not always an integral of motion. There is reason to assume, however, that in some nuclei, when the admixture of states with $j \neq 1/2$ is small, there will be realized a case of weak coupling even when β is not very small. In the case of weak coupling, in the first approximation the coupling of the outer nucleon with the nonspherical part of the core potential can be neglected.

First, let us consider in this approximation the rotational states of an axial nucleus. Usually in nuclear physics in investigating single nucleon states, it is assumed that the nucleus is not rotating. If the nucleus is rotating, the rotational and nucleon motions affect each other. Let us assume that this influence can be described by an operator proportional to the scalar product of the corresponding angular momenta. Then in the weak coupling approximation the Hamiltonian of an axial nucleus will be of the form

$$H = A\hat{\mathrm{R}}^2 + W\hat{\mathrm{R}}\hat{\mathrm{j}} + H_p, \qquad (7)$$

where A is a parameter determined by the moment of inertia of the nucleus, and W is a parameter characterizing the strength of the coupling between the momentum of the outer nucleon and the rotation angular momentum.

It should be noted that Zaretskii & Shut'ko[12] already made an attempt to take into account the additional interaction of the nucleon spin with the rotation of the nucleus. The operator of this interaction, which they called quasi-magnetic interaction of the nucleon spin with the rotation, was chosen by analogy with "Gund's case b" for diatomic molecules in the form

$$\gamma(\hat{\mathrm{R}}+\hat{\mathrm{L}})\,\mathrm{S},$$

where $\hat{\mathrm{L}}$ is the operator of the nucleon orbital angular momentum, and S is the nucleon spin operator.

Invoking (6), we find $\hat{\mathrm{R}}\hat{\mathrm{j}}=\frac{1}{2}(\hat{J}^2-\hat{R}^2-\hat{j}^2)$. Inserting this value and (6) into (7), we readily obtain the mean value of operator (7) in the state with definite values of R and J and $j=1/2$:

$$E=AR(R+1)+\frac{W}{2}\{J(J+1)-R(R+1)\}+E_0'. \tag{8}$$

The quantum number R, corresponding to rotation of an even nuclear core, takes on only even values, consequently

$$R=J+\frac{1}{2}(-1)^{J+1/2}.$$

Inserting this value into (8), we finally obtain

$$E(J)=A\left\{J(J+1)+a(-1)^{J+1/2}\left(J+\frac{1}{2}\right)\right\}+E_0, \tag{9}$$

where

$$a=\left(1-\frac{W}{2A}\right). \tag{10}$$

As regards form, Eq.(9) agrees exactly with the formula of Bohr & Mottelson for the case of strong coupling with $K=\Omega=1/2$. However, the physical meaning of the constant a is now different. In the work of Bohr & Mottelson the parameter a is defined by

$$a^{BM}=\sum(-1)^{j-1/2}\left(j+\frac{1}{2}\right)|C_j|^2,$$

where $|C_j|^2$ is the probability that the nucleon in a given state will have angular momentum j.

According to (9), interaction of the outer nucleon with the rotation of the nucleus leads to shift and splitting of the rotational levels of the nuclear core. For $W/A<4$ the ground state of the nucleus corresponds to core at rest and has spin 1/2. For $W/A>4$, the spin of the ground state of the nucleus equals 3/2, i.e., the nuclear core in the ground state rotates.

In the case of nonaxial odd nuclei the nuclear core has the shape of a triaxial ellipsoid. In this case, with weak coupling ($j=1/2$) the Hamiltonian of the core and the outer nucleon can be written in the form

$$H=\frac{\hbar^2}{B\beta^2}\left\{\frac{1}{8}\sum_{i=1}^{3}\frac{(\hat{J}_i-\hat{j}_i)^2}{\sin^2\left(\gamma-\frac{2}{3}\pi i\right)}+\lambda\hat{\mathbf{J}}\hat{\mathbf{j}}\right\}+H_p.$$

The variation of the eigenvalues of this operator for the cases $\gamma=10^\circ$ and $\gamma=22^\circ$ as a function of the dimensionless parameter λ is shown in Fig.6. In

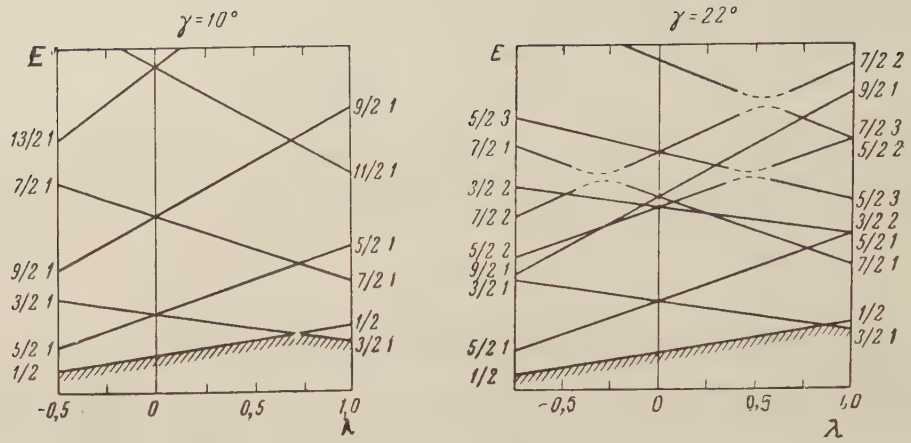

Fig.6. Energy of the rotational states of odd nonaxial nuclei (weak coupling case $j = 1/2$) as a function of the parameter γ, characterizing the coupling of the rotation momentum with the momentum of the nucleon.

Ref.11 we calculated the probabilities for E2 and M1 transitions between the rotational states of nuclei that pertain to the case of weak coupling.

It should be emphasized that the theory of rotational states of nonaxial nuclei is still in a very early stage of development.

IV. Theoretical calculations of the equilibrium shape of nuclei

The problem of the equilibrium shape of a nucleus with one outer nucleon was investigated by Bohr[13]. In his work, Bohr postulated that the shape of the nucleus remains axially symmetric and determined the deviation from spherical symmetry. Filippov[14] showed that in the case of one nucleon outside the closed shells precise solution of the problem without recourse to this simplification leads to the same results as the approximate solution deduced by Bohr.

In the presence of several nucleons outside the filled shells investigation of the equilibrium shape of the nucleus becomes appreciably more complicated owing to the necessity of taking into account correlation in the motion of the outer nucleons. This correlation appears because of direct interaction of the outer nucleons with each other and also because of the Pauli exclusion principle.

Davydov & Filippov[15] investigated the equilibrium shape of a nucleus on the assumption that a pair of outer nucleons of the same type interacts with the core as a whole. It was shown that this assumption in a number of cases leads to a nonaxial shape. Filippov[14] investigated the opposite case, when one can neglect the interaction between the outer nucleons, i.e., when the correlation in the motion of the outer nucleons is due only to the Pauli principle. Filippov showed that in the presence of three nucleons in the shell with $j=5/2$ the energy minimum of the nucleus corresponds to the nuclear shape characterized by the nonaxiality parameter $\gamma = \pi/6$. In the general case, however, partial filling of the shell with nucleons of one type leads to an axial shape. When the shell is less than half filled the energy minimum corresponds to a nuclear shape with $\gamma = \pi/3$, i.e., to an oblate ellipsoid of revolution with its symmetry axis parallel to the Y axis. When the shell is more than half filled, the energy minimum corresponds to $\gamma = 0$, i.e., the nucleus is a prolate ellipsoid of revolution with its symmetry axis aligned with the Z axis. Hence in nuclei in which one shell is less than half filled with protons (neutrons), while another shell is more than half

filled with neutrons (protons) the equilibrium shape of the nucleus may not have an axial symmetry axis. Filippov showed that the configurations

$\left(\frac{5}{2}\right)^1\left(\frac{7}{2}\right)^{-1}$; $\left(\frac{5}{2}\right)^1\left(\frac{7}{2}\right)^{-3}$; $\left(\frac{5}{2}\right)^2\left(\frac{7}{2}\right)^{-1}$; $\left(\frac{5}{2}\right)^2\left(\frac{7}{2}\right)^{-2}$; $\left(\frac{5}{2}\right)^2\left(\frac{7}{2}\right)^{-3}$; $\left(\frac{5}{2}\right)^1\left(\frac{9}{2}\right)^{-1}$ and others

give rise to a nonaxial shape.

Thus correlation in the motion of the outer nucleons leading to competing axial deformations of the nucleus along the Y axis and the Z axis can, in a number of cases, result in a nonaxial shape of the nucleus. The nuclear shape will be close to axial when one of the competing factors predominates over the other. This situation obtains in strongly deformed nuclei.

Studies carried out by Filippov substantiate the calculations carried out earlier by Geilikman[16] and Zaikin[17], who consider the equilibrium nuclear shape for specific forms of single particle potential, but without taking into account spin-orbit interaction.

Moscow State University

References

1. A.S.Davydov, Izv.AN SSSR, Ser.fiz., 23, 792 (1959). (Trans.Bulletin, 23, 788.)
2. A.S.Davydov & G.F.Filippov, Zhur.eksp.i teor.fiz., 35, 440 (1958). (Trans. Soviet Physics - JETP.)
3. A.S.Davydov & V.S.Rostovskii, Ibid., 36, 1788 (1959). (Trans.Ibid.)
4. W.King & M.Johns, Canad.J.Phys., 37, 755 (1959).
5. G.DeMille, T.Kavanagh, R.Moore, R.Weaver & W.White, Ibid., 37, 1036 (1959).
6. D.M.Van Patter, Nucl.Phys., 14, 42 (1959/60).
7. E.P.Grigor'ev & M.P.Avotina, Izv.AN SSSR, Ser.fiz., 24, 324 (1960). (Trans.Bulletin, 24, 311.)
8. A.S.Davydov, N.S.Rabotnov & A.A.Chaban, Zhur.eksp.i teor.fiz., 38, 1311 (1960). (Trans.Soviet Physics - JETP.)
9. A.B.Migdal, Ibid., 37, 249 (1959). (Trans.Ibid.)
10. A.A.Chaban, Ibid., 38, 1630 (1960). (Trans.Ibid.)
11. A.S.Davydov, Nucl.Phys., 15 (1960).
12. D.F.Zaretskii & A.V.Shut'ko, Zhur.eksp.i teor.fiz., 32, 370 (1957). (Trans.Soviet Physics - JETP.)
13. A.Bohr, Dan.Mat.-Fys.Medd., 26, No.14 (1953).
14. G.F.Filippov, Zhur.eksp.i teor.fiz., 38, 1316 (1960). (Trans.Soviet Physics - JETP.)
15. A.S.Davydov & G.F.Filippov, Ibid., 36, 1467 (1959). (Trans.Ibid.)
16. B.T.Geilikman, Ibid., 35, 989 (1958). (Trans.Ibid.)
17. D.I.Zaikin, Ibid., 35, 529 (1958). (Trans.Ibid.)

GAMMA-RADIATION FROM THE $Cl^{35}(n,\gamma)Cl^{36}$ REACTION

- L.V.Groshev, A.M.Demidov & V.N.Lutsenko

Some years ago we measured the spectrum of γ-rays emitted in thermal neutron capture by Cl^{35} by means of a magnetic Compton spectrometer with a resolution of 2 percent.[1] In the present report we give the results of new measurements of the same spectrum, obtained with the Compton magnetic spectrometer described in Ref. 2, which also contains a description of the experimental arrangement.

For these measurements we used NaCl: weight of sample - 1.3 kg; dimensions - 50 x 100 x 190 mm. We chose this salt because the presence in the spectrum of the lines accompanying β-decay of Na^{24} gave us two useful reference points for plotting the calibration curve. Inasmuch as the thermal neutron capture cross section for chlorine is 33.6 barns, while for sodium it is 0.505 barns, there could be evinced in the spectrum only the most intense lines from the $Na^{23}(n,\gamma)Na^{24}$ reaction. The energies of these lines were precisely known from our earlier measurements with the old instrument.

The γ-spectrum obtained by subtracting the background from the experimental spectrum is reproduced in Figs.1 & 2. This background is due to a number of caused. First, there is the background radiation from the reactor channel. This part of the background was measured with a similar sample but surrounded with a layer of boron carbide. The background radiation 0.477, 2.223, 4.944 and 7.363 Mev γ-lines, which are due to the $B^{10}(n,\alpha,\gamma)Li^{7}$, $H(n,\gamma)D$, $C^{12}(n,\gamma)C^{13}$ and $Pb^{207}(n,\gamma)Pb^{208}$ reactions, were not subtracted from the experimental spectrum inasmuch as their intensity changes when the sample is surrounded with boron carbide.

The second cause giving rise to a background is detection by the spectrometer of electron pairs produced in the converter. This part of the background was determined by measuring the positron spectrum; to this end both magnet fields were reversed. We also subtracted the coincidences due to electrons ejected from the window of the separator and chance coincidences, which amounted to ~0.5 coinc/ /3 min. The total background subtracted from the experimental spectrum amounted to 2 coinc/3 min at 1 Mev and 10 coinc/3 min at 5 Mev.

In the table below we list the energies and intensities of the resolved γ-lines. In determining the γ-ray energies we used the calibration curve plotted on the basis of a number of reference points (see Ref.2). In evaluating the intensities we took into account the spectral response of the spectrometer (in particular, the influence of electron scattering in the converter and pass-through counter) and the energy dependence of the γ-ray absorption in the sample and along the path from the sample to the converter. In the energy range from 1 to 8 Mev the absorption coefficient for the sample changes by a factor of ~1.5; the absorption in the channel by a factor of ~1.9.

The intensities listed in the table are expressed in terms of the number of photons per 100 captured neutrons. They were obtained by normalizing all the energy carried off by the γ-rays to the neutron binding energy. The error in determining the absolute intensities is evaluated to be 10% for the intense lines, and may be as great as 50% for the weak lines and γ-lines with $h\nu \lesssim 0.6$ Mev.

While chlorine has two stable isotopes: Cl^{35} and Cl^{37}, 99.6% of the captures occur in Cl^{35}. Hence one can safely attribute all the observed γ-lines to transitions in Cl^{36}.

Utilizing the data from the table we constructed the scheme of γ-transitions in Cl^{36} reproduced in Fig.3. In constructing the scheme we also used the data on the level energies obtained by Paris et al[4] in investigating the (d,p) reaction. In this work the level diagram was investigated in detail only up to 4.04 Mev. We shall discuss the higher lying levels below. The neutron binding energy was taken from the work of Giese & Benson[3].

We note that in our case the accuracy in determining the line energies is determined primarily by the uncertainty in the energy values for the lines that were used in plotting the calibration curve. Since this does not affect the relative energies, the energy difference between close lines could be determined with high accuracy. This in conjunction with the possibility of more precise measurement of the γ-line energies in the region below 2 Mev, enabled us to determine the energy of some levels more accurately than was done in the work of Paris et al[4]. These more accurate data are listed in the extreme left column in Fig.3.

The angular distribution of protons from the (d,p) reaction was investigated by the photographic plate technique by Teplov[5]. The values of the orbital momenta found by Teplov are listed at the extreme right in Fig.3. We note that the angular distributions determined by Teplov for high-lying states pertain to groups of levels.

For the initial Cl^{35} state we assume $l = 2$, inasmuch as neutron capture in the thermal region is determined primarily by the negative energy (-120 ev) level with spin and parity 2+ (Brugger et al[6]). However, an admixture of 1+ state is not entirely excluded.

In constructing the transition scheme shown in Fig.3, we first plotted the γ-lines for which the energies within the limits of the experimental error agree with the level energy differences reported by Paris et al[4]. Some transitions could be inserted in more than one location; in these cases we have indicated by dashed lines the transitions that appear more doubtful in view of the available intensity data.

After plotting these transitions, we still had a number of γ-lines, apparently, corresponding to cascades passing through levels lying above 4.04 Mev. Some of these γ-rays may form two-step cascades. Assuming the existence of such cascades, we introduced into the scheme levels with energies 4.138, 4.589, 4.757, 5.016, 5.516 and 6.344 Mev.

The results of coincidence measurements on the γ-rays from the $Cl^{35}(n,\gamma)Cl^{36}$ reaction obtained in the investigations listed under Refs.7-10 are generally in agreement with our scheme.

We note two interesting features in the scheme for Cl^{36}: the existence of two close levels at 1.957 and 1.949 Mev, and the presence of a very intense low energy transition between the 2.467 and 1.949 Mev levels. A skeletal scheme showing the levels of particular interest is given in Fig.4.

Teplov[5], measuring the angular distribution of protons for the 1.95 Mev level, found that it corresponds to a mixture of orbital momenta 0 and 3, which can only be explained by postulating the existence of two levels. Paris et al[4] detected only one level having an energy of 1.952 Mev. Segel[10], investigating coincidences of the γ-rays following thermal neutron capture in Cl^{35}, found that the relative intensity of the transitions departing from the 1.95 Mev level varies depending on whether it is fed by the cross-over 6.621 Mev transition from the initial state or by the 6.110—0.518 Mev cascade. On the basis of his results Segel inferred that there are two levels at this energy (1.95 Mev).

In our spectrum the existence of two levels at 1.95 Mev was clearly evinced in the splitting of the peak at this energy. This peak and its resolution into two γ-lines with a separation of 8 ± 1 kev are shown in Fig.5.

On the basis of the 6.621 Mev γ-rays alone, we cannot determine which of the levels of this doublet is fed by the transition from the initial state. However, from the fact that the energy difference between the 6.621 and 6.110 Mev γ-rays (0.511 ± 0.002 Mev) is less than the energy of the 0.5.8 ± 0.002 Mev line, it would follow that the 6.621 Mev transition feeds the 1.957 Mev level, and the 6.110—0.518 Mev cascade populates the 1.949 Mev level. Analysis of the cascades

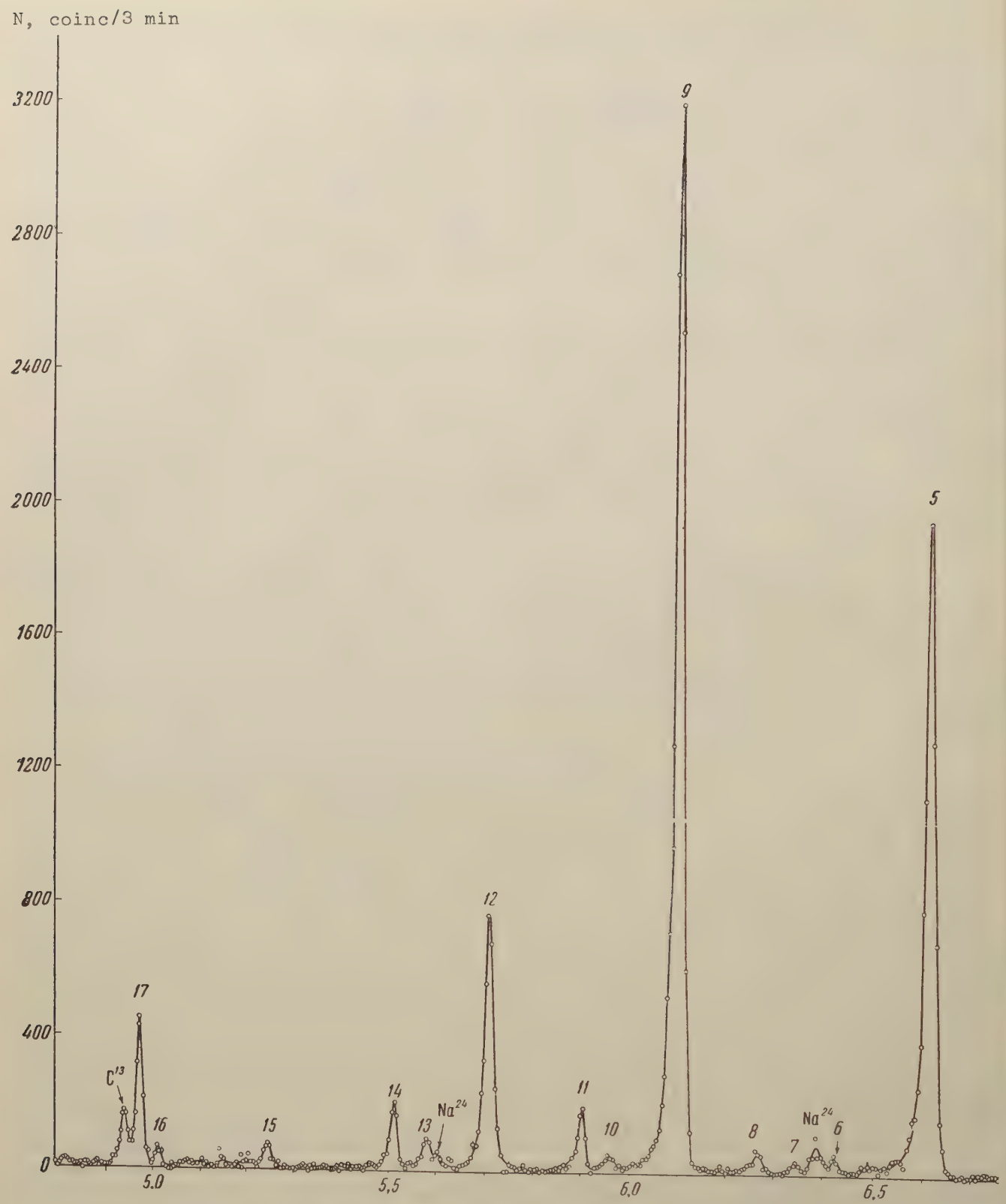

Fig.1. NaCl γ-spectrum in the $h\nu$ range from 4.8 to 8.7 Mev.

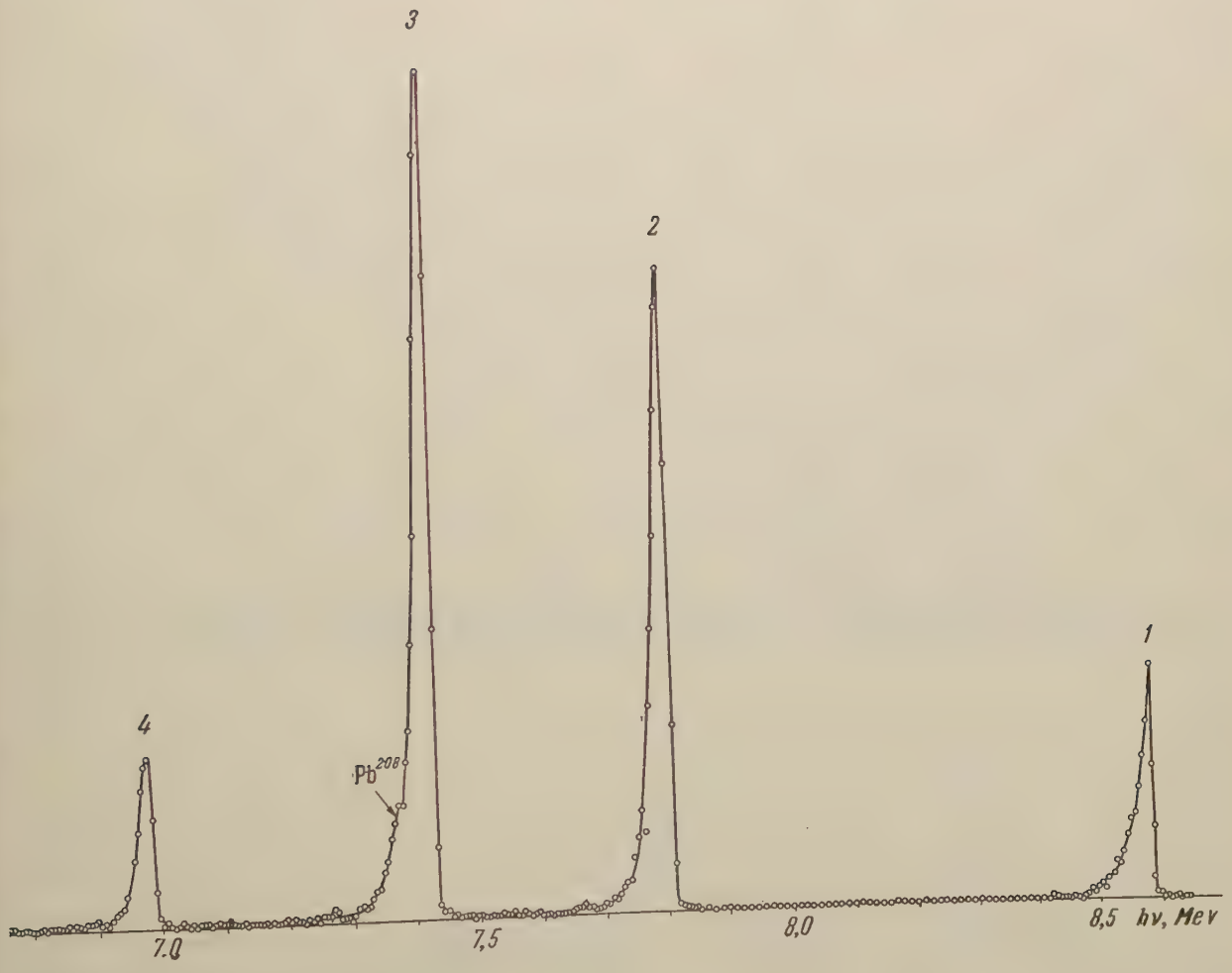

Fig.1. continued

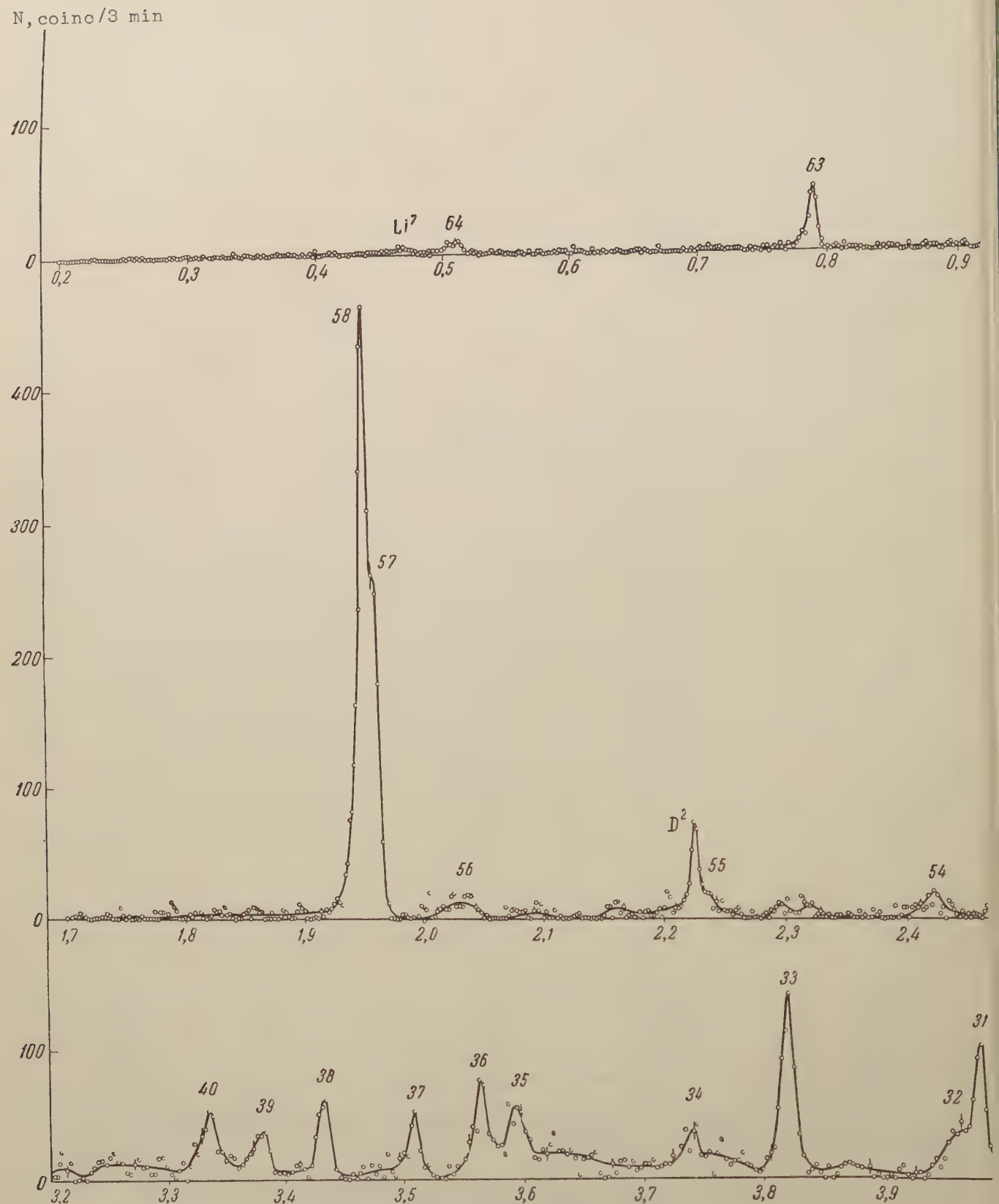

Fig.2. NaCl γ-spectrum in the $h\nu$ range from 0.2 to 4.8 Mev.

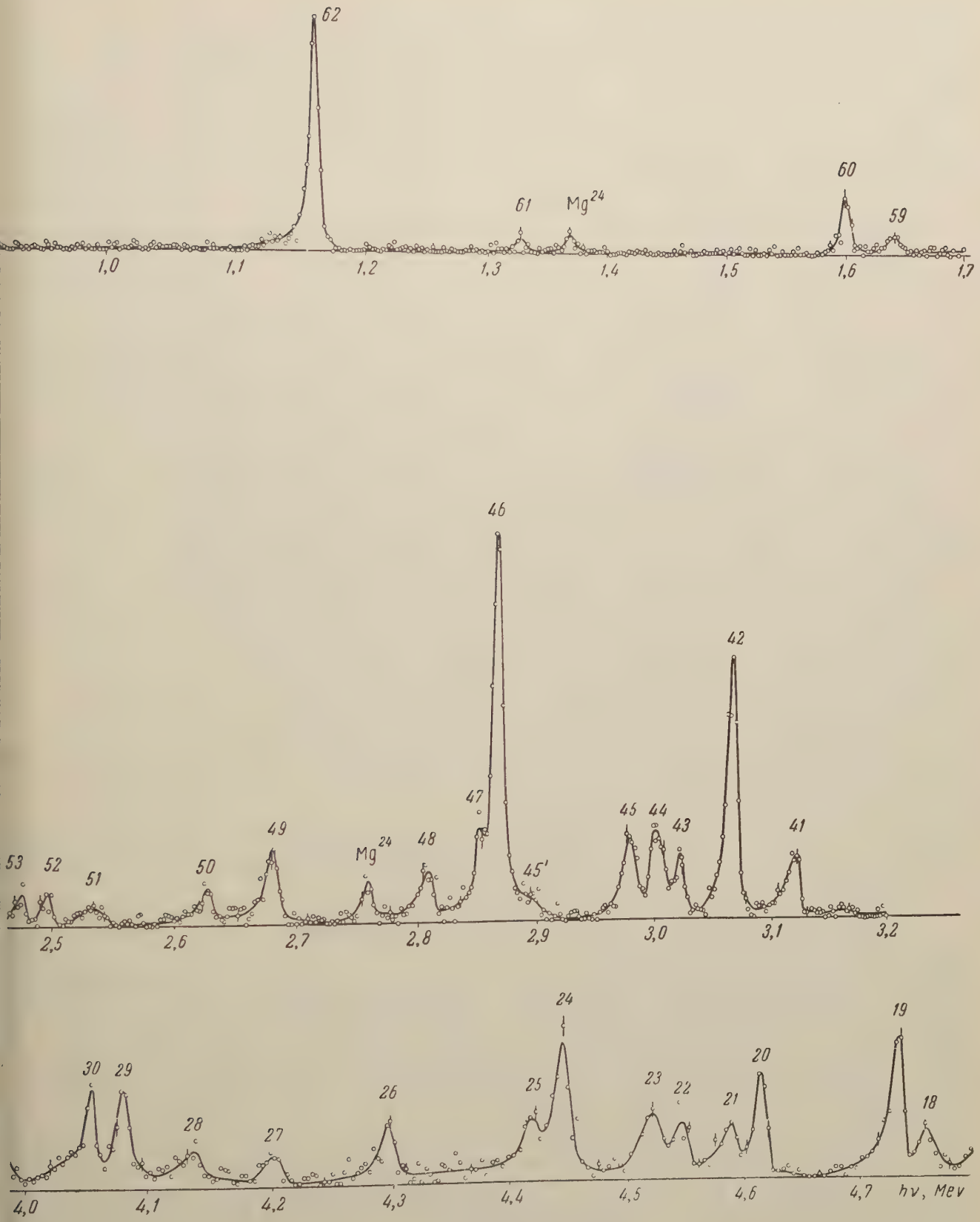

Fig.2. continued

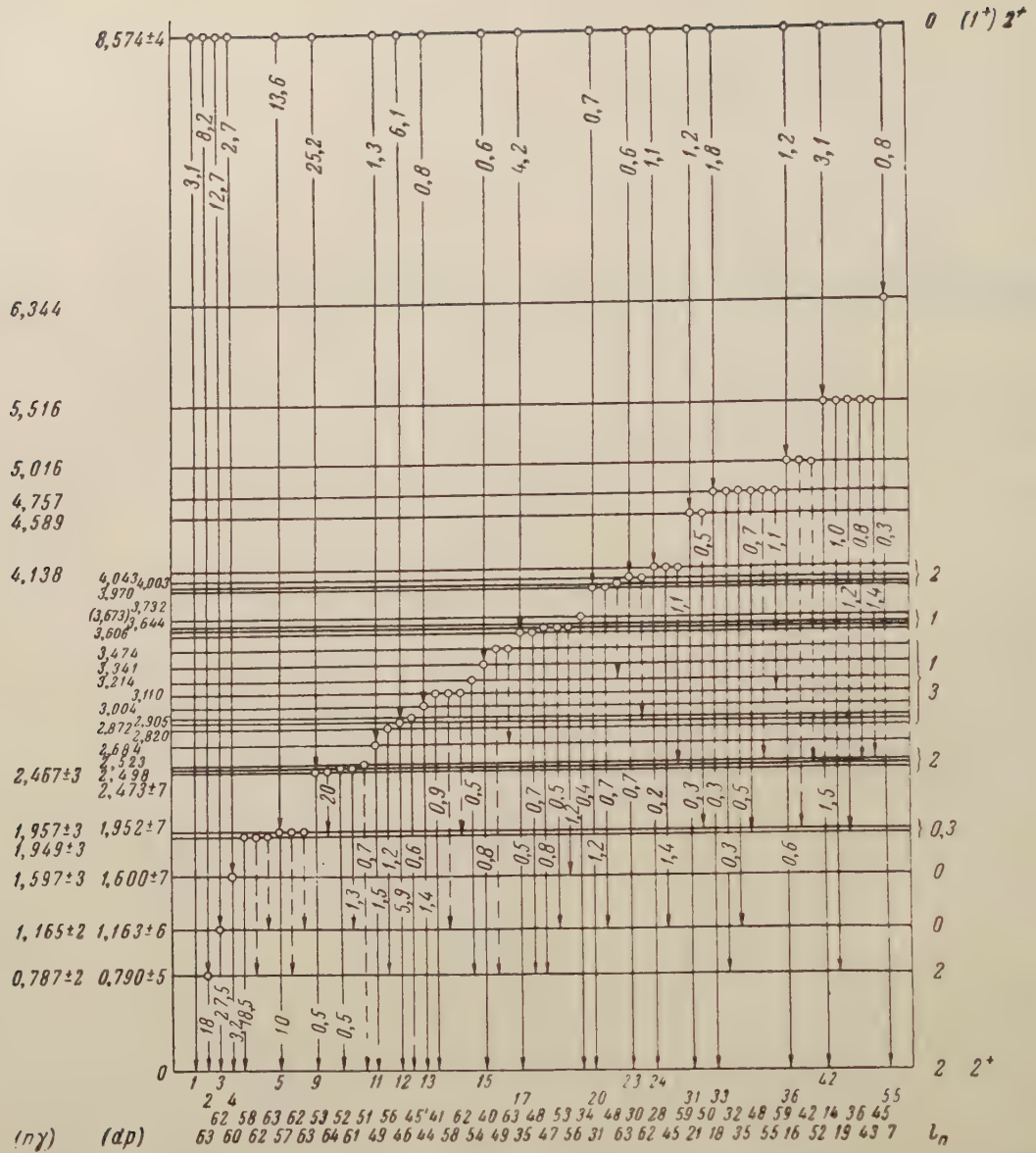

Fig.3. Scheme of γ-transitions in Cl^{36}.

substantiates this inference (see Fig.4). It also follows from this analysis that the 1.949 and 1.957 Mev states must be partially depopulated by a 1.16—0.79 or 0.79—1.16 Mev cascade, which is in good agreement with the data of Segel[10] obtained from analysis of the coincidence spectra. At present we cannot decide between the alternate sequences of the 0.79 and 1.16 Mev γ-rays inasmuch as the sum of their energies within the limits of the experimental error agrees with either 1.949 or 1.957 Mev.

The high intensity of the transition between the 2.467 and 1.949 Mev levels gives reason to assume that this is an electric dipole transition. The existence of such a transition imposes certain limitations on the choice of assignments for the levels listed in Fig.4, if we assume definite values for the angular momentum of the initial state (2+ or 1+) and the multipole order of the transition from

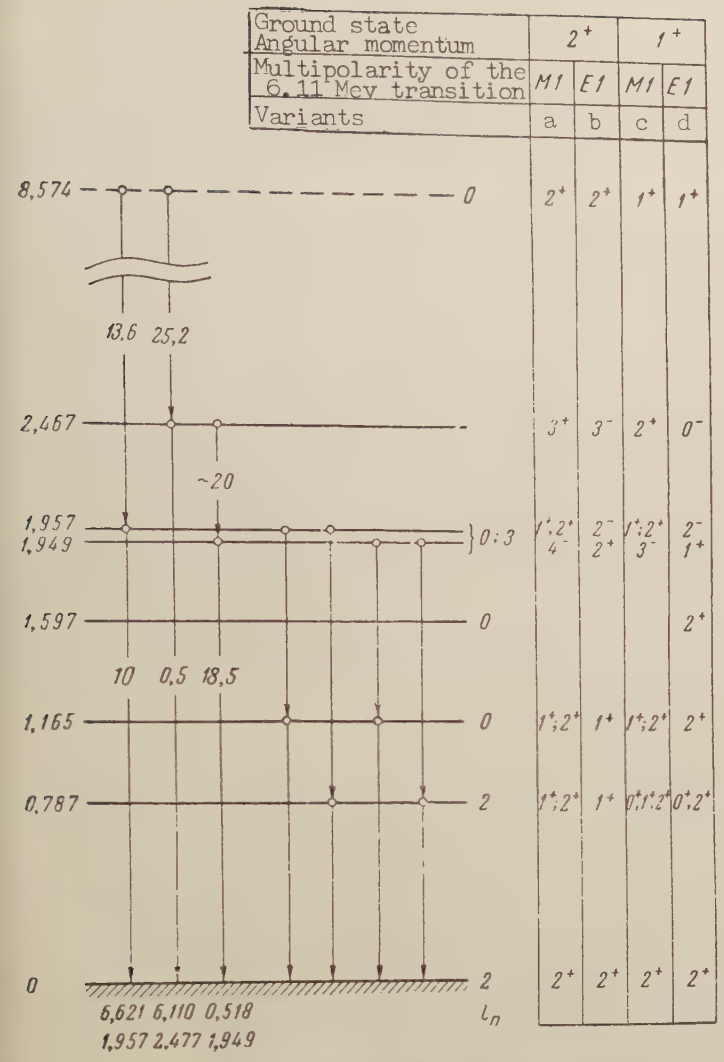

Fig.4. Part of the Cl^{36} γ-transition scheme and four versions of the spin and parity assignments.

the initial state to the 2.467 Mev level. This transition (6.11 Mev) is the most intense of all the transitions departing from the initial level and, consequently, it must be either E1 or M1. Accordingly, we carried out spin and parity assignments for the four possible variants, taking into account the orbital momenta determined by Teplov. The results are shown in the table in Fig.4.

To illustrate the reasoning employed in arriving at the different spin and parity assignments, we give the detailed steps for variant "d": inasmuch as the 6.11 Mev transition is E1, the assignment for the 2.467 Mev level may be 0-, 1- or 2-. The fact that there is no intense transition from this level to the ground state indicates that we can give preference to 0-. The existence of an E1 transition between the 2.467 and 1.949 Mev levels requires that for the 1.949 Mev level $l_n = 0$ rather than 3, and, consequently, of the two possible assignments 1+ and 2+, we must choose 1+. Then for the 1.957 Mev level we have $l_n = 3$ ($j_n = 7/2$), and J^π = 2-, 3-, 4- or 5-; the existence of the intense 6.621 Mev transition narrows the assignment to 2-. For the 1.60 and 1.16 Mev levels, which have $l_n = 0$, we must make the assignment 2+, inasmuch as there are no intense transitions from these levels to the 2.467 Mev level. The fact that there is no transition between the 2.467 and 0.787 Mev levels and that there is a transition to this level from the initial state limits the possible assignments to 0+ and 2+.

Similar analyses were carried out for the other variants.

It must be noted that more or less serious objections can be raised against each of the variants. Thus in variants "a" and "c" the 2.467 Mev M1 transition is strongly forbidden relative to the 0.518 Mev E1 transition.

In the "b" variant, it is difficult to explain the strong forbiddenness of the 2.467 Mev E1 transition relative to the 0.518 Mev E1 transition.

In variant "d" the forbiddenness of the 2.467 Mev transition relative to the 0.518 Mev transition is satisfactorily explained, but this variant like variant "b", involves the assumption that the assignment for the initial state is 1+,

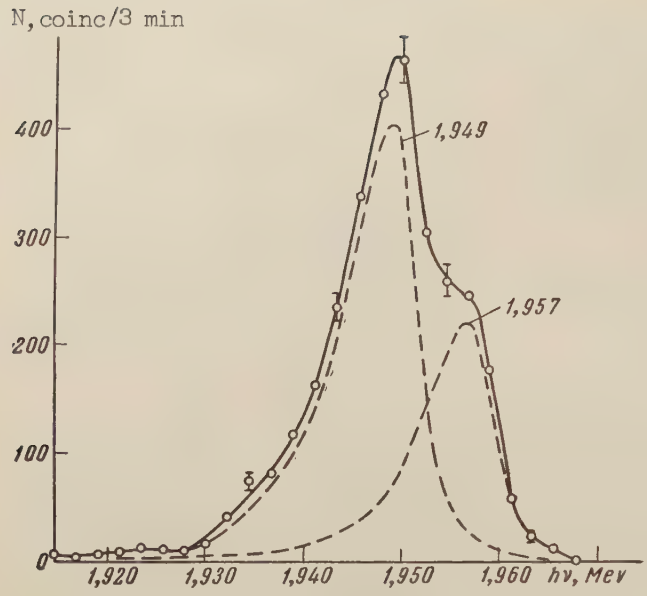

Fig.5. Resolution of the 1.95 Mev doublet.

which is in conflict with the data of Brugger et al[6], if we accept that capture in the thermal region for Cl^{36} is determined primarily by a negative energy resonance.

Trumpy[11] investigated the angular correlation for the 7.42—1.16 Mev cascade and found that the factor a_1 multiplying $\cos^2\theta$ in the expression for the angular correlation equals 0.092 ± 0.025. On the basis of this value he came to the conclusion that this cascade has the characteristics 1+ (M1) 2+ (86% M1 + 14% E2) 2+, which is in good agreement with the assignment arrived at in variant "d". It can readily be shown, however, that the above value for a_1 is also consistent with 2+ (M1) 1+ (m1) 2+.

Thus, on the basis of the present data, it is impossible to choose between the four assignment variants.

No.	hν, Mev	I_γ, %	No.	hν, Mev	I_γ, %
1*	8,573±0,004**	3,1	33*	3,822±0,004	1,8
2*	7,786±0,005	8,2	34*	3,742±0,006	0,4
3*	7,410±0,005	12,7	35*	3,596±0,005	0,5
4*	6,974±0,005	2,7	36*	3,566±0,004	1,2
5*	6,621±0,005	13,6	37	3,510±0,004	0,8
6	6,423±0,008	0,3	38	3,435±0,004	1,0
7*	6,344±0,008	0,3	39	3,383±0,004	0,5
8	6,266±0,006	0,6	40*	3,338±0,005	0,8
9*	6,110±0,005	25,2	41*	3,121±0,004	0,9
10	5,959±0,006	0,3	42*	3,067±0,004	3,6
11*	5,902±0,005	1,3	43*	3,024±0,004	0,8
12*	5,715±0,004	6,1	44*	3,002±0,005	1,4
13*	5,585±0,005	0,8	45*	2,980±0,004	1,4
14*	5,516±0,004	1,5	45'*	2,896±0,005	0,6
15*	5,246±0,005	0,6	46*	2,868±0,003	5,9
16*	5,016±0,004	0,6	47*	2,852±0,004	0,8
17*	4,981±0,004	4,2	48*	2,810±0,004	0,7
18*	4,757±0,005	0,3	49*	2,681±0,003	1,5
19*	4,732±0,004	1,0	50*	2,628±0,004	0,5
20*	4,613±0,004	0,7	51*	2,535±0,007	0,7
21*	4,589±0,005	0,3	52*	2,498±0,003	0,5
22	4,547±0,008	0,4	53*	2,477±0,003	0,5
23*	4,522±0,005	0,6	54*	2,422±0,004	0,5
24*	4,444±0,004	1,1	55*	2,235±0,003	0,8
25	4,417±0,006	0,5	56*	2,033±0,007	1,2
26	4,298±0,004	0,5	57*	1,957±0,003	10,0
27	4,203±0,005	0,2	58*	1,949±0,003	18,5
28*	4,138±0,008	0,2	59*	1,636±0,003	1,1
29	4,080±0,004	0,7	60*	1,597±0,003	3,2
30*	4,053±0,004	0,7	61*	1,329±0,002	1,3
31*	3,980±0,004	1,2	62*	1,165±0,002	27,5
32*	3,957±0,007	0,3	63*	0,792±0,002	18,0
			64*	0,518±0,002	~20

---

*Line plotted in the γ-transition scheme.

**This energy value was taken from the work of Giese & Benson[3] and used as a reference point in determining the transition energies.

References

1. L.V.Groshev, A.M.Demidov, V.N.Lutsenko & V.I.Pelekhov, Atlas spektrov luchei radiatsionnogo zakhvatateplovykh neitronov (Atlas of thermal neutron capture γ-ray spectra), M., 1958.
2. L.V.Groshev, A.M.Demidov, V.N.Lutsenko & A.F.Malov, Present issue of the Bulletin, p.794.
3. C.T.Giese & J.L.Benson, Phys.Rev., 110, 712 (1958).
4. C.H.Paris, W.W.Buechner & P.M.Endt, Phys.Rev., 100, 1317 (1955).
5. I.B.Teplov, Zhur.eksp.i teor.fiz., 31, 25 (1956). (Trans.Sov.Phys.-JETP.)
6. R.M.Brugger, J.E.Evans, E.G.Joki & R.S.Shankland, Phys.Rev., 104, 1054 (1956).
7. A.L.Recksiedler & B.Hamermesh, Phys.Rev., 96, 109 (1954).
8. V.R.Burmistrov, Izv.AN SSSR, Ser.fiz., 23, 902 (1959), (Trans.Bulletin, 23, 890); Atomnaya energiya, 7, 260 (1959), (Trans.Soviet Jour.of Atomic Energy).
9. J.E.Draper & A.A.Fleischer, Bull.Amer.Phys.Soc., II, 4, 476 (1959).
10. R.E.Segel, Phys.Rev., 113, 844 (1959).
11. G.Trumpy, On the Determination of Nuclear Spin by the Study of Neutron Capture Gamma Rays, Blindern, Oslo, 1957.

GAMMA-SPECTRA OF THE ISOTOPES IN THE LANTHANUM FRACTION FROM SPALLATION OF TANTALUM

- E.P.Grigor'ev, S.L.Sakharov & V.O.Sergeev

The γ-spectrum of the lanthanum fraction separated from the rare earth products obtained as a result of bombardment of a tantalum target with 660 Mev protons was investigated on the automatic scintillation spectrometer described in Ref.1.

Among the lanthanum isotopes there were detected La^{135} and La^{132}, which have periods of 18 hr and 4.2 hr, respectively. La^{135} was recently investigated in detail by Mitchell et al[2] who proposed a decay scheme for this isotope. We observed the most intense 470 kev line and the x-ray component, the intensity of which fell off with a period of 18 hr. Availability of the decay scheme enabled us to determine the relative yield of La^{135} from the nuclear reaction.

The γ-spectrum of 4-hour lanthanum is extremely complicated. Hence owing to the relatively low resolution of our instrument we are unable to indicate the energies and relative intensities of the γ-lines with good accuracy. The most intense lines are evinced only by small rises in the spectral curve; they have the following energies: 1.0, 1.5, 2.3, 3.0 and 3.3 Mev. We found that the intensities of all the lines with energies exceeding 1 Mev fall off with the same period. Observation of the decrease in intensity over a time equal to 10 half-lives yielded an average value of T = 4.2 ± 0.1 hr.

The decay curves plotted for different sections of the γ-spectrum are shown in the accompanying figure.

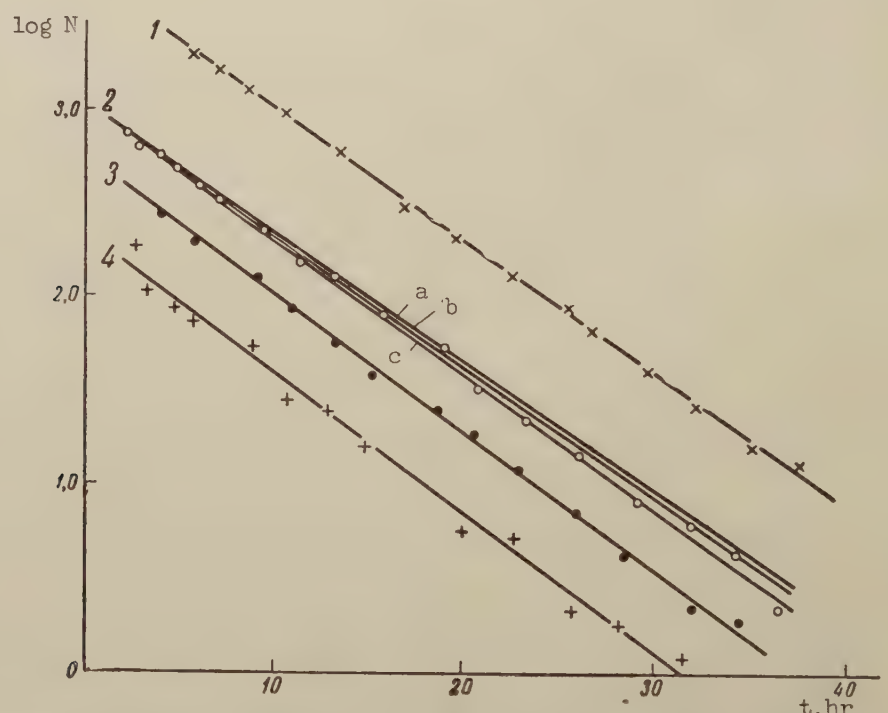

La^{132} decay curves: 1) E_γ = 1.0 Mev, T = 4.20 hr; 2) E_γ = 1.5 Mev (a - T = 4.25 hr, b - 4.30 hr, c - 4.15 hr); 3) E_γ = 2.1 Mev, T = 4.15 hr; 4) E_γ = 2.3 Mev, T = = 4.10 hr.

Two lanthanum isotopes, namely, La^{132} (4.5 hr - Ref.3) and La^{133} (4.0 hr - Ref.4) have periods close to the observed one.

La^{132} - Ba^{132} and La^{133} - Ba^{133} mass differences (in Mev)

ass difference	Calculated according to		Experimental data	
	Levy-Riddel Ref.6	Cameron Ref. 7	From β^+ spectrum	From γ-spectrum
La^{132} - Ba^{132}	4.66	5.20	4.8	3.3
La^{133} - Ba^{133}	1.88	2.77	2.2	

La^{132} decays by emission of positrons with an end-point energy of 3.8 Mev (Refs.5 & 3), while La^{133} decays primarily by electron capture.

We did not observe a 4-hr component in the x-radiation; on the other hand, the intensity of most of the γ-lines fell off with a period of ~4 hr. From this it may be concluded that if La^{133} was present in our fraction, the amount present was less than 10% with respect to the amount of La^{132}. This inference is substantiated by comparison of the disintegration energy with the La^{132} - Ba^{132} and La^{133} - Ba^{133} mass differences calculated by means of the semi-empirical formulas of Levy[6] and Cameron[7]. The calculated results are compared with the experimental data in the accompanying table.

It will be evident from the table that the probability of γ-rays with energy exceeding 2 Mev in the decay of La^{133} is negligible; hence all or most of the high energy γ-radiation must belong to La^{132}.

The decay scheme for La^{132} is not known, hence one cannot determine the number of photons of any given energy per disintegration. However, one can evaluate the number of disintegrations of La^{132} at a given moment from the x- and annihilation radiations and then compare this number with the number of disintegrations of La^{132}. Then knowing the time elapsed since bombardment, one can determine the ratio of the yields of La^{132} and La^{135}. We carried out the calculations and obtained 100:80. Noteworthy is the fact that the yield of La^{133} is appreciably lower. Yet according to the formula of Rudstam[8] the yield of this isotope should not be less than the yield of La^{132} or La^{135}.

Scientific Research Physical Institute,
"A.A.Zhdanov" Leningrad State University

Reference

1. Transactions of the Second Conference on Neutron-Deficient Rare Earth Isotopes, Vol.3, p.121, Dubna, 1960.
2. A.C.G.Mitchell, C.B.Creager & C.W.Kocher, Phys.Rev., 111, 343 (1958).
3. M.M.Gransden & W.S.Bogle, Phys.Rev., 82, 447 (1951).
4. R.C.Naumann, F.L.Reynolds & I.Perlman, Phys.Rev., 77, 398 (1950).
5. W.Ware, Cited in D.Strominger, T.M.Hollander & G.T.Seaborg, Revs.Mod. Phys., 30, 719 (1958).
6. T.Riddel, A Table of Levy's Empirical Atomic Masses, Chalk River, 1957.
7. A.G.W.Cameron, A Revised Semi-Empirical Atomic Mass Formula, Chalk River, 1957.
8. S.Rudstam, Phil.Mag., 44, 1132 (1953).

DETERMINATION OF THE PERIODS OF Dy^{159}, Ho^{160m}, Tm^{166} AND Lu^{173}

- E.P.Grigor'ev, O.V.Larionov, M.K.Nikitin, S.L.Sakharov & V.O.Sergeev

The investigated isotopes - Dy^{159}, Ho^{160m}, Tm^{166} and Lu^{173} - were obtained by bombardment of a tantalum target with 660 Mev protons in the Joint Institute for Nuclear Research synchrocyclotron. The rare earths were first separated chemically from the target, and then the individual elements were separated chromatographically.

Procedure

For determining the periods we used the standard B-2 equipment and MST-17 end-window counters with thin mica windows. The counters were carefully selected as regards length and slope of the plateau, magnitude of the operating voltage, stability in operation with time and under different loads and as regards intrinsic background. The counters were protected against extraneous radiation by lead shields. The source was mounted immediately in front of the window and fixed in position by means of the counter cap, so that the geometry remained constant during the entire measurement time. The sources were surrounded on all sides with aluminum foil, which obviated loss of radioactive material due to crumbling or flaking (such loss may obviously result in apparent reduction of the observed period).

The counter load at beginning of measurement did not exceed 10^4 pulses/min; the total number of pulses recorded by any counter during an experiment did not exceed 10^8; the characteristics of the counters did not noticeably change during the measurement period.

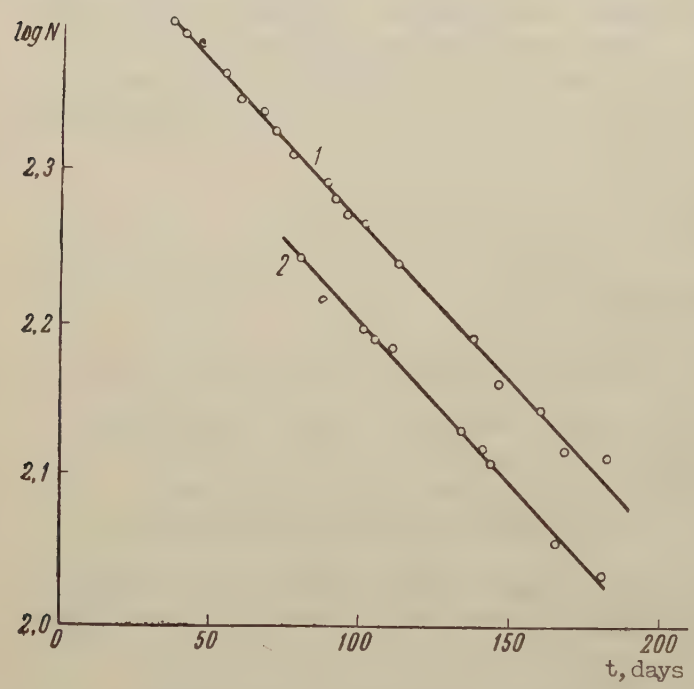

Fig.1. Dy^{159} decay curves: 1) T = 141 ± 10 days according to the data of the first counter, 2) T = 138 ± 10 days according to the data of the second counter.

Since it was difficult for us to check whether the efficiency of the counters remained constant during the course of the measurements, one can only judge of the accuracy of our results by comparing our values with the most precise measurements of other investigators and to some degree from the rectilinearity of the semilogarithmic decay plots.

Dy^{159}

Dy^{159} served as the control isotope. In other investigations this isotope was obtained by the $Dy^{158}(n,\gamma)Dy^{159}$ and $Tb^{159}(d,2n)Dy^{159}$ reactions and its period was determined with good accuracy: T = 134 days (Butement[1]), 140 days (Ketelle[2]) and 144.4 ± 0.2 days (Ketelle & Brosi[3]).

Our curves, obtained on the basis of measurements with three different counters, are shown in Fig.1; the average value is T = = 139 ± 10 days, which is in good agreement with the above periods.

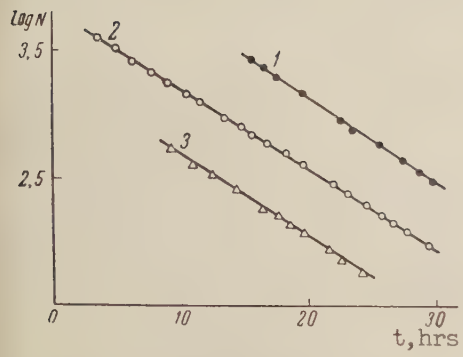

Fig.2.

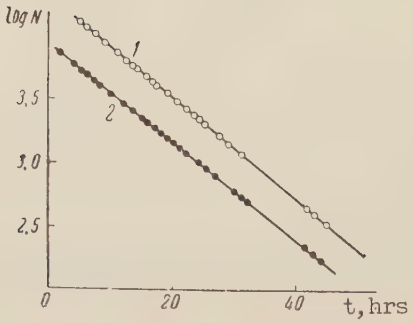

Fig.3.

Fig.2. Ho^{160m} decay curves: 1) T = 4.73 ± 0.10 hrs based on data of the first counter, 2) T = 4.79 ± 0.10 hrs based on data of second counter, 3) T = 4.77 ± 0.10 hrs based on data of third counter.

Fig.3. Tm^{166} decay curves: 1) T = 7.68 ± 0.10 hrs based on data of first counter, 2) T = 7.80 ± 0.08 hrs based on data of second counter.

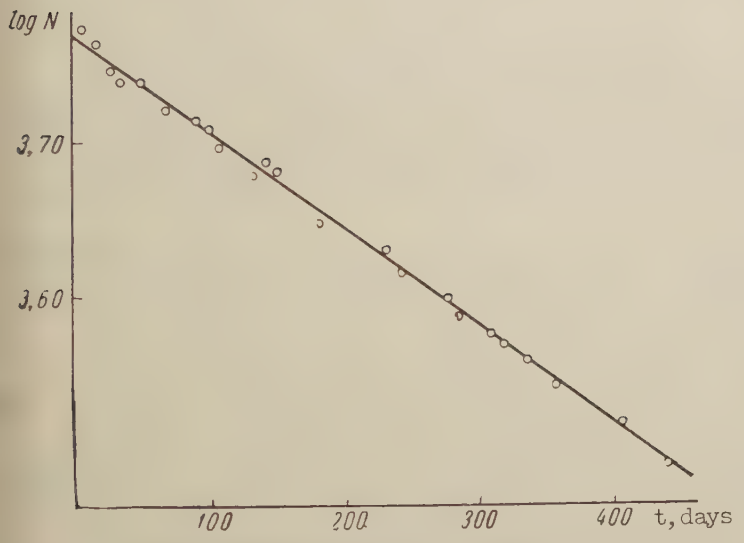

Fig.4. Lu^{173} decay curve: T = 480 ± 30 days.

Ho^{160m}

The spectrum of Ho^{160m} has been thoroughly investigated by a number of authors; however, the values reported by different authors differ appreciably (Table 1). Hence we felt it would be of interest to obtain an accurate value of the half-life. Our Ho^{160m} source was prepared by repeat separation of this isotope from the erbium fraction. Inasmuch as the only long-lived isotope in the erbium fraction was Er^{160} (T = 30 hrs), it was the only impurity evinced in the activity of our Ho^{160m} source. Having measured the decrease in the counting rate over a period of 2 weeks, it was easy to take into account the effect of this impurity.

Table 1

Period of Ho^{160m} according to the data of different authors

	Ref.6*	Refs. 7-10	Ref. 11	Ref.4	Our data
T,hrs	4.6 ± 0.1	5.0	5	5.3 ± 0.2	4.76 ± 0.10

The mean value obtained from three series of measurements is T = 4.76 ± ± 0.10 hrs. The decay curves are shown in Fig.2.

*Wilkinson & Hicks[6] erroneously attributed the 4.6 hr activity to Ho^{161}.

Tm^{166}

Since the rather accurate determination of the period of Tm^{166} by Wilkinson & Hicks[12] other investigators of this isotope did not pay particular attention to determining its half-life. The values

Table 2

Period of Tm^{166} according to the data of different authors

	Ref.12	Refs. 7,13	Ref. 14	Our data
T,hr	7.7 ± 0.1	7.7	8	7.74 ± 0.08

obtained by Wilkinson & Hicks and other authors together with our data are shown in Table 2.

Our source was free of impurities inasmuch as it was obtained as a result of repeat separation of Yb and Tm. That any possible admixture of Yb isotopes was insignificant is proved by the fact that after complete decay of the Tm^{166} insertion of the source yielded no appreciable increase of the counter background. The decay curves are shown in Fig.3.

Lu^{173}

Table 3

Periods of Lu^{173} according to the data of different authors

	Ref.10	Ref.15	Ref.16	Ref.14	Ref.17	Ref.18	Our data
T,days	510	500	480	200	150-200	160	480 ± 30

Our measurements on Lu^{173} were started 9 months after bombardment of the tantalum target and separation of the lutetium fraction, when all the short-lived isotopes had completely decayed. Before starting the measurements we again purified the lutetium to remove possible impurities. Measurements extended over a period exceeding 1 year. The result is shown in Table 3; the decay curve is given in Fig.4.

We also recorded the γ-spectrum of Lu^{173} by means of a scintillation spectrometer. The spectrum is shown in Fig.5. It agrees with the spectrum of Lu^{173} given by Gorodinskii et al[14].

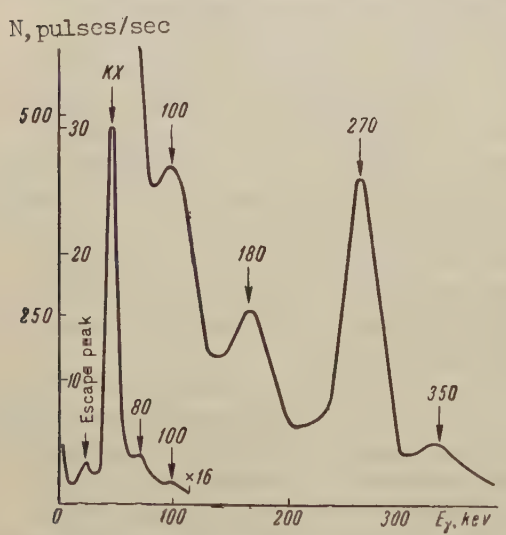

Fig.5. Gamma-spectrum of Lu^{173}.

It will be evident from Table 3 that there is an appreciable difference between the values of the period obtained in the investigations listed under Refs.10, 15 & 16 and the values found in investigating the lutetium fraction separated from a proton bombarded tantalum target (Refs.14, 17 & 18). It will be noted, however, that our results are close to the data of the first group of studies and differ appreciably from the results obtained in the investigations carried out in the Radium and Physical-Technical Institutes in Leningrad. Possibly underestimated values were obtained in the work of Refs.17 & 18 owing to loss of active material due to crumbling or flaking of the source, inasmuch as we understand that in these experiments no special measures to prevent such loss were taken.

Scientific Research Physical Institute,
"A.A.Zhdanov" Leningrad State University

References

1. F.D.S.Butement, Proc.Phys.Soc., A,64, 428 (1951).
2. B.H.Ketelle, Phys.Rev., 80, 758 (1950).
3. B.H.Ketelle & A.R.Brosi, Phys.Rev., Letters, 3, 407 (1959).
4. B.S.Dzhelepov, B.K.Preobrazhenskii, I.M.Rogachev & L.A.Tishkin, Izv. AN SSSR, Ser.fiz., 21, 962 (1957). (Trans.Bulletin, 21, 964.)
5. E.P.Grigor'ev, B.S.Dzhelepov, A.V.Zolotavin, B.Kratsik & G.Bitterlikh, Ibid., 23, 868 (1959). (Trans.Bulletin, 23, 859.)
6. G.W.Wilkinson & H.G.Hicks, Phys.Rev., 79, 815 (1950).
7. W.E.Nervik & G.T.Seaborg, Phys.Rev., 79, 815 (1950).
8. J.W.Mihelich & B.Harmatz, Phys.Rev., 106, 1232 (1954).
9. T.H.Handley, Phys.Rev., 94, 945 (1954).
10. J.W.Mihelich, B.Harmatz & T.H.Handley, Phys.Rev., 108, 989 (1957).
11. G.M.Gorodinskii, A.N.Murin, V.N.Pokrovskii & B.K.Preobrazhenskii, Izv. AN SSSR, Ser.fiz., 21, 1624 (1957). (Trans.Bulletin, 21, 1611.)
12. G.Wilkinson & H.G.Hicks, Phys.Rev., 75, 1370 (1949).
13. M.Michel & D.Templeton, Phys.Rev., 93, 1422 (1954).
14. G.M.Gorodinskii, A.N.Murin, V.N.Pokrovskii & B.K.Preobrazhenskii, Izv. AN SSSR, Ser.fiz., 21, 1004 (1957). (Trans.Bulletin, 21, 1005.)
15. G.Wilkinson & H.G.Hickes, Phys.Rev., 81, 340 (1951).
16. J.W.Bichard, J.W.Mihelich & B.Harmatz, Phys.Rev.Letters, 3, 451 (1959).
17. B.K.Preobrazhenskii, Yu.G.Bobrov, K.Ya.Gromov & B.S.Dzhelepov, Izv.AN SSSR, Ser.fiz., 21, 940 (1957). (Trans.Bulletin, 21, 942.)
18. V.Romanov, M.Iodko & V.Tuchkevich, Transactions of the Second Conference on Neutron-Deficient Rare Earth Isotopes, Vol.3, p.108, Dubna, 1960.

GAMMA-SPECTRA OF THE TANTALUM ACTIVITY FORMED BY PROTON BOMBARDMENT OF TANTALUM

- E.P.Grigor'ev, O.V.Larionov, M.K.Nikitin, S.L.Sakharov & V.O.Sergeev

The investigated activity was obtained by bombarding a tantalum target with 660 Mev protons in the Joint Institute for Nuclear Research synchrocyclotron. The tantalum was first separated from the nuclear reaction products, mainly rare earths and hafnium, and then repurified chemically. The radioactive tantalum isotopes were investigated on the automatic scintillation γ-spectrometer described in Ref.1.

The observed γ-lines can be divided into two groups on the basis of their periods.

The intensity of the 115 kev line at first fell off rather rapidly ($T \approx 8$ hr) and then with a period of 58 ± 10 hr. Corresponding components were also observed in the x-radiation. Comparing these results with the data on tantalum isotopes in the literature, one can attribute these lines to the decay of 53 hr Ta^{177}. According to Mann et al[2] and Felber[3] the most intense line in the γ-radiation of this isotope is located at 113 kev.

The intensity of the strongest γ-lines in the spectrum of the tantalum fraction fell off with a period of 8-11 hr. The line energies and relative intensities are listed in Table 1; the spectrum up to 400 kev is shown in Fig.1.

Table 1

Energies and relative intensities of Ta isotopes decaying with a period of 8-11 hr

E_γ, kev	55 (KX)	115 ± 5	210 ± 10	270	350	500	1150	1700
I_γ	100	10	7	2	2	0.3	0.7	0.3

Two tantalum isotopes with close periods are known, namely, 8 hr Ta^{176} (Refs. 3 & 4) and 11 hr Ta^{175} (Ref.5). We could not assign the lines observed in the energy regions to 1500 kev to a definite isotope owing to complexity of the spectrum and the inadequate resolution of our instrument. On the basis of comparison of our data with the results of Felber[3] and Mihelich et al[5] it may be asserted that both isotopes were present in our tantalum fraction.

Table 2

Energies and relative intensities of the hard γ-lines of the 8 hr tantalum isotope

E_γ, Mev	1.7	2.2-2.3	2.7	2.8
I_γ	3	1	0.3	1

We investigated the high energy part of the γ-spectrum to 3.5 Mev particularly thoroughly, using several different sources.

It was established that the intensity of different sections of the spectrum in the energy region above 1.5 Mev fell off with the same period: $T = 8 \pm 1$ hr. This section of the γ-spectrum is shown in Fig.2. We carried out a resolution of the γ-spectrum into components on the basis of the recorded shapes of the following lines: Th 2.614 Mev, Na^{24} 1.37 & 2.76 Mev and Zn^{65} 1.12 Mev. The results of this analysis are given in Table 2.

On the basis of their period the high energy γ-lines may be attributed to the decay of Ta^{176}. Hitherto only two lines with energies of 88.3 and 202.1 kev have been observed[3] in the spectrum of Ta^{176}. In view of the fact, however, that according to the tables of Cameron[6] and Riddel-Levy[7] the Ta^{176} - Hf^{176} mass difference is 3437 or 2722 kev, one can expect population of high-lying levels in Hf^{176}.

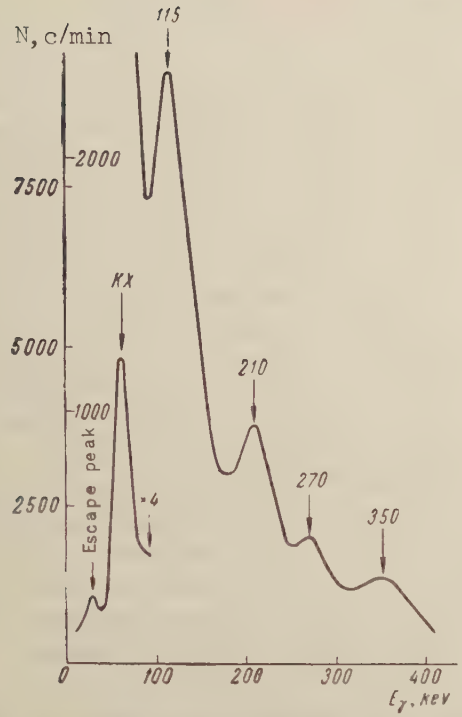

Fig.1. Gamma-spectrum of the tantalum fraction (E_γ to 400 kev).

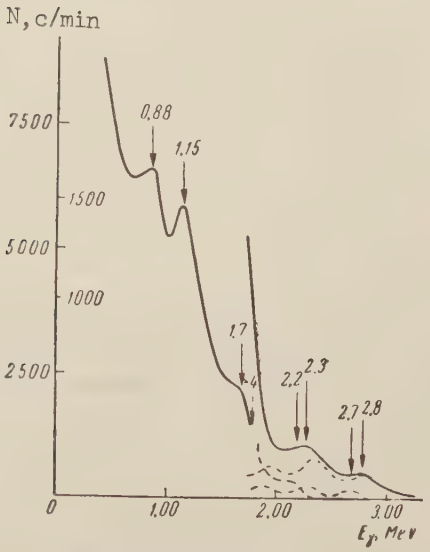

Fig.2. Gamma-spectrum of the tantalum fraction (E_γ to 3.1 Mev).

high energy γ-lines to the decay of Ta^{176}. On the other hand, the Ta^{175} - Hf^{175} mass difference according to Cameron and Riddel is only 1.8 Mev. This supports our assignment of the Accepting this assignment, the Ta^{176} - Hf^{176} mass difference evaluated on the basis of our data on the spectrum of Ta^{176} should be greater than 3 Mev.

Elaboration of the decay scheme for Ta^{176} must await investigation of its conversion electron spectrum with a high resolution spectrometer.

Scientific Research Physical Institute,
"A.A.Zhdanov" Leningrad State University

References

1. Transactions of the Second Conference on Neutron-Deficient Rare Earth Isotopes, Vol.3, p.121, Budna, 1960.
2. L.Mann, R.Nagle & H.West, Bull.Amer.Phys.Soc., 2, 231 (1957).
3. F.F.Felber, Unpublished thesis (1956), cited in D.Strominger, J.M.Hollander & G.T.Seaborg, Revs.Mod.Phys., 30, 754 (1958).
4. G.Wilkinson, Phys.Rev., 80, 495 (1950).
5. J.W.Mihelich, B.Harmatz & T.H.Handley, Phys.Rev., 114, 1082 (1959).
6. A.G.W.Cameron, A Revised Semi-Empirical Atomic Mass Formula, Chalk River, 1957.
7. J.Riddel, A Table of Levy's Empirical Atomic Masses, Chalk River, 1957.

MEASUREMENT OF THE MEAN LIFETIME OF Lu^{175} IN THE 113.8 kev EXCITED STATE

- V.P.Bozhko, I.I.Zalyubovskii & A.I.Tutubalin

We measured the lifetime of the first excited state of Lu^{175}, which forms in β^--decay of Y^{175}, by means of the fast-slow coincidence circuit pictured in Fig.1. Inasmuch as this is a low-lying level and the intensity of the β-branch to it amounts to only 5% of the total number of disintegrations of Yb^{175} (Ref.1), exacting requirements are imposed on the experimental conditions, for it is necessary to distinguish soft β- and γ-radiations of low intensity against an intense high-energy background. Hence the channels of the equipment must have an adequate amplitude discrimination, and the coincidence circuit must have good time resolution with a high selection coefficient. In addition, there are the obvious difficulties connected with the short lifetime of Yb^{175} (4.2 days). In view of these difficulties, there have apparently been no direct measurements of the lifetime of the 114 kev state of Lu^{175}. Although de Waard[3] made an attempt to determine the lifetime, he obtained only an evaluation of the upper bound: $2 \cdot 10^{-9}$ sec.

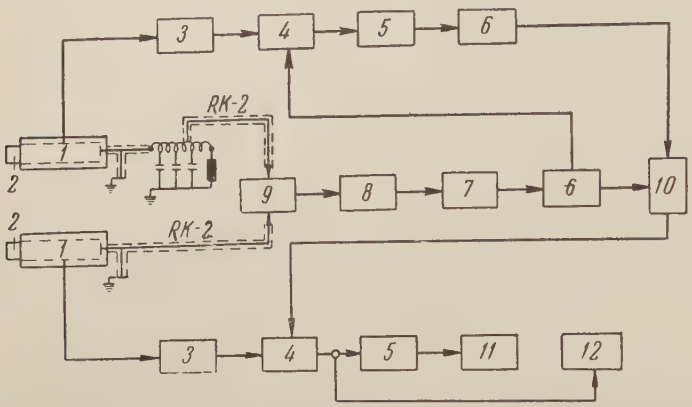

Fig.1. Fast-slow coincidence circuit: 1) FEU-33 photomultiplier, 2) stilbene crystal, 3) linear amplifier, 4) band-pass filter, 5) differential discriminator, 6) shaper, 7) discriminator, 8) amplifier, 9) fast coincidence register, 10) slow coincidence register and shaper, 11) counter, 12) multiple channel analyzer.

The radiation detectors employed in the present work were stilbene crystals (2 in Fig.1) coupled to FEU-33 photomultipliers. The crystal detecting the γ-radiation was not affected by β-particles inasmuch as these were stopped by an aluminum absorber. The crystal detecting β-particles had a thickness of 1 mm and was virtually insensitive to γ-rays. Thus the experimental conditions corresponded to the "nonsymmetrical case" described by Gol'danskii et al[3]. The potential on the photomultipliers was 3.8 kev, which insured the necessary pulse height. The pulses were shaped by shorted sections of RK-2 cable connected to the PM anodes. Equally narrow pulse height intervals were selected in both channels by means of differential discriminators (5).

Fig.2 shows the experimental delayed β-γ and γ-β coincidence curves. The self-comparison procedure employed automatically excludes systematic deviations introduced by the photomultipliers and the associated electronic equipment.[4] The separation between the centers of gravity of these delayed coincidence curves is equal to twice the lifetime of the level: 2τ. The statistical error in 2τ was determined by means of the expression

$$\Delta\tau = \sqrt{D_\tau}, \qquad (1)$$

where

$$D_\tau = \frac{1}{N}\left[\tau^2 + \frac{2}{\alpha}(\tau')^2\right]^*,$$

---

*See Ref.3.

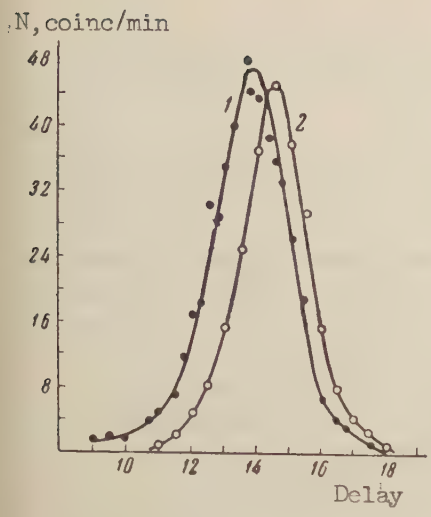

Fig.2. Delayed β-γ (1) and γ-β (2) coincidence curves. Each division on the horizontal scale equals $1.55 \cdot 10^{-9}$ sec.

wherein Π is the total number of counts for the entire curve, τ' is the resolving time for the given case and α is a coefficient that depends on the shape of the coincidence curve.

After correction for the statistical uncertainty and the error introduced by inaccuracy in calibrating the variable delay line, we obtained the following value for the period:

$$T = 0.692\tau = (3.6 \pm 0.6) \cdot 10^{-10} \text{ sec.}$$

It is impossible to find the lifetime of this level directly from the data of Coulomb excitation[5], inasmuch as de-excitation occurs by a mixed transition, so that one must have independent data on the proportion of the multipole mixture, the magnetic moment, and the internal and collective g factors. If one uses the data on the total conversion coefficient and reduced transition probability for the 114 kev level from the work of Martin et al[6], and the data of Hatch et al[7] and Bernstein[8], evaluations give approximately $1.1 \cdot 10^{-10}$ sec for the lifetime of this state. Following Martin et al, in these calculations the admixture of E2 is assumed to be 20%.

Using our value for T, we found the multipole order proportions to be 80% E2 + 20% M1. The calculations were carried out by means of the equation

$$\frac{1}{\tau_\gamma (M1+E2)} = \left(1 + \frac{1}{\delta^2}\right)(1+\alpha)\, T_\gamma (E2), \qquad (2)$$

where $\delta^2 = \frac{T_\gamma (E2)}{T_\gamma (M1)}$, T_γ is the γ-transition probability per sec, and α is the total conversion coefficient.

This proportion of E2 to M1 leads to a value for the gyromagnetic ratio g_k somewhat lower than that given by theory. The theory for a uniformly charged nucleus gives $g_k = Z/A \approx 0.41$. Such deviation of g_k to the side of lower values as compared with theory has been observed in a number of cases.[9]

Even now one can advance a tentative explanation for the tendency towards lower values of g_k for rotational levels such as, for example, the 114 kev level in Lu^{175}.

We still do not know precisely what character of motion in the nucleus leads to the presence of rotational states. Inasmuch as the gyromagnetic ratio is essentially the mean specific charge of the nucleons contributing to the energy of rotation, low values of g_k indicate that only part of the nucleons participates in the rotational motion. In order to determine how large this part may be it is necessary to carry out careful and systematic comparisons of the gyromagnetic ratios and moments of inertia of nuclei, obtained independently from experiments on Coulomb excitation and measurements of the lifetimes and magnetic moments of excited nuclei.

Physical-Technical Institute,
Academy of Sciences of the Ukrainian SSR

References

1. B.S.Dzhelepov & L.K.Peker, Skhemy raspada radioaktivnykh izotopov (Decay schemes of radioactive isotopes), M., 1958.
2. H.de Waard, Phil.Mag., 46, 445 (1955).
3. V.I.Gol'danskii, A.V.Kutsenko & M.I.Podgoretskii, Statistika otschetov pri registratsii yadernykh chastits (Counting statistics in detection of nuclear particles), M., 1959.
4. K.Siegbahn, Beta- and Gamma-Ray Spectroscopy. Amsterdam 1955. (Cited in Russian trans.); D.E.Berlovich, Izv.AN SSSR, Ser.fiz., 20, 1438 (1956). (Trans. Bulletin, 20, 1315.)
5. N.P.Heydenburg & G.M.Temmer, Phys.Rev., 104, 981 (1956).
6. M.Martin, P.Marmier & J.deBoer, Helv.Phys.Acta, 31, 435 (1958).
7. E.Hatch, F.Boehm, P.Marmier & J.M.DuMond, Phys.Rev., 104, 745 (1956).
8. E.M.Bernstein & H.W.Lewis, Phys.Rev., 105, 1524 (1957).
9. G.Goldring & R.P.Scharenberg, Phys.Rev., 110, 701 (1958).

* * * * * * *

GAMMA-RADIATION FROM Zr^{95} + Nb^{95}

- N.A.Voinova, B.S.Dzhelepov & N.N.Zhukovskii

We investigated the γ-radiation from Zr^{95} + Nb^{95} by means of the Elotron under standard conditions.[1] The activity was in the form of a 5 g sample of zirconium sulfate, $Zr(SO_4)_2$, obtained from fission products. The measurements were carried out with a source in which the 65 day Zr^{95} was approximately in equilibrium with its daughter, 35 day Nb^{95}. At the start of the measurements the activity of the source was ~0.8 curie.

The experimental recoil electron spectrum is shown in the accompanying figure. In the energy interval from 100 to 1200 kev there are evident only two lines with energies of 720 ± 5 and 762 ± 2 kev according to the calibration of our instrument. The half-width of the 720 kev line (~2%) within the limits of the statistical uncertainty is equal to the apparatus line width at this energy. This line belongs to Zr^{95} (Refs.2-7). The 762 kev line had an appreciably greater (~0.5%) width than the apparatus width. According to the data of other authors, there are observed in the 700 to 800 kev interval in the electron spectra of Zr^{95} and Nb^{95} K and L conversion lines associated with a 757 ± 2 kev transition in Zr^{95} (Refs. 4-6, 8 & 9) and a 767 ± 1 kev transition in Nb^{95} (Refs.3, 6, 8-13).

On the basis of our data it is impossible to resolve these two lines and evaluate their relative intensities.

After making appropriate corrections for self-absorption in the source, the spectral response and the decay of the Zr^{95} and Nb^{95} in the course of measurements, we arrived at a value of 0.14 ± 0.02 for the intensity ratio of the 720 and 762 kev γ-lines.

We observed no noticeable rise of the spectrum curve above the background in the energy region from 100 to 720 kev. If there are any lines in this energy region their intensity cannot be greater than 0.6% the intensity of the 762 kev line. In the energy region above 770 kev there are no lines with an intensity exceeding 0.5% the intensity of the 762 kev line.

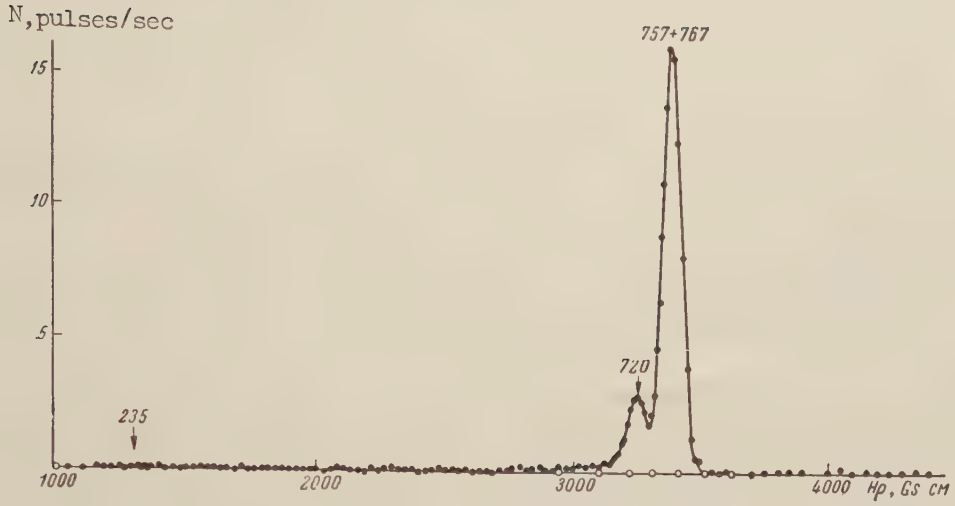

Recoil electrons ejected by the Zr^{95} + Nb^{95} γ-rays.

"V.G.Khlopin" Radium Institute,
Academy of Sciences of the USSR

References

1. B.S.Dzhelepov, N.Zhukovskii, S.Shestopalova & I.Uchevatkin, Nucl.Phys., 8, 250 (1958).
2. C.Mandeville, E.Shapiro, R.Mendenhal, E.Zucker & G.Conclin, Phys.Rev., 89, 559 (1953).
3. H.Slätis & L.Zappa, Arkiv Fys., 6, 81 (1953).
4. P.Mittelman, Phys.Rev., 91, 484 (1953).
5. P.Mittelman, Phys.Rev., 94, 99 (1954).
6. P.Zarubin, Izv.AN SSSR, Ser.fiz., 18, 563 (1954). (Trans.Bulletin, 18, 244.)
7. R.Rhor & R.Birkhoff, Phys.Rev., 98, 1266 (1955).
8. J.Cork, J.Le Blanc, D.Martin, W.Nestor & M.Brice, Phys.Rev., 90, 579 (1953).
9. G.Drabkin, V.Orlov & L.Rusivov, Izv.AN SSSR, Serif.z, 19, 324 (1955). (Trans.Bulletin, 19, 294.)
10. R.Maerker & R.Birkhoff, Phys.Rev., 89, 1159 (1953).
11. E.Strucken & A.Weber, Phys.Rev., 91, 484 (1953).
12. E.Strucken, Z.O'Friel & A.Weber, Phys.Rev., 93, 1053 (1954).
13. K.Johnson, Arkiv Fys., 10, 247 (1956).

GAMMA-RADIATION FROM Tb^{160}

- N.A.Voinova, B.S.Dzhelepov, N.N.Zhukovskii & Yu.V.Khol'nov

The γ-radiation from Tb^{160} was investigated by means of two recoil electron spectrometers, namely, the Ritron and the Elotron. The source was 0.46 g terbium oxide, the initial activity of which was ~800 mC.

The 80 to 300 kev section of the spectrum was investigated on the Ritron (modified as described in Ref.1) by observing photoelectrons. The radiator was a bismuth target with a superficial density of 3.7 mg/cm^2.

In Fig.1 one can clearly discern the following photoelectron lines: L-86, K-196, K-214, K-298 and L-298. The deviation of the left-hand side of the K-298 line from the standard line shape may be due to the presence of K-253 and K-276 lines in the spectrum.

The 200 to 1700 kev interval of the spectrum was investigated by observing recoil electrons under the usual operating conditions for the Elotron and Ritron (Refs.1 & 2). The experimental curves are shown in Figs.2 & 3.

In the recoil electron spectrum obtained on the Elotron (Fig.2) there are evident 11 peaks: of these only the peaks having energies of 298, 392, 1003 and 1311 kev, according to our calibration, have a width close to the apparatus width. The experimental 765, 880, 965, 1113, 1179 and 1274 kev lines are 0.6, 0.3, 0.4, 0.2, 0.2 and 0.4%, respectively, wider than the corresponding apparatus lines. We assume that the broadening of these lines is due to low intensity γ-rays having close energies.

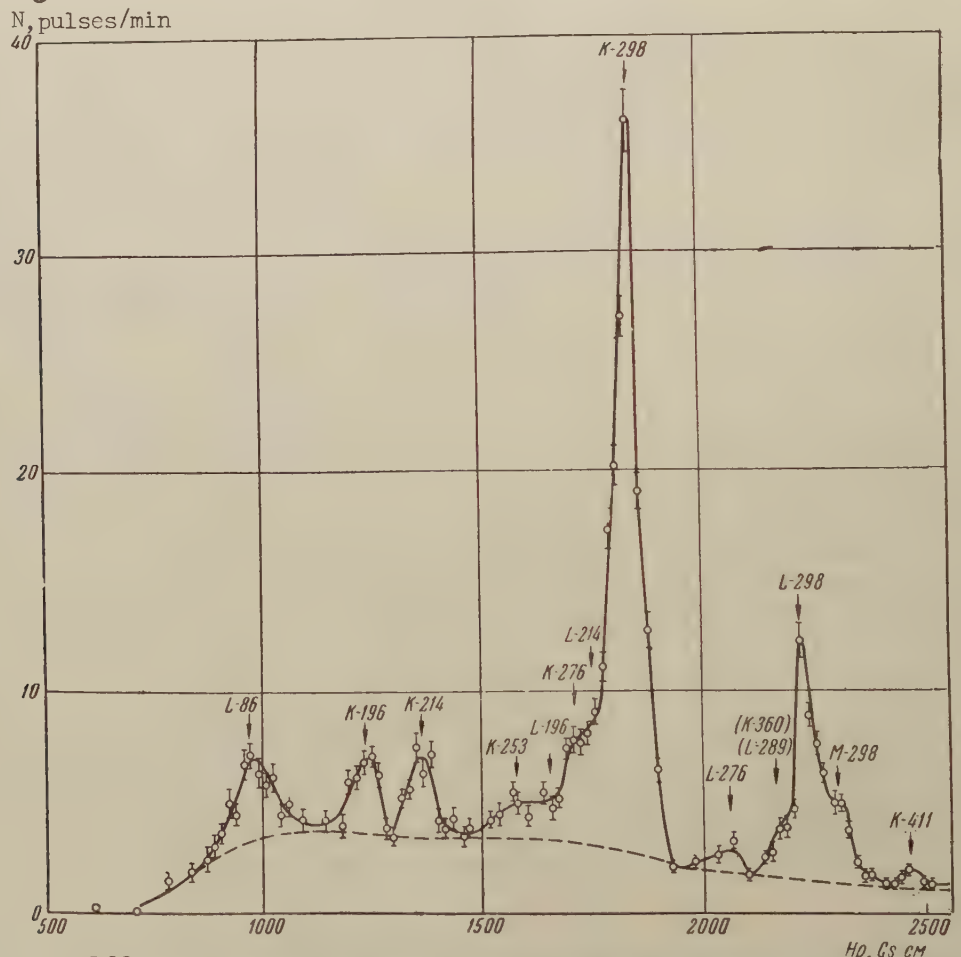

Fig.1. Tb^{160} photoelectron spectrum obtained by means of the Ritron.

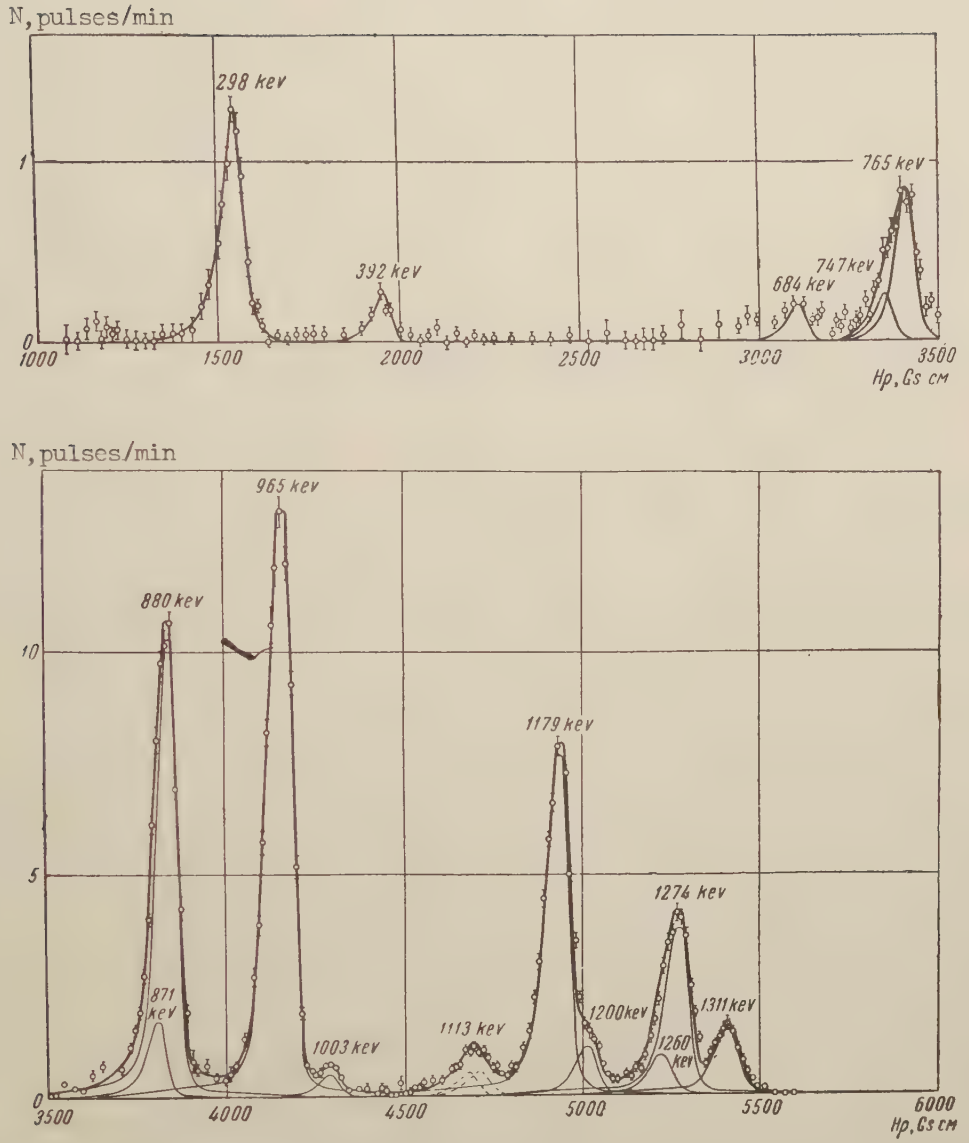

Fig.2. Tb^{160} recoil electron spectrum obtained by means of the Elotron.

In the 650-770 kev energy region, according to the data of Bäckström et al[3], there are γ-lines with energies 681 and 764 kev. In this energy interval we distinguished a γ-line with $h\nu$ = 684 kev. The section of the spectrum corresponding to the 765 kev line may be represented as the sum of two γ-lines with energies of 747 and 765 kev.

In the work of Grigor'ev et al[4] there are indications that in the conversion electron spectrum of Ho^{160} there are evinced K and L conversion lines associated with two transitions having energies of 873 and 880 kev. We inscribed an 880 kev energy apparatus line into the experimental curve at 880 kev; the excess of recoil electrons on the left side of this line corresponds to a line due to 871 kev γ-rays.

The observed 965 kev γ-line is undoubtedly comprised of the two known Tb^{160} γ-lines: 962.5 and 966.3 kev, the intensity ratio of which, according to Bäckström et al[3] who observed photoelectrons, is 1:2.3.

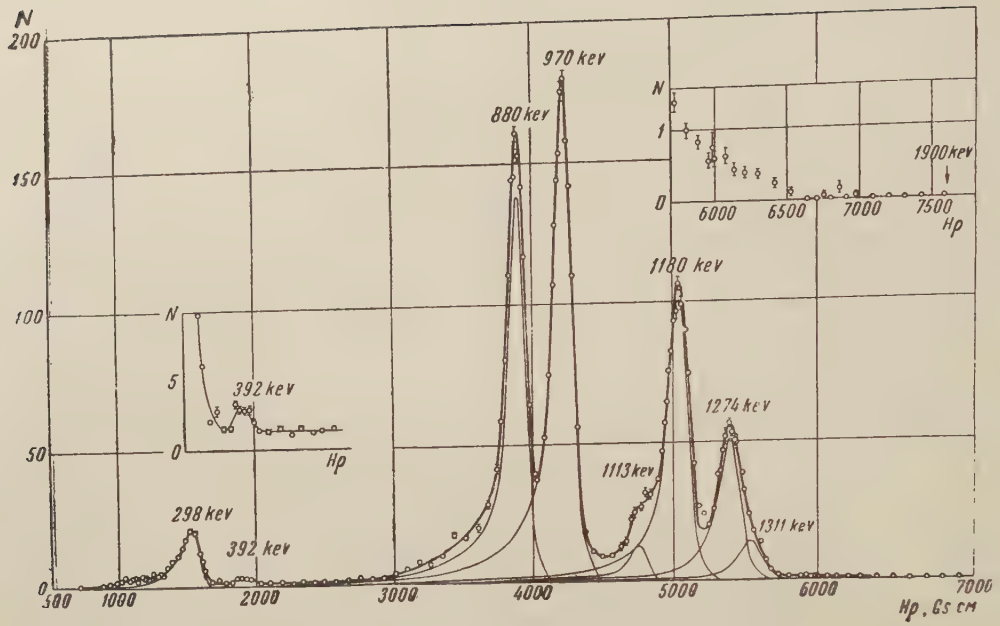

Fig.3. Tb^{160} recoil electron spectrum obtained on the Ritron.

On the right-hand side of the 965 kev line there is a minor rise which we attribute to 1003 kev γ-rays. These γ-rays have not been hitherto observed.

The 1113 kev line (energy value according to our calibration) is located on the left-hand side of the intense 1179 kev line. As resolved, the width of the 1113 kev line is approximately 0.2% greater than the width of the corresponding apparatus line. It may be assumed, therefore, that it consists of two lines of close energies. Accordingly, we inscribed into the experimental plot two lines on the assumption that the energy of one of them is 1115.0 ± 1.7 kev (Bäckström et al[3]); we then obtained an energy of 1110 ± 5 kev for the second line. The best agreement with experiment is obtained if it is assumed that the intensities of these two lines are approximately equal.

On the right-hand side of the 1179 kev line there is clearly evinced a line with $h\nu$ = 1200 kev. The 0.4% broadening of the 1274 kev line is presumably due to the presence of γ-rays with $h\nu$ = 1260 kev. No γ-rays of this energy have hitherto been observed in the radiation from Tb^{160}.

Fig.3 shows the recoil electron spectrum obtained under higher luminosity conditions on the Ritron. There are evident six peaks located at 298, 392, 880, 970, 1180 and 1274 kev.

In the Hρ = 5900 to 6000 region there is some rise of the experimental points above the background. In this region, according to Keshishian et al[5], there are γ-rays with an energy of 1447 kev. On the basis of our data, we can only evaluate the upper bound for the intensity of these γ-rays: 0.2% the intensity of the 965 kev γ-rays. A special search carried out by means of the Ritron showed that if there are any γ-rays in the 1450 to 1900 kev region their intensity does not exceed 0.05% the intensity of the 965 kev γ-line.

Thus, through analysis of the experimental curves (Figs.1-3) we distinguished 17 γ-lines and determined their relative intensities. There are reports in the literature regarding the existence in the spectrum of Tb^{160} of a number of other very weak lines. For some of these we could only evaluate the upper intensity bound.

Energies and relative intensities of the Tb^{160} γ-lines

No.	Our data				Ref. 4		Ref. 3		Ref. 6	Ref. 7	Ref. 8	Ref. 9	Ref. 10	Ref. 11	
	$h\nu$, kev	Elotron recoils	Ritron recoils	Ritron photo-electrons	$\pi\sqrt{2}$ spectr. photoelectron		$\pi\sqrt{2}$ spectr. photoelectron		Scintillation spectrometers					Scint. spectr. crystal diffraction spect. & photoelectrons	
		I_γ			$h\nu$, kev	I_γ	$h\nu$, kev	I_γ	I_γ					$h\nu$, kev	I_γ
1	2	3	4	5	6	7	8	9	10	11	12	13	14	15	16
1	86	—	—	31±5	—	—	86,8±0,3	—	35	38	28	38	—	86,7	38,3
2	—	—	—	—	—	—	94,3±0,6*	0,3	—	—	—	—	—	—	—
3	196	<20	—	7±2	196,1±1,0	10±2	197,0±0,4	—	15	12	23	11,5	(11) 22	197	12,6
4	214		—	7±2	215±1	9	215,6±0,4	—	—	10	—	9	(11)	216	9,8
5	(253)	<2	—	2±2	—	—	—	—	—	—	—	—	—	—	—
6	(276)	—	—	7±3	—	—	—	—	—	—	—	—	—	—	—
7	298±2	77±8	86±6	86±6	297,8±1,0	62±12	298,6±0,4	—	41	74	85	77	44	299	75,4
8	392±5	9±2	3±1	—	—	—	394,5±1,0	—	—	—	8,5	—	2	393	~2,8
9	684±4	2,1±0,8	—	—	—	—	681±2*	1,5	—	—	—	—	2	—	—
10	747±10	2,5±1,0	—	—	—	—	—	—	—	—	—	—	—	—	—
11	765±3	8±1	—	—	—	—	64±2*	—	—	—	—	—	—	765	≤6
12	871±5	(13)	87±6	—	—	—	—	—	100	84	94	85	105	880	85,5
13	880±2	(81) 94±5		—	878±1	77±12	879,3±0,2	94							
14	965±3	100 (33)	100	—	963	100	962,5±0,4	28	100	100	100	100	100 (5	962	30,7 100
15		(67)		—	967		966,3±0,3	66					95)	966	69,8
16	—	—	—	—	~985	<4	—	—	—	—	—	—	—	—	—
17	1003±5	2,8±0,5	—	—	—	—	—	—	—	—	—	—	—	—	—
18	~1070	<5	—	—	~1070	<6	—	—	—	—	—	—	5	—	—
19	1113±5 (1110±5	~2,7	6±2	—	—	—	—	—	—	—	—	—	—	—	—
20	1115±2)	~3 5,7±1,5		—	1112±2	5	1115,0±1,7	4,9	—	—	—	—	—	—	—
21	1179±2	43±3	49±2	—	1178±2	44±9	1177,6±0,3	43	74	43	45	42	50	1179	43,6
22	1200±10	6±3 49±3	~3	—	1201±2	6±1	1199,9±0,8	7,5						1205	7,3
23	1260±10	5 24±2	25±2	—	—	—	—	—	32,5	23	23	23	23	1273	23,7
24	1274±3	19		—	1273±2	24±5	1272,3±0,4	—							
25	1311±2	7,3±1,1	6±2	—	1314	7	1312,4±0,8	6	—	—	—	—	—	1315	9,5
26	1447	—	<0,2	—	—	—	—	—	—	—	—	—	—	—	—

*These γ-rays were detected by observing conversion electrons.

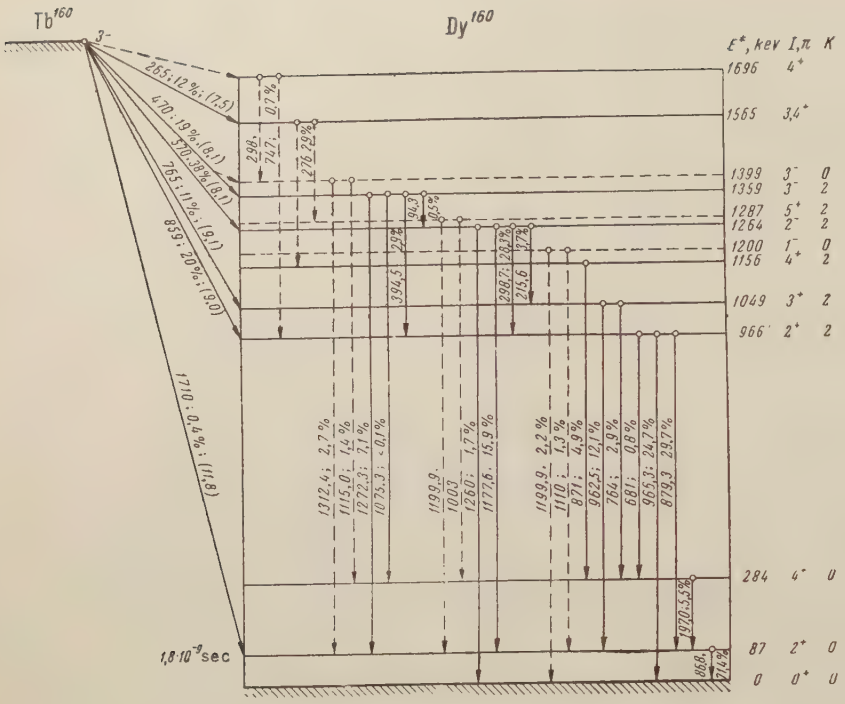

Fig.4. Decay scheme for Tb^{160}.

The evaluated energies and relative intensities of the observed γ-lines are listed in the accompanying table, together with the experimental data of other authors. Until now there have not been available reliable data on the relative intensities of the γ-rays accompanying the decay of Tb^{160} in the entire energy range: the data obtained by means of scintillation spectrometers[6-11] are not accurate owing to the low resolution characteristics of such instruments; the relative intensities deduced from photoelectron observations by Grigor'ev et al[4] comprise an appreciable uncertainty (up to 16-20%).

All the γ-lines observed in our experiments fit into the level diagram for Dy^{160} (Fig.4) constructed on the basis of investigations of Tb^{160} and Ho^{160}. The experimental evidence that the γ-spectrum of Tb^{160} includes an 871 kev line gives reason to infer that the transition between the 1156 and 284 kev levels of Dy^{160} is observed not only in the decay of Ho^{160} (Ref.4) but also in the decay of Tb^{160}.

The new 1003 kev line discovered by us can be inserted in the scheme between the 1287 and 284 kev levels.

The intensity balance for all levels is satisfactory: the average discrepancy does not exceed 5%. The greatest divergences are obtained for the high-lying levels, which may be attributed to the lack of accurate data on the intensities of the β-transitions feeding these levels.

"V.G.Khlopin" Radium Institute,
Academy of Sciences of the USSR

References

1. B.Dzhelepov, V.Prikhodtseva, A.Feoktistov & Yu.Khol'nov, Izv.AN SSSR, Ser.fiz., 20, 1361 (1956). (Trans.Bulletin, 20, 1245.)

2. B.Dzhelepov, N.Zh8kovskii, S.Shestopalova & I.Uchevatkin, Ibid., 22, 841 (1958). (Trans.Bulletin, 22, 835.)

3. G.Bäckström, J.Lindskog, O.Bergman, E.Bashandy & A.Bäcklin, Arkiv.Fys., 15, 121 (1959).

4. E.Grigor'ev, B.Dzhelepov, A.Zolotavin, O.Kraft, B.Kratsik & L.Peker, Izv. AN SSSR, Ser.fiz., 22, 101 (1958). (Trans.Bulletin, 22, 99); G.Bitterlikh, E. Grigor'ev, B.Dzhelepov, A.Zolotavin & B.Kratsik, Program and abstracts, Ninth Annual Conference on Nuclear Spectroscopy, M.-L., 1959; E.P.Grigor'ev, B.S.Dzhele-

pov, A.V.Zolotavin, B.Kratsik & G.Bitterlikh, Izv.AN SSSR, Ser.fiz., 23, 868 (1959). (Trans.Bulletin, 23, 859.)
5. V.Keshishian, H.Kruse, R.Klotz & C.Fowler, Phys.Rev., 96, 1050 (1954).
6. H.Jaffe, NSA, 9, 24B, 95 (1955).
7. H.Thiry, Bull.Roy.Soc.Liege, 26, 29 (1957).
8. O.Nathan, Nucl.Phys., 4, 125 (1957).
9. M.Clark & J.Knowles, BAPS, 11, 2, 231 (1957).
10. Ofer, Nucl.Phys., 5, 331 (1958).
11. M.A.Clark, Canad.J.Phys., 38, 262 (1960).

* * * * * * *

DETERMINATION OF LEVEL SPINS AND PARITIES FROM INELASTIC SCATTERING AND THE PICK-UP REACTION ON Be^9

- O.F.Vemets, L.S.Saltykov, M.V.Sokolov & Yu.V.Tsekhmistrenko

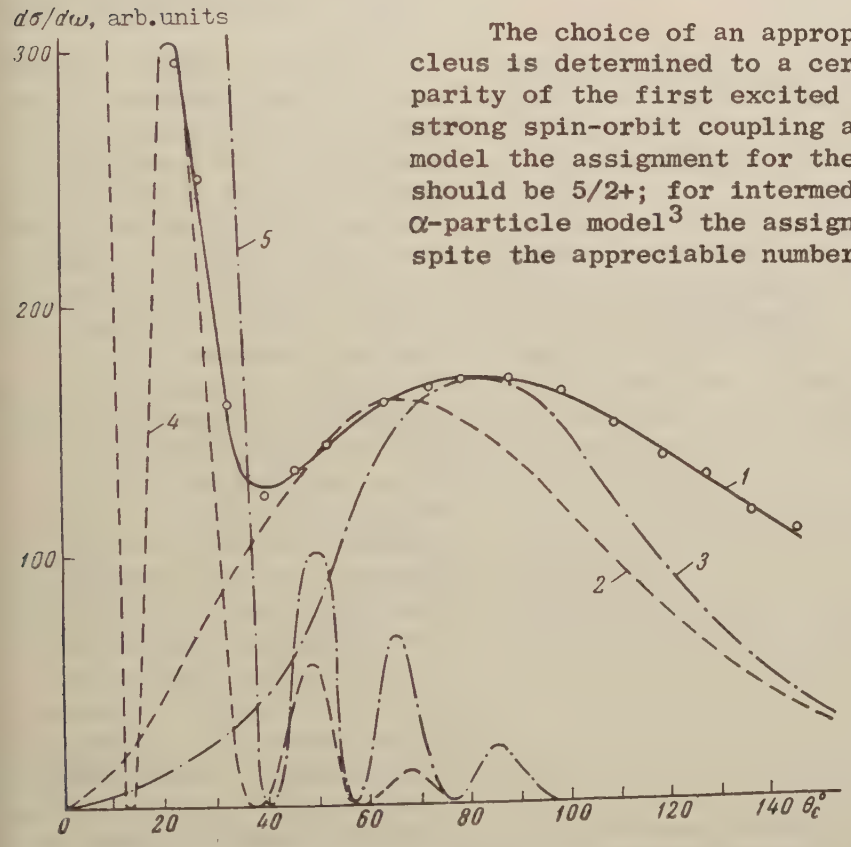

Fig.1. Angular distribution of inealstically scattered protons, Q = -2.43 Mev; 1 - experimental data. Theoretical curves: 2 - direct interaction of the incident proton with one nucleon of the nucleus[6]; 3 - excitation of rotational levels in the α-particle model[7] of Be^9; 4 - dipole electric interaction[8]; 5 - quadrupole electric interaction[8].

The choice of an appropriate model for the Be^9 nucleus is determined to a certain extent by the spin and parity of the first excited level. For the case of strong spin-orbit coupling according to the Klinkenberg[1] model the assignment for the first excited level of Be^9 should be 5/2+; for intermediate coupling[2] and for the α-particle model[3] the assignment should be 5/2-. Despite the appreciable number of studies devoted to the spin and parity of the 2.43 Mev level, so far these parameters have not been definitively established, which is what led us to investigate the angular distribution of inelastically scattered 6.8 Mev protons and 13.6 Mev deuterons from this nucleus.

The (p,d) and (d,t) reactions were investigated for elucidating the nature of the mechanisms involved at the indicated proton and deuteron energies.

The deuteron and molecular hydrogen ion beams were obtained from the cyclotron of the Institute of Physics of the Ukrainian SSR Academy of Sciences. The experimental geometry and the scattered deuteron and triton detector in the

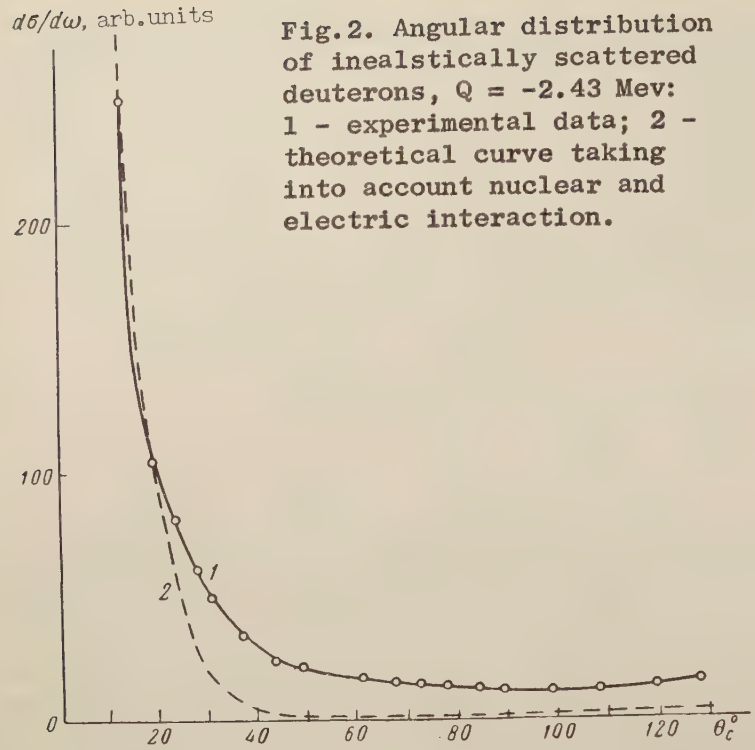

Fig.2. Angular distribution of inealstically scattered deuterons, Q = -2.43 Mev: 1 - experimental data; 2 - theoretical curve taking into account nuclear and electric interaction.

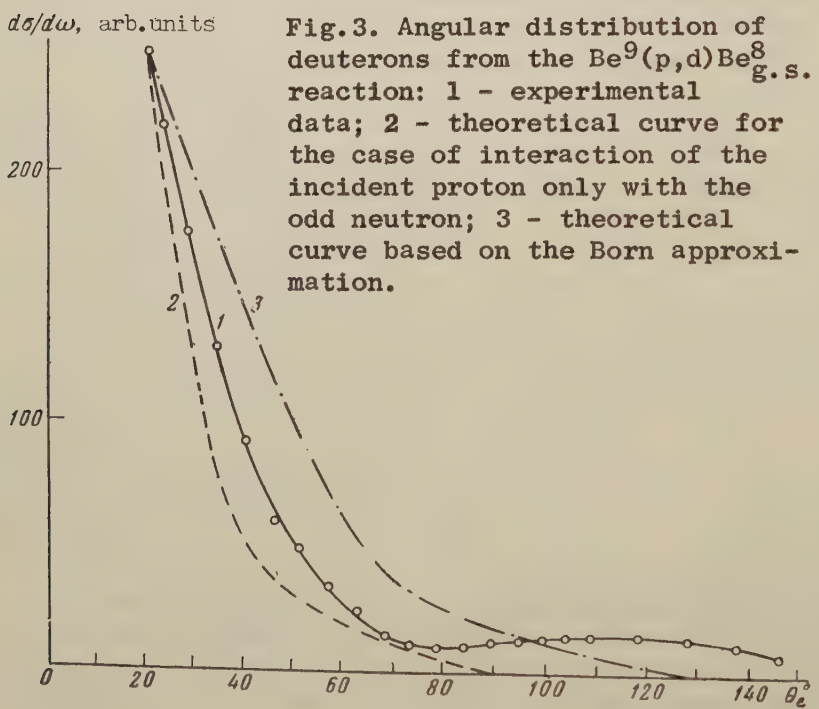

Fig.3. Angular distribution of deuterons from the $Be^9(p,d)Be^8_{g.s.}$ reaction: 1 - experimental data; 2 - theoretical curve for the case of interaction of the incident proton only with the odd neutron; 3 - theoretical curve based on the Born approximation.

case of the (d,t) reaction were the same as in the work of Ref.4; the inelastically scattered protons and deuterons from the (p,d) reaction were recorded by means of a scintillation spectrometer.

Fig.1 shows the angular distribution of inelastically scattered protons together with the results of calculations based on direct interaction of the incident proton with one nucleon of the nucleus, excitation of rotational levels in the α-particle model,[7] and electric interaction[8] (dipole and quadrupole).

In the range of small angles best agreement with experiment is given by curve 4, corresponding to dipole electric interaction, although the values of the effective radius proved to be very large (r = 20.4 f). In the region of large angles, however, no satisfactory agreement with theory is obtained.

The angular distribution of inelastically scattered deuterons is given by curve 1 in Fig.2. The rise in the region of small angles (if one does not assume an anomalously large radius) can be due only to electric interaction; hence for explaining the angular distribution we consider jointly the effects of electric and direct nuclear interactions.

Because of interaction of the neutron with the nuclear core one can attribute to it an effective electric charge αe; then the interaction of the odd neutron in Be^9 with the proton in D_2O will be described by Coulomb's law, while the interaction with the neutron can be described by means of an effective δ-type potential.

Given the above assumptions, the cross section for the final state of Be^9 with $l = 2$ will be

$$\sigma(\theta) \approx \frac{1}{k^2} \operatorname{arc\,tg}^2 \frac{k}{4\gamma} \left\{ e^{-\frac{16\,k^2}{81 M\omega}} \left(1 - \frac{32\,k^2}{405\,M\omega}\right) + \xi \left[\frac{\sin\left(\frac{8}{9} kR\right)}{\frac{8}{9} kR} - \cos\left(\frac{8}{9} kR\right)\right] \right\}^2, \qquad (1)$$

where $\gamma = \sqrt{M\varepsilon_b}$, ω is a parameter of the oscillator potential acting on the outer nucleon in Be^9, and ξ is an empirical parameter.

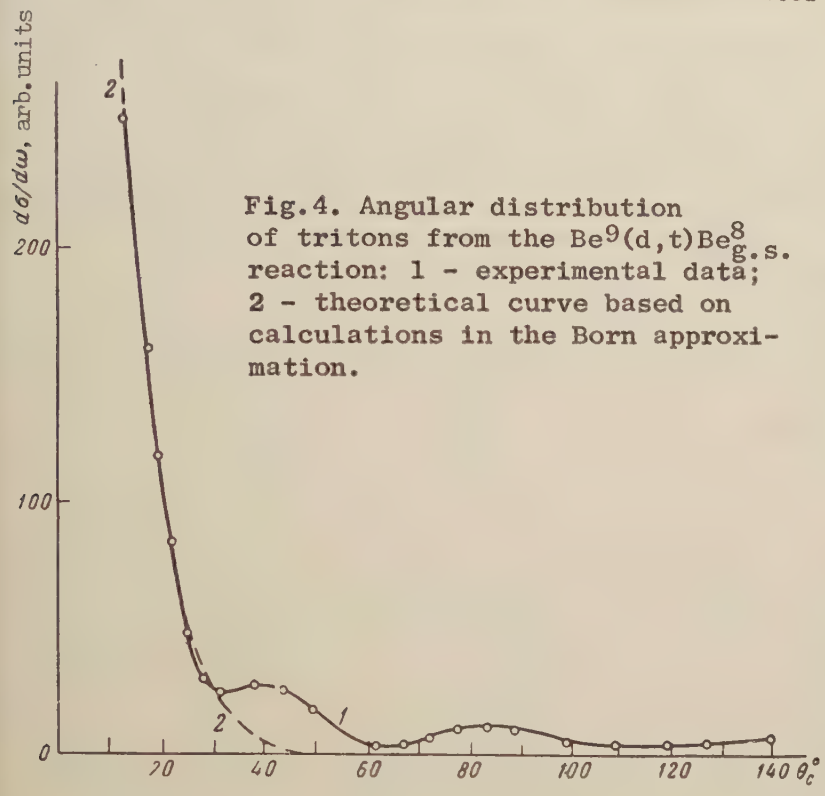

Fig.4. Angular distribution of tritons from the $Be^9(d,t)Be^8_{g.s.}$ reaction: 1 - experimental data; 2 - theoretical curve based on calculations in the Born approximation.

Curve 2 in Fig.2 corresponds to ω = 3 Mev, R = 4f and ξ = 0.01. On the assumption that $l_к$ = 3, no satisfactory agreement with experiment can be obtained.

Thus it follows from inelastic scattering of protons (Δl = 1) and from inelastic scattering of deuterons ($l_к$ = 2) that the spin and parity of the 2.43 Mev level are 5/2+.

The experimental angular distribution of deuterons from the (p,d) reaction is shown by curve 1 in Fig.3; curve 2 gives the results of calculations for the case when the incident proton interacts only with the unpaired neutron[9]; curve 3 gives the results for calculations carried out in the Born approximation[10]. The value of l_n in both cases was taken equal to 1 in accord with the known spins of Be^9 and Be^8 (3/2- and 0+, respectively).

The results of investigation of the (d,t) reaction are given by curve 1 in Fig.4. As in the case of the (p,d) reaction, there can be no doubt regarding the direct mechanism of the process (this is substantiated by the results of observations at other deuteron energies[11-14]).

In the Born approximation (for a triton function of simple form) the angular distribution for interaction of the deuteron with a neutron in the 3/2 state is

$$\sigma(d,t) \approx \frac{1}{k^2} \operatorname{arc\,tg}^2 \frac{k}{4\gamma}\, j_1^2(k_1 R)\, \frac{1}{(k^2+\gamma^2)^2}, \qquad (2)$$

where

$$k = \frac{2}{3} k_t - k_b; \quad k_1 = k_t - \frac{8}{9} k_b; \quad \gamma = \sqrt{M_p \cdot \varepsilon_b}; \quad \varepsilon_d = 2.23 \text{ Mev}.$$

Results of calculations in this approximation are given by curve 2 in Fig.4.

The writers desire to express their gratitute to M.V.Pasechnik for his interest in the work, Yu.A.Bin'kovskii for preparation of the target and the staff of the Cyclotron Laboratory for assistance in carrying out the experiment.

Institute of Physics,
Academy of Sciences of the Ukrainian SSR

References

1. P.F.A.Klinkenberg, Revs.Mod.Phys., 24, 53 (1952).
2. J.B.French, E.C.Halbert & S.P.Pandya, Phys.Rev., 99, 1387 (1955).
3. R.R.Haefner, Revs.Mod.Phys., 23, 228 (1951).
4. N.I.Zaika & O.F.Nemets, Ukr.fiz.zhur. (Ukrainian Physics Journal), 4, 519 (1959).
5. O.F.Nemets, L.S.Saltykov & M.V.Sokolov, Zhur.eksp.i teor.fiz., 38, 1663 (1960). (Trans.Soviet Physics - JETP.)
6. N.Austern, S.T.Butler & H.McManus, Phys.Rev., 92, 350 (1953).
7. J.S.Blair & E.M.Henley, Phys.Rev., 112, 2029 (1958).
8. C.J.Mullin & E.Guth, Phys.Rev., 82, 141 (1951).
9. G.I.Kopaleishvili, Zhur.eksp.i teor.fiz., 30, 1145 (1956). (Trans.Soviet Physics - JETP.)
10. J.Dabrowski & J.Sawicki, Nuovo Cimento, 12, 293 (1954).
11. J.A.Harvey, Phys.Rev., 82, 298 (1951).
12. S.W.Rasmussen, Phys.Rev., 103, 186 (1956).
13. N.A.Vlasov & A.A.Ogloblin, Zhur.eksp.i teor.fiz., 37, 54 (1959). (Trans. Soviet Physics - JETP.)
14. P.Cüer & J.J.Jung, Phys.Rev., 89, 1151 (1953).

SPINS AND PARITIES OF C^{13} LEVELS

- N.I.Zaika, O.F.Nemets & M.A.Tserineo

In this report we give the results of the measurements of the differential cross sections and angular distributions of protons from the $C^{12}(d,p)C^{13}$ reaction at deuteron energies of 4.65, 7.15, 9.55, 12.1 and 13.3 Mev. The deuteron beam with initial energy 13.6 Mev was obtained from the cyclotron of the Physics Institute of the Ukrainian SSR Academy of Sciences. The initial deuteron energy was reduced by means of aluminum absorbers located in front of the target. An auxiliary collimator was mounted after the absorbers. The uncertainty in determining the deuteron energy was ±200 kev.

The experimental geometry and the proton detector were the same as in the work of Ref.1, except that an additional absorber was installed at the entrance of the chamber in order to minimize deuteron pulses in the amplifier channel.

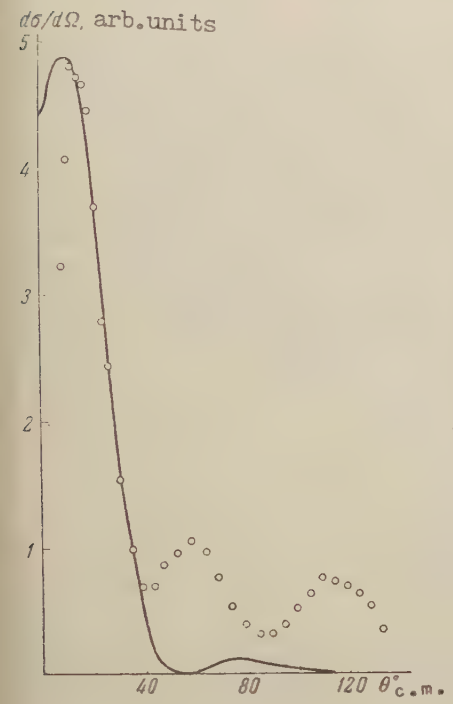

Fig.1.

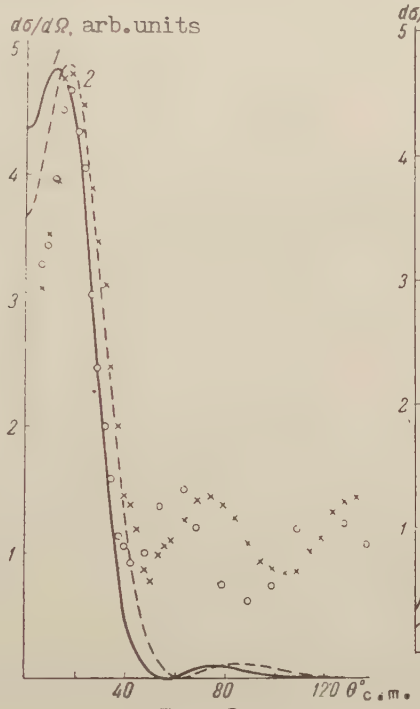

Fig.2.

Fig.3.

Fig.1. Angular distribution of protons from the $C^{12}(d,p)C^{13}_{g.s.}$ reaction. Deuteron energy 13.3 Mev; $r_0 = 4.6$ f and $l_n = 1$.

Fig.2. Same as Fig.1 but for $E_d = 12.1$ Mev (1) and $E_d = 9.55$ Mev (2).

Fig.3. Same as Fig.1 but for $E_d = 7.15$ Mev (1) and $E_d = 4.65$ Mev (2); $r_0 = 5.5$ f.

Figs.1-3 show the angular proton distributions corresponding to the ground state of C^{13}; Figs.4-6, the proton distributions corresponding to the three lowest excited states of C^{13} for deuteron energies of 13.3 and 12.1 Mev.

From comparison with theory[2] one can make the following l_n assignments for the ground state and the first three excited states: 1, 0, 1, and 2, respectively. Then, in view of the fact that the spin of C^{12} is 0+, we obtain for the respective spins and parities 1/2- or 3/2-, 1/2+, 1/2- or 3/2-, and 3/2+ or 5/2+.

According to the shell model with intermediate coupling[3], the corresponding states have spins 1/2-, 1/2+, 3/2- and 5/2+.

The angular proton distribution corresponding to excited states is in good agreement with the distribution according to the theory of the stripping reaction.

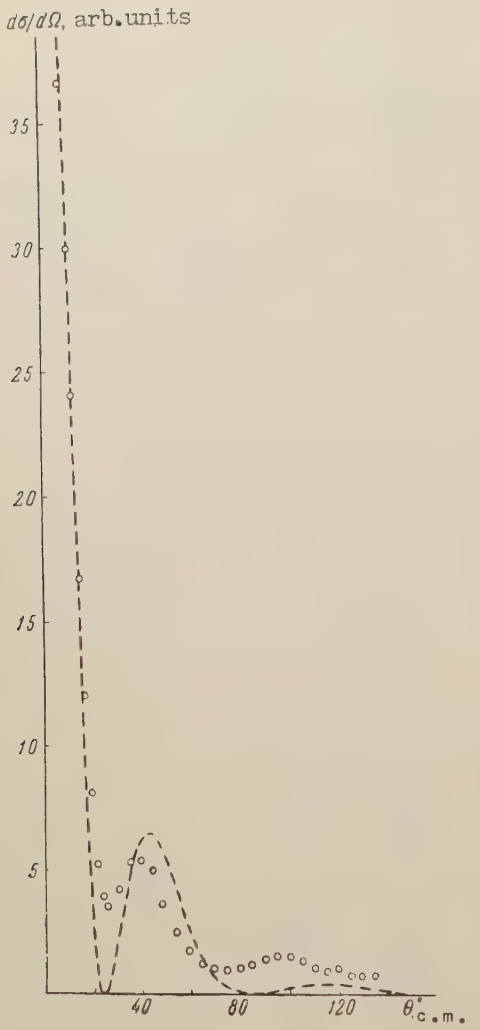

Fig.4.

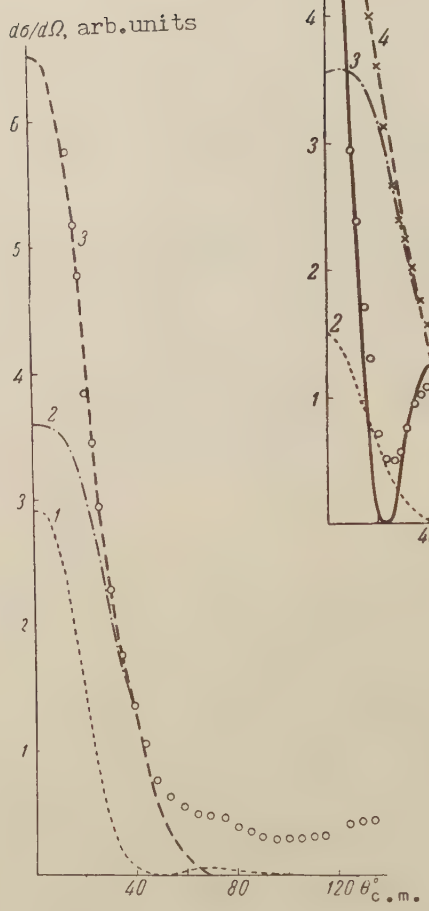

Fig.5.

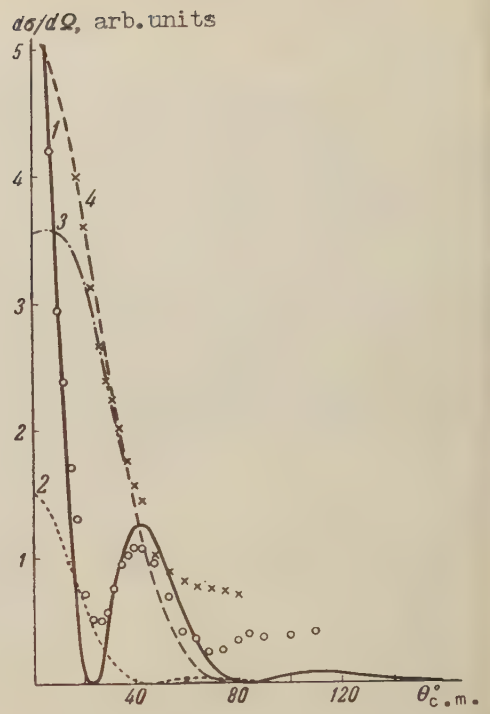

Fig.6.

Fig.4. Angular distribution of protons from the $C^{12}(d,p)C^{13*}$ reaction, corresponding to the first excited state, for E_d = 13.3 Mev, r_0 = 4.6 f and l_n = 0 for the 3.09 Mev level.

Fig.5. Angular distribution of protons from the $C^{12}(d,p)C^{13*}$ reaction, corresponding to the second and third excited states, for E_d = 13.3 Mev and r_0 = 4.6 f: 1 - for the 3.68 Mev level, l_n = 1; 2 - for the 3.86 Mev level, l_n = 2; 3 - (l_n = 1) + (l_n = 2).

Fig.6. Angular distribution of protons from $C^{12}(d,p)C^{13*}$ reaction, corresponding to the first excited state, for E_d = 12.1 Mev and r_0 = 4.6 f: 1 (open circles) - for the 3.09 Mev level, l_n = 0; 2 - for the 3.68 Mev level, l_n = 1; 3 - for the 3.86 Mev level, l_n = 2; 4 (crosses) - (l_n = 1) + (l_n = 2).

In the distribution of protons corresponding to the ground state, however, there are anomalies that are worth noting.

The variation of the cross section at large angles for deuteron energies up to 7.15 Mev and above 9.55 Mev are different: the main peaks in the first case are wider than the theoretical ones, and in the second case, narrower. A similar difference was observed by other authors at energies lower[4] and higher[5] than our

proton energies. This may be connected with contributions from reactions other than stripping, contributions that may differ at different energies.

Measurements of the differential cross sections for angles corresponding to the peak in the angular distribution were carried out by means of a current integrator[6] for protons corresponding to the ground state at deuteron energies at 7.15, 9.55, 12.1 and 13.3 Mev; the cross section values obtained were 24, 18, 14 and 13 mb/sterad, respectively.

The error in the cross section measurements is evaluated to be ±30%.

Institute of Physics,
Academy of Sciences of the Ukrainian SSR &
"Rudjer Boskovich" Institute,
Zagreb, Yugoslavia

References

1. N.I.Zaika & O.F.Nemets, Izv.AN SSSR, Ser.fiz., 23, 1460 (1959). (Trans. Bulletin, 23, 1447.)

2. S.T.Butler, Proc.Roy.Soc. A208, 559 (1951).

3. A.M.Lane, Proc.Roy.Soc., A68, 197 (1955).

4. R.E.Benenson, K.W.Jones & M.T.McEllistrem, Phys.Rev., 101, 308 (1956).

5. H.E.Gove, Ibid., 81, 364 (1951); J.N.McGruer, E.K.Warburton & R.S.Bender, Phys.Rev., 100, 235 (1955); R.G.Freemantle, W.M.Gibson & J.Rotblat, Phil.Mag., 45, 1200 (1954).

6. V.N.Dobrikov, N.I.Zaika & O.F.Nemets, PTE, 4, 23 (1958). (Trans.Instruments & Experimental Techniques.)

ASSIGNMENTS FOR THE LEVELS OF Ti^{47-50} AND Sr^{89}

- N.I.Zaika & O.F.Nemets

Despite the fact that there have been quite a few investigations devoted to the angular distribution of particles from stripping reactions, little is known regarding these reactions where medium and high mass nuclei are concerned.

In particular inferences regarding the spins and parities of different states of titanium isotopes on the basis of the angular distribution of protons from stripping reactions can be drawn only from the work of Bretscher et al[1] who used 10 Mev protons and Ti^{47} and Ti^{48} targets. At deuteron energies of 2.6 Mev (Ref. 2) and 4.16 Mev (Ref.3) there is no characteristic peak in the angular distribution curves, so that it is difficult to draw any deductions regarding the transferred angular momenta. The same thing may be said regarding measurements on Sr^{88} with E_d = 8 Mev carried out by Holt & Marscham[4].

We undertook a series of measurements of the angular distributions of protons from the stripping reactions on Ti^{46}, Ti^{47}, Ti^{48} and Ti^{49} in which the 28 neutron shell is almost filled and on Sr^{88} in which the 50 neutron shell is completely filled. The deuterons were accelerated to 13.6 Mev in the cyclotron of the Institute of Physics of the Ukrainian SSR Academy of Sciences. The experimental geometry and the proton detector were the same as in the work of Ref.5, with the difference that the entrance to the ionization chamber was covered with an absorber stopping deuterons. The targets were polystyrene films impregnated with appropriately enriched TiO_2 or $SrCO_3$ powder.

The presence in the target of oxygen and carbon, which have large stripping reaction cross sections, made it feasible to carry out measurements only for states with $Q \geqslant 3$ Mev; actually the relatively low degree of enrichment hampered measurements even in this region.

Ti^{46}

In the case of Ti^{46} measurements of the angular distribution of protons for the ground state is of greatest interest. This is due to the anomalous value of the spin of Ti^{47}, which is reported[6] to be 5/2 (odd parity). As is known, after filling of the shell with 20 nucleons, there begins filling of the $f_{7/2}$ state, so that in the case of Ti^{47} one might expect the spin and parity of the ground state to be 7/2-; the anomalous spin is the result of interaction of odd nucleons in the $(f_{7/2})^{-3}$ (Ref.7) or the $(f_{7/2})^5$ (Ref.8) configuration and, consequently, neutron capture in the stripping reaction should be accompanied by rearrangement of the outer shell. This may be evinced either in an anomalous angular distribution or a low value of the reaction cross section.

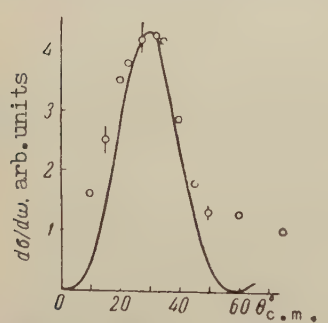

Fig.1. Angular distribution of protons from the $Ti^{46}(d,p)Ti^{47}$ reaction; Q = 6.45 Mev, l_n = 3.

The angular distribution of protons corresponding to the ground state of Ti^{47} is shown in Fig.1. From comparison with the theory[9] it may be inferred that this state is associated with transfer of angular momentum l_n = 3; hence the assignments for the ground state may be 5/2- or 7/2-. The latter value is in agreement with the data from direct measurements[10] of the spin of Ti^{47}.

It should be noted that the cross section for the $Ti^{46}(d,p)Ti^{47}_{g.s}$ reaction (possibly with some contribution from the 0.16 Mev level) proved to be greater than the $Ti^{48}(d,p)Tl^{49}_{g.s}$ cross section, although in the latter case there should be no rearrangement of the configuration inasmuch as Ti^{49} has the normal spin value 7/2.[10]

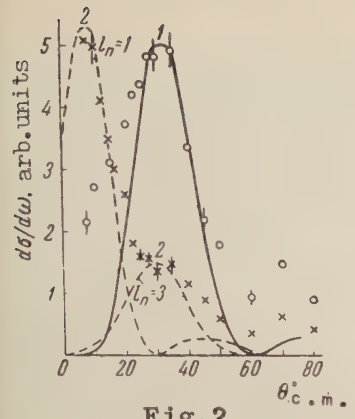

Fig.2

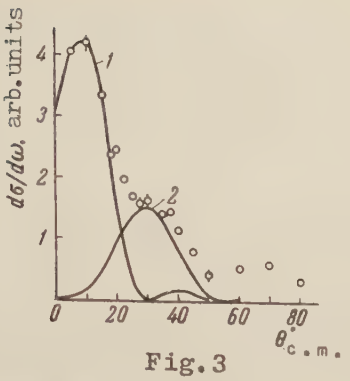

Fig.3

Fig.2. Angular distribution of protons from the reactions: 1) (open circles) - $Ti^{47}(d,p)Ti^{48}$; Q = 8.14 Mev, $l_n = 3$; 2) (crosses) - $Ti^{47}(d,p)Ti^{48*}$; Q = 6.81 Mev, $l_n = 1$ and $l_n = 3$.

Fig.3. Angular distribution of protons: 1 - from the $Ti^{47}(d,p)Ti^{48*}$ reaction; Q = 5.83 Mev, $l_n = 1$; 2 - from an admixture of $Ti^{48}(d,p)Ti^{49}$; Q = 5.81 Mev, $l_n = 3$.

Ti^{47}

In the case of Ti^{47} the transition to the ground state of Ti^{48} may also be accompanied by rearrangement of the $f_{7/2}$ configuration.

As will be evident from Figs.2 & 3, this does not give rise to any anomalies in the angular distributions (the admixture of $l_n = 3$ to the states with $l_n = 1$ (Fig.3) is due to the presence of Ti^{48} in the target).

The l_n value (3) is consistent with the assignment 0+ for the ground state of Ti^{48}. For the 1.33 and 2.31 Mev levels the possible assignments are 1+, 2+, 3+ and 4+ in agreement with the results of Bretscher et al[1].

It should be noted that if for the ground state Q = 8.14 Mev, the energy of the first excited level in Ti^{48} equals 1.33 and not 0.986 Mev, as has been reported[11] on the basis of measurements of neutron capture γ-rays. At the same time, from measurements[12] of the masses of Ti isotopes one might expect Q = 9.41 Mev.

Inasmuch as the ratio of the cross sections for the $Ti^{46}(d,p)Ti^{47}$ and $Ti^{47}(d,p)Ti^{48}_{g.s.}$ reactions should be of the order of $\frac{2J_{47}+1}{2J_{46}+1} : \frac{2J_{48}+1}{2J_{47}+1} = 36$, it is not impossible that we failed to detect the protons from the actual ground state of Ti^{48}. We plan to check this in the near future.

Ti^{48}

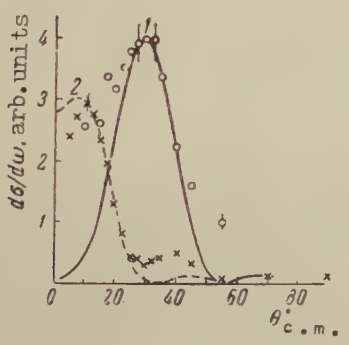

Fig.4. Angular distribution of protons from the reactions: 1 (circles) - $Ti^{48}(d,p)Ti^{49}$; Q = 5.81 Mev, $l_n = 3$; 2 (crosses) - $Ti^{48}(d,p)Ti^{49*}$; Q = 4.46 Mev, $l_n = 1$.

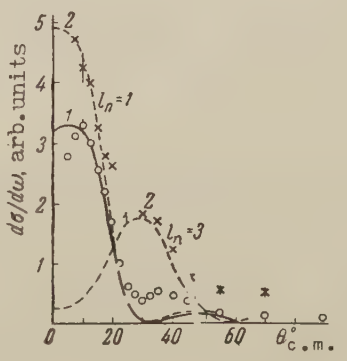

Fig.5. Angular distribution of protons from the reactions: 1 (circles) - $Ti^{48}(d,p)Ti^{49*}$; Q = 4.11 Mev, $l_n = 1$; 2 (crosses) - $Ti^{48}(d,p)Ti^{49*}$, Q = 3.41 Mev, $l_n = 1$ and $l_n = 3$.

The results of measurements for Ti^{48} are shown in Figs.4 & 5. For the ground and 1.35, 1.7 and 2.4 Mev excited states of Ti^{49} the transferred angular momenta values are 3, 1, 1 and 1 + 3, respectively, and the possible spin and parity assignments are 5/2- or 7/2-, 1/2- or 3/2-, 1/2- or 3/2- and 5/2- or 7/2-.

According to Jeffries[10] the spin of Ti^{49} is 7/2, which is in agreement with our results.

Ti^{49}

The angular distributions of protons for Ti^{49} are shown in Figs.6 & 7. Inasmuch as Ti^{50} is an even-even nucleus the spin of the ground state is 0+.

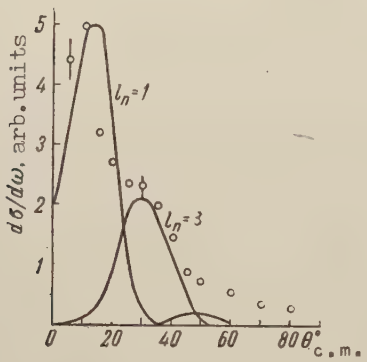

Fig.6

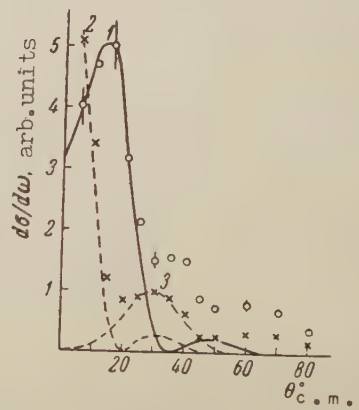

Fig.7

Fig.6. Angular distribution of protons from the $Ti^{49}(d,p)Ti^{50}$ reaction; Q = 8.62 Mev.

Fig.7. Angular distribution of protons from the reactions: 1 (circles) - $Ti^{49}(d,p)Ti^{50*}$; Q = 7.04 Mev, $l_n = 1$; 2 (crosses) - $Ti^{49}(d,p)Ti^{50}$; Q = = 5.82 Mev, $l_n = 0$; 3 (crosses) - from an admixture of $Ti^{48}(d,p)Ti^{49}$; Q = 5.81 Mev, $l_n = 3$.

Hence the reaction with transition to the ground state of Ti^{50} must be accompanied by transfer of an angular momentum $l_n = 3$. At the same time, there is a component corresponding to $l_n = 1$ in the angular distribution. Possibly Ti^{50} has a low-lying level which we were unable to resolve. For the 1.58 and 2.8 Mev levels, $l_n = 1$ and 0, respectively, and the possible assignments are 2+, 3+, 4+ or 5+ and 3- or 4-, respectively.

The isotopic composition of the titanium targets is shown in the accompanying table.

Isotope composition of the titanium targets (%)

Target	Isotopes				
	46	47	48	49	50
Ti^{46}	57,5	4,0	33,0	3,0	2,5
Ti^{47}	3,3	63,0	29,8	2,2	1,7
Ti^{48}	0,7	0,6	97,8	0,5	0,4
Ti^{49}	4,0	4,5	54,0	37,0	0,5

Sr^{88}

The angular proton distributions corresponding to the ground and first excited states of Sr^{89} are shown in Fig.8. The respective l_n values are 2 and 0; accordingly, the spins and parities are 3/2+ or 5/2+ and 1/2+, respectively.

According to the shell model, for the case of spherical nuclei[13] after filling of the 50 neutron shell there beings filling of the $d_{5/2}$ state. This is in agreement with

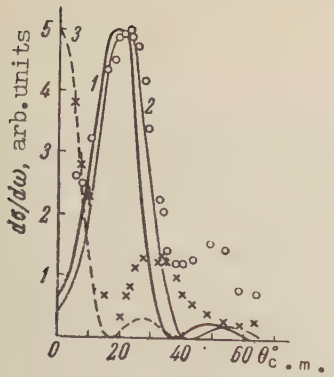

←Fig.8. Angular distribution of protons from the reactions: 1 & 2 (circles) - $Sr^{88}(d,p)Sr^{89}$; Q = 4.32 Mev, $l_n = 2$ (1 - $r_0 = 7.1$ f; 2 - $r_0 = 6.2$ f); 3 (crosses) - $Sr^{88}(d,p)Sr^{89*}$; Q = 3.25 Mev, $l_n = 0$.

our results for the ground state. For the excited state ($g_{7/2}$ according to Klinkenberg[13]) no satisfactory agreement is obtained.

We take this opportunity to express our gratitude to M.V.Pasechnik for his interest in the work and Yu.A. Bin'kovskii for preparing the targets, Yu.V.Gofman and V.N.Dobrikov for assistance in carrying out the measurements and to the personnel of the Cyclotron Laboratory for operating the cyclotron.

Institute of Physics,
Academy of Sciences of the Ukrainian SSR

References

1. M.M.Bretscher, J.O.Alderman, A.Elwyn & F.B.Shull, Phys.Rev., 96, 103 (1954).
2. W.W.Pratt, Phys.Rev., 97, 131 (1955).
3. L.L.Lee, Jr. & W.Rall, Phys.Rev., 99, 1384 (1955).
4. J.R.Holt & T.N.Marscham, Proc.Phys.Soc.A, 66, 565 (1953).
5. N.I.Zaika & O.F.Nemets, Izv.AN SSSR, Ser.fiz., 23, 1460 (1959). (Trans. Bulletin 23, 1447.)
6. R.H.Nussbaum, Revs.Mod.Phys., 28, 423 (1956).
7. D.Kurath, Phys.Rev., 91, 1430 (1953).
8. B.H.Flowers, Phil.Mag., 45, 329 (1954).
9. S.T.Butler, Proc.Roy.Soc., 208, 559 (1951).
10. C.D.Jeffries, Phys.Rev., 92, 1262 (1953).
11. J.W.Knowles, G.Manning, G.A.Bartholomev & P.J.Campion, Phys.Rev., 114, 2065 (1959).
12. G.R.Pieper, Phys.Rev., 88, 1299 (1952).
13. P.F.A.Klinkenberg, Revs.Mod.Phys., 24, 63 (1952).

SPIN OF THE 1.38 Mev LEVEL OF Mg^{24}

- O.F.Nemets & G.A.Prokopets

Investigation of the angular distribution of protons from interactions of charged particles with nuclei can yield information both on the interaction mechanism and on the spin and parity of the final state of the reacting nucleus.

Measurements made on Mg^{24} show that in the 7.3 Mev energy region in the case of inelastic scattering of protons (see Refs.1,2 & 3), in addition to direct interaction, an important role is played by formation of a compound nucleus. From results of experiments on inelastic scattering of deuterons, carried out at energies of 7.5 Mev (Holt & Young[4]), 8.9 Mev (Hinds et al[5]) and 15 Mev (Haffner[6]) it may be concluded that generally direct interaction predominates. Haffner[6] also notes the large contribution in the range of small angles made by electric interaction of the deuteron with the nucleus[7].

In the above listed studies there were not carried out detailed investigations in the region of small angles, although this angular region is of interest inasmuch as results therein can yield additional information on the mechanism of inelastic scattering.

It follows from the experiments of different authors (for example, Refs.8-10) on determination of the spin and parity of various states of Mg^{24} that the most probable assignment for the 1.38 Mev level is 2+.

The 1.38 Mev level may be regarded as a rotational one, inasmuch as the odd-odd Mg^{24} nucleus has collective attributes; moreover, it is strongly deformed, which is important from the standpoint of the inelastic scattering proton mechanism proposed by Yoshida[11].

The present work was concerned with determining the spin of the 1.38 Mev excited level of Mg^{24} by detailed investigation of the angular distribution of inelastically scattered deuterons and protons, particularly in the range of small angles.

The deuteron and proton beams were obtained from the Institute of Physics cyclotron. The spectrometer was an ionization chamber with split electrodes, a design that allows of selective detection of the particles.[12]

The measurements were carried out in the angular range from 2.5 to 140°. The steps were 2.5° in the region of small angles and 5° in the region of large angles. The monitor was a scintillation counter, mounted at an angle of 90° relative to the incident beam.

The statistical uncertainty in determining the relative cross sections was evaluated to be 15% in the range of large angles and up to 25% in the region of small angles. For angles smaller than 12.5° in the case of deuterons and 15° in the case of protons the results are only qualitative owing to the interference of the background due to deuterons elastically scattered in the target and protons undergoing additional inelastic scattering from the gas particles in the chamber and from the nuclei of the 17 mg/cm^2 copper foil covering the entrance to the chamber. The target itself was a magnesium foil with a superficial density of 1.4 mg/cm^2.

Curve 1 in Fig.1 shows the angular distribution of inelastically scattered deuterons obtained in the present investigation. In the same figure we give the theoretical curves corresponding to the mechanism of direct nuclear interaction according to Huby & Newns[13] (curve 2) and electric interaction according to Mullin & Guth[7] (curve 3). The peak at 20° can also be associated with the collective properties of the Mg^{24} nucleus, according to the theory of Mamasakhlisov & Kopaleishvili[14].

The best agreement with theory is obtained for the following parameters.

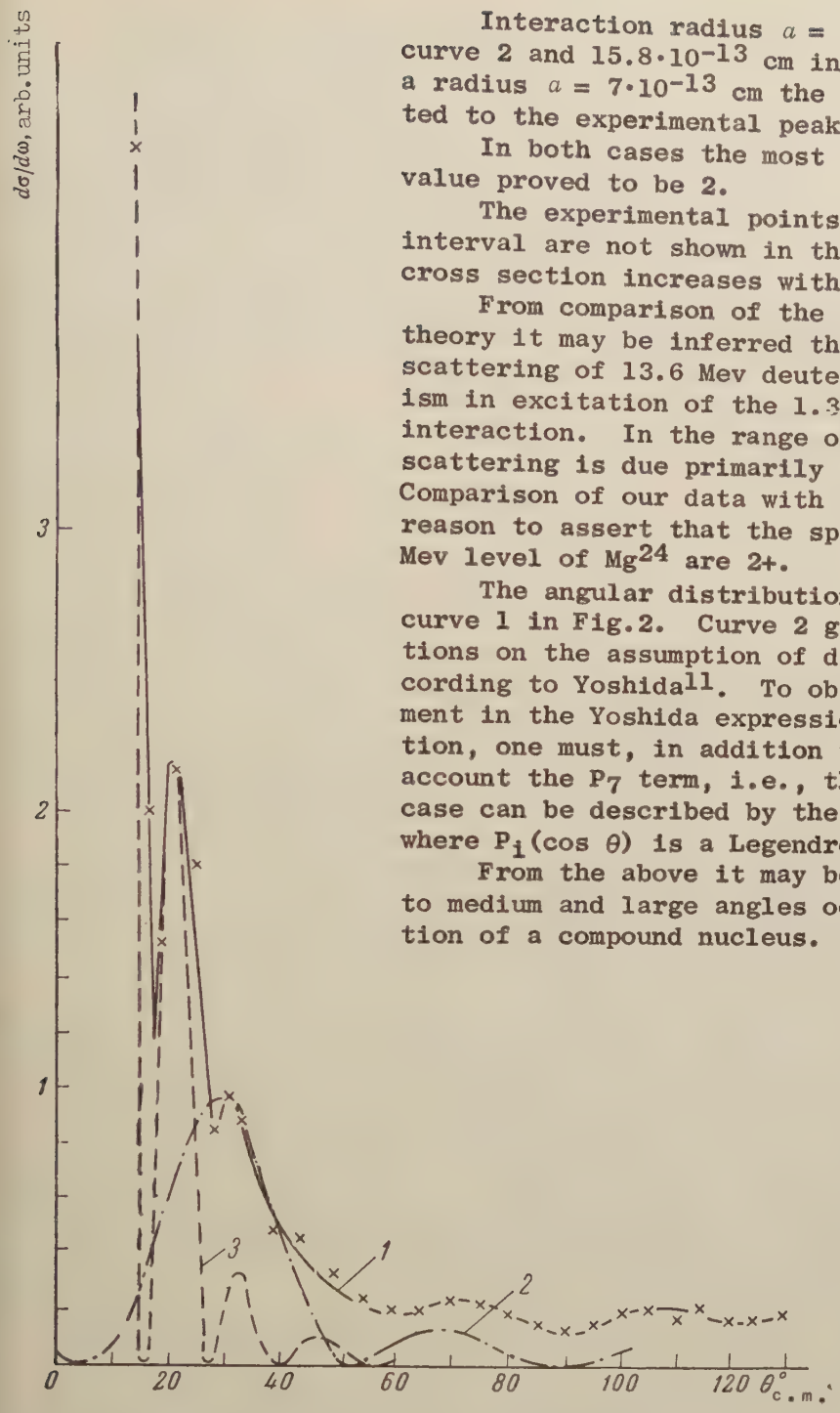

Fig.1. Angular distribution of inelastically scattered deuterons from the $Mg^{24}(d,d')Mg^{24*}$ reaction; Q = -1.38 Mev: 1) our experimental data; 2) theoretical curve for direct nuclear interaction, l = = 2, $a = 6.3 \cdot 10^{-13}$ cm; 3) theoretical curve for electric interaction, $l = 2$, $a = 15.8 \cdot 10^{-13}$ cm.

Interaction radius $a = 6.3 \cdot 10^{-13}$ cm in the case of curve 2 and $15.8 \cdot 10^{-13}$ cm in the case of curve 3; with a radius $a = 7 \cdot 10^{-13}$ cm the peak in curve 2 can be fitted to the experimental peak at $\theta = 20^{\circ}$.

In both cases the most suitable angular momentum value proved to be 2.

The experimental points for the 2.5 to 10° angular interval are not shown in the figure; in this range the cross section increases with decrease of angle.

From comparison of the experimental results with theory it may be inferred that in the case of inelastic scattering of 13.6 Mev deuterons the predominant mechanism in excitation of the 1.38 Mev level of Mg^{24} is direct interaction. In the range of small angles, however, the scattering is due primarily to electric interaction. Comparison of our data with the theoretical curves gives reason to assert that the spin and parity of the 1.38 Mev level of Mg^{24} are 2+.

The angular distribution of protons is shown by curve 1 in Fig.2. Curve 2 gives the results of calculations on the assumption of direct surface interaction according to Yoshida[11]. To obtain agreement with experiment in the Yoshida expression for the angular distribution, one must, in addition to the P_0 term, take into account the P_7 term, i.e., the theoretical curve in this case can be described by the expression $2.2\,P_0 + P_7$, where $P_i(\cos\theta)$ is a Legendre polynomial.

From the above it may be inferred that scattering to medium and large angles occurs primarily with formation of a compound nucleus. At the same time in the range of small angles a significant role must be played by some other mechanism.

The experimental results in this energy region are difficult to compare with the theory of direct nuclear interaction proposed by Austern, Butler & McManus[15].

Somewhat better agreement is obtained with the theory of electric interaction[7] (curve 3 in Fig.2). Best agreement is obtained on the assumption of electric quadrupole transition with an interaction radius $a = 24.7 \cdot 10^{-13}$ cm. Admittedly, however, so large a value of a appears questionable.

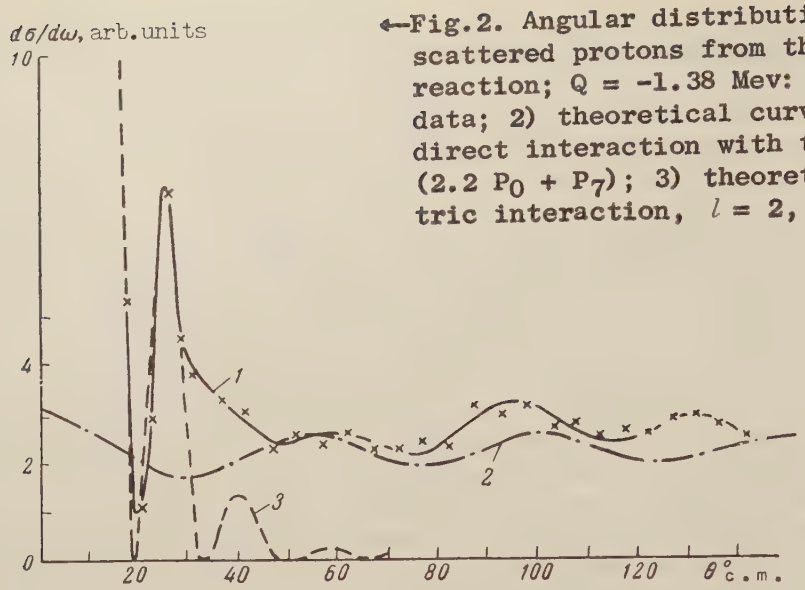

←Fig.2. Angular distribution of inelastically scattered protons from the $Mg^{24}(p,p')Mg^{25*}$ reaction; Q = -1.38 Mev: 1) our experimental data; 2) theoretical curve for the case of direct interaction with the nuclear surface ($2.2\ P_0 + P_7$); 3) theoretical curve for electric interaction, $l = 2$, $a = 24.7 \cdot 10^{-13}$ cm.

Institute of Physics,
Academy of Sciences of the Ukrainian SSR

References

1. G.W.Greenlees, B.C.Haywood, L.G.Kuo & M.Petrowic, Proc.Phys.Soc.A, 70, 331 (1957).
2. P.C.Gugelot & P.R.Phillips, Phys.Rev., 101, 1614 (1956).
3. H.E.Conzett, Phys.Rev., 105, 1324 (1957).
4. J.R.Holt & C.T.Young, Nature, 164, 1000 (1949).
5. J.R.Hinds, R.Middleton & T.Parry, Proc.Phys.Soc.A, 70, 900 (1957).
6. J.W.Haffner, Phys.Rev., 103, 1398 (1956).
7. C.J.Mullin & E.Guth, Phys.Rev., 82, 141 (1951).
8. J.O.Newton, Phys.Rev., 96, 241 (1954).
9. P.J.Grant, J.G.Rutherglen, F.C.Flack & G.W.Hutchinson, Proc.Phys.Soc.A, 68, 369 (1955).
10. P.M.Endt & J.C.Kluyver, Revs.Mod.Phys., 26, 95 (1954).
11. S.Yoshida, Proc.Phys.Soc.A, 69, 668 (1956).
12. O.F.Nemets, Trudy Sessii AN USSR po mirnomu ispol'zoganiyu atomnoi energii (Transactions of the Session of the Ukrainian SSR Academy of Sciences on Peaceful Uses of Atomic Energy), p.145, Kiev, 1958.
13. R.Huby & H.C.Newns, Phil.Mag., 42, 1442 (1951).
14. V.I.Mamasakhlisov & T.I.Kopaleishvili, Zhur.eksp.i teor.fiz., 34, 1169 (1958). (Trans.Soviet Physics - JETP.)
15. N.Austern, S.T.Butler & H.McManus, Phys.Rev., 92, 350 (1953).

SPINS AND PARITIES OF Ca^{41} LEVELS

- N.I.Zaika, O.F.Nemets & V.S.Prokopenko

Using the 13.6 Mev deuteron beam extracted from the Institute of Physics cyclotron, we investigated the angular distribution of protons from the $Ca^{40}(d,p)Ca^{41}$ reaction for the ground state and the 1.95 and 2.42 Mev excited states of the final nucleus. The experimental geometry and detectors were the same as in the work of Ref.1 with the sole difference that a polystyrene absorber stopping all deuterons was installed in front of the chamber.

Earlier experiments of Teplov & Yur'ev[2] involving bombardment of Ca^{40} with low energy deuterons indicated strong nuclear interaction. Hence we felt it would be of interest to carry out measurements at higher deuteron energies.

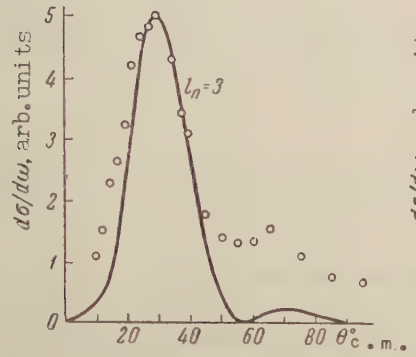

Fig.1

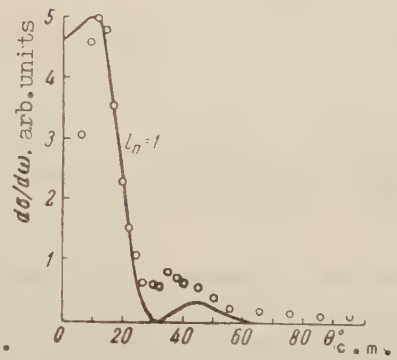

Fig.2

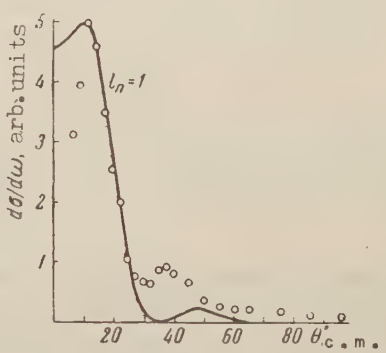

Fig.3

Fig.1. Angular distribution of protons from the $Ca^{40}(d,p)Ca^{41}$ reaction; Q = 6.14 Mev, $l_n = 3$.

Fig.2. Angular distribution of protons from the $Ca^{40}(d,p)Ca^{41}$ reaction; Q = 4.18 Mev, $l_n = 1$.

Fig.3. Angular distribution of protons from the $Ca^{40}(d,p)Ca^{41}$ reaction; Q = 3.69 Mev, $l_n = 1$.

The experimental results are shown in Figs.1-3. The solid curves in the figures give the angular distributions calculated according to the theory of Butler[3]. In all cases the interaction radius was assumed to be $6 \cdot 10^{-13}$ cm.

As indicated in the figures and captions the angular momenta transferred to the nucleus from the neutron are, in agreement with the earlier work of Holt & Marsham[4] and Bockelman & Buechner[5], 3, 1 and 1 for the ground, 1.95 and 2.42 Mev states, respectively.

Inasmuch as the spin and parity of Ca^{40} are 0+, the possible assignments for the ground, 1.95 and 2.42 Mev states of Ca^{41} are 5/2- or 7/2-, 1/2- or 3/2- and 1/2- or 3/2-.

The nuclear shell model for the spherical case predicts 7/2-, 3/2- and 1/2-, respectively.[6]

These results are also in agreement with the data obtained from analysis[7] of the γ-ray spectra emitted in thermal neutron capture by Ca^{40}.

The strong nuclear interaction detected by Teplov & Yur'ev[2] is evinced at E_d = 13.6 Mev only in narrowing of the experimental peak as compared with the theoretical. No significant shift of the peak to the side of smaller angles is observed.

Institute of Physics,
Academy of Sciences of the Ukrainian SSR

References

1. N.I.Zaika & O.F.Nemets, Izv.AN SSSR, Ser.fiz., 23, 1460 (1959). (Trans. Bulletin, 23, 1447.)
2. I.B.Teplov & B.A.Yur'ev, Zhur.eksp.i teor.fiz., 33, 1313 (1957). (Trans. Soviet Physics - JETP.)
3. S.T.Butler, Proc.Roy.Soc.A208, 559 (1951).
4. J.R.Holt & T.N.Marsham, Proc.Phys.Soc., 66, 565 (1953).
5. C.K.Bockelman & W.W.Buechner, Phys.Rev., 107, 1366 (1957).
6. P.Klinkenberg, Revs.Mod.Phys., 26, 63 (1952).
7. L.V.Groshev, A.M.Demidov, V.N.Lutsenko & V.I.Pelekhov, Atlas spektrov gamma-luchei radiatsionnogo zakhvata teplovykh neitronov (Atlas of thermal neutron capture γ-ray spectra) M., 1958.

* * * * * * *

ANGULAR DISTRIBUTION OF PROTONS INELASTICALLY SCATTERED FROM Cr AND Ni ISOTOPES

- M.V.Pasechnik, N.N.Pucherov & V.I.Chirko

The present investigation was concerned with inelastic scattering of 6.8 Mev protons from chromium and nickel isotopes.

The proton beam was extracted from the cyclotron of the Institute of Physics of the Ukrainian SSR Academy of Sciences, focused by quadrupole lenses, deflected 30° by a magnet and then entered the 1.6 meter diameter scattering chamber. The scattering chamber was located outside the reinforced concrete shielding at a distance of 8 meters from the cyclotron.

The target was mounted in the center of the scattering chamber at an angle of 45° to the incident beam. The scattered protons were detected by means of a scintillation spectrometer mounted on a rotating arm. The accuracy in setting the angles was ±0.3°. The experimental procedure was in principle the same as that described in Ref.1.

The energy resolution (4-5%) of the scintillation spectrometer enabled us to resolve proton groups associated with excitation of levels above 1 Mev, provided the separation between levels was not too great. In particular, we clearly distinguished proton groups associated with excitation of the first excited states of Cr^{52} and Ni^{58}.

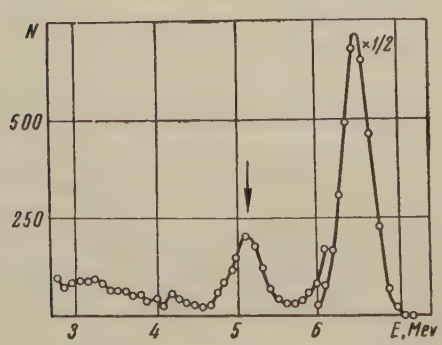

Fig.1. Energy spectrum of protons scattered from Cr^{52} at an angle $\theta_L = 90°$; $E_p = 6.8$ Mev.

The targets were prepared in the form of thin free-standing films 2-4 μ thick and were enriched to at least 95%. In using such nearly monoisotopic targets, it proved feasible to identify proton groups pertaining to individual excited states, i.e., to measure the differential partial cross sections. In view of the appreciable background connected with the presence of strong elastic scattering, measurements at angles smaller than 40° were not performed. We plan to undertake such measurements in the future after making the necessary improvements in the equipment and procedure.

A typical spectrum obtained for protons scattered from Cr^{52} at an angle of 90° is shown in Fig. 1. The differential partial cross section for inelastic scattering was determined from the ratio

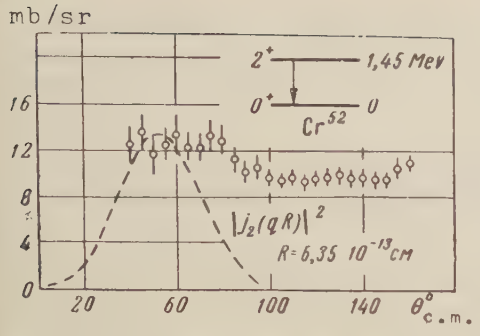

Fig.2. Angular distribution of protons inelastically scattered from Cr^{52} with excitation of the 1.45 Mev level (2+).

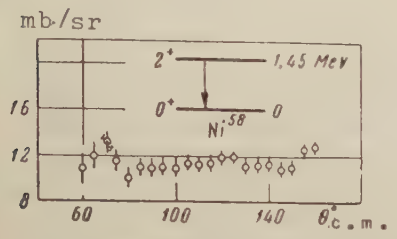

Fig.3. Angular distribution of protons inelastically scattered from Ni^{58} with excitation of the 1.45 Mev level (2+).

of the areas under the peaks of elastic and inelastic scattering in the energy spectrum of protons scattered at a given angle. The differential cross section for elastic scattering was determined on the assumption that in the region of $\theta = 20^{\circ}$ the elastic scattering obeys Rutherford's law[2].

The angular distributions of protons inelastically scattered from Cr^{52} and Ni^{58} are shown in Figs.2 & 3. In both cases we are dealing with distributions of the proton groups associated with excitation of the first excited state. Thus in both cases there is involved a 0+→2+ transition.

It will be evident from the figures that the angular distributions are primarily isotropic, although for Cr^{52} there is a minor hump in the region of angles smaller than 80°.

The other theory is based on the assumption of direct interaction. Simplified calculations show that in this case

$$\frac{d\sigma}{d\omega} \sim \sum_l |C_l j_l(qR)|^2, \qquad (1)$$

where C_l is a constant, $l\hbar$ is the orbital angular momentum carried into the nucleus, R is the radius of the nucleus, and $q = |k_i - k_f|$ is the change in the momentum of the proton as a result of scattering.

Analysis of the angular distributions in the case of inelastic scattering by Cr^{52} and Ni^{58} shows that at a proton energy of the order of 7 Mev inelastic scattering occurs primarily with formation of a compound nucleus.

Kikuchi et al[4] in experiments on scattering of 14.1 Mev protons by Cr^{52} nuclei with excitation of the 1.45 Mev level observed a noticeable asymmetry in the angular distribution relative to 90°. In this case the angular distribution was interpreted by means of Eq.(1), taking $l = 2$ and $R = 6.35 \cdot 10^{-13}$ cm. The dashed line in Fig.2 shows the curve calculated by means of this formula for our case using the same parameters. It will be seen that the calculated curve does not agree with experiment. It must be noted that more precise calculations of the angular distribution for the process of direct interaction[5] show that the angular distribution has a more complex shape than follows from Eq.(1). Nevertheless, it may safely be asserted that if direct interaction does occur, in our case its contribution is minor.

We made evaluations of the differential partial cross section for inelastic proton scattering associated with excitation of the following levels: 1.45 Mev in Ni^{58}, 1.33 Mev in Ni^{60} and 1.17 Mev in Ni^{62}. The evaluations were made in the $140\text{-}160^{\circ}$ region. In the case of Ni^{62} we obtained a cross section value (30 millibarn/steradian) somewhat greater than for the two lighter isotopes (20 mb/sr for Ni^{60} and 10 mb/sr for Ni^{58}). It may be that the value of the cross section obtained for Ni^{60} is an overestimate.

We take this opportunity to thank the personnel of the cyclotron laboratory for the operation of the equipment.

Institute of Physics,
Academy of Sciences of the Ukrainian SSR

References

1. N.N.Pucherov, Ukr.fiz.zhur. (Ukrainian Physics Journal), 4, 313 (1959).
2. A.K.Val'ter, I.I.Zalyubovskii, A.P.Klyucharev, M.V.Pasechnik, N.N.Pucherov & V.I.Chirko, Zhur.eksp.i teor.fiz., 38, 1419 (1960). (Trans.Soviet Physics - JETP.)
3. L.Wolfenstein, Phys.Rev., 82, 690 (1951).
4. K.Kikuchi, S.Kobayashi & K.Matsuda, J.Phys.Soc.Japan, 14, 121 (1959).
5. C.A.Livinson & M.K.Banerjee, Ann.Phys. (N.Y.), 3, 67 (1958).

* * * * * * *

INVESTIGATION OF THE LEVELS OF Cl^{35}

- Yu.P.Antuf'ev, A.K.Val'ter, V.Yu.Gonchar, E.G.Kopanets, A.N.L'vov & S.P.Tsytko

Introduction

Hitherto the $S^{34}(p,\gamma)Cl^{35}$ reaction (Q = 6.373 Mev) has virtually not been studied. In the literature one can find only the brief communication of Hanscome & Malich[1] to the effect that in proton bombardment of a target containing a normal isotopic composition (S^{32} - 95%, S^{33} - 0.74%, S^{34} - 4.24% and S^{36} - 0.017%) there were observed numerous poorly resolved resonances only five of which, in view of absence of induced β-activity, were attributed to the above reaction. The proton energies for these resonances are given as 1.37, 1.61, 1.69, 1.80 and 1.86 Mev.

The authors also note the possibility of the existence of resonances associated with the $S^{32}(p,\gamma)Cl^{33}$ reaction (Q = 2.285 Mev) which, owing to the short half-life of Cl^{33} (T = 2.52 sec), it may have been impossible to distinguish from the resonances associated with the $S^{34}(p,\gamma)Cl^{35}$ reaction.

The most complete data on the low lying levels of Cl^{35} were obtained by Endt et al[2] who investigated inelastic scattering of protons by Cl^{35} and established the existence in this nucleus of levels with excitation energies of 1.221, 1.763, 2.645, 2.695, 3.006, (3.165), 4.058, 4.113 and 4.174 Mev.

Data on the parity of the first two levels in Cl^{35} were obtained in the work of Kistner et al[3], who attribute an even parity to these levels on the basis of their investigation of positron decay of A^{35}.

There are no other experimental data on the levels of Cl^{35} in the literature.

Accordingly, the purpose of the present investigation was further study of the levels of Cl^{35} by means of the $S^{34}(p,\gamma)Cl^{35}$ reaction. We measured the excitation functions and the spectra and angular distributions γ-rays from this reaction.

Experimental Procedure and Results

Excitation function

For investigating the excitation function we used isotopic S^{34} targets and a monoenergetic beam of protons accelerated to 4 Mev in the electrostatic generator of the Physical-Technical Institute of the Ukrainian SSR Academy of Sciences.[4] The isotopic S^{34} targets were prepared by knocking S^{34} ions into tantalum backings in an electromagnetic separator.[5] The targets had a thickness corresponding

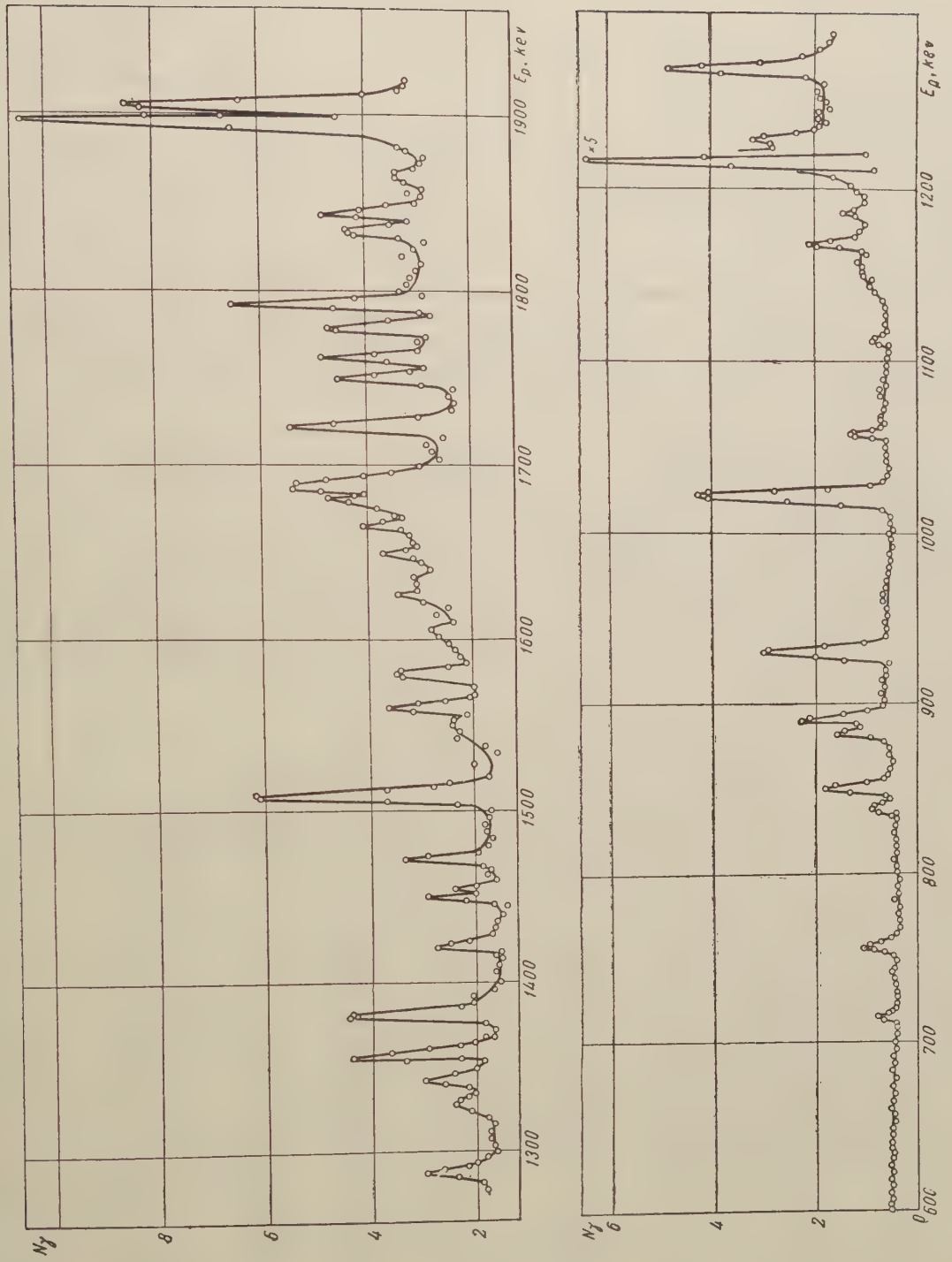

Fig.1. Excitation function for the $S^{34}(p,\gamma)Cl^{35}$ reaction.

to the half-width of the 4-5 kev resonance peaks at a proton energy of 1.0 Mev and proved to be highly stable under bombardment. The temperature of the target was maintained at 250° and the yield from the target did not change over several days of work with the target. The proton current was measured by a current integrator, the sensitivity and linearity of which remained constant within 1% during the entire period of measurement. The proton beam was mono-energetic within 0.1%. The proton energy was measured by means of an electrostatic analyzer to within ±0.05%.

The γ-rays were detected by a 2 cm thick, 3 cm diameter CsI(Tl) crystal which was mounted at a distance of 3 cm from the target at an angle of 60° relative to the direction of the proton beam. In investigating the excitation function we detected γ-rays with energies exceeding 1.5 Mev. The target chamber had a window covered with copper foil 0.05 mm thick, which passed positrons from the target. Opposite the window there was mounted a thin (0.2 cm thick, 3 cm diameter) CsI(Tl) crystal for monitoring any β-activity induced in the target. The β-activity measurements were carried out simultaneously with measurements of the γ-ray yield. The results of measurements of the excitation function for the $S^{34}(p,\gamma)Cl^{35}$ reaction are shown in Fig.1. It will be seen that 44 narrow resonances are observed in the γ-ray spectrum in the energy interval from 0.6 to 1.9 Mev. No induced activity was observed in conjunction with any of the resonances; hence we infer that all the observed resonances may be attributed to the $S^{34}(p,\gamma)Cl^{35}$ reaction.

The proton energies at which γ-resonances occurred, the relative intensities of the resonance peaks and the corresponding level energies in Cl^{35} are listed in the accompanying table. In determining the excitation energies we took the Q value for the $S^{34}(p,\gamma)Cl^{35}$ reaction to be 6.373 Mev, as listed by Endt & Braams[6].

The experimental half-width of all the resonance peaks except those at E_p = = 1020, 1158, 1328 and 1547 kev is 4-5 kev. This width is due apparently to the thickness of the target and the minor energy spread of proton beam. The half-width of the 1020, 1158, 1328 and 1547 kev resonances are 8, 22, 9 and 20 kev,

Resonance energies and characteristics of the levels of Cl^{35} evinced in the $S^{34}(p,\gamma)Cl^{35}$ reaction

No.	E_p, kev	Level energy, Mev	Relative intensity resonance peaks	No.	E_p, kev	Level energy, Mev	Relative intensity resonance peaks
1	715	7,067	0,6	23	1450	7,780	1,4
2	756	7,107	1,0	24	1455	7,785	0,5
3	838	7,180	0,7	25	1471	7,801	2
4	848	7,196	1,8	26	1510	7,836	5,5
5	881	7,228	1,4	27	1547	7,875	0,6
6	889	7,236	2,4	28	1559	7,886	2,1
7	928	7,274	3	29	1578	7,905	1,7
8	1020	7,363	4,5	30	1605	7,931	—
9	1057	7,399	0,9	31	1625	7,950	0,7
10	1112	7,452	0,3	32	1650	7,975	1
11	1158	7,497	0,5	33	1665	7,989	1,3
12	1166	7,505	1,3	34	1681	8,005	1,3
13	1184	7,522	0,6	35	1684	8,008	3,0
14	1214	7,551	4,3	36	1721	8,044	3,5
15	1227	7,564	1,4	37	1751	8,073	2,0
16	1267	7,60	4,0	38	1760	8,081	2,2
17	1286	7,621	1,6	39	1778	8,099	2,5
18	1328	7,662	0,8	40	1791	8,112	4,4
19	1341	7,675	1,4	41	1832	8,151	1,5
20	1355	7,688	3,1	42	1842	8,161	2,0
21	1378	7,711	3,4	43	1896	8,214	8,5
22	1418	7,749	1,5	44	1904	8,221	5,5

respectively.

Gamma-spectra and angular distributions

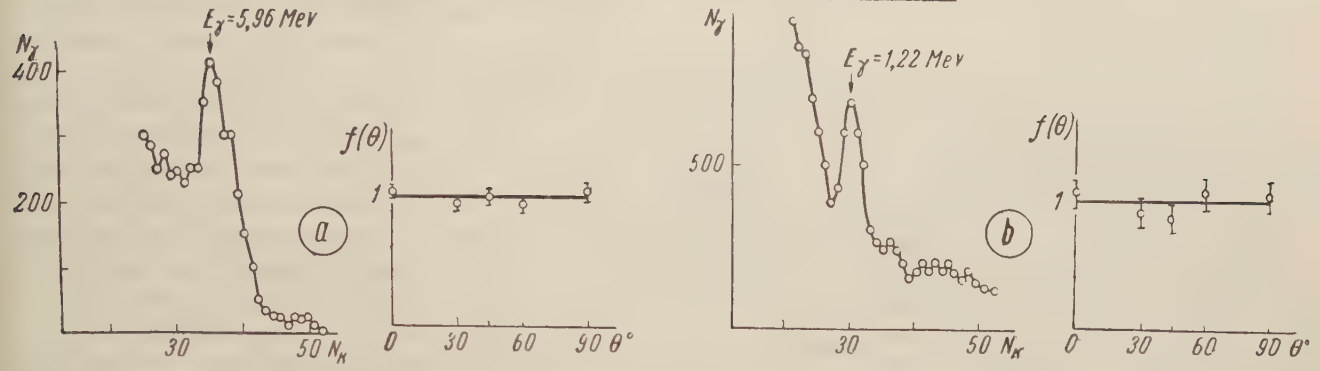

Fig.2. Gamma-ray spectrum and angular distribution for the resonance at E_p = 848 kev; a - angular distribution of 5.96 Mev γ-rays, b - angular distribution of 1.22 Mev γ-rays.

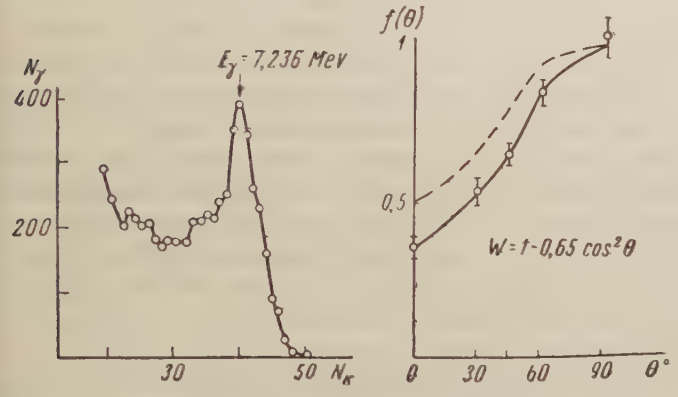

Fig.3. Gamma-ray spectrum and angular distribution for the resonance at E_p = 890 kev.

For investigating the angular distributions and spectra of the γ-rays we used the single crystal scintillation γ-spectrometer described in Refs.7 & 8. The 3 cm diameter, 2 cm thick CsI(Tl) crystal, which was coupled to an FEU-S photomultiplier, could be rotated about the center of the target 150° in either sense relative to the direction of the proton beam. The photomultiplier pulses after amplification were fed into a 50-channel pulse height analyzer.

For obtaining the angular distributions we investigated the spectra at different angles. The γ-ray intensity for each investigated angle was determined from the area under the peak corresponding to the given γ-ray energy. By way of γ-ray monitor in the angular distribution measurements we used a similar CsI(Tl) crystal coupled to an FEU-S photomultiplier mounted at a fixed angle of 90° relative to the proton beam.

The γ-ray spectra and angular distributions were investigated for the E_p = = 848, 881, 890, 929, 1020 and 1214 kev resonances. The experimental curves for three proton energies are shown in Figs.2, 3 & 4. Analysis of the experimental spectra and angular distributions enabled us to draw certain inferences regarding the spin and parity of the resonance levels and the first level in Cl^{35}, and also regarding the γ-transitions between these levels. The proposed γ-transition diagram is shown in Fig.5.

Resonance at 848 kev

The E_p = 848 kev resonance corresponds to a level at 7.196 Mev in Cl^{35}; from this level there occur γ-transitions to the 1.22 Mev level with an abundance $\geqslant$ 95% and to the ground state of Cl^{35} with an abundance not exceeding 5%. The angular distributions for the 5.96 and 1.22 Mev γ-rays, which are in cascade, are isotropic. Such distributions as well as the evaluated intensity ratio between the cross-

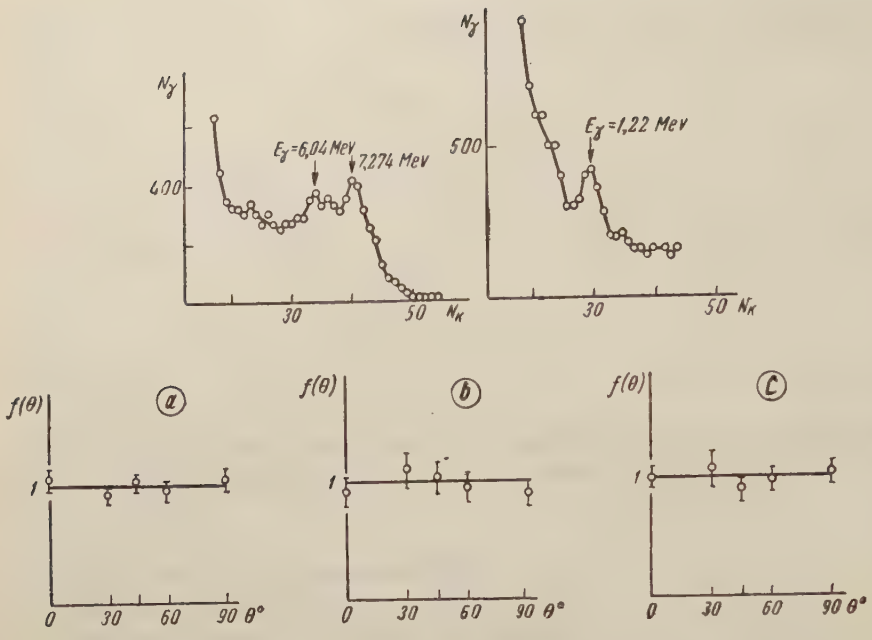

Fig.4. Gamma-ray spectrum and angular distribution for the resonance at E_p = 929 kev: a - angular distribution of 7.27 Mev γ-rays, b - angular distribution of 6.04 Mev γ-rays, c - angular distribution of 1.22 Mev γ-rays.

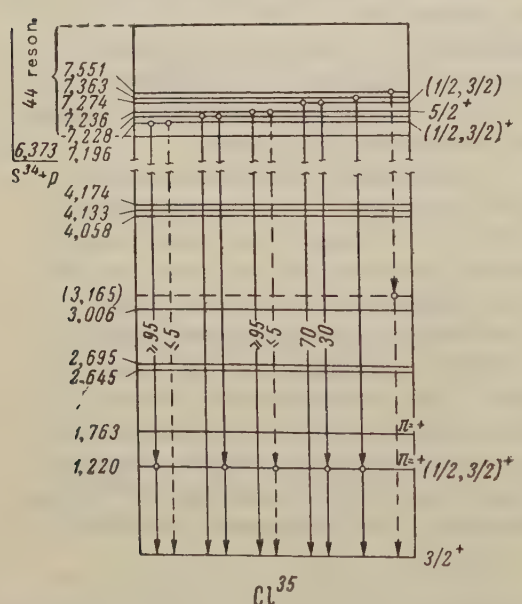

Fig.5. Gamma-transitions in Cl^{35}.

over and cascade transitions are in agreement with the inference that the 1.22 and 7.196 Mev levels both have spin and parity 1/2+. It may be noted that the shell model predicts a spin value of 1/2 for the first excited state of Cl^{35}. This spin value also follows from comparison of Cl^{33} with S^{33}, nuclei which have similar nucleon configurations in the unfilled shell. Theoretically other assignments are possible, but further assumptions must be made to justify them. Thus, for example, the spin of both levels may be 3/2, but then in order to explain the isotropic angular distribution it must further be assumed that the transition from the 7.196 level to the 1.22 level must be pure quadrupole.

Resonance at 890 kev

The E_p = 890 kev resonance corresponds to a level with excitation energy of 7.236 Mev in Cl^{35}. In the spectrum there is one intense line at 7.236 Mev, i.e., corresponding to a transition to the ground state. Analysis of the γ-ray spectrum at different angles showed that there also departs from the 7.236 Mev level a very weak ($\leqslant$ 5%) transition to the 1.22 Mev level. The angular distribution for the transition to the ground state is characterized by

$$W(\theta) = 1 - (0.65 \pm 0.03)\cos^2\theta.$$

Comparison of the deduced angular distribution with the calculated distribution indicates that the spin of the 7.236 Mev level is 5/2. Deviation of the experimental factor multiplying $\cos^2\theta$ from the calculated value (-0.5) can be explained if one assumes that this transition is not pure dipole but has a small admixture of quadrupole radiation with an amplitude ratio E2/M1 = -0.10. In view of this one may hypothesize that the transition from the 7.236 Mev level to the ground state with spin and parity 3/2+ must occur without

change in parity, i.e., that the assignment for the 7.236 Mev level is 5/2+. This assignment is not in conflict with the fact that there is observed a low intensity transition from the resonance 7.236 Mev level to the 1.22 Mev (1/2+) level, inasmuch as this transition may be E2.

Resonance at 929 kev

The E_p = 929 kev resonance corresponds to an excited level at 7.274 Mev from which there occur transitions to the ground state (abundance ~70%) and to the 1.22 Mev (~30%). The experimental angular distributions for the cross-over transition and for the two cascade transitions are isotropic. As in the case of the E_p = = 848 kev resonance, it may be assumed that the spin of the 7.274 Mev level is 1/2. The substantial difference between the intensity ratios of the transitions to the ground and first excited state from the two resonance levels at 7.196 and 7.274 Mev, both with spin 1/2, could be explained on the assumption that these are levels of different types. We believe, however, that this is a matter for further investigation.

Resonances at 881, 1020 and 1214 kev

We carried out a preliminary measurement of the spectra and angular asymmetry of the γ-rays for these three resonances. The γ-ray spectrum associated with the E_p = 881 kev resonance is similar to the γ-ray spectrum for the resonance at 929 kev, i.e., there are γ-transitions of comparable intensity both to the ground state and to the 1.22 Mev level. In contrast to the resonance at E_p = 929 kev, however, there is a noticeable asymmetry in the angular distribution of the γ-rays for the 881 kev resonance. Our preliminary investigation of the angular asymmetry for the transitions from the 7.228 Mev level to the ground state indicates that this resonance level may have spin 3/2.

The γ-rays spectrum for the resonance at 1020 kev is similar to the spectrum associated with the resonance at 848 kev, i.e., the corresponding ~7.363 Mev level decays virtually 100% by cascade transitions through the first excited level of Cl^{35}. No asymmetry in the angular distribution of these γ-rays was observed.

The resonance at E_p = 1214 kev is distinguished from all the other resonances by its great intensity and by the character of the corresponding γ-ray spectrum. In view of this we had some doubt whether this resonance is due to the $S^{34}(p,\gamma)Cl^{35}$ reaction; there are, however, a number of factors which indicate that this is the case. Thus, for example, a resonance at E_p = 1214 kev is observed in using a ZnS target with a natural isotopic content of S^{34} (4.24%), and this resonance increases proportionally in intensity in measurements with a target containing close to 100% S^{34}. Moreover, no induced β-activity is associated with this resonance. In the corresponding γ-ray spectrum there appear two γ-lines with energies of 4.37 and 3.24 Mev.

In order to explain the de-excitation of this level, which differs from the decay mode for the neighboring resonance levels, it may be hypothesized that this resonance level at 7.551 Mev has a high spin value and that therefore transitions from it to levels with low spin values are forbidden. This, however, is in conflict with the great intensity of this resonance. We hope that further investigations of the angular distributions and the correlation of the cascade γ-transitions will help elucidate the nature of this level.

We desire to express our gratitude to M.I.Guseva for preparing the isotopic S^{34} targets, and to A.A.Tsygikalo and Yu.A.Kharchenko and the personnel of the

electrostatic generator for insuring satisfactory operation of the accelerator during our experiments.

Kharkov Physical-Technical Institute,
Academy of Sciences of the Ukrainian SSR

References

1. T.D.Hanscome & C.W.Malich, Phys.Rev., 82, 304 (1951).
2. P.M.Endt, C.H.Paris, A.Sperduto & W.W.Buechner, Ibid., 103, 961 (1956).
3. O.C.Kistner, A.Schwarzschild & B.M.Rustad, Ibid., 104, 154 (1956).
4. A.K.Val'ter & A.A.Tsygikalo, PTE, (Instruments & Exper.Techniques), No.4, 3 (1957).
5. M.I.Guseva, Ibid., No.5, 112 (1957).
6. P.M.Andt & C.M.Braams, Revs.Mod.Phys., 29, 683 (1957).
7. A.K.Val'ter, V.Yu.Gonchar, A.N.L'vov & S.P.Tsytko, Izv.AN SSSR, Ser.fiz., 23, 228 (1959). (Trans.Bulletin, 23, 219.)
8. A.K.Val'ter, V.Yu.Gonchar, A.N.L'vov & S.P.Tsytko, Ibid., 23, 835 (1959). (Trans.Bulletin, 23, 829.)

ELASTIC SCATTERING OF PROTONS BY Ne^{20}

- A.K.Val'ter, A.S.Deineko, P.V.Sorokin & A.Ya.Taranov

There are only two brief communications[1,2] in the literature on investigation of the levels in Na^{21} by means of elastic scattering of protons from Ne^{20} nuclei. These abstracts give only the energies of the levels evinced at proton energies from 0.4 to 4 Mev and the final results of phase-shift analysis, namely, the widths, spins and parities of the evinced levels. It is also reported that the levels for which the spins and parities were determined have a proton (elastic) width $\Gamma_p > 0.7\,\Gamma$.

Owing to the fact that the experimental cross section values are not given, it is impossible to check the assignments by comparing the experimental cross sections with the cross sections calculated on the basis of the inferred spins, parities and level widths. Hence we felt it would be of interest to investigate the p-Ne^{20} elastic scattering cross section for the purpose of checking the data of Heaberli et al[1,2].

Procedure and experimental results

Proton resonance energies and Na^{21} level characteristics

E_p, Mev	Level in Na^{21}, Mev	Level width, kev		Spin & parity	$\frac{\Gamma_p}{\Gamma}$	Reduced width γ^2, Mev cm
		Our data	Ref. 2			
1,81	4,18	121	180	$3/2^-$		$1{,}4\cdot10^{-13}$
1,96	4,32	17	6	$5/2^+$	0,25	$0{,}8\cdot10^{-13}$
2,15	4,50	27	17	$3/2^+$	0,84	$0{,}9\cdot10^{-13}$
2,69	5,02					
3,18	5,48	80	110	$1/2^+$		$0{,}2\cdot10^{-13}$

The p-Ne^{20} elastic scattering cross section was measured by means of the equipment described earlier[3]. By way of target we used gaseous neon of natural isotopic composition (90.5% Ne^{20}) at a pressure of 5 mm Hg. The energy spread of the proton beam was ±8 kev; this was due primarily to loss straggling incident to passage of the protons through the entrance window of the scattering chamber.

The p-Ne^{20} scattering cross section was measured at angles of 55, 90, 125, 141 and 151° in the center of mass system in the proton energy range from 1.6 to 3.4 Mev. The results are shown in Figs.1 & 2, from which it will be evident that there are five clearly pronounced resonances. The proton energies at which these resonances are observed and the corresponding level energies in Na^{21} and level widths are listed in the accompanying table.

The minor anomalies in the curves of Fig.2 are presumably connected with resonance scattering of protons by Ne^{22} nuclei, the content of which in the target was 9.2%.

Discussion

The phase-shift analysis of the experimental data was carried out by the procedure described in Refs.4 & 5. The deduced spins and parities are listed in the accompanying table. We were unable to analyze the resonance at 2.69 Mev inasmuch as it is apparently connected with more than one level.

Our values for the energies, spins and parities of the levels in Na^{21} are in good agreement with the results of Heaberli[2]. As will be evident from the table, however, there is a substantial difference between our results and those of Heaberli as regards the level widths. Inasmuch as the energy resolution in our experi-

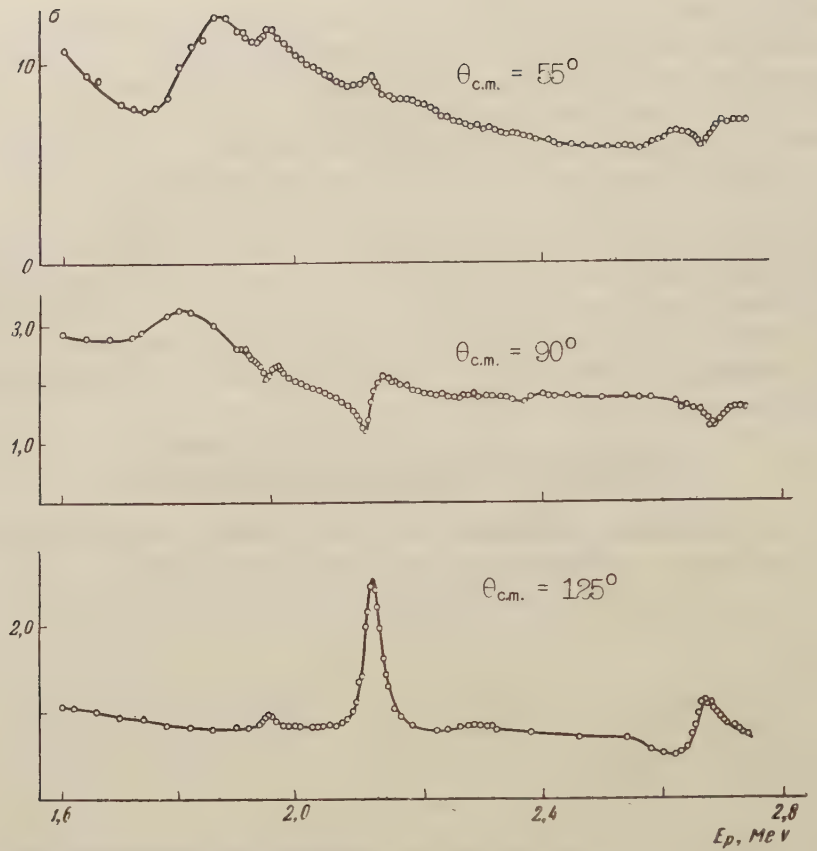

Fig.1. Cross sections (in 10^{-25} cm^2/steradian) for scattering of protons from Ne^{20} at $\theta_{c.m.} = 55, 90$ and 125°.

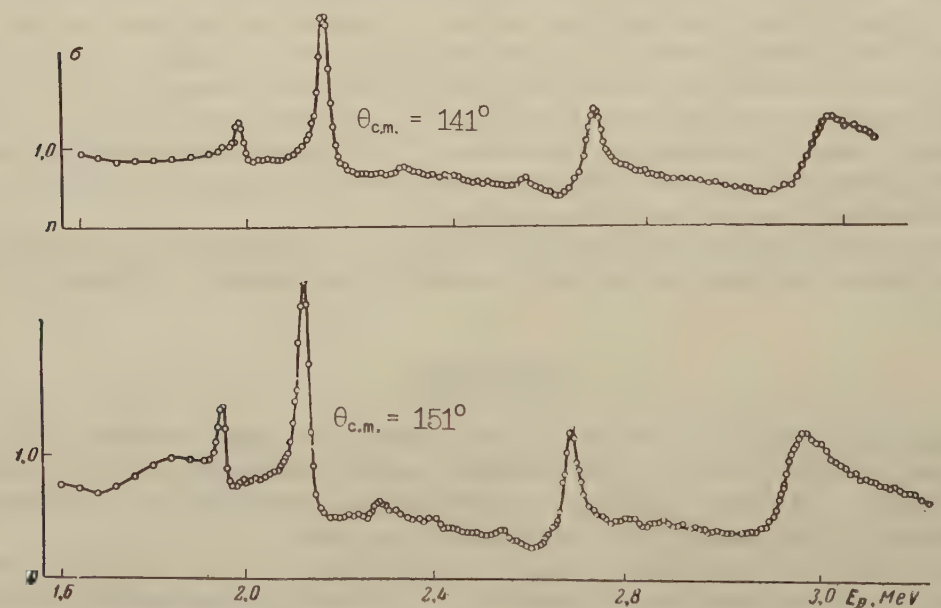

Fig.2. Same as Fig.1 but for $\theta_{c.m.} = 141$ and 151°.

ment was relatively low (±8 kev), it may be that our width values are overestimates.

As will be evident from Fig.1 the resonances at 1.95 and 2.15 Mev at an angle of 125° are symmetrical. It was shown by Smith[6] that for such resonances one can determine Γ_p^2/Γ by using the expression for the resonance scattering integral. The result in this case does not depend on the energy resolution. For the case of scattering of protons by nuclei with spin 0 the area R_s under a symmetrical resonance is related with Γ_p^2/Γ by the equation

$$R_s = \frac{\pi\lambda^2}{4\sigma_{nr}} \cdot \frac{\Gamma_p^2}{\Gamma} H, \qquad (1)$$

where λ is the effective wavelength of the incident proton, σ_{nr} is the cross section for nonresonance scattering, and $H = \sum_L Z^2(lJlJ; \frac{1}{2}L) P_L$ (here l is the proton orbital momentum, J is the level spin and θ is the scattering angle).

On the basis of the areas under the resonance curves we obtained by means of Eq.(1) $\Gamma_p^2/\Gamma = 1 \pm 0.2$ for the resonance at $E_p = 1.95$ Mev and $\Gamma_p^2/\Gamma = 18 \pm 0.2$ for the resonance at $E_p = 2.15$ Mev. From this one can readily establish the lower bounds for the total widths of these levels: $\Gamma \geqslant 1$ kev for the first and $\Gamma \geqslant 18$ kev for the second.

Using our values for the widths we determined the ratio Γ_p/Γ. The results are given in the accompanying table.

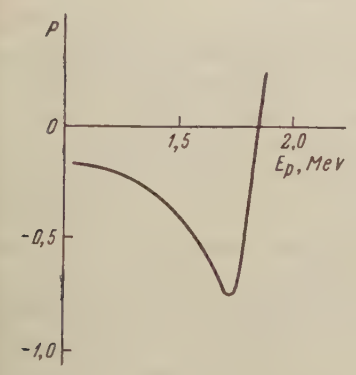

Fig.3. Polarization of protons scattered at an angle of 90° from Ne^{20}.

The great width of the 4.18 Mev level and the fact that its spin and parity are 3/2- give reason to infer that protons scattered from Ne^{21} will be polarized in a rather wide energy interval near $E_p = 1.8$ Mev. Using the results of phase-shift analysis and the equations given in Ref.7, we calculated the energy dependence of the polarization of protons scattered at 90°. The results are shown in Fig.3. The calculations were carried out for the proton energy range from 1 to 1.8 Mev. At higher proton energies one must take into account the influence of the resonances at 1.96 and 2.15 Mev. As will be evident from Fig.3, the polarization of the protons varies smoothly with energy and attains 70%. Elastic scattering from Ne^{20} nuclei can be utilized for determining the polarization of protons with energies from 1 to 1.8 Mev.

References

1. W.Heaberli, A.Galonsky, E.Goldberg & R.Douglas, Phys.Rev., 91, 438 (1953).
2. W.Heaberli, Phys.Rev., 99, 640 (1955).
3. A.K.Wal'ter, A.S.Deineko, I.Ya.Malakhov, P.V.Sorokin & A.Ya.Taranov, Izv. AN SSSR, Ser.fiz., 23, 839 (1959). (Trans.Bulletin, 23, 833.)
4. R.A.Laubenstein & M.I.W.Laubenstein, Phys.Rev., 84, 18 (1951).
5. A.K.Val'ter, I.Ya.Malakhov, P.V.Sorokin & A.Ya.Taranov, Izv.AN SSSR, Ser. fiz., 22, 871 (1958). (Trans.Bulletin, 22, 865.)
6. R.B.Smith, Physica, 24, 1089 (1958).
7. P.V.Sorokin, A.K.Val'ter, I.Ya.Malakhov & A.Ya.Taranov, Zhur.eksp.i teor. fiz., 35, 1386 (1958). (Trans.Soviet Physics - JETP.)

ELASTIC SCATTERING OF PROTONS FROM NUCLEI

- A.P.Klyucharev

On the basis of the experimental results obtained in different laboratories, here and abroad, on proton-nucleus scattering in the range of medium energies it has proved feasible to establish a number of interesting and significant regularities. For example, it has been determined that at proton energies above the potential barrier, the scattering is a diffraction effect, and that the position of the maxima and minima in the curve for the differential cross section vs the scattering angle are determined at a given energy by the mass number of the scatterer and are shifted to the side of smaller angles with increase of the proton energy.[1,2]

The values of the differential cross section calculated on the basis of the optical nuclear model are in satisfactory agreement with the experimental values in an appreciable range of angles and energies.[3,4]

Investigations of proton scattering by medium-Z nuclei at energies lower than the potential barrier showed that the character of the angular dependence of the ratio of the differential cross section determined experimentally to the cross section for Coulomb (Rutherford) scattering - $\sigma(\theta)/\sigma_{Rh}(\theta)$ (θ is the scattering angle) - is quantitatively different for the nuclei of some neighboring elements.[5] With increase in proton energy this difference is gradually effaced. It must be noted that most of the investigations in question were carried out with targets of natural isotopic composition; hence the cross section values are averaged values for the cross sections of the isotopic nuclei comprising the target.

Obviously, a detailed picture of proton-nucleus scattering can be obtained only by studying the effect for different separated isotopes. Research on proton scattering by separated isotopes was first undertaken in the Physical-Technical Institute of the Ukrainian SSR Academy of Sciences (Kharkov). The work is now being continued in collaboration with the Institute of Physics of the Ukrainian SSR Academy of Sciences (Kiev).

Up to now we have investigated the angular distribution of protons elastically scattered from the following separated isotopes: a) at proton energies of 5.45 and 6.8 Mev: Cr^{52}, Cr^{53}, Co^{59}, Ni^{58}, Ni^{60}, Ni^{62}, Cu^{63} and Cu^{65} (Refs.6,7 & 8) and b) at a proton energy of 19.6 Mev: Li^{6}, Li^{7}, Co^{59}, Cu^{63}, Cu^{65}, Ge^{73}, Ge^{74}, Cd^{111}, Cd^{113}, Cd^{116}, Sn^{116}, Sn^{117}, Sn^{118}, Sn^{119}, Sn^{120}, Sn^{122}, Sn^{124}, Pb^{207}, Pb^{208}, Bi^{209} and U^{238} (Ref.9). The proton sources were linear accelerators (5.45 and 19.6 Mev protons) and the Institute of Physics cyclotron (6.8 Mev).

The scattered protons were detected at different angles either by a scintillation spectrometer or nuclear emulsions. The experimental techniques are described in detail in Refs.7 and 10.

Three different procedures were used for preparing the targets in the form of thin foils: electrolytic deposition, vacuum evaporation and vacuum thermal dissociation. These target preparation techniques are described in Ref.11.

The use of the developed detecting techniques in conjunction with thick targets made it possible in most cases to record reliably the elastically scattered protons with complete discrimination of the inelastically scattered protons. An exception was Cr^{53} in the case of bombardment with 6.8 Mev protons (see below). The relative error in the cross section measurements did not exceed 3%.

We shall not discuss in detail here the results obtained for 19.6 Mev protons - they are described in Ref.9. However, we want to mention two interesting facts. Fig.1 shows the angular dependence of the cross section ratio for protons scattered from cadmium 111, 113 and 116. The diffraction scattering pattern is the same for all three isotopes if one neglects the minor displacement of the maxima and minima as a function of the mass number. However, it will be recalled that Cd^{111} has five levels below 600 kev, Cd^{113} has four levels, and Cd^{116} only

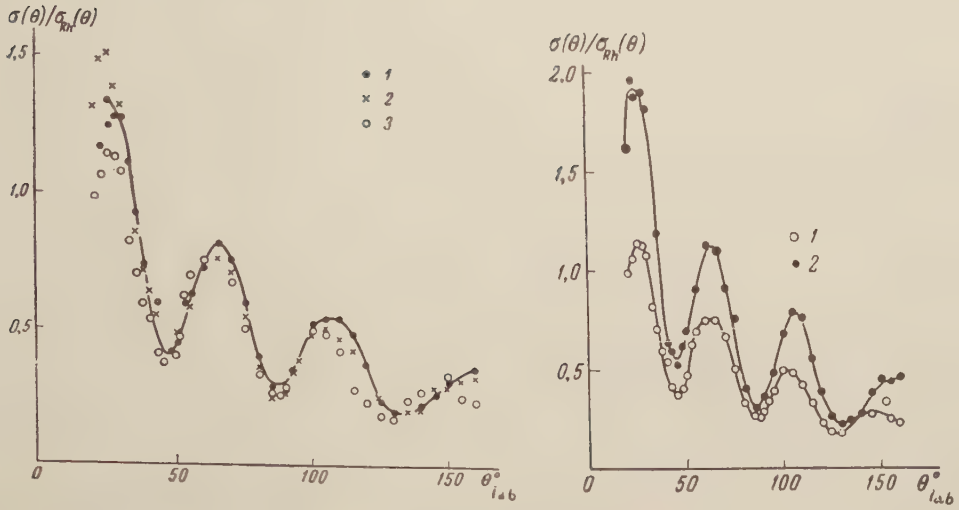

Fig.1. Angular dependence of the ratio of the elastic scattering cross section to the cross section for Coulomb scattering for cadmium isotopes at a proton energy of 19.6 Mev; θ in the laboratory system; 1 - Cd^{111}, 2 - Cd^{114}, 3 - Cd^{116}.
Fig.2. Same as Fig.1 but for Cd^{116} (1) and Sn^{116} (2).

one level.

The inelastically scattered protons associated with these levels could not be discriminated under our experimental conditions. The fact that a diffraction effect pattern is observed in the range of large angles as well indicates that inelastic scattering from the cadmium isotopes at the given energies involves direct interaction so that the contribution of inelastically scattered protons in the region of large angles is relatively small compared to the comtribution from elastically scattered protons.

Fig.2 shows the angular dependences for protons scattered from Cd^{116} and Sn^{116}, both of which are even-even nuclei with the same atomic number. The positions of the maxima and minima in the respective curves are virtually the same. The absolute values of $\sigma(\theta)/\sigma_{Rh}(\theta)$ for Cd^{116} are approximately twice the values for Sn^{116}. Thus the replacement of two neutrons by two protons leads to an appreciable change in the scattering amplitude, whereas change of the number of neutrons by two results in no significant alteration of the curves.

Data on the angular dependence of the ratio of the measured differential cross section for elastic scattering to the cross section for Coulomb scattering in the field of the nucleus for all the investigated isotopic targets (in the energy range below or close to the potential barrier) are summarized in Fig.3.

We note that the angular distribution for Cr^{53} at 6.8 Mev in scattering to large angles is represented by two curves: the upper curve was obtained directly from measurements; the lower curve includes corrections for the angular distribution of inelastically scattered protons with excitation of the 970 and 540 kev levels in Cr^{53}. The data on inelastic scattering were obtained at an energy of 5.4 Mev, but it may be assumed that the curve for inelastic scattering at 6.8 Mev will be quantitatively the same. This assumption is not in conflict with the data on inelastic scattering of 6.8 Mev protons from Cr^{53} with excitation of the 970 kev level and also from neighboring nuclei[12]. Direct interaction at these energies is not observed.

Analyzing the scattering curves shown in Fig.3 we note that at the proton

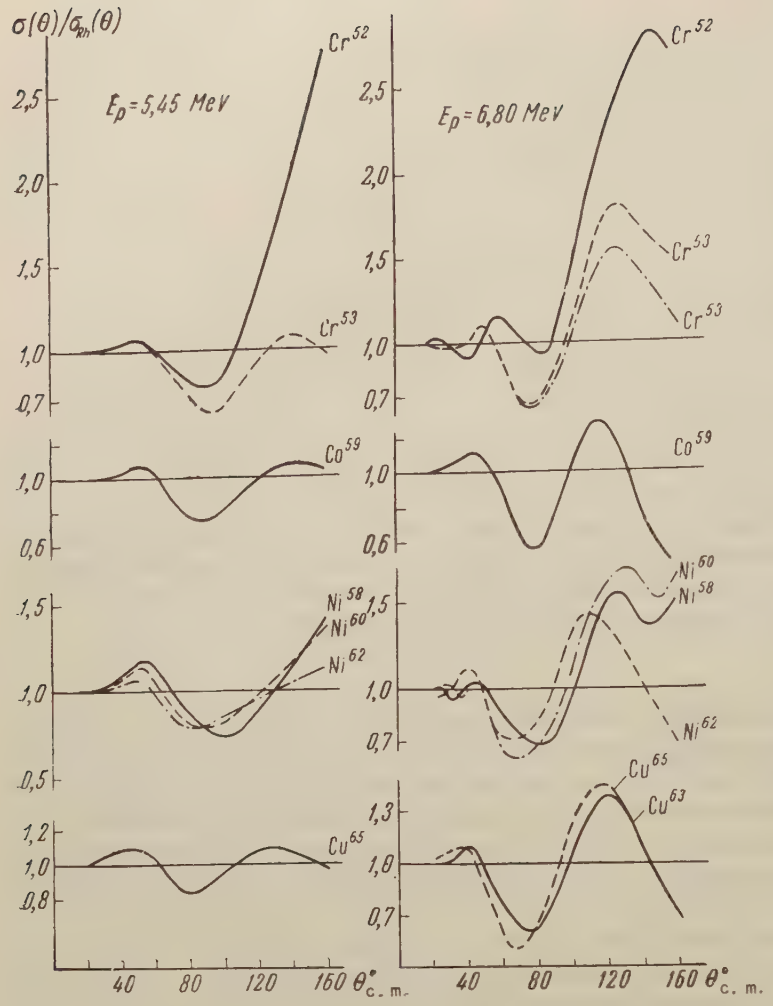

Fig.3. Angular dependence of the cross section for elastic scattering to the cross section for Coulomb scattering at proton energies of 5.45 and 6.8 Mev. θ in the center of mass system.

energy of 5.45 Mev there is a quantitative and a qualitative difference between the angular dependences of $\sigma(\theta)/\sigma_{Rh}(\theta)$ in the range of large angles for even-even nuclei (Cr^{52}, Ni^{58}, Ni^{60} and Ni^{62}) and odd-even nuclei (Co^{59} and Cu^{65}). The angular dependences are similar for odd-even and even-odd nuclei (Cr^{53}, Co^{59} and Cu^{65}). Thus change in the number of nucleons in the nucleus by one results in a quantitative change in the character of the angular distribution of the scattering for proton energies lower than the potential barrier.

Quantitative differences are also observed at these energies for different even-even nuclei, as, for example, in the case of scattering from nickel isotopes. The results obtained at a proton energy of 6.8 Mev, on the one hand, emphasize this difference, and, on the other hand, exhibit a tendency towards smoothing out of this difference. In the angular dependence curve for even-even nuclei a second maximum appears in the region of large angles. With increase of the proton energy above the potential barrier the scattering picture gradually becomes qualitatively similar for even-even as well as for even-odd and odd-even nuclei, that is, diffraction scattering begins to predominate. However, there remains a difference as regards the absolute values of $\sigma(\theta)/\sigma_{Rh}(\theta)$. Most significative here are the data obtained for chromium isotopes. Cr^{53} has only one neutron outside the closed 28 neutron shell, as compared with Cr^{52}. This neutron is weakly bound: its binding energy is 7 Mev, whereas the binding energy of the last neutron in Cr^{52} is 11 Mev. It may be hypothesized that this odd neutron "diffuses" the surface of the Cr^{53} nucleus.

Since the Coulomb potential for both nuclei may be assumed to be the same, the time an incident proton spends within the sphere of action of the nuclear forces will be shorter in the case of Cr^{52} as compared with Cr^{53}. Hence the probability for absorption in the latter case will be greater. The same argument can presumably be applied to odd-even nuclei (Co, Cu) in which the nuclear surface can be "diffused" owing to the presence of an extra odd proton as compared with the neighboring even-even nuclei (Fe, Ni).

Apparently, one can also consider from this standpoint the change in the cross section for scattering at large angles by nickel isotopes: the cross section decreases appreciably with each successive neutron pair increment.

It must be noted that if one regards the even-even nuclei of Ni isotopes as spherical, in the case of Ni^{58} and Ni^{60} there is filled the $3p_{3/2}$ neutron subshell, whereas in the case of Ni^{62} there begins to fill the $4f_{5/2}$ subshell. This can lead to greater "diffusion" of the nuclear surface of the last nucleus and thus to greater absorption of the incident protons at large angles as compared with Ni^{58} and Ni^{60}.

With increase of the incident proton energy the influence of the nuclear surface on the process of interaction of the protons with the nuclei decreases and the above mentioned difference is gradually effaced. As already noted, at energies above the potential barrier, the scattering picture gradually becomes predominantly "diffractive". However, in this case also, the differential cross section depends on the details of the nuclear structure, as is evinced by the results on the angular distribution of protons scattered from Cd^{116} and Sn^{116}.

Physical-Technical Institute,
Academy of Sciences of the Ukrainian SSR

References

1. A.I.Akhiezer & I.Ya.Pomeranchuk, Usp.fiz.nauk, 39, 153 (1949).
2. B.B.Kinsey & T.Stone, Phys.Rev., 103, 975 (1956).
3. A.E.Glassgold, W.B.Cheston, et al, Phys.Rev., 106, 1207 (1957).
4. A.E.Glassgold & P.J.Kellogg, Phys.Rev., 107, 1372 (1957).
5. D.A.Bromly & N.S.Wall, Phys.Rev., 102, 1560 (1956).
6. A.P.Klyucharev & N.Ya.Rutkevich, Zhur.eksp.i teor.fiz., 38, 285 (1960). (Trans.Soviet Physics - JETP.)
7. N.Ya.Rutkevich, V.Ya.Golovnya, A.K.Val'ter & A.P.Klyucharev, Doklady AN SSSR, 130, 1008 (1960). (Trans.Soviet Physics - Doklady.)
8. A.K.Val'ter, I.I.Zalyubovskii, A.P.Klyucharev, M.V.Pasechnik, N.N.Pucherov, & V.I.Chirko, Zhur.eksp.i teor.fiz., 38, 1419 (1960). (Trans.JETP.)
9. R.A.Vanetsian, A.P.Klyucharev & E.D.Fedchenko, Atomnaya energiya, 6, 661 (1959). (Trans.Soviet Journal of Atomic Energy.)
10. R.A.Vanetsian & E.D.Fedchenko, Zhur.eksp.i teor.fiz., 30, 577 (1956). (Trans.Soviet Physics - JETP.)
11. A.D.Bondar', A.S.Emlyaninov, A.P.Klyucharev, L.G.Lishenko, V.N.Medyavik, A.D.Nikolaechuk & O.E.Shalaeva, Transactions of the Tenth All-Union Conference on Nuclear Spectroscopy, Moscow, Jan.1960.
12. N.N.Pucherov, Thesis, Inst.of Physics, Ukrainian Ac.of Sci., 1959.

INVESTIGATION OF THE LEVELS OF K^{41} BY MEANS OF THE $A^{40}(p,\gamma)K^{41}$ REACTION

- A.K.Val'ter, Yu.P.Antuf'ev, V.Yu.Gonchar, A.N.L'vov, E.G.Kopanets & S.P.Tsytko

Introduction

The configuration of the ground state of K^{41}, a nucleus containing 19 protons and 22 neutrons, is $(\pi d_{3/2})^3\ (\nu f_{7/2})^2$; the spin and parity are 3/2+. The excited states of this nucleus have scarcely been studied.

On the basis of the nuclear shell model one can expect to observe a single particle level with spin and parity 7/2-, which corresponds to transition of the last unpaired proton from the $d_{3/2}$ to the $f_{7/2}$ level. Such a level with an energy of 1.29 Mev was actually detected in investigations[1,2] of β-decay of A^{41}.

In investigations of the $A^{40}(d,n)K^{41}$ reaction (Q = 5.62 Mev) there were observed[1,3] levels in K^{41} at 1.34, 3.1 and 4.4 Mev. Investigation of the $K^{40}(n,\gamma)K^{41}$ reaction (Q = 10.109 Mev) led Bartholomew & Kinsey[4] to infer that there may exist two additional levels with energies of 1.66 and 0.72 Mev in K^{41}. The existence of these two levels, however, was not definitely established.

Some data on high lying resonance levels in K^{41} were obtained in studying the $A^{40}(p,\gamma)K^{41}$ reaction (Q = 7.84 Mev) (Refs.1 & 5) and the $K^{40}(n,\gamma)K^{41}$ reaction.

In studying the first of these reactions there were observed five resonances at E_p = 900, 1050, 1080, 1100 and 1235 kev. In studying the second reaction there was observed one level with an excitation energy of 10.109 Mev, corresponding to the binding energy of the attached neutron.

All the above data regarding the levels in K^{41} are summarized in the review article by Endt & Braams[1].

In addition, Freier et al[6] in investigating the elastic scattering differential cross section for p-A^{40} interaction observed resonances at proton energies of 1.90 and 2.48 Mev. In a subsequent investigation[6], we determined the energies of these resonance more accurately and arrived at the following spin and parity assignments for the corresponding levels in K^{41}: 1/2- or 3/2- for the 9.66 Mev level (E_p = 1.86 Mev), and 1.2+ for the 10.23 Mev level (E_p = 2.45 Mev).

In the present work for the purpose of obtaining more data on the levels of K^{41} we investigated the $A^{40}(p,\gamma)K^{41}$ reaction, which enabled us to identify some of the high lying resonance levels of the compound K^{41} nucleus as well as the low lying levels and to determine their spins and parities.

Equipment and Procedure

The protons were accelerated by the electrostatic generator[8] of the Physical-Technical Institute of the Ukrainian SSR Academy of Sciences; this generator is characterized by a high degree of stability and yields a highly monoenergetic proton beam.

The thin A^{40} targets were prepared in the electromagnetic separator by knocking A^{40} ions into a tantalum backing. The thickness of the knocked-in targets was about 3 kev for ~1 Mev protons. The procedure for preparing such targets has been described by Guseva[9]. The isotopic A^{40} targets on tantalum backings withstood a current of the order of 5 microamp for many days without substantial change in the γ-ray yield from the target.

In measuring the excitation function of the reaction, the γ-ray detector was a scintillation counter with a 3 cm diameter, 2 cm thick CsI(Tl) crystal coupled to an FEU-S photomultiplier; the crystal was mounted at 0° to the proton beam. The beam current was measured by a current integrator, the linearity and response of which were checked periodically and found to remain constant during the entire period of the experiment.

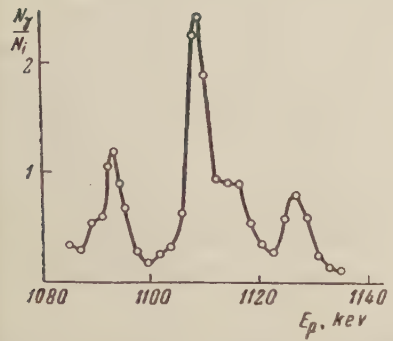

Fig.1. Excitation function of the $A^{40}(p,\gamma)K^{41}$ reaction. N_γ - number of pulses due to γ-rays; N_i - pulses from the current integrator.

The γ-ray spectrum was measured at an angle of 60° relative to the direction of the incident protons by means of the scintillation spectrometer described in Refs.10 & 11. For measuring the γ-ray angular distributions we used a scintillation spectrometer that could be rotated 150° counterclockwise relative to the beam direction about the center of the target.

A similar scintillation spectrometer served as the γ-ray monitor; this was mounted at a fixed angle of 90° relative to the direction of the proton beam.

Experimental Results and Discussion

The excitation function of the $A^{40}(p,\gamma)K^{41}$ reaction was investigated in the proton energy range from 1085 to 1130 kev. The experimental results are shown in Fig.1. Instead of the single resonance at 1100 kev, reported earlier by Broström[5], we detected four resonances at E_p = 1092, 1107.5, 1114 and 1125 kev. The widths of the observed resonance peaks are of the order of 4-5 kev and are, apparently, due to the thickness of the target and the slight energy spread of the proton beam.

We investigated the γ-spectrum corresponding to the two most intense resonances. Analysis of the high energy part of the spectrum associated with the 1092 kev resonance showed that this spectrum comprises γ-lines with energies of 8.9, 7.6, 7.3 and 5.8 Mev. The first of these corresponds to a transition from the 8.91 Mev level to the ground state; the 7.6 and 7.3 Mev lines correspond to transitions to levels at 1.29 and 1.59 Mev, which is substantiated by the presence of γ-lines of energies 1.29 and 1.59 Mev in the soft part of the spectrum. The 5.8 Mev γ-line apparently is due to a cascade transition from the 8.91 Mev level to the known 3.1 Mev level.[1] The presence of a diffuse peak at ~4.5 Mev indicates that there may be a transition from the resonance level to a level at 4.4 Mev (the corresponding γ-line energy is 4.5 Mev) and from the 4.4 Mev level to the ground state. In the soft part of the γ-spectrum associated with this resonance we observed γ-lines with E_γ = 0.60, 0.98, 1.29 and 1.59 Mev, which substantiates the existence of the known[1] levels with energies of 0.72, 1.29 and 1.66 Mev. The 0.98 Mev line may be due to a cascade transition from the 1.59 Mev level to a level at 0.60 Mev.

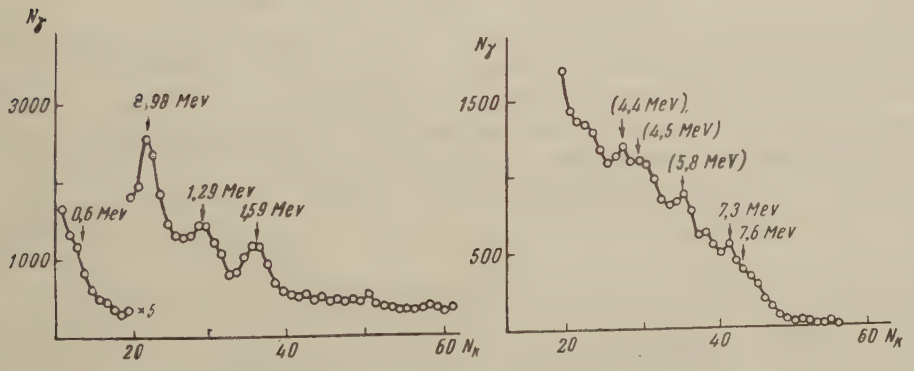

Fig.2. Gamma-ray spectrum for the resonance at E_p = 1107.5 kev.

The low and high energy parts of the γ-spectrum for the 1107.5 kev resonance are shown in Fig.2. There are evident in the spectrum γ-lines with energies of 7.6 and 7.3 Mev, corresponding to transitions to the 1.29 and 1.59 Mev

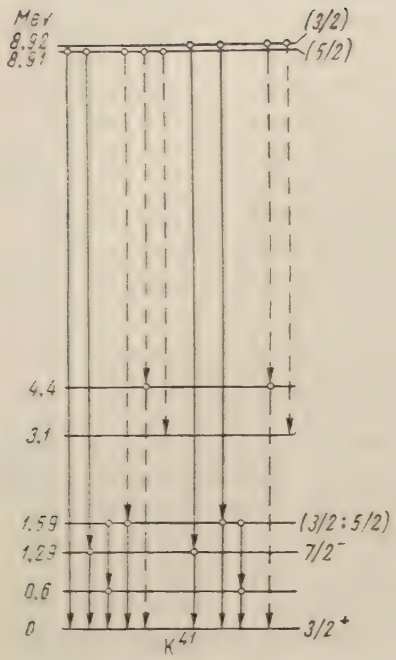

Fig.3. Level scheme for K^{41}.

levels, and a γ-line with E_γ = 5.8 Mev, presumably corresponding to a transition from the 8.92 Mev level to a level at 3.1 Mev. The hypothesized 4.5 and 4.4 Mev lines were not resolved in the spectrum, but it is highly probable that there is a transition from the 8.92 Mev level to the 4.4 Mev level and a further transition from this level to the ground state. We observed no evidence for a cross-over transition from the 8.92 Mev resonance level to the ground state. The soft part of the spectrum for this resonance is similar to the γ-spectrum for the 1092 kev resonance.

On the basis of analysis of the spectra we propose the decay scheme shown in Fig.3. The tentative possible spin assignments arrived at on the basis of preliminary measurements of the angular γ-ray distributions are indicated in parentheses in Fig.3.

We are deeply grateful to M.I.Guseva for preparing the A^{40} targets.

Physical-Technical Institute
Academy of Sciences of the Ukrainian SSR

References

1. P.M.Endt & C.M.Braams, Revs.Mod.Phys., 29, 683 (1957).
2. L.G.Elliot, Phys.Rev., 78, 378 (1950).
3. D.C.Worth, Phys.Rev., 78, 378 (1950).
4. G.A.Bartholomew & B.B.Kinsey, Canad.J.Phys., 31, 927 (1953).
5. K.J.Broström, T.Huus & J.Koch, Nature, 162, 695 (1948).
6. G.D.Freier, K.F.Famularo, D.M.Zipoy & J.Leigh, Phys.Rev., 110, 446 (1958).
7. A.K.Val'ter, I.Ya.Malakhov, P.V.Sorokin & A.Ya.Tarapov, Izv.AN SSSR, Ser. fiz., 23, 846 (1959). (Trans.Bulletin, 23, 839.)
8. A.K.Val'ter & A.A.Tsygikalo, PTE (Instruments & Exper.Techniques), 4, 3 (1957).
9. M.I.Guseva, Ibid., 5, 112 (1957).
10. N.G.Afanas'ev & V.Yu.Gonchar, Atomnaya energiya, 4, 289 (1958). (Trans. Sov.Journ.of Atomic Energy.)
11. N.G.Afanas'ev & V.Yu.Gonchar, Transactions of the Session of the Ukrainian SSR Ac.of Sci.on the Peaceful Uses of Atomic Energy, p.169, Kiev, 1958.
12. Yu.P.Antuf'ev, A.K.Val'ter, V.Yu.Gonchar, E.G.Kopanets, A.N.L'vov, P.M. Tutakin & S.P.Tsytko, in "Yadernye reaktsii pri malykh i srednikh energiyakh" (Nuclear reactions at low and medium energies), p.294, M., 1958.

EXPERIMENTAL AND THEORETICAL STATE-MIXING COEFFICIENTS AND POLARIZATION OF NUCLEONS IN DEFORMED NUCLEI

- D.A.Varshalovich

The state of a nucleon in an axially deformed nucleus without L-S coupling can be characterized by the quantum numbers Σ, Λ and Ω; these are the projections of the spin s, orbital l and total angular momenta j of the nucleon on the nuclear symmetry axis; it will be noted that $\Sigma + \Lambda = \Omega$ inasmuch as $s + l = j$. The presence of Russel-Saunders interaction, however, mixes the states with different Σ and Λ but the same Ω, i.e., part of the time the nucleon will be in the state with $\Sigma = +\frac{1}{2}$ and $\Lambda = \Omega - \frac{1}{2}$, and part of the time in the state with $\Sigma = -\frac{1}{2}$ and $\Lambda = \Omega + \frac{1}{2}$.

Accordingly, the wave function of the nucleon in a deformed nucleus can be represented as the superposition of two functions:

$$\Psi(\Omega) = \alpha\Phi^{+} + \beta\Phi^{-}. \qquad (1)$$

The functions Ψ and Φ are normalized, and α^2 and β^2 are the expectation coefficients, i.e., they characterize the probability of finding the nucleon in one state or the other.

We define the polarization of a nucleon in a deformed nucleus as double the mean value of the projection of the spin on the nuclear symmetry axis:

$$P \equiv 2\langle s\rangle = \alpha^2 - \beta^2; \quad -1 \leqslant P \leqslant 1 \qquad (2)$$

and inversely

$$\alpha^2 = \frac{1+P}{2}; \qquad \beta^2 = \frac{1-P}{2}. \qquad (3)$$

The values of the coefficients α and β and of the polarization P can be calculated theoretically using the Nilsson wave functions.[1] There are, however, a number of factors owing to which the wave functions of an actual nucleus may differ appreciably from the Nilsson wave functions:

1) the basic assumption of the Nilsson model regarding axial symmetry of the nuclear field[2] may not be fulfilled;

2) the Nilsson functions were calculated on the assumption of complete decoupling of the single particle and collective motions, which is valid only in the first approximation; coupling between these motions leads to mixing of the Nilsson configurations;[3]

3) residual pair interaction of the nucleons not entering into the self-consistent nuclear field also leads to change in the wave functions;[4]

4) Nilsson may not have selected with sufficient accuracy the parameters of the model characterizing the self-consistent nuclear field;[1]

5) finally, the wave functions depend on the deformation of the nucleus, and the values of the deformation parameter in many cases may have been determined with appreciable error.

All these factors can appreciably alter the wave functions. Hence we believe it is of interest to compare the theoretical and empirical values of the polarization of the nucleon and the theoretical and experimental values of the coefficients α and β.

The magnitude of the nucleon polarization P and of the coefficients α and β can be determined from the experimental values of the magnetic moments μ of deformed nuclei. The contributions of the internal and collective motions of nucleons to the magnetic moment of the nucleus are determined by the gyromagnetic ratios g_Ω and g_R. According to the collective nuclear model, $g_R = Z/A \approx 0.4$, which is in satisfactory agreement with the experimental values of g_R for different nuclei (0.2 to 0.5), particularly if one bears in mind that in many cases the experimental values of g_R were determined with a substantial uncertainty.

If μ and g_R are known, we can find

$$g_\Omega = \frac{J}{\Omega}\left(\frac{\mu - g_R}{\Omega}\right) + \frac{\mu}{\Omega^2} + g_R\left[1 - \left(\frac{J}{\Omega}\right)^2\right], \tag{4}$$

where J is the total angular momentum of the nucleus.

In contrast to g_R, the value of g_Ω depends substantially on the configuration of the state and for different states not only as regards absolute magnitude but also sign:

$$g_\Omega \Omega = g_s \langle s \rangle + g_l \langle l \rangle, \tag{5}$$

where g_s and g_l are the spin and orbital gyromagnetic ratios for a free nucleon:

$$g_s = \left\{\begin{matrix} +5.58 \\ -3.82 \end{matrix}\right\} \quad \text{and} \quad g_l = \left\{\begin{matrix} 1 \\ 0 \end{matrix}\right\}. \tag{6}$$

From (5), recalling that $\langle s \rangle = \frac{1}{2} P$ and $\langle l \rangle = \Omega - \frac{1}{2} P$, we obtain

$$P = 2\Omega \frac{g_\Omega - g_l}{g_s - g_l}. \tag{7}$$

Thus by means of (4) one can calculate g_Ω from the experimental values of μ and g_R (or assuming $g_R = Z/A$). Having g_Ω, one can find the polarization P of the last unpaired nucleon by means of Eq.(7). Finally, having P one can calculate $|\alpha|$ and $|\beta|$ by means of Eq.(3).

All the enumerated quantities are given in Tables 1 and 2 for odd-proton and odd-neutron nuclei. For purposes of comparison we also list the values of $|\alpha|$ and $|\beta|$ determined from the Nilsson wave functions using the indicated values of the deformation parameter δ. In the last column we give the asymptotic quantum numbers determined from comparison of the experimental level schemes with the theoretical scheme of Nilsson. It will be evident from the table that in actual nuclei states with $\Sigma = +1/2$ and $\Sigma = -1/2$ mix to an appreciably greater extent than follows from the Nilsson functions. The differences are, however, not large so that the sign of the polarization P, except for the case of W^{183}, agrees with the sign of Σ given in the last column. This agreement, on the one hand, supports the Nilsson classification of states according to asymptotic quantum numbers and, on the other hand, allows of checking in each specific case whether the configuration of the state is correctly defined. In particular, the observed divergences for the ground state of W^{183} suggest that it has a different configuration. This is also indicated by the other anomalies observed in the characteristics of this nucleus, for example, the appreciable divergence between the theoretical and experimental values of the parameter a characterizing the position of the energy levels with $K = 1/2$. Possibly the noted divergences of W^{183} and the deviations of α, β and P for other odd-neutron nuclei are partially due to renormalization of the geomagnetic ratios g_s and g_l for the nuclear neutrons.

In the case of Np^{237} ($\mu = 6$ n.m.) and Pu^{241} ($\mu = 1.4$ n.m.) the polatizations are 2.40 and 1.23, respectively, which is in conflict with (2). Apparently, the

Table 1

Nuclei with odd-Z

Nucleus	J^*	μ, n.m.*	g_Ω**	P_{exp}	$\lvert\alpha_{exp}\rvert$	$\lvert\beta_{exp}\rvert$	δ	$\lvert\alpha_{theo}\rvert$	$\lvert\beta_{theo}\rvert$	Ω	π	$[Nn_z\Lambda\Sigma]$
$_{11}Na^{23}$	3/2	+2,217	(+2,15)	+0,75	0,94	0,35	0,37	0,97	0,27	3/2	+	[211+]
$_{13}Al^{27}$	5/2	+3,641	(+1,89)	+0,93	0,98	0,19	0,35	1,00	0,00	5/2	+	[202+]
$_{63}Eu^{153}$	5/2	+1,5	+0,65	−0,38	0,56	0,83	0,30	0,36	0,93	5/2	+	[413−]
$_{65}Tb^{159}$	3/2	(+) 1,52	+1,49	+0,32	0,81	0,58	0,31	0,94	0,35	3/2	+	[411+]
$_{67}Ho^{165}$	7/2	(+) 3,31	+1,12	+0,18	0,77	0,64	0,30	0,95	0,32	7/2	−	[523+]
$_{69}Tu^{169}$	1/2	−0,20 (3)	−2,20	−0,70	0,39	0,92	0,28	0,40	0,92	1/2	+	[411−]
$_{71}Lu^{175}$	7/2	+2,0	+0,66	−0,52	0,49	0,87	0,28	0,22	0,98	7/2	+	[404−]
$_{73}Ta^{181}$	7/2	+2,1	+0,70	−0,46	0,52	0,85	0,23	0,24	0,97	7/2	+	[404−]
$_{73}Ta^{181m}$	5/2	+3,0 (3)	(+1,52	+0,57	0,89	0,46	0,23	0,98	0,22	5/2	+	[402+]
$_{75}Re^{185}$	5/2	+3,171	+1,55	+0,60	0,90	0,45	0,19	0,97	0,25	5/2	+	[402+]
$_{75}Re^{187}$	5/2	+3,176	+1,55	+0,60	0,90	0,45	0,19	0,97	0,25	5/2	+	[402+]
$_{77}Ir^{191}$	3/2	+0,16	(−0,09)	−0,71	0,38	0,93	0,14	0,24	0,97	3/2	+	[402−]
$_{77}Ir^{193}$	3/2	+0,17 (3	(−0,08	−0,71	0,38	0,93	0,12	0,28	0,96	3/2	+	[402−]
$_{93}Np^{237}$	5/2	(+) 6,0 (2,5)	(+3,20)	+2,40	—	—	0,25	0,90	0,45	5/2	+	[642+]
$_{93}Np^{237m}$	5/2	+2,0	(+0,96)	−0,05	0,69	0,73	0,25	0,48	0,88	5/2	−	[523−]
$_{95}Am^{241}$	5/2	(+) 1,4	(+0,63)	−0,30	0,59	0,81	0,27	0,47	0,89	5/2	−	[523−]
$_{95}Am^{243}$	5/2	(+) 1,4	(+0,63)	−0,30	0,59	0,81	0,27	0,47	0,89	5/2	−	[523−]

Table 2

Nuclei with odd-N

Nucleus	J^*	μ, n.m.*	g_Ω **	P_{exp}	$\lvert\alpha_{exp}\rvert$	$\lvert\beta_{exp}\rvert$	δ	$\lvert\alpha_{theo}\rvert$	$\lvert\beta_{theo}\rvert$	Ω	π	$[Nn_z\Lambda\Sigma]$
$^{21}Ne_{11}$	3/2	−0,5 (1)	(0,89)	+0,70	0,92	0,39	0,37	0,98	0,22	3/2	+	[211+]
$^{25}Mg_{13}$	5/2	−0,855	(−0,67)	+0,80	0,95	0,32	0,36	1,00	0,00	5/2	+	[202+]
$^{155}Gd_{91}$	3/2	−0,32	(−0,63)	+0,50	0,87	0,50	0,31	0,91	0,42	3/2	−	[521+]
$^{157}Gd_{93}$	3/2	−0,37 (4)	(−0,69)	+0,54	0,88	0,48	0,31	0,91	0,42	3/2	−	[521+]
$^{161}Dy_{95}$	5/2	−0,38 (5)	(−0,38)	+0,50	0,87	0,50	0,30	0,88	0,47	5/2	−	[752+]
$^{163}Dy_{97}$	5/2	+0,53 (5)	+0,18	−0,24	0,62	0,79	0,30	0,44	0,90	5/2	+	[523−]
$^{167}Er_{99}$	7/2	−0,5 (1)	(−0,30)	+0,55	0,88	0,47	0,29	0,93	0,37	7/2	+	[633+]
$^{171}Yb_{101}$	1/2	+0,43 (5)	+1,38	−0,36	0,57	0,82	0,28	0,48	0,88	1/2	−	[521−]
$^{173}Yb_{103}$	5/2	−0,67 (5)	(−0,53)	+0,70	0,92	0,39	0,28	0,94	0,33	5/2	−	[512+]
$^{177}Hf_{105}$	7/2	+0,61 (3)	+0,20	−0,37	0,56	0,83	0,27	0,32	0,94	7/2	−	[514−]
$^{179}Hf_{107}$	9/2	−0,47 (3)	−0,20	+0,48	0,86	0,51	0,26	0,96	0,30	9/2	+	[624+]
$^{183}W_{109}$	1/2	+0,118	+0,16	−0,04	0,69	0,72	0,21	0,92	0,41	1/2	−	[510+]
$^{189}Os_{113}$	3/2	+0,656	(+0,46)	−0,36	0,57	0,83	0,16	0,46	0,89	3/2	−	[512−]
$^{233}U_{141}$	5/2	(+) 0,51	+0,13	−0,17	0,64	0,77	0,24	0,57	0,82	5/2	+	[633−]
$^{235}U_{143}$	7/2	(−) 0,34	−0,23	+0,42	0,84	0,54	0,24	0,91	0,42	7/2	−	[743+]
$^{241}Pu^{147}$	5/2	(−) 1,4	(−0,94)	+1,23?	—	—	0,27	0,90	0,44	5/2	+	[622+]

---

*The experimental values of J and μ were taken from Ref.5.

**The values of g_Ω given in parentheses were calculated on the assumption that $g_R = Z/A$.

indicated values of μ for these nuclei are too high. For P to be smaller than unity, the magnetic moments must be < 3.7 n.m. for Np^{237} and < 1.1 n.m. for Pu^{241}.

The asymptotic quantum numbers Λ and Σ indicated in the last columns of Tables 1 & 2 actually pertain not to the entire wave function but only to the main configuration, i.e., to Φ^+ with $\alpha^2 > \beta^2$ or to Φ^- with $\beta^2 > \alpha^2$. The selection

rules with respect to the quantum numbers Λ and Σ for γ-, β- and other transitions define for what changes of Λ and Σ the matrix element of the transitions between the main configuration vanishes. When there is an admixture of states with other values of Λ and Σ, the forbidden transition occurs but is retarded as compared with the fully allowed transition. The transition probability depends on the magnitude of this admixture, i.e., essentially on the coefficients α and β. Thus α_{exp} and β_{exp} determine the extent to which the selection rules with respect to asymptotic quantum numbers are fulfilled in each specific case.

Thus the values of the polarization P and the coefficients α and β determined from the experimental values of μ, show that the Nilsson functions are in satisfactory agreement with experiment, that the classification of states according to quantum numbers is meaningful, and that the selection rules with respect to Λ and Σ are valid.

Leningrad Physical-Technical Institute,
Academy of Science of the USSR

References

1. S.G.Nilsson, Kgl.Danske Vid. Selskab. Mat.-Fys. Medd., 29, No.16 (1955).
2. A.S.Davydov & G.F.Fillipov, Zhur.eksp.i teor.fiz., 33, 723 (1957). (Trans. Soviet Physics - JETP.)
3. A.K.Kerman, Kgl.Danske Vid.Selskab.Mat.-Fys.Medd., 30, No.15 (1956).
4. J.N.L.Gauvin, Nucl.Phys., 8, 213 (1958).
5. K.F.Smith, Progr.Nucl.Phys., 6, 52 (1957).

INTERNAL BREMSSTRAHLUNG ACCOMPANYING β-DECAY OF P^{32}

- K.A.Korotkov & A.M.Chernikov

In recent years there have appeared a number of reports[1-5] on measurements of the P^{32} spectrum of internal bremsstrahlung (hereinafter IB) up to an energy of 1100 kev. Some authors[1,2] found that the Knipp-Uhlenbeck[6] theory does not agree with the experimental results, while others[3-5] report agreement. In view of this disparity we undertook an investigation of the IB spectrum accompanying β-decay of P^{32} in the energy range from 20 to 1215 kev.

For the measurements we used a single-channel scintillation spectrometer with a 29 mm diameter, 14 mm thick NaI(Tl) crystal packed in an aluminum container. Prior to measurements, the equipment was heated for three hours and before each measurement we checked the energy calibration and channel width. The temperature in the laboratory was maintained constant.

The β-particles from the P^{32} were absorbed by a beryllium disk 1.025 g/cm^2 thick (Fig.1), which was located midway between the source and the crystal over the opening of the collimator. The collimator, a 50 mm thick disk 17 mm in diameter, was covered with a 10 mm thick layer of plexiglass. The photomultiplier was shielded with a cylinder of bakelite varnish-impregnated cellophane cylinder (wall thickness 8 mm) and lead (10 cm thick). The purpose of all these measures was to reduce to a minimum the external bremsstrahlung produced in the plexiglass, air and surrounding objects. To suppress the K x-rays from the lead collimator the entrance side of the hole was lined with 0.5 mm Fe, and the side toward the crystal with 0.7 mm Cd + 1.5 mm Fe.

The P^{32} sources were prepared from a solution of Na_2HPO_4 by evaporation on a ~0.4 μ thick plastic film. The film was mounted on an inner plexiglass ring of inner diameter 50 mm, outer diameter 84 mm and thickness 0.5 mm. This ring in turn was centered over a plexiglass ring supported on three 2 mm diameter plexiglass rods. The sources were coated with a thin layer of zapon lacquer.

We obtained the spectra of two different sources with activities of 2 and 0.11 mC. The intensity of the background observed in the absence of the source was of the order of 15% relative to the intensity of the IB spectrum at 1200 kev. The statistical uncertainty in all the experimental points was less than 3%; this corresponds to a 4-8 hour counting time per channel in the range of high energies.

The spectrometer was calibrated with reference to the following γ-lines: Zn^{65} 1.12 Mev, Cs^{137} 662 kev, Au^{198} 412 kev, Cr^{51} 323 kev, Hg^{203} 279 kev and the 75 kev Kα x-ray line of Pb (P^{32} + Pb radiator).

The observed pulse distributions were corrected for the background, the energy resolution of the spectrometer, the yield of x-rays from the iodine of the crystal, the external bremsstrahlung from the Be absorber, the recoil electron spectrum, the efficiency of the NaI(Tl) crystal in detecting photons, the absorption of γ-rays by the beryllium and Al + MgO absorbers (packing of the crystal), the geometric efficiency and the rate of decay. In addition, we introduced an appropriate correction taking into account the presence of other isotopes in the source.

The above enumerated corrections to the experimental spectrum were introduced by the procedure proposed by Liden & Starfelt[7]. Two of the corrections (for bremsstrahlung from the Be absorber and the yield of K x-rays from the iodine of the crystal) were taken from the work of Liden & Starfelt[2] and Novey[3], respectively. This was justified inasmuch as our experimental conditions were virtually identical with those of the cited authors.

Evaluations showed that the error involved in introducing the corrections to the IB spectrum amounts to about 6% in the region of high energies and 2.5-3% in the region of low and medium energies. This evaluation does not include the statistical error in measurement.

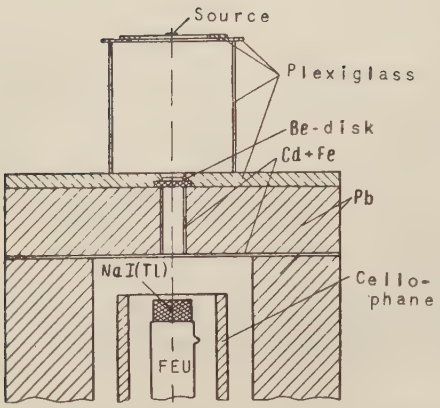

Fig.1. Experimental arrangement for investigating the IB accompanying β-decay of P^{32}.

The spectrum corrected in this manner was compared with the spectrum computed according to the theory of Knipp & Uhlenbeck[6]. According to this theory, the probability for emission of a photon with energy between k and $k+dk$ is given by

$$S(k) = \int_{1+k}^{w_0} P(w_e)\,\Phi(w_e, k)\,dw_e,$$

where w_e is the energy of the primary electrons, k is the photon energy, w_0 is the end-point energy of the β-spectrum, $P(w_e)$ is the probability for emission of a β-particle with energy w_e, and $\Phi(w_e, k)$ is the probability for emission of a photon with energy k from an electron with energy w_e:

$$\Phi(w_e, k) = \frac{\alpha}{\pi k}\frac{p}{p_e}\left\{\frac{w^2+w_e^2}{pw_e}\ln(w+p) - 2\right\}.$$

Here p_e is the electron momentum prior to emission of the photon, w and p are the energy and momentum of the electron after emission ($w = w_e - k$), and α is the fine structure constant. In order to take into account the Coulomb effect one must, according to Nilsson[8] and Lewis & Ford[9] replace $P(w_e)$ by the experimental β-distribution and take $\Phi(w_e, k)$ in the form

$$\Phi(w_e,\ k,\ z) = \Phi(w_e,\ k,\ 0)\,\frac{F(w,\ z)}{F(w_e,\ z)},$$

where $F(w, z)$ is the Fermi function for allowed β-transitions.

In the first approximation one can write

$$\Phi_1(w_e,\ k,\ z) = \Phi(w_e,\ k,\ 0)\,\frac{1+\pi\alpha w/p}{1+\pi\alpha z w_e/p_e}.$$

In Fig.2, curve 1 is the curve calculated according to the Knipp-Uhlenbeck theory, curve 2 is calculated taking into account the Coulomb correction, and 3 gives the experimental points (the results of three series of measurements with the same geometry, using two different sources).

Comparison of the experimental and theoretical data shows that in the energy interval from 20 to 65 kev the experimental points lie somewhat above the calculated ones, which can be explained by the presence of external bremsstrahlung from the source, which we did not take into account. There is a weak rise above the smooth curve in the 65 to 175 kev region. This hump was observed in the work of other authors[1-3]. We explain it by omission of a correction for the back reflection of γ-rays from the photomultiplier, although it must be noted that in the work of Liden & Starfelt[2] such a correction was introduced, but a bump was still observed. In the energy range above 175 to 200 kev the experimental points deviate increasingly from the theoretical curves. The absolute values of the experimental ordinates in the 250 kev region lie approximately 15% above the values given by theory, at 500 kev the upward deviation is 28%, and at 1215 kev - 80%. These differences are appreciably greater than the experimental error.

The corrected theory taking into account the Coulomb effect in the first approximation also does not agree with experiment although the divergence in the range of high energies is somewhat reduced. The total IB γ-ray energy per β-decay evaluated from our results is $2.89\cdot10^{-3}$ mc^2/β which is 22% higher than the theoretical value of $2.37\cdot10^{-3}$ mc^2/β.

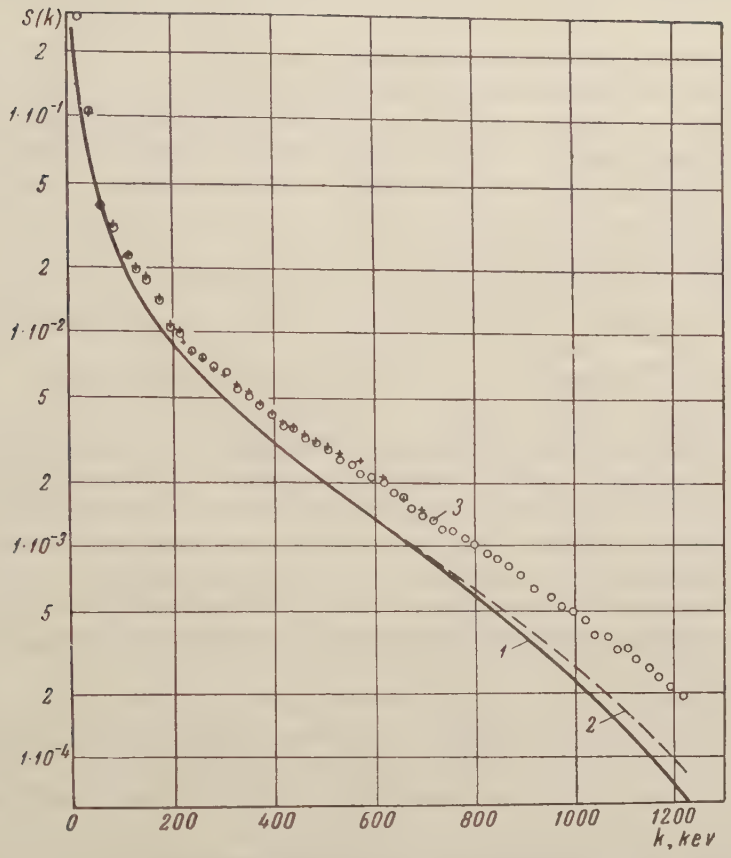

Fig.2. Spectrum of internal berhmsstrahlung accompanying β-decay of P^{32}: 1 - curve calculated according to the Knipp & Uhlenbeck theory (z = 0), 2 - curve calculated taking into account the Coulomb correction (z ≠ 0), 3 - experimental points.

In general our results are in good agreement with the data of Liden & Starfelt.[2]

Voronezh State University

References

1. A.Michalowicz, J.phys.et radium, 15, 156 (1954).
2. K.Lidén & N.Starfelt, Phys.Rev., 97, 419 (1955).
3. T.B.Novey, Phys.Rev., 89, 672 (1953).
4. M.Goodrich & W.B.Payne, Phys.Rev., 94, 405 (1954).
5. P.Bolgiano, L.Madanski & F.Rasetti, Phys.Rev., 89, 679 (1953).
6. J.K.Knipp & G.E.Uhlenbeck, Physica, 3, 425 (1936).
7. K.Lidén & N.Starfelt, Arkiv Fys., 7, 427 (1954).
8. S.B.Nilsson, Arkiv Fys., 10, 467 (1956).
9. R.R.Lewis & G.W.Ford, Phys.Rev., 107, 756 (1957).

EXCITATION OF COLLECTIVE NUCLEAR LEVELS IN STRIPPING REACTIONS

- A.M.Korolev

Introduction

The theory of the stripping reaction in the case of direct interaction of a deuteron with the nuclear surface was developed by Butler,[1] who determined the angular distribution of the captured nucleon. Butler also pointed out that stripping reaction experiments could be of great help in determining the spin and parity of the excited and ground states.

Bhatia et al[2] found the angular distribution for the stripping reaction in the Born approximation; their results do not differ significantly from those of Butler.

More systematic calculations were carried out by Tobocman[3], who took into account the scattering of the deuteron and proton by the nucleus.

None of these theories, however, can satisfactorily explain the large-angle angular distribution of the (d,p) reaction products.[4] Hence we felt it would be of interest to analyze theoretically the mechanism of the stripping reaction, but in terms other than those of the single-particle nuclear and Coulomb interactions.

In addition to producing a compound nucleus, the (d,p) reaction may involve a collective interaction of the nucleons with the nuclear surface, in which case it is possible that neutron capture may result not in the ground state, but in a collective excited state.

Several authors[5,6] have investigated the excitation of such collective levels in the strong coupling limit for highly deformed nuclei, when primarily rotational levels are excited. In the present work we shall consider a different limit, namely, that of weak coupling, when the collective oscillation spectrum is essentially of a vibrational nature, the initial nucleus is spherical, and the final nucleus obtained after neutron capture is weakly deformed. In our opinion such nuclei exhibit several interesting properties in relation to the stripping reaction.

1. Statement of the problem

We shall consider stripping reactions (also called (d,p) reactions) on even-even spherical nuclei with some (but not very many) nucleons outside the closed shell. After capture of a neutron by such a system, the resulting nucleus may be in the ground state or it may be in a collective or single-particle excited state. The nucleon-nuclear surface collective interaction is most likely to excite collective states.

Since the collective interaction is weak compared to the interaction due to the nuclear potential, we may use the Born approximation for our calculations.

According to Bohr's generalized model,[6] the Hamiltonian for the nucleon-nuclear surface interaction, responsible for the neutron capture in the stripping reaction, is of the form

$$H' = -V_p R_0 \delta(r_p - R_0) \sum_\mu \alpha_{2\mu} Y_{2\mu}(\theta_p \varphi_p) - V_n R_0 \delta(r_n - R_0) \sum_\mu \alpha_{2\mu} Y_{2\mu}(\theta_n \varphi_n). \qquad (1)$$

The first and second terms in this equation describe the interaction of the proton and the neutron, respectively, with the nuclear surface, and the $\alpha_{2\mu}$ are given in terms of the phonon creation and destruction operators b_μ and b_μ^* by

$$\alpha_{2\mu} = \sqrt{\frac{\hbar}{2B\omega}}\,(b_\mu + (-1)^\mu b^*_{-\mu}). \tag{1a}$$

The initial state of the system consists of an incident deuteron with wave vector k_d and the even-even target nucleus in its ground state. The final state consists of an outgoing proton with wave vector k_p and the newly formed nucleus, with the captured neutron, in the ground state or in an excited state with binding energy E_β. The wave functions of these states are

$$\Psi_i(\mathbf{r}_p\mathbf{r}_n) = \frac{1}{(2\pi)^{3/2}}\, e^{i\frac{\mathbf{k}_d}{2}(\mathbf{r}_p+\mathbf{r}_n)}\varphi_d(|\mathbf{r}_p-\mathbf{r}_n|)\, X_1^{m_d}\Phi_0, \tag{2}$$

and

$$\Psi_f(\mathbf{r}_p\mathbf{r}_n) = \frac{1}{(2\pi)^{3/2}}\, e^{ik_p\left(\mathbf{r}_p-\frac{M}{M_f}\mathbf{r}_n\right)} X_{S_p}^{\mu_p}\Phi_N^{JM}(\mathbf{r}_n). \tag{2a}$$

If we start with the Hulthen approximation for the two-particle meson potential, the radial part of the deuteron wave function will be[7]

$$\varphi_d(r) = N\,\frac{e^{-\alpha r}}{\alpha r}(1-e^{-\alpha r}). \tag{2b}$$

In Eq. (2), $X_1^{m_d}$ is the spin function of the deuteron, describing the triplet two-particle state, while $X_{S_p}^{\mu_p}$ and $X_{S_n}^{\mu_n}$ are the neutron and proton spin functions, respectively.

Let us assume that the nucleus produced in the reaction has total angular momentum J with z-component M, and principal collective-level number N_0.

The wave function of this nucleus must then describe a system consisting of an even-even core and a neutron interacting with its surface.[8] It is of the form

$$\Phi_{N_0}^{JM}(r) = \sum_{Nk'Rl_n} a_{Nk'Rl_n}^{N_0JM}\,\widetilde{\Phi}_N[Rs(k')\,t'_n;\ JM]\,\varphi_{ln}(r_n). \tag{3}$$

The sum in (3) is over the phonon number $N = 0, 1, 2$, the angular momentum R of the core, and the spin k' and orbital angular momentum l_n of the odd neutron.

The $\widetilde{\Phi}_N[Rs(k')\,l_n;\ lM]$ functions depend on both the spin and the angle variables of the odd nucleon.

They form a complete set of orthonormal functions according to

$$\widetilde{\Phi}_N[Rs(k')\,l_n;\ JM] = \sum_{\mu_n m_n}(RsM-m_n-\mu_n\,|\,Rsk'M-m_n)\times$$
$$\times(k'l_nM-m_nm_n\,|\,k'l_nJM)\,Y_{l_nm_n}(\theta_n\varphi_n)\,X_S^{\mu_n}\Phi_{NR}^{M-m_n-\mu_n}. \tag{3a}$$

Thus the collective nucleon-nuclear surface interaction is accounted for in our method both by our choice of Hamiltonian (1) and by our choice of the final-nucleus wave function, in which collective effects are included.

We now go on to the Born approximation for the transition matrix element for the stripping reaction.

Using our interaction Hamiltonian and initial and final wave functions of Eqs. (2) and (2a), we obtain

$$M = \int\Psi_i^* H'\Psi_f\, d\mathbf{r}_n d\mathbf{r}_p d\sigma_n d\sigma_p d\gamma = M_p + M_n, \tag{4}$$

where the interaction of the proton with the nuclear surface is accounted for in

$$M_p = -V_p R_0^3 \sum_\mu \int \Psi_i^* (\mathbf{R}_0, \mathbf{r}_n) \alpha_{2\mu} Y_{2\mu} (\theta_p \varphi_p) \Psi_f (\mathbf{R}_0, \mathbf{r}_n) d\Omega_p d\mathbf{r}_n d\sigma_p d\sigma_n d\gamma, \tag{4a}$$

and the interaction of the neutron is accounted for in

$$M_n = -V_n R_0^3 \sum_\mu \int \Psi_i^* (\mathbf{r}_p, \mathbf{R}_0) \alpha_{2\mu} Y_{2\mu} (\theta_n \varphi_n) \Psi_f (\mathbf{r}_p, \mathbf{R}_0) d\Omega_n d\mathbf{r}_p d\sigma_n d\sigma_p d\gamma. \tag{4b}$$

The integration in Eqs. (4)-(4b) is over both the space and the spin variables of the neutron and proton, as well as over the collective variables.

2. Neutron part of the transition matrix element

Before going on to a calculation of M_n, we point out one of its properties which will make the calculation somewhat simpler. Expression (1a) for the $\alpha_{2\mu}$ operators guarantees that only the single-phonon amplitude in Ψ_f gives a nonzero contribution to the matrix element. For this reason the sum over N and R in (3) will vanish, and the expansion coefficients will be of the simple form[8]

$$a_{1k'2l_n}^{N_0 J} = -\tilde{g}_n [(2l_n + 1)(2k' + 1)]^{1/2} (l_n 200 / l_n 2 l_0 0) W (l_0 2Jk'; l_n s), \tag{5}$$

where

$$B_{l_n} = \frac{\varphi_{l_n} (\beta B_0)}{\sqrt{N (W_J) (W_J - E_{l_n 1} - 2\tilde{g}_n \alpha_{l_n 2})}} \quad \text{and} \quad \tilde{g}_n = V_n R_0 \sqrt{\frac{\hbar}{2B\omega}} \left(\frac{5}{4\pi}\right)^{1/2}.$$

Inserting (2) and (2a) into (4b) and making use of (5), we obtain

$$\begin{aligned} M_n = \frac{1}{(2\pi)^3} \tilde{g}_n V_n R_0^3 \sum_{k' l_n} \sum_{\mu \mu_n} \sum_{m_n} [(2l_n + 1)(2k' + 1)]^{1/2} \times \\ \times (l_n 200 \,|\, l_n 2 l_0 0) (2s\mu\mu_n \,|\, 2sk'\mu + \mu_n) (k' l_n \mu + \mu_n m_n \,|\, k' l_n JM) \times \\ \times W (l_0 2Jk'; l_n s) \langle 0 \,|\, \alpha_{2\mu} \,|\, 1 \rangle \langle m_d \,|\, \mu_n \mu_p \rangle B_{l_n} L_{l_n m_n}^{(n)}, \end{aligned} \tag{6}$$

where $\langle 0 \,|\, \alpha_{2\mu} \,|\, 1 \rangle$ and $\langle m_d \,|\, \mu_n \mu_p \rangle$ are the matrix elements taken over the collective and spin variables, and

$$L_{l_n m_n}^{(n)} = \int e^{-i \frac{\mathbf{k}_d}{2} (\mathbf{r}_p + \mathbf{R}_0)} \varphi_d (|\mathbf{r}_p - \mathbf{R}_0|) Y_{2\mu} (\theta_n \varphi_n) e^{i \mathbf{k}_p \left(\mathbf{r}_p - \frac{M}{M_f} \mathbf{R}_0\right)} \times Y_{l_n m_n} (\theta_n \varphi_n) \varphi_{l_n} (\beta R_0) d\mathbf{r}_p d\Omega_n. \tag{6a}$$

The remaining notation is the same as in Ref. 8.

The integration in (6a) is not particularly difficult to perform. We write $\mathbf{r}_p - \mathbf{R}_0 = \mathbf{r}$, so that $d\mathbf{r}_p d\Omega_n = d\mathbf{r} d\Omega_n$ ($\mathbf{R}_0$ is a vector of fixed length), expand the plane waves in spherical harmonics[9]

$$e^{i\mathbf{k}\mathbf{r}} = 4\pi \sum_{lm} i^l j_l (kr) Y_{lm}^* (\theta_k \varphi_k) Y_{lm} (\theta_r \varphi_r), \tag{7}$$

and use the known expression for the integral of a product of three spherical functions.[9] After some relatively simple operations we arrive at

$$L_{l_n m_n}^{(n)} = (4\pi)^{1/2} \sum_L \left[\frac{5}{4\pi} (2l_n + 1)\right]^{1/2} (l_n 200 \,|\, l_n 2L0) (l_n 2 m_n \mu \,|\, l_n 2L0) \times Q (K) j_L (kR_0) \varphi_{l_n} (\beta R_0), \tag{8}$$

where

$$Q (K) = \int_0^\infty \frac{\sin Kr}{Kr} \varphi_d (r) r^2 dr = \frac{N_d}{\alpha} \left[\frac{1}{K^2 + \alpha^2} - \frac{1}{K^2 + (\alpha + \varkappa)^2}\right], \tag{8a}$$

$j_L (kR_0)$ is a spherical Bessel function, and the dependence of $L_{l_n m_n}^{(n)}$ on the proton scattering angle ϑ_p is defined by

$$K = \sqrt{k_p^2 + \frac{k_d^2}{4} - k_p k_d \cos\vartheta_p} \quad \text{and} \quad k = \sqrt{k_p^2 + k_d^2 - 2k_p k_d \cos\vartheta_p}.$$

We insert (8) into (6) and sum the Clebsch-Gordan coefficients[10] over μ, m_n, k' and L obtaining

$$M_n(k, K) = (\pi)^{-3/2}\tilde{g}_n^2 R_0^2 i^{l_0}(sl_0\mu_n 0 \mid sl_0 J\mu_n) Q(K) j_{l_0}(kR_0)(2l_0+1)^{1/2} \times \\ \times \sum_{l_n}(l_0 200 \mid l_0 2l_n 0)^2 \varphi_{l_n}(\beta R_0) B_{l_n} \langle m_d \mid \mu_p \mu_n\rangle. \tag{9}$$

Here we must note the following properties of the matrix element whose square gives the angular distribution of the protons in the stripping reaction.

Eq.(9) shows that both when the neutron is captured into the ground state or a single-particle excited state and when a collective level is excited, the proton angular distribution is determined by the orbital angular momentum l_0 of the corresponding single-particle level, as though the nucleus were spherical.

Thus it is immaterial that the state of the neutron interacting with the nuclear surface is a mixture of states with different orbital angular momenta; these different states are not evinced in the angular distribution, and experiments show only one peak, rather than the three one might expect.[11] The angular distribution will be the same as that obtained by Butler[1] (or, more accurately, identical with that deduced by Bhatia[2]).

3. The proton part of the transition matrix element

According to (4a), (2), (2a) and (5) the proton part of the transition matrix element will be of the form

$$M_p = \frac{1}{(2\pi)^3} V_p R_0^3 \sum_{k' l_n \mu\mu_n} \sum_{m_n} [(2l_n+1)(2k'+1)]^{1/2}(l_n 200 \mid l_n 2l_0 0) \times \\ \times (2s\mu\mu_n \mid 2sk'\mu+\mu_n)(k' l_n \mu+\mu_n m_n \mid k' l_n J M) W(l_0 2Jk'; l_n s) \times \\ \times \langle 0 \mid \alpha_{2\mu} \mid 1\rangle \langle m_d \mid \mu_p \mu_n\rangle B_{l_n} L_{l_n m_n}^{(p)}, \tag{10}$$

where

$$L_{l_n m_n}^{(p)} = \int e^{-i\frac{k_d}{2}(R_0+r_n)} \varphi_d(\mid R_0 - r_n \mid) Y_{2\mu}(\theta_p \varphi_p) e^{ik_p\left(r_p - \frac{M}{M_f}R_0\right)} \times Y_{l_n m_n}(\theta_n \varphi_n)\varphi_{l_n}(\beta R_0)\, dr_n\, d\Omega_n. \tag{10a}$$

We shall integrate (10a) in the same way as we did (6a). In this case, however, we shall have need of the following relations, which may be obtained by expanding the plane wave $e^{i(k_1+k_2)r}$ in spherical Bessel functions:

$$i^l j_l(\mid k_1 + k_2 \mid r) Y_{lm}^*(\theta\varphi) = 4\pi \sum_{l_1 m_1} \sum_{l_2 m_2} i^{l_1+l_2}\left[\frac{(2l_1+1)(2l_2+1)}{4\pi(2l+1)}\right]^{1/2}(l_1 l_2 00 \mid l_1 l_2 l0) \times \\ \times (l_1 l_2 m_1 m_2 \mid l_1 l_2 lm) j_{l_1}(k_1 r) j_{l_2}(k_2 r) Y_{l_1 m_1}^*(\vartheta_1\varphi_1) Y_{l_2 m_2}^*(\vartheta_2\varphi_2); \tag{11}$$

$$h_l^{(1)}(\mid k_1 + k_2 \mid r) Y_{lm}^*(\theta\varphi) = 4\pi \sum_{l_1 m_1} \sum_{l_2 m_2}\left[\frac{(2l_1+1)(2l_2+1)}{4\pi(2l+1)}\right]^{1/2}(l_1 l_2 00 \mid l_1 l_2 l0) \times \\ \times (l_1 l_2 m_1 m_2 \mid l_1 l_2 lm) h_{l_1}^{(1)}(k_1 r) i_{l_2}(k_2 r) Y_{l_1 m_1}^*(\vartheta_1\varphi_1) Y_{l_2 m_2}^*(\vartheta_2\varphi_2)$$

$$\text{for } k_1 > k_2, \tag{11a}$$

where $\theta\varphi$, $\vartheta_1\varphi_1$ and $\vartheta_2\varphi_2$ are the directions of $k_1 + k_2$, k_1 and k_2, respectively. The $h_{l_1}^{(1)}(kr)$ and $i_{l_2}(kr)$ functions are, to within phase factor[9], spherical Hankel functions of the first kind and Bessel functions of an imaginary argument; the phase factors are chosen so as to make these functions real.

If $h_l^{(1)}(kr)$ is represented by an integral along the real axis, Eq.(11a) turns out to be a consequence of (11). These relations are a generalization of the well-known[12] corresponding relations in the theory of Bessel functions for $l = 0$.

In order to integrate (10a) we replace $dr_n d\Omega_p$ by $dr\, d\Omega_p$ and $R_0 - r_n$ by r, and use Eq.(11a) for $\varphi_{l_n}(\beta r_n) = N_{l_n} h_{l_n}^{(1)}(\beta |R_0 - r|)$.

After some tedious operations involving (11) and (11a) and similar relations, the integral in (10a) can be taken and we arrive at

$$L_{l_n m_n}^{(p)}(\vartheta_p) = 4\pi \frac{N_d}{\alpha} \sum_{l_1 m_1} \sum_{l_2 m_2} i^{l_n + l - l_1} \left[\frac{5(2l_1+1)(2l_2+1)}{4\pi(2l+1)(2l_n+1)}\right]^{1/2} (l_1 200 | l_1 2l0) \times$$

$$\times (l_1 2 m_1 \mu | l_1 2lm)(l_1 l_2 00 | l_1 l_2 l_n 0)(l_1 l_2 m_1 m_2 | l_1 l_2 l_n m_n) \times j_l(kR_0) Y_{lm}(\vartheta_k \varphi_k) F_{l_1 l_2}(\alpha, \beta, q), \qquad (12)$$

where

$$F_{l_1 l_2}(\alpha, \beta, q) = \left\{\varphi_{l_1}(\beta R_0) P_{l_2}(\alpha, \beta, q) + e^{-\alpha R_0} \sum_{LL'} i^L [(2l_2+1)(2L+1)^2]^{1/2} \times \right.$$

$$\left. \times (l_2 L 00 | l_2 L L' 0)^2 P_{L'}(\alpha, \beta, q) \left[(1+\alpha R_0) j_L(qR_0) + qR_0 \frac{dj_L(qR_0)}{(qR_0)} H_{Ll_1}^{(0)}(\beta R_0) + j_L(qR_0) H_{Ll_1}^{(1)}(\beta R_0)\right]\right\}; \qquad (12a)$$

here

$$H_{Ll_1}^{(0)}(\beta R_0) = (\varphi_L(\beta R_0) i_{l_1}(\beta R_0) - i_L(\beta R_0) \varphi_{l_1}(\beta R_0)); \qquad (12b)$$

$$H_{Ll_1}^{(1)}(\beta R_0) = \left(i_{l_1}(\beta R_0) \frac{d\varphi_L(\beta R_0)}{d(\beta R_0)} - \varphi_{l_1}(\beta R_0) \frac{di_L(\beta R_0)}{d(\beta R_0)}\right); \qquad (12c)$$

$$P_{l_2}(\alpha, \beta, q) = \int_{-1}^{+1} \frac{P_{l_2}(t)\, dt}{\Delta^2 - 2i\beta q t}. \qquad (12d)$$

The function $P_{l_2}(t)$ in (12d) is a Legendre polynomial, and $\Delta^2 = q^2 + \alpha^2 - \beta^2$.

For the four lowest values of l_2 this integral will be of the form

$$P_0(\alpha, \beta, q) = \frac{1}{2\beta q} \operatorname{arctg} \frac{2\beta q}{\Delta^2}, \qquad (13a)$$

$$P_1(\alpha, \beta, q) = \frac{i}{2\beta q}\left(1 - \frac{\Delta^2}{2\beta q} \operatorname{arctg} \frac{2\beta q}{\Delta^2}\right), \qquad (13b)$$

$$P_2(\alpha, \beta, q) = \frac{1}{4\beta q}\left[\frac{3\Delta^2}{2\beta q}\left(1 - \frac{\Delta^2}{2\beta q} \operatorname{arctg} \frac{2\beta q}{\Delta^2}\right) - \operatorname{arctg} \frac{2\beta q}{\Delta^2}\right], \qquad (13c)$$

$$P_3(\alpha, \beta, q) = \frac{i}{4\beta q}\left[5\left(\frac{1}{3} - \frac{\Delta^4}{(2\beta q)^2} + \frac{\Delta^6}{(2\beta q)^3} \operatorname{arctg} \frac{2\beta q}{\Delta^2}\right) - 3\left(1 - \frac{\Delta^2}{2\beta q} \operatorname{arctg} \frac{2\beta q}{\Delta^2}\right)\right]. \qquad (13d)$$

The spherical coordinates $\vartheta_k \varphi_k$ give the angle between $\mathbf{k} = \mathbf{k}_p - \mathbf{k}_d$ and $\mathbf{q} = \frac{\mathbf{k}_d}{2} + \frac{M}{M_f}\mathbf{k}_p$. If we neglect recoil of the nucleus, $\mathbf{q} = \frac{\mathbf{k}_d}{2}$, and then ϑ_k is simply related to the proton emission angle by

$$\cos \vartheta_k = \frac{k_p \cos \vartheta_p - \frac{k_d}{2}}{k(\vartheta_p)}. \qquad (14)$$

Inserting (12) into (10) and using Racah techniques to sum the Clebsch-Gordan coefficients over μ, m_n and k', we arrive at

$$M_p(k,q)=\frac{1}{2\pi}\tilde{g}_n\tilde{g}_p\frac{N_d}{\alpha}\sum_{l_1l_2}\sum_{ll_n}\sum_m i^l\sqrt{\frac{(2l_1+1)}{(2l+1)}}(2l_n+1)(2l_2+1)(l_1200\,|\,l_1 2l0)\times$$

$$\times(l_n200\,|\,l_n2l_00)(l_nl_200\,|\,l_nl_2l_10)(l_2l_00m\,|\,l_2l_0lm)(sl_0\mu_nm\,|\,sl_0JM)\times$$

$$\times W(l_2l_nl2;\,l_1l_0)\langle m_d\,|\,\mu_n\mu_p\rangle\, j_l(kR_0)\,Y_{lm}(\vartheta_k\varphi_k)\,B_{l_n}\times(F_{l_1l_2}(\alpha,\beta,q)-F_{l_1l_2}(\varkappa,\beta,q)). \quad (15)$$

If $q^2-\beta^2+\alpha^2\gg 2\beta q$, then $P_{l_2}(\alpha,\beta,q)\sim\left(\frac{2\beta q}{\Delta^2}\right)^{l_2}$ and the greatest contribution to (15) is from the $l_2=0$ wave. In this case the expression is greatly simplified, and we have

$$M_p(k,q)=\frac{1}{2\pi}\tilde{g}_n\tilde{g}_p\sum_{m_0}i^{l_0}\langle m_d\,|\,\mu_n,\mu_p\rangle\,(sl_0\mu_nm_0\,|\,sl_0JM)\,j_{l_0}(kR_0)\,Y_{l_0m_0}(\vartheta_k\varphi_k)\times$$

$$\times\sum_{l_n}(l_0200\,|\,l_02l_n0)^2\,B_{l_n}(F_{l_n0}(\alpha,\beta q)-F_{l_n0}(\varkappa,\beta,q)). \quad (16)$$

4. Proton angular distribution from the stripping reaction

In the Born approximation the expression for the differential cross section for stripping is

$$d\sigma=\frac{1}{4\pi^2\hbar^4}M_p^*M_d^*\frac{k_p}{k_d}M^2\,d\Omega_p, \quad (17)$$

where M_p^* and M_d^* are the reduced masses of the proton and deuteron, respectively. Further, the square of the matrix element must be averaged over the triplet states of the deuteron and summed over all possible states of the system after the interaction, i.e., over the quantum numbers M and μ_p of the nucleus and proton. When this is done in (15), the proton angular distribution in the (d,p) reaction is given by

$$d\sigma=\frac{\tilde{g}_n^2R_0^4}{\pi(2\pi\hbar)^4}(2J+1)M_p^*M_d^*\frac{k_p}{k_d}\Big\{\tilde{g}_n^2Q^2(\alpha,K)\,j_{l_0}(kR_0)\,G_{l_0}^2(\beta)+$$

$$+\tilde{g}_n\tilde{g}_p\sum_l[G_{l_0}^*(\beta)\,D_{l0}(\alpha,\beta,q)+G_{l_0}(\beta)\,D_{l0}^*(\alpha,\beta,q)]\,j_{l_0}(kR_0)\,j_l(kR_0)\,Y_{l0}(\vartheta_k)\,Q(\alpha,k)+$$

$$+\tilde{g}_p^2\sum_{l'l}\sum_{Lm}\left[\frac{(2L+1)(2l+1)}{4\pi(2l'+1)}\right]^{1/2}(lL00\,|\,lLl'0)\,(lLm0\,|\,lLl'm)\,D_{lm}^*D_{l'm}\times j_l(kR_0)\,j_{l'}(kR_0)y_{L0}(\varsigma_k)\Big\}\,d\Omega_p, \quad (18)$$

where

$$G_{l_0}(\beta)=(2l_0+1)^{1/2}\sum_{l_n}(l_0200\,|\,l_02l_n0)^2\,\varphi_{l_n}(\beta R_0)\,B_{l_n}, \quad (18a)$$

$$D_{ilm}=\sum_{l_1l_2}\sum_{l_n}i^{l-l_0}\sqrt{\frac{(2l_1+1)}{(2l+1)}}(2l_n+1)(2l_2+1)(l_1200\,|\,l_12l0)\times$$

$$\times(l_n200\,|\,l_n2l_00)(l_nl_200\,|\,l_nl_2l_10)(l_2l_00m\,|\,l_2l_0lm)\times W(l_2l_nl2;\,l_1l_0)(F_{l_1l_2}(\alpha)-F_{l_1l_2}(\varkappa))Bl_n\frac{N_d}{\alpha}. \quad (18b)$$

Our result for the proton angular distribution has the following attributes. The first term, related to the neutron-nuclear surface collective interaction, gives a proton angular distribution that is almost the same as Butler's.[1,2] The third term, related to the collective interaction involving the proton, gives a different angular distribution.

Since (18) is a superposition of spherical Bessel functions with different l, the angular distribution it gives is considerably more complicated.

Because the cutoff factor $\left[\alpha^2+\left(k_p-\frac{k_d}{2}\right)^2\right]^{-2}$ does not appear, the $j_l(kR_0)$ with large l will contribute significantly to the angular distribution at large angles. The second term results from interference between the above two processes. Inasmuch as the $F_{l_1 l_2}$ function entering into the third term is proportional to $\arctan\frac{2\beta q}{\Delta^2}$, the proton contribution to the angular distribution must have a resonance character with a half-width $\Gamma = 2\beta q \sim \sqrt{2E_d E_\beta}$ (where E_β is the resulting energy level of the final nucleus).

The total cross section becomes a maximum when the incident deuteron energy is $E_d = 2\left(E_\beta - \frac{\varepsilon_d}{2}\right)$. These resonances will be quite wide: as much as 10 Mev.

Far from these resonances, only the $l_2 = 0$ terms contribute significantly to (18) and (18a) (since $F_{l_1 l_2} \sim \left(\frac{\Gamma}{\Delta^2}\right)^{l_2}$). Then the expression for the differential cross section is greatly simplified, becoming

$$d\sigma = \frac{\tilde{g}_n^2 R_0^4}{\pi(2\pi\hbar)^4}(2J+1)M_p^* M_d^* \frac{k_p}{k_d} j_{l_0}^2(kR_0)\{Q^2(K)G_{nl_0}^2(\beta) + \\ + 2Q(K)G_{nl_0}(\beta)G_{pl_0}(\alpha,\beta,q)Y_{l_0 0}(\vartheta_k) + (2l_0+1)G_{pl_0}^2(\alpha,\beta,q)\}\,d\Omega_p. \qquad (19)$$

In this case the angular distribution will have a main maximum, corresponding to the function $j_{l_0}(kR_0)$, but this maximum may be shifted somewhat, due to the interference term.

Furthermore, one must expect an important contribution to the angular distribution at large angles. Since the interference term in (18) and (19) changes sign on going through resonance, the angular distribution should change radically when the deuteron energy is varied through this region.

The expressions obtained for the angular distribution are valid not only for collective levels, but also for single-particle levels. One must, however, recall that in addition to the collective interaction there occurs interaction of nucleons in the potential well.[2]

Noting that the neutron contribution to the matrix element is the same as the matrix element obtained by Bhatia, we can write the differential cross section with the inclusion of the potential interaction, in arbitrary units, in the form

$$d\sigma = Aj_{l_0}^2(kR_0)\{Q^2(K) - 2\sqrt{4\pi}\,Q(K)C(\beta,q)Y_{l_0 0}(\vartheta_k) + (2l_0+1)C^2(\beta,q)\}\,d\Omega_p. \qquad (20)$$

Here A is an arbitrary constant, and C is a parameter which characterizes the relative efficiency of the collective interaction compared to the potential interaction. Since the collective interaction is weak, the third term in (20) is unimportant. However, the interference term, as was mentioned above, changes the angular distribution at large angles, due to the potential interaction, so that the total distribution will differ from that of Butler.

One may expect to observe the above effects in stripping reactions on nuclei with several protons outside the closed shell, for which the collective interaction of the proton with the nucleus will be as large as possible without too much deformation of the even-even nucleus.

Institute of Physics
Academy of Sciences of the Ukrainian SSR

References

1. S.T.Butler, Proc.Roy.Soc.A, 208, 559 (1951).
2. A.Bhatia, K.Huang, R.Huby & H.Newns, Phil.Mag., 43, 485 (1952); R.Huby, Proc.Roy.Soc.A, 215, 385 (1952); S.Joshida, Prog.Theor.Phys., 10, 1 (1953).
3. W.Tobocman, Phys.Rev., 94, 1655 (1954).
4. T.F.Stratton, I.M.Blair, K.F.Famularo & R.V.Stuart, Phys.Rev., 98, 629 (1955); N.I.Zaika & O.F.Nemets, Izv.AN SSSR, Ser.fiz., 23, 1460 (1959). (Trans. Bulletin, 23, 1447.)
5. J.Sawicki, Nucl.Phys., 6, 575 (1958); G.R.Satchler, Ann.Phys., 3, 241 (1958).
6. A.Bohr, Kgl.Danske Vid.Selskab.Mat.-Fys.Medd., 26, No.14 (1952); A.Bohr & B.Mottelson, Kgl.Danske Vid.Selskab.Mat.-Fys.Medd., 27, No.16 (1953).
7. L.Rosenfeld, Nuclear forces. Amsterdam, 1948.
8. A.M.Korolev, Izv.AN SSSR, Ser.fiz., 23, 1487 (1959). (Trans.Bulletin, 23, 1470.)
9. J.M.Blatt & V.F.Weisskopf, Theoretical Nuclear Physics, N.Y., 1952. (Cited in Russian translation.)
10. L.S.Biedenharn, J.M.Blatt & M.E.Rose, Revs.Mod.Phys., 24, 249 (1952).
11. S.T.Butler, Phys.Rev., 106, 272 (1957).
12. G.N.Watson, A Treatise on the Theory of Bessel Functions, Cambridge,N.Y. 1944. (Cited in Russian translation.)

BETA-TRANSITIONS IN WEAKLY DEFORMED NUCLEI

- B.D.Konstantinov & V.I.Ovcharenko

Introduction

The shell model provides a convenient means for classifying the degree of forbiddenness of β-transitions. It cannot, however, explain the existence of two groups of ft values for allowed transitions. To explain the experimentally observed ft values one must turn to Bohr's unified model[1].

Several authors[2-4] have used this model for theoretical β-transition studies taking into account the interaction of the odd nucleon with the nuclear surface (mostly for the case of strong coupling).

Below we give a calculation of the nuclear matrix elements based on the work of Korolev[5], who deduced the wave functions and energy levels of odd nuclei on the weak-coupling side of intermediate coupling. Nonadiabatic terms and the two-phonon states are included in the treatment.

We shall restrict our considerations to the nonrelativistic approximation for allowed and once forbidden β-transitions, assuming scalar and tensor interactions between nucleons and the electron-nutrino field.

1. Formulation of the problem

In order to find the ft values one must know the nuclear matrix elements.

We calculate the matrix elements for allowed and once forbidden β-transitions between nuclei consisting of an even-even spherical core and an "extra" (odd) nucleon.

The wave functions of such a system[5] can be written

$$\Psi_{JM}(\mathbf{r}) = \sum_{RsKlN} a^{N_0 JM}_{RsKlN}\, \psi_l(r,k)\, \Phi_N[Rs(K)\,l;\, JM], \tag{1}$$

where R is the nuclear surface angular momentum, s is the nucleon spin, $K = R + s$, l is the orbital angular momentum of the nucleon, J is the total nuclear angular momentum, M is its z component, N is the number of phonons, and N_0 is the principal quantum number of the collective energy level.

Further, $\psi_l(r,k)$ is the radial part of the wave function for a nucleon in the spherically symmetric field $V(r)$. The angle and spin parts $Y_{lm}(\vartheta,\varphi)$ and $\chi_s^{m_s}$ of the nucleon wave function are included in $\Phi_N[Rs(K)\,l;\, JM]$.

The $\Phi_N[Rs(K)\,l;\, JM]$ wave functions correspond to a definite scheme for coupling the angular momenta, and they form a complete set of orthogonal functions according to

$$\Phi_N[Rs(K)\,l;\, JM] = \sum_{m,m_s} (KlM - m\,m \,|\, KlJM) \times$$
$$\times\, (RsM - m - m_s m_s \,|\, RsKM - m)\, Y_{lm}(\vartheta,\varphi)\, \chi_s^{m_s}\, \Phi_N^{M-m-m_s}(R), \tag{2}$$

where $\Phi_N^{M-m-m_s}(R)$ is the wave function of the even-even core with spin R in the representation in which the phonon number N is diagonal.

We shall use the notation

$$T^{Jn}_{l'l''}(\tau) = \frac{(l'\,200\,|\,l'2l''0)\,\psi_{l'}(R_0)\,\psi_{l''}(R_0)}{(W_J - E_{l''n} + \tau)}, \tag{3a}$$

$$\varepsilon_{l2} = 2\tilde{g}^2 \sum_{l'} \left[T^{J_2}_{ll'}(0)\right]^2 (W_J - E_{l'2}), \tag{3b}$$

$$N(W_J, l_0) = 1 + \tilde{g}^2 \sum_l \left[T^{J1}_{l_0 l}(\varepsilon_{l2})\right]^2 + 2\tilde{g}^4 \sum_{ll'} \left[T^{J1}_{l_0 l}(\varepsilon_{l2})\, T^{J2}_{ll'}(0)\right]^2, \tag{3c}$$

and

$$\tilde{g}^2 = kR_0 \left(\frac{\hbar}{2B\omega}\right)^{1/2} \left(\frac{5}{4\pi}\right)^{1/2}, \tag{3d}$$

$$E_{ln} = E_l + n\hbar\omega_2, \tag{3e}$$

where E_l is a single-particle level, $\hbar\omega_2$ is a collective level, and R_0 is the nuclear radius.

Then assuming that there exist only two quanta of surface excitation, the $a^{N_0 JM}_{RsKlN}$ amplitudes for the no-phonon, one-phonon, and two-phonon states are of the form

$$a^J_{l_0 l} = \frac{\delta_{ll_0}}{\sqrt{N(W_J, l_0)}}, \tag{4a}$$

$$B^{l_0 J}_{2Kl} = -\tilde{g}(2K+1)^{1/2} W(l_0 2JK; ls)(2l_0+1)^{1/2} T^{J1}_{l_0 l}(\varepsilon_{l2})\, a^J_{l_0 l_0}, \tag{4b}$$

$$C^{l_0 J}_{RKl} = \sqrt{2}\ \tilde{g}^2 \sum_{l'} (2K+1)^{1/2}(2R+1)^{1/2} W(KRJl_0; sl)\, W(2Rl'l_0; 2l) \times$$
$$\times (2l_0+1)^{1/2}(2l'+1)^{1/2} T^{J1}_{l_0 l'}(\varepsilon_{l2})\, T^{J2}_{l'l}(0)\, a^J_{l_0 l_0}. \tag{4c}$$

The angular momentum l_0 above is determined by the inequality

$$J - \frac{1}{2} \leqslant l_0 \leqslant J + \frac{1}{2} \tag{5}$$

and the level parity, while the energy is given by

$$W_J = E_{l_0} + \tilde{g}^2 \sum_l \frac{(l_0 200 \mid l_0 2l0)^2\, \psi^2_l(R_0)\, \psi^2_{l_0}(R_0)}{W_J - E_l - \hbar\omega_2 - \varepsilon_{l2}(W_J)}. \tag{6}$$

We shall use this model to calculate the nuclear matrix elements.

2. Calculation of the nuclear matrix elements

In this section we calculate the squares of the nuclear matrix elements for allowed and first forbidden β-transitions with the wave functions given by (1).

Allowed transitions

For allowed transitions the squares of the matrix elements are of the form

$$\left|\int 1\right|^2 = \frac{1}{2J+1} \sum_{M=-J}^{+J} \sum_{M'=-J'}^{+J'} \left|\int \Psi^{*(f)}_{J'M'} \Psi^{(i)}_{JM}\, d\tau\right|^2, \tag{7}$$

$$\left|\int \vec{\sigma}\right|^2 = \frac{1}{2J+1} \sum_{M=-J}^{+J} \sum_{M'=-J'}^{+J'} \left|\int \Psi^{*(f)}_{J'M'} \vec{\sigma} \Psi^{(i)}_{JM}\, d\tau\right|^2, \tag{8}$$

where $\Psi^{(f)}_{J'M'}$ is the daughter-nucleus wave function with angular momentum J', and $\Psi^{(i)}_{JM}$ is the initial-nucleus wave function with angular momentum J.

To obtain the result of (7), one must sum Clebsch-Gordan coefficients over the magnetic quantum numbers m and m_s, and Racah coefficients over the angular

momenta R, K and l. As a result of this summation one obtains

$$\left|\int 1\right|^2 = \left[a^{J'}_{l'_0 l'_0} a^{J}_{l_0 l_0} I^0_{l'_0, l_0} + \sum_l \frac{B^{J'}_{ll'_0} B^{J}_{ll_0}}{(2l_0+1)} I^0_{l,l} + \sum_{l,l'} \frac{C^{J'l'}_{ll'0} C^{Jl_0}_{ll'}}{(2l_0+1)(2l'+1)} I^0_{ll}\right]^2 \delta_{J'J}\delta_{l'_0 l_0}, \tag{9}$$

where the $a^J_{l_0 l_0}$, B^J_{l,l_0} and $C^{Jl_0}_{l,l'}$ are given by

$$a^J_{l_0 l_0} = \frac{1}{\sqrt{N(W_J, l_0)}}, \tag{10a}$$

$$B^J_{ll_0} = -\tilde{g}(2l_0+1)^{1/2} T^{J1}_{l_0 l}(\varepsilon_{l2})\, a^J_{l_0 l_0}, \tag{10b}$$

$$C^{Jl_0}_{ll'} = \sqrt{2}\,\tilde{g}^2 (2l_0+1)^{1/2}(2l'+1)^{1/2} T^{J1}_{l_0 l'}(\varepsilon_{l2})\, T^{J2}_{l'l}(0)\, a^J_{l_0 l_0}, \tag{10c}$$

and $I^\lambda_{l',l}$ is the integral

$$I^\lambda_{l',l} = \int \psi^{*(f)}_{l'}(r,\ k)\, \psi^{(i)}_l(r, k)\, r^{\lambda+2}\, dr, \tag{11}$$

in which $\psi_l(r, k)$ is the radial part of the wave function for a nucleon in the nuclear field $V(r)$.

The expression in (8) was obtained, following Condon and Shortley[6], by first finding the matrix elements

$$(\alpha' J' M' | \mathrm{s} | \alpha J M)$$

with the angular-momentum coupling scheme

$$\mathbf{J} = \mathbf{R} + \mathbf{s} + \mathbf{l} = \mathbf{K} + \mathbf{l}.$$

Then by summing products of Racah coefficients over R, K and l one arrives at

$$\left|\int \vec{\sigma}\right|^2 = 4(2J'+1)[s(s+1)(2s+1)]\, W^2(J'1\, l_0 s;\, Js) \times$$
$$\times \left\{a^{J'}_{l'_0 l'_0} a^{J}_{l_0 l_0} I^0_{l'_0 l_0} + \sum_l \frac{B^{J'}_{ll'_0} B^{J}_{ll_0}}{(2l_0+1)} I^0_{ll} + \sum_{ll'} \frac{C^{J'l'}_{ll'0} C^{Jl_0}_{ll'}}{(2l_0+1)(2l'+1)} I^0_{ll}\right\}^2 \delta_{l'_0 l_0}. \tag{12}$$

As will be evident from (9) and (12), for allowed transitions we obtain the usual selection rules for J (namely $\Delta J = 0$ for $\left|\int 1\right|^2$ and $\Delta J = 0, \pm 1$ for $\left|\int \vec{\sigma}\right|^2$) and conservation of parity $l'_0 = l_0$.

First forbidden transitions

For this case one has to calculate the squares of the matrix elements

$$\int \mathbf{r}, \quad \int (\vec{\sigma}\mathbf{r}), \quad \int (\vec{\sigma}\times\mathbf{r}) \quad \text{and} \quad \int B_{kj},$$

where

$$B_{kj} = \sigma_k x_j + \sigma_j x_k - \frac{2}{3}\delta_{kj}(\vec{\sigma}\mathbf{r}).$$

In calculating $\left|\int \mathbf{r}\right|^2$ the radius vector r is treated as a tensor operator of rank one whose components are given by the spherical harmonics according to

$$r_m = \sqrt{\frac{4\pi}{3}}\, rY_{1m}(\vartheta,\ \varphi) = \sqrt{\frac{4\pi}{3}}\, Y_{1,m}(\mathbf{r}).$$

Then making use of the formula for the integral of three spherical functions[7] and performing some calculations similar to those used to obtain (9), one arrives at

$$\left|\int \mathbf{r}\right|^2 = \frac{4\pi}{3}\sum_{m=-1}^{+1}\left|\int Y_{1,m}(\mathbf{r})\right|^2 = (2J'+1)\,W^2(sl_0'J1;\ J'l_0)\,Q(J',\ J;\ l_0',\ l_0), \tag{13}$$

where

$$\begin{aligned} Q(J',\ J;\ l_0',\ l_0) = [&a^{J'}_{l_0'l_0'}\, a^{J}_{l_0l_0}(2l_0+1)^{1/2}(1l_000\,|\,1l_0l_0'0)\,I^1_{l_0'\ l_0} + \\ &+ \sum_{ll'} B^{J'}_{l'l'_0} B^{J}_{ll_0}(2l+1)^{1/2}(1l00\,|\,1ll'0)\,W(2l_0'l1;\ l'l_0)\,I^1_{l'l} + \\ &+ \sum_{\substack{ll'\\ l_1l_2}} C^{J'l_0'}_{l'l_1} C^{Jl_0}_{ll_2}(2l+1)^{1/2}(1l00\,|\,1ll0)\,W(2l_0'l_21;\ l_1l_0)\,W(2l'l_21;\ l_1l)\,I^1_{l'l}\ ]^2. \end{aligned} \tag{14}$$

To calculate the other matrix elements for this case it is convenient to write $(\vec{\sigma}\mathbf{r})$, $(\vec{\sigma}\times\mathbf{r})$ and B_{kj} in the form

$$(\vec{\sigma}\mathbf{r}) = \sum_{m=-1}^{+1}(-1)^m\sigma_m r_{-m} = -\sqrt{3}\sum_{m=-1}^{+1}(11m,-m\,|\,1100)\,\sigma_m r_{-m},$$

$$(\vec{\sigma}\times\mathbf{r}) = i\sqrt{2}\sum_{q=-1}^{+1}(11m-q,\ q\,|\,111m)\,\sigma_q r_{m-q} = \sqrt{\frac{4\pi}{3}}\, Y_{1,m}(\vec{\sigma}\mathbf{r})$$

and

$$\sum_{kj}\left|\int B_{kj}\right|^2 = \frac{4\pi\cdot 8}{15}\sum_{m=-2}^{+2}\left|\int Y_{2m}(\vec{\sigma})\right|^2,$$

$$Y_{2m}(\vec{\sigma}) = \sqrt{\frac{15}{8\pi}}\sum_{q=-1}^{+1}(11m-q,\ q\,|\,112q)\,\sigma_q\, r_{m-q}.$$

In this notation it is easy to make use of the expressions[8] for the form factors of the first forbidden transitions; in it, in addition, one can calculate the matrix elements by means of known rules for products of tensor operators.[7] In this way one obtains

$$\left|\int(\vec{\sigma}\mathbf{r})\right|^2 = \frac{3}{2J+1}\left|{}^{J'l_0'}\mathfrak{M}_0^{Jl_0}\right|^2, \tag{15}$$

$$\left|\int(\vec{\sigma}\times\mathbf{r})\right|^2 = \frac{4\pi}{3}\sum_{m=-1}^{+1}\left|\int Y_{1m}(\vec{\sigma}\times\mathbf{r})\right|^2 = \frac{2}{2J+1}\left|{}^{J'l_0'}\mathfrak{M}_1^{Jl_0}\right|^2, \tag{16}$$

$$\sum_{kj}\left|\int B_{kj}\right|^2 = \frac{32\pi}{15}\sum_{m=-2}^{+2}\left|\int Y_{2m}(\vec{\sigma})\right|^2 = \frac{4}{2J+1}\left|{}^{J'l_0'}\mathfrak{M}_2^{Jl_0}\right|^2, \tag{17}$$

where

$${}^{J'l_0}\mathfrak{M}_\varkappa^{Jl_0} = (-1)^{l_0-l_0'+1}\,2\,[(2J'+1)(2J+1)(2\varkappa+1)]^{1/2}[s(s+1)(2s+1)]^{1/2}\times \begin{Bmatrix} \varkappa & J' & J \\ 1 & s & s \\ 1 & l_0' & l_0 \end{Bmatrix} Q(J',\ J;\ l_0',\ l_0). \tag{18}$$

The Racah coefficient in (13) and the 9-j symbol[7] in (18) imply the selection rules

$$J' - J = 0 \qquad \text{for } \left|\int (\vec{\sigma}\mathbf{r})\right|^2,$$

$$J' - J = 0, \pm 1 \qquad \text{for } \left|\int \mathbf{r}\right|^2 \text{ and } \left|\int (\vec{\sigma}\times\mathbf{r})\right|^2,$$

$$J' - J = 0, \pm 1, \pm 2 \text{ for } \sum_{kj}\left|\int B_{kj}\right|^2.$$

The factor $Q(J', J; l_0', l_0)$ in (18) differs from zero when

$$l_0' - l_0 = 2n + 1,$$

where n is an integer. Thus first degree forbidden transitions are accompanied by a change in parity.

The radial integrals (11) entering into the expressions for the matrix elements are calculated in the Appendix.

As an example, we have treated the specific β-transition $_{50}Sn_{71} \rightarrow {}_{51}Sb_{70}$. This transition belongs to the group of allowed unfavored transitions in which the nuclear spin changes by one unit.

The numerical values used in the calculation were the following. The nuclear radius was calculated by the formula

$$R_0 = (1.27 \cdot A^{1/3} + 0.6)\cdot 10^{-13} \text{ cm},$$

and the energy of the first collective level of the even-even nucleus was taken as $\hbar\omega_2$ = 1.3 Mev.[9]

The odd nucleon-nuclear surface coupling constant was chosen so as to obtain the correct binding energy for the odd nucleon. With these parameters one obtains $\left|\int\vec{\sigma}\right|^2 = 1.35\cdot 10^{-2}$.

This, in turn, leads to $\log ft_{theo} = 5.549$, which compares favorably with the experimental value[10] of $\log ft = 5.0$.

It is thus seen that when collective effects are taken into account the agreement with experiment is relatively good.

We desire to express our deep gratitude to A.M.Korolev for his constant interest in the work and valuable advice.

Appendix

Calculation of the Radial Integrals

The expressions for the nuclear matrix elements contain integrals of the form

$$I^{\lambda}_{l'l} = \int_0^{\infty} \psi^{*(f)}_{l'}\, \psi^{(i)}_{l}\, r^{\lambda+2}\, dr. \qquad \text{(A1)}$$

To calculate these integrals one needs to know the radial wave functions of the proton and neutron.

The normalized radial wave functions of the neutron in a spherical rectangular potential well of depth V_0 are given[11] by

$$\psi_l(r) = A_l J_{l+1/2}(kr)(kr)^{-1/2}, \qquad r < R_0, \qquad \text{(A2)}$$

$$\psi_l(r) = B_l K_{l+1/2}(\alpha r)(\alpha r)^{-1/2}, \qquad r > R_0, \tag{A3}$$

where $J_{l+1/2}(kr)$ is the usual Bessel function of semi-integral order, $K_{l+1/2}(\alpha r)$ is a modified Hankel function, and

$$k = \sqrt{\frac{2M(V_0 - |E_l|)}{\hbar^2}}, \qquad \alpha = \sqrt{\frac{2M|E_l|}{\hbar^2}};$$

$$A_l = \left\{ \frac{2k^3}{(kR_0)^2 \left[\frac{K_{l-1/2}(\alpha R_0) K_{l+3/2}(\alpha R_0)}{K^2_{l+1/2}(\alpha R_0)} J^2_{l+1/2}(kR_0) - J_{l-1/2}(kR_0) J_{l+3/2}(kR_0) \right]} \right\}^{1/2}, \tag{A4}$$

$$B_l = \left\{ \frac{2\alpha^3}{(\alpha R_0)^2 \left[\frac{K_{l-1/2}(\alpha R_0) K_{l+3/2}(\alpha R_0)}{K^2_{l+1/2}(\alpha R_0)} J^2_{l+1/2}(kR_0) - J_{l-1/2}(kR_0) J_{l+3/2}(kR_0) \right]} \right\}^{1/2} \times$$

$$\times \frac{J_{l+1/2}(kR_0)}{K_{l+1/2}(\alpha R_0)}. \tag{A5}$$

To obtain the proton wave functions we solve the Schroedinger equation with the potential

$$V(r) = -V_0' \quad \text{for} \quad r < R_0, \tag{A6}$$

$$V(r) = \frac{Ze^2}{r} \quad \text{for} \quad r > R_0. \tag{A7}$$

The inner-region solution regular at $r = 0$ is given by a Bessel function in the form

$$\psi_l(r) = C_l J_{l+1/2}(\beta r)(\beta r)^{-1/2}, \quad r < R_0, \tag{A8}$$

where

$$\beta = \sqrt{\frac{2M(V_0' - |E_l'|)}{\hbar^2}}.$$

The outer-region solution finite in the limit as $r \to \infty$ is of the form

$$\psi_l(r) = D_l \frac{W_{b,l+1/2}(\gamma r)}{(2\gamma r)}, \quad r > R_0. \tag{A9}$$

where

$$\gamma = \sqrt{\frac{2M|E'_l|}{\hbar^2}}, \quad b = -\frac{2MZe_2}{\hbar^2 2\gamma},$$

and $W_{b,l+1/2}(2\gamma r)$ is Whittaker's function.[12]

Integrals involving $W_{b,\,l+1/2}(2\gamma r)$, are quite complicated in general. It is known, however,[12] that

$$W_{b,\,l+1/2}(x) = e^{-\frac{1}{2}x} x^b \{1 + O(x^{-1})\} \tag{A10}$$

for $|\arg x| < \pi$ in the limit as $x \to \infty$, and

$$\int_x^\infty t^{n-1} e^{-t}\, dt = x^{\frac{1}{2}(n-1)} e^{-\frac{1}{2}x} W_{1/2(n-1),\,1/2\,n}(x). \tag{A11}$$

This last equation is valid for all n.

By calculating $2\gamma R_0$ it can be shown that in a sufficiently large energy interval, $2\gamma R_0 > 1$. This then makes it possible to use not the exact solution (A9) but

its asymptotic form

$$\psi_l(r) = D_l\,(2\gamma r)^{b-1}\,e^{-\gamma r},\ r > R_0. \tag{A12}$$

One may now use (A10) and (A11), set (A12) equal to (A8) at R_0, and make use of normalization to arrive at

$$C_l = \left\{\frac{2\beta^3}{(\beta R_0)^2\left[\left(1+\frac{1}{\gamma R_0}\right)J^2_{l+1/2}(\beta R_0) - J_{l-1/2}(\beta R_0)\,J_{l+3/2}(\beta R_0)\right]}\right\}^{1/2}, \tag{A13}$$

$$D_l = \left\{\frac{2\,(2\gamma)^3}{(2\gamma R_0)^2\left[\left(1+\frac{1}{\gamma R_0}\right)J^2_{l+1/2}(\beta R_0) - J_{l-1/2}(\beta R_0)\,J_{l+3/2}(\beta R_0)\right]}\right\}^{1/2} \times \frac{J_{l+1/2}(\beta R_0)}{(2\gamma R_0)^{b-1/2}e^{-\gamma R_0}}. \tag{A14}$$

Having obtained the wave functions, we calculate the integral (A1), which we write in the form

$$I^{\lambda}_{l'l} = I^{\lambda(1)}_{l'l} + I^{\lambda(2)}_{l'l}, \tag{A15}$$

where

$$I^{\lambda(2)}_{l'l} = \int_{R_0}^{\infty} \psi^{*(f)}_{l'}\,\psi^{(i)}_{l}\,r^{\lambda+2}\,dr = D_{l'}\,B_l\,\frac{\sqrt{\pi}\,R_0^{\lambda}\,(2\gamma R_0)^b}{2^2\alpha\,(\alpha+\gamma)\,\gamma}\,e^{-(\alpha+\gamma)R_0}, \tag{A16}$$

and the integral

$$I^{\lambda(1)}_{l'l} = \int_0^{R_0} \psi^{*(f)}_{l'}\,\psi^{(i)}_{l}\,r^{\lambda+2}\,dr$$

has been calculated for

$$\lambda = 0,\quad l' = l,$$

$$\lambda = 1,\quad l' = l \pm 1.$$

Writing

$$G_{l-k+1/2}(a,\,b) = \int_0^{R_0} rJ_{l-k+1/2}(ar)\,J_{l-k+1/2}(br)\,dr =$$

$$= \frac{bR_0 J_{l-k+1/2}(aR_0)\,J_{l-k-1/2}(bR_0) - aR_0\,J_{l-k-1/2}(aR_0)\,J_{l-k+1/2}(bR_0)}{a^2-b^2} \tag{A17}$$

and

$$H_{l+n+1/2,\ l+n-1/2}(a,\,b) = \int_0^{R_0} r^2 J_{l+n+1/2}(ar)\,J_{l+n-1/2}(br)\,dr =$$

$$= \sum_{k=1}^{l+n} (-1)^{k-1}\,\frac{2\,(l+n-k+1/2)}{a^{\frac{1+(-1)^{k-1}}{2}}\,b^{\frac{1+(-1)^k}{2}}}\,G_{l+n-k+1/2}(a,\,b) +$$

$$+\frac{1}{\pi}\cdot\frac{1}{(ab)^{1/2}}\cdot\frac{\sin(a-b)R_0 - (a-b)R_0\cos(a-b)R_0}{(a-b)^2} +$$

$$+(-1)^{l+n}\frac{1}{\pi}\cdot\frac{1}{(ab)^{1/2}}\cdot\frac{\sin(a+b)R_0 - (a+b)R_0\cos(a+b)R_0}{(a+b)^2}, \tag{A18}$$

we obtain $I^{\lambda(1)}_{l'l}$ for the cases of interest, namely,

$$I^{0(1)}_{ll} = \frac{A_l C_l}{(\beta k)^{1/2}}\,G_{l+1/2}(\beta,\,k), \tag{A19}$$

$$I^{1(1)}_{l+1,l} = \frac{C_{l+1}A_l}{(\beta k)^{1/2}} H_{l+1+1/2,\ l+1-1/2}(\beta, k), \tag{A20}$$

$$I^{1(1)}_{l-1,l} = \frac{C_{l-1}A_l}{(\beta k)^{1/2}} H_{l+1/2,\ l-1/2}(k, \beta). \tag{A21}$$

The constants A_l, B_l, C_l and D_l are given by (A4), (A5), (A13) and (A14), respectively.

Institute of Physics,
Academy of Sciences of the Ukrainian SSR

References

1. A.Bohr, Klg.Danske Videnskab. Selskab, Mat.-fys.Medd., 26, No.14 (1952).
2. A.Bohr, Ibid., 27, No.16 (1953).
3. M.Redlich & E.Wigner, Phys.Rev., 95, 122 (1955).
4. S.G.Nilsson, Klg.Danske Videnskab.Selskab, Mat.-fys.Medd., 29, No.16 (1955).
5. A.M.Korolev, Izv.AN SSSR, Ser.fiz., 23, 1492 (1959). (Trans.Bulletin 23, 1475.)
6. E.U.Condon & G.H.Shortley, The Theory of Atomic Spectra,Cambridge, 1944. (Cited in Russian translation.)
7. A.Edmonds, in Deformatsiya atomnykh yader (Deformation of nuclei), Edited by L.Sliv., M.1958.
8. E.Konopinskii, Beta-i gamma-spektroskopiya (Beta- and gamma-spectroscopy), M. 1959.
9. G.Scharff-Goldhaber, Phys.Rev., 90, 587 (1953).
10. B.S.Dzhelepov & L.K.Peker, Skhemy raspada radioaktivnykh yader (Decay schemes of radioactive nuclei), M.-L. 1958.
11. L.I.Schiff, Quantum Mechanics, N.Y., 1949. (Cited in Russian translation.)
12. E.T.Whittaker & G.N.Watson, A Course in Modern Analysis, Cambridge 1940. (Cited in Russian translation.)

MAGNETIC AND QUADRUPOLE MOMENTS OF WEAKLY DEFORMED NUCLEI

- Yu.L.Gurin, A.M.Korolev & B.D.Konstantinov

In order to check the validity of the Bohr-Mottelson model,[1] we calculated the magnetic and quadrupole moments of deformed nuclei for strong coupling between the odd nucleon and the nuclear collective modes. These quantities have already[2] been calculated for intermediate coupling of the odd nucleon with the nuclear surface in the specific case of odd nuclei close to the magic numbers. In the paper cited, however, comparison with experiment was not carried out for a sufficiently large number of nuclei, which is necessary for a true verification of the phonon treatment of collective excitations in the Bohr-Mottelson unified model.

Since several parameters enter into the theory, the results will not be unambiguous unless these parameters are determined from other experiments. It is to obtaining such unique results that the present work is devoted.

We consider magnetic and quadrupole moments of odd nuclei consisting of an even-even spherical core with an "extra" nucleon. The wave functions and energy levels of such nuclei have been obtained[3] in the two-phonon approximation on the assumption of intermediate coupling.

The expressions obtained[2] for the magnetic and quadrupole moments are

$$\mu = \mu_1 - \mu_2, \tag{1}$$

where

$$\mu_1 = J\Big[g_J a^2_{l_0 l_0} + \sum_{l,\,j} g_j (2j+1)\, W^2(2jl_0 s;\, Jl)\, B^2_{ll_0} + \sum_{R,\,l,\,j} g_j (2j+1)(2R+1)\, W^2(Rjl_0 s;\, Jl)\, Q_{l_0 l}\Big], \tag{2}$$

$$\mu_2 = J\Big[\sum_{l,\,j} (g_j - g_R)(2j+1)\frac{J(J+1) - j(j+1) + 6}{2J(J+1)}\, W^2(2jl_0 s;\, Jl)\, B^2_{ll_0} + \sum_{R,\,l,\,j} (g_j - g_R)(2j+1)(2R+1)\frac{J(J+1) + R(R+1) - j(j+1)}{2J(J+1)} \times W^2(Rjl_0 s;\, Jl)\, Q_{l_0 l}\Big]. \tag{3}$$

The total quadrupole moment of such nuclei may be written

$$Q = Q_s + Q_p, \tag{4}$$

where Q_s is the part due to the deformed nuclear surface, and Q_p is the part due to the odd nucleon. These two contributions are described by

$$Q_s = 6Z(5\pi)^{-1/2} R_0^2 e_2 (2J+1)^{1/2} (2J\,0J \mid 2JJJ)\, W(sl_0 J2;\, Jl_0) \times \Big[a_{l_0 l_0} B_{l_0 l_0} + \sqrt{2} \sum_{ll'} W(2l_0 l2;\, l'l_0)\, B_{ll_0} C^{l_0}_{ll'}\Big]; \tag{5}$$

$$Q_p = 2(2J+1)^{1/2} (2J\,0J \mid 2JJJ)\, W(sl_0 J2;\, Jl_0) \times \Big[(2l_0+1)^{1/2} (2l_0\,00 \mid 2l_0\, l_0 0)\, I_{l_0 l_0} a^2_{l_0 l_0} + \sum_{ll'} (2l+1)^{1/2} (2l00 \mid 2ll'0)\, W(2l_0 l'2;\, ll_0)\, I_{l'l} B_{l'l_0} B_{ll_0} + \sum_{ll'l_1 l_2} (2l+1)^{1/2} (2l00 \mid 2ll'0)\, W(2l_2 l_0 2;\, l_0 l_1)\, W(2l_2 l'2;\, ll_1)\, I_{l'l} C^{l_0}_{l'l_1} C^{l_0}_{ll_2}\Big], \tag{6}$$

where

$$I_{l'l} = \int \psi^*_{l'}(r,\, k)\, \psi_l(r,\, k)\, r^4\, dr. \tag{7}$$

The previous work[2] also gives expressions for the $a_{l_0 l_0}$, B_{ll_0} and $C^{l_0}_{ll'}$ in the

no-phonon, one-phonon, and two-phonon states.

The ground state energy of the nucleus, which enters into the expressions for the amplitudes, is given by[3]

$$W_J = E_{l_0} + \tilde{g}^2 \sum_l \frac{(l_0\,200 \mid l_0\,l0)^2\,\psi_l^2(R_0)\,\psi_{l_0}^2(R_0)}{W_J - E_l - \hbar\omega - 2\tilde{g}^2\alpha_{l2}(W_J)}. \qquad (8)$$

For our numerical calculations we have chosen the following nuclei: Sr^{87}, Zr^{91}, Mo^{95}, Ba^{135}, Ba^{137}, Nd^{143}, Nd^{145}, Hg^{199}, Hg^{201} and Pb^{207} (each of which has one or more neutrons outside the closed shell) and Co^{59}, Cu^{63}, In^{115}, Sb^{121}, Tl^{203} and Bi^{209} (each of which has one or more protons outside the closed shell).

When calculating the magnetic and quadrupole moments, the following parameters should be determined from other experimental data: the nuclear radius R_0, the depth V_0 of the potential well, the energy $\hbar\omega$ of the first collective level of the even-even nucleus, and the nucleon-surface coupling constant $\tilde{g}$.

The nuclear radius was calculated by the formula

$$R_0 = (1.27A^{1/3} + 0.6)\cdot 10^{-13}\ \text{cm}.$$

The depth V_0 of the well was obtained from the binding energy of the last nucleon of the even-even nucleus.[4] When a proton was used for such a calculation, a correction was introduced to take account of the Coulomb interaction between the odd nucleon and the core. The binding energy of the nucleon was taken as the difference between the experimental binding energies of corresponding odd and even-even nuclei.[5-7] Exceptions here were Nd^{145}, Ba^{135} and Ba^{137}. The binding energy of the odd nucleon in Nd^{145} was evaluated in the following way. All of the neighboring odd nuclei have almost the same binding energy for their last neutron: $W_J(Nd^{143}) = -6.001$ Mev, $W_J(Nd^{147}) = -5.732$ Mev, and $W_J(Nd^{149}) = -5.853$ Mev.

Since the structure of Nd^{145} is no different from that of the neighboring odd nuclei, the binding energy of the odd nucleon was chosen in the same region, namely, $W_J = -5.850$ Mev. The Ba^{135} and Ba^{137} neutron binding energies were obtained from Zeldes.[8] The collective-level energy $\hbar\omega$ was taken from experiment.[9] In the calculations for Ba^{135} $\hbar\omega$ was evaluated on the basis of the liquid drop model.

The coupling constant $\tilde{g}$ was chosen so as to make the ground state energy given by (8) agree with experiment. In nuclei containing an odd proton, one of the parameters of the theory is $G = \tilde{g}\psi_l^2(\beta R_0)$. It is chosen in this way because when one includes the Coulomb interaction in order to calculate $\psi_l^2(\beta R_0)$, difficulties arise. Since the l dependence of $\psi_l^2(\beta R_0)$ is relatively weak, the mean value of this function may be taken outside the summation sign in (8).

The $I_{ll'}$ integral in the expression for Q_p was replaced by the mean square nuclear radius $3/5\,R_0^2$.

Tables 1 and 2 present the magnetic and quadrupole moments of the enumerated nuclei evaluated according to the single-particle shell model and the Bohr-Mottelson model, together with the experimental values[10-12].

It will be evident from the tables that for slightly deformed nuclei better agreement with the experimental data is given by the Bohr-Mottelson model than by the shell model.

On the whole, in fact, the unified model magnetic-moment results agree well with experiment. Exceptions are Nd^{143}, Hg^{201} and Bi^{209}. Since we don't know the first collective level of Pb^{208}, it would seem that the liquid-drop value $\hbar\omega = 1.3$ Mev does not correspond to reality. Hence the magnetic moment of Bi^{209} turned out to be small by a factor of 2. The Nd^{143} nucleus lies almost at the boundary of the region of deformed nuclei, where this model may not be entirely applicable.

Table 1

Magnetic and Quadrupole Moments of Nuclei with an Odd Neutron

Nucleus	Z	N	A	Ground state	μ (n.m.) single-particle	μ (n.m.) theoretical	μ (n.m.) experimental	Q, e x 10^{-24} cm^2 theo.	Q, e x 10^{-24} cm^2 exper.
Sr	38	49	87	$g_{9/2}$	−1,913	−1,077	−1,089—1,3	1,273	0,850
Zr	40	51	91	$d_{5/2}$	−1,913	−1,560	−(1,9±0,2)	−0,818	−0,460
Mo	42	53	95	$d_{5/2}$	−1,913	−0,998	−0,914	−0,819	
Ba	56	79	135	$d_{3/2}$	1,149	0,520	0,835	−0,657	0,510
Ba	56	81	137	$d_{3/2}$	1,149	0,871	0,935	0,450	0.510
Nd	60	83	143	$f_{7/2}$	−1,913	−1,761	−(1,0±0,2)	−1,355	−(1,1±0,1)
Nd	60	85	145	$f_{7/2}$	−1,913	−1,042	−(0,69±0,10)	−3,094	
Hg	80	119	199	$P_{1/2}$	0,638	0,646	0,504	0	0
Hg	80	121	201	$P_{3/2}$	−1,913	−1,192	−0,559	−1,793	0,600
Pb	82	125	207	$P_{1/2}$	0,638	0,776	0,589	0	0

Table 2

Magnetic and Quadrupole Moments of Nuclei with an Odd Proton

Nucleus	Z	N	A	Ground state	μ (n.m.) single-particle	μ (n.m.) theo.	μ (n.m.) exper.	Q, e x 10^{-24} cm^2 single-particle	Q, e x 10^{-24} cm^2 theo.	Q, e x 10^{-24} cm^2 exper.
										0,500
Co	27	32	59	$f_{7/2}$	5,793	4,730	4,648	0,08	+0,456	−(0,13±
Cu	29	34	63	$P_{3/2}$	3,793	2,759	2,226	−0,06	−0,563	±0,01)
In	49	66	115	$g_{9/2}$	6,793	5,355	5,500	0,15	+3,651	1,161
Sb	51	70	121	$d_{5/2}$	4,793	4,993	3,360	−0,13	−0,205	−(0,3±0,2)
Tl	81	122	203	$S_{1/2}$	2,793	1,778	1,612	0	0	0
Bi	83	126	209	$h_{9/2}$	2,623	1,824	4,082	−0,2	−0,994	−0,4

The agreement between theory and experiment is somewhat worse for the quadrupole moments, but nevertheless, if one bears in mind that we are using a rough model, it is satisfactory. In some cases, however, theory and experiment differ by a factor of 3 or 4. This would seem to be due to the fact that we have not included spin-orbit coupling in our calculations, and to our choice of the liquid-drop value for the mass parameter B which is known actually to be somewhat too low. This is not so crucial in the magnetic-moment calculation, since there B enters the expression for the coupling constant $\tilde{g}$, which is a parameter in the theory and is determined from the binding energy of the odd nucleon.

Institute of Physics,
Academy of Sciences of the Ukrainian SSR

References

1. A.Bohr & B.Mottelson, Klg.Danske Videnskab.Selskab, Mat.-fys.Medd., 27, No.16 (1953).

2. B.D.Konstantinov & A.M.Korolev, Izv.AN SSSR, Ser.fiz., 23, 1497 (1959). (Trans.Bulletin, 23, 1480.)

3. A.M.Korolev, Ibid., 23, 1492 (1959). (Trans.Bulletin, 23, 1475.)

4. A.E.S.Green & K.Lee, Phys.Rev., 99, 772 (1955).

5. A.H.Wapstra, Physica, 21, 385 (1955).

6. J.R.Huizenga, Physica, 21, 410 (1955).

7. R.A.Demirkhanov, T.I.Gutkin & V.V.Dorokhov, Zhur.eksp.i teor.fiz., 35, 917 (1958). (Trans.Soviet Physics - JETP.)

8. N.Zeldes, Nucl.Phys., 7, 27 (1958).

9. G.Scharff-Goldhaber, Phys.Rev., 90, 587 (1958).

10. P.F.A.Klinkenberg, Revs.Mod.Phys., 24, 63 (1952).
11. E.F.Kyul'ts, V.V.Kunts & V.G.Hartman, Uspekhi fiz.nauk, 55, 537 (1955).
12. B.S.Dzhelepov & L.K.Peker, Skhemy raspada radioaktivnykh yader (Decay schemes of radioactive nuclei), M.-L., 1958.

* * * * * * *

DOUBLE-FOCUSING MAGNETIC SPECTROMETER

- A.S.Deineko, A.I.Popov, P.V.Sorokin & A.Ya.Taranov

Introduction

The use in nuclear spectrographs of different types of magnetic and electrostatic fields in conjunction with appropriate detectors has made it possible to investigate in detail different complex nuclear particle spectra.

At present there are in use a number of double focusing spectrometers with inhomogeneous fields. In such spectrometers double focusing is obtained only with a total angle of deflection of about π radians.[1,2] In view of this, such spectrometers are relatively bulky and heavy. In addition, it must be borne in mind that realization of an inhomogeneous field with a given configuration is connected with practical difficulties; hence it may be expedient to use spectrometers of the types proposed by Camac[3] and Prowse & Gibson[4]. These double focusing spectrometers have an inhomogeneous field only in the regions of entrance and exit of the beam and work with smaller angles of deflection, for example, 90°. In such spectrometers focusing in the plane perpendicular to the field is realized by a homogeneous field between the pole pieces, while focusing in the plane parallel to the field is obtained by means of an inhomogeneous field at the entrance and exit from the magnet.

In this report we describe a double focusing magnetic spectrometer with a wedge type magnetic field. This spectrometer was designed for investigating the products of nuclear reactions induced by means of an electrostatic accelerator.

1. Design parameters

Bearing in mind the fact that the energy of the products of nuclear reactions under our conditions generally does not exceed 8 Mev, we estimated that the required value of $H\rho$ need not exceed $4 \cdot 10^5$ oe·cm. With relatively narrow gaps in an Armco iron magnet one can readily obtain a uniform field of up to 15 000 oe. From this we evaluated the radius of curvature of the particle trajectory in a magnetic field: $R_0 = 320$ mm. The design deflection angle was specified as 90°.

To provide for the possibility of measuring the angular distribution of reaction products in the angular range from 0 to 150°, given the design dimensions of the magnet, we found that the distance l_1 from the target to the entrance to the magnet had to be 400 mm. On the basis of the proposed experimental conditions, we assumed a design value of $4 \cdot 10^{-3}$ sterad for the solid angle of the spectrometer. For conditions of double focusing this solid angle can be realized with a path width of 100 mm and height of 16 mm. In this case the entrance angle α in the plane perpendicular to the field is 5.7°. With this aperture one can obtain resolution of ~0.1% for first order focusing.

According to Gross[5]:

$$\operatorname{tg}\varepsilon_2 = \frac{1}{2}\left[\operatorname{tg}(\Phi-\psi) + \frac{1}{\Phi - \operatorname{ctg}\eta}\right] \tag{1}$$

and

$$\frac{1}{l_2} = \frac{1}{2}\left[\operatorname{tg}(\Phi-\psi) - \frac{1}{\Phi - \operatorname{ctg}\eta}\right] \tag{2}$$

(where l_2 is the distance from the exit from the magnet to the point at which double focusing is realized, i.e., to the image,

$$\operatorname{tg}\psi = \operatorname{tg}\varepsilon_1 + \frac{1}{l_1} \quad \text{and} \quad \operatorname{tg}\eta = \operatorname{tg}\varepsilon_1 - \frac{1}{l_1},$$

where ε_1 and ε_2 are the angles of entrance and exit of the particles into and from the magnetic field, l_1 is the distance from the target to the entrance to the magnet, and Φ is the angle of deflection of the principal trajectory of the particles in the magnetic field). Using these equations, we determined ε_1 and ε_2 so that double focusing would be realized for l_2 = 700 mm. Calculations yielded $\varepsilon_1 = 46^\circ$ and $\varepsilon_2 = 4^\circ 51'$.

The expected resolution of the spectrometer for first order focusing[6]

$$\left(\frac{\Delta p}{p}\right)_{\min} = \frac{h_y y_0 + h_{\alpha\alpha}\alpha^2}{h_{\Delta p/p}}, \tag{3}$$

where

$$h_y = \frac{\cos(\Phi-\varepsilon_1)\cos\varepsilon_2 - l_2\sin\Omega}{\cos\varepsilon_1\cos\varepsilon_2};$$

$$h_{\alpha\alpha} = \left\{\left[\left(\frac{\cos\varepsilon_1\cos\varepsilon_2}{l_2\sin\Omega - \cos\varepsilon_2\cos(\Phi-\varepsilon_1)}\right)^2 - \cos\Phi\right](1 + l_2\operatorname{tg}\varepsilon_2) + l_2\sin\Phi\right\};$$

$$h_{\Delta p/p} = (1-\cos\Phi)(1 + l_2\operatorname{tg}\varepsilon_2) + l_2\sin\Phi;$$

$$\Omega = \Phi - \varepsilon_1 - \varepsilon_2;$$

y_0 is the size of the source in the plane perpendicular to the field, and α is the aperture in this plane.

In the above equations the linear dimensions are expressed in units of the radius of curvature of the particles in the magnetic field. For our spectrometer ($\alpha = 2.85^\circ$) with y_0 = 1 mm, the expected resolution is 0.1%. The magnification of the magnet in the plane perpendicular to the field is 0.91; in the plane parallel to the field - 2.7. The shape of the pole pieces and the particle trajectory in the plane perpendicular to the field are shown in Fig.1.

2. Description of the Spectrometer

A photograph of the spectrometer is reproduced in Fig.2. The yoke of the three-leg electromagnet is made of Armco iron. The magnet coils are would of 14 mm^2 section copper bus. Each coil has 320 turns. The resistance of the coils connected in series is 1.38 ohm. At the maximum current of 40 amp the power consumption is 2.2 kw. The magnet coils are water cooled.

The electromagnet is supplied from a motor-generator. The current is regulated to within 0.05% in the range from 4 to 40 amp, which corresponds to variation of the field from 2 to 15 koe. The corresponding detectable proton energy range is 0.2 to 8 Mev.

The side walls of the vacuum chamber are made of steel and are continuations of the magnet shoes. The walls are made parallel to within 0.05 mm. The vacuum chamber is connected to the scattering chamber by means of a sylphon bellows.

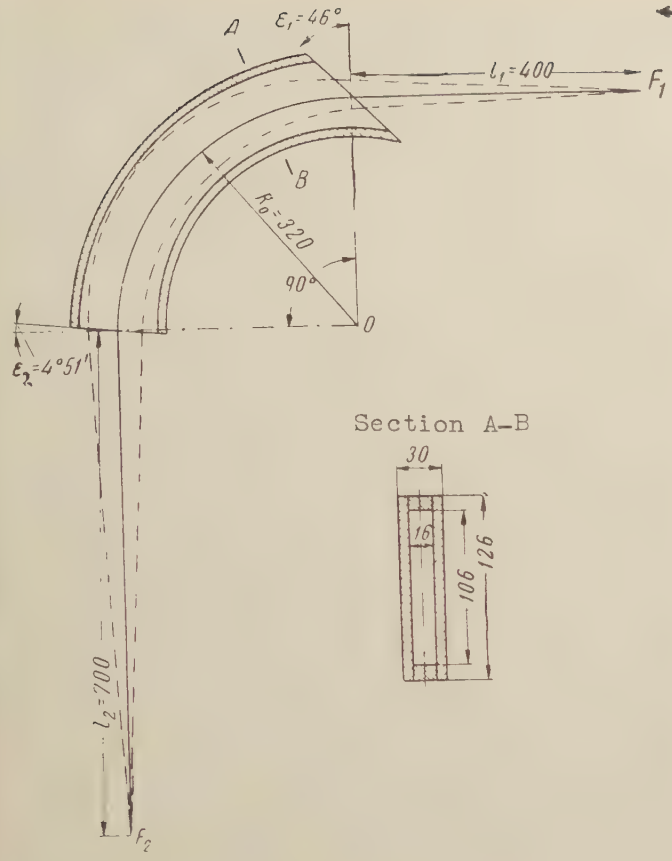

←Fig.1. Shape of the pole pieces and particle trajectory in the plane perpendicular to the magnetic field.

Fig.2. General view of spectrometer.

The chamber exit has provision for mounting detectors, which may be either an appropriate crystal coupled to a photomultiplier or a nuclear emulsion plate.

The magnetic field in the chamber was measured by the proton resonance technique.

The magnet together with the scattering chamber is mounted on a platform which allows of rotating the magnet from 0 to 150° counterclockwise and 0 to 20° clockwise relative to the incident beam. The entire assembly is mounted on rails.

3. Tests of the Spectrometer

In testing the new instrument we determined the following characteristics: a) the variation of the magnetic field as a function of the current in the magnet windings, b) the configuration of the magnetic field, c) the resolution of the instrument, d) the effective solid angle and e) realization of double focusing.

The variation of the field in the gap as a function of the current through the windings is shown in Fig.3. The residual magnetic field after full scale variation of the current 0→40→0 amp is 160 oersted.

We investigated the configuration of the field along the particle trajectory over a path width of 6-7 cm for two values of the field in the gap: H_o = 3.032 koe and H_o = 5.851 koe. It was found that the field configuration does not change with increase in the field strength and that the maximum deviation of the field along the principal trajectory from the design value is 0.3%. The maximum inhomogeneity of the field along the path is 0.03% per cm. The "optical" properties of the spectrometer were investigated by means of a Po^{210} α-particle source measuring 1 x 8 mm.

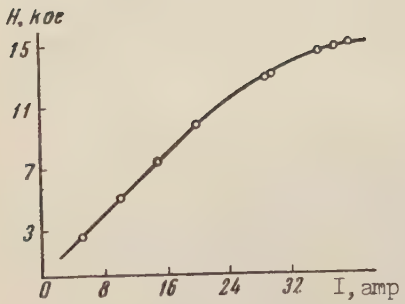

Fig.3. Variation of the field strength with the current through the windings.

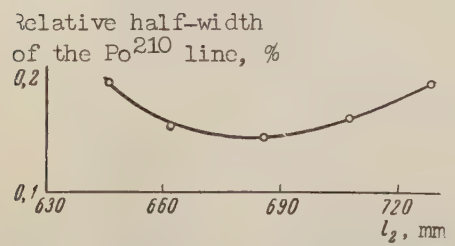

Fig.4. Variation of the momentum resolution as a function of the distance l_2 from the magnet exit to the detector.

In order to determine the best position for the detector we investigated the variation of the resolution as a function of the distance l_2 from the magnet to the detector. The results are shown in Fig.4; the α-particles were detected by a scintillation counter with a CsI crystal. The width of the detector slit in this case was 1 mm. It will be seen that the best resolution (0.15%) is obtained for l_2 = 686 mm; this value of l_2 is in good agreement with the design value of 700 mm.

The resolution of the spectrometer was determined experimentally by means of a scintillation counter with a CsI crystal and a nuclear emulsion plate (type K-1 emulsion, thickness 50 μ).

The experimental line shapes obtained for an α-particle source are shown in Fig.5. The curve on the right was obtained with a scintillation counter (detector slit width 1 mm). The line width at half-height in this case is 0.15 ± 0.03%. At the left is the line shape recorded by means of a photographic plate. The vertical axis is laid off in the number of tracks in a 0.25 x 1.5 cm strip; the horizontal axis in terms of the distance in millimeters along the photographic plate. The zero level was chosen arbitrarily. The width of this line at half-height is 2 mm (equivalent resolution 0.16%). The measured value is in good agreement with R = = 0.1% calculated by means of Eq.(3).

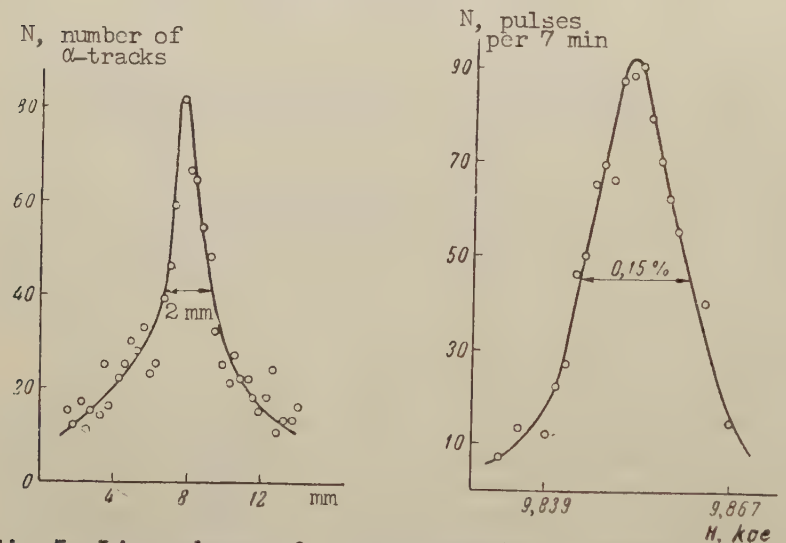

Fig.5. Line shapes for an α-particle source recorded by means of a photographic plate (at left) and a scintillation counter (at right).

To measure the solid angle correctly the dimensions of the detector must exceed the dimensions of the image. The size of the image with a 1 x 8 mm source was determined by means of a nuclear emulsion photographic plate. In the plane perpendicular to the field the size of the image was 2 mm; in the plane parallel to the field - 25 mm.

The effective solid angle Ω was determined as N/N_0, where N is the number of α-particles recorded by a 5 x x 30 mm detector and N_0 is the intensity of the source. We obtained Ω = (3.56 ± 0.23)· $\cdot 10^{-3}$ sterad. This is in good agreement with the design value of $4 \cdot 10^{-3}$ sterad. The good agreement of the experimental and design data indicate that double focusing is actually realized in the spectrometer.

Thus tests of the spectrometer showed that the experimental values of the different parameters are close to the design values and that the spectrometer can be utilized for investigating the energy and angular distributions of the products of nuclear reactions.

Kharkov Physical-Technical Institute,
Academy of Sciences of the Ukrainian SSR

References

1. C.Mileikowsky, Arkiv.Fys., 7, 57 (1954).
2. S.Rubin & P.C.Sachs, Rev.Sci.Instr., 26, 1029 (1955).
3. M.Camac, Rev.Sci.Instr., 22, 197 (1951).
4. D.J.Prowse & W.H.Gibson, J.Scient.Instrum., 33, 129 (1956).
5. W.G.Gross, Rev.Sci.Instr., 22, 717 (1951).
6. A.Lovati & H.J.Tyren, Rev.Sci.Instr., 33, 151 (1956).

PREPARATION OF ISOTOPE TARGETS FOR NUCLEAR STUDIES

- A.D.Bondar', A.S.Emlyaninov, A.P.Klyucharev, L.G.Lishenko, V.N.Medyanik, A.D.Nikolaichuk & O.E.Shalaeva

In the present report we describe the techniques successfully employed in preparation of target foils of 16 different elements.

While basically some of our procedures are similar to those used in working with "large" quantities of isotopes, when it comes to milligram amounts certain modifications become necessary.

We used three different procedures for preparing free (unbacked) metal foils: 1) electrolytic deposition, 2) vacuum evaporation, and 3) thermal dissociation.

In all cases choice of the backing on which the metal is deposited is important, inasmuch as for most experiments a free foil is required and the backing must be stripped off or removed in some manner.

Each of the above mentioned procedures has its own peculiarities. Thus, in the case of electrolytic deposition important considerations are choice of an electrolyte with a minimum content of the deposited element, the electrolysis conditions and recovery of the isotope remaining in the electrolyte.

In employing the vacuum evaporation procedure one must be careful in choosing the material for and the design of the evaporator.

In using the thermal dissociation technique important factors are the chemical compound to be decomposed and the temperature conditions at different stages of the process.

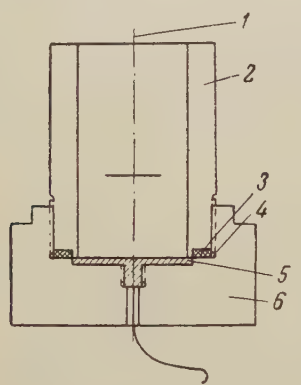

←Fig.1. Electrolytic cell: 1) anode (platinum or graphite) (this can also be used for stirring the electrolyte), 2) cylinder of glass or plastic, 3) rubber gasket, 4) cathode-backing, 5) copper contacting plate to cathode, 6) cell base of acrylic resin.

We prepared free foils of Ni, Cu, Zn, Cd, Co, Mn, Fe, Ag, Cr, Pb and Sn by the electrolytic deposition procedure.[1-6] The electrolysis was carried out in cells made either of ordinary glass or acrylic plastic of the type shown in Fig.1. The conditions of electrolysis found suitable for most of the enumerated foils are given in the accompanying table.

For preparing 5 μ thick lead foils we used the following procedure: some 30-50 mg of the selected Pb isotope were formed into 1 cm long rods which were then used as the anode. The electrolyte was 25% hydrochloric acid to which there were added 0.5 g per liter gelatin. To insure uniform deposition of the Pb, the anode was eccentrically rotated at the rate of 30 rpm. The electrolysis was carried out for a period of 7-8 hours. During this time the lead went into solution and almost all of it was deposited on the backing. For complete extraction of the Pb from the solution we then shifted to a platinum anode and continued the electrolysis for another 10-12 hours. The current density was 0.03 amp/dm^2. The cathode was a 50-100 μ thick tin foil, which at the end was dissolved in ammonium polysulfide.

The method of vacuum evaporation with direct heating was used to prepare germanium and beryllium foils. This is a familiar procedure and has frequently been described in the literature. The specific problem in our case was to reduce loss of the isotopes to a minimum. To this end we prepared special crucibles. In the case of germanium we used crucibles of graphite of the type shown in Fig. 2. This crucible design resulted in a significant decrease of the evaporation losses. The germanium and beryllium were evaporated onto tantalum backings. By

Composition of electrolytes and electrolysis conditions

No.	Foil	Electrolyte composition (per liter sol.)	Cathode	Anode	Electrolyte temp. °C	Current density amp/dm²	Foil thickness, μ	Backing (cathode) solvent	Ref.	Remarks
1	Ni	$NiSO_4 \cdot 7H_2O$ 40 g $2Na_3C_6H_5O_7 \cdot 11H_2O$ 35 g	Polished steel	Platinum	70	0,73	1—20	—	[1]	Stir solution during electrolysis.
2	Cu	$CuSO_4 \cdot 5H_2O$ 26 g $(NH_4)_2C_2O_4$ 58 g $H_2C_2O_4$ 33 g NH_4OH (25%) 150 ml	"	"	50	1,23	1,5—10	—	[2]	
3	Co	a) $CoSO_4 \cdot 7H_2O$ 300 g NaCl 20 g H_3BO_3 30 g в) $CoSO_4 \cdot 7H_2O$ 196 g H_3BO_3 43,3 g	" " "	Platinum or graphite Platinum	55 55	0,25 4,08	1—5 3—10	— —	[3]	Stir solution during electrolysis. Deposition is faster with second solution.
4	Zn	$ZnSO_4 \cdot 7H_2O$ 100 g $(NH_4)_2SO_4$ 30 g $KAl(SO_4)_2 \cdot 12H_2O$ 5 g	Aluminum	"	18—20	1,25	2—10	—	[4]	
5	Cd	$CdSO_4 \cdot {}^8/_3 H_2O$ 60 g $(NH_4)_2SO_4$ 30 g $Al_2(SO_4)_3$ 50 g Gelatin 0,5 g	"	"	40	0,75	6—10	—	[4]	
6	Mn	$MnSO_4$ 150 g $(NH_4)_2SO_4$ 75 g Glycerin 50 ml	"	"	18	14	3—10	Na_2CO_3 100 hl^{-1} NaOH 50 hl^{-1}	[5,6]	Stir solution during electrolysis.
7	Fe	$FeSO_4 \cdot 7H_2O$ 120 g $(NH_4)_2SO_4$ 120 g	Copper	"	40	1,7	4—10	CrO_3 250 hl^{-1} H_2SO_4 25 hl^{-1}	[4]	
8	Ag	Ag_2SO_4 30 g KJ 600 g NH_4OH (25%) 75 ml $Na_4P_2O_7$ 60 g	"	"	60	0,9	5—10	Water solution of $AgNO_3$	[6]	
9	Cr	CrO_3 500 g H_2SO_4 or $Cr_2(SO_4)_3$ 3 g	"	"	60—80	30	2—5	HNO_3 (1 : 1)	[4]	Rate of deposition decreases with rising temperature.
10	Sn	$Na_4P_2O_7$ 40 g $SnCl_2$ 16 g $SnCl_2 \cdot 2H_2O$ 4 g	Polished copper	"	50	0,5	2—5	Chromic acid	[1]	

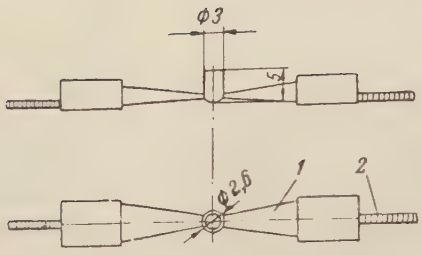

Fig.2. Graphite crucible (dimensions indicated in mm): 1) graphite, 2) copper cable.

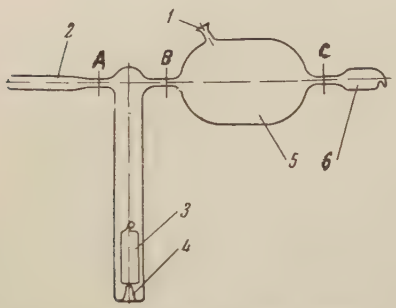

Fig.3. Apparatus for preparing titanium and zirconium iodides: 1) branch tube for introducing the sample, 2) branch tube for connecting to the vacuum system, 3) ampoule with iodine, 4) striker, 5) main bulb, 6) ampoule; A, B and C - points at which the apparatus is sealed off in successive stages.

evaporation one can also prepare foils of alkali and alkaline earth metals and of some lanthanides reduced beforehand from their oxides. By way of reducing agent we used lanthanum. So far, by this procedure we have succeeded only in preparing magnesium isotope foils.

The thermal dissociation procedure was used to prepare foils of Zr, Ti and Cr. In the case of all three metals we prepared the films by decomposition of the iodides. The zirconium and titanium iodides were prepared in the following manner.[7,8]

The molybdenum glass apparatus used is shown in Fig.3. A quantity of Zr or Ti (20-30 mg) is loaded into bulb 5 through tube 1 which is then sealed off. The apparatus is then connected to the vacuum system and pumped to $2\text{-}4\cdot10^{-5}$ mm Hg. After 40-60 min pumping, the tube is sealed off at point A. The ampoule 3 charged with iodine, the amount of which should somewhat exceed the stoichiometric proportion, is then broken by impact against the striker 4 and the iodine is distilled over into bulb 5. Then the apparatus is sealed off at point B. The bulb 5 together with ampoule 6 is placed in a furnace and heated to 240-250° in the case of Ti and 250-260° in the case of Zr. These are the temperatures at which the respective iodides form. The iodide with the excess iodine is then driven over into ampoule 6 which is sealed off at point C.

The sealed off ampoule with the Zr or Ti iodide is then placed in a glass cylinder, the quartz mouth of which is connected with the deposition chamber in which a vacuum of 10^{-5} mm Hg is maintained. This chamber contains the molybdenum backing up to 0.1 mm thick and 25 mm in diameter, which is heated by a tungsten spiral in an alundum crucible up to 1250° in the case of Zr and to 1100-1150° for Ti (the temperature was monitored by an optical pyrometer). Upon attainment of the indicated temperature, the ampoule containing the iodide is broken and the iodide is gradually sublimated by heating it with a gas burner to 220-250°. Upon impinging on the heated backing, the iodide decomposes; the iodine is evacuated and condenses in a trap, while the zirconium or titanium remains deposited on the backing. Finally, the backing is dissolved in nitric acid diluted 1 to 1. By means of this procedure we prepared Ti and Zr foils from 1 to 10 μ thick.

Foils of Cr prepared by electrolysis were found to be brittle and disintegrated spontaneously after 5-7 days. Hence we undertook to prepare such films by decomposition of chromium iodide.[9] There are data in the literature[1,10] that chromium iodide forms at a temperature of 700-900°, which would involve the use of special heat resistant materials and complex apparatus.

We developed a new method for preparing chromium iodide by means of which the iodide can be obtained at the temperature of 300° in an apparatus of molybdenum glass. The chromium is first deposited from a sulfuric colution onto a mercury cathode. The resultant amalgam is filtered through chamois by suction.

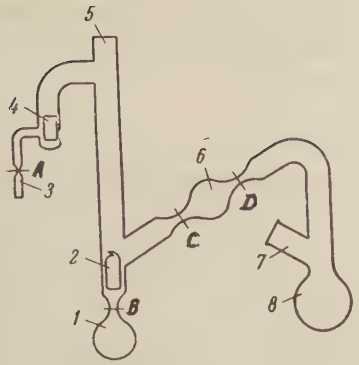

Fig.4

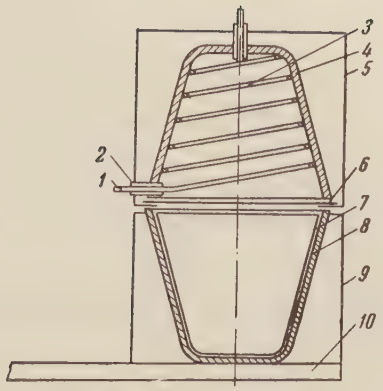

Fig.5

Fig.4. Apparatus for preparing chromium iodide: 1) receiver for mercury, 2) ampoule with iodine, 3) branch tube for connecting to vacuum pump, 4) striker, 5) branch tube for introducing the ampoule with iodine and the striker, 6) ampoule for chromium iodide, 7) tube for introducing the amalgam, 8) retort; A,B,C, & D - points at which apparatus is sealed off.

Fig.5. Diagram of chromium iodide evaporator and backing heater: 1) current leads, 2) insulators, 3) tungsten spiral, 4) ceramic crucible, 5) molybdenum cover, 6) molybdenum backing, 7) molybdenum liner, 8) ceramic crucible, 9) molybdenum cup, 10) holder-rod.

After removal of the excess mercury, there remains a silvery chromium amalgam on the chamois. All further operations are carried out in the special apparatus diagramed in Fig.4. The amalgam is charged into the retort 8 through the tube 7. Then the ampoule 2 with twice the stoichiometric amount of iodine is introduced into the tube 5; then after introducing the striker, the tubes 5 and 7 are sealed off. The apparatus is then connected by means of tube 3 to the vacuum pump, while the retort 8 is placed in a furnace and heated to 200°. The amalgam decomposes as the mercury is distilled over into receiver 1; upon elimination of the mercury the apparatus is sealed off at point A and the receiver with the mercury is sealed off at point B. Then by means of the striker 4 the ampoule with iodine is broken and the iodine is distilled over into the retort. Next the apparatus is sealed off at point C. The retort with ampoule 6 is heated to 300° for 30-40 min. The chromium iodide formed (a black powder) collects in the ampoule, while the excess of iodine and the mercury iodide are distilled over into the retort by heating the ampoule to 300°, after which the ampoule with the chromium iodide is sealed off at point D.

The ampoule containing the chromium iodide is then broken under toluene. The chromium iodide together with the toluene is placed in the ceramic crucible 8 (see Fig.5), lined with sheet molybdenum 7. The crucible is placed in the vacuum chamber which is then evacuated.

The toluene evaporates and condenses in the trap. When all the toluene is evaporated, the backing of 0.1 mm thick sheet molybdenum is heated to ~1050° (the temperature was measured by means of an optical pyrometer) and then by means of the special holder-rod 10 the crucible 8 is brought up flush against the molybdenum backing 6 as illustrated in Fig.5.

Thanks to the molybdenum liner 7 of the crucible, the chromium oxide is heated to approximately 800° and evaporates. Impinging on the heated backing, the vapor decomposes. The chromium is deposited on the backing, while the iodine is

caught and condensed in a trap. A vacuum of the order of $2\text{-}4 \cdot 10^{-5}$ mm Hg was maintained in the chamber. Depending on the amount of chromium iodide prepared and the dissociation time (from 10 to 15 min) there were obtained chromium foils from 1 to 15 μ thick. The molybdenum backing was dissolved in 1:1 nitric acid. Thus we were able to obtain ductile chromium foils.

Isotope targets prepared by the described procedures were repeatedly subjected to bombardment by 5.5, 6.8 and 20 Mev protons with no noticeable impairment of their mechanical properties.

Physical-Technical Institute
Academy of Sciences of the Ukrainian SSR

References

1. N.G.Klyuchnikov, Rukovodstvo po neorganicheskomu sintezu (Manual on inorganic synthesis), M.-L., 1953.
2. A.Levin, Zhur.prikl.khim. (Journal of Applied Chemistry), 14, 74 (1941).
3. R.A.Sharp, R.M.Diamond & G.Wilkinson, Phys.Rev., 101, 1439 (1956).
4. V.I.Lainer & N.G.Kudryavtsev, Osnovy gal'vanostegii (Fundamentals of galvanostegy), Part 1, M., 1953; Part 2, M., 1946.
5. P.I.Terekhov, A.K.Raikhshtadt & A.N.Ivanova, Trudy II Konferentsii po korrozii metallov (Transactions of the Second Conference on the Corrosion of Metals), M.-L., 1943.
6. L.I.Kadaner, Noveishie dostizheniya gal'vanostegii (Latest advances in galvanostegy), Kharkov, 1951.
7. G.I.Stepanova & F.I.Busol, Atomnaya energiya, No.10, 344 (1957). (Trans. Soviet Journal of Atomic Energy.)
8. K.L.Sinel'nikov, F.I.Busol & G.I.Stepanova, Ibid., No.2, 169 (1958). (Trans.Ibid.)
9. A.H.Sully, Chromium, N.Y., 1954. (Cited in Russian trans., 1958.)
10. G.Brauder, Handbuch der praparatiren anorganischen chemie, Stuttgart, 1951. (Cited in Russian trans., 1956.)

DETERMINATION OF THE RATIO OF K AND L X-RAY PHOTONS IN THE RADIATION FROM SOME NEUTRON-DEFICIENT ISOTOPES

- V.D.Vitman, B.S.Dzhelepov. A.A.Pavlov, S.V.Semenov & S.A.Shestopalova

1. Description of the Experiments

We measured the relative intensities of the K and L x-rays from Ho^{160}, Dy^{159}, Nd^{140} + Pr^{140} and Sm^{145} by means of a proportional counter. All the sources were obtained as a result of chromatographic separation of the group of rare earths extracted chemically from a tantalum target bombarded with 660 Mev protons on the Joint Institute for Nuclear Research synchrocyclotron. The holmium, dysprosium and neodynium fractions were obtained after 3-4 hour bombardment; the samarium fraction after more prolonged irradiation in a diffuse beam. The individual fractions were investigated some time after separation so that the isotopes with short periods had decayed completely and the studied activities were virtually the pure enumerated isotopes.

The aluminum counter had a diameter of 100 mm, a length of 400 mm and a wall thickness of 2 mm; it was mounted inside an airtight stell housing into which the x-irradiation entered through a 20 mm diameter window covered with a ~180 μ thick beryllium plate (superficial density 30 mg/cm^2).

The same pressure was maintained in the counter and housing. The radiation entered the detecting volume of the counter through a 25 x 25 mm window covered with a very thin (~1 μ) cellophane film, after passing through a ~10 mm thickness of the working mixture along the path from the housing window to the counter. Most of the secondary electrons ejected from the housing window were absorbed along this path and did not enter the counter. Between the source and housing window there was a collimator, the dimensions of which could be varied depending on the experimental conditions.

The counter was filled with a mixture of 80% A + 20% CH_4 to a total pressure of 700 mm Hg. The argon and methane were purified beforehand by passing over metallic calcium heated to 250-300°.

The recording equipment consisted of a linear non-jamming amplifier, a single channel pulse height analyzer and a "Floks" type scaler. The high voltage for the counter was supplied from a VS-10 rectifier.

The apparatus was calibrated in energy with reference to the x-ray lines of a number of known isotopes, namely, Zn^{65} (Cu K_α = 8.05 kev), Se^{75} (As K_α = 10.5 kev), In^{114} (In K_α = 24.1 kev), Cs^{137} (Ba K_α = 30.8 kev) and Sm^{145} (Pm K_α = 38.4 kev). The relative line half-width was 15% for $h\nu$ = 10.5 kev and 12% for 24.1 kev.

2. Experimental Results

The ratio of L to K x-ray photons was assumed to be proportional to the ratio of the areas under the L and K lines:

$$\frac{N_L}{N_K} = k\,\frac{S_L}{S_K}.$$

The proportionality coefficient in the above equation must take into account the efficiency of the counter in detecting the K and L x-radiation and the absorption of the radiation along the path from the source to the detecting volume of the counter. We determined the areas S_L and S_K under the x-ray lines in the following manner. From the experimental x-ray spectrum (curve a in the figure) we subtracted the background (curve c) which was due to γ-radiation from the source and to a minor degree to the intrinsic background of the counter and cosmic rays.

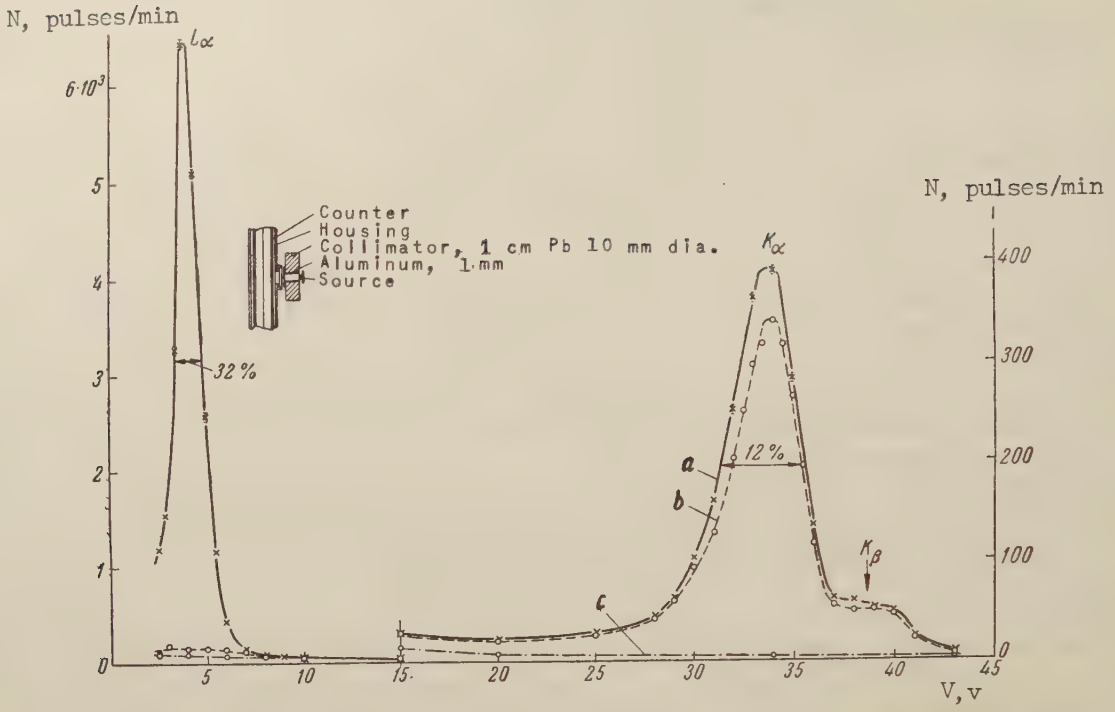

Spectrum of Sm^{145} x-rays: a) spectrum without absorber, b) spectrum with 1 mm aluminum absorber, c) background. The insert shows the experimental arrangement.

To determine the background the source was covered with an absorber slug of 0.8 mm cadmium, 0.5 mm copper and 0.5 mm aluminum. This absorber stopped virtually all the electromagnetic radiation with energy $\leqslant 60$ kev and transmitted virtually 100% of the γ-radiation with energy > 200 kev.

If in the γ-spectrum of the source there are only photons with energy > 200 kev the experimental background can be subtracted directly from the experimental spectrum.

If, on the other hand, the γ-spectrum of the source includes gammas with energies between 70 and 200 kev, one must make an appropriate correction for the absorption of these γ-rays in the slug.

Gammas with energies from 4 to 70 kev are detected by the counter and can be subtracted from the experimental spectrum (in accord with the line shape determined from separate experiments). Where our particular sources were concerned there were no noticeable γ-lines in the energy from 4 to 60 kev.

To separate the effects associated with the L and K radiations we recorded the "shape of the K line" (curve b in figure). To this end the source was covered with a ~1 mm thick aluminum absorber, which completely stopped the L x-rays. The shape of the K line obtained in this manner was then inscribed into the experimental spectrum and the ratio S_L/S_K determined.

For evaluating the efficiency ϵ of the counter and the absorption of the radiation along the path to the counter we used the x-ray mass absorption coefficients μ_m tabulated by Allen[1]. The counter efficiency was calculated approximately: in the case of our geometry the mean path of a photon in the counter can with sufficient accuracy be taken equal to the diameter of the counter. Evaluations showed that the error involved in calculating the effective mean path does not exceed 2%. In evaluating the error in ϵ we also took into account the possible error in the values of μ_m. For L x-radiation the efficiency is close to

Table 1

Determination of the ratio N_L/N_K

Isotope	S_L/S_K	Counter efficiency, %		Fraction entering counter, %		$K=\frac{\Pi_K \varepsilon_K}{\Pi_L \varepsilon_L}$	N_L/N_K
		ε_L	ε_K	Π_K	Π_L		
$Nd^{140}+Pr^{140}$	2,20±0,12	99,75±0,03	2,18±0,08	98,7±0,1	25,1±1,6	0,086±0,09	0,19±0,03
Sm^{145}	3,8±0,5	99,17±0,11	1,78±0,07	98,9±0,1	37,7±2,0	0,047±0,005	0,18±0,04
Dy^{159}	8,7±0,5	95,7±0,3	1,28±0,07	99,0±0,1	53,8±2,0	0,246±0,022	0,21±0,04
Ho^{160}	7,6±1,1	95,1±0,3	1,21±0,08	92,6±0,2	16,1±0,7	0,073±0,008	0,56±0,15

Table 2

Determination of the ratio λ_L/λ_K

Isotope	N_L/N_K	n_{KL} (Ref. 3)	ω_K (Ref. 2)	ω_L	W_K	W_L	λ_L/λ_K	Remarks
$Nd^{140}+Pr^{140}$	0,19±0,03	0,89±0,02	0,89±0,02	0,12±0,02	0	0	$0,5\ \begin{cases}+0,6\\-0,4\end{cases}$	No intense γ-transitions
Nd^{140}	—	—	—	—	—	—	$0,8\ \begin{cases}+1,6\\-0,7\end{cases}$	*
Sm^{145}	0,18±0,04	0,88±0,02	0,90±0,02	0,13±0,02	0,67±0,01	0,103±0,007	$0,6\ \begin{cases}+3,0\\-0,6\end{cases}$	W_K, W_L calc. basis data of Ref. 5
Dy^{159}	0,21±0,04	0,86±0,02	0,91±0,02	0,16±0,03	0,05	0,02	$0,3\ \begin{cases}+0,7\\-0,3\end{cases}$	W_K, W_L calc. basis data of Ref. 6
Ho^{160}	0,56±0,15	0,85±0,02	0,92±0,02	0,18±0,03	0,24±0,04	0,88±0,09	$1,2\ \begin{cases}+3,8\\-1,1\end{cases}$	W_K,W_L calc. basis data of Ref. 7

***In calculating λ_L/λ_K for Nd^{140} we took the theoretical branching ratio in the decay of Pr^{140} according to Dzhelepov[8]: β^+ - 53%, K - 41%, L - 6%.**

100%. For N_L/N_K we calculated the limit error.

The results obtained are listed in Table 1.

3. Bounds for the Ratio λ_L/λ_K

Having determined N_L/N_K one can attempt to find the ratio of probabilities for electron capture from the L and K shells.

If the electron capture leads directly to the ground state of the product nucleus, contributions to N_L and N_K are made only by processes arising incident to filling of the vacancies in the K and L shells.

If, however, capture leads to excited states of the product nucleus, then in the de-excitation of these states there occurs conversion, new vacancies appear in the atomic shells and additional K and L radiation is produced incident to filling of these vacancies. No matter how complicated the decay scheme the ratio of L to K capture probabilities can be expressed in terms of N_L/N_K by means of the formula

$$\frac{\lambda_L}{\lambda_K} = \frac{\left(\frac{N_L}{N_K}\cdot\frac{\omega_K}{\omega_L} - n_{KL}\right)(1+W_K) - W_L}{1+W_L - \left(\frac{N_L}{N_K}\cdot\frac{\omega_K}{\omega_L} - n_{KL}\right)W_K}, \tag{1}$$

where ω_K and ω_L are the fluorescence yields from the K and L shells, n_{KL} is the number of vacancies forming in the L shell owing to filling of one vacancy in the K shell, and W_K and W_L are the numbers of conversion electrons per decay.

The values of ω_K and n_{KL} are fairly well known and can be taken from the literature[2,3]. A substantial uncertainty in evaluating λ_L/λ_K is introduced by ω_L; the L shell fluorescence yield ω_L depends on the distribution of vacancies over the L subshells (n_1, n_2, n_3) and can be calculated by means of the equations given by Wapstra et al[4]:

$$\omega_L = \frac{n_1\nu_1 + n_2\nu_2 + n_3\nu_3}{n_1+n_2+n_3},$$

where

$$\begin{aligned}\nu_1 &= \omega_{L_1} + f_{12}\omega_{L_2} + (f_{13} + f_{12}f_{23})\,\omega_{L_3},\\ \nu_2 &= \omega_{L_2} + f_{23}\omega_{L_3},\\ \nu_3 &= \omega_{L_3};\end{aligned}$$

here ω_{L_i} is the fluorescence yield from the L_i subshell, and f_{12}, f_{13} and f_{23} are Coster-Krönig transition coefficients.

The vacancy distribution can be calculated by means of the formula

$$n_i = \frac{L_i}{K+L} + W_{L_i} + n_{KL_i}\left(\frac{K}{K+L} + W_K\right),$$

where $\frac{L_i}{K+L}$ is the fraction of captures in the L_i subshell, W_{L_i} is the number of conversion L_i electrons per disintegration, n_{KL_i} is the number of vacancies in the K shell.

In practice, however, L capture occurs virtually entirely from the L_1 subshell. The values of ω_{L_i}, n_{KL_i} and the Coster-Krönig coefficients can be taken from Listengarten's[3] review article on the Auger effect; the W_{L_i} can be determined from the corresponding conversion electron spectra.

In Table 2 we list the calculated values of λ_L/λ_K and the quantities necessary to calculate these ratios. The uncertainties indicated for ω_K, ω_L and n_{KL} give the bounds within which the given quantity may lie, judging from the curves given by Listengarten[3]. The uncertainty in N_L/N_K is determined primarily by the uncertainties in evaluating Π_L and ε_K. The uncertainties indicated for W_K and W_L

were taken from the references listed under "Remarks". Inasmuch as all the uncertainties are nonstatistical in character, we believe it is correct to indicate the bounds for the values of λ_L/λ_K when this quantity is determined according to Eq.(1).

Table 2 shows that the uncertainty in determining λ_L/λ_K is very substantial; this stems from the fact that λ_L/λ_K is determined as a small difference between two large quantities.

The physical reason for the large uncertainty is that the L peak comprises more x-rays connected with K capture than with L capture; thus, for example, in the case of $Nd^{140} + Pr^{140}$, if there were no L capture at all, the L peak would be only 1/3 lower.

It must be emphasized that the above method for determining λ_L/λ_K from N_L/N_K is not suitable for small values of the ratio and can yield a satisfactory accuracy only in anomalous cases when $\lambda_L > \lambda_K$.

"D.I.Mendeleev" All-Union Scientific Research Institute of Metrology.

References

1. Handbook of Chemistry and Physics (34th edition), Cleveland, Ohio, 1952.
2. K.Siegbahn, Beta- and Gamma-Ray Spectroscopy, N.Y., 1955. (Cited in Russian trans., 1959.)
3. M.A.Listengarten, Izv.AN SSSR, Ser.fiz., 24, No.9 (1960). (Trans.Bulletin, 24, No.9.)
4. A.Wapstra, G.Nijgh & R.van-Lieshout, Nuclear Spectroscopy Tables, Amsterdam, 1959.
5. A.R.Brosi, B.H.Ketelle, H.C.Thomas & R.J.Kerr, Phys.Rev., 113, 239 (1959).
6. B.H.Ketelle & A.R.Brosi, Ibid., 116, 98 (1959).
7. E.P.Grigor'ev, B.S.Dzhelepov, A.V.Zolotavin, B.Kratsik & G.Bitterlikh, Izv.AN SSSR, Ser.fiz., 23, 868 (1959). (Trans.Bulletin, 23, 859.)
8. B.S.Dzhelepov, Obzor po Nd i Pr. (Survey of Nd and Pr.) Transactions of the Tenth All-Union Conference on Nuclear Spectroscopy, Moscow, Jan., 1960.

Bulletin of the Academy of Sciences of the USSR - Physical Series
Vol.24, No.7 - July 1960
Transactions of the Tenth All-Union Conference on Nuclear Spectroscopy
(Continued from Vol.24, No.3; to be continued in Vol.24, Nos.9 & 12, Vol.25,No.1)

TABLE OF CONTENTS

	Page Orig.	Trans.
Formation of Eu^{145} in spallation of tantalum - A.A.Bashilov, O.V.Larionov, M.K.Nikitin & V.B.Smirnov	788	791
Magnetic gamma-spectrometer with high resolution - L.V.Groshev, A.M.Demidov, V.N.Lutsenko & A.F.Malov	791	794
Conversion electron spectrum of neutron-deficient lutetium isotopes in the 1000 to 3500 kev region - B.S.Dzhelepov, I.F.Uchevatkin & S.A.Shestopalova	802	805
Conversion electron spectrum of Lu^{167} + Yb^{167} - A.S.Basina, B.S. Dzhelepov & V.A.Chikhladze	807	810
Conversion electron spectrum of the dysprosium fraction from spallation of tantalum - A.S.Basina, K.Ya.Gromov & B.S.Dzhelepov	811	813
On the 106 kev transition in Tm^{167} - A.S.Basina & V.A.Morozov	817	819
The (n,2n) and (γ,n) reactions on Au^{197} - M.A.Bak, K.A.Petrzhak & Chen' Tya-mei	818	820
Rotational energy of even-even and odd nuclei - A.S.Davydov	820	822
Gamma-radiation from the $Cl^{35}(n,\gamma)Cl^{36}$ reaction - L.V.Groshev, A.M.Demidov & V.N.Lutsenko	833	834
Gamma-spectra of the isotopes in the lanthanum fraction from spallation of tantalum - E.P.Grigor'ev, S.L.Sakharov & V.O.Sergeev	839	844
Determination of the periods of Dy^{159}, Ho^{160m}, Tm^{166} and Lu^{173} - E.P.Grigor'ev, O.V.Larionov, M.K.Nikitin, S.L.Sakharov & V.O. Sergeev	841	846
Gamma-spectra of the tantalum activity formed by proton bombardment of tantalum - E.P.Grigor'ev, O.V.Larionov, M.K.Nikitin, S.L. Sakharov & V.O.Sergeev	845	850
Measurement of the mean lifetime of Lu^{175} in the 113.8 kev excited state - V.P.Bozhko, I.I.Zalyubovskii & A.I.Tutubalin	847	852
Gamma-radiation from Zr^{95} + Nb^{95} - N.A.Voinova, B.S.Dzhelepov & N.N.Zhukovskii	850	854
Gamma-radiation from Tb^{160} - N.A.Voinova, B.S.Dzhelepov, N.N. Zhukovskii & Yu.V.Khol'nov	852	856
Determination of level spins and parities from inelastic scattering and the pick-up reaction on Be^{9} - O.F.Nemets, L.S.Saltykov, M.V. Sokolov & Yu.V.Tsekhmistrenko	858	861
Spins and parities of C^{13} levels - N.I.Zaika, O.F.Nemets & M.A. Tserineo	862	865
Assignments for the levels of Ti^{47-50} and Sr^{89} - N.I.Zaika & O.F.Nemets	865	868
Spin of the 1.38 Mev level of Mg^{24} - O.F.Nemets & G.A.Prokopets	869	872
Spins and parities of Ca^{41} levels - N.I.Zaika, O.F.Nemets & V.S. Prokopenko	872	875
Angular distribution of protons inelastically scattered from Cr and Ni isotopes - M.V.Pasechnik, N.N.Pucherov & V.I.Chirko	874	876
Investigation of the levels of Cl^{35} - Yu.P.Antuf'ev, A.K.Val'ter, V.Yu.Gonchar, E.G.Kopanets, A.N.L'vov & S.P.Tsytko	877	878

Elastic scattering of protons by Ne^{20} - A.K.Val'ter, A.S.Deineko, P.V.Sorokin & A.Ya.Taranov	884	885
Elastic scattering of protons from nuclei - A.P.Klyucharev	887	888
Investigation of the levels of K^{41} by means of the $A^{40}(p,\gamma)K^{41}$ reaction - A.K.Val'ter, Yu.P.Antuf'ev, V.Yu.Gonchar, A.N.L'vov & S.P.Tsytko	891	892
Experimental and theoretical state-mixing coefficients and polarization of nucleons in deformed nuclei - D.A.Varshalovich	895	895
Internal bremsstrahlung accompanying β-decay of P^{32} - K.A.Korotkov & A.M.Chernikov	899	899
Excitation of collective nuclear levels in stripping reactions - A.M.Korolev	903	902
Beta-transitions in weakly deformed nuclei - B.D.Konstantinov & V.I.Ovcharenko	912	910
Magnetic and quadrupole moments of weakly deformed nuclei - Yu.L.Gurin, A.M.Korolev & B.D.Konstantinov	920	918
Double-focusing magnetic spectrometer - A.S.Deineko, A.I.Popov, P.V.Sorokin & A.Ya.Taranov	924	921
Preparation of isotope targets for nuclear studies - A.D.Bondar', A.S.Emlyaninov, A.P.Klyucharev, L.G.Lishenko, V.N.Medyanik, A.D.Nikolaichuk & O.E.Shalaeva	929	926
Determination of the ratio of K and L x-ray photons in the radiation from some neutron-deficient isotopes - V.D.Vitman, B.S.Dzhelepov, A.A.Pavlov, S.V.Semenov & S.A.Shestopalova	934	931

Translated in 1961 by
Columbia Technical Translations
5 Vermont Avenue, White Plains, N.Y.

Transactions

of the

First All-Union Conference on Electronic and Ionic Collisions

(Riga, June 26 to July 3, 1959)

REGARDING THE FIRST ALL-UNION CONFERENCE ON ELECTRONIC AND IONIC COLLISIONS

- L.A.Sena & G.F.Drukarev

The First All-Union Conference on Electronic and Ionic Collisions, organized by the Academy of Sciences of the Latvian SSR, was held from June 26 to July 3, 1959 in Riga. Representatives from several score scientific-research institutes, universities and other organizations, located in the principal cities of the Soviet Union, attended the conference.

The subjects discussed at the conference were inelastic collisions of electrons with atoms and molecules and the processes involved in encounters of heavy particles (ionization, charge exchange, formation and disintegration of negative ions). The reports were grouped according to subject: each series of reports on specific investigations was preceded by a review of developments in the given field.

The Conference was opened by the review of L.A.Vainstein* which described the present state of methods of calculating electron-atom collision cross sections. Particular attention was given to the problem of collisions of electrons with complex atoms, where a general analysis can be carried out only using the algebraic technique developed by Racah. The report considered two specific cases of particular interest: a transition between terms of the same configuration and transitions with change of configuration for one electron. The results of actual calculations of the excitation function were given in the reports of R.Ya.Damburg & V.Ya.Kravchenko, V.Ya. Vel'dre & R.Ya.Damburg, R.K.Peterkop, and L.A.Vainshtein & G.G.Dolgov. In the last report, "Computer Calculation of the Cross Section for Excitation of Atoms by Electron Impact", there was demonstrated the significant role of partial waves corresponding to large values of the orbital momentum of the scattered electron, even near the excitation threshold.

A review of the use of variational methods in collision theory was presented by Yu.N.Demkov. Experimental investigations of the excitation functions were described in reports submitted by I.P. Zapesochnyi & S.M.Kishko, I.P.Bogdanova, V.E.Yakhontova, and L.M. Volkova & A.M.Devyatova.

"Dissociation of Large Molecules Under Electron Impact" was the title of a report presented by M.V.Gur'ev, M.V.Tikhomirov & N.N. Tunitskii.

The problem of collision of heavy particles was introduced by the review of N.V.Fedorenko entitled "Ionization in Ion-Atom Collisions." Experimental investigations in this field carried out in the Leningrad Physical-Technical Institute were described in a series of reports presented by Yu.F.Bydin & A.M.Bukhteev, L.G.Filippenko & I.P.Flaks, I.P.Flaks & L.F.Filippenko, and V.V.Afrosimov, R.N.Il'in & E.S.Solov'ev.

---

*See "Methods of Calculating the Cross Sections for Excitation of Atoms by Electrons" by L.A.Vainshtein & I.I.Sobel'man, p.943.

Among the reports devoted to charge exchange of ions and atoms were "On the Maximum Cross Section for Nonresonance Single Electron Charge Exchange" by N.V.Fedorenko & V.A.Belyaev, "Resonance Charge Exchange of Alkali Metal Ions and Atoms" by A.M.Bukhteev & Yu. F. Bydin, "Resonance Charge Exchange of Positive Alkali Metal Ions" by D.V.Chkuaseli, U.D.Nikoleishvili & A.I.Guldamishvili, and "Further Investigation of Resonance Charge Exchange of Positive Cesium Ions" by R.M.Kushnir & I.M.Buchma. V.L.Tal'roze presented a report entitled "Elementary Processes Involved in Collision between Slow Ions and Molecules."

Investigations carried out at the Kharkov Physical-Technical Institute were described in a review presented by Ya.M.Fogel' and in the reports, "Loss of Electrons by Fast Atoms in Single Collisions with Gas Molecules" by Ya.M.Fogel', V.M.Ankudinov & D. V. Pilipenko, and "Ionization of Gas Ions in Collisions with Negative Hydrogen Ions" by Ya.M.Fogel', A.G.Koval & Yu.Z.Levchenko.

Analyzing the results obtained in these investigations, Ya.M. Fogel' showed that the regularities governing the formation of negative ions are consistent with the adiabatic hypothesis of Massey. The Massey criterion was the subject of a report presented by G.F. Drukarev. Drukarev also presented a review of "Modern Methods of Calculating Atomic Collision Cross Sections."

In addition to the discussions of individual reports, there was held a symposium in the course of which there was a free exchange of views regarding certain problems that aroused particular interest at the Conference, in particular, ionization by heavy particles near the energy threshold, multiple ionization by electron impact and resonance charge exchange.

METHODS OF CALCULATING THE CROSS SECTIONS FOR EXCITATION OF ATOMS BY ELECTRONS

- L.A.Vainshtein & I.I.Sobel'man

Of late there has been a growing interest in the elementary processes by which atoms are excited and ionized by electrons. The number of theoretical studies, in particular, has increased significantly in the last few years. At the same time, experimental data is being accumulated (by Frish's group[1] in the U.S.S.R. and by Fite's group[2] and others abroad). As a result it is now becoming possible to compare calculations more systematically with experiment. The theoretical investigations are based on many different approximation methods, and it would be impossible within the framework of the present paper to describe these in detail. Furthermore, there have been many review articles on this subject: in addition to the well known monographs of Mott & Massey (Theory of Atomic Collisions) and Massey & Burhop (Electronic and Ionic Impact Phenomena), there have recently appeared two new review articles by Massey.[3] It should be noted, however, that so far all of the more concrete calculations have considered only the simplest transitions. In the more complicated cases it is difficult even to write out the wave equation for the exciting electron. In what follows we shall turn to the general equations of the theory of collisions between atoms and electrons, and then, using these equations, we shall briefly characterize the approximation methods.

The problem of collision theory is to solve the Schrödinger equation for the wave function Ψ of a system composed of an N-electron atom and an external electron. In order to solve the problem in practice Ψ must be expanded in a set of functions $\Psi(\Gamma)$ in which the internal electron variables are separated, as are the radius and the angle variables of the external electron. The most convenient representation is then that in which the total angular moments are diagonal, i.e., in which $\Gamma = \gamma LSk\tilde{l}^{\pi}/_2 L_T S_T$, where γLS are the quantum numbers of the atomic state, $k\tilde{l}^{\pi}/_2$ are the quantum numbers of the partial wave of the external electron, and L_T and S_T are the total orbital and spin moments of the system. If the atomic wave functions are assumed known, the problem is to find the radial part $F_\Gamma(r)$ of the external-electron wave function.

In general (that is, not restricted to the framework of perturbation theory), these functions must be found from a set of integro-differential equations with certain boundary conditions:

$$F_\Gamma(0) = 0; \quad F_\Gamma \sim \delta_{\Gamma\Gamma_0} \sin\left(k_0 r - \frac{\tilde{l}_0\pi}{2}\right) + T_{\Gamma\Gamma_0} \exp i\left(kr - \frac{\tilde{l}\pi}{2}\right). \tag{1}$$

The set of equations for $F_\Gamma(r)$ is obtained from the variational principle

$$\delta_{F_\Gamma} \langle \Psi | H - E | \Psi \rangle = 0. \tag{2}$$

The excitation cross section is given by the $T_{\Gamma\Gamma_0}$ matrix, namely,

$$\sigma^{\gamma LS}_{\gamma_0 L_0 S_0} = \frac{4\pi a_0^2 k}{k_0^3} \sum_{\tilde{l}\tilde{l}_0 L_T S_T} \frac{(2S_T+1)(2L_T+1)}{2(2S_0+1)(2L_0+1)} |T_{\Gamma\Gamma_0}|^2. \tag{3}$$

The actual explicit form of the equations is strongly dependent on the approximation wave functions, since exact functions are obtainable only for the hydrogen atom. It would seem that the Hartree-Fock functions are the most accurate ones available for actual calculation.

The general form of the equations for $F_\Gamma(r)$ is quite complicated. Racah techniques[4] have made it possible to obtain general expressions for the matrix elements in (2). However, the calculations become quite complicated because one must take into account the fact that the single-electron radial functions are not orthogonal. A rigorous treatment of this lack of orthogonality leads to equations that have been studied so little that it is scarcely feasible to use them at the present time. These equations become much simpler, however, if a) one accounts for lack of orthogonality only between the radial functions of the external and valence electrons, and b) one drops some of the terms which contain products of integrals arising from this lack of orthogonality and from multipole interactions of the second and higher order.

Such a simplified set of equations is of the form

$$\left[\hat{L}_\Gamma - \hat{U}_{\Gamma\Gamma} - \frac{k^2}{2}\right] F_\Gamma = \sum_{\Gamma'}{}' \hat{U}_{\Gamma\Gamma'} F_{\Gamma'}; \tag{4}$$

$$\hat{U}F = \sum_\varkappa \alpha^\varkappa y_\varkappa(r) F(r) - \sum_\varkappa \beta^\varkappa [y_\varkappa^{\text{ex}}(r) - \delta_{\varkappa_0} \lambda \Delta(PF)] P(r), \tag{5}$$

where $y_\varkappa(r)$ and $y_\varkappa^{\text{ex}}(r)$ are the direct and exchange potentials, $P(r)$ is the radial function of the optical electron in the atom, and $\Delta(PF)$ is a nonorthogonality integral.

To simplify the notation, the indices Γ and Γ' are suppressed in Eq.(5). The operator $\hat{L}_\Gamma$ includes the kinetic and centrifugal energies and the interaction between the nucleus and the internal electrons. The coefficients $\alpha^\varkappa$ and $\beta^\varkappa$ depend on the orbital and spin angular momentum quantum numbers. In general, they are of quite complicated form, and for lack of space we will not give them here. We note only that they can be expressed in terms of Racah's W-coefficients, Clebsch-Gordan coefficients, and other Racah coefficients. These have been tabulated for the hydrogen atom.[5]

The value of the parameter λ depends on whether the expression for the energy of the system is chosen as

$$E = E_{\gamma LS} + \frac{k^2}{2} \quad \text{or} \quad E = E_{\gamma' L' S'} + \frac{k'^2}{2}.$$

Since the energy $E_{\gamma LS}$ or $E_{\gamma' L' S'}$ of the atom must be calculated in the same approximation as the atomic wave functions, the two representations for E lead to different values of λ. This is the well known "prior-post" divergence of the literature, related to the approximate nature of the atomic wave functions. Whether one uses the prior- or post-approximation makes a difference only in those terms which contain nonorthogonality integrals. But in our approximation the difference vanishes when one uses semiempirical radial wave functions for the optical electron.

Let us now briefly describe the approximation methods employed in collision theory. In most of the calculations performed in the past, the collision process is approximated by two states. In this approximation Eqs.(4) are reduced to the pair of equations

$$\left[\hat{L}_{\Gamma_0} - \hat{U}_{\Gamma_0} - \frac{k_0^2}{2}\right] F_{\Gamma_0} = \hat{U}_{\Gamma_0\Gamma} F_\Gamma \quad \text{and} \quad \left[L_\Gamma - U_\Gamma - \frac{k^2}{2}\right] F_\Gamma = \hat{U}_{\Gamma\Gamma_0} F_{\Gamma_0}; \tag{6}$$

which means that all virtual transitions are neglected. In particular, excitation of the atom by the external electron is completely ignored. For elastic scattering, polarization of the atom by the external electron can be partially accounted for by introducing an additional potential (varying as $1/r^4$) into $U_{\Gamma 0}$. No such procedure has been developed, however, for inelastic scattering.

If one drops the right side in the first of Eqs.(6), we arrive at the so-called method of deformed waves. In this treatment the transition amplitude can be obtained by quadrature when one solves the independent homogeneous equations for $F_\Gamma^*(r)$. One then arrives at

$$|T_{\Gamma\Gamma_0}|^2 = \frac{1}{k^2}\left|\int_0^\infty F_\Gamma^* U_{\Gamma\Gamma_0} F_{\Gamma_0}^* dr\right|^2. \tag{7}$$

It is seen that $T_{\Gamma\Gamma_0}$ is given by the off-diagonal matrix element of the interaction, taken for the independent wave functions of the set $\Psi(\Gamma)$. In other words, the deformed-wave method gives the most accurate solution of the problem in the first approximation of perturbation theory.

The exact solution of (6) is often called the strong-coupling approximation, since it takes into account the influence of the inelastic scattering on the elastic. As has been shown by Seaton's[6] calculations for oxygen, strong coupling may be important for transitions between the terms of a given configuration. When it comes to exciting levels in simple atoms such as H or H_e, however, strong coupling would seem to play a smaller role, of the order of 10%.

The $F_\Gamma^*(r)$ are solutions of a rather complicated integro-differential equation of the Hartree-Fock type with a given potential. It is therefore often necessary to use a better approximation. Foremost among these is the familiar Born approximation, in which $F_\Gamma^*(r)$ is the l-component of a plane wave (i.e., essentially a Bessel function of the order of $l + 1/2$).

The integro-differential equations (6) can be rewritten in the form of integral equations. In some cases this is very helpful, since one can then obtain some general information on the cross section. The first approximation in the integral-equation method turns out to be intermediate between the Born approximation and the deformed-wave approximation. The question of the accuracy of the different approximations has been discussed by Drukarev[7].

We note that the $\hat{U}$ operators include both exchange and direct interactions. Therefore each approximation method can, in turn, be split in two, namely, with and without exchange.

Finally, we return to Eq.(3) for the total cross section. We note that this expression includes a sum over l and l_0. Until recently actual calculations have, as a rule, been restricted to s

and p waves, but lately it has become clear that even at energies as little as 10 ev above threshold, one must take other waves into account as well. This fact complicates the calculations considerably, and makes it necessary to have recourse to electronic computers for performing the computations. Furthermore, with the inclusion of more partial waves, the Born approximation becomes more important, for only by its means is it possible to sum analytically over l and l_0. This essentially corresponds to turning back from partial spherical waves to plane waves.

"P.N.Lebedev" Physical Institute,
Academy of Sciences of the USSR

References

1. S.Frish, Uspekhi fiz.nauk, 61, 461 (1957); S.Frish & V. Yakhontova, Optika i spektroskopiya, 4,402 (1958); V.Yakhontova, Vestnik, Leningrad State University, 10, 27 (1959).

2. W.Fite, Phys.Rev., 112, 1151 (1958).

3. H.Massey, Revs.Mod.Phys., 28,171 (1956); Uspekhi fiz. nauk, 64, 589 (1958); Handb. d. Phys., 36 (1956).

4. C.Racah, Phys.Rev., 62, 438 (1942); Ibid., 63,367 (1943). A.Edmonds, Angular momenta in quantum mechanics (In Collection of articles: Deformation of Nuclei), Russian trans., M.,1958.

5. J.Percival & M.Seaton, Proc.Cambridge Philos.Soc., 53, 654 (1957).

6. M.Seaton, Philos.Trans.Roy.Soc., London, A,245, 469 (1953).

7. G.Drukarev, Zhur.eksp.i teor.fiz., 31,288 (1956)(Trans. Soviet Physics - JETP.); Vestnik, Leningrad State University, No. 22, 65 (1958).

PARTIAL EXCITATION CROSS SECTIONS FOR HYDROGEN ATOMS

- R. K. Peterkop

In the present work we use the Born approximation to calculate some partial cross sections for excitation of a hydrogen atom from its ground state to levels in the discrete and continuous spectrum.

As is known[1], in the Born approximation the excitation amplitude for the nlm level may be written, in atomic units

$$a_{nlm}(\mathbf{q}, \mathbf{c}) = -\frac{1}{2\pi}\iint \exp(i\mathbf{q}\mathbf{r}_1)\,\psi_1(\mathbf{r}_2)\,\frac{1}{r_{12}}\exp(-i\mathbf{c}\mathbf{r}_1)\,\psi^*_{nlm}(\mathbf{r}_2)\,d\mathbf{r}_1\,d\mathbf{r}_2 \quad (n \neq 1), \tag{1}$$

where q is the momentum of the incident electron, and c is the momentum of the scattered electron. The cross section for excitation of the level with principal quantum number n (in units of πa_0) is

$$Q_n(q) = 1/\pi \sum_{lm} \frac{c}{q} \int |a_{nlm}(\mathbf{q}, \mathbf{c})|^2\, d\Omega_c. \tag{2}$$

A similar expression is obtained for $Q_k(q)$, the cross section for excitation of level k in the continuum, referred to a unit momentum interval of the excited atomic electron.

In what follows it will be convenient to make use of the quantity $\sigma(q, c)$, the cross section per unit interval of the scattered-electron momentum. As we showed elsewhere[2], in the discrete spectrum $\sigma(q, c) = cn^3 Q_n(q), (c = \sqrt{q^2 - 1 + n^{-2}})$, while in the continuous one, $\sigma(q, c) = \frac{c}{k} Q_k(q), \quad (c = \sqrt{q^2 - 1 - k^2})$. Expanding the integrand in Eqs.(1) and (2) in spherical functions, expressing the integrals so obtained in terms of angle variables by means of Clebsch-Gordan coefficients, summing over m, and using the explicit expressions for the radial functions, we obtain

$$\sigma(q, c) = \sum_{ltL} \sigma_{ltL}(q, c), \tag{3}$$

where

$$\sigma_{ltL}(q, c) = 2^8 \frac{c^2}{q} \frac{2t+1}{2l+1} \frac{(lt00/L0)^2}{1 - \exp\left(-\frac{2\pi}{k}\right)} \prod_{p=0}^{l} (1 + p^2k^2) \times \left[\frac{2^l}{(2l+1)!} \int_0^\infty \int_0^\infty j_L(qr_1)\,\gamma_l(r_1, r_2)\,j_t(cr_1)\,r_1^2 r_2^{l+2} \times \right.$$

$$\left. \times \exp(-r_2 - ikr_2)\, F\left(1 + l + \frac{i}{k},\ 2l + 2,\ 2ikr_2\right) dr_1\, dr_2 \right]^2. \tag{4}$$

Here $j_s(x)$ is the spherical Bessel function, $F(\alpha, \beta, x)$ is a confluent hypergeometric function, $\gamma_l(r_1, r_2) = \min\left[\frac{r_1^l}{r_2^{l+1}}, \frac{r_2^l}{r_1^{l+1}}\right]$ and $(lt00|L0)$ is a Clebsch-Gordan coefficient.

The expression for the discrete-spectrum cross section $\sigma_{ltL}(q, c)$ is obtained by dropping the factor $\left[1 - \exp\left(-\frac{2\pi}{k}\right)\right]^{-1}$ and replacing k by $-\frac{i}{n}$.

It is clear that $\sigma_{ltL}(q, c)$ is the cross section for the process in which an incident electron with angular momentum L and momentum q is scattered into a state with angular momentum t and momentum c, while an atomic electron is raised from the ground state to the state with momentum $k = \sqrt{q^2 - 1 - c^2}$ and angular momentum l.

Let us write

$$\sigma_l \equiv \sum_{tL} \sigma_{ltL}; \tag{5}$$

then σ and σ_l can be written in the form

$$\sigma(q, c) = \int_0^\pi w(q, c, \theta) \sin\theta\, d\theta, \qquad \sigma_l(q, c) = \int_0^\pi w_l(q, c, \theta) \sin\theta\, d\theta, \tag{6}$$

where θ is the scattering angle of the incident electron.

Obviously,

$$w(q, c, \theta) = \sum_l w_l(q, c, \theta). \tag{7}$$

We then obtain the following results.

In the continuous spectrum

$$w(q, c, \theta) = \frac{2^{11} \cdot c^2}{q\left[1 - \exp\left(-\frac{2\pi}{k}\right)\right]} \frac{\left[x^2 + \frac{1}{3}(1 + k^2)\right] \exp(-2\omega)}{x^2 [1 + (k + x)^2]^3 [1 + (k - x)^2]^3} \tag{8}$$

$$w_0(q, c, \theta) = \frac{2^7 \cdot c^2}{q\left[1 - \exp\left(-\frac{2\pi}{k}\right)\right]} \frac{[2x \cos y + (x^2 - 1 - k^2) \sin y]^2 \exp(-2\omega)}{x^6 [1 + (k + x)^2]^2 [1 + (k - x)^2]^2}; \tag{9}$$

in the discrete spectrum

$$w(q, c, \theta) = \frac{2^{11} \cdot c^2}{q} \cdot \frac{\left[x^2 + \frac{1}{3}\left(1 - \frac{1}{n^2}\right)\right]\left[x^2 + \left(1 - \frac{1}{n}\right)^2\right]^{n-3}}{x^2\left[x^2 + \left(1 + \frac{1}{n}\right)^2\right]^{n+3}}, \tag{10}$$

$$w_0(q, c, \theta) = \frac{2^7 \cdot c^2}{q} \frac{[2x \cos z + (x^2 - 1 + 1/n^2) \sin z]^2 [x^2 + (1 - 1/n)^2]^{n-2}}{x^6 [x^2 + (1 + 1/n)^2]^{n+2}}, \tag{11}$$

where

$$x^2 = q^2 - 2qc \cos\theta + c^2; \quad \omega = \frac{1}{k} \operatorname{arc\,tg} \frac{2k}{1 - k^2 + x^2};$$

$$y = \frac{1}{2k} \ln \frac{1 + (k + x)^2}{1 + (k - x)^2}; \qquad z = n \operatorname{arc\,tg} \frac{2x}{n(1 - 1/n^2 + x^2)};$$

$$w_1(q, c, \theta) = \frac{3(q^2 - c^2)}{x^2} w_0(q, c, \theta). \tag{12}$$

It follows from (12) that $c \to 0$ as $\frac{\sigma_1}{\sigma_0} \to 3$, and $c \to \infty$ as $\frac{\sigma_1}{\sigma_0} \to \infty$.

We have calculated the cross sections σ_{000}, σ_{101}, σ_0, σ_1 and σ for an incident electron momentum $q = 1.2$ (or an energy of 19.6 ev). The results are shown in Fig.1 (where instead of σ_i we have plotted $\frac{1}{c^2}\sigma_i$). Fig.2 gives the cross sections $Q_{2ltL}(q) = \frac{1}{c^{2s}}\sigma_{ltL}(q, c)$ for excitation of the $n = 2$ level for different incident electron momenta.

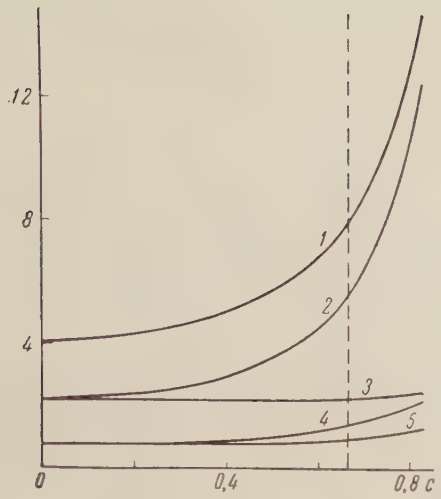

Fig.1. 1) $\frac{1}{c^2}\sigma$, 2) $\frac{1}{c^2}\sigma_1$, 3) $\frac{1}{c^2}\sigma_{101}$, 4) $\frac{1}{c^2}\sigma_0$, 5) $\frac{1}{c^2}\sigma_{000}$.

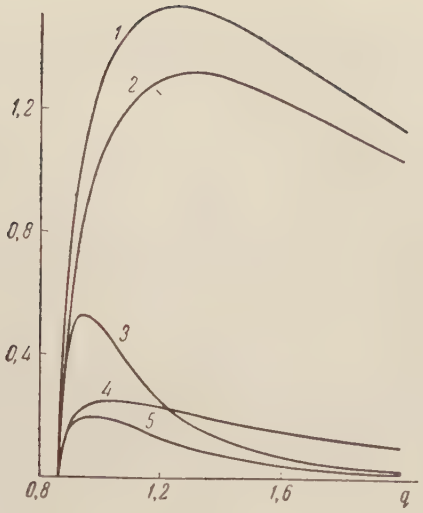

Fig.2. 1) Q_2, 2) Q_{21}, 3) Q_{2101}, 4) Q_{20}, 5) Q_{2000}.

The dashed line in Fig.1 denotes the boundary between the continuous and discrete spectra ($n \Rightarrow \infty$).

The continuum values of σ, σ_1, σ_{101} and σ_0 have been calculated by numerical integration. In Fig.2 the curves for Q_{21} and Q_{20} are those of Elsasser.[3] To obtain σ for the discrete spectrum we used the results of McCarroll.[4]

Noting (see Section 15 of Schiff[5]) that

$$j_l(cr) \xrightarrow[c\to 0]{} \frac{c^l r^l}{1.3.5\ldots(2l+1)} \tag{13}$$

from (4) we obtain

$$\sigma_{lL}(q, c) \xrightarrow[c\to 0]{} a_{lL}(q)\, c^{2l+2}. \tag{14}$$

Then in the limit as $c \to 0$, we find that

$$\sigma_l(q, c) \approx \sigma_{l0l}(q, c) \approx a_{l0l}(q)\, c^2. \tag{15}$$

Therefore, close to the excitation threshold ($c \to 0$) the main contribution to the cross section is from the scattered s-waves. According to Wigner[6], this should be true for the discrete spectrum also in an exact calculation. It is seen from Figs.1 and 2 that when the p-level is excited, the amount of scattered s--waves decreases much more rapidly with increasing c (or q) than it does when the s-level is excited.

The ionization cross section close to the ionization threshold ($q \to 1$ or $E = \frac{q^2}{2} - \frac{1}{2} \to 0$) is of the form

$$\sigma^{ion}(E) = \int_0^{\sqrt{2E}} \sigma(q, c)\, dc \approx \frac{\sqrt{8}}{3} \sum_l a_{l0l}(1)\, E^{1,5}. \tag{16}$$

The partial ionization cross section σ_{llo}^{ion} $(l = 0, 1, 2)$ close to threshold was calculated by Geltman[7] in an approximation differing from the Born approximation in that $\exp(icr)$ in Eq.(1) is replaced by $(2\pi)^{3/2}\psi_c^-(r)$ (the notation is that of Section 113 of Landau and Lifshits[8]). Correspondingly, one replaces $j_l(cr)$ in Eq. (4) by $\frac{1}{c}\sqrt{\pi/2}R_{cl}(r)$ (where $R_{cl}(r)$ is the radial function for a Coulomb potential). Further, Geltman took into account exchange forces. He did not, however, bear in mind the fact that the flux of electrons leaving the atom is double the total number of electrons scattered in ionization; his result for hydrogen is therefore too high by a factor of two.

When the plane wave is replaced by the Coulomb wave function, the behavior of the cross section at threshold is considerably altered. Using the expression (see, for instance, Section 36 of Landau and Lifshits[8])

$$R_{cl}(t) \xrightarrow[c\to 0]{} \sqrt{c}\sqrt{2/r}I_{2l+1}(\sqrt{8r}), \tag{17}$$

for the radial function, (14) and (16) are replaced, in Geltman's approximation, by

$$\sigma_{llL}(q, c) \xrightarrow[c\to 0]{} a_{llL}(q)\,c \quad \text{and} \quad \sigma^{ion}(E) \xrightarrow[E\to 0]{} \sum_{llL} a_{llL}(1)\,E. \tag{18}$$

Thus in this approximation one must include all the scattered waves up to the threshold.

For comparison, we give the numerical values of the coefficients which characterize the dependence of the ionization cross section on the energy. According to Geltman*, $\sum_{l=0}^{2}\sigma_{llo}^{ion} = 0.022\ \pi a_0^2\,(\text{ev})^{-1}$.

In the Born approximation $\sum_{l=0}^{\infty}\sigma_{llo}^{ion} \approx \sigma_{000}^{ion} - 0.017\ \pi a_0^2\,(\text{ev})^{-1.5}$.

The total cross section in the Born approximation is $0.078\ \pi a_0^2\,(\text{ev})^{-1.5}$.

Experiment[9] gives $0.078\,\pi a_0^2\,(\text{ev})^{-1}$.

Inasmuch as the electron-nucleus forces are Coulomb, Geltman's approximation is, according to Wigner, the more accurate one. Experiment also gives a roughly linear dependence of the ionization cross section on energy. But it should be noted that one cannot simply apply Wigner's results directly to our case, since three particles are formed after ionization and one must take into account the interaction between electrons. For instance, the role of the electron knocked out of the atom is not clear. In Geltman's approximation it is ignored, while in the Born approximation it is assumed that it screens the nucleus completely. Wanier[10], applying classical methods to the study of ionization, found that the cross section varies with the energy to the 1.12689 power.

---

*The result as calculated by Geltman is $0.044\ \pi a_0^2\,(\text{ev})^{-1}$.

It would be desirable to obtain more accurate experimental data on the behavior of the ionization cross section near threshold.

References

1. N.F.Mott & H.S.W.Massey, The Theory of Atomic Collisions, Oxford, 1933. (Cited in Russian trans., 1951.)
2. R.K.Peterkop, Izv. (Bulletin), Latvian SSR Ac. of Sci., No.10, 91 (1959).
3. W.Elsasser, Z.Phys., 45, 522 (1926).
4. R.McCarroll, Proc.Phys.Soc.A, 70, 460 (1957).
5. L.I.Schiff, Quantum Mechanics, N.Y.,1955. (Cited in Russian trans., 1957)
6. E.P.Wigner, Phys.Rev., 73, 1002 (1948).
7. S.Geltman, Ibid., 102, 171 (1956).
8. L.D.Landau & E.M.Lifshits, Kvantovaya mekhanina (Quantum Mechanics), M.-L., 1948.
9. W.Fite & R.Brackmann, Phys.Rev., 112, 1141 (1958).
10. G.Wanier, Ibid., 90, 817 (1953).

EXCITATION CROSS SECTIONS FOR SOME SPECTRUM LINES OF KRYPTON AND XENO

- L.M.Volkova, A.M.Devyatov & A.V.Kuralova

In the present work we determined the excitation cross sections for five lines of krypton and ten lines of xenon. The excitation function curves were plotted by the method of photographic photometry.

The electron gun consisted of an indirectly heated oxide-coated cathode and three electrodes. By appropriate choice of the electrode potentials relative to the cathode, we obtained the optimum operating condition for the electron gun: small variation in the magnitude of the electron current and shape of the electron beam with changes of the potential V_3 on the third anode, which controlled the energy of the exciting electrons. To determine the necessary experimental conditions we first checked the variation in the intensity of the spectrum lines as a function of the electron current at a pressure of $3 \cdot 10^{-3}$ mm Hg at which the electron free path in Kr (14 cm) is much greater than the dimensions of the impact space. The variation was found to be linear up to 1600 μa.

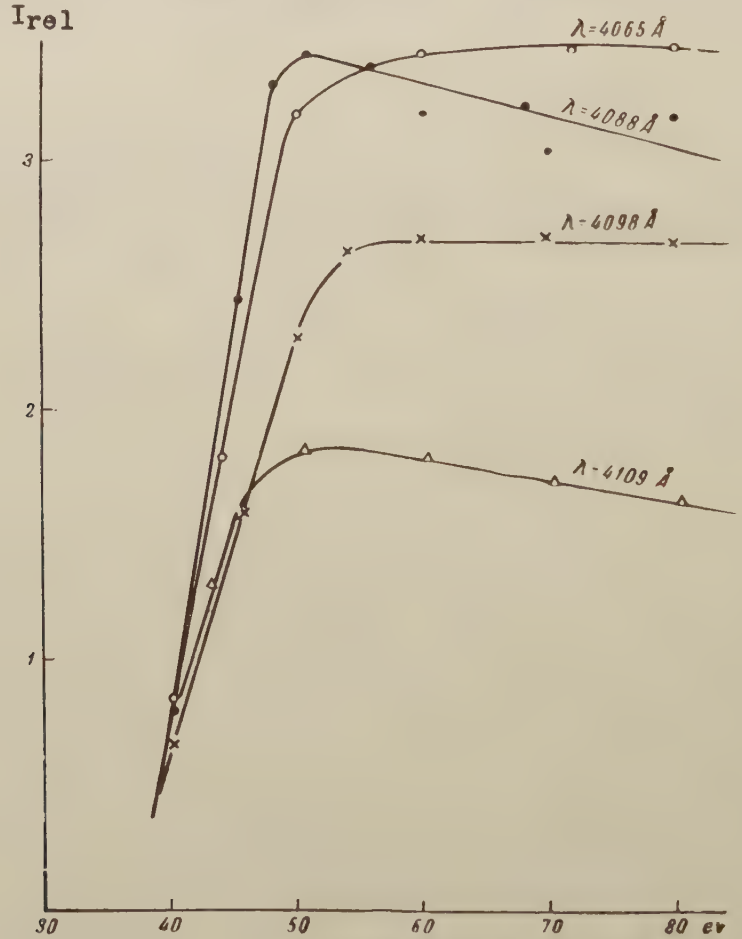

Fig.1. Energy variation of the excitation function for four Kr II lines.

The measurements were carried out with a current of 400 μa. The main measurements for determining the energy dependence of the excitation functions were carried out by the conventional method of recording the spectra at different electron energies; the resultant spectrograms were then processed by the method of photographic photometry. We obtained the excitation functions for a number of lines of krypton and xenon. Part of the data were published in Refs. 3 & 4. Subsequently, we also measured the excitation function of four Kr II lines, which are shown plotted to an arbitrary scale in Fig.1. It must be emphasized that the ordinates of these curves and those reproduced in the other figures are not comparable. Figs.2 & 3 show the excitation function curves for the 4318/19 Å and 4351 Å Kr I lines. The curves for the 4318/19 Å line

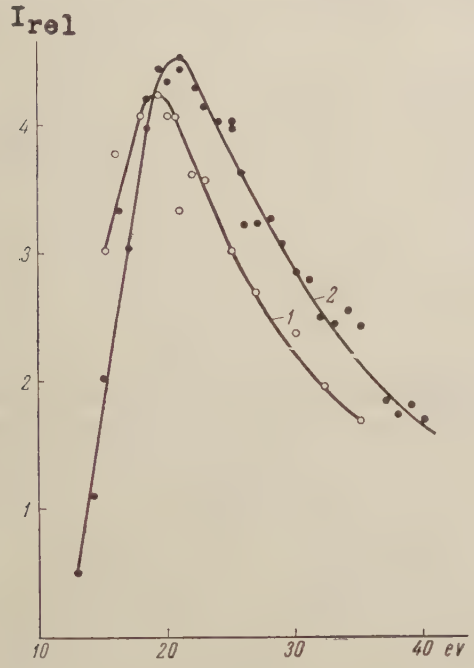

Fig.2

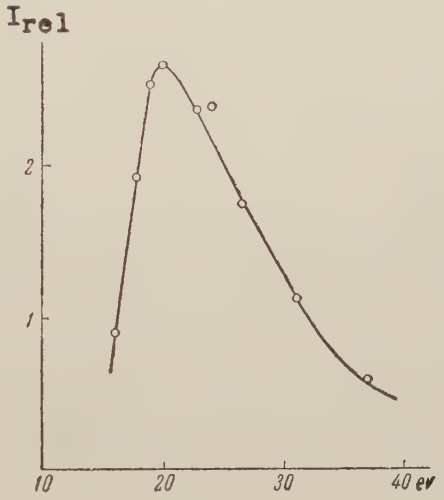

Fig.3

Fig.2. Variation of the excitation function for the Kr I 4318/19 Å line: 1) determined by the usual procedure, 2) in a retarding electric field.
Fig.3. Variation of the excitation function for the Kr I 4351 Å line.

were obtained by the usual method and by the method of a retarding electric field[1,2]. In using the latter method, a retarding field capable of returning all the electrons before they enter the receiver, is applied between the cathode and the electron receiver. Thus the field in the impact space varies from the value of the voltage on the third anode (+50 v) to the retarding voltage (-6 v).

By means of the formulas given in Ref.1 one can determine the electron energy at each point in the electron beam. The essential condition for successful use of this method is that the lines of force of the electric field must be parallel to each other at the axis of the impact gap. To this end the diameter of the last anode and the receiver (37 mm) was made greater than the distance between them (20 mm) and the diameter of the electron beam (4 mm). The sides of the third anode and receiver, bounding the impact space,

were covered with a fine 250 μ mesh screen. Prior to each measurement the electron beam was photographed to determine the electron current density. As will be evident from Fig.2, the curves obtained by the two different methods agree within the limits of the experimental error.

Line		Set value of V_3, v	$q \cdot 10^{20}$, cm^2 at set V_3	$q \cdot 10^{20}$, cm^2 at V_{3max}
Kr	4263,29	20	0,65	0,65
	4273,97	20	1,5	1,5
	4318,55	20	2,53	2,53
	4351,36	20	0,8	0,8
	4463,69	20	1,19	1,19
Xe I	4624,27	60	0,33	1,37
	4671,23	60	0,097	1,16
Xe II	4330,52	60	1,66	2,33
	4414,84	60	1,63	2,37
	4462,19	60	1,73	2,81
	4603,03	60	2,28	3,22
	4615,50	60	0,19	0,28
	4668,49	60	0,37	0,46
	4876,50	60	0,32	0,53
	5044,92	60	0,29	0,37

We also measured the absolute excitation cross sections q_{ik} for the five lines of Kr and the ten lines of Xe, the excitation function curves for which were given in Refs.3 & 4. The absolute cross section values were determined by comparing the intensity of the investigated lines with the intensity of the continuous spectrum of a tungsten ribbon filament lamp of a known brightness temperature. This method of determining absolute cross sections is described in Ref.5. The cross section values for the five lines of Kr and ten lines of Xe are listed in the accompanying table. The uncertainty in our measurements is evaluated as ±30%.

Physics Faculty,
Moscow State University

References

1. S.D.Gvozdover, Teoriya elektronnykh priborov sverkhvysokikh chastot (Theory of superhigh frequency electronic instruments), M., 1956.

2. I.P.Bogdanova, Vestnik, Leningrad State Univ., 18, 16 (1959).

3. A.M.Devyatov & N.A.Kaptsov, Vestnik, Moscow State Univ., 3, 27 (1955).

4. Sin San Guk & A.M.Devyatov, Ibid., 1, 64 (1957).

5. L.M.Volkova, Optika i spektroskopiya, 6, 274 (1959).(Trans. Optics & Spectroscopy.)

ON THE EXCITATION FUNCTIONS OF NITROGEN AND CARBON DIOXIDE MOLECULES IN ENCOUNTERS WITH ELECTRONS

- I.P.Zapesochnyi & S.M.Kishko

Hitherto the excitation functions of the spectrum bands of diatomic molecules, i.e., the variation of the intensity of the molecular bands as a function of the energy of the exciting electrons, have scarcely been studied. The few investigations reported in the literature have been concerned primarily with the bands of molecules in an ionized state (N_2^+ and CO^+). As for normal, nonionized diatomic molecules, the band spectra of which are less intense, measurements have been carried out only for a few bands of nitrogen.[1]

These measurements were performed 25 years ago and the intensity was determined by the photographic technique. Owing to the relatively high nitrogen pressures (~0.1 mm Hg) employed in the experiments, there occurred multiple collisions of the electrons with the nitrogen molecules, as well as other secondary processes, which led to distortion of the true shape of the excitation function curves. As was shown earlier by one of us[3] the true form of the optical excitation function can be obtained only in the absence of multiple collisions, second order impact and step excitations (this will obtain only at low gas pressures and minimal electron current densities) and also provided the electron beam is reasonably monoenergetic.

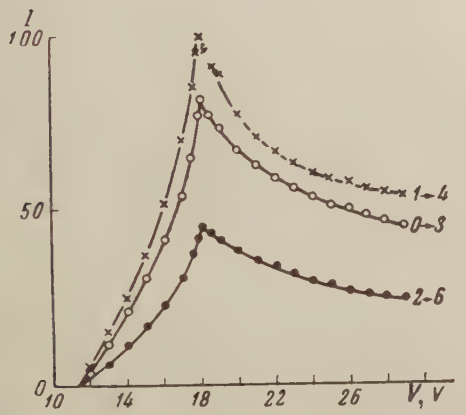

Fig.1. Excitation functions of the bands of the second positive system of N_2.

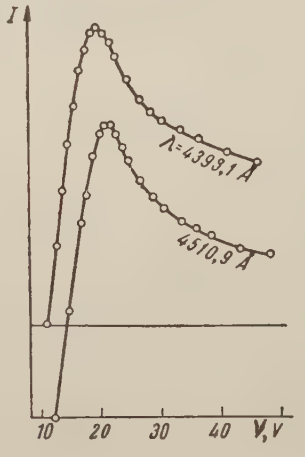

Fig.2. Excitation functions of the bands of the Angström system of CO.

These were the favorable conditions under which we carried out our experiments on measuring the excitation functions of the bands of normal N_2 and CO molecules in the visible region. The band intensities were measured by the photoelectric technique (photomultiplier with a dc amplifier).

The experimental apparatus and procedure were described earlier[3] so that here we shall give only the results of our experiments.

Fig.1 shows the excitation functions of the 0→3, 1→4 and 2→6 bands of the second positive system ($C^3\Pi \rightarrow B^3\Pi$) of molecular nitrogen;

Fig.2 gives the excitation functions of the 0→0 and 1→1 bands of the Angström system ($B^1\Sigma \rightarrow A^1\Sigma$) of carbon monoxide. As will be evident from the figures, the excitation functions of all the investigated bands of N_2 and CO begin immediately above the excitation potential of the upper electronic levels $B^1\Sigma$ (for N_2) and $C^3\Pi$ (for CO), the excitation potentials of which are equal to 11 and 10.8 v, respectively.[4]

The peaks of the excitation function curves for all the bands of the given system coincide (within the limits of error in measuring the accelerating potential, equal to 1 v) and are located at 18 v for N_2 and at 20 v for CO. With further increase of the accelerating potential, the curves fall off, at first rapidly and then very slowly.

The excitation functions of the N_2 bands are characterized by a sharper peak, which lies closer to the excitation potential (~7 ev), while the maximum in the curves for CO is somewhat rounded and is located somewhat further from the excitation potential of the band (~9 ev). The reason for this apparently lies in the different multiplicity of the electron levels of the respective molecules (triplet for N_2 and singlet for CO).

These results were obtained at a pressure of $4.5 \cdot 10^{-3}$ mm Hg for nitrogen and $3 \cdot 10^{-3}$ mm Hg for carbon monoxide and electron densities in the beam less than $1 \cdot 10^{-3}$ amp/cm^2. The velocity spread in the electron beam was about 1 v. It is interesting to note that, as was shown for the case of nitrogen in Ref.3, with increase of the gas pressure the position of the excitation function maximum shifts to the side of lower potentials (owing to onset of multiple collisions).

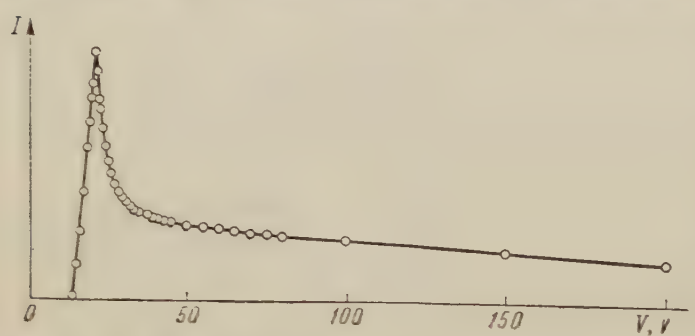

Fig.3. Excitation function of the 0→3 band of the second positive system of N_2.

For example, in measuring the excitation function of the 0→4 band of oxygen even at pressure of 10^{-2} mm Hg there occurs some distortion of the curve, which in this case virtually coincides with the corresponding curve given by Langstroth[1].

Fig.3 shows the excitation function of the 0→3 band of N_2 as measured in a relatively wide range of electron velocities (up to 200 ev). It will be seen that the slow descent of the curve after the peak is essentially monotonic.

It is evident from our experimental results that the excitation functions of the investigated bands of normal N_2 and CO molecules have no noticeable secondary maxima (the relative intensities were measured with an accuracy of 2-5%). In contrast, the excitation functions of the ionic bands of these molecules exhibit fine structure, i.e., have a number of clearly pronounced maxima.[5]

Optics Faculty,
Uzhgorod State University

References

1. G.O.Langstroth, Proc.Roy.Soc.A, 143, 166 (1934).
2. I.P.Zapesochnyi, Vestnik, Leningrad State University, No.11, 67 (1954).
3. S.M.Kishko & M.Yu.Kuchinka, Optika i spektroskopiya, 6, 580 (1959),(Trans. Optics & Spectroscopy.)
4. G.Herzberg, Spectra and Structure of Diatomic Molecules. (Cited in Russian trans.)
5. I.P.Zapesochnyi & S.M.Kishko, Izv.AN SSSR,Ser.fiz., 23, 965 (1959). (Trans. Bulletin 23, 954.)

EXPERIMENTAL INVESTIGATION OF THE EXCITATION FUNCTIONS OF ATOMIC SPECTRUM LINES

- I.P.Bogdanova

A significant role in the emission of glow discharges in rarefied vapors and gases is played by inelastic collisions of free electrons with the atoms of the gas. Hence determination of the cross section for inelastic electron-atom collisions and the variation of the cross section with the electron velocity is of great interest.

At present the most commonly employed procedure for experimental investigation of the optical excitation functions is the double field method of Hanle[1]. This procedure allows of measuring the excitation function of spectrum lines with a relatively high excitation potential. The Hanle procedure is not applicable for measurement of the excitation functions of spectrum lines with an excitation potential of the order of 1.5-3 v.

In order to obtain intense beams of low velocity electrons one can use a retarding field. However, measurement of the excitation function in a retarding field is feasible only if the atom emits at virtually the same point in space where the collision occurred. Simple calculations showed that for most atoms the displacement during the time the atom is in the excited state should be of the order of 10^{-4} cm. So small a displacement can be neglected in measuring the excitation function.

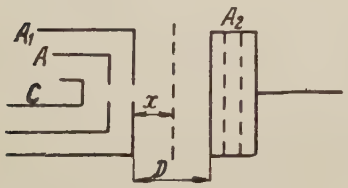

Fig.1. Arrangement of electron gun.

Consider an electron gun with the electrode arrangement shown in Fig.1. The electron beam from the cathode C, after passing through the apertures A and A_1, enters the space between electrodes A_1 and A_2 in which the electron-atom collisions are observed. In the Hanle procedure these electrodes are under equal potentials, and the electrons in the space between A_1 and A_2 move uniformly. Now, if we apply a negative potential to A_2, the electric field between electrodes A_1 and A_2 will slow down the electrons; they will not reach A_2, but will stop in a certain plane between the electrodes and then begin to move back towards A_1. In the presence of a space charge the potential distribution between the electrodes will not be a linear function of the distance between them.

A similar problem was treated by Lukoshkov[2] and Gvozdover[3]. One can apply the results of their calculations to our case; to this end we need only determine the relation between the coordinates of the cross section of the beam and the potential in this cross section.

In the case of a not greatly divergent beam, the potential distribution in the space between electrode A_1 and the plane in which the electrons are turned back must satisfy Poisson's equation

$$\frac{d^2V}{dx^2} = 2en(x). \qquad (1)$$

If the electron current density is known, we have

$$I_0 = en(x)\, v(x) = en(x)\sqrt{\frac{2e}{m}V(x)},$$

where $n(x)$ is the electron concentration, and $v(x)$ is the electron velocity. From the above we obtain

$$n(x) = \frac{I_0}{e\sqrt{\frac{2e}{m}V(x)}}, \tag{2}$$

i.e., in the limit $n(x) \to \infty$ as $V(x) \to 0$. Actually, however, $n(x)$ is finite inasmuch as $\Delta v \neq 0$. For solution of Eq.(1) there are introduced the dimensionless quantities

$$S = x,\ \omega = \sqrt{\frac{V}{V_1}} \quad \text{and} \quad \alpha = \frac{2I_0}{I_1}, \tag{3}$$

where $I_1 = \frac{4}{9}\sqrt{2e/m}\,\frac{V_1^{3/2}}{D^2}$ and V_1 is the potential of electrode A_1.

Then, solving Eq.(1), we obtain the relation between S and ω, i.e., essentially between V and x:

$$S = \frac{4}{3b^2}\left[(b - 2\gamma_0^2)\sqrt{b + \gamma_0^2} - (b\omega - 2\gamma_0^2)\sqrt{b\omega + \gamma_0^2}\right], \tag{4}$$

where $b = \frac{16}{9}\alpha$.

In Eq.(4) γ_0 is the value of the reduced potential in the plane where the electrons are turned back; α can be determined by means of Eq.(3) if the potential on electrode A_1, the distance between A_1 and A_2 and the current density I_0 are known. The current density I_0 must be measured experimentally. The value of γ_0 can be taken from the γ_0 vs α curves given by Gvozdover[3].

Thus, solving Eq.(4) we can determine the electron velocity at different points in the beam, and then Eq.(2) gives us the electron concentration at any cross section of the beam.

It must be borne in mind that the electrode system under consideration is a type of klystron device, so that under certain conditions there can be excited microwave oscillations in the system. Such oscillations will give rise to density pulsation of the beam owing to velocity bunching. This factor must be taken into account in specifying the operating conditions. Generally, intense oscillations appear when a positive potential of ~200-300 v is applied to electrode A_1; consequently, to prevent oscillations it is advisable to apply lower potentials to electrode A_1.

Moreover, measurements of the excitation functions are carried out at pressures of 10^{-4}-10^{-3} mm Hg. The presence of the gas, on the one hand, tends to suppress oscillations, but, on the other hand, makes the problem of finding the function $V(x)$ somewhat ambiguous, inasmuch as the positive ions forming along the path of the electron beam partially compensate the negative space charge of the beam.

In order to check the validity of the above calculations and elucidate the role of any possible interfering factors, we carried out measurements of the known excitation functions of the 5461 and 5791 Å lines of mercury. The measurements were carried out with the following potentials on the electrode:

1) V_{A_1} = +21 v,
V_{A_2} = -4 v,
I_0 = 40 μa,

2) V_{A_1} = +21 v,
V_{A_2} = -8 v,
I_0 = 60 μa,

(I_0 is the current measured in the circuit of electrode A_2 when there is applied to it a potential equal to the potential on electrode A_1). The mercury vapor pressure was 10^{-3} mm Hg.

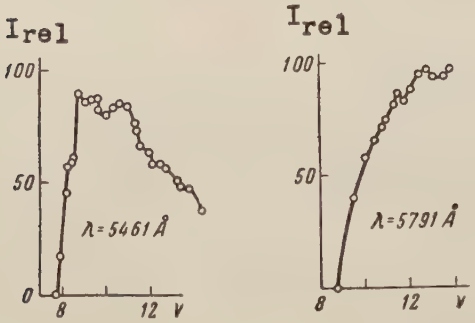

Fig.2. Excitation functions of the 5461 and 5719 Å lines of Hg.

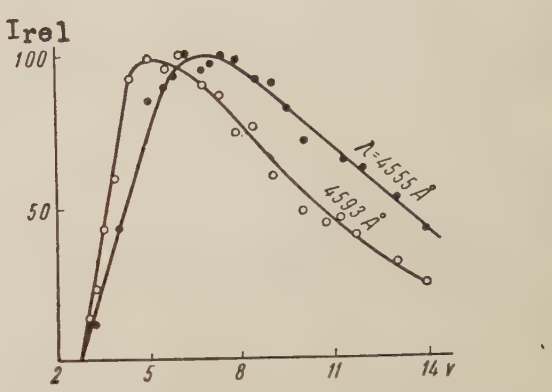

Fig.3. Excitation functions of the components of the second doublet of the principal series of cesium.

The measurement results are shown in Fig.2. Comparison of these results with the data of Frish & Zapesochnyi[4] shows satisfactory agreement. As will be evident from Fig.2, the excitation function of the 5461 Å line exhibits fine structure; the positions of the peaks in the excitation function curve agree within 0.5 v with the positions reported by Frish & Zapesochnyi.

This means that under our experimental conditions the influence of oscillations (if any) was minor and that the positive ions did not significantly compensate the negative space charge of the beam.

Hence, using the retarding field technique, we measured the variation of the excitation functions of the components of the 4555 & 4593 Å doublet in the principal series of cesium ($6^2S_{1/2} - 7^2P_{1/2,3/2}$). The excitation potential of these lines is 2.70 v. The measurements were carried out at a cesium pressure of 10^{-3} mm Hg (110°). At this pressure the doublet is reabsorbed.

The retarding field was realized between electrodes A_1 and A_2 (Fig.1) which were maintained at the following potentials:

1) V_{A_1} = +30 v,
V_{A_2} = -10 v,
I_0 = 100 μa,

2) V_{A_1} = +30 v,
V_{A_2} = -15 v,
I_0 = 70 μa,

3) V_{A_1} = +30 v,
V_{A_2} = -10 v,
I_0 = 70 μa.

The current was regulated by the auxiliary electrode A, located between the cathode C and electrode A_1. The relative intensities were gaged by the photographic procedure. The experimental results are shown in Fig.3. For convenience of comparison, the ordinates have been reduced to the same scale. The accuracy of measurement of

the relative variation in intensity for the doublet is 5%. As will be evident from Fig.3, the deviation of the experimental points from the smooth curve is appreciable, but owing to the uncertainty in the experimental data we were unable to draw a curve through the experimental points.

If one knows the vapor pressure, the dimensions of the vessel and the absolute values of the f numbers (oscillator strength), one can allow for the effect of reabsorption on the intensity ratio of the doublet components. In the present case we allowed for reabsorption on the assumption that all the emitting atoms are concentrated in the path of the beam, and all the absorbing atoms in the remaining part of the vessel. For an electron velocity corresponding to 14 v we obtained the intensity ratio $I_{4555}/I_{4593} = 8 \pm 1$.

It will be seen from Fig.3 that near the excitation threshold the excitation curve of the weaker component rises more steeply than the curve of the stronger component. As a result, obviously, the intensity ratio of the doublet components changes with increasing electron velocity. Thus, for example, at an electron velocity corresponding to 2.9 v the intensity ratio is 2.0; at an electron velocity corresponding to 5.5 v the ratio increases to 4.3 and then to 8 in the region of 14 v.

I desire to express my gratitude to S.E.Frish for his guidance and interest in the work.

References

1. W.Hanle, Z.Phys., 56, 94 (1929).
2. V.S.Lukoshkov, Zhur.eksp.i teor.fiz., 6, 624 (1936).
3. S.D.Gvozdover, Teoriya elektronnykh priborov sverkhvysokikh chastot (Theory of superhigh frequency electronic instruments), M., 1956.
4. S.E.Frish & I.P.Zapesochnyi, Doklady AN SSSR, 95, No.5, 971 (1954); Izv.AN SSSR,Ser.fiz., 19, 5 (1956).(Trans. Bulletin, 19,1.)

EXPERIMENTAL DETERMINATION OF THE CROSS SECTIONS FOR EXCITATION OF THE $2^1S - n^1P$ SERIES LINES OF HELIUM BY ELECTRON IMPACT

- V. E. Yakhontova

As is known, the cross sections for excitation of spectrum lines by electron impact can be determined by the optical procedure.[1] The gas, enclosed in a special tube, is excited by a monoenergetic electron beam, and the intensity of the excited lines is determined spectroscopically. Usually the gas pressure in the tube and the current density are made low enough so that the only source of radiation of the given wavelength is excitation of the atoms by electron collisions and spontaneous transitions. In this case the intensity I_{jk} of the line corresponding to transitions from a level j to another level k is given by the expression

$$I_{jk} = CN \frac{i}{e} Q_{jk} h\nu_{jk} , \qquad (1)$$

where N is the number of atoms per unit volume, e is the electron charge, i is the beam current, Q_{jk} is the effective cross section for excitation of the line and C is a constant dependent on the geometry of the experiment.

Hence having measured the line intensity under conditions where Eq.(1) is valid one can readily calculate the cross section for excitation of the line. In practice the applicability of Eq.(1) is verified by checking whether the variation in the line intensity as a function of the current strength or pressure is linear.

Linear variation of the intensity with the current strength is observed for all the known lines of helium in a rather wide range. Direct proportionality between the intensity and the pressure for most helium lines persists up to a pressure of 0.005 mm Hg and higher. In the case of the $2^1S - n^1P$ series lines, however, some deviation from linearity begins at extremely low pressures: $\sim 10^{-5}$ mm Hg. Measurement of line intensities at so low a pressure is difficult owing to the low level of the intensity. Hence determination of the cross sections for excitation of these lines by the above described procedure is impractical.

This distinctive behavior of the $2^1S - n^1P$ series lines is explained by increase in the population of the n^1P levels owing to absorption of the $1^1S - n^1P$ resonance radiation. As a result of this absorption, the intensity of the line corresponding to the transitions to the unexcited level decreases, while the intensity of the line corresponding to the transition to the 2^1S level increases accordingly. Thus there occurs "transformation" of the resonance radiation to $2^1S - n^1P$ radiation, and the tube in which the excitation occurs becomes a space source, the brightness of which depends on the gas pressure as does the distribution in brightness along the radius of the tube.

Let us see how the intensity of a $2^1S - n^1P$ line changes with increase of pressure. At very low pressures the absorption of resonance radiation is insignificant. Consequently, excitation of the atoms to the n^1P level occurs only by electron impact in the volume of the beam, and the intensity of the line will be given by

Eq.(1). With increase of the pressure, however, the intensity of the line increases more rapidly than according to the linear law. The character of the pressure dependence of the intensity is determined, first, by increase of the total radiation flux and, second, by variation in the brightness distribution of this radiation along the radius of the tube. Beginning with a certain pressure, the $1^1S - n^1P$ radiation will be completely absorbed in the volume of the tube. From this point on the line intensity again becomes proportional to the pressure and is described by a formula similar to Eq.(1) but containing an additional factor taking into account the "transformation" of radiation:

$$I_{jk} = CN \frac{i}{e} \frac{\sum_{l=0}^{j-1} A_{jl}}{A_{jk}} Q_{jk} h\nu_{jk}; \qquad (2)$$

here A_{jl} is the probability for a spontaneous transition from level j to level l. Consequently, for determining the cross section for excitation of a line of the $2^1S - n^1P$ series one can measure the line intensity at a relatively high pressure and calculate the cross section by means of Eq.(2). The pressure must, on the one hand, be sufficiently high to insure complete absorption of the $1^1S - n^1P$ resonance radiation, and, on the other hand, not be so high that the line intensity will be significantly affected by various secondary processes, such as, for example, second order impact and reabsorption.

We determined the cross sections for the excitations of two helium lines, namely, λ = 5016 Å ($2^1S - 3^1P$) and λ = 3965 Å ($2^1S - 4^1P$). The measurements were carried out in the apparatus described earlier[2]. The gas was excited by an electron beam directed along the axis of the cylindrical glass tube. The optical part of the set-up consisted of the excitation tube, a condenser lens and a monochromator. An image of the tube axis (electron beam) was focused by means of the condenser lens in the plane of the entrance slit of the monochromator. The light intensity was measured by an FEU-17 photomultiplier coupled to a dc amplifier. As reference, for determining the absolute intensity values, we used a tungsten filament lamp with a known energy distribution.

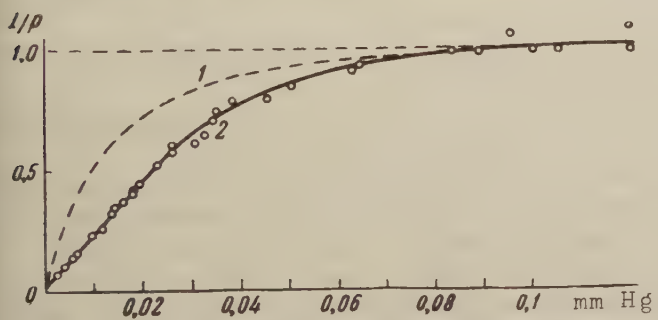

Fig.1. Variation in the intensity of the 5016 Å helium line with pressure: 1) curve plotted according to Eq.(3), 2) experimental curve.

The measurements were carried out at relatively high gas pressure: 0.1 mm Hg. The line excitation cross sections were calculated by means of Eq.(2). In order to determine the pressure beginning with which formula (2) could be considered valid, we measured the variation in the intensity of the lines with pressure.

The experimental results are shown by curves 2 in Figs.1 & 2; it will be apparent that beginning with a pressure of the order of 0.1 mm Hg the experimental curves have a horizontal section.

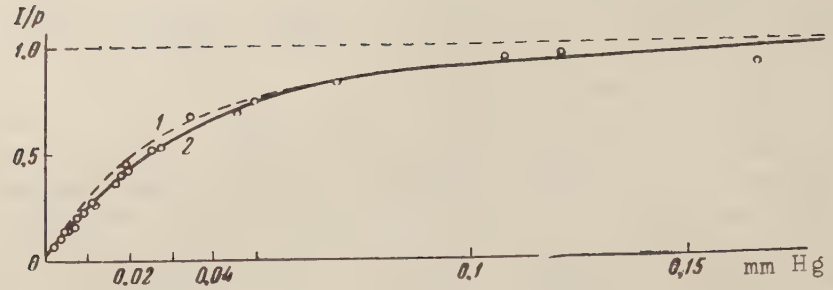

Fig.2. Same as Fig.1 but for the 3964 Å line of He.

Consequently, in this region the intensity is proportional to the pressure, and presumably, the conditions for which Eq.(2) was derived are fulfilled. However, it might be that the presence of the horizontal section in the experimental curves may be explained simply by fortuitous compensation of the increase in line intensity owing to "transformation" of the radiation by decrease in the intensity owing to some secondary processes. Hence we carried out a special investigation to determine how the intensity of the given lines at a pressure of 0.1 mm Hg is affected by second order collisions, step excitation, and reabsorption of the radiation. It was found that these processes have virtually no effect on the intensity of the 5016 Å line and that they have only a weak influence on the intensity of the 3965 Å line: they reduce the intensity by about 5%. This was taken into account in computing the cross section for excitation of the 3965 Å line.

In order to determine whether the $1^1S - n^1P$ radiation was completely absorbed at 0.1 mm Hg, we also carried out an approximate theoretical calculation of the variation in the intensity of the $2^1S - n^1P$ series lines as a function of pressure.[3] As a result there was obtained the following expression for the line intensity:

$$I_{jk} = CN \frac{i}{e} \frac{\sum_{l=0}^{j-1} A_{jl}}{A_{jk}} Q_{jk} h\nu_{jk} \left\{1 - \frac{2(1-\eta)}{(\gamma r_0)^2} \cdot \frac{1 + \gamma r_0 \operatorname{sh} \gamma r_0 - \operatorname{ch} \gamma r_0}{1 + \frac{1-\sqrt{\eta}}{1+\sqrt{\eta}} e^{-2\gamma R}} \times \left[e^{-\gamma H \frac{d_1}{d_2}} + \frac{1-\sqrt{\eta}}{1+\sqrt{\eta}} e^{-\gamma \left(2R - H \frac{d_1}{d_2}\right)} \right] \right\}. \quad (3)$$

Here R is the radius of the experimental tube, r_0 is the radius of the electron beam, $\eta = \frac{A_1}{A_1 + A_2}$, A_1 is the probability for $2^1S - n^1P$ transitions, A_2 is the probability for $1^1S - n^1P$ transitions, $\gamma = 2x\sqrt{\eta}$, x is the absorption coefficient of the medium, $2H$ is the height of the monochromator entrance slit, d_1 is the distance from the source to the condenser lens, and d_2 is the distance from the condenser lens to the plane of the slit. Curves 1 in Figs.1 & 2 were plotted for the 5016 and 3965 Å lines according to Eq.(3). It will be evident from the figures that although the theoretical curves lie somewhat higher than the experimental ones, they are similar in character. Some divergence between the theoretical and experimental curves may be attributed to the necessarily approximate nature of the method.

In determining the excitation cross sections we assumed (on the basis of analysis of the shape of the experimental curves) that at a pressure of 0.1 mm Hg the conditions for which Eq.(2) is valid were

fulfilled. This means that I/p (Figs.1 & 2) attained its maximum value. Our theoretical curves tend to substantiate this assumption. It is evident from the theoretical curves that at a pressure of 0.1 mm Hg the value of I/p for the 5016 Å line does attain its maximum (saturation) value, while for the 3965 Å line, I/p differs from the maximum value by 9%. Hence in calculating the cross section for the 3965 Å line we introduced the correction factor of 0.91 into Eq.(2).

As a result of our measurements and calculations we obtained the following values for the excitation cross sections (corresponding to an electron energy of 100 ev, i.e., the excitation maximum): $Q_{jk} = 3.5 \cdot 10^{-20}$ cm^2 for the 5016 Å line, and $Q_{jk} = 1.5 \cdot 10^{-20}$ cm^2 for the 3965 Å line. We note that Lees[4], who measured the excitation cross sections for the same lines without taking absorption into account, obtained $100 \cdot 10^{-20}$ cm^2 for the 5016 Å line, and $34 \cdot 10^{-20}$ cm^2 for the 3965 Å line.

References

1. H.S.W.Massey & E.H.S.Burhop, Electronic and Ionic Impact Phenomena, Oxford, 1952. (Cited in Russian trans.)

2. V.E.Yakhontova, Vestnik, Leningrad State University, No.10, 27 (1959).

3. V.E.Yakhontova & M.I.Kliot-Dashinskii, Optika i spektroskopiya, 7, 446 (1959). (Trans. Optics & Spectroscopy.)

4. J.Lees, Proc.Roy.Soc.A 137, 173 (1932).

RESONANCE CHARGE EXCHANGE OF ALKALI METAL IONS AND ATOMS

- A.M.Bukhteev & Yu.F.Bydin

Introduction

Investigation of resonance charge exchange of alkali metal ions and atoms in slow collisions is of interest both from the practical standpoint and as regards the theory of interaction of atomic particles.

Firsov[1] carried out theoretical calculations of the resonance charge exchange cross section for elements in which the normal state of the atom and ion is the S state. Inasmuch as alkali metals satisfy this condition, measurement of the charge exchange cross section for alkali metals and of the variation of the cross section as a function of the ion velocity provides a means for verifying Firsov's theory.

Recently, in connection with development of cesium diodes (devices in which heat is converted directly into electricity) and the use in these diodes of cesium ions for compensation of space charge, the question of the magnitude of the charge exchange cross section and its energy dependence for cesium and other alkali metals has become particularly important.

Earlier[2] we measured the resonance charge exchange cross section for potassium.

The present work was concerned with measurements of the effective charge exchange cross sections for Cs, Rb, Na and K in the ion energy range from 150 to 2100 ev. The measurements were carried out by the method of extracting slow positive ions forming as a result of charge exchange in a chamber filled with the vapor of the investigated alkali metal. The data on the vapor pressure of potassium, necessary for determining the resonance charge exchange cross section, were taken from Ditchburn & Gilmour[3]. Inasmuch as the data in the literature on the vapor pressure of Cs, Rb and Na are characterized by an appreciable divergence, in determining the charge exchange cross section for these metals we used an indirect method utilizing the results obtained for potassium (see below).

Apparatus and Procedure

The positive alkali metal ions were obtained from a thermionic source 1 (Fig.1), which consisted of a nickel plate 2 heated by the radiation from a tungsten spiral; the nickel plate was coated with an aluminosilicate mixture formulated according to Eremeev[4].

Mass spectrometric analysis showed that such a source yields primarily ions of the alkali metal, the carbonate of which was used in preparing the aluminosilicate mixture. The percentage of ions of other alkali metals in the ion beam varied, depending on the purity of the initial materials, from 0.3 to 7%.

The ions accelerated by the field of aperture 3, were focused by means of the system of electrodes 4 and, passing through the collimator 5 with a 0.8 mm diameter opening, entered the charge exchange chamber 6. The charge exchange chamber (Fig.2) was made in the form

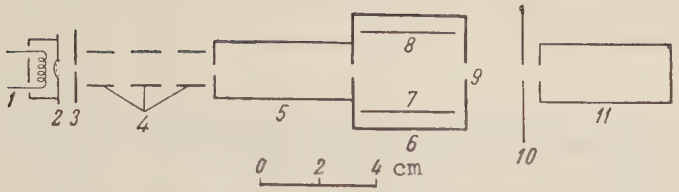

Fig.1. Diagram of apparatus: 1) thermionic source, 2) nickel plate coated with aluminosilicate mixture containing the carbonate of the investigated alkali metal, 3) accelerating aperture, 4) system of focusing electrodes, 5) collimator, 6) charge exchange chamber, 7 & 8) electrodes drawing out the slow ions, 9) exit aperture in the charge exchange chamber, 10) aperture for blocking secondary emission from the Faraday cup, 11) Faraday cup.

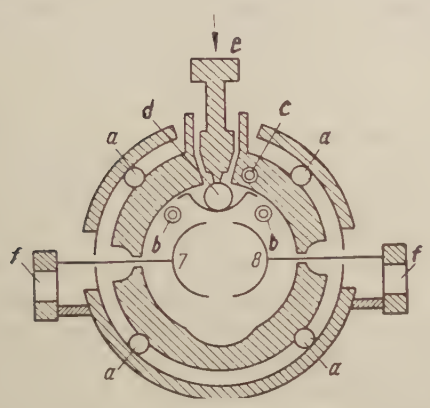

Fig.2. Charge exchange chamber: a) porcelain insulators, b & c) tungsten heater spirals, d) glass ampoule, e) striker for crushing ampoule, f) quarts insulators supporting electrodes 7 and 8.

of a massive (to enhance the thermal inertia) copper cylinder. The porcelain insulators a provide for thermal and electric insulation of the chamber from the rest of the apparatus. The chamber and the electrodes 7 & 8 (Figs.1 & 2) were heated by the radiation from two tungsten spirals b (Fig.2). During the actual intervals of measurement these spirals were switched off and the requisite temperature was maintained in the chamber by means of the auxiliary heater spiral c. The temperature in the chamber was measured to within $\pm 0.3^{\circ}$ by a resistance thermometer, mounted in the chamber wall. In each case the temperature maintained in the chamber was such as to insure a vapor pressure of $(4\text{-}7)\cdot 10^{-5}$ mm Hg of the given alkali metal.

The electrodes 7 & 8 (Figs.1 & 2), which served to collect the slow ions, were mounted at the ends of molybdenum rods extending out to the quartz insulators f outside the chamber. One of these electrodes, which served as the measuring electrode, was connected to an EMU-3 electrometer with a sensitivity of $6\cdot 10^{-13}$ amp per scale division.

The chamber housing in all experiments was maintained at a potential of +18 v relative to the ground; this was necessary in order to block secondary emission from the chamber walls and prevent drift of the slow positive ions towards the chamber housing.

Positive ions that had not undergone charge exchange and fast neutral ions forming in the chamber left the chamber through the opening 9 (Fig.1) and entered the Faraday cup 11, the current I to which was measured by means of a vacuum tube electrometer.

After a number of control tests, we switched on the primary beam, and applying a positive potential to electrode 8, directed the slow

ions onto electrode 7. The ion current I_S attained saturation at an accelerating potential difference equal to 4-6 v, and completely disappeared upon application of a retarding potential difference of the same magnitude.

The ratio $I_S/(I + I_S)$ within the limits of the measurement error did not depend on the magnitude of the primary current and varied linearly with the alkali metal vapor pressure, which was evidence that the collisions were primarily single encounters.

We evaluated the charging cross section Q by means of the formula

$$Q = -\frac{\ln\left(1 - \frac{I_S}{I + I_S}\right)}{nx},$$

where n is the number of alkali metal atoms per 1 cm^3, and x is the path length in the alkali metal vapor; this was assumed to be equal to the length of the charge exchange chamber. As noted above, for determining n we used the data of Ditchburn & Gilmour[3] on the temperature dependence of the vapor pressure of potassium.

In this manner we measured the charge exchange cross section Q and its energy dependence for potassium.

The reliability of cross section determinations for the other alkali metals by the same procedure would be doubtful. There is appreciable divergence in the data in the literature on the vapor pressure of Cs, Rb and Na at different temperatures.[5] Moreover, use of different methods of measuring the vapor pressure and its temperature dependence for different alkali metals could lead to serious and undeterminable errors. All this could distort the true charge exchange cross section values for the alkali metals. Hence we carried out an indirect comparison of the cross sections Q for Cs, Rb, Na and K by measuring the vapor pressures of these metals on the basis of their surface ionization on oxidized tungsten.

It is known from the data in the literature[6] that the coefficient of surface ionization of Cs, Rb and K on oxidized tungsten is 100%; there are also data[6] indicating that it is close to 100% for Na

A special assembly consisting of two semicylinders with slits and a tungsten filament strung along their axis was mounted opposite a slit cut in the charge exchange chamber. After cleansing and purification of the filament by heating, the filament was oxidized under appropriate conditions and the assembly was ready for measurements.

By means of this assembly we recorded the variation of the surface ionization current i as a function of the filament heat; these dependences enabled us to choose for each alkali metal the "working point" on the filament temperature scale.

We then determined the variation of the ratio $I_S/(I + I_S)$ with the surface ionization current i with changes in the chamber temperature at a constant value of the filament heat corresponding to the chosen working point. These dependences, as might have been expected when plotted proved to be straight lines passing through the origin and enabled us to determine the cross section ratios for Cs, Rb, Na and K at a certain energy.

Thus, if one makes use of the relationship

$$i \approx n\sqrt{\frac{kT}{2\pi M}},$$

following from the kinetic theory of gases, one can readily obtain the following formula for the charge exchange cross section ratio of any two alkali metals:

$$\frac{Q_l}{Q_m} = \frac{\ln\left(1-\frac{I_S}{I+I_S}\right)_l}{\ln\left(1-\frac{I_S}{I+I_S}\right)_m} \cdot \sqrt{\frac{M_m T_l}{M_l T_m}},$$

where the indices l and m designate the respective alkali metals, M is the mass of an atom of the given alkali metal, and T is the temperature of the charge exchange chamber corresponding to a certain value (calculated) of the surface ionization current i.

Thus from the ratios obtained and the measured cross section for potassium we evaluated the cross sections for Cs, Rb and Na at the given energy. In order to obtain the energy dependences of the charge exchange cross sections for Cs, Rb and Na, we recorded the energy dependences of $I_S/(I + I_S)$ for these elements at a constant surface ionization current and a constant filament heat corresponding to the chosen working point.

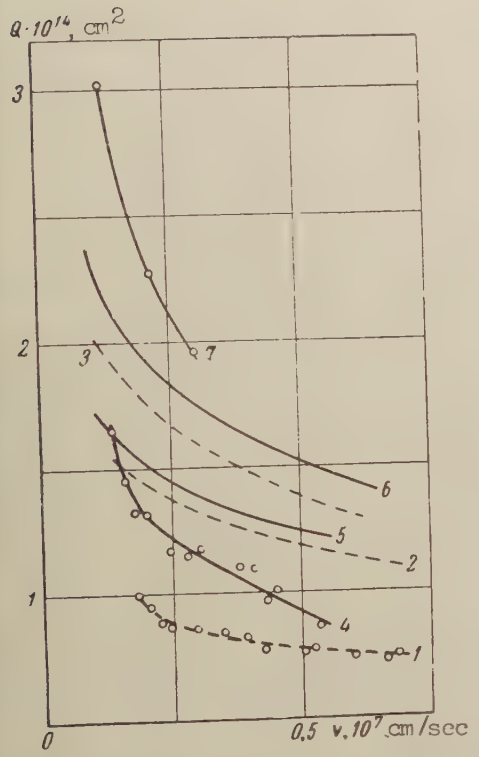

It will be evident that the reliability of our results depends mainly on whether the coefficient of surface ionization on oxidized tungsten is actually 100% for all the investigated alkali metals under our experimental conditions. This is undoubtedly so for Cs and Rd; it is possible that for K also the coefficient of surface ionization under the conditions of our experiment is nearly 100%. For Na, however, the coefficient may differ substantially from 100%. Hence the data for Na may be doubtful, and the cross section values obtained for Na may comprise an appreciable systematic error.

A certain systematic error may be comprised in all the data for Cs, Rb and Na inasmuch as the resonance charge exchange cross sections for these alkali metals were determined in terms of the cross section for K. In our evaluation the mean random error in determining the cross section for resonance charging of Cs, Rb, Na and K in the range of high energies did not exceed 10%, and with decrease of energy increased to about 15%.

Fig.3. Variation of the charge exchange cross section Q with the ion velocity for Cs (solid curves) and Rb (dashed curves): 1 & 4) experimental curves, 2 & 5) theoretical curves calculated according to the formula of Demkov[7], 3 & 6) theoretical curves calculated according to the formula of Firsov[1], 7) experimental curves of Kushnir[8] for Cs^+.

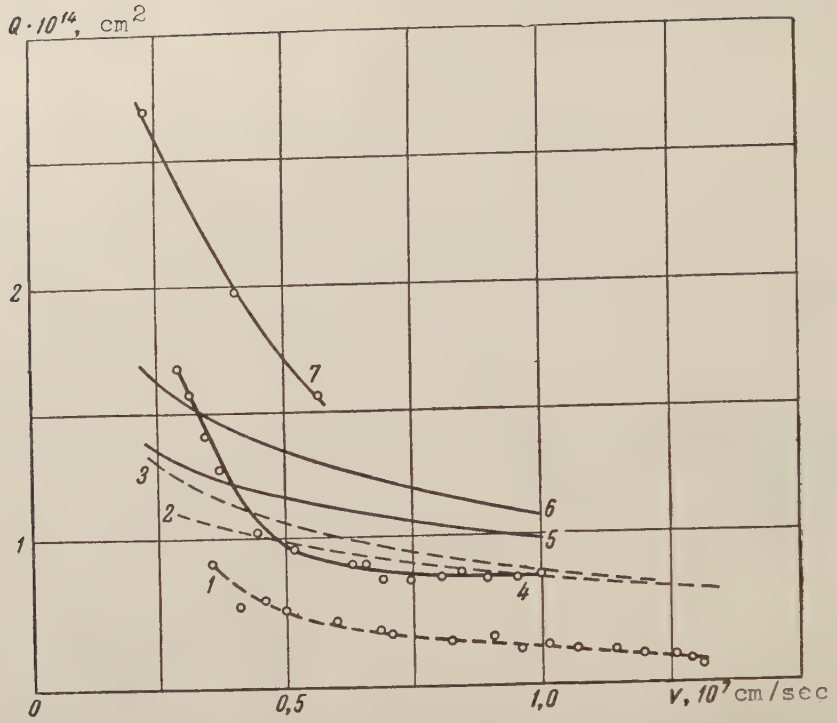

Fig.4. Variation of Q with the ion velocity for K (solid curves) and Na (dashed curves). Curve designation same as in Fig.3. As in Fig.3 the vertical scale is uniform (the figure 0 pertains only to the horizontal scale).

Results and Comparison with Theory

The experimental results are shown in the form of curves giving the variation of the cross section Q as a function of the ion velocity v in Figs.3 & 4. In these figures we also give the curves calculated according to the formulas of Firsov[1] (curves 3 & 6) and Demkov[7] (curves 2 & 5). Curves 7 in both figures were plotted on the basis of the experimental data of Kushnir[8] for resonance charging of Cs^+ (Fig.3) and K^+ (Fig.4).

It will be evident from the figures that in the investigated velocity range the values of the cross section Q for different alkali metals differ little for any given velocity: the difference is only 40-50% in the range of low velocities in our measurement interval and 15-25% in the range of high velocities.

The cross section Q for all the alkali metals monotonically decreases with increasing velocity, the rate of decrease in the range of low velocities being somewhat more rapid than in the range of high velocities in the investigated velocity range.

The theoretical Q vs v curves in all cases lie above the corresponding experimental curves. In the range of low velocities within our experimental velocity interval for all the alkali metals there is observed a more rapid increase of Q with decrease of v than is pre-

dicted by theory. In the range of high velocities, the slope of the theoretical Q vs v curves generally agrees with the slope of the experimental curves, but the theoretical values of Q are 1.5-1.2 times higher than the experimental values.

The experimental data of Kushnir[8] for Cs and K ions in the velocity range common to our experiments and those of Kushnir yield cross section values 50-60% higher than ours.

In view of the lack of reliable data on the temperature dependence of the vapor pressure of Cs, Rb, Na and K and the difficulty of measuring the vapor pressure of these metals in the range from 10^{-5} to 10^{-4} mm Hg, the agreement between theory and experiment may be regarded as acceptable, except for the velocity region where experiment yields a more rapid increase of Q with decrease of ion velocity than is indicated by theory.

We desire to express our deep gratitude to V.M.Dukel'skii for his interest in the work and valuable advice.

Physical-Technical Institute,
Academy of Sciences of the USSR

References

1. O.B.Firsov, Zhur.eksp.i teor.fiz., 21, 1001 (1951).
2. Yu.F.Bydin & A.M.Bukhteev, Zhur.tekh.fiz., 29, 12 (1959). (Trans. Soviet Physics – Technical Physics.)
3. R.W.Ditchburn & J.S.Gilmour, Revs.Mod.Phys., 13, 310 (1941).
4. M.A.Eremeev & A.Kh.Ash, Zhur.tekh.fiz., 23, 435 (1953).
5. D.A.Jackson, Proc.Roy.Soc., 143, 455 (1934).
6. S.Datz & E.H.Taylor, J.Chem.Phys., 25, 3, 399 (1956).
7. Yu.N.Demkov, Uch.zap. (Scientific notes), Leningrad State University, No.146, Issue 8, 74 (1952).
8. R.M.Kushnir, Ukr.fiz.zhur. (Ukrainian Physics Journal), 3, 788 (1958).

RESONANCE CHARGE EXCHANGE OF POSITIVE ALKALI METAL IONS

- D.V.Chkuaseli, U.D.Nikoleishvili & A.I.Guldamashvili

Investigation of the interaction of fast ions with gas atoms is of great interest not only as regards the theory of interaction of charged particles with the atoms of a gas, but also for understanding the properties of plasma and processes occurring in particle accelerators, electromagnetic separators, mass spectrometers and similar equipment.

Of all the possible forms of interaction, the most probable process of resonance charge exchange is of particular interest.[1,2]

We developed a new procedure, different from the technique used earlier[3-5], for the purpose of measuring the resonance charge exchang cross section for positive singly charged ions of alkali metals. The difference between our procedure and the earlier techniques is that w used a molecular beam of the investigated substance as a target instead of the usual collision chamber with the investigated gas. This procedure allows of making rather accurate absolute determinations.

Apparatus

The experiments on charge exchange of positive singly charged K, Cs and Rb atoms were carried out in a small electromagnetic separator.[6] The chamber with the ion source and the receiving-measuring device is diagramed in Fig.1.

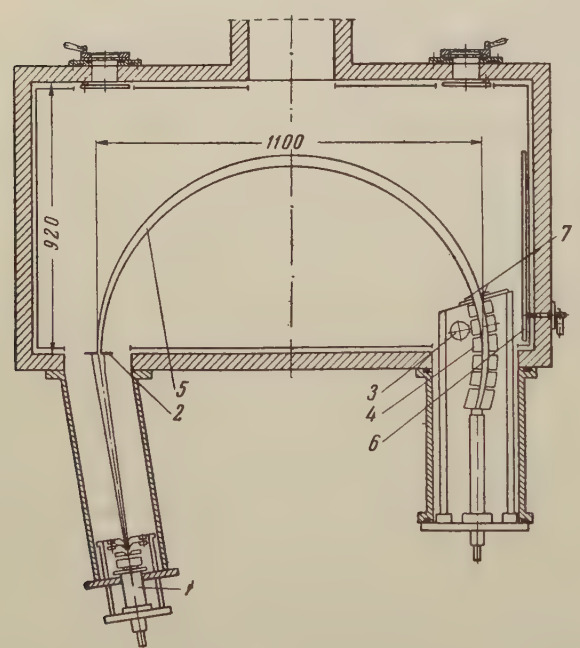

Fig.1. Chamber with ion source and receiving-measuring device: 1) ion source, 2) entrance aperture, 3) molecular source, 4) receiving-measuring device, 5) ion beam, 6) cooled plate (for freezing out the alkali metal vapor), 7) adjustable diaphragm.

For obtaining the positive alkal metal ions we used an ion source ut lizing surface ionization. The ion source is located outside the magne tic field. The beam is shaped and defined by means of an ion optical system and an entrance aperture, an under the influence of the magnetic field is focused at an angle of 180 The mean beam trajectory radius is 555 mm.

The monoenergetic ion beam of th most abundant isotope of the select ed alkali metal passes through the adjustable diaphragm with a 4 x 20 mm slit and enters the receiving-measuring device, which is located in the magnetic field of the separa tor. This movable diaphragm, the position of which can be adjusted

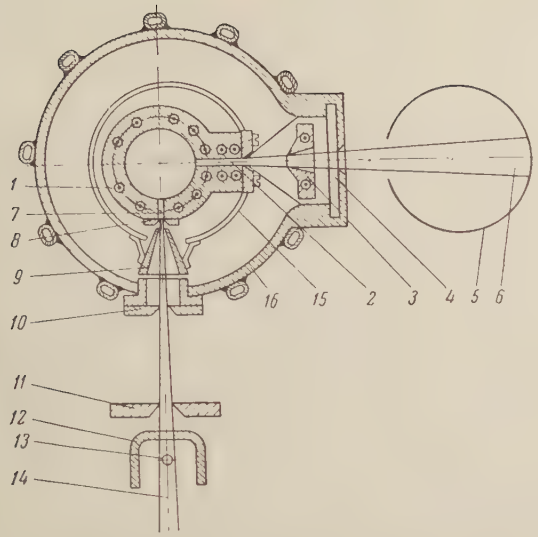

Fig.2. Molecular source: 1) furnace, 2) main channel, 3) hot aperture, 4) shutter, 5) cylinder trap, 6) main beam, 7) auxiliary channel, 8-11) system of defining apertures and baffles, 12) anode, 13) ionizer, 14) auxiliary beam, 15) heat shield, 16) cooled housing.

from outside the vacuum chamber, also serves as the "sighting" target for adjusting the instrument. Behind the diaphragm there are five pairs of plane parallel plates electrically insulated from each other. The second pair of plates is used as the measuring pair, the other are shielding plates.

Opposite the second pair of plates, there is a twin beam molecular source with a monitor (Fig.2).

The principal channel of rectangular shape (0.42 x 30 x 12 mm) with a system of defining plates, baffles and aperture serves for obtaining the main molecular beam, i.e., the target bombarded by the ion beam.

The second channel, oriented at an angle of 90° relative to the main channel, and a system of adjustable apertures, the positions of which are check by a cathetometer, is intended for the auxiliary molecular beam.

The intensity of the auxiliary molecular beam is measured by a monitor by the method of surface ionization. The intensity of the main molecular target beam is measured by the method of weighing. This is accomplished by a special sorption scale mounted on a separate support in the vacuum. The sorption scale consists of a helix of fine quartz filament from which a trap is suspended. The main molecular beam condenses in this trap, which is a cylindrical cup made of copper foil. The deflection of the scale under the weight of the condensed molecular beam material is measured by a KM-1 type cathetometer. The mean sensitivity of the scale is $3 \cdot 10^{-7}$ g. Back-scattering of the atoms from the trap was taken into account in evaluating the beam intensity.

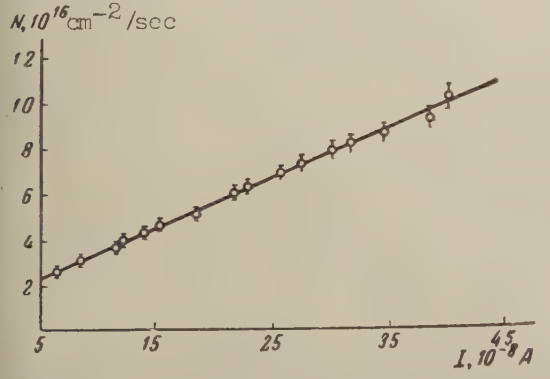

Fig.3. Variation of the intensity N of the molecular beam with the monitor current I.

The intensities of the main and auxiliary molecular beams were measured simultaneously. As a result there were obtained calibration curves plotted in terms of the intensity N of the main molecular target beam against the monitor current I.

During the actual measurements of the charge exchange cross section the values of the intensity of the main molecular target beam were determined from the monitor current by means of the calibration curves, inasmuch as the set-up precludes direct weighing during the charge exchange experiments.

Fig.3 shows a typical calibration curve for cesium. Similar curves were obtained for potassium and rubidium. The reproducibility from experiment to experiment remained within ±10% for potassium and ±6% for rubidium and cesium.

As noted, the calibrated molecular beam is used as the target. The molecular and ion beams intersect at a right angle in the space between the second pair of plates so that the horizontal planes of symmetry of the beams and the system of plates coincide.

The primary ion beam current was measured by a 100 mm deep Faraday cup. Appropriate measures were taken to prevent emergence of secondary electrons and negative ions from the Faraday cup. There were installed shielding plates between which there was applied a transverse electric field symmetrical relative to the earth and the ion beam. Thus the Faraday cup circuit allowed of measuring the true ion beam.

Measurements of the Charge Exchange Cross Section

For the purpose of determining the true geometry of the receiving-measuring device we photographed the trajectories of the molecular, ion and fast atom beams for the case of resonance charge exchange of magnesium (Fig.4).

Fig.4. Beam trajectories: 1) ion beam, 2) molecular beam, 3) fast atoms resulting from charge exchange interaction, 4) molecular source.

As will be evident from Fig.4, the divergence between the ion beam and the trajectory of the fast ions resulting from charge exchange in the deflection range (60 mm) is sufficient for separate detection of these particles. Hence our procedure allows of determining the charge exchange cross section both by detecting the fast neutral atoms and by the potential method. It should be noted, that in addition to the charge exchange cross section, this procedure allows of measuring the stripping cross section.

In the present experiment, however, the charge exchange cross section for alkali metal ions was measured by the potential procedure.[2-5]

In measuring the charge exchange cross section it was assumed that in the ion energy range from 5 to 30 kev the stripping cross section is much smaller than the charge exchange cross section hence no special measures for measuring the stripping cross section were taken.

The geometry of the receiving-measuring device precludes detection of ions scattered at angles smaller than $\pm 45^{\circ}$. However, as is known from the angular distribution of scattered ions[1,2], the scattering at such small angles is virtually zero.

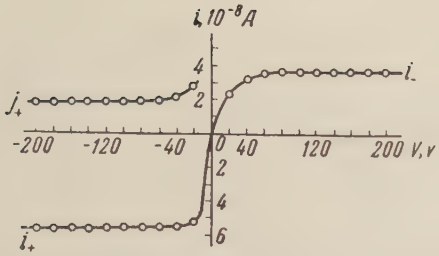

Fig.5

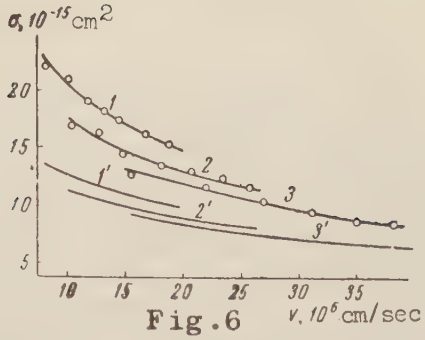

Fig.6

Fig.5. Current-voltage characteristic for the measuring plates.

Fig.6. Variation of the resonance charge exchange cross section with the primary ion velocity: 1, 2 & 3 - experimental curves for cesium, rubidium and potassium, respectively; 1', 2' & 3' - corresponding theoretical curves calculated according to the formula of Firsov[7].

Thus the production of slow ions and electrons as a result of interaction of fast singly charged ions with gas atoms is due primarily to ionization and charge exchange processes.

The number of slow ions and electrons formed as a result of ionization of the gas ions is the same, and hence their currents compensate and cancel each other. Consequently, the charge exchange cross section is given by the formula

$$\sigma_{ce} = \frac{j^+ v}{I^+ N l},$$

where j^+ is the difference between the absolute values of the positive and negative saturation currents as taken off the current-voltage characteristic (see Fig.5), I^+ is the primary ion current, N is the intensity of the molecular beam, v is its mean linear velocity, and l is the path length of the ion beam in the molecular beam.

The results of measurement of the cross section for resonance charge exchange of positive singly charged cesium, rubidium and potassium ions in the primary ion energy range from 5 to 30 kev are given in Fig.6. In the same figure we give the theoretical curves calculated by means of the formula of Firsov[7]. In order not to encumber the figure we do not show the curves calculated by means of Demkov's formula[8]. As will be evident from Fig.6, the charge exchange cross section monotonically decreases with increase of the primary ion velocity. The cross section also decreases in going to atoms with a higher ionization potential.

On the average, the experimental resonance charge exchange cross section values are one and a half times higher than the corresponding theoretical values.

The reproducibility of the experimental results lies within ±15% for potassium and ±10% for rubidium and cesium. Accordingly, these are the values of the mean measurement error. This error is due primarily to the uncertainty in determining the intensity of the molecular beam.

References

1. L.A.Sena, Stolknoveniya elektronov i ionov s atomami gaza (Collisions of electrons and ions with gas atoms), M.-L., 1948.
2. H.S.W.Massey & E.H.S.Burhop, Electronic and Ionic Impact Phenomena, Oxford, 1952, (Cited in Russian trans.)
3. Kenne, Phil.Mag., 40, 269 (1949).
4. Hasted, Proc.Roy.Soc. A205, 421 (1951).
5. N.V.Fedorenko, Zhur.tekh.fiz., 24, 2113 (1954).
6. V.M.Gusev, D.V.Chkuaseli & M.I.Guseva, Atomnaya energiya, 9, 215 (1957). (Trans. Soviet Journal of Atomic Energy.)
7. O.B.Firsov, Zhur.eksp.i teor.fiz., 27, 1001 (1951).
8. Yu.N.Demkov, Uch.zap. (Scientific notes), Leningrad State University, No.146, Issue 8, 74 (1952).

DISSOCIATION OF LARGE MOLECULES UNDER ELECTRON IMPACT

- M.V.Gur'ev, M.V.Tikhomirov & N.N.Tunitskii

This contribution is concerned with the interaction of electrons with large molecules in the general case. Commonly, the effect of electron impact on organic molecules is investigated by means of a mass spectrometer. As a result of ionization and dissociation under electron impact there is formed a large number of diverse ions; these ionic fragments comprise the so-called mass spectrum of the electron bombarded substance.

The design of conventional mass spectrometers is such that a time of the order of 10^{-6} sec elapses between the formation of the ions and the final shaping of the beam. Only a small fraction of the ions (up to 0.5%) can form during a time of this order of magnitude. The initial ions in such dissociations are usually called metastable.

There have been numerous investigations of the mass spectra of organic substances under electron bombardment.[1] From an analysis of the results it may be inferred that the most probable fragments contain 3-4 hydrogen ions regardless of the structure of the molecule (in the absence of double bonds) and of its composition (provided the number of substituent atoms replacing the hydrogens and carbons in the hydrocarbon skeleton is not too great).

In the case of the relatively simple normal (unbranched) paraffins we find that their mass spectra are very similar, while above C_{16} they are virtually identical[2] except for molecular ions, the fraction of which is small and decreases exponentially with increase in the size of the molecule[3]. By way of illustration the mass spectrum of n-tetracosane ($C_{24}H_{50}$) is reproduced in the accompanying figure.

It is usually assumed that as a result of electron impact there forms a molecular ion and that the excitation energy received by it is distributed over all its degrees of freedom until there is concentrated at some particular bond a sufficient energy to rupture it, i.e., to produce dissociation. Thus it is assumed that the molecular ion as a whole is involved in the dissociation process. Rosenstock et al[4] made an attempt to calculate the probabilities for different dissociation processes on the basis of this assumption by means of the theory of absolute reaction rates. As was recently shown by Friedman et al[5], the mass spectra at low electron energies (1-2 ev above the ionization potential of the molecule) cannot be even qualitatively explained on this basis. Our tentative calculations[6] showed that at the usual electron energies (~70 ev), large molecules (C_{44}) theoretically should not dissociate under electron impact, although experiment shows that they actually do.

All these discrepancies are obviated if we hypothesize that the energy brought in by the electron does not have time to be distributed over the entire molecule prior to its dissociation. This means that in the processes accompanying molecular dissociation there is excited only a limited number of vibrational degrees of freedom and that the dissociation occurs in the immediate region of excitation, i.e., that dissociation of large molecules is a localized effect.

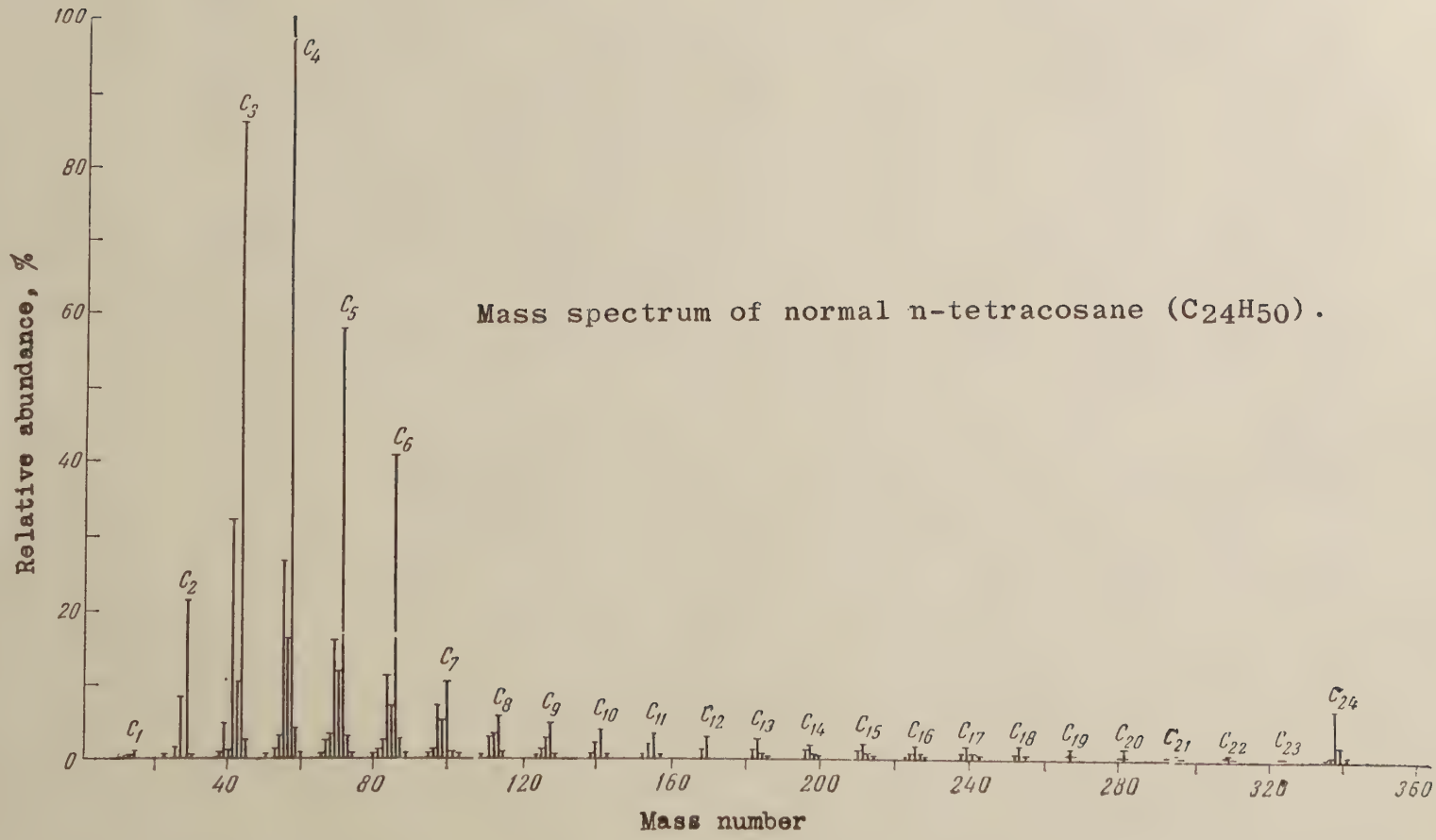

Mass spectrum of normal n-tetracosane ($C_{24}H_{50}$).

The proposed hypothesis is susceptible of experimental verification. Thus assuming that the electron can with equal probability "hit" any part of the molecule and the excitation energy brought in by the electron is distributed only within a limited region, one may obviously expect this part of the molecule to "drop out" in the form of an ionic fragment. This means that fragment ions must form with approximately equal probability from any part of the molecule. Our experiments with a number of substances, for example, with unbranched C_9H_{20} molecules tagged in the center with C^{13} showed that the principal fragments are $C_2H_5^+$, $C_3H_7^+$ and $C_4H_9^+$ ions and that the C^{13} content in these ions is very close to that calculated for equally probable formation of these ions from any part of the molecule.[7] For example, 46% of the $C_3H_7^+$ ions contain a C^{13} atom.

In the process of formation from the central parts of the molecule these atoms apparently capture a hydrogen atom from the other parts of the molecule. As analysis of the data[8] on the appearance potential for $C_nH_{2n+1}^+$ ions shows, transition of a hydrogen atom from one ionic fragment to another leads to appreciable compensation of the excitation energy necessary for rupture of a second C—C bond.

It is interesting to note that this mechanism of formation of the principal ionic fragments apparently operates in the entire investigated energy interval from 1000 ev to an energy 1-2 ev above the appearance potential for the corresponding ion.*

In cases when there occurs rupture not only of a C—C but also of a C—H bond the fragment ions must also, according to our hypothesis, form from "pieces" of the molecule. As was found earlier, for methane and ethane the isotope effect of detachment of hydrogen and deuterium atoms depends on the size of the ions from which they are "detached".[9] Similar results obtained by us for fragment ions of deutero-octane[10] show that the isotope effect is such as though the fragments comprising a detached hydrogen atom form not from the entire octane molecule with 18 hydrogen atoms (C_8H_{18}) but from pieces of the molecule: C_2H_5, C_3H_7, C_4H_9, and so on, i.e., from parts of the molecule corresponding in composition to the ionic fragments forming owing to rupture of certain C—C bonds.

It follows from our hypothesis also that the mass spectra should not depend on the size of the molecule above a certain minimal size (the size above which the influence of the chain ends become minor). This is in agreement with results of experiments at electron energies of 50-70 ev.[2] We obtained the ionization curves for $C_3H_7^+$ forming from C_8H_{18} and $C_{19}H_{40}$. We found that these curves are very close right up to the appearance potential.

Thus, the mass spectra of such molecules are similar not only at an electron energy of 50-70 ev but at all electron energies. It follows therefore that the interaction of an electron with a molecule does not depend on the size of the molecule, which substantiates our hypothesis regarding the localized character of this interaction.

---

*The mass spectra at high electron energies were investigated by Yu. M. Miller.

It may apparently be assumed that dissociation of molecules under electron impact occurs within a time of the order of 10^{-13} sec, inasmuch as if the dissociation time were appreciably longer the energy would have time to be partitioned over the entire molecule.

In the case of the presence of double bonds in the molecule, however, it may be assumed that the excitation energy will be readily transferred through the system of conjugated bonds (as occurs, for example, in chemical reactions). In the case of a benzene molecule, which consists of a closed system of conjugated bonds, the excitation energy should readily be distributed over the entire molecule, which should reduce the probability for dissociation. Hence in the mass spectrum of benzene the fraction of molecular ions should be large compared with fragment ions, and this is in fact borne out by experiment.[2] Analogous arguments can be applied to other molecules and generally yield qualitative agreement with experiment.

"L.Ya.Karpov" Physical-Chemical Institute

References

1. F.H.Field & J.L.Franklin, Electron Impact Phenomena, N.Y., 1957.

2. Catalog of Mass-Spectral Data, Amer.Petroleum Inst., Research Project, 44, 1955.

3. M.V.Gur'ev, Zhur.fiz.khim., 34, 475 (1960). (Trans. Russ. Jour. Phys. Chem.)

4. H.M.Rosenstock, M.B.Walenstein, A.L.Warhaftig & H.Eyring, Proc. Nat. Acad. Sci. U.S., 38, 667 (1952).

5. L.Friedman, F.A.Long & M.Wolfsberg, J.Chem.Phys., 30, 1605 (1959).

6. M.V.Gur'ev, Thesis, "L.Ya.Karpov" Phys.-Chem.Inst.,M.,1959.

7. M.V.Gur'ev, M.V.Tikhomirov & N.N.Tunitskiı, Doklady AN SSSR, 123, 120 (1958). (Trans. Doklady.)

8. D.P.Stevenson, Trans.Faraday Soc., 49, 867 (1953).

9. D.O.Shissler, S.O.Tomson & J.Turkevich, Disc.Faraday Soc., 10, 46 (1951).

10. M.V.Gur'ev & M.V.Tikhomirov, Zhur.fiz.khim., 32, 2731 (1958).

MODERN METHODS FOR CALCULATING ATOMIC COLLISION CROSS SECTIONS

- G. F. Drukarev

1. Encounters between atoms may be divided into fast and slow collisions depending on whether the velocity v of the nuclei is high or low compared to

$$v_0 = \frac{e^2}{\hbar}.$$

In the case of slow collisions ($v \ll v_0$) the system of nuclei and electrons may be treated as a quasimolecule. Mathematically this is expressed by the method of perturbed stationary states, in which the system wave function is expressed in terms of the molecular wave functions of the electrons.

In the case of fast collisions ($v \gg v_0$) one may use the wave functions of isolated atoms for purposes of mathematical description.

In most problems of practical interest the de Broglie wavelength is much smaller than atomic dimensions. Hence the motion of the nuclei can be handled by a semiclassical approximation. One may naturally expect that in such an approximation the same cross sections will be obtained as with a parametric method, in which the nuclei are assumed to travel on fixed trajectories, and the electron wave function satisfies the Schroedinger equation*

$$\left(H_e - i\frac{\partial}{\partial t}\right)\Psi = 0. \qquad (1)$$

Using simplest examples, Bates and McCarroll[1] have shown that the method of perturbed stationary states with semiclassical nuclear wave functions is indeed equivalent to the parametric method.

2. The simplest case is represented by those processes in which a single electron changes its state. Then the electron undergoing the transition is described by means of two-center wave functions.

Let A and B be two force centers (atoms or ions) with masses M_A and M_B, and let the electron move in the field of these two centers. Denote the coordinates of the electron with respect to A, B and the center of mass by $\mathbf{r}_1$, $\mathbf{r}_2$ and $\mathbf{r}$, respectively, and the separation between the nuclei by R, so that

$$\mathbf{r}_1 = \mathbf{r} + \frac{M_B}{M_A + M_B}\mathbf{R} \text{ and } \mathbf{r}_2 = \mathbf{r} - \frac{M_A}{M_A + M_B}\mathbf{R}. \qquad (2)$$

For stationary nuclei the state of the electron will be described by a function $\chi(\mathbf{r}, \mathbf{R})$, which satisfies the equation

$$H_e\chi_n(\mathbf{r}, \mathbf{R}) = \varepsilon_n(R)\,\chi_n(\mathbf{r}, \mathbf{R}), \qquad (3)$$

---

*Here and below we use atomic units: $\hbar = m_e = e = 1$.

where

$$H_e = -\frac{1}{2}\Delta_r + U_A(\mathbf{r}_1) + U_B(\mathbf{r}_2). \tag{4}$$

One must distinguish two different types of χ functions. The first of these is χ_A, which, as $R \to \infty$ and for $\mathbf{r}_1 = \text{const}$, approaches a function $\psi_A(\mathbf{r}_2)$ describing the system $A + e$. The second is χ_B which, as $R \to \infty$ and for $\mathbf{r}_2 = \text{const}$, approaches $\psi_B(\mathbf{r}_r)$ describing the system $B + e$. We assume here that both systems $A + e$ and $B + e$ are stationary in the limit as $R \to \infty$.

In order to deal with collisions it is helpful to introduce functions which, in this limit, describe moving systems $A + e$ and $B + e$. Such functions were introduced and used for constructing their theory both by Bates and McCarrol[1] and by Bates.[2]

We shall treat the problem by the parametric method, writing $\mathbf{R} = \mathbf{R}(t)$.

Assume that in the laboratory coordinate system A is stationary, and B moves with velocity $\mathbf{v}$.

In the center-of-mass system the velocities of A and B will be, respectively,

$$\mathbf{v}_A = -\frac{M_B}{M_A + M_B}\mathbf{v} \quad \text{and} \quad \mathbf{v}_B = \frac{M_A}{M_A + M_B}\mathbf{v}.$$

We introduce the functions

$$\varphi_{An} = \chi_{An}(\mathbf{r}, \mathbf{R}) \exp\left[-i\left(v_A^2/2 + \varepsilon_n(\infty)\right)t + i\mathbf{v}_A\mathbf{r}\right] \tag{5}$$

and

$$\varphi_{Bm} = \chi_{Bm}(\mathbf{r}, \mathbf{R}) \exp\left[-i\left(v_B^2/2 + \varepsilon_m(\infty)\right)t + i\mathbf{v}_B\mathbf{r}\right] \tag{6}$$

(the functions of Bates and McCarroll differ from (5) and (6) by the factor $\exp\left\{-i\int_{-\infty}^{t}[\varepsilon_{n,m}(\mathbf{R}) - \varepsilon_{n,m}(\infty)]\,dt\right\}$).

As $R \to \infty$, (5) and (6) become

$$\varphi_{An} = \psi_{An}(\mathbf{r}_1) \exp\left[-i\left(v_A^2/2 + \varepsilon_n(\infty)\right)t + i\mathbf{v}_A\mathbf{r}\right] \tag{7}$$

and

$$\varphi_{Bm} = \psi_{Bm}(\mathbf{r}_2) \exp\left[-i\left(v_B^2/2 + \varepsilon_m(\infty)\right)t + i\mathbf{v}_B\mathbf{r}\right]. \tag{8}$$

The functions of (7) and (8) describe, respectively, the system $A + e$ moving with velocity v_A, and the system $B + e$ moving with velocity v_B.

3. The operator $L = H_e - i\frac{\partial}{\partial t}$ acting on the wave functions of (5) and (6) gives

$$L\varphi_{An} = \{-i\mathbf{v}\left[\nabla_R\chi_{An}(\mathbf{r}_1, \mathbf{R})\right]_{r_1} + \left[\varepsilon_n(R) - \varepsilon_n(\infty)\right]\chi_{An}(\mathbf{r}_1, \mathbf{R})\} \times \exp\left\{-i\left[\varepsilon_n(\infty) + v_A^2/2\right]t + i\mathbf{v}_A\mathbf{r}\right\} \tag{9}$$

and

$$L\varphi_{Bm} = \{- iv\,[\nabla_R \chi_{Bm}(\mathbf{r}_2, \mathbf{R})]_{\mathbf{r}_2} + [\varepsilon_m(R) - \varepsilon_m(\infty)]\,\chi_{Bm}(\mathbf{r}_2, \mathbf{R})\} \times \\ \times \exp\{- i\,[\varepsilon_m(\infty) + v_B^2/2]t + iv_B r\}. \quad (10)$$

It is seen from this that φ_{An} and φ_{Bm} satisfy the Schroedinger equation in the limit as $R \to \infty$.

At high velocities we may make the approximation of replacing $\chi_{A,B}$ by the atomic wave functions $\psi_A(\mathbf{r}_1)$ and $\psi_B(\mathbf{r}_2)$, respectively, which means that we use (7) and (8) in place of (5) and (6). Then Eqs.(9) and (10) become

$$L\varphi_A = U_B(\mathbf{r}_2)\,\varphi_A \quad (11)$$

and

$$L\varphi_B = U_A(\mathbf{r}_1)\,\varphi_B. \quad (12)$$

4. We shall write the electron wave function $\Psi(r, t)$ satisfying the equation

$$L\Psi = 0, \quad (13)$$

in the form

$$\Psi = \sum_s a_{As}(t)\,\varphi_{As}(\mathbf{r}, t) + a_{Bs}(t)\,\varphi_{Bs}(\mathbf{r}, t). \quad (14)$$

When making approximate calculations in practice, one uses a finite number of the terms of (14).

When such a finite number of terms is used, (14) does not satisfy the Schroedinger equation (13), but, like the exact wave function, can satisfy the equation

$$\int \varphi^*_{B,As} L\Psi d\mathbf{r} = 0. \quad (15)$$

Then Eq.(15) can be obtained from a variational principle similarly as is done for electron scattering by atoms.[3]

Inserting (14) into (15) we obtain a set of equations for the $a_{A,Bs}$, and to this we must add the initial conditions corresponding to the given specific problem.

The expression

$$W = |a_n(\infty)|^2 \quad (16)$$

gives the transition probability to the state n, and refers to a particular value of the impact parameter ρ, so that $W = W(\rho)$.

The total cross section is obtained by integrating over all impact parameters:

$$Q = 2\pi \int_0^\infty W(\rho)\,\rho d\rho. \quad (17)$$

Usually the trajectory is assumed to be rectilinear (which is reasonable for scattering angles as small as those that are encountered in practice). Then one may write $\rho = R_{\min}$.

Choosing the Z axis along the direction of motion, and setting $t = 0$ at $R = R_{\min}$, we have

$$R = (\rho^2 + Z^2)^{1/2}, \tag{18}$$
$$Z = vt. \tag{19}$$

Below we give the equations deduced for some specific processes when a finite number of terms is used in (14), and discuss the approximate solution of these equations.

5. Consider excitation of the B atom in collision with the atom:

$$(A + e)_0 + B \to (A + e)_n + B.$$

We keep only φ_{A0} and φ_{An} in (14). Inserting the resulting expression into (15) and dropping the index A, we obtain

$$i \frac{\partial a_0}{\partial t} = \langle 0 | L | 0 \rangle a_0 + \langle 0 | L | n \rangle a_n \tag{20}$$

and

$$i \frac{\partial a_n}{\partial t} = \langle n | L | n \rangle a_n + \langle n | L | 0 \rangle a_0, \tag{21}$$

with the initial conditions $a_n(-\infty) = 0$, and $a_0(-\infty) = 1$.

Bates[4] has gone through an approximate solution of Eqs.(20) and (21) for a_n small compared with a_0 and the off-diagonal matrix elements small compared with the diagonal ones.

In this case (20) can be written

$$i \frac{\partial a_0}{\partial t} = \langle 0 | L | 0 \rangle a_0, \tag{22}$$

and the solution with the initial condition $a_0(-\infty) = 1$ is

$$a_0(t) = \exp\left[-i \int_{-\infty}^{t} \langle 0 | L | 0 \rangle \, dt'\right]. \tag{23}$$

Inserting (23) into (21), we obtain

$$ia_n(t) = \exp\left[-i \int_{-\infty}^{t} \langle n | L | n \rangle \, dt'\right] \times$$
$$\times \left\{ \int_{-\infty}^{t} dt' \langle n | L | 0 \rangle \exp\left[-i \int_{-\infty}^{t'} (\langle 0 | L | 0 \rangle - \langle n | L | n \rangle) \, dt''\right]\right\}. \tag{24}$$

The desired quantity $|a_n(\infty)|$ is, according to (24),

$$|a_n(\infty)| = \left| \int_{-\infty}^{\infty} \langle n | L | 0 \rangle \exp\left[i \int_{-\infty}^{t'} (\langle n | L | n \rangle - \langle 0 | L | 0 \rangle) \, dt''\right] dt'\right|. \tag{25}$$

Using Eqs.(7), (8), (11) and (12), the matrix elements for fast collisions may be written

$$\langle 0 | L | 0 \rangle = U_{00}; \qquad \langle n | L | n \rangle = U_{nn};$$
$$\langle n | L | 0 \rangle = U_{n0} \exp[i(\varepsilon_n - \varepsilon_0) t], \tag{26}$$

where

$$U_{\alpha\beta} = \int \psi^*_{A\alpha}(\mathbf{r}_1) \, U_B(\mathbf{r}_2) \, \psi_{A\beta}(\mathbf{r}_1) \, d\mathbf{r}_1.$$

6. Let us now consider charge exchange

$$(A + e)_0 + B \rightarrow A + (B + e)_n.$$

For this case we retain the functions φ_{A0} and φ_{Bn} in (14). Then the equations for a_{A0} and a_{Bn} become

$$\{1 - |\langle Bn | A0\rangle|^2\}\, i\frac{\partial a_{Bn}}{\partial t} = \{\langle Bn|L|A0\rangle - \langle Bn|A0\rangle\langle A0|L|A0\rangle\} a_{A0} + \\ + \{\langle Bn|L|Bn\rangle - \langle Bn|A0\rangle\langle A0|L|Bn\rangle\} a_{Bn}; \tag{27}$$

$$\{1 - |\langle Bn|A0\rangle|^2\}\, i\frac{\partial a_{A0}}{\partial t} = \{\langle A0|L|A0\rangle - \langle A0|Bn\rangle\langle Bn|L|A0\rangle\} a_{A0} + \\ + \{\langle A0|L|Bn\rangle - \langle A0|Bn\rangle\langle Bn|L|Bn\rangle\} a_{Bn} \tag{28}$$

and the initial conditions are

$$a_{Bn}(-\infty) = 0 \quad \text{and} \quad a_{A0}(-\infty) = 1.$$

We note that Eqs.(27) and (28) are invariant under the transformation

$$L \rightarrow L + F(t);$$

$$a \rightarrow a \exp\left[i\int_{-\infty}^{t} F(t)\, dt\right]. \tag{29}$$

Charge exchange in slow collisions has been treated by Bates and McCarroll[1], and in fast collisions by Bates[2]. In both cases approximate solutions were obtained for (27) and (28). The approximation reduces essentially to considering a_{Bn} small compared with a_{A0}, and the off-diagonal elements small compared to the diagonal ones. Further, the integral $\langle Bn|A0\rangle$ is also considered small.

Then in Eq.(27) one should drop terms containing $|\langle Bn|A0\rangle|^2$ and $a_{Bn}\langle Bn|A0\rangle\langle A0|L|Bn\rangle$, since they are of higher order than the others, and for the same reason one should drop terms containing $|\langle Bn|A0\rangle|^2$, $\{\langle A0|L|Bn\rangle\langle A0|Bn\rangle\langle Bn|L|Bn\rangle\} a_{Bn}$ and $\langle A0|Bn\rangle\langle Bn|L|A0\rangle a_{A0}$, in (28). This leads to the simplified set of equations

$$i\frac{\partial a_{A0}}{\partial t} = \langle A0|L|A0\rangle a_{A0}; \tag{30}$$

$$i\frac{\partial a_{Bn}}{\partial t} = \{\langle Bn|L|A0\rangle - \langle Bn|A0\rangle\langle A0|L|A0\rangle\} a_{A0} + \langle Bn|L|Bn\rangle a_{Bn}. \tag{31}$$

From (30) we obtain

$$a_{A0} = \exp\left[-i\int_{-\infty}^{t}\langle A0|L|A0\rangle\, dt'\right]. \tag{32}$$

Inserting (30) into (31), integrating, and setting $t = \infty$, we arrive at

$$a_{Bn}(\infty)| = \left|\int_{-\infty}^{\infty}\exp\left[i\int_{-\infty}^{t} dt'\,(\langle Bn|L|Bn\rangle - \langle A0|L|A0\rangle)[\langle Bn|L|A0\rangle - \right.\right. \\ \left.\left. - \langle Bn|A0\rangle\langle A0|L|A0\rangle]\, dt\right]\right|. \tag{33}$$

Below we give expressions for the matrix elements appearing in (33).

For slow collisions, Eqs.(2), (5), (6), (9) and (10) lead to

$$\langle A0 \mid L \mid A0\rangle = \varepsilon_0(R) - \varepsilon_0(\infty); \tag{34}$$

$$\langle Bn \mid L \mid Bn\rangle = \varepsilon_n(R) - \varepsilon_n(\infty); \tag{35}$$

$$\langle Bn \mid L \mid A0\rangle - \langle Bn \mid A0\rangle \langle A0 \mid L \mid A0\rangle = -iv\int \chi^*_{Bn}(\mathbf{r}_2, \mathbf{R})\,[\nabla_R \chi_{A0}(\mathbf{r}_1, \mathbf{R})]_{\mathbf{r}_1} \exp(-iv\mathbf{r}_1)\,d\mathbf{r}_1 \times$$
$$\times \exp[i(\varepsilon_0(\infty) - \varepsilon_n(\infty) + v^2/2)\,t]. \tag{36}$$

For fast collisions, (7), (8), (11) and (12) lead to

$$\langle A0 \mid L \mid A0\rangle = \int \psi^*_{A0}(\mathbf{r}_1)\,U_B(\mathbf{r}_2)\,\psi_{A0}(\mathbf{r}_1)\,d\mathbf{r}_1; \tag{37}$$

$$\langle Bn \mid L \mid Bn\rangle = \int \psi^*_{Bn}(\mathbf{r}_2)\,U_A(\mathbf{r}_1)\,\psi_{Bn}(\mathbf{r}_2)\,d\mathbf{r}_2; \tag{38}$$

$$\langle Bn \mid L \mid A0\rangle - \langle Bn \mid A0\rangle \langle A0 \mid L \mid A0\rangle = \Big\{\int \psi^*_{Bn}(\mathbf{r}_2)\,U_B(\mathbf{r}_2)\,\psi_{A0}(\mathbf{r}_1)\exp(-iv\mathbf{r}_1)\,d\mathbf{r}_1 -$$
$$-\Big[\int \psi^*_{A0}(\mathbf{r}_1)\,U_B(\mathbf{r}_2)\,\psi_{A0}(\mathbf{r}_1)\,d\mathbf{r}_1\Big]\Big[\int \psi^*_{Bn}(\mathbf{r}_2)\,\psi_{A0}(\mathbf{r}_1)\exp(-iv\mathbf{r}_1)\,d\mathbf{r}_1\Big]\Big\} \times$$
$$\times \exp[i(\varepsilon_0(\infty) - \varepsilon_n(\infty) + v^2/2)\,t]. \tag{39}$$

7. Requiring special consideration is the phenomenon of resonant charge exchange (when A and B are identical and the transition takes place without change in energy).

For this case we use the two-center functions symmetrized or antisymmetrized with respect to interchange of the nuclei. We denote these functions by χ_+ and χ_-, and the energies corresponding to them by ε_+ and ε_-. From χ_+ and χ_- we can construct new functions χ_A and χ_B according to

$$\chi_A = 2^{-1/2}(\chi_+ + \chi_-), \tag{40}$$

$$\chi_B = 2^{-1/2}(\chi_+ - \chi_-). \tag{41}$$

In analogy with (5) and (6), we introduce the functions

$$\varphi_A = \chi_A \exp[-i[\varepsilon(\infty) + v_A^2/2]\,t + i\mathbf{v}_A\mathbf{r}] \tag{42}$$

and

$$\varphi_B = \chi_B \exp[-i(\varepsilon(\infty) + v_B^2/2]\,t + v\mathbf{v}_B\mathbf{r}] \tag{43}$$

where now $\mathbf{v}_B = -\mathbf{v}_A = \mathbf{v}/2$), and $\varepsilon(\infty)$ is the common limit of both $\varepsilon_+(R)$ and $\varepsilon_-(R)$ as $R \to \infty$.

Writing Ψ in the form

$$\Psi = a_A\varphi_A + a_B\varphi_B, \tag{44}$$

we obtain a set of equations of the form of (27) and (28) for a_A and a_B. It is, however, more convenient to consider the functions

$$\varphi_+ = 2^{-1/2}(\varphi_A + \varphi_B), \tag{45}$$

$$\varphi_- = 2^{-1/2}(\varphi_A - \varphi_B) \tag{46}$$

and to write Ψ in the form

$$\Psi = a_+\varphi_+ + a_-\varphi_-, \tag{47}$$

where

$$a_+ = 2^{-1/2}(a_A + a_B), \tag{48}$$
$$a_- = 2^{-1/2}(a_A - a_B). \tag{49}$$

This representation is convenient in that the symmetry properties lead to the relation

$$\langle + | L | - \rangle = \langle - | L | + \rangle = 0 \tag{50}$$

(the symbols + and - tell whether φ_+ or φ_- enters into the matrix elements). As a result, the equations for a_+ and a_- separate into the two independent equations

$$\langle + 1 + \rangle \; i\frac{\partial a_+}{\partial t} = \langle + | L | + \rangle a_+ \tag{51}$$

and

$$\langle - 1 - \rangle \; i\frac{\partial a_-}{\partial t} = \langle - | L | - \rangle a_-, \tag{52}$$

which are immediately integrable.

It follows from (48) and (49) that the initial conditions for a_+ and a_- are

$$a_+(\infty) = a_-(-\infty) = 2^{-1/2}. \tag{53}$$

Using this fact, the solution of (51) and (52) becomes

$$a_+(t) = 2^{-1/2}\left[\exp\left(-i\int_{-\infty}^{t}\frac{\langle + | L | + \rangle}{\langle + 1 + \rangle}dt'\right) + 1\right];$$
$$a_-(t) = 2^{-1/2}\left[\exp\left(-i\int_{-\infty}^{t}\frac{\langle - | L | - \rangle}{\langle - 1 - \rangle}dt'\right) - 1\right]. \tag{54}$$

Again, as is seen from (48) and (49), the charge-exchange probability is

$$W = \frac{1}{2}|\, a_+(\infty) - a_-(\infty)\,|^2. \tag{55}$$

Inserting (54), we obtain

$$W = \sin^2\left[1/2\int_{-\infty}^{\infty}\lambda(t)\,dt\right], \tag{56}$$

where

$$\lambda = \frac{\langle + | L | + \rangle}{\langle + 1 + \rangle} - \frac{\langle - | L | - \rangle}{\langle - 1 - \rangle}. \tag{57}$$

Using Eqs.(42), (43), (45) and (46), one can express the matrix elements in (57) in terms of integrals containing χ_+ and χ_-. Simple, but relatively torturous operations lead to the result

$$\lambda = [\varepsilon_+(R) - \varepsilon_-(R)]\left[1 - \frac{\mu_+}{1-\sigma} - \frac{\mu_-}{1+\sigma}\right] + \frac{2\delta v}{1-\sigma^2}, \tag{58}$$

where

$$\mu_{\pm} = \int |\chi_{\pm}|^2 \sin^2 (1/2\ \mathbf{vr})\, d\mathbf{r}, \tag{59}$$

$$\sigma = 1/2 \int (|\chi_{+}|^2 - |\chi_{-}|^2) \cos \mathbf{vr}\, d\mathbf{r} \tag{60}$$

$$\delta = 1/4 \int \{(\chi_{+} + \chi_{-})^* [\nabla_R (\chi_{+} - \chi_{-})]_{r_1} - (\chi_{+} - \chi_{-})^* [\nabla_R (\chi_{+} + \chi_{-})]_{r_2}\} \sin (\mathbf{vr})\, d\mathbf{r}. \tag{61}$$

For low velocities, $\mu_{\pm} \sim v^2$, while $\delta \sim v$.
Neglecting terms of order v^2 in (58), we obtain

$$\lambda \approx \varepsilon_{+} (R) - \varepsilon_{-} (R). \tag{62}$$

For high velocities σ and δ become small as a result of strongly oscillating factors in the integrands, and $\mu_{\pm} \approx \frac{1}{2}$.
Then, as is seen from (58),

$$\lambda \ll |\varepsilon_{+} (R) - \varepsilon_{-} (R)|.$$

References

1. D.R.Bates & R.McCarroll, Proc.Roy.Soc.A, 245, 175 (1958).
2. D.R.Bates, Ibid., 247, 294 (1958).
3. Yu.N.Demkov, Variatsionnye printsipy v teorii stolknovenii (Variational principles in collision theory), M., 1958.
4. D.R.Bates, Proc.Phys.Soc., 73, 227 (1959).

FURTHER INVESTIGATION OF RESONANCE CHARGE EXCHANGE OF POSITIVE CESIUM IONS

- R.M.Kushnir & I.M.Buchma

The present work was a continuation of our earlier investigations[1] of resonance charge exchange of cesium ions; the experiments were extended into the range of higher ion energies to encompass the range from 100 to 2000 ev. The measurements were carried out by the method of drawing the slow ions forming as a result of charge exchange to an auxiliary electrode in the form of a cylinder.

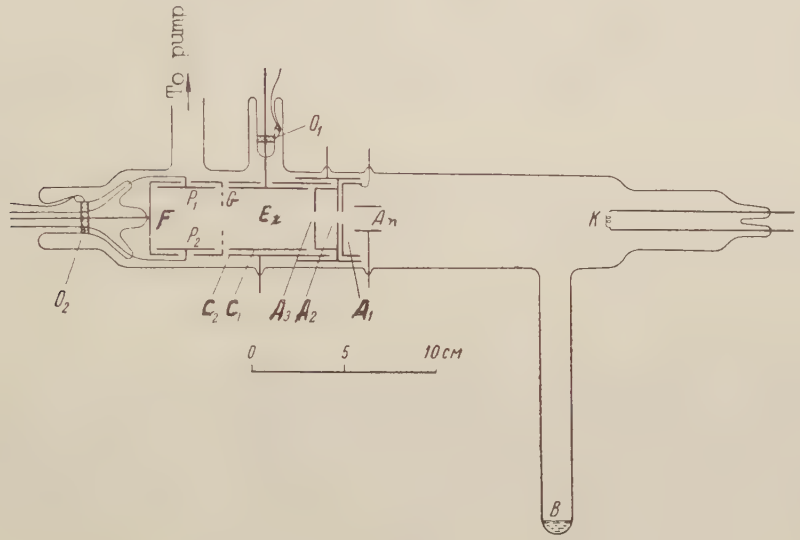

Fig.1. Diagram of apparatus: K - cathode, An - anode, A_1, A2 & A3 - circular apertures (3 mm diameter), Ex - charge exchange chamber, C_1 - measuring cylinder, C_2 - shielding cylinder, F - Faraday cup, P_1 & P_2 - plate electrodes in Faraday cup, G - grid, O_1 & O_2 - guard rings, B - branch tube containing cesium.

The experimental apparatus is diagramed in Fig.1. The envelope was made of special glass characterized by high resistance to alkali metal vapor. The ion source was a low voltage arc (4-4.5 v, 30 ma) ignited in the cesium vapor between the heated tungsten cathode K and the anode An. The ion beam was extracted from the plasma through the aperture A_1, maintained at zero potential. The ions were accelerated to the requisite velocity between apertures A_1 and A_2 and entered the charge exchange chamber Ex. The slow ions forming as a result of charge exchange in the chamber were drawn to the measuring cylinder C_1; the remaining unaffected ions in the beam entered the Faraday cup F. This was separated from the chamber by the grid G. A weak (10 v) transverse electric field was applied between the plate electrode P_1 and P_2 in the cup; this served to prevent exit from the cup of secondary electrons and slow ions. The ion current was measured by means of an M-21 galvanometer.

The guard rings O_1 and O_2 served to shield the measuring electrode from the conduction current on the inside surface of the glass. The procedure as regards outgassing of the vacuum system, controlling the cesium vapor pressure in the measuring device and measurement of the temperature of the branch tube with the metal in the liquid phase was the same as described earlier in Refs.1 & 2. The cesium vapor pressure was determined by means of the equation[3]:

$$\log p = 9.86 - \frac{3774}{T},$$

where p is the pressure of the saturated cesium vapor in microns Hg and T is the temperature of the liquid metal.

The charge exchange cross section was determined on the basis of the exponential equation for attentuation of the beam. This equation is predicated on linear variation of $\log I_0/I$ with p_0. In our case

$$I_0 = I_F + I_C + I_e$$

and

$$I = I_F + I_e,$$

where I_F is the current measured by the Faraday cup, i.e., the flux of ions passing through the charge exchange chamber without losing their charge, I_C is the current of slow ions forming in the charge exchange chamber, I_e is the correction for the secondary electron current, and p_0 is the pressure of the saturated cesium vapor reduced to 0°.

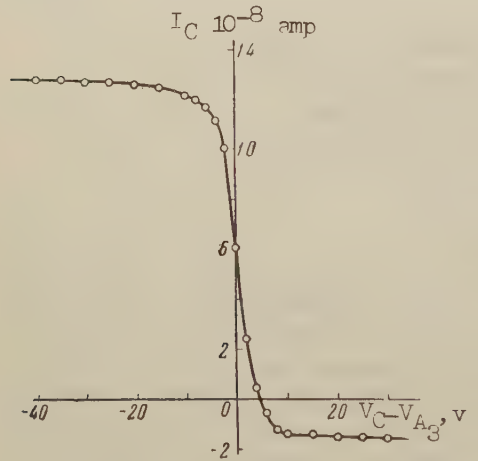

Fig.2. Volt-ampere characteristic of the current to the measuring cylinder: E = 900 ev, $p_0 = 2.6 \cdot 10^{-4}$ mm Hg.

For determining I_C a small potential, negative relative to A_3, was applied to the measuring cylinder C_1 and the variation of the ion current I_C as a function of the potential V_C was recorded. The potential on the Faraday cup was maintained equal to the potential on aperture A_3. By way of illustration the curve obtained for 900 ev ions is shown in Fig.2. I_C was taken to be the saturation current with $V_C < V_{A_3}$.

With the potential V_C on the measuring cylinder positive relative to the potential V_A on aperture A_3 there flowed to the cylinder a small electron current, presumably due to secondary emission from A_3. Thus I_e was taken to be the saturation current to the measuring cylinder with $V_C > V_{A_3}$. At ion energies of 100 and 200 ev this current was negligibly small.

The ion current I_F to the Faraday cup was measured simultaneously with the saturation current I_C.

The experimental data were then used to plot $\log I_0/I$ vs p_0. In all cases the plots were straight lines. From the slope of these lines, which in our case were described by

$$\log \frac{I_0}{I} = \frac{5Q}{2.3} p_0,$$

we evaluated the resonance charge exchange cross section Q for ions of the given energy.

In order to investigate the ion velocity dependence of the charge exchange cross section we carried out experiments at the following ion energies: 100, 200, 400, 700, 900, 1200, 1600 and 2000 ev. For each of these energies we carried out a large number of measurements at different pressures of the saturated cesium vapor in the temperature range from 90 to 115°. Below we give the average charge exchange cross section values:

E, ev	100	200	400	700	900	1200	1600	2000
Q, $\frac{cm^2}{cm^3\ mm\ Hg}$	1100	910	835	790	775	725	695	690

As in our earlier investigation[1] the accuracy of our measurements is determined primarily by the accuracy in determining the pressure of the saturated cesium vapor. Otherwise the total error in Q owing to inaccuracy in measuring I_F, I_C and I_e does not exceed 10%.

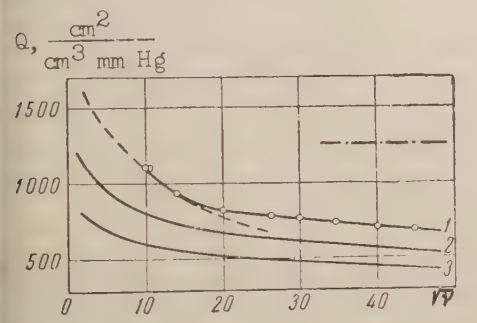

Fig.3. Variation of the charge exchange cross section with the ion velocity in cesium vapor: 1 - our data (dashed section - data of Ref.1); 2 & 3 - theoretical curve based on the formulas of Firsov[4] and Demkov[5], respectively; the dash-dot line is calculated by the limit formula of Sena[6].

Fig.3 shows the variation of the charge exchange cross section Q with ion velocity (curve 1). It will be seen from the figure that the curve based on the present data merges smoothly into the curve obtained earlier by one of us[1] (dashed curve) for the resonance charge exchange cross section in the range of low ion energies.

For purposes of comparison with theory, in Fig.3 we also give the theoretical curves for the ion velocity dependence of the charge exchange cross section calculated according to the formulas of Firsov[4] and Demkov[5]. The dash-dot line gives the value of Q calculated for cesium by means of the approximate limit formula of Sena.[6] It will be evident from Fig.3 that our experimental charge exchange cross sections are somewhat higher than the values calculated by means of the Firsov and Demkov formulas and are appreciably lower than indicated by the limit formula of Sena. The experimental curve is characterized by a steeper rise in the range of low velocities as compared with the Firsov and Demkov theoretical curves. The theoretical curve based on Firsov's formula is closer as regards both shape and position to the experimental curve; in fact, the divergence between the Firsov curve and the experimental curve lies within the limit of the errors of experiment and theory.

We desire to express our deep gratitude to L.A.Sena for valuable advice.

"I.Franko" L'vov State University

References

1. R.M.Kushnir, Ukr.fiz.zhur. (Ukrainian Physics Journal), 3, 788 (1958).
2. R.M.Kushnir, Ibid., 3, 343 (1958).
3. S.Dushman, Scientific Foundations of Vacuum Technique, N.Y., 1949. (Cited in Russian trans.)
4. O.B.Firsov, Zhur.eksp.i teor.fiz., 21, 1001 (1951).
5. Yu.N.Demkov, Uch.zap. (Scientific notes), Leningrad State University, No.146, Issue 8, 74 (1957).
6. L.A.Sena, Stolknoveniya elektronov i ionov s atomami gaza (Collisions of electrons and ions with gas atoms), M.-L., 1948.

INDIRECT EVALUATION OF ELECTRON ATTACHMENT CROSS SECTIONS

- M. V. Konyukov

1. In the positive column of a glow discharge the energy received by the electrons from the longitudinal field is balanced by losses occurring at the walls and in interactions between the electrons and the other components of the plasma.

The electron energy balance equation includes losses of all kinds, but if one separates out the fraction γ_i of energy lost in collisions, the balance equation reduces to a set of equations of the form

$$\gamma_i e U_e E_z = \int_0^\infty \varkappa_i \frac{m_e v_e^2}{2} Q_i(v)\, v_e f(T_e, v_e)\, dv_e, \tag{1}$$

where U_e is the electron drift velocity, E_z is the longitudinal electric field, $\varkappa_i$ is the fraction of the electron energy lost in each collision, Q_i is the collision cross section and $f(T_e, v_e)$ describes the electron velocity distribution at an electron temperature T_e. If the distribution function is known and the electron-temperature dependences of U_e and E_z are available from experiment, Eq.(1) is a Fredholm integral equation of the first kind, giving the cross section for the i-th process as a function of the electron velocity.

2. One of the processes the cross section of which can be studied by Eq.(1) is electron sticking or attachment. Introducing the dimensionless parameters $\varepsilon = \frac{m_e v_e^2}{2kT_0}$ and $\tau = \frac{T_e}{T_0}$, writing

$$\varphi(\tau) = \frac{\gamma_i e U_e E_z (2\pi m_e)^{1/2}}{4\tau^{1/2}(kT_0)^{3/2}},$$

and noting that $\varkappa_i = 1$, we obtain

$$\varphi(\tau) = \int_0^\infty Q(\varepsilon)\, \frac{\varepsilon^2}{\tau^2} \exp\left(-\frac{\varepsilon}{\tau}\right) d\varepsilon. \tag{2}$$

The particular form of the kernel in (2) suggests that we attempt to solve the equation by an expansion in Laguerre polynomials. On the other hand, when we note that under actual conditions $\varphi(\tau)$ is an interpolation polynomial passing through the experimental points, we see that it is simpler to obtain a solution in the form of a polynomial.

If the interpolation polynomial $\varphi(\tau)$ starts with a term not containing τ, the solution $Q(\varepsilon)$ to be found is of the form

$$Q(\varepsilon) = q_{-1}\varepsilon^{-1} + q_0 + q_1\varepsilon + \ldots + q_{n-1}\varepsilon^{n-1}. \tag{3}$$

Inserting (3) into (2) and performing some elementary operations, we arrive at

$$q_{m-1} = \frac{a_m}{\Gamma(m+r)} \tag{4a}$$

$$Q(\varepsilon) = \frac{a_0}{\Gamma(2)}\varepsilon^{-1} + \frac{a_1}{\Gamma(3)} + \ldots + \frac{a_n}{\Gamma(n+2)}\varepsilon^{n-1}, \tag{4b}$$

where $a_0, a_1, \ldots, a_n$ are the coefficients of the interpolation polynomial, and $\Gamma(n)$ is the gamma function of an integral argument. Equation (4b) will give the desired estimate of the electron attachment cross section from indirect measurements in the positive column.

3. Consider two positive columns one of which contains a third charged component, namely, negative ions. If the concentrations are low and the electron temperatures in both discharges are the same, the radial motion of the electrons and positive ions, as well as losses at the walls, will be practically the same.[1] The energy balance, however, will be different because of losses due to the interaction of the electrons with the electronegative component. This then leads to a difference in the longitudinal gradient necessary to maintain the discharge with the negative ions. We shall call such positive columns Schottky equivalents.

Writing out the energy balance equations for an electron in the equivalent columns and subtracting one equation from the other, we obtain

$$(eU_eE_z)' - (eU_eE_z) = \int_0^\infty \left\{ \frac{2m_e}{M} Q_{\text{ela}} + Q_{\text{att}} + \sum_{(k)} \frac{2eV_k}{m_e v_e^2} \right\} \times$$

$$\times \frac{m_e v_e^2}{2} v_e 4\pi \left(\frac{m_e}{2\pi k T_e} \right)^{3/2} \exp\left(- \frac{m_e v_e^2}{2kT_e} \right) v_e^2 dv_e, \qquad (5a)$$

where Q_{ela}, Q_{att} and Q_k are the cross sections for the elastic interaction, attachment, and inelastic interaction with the electronegative component, V_k is the excitation potential for the k-th level, and the prime denotes the equivalent column with the additional component. If as the electronegative gas we chose a halogen, and the fundamental process giving rise to negative ions is taken to be dissociative attachment[2], the Q_{att} term will, in a wide electron temperature range, be greater than $(2m_e / M)\, Q_{\text{ela}}$ and $(2eV_k / m_e v_e^2)\, Q_k$. Under such conditions the excess energy released by the electrons goes essentially for compensation of attachment losses. Equation (5a) then can be written

$$(eU_eE_z)' - (eU_eE_z) = \int_0^\infty Q_{\text{att}} \frac{m_e v_e^2}{2} v_e 4\pi \left(\frac{m_e}{2\pi k T_e} \right)^{3/2} \exp\left(- \frac{m_e v_e^2}{2kT_e} \right) v_e^2 dv_e, \qquad (5b)$$

which agrees with (2) when one writes it in dimensionless variables and takes

$$\varphi(\tau) = \frac{(2\pi m_e)^{1/2} [(eU_eE_z)' - (eU_eE_z)]}{4\tau^{1/2} (kT_0)^{3/2}}.$$

By measuring the electron drift velocity and the longitudinal field in equivalent columns at various electron temperatures, one can obtain φ for several values of τ. Then the interpolation polynomial is constructed to pass through the points obtained, and its coefficients a_k can be used to calculate the q_k.

4. In conclusion some remarks should be made concerning our method for calculating the attachment cross section and its applicability to other processes.

In order to find $\varphi(\tau)$ one must know the electron-temperature dependence. In a column containing no negative ions, this is found by using probes. This is a difficult procedure when there are negative ions present, but the relation between the longitudinal electric field and the temperature can be established by measuring the intensity of the spectrum lines of the parent gas in equivalent columns. The required changes in the electron temperature can be realized by varying either the partial pressure of the parent gas or the discharge current, since Eq.(5b) is independent of the concentration of the neutral atoms of the parent gas and of the electrons. The solution represented by (4b) is an approximation in the sense that it insures the agreement between the calculated E_z values and those obtained experimentally by measuring $\varphi(\tau)$ (these calculations may be carried out in the usual way[3]).

Methods similar to those discussed here can be developed for finding the cross sections for ionization and excitation of various levels by measuring the ionization frequencies and intensities of spectrum lines. They will in general be analogous to the method of finding the energy dependence of the attachment cross section from measurements of the mean cross section.[4]

I am grateful to N.I.Bakievich for valuable advice.

Tula Pedagogical Institute

References

1. M.V.Konyukov, Izv.AN SSSR,Ser.fiz., 23, 971 (1959).(Trans. Bulletin, 23, 960.)
2. M.A.Biondi, Phys.Rev., 109, 2005 (1958).
3. Mirdel, Wiss. Veroff. Simens-Werke, 17 (3), 71 (1938).
4. M.A.Biondi & R.E.Fox, Phys.Rev., 109, 2012 (1958).

ENERGY TRANSFER IN MOLECULAR COLLISIONS

- A.I.Osipov & E.V.Stupochenko

Excitation of internal molecular degrees of freedom is one of the more important elementary kinetic processes. In particular, such phenomena as ultrasonic dispersion in diatomic gases, distribution of adsorbed gases on solid surfaces, and thermal dissociation of diatomic molecules cannot be understood without studying the transformation of translational into vibrational energy. In addition to such conversion processes, an important role may also be played by transfer of vibrational energy. This is of importance, for instance, in transport theory.[1]

The quantitative description of energy transfer processes involves cross sections and transition probabilities. In the present paper we discuss a semiclassical method for calculating such probabilities, and we determine the probability for the transformation of translational (kinetic) into vibrational energy in molecular collisions under strongly nonadiabatic conditions, as well as the probability for transfer of vibrations in molecular collisions. The calculations are performed for head on collision of diatomic molecules, in which the nuclei of the colliding molecules all lie on one straight line.

The transition probabilities are obtained from an asymptotic solution of the time-independent Schroedinger equation which describes the collision process.

Let $V(r,x)$ be an arbitrary potential describing the molecular interaction, where r is the relative motion coordinate and x represents the set of intramolecular coordinates. Under such general conditions the Schroedinger equation is very difficult to solve, even using perturbation theory (the method of deformed waves). To avoid these difficulties, Zener[2] suggested a simplification in which the relative coordinate of the colliding molecules is treated as a parameter whose time dependence is given classically. Then for a practical determination of the transition probabilities, Zener uses the set of equations

$$i\hbar \frac{\partial \psi(x, t)}{\partial t} = [H_{\mathrm{mol}}(x) + V(r(t), x)]\,\psi(x, t), \tag{1}$$

$$M \frac{d^2 r}{dt^2} = -\frac{dV_{nn}(r)}{dr}, \tag{2}$$

where $V_{nn} = S\psi^*_n(x)V(r,x)\psi_n(x)dx$ and the $\psi_n(x)$ are the eigenfunctions of the unperturbed molecular Hamiltonian.

Under some conditions it is easier to solve this set of equations than to deal with the time-independent Schroedinger equation. However, the conditions under which such an approximation is valid have not yet been clarified. Usually, it has merely been asserted that for sufficiently high relative velocities (quasi-classical relative motion) and when $\Delta E \ll E$ (where ΔE is the energy transferred, and E is the kinetic energy originally available), the results obtained by Zener's method are the same as those obtained by the deformed wave method.[3,4] It turns out, however, that these conditions are insufficient if

one wants to describe the relative motion in this problem classically. Our derivation of Eqs.(1) and (2) from the time-independent Schroedinger equation shows that in addition to the above conditions, it is necessary that

$$\left|1-\frac{V_{mm}}{V_{nn}}\right|\ll 1. \tag{3}$$

This condition is fulfilled automatically if the amplitude of oscillation of the atoms in the molecule is much smaller than the effective range of the intermolecular forces. In this case, we have

$$V(r, x)=V(r)+x\frac{\partial V}{\partial x}\Big|_{x=0}+\ldots \tag{4}$$

and V_{nn} will differ from V_{mm} by a quantity of higher order. In practice condition (3) is fulfilled for the first few vibrational levels and has a rather simple physical meaning: in the total Hamiltonian the relative coordinate can be treated as a time-varying parameter only if the molecular vibrations do not affect the relative motion.

Let us now use this method to find the probability for transformation of kinetic to vibrational energy in the collision of atoms with molecules under highly nonadiabatic conditions.

In the representation in which the unperturbed Hamiltonian is diagonal, Eq.(1) can be written

$$i\hbar\frac{da_k}{dt}=\sum a_m(t)V_{km}(r(t))\exp i\omega_{km}t,$$

$$a_m(-\infty)=\delta_{mn}.$$

Under highly nonadiabatic conditions,

$$\omega_{km}\tau\ll 1 \tag{6}$$

(where τ is the duration of the collision), and the exponential in Eq.(5) can be replaced by unity. The solution of such a set of equations reduces to finding the eigenfunctions and eigenvalues of the V_{km} matrix.

We invoke (4) and assume, as one usually does, that the molecular interaction potential is determined by the interaction of only the nearest atoms in the collision, i.e., that

$$V(r, x)=V(r-\lambda x),$$

where λ depends on the mass ratio of the atoms in the molecule. It can then be shown that the transition probabilities for our problem are of the form

$$P_{nm}=|a_m(\infty)|^2=\left|\int_{-\infty}^{\infty}\psi_m^*(x)\exp -i2\lambda k_n\, x\psi_n(x)\,dx\right|^2, \tag{7}$$

where $k_n=\frac{Mv_n}{\hbar}$ is the wave number of the incident atom.*

---

*Nikitin[5] solved a similar problem for oscillators. The expressions he obtained for the transition probabilities, however, are valid only for sufficiently large values of n.

Let us try to understand this formula by applying it to a special case. Let $n = 0$, and let the ψ_m be oscillator eigenfunctions. Then

$$P_{0m} = e^{-q^2} \frac{q^{2m}}{m!}, \tag{8}$$

where $q = 2k_0 \lambda x_0$, and $x_0 = \sqrt{\frac{\hbar}{2\mu\omega}}$ is the expectation value of the oscillator amplitude in the first excited state.

It is evident from (8) that for $q \ll 1$, the most probable transition is $0 \longrightarrow 1$, for which $P_{01} = q^2 = 4\lambda^2 k_0^2 x_0^2$.

For $q \gg 1$, the maximum probability is for transitions to a level with $m \sim q^2$. In both cases the energy transferred is $q^2\hbar\omega = 4\lambda^2 \frac{M}{\mu} E_{\text{kin}}$ in agreement with the corresponding classical result. We emphasize the following fact. Equation (7) is obtained by our method only if (4) is fulfilled. It can, however, be shown that this formula will be valid for any arbitrary interaction potential[6] provided condition (6) is fulfilled; in the case of an oscillator this condition becomes

$$\omega\tau \ll 1.$$

Our method can also be used to find the probability for transfer of vibrational energy in molecular collisions, regardless of the adiabaticity of the collision process.

As before, we proceed from Eqs.(1) and (2). In the representation in which the unperturbed Hamiltonian $H_{\text{mol}}(x) = H_1(x_1) + H_2(x_2)$ is diagonal, Eq.(2) becomes

$$i\hbar \frac{da_{kl}}{dt} = \sum_{pq} a_{pq}(t) V_{(kl)(pq)}(r(t)) \exp i\omega_{(kl)(pq)} t, \tag{9}$$

$$a_{kl}(-\infty) = \delta_{km}\delta_{ln}.$$

Since the probability for transfer of vibrations is much greater than the probability for transformation of kinetic to vibrational energy,[7] it is reasonable to attempt to solve (9) by perturbation theory, assuming in the first approximation that a_{pq} is different from zero only if

$$\omega_{(kl)(pq)}\tau \equiv \frac{(E_k + E_l - E_p - E_q)\tau}{\hbar} \ll 1. \tag{10}$$

As before, we find that the probability for transfer of vibrational energy is

$$P_{nl}^{mk} = |a_{kl}(\infty)|^2 = \left| \int_{-\infty}^{\infty} \psi_{kl}^{*}(x_1, x_2) \exp - \frac{i}{\hbar} x_1 x_2 \beta(\infty)\, \psi_{mn}(x_1 x_2)\, dx_1 dx_2 \right|^2,$$

where

$$\beta(\infty) = \frac{\lambda_1 \lambda_2}{2} \int_{-\infty}^{\infty} \frac{d^2V}{dr^2} dt, \tag{11}$$

and λ_1 and λ_2 are the analogs of λ in the preceding problem.

Again, let us turn to a special case. Assume the initial state of the colliding molecules is such that $|k - m| \ll m$ and $|l - n| \ll n$, and let $|k - m| = |l - n| = q$. Replacing the matrix ele-

ment in (11) by the appropriate Fourier component, we find that the probability for transfer of vibrational energy is

$$P_{nl}^{mk} = J_0^2\left(\frac{\beta x_{0n} x_{0k}}{2\hbar}\right) J_q^2\left(\frac{\beta x_{0n} x_{0k}}{2\hbar}\right),$$

where J_i is a Bessel function, and x_{0k} is the expectation value of the oscillator amplitude in the k-th state. When $\frac{\beta x_{0n} x_{0k}}{2\hbar} \ll 1$, corresponding to an adiabatic collision $(\omega\tau \gg 1)$ Eq.(12) goes over into the usual expression given by perturbation theory,[7] and for this case the most probable transfer is of a single quantum; then the probability is

$$P_{n,\,n-1}^{m,\,m+1} \sim \frac{1}{(\omega\tau)^2}.$$

In the opposite limit $(\omega\tau \ll 1)$, the probability is of the form

$$P_{nl}^{mk} \sim (\omega\tau)^2$$

and is also small. In order words, if $\omega\tau \ll 1$, the collision is so fast that the vibrational quanta do not have enough time to go over from one molecule to another.

The maximum value of the probability occurs when $\omega\tau \sim 1$, that is, when the duration of the collision is of the same order as the vibration period of the oscillator.

Moscow State University

References

1. Fizicheskaya gazodinamika (Physical Gas Dynamics), p.59, M., 1959.
2. C.Zener, Phys.Rev., 38, 277 (1932).
3. C.Zener, Proc.Cambridge Phil.Soc., 29, 136 (1933).
4. B.Widom & S.Bauer, J.Chem.Phys., 21, 1670 (1953).
5. E.Nikitin, Thesis, Inst. of Chem.Phys., M., 1958.
6. A.Osipov, Nauchn. dokl. vyssh. shkoly. (University Scientific Reports), Phys.-Math. Series, No.4, 149 (1958).
7. Takayanagy, Progr. Theoret. Phys., 8, 111 (1952).

THEORY OF THERMAL DISSOCIATION OF DIATOMIC MOLECULES

- E.E.Nikitin & N.D.Sokolov

Thermal dissociation of diatomic molecules,

$$AB + M \xrightarrow{K_d} A + B + M, \qquad (1)$$

has been treated by Rice[1,2] and Careri.[3-5] Careri, basing his work on simple collision theory, takes as a premise that dissociation of molecules can occur by direct transition from one of the low vibrational levels of the bound state to the dissociated state. Theoretical calculations supported by direct experimental evidence (as for instance, the data on ultrasonic relaxation[6]), however, show that in molecular collisions generally the energy transferred is very small compared to the dissociation energy D.

Rice,[1,2] on the other hand, bases his calculations on the correct assumption that the molecule undergoes transition into the energy continuum from one of the upper vibrational levels; he does not, however, take into account the breakdown of the Boltzmann distribution of the molecular vibrational levels.

Recently several models for dissociation have been proposed (in connection with the stochastic theory of chemical reactions) which take into account the fact that dissociation takes place in a sequence of steps.[7-14] In one of our works[10] we showed that if one wants to calculate the dissociation rate, one must not ignore the fact that the vibrations are not in general harmonic and that consequently the number of vibrational quanta decreases as the available vibrational energy of the molecule increases. By using this and taking into account rotations, one can calculate the dissociation rate K_d.

Let $P_{k,k-1}$ be the probability for transition from level k to level $k-1$ for some molecule AB in a single collision with a molecule M. The probability of vibrational excitation of the molecule AB in the transition from level $k-1$ to level k can, clearly, be written in the form

$$P_{k-1,k} = P_{k,k-1} \exp(-E_{k,k-1}/kT),$$

where $E_{k,k-1}$ is the difference in energy between levels k and $k-1$.

Let $x_k(t)$ be the distribution function, i.e., the population of the k-th level. Then the equations of motion can be written in the form

$$\frac{dx_k}{dt} = Z\{\alpha_k P_{k,k-1} x_{k-1} - (P_{k,k-1} + \alpha_{k+1} P_{k+1,k}) x_k + P_{k+1,k} x_{k+1}\}$$
$$(k = 0 \ldots n) \qquad (2)$$

with the boundary conditions $x_{-1} = x_{n+1} = 0$. Here Z is the number of collisions per second, $P_{n,n+1}\alpha_{n+1} \equiv P_\infty$ is the probability for a transition from the highest discrete state to a state in the continuum, and $\alpha_k = \exp(-E_{k,k-1}/kT)$.

Equations (2) are deduced on the assumption that transitions

take place only between neighboring vibrational levels in the discrete spectrum, and that dissociation is possible only from the highest lying discrete level.

The general solution of (2) is of the form

$$x_k(t) = \sum_{m=0}^{n} A_k(\mu_m) \exp(\mu - \mu_m t), \tag{3}$$

where the μ_m are eigenvalues of the matrix B on the right side of (2) (the index m enumerates these eigenvalues in order of increasing μ_m).

If $P_\infty = 0$, the eigenvalues of the corresponding matrix $B^{(0)}$ form the sequence $\mu_m^{(0)}$. Thermal equilibrium then corresponds to the first eigenvalue $\mu_0^{(0)} = 0$.

If $P_\infty \neq 0$, local perturbation theory[15] tells us that all the μ_m will be displaced in the same direction relative to the $\mu_m^{(0)}$. When $P_\infty > 0$, we have $\mu_m > \mu_m^{(0)}$. If $\mu_0 \ll \mu_1$, it follows from (3) that for $t > 1/\mu_1$, the distribution function decreases exponentially, which corresponds to dissociation. Then μ_0 is the dissociation rate, and μ_1 is the vibrational relaxation rate. Calculation shows that in most cases $\mu_0 \ll \mu_1$.

Under these conditions the lowest eigenvalue of B can be found by expanding the corresponding determinant in powers of μ, and keeping only the first two terms.

Calculation gives

$$\mu_0 = z \left/ \left[\sum_{j=0}^{n} \exp(-E_j/kT) \sum_{s=j}^{n+1} \exp(E_s/kT) \middle/ P_{s,s-1} \right] \right. . \tag{4}$$

The second sum in the brackets does not significantly depend on the lower limit, since the terms increase greatly as s is increased. We can therefore change the order of summation in (4), and the lower limit in the sum over s can be changed to unity. Then the sum over j becomes equal to the sum over the vibrational states Q of the molecule AB. Bearing in mind that the equilibrium distribution function is given by

$$x^{(0)} = \exp(-E_n/kT)/Q,$$

Eq.(4) can be rewritten in the form

$$\mu_0 = z \left/ \left[1/x_n^{(0)} P_\infty + \sum_{k=1}^{n} 1/x_k^{(0)} P_{k,k-1} \right] \right. . \tag{5}$$

It is easy to show that the sum in (5) is determined essentially by a few of its largest terms. The first term in the brackets is small compared to the sum, since the probability for transition to a continuum state is much greater than the probability for vibrational transitions.[16,17] On the other hand, as $E \to 0$, the terms of the sum decrease as $\exp(E/kT)$. The largest terms of the sum correspond to the transition region between adiabatic and nonadiabatic collisions, i.e., they are given by the relation

$$E_{k,k-1}/\hbar\alpha\bar{v} \approx 1, \tag{6}$$

where α^{-1} is the effective range of the exchange forces, and $\bar{v}$ is the mean thermal velocity of the colliding molecules. Recalling that α is related to the fundamental frequency of a diatomic molecule by

$$\omega_0 \approx \alpha \sqrt{2D/m},$$

where m denotes the reduced mass of AB, we may rewrite (6) in the form

$$E_{k,k-1} \approx \hbar\omega_0 \sqrt{\frac{kT}{D}}$$

(assuming that the ratio of the reduced mass of AB to the reduced mass of the colliding molecules is close to unity). Under nonadiabatic conditions, the probability for the corresponding single-quantum transition is of the order of one.

It is easily shown that no great importance should be attached to our earlier assumption that only single-quantum transitions take place and that dissociation is possible only from the highest lying level. Indeed, this assumption will be invalid only if $E_{k,k-1}/\hbar\alpha\bar{v} \leqslant 1$, and this is possible only in an energy interval of the order of kT about the dissociation cutoff. This, in turn, can lead to an ambiguity of the same order of magnitude in the effective dissociation energy and to a small ambiguity in the dissociation rate constant.

Replacing the sum in (5) by an integral, we now have

$$\mu_0 = \frac{Z\frac{\hbar\alpha\bar{v}}{kT}\exp(-D/kT)}{Q} \approx \frac{Z\frac{\hbar\omega_0}{\sqrt{DkT}}\exp(-D/kT)}{Q}. \qquad (7)$$

The dissociation rate K_d is equal to μ_0 averaged over all the rotational and electron states of AB, namely,

$$K_d = g_e \int \mu_0 (D_{\text{ef}}) \exp(-\mathscr{E}_{\text{ro}}/kT)\, d\mathscr{E}_{\text{ro}}/kT = \frac{g_e g_{\text{ro}} Z\frac{\hbar\alpha\bar{v}}{kT}\exp(-D/kT)}{Q}, \qquad (8)$$

where D_{ef} is the effective dissociation energy of the rotating AB molecule. Because of centrugal forces, D_{ef} is smaller than D. When we integrate (8) we obtain an additional term multiplying the exponential ($g_e g_{\text{ro}} > 1$; the first term is due to the increased electron statistical weight of the excited vibrational level).

The nonequilibrium distribution function corresponding to exponential dissociation is given by the first eigenvector $l_n(\mu_0)$ of B. The $l_n(\mu_0)$ are easily found using the general relations for the eigenvectors of Jacobian matrices, since the expression for μ_0 is known. We will not go into this question at this time. We note only that the percent depopulation of the upper vibrational level proves to be of the order of

$$\exp[(D - E_p)/kT],$$

where p is the number of the vibrational level, reckoning from the dissociation cutoff. This result agrees, in particular, with earlier results for a dissociating harmonic oscillator.[9,13]

Since in the actual case of an anharmonic oscillator the vibrational energy spacing in the neighborhood of dissociation cutoff is small compared to kT, many levels are comprised in the region of significant depopulation. One may therefore say that in a dissociation reaction the distribution is highly "non-Boltzmann". For a harmonic oscillator, on the other hand, the opposite conclusion follows if $\hbar\omega_0 / kT \gg 1$.

Let us consider, for instance, the dissociation of bromine in the reaction

$$Br_2 + A \rightarrow Br + Br + A .$$

Calculation of g_{ro} and integration of (8) gives $g_{ro} \approx 7$. Owing to centrifugal expansion of the Br_2 molecule the collision rate of a vibrationally excited molecule may be some 2-4 times greater than the gas-kinetic collision rate Z_0. Further, the statistical weight of the stable electronic states converging towards the dissociation cutoff D is 5.[1] Thus an evaluation of K_d from (8) for the condition $\hbar\omega_0 / kT \ll 1$ gives

$$K_d \approx 5 \cdot 10^{-2} Z_0 (D / kT)^{3/2} \exp(-D / kT). \qquad (9)$$

Hence for $T = 2000^{\circ}K$, and setting $Z_0 = 4.35 \cdot 10^{12} T^{1/2}$ cm^3 mole^{-1} sec^{-1}, we arrive at

$$K_d = 4 \cdot 10^{14} \exp(-D / kT);$$

the experimental value of the rate constant at this temperature[18] is $K_d = 5 \cdot 10^{14} \exp(-D/kT)$.

At other temperatures (1000 to 1500°K) the agreement between the experimental and theoretical values of K_d is also satisfactory. Similar results are obtained also for the dissociation of iodine and hydrogen in an argon atmosphere.[19,20]

Since dissociation is a complex stochastic process of successive vibrational excitation of the AB molecules, followed by their dissociation, the breakdown of the Boltzmann distribution reduces K_d compared to its equilibrium value $(K_d)_{equi} = K K_{rec}$ where K is the equilibrium constant of reaction (1).[8] The recombination constant K_{rec} should be about equal for the nonequilibrium and equilibrium processes, since the recombination rate is determined essentially by the transition rate of two colliding atoms from a continuum state to one of the high-lying vibrational levels of the bound state. According to Willard (as cited by Palmer & Hornig[18]), the value of $(K_d)_{equi}$ for dissociation of Br_2 at T = 300° is about equal to $10^{16} \exp(-D / kT)$; the value of K_d according to (9) is about $10^{15} \exp(-D/kT)$, i.e., approximately one tenth the equilibrium value. This difference is therefore connected with breakdown of the vibrational equilibrium distribution of the Br_2 molecule in the initial stage of the dissociation.

Several authors[1,21] have remarked on the high value of the factor multiplying the exponential in the expression for $(K_d)_{equi}$ for diatomic molecules as compared to Z_0. This divergence is due,

on the one hand, to the same factors that make $(K_d)_{equi}$ greater than K_d. There are two such factors: the high (equilibrium) population of the upper vibrational levels, and long-range forces. The last follows from the work of Russell and Simons,[22] who found the dependence of K_{rec} (and therefore also of $(K_d)_{equi}$) on the strength of the van der Waals interaction between the molecule M and the recombining atoms. The long-range forces, however, do not affect K_d, since they are of importance only for transitions from the highest vibrational levels to the continuum, which means that these forces have no effect on the rate of the most rapid stage of the dissociation process. On the other hand, the increase over Z_0 of the factor multiplying the exponential in the expression for $(K_d)_{equi}$ is favored by the factors we have treated above, namely, rotation of the dissociating molecule, the presence of several stable electronic states, and some increase in the diameter of the vibrationally excited molecule.

It follows from all the above that (K_d) depends on the concentration of the reaction products, although it is usually defined as a real constant. This means that the ordinary kinetic equation

$$-\frac{d}{dt}[AB] = K_d[AB][M] - K_{rec}[A][B][M] \qquad (10)$$

for a dissociation and recombination process is invalid over the entire interval of variation in the concentrations of A, B and M inasmuch as it does not take into account the difference between K_d and $(K_d)_{equi}$.

Institute of Chemical Physics,
Academy of Sciences of the USSR

References

1. O.K.Rice, J.Chem.Phys., 9, 259 (1941).
2. O.K.Rice, Ibid., 21, 750 (1953).
3. G.Careri, Nuovo Cimento, 6, 94 (1949).
4. G.Careri, Ibid., 7, 155 (1950).
5. G.Careri, J.Chem.Phys., 21, 749 (1953).
6. J.C.McCoubrey & M.D.McGrath, Quart.Rev., 11, 87 (1957).
7. E.E.Nikitin & N.D.Sokolov, J.Chem.Phys., 31,1371 (1959).
8. E.E.Nikitin & N.D.Sokolov, Doklady AN SSSR, 124, 366 (1959).(Trans. Doklady.)
9. E.E.Nikitin, Ibid., 116, 584 (1957).(Trans. Ibid.)
10. E.E.Nikitin, Ibid., 119, 526 (1958).(Trans. Ibid.)
11. E.E.Nikitin, Zhur.fiz.khim., 33, 572 (1959).
12. K.E.Shuler, Seventh International Symposium on Combustion, 1958.
13. E.W.Montroll & K.E.Shuler, Advances Chem.Phys.1,361 (1958).
14. S.K.Kim, J.Chem.Phys., 28, 1057 (1958).
15. I.M.Lifshits, Zhur.eksp.i teor.fiz., 17, 1017 (1947).
16. E.E.Nikitin, Thesis, Inst. of Chem.Physics, 1958.
17. A.I.Osipov, Vestnik, Moscow State Univ., 4, 97 (1958).
18. H.B.Palmer & D.F.Hornig, J.Chem.Phys., 26, 98 (1957).
19. D.Britton, N.Davidson & G.Schott, Disc.Far.Soc.,17, 58 (1954).

20. M.Camae and others, Chemical Relaxation in Air, Oxygen and Nitrogen, Preprint No.802, Inst. Aeron. Sci., 1958.
21. N.N.Semenov, O nekotorykh problemakh khimicheskoi kinetiki i reaktsionnoi sposobnosti (Regarding certain problems of chemical kinetics and reactivity), M., 1954.
22. K.Russell & J.Simons, Proc.Roy.Soc.A, 217, 271 (1953).

ELEMENTARY PROCESSES INVOLVED IN COLLISIONS BETWEEN SLOW IONS AND MOLECULES

- V. L. Tal'roze

Collisions of slow ions with molecules are the principal form of ionic encounters leading to chemical conversions in plasmas and substances subjected to radioactive radiation. The principal forms of such conversion are transfer of charge (charge exchange) and transfer of heavy particles. The basic technique for investigating these elementary processes is the mass spectroscopic procedure.

Systematic investigations of transitions of heavy particles were carried out in our laboratory[1] and by Schissler & Stevenson[2] and Field et al[3] in the U.S.A. For the purpose of investigating such ion-molecule reactions there was developed in our laboratory a mass spectrometer with a highly monoenergetic electron beam.[4] The secondary ions - the reaction product - were identified from the appearance potentials and from the variation of the ratio of the secondary and primary ion currents as a function of the pressure in the region of ionization. There was developed a pulse method for determining the reaction rate constants: ionization with a microsecond electron pulse, variation of the reaction period, and a short ion extraction pulse.[5]

Specifically, we investigated processes of the type

$$H_2^+ + H_2 = H_3^+ + H,$$

or in general

$$RH^+ + M = R + MH^+ \text{ - transition of a proton}$$

and

$$RH + M^+ = R + MH^+ \text{ - transition of an H atom.}$$

The last process was also investigated by Schissler & Stevenson[2] and Field et al[3]. In addition, Schissler & Stevenson detected processes of the type

$$CH_3^+ + CH_4 = C_2H_5^+ + H_2 \text{ - synthesis of a C—C bond,}$$

and recently Field & Lampe[6] observed a process of the type

$$R^+ + R_1H = RH + R_1^+ \text{ - transition of an } H^- \text{ ion.}$$

It is evident from the results of all these investigations that the above-mentioned and similar processes do not require an activation energy and their cross section, when they are exothermic, is of the order of magnitude of the gas kinetic cross section or even somewhat larger.

However, the inference regarding the absence of an activation energy cannot be extended to all ion-molecular reactions with tran-

sition of heavy particles, particularly to reactions which involve complex rearrangement of double or triple bonds. Thus, for example, Pshezhetskii & Dmitriev[7] showed that the reaction

$$N_2^+ + O_2 = NO^+ + NO,$$

being exothermic, requires an activation energy of ~7 kcal/mole. And actually, as our experiments showed, this reaction is not observable under mass spectrometer conditions where secondary processes with a cross section less than 10^{-19} cm are virtually undetectable.

Of particular interest is the question of the intimate mechanism of the elementary event in such processes. Our experiments showed that there is pronounced anisotropy in the velocity distribution of the products of ion-molecular reactions (preferentially forward). On the other hand, careful measurements (sensitivity up to 10^{-3} ev) of the kinetic energy of the reaction products showed that in the case of the reactions

$$H_2O^+ + H_2O = H_3O^+ + OH,$$

$$NH_3^+ + NH_3 = NH_4^+ + NH_2,$$

$$H_2^+ + H_2O = H_3O^+ + H$$

and

$$H_2^+ + H_2 = H_3^+ + H,$$

the energy released as the result of the process initially remains in the form of excitation of the product particles, and only an insignificant fraction of it is converted to kinetic energy. These results indicate that in the course of the elementary event there is formed an intermediate particle; hence one can only formally characterize the process as we did above, i.e., call it "transition" of a proton or hydrogen atom. It was shown, for example, that in the case of the endoergic reaction

$$C_2H_4^+ + C_2H_4 = C_2H_5^+ + C_2H_3 - 0.3 \text{ ev}$$

the kinetic energy of the primary ion (up to 15 ev) does not allow of overcoming the barrier due to the endoergic nature of the reaction and attaining a reaction cross section detectable in a mass spectrometer.

The other line of research in our work was investigation of the second type of conversions occurring in encounters of ions with molecules, namely, charge exchange processes. Whereas there have been many investigations of charge exchange of atomic ions in encounters with atoms and diatomic molecules, the only thorough study of charge exchange of ions with polyatomic molecules is that reported by Lindholm[8]. He investigated the charge exchange of atomic ions with relatively simple molecules (H_2O, N_2O, CO_2, NH_3, H_2S and CH_4) and observed the processes of nondissociative charge exchange, for example,

$$F^+ + H_2O = F + OH^+ + H + q, \qquad (I)$$

where q is the thermal effect or heat of the process.

The basic postulate from the standpoint of which Lindholm treats all his results is that decisive as regards the cross section for the process is its degree of "resonance", i.e., in cases when q is zero or somewhat greater than zero, there is observed a large cross section; it is understood that q includes the energy of metastable excitation of the incident ion. Inasmuch as, for example, the F^+ ion in reaction (I) is excited, there is evinced a large cross section for the process of dissociative charge exchange for which there is required an energy of 18.7 ev, i.e., an energy close to the energy of recombination of the metastable excited F^+ ion (20.1 ev).

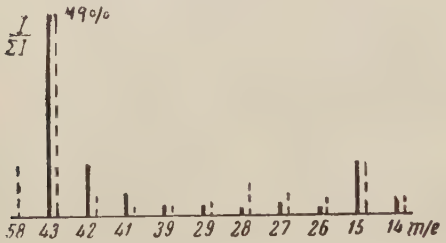

Fig.1. Mass spectra of acetone obtained for charge exchange of ~500 ev Xe^+ ions (solid lines) and ionization by 60 ev electrons (dashed lines).

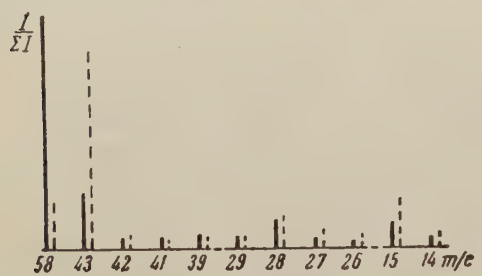

Fig.2. Mass spectra of acetone obtained for charge exchange of ~500 ev CH_3^+ ions (from acetone) and ionization by 60 ev electrons (dashed lines).

According to Lindholm, conversion of the kinetic energy of the incident ion to internal energy in such processes (at the 500 ev ion energy used in Lindholm's experiments) plays no significant role; in other words, in such systems one can justifiably speak of rigorous fulfillment of Massey's adiabatic criterion.

We investigated a large number of charge exchange processes involved in the interaction of atomic and intermolecular ions with simple and complex molecules in the incident ion energy range from 10 to 10^3 ev. These experiments were carried out in the special double mass spectrometer described in Ref.9 with detection of the secondary ions by means of a secondary-electron multiplier.

The primary ions were obtained by bombardment of the appropriate gas with 20 to 80 ev electrons in an "ion gun" at gas pressures of 10^{-5}-10^{-4} mm Hg. The gas pressure in the charge exchange chamber was 10^{-5}-10^{-4} mm Hg.

It was found that charge exchange processes involving polyatomic molecules lead to a large number of different modes of dissociative ionization. By way of illustration in Fig.1 we show the mass spectrum obtained for charge exchange of 500 ev Xe^+ ions with acetone molecules (the intensity of the individual lines has been normalized to the integral intensity of all the lines). The total cross section for charge exchange according to our measurements is four times smaller than the cross section for resonance charge exchange of A^+ ions in argon at the same energy.

By appropriate choice of the primary ions one can eliminate a number of modes of dissociation and obtain a charge exchange mass spectrum in which many lines of fragmentary ions are weakened compared to the mass spectrum obtained by conventional bombardment with

electrons (with an energy of some tens of electron-volts or higher - Fig.2). The fundamental fact that we want to emphasize here is that in the usual charge exchange mass spectrogram there are present lines associated with fragmentary ions, which should not be observed if it is assumed that the incident ion is not excited and the kinetic energy of the ion is not converted into energy of the process. Thus, for example, the elementary process

$$Xe^+ + C_2H_4 = Xe + CH_2^+ + CH_2 \qquad (II)$$

should require for its realization an energy of 7 ev, if it is assumed that the incident ion is not excited. Yet in actual fact in the charge exchange mass spectrum for C_2H_4 obtained for an incident ion energy of 250 ev (Fig.3), there is evident an intense line at *m/e* = 14, i.e., associated with the fragmentary CH_2^+ ion.*

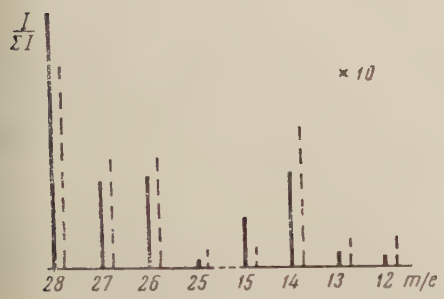

Fig.3. Mass spectra of ethylene obtained for charge exchange of 250 ev Xe^+ ions (solid lines) and ionization by 60 ev electrons (dashed lines).

Assuming that the kinetic energy in the given energy range cannot lead to realization of so strongly endothermic a process with an appreciable cross section, it could be hypothesized that the appearance of the fragmentary ions is indicative of the presence in the incident beam of ions with an appreciable metastable excitation. However, judging from the data of Lindholm for ions of inert gases obtained by electron bombardment, metastable excitation cannot be significant. This and other facts led us to consider a different possible cause of such endoergic processes and to investigate experimentally the role of conversion of kinetic energy in charge exchange involving not very fast ions in encounters with polyatomic molecules. It was found that in contrast to the case of charge exchange in encounters with atoms and simple molecules, such energy conversion plays a very significant role even in the case of very slow ions and can lead to realization of charge exchange processes with an appreciable cross section even close to the threshold determined simply by the laws of conservation of energy and momentum.

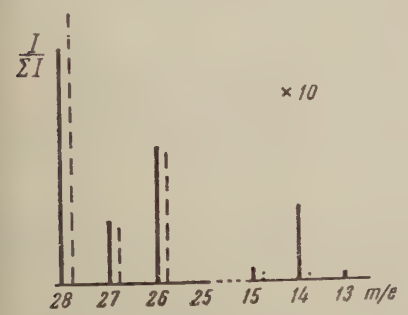

Fig.4. Mass spectra of ethylene obtained for charge exchange of Xe^+ ions with an energy of 70 ev (solid line) and 40 ev (dashed line).

This can be illustrated by the results of our investigation of charge exchange of Xe^+ in ethylene. Fig.4 shows the mass spectra of C_2H_4 obtained for charge exchange of Xe^+ ions with energies of 70 and 40 ev. It will be evident that with decrease of the kinetic energy the relative intensity of the *m/e* = 14 line is sharply reduced, i.e., the intensity of this line falls virtually to zero at ion energies below

---

*The total charge exchange cross section for $Xe^+ + C_2H_4$ proved to be eight times smaller than the cross section for $A^+ + A$.

70 ev. Consequently, process (II) occurs primarily at the expense of the kinetic energy of the Xe ions.

Thus conversion of kinetic energy into energy of the process can play a significant role in charge exchange of ions interacting with complex molecules. On the other hand, the "resonance factor" also remains significant. An example of the influence of this factor is furnished by the investigations of Lindholm of charge exchange of A^+ ions in methane; in the resultant mass spectrum the line corresponding to CH_4^+ ions is virtually absent, while the lines identified with the fragmentary CH_3^+ and CH_2^+ ions have an appreciable intensity. However, as our experiments show, with increase in complexity of the molecule, the role of the "resonance factor" becomes weaker and together with intense lines associated with resonance (dissociative or nondissociative) charge exchange, there appear in the spectrum intense lines of ions for the formation of which there is sufficient energy. This circumstance makes it possible to utilize the charge exchange mass spectrum of complex molecules for determining the presence of metastable excitation of the incident ions (from the appearance potentials of fragmentary ions knows from the data on electron impact*). In doing so, however, one must bear in mind what has been said above regarding the kinetic energy in the processes in question and the consequent necessity of checking the data using primary ions with an energy below the threshold value.

Worthy of attention from the theoretical standpoint is the question of difficulty or ease of conversion of the kinetic energy of the incident ion into energy of the charge exchange process in the case of complex molecules and the weakening of the "resonance factor" in such cases. Both these effects are apparently connected with increase in the number of intersecting and overlapping energy levels with increase in complexity of the molecule. The closest analogs to these effects in the field of optical spectroscopy is the transition from line spectra characteristic of atoms to the band spectra of simple molecules and the broad absorption peaks exhibited by complex molecules.

Of particular interest for future investigation are cases when there are possible from the energy standpoint both charge exchange processes and processes involving transition of a heavy particle. The question of the ratio of the cross sections for these processes is of exceptional importance in the fields of the chemistry of electric discharges and plasma physics.

The following participated in the investigations described in the present report: E.L.Frankevich (transitions of heavy particles), G.K. Lavrovskaya, M.I.Markin (charge exchange processes), L.L.Dekabrun, G.D.Tantsyrev and A.K.Lyubimova (development of the experimental apparatus).

Institute of Chemical Physics
Academy of Sciences of the USSR

---

*Data on the excitation of an incident molecular ion can sometimes be obtained by investigating the impact dissociation of this ion in encounters with neutral particles. The role of excitation in processes of this type was first discovered by Tunitskii et al[10].

References

1. V.L.Tal'roze & E.L.Frankevich, Trudy I Vses. soveshchaniya po radiatsionnoi khimii (Transactions of the First All-Union Conference on Radiation Chemistry) M., 1957; V.L.Tal'roze & A.K.Lyubimova, Doklady AN SSSR, 86, 909 (1952).

2. D.O.Schissler & D.P.Stevenson, J.Chem.Phys., 23, 1353 (1955); Ibid., 24, 926 (1956); Ibid., 29, 282 (1958).

3. F.H.Field, J.L.Franklin & F.W.Lampe, J.Amer.Chem.Soc., 79, 2419, 6132 (1957).

4. E.L.Frankevich & V.L.Tal'roze, PTE (Instruments & Experimental Techniques), No.2, 48 (1957).

5. V.L.Tal'roze & E.L.Frankevich, Izv.AN SSSR,Ser.khim., No.7, 1351 (1959).

6. F.H.Field & F.W.Lampe, J.Amer.Chem.Soc., 80, 5587 (1958).

7. S.Ya.Pshezhetskii & M.T.Dmitriev, Deistvie ioniziruyushchikh izluchenii na neorganicheskie i organicheskie sistemy (Action of ionizing radiations on inorganic and organic systems), M., 1958.

8. E.Lindholm, Z.Naturforsch., 9a, 535 (1954).

9. V.L.Tal'roze, L.L.Dekabrun, E.L.Frankevich, G.D.Tantsyrev, O.D.Vetrov, A.K.Lyubimova, G.K.Lavrovskaya, V.D.Grishin, V.E.Skurat & A.Ya.Yukhvidin, PTE, No.6 (1960).(Trans. Instruments & Experimental Techniques.)

10. N.N.Tunitskii, R.M.Smirnova & M.V.Tikhomirov, Doklady AN SSSR, 102, 1083 (1955); M.V.Tikhomirov, M.V.Kolotyrkin & N.N. Tunitskii, Ibid., 102, 903 (1955). (Trans. Doklady.)

INVESTIGATION OF ELECTRON LOSS DUE TO SCATTERING BY THE RESIDUAL GAS IN AN ACCELERATOR CHAMBER

- A.G.Vlasov, A.A.Vorob'ev, A.N.Kislov & R.P.Meshcheryakov

Introduction

It is a known fact that the efficiency of cyclic accelerators depends greatly on the residual gas pressure in the vacuum chamber.[1] The rapid decrease in radiation intensity observed with increase of pressure in the chamber is evidence of the large number of accelerated particles lost owing to scattering by the residual gas. In designing cyclic accelerators one must take this loss into account in specifying the dimensions of the vacuum chamber. Extant methods of calculating the loss of accelerated particles yield extremely divergent results (by as much as 2 orders of magnitude). The purpose of the present work, accordingly, was experimental verification of the theoretical calculations of the scattering loss in the residual gas with a view to determining the best method of calculating the loss.

Methods of calculating the loss and comparison of computed results

Collisions of the accelerated electrons with the molecules and atoms of the residual gas in the accelerator chamber lead to an increase in the amplitude of the betatron oscillations. Despite the damping of the betatron oscillations in the process of acceleration, their amplitude owing to scattering of electrons by the residual gas may increase to half the aperture of the vacuum chamber, which leads to loss of electrons at the injector anode and chamber walls. In considering the excitation of the betatron oscillations owing to electron collisions with the molecules and atoms of the residual gas one must take into account elastic and inelastic collisions, single and multiple scattering and the damping of the oscillations in the process of acceleration.

Thus calculation of the electron loss owing to scattering by the residual gas involves two groups of problems: first, problems connected with the process of electron scattering by the molecules and atoms of the residual gas, with determination of the scattering cross sections, the angular distribution of the scattered electrons, etc., and second, problems connected with the dynamics of electron motion in the accelerator.

The most important results of calculations and experiments devoted to problems in the first category will be found in the monographs listed under Refs.2 & 4. A number of authors[5-12] have also considered the dynamics of the particle motion, taking into account scattering and loss of the accelerated particles owing to scattering.

Here we shall consider only the final results of calculations of the electron loss owing to scattering by the method proposed by Blachman & Courant[4,5], Greenberg & Berlin[7,8] and Matveev[9,10].

Blachman & Courant[5] in calculating the proton loss took into account only multiple scattering and deduced a formula for calculating the allowable pressure in the vacuum chamber for a given percent loss

Blachman & Courant took into account the damping of the betatron oscillations by introducing the coefficient 1/2.

Thus according to Blachman & Courant the air pressure in mm Hg in the accelerator chamber at a temperature of 300°K equals

$$p = 0.667 n E_j eV \cdot \eta \frac{b_2^2}{R_0^3}, \qquad (1)$$

where n is the index of the fall off of magnetic field with radius, E_j is the injection energy in kev, eV is the energy acquired by the accelerated particles per revolution in kev, b_2 is the half-height of the chamber in cm, R_0 is the radius of the equilibrium orbit in cm, and η is a coefficient taking into account the specified loss in percent: for 10% loss $\eta = 0.089$, and for 50% loss $\eta = 0.2$.

In using this equation for evaluating the electron loss one must introduce a correction coefficient of 1/4, inasmuch as this expression does not take into account single and inelastic scattering. Obviously, evaluation of the electron loss by means of this formula is only approximate.

The method of calculation proposed by Greenberg & Berlin[7,8] takes into account elastic and inelastic collisions, single and multiple scattering and damping of the betatron oscillations. In their publications these authors do not give a final formula for calculating the loss at a given pressure, but do give the upper and lower bounds. Obviously, the upper bound must be an overestimate, the lower bound an underestimate, so that intermediate values determined by this method should be closest to the actual loss. Curves given by these authors can be used for determining the loss in an accelerator chamber at any given pressure.

In deducing his computation formulas Matveev took into account damping of the betatron oscillations and not only the vertical but also the radial betatron oscillations. In view of the cumbersome nature of the calculations by the Matveev method (numerical calculations are possible only by means of a computer) for our evaluations we used the curves given by Matveev in Ref.10.

The results of numerical calculations of the particle loss due to scattering for a number of accelerators by the methods of the cited authors are compared in the accompanying table.

In column 9 we list the values of the pressure calculated according to Eq.(1) for a 10% particle loss. In columns 10 through 14 we give the values of the pressure calculated by the method of Greenberg & Berlin allowing for 10% loss; here the indices δ and w denote the initial particle distributions over betatron oscillation energies (in the δ distribution all the particles after injection are assumed to be in the equilibrium orbit; the w distribution is homogeneous, i.e., the particles after injection uniformly fill the entire chamber). The δ distribution leads to an overestimate of the allowable pressure inasmuch as the calculated loss in this case is smaller than the actual loss, while in the case of the w distribution the calculated pressure values are underestimates. The superscripts ^{u,i} and ^{l} denote the upper bound, the intermediate value and the lower bound for the losses, respectively. Columns 15 & 16 give the pressures calculated for a 10% particle loss by the method of Matveev.

Analysis of the results given in the table leads to the following deductions.

Comparison of the results of calculations of scattering of the accelerated particles (electrons and protons) by the residual gas according to three methods of calculation

Accelerator	Location	Energy, Mev	R_0, cm	$2b$, cm	E_j, kev	eV, ev	$A = \frac{b}{R_0}$	Pressure p in mm Hg for 10% loss							
								Blachman & Courant	Acc. to Greenberg & Berlin					Matveev	
									P_δ^u	P_δ^i	P_δ^l	P_w^u	P_w^i	P_δ	P_w
1	2	3	4	5	6	7	8	9	10	11	12	13	14	15	16
Electrons															
Betatron	Tomsk Polytechnic	15	13,5	5,6	30	13,5	0,207	40	1,35	3,4	9,8	0,13	0,24	2,1	0,18
		25	21	5,9	40	36,5	0,14	58	1,8	4,5	13	0,18	0,32	3	0,25
Synchrotron	Cornell	300	100	—	80	1500	—	3,7	0,22*	0,62*	2*	0,021*	0,04*	0,45	0,023
Protons															
Synchrotron	Berkeley	300	100	—	80	1500	—	3,7	0,22*	0,62*	2*	0,021*	0,04*	0,45	0,023
	Birmingham	1300	450	10	2000	200	0,0111	7*	0,68*	1,4*	6,2*	0,04*	0,07*	0,82	0,05
		1300	450	10	500	200	0,0111	1,75	0,17	0,35	1,55	0,01*	0,0175	0,2	0,01
	Brookhaven	3000	915	16,3	10^3	1150	0,00884	11*	1,7*	3,6*	16,1*	0,09*	0,19*	2,0	0,12
		10^4	2400	20	$4 \cdot 10^3$	$5 \cdot 10^3$	0,00417	6,5*	0,77*	1,8*	8,7*	0,04*	0,1*	1,2	0,06

*The values identified by asterisks are taken from Refs. 5 & 8; the other values are calculated according to the formulas by the cited authors.

1. Calculations by the method of Blachman & Courant give the highest pressure values for which the particle loss does not exceed 10%, which means that the losses are not fully taken into account by this method of calculation.

2. Lower pressure values for 10% loss are given by calculations by the method of Greenberg & Berlin (intermediate loss values) and by the method of Matveev. The method of Greenberg & Berlin gives pressure values 1.5-1.7 times higher than Matveev's computations. This can be explained by the fact that Greenberg & Berlin did not take into account the loss due to radial oscillations (they treated the two dimensional problem while Matveev formulated the problem in four dimensional phase space).

3. It will also be evident that there is an appreciable divergence (1-2 orders of magnitude) between the results of calculations by the different methods. This shows the importance of experimental verification of the theoretical results.

Experimental procedure and apparatus

In the process of injection a large number of electrons is introduced into the chamber. During the period of acceleration, particularly immediately after injection, there is a large output of electrons owing to acceleration due to collisions with the walls of the chamber and with the injector anode; these collisions are due primarily to betatron and radial-phase oscillations of large amplitude. The best way to obtain data on electron scattering by the gas is to measure the distribution of the radiation from some section of the accelerator wall (i.e., the radiation due to electrons leaving the accelerator) during the entire period of acceleration and to vary the chamber pressure or fill the chamber with different gases, leaving all the other parameters constant. Choice of this procedure is dictated by the fact that it is impossible to install detectors for the scattered electrons directly in the chamber of an operating accelerator, since such extraneous counters would disturb the operation of the accelerator.

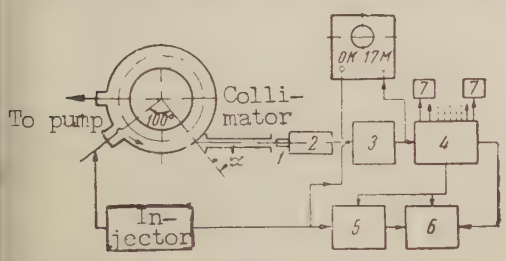

Fig.1. Block diagram of the equipment for measuring the radiation from a given section of the chamber wall.

The most suitable detector for the radiation from the chamber wall is a scintillation counter inasmuch as other forms of counters either have an excessively long pulse time (Geiger counters) or yield an average current (ionization chambers). By using scintillators with a decay time of the order of 0.1-0.2 μsec one can count the number of emitted photons with a fair degree of precision.

A block diagram of our experimental set-up is shown in Fig.1. The scintillator 1 is coupled by a suitable light pipe to an FEU-19M type photomultiplier 2. The scintillator is aimed at the selected section of the chamber wall by means of the collimator. The scintillator, light pipe and photomultiplier are shielded with lead to minimize the influence of extraneous radiation. A photon from the chamber wall produces a flash in the scintillator, which is detected by the photo-

multiplier. The pulse from the photomultiplier is fed into a wide band amplifier; the pulse from the amplifier goes to the "Kashtan" type discriminator 3; the signal from the discriminator is fed into the 16-channel time analyzer consisting of an oscillator 5, a divider 6 and a matrix 4. Our time analyzer was similar to that described by Belyavskii[13] but had a resolving time of 0.2 μsec. The pulses from each channel of the time analyzer are counted and registered by PS-10 000 type scalers 7. The operating time of each channel is controlled by the divider and can be varied from 2 μsec to several minutes. We used channel times of 16, 32, 64 and 256 μsec.

Results of measurement and comparison with calculated values

The measurements were carried out on the 15 Mev betatron of the Tomsk Polytechnic Institute. To find the best section of the chamber wall for the radiation measurements, we measured the distribution of the radiation over a period of acceleration around the periphery of the accelerator in the plane of the orbit. The tests showed that one can carry out measurement at azimuthal angles from 90 to 360° (reckoning from the position of the injector). In the 0 to 90° azimuth range there is a large amount of radiation produced by electrons from the injector that have not completed even one revolution. Accordingly, for our experiment we settled on the section of the chamber located at an azimuth of 100°. It was found that the radiation from the section of the chamber wall (the section defined by the collimator equals about 1 cm^2) depends on the angle α of the collimator relative to the chamber radius at that point (see Fig.1).

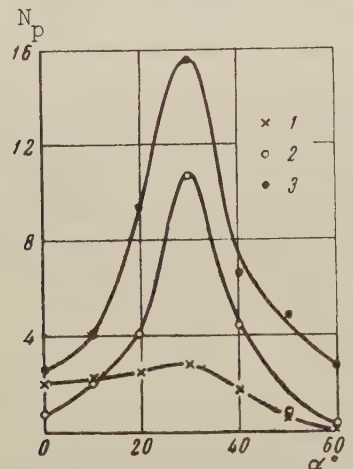

Fig.2. Angular distribution of the radiation in the process of acceleration in the 15 Mev betatron - 80 (1), 270 (2), and 1180 (3) μsec after injection.

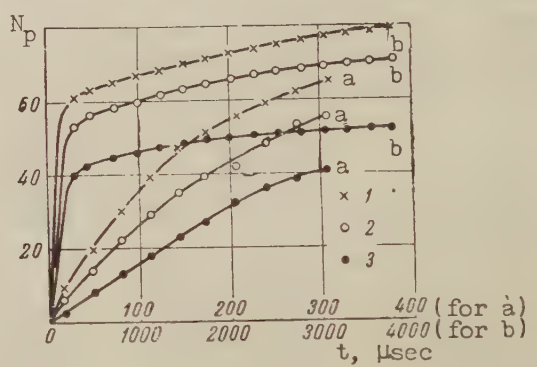

Fig.3. Variation in the radiation from the 100° azimuth section of the chamber wall as a function of the acceleration time with the chamber filled with air at pressures of 1) $1 \cdot 10^{-5}$, 2) $1 \cdot 10^{-6}$, and 3) $5 \cdot 10^{-7}$ mm Hg.

The measured angular distribution of the radiation is shown in Fig.2. For subsequent measurements we chose $\alpha = 30°$.

Fig.3 shows the variation of the radiation intensity (number of photons) as a function of the acceleration time with the chamber

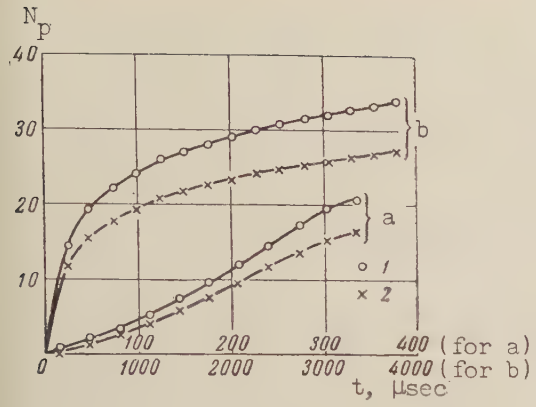

Fig.4. Variation of the radiation from the 100° azimuth section of the chamber wall as a function of the acceleration time with the chamber filled with helium (1) & hydrogen (2). Pressure $1 \cdot 10^{-6}$ mm Hg.

filled with air at different pressures. The dependences are plotted taking into account the variation of the electron energy in the process of acceleration.

Fig.4 shows the variation of the radiation intensity with the acceleration time with the chamber filled with helium and hydrogen at a pressure of 10^{-6} mm Hg. Prior to filling of the chamber with helium and hydrogen it was thrice purged with the given gas and evacuated to $5 \cdot 10^{-7}$ mm Hg, which assured a gas purity of 90 to 95%.

The character of the curves in Fig.4 shows that the radiation and, consequently, the scattering in the chamber filled with helium occurs more slowly than in the chamber filled with air and still more slowly when the chamber is filled with hydrogen. Similar results should be yielded by theoretical calculations (these were not carried out for the 15 Mev betatron) inasmuch as the atomic number Z enters into the formula for the cross section so that the scattering must decrease with decrease of Z.

In order to obtain a quantitative picture we carried out measurements of the orbital current in the accelerator and its decrease in the process of acceleration. The measurement procedure was similar to that described in Refs. 14 & 15. These measurements showed that at the

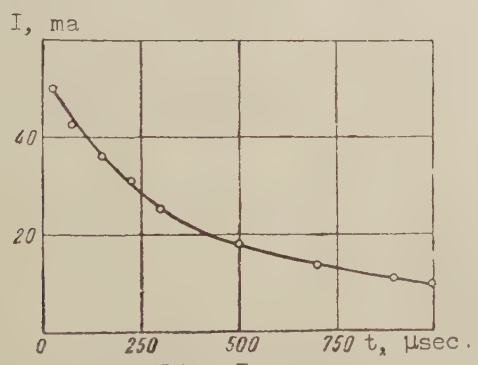

Fig.5

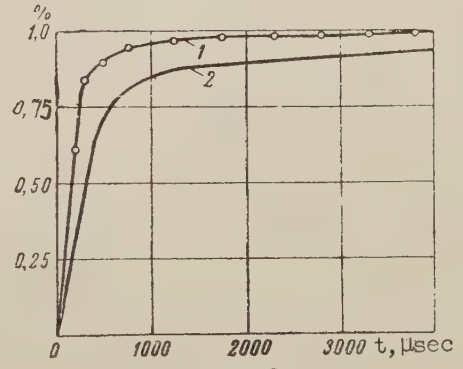

Fig.6

Fig.5. Variation of the orbital current in the 15 Mev betatron as a function of the acceleration time. Current pulse duration - 4 μsec.

Fig.6. Output (1) of electrons from the accelerator and electron loss (2) calculated theoretically as a function of the acceleration time at a pressure of 10^{-6} mm Hg with the 15 Mev betatron chamber filled with air.

beginning of acceleration the number of electrons in the equilibrium orbit is $(7-8) \cdot 10^{11}$. Fig.5 shows the variation in the orbital current as a function of the acceleration time to 1000 μsec. Further decrease of the orbital current occurs very slowly and we were unable to measure it with adequate accuracy. Evaluation based on the yield of hard

gammas from a tungsten target gives a value of 10^8 electrons for the period of acceleration.

Fig.6 shows the variation of the yield of electrons with the accelerating time with the 15 Mev betatron chamber filled with air; this dependence was obtained from the experimental data (Fig.3), taking into account the variation of the orbital current during the acceleration period (Fig.5). The percentages are referred to the current carried in the accelerator. In Fig.6 we also show the theoretical variation of the electron loss due to scattering in gas at a pressure of 10^{-6} mm Hg calculated by the method of Greenberg & Berlin in the case of filling of the 15 Mev betatron chamber with air. The theoretical variation of the electron loss with time calculated by Matveev for a different accelerator[10] is similar to that given by the curves in Fig.6. For our calculations we assumed an injection energy of 30 kev, i.e., the value used in our experiments. With increase of the injection energy the electron loss decreases. The variation of loss with acceleration time in this case is similar to that shown in Fig.3, but the curve lies somewhat lower.

Conclusions

Comparison of the curves shown in Fig.6 shows that calculations by the method of Greenberg & Berlin and by the method of Matveev give fairly accurate values of the electron loss owing to scattering by the residual gas, inasmuch as the results obtained by the two methods differ by a factor of only 1.5-1.7.

While the method of Blachman & Courant can be used for evaluating the proton loss owing to scattering by the gas, for electrons this method yields an underestimate (see table). The fairly good agreement of the experimental and theoretical results also indicates that our measurement procedure was a reasonably reliable one.

We desire to thank V.G.Shestakov for aid in measuring the orbital current and the staff of the Institute for assistance in carrying out the investigation.

Scientific Research Institute at
"S.M.Kirov" Tomsk Polytechnic Institute

References

1. W.B.Jones & H.R.Kratz, Rev.Sci.Inst. 26, 809 (1955).
2. L.A.Sena, Stolknoveniya elektronov i ionov s atomami gaza (Collisions of electrons and ions with gas atoms), M.-L., 1948.
3. N.F.Mott & H.S.W.Massey, Theory of Atomic Collisions, Oxford, 1933. (Cited in Russian trans.)
4. H.S.W.Massey & E.H.S.Burhop, Electronic and Ionic Impact Phenomena, Oxford 1952. (Cited in Russian trans.)
5. N.M.Blachman & E.D.Courant, Phys.Rev., 74, 140 (1948).
6. N.M.Blachman & E.D.Courant, Ibid., 75, 315 (1949).
7. J.M.Greenberg & T.H.Berlin, Ibid., 74, 1243 (1948).
8. J.M.Greenberg & T.H.Berlin, Rev.Sci.Inst.,22, 293 (1951).
9. A.N.Matveev, Zhur.tekh.fiz., 286, 1829 (1958),(Trans. Soviet Physics - Technical Physics.)

10. A.N.Matveev, Thesis, Moscow State University, 1958.
11. M.J.Moravcsik, Phys.Rev., 100, 1009 (1955).
12. G.Bernardini, Symposium, CERN, 1, 461 (1956).
13. A.I.Belyavskii, PTE (Instruments & Experimental Techniques), No.1 (1957).
14. L.Bess & A.O.Hanson, Rev.Sci.Inst., 19, 108 (1948).
15. Yu.S.Korobochko, Zhur.tekh.fiz., 27, 1603 (1957). (Trans. Soviet Physics - Technical Physics.)

PROCEDURE FOR MEASURING TOTAL PARTICLE COLLISION CROSS SECTIONS IN DENSE PLASMA

- L.V.Dubovoi & O.M.Shvets

Introduction

The technique of probing with high frequency fields can be used for determining the probability for particle collision in gas discharge plasma. Thus, development of procedures for measuring the conductance and susceptance of plasmas not under the influence of an external magnetic field led to a new convenient method of determining the probability for scattering of thermal neutrons by neutral particles.[1]

In the present report we propose a method for measuring the total cross sections for the interaction of electrons or ions in a plasma, based on utilizing the properties of plasma in a magnetic field.

The method is based on the variation of the conductivity of plasma in the region of cyclotron resonance as a function of the cross section for collisions of particles in the discharge. The presence of a magnetic field allows of separating the conductivity of the plasma into components associated with the type of particles for which conditions of resonance are fulfilled.

The mechanism of the phenomenon is analogous to the processes occurring in a cyclotron; the quantitative aspects of the problem have been considered by a number of authors[2-4]. According to theory, the loss in the plasma as measured directly from the absorption of the probing hf oscillations is proportional to the real part of the transverse conductivity of the discharge, which in the case of a Maxwellian velocity distribution of the electrons or ions is given by

$$\sigma = \frac{ne^2}{2M}\left(\frac{\nu_c}{\nu_c^2 + (\omega - \omega_c)^2}\right), \qquad (1)$$

where e is the charge and M is the mass of the "resonating" particles, n is their concentration, ν_c is the collision frequency, ω_c is the cyclotron frequency of the particles, and ω is the frequency of the hf electric field E applied perpendicular to the magnetic field. When the cyclotron frequency coincides with the oscillator frequency and the inequality $\nu_c/\omega < 1$ is fulfilled, there must be observed a resonance change in the conductivity of the plasma. The condition $\nu_c/\omega < 1$ is equivalent to the requirement that during the time between two successive collisions the particle complete at least one revolution in the magnetic field. Under these conditions the half-width of the resonance line at half-value of the conductivity is given by the relation

$$\Delta\omega / \nu_c = 1. \qquad (2)$$

In view of neglect in (1) of the influence of polarization fields arising at high densities this relation is valid only if the conditio

$$K = \omega_0^2 / \omega^2 < 1, \qquad (3)$$

is fulfilled; here ω_0 is the Langmuir frequency of the investigated particles. Nonfulfillment of this inequality leads to variation of

the resonance line half-width with the plasma density (not to be confused with line broadening owing to Coulomb collisions), shift of the hf absorption peak into the region of nonresonance values of the magnetic field for the given frequency and to deviation from linear variation of the conductivity with density[4,5].

Thus by means of Eqs.(1) and (2) we can on the basis of the measured hf power absorbed in the region of cyclotron resonance determine the collision frequency of the investigated particles in the plasma. The total collision cross section can then be determined from the value of ν_c and the particle temperature obtained from an independent experiment.

Experimental Results

With a view to checking the theory underlying the proposed procedure for the case of cyclotron resonance of electrons, in designing the experimental apparatus we insured fulfillment of the basic premises of (1) (Maxwellian velocity distribution of the particles, a not excessively high density and a wavelength λ of the probing signal much greater than the transverse dimensions R of the plasma volume). The discharge in hydrogen was excited in a Pyrex tube 12 cm in diameter by the field of a flat plate capacitor coupled to a ~60 watt oscillator. The oscillator frequency was 80 Mc; a constant magnetic field uniform to within 1% in the discharge volume was applied at right angles to the hf electron field. We measured the hf power absorbed in the plasma in the region of electron cyclotron resonance at different discharge parameters. By means of calibration curves for the oscillator, controlled by a resistive load, the absorption data were converted to conductivity values.

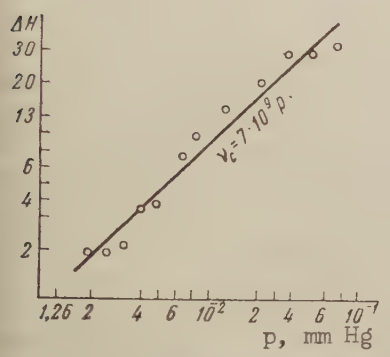

Fig.1. Variation of the half-width of the resonance peaks for electrons with pressure.

The degree of "Maxwellization" and the electron temperature and density were determined by the method of a double probe.[6]

The observed variation of the resonance line half-width with pressure is shown in Fig. 1; it will be seen that it is virtually linear which means that the electrons interacted primarily with neutral atoms. The corresponding effective collision frequency of the electrons with neutrals at the measured electron temperature (11-12 ev) is $7 \cdot 10^9$ sec^{-1} mm^{-1} Hg, whence the collision probability is 35 cm^2/cm^3 at 1 mm Hg, and the effective collision cross section is $10 \cdot 10^{-16}$ cm^2. This value for the cross section is in good agreement with the data obtained by other methods[7].

The described experimental arrangement served as the model for checking and developing a procedure applicable to conditions of ionic cyclotron resonance where there is virtually always fulfilled the conditions $\lambda/R \gg 1$. In case of need to determine the electron collision cross section in plasma of density greater than 10^8 cm^{-3}, the procedure must be appropriately modified to insure fulfillment of inequality (3). The effects connected with polarization of the plasma can readily be elimi-

nated either by appropriate choice of the configuration of the discharge volume[3] or by going over to a higher frequency of the probe signal. The presence of strong magnetic fields in modern equipment makes the second way of eliminating polarization effects preferable. Equations relating the half-width of the signal attenuation curve with collision processes for the case when $\lambda/R \ll 1$ are given by Al'pert et al[8]. The preliminary results of our experiments utilizing the standard techniques for determining the dissipation of waves propagating in a lossy dielectric indicate that experiment gives a satisfactory agreement with theory in the frequency range from 3000 to 9500 Mc. The results obtained by Schneider & Hofmann on cyclotron resonance at 24.3 kMc in the plasma of an acetylene-oxygen flame at 7.5 mm Hg are also consistent with theory. In the last cited case the influence of polarization effects should be evident only at densities exceeding 10^{13} cm^{-3}.

After perfecting the procedure in experiments with electrons, we undertook an attempt to measure the total collision cross sections for thermal protons with neutral particles. The plasma in the form of a cylinder 2-2.5 cm in diameter and 25 cm in length was produced by a Phillips type discharge in a 5 cm diameter quartz tube. The constant magnetic field was applied parallel to the axis of the tube; perpendicular to it we applied an alternating field by means of a flat plate capacitor which was part of a resonance circuit coupled to a low power GSS-6 type oscillator. By means of appropriate calibration curves, prepared beforehand, the indicated voltage was converted to conductivity values. The measurement circuit allowed of direct observation on the oscillograph screen of the shape of the hf power absorption as a function of the magnetic field. The measurements were carried out at a frequency of 2.2 Mc; the plasma density was measured by standard microwave techniques.[8]

To extend the applicability of the procedure into the range of higher densities, we used the technique, proposed by Stix[4,10], for compensating the intraplasma ionic polarization field by longitudinal displacement of electronic charges from neighboring regions not affected by the hf field. To provide the necessary conditions the length of the capacitor was made shorter than the overall length of the plasma cylinder.

The efficiency of the compensation processes connected with fulfillment of the inequality $\frac{nl^2}{2\cdot 10^{10}} \ll 1$ (l is the length of the capacitor in cm) was checked by comparing the half-width of the resonance lines with monotonic increase of the particle density in the discharge from $5\cdot 10^7$ to 10^{12} cm^{-3} ($K = 0.45 < 1$ and $K \approx 10^4 \gg 1$, respectively). In agreement with the theory of Stix[4], under the conditions of our experiment ($\frac{1}{2} l = 8$ cm) up to $n \approx 10^{11}$ cm^{-3} the half-width of the curves remained constant and the position of the resonance corresponded to exact equality of ω and ω_c, in contrast to the results obtained in the experiments of Dubowoj[11], where measures to eliminate polarization were not undertaken and where the effect of intrinsic plasma fields began to play a predominant role at $K = \frac{\omega_0^2}{\omega^2} \approx 1$.

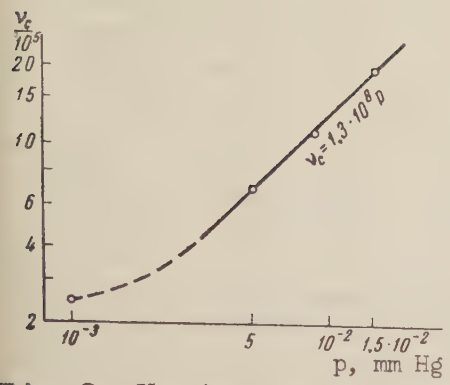

Fig.2. Variation of the proton-neutral particle collision frequency with pressure.

The pressure dependence of the collision frequency obtained in the absence of polarization effects from the corresponding values of the resonance line half-width is shown in Fig.2. At pressures greater than $4 \cdot 10^{-2}$ mm Hg the collision frequency of thermal H^+ ions with the neutral component of the plasma is $1.3 \cdot 10^8$ sec^{-1} mm^{-1} Hg. The corresponding value of the collision probability for ion velocities at the operating temperature of the tube, namely, 330°K (in discharges with a low degree of ionization such as ours the ion temperature may be taken equal to the temperature of the neutral particles) is 550 cm^2/cm^3 at 1 mm Hg and the collision cross section is $155 \cdot 10^{-16}$ cm^2.

It is difficult at present to discriminate between the two processes competing under the conditions of our experiments: scattering of the ions by neutral particles and resonance charge exchange between them; the ratio between the numbers of atomic and molecular ions under our conditions is not known. However, rather arbitrary extrapolation of the proton-neutral particle interaction cross section values obtained by Dalgarno & Yadav[12] into the region of thermal energies leads to values of the same order of magnitude as those obtained in our experiments.

To determine the influence of the ion energy on the magnitude of the cross section for interaction of the ions with neutral particles the intensity of the hf field was increased to the value at which the energy acquired by the particles as a result of interaction with the alternating field begins to exceed the thermal energy. The additional energy acquired by the particles was evaluated by means of the formulas developed by Amoignon & Rommel[13] in working with omegatron type mass spectrometers. The values of the field strength and the time between "start" and "finish", equal to the time between two successive interactions, were taken directly from experiment. Our preliminary measurements and calculations indicate that the ion-neutral particle collision frequency increases in proportion to the ion velocity in the energy range between thermal, corresponding to room temperature, and the value exceeding this by a factor of 4-5. It would appear therefore that the interaction cross section remains constant in the investigated energy interval.

In conclusion, we want to note that the presence of high noise levels characteristic of dense plasmas leads to a sharp increase in the interaction cross section for electrons and ions in the gas discharge so that in measuring "pure" cross sections this effect must be rigorously controlled.

Conclusions

The results of experimental investigations of the properties of plasma with a high concentration of charged particles cannot be adequately described by any theory taking into account only pair collisions. Strong intraplasma fields connected with macroscopic charges

and currents in dense plasmas lead to the appearance of new interaction mechanisms, mechanisms which in some cases may play a predominant role. Such processes can be investigated only in plasmas of sufficiently high concentration, i.e., in the range of concentrations where the methods of investigating interactions now available to experimenters become inapplicable.

On the basis of our preliminary results it may be asserted that the proposed procedure can be used for measuring particle interaction cross sections in plasmas having densities from 10^6 to 10^{14} cm^{-3}. When used for measuring the collision cross sections of electrons in a gas discharge in a magnetic field the procedure yields correct results. In the future it would be desirable to improve the procedure to make possible simultaneous measurements of the collision frequency and the electron density. In view of the possible presence of impurities in Phillips type discharges (impurities connected with cathode sputtering of the electrodes), we cannot claim that our cross section data for the interaction of protons with neutral particles are particularly accurate; we have presented these data primarily to demonstrate the potentialities of the procedure.

References

1. J.M.Anderson & L.Goldstein, Phys.Rev., 102, 933 (1956).
2. D.C.Kelly, H.Margenau & S.C.Brown, Ibid., 108, 1367 (1957).
3. D.Dresselhaus, A.F.Kip & C.Kittel, Ibid., 100, 618 (1955).
4. J.Stix, Phys.Fluids, 1, 308 (1958).
5. K.Körper, Z.Naturforsch. 12a, 815 (1957).
6. Yu.M.Kagan, Vestnik, Leningrad State Univ.,No.4, 79 (1957).
7. R.B.Brode, Revs.Mod.Phys., 5, 256 (1933).
8. Ya.L.Al'pert, V.L.Ginzburg & E.L.Feinberg, Rasprostranenie radiovoln (Propagation of radio waves), p.324, M., 1953; also see Worton, Howard & Heintz, Transactions of the Second International Conference on Peaceful Uses of Atomic Energy, Geneva, 1958.
9. J.Schneider & F.W.Hofmann, Phys.Rev.Letters, 1, 408 (1958).
10. T.Stix & R.Palladino, Phys.Fluids, 1, 446 (1958).
11. L.Dubowoj et al, Proc.Gen.Conf. a Conf. 15 (P) 2211 (1958).
12. A.Dalgarno & H.Yadav, Proc.Phys.Soc.A, 72, 1087 (1958).
13. J.Amoignon, G.Rommel, Le Vide, 12, 377 (1957).

List of Reports and Reviews presented at the First All-Union Conference on Electronic and Ionic Collisions, which are being published in other Journals

1. R. Ya. Damburg & V. Ya. Kravchenko: Evaluation of cross sections for scattering of electrons by alkali atoms, taking into account strong coupling. Izv. (Bulletin), Ac. of Sci. of the Latvian SSR (1960).

2. V. Ya. Vel'dre & R. Ya. Damburg: On the choice of the atomic electron function for the collision problem. Izv. (Bulletin), Latvian SSR Ac. of Sci., No.7, 57 (1959) and No.11, 69 (1959).

3. L. A. Vainshtein & G. G. Dolgov: Computer calculation of the cross section for excitation of atoms by electron impact. Optika i spektroskopiya, 7, 3 (1959). (Trans. Optics & Spectroscopy.)

4. Yu. N. Demkov: Variational methods in collision theory (review). Monograph.

5. N. V. Fedorenko: Ionization in ion-atom collisions (review). Uspekhi fiz.nauk, 68, 481 (1959). (Trans. Soviet Physics - Uspekhi.)

6. Yu. F. Bydin & A. M. Bukhteev: Ionizations of fast sodium, potassium, rhubidium and cesium atoms in collisions with hydrogen, deuterium, nitrogen and oxygen molecules. Zhur.tekh.fiz., 30, 546 (1960).(Trans. Soviet Physics - Technical Physics.)

7. L. G. Filippenko & I. P. Flaks: Scattering of multicharged ions accompanied by electron attachment. Zhur.tekh.fiz., 30, 49 (1959). (Trans. Soviet Physics — Technical Physics.)

8. I. P. Flaks & L. G. Filippenko: Ionization of inert gases by doubly and triply charged ions. Zhur.eksp.i teor.fiz., 38, 719 (1960). (Trans. Soviet Physics - JETP.)

9. V. V. Afrosimov, R. N. Il'in & E. S. Solov'ev: Ionization of argon with formation of multiply charged ions. (In press.)

10. N. V. Fedorenko & V. A. Belyaev: On the maximum cross section for nonresonance single electron charge exchange. Zhur.eksp.i teor.fiz., 37, 1808 (1959). (Trans. Soviet Physics - JETP.)

11. Ya. M. Fogel': Production of negative ions in atomic collisions (review). (In press.)

12. Ya. M. Fogel', A. G. Koval'i & Yu. Z. Levchenko: Ionization of gas ions in collisions with negative hydrogen ions. Zhur.eksp. i teor.fiz., 38, 1053 (1960). (Trans. Soviet Physics - JETP.)

13. Ya. M. Fogel', V. A. Ankudinovi & D. V. Pilipenko: Loss of electrons by fast atoms in single collisions with gas molecules. Zhur.eksp.i teor.fiz., 38, 26 (1960). (Trans. Soviet Physics - JETP.)

14. G. F. Drukarev: Regarding the Massey criterion. Zhur.eksp.i teor.fiz., 37, 847 (1959). (Trans. Soviet Physics - JETP.)

15. M. D. Gabovich: On the role of step processes in the production of protons in ion sources. Zhur.tekh.fiz., 30, 354 (1960). (Trans. Soviet Physics - Technical Physics.)

16. I. A. Grishaev, A. N. Fisun, A. N. Litvinenko, A. S. Grizhko, B. I. Shramenko & V. M. Onishchenko: Measurement of the losses of fast electrons in their passage through matter. Zhur.eksp. i teor.fiz., 37, 1455 (1959). (Trans. Soviet Physics - JETP.)

Bulletin of the USSR Academy of Sciences - Physical Series
Transactions of the First All-Union Conference
on Electronic and Ionic Collisions
Vol.24, No.8 - August 1960

TABLE OF CONTENTS

	Page Orig.	Trans.
Regarding the First All-Union Conference on Electronic and Ionic Collisions - L.A.Sena & G.F.Drukarev	941	941
Methods of calculating the cross sections for excitation of atoms by electrons - L.A.Vainshtein & I.I.Sobel'man	943	943
Partial excitation cross sections for hydrogen atoms - R.K.Peterkop	946	947
Excitation cross sections for some spectrum lines of krypton and xenon - L.M.Volkova, A.M.Devyatov & A.V.Kuralova	950	952
On the excitation functions of nitrogen and carbon dioxide molecules in encounters with electrons - I.P.Zapesochnyi & S.M.Kishko	953	955
Experimental investigation of the excitation functions of atomic spectrum lines - I.P.Bogdanova	956	958
Experimental determination of the cross sections for excitation of the $2^1S - n^1P$ lines of helium by electron impact - V.E.Yakhontova	960	962
Resonance charge exchange of alkali metal ions and atoms - A.M.Bukhteev & Yu.F.Bydin	964	966
Resonance charge exchange of positive alkali metal ions - D.V.Chkuaseli, U.D.Nikoleishvili & A.I.Guldamashvili	970	972
Dissociation of large molecules under electron impact - M.V.Gur'ev, M.V.Tikhomirov & N.N.Tunitskii	975	977
Modern methods for calculating atomic collision cross sections - G.F.Drukarev	979	981
Further investigation of resonance charge exchange of positive cesium ions - R.M.Kushnir & I.M.Buchma	986	989
Indirect evaluation of electron attachment cross sections - M.V.Konyukov	989	993
Energy transfer in molecular collisions - A.I.Osipov & E.V.Stupochenko	992	996
Theory of thermal dissociation of diatomic molecules - E.E.Nikitin & N.D.Sokolov	996	1000

Elementary processes involved in collisions between slow ions and molecules - V.L.Tal'roze 1001 1006

Investigation of electron loss due to scattering by the residual gas in an accelerator chamber - A.G.Vlasov, A.A.Vorob'ev, A.N.Kislov & R.P.Meshcheryakov 1006 1012

Procedure for measuring total particle collision cross sections in dense plasmas - L.V.Dubovoi & O.M.Shvets 1013 1020

List of reports presented at the Conference, being published in other journals 1018 1025

Translated in 1961 by
Columbia Technical Translations
5 Vermont Ave., White Plains, N.Y.

Transactions

of the

Tenth All-Union Conference on Nuclear Spectroscopy

(Moscow, 19-27 January 1960)

(Continued from Vol.24, Nos.3 & 7;
to be continued in Vol.24, No.12 & Vol.25, No.1)

PRESENT STATE OF BETA-DECAY THEORY

- V.A.Lyubimov

I. Fundamental Qualitative Results

1. Parity nonconservation in β-decay

Although the study of β-decay goes back several decades, the present concepts are radically different from those held prior to 1957. In the two years following the experimental confirmation of parity nonconservation in β-decay a number of brilliant theoretical and experimental investigations led to the creation of a theory of weak interactions, with β-decay as one example of this larger class of phenomena. The remarkable success in this field is explained not so much by progress in the development of experimental methods, as by the "liberating" influence that the elementary fact - violation of a basic conservation law - exercised on the minds and hands of investigators.

The puzzling question is often asked: why was the experiment that led to discovery of nonconservation of parity not performed ten or twenty years ago?

The classical theory of β-decay is based on the assumption that the interaction Hamiltonian must be invariant with respect to the several transformations characterizing the properties of space-time: Lorentz transformations, space inversion, time reversal and charge conjugation. In consequence of these requirements the old theory contained no expressions dependent on nonconservation of parity. It was possible to question the specific form of the theory, but it would have been strange to doubt the validity of any of the conservation laws upon which it was based. For this reason an experiment of the type performed by Wu et al would have appeared pointless even five years ago.

Were it not for developments in other fields of physics, consistent investigation of β-decay within the framework of the old concepts would not have led to the necessity of renouncing parity conservation. Only the discovery of contradictions in the properties of K-mesons (the "tau-theta puzzle") brought the necessity of hypothesizing parity nonconservation in weak interactions. This hypothesis was introduced by Lee and Yang,[1] who predicted a whole series of new effects, in particular, angular asymmetry in the β-decay of polarized nuclei. This phenomenon was quickly discovered in the experiment of Wu et al.[2] This test is especially convincing because the very result of the experiment, namely, an asymmetry in the number of electrons emitted parallel and antiparallel to the nuclear polarization, is not invariant with respect to space inversion and demonstrates parity nonconservation without any theoretical assumptions.

The resultant changes in our conceptions of space and time forced a complete reconsideration of the fundamental assumptions of classical β-decay theory. Whereas the old interaction Hamiltonian represented a superposition of five relativistically invariant interaction types, which were characterized by five real coupling constants, now the number of constants had to be doubled, since half of them should represent parity nonconservation. Moreover, all the coupling constants may in general be complex, since a priori we are not able to say anything about invariance under time reversal.

Thus, from this new point of view, the β-interaction Hamiltonian contains twenty unknown parameters. Naturally, a theory with twenty unknown parameters is far from complete. Hence the task of the experimenters lies in quantitative determination of these constants, and that of the theoreticians, in the elaboration of a complete theory in which all constants are reduced to a single one: the "charge" of the weak interactions. This comprehensive program has essentially

been realized in the course of the past few years. Below we will discuss only the most significant experimental and theoretical investigations which, step by step, have led to the present understanding of β-decay and weak interactions.

2. Longitudinal polarization of electrons. The two-component electron in β-decay.

Naturally, with the increase in the number of β-interaction constants there is a corresponding enlargement of the class of phenomena which permit determination of these constants (experiments with polarized particles involved in weak interactions). One of these effects is the appearance of longitudinally polarized electrons in β-decay, predicted by Landau.[3]

The first experiments which measured the longitudinal polarization of β-electrons were performed soon after the discovery of parity nonconservation, almost simultaneously by American[4] and Soviet[5,6] physicists.

These experiments showed that the β-electrons are polarized antiparallel to their motion. Soon Deutsch[7] demonstrated that the positrons are polarized parallel to their motion. Further, it was shown by many experimenters that in allowed transitions and, what is particularly significant, in first forbidden Coulomb transitions[8] the electron polarization is equal to v/c to within 2-5%. This is a necessary and sufficient condition that the coupling constants satisfy the relations

$$C_A = C'_A,\ C_V = C'_V,\ C_S = -C'_S,\ C_T = -C'_T,\ C_P = -C'_P, \tag{1}$$

where the primed (unprimed) constants depend (do not depend) on parity nonconservation. Thus the results of these experiments reduce by exactly one-half the number of independent β-interaction constants.

It is interesting to note that under these conditions (1) the electron enters into the β-interaction only through two components, a circumstance that is very important where the new theory is concerned. Actually, in the case of nonconservation of parity the β-decay Hamiltonian can be written in the general form

$$\sum_\alpha (\overline{\Psi}_n O_\alpha \Psi_p)(\overline{\Psi}_\nu (C_\alpha - \gamma_5 C'_\alpha) O_\alpha \Psi_e),$$

where the O_α are interaction operators and the Ψ are four-component wave functions for the neutron, proton, neutrino and electron. Assuming that the coupling constants satisfy conditions (1) and noting that $(1+\gamma_5)O_\alpha = O_\alpha(1+\gamma_5)$ for S, T and P interaction and $(1-\gamma_5)O_\alpha = O_\alpha(1+\gamma_5)$ for A and V interaction, we obtain for the interaction Hamiltonian

$$\sum_\alpha C_\alpha (\overline{\Psi}_n O_\alpha \Psi_p)(\overline{\Psi}_\nu O_\alpha (1+\gamma_5)\Psi_e).$$

We see that the electron wave function enters in the combination $(1+\gamma_5)\Psi_e$, which is a formal expression of the fact that the electron appears in the β-interaction as a two-component quantity.

After the establishment of relations (1) it became possible to distinguish among an extensive class of phenomena a minimum number of "key" effects depending only on six independent combinations of coupling constants and matrix elements, effects, investigation of which would permit complete determination of all the β-interaction constants:[9]

$$1)\ N_0 = (|C_S|^2 + |C_V|^2)|M_F|^2 + (|C_T|^2 + |C_A|^2)|M_{GT}|^2;$$

$$2)\ N_1 = -\lambda_{jj'}(|C_T|^2 + |C_A|^2)|M_{GT}|^2 - 2\delta_{jj'}\sqrt{\frac{j}{j+1}} \times \mathrm{Re}(C_S C_T^* + C_V C_A^*) M_F M_{GT}^*;$$

$$3)\ N_3 = (|C_V|^2 - |C_S|^2)|M_F|^2 + {}^1/_3(|C_T|^2 - |C_A|^2)|M_{GT}|^2; \qquad (2)$$

$$4)\ N_4 = 2\delta_{jj'}\sqrt{\frac{j}{j+1}}\,\mathrm{Im}(C_V C_A^* - C_S C_T^*) M_F M_{GT}^*;$$

$$5)\ N_\nu = -\lambda_{jj'}(|C_T|^2 - |C_A|^2)|M_{GT}|^2 + 2\delta_{jj'}\sqrt{\frac{j}{j+1}} \times \mathrm{Re}(C_S C_T^* - C_V C_A^*) M_F M_{GT}^*;$$

$$6)\ N_5 = 2\delta_{jj'}\sqrt{\frac{j}{j+1}}\,\mathrm{Im}(C_V C_A^* + C_S C_T^*) M_F M_{GT}^*.$$

The quantity N_0 defines the total probability for β-decay; N_3, the angular $e-\nu$ correlation; N_1, the angular distribution of the electrons in the decay of oriented nuclei; N_ν, the angular distribution of the neutrinos in β-decay of oriented nuclei. N_4 can be measured by studying the asymmetry in the distribution of recoil nuclei relative to the plane through the direction of the electron momentum and the nuclear spin. Finally, the coefficient N_5 can be determined by experiments on the decay of oriented nuclei in which the measurements include, in addition to the direction of the emitted electron, either the polarization of the recoil nucleus or the direction of the γ-ray from the following γ-transition.

At present all these combinations have been studied experimentally.

3. Two-component neutrino theory

Following the work of Lee & Yang on parity nonconservation in weak interactions, the two-component neutrino theory was elaborated by Landau[3], Salam[10], and Lee & Yang[11].

Back in 1929 Weyl[12] noted that for spin 1/2 particles with zero rest mass the Dirac equation degenerates into two equations which are satisfied by two-component wave functions. However, these equations are not invariant with respect to space inversion and hence no physical meaning was ascribed to them. With the knowledge that parity is not conserved in weak interactions there is no longer any objection to the hypothesis that the neutrino is described by one of the two equations:

$$i\frac{\partial\varphi}{\partial t} = \vec{\sigma}\mathrm{p}\varphi$$

or

$$i\frac{\partial\chi}{\partial t} = -\vec{\sigma}\,\mathrm{p}\chi,$$

where $\mathrm{p} = -i\nabla$, $\vec{\sigma}$ are the Pauli spin matrices, and φ and χ are two-component wave functions.

In the two-component theory the neutrino ought to be completely polarized relative to its momentum direction; further, the neutrino and antineutrino should have opposite polarizations. Precisely which direction of polarization the neutrino actually has in Nature (right- or left-handed helicity) only experiment can determine. The wave function of the two-component neutrino must enter the interaction Hamiltonian in the form $(1 \pm \gamma_5)\Psi_\nu$. This implies that the following relations must obtain between the coupling constants:

$C_\alpha = C'_\alpha$, if the neutrino has left helicity,

and (3)

$C_\alpha = -C'_\alpha$, if the neutrino has right helicity.

If we take into account the conditions (1), corresponding to the two-component electron, we find that the two-component neutrino theory is tenable only provided the β-interaction is either solely A and V (left-handed neutrino) or solely S, T and P (right-handed neutrino).

Thus to provide evidence for the two-component neutrino theory one can either directly measure the neutrino polarization or show that only certain definite interaction types are evinced in β-decay.

The neutrino polarization was measured by Goldhaber et al[13]. In this experiment the direction of flight of the neutrino from K-capture in Eu^{152m} was determined by resonance absorption of the γ-rays, and the neutrino polarization by measurement of the circular polarization of the γ-rays. The experiment showed that the neutrino is polarized antiparallel to its motion. On the other hand, in a number of β-ν angular correlation studies[14-16] involving different techniques it was demonstrated that the A and V forms of interaction are realized in β-decay.

The two-component neutrino theory can also be checked by measurement of the cross-section for the capture of antineutrinos by protons, a process which is the reverse of β-decay. Because the two-component theory places one-half of all the neutrinos in a given state, while the four-component theory only one-quarter, the theoretical cross-section in the first case is twice as large as in the second. An experiment of this nature was performed by Reines and Cowan.[17] The observed cross-section, averaged over the neutrino energy, $\sigma = (11.0 \pm 2.6) \cdot 10^{-44}$ cm^2, agrees with the two-component theory.

4. Universal theory of the interaction of four fermions (Feynman & Gell-Mann[18] and Marshak & Sudarshan[19])

The experimental proof of the two-component character of the electron in β-decay and confirmation of the elegant two-component neutrino theory allow us to attempt a further generalization: we hypothesize that all particles appear in the β-interaction solely in the two-component form. This implies additional conditions and leads to an equality between the vector and axial-vector interaction constants: $|C_A| = |C_V|$. The interaction Hamiltonian assumes the simple symmetric form:

$$\Sigma C_\alpha \{[\overline{\Psi}_n (1 \mp \gamma_5) O_\alpha (1 \pm \gamma_5) \Psi_p][\overline{\Psi}_\nu (1 - \gamma_5) O_\alpha (1 + \gamma_5) \Psi_e]\} = G (\overline{\Psi}_n \gamma_\mu (1 \pm \gamma_5) \Psi_p)(\overline{\Psi}_\nu \gamma_\mu (1 + \gamma_5) \Psi_e)$$

with a single constant: the "charge" of the weak interaction.

The choice of sign between the A and V interaction constants can be determined only by experiment, for the proton helicity is unknown a priori. Studies of the angular correlation of electrons and protons from the decay of polarized neutrons by Burgy et al[20] show that the A and V interaction constants have opposite signs.

The second statement of the theory is that all weak processes have the universal form of the interaction of four fermions with a single constant G:

$$G (\overline{A} \gamma_\mu (1 + \gamma_5) B)(\overline{C} \gamma_\mu (1 + \gamma_5) D),$$

where strange particles, e.g., $(\overline{\Lambda}^0, p)$ enter on an equal footing with the particle pairs $(\overline{p}, n)$, $(\overline{\nu}, e)$ and $(\overline{\nu}, \mu)$.

The great success of the theory is that it satisfactorily explains the nonconservation of parity also in those processes in which the leptons are not present

as carriers of parity violation. Actually, in the universal theory all particles enter in two-component form. Their wave functions enter the Hamiltonian in the form $(1 + \gamma_5)\,\Psi$, which is non-invariant with respect to space inversion, and thus they lead to parity violation in weak interactions.

The basic verification of the universal theory is the very near equality of the μ-decay constant with the V interaction constant in β-decay. The close equality (within 5%) was, however, not an obvious consequence, since the β-decay constant could be renormalized due to the strong interactions (the (n, p) part). Hence the third assumption of the universal theory is that the vector interaction constant is not renormalized.

This assumption is based on a profound analogy with quantum electrodynamics. There the electromagnetic interaction is such that the strong interactions do not influence the value of the electric charge. This property is a consequence of conservation of the electric current for arbitrary charged particles.

From the vector part of the weak interaction Hamiltonian one can construct an expression, analogous to the electric current; the assumption that this weak interaction vector current is conserved leads to the universal nature of the vector interaction constant.* On the contrary, from the axial-vector part of the interaction Hamiltonian one cannot obtain conservation of current; hence the constant C_A must be renormalized in β-decay. This is confirmed by experiment: precise measurements of the neutron lifetime by Spivak et al[22] yielded $C_A = -(1.24 \pm 0.04)\,C_V$.

Strictly speaking, the necessity of renormalizing the constant C_A in β-decay casts doubt on the uniqueness of the choice, V - A, deduced from the experiment of Burgy et al[20] on the decay of polarized neutrons, for in principle strong interaction could lead to a change in the sign of C_A. However, from the helicity of the positron in μ^+-decay,[23] where there is no strong interaction renormalization, it follows that the A and V interaction constants have opposite signs.

5. Symmetry transformations. Time reversal.

Up to this point we have considered solely the consequences of parity nonconservation in the weak interactions. Now we turn to experimental tests of other symmetry transformations: charge conjugation (charge parity) and time reversal (time parity).

Already from the experiment of Wu et al[2] it followed that along with parity, charge conjugation invariance was violated.[24] For a proof of time reversal invariance it is necessary to show that the coupling constants in the interaction Hamiltonian are real numbers.** Thus a test of time reversal invariance is possible in those experiments which depend on the combination

$$N_4 = N_5 = 2\delta_{jj'}\sqrt{\frac{j}{j+1}}\,\mathrm{Im}\,C_V\,C_A^*\,M_F\,M_{GT}^*,$$

containing the imaginary part of the interaction constants. The degree of time reversal violation is conveniently characterized by the phase between the A and V constants:

---

*The first to call attention to this were Gershtein and Zel'dovich.[21]

**Even before the experimental discovery of parity nonconservation in β-decay Landau[3] proposed that all interactions are invariant under the combined inversion, namely, simultaneous application of space inversion and charge conjugation. As follows from the Pauli-Lüders theorem, conservation of combined parity is equivalent to time reversal invariance.

$$C_V = G_V \quad \text{and} \quad C_A = G_A e^{i\varphi},$$

where the G's are real.

According to (2) it is necessary, in experiments containing combinations of N_4 or N_5 to measure three vectors:

a) The triad I_0, I_f and P_n: the polarization direction of the nucleus before and after β-decay, and the direction of the electron momentum. This combination is studied by measurements of β-γ angular correlation in the decay of polarized nuclei. The results of experiments with polarized Mn^{52} give[26]

$$135^\circ < \varphi < 250^\circ.$$

b) The triad I_0, P_e and P_n. Studying the decay of polarized neutrons, Burgy et al[20] detected electrons and recoil protons at right angles. The number of coincidences was found to be independent of the neutron polarization direction; hence it follows that

$$\varphi = (180 \pm 8)^\circ.$$

c) If the Fermi nuclear matrix element is known, time reversal invariance can also be tested by comparing the real part of the ratio of the constants with the absolute value of the ratio. In this case the real part can be determined, for example, from the angular distribution of the electrons in the β-decay of oriented nuclei:[2]

$$\frac{N_1}{N_0} = \frac{-\lambda_{jj'} |C_A|^2 M_{GT}^2 - 2\delta_{jj'} \sqrt{\frac{j}{j+1}} \operatorname{Re}\left[C_V C_A^* M_F \cdot M_{GT}^*\right]}{|C_V|^2 M_F^2 + |C_A|^2 M_{GT}^2} = \frac{-\lambda_{jj'} |X|^2 - 2\delta_{jj'} \sqrt{\frac{j}{j+1}} \operatorname{Re} X}{1 + |X|^2},$$

and the absolute value from the total probability for β-decay:

$$N_0 = |C_V|^2 M_F^2 (1 + |X|^2).$$

Here $X \equiv \frac{C_A}{C_V} \frac{M_{GT}^*}{M_F^*}$; $C_V = G$, where G is the constant of the universal four-fermion weak interaction. The value of $G = (1.40 \pm 0.01)$ erg cm^{-2} is known from the ft value for positron decay of O^{14} ($0^+ \to 0^+$ transition). Hence we find

$$|X|^2 - (\operatorname{Re} X)^2 = (\operatorname{Im} X)^2 = \left(\operatorname{Im} \frac{C_A}{C_V} \frac{M_{GT}^*}{M_F^*}\right)^2.$$

The Fermi matrix element can be calculated from transitions in light nuclei in which isotopic spin does not change. Examples of nuclei which would serve are Al^{24}, P^{28}, Cl^{32} and Sc^{40}. In these cases it would be very important to study the β-γ correlation along with the measurement of the circular polarization of the γ-rays (N_1/N_0 combination) and obtain more accurate ft values (N_0 combination).

In the case of the neutron, where the matrix elements are known, the combination N_1/N_0 was determined by Burgy et al[20] and N_0 by Spivak et al[22], who measured the neutron lifetime. From these data it follows that $\varphi = (177 \pm 6)^\circ$.

d) In calculations of the shape of the β-spectrum, the electron polarization, and other phenomena to higher orders in the perturbation expansion, terms appear which depend on the imaginary part of the coupling constant. Thus investigation of anomalies in the shape of the β-spectrum or electron polarization may in some cases enable us to judge of time reversal invariance. An example of this is β-decay of Bi^{210} (RaE). Measurement of the β-spectrum shape leads to $\varphi = (180 \pm 7)^\circ$,

while the deviation of the electron polarization from v/c implies $\varphi = (178.5 \pm 2.5)^\circ$. We will consider this case in greater detail below.

II. Higher Order Effects

By the end of 1958 all the fundamental conclusions of present-day β-decay theory had been experimentally confirmed. However, in most cases the tests were solely qualitative, although several crucial experiments, determining the true interaction forms, yielded definitive, "yes-or-no" results. Naturally, the next stage in testing the theory must be quantitative.

The fundamental results of β-decay theory are the following:

1. In allowed transitions the β-spectrum has the Fermi shape.
2. The electrons are fully polarized, the polarization being equal to v/c.
3. The neutrino is described by a two-component field (A and V interaction).
4. The vector interaction constant is not renormalized.
5. Time reversal invariance holds.

But what if more precise measurements were to show that in some cases, say, the β-spectrum for allowed transitions differs from the Fermi shape or that the electron polarization is not equal to v/c? Would this mean the theory is wrong? Not necessarily; not in all cases. Moreover, for some phenomena the very absence of such deviations would more strongly contradict the theory than the appearance of such anomalies. The point is that hitherto we have considered the deductions from the theory qualitatively, that is to say, in the first approximation. If the calculations are extended to a higher degree of accuracy, taking into account small but, in principle, real effects, the internal logic of the theory should lead to the appearance of certain deviations from the "normal", so that observation of such "anomalies" may well be the next important stage in the confirmation of the theory.

1. Gell-Mann's theory of weak magnetism[27]

As we already mentioned, the analogy between the vector part of weak interaction and electromagnetic interaction proved extremely fruitful. Extending this analogy, we can write an expression for a β-interaction identical in form to the electromagnetic interaction of a current with a field. Special interest is associated with the application of this idea to the calculation of first order terms in β-interaction. For example, in the case of the $1^+ \to 0^+$ β-transition, axial-vector interaction is allowed by the selection rules. However, we can include here also vector interaction in the next higher order, allowed by the selection rules.

Such a vector interaction, by analogy with electromagnetic interaction, is magnetic dipole interaction:

$$-\frac{\mu e}{2M}[\nabla \times \mathrm{A}]_z \to -\frac{\mu G}{2M}[\nabla \times (e^+ \alpha (1+\gamma_5)\nu)]_z,$$

where μ is the magnetic moment of the transition.

Just as the interaction of electric charges leads to the appearance of a magnetic field, so in allowed axial-vector interactions there appears a vector part, which may be likened to weak magnetism.

Inclusion of the weak magnetism leads, for example, to a deviation of the β-spectrum from the Fermi shape by a factor

$$\left(1 + \frac{8}{3} aE\right).$$

The matrix element in the correction coefficient a can be calculated from the magnetic γ-transition matrix element in an isobaric nucleus, provided the β-transition occurs between levels with the same parity and isotopic spin values as in the γ-transition. Thus

$$|a| = \frac{1}{E_\gamma}\left[\frac{^3/_4 \cdot 137 \cdot \Gamma_\gamma}{E_\gamma}\,\frac{ft}{(ft)_{O^{14}}}\right]^{1/2}$$

(Γ_γ is the width and E_γ is the energy of the γ-transition; E is the energy of the β-electron.) The sign of the coefficient can be found from the relation

$$a \sim \frac{\mu_p - \mu_n}{2{,}4M} \sim + \frac{2}{M}$$

(μ_p is the magnetic moment of the proton and μ_n the moment of the neutron).

We do not as yet have a full experimental test of these deductions, that is, determination of the β-spectrum shape and simultaneous measurement of the probability for the corresponding γ-transition.

For the triad $N^{12} \rightarrow C^{12} \rightarrow B^{12}$ there are data on the γ-radiation width but none on the shape of the β-spectrum.

Daniel[28] observed a deviation from the allowed β-spectrum shape in P^{32} amounting to ~10% near the end of the spectrum. However, the sign and magnitude of the deviation $\left(a_{exp} \approx -\frac{20}{M}\right)$ do not agree with the above estimate (see below).

Weak magnetism also affects β-γ angular correlation, where it leads to anisotropy even in allowed transitions. Bohemn et al[29] observed β-γ asymmetry (a_{exp} = = +0.94±0.28%) in the decay of F^{20}. Evaluation of the effect due to weak magnetism gives $a \approx +\ 0.45\%$.

We must add, however, that in all cases investigated to date the observed deviations may be the result of collateral effects (such as nucleon motion in the nucleus, axial-vector interaction of higher order, etc.). Therefore the question of the experimental confirmation of weak magnetism remains open.

2. Deviation of the β-spectrum from the Fermi shape and deviation of the electron polarization from v/c

RaE. The most convincing case of a deviation of the electron polarization from v/c is that of β-decay of RaE. The results of measurements by several groups (Refs.30-33) give a value of approximately -0.7 v/c.

Although RaE undergoes a first forbidden Coulomb transition ($1^- \rightarrow 0^+$), its β-spectrum is significantly different from the Fermi shape characteristic of all other known allowed transitions and first forbidden Coulomb transitions. Yamada[34] and others[35] found a satisfactory explanation by considering the change of the electron wave function in the field of the nucleus. They showed that for several important matrix elements interference in the expression for the β-decay probability can lead to a cancelling of the leading terms (which depend weakly on energy), so that higher order terms in the expansion, which depend strongly on energy, begin to play an important role. This then permits a theoretical reproduction of the experimentally observed β-spectrum.

Lewis[36], and also Fujita et al[37], called attention to the fact that in this case the spectrum shape is sensitive to possible violation of time reversal invariance. Indeed, this sensitivity is so great that it is possible to explain the experimental shape by invoking only a very small degree of time reversal violation.

Within Yamada's theoretical framework Geshkenbein, Rudnik & Nemirovskaya[38], and others[39], showed that in the event of agreement of the β-spectrum with experiment, the electron polarization actually ought to differ from v/c and lie in a narrow interval, which in fact includes experimental value.

Thus the discovery of the electron polarization deviation finds its explanation in the theory which at the same time explains the anomaly in the spectrum shape. The close agreement between the experimental and theoretical values for the electron polarization in RaE is a strong argument in favor of the theory of Yamada et al, and, consequently, in the conclusions of Lewis and others, that time reversal invariance holds to great accuracy.

Geshkenbein et al[38] studied the effect on electron polarization of a possible violation of time reversal invariance, since measurements giving the dependence of the polarization on electron energy in principle allow a more precise estimate of the degree of violation.

Data on the RaE polarization energy dependence obtained by the group at the Institute for Theoretical and Experimental Physics[40] lead to the conclusion that time reversal invariance holds to great accuracy:

$$\varphi = (178 \pm 2.5)^{\circ}.$$

P^{32}. Recently Spivak et al[41] made precise measurements of the electron polarization in a number of elements and found small deviations from v/c. The most serious case is that of P^{32}, for in this case the β-transition is allowed.

Geshkenbein and Rudnik[42] found a satisfactory explanation of this. As we mentioned above in connection with weak magnetism, the P^{32} β-spectrum differs from the Fermi shape because the ft value for P^{32} is large. This means that the Gamow-Teller matrix element ($1^+ \rightarrow 0^+$ transition) is unusually small for an allowed transition; therefore higher order terms, allowed by the selection rules, play a significant role in the decay probability. Among such terms are the vector interaction (weak magnetism) and the second forbidden Gamow-Teller term.

By way of major supplementary term there was considered the second forbidden term. In the case of P^{32} identical formulas are obtained[42] both for the β-spectrum and for the electron polarization:

$$C(E) = \left(1 + \frac{a}{E}\right);$$
$$\sigma(E) = -\left(1 - \frac{a}{E}\right)\frac{v}{c}. \qquad (4)$$

From the β-spectrum deviation it follows that $a = 0.1$. Consequently, a 340 kev electron ought to have a polarization equal to $-0.94\ v/c$, which agrees with the value measured by Spivak et al[41], namely, $\sigma_{exp} = -(0.94 \pm 0.04)\ v/c$.

Equations (4) are of fundamental significance, for they relate deviations in the β-spectrum with deviations in the degree of polarization. Undoubtedly, qualitatively such relations hold not only for allowed transitions but in general for arbitrary transitions.

Au^{198}. Polarization anomalies for low energy (~100 kev) electrons in gold were observed long ago by several groups.* On the other hand, a number of experiments[8,45] showed that for energies of ~400 kev the polarization is complete. One might think that here we have contradictory experimental results. Alikhanov et al[46] measured the electron polarization at several energies and showed both by absolute and by relative measurements (relative to the polarization of the electrons from Tm^{170}) that for energies > 300 kev polarization is indeed complete (-0.99 ± 0.03 v/c), while for 100 kev the value is $-0.83 \pm 0.05\ v/c$. However, other measurements[47]

*Notably in the work of A.I.Alikhanov, G.P.Eliseev and V.A.Lyubimov; also see Refs.43 & 44.

show that the β-spectrum deviates from the Fermi shape in the low energy region (< 250 kev) but agrees for higher energies. This serves to explain, at least qualitatively, why the electron polarization for Au^{198} is anomalous in the low energy region.

3. Equality of the coupling constants in different weak interactions

First of all we must determine what is meant by "equality of the coupling constants" (say, $C_A = C_V$) in the universal four-fermion interaction. The fact that the axial-vector interaction is renormalized as a result of the strong interactions indicates that by equality of the constants we should understand equality of the "bare" charges (constants), not perturbed by any additional interactions.

The hypothesis of the conserved vector current in the weak interactions, which precludes changes due to strong interaction renormalization, still does not imply that the constant C_V remains unaltered despite possible electromagnetic and weak interactions. Thus a comparison of the constant C_V in β-decay with that in μ-decay ought to make allowance for radiative corrections, as regards both electromagnetic and the weak interactions. First order electromagnetic radiative corrections to the constants for μ- and β-decay were calculated by Kinoshita and Sirlin[48] and Berman[49].

In μ-decay the correction leads to a 0.4% increase in the meson lifetime.

In β-decay the radiative correction is divergent; the correction cannot be calculated exactly and requires a cut-off parameter. If the cut-off is taken equal to the nucleon mass, the radiative correction leads to a reduction in the lifetime of O^{14} by 1.7%. From this it follows that $G = 1.40 \pm 0.01$ erg cm^{-2}, and the corrected μ-meson lifetime $\tau_\mu = (2.31 \pm 0.05)$ μsec. The latest measurements, by Lundby et al[50], give $\tau_{\mu\ exp} = (2.215 \pm 0.017)$ μsec. Thus there is some difference (~5%) between the μ- and β-decay constants.* But, as we already mentioned, along with electromagnetic corrections to the weak interactions, one ought to include radiative corrections due to the weak interactions themselves. In order to estimate these corrections we must first examine the structure of weak interactions.

III. Structure of the Weak Interactions. Limits to the Applicability of the Universal Four-Fermion Interaction Theory

As we indicated above, the universal interaction has the form

$$G\,(\bar{A}\gamma_\mu(1+\gamma_5)\,B)\,(\bar{C}\gamma_\mu(1+\gamma_5)\,D); \qquad (5)$$

this has been substantiated by numerous experiments. We ask, is this a rigorous expression for the weak interactions, or is it an approximation, valid only for low energies?

At present there are two ways of describing the weak interactions, to which we now turn.

1. Fermion interaction through an intermediate vector boson.

Analogy with electrodynamics can help us to write a more general expression

---

*Apparently, this difference cannot be explained as an error in calculating the radiative correction in β-decay, for any increase in the cut-off value would lead to still greater disagreement between the constants.

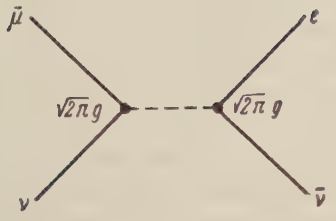

Fig.1. Diagram of $\mu \to e + \nu + \bar{\nu}$ decay via a vector boson.

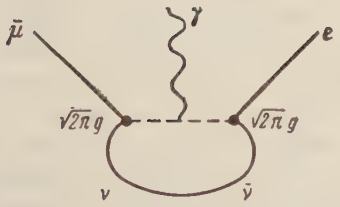

Fig.2. Diagram of $\mu \to e + \gamma$ decay.

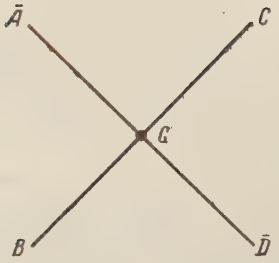

Fig.3. Point interaction of four fermions.

for the interaction of four fermions. Electrodynamic interactions proceed by the emission and absorption of photons by charged particles. We may describe the weak interactions in a similar fashion: a fermion pair - current - emits a weak interaction quantum, which then decays into some appropriate fermion pair, e.g., $(\bar{p},n)$, $(\bar{\nu}e)$, $(\bar{\nu}\mu)$ or $(\bar{\Lambda}^0 p)$. An interaction of this type is diagramed in Fig.1.

Generally the quantum of the interaction is taken to be charged: a vector boson. The mass of this particle must be great. If this were not so, then in interaction with fermions the boson would suffer recoil; for low energies we would not have the form of the fermion interaction given by Eq.(5) and confirmed by experiment. Since in this theory the weak interactions proceed by two steps - creation of the vector boson and its subsequent decay - then between the constant which couples the vector boson to the fermion current and the coupling constant of the weak interactions there must be a relation of the form

$$\frac{4\pi g^2}{M_0^2} = G, \tag{6}$$

where M_0 is the mass of the vector boson, g is dimensionless, and G has the dimensions M^{-2} ($\hbar = c = 1$). Although this theory is very attractive in its original form, it is in conflict with experiment.

If the interaction takes place via a vector boson, then μ-decay with no neutrino emission is possible (Fig.2): the neutrino and antineutrino annihilate, while the boson emits a photon. The probability for such a process can be calculated and represents 10^{-4} of the total μ-decays. However, it has been experimentally established[51] that the probability for the $\mu \to e + \gamma$ decay is less than 10^{-6} of the normal probability.

Pontecorvo[52] advanced the hypothesis that the neutrino which appears in the pair with the μ-meson is not equivalent to the neutrino in the electron pair. In this case the annihilation $\nu_\mu + \bar{\nu}_e$ as portrayed in Fig.2 is not possible, and the decay $\mu \to e + \gamma$ is forbidden. Thus interaction through an intermediate boson remains possible. Pontecorvo's hypothesis contradicts neither the universal theory of weak interactions nor experiment; however, if the helicities of ν_μ and ν_e turn out to be identical, experimental confirmation of this hypothesis will be difficult.

The idea[53] has been advanced that the analogy between the weak interactions and electrodynamics is not fortuitous but has a physical basis, including the consequence that the vector boson coupling constant is precisely equal to the charge of the electromagnetic interaction: e^2 ($e^2 = 1/137$ dimensionless). In this event it follows from Eq.(6) that the mass of the vector boson ought to be approximately 100 times greater than the nucleon mass.

2. Direct interaction of four fermions

On the other hand, one can assume that the four fermions interact directly with one another (Fig.3) and that the Hamiltonian (5) rigorously describes the interaction. The question arises: does this form of the interaction remain unaltered as one goes to higher energies, and if not, up to what energies is it valid?

Weak interactions of higher order ought to be proportional to the energy raised to some power determined by the interaction order. This can be seen from dimensional considerations, since the constant G, which is the expansion parameter, has the dimensions M^{-2}. From this follows a very important basic conclusion: the radiative corrections to the weak interactions will diverge. No matter how small the constant G, in those virtual processes in which only weakly interacting particles take part, arbitrarily large values of the energy are possible (e.g., in $(\mu\bar{\nu})$ $(e\bar{\nu})$ interactions), so that the expansion parameter of the energy and coupling constant combined becomes greater than unity. This means[54] that the energy of the interaction must be limited so that the maximum of $G\Lambda^2$, where Λ is a cut-off parameter, is less than unity. Hence the form (5) of the interaction is not accurate; it is valid only in the region of energies less than Λ.

Several experiments permit one to determine the upper limit to the applicability of this weak interaction theory. In particular, the limit can be inferred from the decay $\mu \to e + \gamma$ ($\Lambda \lesssim 50$ Bev) and from the difference between the constants for μ- and β-decay, which we mentioned earlier. If we accept that this difference is determined by the radiative corrections to the weak interaction in μ-decay (since in β-decay the corrections are small), then according to calculations by Ioffe,

$$\frac{C_{V\mathrm{p}}^2}{C_{V\mu}^2} = 1 - 2\sqrt{2}G\cdot\Lambda^2/\pi^2,$$

From this we obtain the upper bound for the cut-off:

$$\Lambda \lesssim 120 \text{ Bev}.$$

We note that this estimate holds even if there are two different neutrinos: "electron" and "muon" neutrinos. Therefore a more accurate determination of the agreement between the μ- and β-decay constants would permit one to exclude the hypothesis of the heavy (mass $\sim$100 nucleon masses) vector boson.

I desire to express my gratitude to A.I.Alikhanov for valuable comments and to B.L.Ioffe for discussion of several questions.

References

1. P.D.Lee & C.N.Yang, Phys.Rev., 104, 254 (1956).

2. C.S.Wu, E.Ambler, R.W.Hayward, D.D.Hoppes & R.P.Hudson, Ibid., 105, 1413 (1957).

3. L.D.Landau, Zhurleksp.i teor.fiz., 32, 405 (1957); Ibid., 32, 407 (1957). (Trans.Soviet Physics - JETP.)

4. H.Frauenfelder, R.Bobone, E.van Goeler, N.Levine, H.R.Levis, R.N.Peakock, A.Rossi & G.DePasquali, Phys.Rev., 106, 386 (1957).

5. A.I.Alikhanov, G.P.Eliseev, V.A.Lyubimov & B.V.Ershler, Zhur.eksp.i teor. fiz., 32, 1344 (1957). (Trans.Soviet Physics - JETP.)

6. M.E.Vishnevskii, V.K.Grigor'ev, V.A.Ergakov, S.Ya.Nikitin, E.V.Pushkin & Yu.V.Trebukhovskii, Nucl.Phys., 4, 271 (1957).

7. M.Deutsch, B.Gittelman, R.W.Bauer, L.Grodzins & A.W.Sunyar, Phys.Rev., 107, 1733 (1957).

8. A.I.Alikhanov, G.P.Eliseev & V.A.Lyubimov, Zhur.eksp.i teor.fiz., 34, 1047 (1958). (Trans.Soviet Physics - JETP.)

9. B.L.Ioffe & V.A.Lyubimov, Ibid., 34, 1321 (1958). (Trans.Ibid.)

10. A.Salam, Nuovo cimento, 5, 299 (1957).

11. P.D.Lee & C.N.Yang, Phys.Rev., 105, 1671 (1957).

12. H.Weyl, Z.Phys., 56, 330 (1929).

13. M.Goldhaber, L.Grodzins & A.W.Sunyar, Phys.Rev., 109, 1015 (1958).

14. W.B.Herrmannsfeld, D.R.Maxson, P.Stähelin & J.S.Allen, Ibid., 107, 641 (1957); R.L.Burman, P.Stähelin & J.S.Allen, Phys.Rev.Letters, 1, 61 (1958).

15. N.A.Burgov & Yu.V.Terekhov, Zhur.eksp.i teor.fiz., 35, 932 (1958). (Trans. Soviet Physics - JETP.)

16. K.H.Lauterjung, B.Schimmer & H.Maier-Leibnitz, Report at the Second International Conference on Peaceful Uses of Atomic Energy, Geneva, 1958; Proc.of the CERN Conference on High Energy Physics, 1958, Report of M.Goldhaber.

17. F.Reines & C.Cowan, Phys.Rev., 113, 273 (1959).

18. R.P.Feynman & M.Gell-Mann, Ibid., 109, 193 (1958).

19. R.E.Marschak & E.C.Sudarshan, Proc.of Padua - Venice Conference on Mesons and New Discovered Particles, 1957.

20. M.Burgy, W.Krohn, T.Novey, G.Ringo & V.Telegdi, Phys.Rev., 110, 1214 (1958).

21. S.S.Gershtein & Ya.B.Zel'dovich, Zhur.eksp.i teor.fiz., 29, 698 (1955). (Trans.Soviet Physics - JETP.)

22. A.N.Sosnovskii, P.E.Spivak, Yu.A.Prokof'ev, I.E.Kuzhikov & Yu.P.Dobrynin, Proc.of the CERN Conference on High Energy Physics, 1958, Report of M.Goldhaber.

23. H.Anderson, Ibid.

24. B.L.Ioffe, L.B.Okun' & A.P.Rudik, Zhur.eksp.i teor.fiz., 32, 396 (1957). (Trans.Soviet Physics - JETP.)

25. G.Lüders, Kgl.Danske Videnskab.Selskab., Mat.-fys.Medd., 28, No.5 (1954); W.Pauli, in "Niels Bohr and the Development of Physics". London, 1955.

26. E.Ambler, R.W.Hayward, D.D.Hoppes & R.P.Hudson, Proc.Rehovath Conference, 1957. Report of C.S.Wu.

27. M.Gell-Mann, Phys.Rev., 111, 362 (1958).

28. H.Daniel, Nucl.Phys., 8, 191 (1958).

29. F.Bohemn, V.Soergel & B.Stech, Phys.Rev.Letters, 1, 77 (1958).

30. A.I.Alikhanov, G.P.Eliseev & V.A.Lyubimov, Zhur.eksp.i teor.fiz., 35, 1061 (1958). (Trans.Soviet Physics - JETP.)

31. J.Geiger, G.Ewan, R.Graham & D.MacKenzie, Phys.Rev., 112, 1684 (1958).

32. W.Bühring & J.Heintze, Phys.Rev.Letters, 1, 176 (1958).

33. H.Wegener, H.Bienlein & H.v.Issendorff, Phys.Rev.Letters, 1, 460 (1958).

34. M.Yamada, Progr.Theor.Phys., 10, 252 (1953).

35. E.A.Plassmann & L.M.Langer, Phys.Rev., 96, 1593 (1954); H.Takebe, S. Nakamura, & M.Taketani, Progr.Theor.Phys., 14, 317 (1955).

36. R.Lewis, Phys.Rev., 108, 905 (1957).

37. J.Fujita, M.Yamada, Z.Matumoto & S.Nakamura, Phys.Rev.,108, 1104 (1957).

38. B.V.Geshkenbein, A.B.Rudik & S.A.Nemirovskaya, Zhur.eksp.i teor.fiz., 36, 517 (1959).

39. A.Bincer, E.Church & J.Weneser, Phys.Rev.Letters, 1, 95 (1958); H.Wegener, Z.Phys., 154, 553 (1959).

40. A.I.Alikhanov, G.P.Eliseev & V.A.Lyubimov, Nucl.Phys., 13, 541 (1959).

41. L.A.Mikaelyan & P.E.Spivak, Zhur.eksp.i teor.fiz., 37, 1168 (1959). (Trans.Soviet Physics - JETP.)

42. B.V.Geshkenbein & A.P.Rudik, Ibid., 38, 1894 (1960). (Trans.Ibid.)
43. M.E.Vishnevskii, S.Ya.Nikitin & E.V.Pushkin, Vsesoyuznaya konferentsiya po yadernym reaktsiyam pri malykh i srednikh energiyakh (All-Union Conference on Nuclear Reactions at Low and Intermediate Energies), M., 1957.
44. J.E.Turner, G.A.Gard & P.E.Cavanagh, Paper S1, Bulletin of Conference on Weak Interactions, Gatlinburg, Tennessee, 1957.
45. N.Benczer-Koller, A.Schwarzchild, J.B.Vise & C.S.Wu, Proc.Rehovath Conference, 1957. Report of C.S.Wu.
46. A.M.Alikhanov, G.P.Eliseev & V.A.Lyubimov, Zhur.eksp.i teor.fiz., 39, 587 (1960). (Trans.Soviet Physics - JETP.)
47. R.M.Steffen, Proc.Rehovath Conference, 1957.
48. T.Kinoshita & A.Sirlin, Phys.Rev., 113, 1652 (1958).
49. S.Berman, Ibid., 112, 267 (1958).
50. J.Fischer, B.Leontic, A.Lundby, R.Mennier & J.P.Street, Phys.Rev.Letters, 3, 349 (1959).
51. T.O'Kiefe, M.Rigby & J.Wormald, Proc.Phys.Soc., 73, 951 (1959).
52. B.Pontecorvo, Zhur.eksp.i teor.fiz., 37, 1751 (1959). (Trans.Soviet Physics - JETP.)
53. A.Salam & J.C.Ward, Nuovo cimento, 11, 568 (1959).
54. B.L.Ioffe, Report presented at the Tenth All-Union Conference on Nuclear Spectroscopy, M., January 1960.

INVESTIGATION OF THE FINE STRUCTURE OF ALPHA-RADIATION FROM U^{234} AND U^{235}

- S.A.Baranov, A.G.Zelenkov & V.M.Kulakov

We investigated the fine structure of the α-spectrum of uranium 234 and uranium 235 by means of the large double focusing magnetic spectrometer described in Refs.1 & 2. The difficulty inherent in such investigations stems from the long period of U^{235} ($7.1 \cdot 10^8$ years) and the complexity of the α-spectrum. Hence detailed data on the α-decay of these uranium isotopes can be obtained only with the aid of an instrument with high luminosity and good resolution.

The source was enriched in U^{235} and prepared by vacuum evaporation. The thickness of the active layer was ~10 μg/cm^2. With an effective source area of 3 to 5 cm^2 the apparatus line half-width did not exceed 6 to 7 kev. Several exposures with a total duration of about 700 hours were necessary to investigate the relatively broad region covered (~650 kev). The spectrograph was calibrated in energy by the usual procedure of measuring the magnetic field in the gap and the coordinates corresponding to different positions of the same α-particle group in the focal plane. Such calibration in general may prove different for different energy ranges owing to variation of the configuration of the magnetic field with field strength. Hence our calibration was checked with reference to three monoenergetic α-particle groups of different energies, namely, 6110 kev (Cm^{242}), 5495 kev (Pu^{238}) and 4768 kev (U^{234}). On the basis of the test results we can assert that the calibration of our instrument remained constant within ~1 kev in the energy range from 4650 to 6400 kev and can be described by the following formula

$$E = E_0(1 + 2.28_5 \cdot 10^{-4} x + 0.2_2 \cdot 10^{-7} x^2),$$

where E_0 is the energy of the particles moving along the central orbit, and x is the distance in mm measured along the photographic plates from the point of intersection of the focal plane with a circle of radius ρ_0.

In view of the fact that the calibration remains constant in a relatively wide energy range gives reason to infer that it remains the same in the energy interval involved in the present investigation, namely, from 4150 to 4800 kev.

By way of "standard" we used the U^{234} α-particle group corresponding to the transition to the ground state of Th^{230} (E_α = 4768 kev). In the α-spectrum of U^{234} (Fig.1 and Table 1) we observed the three known groups corresponding to transitions to the rotational levels of Th^{230} (0+, 2+ and 4+). This is the first time the transition to the 4+ level has been observed by means of a magnetic spectrometer. Our values for the energies and relative intensities of these three groups are in good agreement with the results of other investigations[3-6].

The results of investigation of the fine structure of α-decay of U^{235} are shown in Figs.1, 2 & 3 and Table 2. We identified 13 groups of α-particles in the spectrum of U^{235}. Our results are not in conflict with the data of Chiorso[7] and Vorob'ev et al[8], who studied the α-activity by means of ionization chambers. However, our results do differ substantially as regards intensities and energies from the data of Pilger et al[9-11]. The most serious divergence obtains for the highest intensity groups (Fig.2).

Table 1

Fine structure of the U^{234} α-spectrum

α-Group	E_{excit}, kev	I, %
α_0 (0+)	0	72,5 ±3,0
α_1 (2+)	53,5±1	27,5 ±1,5
α_2 (4+)	173±2	≤0,37 ±0,11

Analysis of the experimental data gives reason to assert that the fine structure groups observed in the spectrum of U^{235} correspond to transitions to four or five single particle levels in Th^{231}. The α_{13}, α_8 and α_{10} groups are characterized by the lowest hindrance factors. Inasmuch as the ground

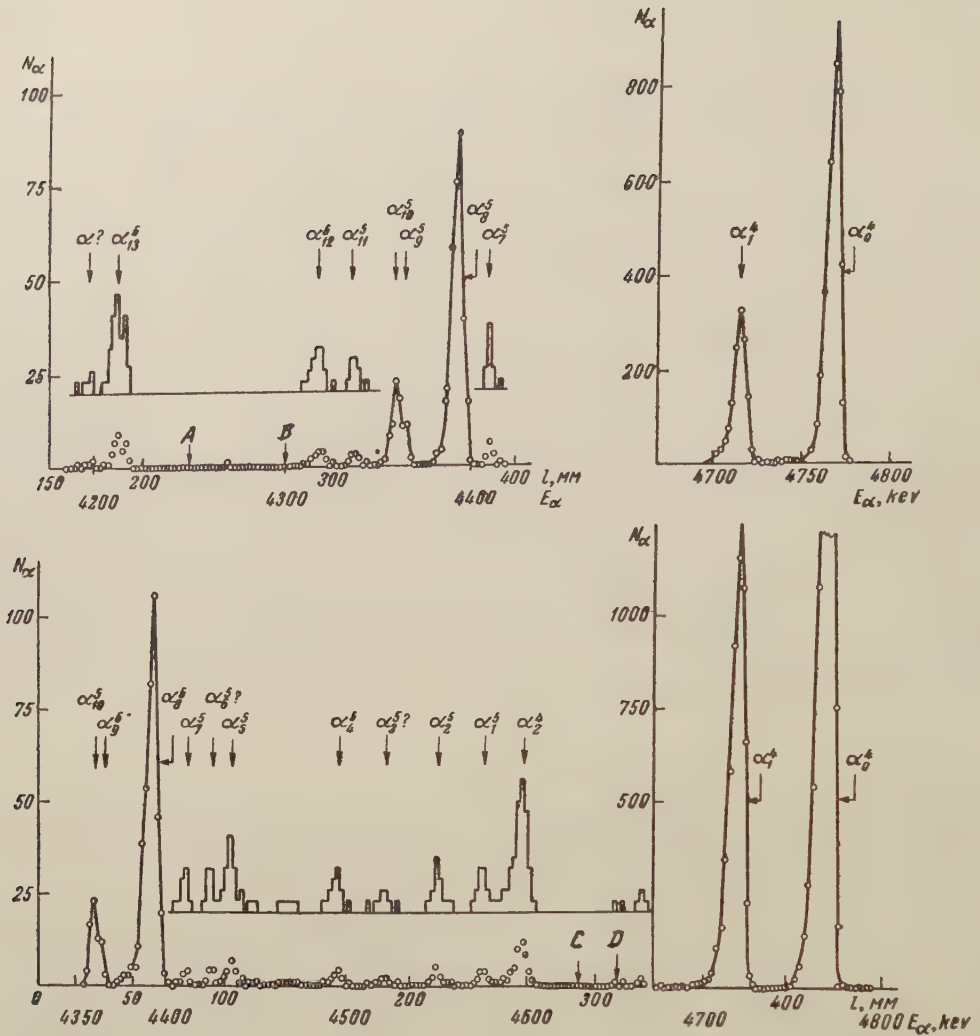

Fig.1. Spectrum of α-particles from U^{234} and U235. N_α = number of α-particles; l = coordinate of the photographic plate in mm. The α-groups identified by the superscript 4 pertain to U^{234}; those identified by the superscript 5 pertain to U^{235}. The α-particle tracks were counted at intervals of 0.3 mm. The spectrum shown at the bottom of the figure was recorded at the same time.

state of U^{235} has spin 7/2 and odd parity[11], it may be assumed that these α-decays lead to levels in Th^{231} with close spin values. According to classifications[12,13] based on Nilsson's diagrams Th^{231} should have levels corresponding to states with K = 7/2- (743) and K = 5/2- (752). If we assume that the α_{13} group, characterized by the lowest hindrance factor ($m \approx 2.2$) corresponds to a favored transition to the 7/2- (743) state, one can identify levels 7, 8, 10 and 13 (Fig.3) as levels belonging to one rotational band based on the single particle 5/2- (752) state.

The anomalously small separation between levels 7 and 8 can be explained by strong "interaction between rotational levels"[14] belonging to states with 5/2- (752) and 7/2- (743), which should lead to a substantial shift of levels 8, 10 and 12 relative to level 7. The energy intervals between levels 8 (I = 7/2), 10 (I = 9/2) and 12 (I = 11/2) agree within the limits of the measurement error with the assignment K = 5/2. However, the value of the moment of inertia for this state

Table 2

Fine structure of the U^{235} α-spectrum.

α-Groups	α-Particle energy, kev*	I, %***	Hindrance factor, m	α-Groups	α-Particle energy, kev*	I, %***	Hindrance factor, m
α_1	4578	1,5	$5\cdot10^3$	α_8	4394	62	5,4
α_2	4550	3	$(1\div2)\cdot10^3$	α_9	4368	(6)	35
α_3 (?)	4522	<1	$\sim5\cdot10^3$	α_{10}	4362	(11) } 17	17
α_4	4496**	1	$(1\div2)\cdot10^3$	α_{11}	4339	1,5	80
α_5	4438	3	$(2\div3)\cdot10^2$	α_{12}	4320	3	30
α_6 (?)	4426	1,5	$\sim4\cdot10^2$	α_{13}	4214	5,5	2;2
α_7	4412	2	$\sim2\cdot10^2$				

*In evaluating the energy we used the most intense α-group of U^{234} (E_α = 4768 kev) as the "standard". The uncertainty in the energy values is ± 2 kev.

**Coincides in energy with the α_0 group of U^{236}.

***The intensity values are based on three experiments.

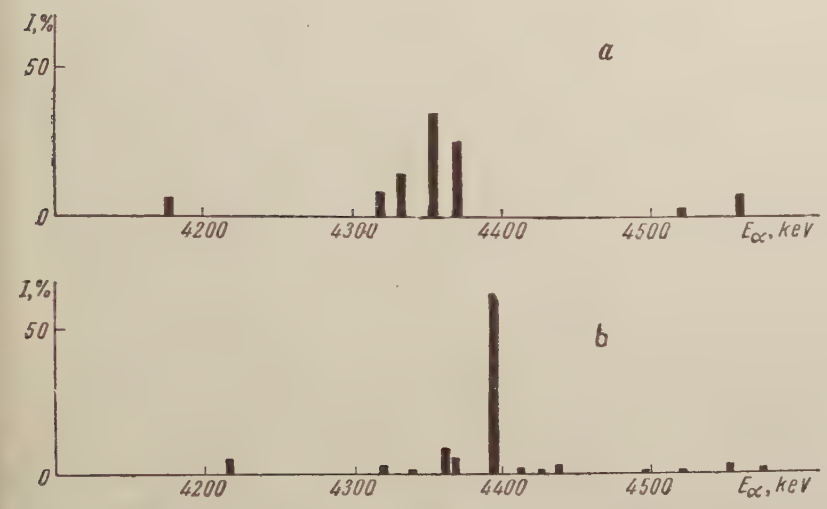

Fig.2. Results of measurement of the α-spectrum of U^{235}: a) data of Pilger et al[9-11], b) our data.

differs greatly from its value in neighboring even-even nuclei ($\frac{3\hbar^2}{J} \approx 49$-53 kev) and approaches the solid body value $\Delta J/J_{sb} = \frac{J_{odd} - J_{ee}}{J_{sb}} \approx 60$ %. Theory also predicts a substantial increase of the moment of inertia for the 5/2- (752) state; evaluations carried out by means of the formulas given by Prior[15] and Grin' et al[16] for a deformation parameter $\beta \approx 0.23$ yield $\Delta J/J_{sb} \approx$ 30-50%.

As a result of the above mentioned interaction of states each of the levels of the rotational band, except for level 7, will be characterized by a superposition of states with K = = 5/2 and K = 7/2. According to Prior[17] this should probably result in a substantial increase in the intensity of the α-transitions to levels 8, 10 and 12. Accordingly, one can expect the intensity ratios of the α-transitions to be described in the first approximation by the formulas for favored transitions with K = 7/2. Theoretical evaluation of the intensities of the transitions to the 7/2, 9/2 and 11/2 levels yields 100:15:2, while the experimental ratios for the transition intensities to levels 8, 10 and 12 are approximately 100:17:5. As might be expected, the intensity of the transition to level 7 is much lower ($m \approx 2\cdot10^2$).

Levels 9 and 11 can be attributed to a state with 3/2+ (631), inasmuch as the corresponding α-particle groups (α_9 and α_{11}) have relatively small hindrance factors ($m < 100$), characteristic of transitions not connected with change in the projection of the spin of the last odd nucleon on the nuclear axis.[17] The magnitude of the moment of inertia for the indicated identification of the levels is in agreement with theoretical evaluations for 3/2+ ($\Delta J/J_{sb} \approx 20\%$).

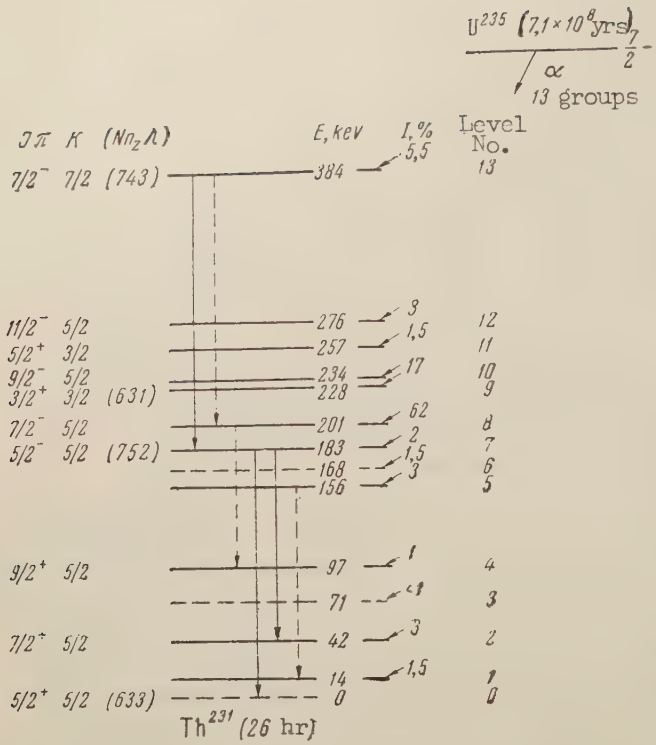

Fig.3. Proposed level diagram for Th^{231}.

The other levels, according to Nilsson's scheme, presumably belong to single particle 5/2+ (633) and 1/2+ (631) states. Transitions to these states involve change of Σ, which should explain the large hindrance factor characteristic of the corresponding α-particle groups.[17] The most probable assignment for the ground state is 5/2+ (633) (see Ref.13).

Theoretical evaluation of the separation between the ground state and the first excited level of Th^{231} yields ~40 kev (compare with the level diagram of U^{233}), which differs greatly from the separation between levels 1 and 2 (~28 kev). We cannot, however, deny the possible existence of a group of α-particles with an energy of 4590 kev and an intensity of ~1%, since such a group would be masked in our measurements by the 4596 kev group of U^{234} α-particles, which corresponds to the transition to the 4+ level in Th^{230}. Hence we arbitrarily assumed that the observed α_1 group goes not to the ground state of Th^{231} but to an excited level at ~14 kev. On this assumption, levels 2 and 4 and possibly 5 or 6 may be identified as rotational levels based on the 5/2+ (633) ground state with spins 7/2, 9/2 and 11/2 (see Fig.3).

Let us compare the level diagram proposed for Th^{231} (Fig.3) with the data on γ-radiation. It must be noted that the γ-spectrum is complex, while the resolution of scintillation spectrometers - the only instruments by means of which the spectrum has been investigated to date - is not high. Hence the results obtained by different authors[8,18-20] conflict in many respects. Among the more or less reliably established γ-transitions is the 184-188 kev transition (55%) and the 195-210 kev transition in cascade with it, and transitions of 143-146 and 105-110 kev energy. From determinations[8,13,20] of the conversion coefficients it follows that the ~185 and ~145 kev transitions are E1 and the ~200 kev transitions is M1. Regarding the 105-110 kev transition it is known only that it must comprise a substantial fraction of dipole radiation.[8] The above mentioned γ-ray data are in conflict with the proposed level diagram. The absence of detectable transitions from level 13 to the rotational levels based on the ground state may be explained by the fact that they are forbidden by the asymptotic quantum number selection rules. The electric dipole transitions (~185 and ~145 kev) are also forbidden by these selection rules which may explain the relatively long lifetime of the ~185 kev state. According to Strominger[21], the lifetime of this state is $(0.77 \pm 0.12) \cdot 10^{-9}$ sec.

Nevertheless the proposed scheme can only be regarded as tentative. In order to establish the definitive scheme one must have additional experimental data, primarily information on the conversion electron spectrum.

We desire to express our gratitude to V.V.Beruchko and A.I.Timoshinov, who participated in the measurements, and V.F.Gorbunov, V.P.Zakharova and V.K.Selikhov for assistance in preparing the sources.

References

1. S.A.Baranov, A.G.Zelenkov, G.Ya.Shchepkin, V.V.Beruchko & A.F.Malov, Atomnaya energiya, 7, 262 (1959) (Trans.Soviet Journal of Atomic Energy); Izv.AN SSSR, Ser.fiz., 23, 1402 (1959) (Trans.Bulletin 23, 1389).
2. L.L.Gol'din & E.F.Tret'yakov, Ibid., 20, 859 (1956) (Trans.Ibid., 20, 781).
3. L.L.Gol'din, E.F.Tret'yakov & G.I.Novikova, Session of the USSR Acad.of Sci.on the Peaceful Uses of Atomic Energy, Phys.-Math.Series, 226, July, 1955.
4. G.Valladas, Compt.rend., 237, 1673 (1953).
5. B.Bochagov, A.Komar & G.Kocharov, Zhur.eksp.i teor.fiz., 32, 1257 (1957). (Trans.Soviet Physics - JETP.)
6. A.P.Komar, G.A.Korolev & G.E.Kocharov, Izv.AN SSSR, Ser.fiz., 22, 824 (1958). (Trans.Bulletin 22, 821.)
7. A.Ghiorso, Phys.Rev., 82, 979 (1951).
8. A.A.Vorob'ev, A.P.Komar & V.A.Korolev, Program of the Tenth Conference on Nuclear Spectroscopy, M.-L., 1960.
9. R.Pilger, F.Stephens, F.Asaro & I.Perlman, Bull.Amer.Phys.Soc., 2, 394 (1957).
10. R.Pilger, Thesis, UCRL, 3877, July 1957. (Not published.)
11. D.Strominger, J.M.Hollander & G.T.Seaborg, Revs.Mod.Phys., 30, 817 (1958).
12. B.R.Mottelson & S.G.Nilsson, Mat.-fys.Skr.Danske Vid.Selskab, 1, N8 (1959).
13. F.S.Stephens, F.Asaro & I.Perlman, Phys.Rev., 113, 212 (1959).
14. A.Kerman, Mat.-fys.Medd.Kgldanske Vid.Selskab, 30, N 15 (1955).
15. O.Prior, Arkiv fys., 14, 451 (1959).
16. Yu.T.Grin', S.E.Drozdov & D.F.Zaretskii, Program of the Tenth Conference on Nuclear Spectroscopy, M.-L., 1960; Zhur.eksp.i teor.fiz., 38, 1297 (1959). (Trans.Soviet Physics - JETP.)
17. O.Prior, Arkiv fys., 16, N.2, 15 (1959).
18. G.W.Malich, Bull.Amer.Phys.Soc., Ser.II, 1, 43 (1956).
19. S.A.E.Johnson, Arkiv fys., 10, 97 (1956).
20. F.S.Stephens, Thesis, UCRL, 2970 (June, 1955).
21. D.Strominger, Phys.Rev., 114, 502 (1959).

THE AUGER EFFECT
(A Review)

- M.A.Listengarten

Introduction

When internal conversion, electron capture, the photoelectric effect, or any other process which ionizes the internal shells of an atom leaves a vacancy in such a shell, this vacancy is filled in a time of the order of 10^{-17}-10^{-14} sec by an electron from one of the higher levels. The energy emitted in such a transition is equal to the difference in the ionization energy of the two levels. This transition energy may be carried off by electromagnetic radiation (characteristic x-rays) or by an electron from another shell, which, as a result, leaves the atom. The latter process is called the Auger effect, and the emitted electron is called an Auger electron.

An understanding of the Auger effect is necessary both to differentiate internal-conversion electrons and β-particles from Auger electrons when a nucleus is undergoing radioactive decay, and if one wants to use the number of Auger electrons to calculate the number of initial vacancies in the shell. Such a calculation can be used, for instance, to determine the number of K-captures or the number of conversions.

Investigation of the Auger effect should yield information on the following quantities: (1) the number of different Auger-electron lines, (2) their energies, (3) the relative intensities of the separate Auger-electron lines (or line groups), (4) the absolute probability for the Auger effect (line widths), (5) the Auger-effect-x-ray branching ratio for filling the initial vacancies.

I. Classification of Auger Electrons

An atom with a single vacancy, or hole, will be left, as a result of the Auger effect, with two holes. We will label series of Auger electrons by the shell in which the initial vacancy occurred (e.g., K series, L series). We will label groups of Auger electrons by the shells containing the two holes resulting from the Auger effect (e.g., K-LL, K-LM, K-MN groups of the K series). Finally each group consists of several Auger-electron lines differing in their energy.

The notation used for the different Auger lines of each group depends on the method one uses to characterize the states of the doubly ionized atom. In different regions of the atomic number Z and for instruments with different resolutions one will in general use different quantum numbers. Their choice will depend on whether one need take into account, first, relativistic effects, and, second, residual interaction between the electrons (or holes). By residual interaction we understand that part of the electromagnetic interaction of the electrons which cannot be included in the average centrally symmetric atomic potential. One then has four possibilities.

1. jj coupling. The Auger electron lines are denoted by the same shell and subshell indices (e.g., K, L_1, L_2, L_3, M_1) as are used to denote the single-electron energy states of the atom in x-ray spectroscopy. For instance, the K-LM group should contain fifteen lines since there are three L and five M subshells. The emission of electrons of the K-LL group can leave the L shell, consisting of three subshells, in six different energy states with the configurations given in the second line of Table 1. One then obtains the six lines given in the first line of the table. This classification takes into account relativistic effects, but not the residual interaction, and is known as the jj coupling limit. The system consisting of the Z - 2 electrons (or, equivalently, the two holes) is

then characterized merely by the quantum numbers of the individual single-electron states predicted by the relativistic theory for the centrally symmetric field. The jj coupling limit can be used to classify Auger electrons for $Z \geqslant 30$--40.

2. Nonrelativistic single-electron approximation. Here neither the residual interaction nor the relativistic effects are included. This approximation can be used when the resolution is low for $Z < 40$; but it is good for large Z only for the external shells. In the nonrelativistic approximation the L_2 and L_3 subshells, the M_2 and M_3 subshells, etc., are not split. Then the K-LL group will have only three lines (as in line 10 of Table 1), namely, $K\text{-}L_1L_1$, $K\text{-}L_1L_{2+3}$, and $K\text{-}L_{2+3}L_{2+3}$. These lines correspond to the three possible states of the L shell of a doubly ionized atom in the nonrelativistic single-electron approximation. Their configuration is given in line 9 of Table 1.

Until recently it was thought that the above classifications exhaust the possibilities. But not long ago Siegbahn et al[1] reported observing not six, but seven Auger electrons in the K-LL group of copper. This report led to much experimental and theoretical work devoted to the number of lines in a group[2-5]. Two new possibilities for the classification of Auger lines were brought forward (they were already discussed by Ference[6] back in the thirties).

3. The LS coupling limit. Relativistic effects are not included, but the residual interaction (which, in the nonrelativistic approximation, is entirely electrostatic) is taken into account. This classification is applicable to very small Z (say, less than 20) and when the resolution is good enough for quite weak lines to be distinguished. For small Z, as well as for the shells furthest away from the nucleus, the binding energy becomes so small that the weak two-particle residual interaction contributes measurably. In the nonrelativistic approximation the total orbital angular momentum L and the total spin S (but not the angular momentum and spin of the separate electrons) are conserved separately. The interaction energy depends on L and S. The six lines of the K-LL group possible in this approximation are shown in lines 6-8 of Table 1.

4. Intermediate coupling. For $20 \leqslant Z \leqslant 40$ (and for even lower and higher Z if the resolution is high) neither the residual interaction nor the relativistic effects may be neglected if one wants to explain the nature of the weak Auger lines. In general the energy of the atom depends on the total angular momentum J of the system of electrons (or holes). This leads to splitting of each line obtained in the jj or LS coupling schemes, into several lines (multiplet components) depending on J. The nine lines possible in the K-LL group are shown in Table 1. Their classification in LS terms is given in lines 4 and 9 (or 4 and 10) of the Table, and corresponds to the splitting of each of the two ^3P lines into the three components with $J = L + S$, $J = L$, and $J = L - S$.

The same lines can be classified with equal validity in jj-coupling terms (lines 1 & 3 or 2 & 3 in Table 1), which corresponds to splitting into components depending on how the angular momenta j_1 and j_2 of the two holes couple to give J. Obviously, $|j_1 - j_2| \leqslant J \leqslant j_1 + j_2$.

The intermediate coupling classification is valid for all Z, but outside the $20 \leqslant Z \leqslant 40$ interval it may not be reasonable to use it in describing the states of the internal subshells, since the different multiplet components in the Auger spectrum will have energies which are almost equal and intensities which differ greatly. In dealing with Auger emission from the outer subshells, on the other hand, the region of applicability of the intermediate coupling classification increases in the direction of large Z.

The Pauli principle restricts the possible states in the intermediate coupling classification. For instance, when the atom has spin $S = 0$, the two-electron

Table 1

Auger lines of the K-LL group.*

Relativistic single-electron approximation (jj coupling limit)	1) line denoted by 2) L shell configuration $(nl_j)^N$	$K-L_1L_1$ $(2s_{1/2})^0(2p_{1/2})^2\times$ $\times(2p_{3/2})^4$	$K-L_1L_2$ $(2s_{1/2})^1(2p_{1/2})^1\times$ $\times(2p_{3/2})^4$		$K-L_1L_3$ $(2s_{1/2})^1(2p_{1/2})^2\times$ $\times(2p_{3/2})^3$		$K-L_2L_2$ $(2s_{1/2})^2(2p_{1/2})^0\times$ $\times(2p_{3/2})^4$	$K-L_2L_3$ $(2s_{1/2})^2(2p_{1/2})^1\times$ $\times(2p_{3/2})^3$		$K-L_3L_3$ $(2s_{1/2})^2(2p_{1/2})^2\times$ $\times(2p_{3/2})^2$	
Intermediate coupling	3) in jj terms	0;1*	1	0	1	2	0;1*	2	1*	0;1*	2;3*
	4) in LS terms: $^{2j+1}L_J$	$^1S_0$	$^1P_1$	$^3P_0$	$^3P_1$	$^3P_2$	$^1S_0$	$^1D_2$	$^3P_1$****	$^3P_0$	$^3P_2$
	5) total atomic angular momentum J	0	1	0	1	2	0	2	1*	0	2
LS coupling limit	6) atomic state	^1S	^1P	^3P			^1S	^1D	^3P		
	7) atomic spin S	0;1*	0	1			0;1*	0;1*	0;1*		
	8) orbital angular momentum L	0	1				0	2	1		
Nonrelativistic single-electron approximation	9) L shell configuration $(nl)^N$	$(2s)^0(2p)^6$	$(2s)^1(2p)^5$				$(2s)^5(2p)^4$				
	10) line denoted by	$K-L_1L_1$	$K-L_1L_{2+3}$				$K-L_{2+3}L_{2+3}$				

*Here n is the principal quantum number, l is the orbital and j is the total electron angular momentum, L and J are the same for the atom, s, p, d... correspond to l = 0, 1, 2, ... (with similar notation for L), S is the atomic spin, N is the number of electrons with given n, l and j, and a six-pointed asterisk at the number indicates that the given state is forbidden by the Pauli principle.

**This configuration does not occur in Auger transitions (see text).

(or two-hole) spin function will be antisymmetric, and then the coordinate function of the equivalent electrons must be symmetric. Thus if both holes are in the $2s$ or $2p$ state,* then if S = 0 only even L are possible, and if S = 1 only odd L.

Thus in intermediate coupling there may be 9 lines in the K-LL group. Three of these, namely K-L_1L_2 (with J = 0), K-L_1L_3 (with J = 2), and K-L_3L_3 (with J = = 0), are very weak. These nine lines fuse into six in the jj and LS coupling limits, and into three in the nonrelativistic limit. For inequivalent electrons or holes (e.g., for a $2s$ and a $2p$ or a $2p$ and a $3p$ hole), combinations of S, L and J of all parities are possible. Thus the fifteen lines of the K-LM group split into 36 lines in intermediate coupling (these are given in Table 8). States forbidden by the Pauli principle are indicated by a six-pointed asterisk in Table 1.

If before the Auger transition took place in the atom there were already two (or more) vacancies, the classification of Auger electrons which includes the residual interaction (that is, cases 3 and 4) becomes even more complicated, in that the initial energy of the atom may be different depending on the coupling of the angular momenta of the holes in the initial state, that is, before the Auger transition.

The line which Sokolovski et al[1], thought to be a seventh K-LL line in copper would seem actually to be not an Auger line, since its energy does not correspond to the calculated value according to intermediate coupling.[4] A weak seventh K-LL line with the correct energy has been observed[3] in the spectrum of plutonium.

In most cases the most useful analysis of the Auger spectrum is by jj coupling, since, as has already been mentioned, the other lines are very weak and have energies almost equal to the main lines.

II. Auger electron energies

The kinetic energy $E(V - X_iY_j)$ of an Auger electron is given by

$$E(V - X_iY_j) = E(V) - E(X_i) - E(Y_j) - \Delta E_{X_iY_j}. \qquad (1)$$

Here V denotes the shell with the initial vacancy, X_i and Y_j are the shells (or subshells) in which vacancies are produced by the Auger transition, and $E(V)$, $E(X_i)$ and $E(Y_j)$ are the binding energies of the electron on these shells or subshells.

If one considers the electron from the X_i subshell to fill the vacancy, and that from Y_j shell to be emitted, then $E(V) - E(X_i)$ is the energy liberation in the transition, and $E(Y_j) + \Delta E_{X_iY_j}$ is the binding energy of an electron in the Y_j subshell in an atom singly ionized in the X_i subshell. Since the X_i and Y_j electrons are indistinguishable, one may equally consider $E(V) - E(Y_j)$ to be the energy liberated, and $E(X_i) + \Delta E_{X_iY_j}$ to be the binding energy of the electron in the X_i subshell in the atom ionized in the Y_j shell.

The values of $E(V)$, $E(X_i)$ and $E(Y_j)$ are well known. The most difficult quantity to determine is $\Delta E_{X_iY_j}$. A convenient empirical method for finding this quantity was suggested by Bergstrom and Hill[7]. According to them, when the atom is ionized in the X_i subshell, $E(Y_j)$ increases as though it were due to some increase ΔZ in the atomic number Z of the atom, or one may write

---

*In these states J must be even (see, for instance, Asaad and Burhop[4]).

$$\Delta E^{(Z)}_{X_iY_j} = \Delta Z\,[E^{(Z+1)}(Y_j) - E^{(Z)}(Y_j)]. \qquad (2)$$

The index Z refers to the element in which the Auger transition takes place. By choosing a reasonable value for ΔZ (see below), one can find $\Delta E_{X_iY_j}$ according to Eq.(2), and then use (1) to find the Auger electron energy.

Compared with other methods of finding the Auger electron energies, the Bergstrom-Hill method for all its simplicity gives the best results for all groups and series (except the K-LL group!).

In the intermediate coupling calculation, the Auger electron energy depends on the total angular momentum J of the atom with holes in the X_i and Y_j shells, i.e.,

$$\Delta E_{XY} = \Delta E_{YX} = \Delta E_{XY}(J).$$

Accurate measurement of the energy of K-LL electrons should be compared with the Asaad-Burhop[4] intermediate coupling calculations. Nevertheless, because of its simplicity, the ΔZ calculation is sometimes useful for rough estimates also for the K-LL group.

1. The K-LL group. The Asaad-Burhop intermediate coupling values for the energies of the nine lines in the K-LL group are given by

$$\begin{aligned}
&1.\ K-L_1L_1\,(^1S_0).\quad E(K)-E(L_1)-E(L_1)-F^0(2020);\\
&2.\ K-L_1L_2\,(^1P_1).\quad E(K)-E(L_1)-E(L_2)-F^0(2120)-\\
&\qquad -\left\{\left[\left(\tfrac{1}{3}G^1(2120)-\tfrac{1}{4}\zeta\right)^2+\tfrac{1}{2}\zeta^2\right]^{1/2}-\tfrac{3}{4}\zeta\right\};\\
&3.\ K-L_1L_3\,(^3P_1).\quad E(K)-E(L_1)-E(L_3)-F^0(2120)+\\
&\qquad +\left\{\left[\left(\tfrac{1}{3}G^1(2120)-\tfrac{1}{4}\zeta\right)^2+\tfrac{1}{2}\zeta^2\right]-\tfrac{3}{4}\zeta\right\};\\
&4.\ K-L_1L_2\,(^3P_0).\quad E(K)-E(L_1)-E(L_2)-F^0(2120)+\tfrac{1}{3}G^1(2120);\\
&5.\ K-L_1L_3\,(^3P_2).\quad E(K)-E(L_1)-E(L_3)-F^0(2120)+\tfrac{1}{3}G^1(2120);\\
&6.\ K-L_2L_3\,(^1D_2).\quad E(K)-E(L_2)-E(L_3)-F^0(2121)+\tfrac{2}{25}F^2(2121)-\\
&\qquad -\left\{\left[\left(\tfrac{3}{25}F^2(2121)+\tfrac{1}{4}\zeta\right)^2+\tfrac{1}{2}\zeta^2\right]^{1/2}-\tfrac{3}{4}\zeta\right\};\\
&7.\ K-L_3L_3\,(^3P_2).\quad E(K)-E(L_3)-E(L_3)-F^0(2121)+\tfrac{2}{25}F^2(2121)+\\
&\qquad +\left\{\left[\left(\tfrac{3}{25}F^2(2121)+\tfrac{1}{4}\zeta\right)^2+\tfrac{1}{2}\zeta^2\right]^{1/2}-\tfrac{3}{4}\zeta\right\};\\
&8.\ K-L_3L_3\,(^3P_0).\quad E(K)-E(L_3)-E(L_3)-F^0(2121)-\tfrac{1}{10}F^2(2121)+\\
&\qquad +\left\{\left[\left(\tfrac{3}{10}F^2(2121)-\tfrac{1}{2}\zeta\right)^2+2\zeta^2\right]^{1/2}-\tfrac{3}{2}\zeta\right\};\\
&9.\ K-L_2L_2\,(^1S_0).\quad E(K)-E(L_2)-E(L_2)-F^0(2121)-\tfrac{1}{10}F^2(2121)-\\
&\qquad -\left\{\left[\left(\tfrac{3}{10}F^2(2121)-\tfrac{1}{2}\zeta\right)^2+2\zeta^2\right]^{1/2}-\tfrac{3}{2}\zeta\right\}.
\end{aligned} \qquad (3)$$

Here

$$\zeta = \tfrac{2}{3}[E(L_2) - E(L_3)]; \qquad (4)$$

$E(K)$, $E(L_1)$, $E(L_2)$ and $E(L_3)$ are the binding energies of the electron on the K and L subshells. If the energies are all expressed in kev, then

$$\begin{aligned} F^0(2020) &= 0.00408\,(Z-3.8)\,(1-1.76\cdot10^{-5}Z^2);\\ F^0(2120) &= 0.00441\,(Z-4.0)\,(1-3.25\cdot10^{-5}Z^2);\\ G^1(2120) &= 0.00239\,(Z-2.6);\\ F^0(2121) &= 0.00494\,(Z-4.5)\,(1-2.5\cdot10^{-5}Z^2);\\ F^2(2121) &= 0.00239\,(Z-5.1). \end{aligned} \qquad (5)$$

The Asaad-Burhop calculations are performed in the nonrelativistic approximation. The $(1-\alpha Z^2)$ factors in (5) are introduced in order to take account of relativistic effects. The numerical values of α in these factors are chosen so as to make the electron energies agree as well as possible with the measurements of Mladenovic and Slätis[8] for Z = 83.

The $(Z-\sigma)$ factors in (5) describe screening effects. The parameter σ is chosen from the requirement that for Z = 80 the values of F and G in (5) agree with calculations based on the Hartree[9] self-consistent field method.

Table 2 gives the experimental energies of the main lines of the K-LL group, as well as the theoretical values according to (3)-(5) based on the binding energy tables of Wapstra, et al[10].

The theoretical and experimental absolute values of the energies do not agree very well. For Z = 29, for instance, the difference of roughly 60 ev is about 60 times greater than the uncertainty of measurement. However, the Asaad-Burhop calculation gives the relative positions of the lines extremely well, namely to within about 5 ev for Z = 29, or to about 50 ev for Z = 94 (which is 0.05% in both cases).

Table 3 gives the relative line energies according to the most accurate measurements.[2,3] In these measurements, as well as in others,[20] seven K-LL lines were observed for Z = 29, 93 and 94. Comparing the energy of the seventh line with the energies of the weak lines according to the intermediate coupling theory, one sees that only in the Z = 94 case is this an Auger line. The difference between the calculated and observed energies for all six lines is explained by saying that the Asaad-Burhop calculation takes screening correctly in account only for Z = 80. The screening correction should displace all the lines of a group about equally and for all these lines it can be introduced by adding to the right side of (3) the term

$$+\ 0.0011\cdot(80 - Z) \qquad (6)$$

The energy 0.0011 kev is chosen so as to obtain agreement between experiment and theory for Z = 29. In Table 2 the theoretical values are given without this correction. When it is used, the agreement is significantly improved for Z = 32, 47 and 62 as well. The remaining difference for $Z \geqslant 84$ may be attributed to uncertainties in the binding energy values for these heavy elements. It seems, furthermore, that there exist systematic errors in the energy measurements.[15,20]

It should be noted that the seventh line reported by Evan et al[3] was actually deduced from the modified shape of the close intense line. For heavier elements the width of the K level becomes so great (up to 100 ev), that close-lying weak Auger lines cannot be separated from the six principal lines by any increase in resolution of the instrument.

Since the binding energy and relativistic corrections in Eqs.(3)-(5) are obtained from experiment, the energies calculated from these formulas are semi-empirical.

Table 2

Experimental and theoretical energies of K-LL electrons (kev)

Line	Z = 29		Z = 32		Z = 47		Z = 62	
	Exper. [2]x	Theo. [4]	Exper. [2]	Theo. [4]	Exp. [11]*	Theo. [4]	Exp. [12]	Theo. [4]
$K-L_1L_1(^1S_0)$	6,739 ±0,006	6,678	8,212±0,006	8,151	17,74	17,732	31,15	31,144
$K-L_1L_2(^1P_1)$	6,867 ±0,004	6,811	8,367±0,004	8,309	18,02	18,012	31,60	31,579
$K-L_1L_3(^3P_1)$	6,909 ±0,006	6,851	8,415±0,006	8,356	18,18	18,174	32,19	32,151
$K-L_2L_2(^1S_0)$	7,006 ±0,0025	6,952	8,524±0,004	8,470	18,29	18,264	—	31,958
$K-L_2L_3(^1D_2)$	7,0345±0,001	6,980	8,561±0,0025	8,508	18,46	18,442	32,58	32,561
$K-L_3L_3(^3P_2)$	7,063 ±0,0025	7,008	8,601±0,0025	8,547	18,65	18,624	33,19	33,169

Line	Z = 64		Z = 74		Z = 78		Z = 79	
	Exper. [12]	Theo.[4]	Exper. [13]	Theo. [4]	Exper. [14]	Theo. [4]	Exper. [15]	Theo. [4]
$K-L_1L_1(^1S_0)$	—	33,235	45,07±0,05	45,077	50,35	50,372	51,87	51,743
$K-L_1L_2(^1P_1)$	33,68	33,696	45,63±0,05	45,653	51,06	51,003	52,51	52,391
$K-L_1L_3(^3P_1)$	34,39	34,357	46,95±0,05	46,956	52,68	52,676	54,26	54,168
$K-L_2L_2(^1S_0)$	—	34,096	—	46,149	—	51,541	53,10	52,944
$K-L_2L_3(^1D_2)$	34,85	34,789	47,50±0,05	47,492	53,28	53,260	54,89	54,766
$K-L_3L_3(^3P_2)$	35,58	35,488	48,86±0,05	48,843	55,03	54,983	56,64	56,594

Line	Z = 80			Z = 83			Z = 84		
	Exper. [7]	Theo [4]	Theo [5]	Exper. [16]	Exper. [8]	Theo [4]**	Exp. [17]	Exp. [18]	Theo. [4]
$K-L_1L_1(^1S_0)$	53,18±0,04	53,157	53,293	57,458±0,020	57,466±0,020	57,460	58,92	59,07	58,944
$K-L_1L_2(^1P_1)$	53,79±0,04	53,816	53,713	58,147±0,020	58,186±0,020	58,171	59,92	59,75	59,678
$K-L_1L_3(^3P_1)$	55,71±0,04	55,705	55,780	60,423±0,020	60,417±0,020	60,424	62,17	62,19	62,058
$K-L_2L_2(^1S_0)$	(54,32)	54,378	54,133	58,783±0,020	—	58,776	—	—	60,306
$K-L_2L_3(^1D_2)$	56,35±0,05	56,312	56,199	61,070±0,020	61,090±0,020	61,078	62,77	62,83	62,735
$K-L_3L_3(^3P_2)$	58,27±0,05	58,253	58,266	63,367±0,020	63,404±0,020	63,385	65,33	65,33	65,169

Line	Z = 93			Z = 94	
	Exper. [19]	Exper. [20]	Theo. [4]	Exper. [3]	Theo. [4]
$K-L_1L_1(^1S_0)$	73,41	73,7	73,532	75,18±0,015	75,259
$K-L_1L_2(^1P_1)$	74,25	74,6	74,401	76,05±0,015	76,160
$K-L_1L_3(^3P_1)$	78,21	78,52	78,335	80,24±0,015	80,304
$K-L_2L_2(^1S_0)$	—	75,3	75,138	76,78±0,04	76,927
$K-L_2L_3(^1D_2)$	78,95	79,32	79,126	81,06±0,015	81,125
$K-L_3L_3(^3P_2)$	82,99	83,3	83,122	85,30±0,015	85,331

*The energies here are those given by Goeffrion and Nadeau[21], who demonstrated a systematic error in the work of Johnson and Foster.[11]

**Some of the parameters in the theoretical formulas of Asaad and Burhop are chosen so as to give the best possible fit to the experimental results of Mladenovic and Slätis.[8]

xThe numbers in brackets in this and the following tables are References.

Table 3

Relative position of the K-LL lines (ev)

Line	Z = 29		Z = 32		Z = 93		Z = 94	
	Exper. [2]	Theo. [4]	Exper. [2]	Theo. [4]	Exper. [20]	Theo. [4]	Exper. [3]	Theo [4]
$K-L_1L_1\,(^1S_0)$	0	0	0	0	0	0	0	0
$K-L_1L_2\,(^1P_1)$	128	133	155	158	900	869	860	901
$K-L_1L_3\,(^3P_1)$	176	173	201	205	4820	4803	5060	5046
$K-L_1L_2\,(^3P_0)$	—	164	—	189	—	1818	—	951
$K-L_1L_3\,(^3P_2)$	—	184	—	220	—	4898	5220	5141
$K-L_2L_3\,(^1D_2)$	296	302	349	357	5620	5594	5880	5866
$K-L_3L_3\,(^3P_2)$	324	330	389	396	9600	9590	10120	10072
$K-L_3L_3\,(^3P_0)$	—	317	—	381	—	9522	—	10004
$K-L_2L_2\,(^1S_0)$	267	273	312	319	1600	1606	1600	1668
	97	?	—	—	4450	?	—	—

Asaad[5] calculated Auger electron energies without the use of empirical parameters only for six lines of the K-LL group for Z = 80 (mercury). These were relativistic calculations with jj coupling (but without the residual interaction). A screening correction was obtained by the Hartree self-consistent field method[9] with further corrections for exchange. The actual calculations were performed by electronic computers. The results are included in Table 2 (for Z = 80).

The Bergstrom-Hill ΔZ parameter for the K-LL group in the region Z = 80 to 85 has the following values: $\Delta Z = 0.54$ for Auger electrons from the L_1 subshell, $\Delta Z = 0.55$ for L_2 electrons, and $\Delta Z = 0.76$ for L_3 electrons.[7] This means that ΔE_{XY} in (1) and (2) is roughly the same for all lines of this group. The values of ΔE_{XY} and ΔZ for other Z can be found from the conditions (a) that $\Delta Z = 0.8$ for K-L_3L_3 lines, and (b) ΔE_{XY} is the same for all lines. For Z = 62, for instance, this gives $\Delta Z(L_1) \approx \Delta Z(L_2) \approx 0.65$, which agrees with experiment.[12]

In calculating the relative positions of the lines, the Bergstrom-Hill method is considerably inferior to the methods of Eqs.(3)-(5). If, however, one does not use the correction of (6), then away from the $Z \approx 80$ region the Bergstrom-Hill method gives absolute energy values of better accuracy than does the Asaad-Burhop method.

2. The K-LM group. Asaad and Burhop[4] also performed intermediate coupling calculations for the K-LM group. As an illustration, Fig.1 shows the transition from the LS coupling limit to the jj coupling limit for the $(2p)^5(3p)^5$ configuration of the L and M shells of an atom doubly ionized in these shells. When Z goes from 0 to ∞, the parameter η_0 goes from 0 to 1. In Fig.1 we have $\eta_0 = [1 + (30/Z_0)^3]^{-1}$; $Z_0 = [(Z - 3.3)\,(Z - \sigma)]^{1/2}$. The Slater screening constant σ is 10.25 for the K-$LM_{1,2,3}$ lines, and 20.15 for the K-$LM_{4,5}$ lines. In practice, however, the Asaad-Burhop results cannot be used to identify lines in this group for two reasons. First, only the displacements of the lines belonging to a single configuration are given, with no information about the relative position of lines belonging to the different configurations. Second, the nonrelativistic approximation is used with a very rough screening correction, which leads to results that are too inaccurate.*

---

*For instance, measurements[13] give an energy difference of 1.11±0.05 kev between the K-L_2M_3 and K-L_3M_2 lines for Z = 74. Bergstrom and Hill get 1.02 kev for this case with $\Delta Z = 1$. According to Fig.2, this difference is 0.62 kev. A similar conclusion will be reached if one compares the Asaad-Burhop calculations with experiment[8] for Z = 83.

Thus if one wants to calculate the K-LM or any other Auger group energies (other than K-LL) the best method to date is that of Eqs.(1) and (2) with a suitable choice of ΔZ.

Analysis of the experimental data for the electron energy gives[8] $\Delta Z \approx 0.60$ for the K-$LM_{1,2,3}$ lines when Z = 83. The same value of ΔZ was found[18] for Z = = 84. For Z = 74, Gallagher & Strominger[13] obtained $\Delta Z \approx 1$ for the same lines, so that energies calculated according to

$$E(K - L_i M_j) = E^{(Z)}(K) - E^{(Z)}(L_i) - E^{(Z+1)}(M_j),$$

agree well with experiment.

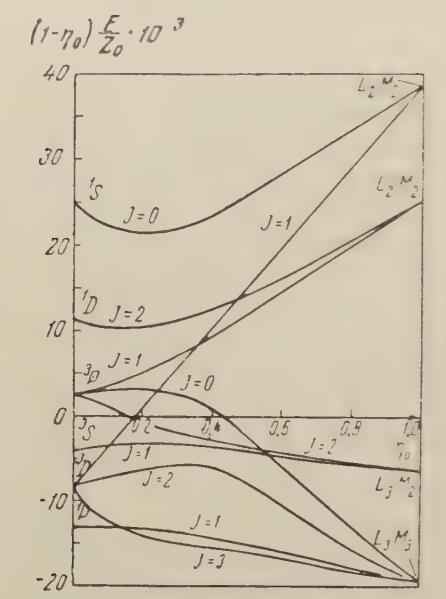

Fig.1. Transition from LS to jj coupling[4] with increasing Z for the $(2p)^5(3p)^5$ configuration. The ordinate is proportional to the line energy, and the abscissa gives η_0 (whose relation to Z is given in the text). The energy E is given in atomic units (27.2 ev).

3. Other groups of the K series. There are only scanty data on the line energies in the K-LN, K-MM and other groups. The energies are usually calculated by the Bergstrom-Hill method with the choice Z = 1, and the Y_j in Eq.(2) taken for the subshell which is further from the nucleus.

4. The L series. Sujkowski and Slätis[22] measured the energies and, very roughly, the relative intensities of the fifty-four lines in the L-MM and L-MN groups of Bi and Tl. They subjected their results to a detailed comparison with theory for various ΔZ values, as well as with earlier experimental results. The result is that these authors also find that $\Delta Z = 1$ gives the best fit for Z = 81-83. With this value the energy values obtained according to (1) and (2) are close to the experimental ones, with a mean deviation of the order of 10 ev. If one were to take $\Delta Z = 0$, this mean deviation would be of the order of 100 ev, so long as one does not alter the interpretation of any of the lines. Risch[23] found that for the L-MN group, ΔZ is different for different lines, lying in the region $0.7 \leqslant \Delta Z \leqslant 1.3$ (this also for Z = 81-83), The average value of ΔZ is about 1.

5. Further remarks on Auger electron energies. If the original vacancy in the L shell results from L conversion, L capture, or K_α(K-$L_{2,3}$) x-radiation, the L series of Auger electrons is emitted by a singly ionized atom. At the same time a definite fraction of the vacancies in the L shell is formed by K-LL Auger transitions, and this gives rise to an L series of Auger electrons from a doubly ionized atom. The line energies for electrons from a doubly ionized atom will differ greatly from the corresponding line energies for a singly ionized one, even approaching the energies corresponding to an atom with atomic number Z+1. This effect is discussed by Sujkowski and Slätis,[22] who were not able to observe the corresponding electrons. Such ionization differences should affect the energies in the M and N series even more greatly, since these can be emitted by multiply ionized atoms.

Auger electron energies depend on the mechanical motion of the emitting atom. For instance, in the α-decay of Bi^{212}, the Auger lines of Tl^{208} are broadened by ±112 ev as a result of recoil. In measuring coincidences between Auger electrons and α-particles at certain angles one obtains a definite energy shift; Burde & Cohen[24] took this shift into account.

From the calculated Auger electron energies one should subtract the work function of the metal if the electron binding energy values are based on the x-ray absorption edge in the metal (see, for instance, Wapstra, et al[10]).

The work function decreases[25] from 11 ev for Z = 3 (Li) to 5 ev for Z = 37 (Rb), and is equal to about 4 ev for Z $\geq$ 60. In gases the work function is zero. The theoretical values in Table 1 are given without this correction.

As for semiconductors (for instance, CuO), the electron energy levels in them lie deeper than in metals. Therefore the K-L_2L_3 electrons from CuO have energies 1.0 ± 0.3 ev lower than the corresponding Auger electrons from metallic copper.[26]

III. Group and Line Intensities

1. Methods for calculating Auger-effect probabilities. The first theoretical discussion of the probability for the Auger effect was that of Wentzel,[27] who found that in the nonrelativistic approximation this probability is independent of Z, and is equal to ~10^{15}sec^{-1}. As long ago as 1935 Pincherle[28] calculated the probabilities of all possible Auger transitions for shells and subshells up to $4p$ inclusive (the configuration of krypton), using the nonrelativistic approximation and unscreened hydrogen-like electron wave functions.

In the nonrelativistic approximation one assumes that the perturbation causing the first electron to undergo transition from its initial bound state to the final free state outside of the atom is its electrostatic interaction with the second electron which fills the hole in the transition. Let $\psi_i(r_1)$ be the Schrödeinger wave function of the first electron in its initial state, and $\psi_{f\,\mathrm{fr}}(r_1)$ its wave function in the final state. Similarly, let $\psi_i(r_2)$ and $\psi_f(r_2)$ be the initial and final state wave functions of the second electron. Then according to the usual quantum mechanical formula, the probability W_a for the Auger transition is

$$W_a = \frac{2\pi}{\hbar}\sum_{if}\left|\iint \psi^*_{f\,\mathrm{fr}}(\mathbf{r}_1)\,\psi^*_f(\mathbf{r}_2)\,V(\mathbf{r}_1-\mathbf{r}_2)\,\psi_i(\mathbf{r}_1)\,\psi_i(\mathbf{r}_2)\,(d\mathbf{r}_1)\,(d\mathbf{r}_2)\right|^2; \tag{7}$$

where the perturbation energy $V(\mathbf{r}_1 - \mathbf{r}_2) = e^2/|\mathbf{r}_1 - \mathbf{r}_2|$.

Because the two electrons are indistinguishable, one may also consider the first electron $(\mathbf{r}_1)$ to fill the vacancy, while the second $(\mathbf{r}_2)$ leaves the atom. This possibility will be correctly accounted for if one replaces the products of wave functions in (7) by antisymmetric combinations of the single-electron functions (in accordance with the Pauli principle). Then in the integrand of (7) there appears another term which differs from (7) only in the replacement of

$$\psi^*_{f\,\mathrm{fr}}(\mathbf{r}_1)\;\psi^*_f(\mathbf{r}_2) \quad \text{by} \quad \psi^*_{f\,\mathrm{fr}}(\mathbf{r}_2)\,\psi^*_f(\mathbf{r}_1).$$

In the relativistic theory one assumes that the transition of the first electron from its initial state (described by a relativistic Dirac electron wave function $\psi_i(\mathbf{r}_1)$ into the final state $(\psi_{f\,\mathrm{fr}}(\mathbf{r}_1))$. is brought about by the interaction of the electron with the electromagnetic radiation emitted when the second electron fills the hole. The vector and scalar potentials A_{if} and φ_{if} for the transition are related to the wave functions of the electrons filling the initial vacancy by the equations

$$A_{if} = -e\int[(\exp ik|\mathbf{r}_1-\mathbf{r}_2|)/|\mathbf{r}_1-\mathbf{r}_2|]\,\psi^*_f(\mathbf{r}_2)\,\vec{\alpha}\,\psi_i(\mathbf{r}_2)\,(d\mathbf{r}_2)$$

and

$$\varphi_{if} = -e\int[(\exp ik|\mathbf{r}_1-\mathbf{r}_2|)/|\mathbf{r}_1-\mathbf{r}_2|]\,\psi^*_f(\mathbf{r}_2)\,\psi_i(\mathbf{r}_2)\,(d\mathbf{r}_2). \tag{8}$$

Thus

$$W = \frac{2\pi}{\hbar} \sum_{if} |e \int \psi^*_{f\,\mathrm{fr}}(\mathbf{r}_1)\,(\vec{\alpha}\mathbf{A}_{if} - \varphi_{if})\,\psi_i(\mathbf{r}_1)\,(d\mathbf{r}_1)|^2; \qquad (9)$$

here $k = \frac{E_i - E_f}{\hbar c}$, where $E_i - E_f$ is the energy liberated when the second electron fills the vacancy, and $\vec{\alpha}$ represents the set of Dirac matrices.

The relativistic expressions for the Auger probabilities are similar to the corresponding expressions for the internal-conversion probabilities. They differ, however, in that in internal conversion the electromagnetic field causing the transition is produced by the nucleons; in the present case this field is produced by the electrons, and it thus becomes necessary to make use of the Pauli principle in (9) to take account of the indistinguishability of the electrons (as was done in the nonrelativistic approximation).

A relativistic theory of the Auger effect was given by Massey and Burhop[29] in 1936. These authors, however, in integrating Eqs.(8) and (9) and in performing the numerical calculations using hydrogen-like Coulomb electron wave functions, committed a number of errors. In 1957 we deduced the correct expressions for the Auger probabilities and undertook numerical calculations in which screening effects were included. In 1959 Asaad[5] published results of relativistic calculations with screening for Z = 80 for the K-LL group.

2. Absolute probabilities for the Auger effect. Table 4 gives the transition probabilities for the K-LL group in atomic units, as calculated by various authors on the basis of various different assumptions. The absolute values of the intensities can be obtained from the relative-intensity tables given below.

Table 4

K-LL transition probabilities per 10^3 atomic time units*

Line	nr; us All Z Ref.28	nr; H Z = 47 Ref.30	r; H Z = 79 Ref.22	nr; T-F Z = 79 Ref.31	nr; Ha Z = 80 Ref.5	r; Ha Z = 80 Ref.5
$K - L_1L_1$	2,5	2,54	1,74	2,02	2,04	9,01
$K - L_1L_{2+3}$	8,83	8,65	18,73	7,10	7,16	20,32
$K - L_{2+3}L_{2+3}$	24,3	17,11	—	19,25	17,58	19,86
$\Sigma K - LL$	35,6	28,30	—	28,37	26,78	49,19

*One atomic time unit is $2.42 \cdot 10^{-17}$ sec. To find the transition probabilities per second, the tabulated data should be multiplied by $4.134 \cdot 10^{13}$. To find the partial widths of the Auger lines in ev, the tabulated data should be multiplied by $27.2 \cdot 10^{-3}$. The notation is the following: r = relativistic calculation; nr = nonrelativistic approximation; us = calculation for an unscreened atom; H = = calculation with hydrogen-like wave functions and with Z replaced by Z - σ (where σ is the Slater screening constant); T-F = screening according to the Thomas-Fermi statistical model (without exchange); Ha = screening according to the Hartree self-consistent field.

Calculations made in the nonrelativistic approximation lead in general to very similar results and can be used for light atoms. In heavy atoms, however, the relativistic corrections become quite important: they increase the emission probability for the K-LL group by 80%, while the probability of the $K\text{-}L_1L_1$ transition is multiplied for the same reason by a factor of 4.

Table 5

Experimentally observed relative intensities of the lines in the K-LL group

Line	Z = 26 [32]	Z = 29 [33]	Z = 29 [2]	Z = 32 [2]	Z = 47 [11]	Z = 62 [12]	Z = 69 [34]	Z = 74 [13]	Z = 78 [14,3]	Z = 79 [15]	Z = 80 [7]	Z = 83 [35]	Z = 83 [8]	Z = 83 [16]	Z = 84 [18]	Z = 84 [8,17]	Z = 94 [3]
$K-L_1L_1$	1,0	1,0	1,0	1,0	1,0	1,0	1,0	1,0	1,0	1,0	1,0	1,0	1,0	1,0	1,0	1,0	1,00
$K-L_1L_2$	2,3±0,2	2,8±0,2	3,1	3,3	1,3±0,2	1,2	1,6	2,1	1,4±0,25	1,7	1,2	1,8	1,8	1,72	~1,45	1,6	1,86±0,10
$K-L_1L_3$			1,3	0,9	1,3±0,2	1,5	1,5	0,7	0,9±0,2	1,2	0,7	1,3	1,1	0,91	~0,65	0,9	0,65±0,08
$K-L_2L_2$			1,9	1,0	0,5±0,2			—	0,2±0,1	0,3	0,2	0,2	~0,2	0,17	<0,15	0,5	0,11±0,04
$K-L_2L_3$	6,6±0,6	9,1±1,0	14,3	14,3	3,2±0,4	2,6	2,0	1,9	1,4±0,25	1,4	1,4	2,3	1,6	1,64	~1,35	1,4	1,11±0,07
$K-L_3L_3$			1,9	2,0	1,8±0,2	0,9	0,9	0,8	0,8±0,2	0,8	0,6	1,2	0,8	0,69	~0,70	0,6	0,40±0,05

3. Relative intensities of Auger-electron groups and lines; the K-LL group. The group in which the line intensities have been most thoroughly studied is the K-LL group. Table 5 gives the experimental values of the relative line intensities according to several authors.

Table 6 gives the average values of the experimental relative intensities for all Z, with the data of Refs.2, 3, 8, 11 and 16 given the greatest weight. For large and medium Z, these values are pretty well established. The uncertainties are of the order of 40% for $K-L_2L_2$ and about 10% for the other lines. For $Z < 50$ the relative intensities are not as reliable, in view of the discrepancies between the results of Sokolovski & Nordling[2] and Moussa et al[32,33]. For these values of Z the uncertainty is of the order of 30-35%.

Table 7 gives a comparison of experiment with various theories. It will be evident from Tables 7a and 7b that the nonrelativistic theory does not give sufficiently good agreement with experiment even for low values of Z. The Asaad-Burhop (intermediate coupling) improvement of the theory does not significantly affect these results. For Z = 29 the intensity ratios for some of the lines differ from the Asaad-Burhop predictions by a factor of as much as five (for instance for the $K-L_2L_2/K-L_1L_1$ ratio).

For Z = 80 the difference between jj coupling and intermediate coupling in the nonrelativistic theory becomes negligible (compare columns 5 and 6 of Table 7c).

For the heavy elements the latest results calculated relativistically for the K-LL spectrum (Table 7c) are in satisfactory agreement with experiment. The nonrelativistic approximation for Z = 94 (Table 7d) gives results which are in poorer agreement with experiment than the relativistic calculation for Z = = 80. Nevertheless the intermediate coupling theory gives good agreement for the intensity ratio of the two components which, according to this theory, make up the $K-L_1L_3$ line.

Table 8 gives the relative intensities of the K-LL and K-LM groups as calculated by Asaad and Burhop[4]. They obtained the matrix elements for the K-LL calculation from Burhop's results,[30] and for the K-LM calculation from unpublished work of Rubinstein and Snyder.

Tables 4-8 contain all the theoretical results on the intensity of K-LL lines published up to 1959, as well as most of the experimental data.

4. K-LX and K-XY groups (where X and Y stand for any shells other than K or L). Although the experiments on K-LX groups are not very accurate, one may nevertheless conclude from Table 9 that the theory

Table 6

Averaged experimental relative intensities of lines in the K-LL group

Line	$Z = 30$	$Z = 40$	$Z = 50$	$Z = 60$	$Z = 70$	$Z = 80$	$Z = 90$	$Z = 100$
$K - L_1L_1$	1,0	1,0	1,0	1,0	1,0	1,0	1,0	1,0
$K - L_1L_2$	3,2	2,0	1,4	1,4	1,5	1,6	1,7	1,9
$K - L_1L_3$	1,1	1,2	1,3	1,2	1,1	0,9	0,7	0,6
$K - L_2L_2$	1,4	0,8	0,5	0,3	0,2	0,15	0,10	0,10
$K - L_2L_3$	~13	~5	~3,3	~2,5	1,9	1,5	1,2	1,1
$K - L_3L_3$	1,9	1,8	1,6	1,3	1,0	0,7	0,5	0,3
$K - LL/K - L_1L_1$	~22	~12	~9	~7,7	6,7	5,8	5,2	5,0

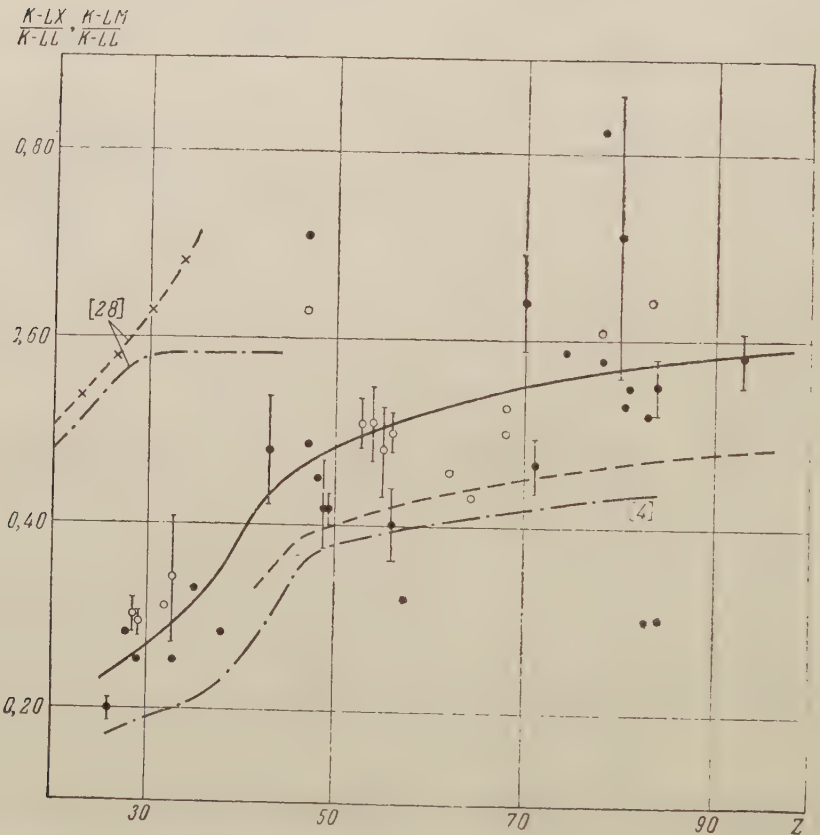

Fig.2. The K-LM/K-LL (open circles) and K-LX/K-LL (solid circles) ratios for different Z. The solid curve gives the average experimental results for the K-LX/K-LL ratio; the dashed curve for the K-LM/K-LL ratio. The dot-dash curve gives the Asaad-Burhop[4] and Pincherle[28] results for K-LM/K-LL; the dash-cross curve gives the Pincherle[28] results for K-LX/K-LL.

corresponds only very approximately to experiment. For large Z the deviation can be explained by the fact that the theory does not include relativistic effects.

Table 10 gives the measured K-LX/K-LL and K-XY/K-LL ratios for various Z. The ratios are also shown in Figs.2 and 3. The same figures also give the theoretical curves for K-LX/K-LL, K-LM/K-LL, K-XY/K-LL and K-MM/K-LL according to Pincherle[28] and Asaad & Burhop[4]. In addition to the theoretical calculations

Table 7

Comparison of theoretical and experimental relative line intensities for the K-LL group*

a) $Z \leqslant 32$

Line	All Z	Z = 18	Z = 26		Z = 29			Z = 32	
	Theo; one-electron approx.		Exper.	Theo.	Exper.		Theo.	Exp.	Theo.
	nr; us Ref. 28	nr; Ha Ref. 36	[32]	nr; H; intermed. coupling Ref. 4	[33]	[2]	nr; H; intermed. coupling Ref. 4	[2]	nr; H; intermed. coupling Ref. 4
$K-L_1L_1(^1S_0)$	1,00	1,00	1,00	1,00	1,00	1,00	1,00	1,00	1,00
$K-L_1L_2(^1P_1)$						3,1	2,84	3,3	2,70
$K-L_1L_2(^3P_0)$ (weak)	3,54	3,26	2,3±0,2	3,62	2,8±0,2	— 4,4	0,05 3,49	— 4,2	0,05 3,48
$K-L_1L_3(^3P_1)$						1,3	0,36	0,9	0,49
$K-L_1L_3(^3P_2)$ (weak)						—	0,24	—	0,24
$K-L_2L_2(^2S_0)$						1,9	0,39	1,0	0,37
$K-L_2L_3(^1D_2)$	9,8	8,2	6,6±0,6	6,93	9,1±1,0	14,3 18,1	5,63 6,84	14,3 17,3	5,39 6,78
$K-L_3L_3(^3P_2)$						1,9	0,79	2,0	0,97
$K-L_3L_3(^3P_0)$ (weak)						—	0,03	—	0,05

b) $Z = 47$

Line	Exper.	Theory (nr; H)		
		$j-j$-cpling		interm. coupling
	[11]	[30]	Burhop** (1954)	[4]
$K-L_1L_1$	1,00	1,00	1,00	1,00
$K-L_1L_2$	1,3±0,2	1,17	1,13	1,82
$K-L_1L_3$	1,3±0,2	2,25	2,26	1,66
$K-L_2L_2$	0,5±0,2	0,96	0,38	0,24
$K-L_2L_3$	3,2±0,4	2,55	4,03	4,71
$K-L_3L_3$	1,8±0,2	3,23	2,30	1,90

**According to Bergstrom.[37]

c) $Z \approx 80$

Line	Experiment Z = 80 (see Table 6)	Nonrelativistic theory			Relativistic theory		
		Z = 79	Z = 80		Z = 79		Z = 80
		one-electron approximation nr; T-F [31]	intermed. coupling		$j-j$-coupling		
			nr; H[4]	nr; Ha [5]	nr; H[5]	r; H[22]	r; Ha [5]
$K-L_1L_1$	1,0	1,00	1,00	1,00	1,00	1,00	1,00
$K-L_1L_2$	1,6	1,16	1,20	1,27	1,18	5,5	1,44
$K-L_1L_3$	0,9	2,35	2,27	2,25	2,33	5,3	0,82
$K-L_2L_2$	0,15		0,15	0,25	0,25	—	0,09
$K-L_2L_3$	1,5	9,51	4,32	5,37	5,54	—	1,46
$K-L_3L_3$	0,7		2,40	3,00	3,03	—	0,66

d) $Z = 94$

Line	Exper. [3]	Theory, extrapolation of Ref. 4 (intermed. coupling) nr; H
$K-L_1L_1(^1S_0)$	1,00	1,00
$K-L_1L_2(^1P_1)$	1,86±0,10	1,06
$K-L_1L_2(^3P_0)$	—	0,05
$K-L_2L_2(^1S_0)$	0,11±0,04	0,14
$K-L_1L_3(^3P_1)$	0,60±0,06	2,12
$K-L_1L_3(^3P_2)$	0,05±0,03	0,24
$K-L_2L_3(^1D_2)$	1,11±0,07	4,28
$K-L_3L_3(^3P_0)$	—	0,29
$K-L_3L_3(^3P_2)$	0,40±0,05	2,7

*For the meaning of us, nr, H, Ha, etc., see Table 4.

Table 8

Relative intensities of lines in the K-LL and K-LM groups, as calculated by Asaad & Burhop[4] in the intermediate coupling approximation (nonrelativistic approximation with H-like wave functions)

Line	$Z = 25$	$Z = 30$	$Z = 37$	$Z = 47$	$Z = 80$
$K - L_1L_1\ (^1S_0)$	1,00	1,00	1,00	1,00	1,00
$K - L_1L_2\ (^1P_1)$	2,99	2,80	2,40	1,77	1,15
$K - L_1L_2\ (^3P_0)$	0,047	0,047	0,047	0,047	0,047
$K - L_1L_3\ (^3P_1)$	0,24	0,40	0,80	1,42	2,03
$K - L_1L_3\ (^3P_2)$	0,24	0,24	0,24	0,24	0,24
$K - L_2L_2\ (^1S_0)$	0,41	0,38	0,32	0,24	0,15
$K - L_3L_3\ (^1D_2)$	6,08	5,54	5,08	4,71	4,32
$K - L_2L_3\ (^3P_0)$	0,012	0,038	0,096	0,185	0,28
$K - L_3L_3\ (^3P_2)$	0,47	0,86	1,30	1,72	2,12
$K - L_1M_1\ (^3S_1)$	0,001	0,001	0,001	0,002	0,002
$K - L_1M_1\ (^1S_0)$	0,17	0,19	0,20	0,29	0,31
$K - L_1M_2\ (^3P_0)$	0,005	0,006	0,007	0,011	0,013
$K - L_1M_2\ (^1P_1)$	0,19	0,18	0,17	0,49	0,18
$K - L_1M_3\ (^3P_1)$	0,035	0,059	0,114	0,25	0,31
$K - L_1M_3\ (^3P_2)$	0,027	0,031	0,037	0,057	0,062
$K - L_2M_1\ (^3P_0)$	0,005	0,005	0,005	0,006	0,006
$K - L_2M_1\ (^1P_1)$	0,146	0,138	0,118	0,150	0,152
$K - L_3M_1\ (^3P_1)$	0,100	0,115	0,170	0,25	0,28
$K - L_3M_1\ (^3P_2)$	0,023	0,024	0,024	0,033	0,035
$K - L_1M_4\ (^3D_1)$		0,001	0,002	0,010	0,010
$K - L_1M_4\ (^1D_2)$	—	—	0,001	0,004	0,009
$K - L_1M_5\ (^3D_2)$	—	0,001	0,003	0,015	0,010
$K - L_1M_5\ (^3D_3)$	—	0,002	0,005	0,022	0,022
$K - L_2M_2\ (^1S_0)$	0,080	0,077	0,059	0,087	0,071
$K - L_3M_2\ (^3S_1)$	0,001	0,001	0,001	0,001	0,001
$K - L_3M_3\ (^1P_1)$	—	—	0,0004	0,001	0,001
$K - L_3M_3\ (^3P_0)$	0,020	0,029	0,058	0,125	0,142
$K - L_2M_3\ (^3P_1)$	—	0,0002	0,0004	0,0009	0,0010
$K - L_3M_2\ (^3P_2)$	0,087	0,34	0,39	0,75	0,80
$K - L_2M_3\ (^1D_2)$	1,08	0,93	0,88	1,035	0,93
$K - L_2M_2\ (^3D_1)$	0,001	0,001	0,001	0,002	0,002
$K - L_3M_3\ (^3D_2)$	0,015	0,016	0,088	0,60	0,70
$K - L_3M_3\ (^3D_3)$	—	0,002	0,003	0,005	0,005
$K - L_3M_4\ (^3P_0)$	—	—	0,0002	0,0007	0,0014
$K - L_3M_4\ (^3P_1)$	—	—	0,0003	0,0012	0,0030
$K - L_2M_5\ (^3P_2)$	—	—	0,0006	0,0026	0,0058
$K - L_2M_4\ (^1P_1)$	—	—	0,0004	0,0014	0,0023
$K - L_3M_5\ (^3D_1)$	—	—	0,0004	0,0019	0,0041
$K - L_2M_4\ (^3D_2)$	—	—	0,0049	0,028	0,053
$K - L_3M_4\ (^3D_3)$	—	—	0,0099	0,138	0,315
$K - L_3M_5\ (^1D_2)$	—	—	0,0014	0,0055	0,0057
$K - L_3M_4\ (^3F_2)$	—	—	0,0015	0,0057	0,0146
$K - L_3M_5\ (^3F_3)$	—	—	0,0084	0,0225	0,040
$K - L_3M_5\ (^3F_4)$	—	—	0,0135	0,070	0,137
$K - L_2M_5\ (^1F_3)$	—	—	0,049	0,158	0,263
$\sum_i K - L_1M_i$	0,428	0,471	0,540	0,851	0,929
$\sum_i K - L_2M_i$	1,312	1,151	1,118	1,471	1,486
$\sum_i K - L_3M_i$	0,246	0,527	0,770	2,010	2,485
$\frac{K - LM}{K - LL}$	0,172	0,190	0,215	0,382	0,432

Table 9

Relative intensities of lines in K-LX groups*

Line	Experiment							Theory					
					Z = 83			intermediate coupling		Intermed. coupling			
	Z = 29 [33]	Z = 47 [11]	Z = 74 [13]	Z = 78 [14]	[8]	***	Z = 93 [20]	All Z nr;us [23]	Z = 47 nr;H [30]	Z = 29	Z = 47	Z = 76	Z = 83
										nr; H [4]			
$K-L_1L_1$	1,00	1,00	1,00	1,00	1,00	1,00	1,00	1,00	1,00	1,00	1,00	1,00	1,00
$K-L_1M_1$	0,95	0,8±0,2	0,5±0,2	0,5	0,4	0,4	1,7	0,5	0,49	0,19	0,29	0,30	0,31
$K-L_1M_2$		0,8±0,2	0,4±0,2	0,3	0,5	0,3		1,0	1,24	0,19	0,20	0,19	0,19
$K-L_1M_3$			0,5±0,2	0,5	0,8	0,5				0,09	0,31	0,35	0,37
$K-L_2M_1$	1,75	0,2±0,1**						0,7	0,18	0,14	0,15	0,16	0,16
$K-L_3M_1$		1,6±0,3	0,4±0,2	—	—	⩽0,1				0,08	0,28	0,31	0,32
$K-L_2M_3$			0,25±0,1**	0,4**	0,7**	0,4**		4,5	2,5	0,96	1,04	0,95	0,93
$K-L_2M_2$		—	—	—	—	—	—			0,14	0,09	0,07	0,07
$K-L_3M_2$		1,7±0,3**	0,6±0,2	0,5**	0,7**	0,5**	1,3			0,31	0,75	0,79	0,80
$K-L_3M_3$			0,7±0,3**	0,4	1,0**	0,45**				0,05	0,73	0,82	0,85
$K-L_1M_{4,5}$	—	same as $K-L_2M_1$	same as $K-L_2M_3$	same as $K-L_2M_3$	same as $K-L_2M_3$	same as $K-L_2M_3$		0,1	0,5	—	0,05	0,05	0,05
$K-L_2M_{4,5}$	—	—	—	—	—	—		1,4	0,61	—	0,19	0,27	0,32
$K-L_3M_{4,5}$	—	0,55±0,20	0,4±0,2**	0,25**	—**	0,1**				—	0,25	0,46	0,52
$K-L_1N_{1-3}$	—	same as $K-L_3M_{2,3}$	same as $K-L_3M_3$	same as $K-L_3M_2$	same as $K-L_3M_2$	same as $K-L_3M_2$		0,19	—	—	—	—	—
$K-L_2N_{1-3}$	—	0,3±0,2	same as $K-L_3M_{4,5}$	same as $K-L_3M_{4,5}$	same as $K-L_3M_3$	same as $K-L_3M_3$		0,33	—	—	—	—	—
$K-L_3N_{1-3}$	—	0,55±0,20	0,15±0,1	0,3	—**	0,2**	0,2		—	—	—	—	—
$K-L_1N_{4-7}+K-L_1O$	—	same as $K-L_2M_{4,5}$	—	same as $K-L_3M_{4,5}$	same as $K-L_3M_3$	same as $K-L_3M_3$	—	—	—	—	—	—	—
$K-L_2N_{4-7}+K-L_2O$	—	—	—	—	same as $K-L_3M_{4,5}$	same as $K-L_3M_{4,5}$	—	—	—	—	—	—	—
$K-L_3N_{4-7}+K-L_3O$	—	—	—	—	same as $K-L_3N_{1-3}$	same as $K-L_3N_{1-3}$	—	—	—	—	—	—	—

*The interpretation of some of the lines is now better established than was indicated in the original experimental papers.

**Includes the intensity of a line with the same energy.

***Calculations of E.M.Krisyuk based on Fig.2 in Zernovoi et al[16].

Table 10

Relative intensities of groups in the K series

Z	$\frac{K-LX}{K-LL}$	$\frac{K-XY}{K-LL}$	Ref.	Remarks
26	0,20±0,01		[39]	
28	0,28		[40]	
29	0,252		[41]	
—	0,292±0,010	0,016±0,002	[42]	
—	0,30 ±0,02	0,017±0,004	[33]	
32	0,31		[6]	$K-LM$
33	0,34 ±0,07	0,013±0,004	[43]	$K-LM$ & $K-MM$
—	0,25		[44]	
35	0,33		[45]	
38	0,28		[46]	
43	0,48±0,06	0,05±0,01	[38], [47]	
47	0,49	0,054	[47]	$K-MM$
—	0,71	0,075	[11]	$\frac{K-LM}{K-LL}=0,63$; $\frac{K-MM}{K-LL}=0,058$
48	0,45	0,056	[48]	$K-MM$
49	0,417±0,016	0,076±0,008	[49]	
—	0,429±0,05	0,05 ±0,02	[38], [47]	
53	0,51±0,03*	0,035±0,010	[50]	$K-L(M,N)$ & $[(K-MM)+(K-NN)]$
54	0,51±0,04		[51]	$K-LM$
55	0,48±0,05		[51]	$K-LM$
56	0,40±0,04	0,08±0,02	[49]	
—	0,50±0,02	0,08±0,04	[52]	$K-LM$ & $K-MM$
57—58	0,32		[53]	
62	0,457		[12]	$K-LM$
64—65	0,43		[54]	} $K-KM$
68	0,50		[55]	
—	0,525	0,075	[56]	$K-LM$ & $K-MM$
70	0,64±0,05		[18]	
71	0,477±0,03	0,10±0,04	[57]	
74	0,585		[13]	$K-LM$ & $K-LN$
78	0,82	0,25**	[58]	$K-LM, K-LN$ & $K-MM$; $K-LM/K-LL\sim 0,61$
—	0,58		[14]	$K-LM$ & $K-LN$
80	0,71±0,015		[49]	
80—81	0,53±0,06		[59]	
81	0,55		Herrlander cited in [18]	
83	0,64		[8]	
—	0,52		[16]	$K-LM$
—	⩾0,4		[35]	
84	0,55±0,03		[18]	
—	0,40		Hoff cited in [18]	
93	0,58±0,03	0,085±0,008	[20]	$\frac{K-MM}{K-LL}=0,046$

*Some use is made of the results of Bergstrom.[51]

**According to Broyles et al[49], the value measured by Steffan et al[58] is 0.025.

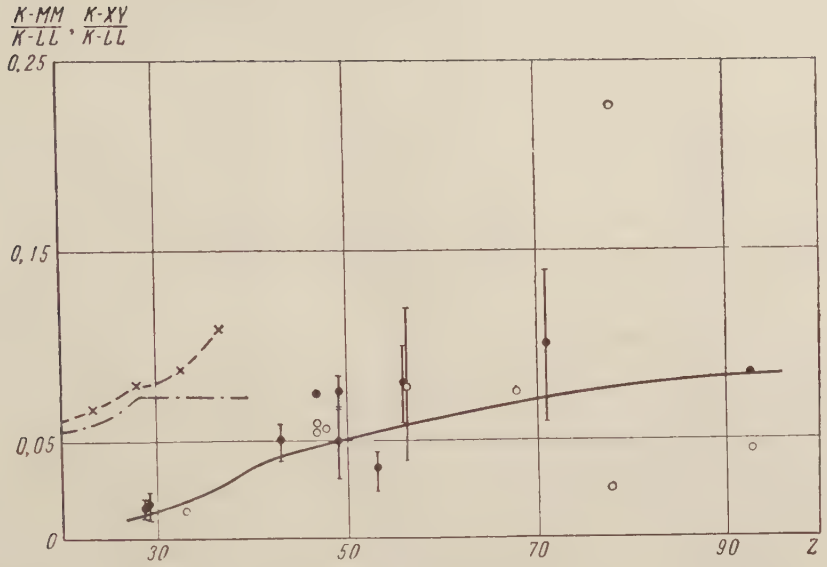

Fig.3. The K-MM/K-LL (open circles) and K-XY/K-LL (solid circles) ratios. The solid curve approximates the mean values. Pincherle's[2] theoretical results are given by the dot-dash curve for K-MM/K-LL and by the dash-cross curve for K-XY/K-LL.

given in Tables 8 and 9 and Figs.2 and 3, there exist also the calculations of Rubinstein and Snyder (Ref.36 and some unpublished work). Their calculations give

for Z = 18, $(K\text{-}L_1M):(K\text{-}L_{2+3}M):(K\text{-}LL) = 0.04:0.11:1.00$;

for Z = 47 (cited in Ref.38), $(K\text{-}LL):(K\text{-}LX):(K\text{-}XY) = 1.000:0.312:0.022$.

The 0.312 result is much lower than the experimentally observed value in this region of Z.

The various theoretical results disagree, which is probably due to errors in calculation rather than differences in the basic assumptions. Figures 2 and 3 show curves of average experimental results. When the error in measurement is reported as the same, the later result is given the greater weight. The errors for K-LX/K-LL are of the order of 5-10% in the middle of the curve, and 10-15% at its ends; for K-XY/K-LL this error is about 20-25%.

An important fact is that the K-LM, K-LN, and K-LO spectra overlap to some extent in all atoms having N or O electrons. Therefore whenever an author claims to have measured the K-LM/K-LL ratio, he has actually measured at best

$$\frac{(K-LM)+(K-L_1(N+O))}{K-LL},$$

while for Z > 72, he has measured

$$\frac{(K-LM)+(K-L_{1+2}(N+O))}{K-LL}$$

For relatively low Z and poor resolution, the ratio does, in fact, turn out to be K-LX/K-LL. For large Z and for sufficiently good resolution, one can use Table 11 to obtain a correction to the measured K-LM/K-LL value in order to determine K-LX/K-LL (using, for instance, the data of Mladenovic and Slätis[8]). This situation was taken into account in constructing the average curve in Fig.2. The K-LX/K-LL curve differs greatly from the straight line the authors of several review articles[10,18,37] and others have given for this case; its shape approaches

Table 11

Average values of line intensities in the K-LX groups

Line	$Z = 47$	$Z = 74$	$Z = 83$
$K - L_1L_1$	1,00	1,00	1,00
$K - L_1M_1$	0,5	~0,45	0,4
$K - L_1M_2$	~0,25	0,3	~0,35
$K - L_1M_3$	0,3	0,3	~0,35
$K - L_1M_{4+5}$	<0,05	<0,05	<0,05
$K - L_2M_1$	~0,15	~0,15	~0,15
$K - L_2M_2$	~0,05	<0,05	<0,05
$K - L_2M_3$	0,8	0,4	~0,35
$K - L_2M_{4+5}$	0,1	~0,05	~0,05
$K - L_3M_1$	~0,25	0,2	0,1
$K - L_3M_2$	0,5	0,4	~0,35
$K - L_3M_3$	0,5	~0,45	0,4
$K - L_3M_{4,5}$	0,3	0,1	0,1
$\Sigma K - LM$	~3,75	~2,85	2,65
$K-L_1M : K-L_2M : K-L_3M$	1 : 1 : 1,4	1 : 0,6 : 1,05	1 : 0,5 : 0,85
$K - L_1N_{1-3}$	0,2	0,2	0,2
$K - L_1N_{4-7}$	—	—	—
$K - L_2N_{1-3}$	0,2	0,1	0,1
$K - L_2N_{4-7}$	~0,05	<0,05	<0,05
$K - L_3N_{1-3}$	0,3	0,2	~0,15
$K - L_3N_{4-7}$	~0,05	<0,05	<0,05
$K - LO$	—	~0,1	~0,1
$\Sigma K - L(N+O)$	0,8	<0,65	0,6
$K - LX$	~4,55	3,5	~3,25
$K - L(N+O)/K - LM$	~0,21	~0,23	~0,23
$K - LL/K - L_1L_1$	~9,7	~6,3	~5,65
$K - LM/K - LL$	~0,39	~0,46	~0,47
$K - LX/K - LL$	~0,47	~0,55	~0,57

that of the Asaad-Burhop K-LM/K-LL curve, although it lies somewhat higher. Similarly, the curve of Fig.10 differs from the results of Wapstra et al[10].

Table 11 is constructed on the basis of several experimental works[8,11,13,14,16,20] and on the assumption that both K-LN/K-LM and K-LO/K-LN are of the order of 0.2 to 0.25 (in analogy with internal conversion[60]) and that (K-L,N):K-L_2N):(K-L_3N) ≈ (K-L_1M):(K-L_2M):(K-L_3M), according to the same analogy.

These assumptions do not contradict experiment. Some of the coincident lines have been "resolved" by using the theoretical values for their intensity ratios. The K-LX/K-LL ratio is taken from Fig.2. The value of K-LM/K-LL obtained is rather close to the result of Asaad & Burhop[4], while the ratios (K-L_1M):(K-L_2M):(K-L_sM) differ from theirs in that the fraction of K-L_1M increases with increasing Z.

Table 12 gives Pincherle's[28] theoretical results for K-XY groups; no more accurate results exist. Scant experimental data giving the intensities of some individual K-XY lines can be found only in two articles.[11,20]

The total probability for K-LX + K-XY Auger transitions was calculated by Mokhov and Urin[61] for $Z \approx 47$ (in the nonrelativistic approximation with hydrogen-like wave functions). The probability obtained from their calculations is

$$W_a(K - LX + K - XY) = 17.6 \cdot 10^{-3} \text{ a u}$$

or, if one takes W_a(K-LL) from Burhop[30], one obtains [(K-LX) + (K-XY)]/(K-LL) = = 0.625. This is considerably closer to the experimental results than Pincherle's value of 0.82. The Mokhov-Urin method, however, cannot be used to calculate the individual line intensities.

5. The L series. The intensity ratios of lines in the L_1-XY, L_2-XY, and L_3-XY groups depend on the relative number of initial vacancies in the given subshell, and differ for different modes of excitation. For instance, if the Auger

Table 12

Relative K-XY line intensities

Line	Theo.[28] nr; us Ali Z	Exper. [11] Z = 47	Line	Theo.[28] nr; us Ali Z	Exper. [11] Z = 47
$K-L_1L_1$	1,00	1,00	$K-M_{4,5}N_1$	0,004	
$K-M_1M_1$	0,06		$K-M_{4,5}N_{2,3}$	0,06	
$K-M_1M_{2,3}$	0,21	0,18±0,10	$K-N_1N_1$	0,004	
$K-M_1M_{4,5}$	0,01		$K-N_1N_{2,3}$	0,01	
$K-M_1N_1$	0,02		$K-N_{2,3}N_{2,3}$	0,02	
$K-M_1N_{2,3}$	0,06	0,05			
$K-M_{2,3}M_{2,3}$	0,53	0,3±0,02	$K-MM/K-LL$ for $Z>29$	0,075	0,058
$K-M_{2,3}M_{4,5}$	0,24	0,05			
$K-M_{2,3}N_1$	0,05		$K-XY/K-LL$ for $Z=36$	0,103	
$K-M_{2,3}N_{2,3}$	0,16				
$K-M_{4,5}M_{4,5}$	0,02				

transition follows L shell conversion of an M1 gamma, the L_1-X_iY_j lines will be more intense than those excited by E2 gammas, which rarely produce vacancies in the L_1 shell. On the other hand, the relative intensities of lines in a given group (e.g., L_2-X_iY_j lines with different i and j) do not depend on the mode of excitation. There have, however, been very few studies of these relative intensities. For the existing data see Section VI.

IV. Fluorescence Yield for the K Shell

The yield ω_K of K fluorescence is defined as the ratio

$$\omega_K = \frac{W_{XK}}{W_{XK}+W_{aK}}, \tag{10}$$

where W_{XK} is the probability for x-radiation of the K series, and W_{aK} is the probability for Auger emission of K series.

The Auger yield a_K is defined as the ratio $\frac{W_{aK}}{W_{XK}+W_{aK}}$.

It is convenient to represent ω_K in the following way. Since the probability for x-radiation is proportional to Z^4, while the Auger effect depends only weakly on Z, Eq.(10) can be written

$$\omega_K = \frac{aZ^4}{aZ^4+b} \quad \text{or} \quad \left(\frac{\omega_K}{1-\omega_K}\right)^{\frac{1}{4}} = BZ \quad \left(B=\frac{a}{b}\right). \tag{11}$$

When one takes account of screening, one replaces Z by Z - σ; therefore with screening one obtains

$$[\omega_K/(1-\omega_K)]^{\frac{1}{4}} = -A+BZ \qquad (\text{where } A=\sigma B).$$

Finally, assuming that one can obtain the relativistic correction by replacing Z by $Z(1-\alpha Z^2)$, we arrive at[62]

$$[\omega_K/(1-\omega_K)]^{\frac{1}{4}} = -A+BZ-CZ^3 \quad (C=\alpha A). \tag{12}$$

The constants A, B and C are obtained from experiment by a least-squares fit. Empirical and semi-empirical curves for the K fluorescence yield and the values of A, B and C have been published in several papers.[10,18,37,38,49,62,63,64]

Table 13

Constants of Eq.(12) as found by various authors

Constants	Ref.63 (1955)	Ref.38 (1956)	Ref.10 (1959)
$A \cdot 10^4$	4.4	2.47	6.4
$B \cdot 10^4$	3,46	3,318	3,40
$C \cdot 10^6$	1.35	1,14	1,03

Table 13 gives the values of A, B and C as obtained by a least-squares fit. Table 14 compares the latest (1956-1959)* experimental values of ω_K with the theoretical ones obtained from Eq.(12) with the constants taken from Wapstra[10] and Bergstrom.[38]

It cannot be said that the 1959 semi-empirical curve[10] is in better agreement with the new experiments than the 1956 curve, based on earlier measurements.[38]

For the region $23 \leqslant Z \leqslant 57$, the two curves are very similar. They both give the K fluorescence yield and the Auger yield with an error no greater than 10% at the edges of this region, and they give the same results for $Z \approx 40$-45. Both papers we are discussing[10,38] give results for the fluorescence yield for $Z < 23$ and the Auger yield for $Z > 57$ which differ considerably from each other and from experiment, especially for small Z. For $Z < 20$, different experiments give ω_K values differing by a factor of 5. For $Z > 90$ different experiments[12,20] give Auger yield a_K values differing by a factor of 2.

Table 14

K fluorescence yield (comparison of 1956-1959 experimental results with theory according to Eq.(12))

Z	Experiment	Ref.	Constants from [10]	Constants from [38]	Z	Experiment	Ref.	Constants from [10]	Constants from [38]
10	0.043±0.004	[65]	0,006	0,009	40	0,70 ±0,92	[64]	0,696	0,698
12	0.008±0.003	[66]	0.014	0.020	41	0,73 ±0.02	[64]	0.715	0,715
13	0.008±0.003	[65]	0.020	0.028	42	0.73 ±0.02	[64]	0.733	0.731
13	0.043±0.002	[67]			43	0,70 ±0.03	[38]	0,750	0,748
22	0.18 ±0.01	[68]	0,170	0,191	45	0,786±0,015	[64]	0,780	0,778
23	0.304±0.013	[67]	0,199	0,220	46	0,790±0,014	[64]	0,793	0,789
23	0,23 ±0,02	[69]			47	0,821±0,015	[64]	0,805	0,800
24	0,219±0,012	[70]	0,229	0,250	48	0,827±0,014	[64]	0,817	0,811
25	0.308±0.015	[65]	0.261	0.280	49	0.87 ±0.03	[66]	0,828	0,821
26	0.308±0.015	[64]	0.293	0.311	50	0.836±0.015	[74]	0.838	0,830
27	0.31 ±0.01	[71]	0.327	0.343	50	0.846±0.012	[64]		
28	0.366±0.011	[64]	0,359	0,376	53	0.91 ±0.03	[50]	0.863	0,856
28	0.33 ±0,02	[72]			57	0,88 ±0,01	[75]	0,889	0,882
29	0.39 ±0.02	[72]			68	0,955±0,022	[55]	0,932	0,925.
29	0.410±0.012	[64]	0.392	0.409	70	0,936±0,010	[18]	0,937	0,930
29	0.42 ±0.02	[69]			84	0,942±0,005	[18]	0,958	0,950
30	0.44 ±0.02	[72]	0.426	0.442	92	0,967±0,010	[18]	0,963	0,955
30	0.446±0.012	[64]			93	0.938±0,010	[20]	0,963	0,955
31	0,47 ±0.02	[69]	0,458	0,471					
31	0,53 ±0,03	[73]							

The results of Frey et al[65] and of Rightmire et al[66] are not remarkable for their accuracy. However, the value $\omega_K = 0.045 \pm 0.002$ obtained by Susor and Charpak[67] for aluminum, is probably correct** and is an indication that for small Z the ω_K values given by the earlier[38] and especially the later[10] semi-empirical curves are too low.

For reference, Table 15 gives the Wapstra et al[10] values of ω_K. The uncertainty given by the authors is 0.005, independent of Z, although for $Z < 30$ and $Z > 90$ it is in fact two to three times greater.

---

*For data earlier than 1956, see Gray[18] and Bergstrom.[38]

**This opinion of the relative value of different ω_K measurements was given by A.A.Konstantinov, whom the author thanks for valuable discussions.

Table 15

K fluorescence yield according to Wapstra's[10] semi-empirical curve

Z	ω_K	Z	ω_K	Z	ω_K	Z	ω_K
14	0,027	36	0,605	58	0,895	80	0,954
16	0,049	32	0,653	60	0,904	82	0,956
18	0,081	40	0,696	62	0,913	84	0,958
20	0,120	42	0,733	64	0,920	86	0,959
22	0,170	44	0,766	66	0,926	88	0,961
24	0,229	46	0,793	68	0,932	90	0,962
26	0,293	48	0,817	70	0,937	92	0,963
28	0,359	50	0,838	72	0,941	94	0,964
30	0,426	52	0,855	74	0,945	96	0,965
32	0,490	54	0,870	76	0,948	98	0,966
34	0,550	56	0,883	78	0,952	100	0,967

Further refinements in ω_K measurements for different Z are very important. Situations have been noted[62] in which a 10% error in ω_K led to a 250% error in the measured value of the K to L capture ratio.

By using Tables 6 and 15 and Figs.2 and 3 together with data on the relative intensity of K series x-radiation[10], one can calculate the number of holes forming in each of the L subshells per vacancy filled in the K shell. The results of such calculation are given in Fig.4. For n_{K-L_2}, for instance, we made use of the equation

$$n_{K-L_2} = (1-\omega_K)\frac{2(K-L_2L_2)+(K-L_2L_1)+(K-L_2L_3)+(K-L_2X)}{(K-LL)+(K-LX)+(K-XY)} + \omega_K \frac{W_{X(L_2-K)}}{W_{XK}}. \quad (13)$$

As intermediate values, we used the averaged values of the ratios $(K\text{-}L_1X):(K\text{-}L_2X):(K\text{-}L_3X)$ (Table 16). These were obtained by interpolating and extrapolating the data of Table 11. For Z = 30 we took $(K\text{-}L_2X):(K\text{-}L_3X)$ from Asaad and Burhop[4], and $(K\text{-}L_1X):(K\text{-}L_{2,3}X)$ as the average of their result and those of Bellicard[33]. The ratios have errors of the order of 5 to 10%. The same table gives the number of vacancies in each subshell per electron of the K series, entering into (13). The error here is also of the order of 5 to 10%. The error in the results given in Fig.4 is of the order of one-third of the value of n_{K-L_1}. The sum $\sum_i n_{K-L_i}$ according to Fig.4 is about 5% greater than Fink's value.[77] For $Z \geqslant 50$, the value of n_{K-L_1} given by Fig.4 is almost the same as that of Wapstra.[10]

In order to obtain a theoretical value for the K fluorescence yield, one must calculate the probability of Auger and radiative transitions of the K series. This was first done by Wentzel[27]. Nonrelativistic calculations of Burhop[4] and Pincherle[28] give B = 0.032 in Eq.(11). More accurate calculations were performed only for some isolated values of Z. According to Rubinstein and Snyder[36] (a nonrelativistic calculation including screening by the Hartree self-consistent field), ω_K is 0.13, 0.67 and 0.8 for Z = 18, 36 and 47, respectively. Relativistic calculations by Burhop and Massey[29,76] using hydrogen-like wave functions indicate that relativistic effects increase the Auger yield (i.e., the value of $1-\omega_K$) by a factor of 2 for Z = 79, and by 20% for Z = 47. Finally, Asaad[5] found that ω_K = = 0.961 for Z = 80 (a relativistic calculation with screening included by the self-consistent field method, and with corrections for exchange).

In his calculations Asaad used the following values: $W_a(K\text{-}LL) = 49{:}19\,10^{-3}$ $(au)^{-1}$ (see Table 4), $W_X(K\text{-}L) = 1{\cdot}713\ (au)^{-1}$ (here $W_X(K\text{-}L)$ is the probability for K-L x-radiation), and $W_{X,K} = 2.186\ (au)^{-1}$ (the total K series x-ray proba-

Table 16

Average values for $\frac{K-L_1X}{K-LX}$, $\frac{K-L_2X}{K-LX}$ and $\frac{K-L_3X}{K-LX}$ and the number of vacancies in the L subshells caused by Auger transitions per K series Auger electron

Z	$\frac{K-L_1X}{K-LX}$	$\frac{K-L_2X}{K-LX}$	$\frac{K-L_3X}{K-LX}$	Vacancies in the subshells		
				L_1	L_2	L_3
30	0,28	0,49	0,23	0,28	0,77	0,68
40	0,29	0,37	0,34	0,38	0,60	0,68
50	0,30	0,29	0,41	0,45	0,50	0,68
60	0,33	0,26	0,41	0,50	0,45	0,65
70	0,37	0,24	0,39	0,55	0,43	0,59
80	0,40	0,23	0,37	0,60	0,43	0,53
90	0,43	0,21	0,36	0,65	0,43	0,46
100	0,45	0,20	0,35	0,70	0,45	0,40

bility.[5,76] In accord with Pincherle[28], it was assumed that

$$\frac{(K-LX)+(K-XY)}{K-LL}=0.82.$$

The value 0.961 is somewhat greater than the experimental average for Z = = 80. If, however, one takes $\frac{(K-LX)+(K-XY)}{K-LL}$ from Figs.2 and 3, one obtains ω_K = 0.955, which is closer to the data of Table 15.

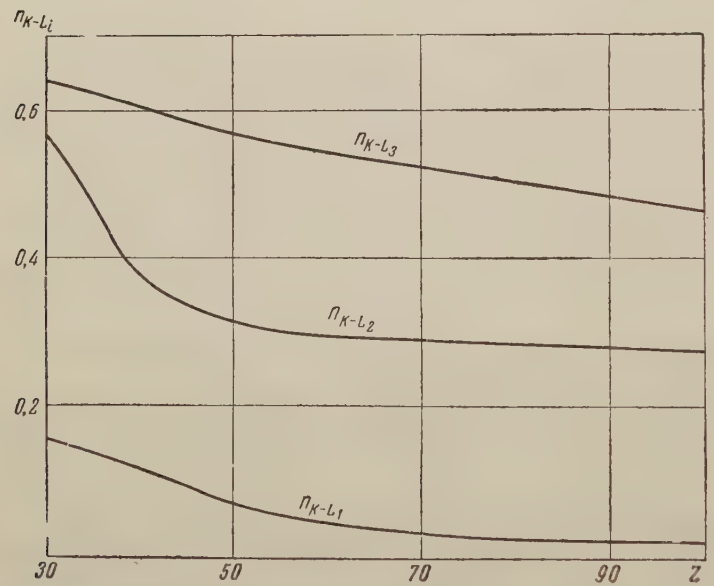

Fig.4. Number of holes produced in the L subshells per one vacancy in the K shell.

V. Coster-Kronig Transitions

A special type of Auger effect is one in which the hole goes from one subshell to another in the same shell. Such transitions are called Coster-Kronig transitions. In such transitions there are ejected very low energy electrons from the outer shells. From energy considerations alone it is possible for transitions of the form $L_1 - L_2N$, $L_1 - L_3M_{4,5}$ and the like to occur but not for all values of Z. Thus, for instance, an $L_1 - L_3M_5$ transition is possible only for those Z for which the difference in binding energy between the L_1 and L_3 subshells is greater than the binding energy of the M electron in the Z + 1 atom. For this (most important) case we must have either $Z < 50$ or $Z > 73$. The probability for such transitions increases with increasing energy of the ejected electron.

Many important phenomena of x-ray spectroscopy are related to the Coster-Kronig effect: for $Z > 73$ there is a sharp increase in the width and decrease in the relative intensity of x-ray lines associated with transitions from the L_1

Table 17

Z regions in which the most important Coster-Kronig transitions of the L and M series are possible

Transition	Z	Transition	Z	Transition	Z	Transition	Z
a) $L-LX$-Group							
$L_1-L_3M_1$	$\leqslant 32$	$L_2-L_3M_1$	For no Z	$L_1-L_2M_1$	$\leqslant 29$	$L_1-L_2N_1$	$\leqslant 70$
$L_1-L_3M_2$	$\leqslant 36$	$L_2-L_3M_2$		$L_1-L_2M_2$	$\leqslant 33$	$L_1-L_2N_2$	$\leqslant 76$
$L_1-L_3M_3$	$\leqslant 36$ & $\geqslant 91$	$L_2-L_3M_3$	$\leqslant 99$	$L_1-L_2M_3$	$\leqslant 34$	$L_1-L_2N_3$	$\leqslant 80$
$L_1-L_3M_4$	$\leqslant 49$ & $\geqslant 77$	$L_2-L_3M_{4,5}$	$\leqslant 30$ & $\geqslant 91$	$L_1-L_2M_4$	$\leqslant 40$	$L_1-L_2N_4$	$\leqslant 91$
$L_1-L_3M_5$	$\leqslant 50$ & $\geqslant 74$			$L_1-L_2M_5$	$\leqslant 42$	$L_1-L_2N_5$	$\leqslant 94$
$L_1-L_2N_{6,7}$; L_1-L_2O; $L_1-L_3(N, O)$ & $L_2-L_3(N, O)$ possible for all values of Z for which there are N and O electrons							
b) $M-MX$-Group							
$M_1-M_2M_{4,5}$	$\leqslant 33$	$M_1-M_3M_{4,5}$	$\leqslant 33$	$M_2-M_4M_{4,5}$	$\leqslant 34$	$M_3-M_5N_5$	$\leqslant 90$
$M_1-M_2N_1$	$\leqslant 46$	$M_1-M_3N_1$	$\leqslant 49$	$M_3-M_4N_{4,5}$	$\leqslant 84$	$M_3-M_5N_4$	$\leqslant 88$
$M_1-M_2N_{2,3}$	$\leqslant 52$	$M_1-M_3N_5$	$\leqslant 86$	$M_3-M_4N_3$	$\leqslant 70$	$M_3-M_5N_3$	$\leqslant 76$
$M_1-M_2N_{4,5}$	$\leqslant 70$	$M_1-M_5M_5$	$\leqslant 44$	$M_3-M_4N_2$	$\leqslant 65$	$M_3-M_5N_2$	$\leqslant 70$
$M_1-M_2N_{6,7}$	$\leqslant 90$	$M_2-M_3M_{4,5}$	$\leqslant 47$ & $\geqslant 66$	$M_3-M_4N_1$	$\leqslant 54$	$M_3-M_5N_1$	$\leqslant 56$
$M_1-M_4M_{4,5}$	$\leqslant 42$	$M_2-M_4N_1$	$\leqslant 87$	$M_3-M_4M_{4,5}$	$\leqslant 35$	$M_3-M_5M_5$	$\leqslant 36$

subshell, and intense satellites appear in the L series.[78-82] A theoretical calculation of the probability for Coster-Kronig transitions and of their contribution to the width of the levels has been carried out[31] only for Z = 79. Some approximate results were also obtained by Pincherle[28].

Table 17 gives the Z regions in which L and M series Coster-Kronig transitions are possible. The ratio of the number of vacancies filled by Coster-Kronig transitions to the total number of initial vacancies in the given subshell is known as the Coster-Kronig yield, and is denoted by $f_{X_iX_j}$ (the relative probability for a hole transition from the X_i subshell to the X_j subshell).

The term "Auger yield" is usually used only for transitions in which the initial and final vacancies are in different shells. The sum of the Auger yield, the Coster-Kronig yield, and the fluorescence yield is unity for each of the subshells.

VI. Fluorescence yield for the L shell

It is possible to calculate and tabulate the Z dependence of the fluorescence yield only for each of the three L subshells, i.e., ω_{L1}, ω_{L2} and ω_{L3}. The average fluorescence yield $\bar{\omega}_L$ for the shell as a whole may be different for different experiments and for different isotopes. This is because the initial vacancies may be distributed over the three subshells differently as a result of internal conversion of γ-rays of different multipole orders and energies, of L capture with different transition energies, and of atomic excitation by x-rays or particles.

Let us write n_1, n_2 and n_3 for the relative numbers of initial vacancies in the three L subshells, so that

$$n_1 + n_2 + n_3 = 1; \tag{14}$$

further, let ω_1, ω_2 and ω_3 be the fluorescence yields for each of the three subshells; let a_1, a_2 and a_3 be the corresponding Auger yields, and f_{12}, f_{13} and f_{23} the corresponding Coster-Kronig yields (the hole undergoes transition from the L subshell denoted by the first index to the subshell denoted by the second). In addition, let X_1, X_2 and X_3 be the number of x-ray quanta with energies corresponding

to transitions to each of the subshells, and let A_1, A_2 and A_3 be the number of Auger electrons.

Then the mean fluorescence yield $\bar{\omega}_L$ and the mean Auger yield $\bar{a}_L$ (the number of x-rays plus the number of Auger electrons per initial vacancy in the L shell) will be

$$\bar{\omega}_L = X_1 + X_2 + X_3 \quad \text{and} \quad \bar{a}_L = A_1 + A_2 + A_3, \tag{15}$$

and further

$$\begin{aligned} X_1 &= \omega_1 n_1; & A_1 &= a_1 n_1; \\ X_2 &= \omega_2 (n_2 + f_{12} n_1); & A_2 &= a_2 (n_2 + f_{12} n_1); \\ X_3 &= \omega_3 [n_3 + f_{13} n_1 + f_{23} (n_2 + f_{12} n_1)]; & A_3 &= a_3 [n_3 + f_{13} n_1 + f_{23} (n_2 + f_{12} n_1)]. \end{aligned} \tag{16}$$

According to (16) the number of x-ray transitions to the L_2 level, for instance, is given by the number n_2 of initial vacancies in the L_2 shell and the number $f_{12} \cdot n_1$ of holes undergoing transition from L_1 to L_2.

From the requirement that

$$\bar{\omega}_L + \bar{a}_L = 1 \tag{17}$$

for arbitrary $n_i \geqslant 0$ consistent with (14), follow the three obvious identities

$$\omega_3 + a_3 = 1, \quad \omega_2 + a_2 + f_{23} = 1 \quad \text{and} \quad \omega_1 + a_1 + f_{12} + f_{13} = 1. \tag{18}$$

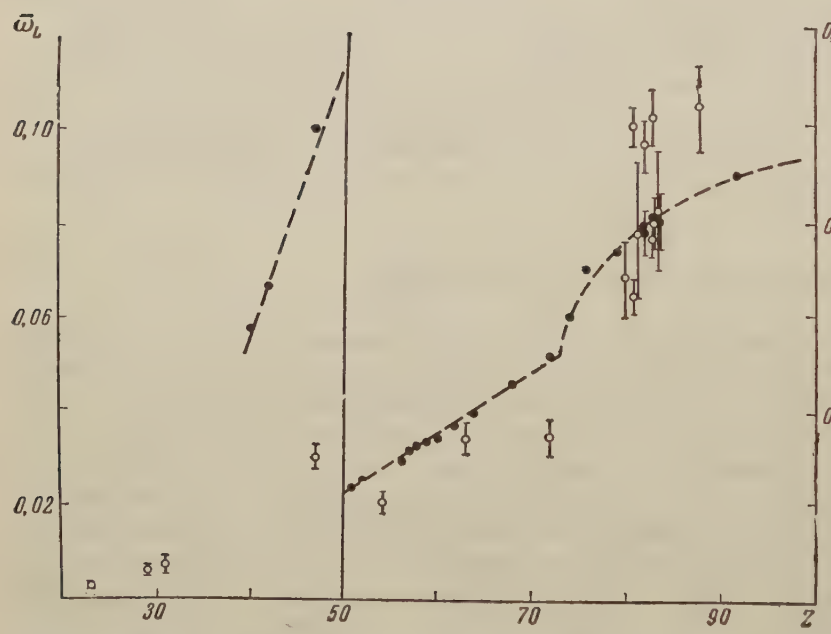

Fig.5. Mean fluorescence yield for the L shell. The solid circle points and the dashed line give $\bar{\omega}_L$ for soft x-ray excitation.[83] The open circles give ω_L as obtained from radioactive decay data. For Z < 50 the ordinate scale is increased by a factor of five.

If the excited states are produced by photons whose energy is greater than $E(L_3)$, but less than $E(L_2)$, then $n_1 = n_2 = 0$ and ω_3 can be measured independently. If the L shell is excited by soft x-rays, then $n_1 : n_2 : n_3 \approx 1:2:3$.[63] In excitation by electrons, $n_1 : n_2 : n_3 \approx 1:1:2$.[63] In internal conversion and in electron capture with transition energies less than the K-shell binding energy, the n_i are proportional to the L-subshell conversion coefficients or the L-subshell capture probabilities.

If K conversion or K capture are possible on the basis of energy considerations, then one must add to the number of vacancies produced by L capture or conversion

Table 18

Mean L-shell fluorescence yield $\bar{\omega}_L$ for several Z, as obtained from radioactive decay studies

Z (daughter)	$\bar{\omega}_L$	Ref.	Type of decay	Subshell excitation	$\bar{\omega}_L$ acc. Fig 5	$\bar{\omega}_L$ acc. to Lay's curve[83]
23	0,0024±0,0003	[69]	Electron capture in Cr^{51}	1 : 2,1 : 2,4	—	—
29	0,0056±0,0008	[69]	" Zn^{65}	1 : 2,1 : 2,4	—	—
31	0,0064±0,0009	[69]	" Ge^{71}	1 : 2,1 : 2,4	—	—
47	0,029 ±0,003	[84,85,77]	" Cd^{109}	1 : 1,8 : 2,8	0,047	0,095
			$E3$-conversion in Ag^{109}			
54	0,10±0,01	[86]	Electron capture in Cs^{131}	1 : 1,5 : 2,8	0,08	0,14
63	0,17±0,02	[87]	" Cd^{153}*	1 : 0,45 : 0,75	0,155	0,19
72	0,17±0,02	[88]	" Ta^{179}**	1 : 6 : 9	0,23	0,26
80	0,34±0,04	[89]	" Tl^{204}	1 : 1,7 : 2,3	0,35	0,38
80	0,37±0,04	[90]	Conversion (mainly $E2$) in Hg^{199}	1 : 3,3 : 3,5	0,35	0,38
81	0,50±0,02	[24]	$M1$-conversion in Tl^{208}	1 : 0,1 : 0,01	0,39	0,39
81	0,39±0,08	***		1 : 0,1 : 0,01	0,39	0,39
81	0,32±0,02	[82]		1 : 0,1 : 0,01	0,39	0,39
82	0,39±0,02	[72]	Excitation by x-rays	~1 : 2 : 3	0,39	0,40
81—83 (av.)	0,48±0,02	[23]	Conversion (mainly $M1$) in Tl^{208}, Bi^{212}, Pb^{208}	1 : 0,5 : 0,8	0,39	0,40
83	0,51±0,03	[24]	Conversion (mainly $M1$) in Bi^{212}	1 : 1,5 : 2,8	0,38	0,41
	0,40±0,03	[82]		1 : 1,5 : 2,8	0,38	0,41
83	0,40±0,02	***	$M1$-conversion in Bi^{210}	1 : 0,1 : 0,01	0,41	0,41
83	0,41±0,07	****		1 : 0,1 : 0,01	0,41	0,41
83	0,38±0,02	[91]		1 : 0,1 : 0,01	0,41	0,41
88	0,52±0,04	[92]	$E2$-conversion in Ra^{226}	1 : 32 : 26	0,51	0,43

*Coincidence counting eliminated L x-rays after conversion.

**Only L x-rays in coincidence with K x-rays were counted.

***According to Ross et al[81] on the basis of measurements by different authors before 1955.

****Based on the measurements of Kinsey[93].

the number of vacancies produced in the K shell by K-L transitions, which can be calculated with the aid of Fig.4.

Fig.5 gives the mean fluorescence yield $\bar{\omega}_L$ as found by various authors. The solid circles and dashed line give the results of Lay[83], which were obtained by x-ray excitation of the atoms, so that $n_1 : n_2 : n_3 = 1:2:3$ (or, according to Ross, et al.,[81] 1:1.7:2.6). The open circles represent values of ω_L obtained from radioactive decay (data taken from Table 18).

For $Z < 80$, the radioactive decay values of $\bar{\omega}_L$ are found to be much lower than those obtained from x-ray excitation. For $Z > 80$ the opposite seems to be true at first glance. However, it has been pointed out by Winkenbach[82] that in the light of new measurements of the number of initial vacancies in ThC', the value of 0.50 for $\bar{\omega}_L$ for Z = 81-83 is an overestimate.

It is seen from Table 18 that when the K shell is excited, the radioactive $K\text{-}L_2$ and $K\text{-}L_3$ transitions cause $n_1 : n_2 : n_3$ to depend only weakly on the nature of the initial excitation. Further, it may be noted that for $Z \approx 82$ the mean value of ω_L is fortunately nearly the same for different modes of excitation.

The methods for finding the Auger, fluorescence, and Coster-Kronig yields for the L shell have been discussed most thoroughly by Ross et al[81], and by Kinsey[93].

The quantities measured in experiments are the ratios $A_1 : A_2 : A_3$ and $X_1 : X_2 : X_3$ and the mean fluorescence yield $1 - \bar{a}_L = \bar{\omega}_L$. With this data it is a simple matter to use (15) to obtain the A_1, A_2, A_3, X_1, X_2 and X_3. If $n_1 : n_2 : n_3$ is known, one may use (16) and (18) to obtain the four quantities

Table 19

Measured values of the fluorescence ω_i the Auger a_i and the Coster-Kronig yield f_{ik} for the L subshells

Measured quantity	$Z=56$ [94]	$Z=81\div83$ (average) [24]	$Z=81\div83$ (average) [23]	$Z=83$ [81]***	$Z=83$ [95]	$Z=82$ (mean value)****
a_1	$0,28\pm0,06$	0,15	$0,07\pm0,02$	$0,11\pm0,03$	0,11	0,12
a_2	$0,63\pm0,24$	0,34	$0,46\pm0,09$	$0,62\pm0,14$	0,68	0,55
a_3	$0,95\pm0,01$	0,54	$0,59\pm0,05$	$0,60\pm0,05$	0,66	0,66
f_{12}	$0,66\pm0,07$	0,24	0,19**	$0,19\pm0,05$	0,16	0,16
f_{13}		0,52	0,58**	$0,58\pm0,05$	0,62	0,60
f_{23}	$0,26\pm0,26$	0*	0*	$0,06^{+0,14}_{-0,06}$	0*	0
ω_1	$0,06^{+0,13}_{-0,06}$	0,09	0,16	$0,12\pm0,01$	0,11	0,12
ω_2	$0,11^{+0,50}_{-0,11}$	0,66	0,54	$0,32\pm0,04$	0,32	0,45
ω_3	$0,05\pm0,01$	0,46	0,41	$0,40\pm0,05$	0,34	0,34

	$Z=73$	$Z=74$	$Z=77$	$Z=78$	$Z=79$	$Z=81$	$Z=82$	$Z=83$	$Z=90$	$Z=92$	—
	[96]					[82]	[97]	[96]	[97]		—
ω_3	0,191	0,207	0,244	0,262	0,276	$0,33\pm0,02$	0,32	0,337 0,367	0,42	0,44	0,34

*Assumed in order to obtain the other quantities.

**According to Ross et al[81].

***Calculated by Ross et al[81] from various data[81,98-100] on the L Auger and L fluorescence spectra in RaD decay and in x-ray excitation.

****Assumed here, using Kinsey's[93] results.

$$\omega_1=\frac{X_1}{n_1};\quad a_1=\frac{A_1}{n_1};\quad \frac{1}{\omega_3}=1+\frac{A_3}{X_3};\quad \frac{1}{a_3}=1+\frac{X_3}{A_3}. \tag{19}$$

In order to obtain the remaining five quantities, ω_2, a_2, f_{12}, f_{13} and f_{23}, one needs another relation independent of (14)-(18). There are two ways to obtain it.

First, one may set $f_{23}=0$ (which will not alter the final result too drastically[81]). The according to (16)

$$\frac{1}{\omega_2}=1+\frac{A_2}{X_2}\ (\text{if}\quad f_{23}=0). \tag{20}$$

The remaining quantities can be written in terms of ω_2 in the form

$$a_2=\omega_2\frac{A_2}{X_2};\quad f_{12}=\frac{1}{n_1}\left[\frac{X_2}{\omega_2}-n_2\right];\quad f_{13}=1-a_1-\omega_1-f_{12}. \tag{21}$$

Second, one may use the results of additional series of measurements of the L spectrum for the same Z but with a different distribution of the vacancies over the subshells (say, by exciting L fluorescence by x-rays or by studying the radioactive decay of two different isotopes). According to (16), $\frac{A_1}{X_1}$, $\frac{A_2}{X_2}$ and $\frac{A_3}{X_3}$ should be dependent upon the distribution of the initial vacancies for a given Z. It is sufficient, for instance, to find $X_1'\colon X_2'\colon X_3'$ and $\bar{\omega}_L'$ depending on a new distributio

Table 20

Relative L series Auger line intensities*

Line	Z = 81	Z = 83	Z = 81 ÷ 83	Z = 83	Z = 83
	[24]		Average from [23]	Average from [98,99]	[95]
	$Bi^{213} \xrightarrow{\alpha} Tl^{209}$	$Po^{212} \xrightarrow{\beta} Bi^{212}$	$Pb^{212} \xrightarrow{\beta} Bi^{212} \xrightarrow{\beta(\alpha)} Po^{212}(Tl^{208})$	$Pb^{210} \xrightarrow{\beta} Bi^{210}$	$Pb^{210} \xrightarrow{\beta} Bi^{210}$
$L_1 - MM$	22,5	8,5	4,0±1,5	12	—
$L_1 - M(N+O)$	3,5	—	1,3±0,3	3,3	—
$L_1 - N(N+O)$	—	—	0,2	1,6**	—
$\Sigma(L_1 - XY)$	26	8,5	5,5±1,8	~17	15
$L_2 - MM$	10	12,5	18,6±2,2	20	—
$L_2 - M(N,O)$	11	9,5	6,4±0,4	6,7	—
$L_2 - N(N,O)$	—	—	0,6	**	—
$\Sigma(L_2 - XY)$	21	22	25,6±2,6	~27	25
$L_3 - MM$	37,6	53,0	50,1±0,7	41	—
$L_3 - M(N+O)$	15,5	16,5	17,6±1,1	12	—
$L_3 - N(N+O)$	—	—	1,2±0,2	3	—
$\Sigma(L_3 - XY)$	53,1	69,5	68,9±2,2	56	60
$L - XY$	100	100	100	100	100

*The L_i-M_4M_5 line is the most intense in each of the L_i-XY groups[22] (for Z = 81-83).

**Lines coincide.

$n_1 : n_2 : n_3$. By combining the results of two such experiments one can find ω_2 for instance from the expression

$$\omega_2 = \frac{X_2 n_1' - X_2' n_1}{n_2 n_1' - n_2' n}, \qquad (22)$$

and then use (16) and (21) to find the four remaining quantities a_2, f_{12}, f_{13} and f_{23}. From the remaining measurements one can either find ω_1, a_1, etc., by going through the procedure again, or one can fill in the gaps in the first series of measurements. Table 19 gives the fluorescence, Auger, and Coster-Kronig yields for the L subshells for those few cases in which they could be measured. To find them, the various authors[23,24,81,95] have used the data collected in Table 20.

Auger and Coster-Kronig yields for the L subshells could be calculated if one knows the radiation widths Γ_{X_i} and total widths Γ_i of the levels involved, as well as their widths Γ_{a_i} and Γ_{ik} with respect to Auger and Coster-Kronig transitions (where $i, k = 1, 2, 3$). Then

$$\omega_i = \frac{\Gamma_{X_i}}{\Gamma_i}; \quad a_i = \frac{\Gamma_{a_i}}{\Gamma_i}; \quad f_{ik} = \frac{\Gamma_{ik}}{\Gamma_i}; \quad \Gamma_i = \Gamma_{X_i} + \Gamma_{a_i} + \sum_{k>i} \Gamma_{ik}. \qquad (23)$$

There is still too little experimental and theoretical data on the widths for the yields to be reliably calculated in this way. Attempts to perform such a calculation have been undertaken by Kinsey[93] for Z = 73 to 92, and later by Kinsey's method[86,62] for Z = 54 and Z = 47. The results are given in Table 21.

It has often been said that the values of ω_i in Table 21 are too low, at any rate for Z < 90. This is because the calculations are based on values of Γ_{X_i} taken from Massey and Burhop[76], which are too low. For instance, Massey and Burhop find by interpolation that the probability for the K-L_3 transition for Z = 80 is 1.020 per atomic time unit, while by more accurate calculations[5] it is 1.163, a difference of 14%. The width of the K level for Z = 79 and Z = 51 is, according to these authors 10-15% less than the average experimental value as

Table 21

Fluorescence and Auger yields for the L subshells, as calculated from the total and radiation widths of the levels

Calculated quantity	Z = 47 [62]	Z = 54 [86]	Z = 73 [93]	Z = 75 [93]	Z = 77 [93]	Z = 79 [93]	Z = 81 [93]	Z = 83 [93]	Z = 90 [93]	Z = 92 [93]
ω_1	0,011	0,017	0,17	0,110	0,100	0,090	0,090	(0,100)	(0,150)	(0,160)
ω_2	0,032	0,025	0,31	0,33	0,37	0,39	0,43	0,46	0,56	0,59
ω_3	0,030	0,03	0,18	0,20	0,23	0,25	0,27	0,30	0,39	0,41
a_1		0,983					0,12	0,08		
a_2		0,975	0,69	0,67	0,63	0,61	0,57	0,54	0,44	0,41
a_3		0,970	0,82	0,80	0,77	0,75	0,73	0,70	0,61	0,59
f_{12}		0*					0,12**	0,12**		
f_{13}		0*	0	0,42	0,54	0,65	0,67	(0,70)	(0,60)	(0,60)
f_{23}		0*	0*	0*	0*	0*	0*	0*	0*	0*
$\bar{\omega}_L$***		0,03	0,18	0,21	0,24	0,27	0,29	0,32	0,40	0,42

*Assumed to obtain the other quantities.

**Added by Kinsey[93] to the calculated values in order to obtain the best agreement with his experiments.

***We take the excitation ratios $L_1:L_2:L_3 = 100:10:1$.

Table 22

Level widths and fluorescence, Auger, and Coster-Kronig yields

Subshell	Γ_i, ev: Z = 47 [101]	Z = 47 [107]	Z = 51 [103]	Z = 52 [103]	Z = 53 [106]	Z = 54 [106]	Z = 73 *	Z = 74 [109]	Z ≈ 55 (assumed)	Γ_{X_i}, ev: Z = 55 [76] **	Z = 54÷56 (assumed)	ω_i: Z = 54÷56 (found from Γ_{X_i}/Γ)	a_i: = 54÷56 [94] ***	f_{ik}: Z = 54÷56 [94] ***
L_1		5,3	5,6	4,9			2,8	4,9	3,0	0,115	0,16	~0,05	0,3	f_{12}~0,6
L_2	2,3	2,2	4,7	4,6			3,0	3,0	2,5	0,153	0,22	~0,09	~0,7	f_{13}<0,05
L_3	2,4	2,0	4,1	4,7	2,6±0,1	<4,06	3,4	3,4	2,6	0,125	0,18	~0,07	0,93	f_{23}~0,2

*Assumed by Kinsey[93] as the most accurate value.

**The intensity ratios of x-rays from the L → N, O and L → M transitions are taken from Kinsey and Bethe.[93,108]

***Using the value of ω_i chosen here and the estimates made.

given by Sachenko.[101] Since ω_3 is relatively well measured, Tables 21 and 19 point to the same conclusion (the difference in ω_3 is about 10-20% for Z > 73).

The reason Massey and Burhop have this low value of ω_i is that they use the Slater screening constant. This method for including screening will also lead to an L shell conversion probability too low by 30%.[102] A second reason why the ω_i in Table 21 are so small is that the total width measured by Sandstrom[103] and used by Fink and Robinson[86] to calculate ω_i is an overestimate by a factor of 2.* As a consequence, the calculated L-shell fluorescence yield is clearly smaller than the experimental values of $\bar{\omega}_L$ for Z < 90. On the other hand, Kinsey's extrapolation to heavy elements gives results in good agreement with measurement for Z = 94 (see Vandenbroch et al[104], and a reference to N.H.Lazar by Foucher[105]). By comparing recently measured fluorescence yields for Z < 80 with Lay's results

---

*In using Table 22 to compare widths for different Z's, one should bear in mind the fact that Γ_{L_i} increases sharply for Z < 50 and Z > 74.

(see Fig.5), one sees definitely that for small and intermediate Z values Lay's results are too high.

Table 22 is an attempt to give an estimate of the widths corresponding to the Auger, fluorescence, and Coster-Kronig yields for Z = 54-56. The value for Γ_{L_3} is taken from Green.[106] According to all the data, Γ_{L_2} is of the same order as Γ_{L_3}. The value of Γ_{L_1} is obtained by decreasing Sandstrom's[103] results by the same factor as is necessary to obtain the corrected value of Γ_{L_3}. Such a choice is supported by the data for Z = 73 and Z = 47.[93,107] The radiation widths are found by interpolating the Massey-Burhop[76] results. The contribution from $L \longrightarrow (N,0)$ transitions is included in a well known way.[93,108] On the basis of the above discussion, the Massey-Burhop widths are multiplied by 1.4. The values of ω_i obtained from Eq.(22) are close to those of Burford and Haynes[94]; the a_i are taken from Burford and Haynes on the basis of the ω_i obtained. In this Z region f_{12} should play a predominant role, since low-energy L_1–L_2N Coster-Kronig transitions may take place (see Table 17). On the other hand, f_{13} should be small, since L_1-L_3M transitions are impossible for $50 \leqslant Z \leqslant 73$, while L_1-L_3N electrons have high energy. Coster-Kronig electrons of the L_2-L_3N type will give a contribution to f_{23}. The sum $f_{13} + f_{12}$ is taken from Burford and Haynes.[94]

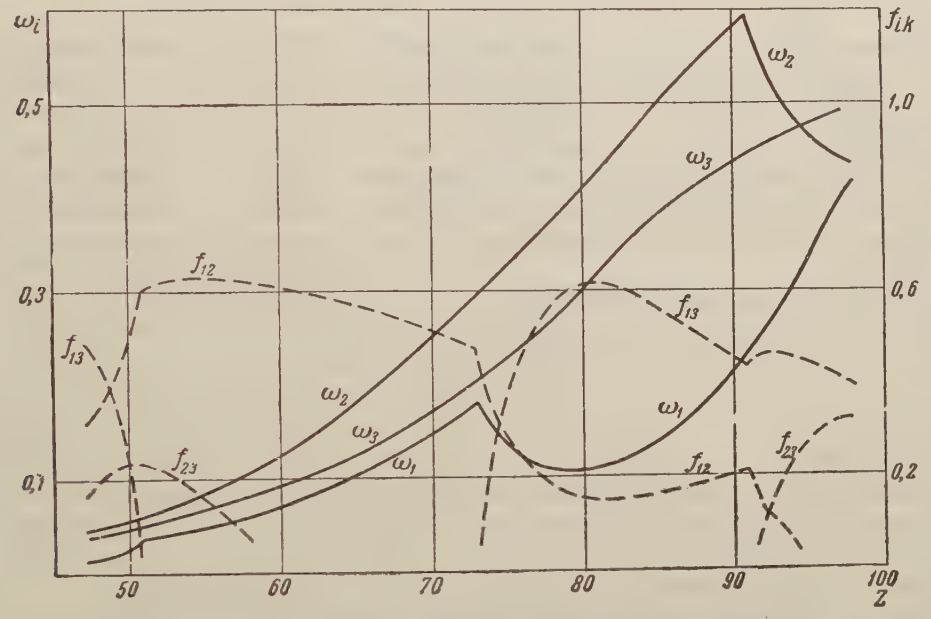

Fig.6. Fluorescence yields ω_i (solid curves) and Coster-Kronig yields f_{ik} (dashed curves) for the L subshells (i, k = 1, 2, 3).

Fig.6 gives curves for the fluorescence and Coster-Kronig yields for the L subshells. The curves are constructed in exactly the same way as Kinsey's.[93] From considerations similar to his, radiation, Auger, and Coster-Kronig widths were chosen for each Z from 47 to 98. The method is different from Kinsey's in that 1) experimental data for Z = 47, 54 and 56 (Tables 19 and 22) is included, and the curves are extended to Z = 47; 2) Z = 55 and Z = 82 where used as check points, for which all data was taken from Tables 19 and 22; 3) the Auger widths were assumed not to be constant, but to increase linearly from Z = 47 to Z = 82, and even more rapidly for Z > 82; 4) the Massey-Burhop[76] radiation widths were increased by 40%, 20% and 10% for Z = 51, 79 and 92, respectively; 5) as indicated in Table 17, use was made of the fact that the Coster-Kronig width Γ_{ik}

changes sharply at Z = 51, 73, 91 and 92. For other Z regions, the Γ_{ik} values obtained for Z = 55 and 82 were reduced (increased) continuously with Z in accordance with the increase (reduction) of the Coster-Kronig electron energies. It was assumed that the L_2-$L_3M_{4,5}$ transitions cause Γ_{23} to increase for Z > 91 in the same way as Γ_{13} increases for Z > 73. Of particular interest would be an experimental verification of the cusp in the curves at Z = 91 and 92, as has already been done for Z = 51 and 73.

The most accurate curve is that for ω_3 for it passes essentially through experimental points given in Table 19 (the error is less than 10% for Z = 73 to 92, and of the order of 15-20% for other Z). The curves for ω_1, ω_2 and f_{13} have an uncertainty of about 20%. The f_{23} and f_{12} curves are the least accurate; they may contain errors greater than 40%.

A comparison of the measured and calculated $\bar{\omega}_L$ is given in Table 18. The measured values fall in the vicinity of those calculated from Fig.6, differing from them roughly equally in both the positive and negative directions.

It seems that in spite of the rather poor accuracy of the data of these curves, until better yield measurements are obtained for the L shell, they are more reliable than, for instance, those of Lay.

VII. Fluorescence yield for the M shell

It was found that under x-ray excitation[83] $\bar{\omega}_M = 0.06$ for Z = 92. For Z = 83 ($Pb^{210} \rightarrow Bi^{210}$ decay), $\bar{\omega}_M = 0.046$ (H.Jaffe, cited by Burhop[62]). Burhop has suggested the following approximate expression: $\bar{\omega}_M = 1.7 \cdot 10^{-9}(Z-13)^4$.

The calculations of Ramberg and Richtmyer[31] for Z = 79 allow one to evaluate the fluorescence yields for the M subshells. One obtains 0.0050 (M_I), 0.0084 (M_{II}), 0.0045 (M_{III}), 0.017 (M_{IV}) and 0.019 (M_V). Most of the vacancies in the M_I, M_{II} and M_{III} subshells are filled by Coster-Kronig transitions.

Scientific Research Physics Institute,
"A.A.Zhdanov" Leningrad State University

References

1. E.Sokolovski, C.Nordling & K.Siegbahn, Arkiv fys., 12, 301 (1957).
2. E.Sokolovski & C.Nordling, Arkiv fys., 14, 557 (1959).
3. G.T.Evan, J.S.Geiger, R.L.Graham & D.R.McKenzie, Canad.J.Phys., 37, 174 (1959).
4. W.N.Asaad & E.H.Burhop, Proc.Phys.Soc., 71, 369 (1958).
5. W.N.Asaad, Proc.Roy.Soc., 294, 555 (1959).
6. M.Ference, Phys.Rev., 51, 720 (1937).
7. I.Bergstrom & R.Hill, Arkiv fys., 8, 21 (1954).
8. M.Mladenovic & H.Slätis, Arkiv fys., 9, 41 (1955).
9. D.Hartree & W.Hartree, Proc.Roy.Soc., A, 149, 210 (1935).
10. A.Wapstra, G.Nijgh & R.Van-Lieshout, Nuclear Spectroscopy Tables, Amsterdam, 1959.
11. F.A.Johnson & J.S.Foster, Canad.J.Phys., 31, 469 (1953).
12. B.V.Bobykin & N.I.Novik, Izv.AN SSSR, Ser.fiz., 21, 1556 (1957). (Trans. Bulletin 21, 1546.)
13. G.Gallagher & D.Strominger, J.Unik.Phys.Rev., 110, 725 (1958).
14. G.T.Evan, Canad.J.Phys., 35, 672 (1957).
15. J.Mihelich, Phys.Rev., 32, 415 (1952).
16. A.Zhernovoi, E.Krisyuk & G.Latyshev, Zhur.eksp.i teor.fiz., 32, 682 (1957). (Trans.Soviet Physics - JETP.)

17. M.Mladenovic & H.Slätis, Arkiv.fys., 8, 65 (1954).
18. P.Gray, Phys.Rev., 101, 1306 (1956).
19. J.O.Rasmussen, F.T.Canavan & J.M.Hollander, Phys.Rev., 107, 141 (1957).
20. D.Hoffman & B.Dropesky, Phys.Rev., 109, 1211 (1958).
21. G.Goeffrion & G.Nadeau, Canad.J.Phys., 35, 1284 (1957).
22. Z.Sujkowski & N.Slätis, Arkiv.fys., 14, 101 (1958).
23. K.Risch, Z.Phys., 150, 87 (1958).
24. J.Burde & S.Cohen, Phys.Rev., 104, 1085 (1956).
25. J.S.Släter, Phys.Rev., 98, 1039 (1955).
26. G.Nordling, E.Sokolovsky & K.Siegbahn, Arkiv fys., 13, 483 (1958).
27. G.Wentzel, Z.Phys., 43, 524 (1927).
28. L.Pincherle, Nuovo cimento, 12, 81 (1935).
29. H.Massey & E.Burhop, Proc.Roy.Soc.A, 153, 661 (1936).
30. E.Burhop, Proc.Roy.Soc., A, 148, 272 (1935).
31. E.Ramberg & F.Richtmyer, Phys.Rev., 51, 913 (1937).
32. A.Moussa & J.Bellicard, J.phys.et radium, 15a, 85 (1952); J.B.Bellicard, Theses, Paris, 1956.
33. J.Bellicard, A.Moussa & S.Haynes, Nucl.Phys., 3, 307 (1957).
34. J.Cork, M.Brice, D.Martin, L.Schmidt & R.Helmer, Phys.Rev., 101, 1042 (1956).
35. C.D.Ellis, Proc.Roy Soc.A, 139, 336 (1933).
36. R.A.Rubinstein & J.N.Snyder, Phys.Rev., 97, 1653 (1955); Ibid., 99, 189 (1955).
37. I.Bergstrom in K.Siegbahn (editor), Beta- and Gamma-Ray Spectroscopy, N.Y.1955.
38. J.Laberrigue-Frolov & P.Radavanyi, J.phys.et radium, 17, 944 (1956).
39. J.Bellicard & A.Moussa, J.phys.et radium, 18, 115 (1957).
40. E.Plassman & F.Scott, Phys.Rev., 84, 156 (1951).
41. T.Yuasa, Physica, 18, 1267 (1952).
42. J.Perkins & S.Haynes, Phys.Rev., 92, 687 (1953).
43. E.Grigor'ev, A.Zolotavin, V.Klement'ev & R.Sinitsyn, Izv.AN SSSR, Ser. fiz., 23, 159 (1959). (Trans.Bulletin 23, 153.)
44. F.Scott, Phys.Rev., 84, 659 (1954).
45. S.Thulin, Cited in Ref.37.
46. J.Scholey, Cited in Ref.18.
47. J.Laberrigue-Frolov & P.Radvanyi, Compt.rend.242, 901 (1953).
48. O.Huber, F.Humbel, H.Schneider & A.de-Schalit, Helv.phys.acta, 25, 3 (1952).
49. C.Broyles, D.Thomas & S.Haynes, Phys.Rev., 89, 715 (1953).
50. R.N.Forest & H.T.Easterday, Phys.Rev., 112, 950 (1959).
51. I.Bergstrom, J.Arkiv.fys., 5, 191 (1952).
52. T.Asuma, J.Phys.Soc.Japan, 9, 443 (1954).
53. K.Ya.Gromov, B.S.Dzhelepov, A.G.Dmitriev & B.K.Preobrazhenskii, Izv.AN SSSR, Ser.fiz., 22, 153 (1958). (Trans.Bulletin, 22, 151.)
54. B.S.Dzhelepov. B.K.Preobrazhenskii, I.M.Rogachev & P.A.Tishkin, Ibid., 22, 126 (1958). (Trans.Bulletin, 22, 125.)
55. V.Brabets, K.Gromov, B.Dzhelepov & V.Morozov, Ibid., 23, 812 (1959). (Trans.Bulletin, 23, 805.)
56. B.S.Dzhelepov, B.K.Preobrazhenskii & V.A.Sergienko, Ibid., 22, 945 (1959). (Trans.Bulletin, 22, 936.)
57. A.Buford, J.Perkins & S.Haynes, Phys.Rev., 99, 3 (1956).
58. R.Steffen, O.Huber & F.Humbel, Helv.phys.acta, 22, 167 (1949).
59. J.Passel, M.Michel & I.Bergstrom, Phys.Rev., 95, 999 (1954).
60. M.A.Listengarten, Izv.AN SSSR, Ser.fiz., 22, 759 (1958). (Trans.Bulletin, 22, 855.)

61. V.Mokhov & M.Urin, Zhur.eksp.i teor.fiz., 30, 209 (1956). (Trans.Soviet Physics - JETP.)
62. E.H.S.Burhop, J.phys.et radium, 16, 625 (1955).
63. E.H.S.Burhop, Auger Effect and Other Radiationless Transitions - Cambridge, 1952.
64. C.E.Roos, Phys.Rev., 105, 931 (1957).
65. W.F.Frey, R.E.Johnston & J.I.Hopkins, Phys.Rev., 113, 1057 (1959).
66. R.Rightmire, I.Simanton & T.Kohman, Phys.Rev., 113, 1067 (1959).
67. F.Susor & G.Charpak, J.phys.et radium, 20, 462 (1959).
68. H.Hagedorn & T.Konijn, Physica, 23, 1069 (1957).
69. A.A.Konstantinov, Program of the Tenth All-Unions Conference on Nuclear Spectroscopy, M., 1960.
70. T.Konijn, H.Hagedorn & B.Van-Nojen, Physica, 24, 377 (1958).
71. T.Konijn, H.Hagedorn & B.Van-Nojen, Physica, 24, 129 (1958).
72. E.Patronis, C.Braden & L.Wyle, Phys.Rev., 105, 861 (1957).
73. P.W.Drewer & A.Molik, Phil.Mag., 2, 427 (1957).
74. J.Fairbrother, D.Parkin & B.O'Connor, Proc.Phys.Soc.A, 70, 262 (1957).
75. B.Kettele, H.Thomas & A.Brosi, Phys.Rev., 103, 190 (1956).
76. N.S.Massey & E.K.Burhop, Proc.Cambridge Philos.Soc., 32, 461 (1936).
77. B.L.Robinson & R.W.Fink, Revs.Mod.Phys., 27, 424 (1955).
78. D.Coster & R.Kronig, Physica, 2, 13 (1935).
79. J.N.Cooper, Phys.Rev., 61, 234 (1942).
80. J.N.Cooper, Phys.Rev., 65, 155 (1944).
81. M.A.Ross, A.J.Cochran, J.Hughes & N.Feather, Proc.Phys.Soc.A, 68, 612 (1955).
82. H.Winkenbach, Z.Phys., 152, 387 (1958).
83. H.Lay, Z.Phys., 91, 533 (1934).
84. E.Der Meteosian, Phys.Rev., 92, 938 (1953).
85. G.Betolini, A.Bizi, E.Lazzarini & L.Zappa, Nuovo cimento, 11, 539 (1954).
86. R.W.Fink & B.L.Robinson, Phys.Rev., 98, 1293 (1955).
87. A.Bisi, E.Germagnoli & L.Zappa, Nucl.Phys., 1, 593 (1956); Nuovo cimento, 4, 764 (1956).
88. A.Bisi, L.Zappa & E.Zimmer, Nuovo cimento, 4, 307 (1956).
89. H.Schmied & R.Fink, Phys.Rev., 107, 1062 (1957).
90. S.Haynes & W.Achor, J.phys.et radium, 16, 635 (1955).
91. R.W.Fink, Phys.Rev., 106, 266 (1957).
92. E.Booth, L.Madansky & F.Rasetti, Phys.Rev., 102, 800 (1956).
93. B.B.Kinsey, Canad.J.Research, 29, 404, 421 (1958).
94. A.Burford & S.Haynes, Bull.Amer.Phys.Soc., 3, 208 (1958).
95. T.Tousset & A.Moussa, J.phys.et radium, 19, 39 (1958).
96. H.Küstner & E.Arends, Ann.Phys., 22, 443 (1935).
97. R.Stephenson, Phys.Rev., 51, 637 (1937).
98. B.Kobayashi, J.Phys.Soc.Japan, 8, 440 (1953).
99. A.A.Bashilov, B.S.Dzhelepov & L.S.Chervinskaya, Izv.AN SSSR, Ser.fiz., 17, 488 (1953).
100. M.Frilley, B.Gokhale & M.Valadares, Compt.rend.Acad.sci., 232, 157 (1951).
101. V.P.Sachenko, Uch.zap. (Scientific notes), Rostov on the Don University, 68, 91 (1958); M.A.Blokhin & V.P.Sachenko, Izv.AN SSSR, Ser.fiz., 21, 1343 (1957). (Trans.Bulletin, 21, 1333.)
102. L.A.Sliv & M.A.Listengarten, Zhur.eksp.i teor.fiz., 22, 29 (1952).
103. A.Sandstrom, Phil.Mag., 22, 497 (1936).
104. S.F.Vandenbroch, H.Dimard, and others. Phys.Rev., 115, 115 (1959).
105. R.Foucher, J.phys.et radium, 20, 508 (1959).
106. E.Green, Phys.Rev., 55, 1072 (1939).
107. L.Parrat, Phys.Rev., 54, 99 (1938).

108. H.A.Bethe, Quantenmechanik der Ein und Zwei Elektronenprobleme, 1933.
109. J.A.Bearden & T.M.Snyder, Phys.Rev., 59, 162 (1941).
110. G.Evan, R.Graham & L.Grodzins, Can.J.Phys., 38, 163 (1960).
111. G.Evan & S.Meritt, Can.J.Phys., 38, 324 (1960).
112. J.O.Newton, Phys.Rev., 117, 1529 (1960).
113. J.C.Nall, O.L.Baird & S.K.Haynes, Phys.Rev., 118, 1278 (1960).
114. R.Marguin & M.Moussa, J.Phys.et radium, 21, 17 (1960).
115. F.Bertrand, M.Charpak & F.Sousor, J.Phys.et radium, 20, 967 (1959).
116. B.Robinson & R.Fink, Revs.Mod.Phys., 32, 117 (1960).

Note Added in Proof:

Some new work[110-116] on Auger electrons appeared early in 1960. The seventh Auger line K-$L_{13}(^3P_2)$ in the K-LL group was observed in Sm (Z = 62) and in Gd (Z = 64).[110-111] The measured intensity agrees with theory. The relative intensities (I_{rel}) of the lines in the K-LL group are given in Table A.[110-113] The following values of I_{rel} are reported K-LX/K-LL = 0.496 (Z = 80)[113], K-XY/K-LL = = 0.094 (Z = 80) and K-LX/K-LL = 0.49 (Z = 70)[114]. Nall, Baird and Haynes[113] measured I_{rel} for fifty lines in the L series (Z = 80). The fluorescence yield ω_K for the K shell is found to be 0.952 (Z = = 80)[113], 0.94 (Z = 75)[112], 0.936 (Z = 70)[114], 0.38 (Z = 28)[115], and 0.093 (Z = 17)[115]. The fluorescence yield ω_L for the L shell is found to be 0.047 (Z = 47)[115], 0.41 (Z = = 80)[113], 0.38 (Z = 81-83) (Lee, cited by Nall[113]), 0.19 (Z = 65), 0.20 (Z = = 70, 0.24 (Z = 72), 0.34 (Z = 80), 0.37 (Z = 80) and 0.385 (Z = 82) (Lazar and Lyon, cited by Robinson and Fink[116]), and $0 \leqslant \bar{\omega}_L \leqslant 0.08$ (Z = 70)[114]. The Auger yields a_i and Coster-Kronig yields f_{ik} for the L subshells are $a_1 = 0.16$, $a_2 = 0.46$, $a_3 = 0.607$, $f_{12} + f_{13} = 0.74$, $f_{23} =$ = 0.22 (Z = 80)[113] and $a_1 = 0.324$, $a_2 = 0.56 \pm 0.07$, $a_3 = 0.95$, $f_{12}+f_{13} = 0.58$, $f_{23} = 0.34 \pm 0.07$ (Z = 56)[113]. These data are in approximate agreement with Tables 19 and 22 for Z = 56 and 82. For the L subshells $\omega_2 = 0.32$ (Z = 80)[113]; the ω_i obtained by C.E.Roos (private communication to Robinson and Fink[116]) are given in Table B. These last two measurements are in sharp disagreement with all previous ones and with estimates for Z = 73 to 82 (Tables 19 and 21), on which the graphs of Fig.5 are based.

Table A

Line	Z = 62 [110]	Z = 64 [111]	Z = 75 [112]	Z = 80 [113]	Line	Z = 62 [110]	Z = 64 [111]	Z = 75 [112]	Z = 80 [113]
$K-L_1L_1$	1,00	1,00	1,00	1,00	$K-L_2L_2$	0,26	0,27	0,1	0,40
$K-L_1L_2$	1,39	1,40	1,4	1,32	$K-L_2L_3$	3,14	3,08	2,0	1,28
$K-L_1L_3$	1,47	1,30	1,1	0,85	$K-L_3L_3$	1,39	1,28	0,95	0,76

Table B

Z	ω_3	ω_2	ω_1
73	0,23	0,23	0,28
78	0,28	0,31	0,35
79	0,32	0,27	0,36
82	0,35	0,24	0,37

INFLUENCE OF MAGNETIC FIELDS ON RESONANCE ABSORPTION OF GAMMA-RAYS

- V.A.Lyubimov & A.I.Alikhanov

Mössbauer's[1] discovery of the emission and resonance absorption of γ-rays without energy loss to nuclear recoil has made it possible to observe the Zeeman splitting of nuclear levels directly and to measure their magnetic moments. Several investigators[2] have independently directed their attention to this possibility, in particular one of the present authors (A.I.A.).

For purposes of observation we chose the 23.8 kev γ-transition in Sn^{119m} (lifetime - $2.67 \cdot 10^{-8}$ sec, i.e., level width - $2.5 \cdot 10^{-8}$ ev). The half-life of Sn^{119m} is 250 days. In spite of the low thermal-neutron capture cross section of Sn^{118}, a source of the required activity is easily prepared. From the 89 kev isomeric level, the Sn^{119m} nucleus undergoes transition to the 23.8 kev level by emitting conversion electrons (from the K shell); from this level it decays to the ground state mainly (87%) through conversion on the L shell, but 13% of the time by emitting the desired γ-rays.

Thus the radiation from Sn^{119m} consists of 23.8 kev γ-rays and Sn x-rays with an energy of about 25 kev.

In a mixture of Sn isotopes there is another very strong emitter of x-rays of almost the same energy (~24 kev). This is In^{113} which is formed from Sn^{112} by neutron capture with a relatively large cross section. For this reason we used a tin sample enriched to 96% Sn^{118}, in which the Sn^{112} impurity was less than 0.05%.

Resonance self-absorption in the source depends on the amount of stable Sn^{119}, which if present in a high concentration will greatly restrict the possible source thickness, and therefore also its intensity. In our sample, the Sn^{119} impurity was of the order of about 1.0%, which is about one ninth the amount in a natural mixture.

Before proceeding to study the influence of a magnetic field on resonance emission and absorption, some preliminary experiments were performed.

The apparatus consisted of a proportional counter filled with a mixture of krypton and propane and adjusted to detect γ-rays with energies between 20 and 30 kev. Between the source and the counter were a palladium plate to absorb the Sn x-rays, and a 2 cm thick plexiglass plate to eliminate the electrons from the β-radioactive impurities in the source.

The tin absorber was placed in direct contact with the source and cooled with it down to 100°K. It was found that cooling reduced the intensity of the soft radiation by 15%. This is explained simply by the occurrence of resonance radiation without recoil with a very narrow ($<10^{-7}$ ev) line width and resonance absorption of it in the Sn^{119} and the absorber. In this way one obtains a curve giving the resonance absorption as a function of temperature (Fig.1, I). By attaching the absorber firmly to the source, one reduces the line width to its minimum value, closest to the natural width, since in this way the Doppler broadening due to relative motion of the source and absorber is eliminated.

A second experiment measured the cross section for resonance absorption. The decrease in intensity was measured as a function of absorber thickness at 100°K (Fig.1, II). These two experiments can be used to establish the magnitude of the resonance effect under our conditions, to compare it with the theoretical curves, and to find the effective Debye temperature of white tin.

In the magnetic-field measurements a magnet with pyramid-shaped pole pieces was used. The distances between the pole pieces was 6 mm, and the maximum field intensity was 20,000 gauss.

A 20 x 4 mm γ-ray source of thickness 5 mg/cm^2 was bonded on one side to a

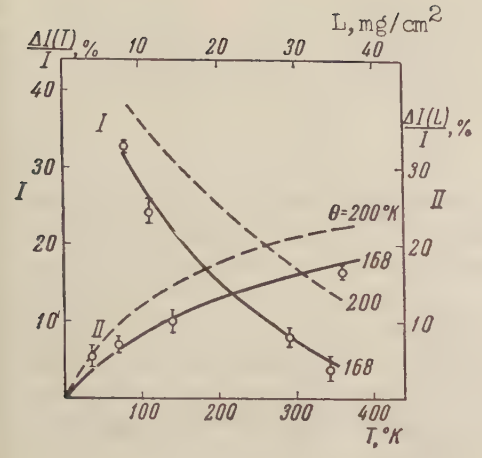

Fig.1. I - temperature dependence of the resonance effect; II - intensity attenuation as a function of absorber thickness at 100°K.

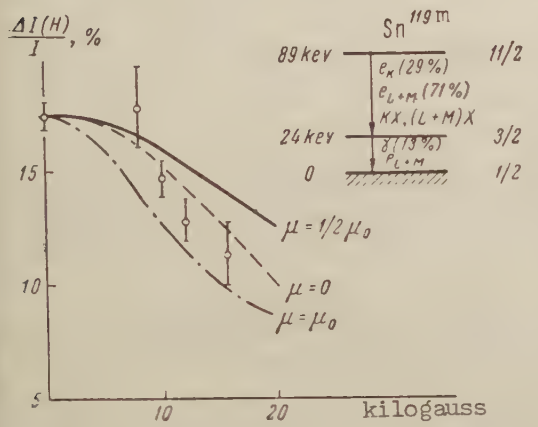

Fig.2. The magnetic-field dependence of the resonance effect.

2 cm thick plexiglass plate, and on the other side to a natural tin absorber of thickness 36 mg/cm^2. The photoelectric effect absorption length for 23.9 kev γ-rays in tin is 70 mg/cm^2, which is much greater than the resonance absorption length in the source and absorber. One end of the plate containing the source was inserted between the poles of the magnet. The source was in thermal contact with a copper rod whose other end was immersed in liquid nitrogen. During the magnetic field measurements, the absorber was at room temperature. In the range of high fields the stray magnetic field at the absorber was equal to about 28% of the field at the location of the source.

The experiment consisted of the following. First, the proportional counter was used to measure the soft radiation, filtered by the 2 cm plexiglass and 60 mg/cm^2 palladium plates, passing through the absorber. When the source was cooled down to 100°K by means of the copper rod, the measured intensity of the soft radiation dropped by 15%. When the magnetic field was turned on with the source and absorber cooled, the soft radiation intensity increased with the magnetic field. The magnetic field, splitting the 23.8 kev level, shifts the energy of the radiation from the source by roughly 10^{-7} ev, while the 23.8 kev level in the absorber, which is located in a weaker magnetic field, is shifted by a much smaller amount. As a result the energy difference between the emitter and absorber decreases and the measured intensity rises.

Fig.2,b shows, in addition to the experimental points, rough calculated curves for the resonance effect as a function of the magnetic field for different magnetic moments of the 23.8 kev level.

We express our deep gratitude to L.A.Artsimovich for providing the samples of enriched tin, to G.M.Kukavadze for his mass-spectrographic analysis, and to V.I.Anan'ev for aid in the measurements.

Institute of Theoretical and Experimental Physics,
Academy of Sciences, U.S.S.R.

References

1. R.L.Mössbauer, Z.Naturforsch, 14a, 211 (1959).
2. R.J.Mössbauer and M.Hamermesh, private communication cited by L.L.Lee, L.Meyer-Schutzmeister, J.P.Schiffer & D.Vincent, Phys.Rev.Letters, 3, 223 (1959).

NEW IRIDIUM AND PLATINUM ISOTOPES: Ir^{184} AND Pt^{187}

- V.I.Baranov, K.Ya.Gromov, B.S.Dzhelepov, Zyong Chong Bai, T.V.Malysheva, V.A.Morozov, B.A.Khotin & V.G.Chumin

Iridium-184

By means of a Danysz type β-spectrometer we investigated the conversion electron spectrum of the iridium fraction forming as a result of spallation of gold bombarded with 660 Mev protons. The iridium was separated carrier-free from the bombarded 1-2 g gold plate.[1]

In the iridium spectrum we observed a number of lines the intensity of which fell off with a period of 3.1 ± 0.3 hours. These lines were identified as L-120, M-120, K-264, L-264, M-264, K-391 and L-391. The experimental data on these lines are summarized in Table 1. The experimental (series I) spectrum of iridium is shown in Fig.1,a.

Table 1

Experimental data on the Ir conversion lines decaying with a period of 3.1 hours

H_ρ, Gs cm	E_e, kev	I_{rel}	T, hr	Identification	E_γ, kev	K/L Exper.	K/L Theo.(E2)	Assignment
1162	107,4	4,2±0,35	3,1±0,3	L	120,0±0,5			
1220	117,4	1,8±0,2	3,1±0,4	M				
1600	189,8±0,4	1,0	3,1±0,3	K	264,0±1	1,2÷1,8	2	(E2)
1891	252,2±0,5	0,7±0,15	3,3±0,5	L				
1932	261,3±0,4	0,25	—	M				
2175	317,3±1	0,26	3,3±0,7	K	391,2±1	4,3	3,1	(E2)
2430	378,8±1	0,06	—	L				

Table 2

Experimental data on the L, M and N lines of the 120 kev transition, obtained by means of the double focusing β-spectrometer

H_ρ, Gs cm	E_e, kev	I_{rel}	Identification	E_γ, kev	$(L_I+L_{II})/L_{III}$ Exper.	$(L_I+L_{II})/L_{III}$ Theor.(E2)	Assignment
1160,8	107,2	1,15±0,25	L_I+L_{II}	119,7±0,3	0,9÷1,4	1,3	(E2)
1170,3	108,8	1,0	L_{III}				
1218,1	117,05	0,7±0,15	M				
1230,0	119,13	0,25±0,15	N				

In addition, we carried out a more detailed investigation of the L, M and N lines of the 120 kev transition on a $\pi\sqrt{2}$ double-focusing β-spectrometer characterized by higher resolution.[2] The data obtained are shown in Table 2; the experimental spectrum is reproduced in Fig.1,b.

From the energy differences between the L_{III}-119.7 and N-119.7 lines and between the K-264 and M-264 lines it may be inferred that these transitions occur in the osmium nucleus. The values of the K/L ratio for the 264 and 391 kev transitions indicate that both these transitions are E2. The value of the ratio $(L_I + L_{II})/L_{III}$ for the 120 kev transition (Table 2) does not conflict with an E2 assignment for this transition, although one cannot exclude E3, E4 or E5. If we assume that the 264 and 120 kev transitions are in cascade, we find that the energy ratio of the 384 and 120 kev levels (3.2) is very close to the theoretical

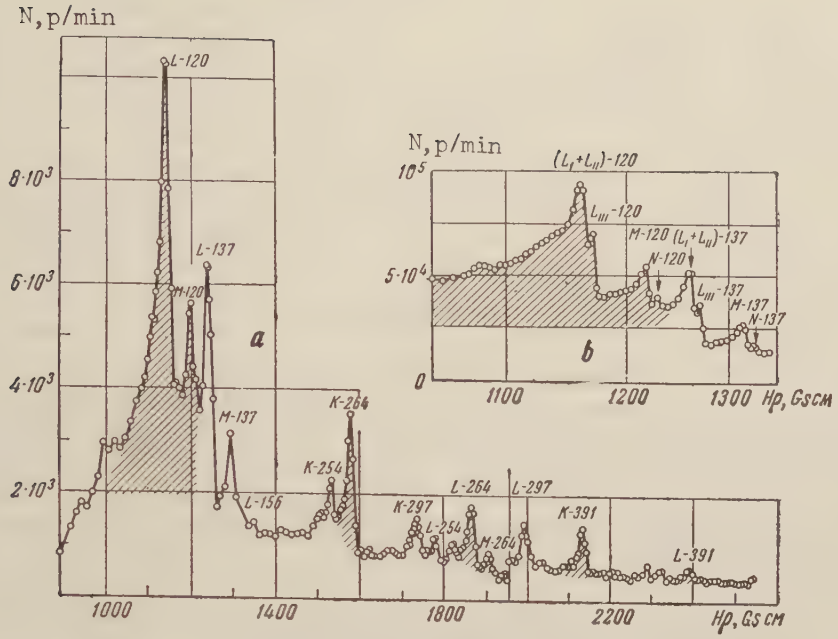

Fig.1. a - Experimental spectrum of the Ir fraction; the hatched sections pertain to Ir^{184}. b - Section of spectrum investigated on the $\pi\sqrt{2}$ double focusing spectrometer.

ratio for the ground state rotational band levels in deformed even-even nuclei. Thus the experimental data give reason to assume that the observed γ-transitions occur in the even-even osmium nucleus.

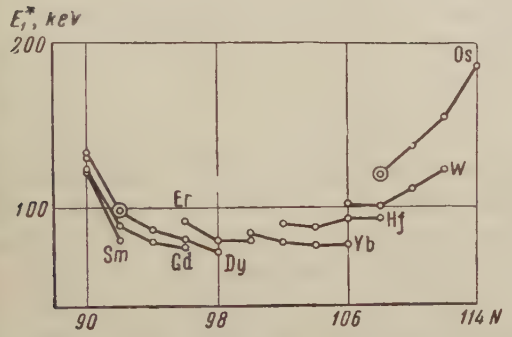

Fig.2. Variation of the energy of the first levels of deformed even-even nuclei with the number of neutrons.

A period of 3.2 hours was observed by Chu[3] for Ir^{190}. But the energies of the first three γ-transitions in Ir^{190} are 186, 356 and 401 kev. We detected no conversion lines associated with transitions of these energies. Consequently, the transitions detected in our experiments do not belong to Ir^{190}.

From the plot of the energies of the first levels of deformed even-even nuclei as a function of the number of neutrons (Fig.2) it may be inferred that the first rotational level at 120 kev may belong to Os^{184} or Os^{182}. The 182 mass assignment may be excluded, however, because no activity with a period of 21-24 hours, characteristic of Os^{182}, was observed in the Os repeatedly separated from the Ir fraction (Fig.3). Moreover, measurements[5] on a 100-channel scintillation spectrometer showed no evidence of γ-radiation belonging to Os^{182}.

On the basis of the above data we propose the decay scheme for Ir^{184} shown in Fig.4.

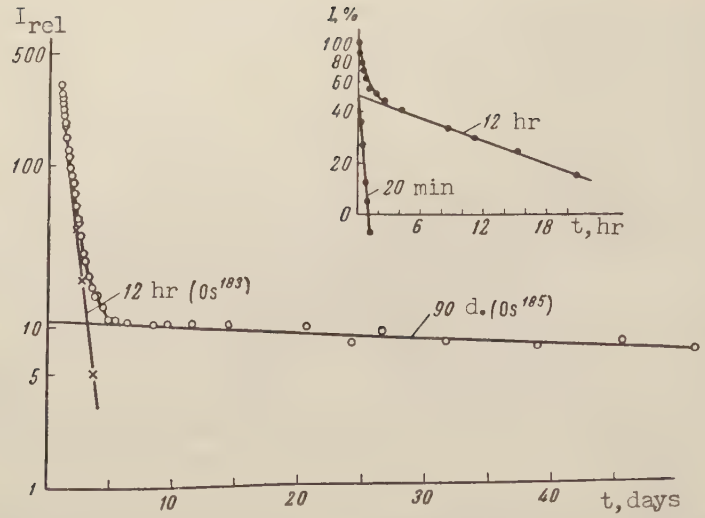

Fig.3. Decay of Os separated from the Ir fraction.

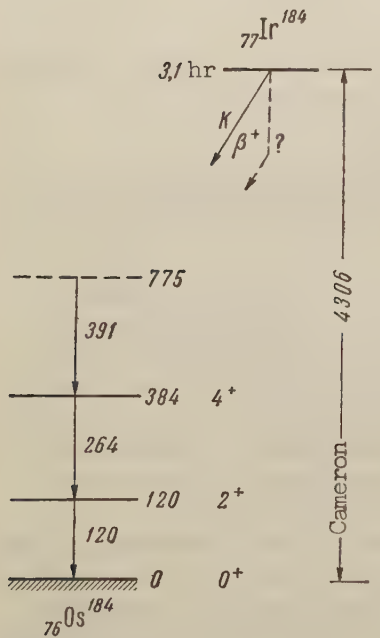

Fig.4. Decay scheme for Ir^{184} (energies in kev).

We note that if this decay scheme is accepted, the relative intensities of the 120, 264 and 391 kev transitions evaluated from the intensities of the conversion electron lines prove to be approximately equal ($I_{120}:I_{264}:I_{391} \approx 13:15:9$). This can be explained if we assume that the decay of Ir^{184} goes primarily to some nonrotational Os^{184} level with high spin. Similar cases are observed in neighboring nuclei: $Ir^{190} \rightarrow Os^{190}$ and Hf^{180m} (Ref.4). In our case it is not impossible that there is excited an isomeric state of Os^{184}. Thus in the osmium repeatedly separated from the Ir fraction there was observed an activity with a period of about 20 min (see insert in Fig.3). This period may be due to an isomer of Os^{184}.

In addition to the above mentioned lines in the spectrum of the Ir fraction we observed a number of other lines belonging to other iridium isotopes:

Ir^{186}: 137, 297 and 435 kev γ-rays (T = 18 ± 2 hours);
Ir^{185}: 254 kev γ-rays (T = 15 ± 1 hour);
Ir^{188}: 156 kev γ-rays.

Platinum-187

For determining the period of Pt^{187} the platinum fraction was first separated from the gold plate bombarded with 660 Mev protons in the synchrocyclotron.[1] Then, at equal time intervals (4 hr) the daughter iridium was separated from this fraction. The conversion electron spectrum of the daughter iridium was investigated on the $\pi\sqrt{2}$ double focusing magnetic spectrometer. The amount of Ir^{187} formed was determined from the intensity of the L-90.5 line[6], taking into account the efficiency of the chemical separation and the degree of covering of the target. The period determined in this manner for Pt^{187} was 2.0 ± 0.4 hours. For control purposes we also determined the period of the known[4] platinum isotope Pt^{186}, from the intensity of the L-137 line belonging to Ir^{186}. We obtained for Pt^{186} a period of 2.5 ± 0.3 hours, which is in good agreement with the data of Smith & Hollander[7]. No conversion lines of Ir^{185} were observed in the daughter iridium spectrum.

Conclusions

1. We discovered a new iridium isotope - Ir^{184} - with a period of 3.1 ± 0.3 hrs. A tentative decay scheme is proposed for this isotope.
2. We found a new platinum isotope - Pt^{187} - with a period of 2.0 ± 0.4 hrs.

"V.I.Vernadskii" Institute of Geochemistry and Analytic Chemistry
of the Academy of Sciences of the USSR &
Joint Institute for Nuclear Research

References

1. T.V.Malysheva, B.A.Khotin, A.K.Lavrukhina, L.N.Kryukova & V.V.Murav'eva, Present issue of the Bulletin, p.1113.
2. I.M.Bekkerman, B.A.Gumenyuk & I.S.Dneprovskii, β-spektrometr tipa BPP (Type BPP β-spectrometer), M., 1959.
3. T.C.Chu, Phys.Rev., 79, 582 (1950).
4. D.Strominger, J.M.Hollander & G.T.Seaborg, Revs.Mod.Phys., 30, 585 (1958).
5. Yu.A.Surkov, G.M.Chernov, A.K.Lavrukhina & Z.V.Khromchenko, Present issue of the Bulletin, p.1123.
6. R.M.Diamond & J.M.Hollander, Nucl.Phys., 8, 143 (1958).
7. W.G.Smith & J.M.Hollander, Phys.Rev., 98, 1258 (1955).

ON THE EXISTENCE OF ISOMERIC STATES OF Te^{119}

- N.G.Zaitseva, M.Ya.Kuznetsova, I.Yu.Levenberg, V.N.Pokrovskii & V.A.Khalkin

The existence of isomeric states of Te^{119} was established in investigating[1] the neutron-deficient isotopes of iodine with $A \leqslant 121$. From the build-up of well known Sb^{119} there were identified two parent periods: 12 ± 1 hr and 4.25 ± ± 0.25 days. It was found that the short-lived Te^{119} is a daughter of I^{119} (21 min), whereas 4.25-day Te^{119} is not.

The existence of Te^{119} isomers is not surprising, for seven odd tellurium isotopes (with A from 121 to 133) have isomeric states, which is consistent with nuclear shell theory.[2] Periods close to those observed by us and equal to 4.5 days (Lindner & Perlman[3,4]) and 16 ± 2 hrs (Dropesky[5] and Fink[6]) were attributed to Te^{119} earlier, but these half-lives were observed in isolation from each other and apparently were regarded as mutually exclusive: thus whereas Dzhelepov & Peker[7] gives only T = 16 hrs for Te^{119}, Seaborg[8] gives only T = 4.5 days.

The purpose of the present work was to obtain more detailed data on the decay of Te^{119} isomers and to establish their relative yield in the spallation reaction of iodine. The Te^{119} isomers were obtained jointly with other Te isotopes by bombarding a KI plate with 250 Mev protons in the Joint Institute for Nuclear Research synchrocyclotron. The tellurium and iodine were separated 15 minutes after the end of irradiation. As a result of the chemical separations (described in detail in Ref.1) there were obtained two radiochemically pure tellurium fractions which we designate Te I and Te II. Fraction Te I was a mixture of isotopes that had formed as a result of spallation of iodine and as a result of decay of various radioactive iodine isotopes. Fraction Te II was a mixture of tellurium isotopes that had built up only as a result of decay of radiochemically pure (at the instant of separation of the other spallation products) iodine. Only the short-lived (12 ± 1 hr) Te^{119} isomer was present in Te II.

We recorded the β- and γ-spectra of Te I and Te II by means of a simple magnetic spectrometer and a scintillation γ-spectrometer (half-width of the Cs^{137} line - 9%). It was established that the radiation from the short-lived isomer comprises an intense 660 kev γ-line, internal conversion electrons corresponding to this line and weak positron radiation with end-point energy ~550 kev. The branching ratios are $\gamma/\beta^+ \geqslant 5$, and $\beta^+/e^- \approx 5$. The period of Te^{119} determined from the decrease in intensity of the 660 kev γ-line and the β^+ radiation proved to be 14 ± 2 hrs. In the spectrum of the Te I fraction there were also detected a number of γ-lines (the most noticeable at 150 and 1200 kev) which decayed with a period of about 5 days. However, in view of the presence of 6-day Te^{118} in the tellurium fraction we had to refrain from attributing these γ-lines to 4.25-day Te^{119}. For the same reason we hesitate to say anything definitive regarding the β^+-decay of this Te^{119} isomer.

There arises the obvious question: which of the observed states is the ground state and which the isomeric? In our earlier work[1] it was established that the rate of growth of Sb^{119} in the Te II fraction as observed over a period of 9 days corresponds to T = 12 ± 1 hr. It follows that 4.5-day Te^{119} does not form in the decay of I^{119}; moreover if it be assumed that this is the ground state, there appears to be no decay to it from the isomeric (13 hr) state. Under the most extreme assumptions the fraction of isomeric transitions does not exceed 1%.

Assuming the inverse arrangement, i.e., that the 13-hour state is the ground state, we made an attempt to separate the metastable and ground states by a chemical method[9,10]. Measurements of the activity of the separated fractions that should have contained Te^{119} in the ground state by means of an MST-40 end window counter and a γ-spectrometer yielded negative results: no 13-hour Te^{119} was detected. This can be explained either by an insignificantly small fraction of

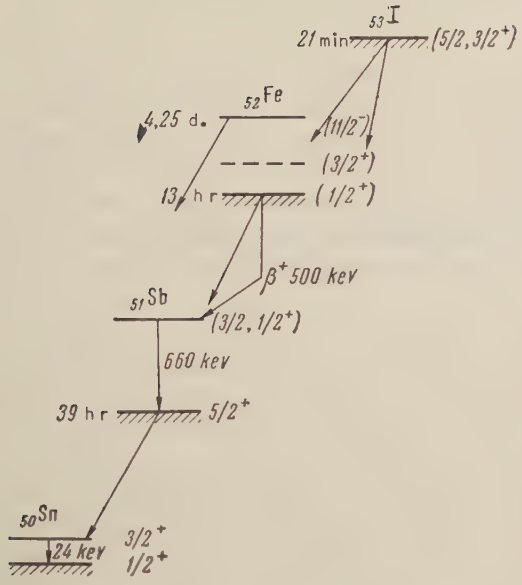

Proposed decay scheme for A = 119.

isomeric transitions or by a large energy difference between the ground and isomeric states and the consequent small conversion coefficient. Moreover, it was established that the intensity of the 660 kev γ-rays from Te I and Te II falls off with T = 13 hrs, so that the fraction of the isomeric transition at best does not exceed 10%.

Thus we failed to obtain direct experimental information on the arrangement of the isomeric and ground states. Nevertheless, we attempted to construct a decay scheme for Te^{119} which would not be in conflict with our experimental data and would satisfy the requirements of the nuclear shell model[2].

On the basis of the nuclear shell model the most probable assignment for I^{119} is 5/2+ or 3/2+. According to the shell model, the ground state of Te^{119} should be 1/2+, and the isomeric state 11/2- (this obtains, for example, in the case of the neighboring odd isotopes, Te^{121}, Te^{123} and Te^{125}). Then decay of I^{119} should occur primarily to the ground state of Te^{119}. Inasmuch as the daughter isotope of I^{119} is 13 hr Te^{119}, we infer that this is the ground state of Te^{119}.

Taking the ground state spin of Sb^{119} to be 5/2+ (Ref.7) and the spin of the excited 660 kev level to be either 3/2+ or 1/2+, we find that the decay from the 1/2+ ground state of Te^{119} to this level of Sb^{119} is allowed (see figure). This is in agreement with the evaluation of log ft, which under the above assumptions, equals ~5.5. This assumption also explains the absence of a 660 kev level in the decay scheme for 4.25-day Te^{119} proposed by Sorokin et al[11], i.e., according to this scheme there are populated levels with much higher spin.

In conclusion, we want to report briefly on the relative cross sections for formation of the Te^{119} isomers in bombardment of iodine with 250 Mev protons. In our work the bombardment time, the duration of the separation operation and the time of separation were measured to within 1 minute; the yields of all the chemical separation reactions were also accurately determined. Hence by relatively simple calculations we were able to establish the relative cross sections for formation of I^{119}, Te^{119} and Te^{119m} both on the basis of the rate of build-up of Sb^{119} in the Te I and Te II fractions and from the variations in intensity of the 660 kev line in their spectra. We obtained for the cross section ratios $\sigma_{Te^{119}} : \sigma_{I^{119}} : \sigma_{Te^{119,m}} = 1 : 1.5 : 3$. The results of determinations of the relative cross sections carried out by different methods on the basis of the data obtained in different series of experiments all agree within ±10%.

References

1. N.G.Zaitseva, M.Ya.Kuznetsova, I.Yu.Levenberg & V.A.Khalkin, Radiokhimiya No.4 (1960). (Trans.Radiokhimiya.)

2. M.G.Mayer & J.H.D.Jensen, Elementary Theory of Nuclear Shell Structure, N.Y., 1955. (Cited in Russian trans.)

3. M.Lindner & J.Perlman, Phys.Rev., 73, 1124 (1948).

4. M.Lindner & J.Perlman, Phys.Rev., 78, 499 (1950).
5. B.Dropesky, Thesis, Univ. Rochester, 1953; see Nucl.Sci.Abstr., 9, 24B (1955).
6. R.W.Fink, Thesis, Univ. Rochester, 1953; see Nucl.Sci.Abstr., 9, 24B (1955).
7. B.S.Dzhelepov & L.K.Peker, Skhemy raspada radioactivnykh yader (Decay schemes of radioactive nuclei), M.-L., 1958.
8. D.Strominger, J.M.Hollander & G.T.Seaborg, Revs.Mod.Phys., 30, 585 (1958).
9. G.T.Seaborg, J.J.Livingood & J.W.Kennedy, Phys.Rev., 57, 363 (1940).
10. R.R.Williams, Radiochemical Studies, Fission Products, 1220. N.Y., 1951.

OPERATION OF AN IONIZATION ALPHA-SPECTROMETER UNDER HEAVY LOADS

- A.A.Vorob'ev & V.A.Korolev

One of the most interesting problems in the field of modern α-spectroscopy is investigation of low intensity α-transitions against the background of more intense transitions. This includes, for example, investigation of α-decay to vibrational levels and odd parity levels in odd-odd nuclei. Extant α-spectrometers are not suitable for the investigation of such weak (10^{-4}-10^{-6}%) transitions. In the case of magnetic α-spectrometers the lower bound of the detectable intensity (10^{-3}-10^{-4}%) is determined primarily by the effect of the tails of the more intense lines.

Ionization α-spectrometers do not have this shortcoming since they allow of working in coincidence with a γ-spectrometer. In this case the tails are completely eliminated since the more intense lines do not yield coincidences. Moreover, it becomes feasible to evaluate the multipolarities and relative intensities of the corresponding γ-transitions and to investigate α-γ angular correlations, in other words, it becomes possible to identify the nuclear levels. However, these advantages of ionization chambers cannot at present be realized mainly owing to the low value of the maximum allowable chamber load. Usually the maximum chamber load does not exceed 100 pulses per sec.

Below we describe a method by means of which one can increase the allowable load to 10^4 pulses per sec.

Electron Collection Time

In the final analysis the duration of pulses produced by an ionization chamber is determined by the electron collection time. It can readily be shown that the pulse rise time on the collecting electrode in a chamber with a grid is described by

$$T = \frac{q}{W_2} + \frac{R \cdot \cos\varphi}{W_1}, \qquad (1)$$

where q is the distance between the collecting electrode and the grid, W_1 and W_2 are the electron drift velocities in front of and behind the grid, R is the α-particle range, and φ is the angle of emission of the α-particles relative to the normal to the electrode surface. By adding some 10-15% methane to the argon filling the chamber (which leads to a sharp increase in the electron drift velocity) and reducing q to ~0.5 cm one can reduce the pulse rise time to about 0.5-0.4 microsec.

Pulse Shaping

Obviously, from the standpoint of maximum reduction of the pulse duration it is expedient to shape the pulses by means of a short-circuited line. In doing this, however, it must be borne in mind that at high loads the pulses at the amplifier input will not be square. The pulse droop is determined from conditions of equality of the charging and discharging currents through the collecting electrode and may be described by the formula

$$V(t) = V_0(1 - nt). \qquad (2)$$

This shape of the input pulses excludes forming them by means of a single short-circuited line, inasmuch as in this case after the main pulse there appears

a negative tail, the magnitude of which equals

$$\delta = 2T_l\, nV_0, \tag{3}$$

where T_l is the line delay time, and n is the number of pulses per unit time. For $n = 10^{-4}$ pulses/sec and $2T_l = 3$ μsec, $\delta = 0.03$

The negative tail can be eliminated if the pulses are formed by means of two short-circuited lines. This method of shaping has the further advantage that with it the constant component of the pulse spectrum is close to zero, and, consequently, there will not occur charging of the stray capacitances and shift of the zero count level with variation in the pulse load.

Influence of the Rise Time on the Pulse Amplitude

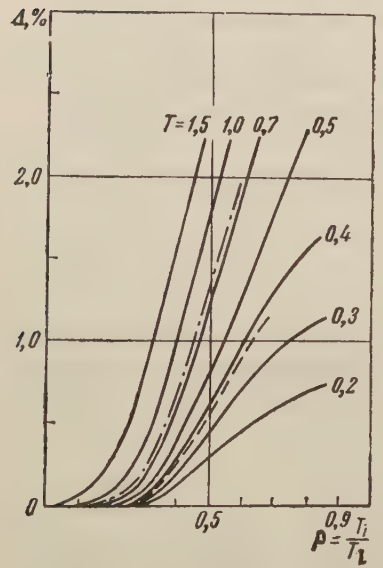

Fig.1. Variation of the rise deficit Δ with the ratio p for different rise times T (in μsec) with T_l = 1.5 μsec. The dash line gives the same dependence for T_l = 2.0 μsec and T = 0.5 μsec; the dash-dot line gives the dependence for T_l = 1.0 μsec and T = 0.5 μsec.

In determining the line parameters and the amplifier pass band one must bear in mind the influence of the pulse rise time on the amplitude of the pulses at the amplifier output. The rise time T is given by Eq.(1). Inasmuch as the rise time will be different for different $\cos\varphi$, this could lead to amplitude scatter of the output pulses.

Let us see to what extent the pulse amplitude will be reduced in going from an ideal instantaneous rise pulse to an input pulse with a rise time T. For simplicity we consider the rise to be linear. Introducing the concept of a rise lag or deficit Δ and performing the necessary calculations we obtain

$$V_T = V_0(1 - \Delta); \tag{4}$$

$$\Delta = \frac{\frac{T_i}{T}\left(e^{\frac{T}{T_i}} - 1\right) - 1}{e^{\frac{2T_l}{T_i}} - 1}, \tag{5}$$

where V_0 is the pulse amplitude at the output in the case of an instantaneous rise input pulse, V_T is the pulse amplitude at the output in the case when the pulse rise time is T, and T_i is the constant of the integrating circuit.

The variation of Δ with T_i for different rise times and different values of the line delay time T_l (1, 1.5 and 2 μsec) is shown in Fig.1. Here the horizontal scale is laid off in $p = T_i/T_l$ rather than T_i.

As will be shown below, the magnitude of p determines the signal-to-noise ratio; hence from this standpoint one should choose the highest possible value of p. Let us assume that we can take Δ = 0.2%. Since collimation is usually employed, this leads to a pulse amplitude scatter of $< 0.1\%$.

As will be evident from Fig.1, the maximum allowable value of p for a given rise time (say, 0.5 μsec) increases with increase of T_l. At the same time, however, the pulse duration also increases.

In designing the delay line we specified T_l = 1.6 μsec. The line was prepared in the following manner. A silver band 12 mm wide was applied to a quartz tube 80 cm long and 26 mm in diameter. This was then covered with 20 μ thick telephone tape and wound with contacting turns of 0.5 mm diameter enameled wire. Appropriate correcting plates were introduced to reduce the parasitic oscillations and improve the shape of the pulse leading edge. The shaping lines prepared in this manner had the following parameters: T_l = 1.6 μsec, Z = 700 ohm, R = 6 ohm, and t_f = 0.2 μsec, where Z is the wave impedance, R is the resistance and t_f is the rise time of the reflected signal.

Signal-to-Noise Ratio

The use of such long lines as shapers makes it necessary to consider the question of signal-to-noise ratio. Actually this question has hitherto not been considered even for the case of a single line (the treatment given by Gillespie[1] is erroneous since the author neglects the presence of a grid current in the input circuit). Calculation of the signal-to-noise ratio is generally analogous to that given by us in Ref.2. Hence below we shall give only the results.

In what follows we use {1,1} to identify the case of single integration-single differentiation (by means of the line), and {1,2} to identify the case of single integration-double differentiation. First we give the results obtained for the pass band in case {1,1}. The spectral transmission factor:

$$F_{11}(\omega) = \frac{\sin^2(\omega T_l)}{1+\omega^2 T_i^2}. \tag{6}$$

The mean square of the noise voltage

$$\overline{U_{11}^2} = \frac{1}{2}\left[a\cdot p\,(e^{-2/p}+2/p-1)+\frac{1-e^{-2/p}}{a\cdot p}\right]; \tag{7}$$

here the noise voltage is measured in units of $\sqrt[4]{\frac{5kTeI_c}{4C^2S}}$ (See Ref.2) and $p=T_i/T_l$, and

$$a = T_l\cdot\sqrt{\frac{eI_c\cdot S}{5kTC^2}}. \tag{8}$$

The first term in Eq.(7) represents the grid current noise; the second term the plate current noise. The amplitude of the output signal (in relative units) is

$$V_{11} = \frac{1}{2}[1-e^{-2/p}]. \tag{9}$$

Inasmuch as V_{11} does not depend on the parameter a, we can readily determine the extremum value of a at which the noise is minimal:

$$a_{\text{extr}} = \frac{1}{p}\sqrt{\frac{1-e^{-2/p}}{e^{-2/p}+2/p-1}}. \tag{10}$$

Obviously, in this case we attain the best signal-to-noise ratio:

$$Q_{\max} = \frac{1-e^{-2/p}}{2\sqrt[4]{(1-e^{-2/p})\cdot[2/p-(1-e^{-2/p})]}}. \tag{11}$$

or the pass band in case {1, 2} there were obtained the following results (for $T_{l1}=T_{l2}$). The mean square of the noise voltage is

$$\overline{U}_{12}^2 = \frac{1}{8}\left[\frac{3-4e^{-2/p}+e^{-4/p}}{a\cdot p} + a\cdot p\,(4\cdot e^{-2/p} - e^{-4/p} + 4/p - 3)\right]. \quad (12)$$

The signal amplitude

$$V = \frac{1}{4}(1-e^{-2/p}). \quad (13)$$

The optimum value of a:

$$a_{\text{extr}} = \frac{1}{p}\sqrt{\frac{3-4e^{-2/p}+e^{-4/p}}{4e^{-2/p}-e^{-4/p}+4/p-3}}. \quad (14)$$

The maximum signal-to-noise ratio

$$Q_{\max} = \frac{1-e^{-2/p}}{4\sqrt{2}\sqrt{(3-4\cdot e^{-2/p}+e^{-4/p})\,[4/p-(3-4e^{-2/p}+e^{-4/p})]}}. \quad (15)$$

Fig.2 shows the variation of the signal-to-noise ratio with the parameter p. The unit here is the maximum signal-to-noise ratio that can be obtained in conventional shaping in an RC network with the same parameters of the first tube and input circuit.[2] In this figure we also give the corresponding values of a_{extr} (dash lines). It will be seen from Fig.2 that Q increases with increase of p and in the {1; 1} case even exceeds by 20% the value that can be obtained by conventional shaping.

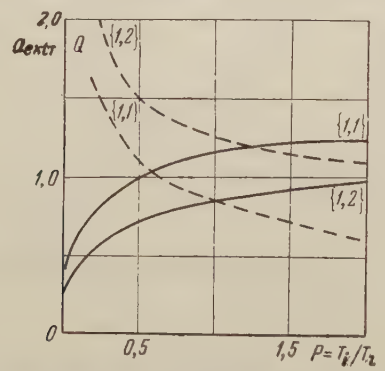

Fig.2. Variation of the signal-to-noise ratio Q (solid curves) and a_{extr} (dash curves) with the parameter p.

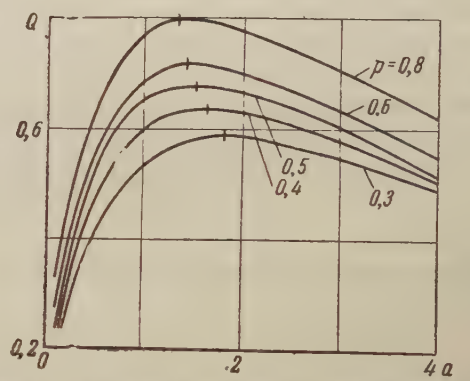

Fig.3. Variation of Q with the parameter a for different values of the ratio p.

Unfortunately, the influence of the deficit Δ is such that one cannot make p greater than 0.4-0.5. Hence the signal-to-noise ratio in case {1,2} is impaired by a factor of 1.5. The line half-width due to radio noise in this case must be ~28 kev. This value of Q, however, can be obtained only when the parameter a has the optimum value and the ratio S/I_g is the same as in the case of conventional shaping. The value of a is given by Eq.(8). Under the operating conditions generally obtaining for the first tube in low noise amplifiers[3] and with $T_l = 1.6$ μsec, $a \approx 0.1$, which is far from the extremum value (Fig.3). Consequently, the problem is to increase the transconductance S of the tube without sacrifice of S/I_g (a small decrease of this ratio is allowable inasmuch as Q is a function of S/I_g to the one fourth power. The best solution of the problem would be to use a high transconductance tube as the first amplifier tube. Tests with 6Zh9P and 6S3P tubes showed, however, that these tubes have an inadmissibly high grid current.

Another way to increase the transconductance is to raise the plate voltage of the first tube. By this means S can be increased by a factor of 3-4, but only

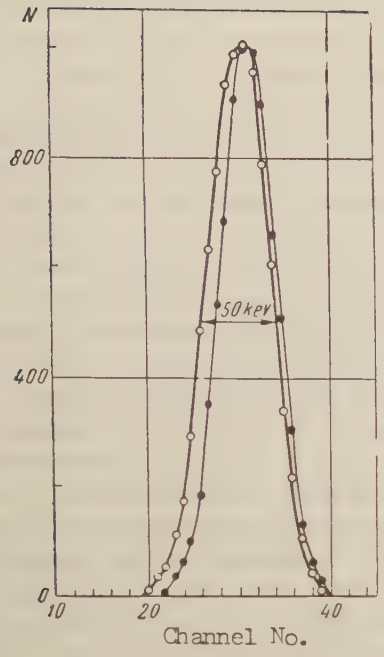

Fig.4. Amplitude distribution of oscillator pulses without load (light line) and with a load of $8 \cdot 10^3$ pulses/sec (heavy line).

at the expense of some decrease of S/I_g. Better results can probably be obtained by parallel operation of 3-4 tubes, inasmuch as in this case S and I_g increase by the same factor.

In our work we did not attempt to use several tubes in parallel but only increased the plate voltage of the 6Zh1P tube from 60 to 120 v. The line half-width due to oscillator pulses in this case proved to be 45 kev (Fig.4) with $p = 0.5$ and $T_l = 1.6$ μsec. This would indicate that connection of three or four tubes in parallel at the amplifier output should reduce the line half-width due to radio noise to ~30 kev.

Tests of the Spectrometer under High Loads

To check the operation of the spectrometer under high loadings we carried out measurements of the α-spectrum of Pu^{238} using a source having an intensity of $8 \cdot 10^3$ pulses/sec and also the spectrum of oscillator pulses applied to the amplifier input simultaneously with the α-particle pulses. Fig.5 shows the oscillogram obtained for oscillator pulses equal in amplitude to pulses from 5 Mev α-particles. The overall pulse duration is 10 μsec (measured to drop of the trailing edge to 0.1% of the crest amplitude).

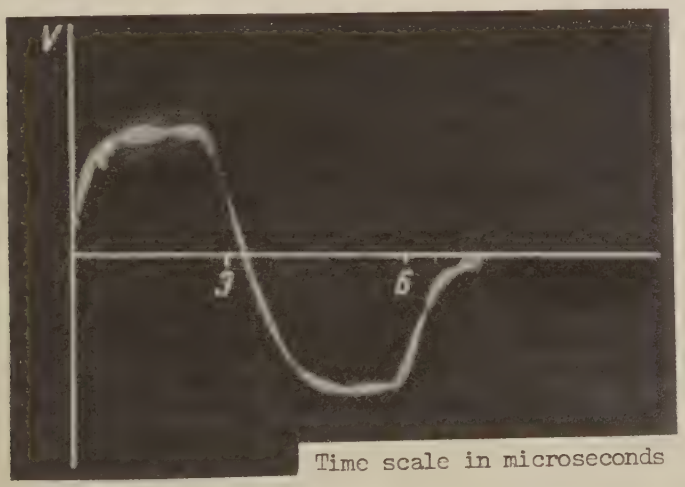

Fig.5. Oscillogram of oscillator pulses shaped by means of two short circuited lines.

The light line in Fig.4 gives the spectrum of oscillator pulses obtained in the absence of α-particle pulses; the heavy line shows the spectrum of the same pulses in the presence of a load ($8 \cdot 10^3$ pulses/sec). In working with heavy loads, we used a specially developed circuit that precluded detection of overlapping pulses. As will be evident from comparison of the curves in Fig.4, application of a heavy load had very little effect on the width and position of the peak.

The recorded α-spectrum of Pu^{238} is shown in Fig.6. As indicated, the line width at half-height in this case was 60 kev.

Analyzing our results, it must be noted that the principal contribution to the line half-width (45 kev) is from radio noise. But, as was shown above, the noise level can be substantially reduced by introducing additional tubes. Thus there is reason to assume that the half-width of the α-line can be brought down to 40-50 kev.

Before concluding, we would like to mention some of the possible applications

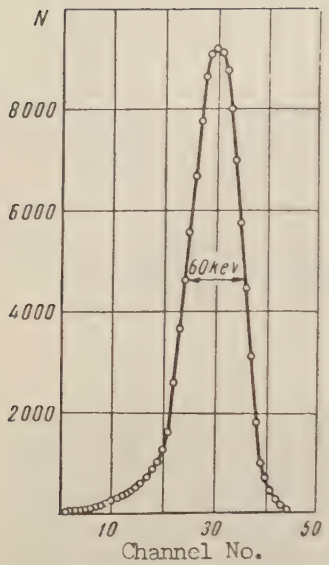

Fig.6. Alpha-spectrum of Pu^{238} recorded at a load of $8 \cdot 10^3$ pulses/ /sec.

of high load spectrometers. As noted in the introduction, by means of such a spectrometer it is feasible to investigate low intensity α-transitions. With the attained value of the allowable load, the minimum detectable intensity in our spectrometer is $5 \cdot 10^{-6}$% the total intensity.

Such spectrometers can also be used for measuring α-γ angular correlation. Actually such measurements are virtually impossible at a low counting rate in the chamber (or more accurately speaking, they are possible only in a very limited number of cases). This partially explains the fact why hitherto ionization chambers have not been used for investigating α-γ angular correlations despite the obvious advantages of this procedure. Increase of the allowable load on the α-spectrometer makes it possible to use it in coincidence with a β-spectrometer. Development of such a coincidence would be extremely useful for nuclear spectroscopy. Finally, spectrometers capable of operating under high loads can be used for investigating nuclear fission against a strong background of α-particle pulses.

We desire to thank I.A.Fadeev and M.F.Sobelevskaya, who participated in the design and construction of the long lines.

Physical-Chemical Institute,
Academy of Sciences of the USSR

References

1. A.B.Gillespie, Signal, Noise and Resolution in Nuclear Counter Amplifiers, N.Y.-London, 1953.

2. A.A.Vorob'ev, V.A.Korolev & G.E.Solyakin, PTE, No.2, 95 (1959). (Trans. Instruments and Experimental Techniques.)

3. A.A.Vorob'ev, V.A.Korolev & G.E.Solyakin, Ibid., No.1, 87 (1959). (Trans. Ibid.)

INVESTIGATION OF ALPHA-DECAY OF U^{235} BY MEANS OF AN IONIZATION ALPHA-SPECTROMETER

- A.A.Vorob'ev, A.P.Komar & V.A.Korolev

The first data on the fine structure of the U^{235} α-spectrum were obtained in 1951 by Ghiorso[1] by means of an ionization chamber. He distinguished three α-particle groups with energies (and relative intensities) of 4.58 (10%), 4.40 (86%) and 4.20 Mev (4%). In 1957 Pilger et al[2] investigated the α-spectrum of U^{235} on a magnetic spectrometer. Their results differ significantly from those of Ghiorso; they reported 4.559 (7%), 4.520 (3%), 4.32-4.37 (group of unresolved lines with a total intensity of 84%) and 4.117 ± 0.004 Mev (6%).

There is also some disagreement between the results of different investigators[2-5] who studied the γ-radiation accompanying α-decay of U^{235}. Thus, Johnsson[4] observed γ-lines with energies of 289 and 389 kev. On the other hand, Pilger et al[2] and Malich[3] showed that there are no γ-rays in the spectrum of U^{235} with energies exceeding 250 kev. Pilger et al observed a γ-line at 165 kev, while no such line was detected in the other investigations. In most of the experimental spectra there is a 145 kev γ-line. Johnsson[4], however, on the basis of control measurements asserts that this line is associated with back scattering of 185 kev γ-rays. Johnsson also observed γ-radiation with an energy of ~110 kev, yielding coincidences with 75 kev photons. An analogous γ-group (109 kev) was observed by Stephens[5], but according to this author this group did not yield coincidences with any other γ-rays.

Firmly established is the presence in the spectrum of an intense (~70% per decay) line with an energy of 185 ± 2 kev and the fact that these γ-rays yield coincidences with the 200 ± 10 kev γ-rays.[2,4] Inasmuch as hitherto no one had investigated the γ-spectra in coincidence with individual α-groups, there has been some degree of ambiguity in locating the γ-transitions in the decay scheme[6].

Below we give the results of investigation of α-decay of U^{235} by means of an ionization α-spectrometer operated in coincidence with a γ-spectrometer. We investigated the α-spectrum without regard to coincidences with γ-rays and also a number of γ-spectra in coincidence with different α-particle groups.

For our measurements we used a source enriched in U^{235}. The most intense line in the spectrum, however, was the characteristic line of U^{234} (98%). We used this line for stabilizing the amplification factor of the α-spectrometer amplifier circuit and as the standard in measuring the U^{235} α-particle energies. We also employed stabilization of the photomultiplier multiplication factor; to this end we used the pulses due to γ-rays from a small Cs^{137} source (~50 pulses/sec) cemented to the crystal. For the principal measurements we used a 30 x 10 mm NaI(Tl) crystal. The half-width of the Cs^{137} line was about 8%; thanks to stabilization, this resolution was maintained virtually constant over a prolonged period.

To enhance the α-spectrum we used electronic collimation, which reduced the counting rate by a factor of 2. The number of coincidences was ~4 per min. At so low a counting rate there was great advantage in using our "two-dimensional" multichannel analyzer (the γ-spectrum was recorded by means of a 50-channel analyzer; the α-spectrum by means of a 28-channel analyzer).

Only one α-γ coincidence experiment was carried out (100 hrs of measurement), but this provided us with sufficient data to plot the γ-spectra in coincidence with any α-particle group, and the α-spectra in coincidence with any γ-line. The use of a two-dimensional analyzer not only greatly reduces the measurement time but enhances the reliability of the results inasmuch as it eliminates possible errors due to instability of the apparatus and variation in the experimental conditions.

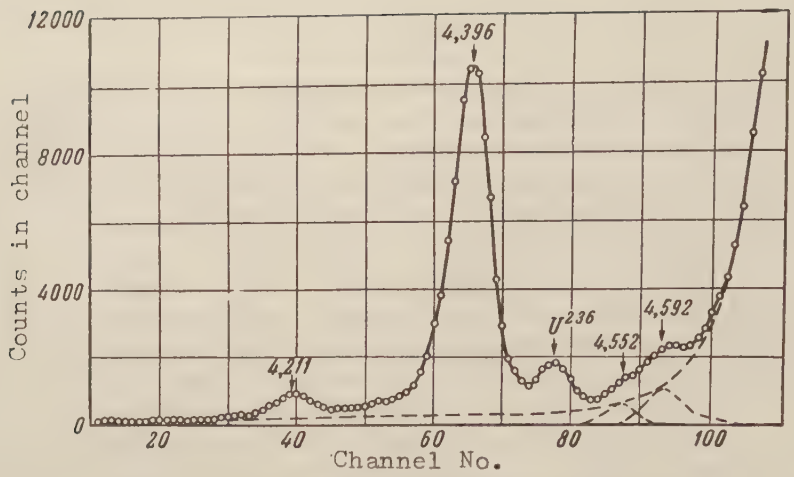

Fig.1. Singles α-spectrum of U^{235}.

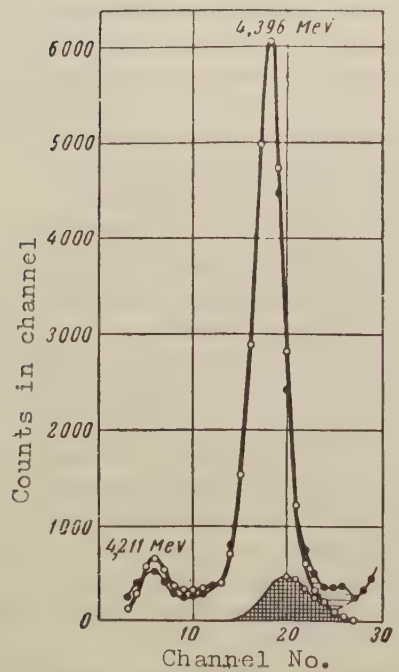

←Fig.2. Alpha-spectrum of U^{235}. Heavy line - α-spectrum in coincidence with γ-rays not discriminated in energy. The double hatched area represents the part of the α_2 line yielding coincidences with 93 kev γ-rays. Light line - α-spectrum without coincidences. The lightly hatched area represents the part of the α-spectrum due to shift of part of the pulses from the α_2 line owing to additional ionization from the L electrons and not evinced in coincidence with the γ-rays (i.e., this is the difference area used in calculating the L shell internal conversion coefficient).

The α-spectrum of U^{235} recorded without coincidences with photons is shown in Fig.1.

The α-group energies, relative intensities and corresponding hindrance factors are listed in Table 1. In evaluating the energies we introduced a small correction (4 kev for the 4.396 Mev line) which took into account the energy dependence of the ionization in the chamber. The measurement uncertainty is evaluated as ± 3 kev. The 4.486 Mev line apparently belongs to U^{236}. It was not evinced in the spectrum (Fig.2) obtained for a source prepared from a different material. In evaluating the intensity of the α_3 line we took into account the small admixture of the main line of U^{238} (E_α = = 4.195 Mev). In evaluating the intensity of the α_0 line we took into account the presence of the 4.594 Mev α-group of U^{234}, corresponding to a transition to the 4+ level. Moreover, the energy and intensity of this line were determined from a spectrum of a natural uranium isotope mixture, wherein the content of U^{235} relative to U^{234} was two times greater than in the enriched source, and where accurate extrapolation of the tail of the U^{234} line by analogy with the U^{238} line was feasible.

Our results for the α-spectrum of U^{235} are in general agreement with the results of Ghiorso, although his data are primarily quantitative in character, particularly as regards energy values. With the resolution of Ghiorso's spectrometer the α_0 and α_1 groups could not be resolved and were recorded as a single group with a relative intensity of 9%. On the other hand, comparing our results with the results of Pilger et al, one notes a significant disparity as regards the energies, particularly for the α_3 group. Even if one attributes their 4.117

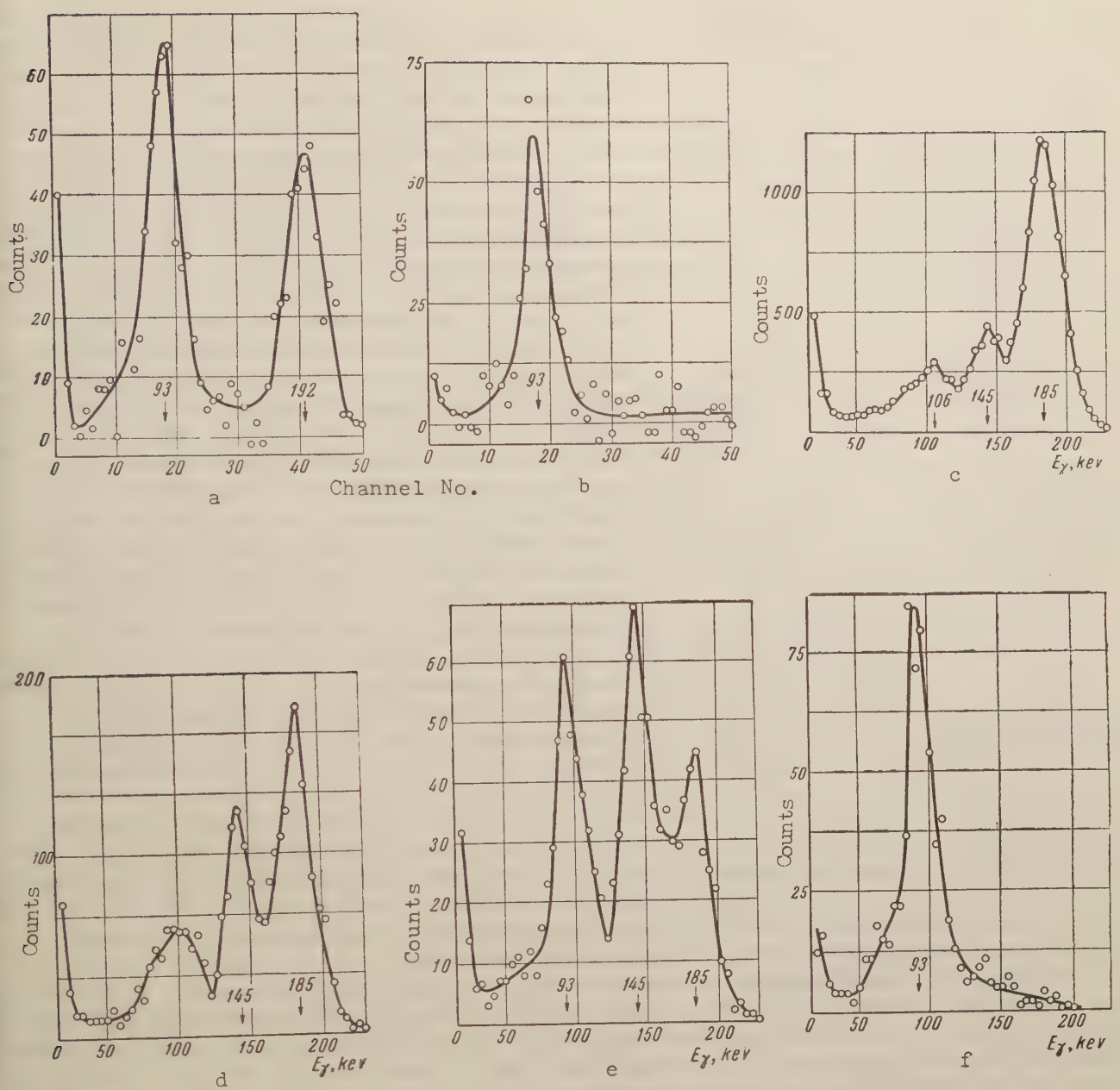

Fig.3. Gamma-spectra in coincidence with different channels of the α-analyzer: a - difference γ-spectrum in coincidence with channels 5-7, b - γ-spectrum in coincidence with channels 9-11, c - γ-spectrum in coincidence with channels 17-19, d - γ-spectrum in coincidence with channel 20, e - γ-spectrum in coincidence with channel 21, f - γ-spectrum in coincidence with channels 22-27.

Mev value for the α_3 group to some accident or malfunction, there still remains a difference of at least 30 kev for the energies of the other groups. We attribute this divergence to incorrect calibration of the spectrometer used by Pilger et al.

Recently Baranov & Zelenkov[7] investigated the α-spectrum of U^{235} on a new high luminosity magnetic spectrometer. They succeeded in resolving a number of lines among which are the lines with energies (and relative intensities) of 4.550 (3.5%), 4.394 (70%) and 4.213 Mev (6%). These energy values are in good agreement with our results.

Table 1

U^{235} α-line energies and intensities

α-Group	E_α, Mev	Level energy	Intensity, %	Hindrance factor
α_0	4,592	0	6,5	1800
α_1	4,552	41	2,5	800
α_2	4,396	199	84	4,6
α_3	4,211	385	7	1,7

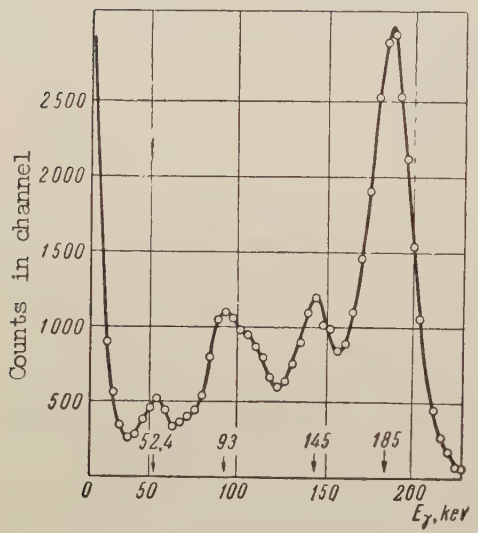

Fig.4. Gamma-spectrum recorded

Fig.3 shows the γ-spectra in coincidence with different channels of the α-analyzer. For calibration of the γ-spectrometer we used the 52.4, 93 and 185 kev lines (see Figs.3 & 4). The α_3 group is accompanied by a γ-cascade. However, knowing the relative intensities of the α-groups without coincidences and the γ-spectrum corresponding to the transition from the intermediate level in the cascade (Fig.3,c), we were able to plot the difference spectra. Thus the γ-spectra shown in Fig.3,a & b represent a γ-transition from the upper state to an intermediate state. There appears to be no cross-over transition to the lowest state. The 93 kev line is Th^{231} K x-radiation. The energy of this transition was evaluated as 192 kev. Possibly this γ-line actually consists of two lines close in energy. We evaluated the K shell internal conversion coefficient (ICC) of the 192 kev transition from the intensity ratio of the 93 and 192 kev lines. In computing the ICC the intensity of the 93 kev line was doubled inasmuch as half the pulses from the α-particles, accompanied by conversion electrons, is shifted to the side of higher energies (Fig.3,b). The calculations yielded a value of 2 ± 0.5 for the K shell ICC.

From comparison of this value with the theoretical values of the ICC (Table 2) it may be inferred that this transition is pure M1.

The α_2 line (Fig.3,c) is accompanied by γ-rays having energies of 185 ± 2, 145 ± 2 and 106 ± 3 kev and relative intensities of 82 : 13.5 : 4.5.

Comparison with the spectra reproduced in Figs.3,d & e shows that the 145 kev radiation is nuclear radiation and is not the result of back-scattering of higher energy γ-rays. The observed variation in the relative intensities of the lines is apparently connected with the fact that after emission of a 145 kev photon the nucleus remains in an excited state which is de-excited by emission of a conversion electron; this leads to a shift of the corresponding α-line. On the

Table 2

Multipole order assignments

E_γ, kev	K shell ICC					L Shell ICC					
	E1	E2	M1	M2	Exp.	E1	E2	M1	M2	Exp.	Type radiation
185	0,089	0,178	2,28	10	0,10± ±0,02	0,018	0,54	0,55	4,7	0,07± ±0,05	E1+ ⩽0,5% M2
145	0,16	0,25	5,7	23		0,036	1,88	1,06	11		E1+ ⩽1,5% M2
106	—	—	—	—		0,083	7,68	2,72	41		1
192	0,07	0,15	2,04	8	2±0,5						M1

other hand, the 185 kev transition apparently goes to the ground state.

The 106 kev γ-line cannot be a Compton peak inasmuch as for an energy of 185 kev the maximum Compton electron energy is 75 kev.

On the other hand, the maximum energy of a back-scattered γ-ray is 110 kev, which is somewhat higher than the observed value of 106 kev.

The NaI(Tl) crystal used in our main series of measurements absorbed 70% of the 185 kev γ-rays; hence in principle back-scattering could occur. We carried out a series of control measurements of the γ-spectrum in coincidence with the α_2 group using a thicker crystal (25 mm) which completely absorbed the 185 kev γ-radiation. The spectrum obtained in this case was identical with that shown in Fig.3,c which proves that the 106 kev γ-line cannot be explained as being due to back-scattering of higher energy gammas.

The multipole orders of the 184, 145 and 106 kev γ-transitions were determined by comparing the measured K and L shell ICC with the theoretical coefficients. For determining the number of decays accompanied by K x-rays we plotted the α-spectrum in coincidence with the 93 kev photons (doubly hatched area in Fig.2). The K shell ICC was evaluated as 0.10 ± 0.02.

For determining the upper bound of the integral L shell ICC we used the difference between the areas under the spectra without and with coincidences (lightly hatched area in Fig.2). In calculating the ICC the measured area was doubled and divided by the total area under the spectrum. Thus we obtained a value of $0.07 \pm$ ± 0.05 for the integral L shell ICC.

Through comparison of the experimental ICC with the theoretical coefficients given by Sliv & Band[8] (Table 2) we determined the multipole orders of these γ-transitions. The assignments were arrived at as follows.

185 kev γ-transition. Pure M1 and M2 transitions are excluded by comparison of the theoretical and experimental K shell ICC; E2 and M1 is excluded on the basis of the L shell ICC. Thus there remains only E1 + M2, wherein the admixture of M2 cannot exceed 0.5%.

145 kev γ-transition. If the assignment is E2 + M1, the admixture of M1 must be less than 5% (K shell ICC), but in this case due to this radiation alone there would be 25 L conversion electrons per 100 γ-rays, which is more than 3 times the observed experimental value for the sum of all the radiations.

Thus the only possible assignment is E1 + M2 with M2 not exceeding 1.5%.

106 kev γ-transition. Regarding this radiation one can only assert that it cannot be pure quadrupole. Thus, in the case of E2 the number of L conversion electrons would amount to 35% of the total number of γ-rays (for M2 the number would be still greater) which, as we showed, cannot be. Hence the 106 kev radiation must comprise an admixture of dipole radiation; if the assignment is E1 + M2, the fraction of E1 must be $\geqslant 90\%$, while if the assignment is M1 + E2, the admixture of M1 must be at least 70%. On the basis of our data alone, one cannot decide between these alternatives. The energies of the observed γ-transitions and the multipole order assignments are listed in Table 2.

On the basis of our data on the α- and γ-spectra, we propose the α-decay scheme for U^{235} shown in Fig.5. According to Nilsson's diagrams, the 141st neutron must occupy a level with $5/2+$ (633). This is the assignment for the ground state of Th^{231}. It must be noted that in this nuclear region in all cases when it has been possible to determine the spin and parity of the ground state the assignments agreed with the predictions from Nilsson's scheme.

The next higher level is apparently a rotational satellite of the ground state. The reduced probabilities for the 185 and 145 kev transitions evaluated on this assumption agree with the experimental values. A level at 185 kev was introduced into the scheme in view of the disparity (exceeding the possible experimental error) between the γ-ray energies and the separations between the α_0

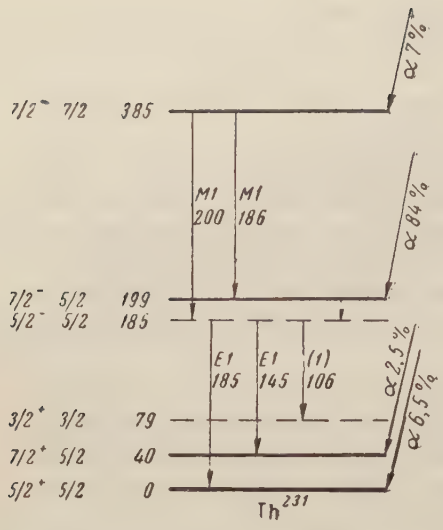

Fig.5. Level scheme for Th^{231}.

& α_2 and α_2 & α_3 groups. The multipole order assignment for the transitions from this level indicates that its spin and parity must be either 5/2- or 7/2-. Both these assignments are allowed by Nilsson's scheme. The 7/2- assignment is improbable, however, in view of the fact that the α-transition to this level is not favored (the ground state of U^{235} is 7/2-). The transition to the 385 kev level is favored, and the spin assignment for this level is 7/2-, which is also consistent with the multipolarity of the γ-transitions from this level.

If the observed 192 kev γ-line actually consists of two lines, on the basis of the shape of the γ-spectrum it may safely be asserted that these lines are of comparable intensity and hence are both M1. But in this case one must attribute a spin 7/2- to the 199 kev level and assume that it belongs to the rotational band with K = 5/2. The small separation (14 ± 5 kev) between the 185 and 199 kev levels may be the result of "interaction" of the 199 kev (7/2- or 5/2) level with the 385 kev (7/2- or 7/2+) level.[9]

Some difficulties are encountered in locating the 106 kev γ-transition in the scheme. If this transition departs from the 185 kev level, the level at 79 kev cannot be the second level of the ground state rotational band: first, because in this case there cannot be a dipole transition, second, because in this case the energy interval rule is not satisfied, and third, because the observed transition intensity is almost one order of magnitude greater than the calculated reduced transition probability (0.5%). If this transition is assumed to depart from the 199 kev level, the absence of intense ~200 and 160 kev transitions from this level is inexplicable. Hence it must be inferred that the 106 kev transition departs from the 185 kev level, and that the 79 kev level is a single particle one.

Nilsson's scheme allows for the existence of single particle levels with the following spins: 5/2-, 3/2+, 7/2- and 1/2+. Inasmuch as 5/2- and 7/2- have already been utilized and the 79 kev level cannot have spin 1/2 (the 106 kev transition is dipole), there remains for it only the assignment 3/2+. It must be emphasized that the above identification of the levels is only tentative in character. It may be asserted, however, that it is not in conflict with the experimental data now available.

We desire to express our sincere gratitude to S.A.Baranov and A.G.Zelenkov for valuable discussions and for making available the results of their investigations prior to publication. We also thank M.F.Sobolevskaya for assistance in carrying out the measurements.

References

1. A.Ghiorso, Phys.Rev., 82, 979 (1951).
2. R.C.Pilger, F.S.Stephens, J.F.Asaro & I.Perlman, Bull.Am.Phys.Soc., Ser. II, 2, 394 (1957).
3. G.W.Malich, Ibid., 1, 43 (1956).
4. S.A.E.Johnsson, Arkiv fys., 10, 97 (1956).
5. F.S.Stephens, Ph.D.Thesis, Univ.of California, 1955.
6. B.S.Dzhelepov & L.K.Peker, Skhemy raspada radioaktivnykh yader (Decay schemes of radioactive nuclei), M.-L., 1958.

7. S.A.Baranov & A.G.Zelenkov & B.M.Kulakov, Present issue of the Bulletin, p.1045.
8. L.A.Sliv & I.M.Band, Tablitsy KVK γ-izlucheniya (Tables of Internal Conversion Coefficients) M.-L., 1958.
9. A.K.Kerman, Kgl.Danske Videnskab.Selskab, Mat.-fys.Medd., 30, N15 (1956).

* * * * * * *

DECAY SCHEME FOR Eu^{147}

- Yu.A.Aleksandrov, Yu.A.Nemilov, M.K.Nikitin & Sh.Piskorzh

We investigated the γ-γ coincidences and angular anisotropy of the 76-120 kev γ-cascade in the decay of 24-day Eu^{147} (Ref.1) by means of a two-channel scintillation spectrometer with a fast-slow coincidence circuit (resolving time $5 \cdot 10^{-8}$ sec). The europium fraction was separated chromatographically from a tantalum target bombarded with fast protons in the Joint Institute for Nuclear Research synchrophasotron. The europium fraction was held for 30 days to allow the major part of the Eu^{146} and Eu^{145} (T = 5 days) activities to die out. The proportion of the listed isotopes in the mixture was checked periodically by investigating the γ-spectrum.

In addition to Eu^{147} there was present in the investigated fraction an activity with T > 50 days belonging to Eu^{148} and Eu^{149}. This activity seriously hampered the investigation.

The conversion electron spectrum of Eu^{147} was investigated by Anton'eva et al[2]. They observed electrons identified with the following γ-transitions: 76.5, 121, 198, 600, 676 and 800 kev. The γ-spectrum of Eu^{147} was also investigated by Gorodinskii et al[3] by means of a scintillation spectrometer. These investigators detected γ-transitions with energies of 80, 124 and 200 kev. Gorodinskii & Firsov[4,5] attempted to measure the γ-γ coincidences in Sm^{147}. In their initial experiments they did not observe coincidences between the 121 and 200 kev transitions and the x-rays from Sm^{147}. Upon increasing the resolving time of the coincidence circuit to $3 \cdot 10^{-6}$ sec, however, these authors observed coincidences of the Sm x-radiation with the 121 kev γ-rays. This they naturally interpreted as indicative of the existence of an isomeric state at 121 kev in Sm^{147}. On the other hand, Berlovich et al[6] measured the upper bound of the mean lifetime of the 121 kev level and obtained $\tau \leqslant 2 \cdot 10^{-10}$ sec.

The absence of coincidences between the 121 and 200 kev transitions indicates the existence of the two levels with these energies in Sm^{147}, while from the data on β-decay of Pm^{147} it follows that one of the first excited states in Sm^{147} is the 121 kev level.

We established the existence of the following cascade transitions: 76-120-600, 120-676 and 200-600 kev. The results of these measurements are shown in Fig.1.

As will be evident from the figure, there are coincidences with all the γ-transitions in this energy region, which is evidence that Sm^{147} does not have an isomeric state. The coincidence peak at ~76 kev in view of its energy cannot be a peak due to addition of K capture x-rays and internal conversion x-rays from the 121 and 200 kev γ-rays in the crystal, as was inferred in the work of Ref.1. The presence of a coincidence peak in the region of 40 kev is explained by coincidences of the K capture x-rays and the internal conversion x-rays from the 121 and 200 kev transitions.

The results of measurements of coincidences with the 76 kev γ-rays are shown in Figs.2 & 3. The presence of a certain number of coincidences in the vicinity

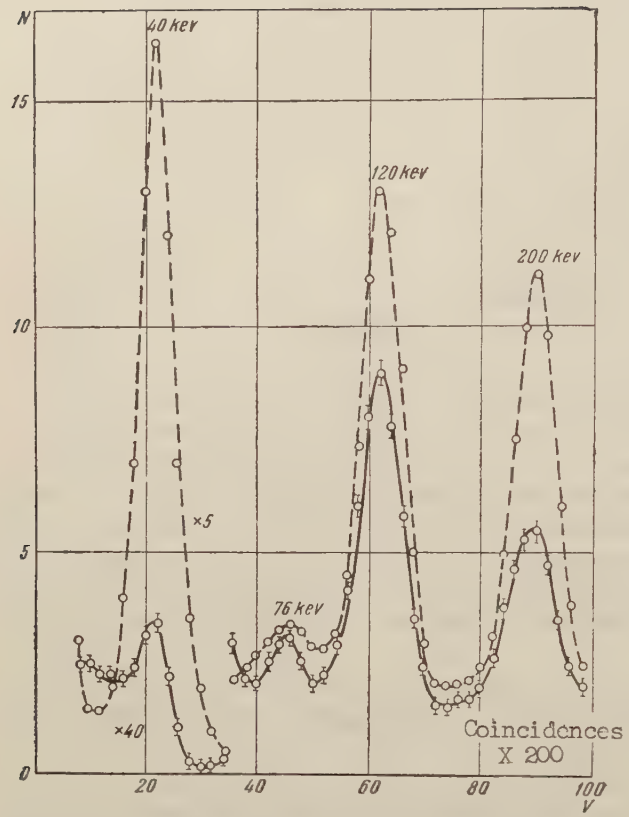

Fig.1. Spectrum of Eu^{147} γ-rays yielding coincidences with the 40 kev x-rays.

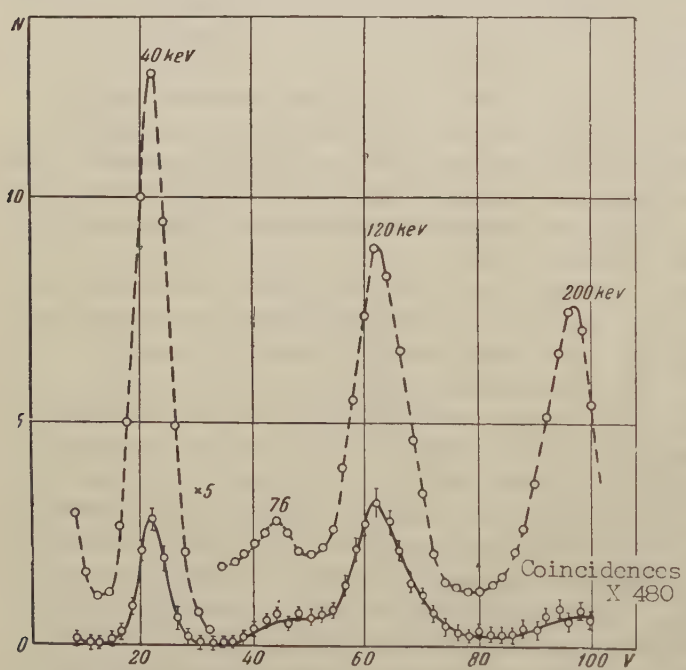

Fig.2. Spectrum of Eu^{147} γ-rays (low energy region) yielding coincidences with the 76 kev γ-rays.

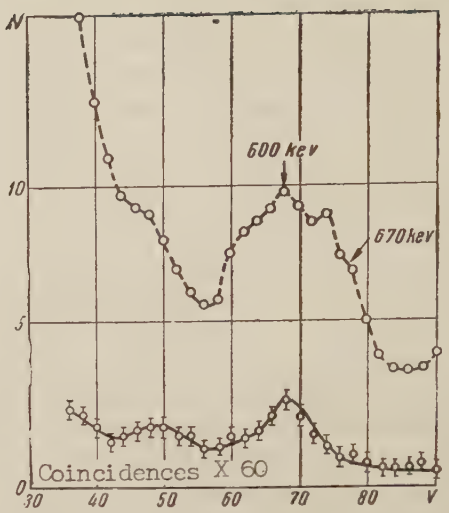

Fig.3. Spectrum of Eu^{147} γ-rays (high energy region) yielding coincidences with the 76 kev γ-rays.

of 80 and 200 kev is explained by the fact that the fixed channel, in addition to 76 kev γ-rays, received and detected part of the Compton distribution from the 600 to 676 kev γ-rays. The shape of the singles γ-spectrum in the high energy region is explained by superposition of the photopeaks from the 540 and 630 kev γ-rays from Eu^{148} or Eu^{149}.

Figs.4 & 5 show the results of measurements of the coincidences with the 120 kev γ-rays. The presence of coincidences in the vicinity of 120 and 200 kev is also explained by the fact that the fixed channel, in addition to 120 kev γ-rays detected part of the Compton distribution from the 600 and 676 kev γ-rays.

Figs.6 & 7 show the results of measurements of coincidences with the 200 kev γ-rays.

We also measured the angular anisotropy $A = \frac{w\,(180°) - w\,(90°)}{w\,(90°)}$ for the 76-120 kev cascade transition, and obtained A = -0.249. From this we determined the coefficient A_2 in the expression for the function $w(\vartheta)$; we obtained $A_2 = 0.21 \pm 0.08$.

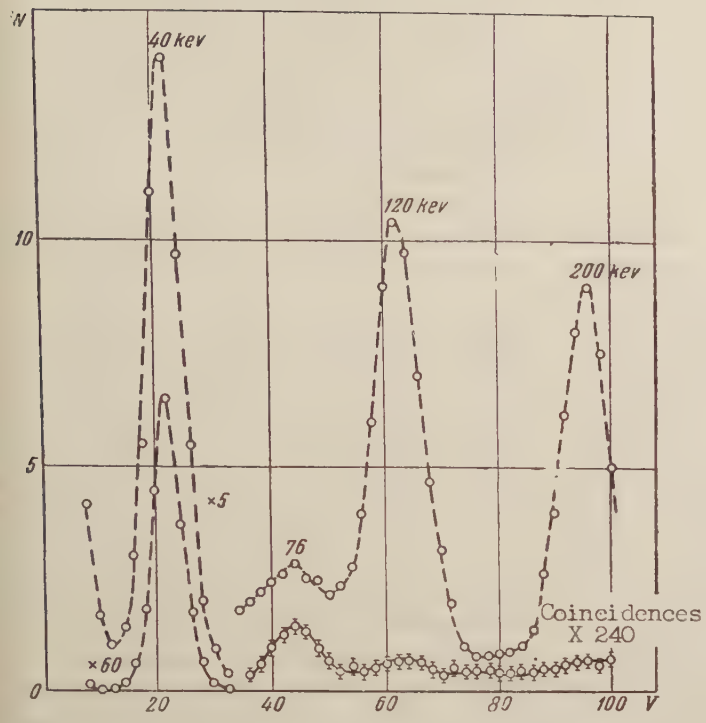

Fig.4. Spectrum of Eu^{147} γ-rays (low energy region) yielding coincidences with the 120 kev γ-rays.

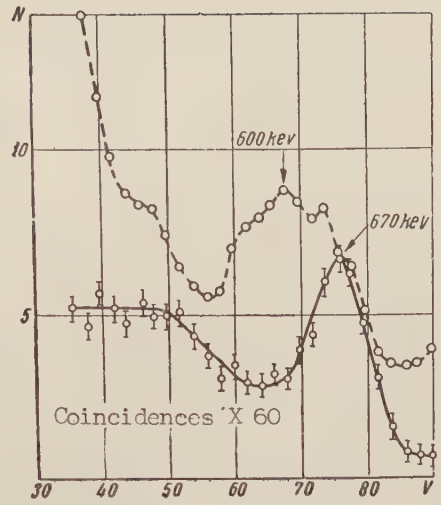

Fig.5. Spectrum of Eu^{147} γ-rays (high energy region) yielding coincidences with the 120 kev γ-rays.

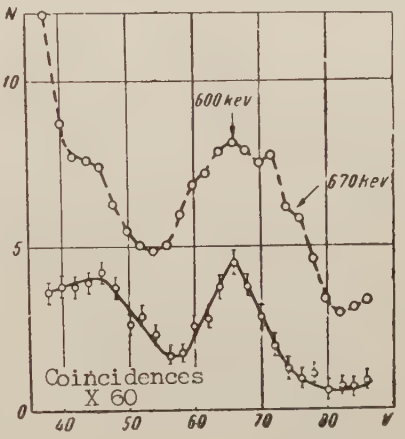

Fig.6. Spectrum of Eu^{147} γ-rays (high energy region) yielding coincidences with the 200 kev γ-rays.

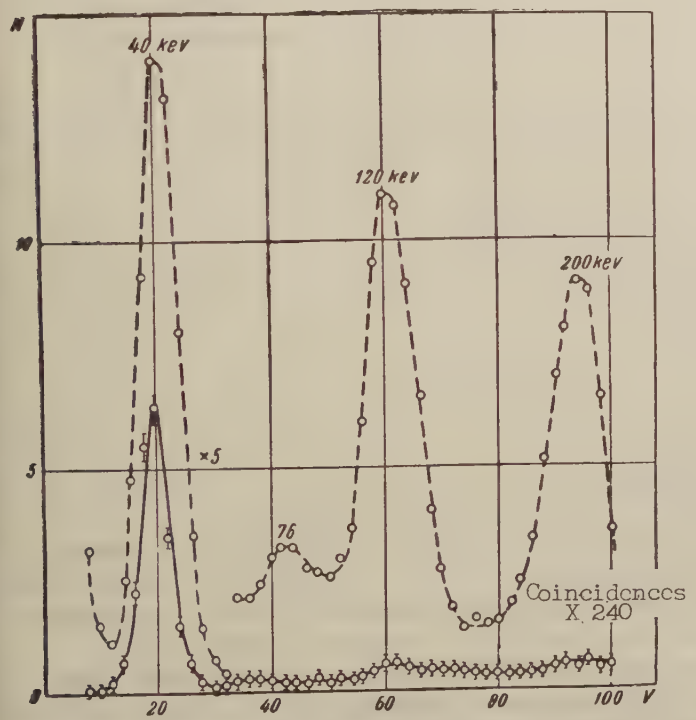

Fig.7. Spectrum of Eu^{147} γ-rays (low energy region) yielding coincidences with the 200 kev γ-rays.

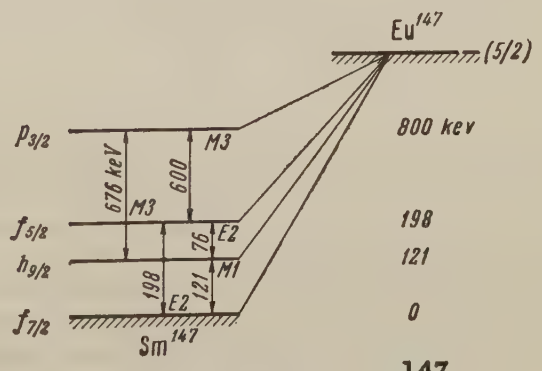

Fig.8. Decay scheme for Eu^{147}.

All our experimental data on γ-γ coincidences are in agreement with the decay scheme plotted by Anton'eva et al[2] on the basis of energy relationships.

The coefficient A_2 was compared with the theoretical values calculated for different level spins and transition multipole orders. The theoretical coefficient for the sequence $f_{7/2}$, $h_{9/2}$ and $f_{5/2}$ and multipolarities $I_1 = 2$ and $I_2 = 1$, is $A_2 = -0.131$. For the configuration sequence given by Anton'eva et al[2] ($h_{9/2}$, $f_{7/2}$ and $f_{5/2}$) the coefficient $A_2 = +0.05$. In their book, Dzhelepov & Peker[7] give the following assignments for the levels: 7/2-, 5/2- and 3/2-; in this case $A_2 = +0.05$. Consequently, our experimental value for the coefficient A_2 agrees within the limits of the experimental error with the sequence $f_{7/2}$, $h_{9/2}$, $f_{5/2}$.

This assignment for the ground state of Sm^{147} is not in conflict with the data on β-decay of Pm^{147}. According to Mayer's single particle model the ground state of Pm^{147} should be $d_{5/2}$. Consequently, the β-transition between the ground states of Pm and Sm is a first forbidden β-transition. The experimental value of log ft, namely, 7.5, is not in conflict with this inference. This assignment is also substantiated by other results of experimental determination of the Sm^{147} ground state spin made by Murakawa[8].

The ground state of Sm^{147} according to the single particle model is a $h_{9/2}$ or $f_{7/2}$ type state.

Now let us consider the possible multipole order assignments for the γ-transitions. The 76 kev transition cannot be E1 inasmuch as its intensity is low. The conversion coefficient and the K/L ratio for this transition have not been measured. The relative intensity of this transition[2] indicates that it is either M1 or E2. According to our measurements, an M1 type transition is not allowed by the spin selection rules. Consequently, this transition must be E2.

According to the K/L ratio for the 120 kev transition obtained by Anton'eva et al this transition must be M1 + E2. The inference drawn by Berlovich et al on the basis of the measured upper bound for the lifetime of the 121 kev level ($\tau \leqslant 2 \cdot 10^{-10}$ sec), that this transition is E1, is apparently incorrect inasmuch as this transition is forbidden by the parity selection rules; according to our results this transition must be M1.

The value of the conversion ratio K/L = 3.4 ± 0.3 for the 200 kev transition obtained by Anton'eva et al is in good agreement with the assumption that this transition is pure E2. This assignment is not in conflict with the spin and parity selection rules.

The 600 and 676 kev transitions according to both the spin and parity selection rules and the relative intensities should be M1.

On the basis of all the above we propose the decay scheme for Eu^{147} shown in Fig.8.

Scientific Research Physical Institute,
"A.A.Zhdanov" Leningrad State University

References

1. G.Gorodinskii, A.Murin, V.Pokrovskii & B.Preobrazhenskii, Izv.AN SSSR, Ser.fiz., 21, 1624 (1957). (Trans.Bulletin 21, 1611.)

2. N.Antoneva, A.Bashilov, B.Dzhelepov & B.Preobrazhenskii, Ibid., 22, 906 (1958). (Trans.Bulletin, 22, 899.)

3. G.Gorodinskii, A.Murin, V.Pokrovskii, B.Preobrazhenskii & N.Titov, Doklady AN SSSR, 112, 405 (1957). (Trans.Soviet Physics - Doklady.)

4. G.Gorodinskii & E.Firsov, Uch.zap.(Scientific notes), Leningrad Pedagogical Institute, 10, 272 (1957).

5. G.Gorodinskii & E.Firsov, Ibid., 197, 176 (1958).
6. E.Berlovich, K.Grotovskii, M.Bonits, V.Breslav & B.Preobrazhenskii, Izv. AN SSSR, Ser.fiz., 21, 1643 (1957). (Trans.Bulletin, 21, 1629.)
7. B.Dzhelepov & L.Peker, Skhemy raspada radioaktivnykh yader (Decay schemes of radioactive nuclei), M.-L., 1958.
8. K.Murakawa, Phys.Rev., 93, 1232 (1954).

* * * * * * *

CONCERNING THE $Yb^{164} \rightarrow Tm^{164} \rightarrow Er^{164}$ DECAY CHAIN

- B.Dalkhsuren, I.Yu.Levenberg, A.N.Murin, Yu.V.Norseev, V.P.Pokrovskii & I.A.Yutlandov

The existence of a 75-min positron activity in the ytterbium fraction obtained by spallation of tantalum bombarded with high energy protons has been established in a number of investigations.[1-3] The end-point energy of the positron spectrum is given as 2400 kev by Nervik & Seaborg[1], 2900 kev by Kalyamin et al[2] and 2940 kev by Abdurazakov et al[3]. The last investigators also detected conversion electrons associated with 91.5 and 211 kev γ-transitions.

Abdurazakov et al proposed a new identification for this activity. They suggested that mass number involved is 164, i.e., hypothesized that there exists the isotope Tm^{164}, decaying by positron emission to the 91.5 and 302 kev levels of Er^{164}.

We attempted to obtain direct proof of the existence of the daughter activity of 75-min Yb and in particular to determine its period. We used the chromatographic technique for separating Yb and the Tm daughter isotopes. The γ-spectra of the separated fractions were measured by scintillation spectrometers coupled to a multiple channel AMA-ZS analyzer and an automatic single channel analyzer.

Our search for Tm^{164} in the daughter activity did not yield conclusive results; this could be attributed to the short half-life of Tm^{164} (at least 15 min elapsed from the appearance of the Yb on the chromatogram to the beginning of measurements of the daughter Tm). Attempts at more rapid separation of Yb and Tm were also not successful inasmuch as in this case the separation was incomplete.

We therefore turned to observation of the build-up of Tm^{164} in the ytterbium fraction. To this end we took a drop of Yb from the leading edge of the separation chromatogram and followed the variation in intensity of the 510 kev γ-rays (annihilation radiation peak). The measurements were started 2-3 min after emergence of the specimen drop from the ion exchange column. The choice of the 510 kev line was dictated by the consideration that the ~3 Mev positron radiation must belong to Tm^{164} (the Tm^{164} - Er^{164} mass difference is 3785 kev according to Riddel[4] and 3097 kev according to Cameron[5]) rather than to Yb^{164} (the Yb^{164} - Tm^{164} mass difference is 1232 and 1301, according to Riddel and Cameron, respectively). Additional favorable factors were the absence of noticeable β^+-radiation from the other Yb isotopes present in the fraction (Yb^{166}, Yb^{169} and Yb^{167}; the last being short-lived, generally decayed completely by the time of separation) and the high intensity of the 510 kev γ-rays in the spectrum of the fraction.

The results of one of our experiments are shown in Fig.1. We show only the initial section of the curve (the measurements were usually continued for a period of 5 to 7 hours, so that the 75-min decay period could readily be followed). The build-up is readily apparent, and the period obtained for Tm^{164} is 2 min. Mainly the measurements were carried out with the aid of a multiple channel analyzer; the time required for recording the complete spectrum was usually 30 sec, so that

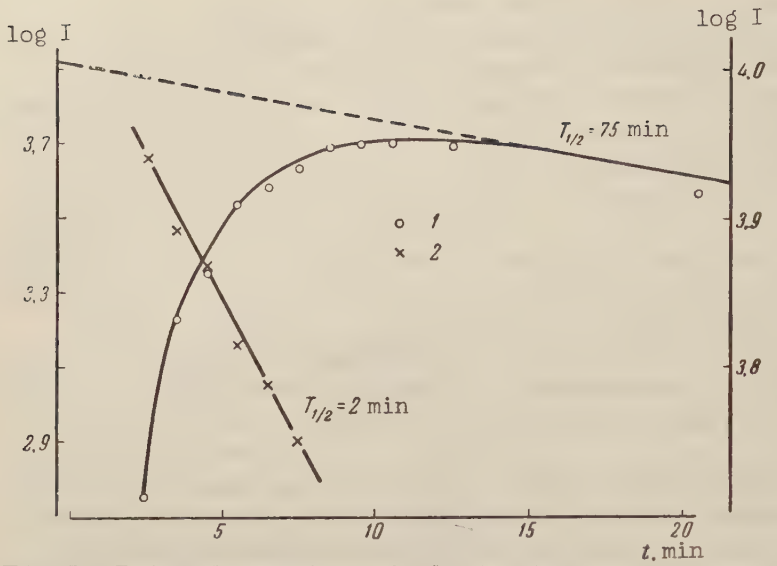

Fig.1. Initial section of the build-up and decay curve for 510 kev γ-rays: 1 - experimental curve (right-hand scale), 2 - results of subtraction (left-hand scale).

we were able to record the full spectrum every minute. A great convenience was the use of an automatic recorder in conjunction with the AMA-ZS analyzer. The data obtained in concurrent measurements with a single channel γ-spectrometer gave excellent agreement with the "multiple channel" data, although they are somewhat less convincing since only about half the points could be obtained for the build-up section of the curve.

The average value of the period T obtained from over ten series of measurements is 2 ± 0.5 min. The fact that T is comparable with the measurement time Δ does not introduce any significant error into determination of T. Thus the intensity of the 510 kev γ-rays (proportional to the amount of daughter Tm) is given to within a constant factor by

$$I(t) = A(e^{-\lambda_1 t} - e^{-\lambda_2 t}),$$

where λ_i is the decay constant, T_1 is the period of the parent isotope, and T_2 is the period of the daughter isotope $(T_1 > T_2)$. Then the intensity $I(t_i)$ at a given instant t_i measured over the interval Δ_i is

$$I(t_i) = \int_{t_i}^{t_i+\Delta_i} I(t)\,dt = A\left(e^{-\lambda_1 t_i}\,\frac{1-e^{-\lambda_1\Delta_i}}{\lambda_1} - e^{-\lambda_2 t_i}\,\frac{1-e^{-\gamma_2\Delta_i}}{\lambda_2}\right).$$

Inasmuch as $\lambda_1 \Delta_i \ll 1$, we have

$$1 - e^{-\lambda_1\Delta_i} \approx \lambda_1 \Delta_i$$

and

$$I(t_i) = A\left(e^{-\lambda_1 t_i} - e^{-\lambda_2 t_i}\,\frac{1-e^{-\lambda_2\Delta_i}}{\lambda_2\Delta_i}\right)\Delta_i.$$

From this it is apparent that with $\Delta_i = \text{const}$ the factor multiplying $e^{-\lambda_2 t}$ is constant and hence does not affect the determination of T_2, carried out by graphic subtraction.

This factor was taken into account in determining the fraction of the 510 kev γ-ray intensity connected with Tm, or, in other words, allowing for the possible presence of positron radiation from Yb^{164}. For T_2 = 2 min and Δ_i = 0.5 min this factor is 0.92. It was found that the intensity of the positron radiation from Yb^{164}, if it exists, amounts to not over 10% relative to the intensity of the positron radiation of Tm^{164}. The relatively high uncertainty of this evaluation is explained by the difficulty of precisely identifying the instant of separation of Yb and Tm in the ion exchange column.

Employing a similar procedure we followed the build-up of 90 kev γ-radiation. In this case it was necessary to take into account the variation of the intensity of the 80 kev γ-rays belonging to Yb^{166} and Tm^{166}, since the 80 and 90 kev γ-rays were not resolved by our scintillation spectrometer. The build-up of γ-80 was investigated by Baranovskii & Pokrovskii; it was also checked in our experiments. The results obtained for γ-90 are in excellent agreement with the results for γ-510.

We also made attempts to follow the variation in the intensity of the 210 kev γ-rays; however, the results obtained were not conclusive owing to the low intensity of this γ-line.

Thus it may be asserted that the existence of the chain

$$Yb \xrightarrow[75\ min]{K} Tm \xrightarrow[2\ min]{K,\beta^+} Er$$

has been established. Further, if we take into account the demonstrated fact that the 80 kev transition actually occurs in the daughter nucleus (between the levels of Er), the 164 mass number assignment proposed by Abdurazov et al[3] for this chain becomes highly probable.

A further argument in favor of the inference that the 91.5 kev transition occurs between the levels of the even-even nucleus is the following. From our measurements we could determine the ratio of the abundance of 90 kev γ-rays to the number of positrons: 0.08 ± 0.03. Abdurazov et al give the ratio of the intensity of the L conversion electrons from the 91.5 kev transition to the intensity of β^+: 0.14 ± 0.03. This gives us the value of the L shell conversions coefficients: α_L = 1.75 ± 1. This value is in good agreement with the theoretical value[7] of 2.16 for E2 radiation, and differs greatly from the other closest values, namely, 0.054 for E1 and 0.45 for M1. Then, on the assumption of E2 radiation, the intensity of the 91.5 kev transition amounts to not over 40% the number of positrons emitted in the $Yb^{164} \rightarrow Tm^{164} \rightarrow Er^{164}$ decay series.

Aside from the 91.5 and 211 kev lines, in our experiments we did not detect any intense (> 10% the number of β^+) lines that could be attributed to Yb^{164} or Tm^{164}. This indicates that the major part of the decays of Yb^{164} and Tm^{164} goes to the ground state (Fig.2). Evaluating log ft for each of these transitions we find that for each of them log $ft \leqslant 5$, which indicates that these transitions are allowed.

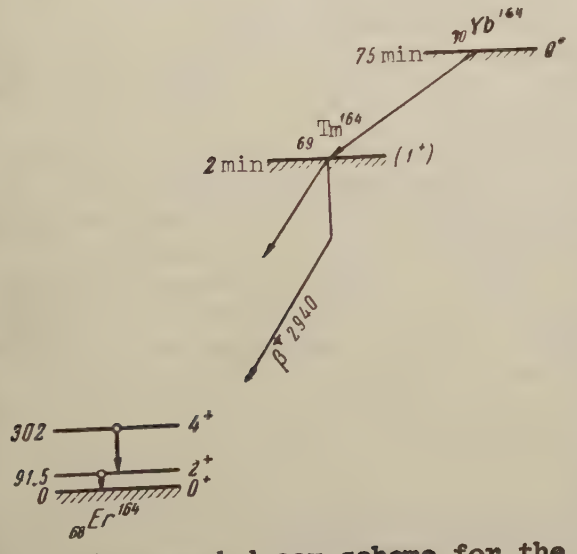

Fig.2. Proposed decay scheme for the A = 164 chain.

This, however, would appear to be in conflict with the possible spin assignments for Tm^{164}.

Thus, according to the theoretical rules[8], which are usually valid, the spin of the odd-odd nucleus $_{69}Tm^{164}_{95}$ should be equal to $|\Omega_p \pm \Omega_n|$, where Ω_p and Ω_n are the spins of the odd (69th) proton and odd (95th) neutron, respectively. According to Nilsson's[9] scheme Ω_p = 1/2+ and Ω_n = 5/2-, so that the spin of Tm^{164} should be 2- or 3-, but neither of these values is consistent with the allowed character of the transition.

It is known, however, that for the 95th neutron there is realized a state with 5/2+, located close to the 5/2- state (for Dy^{161} - see Ref.10). Further, it is known (Refs.10,11) that for Z = 69 there is re-

alized the 1/2+ state, but with decrease in the number of neutrons it is approached ever closer by the 7/2+ state. Thus for Tm^{171} the energy separation between the 1/2+ ground state and the excited 7/2+ state is 636 kev, for Tm^{169} the separation is 316 kev, while for Tm^{167} it is only 176 kev. Thus it is not impossible that in the case of Tm^{164} the last proton is in the 7/2+ state. Then $|\Omega_p \pm \Omega_n|$ may be either 1+ or 6+. The 1+ assignment is consistent with the allowed nature of the transition. These inferences are, naturally, only tentative, and the entire question requires further investigation.

We are grateful to K.Ya.Gromov and E.P.Grigor'ev for valuable discussions.

References

1. W.Nervik & G.Seaborg, Phys.Rev., 97, 1092 (1955).

2. A.V.Kalyamin, I.Yu.Levenberg & V.A.Yakovlev, Atomnaya energiya, 5, 582 (1959). (Trans.Soviet Journal of Atomic Energy.)

3. A.A.Abdurazakov, K.Ya.Gromov, B.S.Dzhelepov, Yu.V.Norseev, G.Ya.Umarov & V.G.Chumin, Izv.AN SSSR, Ser.fiz., 24, 278 (1960). (Trans.Bulletin, 24, 266.)

4. J.Riddel, A Table of Levy's Empirical Atomic Masses, CRP 654, Chalk River, 1957.

5. A.G.W.Cameron, A Revised Semi-Empirical Atomic Mass Formula, CPR 690, Chalk River, 1957.

6. V.I.Baranovskii & V.N.Pokrovskii, Izv.AN SSSR, Ser.fiz., 23, 819 (1959). (Trans.Bulletin, 23, 813.)

7. L.A.Sliv & I.M.Band, Tablista koeffitsentov vnutrennei knoversii γ-izlucheniya (Table of internal conversion coefficients. Part II, L shell), M. 1954.

8. L.K.Peker, Izv.AN SSSR, Ser.fiz., 21, 1029 (1957). (Trans.Bulletin, 21, 1030.)

9. S.G.Nilsson, Kgl.Danske Videnskab Selskab, Mat.-fys.medd., 29, N 16 (1955).

10. B.R.Mottelson & S.G.Nilsson, Ibid., 1, N 8 (1959).

11. B.Harmatz, T.H.Handley & J.W.Mihelich, Phys.Rev., 114, 1082 (1959).

INVESTIGATION OF NEW NEUTRON-DEFICIENT PLATINUM ISOTOPES

- T.V.Malysheva, B.A.Khotin, A.K.Lavrukhina, L.N.Kryukova & V.V.Murav'eva

The present work was undertaken with a view to investigating the neutron-deficient isotopes of platinum forming as the result of spallation of gold bombarded with 660 Mev protons. Gold samples weighing 1-2 g were bombarded in the Joint Institute for Nuclear Research synchrocyclotron, and the active platinum and iridium fractions separated from the product. The platinum isotopes were investigated by studying the conversion electron spectrum and the genetic relationships.

Owing to the lack of a satisfactory technique for separating carrier-free platinum and iridium, we carried out a number of experiments to develop such a procedure. The proposed procedure is based on anion exchange separation of the chloride complexes of platinum and iridium. The chloride complex of tetravalent platinum $(PtCl_6)^{2-}$ is well sorbed by the strongly basic anionite Dowex-I, while the tetravalent complex of iridium $(IrCl_6)^{2-}$ is reduced as a result of evaporation with hydrochloric acid and the reducing action of the resin to the trivalent complex $(IrCl_6)^{3-}$, which is unstable in 8N HCl and is eluted under the given conditions.[1-4] The column was flushed with 8N HCl under pressure insuring an elution rate of 0.7-0.8 ml/min.

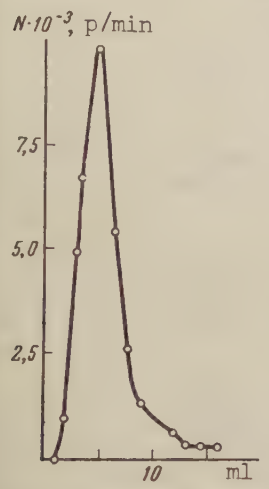

Fig.1. Elution of Ir(III) by 8N HCl.

The elution curve for Ir(III) is shown in Fig.1. The fact that the curve has a horizontal section indicates that at the given moment there began to be elutriated the just formed daughter iridium. The platinum was obtained by ashing the upper resin layers.

To remove the alkali and alkaline earth elements, the platinum and iridium in 0.1-0.4 N HCl solution were passed through a column filled with KU-2 cationite.[5]

The purity of the iridium and platinum depends primarily on the presence of gold, osmium, rhenium, tungsten and tantalum that form from the gold. The gold was eliminated by extraction with ethyl ether; the osmium was eliminated in the form of OsO_4 in the process of solution of the target in boiling aqua regia. The tungsten and rhenium were sorbed on the anionite, but in the subsequent flushing of the target were probably partially eluted. Thus the passing of iridium and platinum through the anionite not only separated these elements but cleansed them of the major impurities.

All the final solutions were further purified from extraneous impurities by double distillation.

The results of investigation of the conversion electron spectrum of the iridium fraction are given in Ref.6 (present issue of the Bulletin, p.1086).

We investigated the conversion electron spectra of the platinum fraction by means of a magnetic, helical orbit β-spectrometer with a resolution of 0.5%. The experimental spectra are shown in Fig.2. The results of the conversion line measurements are summarized in the accompanying table.

In the conversion electron spectrum of the platinum fraction we observed a group of lines the intensity of which fell off with a period of 10-11 days. Five of these lines are associated with a γ-transition of 155 ± 0.3 kev energy belonging to Ir^{188}, which builds up from 10-day Pt^{188}. We detected two known γ-transitions of Pt^{188} with energies of 187.0 ± 0.3 kev and 194.5 ± 0.3 kev (Ref.8) as well as a new γ-transition with E_γ = 171.5 ± 0.4 kev. In addition, we observed lines associated with a 184.0 ± 0.5 kev γ-transition which may be attributed to either Pt^{188} or Ir^{189}.

Results of investigation of the conversion electron spectrum of the platinum fraction

E_e, kev	Half-life		Identification	E_γ, kev		Isotope
	Measured	Tabulated (Ref.7)		Measured	Tabulated (7)	
84,6±0,3	~3 days	3,3—4,4 days	L-98,5	98,5±0,3	97—99	$Pt^{195\,m}$
115,6±0,3	4,3±1 days		(L_I+L_{II})-129,5	129,7±0,3	129,9	
118,1±0,3	4±1 »		L_{III}-129,7			
126,6±0,7	4 days		M-129,9			
129,1±0,2	~5 days		N-129,8			
121,7±0,3	4,5±1 days	3,4—4,5 days	L_I-135,6	135,4±0,3	135,5	$Pt^{193\,m}$
123,5±0,4	3,5±1 »		L_{III}-135,1			
132,3±0,2	~5 days		M-135,6			
134,7±0,3	~5 »		N-135,4			
68,8±0,5	3±1 days.	2,9—3,2 days	(L_I+L_{II})-81,8	82,3±0,5	82,5	Pt^{191}
70,9±0,5	3±1 »		L_{III}-82,1			
79,1±0,5	~5 days		M-82,5			
255,4±0,4	3,2±0,5 »		$(L+L_{II})$-268,4	268,2±0,5	267—268	
191,8±0,5	3,5±0,5 »		K-267,9			
274,9±0,5	3,2±0,5 »		K-351	351±0,5	351—352	
283,6±0,5	2,6±0,5 »		K-359,6	359±0,5	360—361	
64,5±0,4	14+3 hr	11 hr	K-140,6	140,3±0,4	140	Pt^{189}
126,9±0,4	Several hours		L-139,9			
80,8±0,3	~10 »	—	(L_I+L_{II})-93,9	94,0±0,2	—	Pt^{189}
82,7±0,3	~10 »	—	L_{III}-93,9			
90,9±0,2	10,5±0,5 hr	—	M-94,1			
93,3±0,3	10±1 hr	—	N-94,0			
97,7±0,3	10±1 hr	—	?		—	Pt^{189}
229,7±0,2	10÷14 »	—	?		—	Pt^{189}
56,8±0,1	~10 days	10 days	(L_I+L_{II})-69,5	69,5±0,1	69,5	Ir^{189}
58,5±0,1	~10 »		L_{III}-69,4			
95,6±0,3	~10 »	—	K-171,6	171,5±0,4	—	Pt^{188}
157,9±0,4	~10 »		L-171,3			
107,6±0,4	~10 »	—	K-183,7	184,0±0,5	—	Pt^{188} or Ir^{189}
171,4±0,4	~10 »		(L_I+L_{II})-184,5			
110,9±0,4	~10 »	10 days [8]	K-187,0	187,0±0,3	188,5 [8]	Pt^{188}
173,8±0,3	~10 «		(L_I+L_{II})-187,0			
118,5±0,3	~10 »	10 days [8]	K-194,6	194,5±0,3	195,4 [8]	Pt^{188}
181,5±0,3	~10 »		(L_I+L_{II})-194,5			
184,1±0,3	~10 »		L_{III}-195,3			
171,0±0,4	2,5±0,5 hr	—	(L_I+L_{II})-184,1	184,0±0,4	—	Pt^{187}, Pt^{186} or Pt^{184}
172,8±0,4	2,5±0,5 »	—	L_{III}-184,0			
166,4±0,4	3±1 hr	—	(L_I+L_{II})-179,5	179,5±0,4	—	
168,3±0,4	~3 »	—	L_{III}-179,5			
37,4±0,2	<10 hr	—	(L_I+L_{II})-50,5	50,5±0,2	—	
39,2±0,2	<10 »	—	L_{III}-50,4			
80,8±0,3	~10 days	10 days (Period of Pt^{188})	K-154,7	155,0±0,3	155	Ir^{188}
142,2±0,3	11±1 days		(L_I+L_{II})-154,9			
144,0±0,4	10±0,5 days		L_{III}-154,9			
151,8±0,3	11±2 »		M-154,8			
154,4±0,4	11±2 »		N-155,0			
240,5±0,4	11,5±1 hr	13 hr	K-314,4	314,4±0,4	314,4	Ir^{187}
222,5±0,4	14,5±1 »	14—16hr.	K-296,4	296,4±0,4	297	Ir^{186}

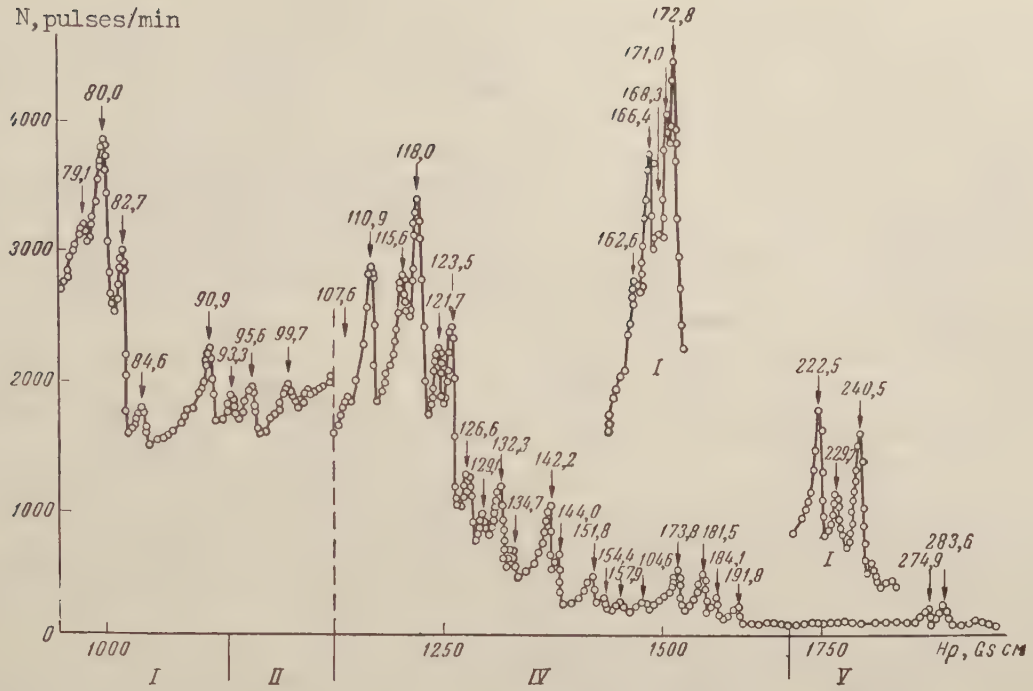

Fig.2. Experimental conversion electron spectra of the platinum fraction on the first (I), second (II), and subsequent days after irradiation. The figures give the conversion electron energies in kev.

The observed group of lines the intensity of which falls off with a period of 3 to 4 days characterizes the well-known transitions of Pt^{195m}, Pt^{193m} and Pt^{191}.

We attributed the conversion lines decaying with a period of 10-11 hours to Pt^{189}. In addition to the lines of the already known[9] 140 kev transition, we observed six new conversion lines; four of them were identified as the $L_I + L_{II}$, L_{III}, M and N lines of a 94.0 ± 0.2 kev transition.

The presence in the platinum fraction spectra of the 314.4 and 296.4 kev γ-transitions belonging to Ir^{187} and Ir^{186} (Ref.10) indicates that in the spallation of gold there forms, in addition to the already known platinum isotope, Pt^{186}, a new isotope, Pt^{187}. No conversion lines corresponding to γ-transitions of Ir^{185} were observed in the platinum fraction spectrum. It may be assumed that the period of Pt^{185} is either very long or, what is more probable, short: $\leqslant$ 20 min.

We also observed four conversion electron lines the intensity of which fell off with a period of 2.5 ± 0.5 hours. We identified these as the $L_I + L_{II}$ and L_{III} lines of a 184 ± 0.4 kev transition and the $L_I + L_{II}$ and L_{III} lines of a 179.5 ± 0.4 kev transition.

On the basis of the period these may be attributed to Pt^{184}, Pt^{186} or Pt^{187} (Ref.6).

The period of the platinum isotopes were determined by separating the daughter iridium from the platinum fraction at equal intervals ranging from 1 to 4 hours (Fig.3). Determination of the integral period of Pt^{186} and Pt^{187} from the activity of 15-hour Ir^{186} and 13-hour Ir^{187} yielded a value of 2.2 ± 0.5 hours, which is in good agreement with the data of Baranov et al[6].

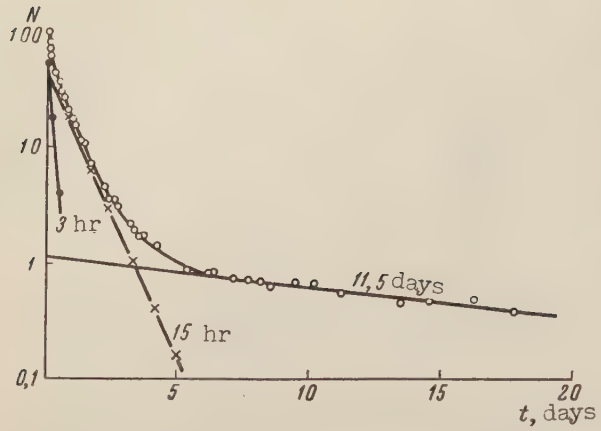

Fig.3. Decay of the daughter iridium activity.

The period of the platinum determined from the activity of the daughter iridium decaying with a period of 3 hours was found to be 2.6 ± 0.6 hours. According to Baranov et al[6] this period may be assigned to the new platinum isotope Pt^{184}.

"V.I.Vernadskii" Institute of Geochemistry and Analytic Chemistry of the Academy of Sciences of the USSR
& Scientific Research Institute of Nuclear Physics at Moscow State University

References

1. K.A.Kraus, F.Nelson & G.W.Smith, J.Phys.Chem., 58, 11 (1954).
2. S.S.Berman & W.A.E.McBryde, Canad. J.Chem., 36, 845 (1958).
3. S.S.Berman & W.A.E.McBryde, Canad.J.Chem., 36, 835 (1958).
4. D.D.Busch, G.M.Prospero & R.A.Nauman, Anal.Chem., 31, 884 (1959).
5. N.K.Pshenitsyn, K.A.Gladyshevskaya & L.M.Ryakhova, Zhur.neorg.khimii, (Jour. of Inorganic Chemistry), 2, 1057 (1957).
6. V.I.Baranov, K.Ya.Gromov, B.S.Dzhelepov, Zyong Chong Bai, T.V.Malysheva, V.A.Morozova, B.A.Khotin & V.G.Chumin, Present issue of the Bulletin, p.1086.
7. D.Strominger, J.M.Hollander & G.T.Seaborg, Revs.Mod.Phys., 30, 585 (1958).
8. Nuclear Data Sheets, 3, 119 (1959).
9. W.G.Smith & J.M.Hollander, Phys.Rev., 98, 1958 (1955).
10. R.M.Diamond & J.M.Hollander, Nucl.Phys., 8, 143 (1958).

NEUTRON-DEFICIENT ISOTOPES OF RARE EARTH ELEMENTS OF THE CERIUM GROUP (SPALLATION PRODUCTS OF EUROPIUM BOMBARDED WITH 660 Mev PROTONS)

- A.K.Lavrukhina, G.M.Kolesov & Tan Syao-en

From the standpoint of theory the justification for detailed investigation of neutron-deficient isotopes of the rare earth elements of the cerium group, which are of undoubted interest to nuclear spectroscopists, is that such investigations yield data on the cross sections for their formations in different nuclear reactions. Hitherto such isotopes have been obtained mainly from reactions with relatively low energy particles. In the range of high bombarding particle energies there is available information only on the yields of individual isotopes of the cerium group, for example, Ce^{134} and Ce^{135} produced by spallation of tantalum by 340 Mev protons[1] and Ce^{134}, Nd^{140} and Gd^{147} obtained by splitting of bismuth by 660 Mev protons[2]. Detailed information on the formation cross sections of rare earth isotopes in spallation of hafnium under bombardment with 660 Mev protons was obtained in the work of Ref.3. It was established that the yields of the cerium group isotopes are substantially smaller than the yields of isotopes of the heavier rare earth elements.

In view of this we felt it would be of interest to investigate the spallation products of europium and samarium, particularly since the process of spallation in this nuclear region has not been studied. Only the cross sections for the (p,pn) and (p,2p) reactions on Ce^{142} at proton energies from 0.4 to 3 Bev are known.[4]

Separation of the rare earth isotopes forming as a result of spallation of europium and samarium is hampered by difficulties connected primarily with the necessity of eliminating the bulk of the target material. We solved the separation problem by using the technique of electrolytic deposition on a mercury cathode. It was found that in electrolysis from acetate-citrate solutions 97-98% of the samarium enters the amalgam[9], while 98-99% of the spallation product elements remain in the solution.[6] We also investigated the composition of radioactive rare earth isotopes of the cerium group forming as a result of bombardment of samarium with protons of different energies and europium and neodymium with 660 Mev protons.[7]

In the present communication we give the results of our investigation of the cross section for formation of rare earth isotopes as a result of spallation of europium bombarded with 660 Mev protons.

Experimental procedure

Europium oxide (99.8% Eu_2O_3) targets weighing 2 to 5 mg were bombarded for 50 min in the internal 660 Mev proton beam of the Joint Institute for Nuclear Research synchrocyclotron. After chemical separation of the rare earth elements from the bulk of the target, they were separated into fractions in a 25 x 0.2 cm ion-exchange column filled with KPS-200 cationite in NH_4^+ form (grain size - 400 mesh). The isotopes were eluted with ammonium lactate, the concentration of which in the process of separation varied from 0.4 to 0.8 n. The eluate drops were collected on a moving tracing paper band, dried under a lamp and scanned with an MST-17 counter. The various fractions were identified from the position of the activity peaks on the chromatogram (Fig.1); the individual rare earth isotopes were identified from the decay periods and radiation energies (Table 1).

The yields of the β^+ and β^--active isotopes were calculated by the procedure described earlier in Ref.8; the yields of the electron capture isotopes were evaluated from the L radiation accompanying K capture[9]. The uncertainties in

Table 1

Characterization of the radioactive isotopes of rare earth elements forming as a result of spallation of europium*

Isotope	$T_{1/2}$	Formation cross section, mb		Isotope	$T_{1/2}$	Formation cross section, mb	
		From Eu	From Hf (Ref.3)			From Eu	From Hf (Ref.3)
$_{57}La^{131}$	60 min	—		Nd^{141}	3 hr	11	0,4 **
La^{132}	4,6 hr	4		$_{61}Pm^{141}$	30 min	73	19 **
La^{135}	19,7 »	2		Pm^{145}	18 day	1,5	
$_{58}Ce^{132}$	4,5 »	1		Pm^{148}	5,3 day	0,15	
Ce^{134}	72 »	13	5	Pm^{149}	50 hr	0,2	
Ce^{135}	22 »	10 **	2,5 **	Pm^{150}	3 »	0,08	
Ce^{133}	8 »	5,5 **		$_{62}Sm^{142}$	72 min	75	6 **
Ce^{137}		10 **	0,3	Sm^{145}	340 day	6,3 **	10 **
Ce^{139}	140 day	—	0,03	Sm^{153}	2 day	—	
$_{59}Pr^{134}$		0,7		$_{63}Eu^{144}$	15 min	53	2 **
Pr^{136}	70 min	14 **		Eu^{145}	5 day	28	8
Pr^{137}		23 **		Eu^{147}	39 »	15 **	30 **
Pr^{138}		15 **		Eu^{148}		11 **	
Pr^{139}	4,5 hr	5	0,6	Eu^{150}	15 hr	5	
Pr^{142}	16 hr	0,4	0,02	Eu^{152}	10 »	3	
Pr^{143}	13 day	0,1	0,007				
$_{60}Nd^{139}$	5,6 hr	72	17	$_{64}Gd^{147}$	36 »	—	12
Nd^{140}	3,3 day	28	4	Gd^{149}	9,3 day	—	2

*The data listed in the table are average values for three experiments.
**Interpolated data.

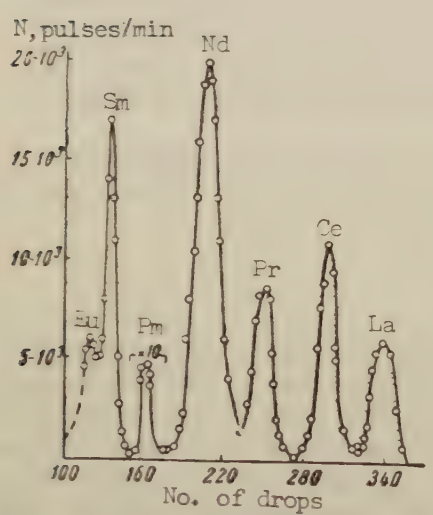

Fig.1. Chromatographic separation of the rare earth elements by ammonium lactate at pH = 5.8 and t = 86-90° (elution rate - 2 drops per min.).

evaluating the yields of these two groups are estimated to be 50 and ~100%, respectively.

The yield of Pr^{134} was calculated from the activities of the daughter Ce^{134}; the yield of Sm^{142} was evaluated on the assumption that the relative intensity of the positron decay branch is 10%. In determining the yields of Nd^{141}, La^{132}, Pr^{139} and Ce^{134} we took into account the contribution of neighboring isobars. In view of the fact that the neighboring isobars for the lightest isotopes - Ce^{132}, Pr^{134}, Pr^{136}, Nd^{139}, Nd^{140}, Sm^{142}, Eu^{144} and Eu^{145} - are not known, in evaluating the yields of these we could not allow for the effect of neighboring isobars. In determining the yields of Ce^{132}, Ce^{134}, Nd^{139}, Nd^{140}, Sm^{142} and Sm^{145} we took into account the contribution from the daughter isotopes.

The proton beam was monitored by measuring the Na^{24} activity of an aluminum foil. The $Al^{27}(p,3pn)Na^{24}$ reaction cross section was assumed to be 10 mb.

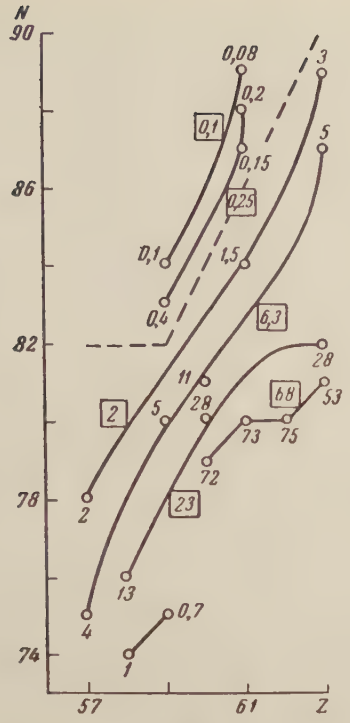

Fig.2

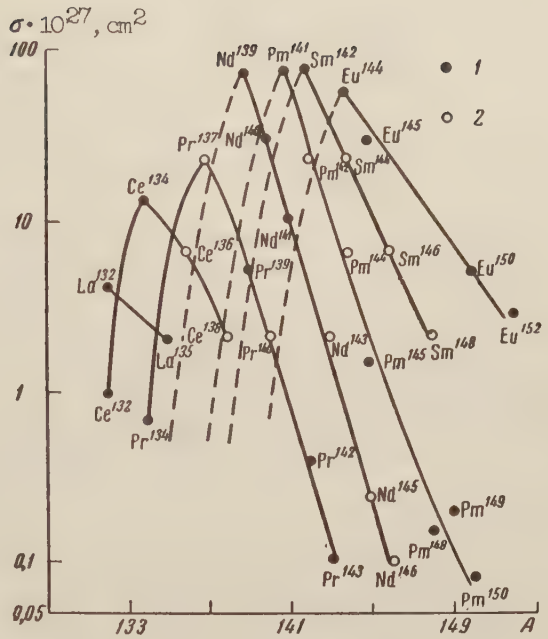

Fig.3

Fig.2. Yields of the radio-isotopes of rare earth elements forming as a result of spallation of europium. Dashed lines - line of nuclear stability. The figures at the points give the formation cross section for the isotope in millibarns; the figures at the curves represent the mean cross section for the given curve.

Fig.3. Mass number distribution of isotope yields: 1) experimental data, 2) interpolated data.

Discussion

A chart of the identified isotopes with independent yields is shown in Fig.2. In the chart isotopes with approximately the same formation cross section are connected by solid lines. The dash line represents the line of maximum nuclear stability. It will be evident that isotopes forming with a maximum yield lie in the region of neutron-deficient isotopes.

Fig.3 shows the distribution of isotope yields for each element according to mass number. A complete bell shaped curve was obtained only for cerium and praseodymium. For the other elements we obtained only the right-hand branch of the curves owing to the lack of information on isotopes with a large neutron deficit in this nuclear region. The isotopes characterized by maximum yield values are Ce^{134}, Pr^{137}, Nd^{139}, Pm^{141}, Sm^{142} and Eu^{144}. Obviously, in most cases these are the lightest known isotopes of the given elements. From the character of the distributions one can predict the yield of as yet unknown lighter isotopes. To this end we need merely draw the left hand branches of the bell shaped curves on the assumption that in each case the peaks have been attained and that the lighter isotopes will form with a smaller yield. The theoretical left-hand branches have been plotted (dashed lines) for neodymium, promethium, samarium and europium. These dashed curves show that isotopes of samarium, promethium and neodymium with mass number one or two units smaller than 142, 141 and 139, respectively, should be produced with relatively high yields (formation cross sections 40 to 10 mb).

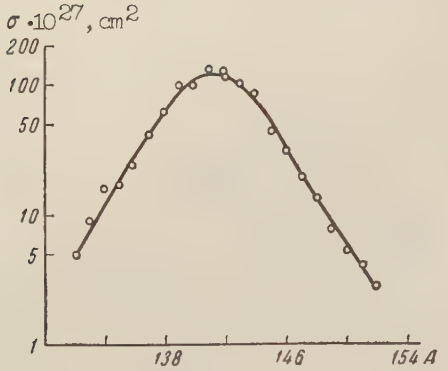

Fig.4. Variation of the cumulative yield of isobars with mass number.

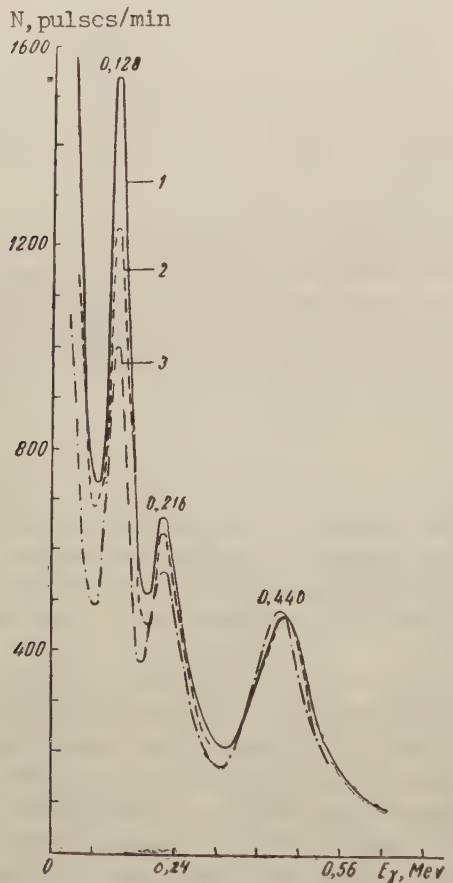

Fig.5. Gamma-spectrum of the daughter Ce fraction separated from Pr: 1 - first measurement, 2 - spectrum after 1 hr 25 min, 3 - after 3 hr 35 min.

Table 2

Abundances of rare earth isotopes in the earth's crust and in the end decay product of spallation of europium by 660 Mev protons

Element	Mass number	Isotope content, %	
		Earth's crust	Spallation product
1	2	3	4
Lanthanum	138	0,089	—
	139	99,911	100
Cerium	136	0,193	13,1
	138	0,25	34,7
	140	88,48	52,2
	142	11,07	—
Praseodymium	141	100	100
Neodymium	142	27,13	41,5
	143	12,2	31,9
	144	23,87	1,9
	145	8,3	14,4
	146	17,18	10,3
	148	5,72	—
	150	5,6	—
Samarium	144	3,16	62,8
	147	15,07	15,8
	148	11,27	10,9
	149	13,84	6,2
	150	7,47	4,3
	152	26,63	—
	154	22,53	—
Europium	151	47,77	100
	153	52,23	—

For praseodymium and cerium with A < 134 and 132, respectively, the cross sections for the formation of any new neutron-deficient isotopes should be < 1 mb.

The cerium group formation cross sections observed in spallation of europium by 660 Mev protons are substantially higher than the cross sections for the formation of these isotopes in spallation of hafnium. It will be evident from the data of Table 1 that the yield of Ce^{134} from europium is three times higher than the yield from hafnium, that of Ce^{137} is 30 times higher, that of Pr^{139} 8 times higher, of Nd^{139} 4 times, of Nd^{147} 7 times, of Pm^{141} 4 times, of Sm^{142} 12 times, and of Eu^{144} 25 times.

It will be evident therefore that bombardment of europium (or samarium) with 660 Mev protons is a more efficient procedure for producing neutron-deficient isotopes of the cerium group of rare earth elements than bombardment of hafnium, for example.

The variation of the cumulative yield of the different isobars as a function of their mass number is shown in Fig.4. It will be seen that the maximum yield obtained in the A = 137 to 145 region. The values of the cumulative yield for each A in this region amounts to 60-120 mb. These cumulative yield values can be utilized for determining the possibility of obtaining samples of relatively long lived isotopes suitable for spectroscopic studies.

The total cross section for the formation of rare earth isotopes in spallation of europium by 660 Mev protons equals 0.9 barns, which amounts to ~50% of the geometrical cross section.

Analysis of the experimental data shows that neutron-deficient isotopes account for 92% of the total yield of all rare earth element isotopes forming in the spallation of europium. The percentages of stable isotopes and neutron-rich isotopes are appreciably smaller: ~6 and 2%, respectively. Also of interest is the isotopic composition of the rare earth elements forming as a result of complete decay of all the radioactive spallation products. The abundances of the different stable isotopes in the end spallation-decay product together with data on the isotopic composition of the corresponding rare earths in the earth's crust are listed in Table 2.

It will be evident from the tabulated data that the isotopic composition of the rare earth elements in the earth's crust differs from the isotopic composition in the product of spallation of europium by 660 Mev protons. Lighter isotopes predominate in the spallation product. Of interest from the standpoint of elucidating the role of nuclear reactions of high energies in the formation of the chemical elements is the ratio of the abundances of Ce^{136} and Ce^{138}. It will be evident from the data of Table 2 that in the earth's crust the ratio of these cerium isotopes is 0.8, while in the europium spallation decay product, the ratio is 0.4. The magnitude of this abundance ratio may be expected to increase with increase of the bombarding proton energy. This fact merits attention, and further investigations employing higher proton energies may yield an answer to the question of at what proton energy the Ce^{136}:Ce^{138} abundance ratio will be the same as in the earth's crust. Thus it may be possible to evaluate the influence of nuclear reactions produced by cosmic rays on the isotopic composition of the earth.

New praseodymium isotope - Pr^{134}

In an earlier contribution[7] we reported the possible formation in the process of splitting of samarium by 660 Mev protons of a new praseodymium isotope, Pr^{134}.

To substantiate the existence of this isotope we carried out a series of experiments in collaboration with V.V.Malyshev; in these experiments, immediately after bombardment of the target, the cerium was separated in radiochemically pure form by extraction of $H_2[Ce(NO_3)_6]$ with ethyl ether from 8 n nitric acid.[10] The daughter cerium was separated five times at hourly intervals from the residual solution. All these fractions contained an activity with T = 72 hours, corresponding to Ce^{134}. Obviously, this isotope forms from Pr^{134}, the period of which is evaluated as ~1 hour from the Ce^{134} activity in the daughter fractions. The γ-spectrum of the daughter cerium after the first separation from the Pr fraction was recorded for us by Yu.A.Surkov and V.G.Karpushin on a 100-channel scintillation spectrometer (Fig.5). There were detected lines with energies of 0.128 ($T \approx 4$-5 hr), 0.216 ($T \approx 17$ hr) and 0.440 Mev.

"V.I.Vernadskii" Institute of Geochemistry and Analytic Chemistry
of the Academy of Sciences of the USSR

References

1. W.Nervik & G.T.Seaborg, Phys.Rev., 97, 1092 (1955).
2. A.V.Kalyamin, A.N.Murin, B.K.Preobrazhenskii & N.E.Titov, Atomnaya energiya, 4, 196 (1958). (Trans.Soviet Journal of Atomic Energy.)
3. A.K.Lavrukhina & A.A.Pozdnyakov, Ibid., 7, 332 (1959).
4. A.A.Caretto & G.Friedlander, Phys.Rev., 110, 1169 (1958).
5. A.K.Lavrukhina & G.M.Kolesov, Transactions of the Conference on Neutron-Deficient Isotopes of the Rare Earths, p.80, Dubna, 1959.
6. A.K.Lavrukhina, G.M.Kolesov & Tan Syao-en, Radiokhimiya (In press). (Trans.Radiokhimiya.)
7. A.K.Lavrukhina & G.M.Kolesov, Transactions of the Conference on Neutron-Deficient Isotopes of the Rare Earths, p.64, Dubna, 1959.
8. A.P.Vinogradov, I.P.Alimarin, V.I.Baranov, A.K.Lavrukhina and others, Session of the USSR Academy of Sciences on the Peaceful Uses of Atomic Energy (OKhN meeting), p.97, M., 1955.
9. T.V.Malysheva & I.P.Alimarin, Zhur.eksp.i teor.fiz., 35, 1103 (1958). (Trans.Soviet Physics - JETP.)
10. A.K.Lavrukhina & Chzhu Pei-tszi, Radiokhimiya (Radiochemistry), 1, 530 (1959).

INVESTIGATION OF THE NEUTRON-DEFICIENT ISOTOPES OF OSMIUM

- Yu.A.Surkov, G.M.Chernov, A.K.Lavrukhina & Z.V.Khromchenko

Investigation of the neutron-deficient isotopes of osmium is of undoubted interest in view of the paucity of experimental data on the decay schemes and structure of nuclei in the iridium-osmium-rhenium region. Particularly scanty are data on the neutron-deficient isotopes of these elements forming in nuclear reactions induced by high energy particles. In view of this the results of our investigation of the neutron-deficient isotopes of osmium obtained by proton bombardment of gold may not be without interest.

Procedure

The neutron-deficient isotopes were produced by 1-2 hours bombardment of a 0.2 g gold sample with 660 Mev protons in the Joint Institute for Nuclear Research synchrocyclotron. The iridium and osmium fractions were radiochemically separated from the irradiated gold, and then at definite intervals the daughter elements, daughter Os and daughter Re, were extracted from these fractions. The purity of the separated elements was checked by appropriate radiochemical procedures. The study was concerned primarily with the Os fraction; the other fractions were investigated to the extent necessary for clarifying the results obtained for the Os isotopes.

For analysis of the β- and γ-radiations of the nuclear reaction products we used a 100-channel scintillation spectrometer and appropriate β- and γ-counting equipment. The γ-spectrometer consisted of a detector (40 x 50 mm NaI(Tl) crystal coupled to an FEU-3 photomultiplier), a linear amplifier, a discriminator and an AI-100 type 100-channel pulse height analyzer. The relative half-width of the characteristic Cs^{137} γ-line recorded by the spectrometer did not exceed 9%. The decay periods were determined from the rate of decrease in the height of the individual peaks in the γ-spectrum and the decay of the integral activity of the separated fractions. The integral activities were measured either by means of a ~4π scintillation counter or by means of end-window β-counters with a solid angle $\leqslant 10\%$.

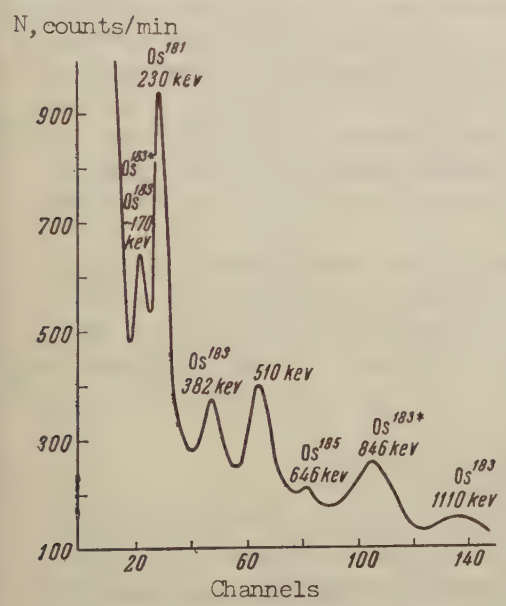

Fig.1. γ-Spectrum of Os isotopes forming as a result of bombardment of gold with 660 Mev protons. The 510 kev peak belongs to Os^{182}.

Investigation of Osmium Isotopes

The γ-spectrum of the osmium isotopes extracted from the proton bombarded gold is shown in Fig.1. On the basis of analysis of the energy distribution and the decay curves for individual γ-lines and the integral β- and γ-activities we identified the following isotopes: Os^{182} (T 20 hr, E_γ = 510 kev), Os^{183} (T $\approx$ 13 hr, E_γ = 168, 382 and 1110 kev), Os^{183m} (T $\approx$ 10 hr, E_γ = 171 and 846 kev) and Os^{185} (T $\approx$ 90 days, E_γ = 646 kev).

All the enumerated isotopes have a half-life $\gtrsim$10 hrs. However, in the γ-spectrum we observed an intense line at 230 kev which decayed with a period of ~2.7 hrs. No such short period γ-rays have hitherto been reported for any neutron-deficient osmium isotopes. Control experiments aimed at checking the purity of the osmium fraction showed that it was free of radioactive im-

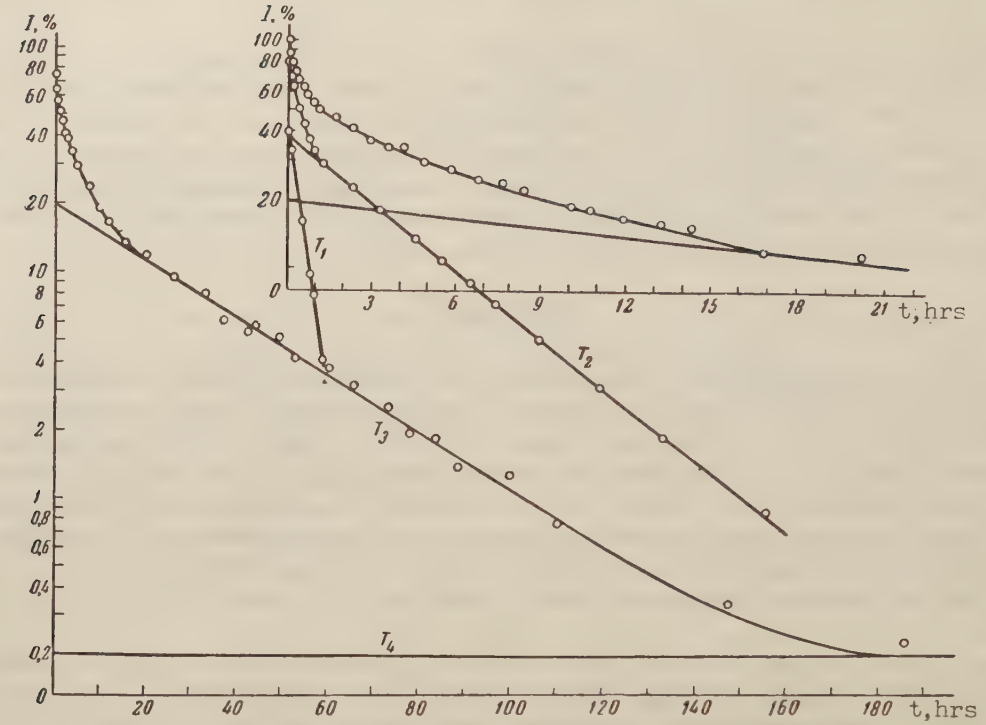

Fig.2. Decay curve for the Os isotope.

purities, which gave reason to infer the existence of a new osmium isotope with a period of about 3 hours. The existence of such an isotope was substantiated by our investigations of daughter Os and daughter Re (see below).

There was not evinced in our experimental spectrum the ~23 min activity (E_γ = = 170 kev) reported by Fester et al[1]. This is explained mainly by the fact that the spectrum was investigated approximately an hour after the end of bombardment when the remaining small fraction of this activity would be unnoticeable against the background of the γ-rays of approximately the same energy from Os^{182} and Os^{183} and the new intense 230 kev line. However, in the measurements of the integral activity of the osmium fraction, which were begun somewhat earlier, we succeeded in observing an activity with a period of ~23 min.

The decay curve obtained for the integral activity of the Os fraction, measured by means of an end-window counter, is shown in Fig.2. By resolution of this curve we obtained the following periods: $T_1 \approx 23$ min, $T_2 \approx 3$ hr, $T_3 \approx 20$ hr, (Os^{182} & Os^{183}) and $T_4 \approx 90$ days (Os^{185}). These results tend to substantiate our identification.

Investigation of the Daughter Osmium Isotopes

Fig.3 shows the γ-spectrum of the daughter Os built up over a period of 3 hours in the Ir fraction separated from the irradiated gold. It will be evident that some of the lines shown in Fig.1 also appear in this spectrum, although with different relative intensities. What is of interest, however, is not the similarity but the difference between these spectra. The new 230 kev line does not appear in Fig.3. The fact that this line is absent from the daughter Os spectrum indicates that if there is an Ir parent of the 2.7 hour Os isotope, it must have a very short period and a mass number probably smaller than 183. Also not evident

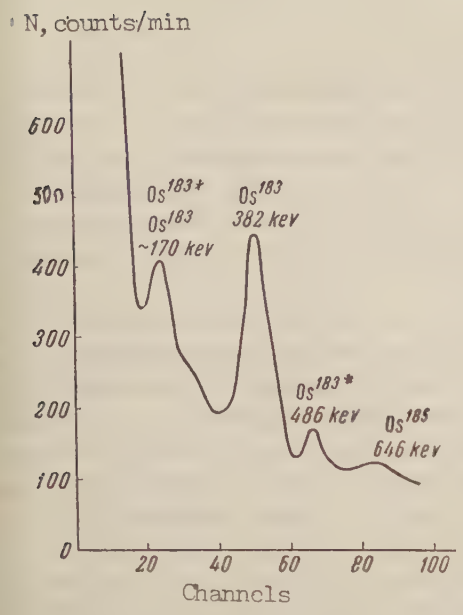

Fig.3. Gamma-spectrum of daughter Os isotopes forming as a result of decay of Ir obtained by 660 Mev proton bombardment of Au.

in the daughter Os spectrum is the line at 510 kev, belonging to Os^{182}, which gives ground for analogous inferences regarding the parent Ir^{182}.

The fact that there are present in the daughter Os spectrum γ-lines associated with Os^{183} and Os^{183m} indicates that there exists the as yet unknown iridium isotope, Ir^{183}, which decays to both the ground state and isomeric state of Os^{183}.

The integral activity decay curve for the daughter Os fraction is shown in Fig.4. Resolution of this curve brought out the following decay periods: $T_1 \approx 23$ min, $T_2 \approx 10$-13 hr (Os^{183} & Os^{183m}), and $T_3 \approx 90$ days (Os^{185}).

The 23 min activity was present in all the investigated daughter Os fractions. In view of this we made an attempt to determine the half-life of the corresponding parent Ir isotope. To this end we carried out repeated separations of the building up daughter Os with precise determination of the chemical yield. At present we have only preliminary data, which indicate that the Ir isotope from which the 23 min Os forms has a period of not less than 5 hours.

The lightest iridium isotope described in the literature[2] is Ir^{184}. From the above said it follows that there also probably exists Ir^{183}, and that there probably do not exist any lighter isotopes (Ir^{182} and Ir^{181}) with $T > 10$ min. In view of this, the mass number assignment - A = 181 - made by Fester et al[1] for the ~23 min Os isotope is mistaken.

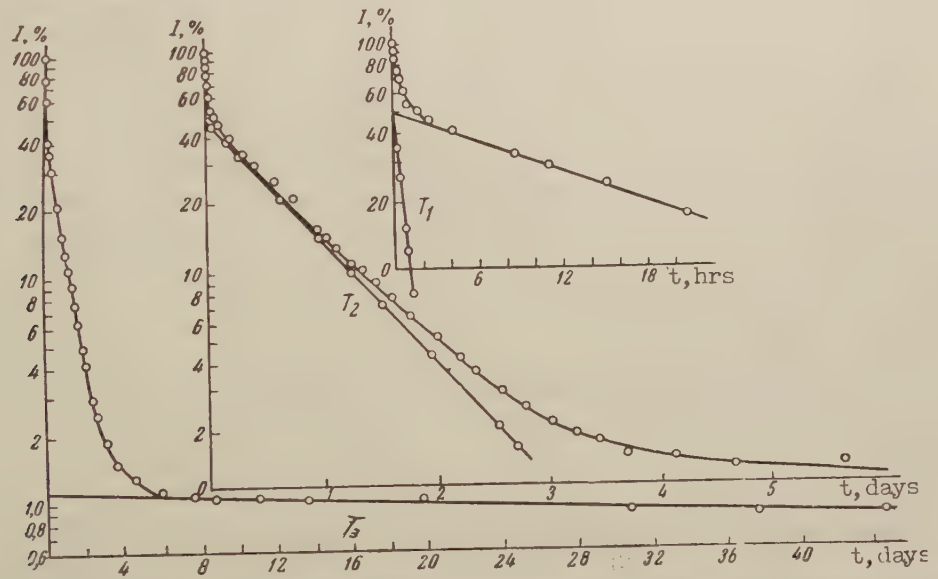

Fig.4. Integral activity decay curve for the daughter Os isotopes.

Investigation of the Daughter Rhenium Isotopes

The activity of the daughter rhenium building up in the Os fraction separated from the bombarded gold was investigated primarily for determining the mass

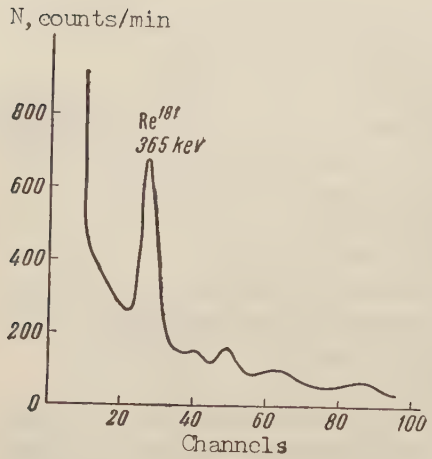

Fig.5. Gamma-spectrum of the daughter Re isotopes forming as a result of decay of the Os fraction obtained by 660 Mev bombardment of Au.

number of the new 2.7 hour osmium isotope.

Fig.5 shows the spectrum of the Re daughter isotopes extracted from the Os fraction. It will be evident that the activity corresponding to the shortest lived osmium isotope (we show the spectrum of the fraction in which there is obviously no decay product of 23 min Os), i.e., to the 2.7 hour Os, is Re^{181} ($T \approx 20$ hr, $E_\gamma = 365$ kev). Consequently, it may be inferred that the detected 2.7 hour activity belongs to Os^{181}.

Fig.6 shows the integral activity decay curve for daughter Re obtained by means of a scintillation counter. From the resolution of the curve it is apparent that almost the entire activity falls off with a period $T_1 \approx 20$ hr (Re^{181}), and that only an insignificant fraction belongs to a long-lived rhenium isotope, probably Re^{183} with a period $T_2 \approx$ ≈ 70 days.

To check this we carried out quantitative determinations of the daughter Re, which was separated at hourly intervals from the Os (in all we extracted six fractions). The measurements of the relative amount of Re^{181} were made by means of a γ-spectrometer with reference to the 365 kev line and also from determinations of the 20-hour activity calculated from the daughter Re decay curve. The data obtained indicate that the parent nucleus of Re^{181} actually does have a period of ~3 hr. Thus there is good reason to assume that the mass number of the new osmium isotope is 181.

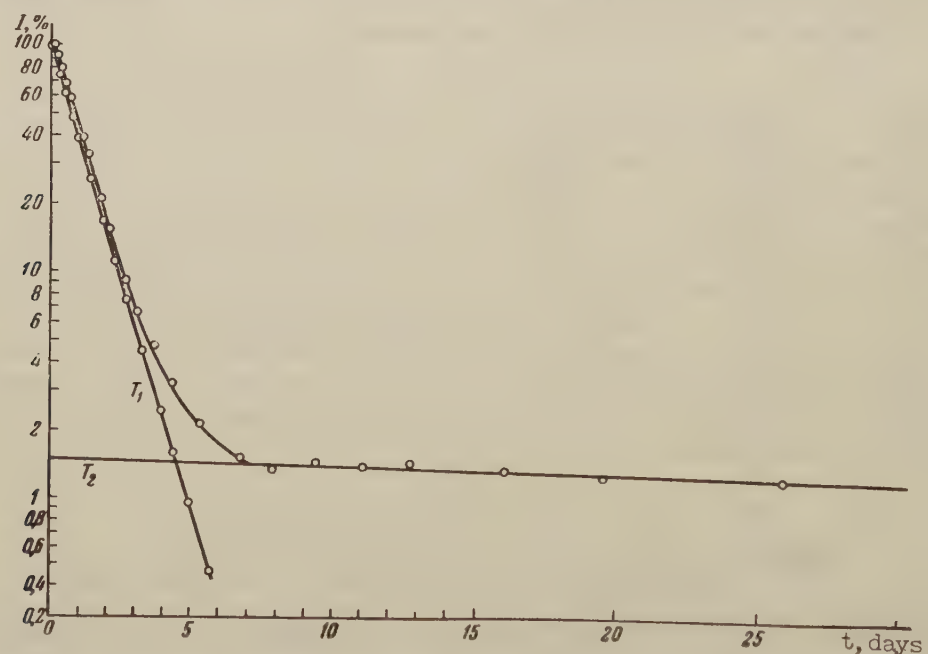

Fig.6. Integral activity decay curve for daughter Re isotopes.

Discussion

The data on neutron-deficient isotopes of Ir, Os and Re forming in nuclear reactions at high bombarding particle energies available at present are, unfortunately, extremely scanty. Hence some of the inferences drawn here, being based on unverified data, may be erroneous. However, the good agreement of our experimental results with those of Fester et al[1] may be taken as confirmation of our identifications of the neutron-deficient isotopes of osmium formed in proton bombardment of gold. As noted above, in our experiments the proton energy was 660 Mev, i.e., one order of magnitude higher than in the work of Fester et al[1] (10-80 Mev). We hoped, therefore, to obtain some new data, mainly on the lightest isotopes of osmium, the yield of which should presumably increase with the proton energy. The results of our experiments give reason to infer the existence of a new neutron-deficient osmium isotope, Os^{181}, forming in the process of bombardment with high energy particles. This isotope decays with a period of 2.7 hours, converting by orbital electron capture to Re^{181}. In the process there are emitted 230 kev γ-rays.

Our data also established the existence of Ir^{183}, which decays by electron capture with a period of several hours. In decaying, this iridium isotope forms both isomers of osmium, Os^{183} and Os^{183m}, the periods of which are 13 and 10 hours, respectively. The branching ratio to these states was not determined owing to the lack of adequate data on the decay schemes for the Os isotopes.

In our investigation we also observed the 23 min activity of osmium reported by Fester et al. Of particular interest is the presence of these 170 kev γ-rays in the radiation from the daughter osmium fraction. Our experimental results and the inferences drawn therefrom tend to substantiate the existence of such an osmium isotope; one cannot, however, make a reliable mass number assignment for it at present. It is not impossible that the 23 min isotope is actually an isomer of one of the osmium isotopes identified by us.

We desire to express our deep gratitude to V.I.Baranov for his constant interest in the work.

References

1. I.S.Fester, I.W.Hilborn & L.Yaffe, Canad.J.Phys., 36, 555 (1958).
2. T.V.Malysheva, B.A.Khotin, A.K.Lavrukhina, L.N.Kryukova & V.V.Murav'eva, Present issue of the Bulletin, p.1113.

BETA-GAMMA ANGULAR CORRELATION IN THE DECAY OF La^{140} AND Ce^{141}

- V.P.Rudakov

The theory of β-γ angular correlation has by now been fairly thoroughly developed.[1-4] It follows from the results of theoretical calculations that it is worthwhile analyzing the correlation only in the case of once forbidden β-transitions inasmuch as in the case of allowed transitions there is no correlation, while in the case of more strongly forbidden transitions interpretation of the results becomes too complicated.

In once forbidden β-transitions with $\Delta j = 0, 1$ the anisotropy coefficient a in the correlation function $W(\theta) = 1 + a\cos^2\theta$ depends on several of the β-transition matrix elements and, in addition, on the angular momenta of the nuclear levels between which the β-transition occurs, on the multipole order of the γ-radiation and on the energy of the β-particles. Obviously, owing to the fact that the anisotropy coefficient depends on a large number of matrix elements one can hardly expect to obtain information on the characteristics of the nuclear levels through analysis of β-γ angular correlation. It makes better sense to investigate correlation in γ-transitions between levels with known spins and parities and then to attempt to evaluate the matrix element ratios. However, in the case of once forbidden β-transitions with $\Delta j = 2$, i.e., in the case of unique β-transitions, the anisotropy coefficient no longer depends on the matrix elements and can be calculated theoretically. In this case investigation of β-γ angular correlation can yield additional information on the assignments for the nuclear levels.

In the present work we carried out measurements of the β-γ angular correlation in the decay of La^{140}, inasmuch as there are data indicating that the β-transition between the ground state of La^{140} and the first excited state of Ce^{140} is a unique transition ($4^- \rightarrow 2^+$).[5] The half-life of La^{140} is ~40 hours. The β-transition in question accounts for less than 10% of all the decays. The end-point energy of this β-spectrum is 2.2 Mev. The energy of the β-rays is 1.6 Mev. The end-point energy of the next lower energy partial spectrum is 1.7 Mev.

Our La^{140} was obtained by neutron irradiation of lanthanum oxide in a pile. The source was prepared in the form of a thin (0.5 mg/cm^2) layer of oxide on an aluminum foil (0.2 mg/cm^2). The measurements were carried out by means of the equipment described earlier[6]. We measured the differential angular correlation for a β-particle energy of 1.8 Mev. The gate of the γ-spectrometer analyzer was adjusted so as to detect γ-rays in the energy interval from 1.0 to 1.6 Mev. As a result of the measurements we obtained $a = 0.12 \pm 0.04$ (the indicated uncertainty is the statistical error). This value of the anisotropy coefficient is not in conflict with the result (0.13) obtained by Jensen[7] in measuring the integral β-γ angular correlation for La^{140} in the β-particle energy range from 1.7 to 2.2 Mev.

On the basis of the work of Dolginov[3] and Hauser[4] we calculated the anisotropy coefficient for a $4^- \xrightarrow{\beta} 2^+ \xrightarrow{\gamma} 0^+$ transition. For a β-particle energy of 1.8 Mev we obtained a value of 0.22 for the anisotropy coefficient.

It will be evident that the calculated and experimental values differ substantially. In the present case one can hardly expect a smoothing out of the correlation and reduction of the experimental value since high energy β- and γ-radiations were detected. Thus there is reason to question the 4- assignment for the ground state of La^{140}. If one assumes that the spin of the ground state of La^{140} is 3-, calculations for a $3^- \xrightarrow{\beta} 2^+ \xrightarrow{\gamma} 0^+$ transition show that the calculated value of the coefficient can be brought into agreement with the experimental value with a reasonable choice of the matrix element ratio values.

In the work of Ref.6 there were carried out measurements of the β-γ angular correlation in the decay of Ba^{139} for the purpose of determining the sign of the

β-interaction constants. The experimental values agreed with the theoretical ones found on the basis of the single particle nuclear model only for a negative value of the ratio of the vector and axial vector interaction constants. In the present work, for the same purpose, we carried out measurements of the correlation in the decay of Ce^{141}. Theoretical analysis of this case is more complicated than in the case of Ba^{139}, inasmuch as it is necessary to take into account five matrix element ratios, two of which remain unknown, arbitrary parameters. Analysis could be carried out by measuring the variation of the anisotropy coefficient as a function of the β-particle energy.

The period of Ce^{141} is 32.5 days. Approximately 75% of all the disintegrations are accounted for by the transition to the 145 kev level in Pr^{141}. The end-point energy of this β-spectrum is 430 kev. The energy of the γ-rays accompanying the β-decay is 145 kev. The β-γ transition of interest to us is characterized by $7/2^- \xrightarrow{\beta} 7/2^+ \xrightarrow{\gamma} 5/2^+$.[5]

The Ce^{141} was obtained by neutron irradiation of cerium oxide in a pile. The measurements were carried out one month after the irradiation, when all extraneous activities had virtually died out. The source was prepared in the form of a thin (0.1 mg/cm^2) oxide layer on aluminum foil. The measurements were carried out for a β-particle energy of 400 kev.

The γ-spectrometer detected γ-rays with a maximum energy of ~150 kev. On the basis of the experimental results we obtained $a = 0.006 \pm 0.020$ (the uncertainty is the statistical error). The absence of noticeable anisotropy precludes the possibility of theoretical analysis of this case.

References

1. A.Z.Dolginov, Zhur.eksp.i teor.fiz., 20, 636 (1950).
2. A.Z.Dolginov, Ibid., 22, 668 (1952).
3. A.Z.Dolginov & I.N.Toptygin, Izv.AN SSSR, Ser.fiz., 20, 1377 (1956). (Trans.Bulletin, 20, 1260.)
4. I.Hauser, Nuovo cimento, Suppl.N 1 (1957).
5. B.S.Dzhelepov & L.K.Peker, Skhemy raspada radioaktivnykh yader (Decay schemes of radioactive nuclei), M.-L., 1958.
6. N.A.Vlasoc & V.P.Rudakov, Zhur.eksp.i teor.fiz., 36, 24 (1959). (Trans. Soviet Physics - JETP.)
7. E.Jensen, NSA, 11, N 6 B (1957).

CONVERSION ELECTRON SPECTRUM OF THE DYSPROSIUM FRACTION FROM THE SPALLATION PRODUCTS OF TANTALUM

- A.A.Abdurazakov, K.Ya.Gromov, B.S.Dzhelepov & G.Ya.Umarov

The conversion electron spectra of dysprosium isotopes formed by spallation of tantalum bombarded with 600 Mev protons were investigated by means of a uniform field magnetic β-spectrograph. The source was prepared by evaporation of drops of the eluate obtained in the process of chromatographic separation of the rare earths; the backings were 0.2 x 8 mm aluminum foil strips 5 μ thick.

At present the following radioactive neutron-deficient isotopes of dysprosium are known: 134-day Dy^{159}, 8-hr Dy^{157}, 10-hr Dy^{155}, 13-hr Dy^{154}, 5-hr Dy^{153} and 2.3-hr Dy^{152}. There are also indications in the literature that there may exist dysprosium isotopes with $A < 153$ and a period shorter than half an hour. Such isotopes could not be observed in our experiments. Our experimental conditions were also unfavorable for observation of the conversion lines of Dy^{159}. Thus in the recorded spectra there could be evinced conversion lines emitted in the following radioactive series:

$$Dy^{157} \xrightarrow[K]{8\ hr} Tb^{157} \xrightarrow[K]{?} Gd^{157};$$

$$Dy^{155} \xrightarrow[K,\beta^+]{10\ hr} Tb^{155} \xrightarrow[K]{5.6\ day} Gd^{155};$$

$$Dy^{154} \xrightarrow[K]{13\ hr} Tb^{154} \xrightarrow[K]{18\ hr\ or\ 8\ hr} Gd^{154};$$

$$Dy^{153} \xrightarrow[K]{5\ hr} Tb^{153} \xrightarrow[K]{62\ hr} Gb^{153} \xrightarrow{236\ day} Eu^{153};$$

$$Dy^{152} \xrightarrow[K]{2.5\ hr} Tb^{152} \xrightarrow[K]{18\ hr} Gd^{152}.$$

The conversion electron energies were determined by means of calibration curves plotted for each spectrogram. For purposes of calibration we utilized the following lines: K-82.98, K- and L_I-326.6 (Dy^{157}), K- and L_I-227.0 and K--508.0 (Dy^{155}), K- and L_I-309.8, K-161.5, K-163.5 and K-180.4 (Tb^{155}), K-212.2 (Tb^{153}), and K- and L_I-344.3 (Tb^{152}). The energies of these conversion electrons had been determined with good accuracy in the work of Mihelich et al[1] and Andersson[3]. In all our experiments these lines had an appreciable intensity and where they occurred in the recorded energy interval were clearly evinced in the spectrogram. In analyzing our results we made only qualitative evaluations of the line intensities.

A series of tantalum targets were bombarded, the bombardment times being 15-20 min, 2 hours and 4 hours. In the case of the 4 hour bombardment, the chromatographic separation was performed 15-20 hours after the end of bombardment. In the case of the targets bombarded 15-20 min and 2 hours, the separation was carried out 2-2.5 hours after irradiation. This variation of the bombardment time and of the interval between the end of bombardment and separation enabled us to obtain sources with different isotopic compositions. This and primarily successive exposure of a series of photographic plates with appropriate exposure times enabled us in most cases to identify the isotopes responsible for the recorded lines. A section of the spectrogram obtained in one series of measurements is reproduced in Fig.1.

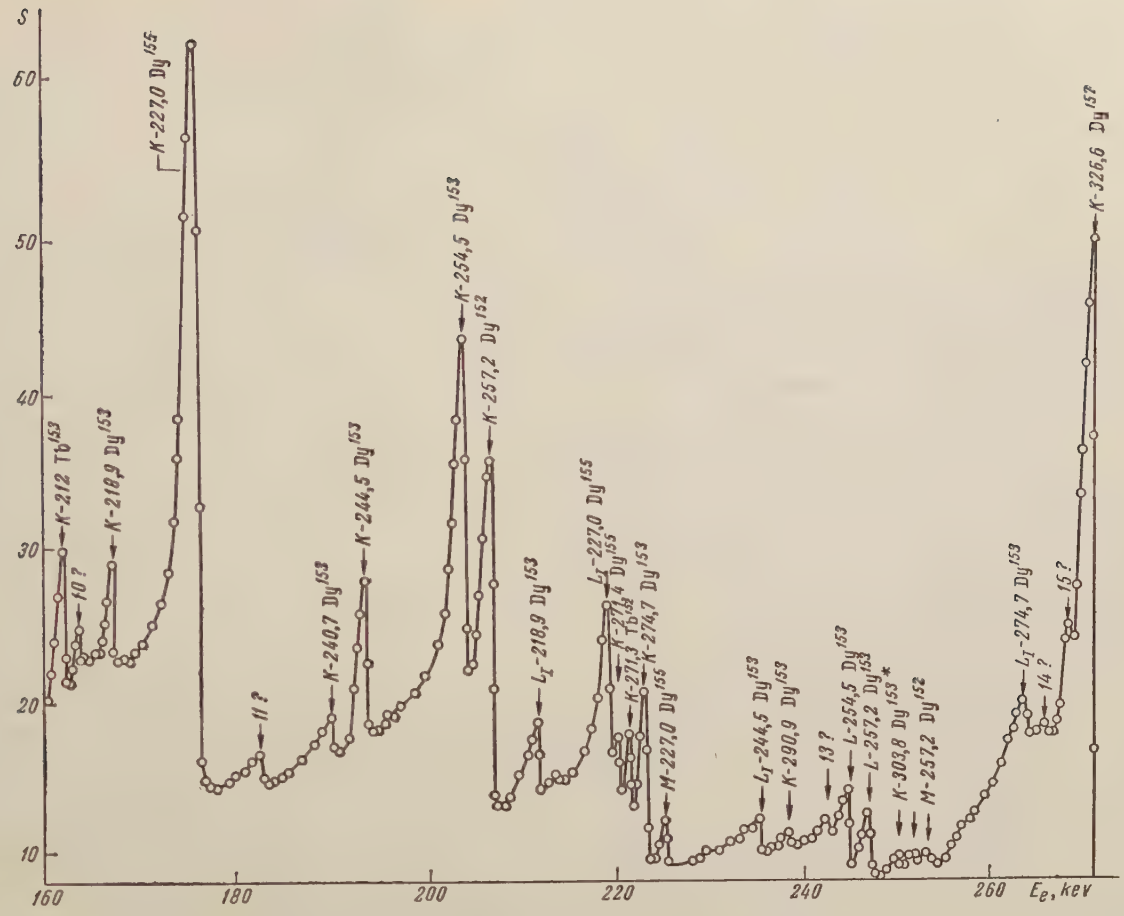

Fig.1. Section of conversion electron spectrum of the dysprosium fraction.

$$1.\ Dy^{157} \xrightarrow[K]{8.2\ hr} Tb^{157} \xrightarrow[K]{?} Gd^{157}$$

The conversion electron spectrum of Dy^{157} was investigated by Mihelich et al[1]. All the more intense lines of Dy^{157} detected by these authors were observed in our experiments as well.

$$2.\ Dy^{155} \xrightarrow[K,\beta+]{10\ hr} Tb^{155} \xrightarrow[K]{5.6\ day} Gd^{155}$$

The conversion electrons emitted in the decay of Dy^{155} were observed in the investigations of Toth & Rasmussen[2] and Dzhelepov et al[4,5]. In these investigations, however, the sources, in addition to Dy^{155}, contained Dy^{157}. Hence unambiguous identifications of the conversion lines were feasible only in the energy range to 300 kev for which there are available the data of Mihelich et al on Dy^{157}. The experimental data now available do not allow of determining to which of the isotopes, Dy^{155} or Dy^{157}, a given conversion line appearing in the energy range above ~300 kev spectrum of a mixed Dy^{155} + Dy^{157} source belongs. In Table 1, our experimental data on the conversion electron spectrum of Dy^{155} are compared with the results of Toth[2] and Dzhelepov et al[5]. The lines that are definitely known to belong to Dy^{157} have been omitted from the Table. There is reason to assume that all or at least most of the remaining (listed) lines belong to Dy^{155}. On the basis of analysis of the data of Table 1, one can draw the following deductions.

Table 1

Conversion electrons of Dy^{155} (T = 10 hr)

No.	Dzhelepov et al[5]		Toth & Rasmussen[2]		Our data			No.	Dzhelepov et al[5]		Toth & Rasmussen[2]		Our data		
	E_e, kev	Identif.	E_e, kev	Identif.	$H\rho$	E_e, kev	Identif.		E_e, kcv	Identif.	E_e, kev	Identif.	$H\rho$	E_e, kcv	Identif.
1	2	3	4	5	6	7	8	1	2	3	4	5	6	7	8
1	—	—	34,4	L_I-43,09	635,5	34,36	L_I-43,0	21	—	—	147,38	L_{II}-155,8	—	—	—
2	—	—	34,82	L_{II}-43,09	639,5	34,77	L_{II}-43,0	22	—	—	148,34	L_{III}-155,8	—	—	—
3	—	—	35,54	L_{III}-43,09	645,2	35,37	L_{III}-43,0	23	—	—	153,59	K-205,7	1417,0	153,48	K-205,5
4	—	—	36,02	K(?)-88,03	648,8	35,86	K-88,0	24	180	K-230	175,13	K-227,0	1527,5	175,13	K-227,0
5	—	—	38,29	K-90,38	671,2	38,18	K-90,4	25	—	—	197,12	L_I-205,7	—	—	—
6	—	—	41,51	M-43,09	698,6	41,24	M-43,0	26	—	—	218,30	L_I-227,0	1735,84	218,28	L_I-227,0
7	—	—	42,74	N-43,14	—	—	—	27	—	—	219,20	K-271,4	1740,2	219,20	K-271,2
8	—	—	56,70	L_I-65,43	825,0	56,71	L_I-65,4	28	—	—	225,02	M-227,0	1767,0	224,97	M-227,0
9	—	—	57,18	L_{II}-65,43	827,6	57,03	L_{II}-65,4	29	—	—	226,65	N-227,0	—	—	—
10	—	—	57,85	L_{III}-65,43	834,8	57,97	L_{III}-65,4	30	—	—	247,67	—	—	—	—
11	—	—	63,42	M-65,43	876,0	63,52	M-65,4	31	270	K-320*	262,84	L_I-271,4	—	—	—
12	—	—	65,13	N-65,43	—	—	—	32			266,02	—	—	—	—
13	—	—	79,31	L(?)-88,03	986,0	79,32	L_I-88,0	33	320	K-370	319,23	—	—	—	—
14	—	—	81,68	L_I-90,38	1002,0	81,74	L_I-90,4	34	400	K-450	381,22	—	2440,0	381,21	K-433,2
15	—	—	88,42	M-90,38	—	—	—	35			432,12	—	2644,0	431,98	K-484,0
16	—	—	90,04	N-90,38	—	—	—	36			446,14	—	2702,0	446,63	K-498,6
17	—	—	103,87	K-155,8	1140,2	103,76	K-155,76	37	465	K-515	455,95	—	2738,8	455,95	K-508,0
18	—	—	106,65	K-115,4	—	—	—	38	610	K-660	—	—	—	—	—
19	—	—	109,45	K-161,4	1173,8	109,43	K-161,43								
20	—	—	132,62	K-184,6	1306,2	132,76	K-184,76								

*In the measurements of Dzhelepov et al this line included the K-326.6 line of Dy^{157}.

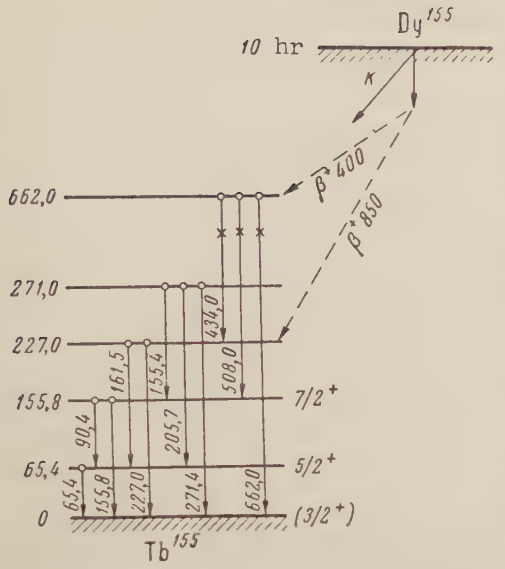

Fig.2. Decay scheme for Dy^{155}.

A. The measurements of Dzhelepov et al[5] in general correctly represent the character of the conversion electron spectrum, although the poor resolution of the instrument used by these investigators did not permit resolution of some of the lines.

B. Our results are in good agreement with the data of Toth & Rasmussen[2].

C. Toth & Rasmussen list but do not identify the conversion lines having energies of 381.2, 432.2, 446.4 and 455.8 kev. We feel there is no alternative to assuming that these are the K lines of transitions having energies of 434, 484, 498.6 and 508 kev, respectively.

The decay scheme for Dy^{155} proposed by Toth & Rasmussen[2] and Dzhelepov et al[5] is substantiated by the $e^- - e^-$ coincidence experiments of Dzhelepov & Sergienko[6]. On the basis of the data of Table 1 one can insert into this scheme a level at 662 kev (Fig.2). As for the positrons appearing in the decay of Dy^{155} and observed in the work of Dzhelepov et al[5] (the end-point energies of the β-spectrum components are 850 and 400 kev), the available data are inadequate to determine which levels of Tb^{155} are fed by the positron decay. It is possible, for example, that the positron decay of Dy^{155} populates the 662 and 227 kev levels of Tb^{155}.

Our data on the conversion electrons of Tb^{155} are in good agreement with the results of Mihelich et al[1].

$$3.\ Dy^{154} \xrightarrow[K]{13\ hr} Tb^{154} \xrightarrow[K]{18\ hr\ or\ 8\ hr} Gd^{154}$$

Alpha-decay of the dysprosium isotope with A = 154 was detected by Toth & Rasmussen[7]. There are no reports in the literature regarding the existence of a K capture branch in the decay of Dy^{154}. There is no reason, however, to doubt that it exists and has a substantial intensity. In our experiments K capture of Dy^{154} could be detected by observing the conversion lines associated with the 123.2 kev γ-transitions appearing in the decay of Tb^{154}. The results obtained by Mihelich et al[1] in investigating the conversion electron spectrum of Tb^{154} show that this is the most intense transition in the decay of this nuclide. We observed no traces of conversion lines associated with the 123.2 kev γ-transition in investigating the spectra of the Dy activities. The reasons for this are not clear: either the period of Dy^{154} as reported by Toth & Rasmussen[7] is incorrect, or the yield of Dy^{154} is much smaller than the yield of the neighboring isotopes.

$$4.\ Dy^{153} \xrightarrow[K]{5\ hr} Tb^{153} \xrightarrow[K]{62\ hr} Gd^{153} \xrightarrow{236\ day} Eu^{153}$$

Dy^{153} was first obtained by Toth & Rasmussen[7] by the $Gd^{152}(\alpha,3n)Dy^{153}$ reaction. These investigators established that the Dy^{153} emits ~3.3 Mev α-particles and that its period is 5 days.

The presence of Dy^{153} in dysprosium fractions obtained by spallation of tantalum has been established in the mass spectrometric measurements of Dobronravova et al[8]. In these experiments it was demonstrated that Tb^{153} forms in the decay of Dy^{153}. Thus it was proved that there exists a K capture branch in the decay of Dy^{153}. An 80 kev line was observed in the γ-spectrum of Dy^{153}. The existence

Table 2

Conversion electrons of Tb^{153} (T = 62 hr)

No.	Michelich et al[1]*			Toth & Rasmussen[2]**		Our data		
	E_e, kev	Intensity	Identification	E_e, kev	Identification	H_ρ	E_e, kev	Identification
1	2	3	4	5	6	7	8	9
1	17,87	45	K-68,1	—	—	—	—	—
2	33,11	450	L_I-41,5	33,28	L_I-41,68	622,0	32,95	L_I-41,4
3	33,56	360	L_{II}-41,5	—	—	627,0	33,47	L_{II}-41,4
4	34,25	400	L_{III}-41,5	34,40	L_{III}-41,68	634,0	34,20	L_{III}-41,4
5	37,26	180	K-87,4	37,44	K-87,61	661,5	37,13	K-87,4
6	—	—	—	39,82	M-41,68	—	—	—
7	—	—	—	41,33	N-41,68	—	—	—
8	43,31	75	L_I-51,7	43,45	L_I-51,84	—	—	—
9	43,76	10	L_{II}-51,7	—	—	—	—	—
10	44,45	10	L_{III}-51,7	—	—	—	—	—
11	49,9	25	M-51,7	—	—	—	—	—
12	51,87	145	K-102,1	52,03	K-102,3	787,0	51,82	K-102,1
13	59,57	1000	K-109,8	59,60	K-109,9	846,8	59,57	K-109,8
14	59,71		L_I-68,1	—	—	—	—	—
15	—	—	—	74,30	K-124,5	—	—	—
16	—	—	—	79,17	L_I-87,55	984,0	79,02	L_I-87,4
17	—	—	—	81,26	—	—	—	—
18	—	—	—	86,79	—	—	—	—
19	—	—	—	91,20	L_I-141,5	—	—	—
20	93,71	25	L_I-102,1	—	—	—	—	—
21	—	—	—	95,37	—	—	—	—
22	101,41	210	L_I-109,8	101,62	L_I-109,9	1126,3	101,46	L_I-109,8
23	109,4	10	N-109,8	—	—	—	—	—
24	—	—	—	120,42	K-170,6	1237,0	120,35	K-170,6
25	124,17	55	K-174,4	124,24	K-174,5	1258,6	124,17	K-174,4
26	107,9	55	M-109,8	—	—	1166,0	108,10	M-109,8
27	—	—	—	133,17	L_I-141,5	—	—	—
28	144,97	45	K-195,2	144,95	K-195,2	1372,2	144,97	K-195,2
29	161,97	195	K-212,2	162,23	K-212,3	1461,0	161,97	K-212,2
30	166,00	10	L_I-174,4	—	—	1482,0	166,10	L_I-174,4
31	186,81	10	L_I-195,2	—	—	—	—	—
32	199,57	60	K-249,8	199,43	K-249,7	1647,2	199,57	K-249,8
33	203,81	30	L_I-212,2	203,24	L_I-212,3	1667,65	203,84	L_I-212,2

---

*Only the γ-transitions are listed in the work of Mihelich et al[1]. The conversion electron energies listed in the table were calculated on the basis of Mihelich's data.

**Toth & Rasmussen[2] made only a qualitative evaluation of the line intensities; they merely divide the lines into a number of intensity classes.

of a K capture branch in the decay of Dy^{153} was substantiated in the work of Basina et al[9] and Dzhelepov & Zvol'skii[10] and in the present experiments. We, and Basina et al[9], observed conversion lines of Tb^{153} in the spectra of the dysprosium fraction, while Dzhelepov & Zvol'skii also observed increase in the intensity of these lines with time.

Our experimental results for the conversion electron spectrum of Tb^{153} are listed and compared with the results of Mihelich et al[1] and Toth & Rasmussen[2] in Table 2.

Table 3

Conversion electrons of Dy^{153} (T = 5-6 hr)

No.	$H\rho$	E_e, kev	Identification	No.	$H\rho$	E_e, kev	Identification
1	578,4	28,60	K-80,6	15	1377,6	146,00	M-147,8
2	596.0	30,33	K-82,3	16	1486,0	166,88	K-218,9
3	753,0	47,63	K-99,6	17	1594,7	188,72	K-240,7
4	935,0	71,9	L_I-80,6	18	1613,3	192,55	K-244,5
5	940,0	72,54	L_{II}-80,6	19	1661,3	202,52	K-254,5
6	947 0	73,62	L_I-82,3	20	1698,1	210,25	L_I-218,9
7	950,0	73,99	L_{II}-82,3	21	1756,5	222,71	K-274,4
8	954,0	74,58	L_{III}-82,3	22	1816,8	235,99	L_I-244,5
9	944,2	80,57	M-82,3	23	1863,8	246,0	L_I-254,5
10	1017,0	84,02	K-136,0 or L_I-92,8	24	1889,4	251,8	(K-303,8)
11	1062,5	91,13	L_I-99,6	25	1953,2	266,10	L_I-274,7
12	1091,0	95,69	K-147,8	26	2261,0	337,79	K-389,8
13	1247,0	122,12	K-174,1	27	2368,5	363,72	(K-415,7)
14	1340,6	139,08	M-147,8				

As will be evident from the table we did not detect a number of weak conversion lines observed by Mihelich et al: K- and L_I-68.1, L_I-, L_{II}-, L_{III}- and M-51.7, L_I-102.1, N-109.8 and L_I-195.2.

On the other hand, it is difficult to understand why Mihelich et al did not observe the L_I-87.4 and N-170.6 lines which were clearly evident in our measurements and in those of Toth & Rasmussen[2] and Anton'eva et al[11].

We attribute the conversion lines listed in Table 3 to $Dy^{153} \rightarrow Tb^{153}$. One can adduce the following arguments in favor of the assertion that these lines appear in the decay of Dy^{153}:

A. It is apparent from an examination of photographic plates exposed in succession for the same source that the period corresponding to the lines listed in Table 3 is close to the period of Dy^{153} and Dy^{155}. One cannot attribute these lines to Dy^{157} or Dy^{155} inasmuch as none of these lines was observed by the authors of Refs.1 and 2, while we, in turn, did not observe the weak lines of Dy^{157} and Dy^{155} detected by these authors.

B. Among the conversion lines in Table 3 there are lines associated with 80.6 and 82.3 kev transitions. As was noted above, Dobronravova et al[8] observed γ-rays of 80 kev energy in the spectrum of Dy^{153}.

C. Basina et al[9] report that the period corresponding to the conversion electrons from the 244 and 255 kev γ-transitions is 5-6 hours.

D. Dzhelepov & Zvol'skii[10] established that the period corresponding to the decay in intensity of the conversion electron lines associated with the 80.8, 82.5 and 99.7 kev γ-transitions is somewhat shorter than the period of Dy^{157}. They evaluated this period as 6-7 hours (from the decay in intensity of the 80.8, 82.5 and 99.7 kev conversion lines).

In view of the above we believe that in the decay of Dy^{153} there occur γ-transitions with energies 80.6, 82.3, 99.6, 147.8, 174.1, 218.9, 240.7, 244.5, 254.5, 274.4 and 389.8 kev. Possibly transitions with energies of 92.8 (or 136.0), 303.8 and 415.7 kev also occur in the decay of this isotope.

No conversion electrons associated with the decay of Gd^{153} to Eu^{153} were detected in our experiments.

5. $Dy^{152} \xrightarrow[K]{2.5\ hr} Tb^{152} \xrightarrow[K,\beta^+]{18\ hr} Eu^{152}$

In 1958 Toth & Rasmussen[7] obtained a new dysprosium isotope, Dy^{152}, by the $Gd^{152}(\alpha,4n)Dy^{152}$ reaction. They found that Dy^{152} emits ~3.5 Mev α-particles and

Table 4

Results of investigation of the conversion electron spectra of 2.3 hr Dy^{152} and 18 hr Tb^{152}

No.	$H\rho$	E_e, kev	Identification
Dy^{152} — 2.3 hours → Tb^{152}			
1	1674,0	205,18	K-257,2
2	1875,0	243,60	L_I-257,2
3	1904,6	255,2	M-257,2
Tb^{152} — 18 hours → Gd^{152}			
1	1327,8	136,70	(K-186,9)
2	1749,0	221,10	K-271,3
3	2075,45	294,07	K-344,3
4	2253,85	335,91	L_I-344,3
5	2357,6	361,07	K-441,3
6	2444,5	382,31	K-432,5
7	3057,0	538,16	K-588,4
8	3162,9	566,00	K-616,2
9	3320,4	607,8	L_I-616,2

that its half-life is 2.5 hours.

The presence of Dy^{152} in the dysprosium fraction obtained by spallation of tantalum was established by Bonch-Osmolovskaya et al[12], Basina et al[9] and in our experiments.

The results of our investigation of the conversion electrons from Dy^{152} and Tb^{152} are shown in Table 4.

The variation in intensity of the lines associated with the 271.3, 344.3, 411.3, 432.5, 588.4 and 616.2 kev γ-transitions in the successively exposed plates gives reason to assert that these γ-transitions arise in the decay of the daughter Tb. We cannot attribute these lines to Tb^{155} or Tb^{153} inasmuch as none of these lines was observed by the authors of Refs.1 and 2. Moreover, none of the lines listed in Table 4 was observed by us in the experiments carried out with the fraction obtained by prolonged bombardment (4 hours bombardment, chromatographic separation 15-20 hours after bombardment).

On the other hand, 1) it is known that a 344.3 kev γ-transition occurs in Gd^{152} (Andersson[3]) and 2) Basina et al[9] observed build-up in the intensity of the conversion lines associated with 344, 432, 586 and 615 kev transitions.

Thus of the known terbium isotopes that might be present in the dysprosium fraction, there remains only Tb^{152}.

Hence it may be safely asserted that the γ-transitions with energies 271.3, 344.3, 411.3, 432.5, 588.4 and 616.2 kev occur in the decay of Tb^{152}. Possibly a transition of 186.9 kev energy is also involved in the decay of Tb^{152}. All the listed γ-transitions except the last were observed in the work of Anton'eva et al[11]; however, these investigators erroneously attributed the transitions to Tb^{151} or Tb^{154}.

As arguments that the 257.2 kev transition occurs in the decay of 2.3 hr Dy^{152} one can adduce the following facts: first, this transition is observed only when the chromatographic separation is carried out immediately after proton bombardment, and, second, from a comparison of the blackenings in successively exposed plates it is evident that the period corresponding to the 257.2 kev transition is shorter than the period (5-6 hr[9]) for the lines associated with the 254.7 kev transaction.

Table 5

Unidentified conversion lines

No.	$H\rho$	E_e, kev	No.	$H\rho$	E_e, kev
1	782,0	51,2	9	1441,0	158,1
2	930,8	71,20	10	1470,5	163,84
3	937,0	72,10	11	1560,2	181,70
4	1100,2	97,18	12	1763,0	224,11
5	1105,0	97,96	13	1853,8	243,9
6	1349,0	140,64	14	1979,0	269,28
7	1388,0	147,96	15	1979,0	271,95
8	1415,0	153,1			

In Table 5 we list the conversion electron lines that we observed in our experiments but were unable to identify. Lines Nos.2,3,9 and 12 probably appear in the decay of Dy or Tb isotopes with T > 15 hr. The other lines presumably belong to Dy^{152} or Dy^{153} (more probably the latter).

Thus as a result of investigation of the spectrum of the dysprosium fraction in the energy range from 25 to 1000 kev:

1) we substantiated the data of other authors on the conversion electron spectra of Dy^{157} (T = 8.2 hr), Dy^{155} (T = 10 hr), Tb^{155} (T = 5.6 hr), and Tb^{153} (T = 62 hr). We obtained evidence for a new level with an energy of 662.0 kev in Tb^{155};

2) we substantiated the existence of a K capture branch in the decay of Dy^{153}.

We obtained the following more accurate values for the energy of the γ-transitions in this isotope: 80.6, 82.3, 99.6, 244.5, 254.5 and 147.8 kev and detected new γ-rays with energies of 174.1, 218.9, 240.7, 274.4, 303.8, 389.8 and 415.7 kev;

3) we established the existence of Dy^{152} in the dysprosium fraction obtained by fast proton bombardment of tantalum. We discovered a new 257.2 kev γ-transition occurring in the decay of Dy^{152} and thus proved the existence of a K capture branch in the decay of Dy^{152};

4) we obtained more accurate values for the γ-rays emitted in the decay of Tb^{152}: 411.3, 271.3, 432.5, 588.4 and 616.2 kev, and discovered a new γ-transition with an energy of 186.9 kev.

We desire to express our deep gratitude to I.A.Yutlandov, S.Khainatskii, V.A.Khalkin and Yu.V.Norseev for carrying out the chemical separations, I.Zvol'skii and A.S.Basina for making available their experimental results on the dysprosium fraction prior to publication and for valuable discussions and to F.M. Abdurazakova for assistance in carrying out the measurements and processing the results.

Central Asian Polytechnic Institute
Joint Institute for Nuclear Research

References

1. J.O.Mihelich, B.Harmatz & T.H.Handley, Phys.Rev., 108, 989 (1957).
2. K.S.Toth & J.O.Rasmussen, Ibid., 115, 150 (1959).
3. B.Andersson, Proc.Roy.Soc., A, (London), 69, 415 (1956).
4. B.S.Dzhelepov, B.K.Preobrazhenskii, I.M.Rogachev & P.A.Tishkin, Izv.AN SSSR, Ser.fiz., 22, 126 (1958). (Trans.Bulletin, 22, 125.)
5. B.S.Dzhelepov, O.E.Kraft, B.K.Preobrazhenskii & G.F.Yushkevich, Ibid., 22, 208 (1958). (Trans.Bulletin, 22, 205.)
6. B.S.Dzhelepov & V.A.Sergienko, Program of the Tenth All-Union Conference on Nuclear Spectroscopy, M., 1960.
7. K.S.Toth & J.S.Rasmussen, Phys.Rev., 109, 121 (1958).
8. A.N.Dobronravova, L.N.Krizhenskii, A.N.Murin & V.N.Pokrovskii, Izv.AN SSSR, Ser.fiz., 22, 815 (1958). (Trans.Bulletin, 22, 809.)
9. A.S.Basina, K.Ya.Gromov & B.S.Dzhelepov. Program of the Tenth All-Union Conference on Nuclear Spectroscopy, Moscow, Jan.1960. (Trans.Bulletin, Vol.24, 813.)
10. B.S.Dzhelepov & I.Zvol'skii, Ibid.
11. N.M.Anton'eva, A.A.Bashilov, B.S.Dzhelepov & B.K.Preobrazhenskii, Doklady AN SSSR, 19, 241 (1958). (Trans.Soviet Physics - Doklady.)
12. N.A.Bonch-Osmolovskaya, B.S.Dzhelepov & O.E.Kraft, Program of the Tenth All-Union Conference on Nuclear Spectroscopy, M., 1960. (Trans.Bulletin, 24, 270.)

DISINTEGRATION OF Nd^{140} AND Pr^{140}

- E.I.Biryukov, O.I.Grigor'ev, B.S.Kuznetsov & N.S.Shimanskaya

1. In the neodymium fraction separated from a tantalum target bombarded with 660 Mev protons there is observed approximately one day after separation virtually one activity with a period of ~3.3 days. This activity can be attributed to neodymium 140, which by pure electron capture converts to Pr^{140}. Pr^{140}, in turn, decays to stable Ce^{140}. In view of the short lifetime of Pr^{140} (~3 min) in working with any Nd^{140} sample we are necessarily dealing with an equilibrium mixture of Nd^{140} + Pr^{140}.

The results of various studies of the radiations from Nd^{140} + Pr^{140}, including ours, are summarized in Table 1.

It will be evident from an examination of the Table that the information on the radiation from these isotopes is far from complete and that the data of different investigators even on the relative intensities of the integral K x- and β-radiations conflict. Some results, as for example the data of Wilkinson & Hicks[1] obtained by the method of absorption disagree significantly with the data of other authors. The decay scheme for Nd^{140} is not known and the energy of the $Nd^{140} \rightarrow Pr^{140}$ transition has not been determined.

Inasmuch as, as will be shown below, precise data on the intensity of the L x-, K x- and β^+-radiations of the equilibrium Nd^{140} + Pr^{140} mixture make it possible to calculate the distribution between the decay branches for Nd^{140} and Pr^{140}, we felt it would be of interest to measure the intensities of the β^+-, γ- and x-radiations, including the L x-radiation, which hitherto had not been investigated.

2. The Nd^{140} + Pr^{140} equilibrium mixture used in the present experiments, like the source employed in the work of the Dzhelepov group[3-5], was obtained by separation from a tantalum target bombarded with 660 Mev protons in the Joint Institute for Nuclear Research synchrocyclotron. In the neodymium fraction obtained by chromatographic separation, in addition to 3-day Nd^{140}, there was at first present a minor admixture of shorter lived activity with a period of a few hours. This activity was presumably due to 5.5 hr Nd^{139}. Thus upon second separation of the Nd fraction in an ion exchange column, in the Pr fraction there was observed an activity with a period of ~4.7 hours obviously due to Pr^{139}. Hence all subsequent measurements were undertaken after the passage of not less than 40-50 hours after the chemical separation, usually after double ion-exchange separation.

The Nd^{140} + Pr^{140} radiation was investigated by means of a γ-spectrometer with a proportional counter (soft L and K x-radiation) and a scintillation spectrometer with an NaI(Tl) crystal (K x- and γ-radiation).

The experimental set-up with the proportional counter was essentially the same as that described earlier in Ref.6. For some of the measurements, however, we used a new proportional counter of somewhat different design, which provided for continuous purification of the working mixture. This substantially enhanced the resultion of the instrument. Moreover, this counter had provision for evacuating the airspace between the source and the ~30 mg/cm^2 entrance window.

The experimental x-radiation spectra of the equilibrium Nd^{140} + Pr^{140} mixture, recorded by means of the proportional counter are reporduced in Figs.1 and 2. There are clearly evident in the spectra L- and K x-radiation peaks with energies close to those of the $L\alpha_1$ and $K\alpha_1$ lines of Pr and Ce. The minor peak in the region of 40 kev is connected with the $K\beta'$ lines of Pr and Ce.

For the K x-radiation measurements there was installed between the source and the entrance window of the counter a beryllium absorber, the thickness of

Table 1

Nd^{140} + Pr^{140} Radiations

Investigation	Observed radiation	β^+ end point, Mev	Intensity								
			LX	KX		β^+	Auger β^+	Conver. electron		γ-1200	γ-1596
				Pr	Ce			(L+K)-1596	(L+K)-1902	γ-510	
Wilkinson & Hicks[1]	K, β^+, γ-510, γ-1200	2,4 -2,5	—	5,0 (3,3)		1,0	—	—	—	1,0	$5 \cdot 10^{-2}$	—
Browne, Rasmussen et al[2] Gorodinskii et al[3]	$K_{\alpha_{1,2}}$, K_{β_1} (Pr & Cl), β^+, γ-510	2,23±0,02	—	2,23	1,07	1,0	—	—	—	—	—	—
	K, γ-110, γ-190, γ-(200÷320), γ-500, γ-510	—	—	—		—	—	—	—	—	—	—
Gromov, Dzhelepov et al[4]	Auger $K - 2L$, $K - LM$; β^+	2,47	—	(1,47)		1,0	0,18	—	—	—	—	—
Dzhelepov et al[5]	β^+, e^--1596, e^--1902	2,38±0,01	—	—		1,0	—	$1,4 \cdot 10^{-5}$	$2,1 \cdot 10^{-3}$	—	—	—
Our data	L, K, β^+, γ-510, γ-1596	—	0,27	2,1		1,0	—	—	—	2,0	—	$8 \cdot 10^{-3}$

which (~1150 mg) was sufficient to absorb virtually all the β-particles from the source. In some of the measurements this elimination of the electrons was realized by means of a magnet producing a 4000 oe field in the gap between the source and counter.

The relative intensities of the L and K radiations, i.e., the I_L/I_K intensity ratio, was determined on the basis of the corrected ratio S_L/S_K of the areas under the L and K peaks. In evaluating the intensity ratio we took into account the efficiencies f_L and f_K of the counter in detecting the L and K x-rays. These efficiencies were determined by means of the formulas of Bisi & Zappa[7] on the basis of the known x-ray absorption coefficients for argon and the geometry of the experiment. In the case of the measurements for which there was an air filled gap between the source and counter window, we introduced a correction f' for absorption of the x-rays in air, which for the L radiation was appreciable. The experimental value found for f'_L was 20%, which was in good agreement with the theoretically calculated value of 19.2%. For the K x-radiation of Nd and Pr the corresponding correction was of the order of 0.5%.

In all, we carried out five series of measurements of I_L/I_K for the equilibrium Nd^{140} + + Pr^{140} mixture. Each series comprised three to seven measurements of this ratio. The average values for S_L/S_K and I_L/I_K are listed in Table 2. It will be seen that our mean value for I_L/I_K is 0.13 with an uncertainty of 25%, according to our evaluation.

We determined the ratio between the K x-radiation and β^+-particle intensities by means of the scintillation spectrometer. The cover of the aluminum container over the upper part of the NaI(Tl) crystal was removed and the surface of the crystal was covered with a 4 mg/cm^2 polyethylene film and a ~1.5 mg/cm^2 aluminum foil. The source was mounted at a distance of 6 cm from the crystal and its radiation was collimated so that the cross section of the radiation beam in the central plane of the crystal would be 2 cm in diameter. In measuring the K x-radiation we introduced a correction for the escape peak due to iodine x-rays from the crystal. According to the data of Axel[9] this correction at an energy of 35 kev should be 26%. The efficiency of the crystal was determined by means of the formula deduced by the method of

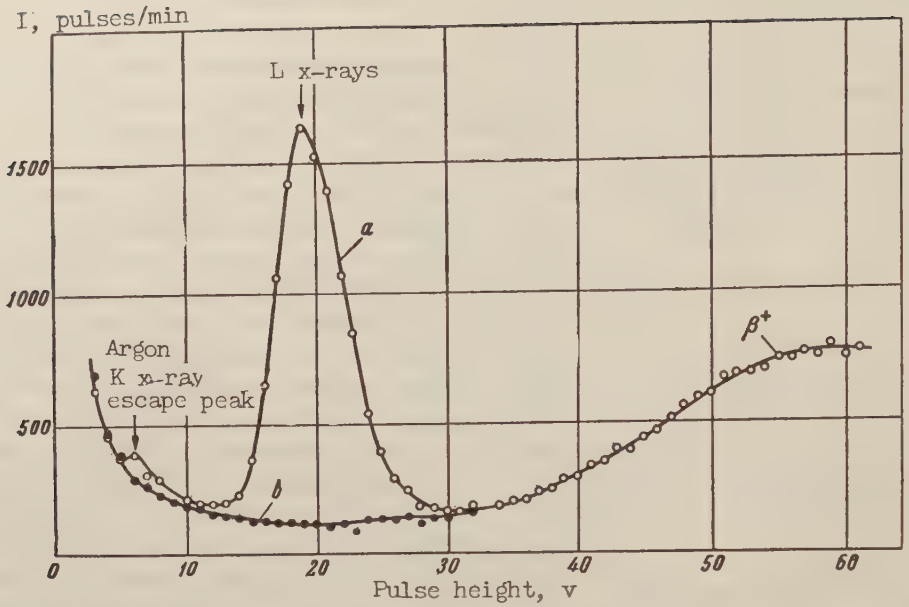

Fig.1. Experimental L x-ray spectrum of Nd^{140} + Pr^{140} recorded by means of the proportional counter: a) without absorber, b) with 26 mg/cm² absorber.

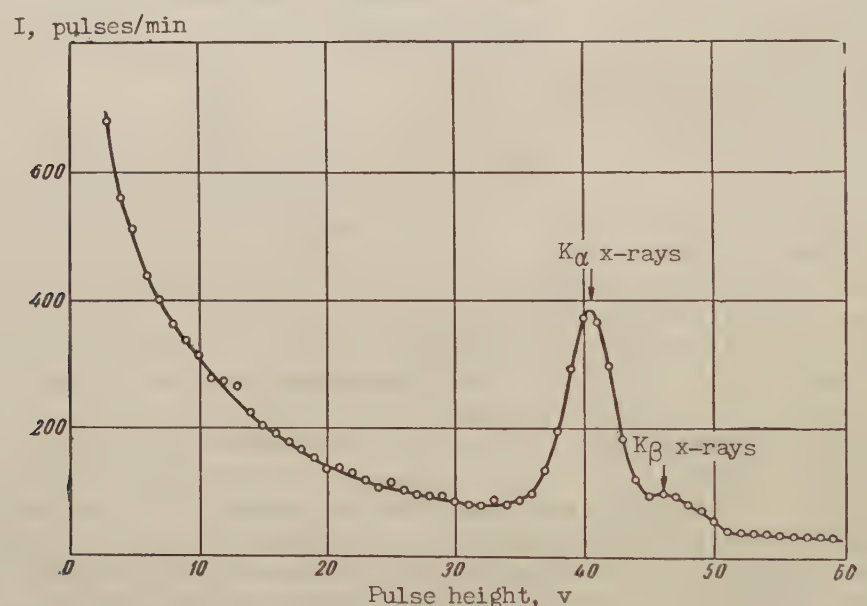

Fig.2. Experimental K x-ray spectrum of Nd^{140} + Pr^{140} recorded with the proportional counter.

Average experimental values of the ratios I_L/I_K and $I_K/I_{\beta+}$ — **Table 2**

S_L/S_K	f_L	$f_{L'}$	f_K	I_L/I_K	$2S_K/S_{\gamma\text{-}510}$	f'_K	$f_{\gamma\text{-}510}$	$I_K/I_{\beta+}$
3,3±0,3	$7{,}14\cdot10^{-3}$	0,80	$22{,}7\cdot10^{-5}$	0,13±0,03	9,9±0,5	0,622	0,132	2,1±0,2

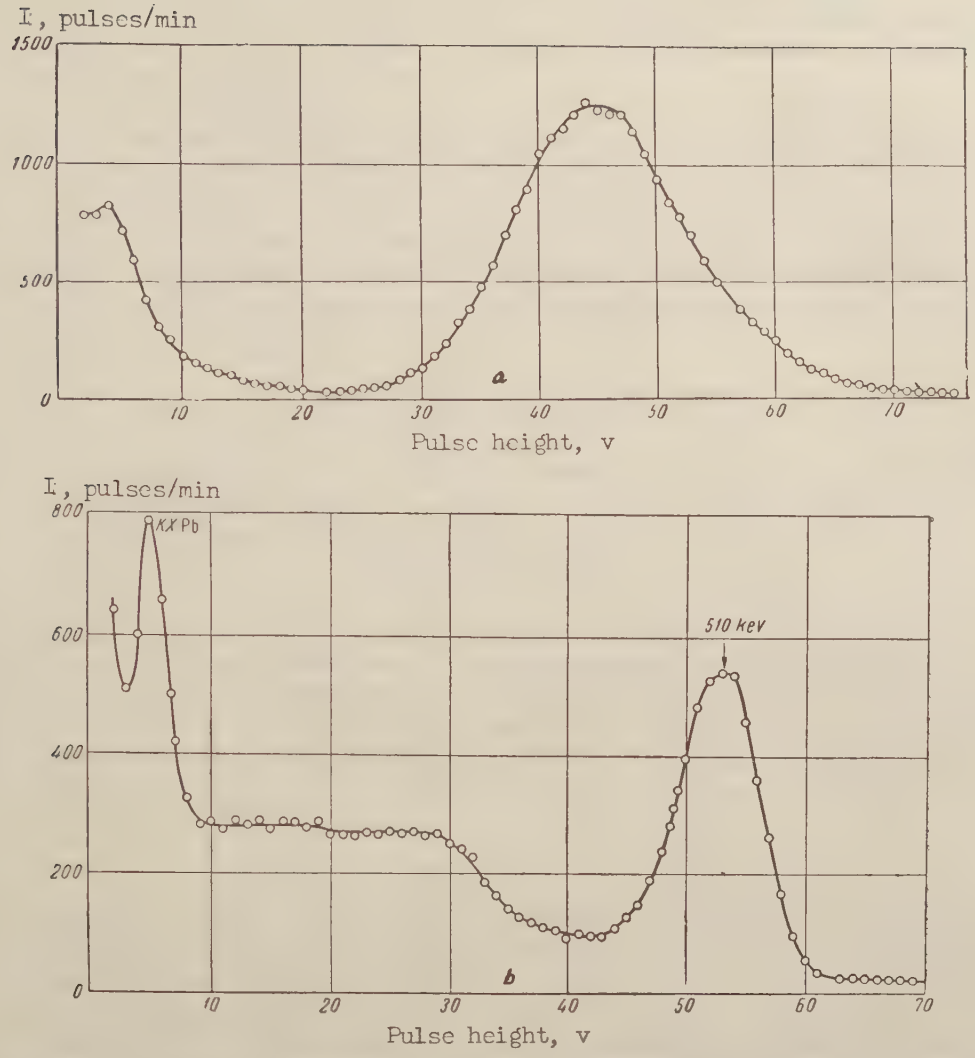

Fig.3. Radiation spectra of Nd^{140} + Pr^{140} recorded on the scintillation spectrometer with an NaI(Tl) crystal: a) K x-radiation, b) annihilation radiation.

Maeder et al[10]. This efficiency curve was checked in a wide energy range by means of sources calibrated beforehand with a 4π counter.

One of the experimental K x- and γ-radiation spectra in the energy region to 650 kev is shown in Fig.3. Aside from the intense K x-radiation peak, there is evident in this region only a peak in the vicinity of 510 kev due to annihilation radiation. The intensity of the positron emission was determined on the basis of the area of this annihilation peak. In determining it, in addition to the efficiency of the crystal in detecting photons of this energy, we took into account the absorption of the annihilation radiation in the 1700 mg/cm^2 lead absorber located near the source.

The absolute intensity of the β^+-radiation was also measured by means of a calibrated counting set-up with an end-window counter. In these experiments the positrons could be deflected by a magnetic field or absorbed by a beryllium absorber. This enabled us to determine the correction connected with the efficiency of the counter in detecting the L and K radiation in determining $I_{\beta+}$.

As a result of measurements of the intensity of the annihilation radiation

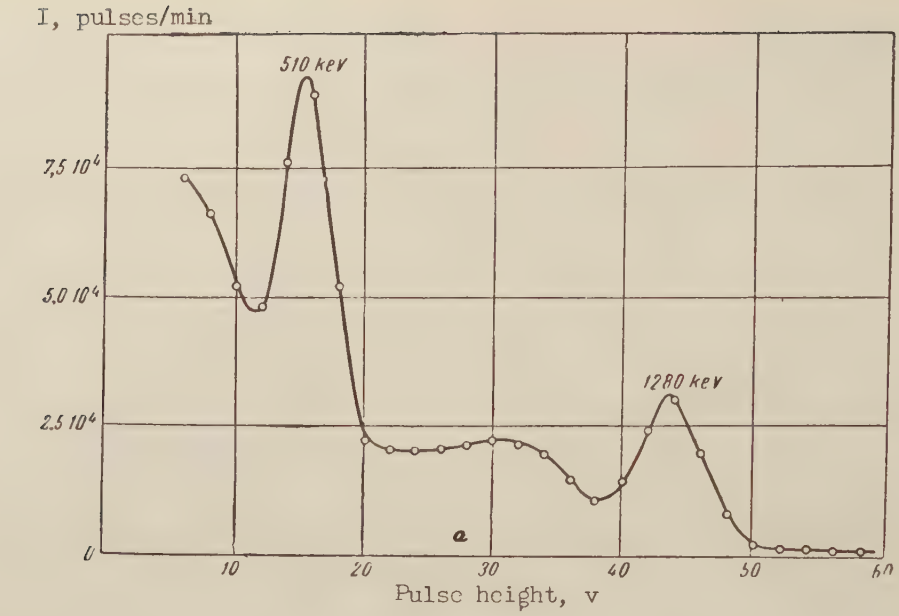

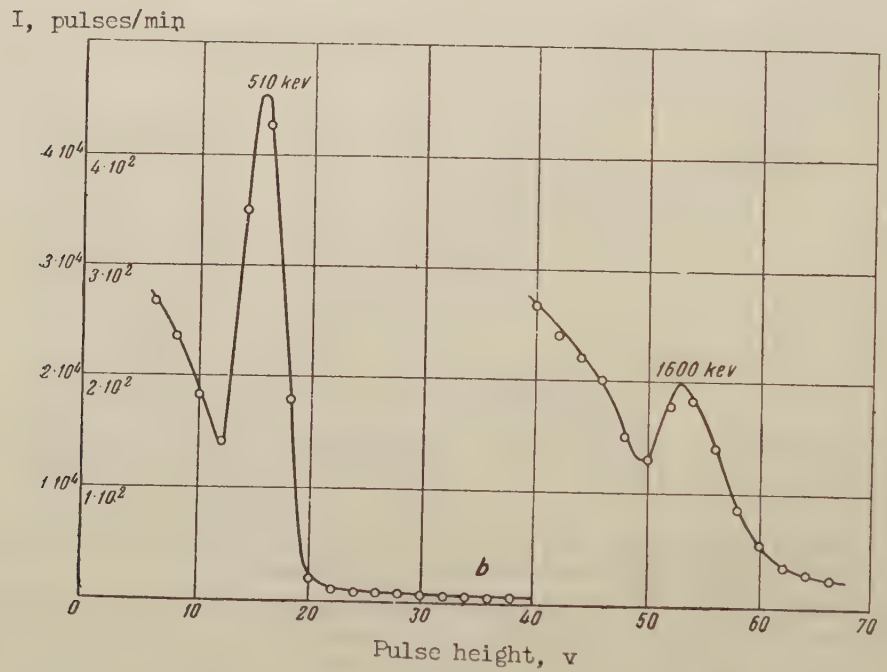

Fig.4. a) Spectrum of Na^{22} γ-radiation in the range from 250 to 2000 kev; b) spectrum of Nd^{140} + Pr^{140} γ-radiation in the same energy region. Both spectra were recorded under identical conditions.

and the β^+-particles we obtained a value of 2.04 ± 0.10 for the ratio $I_{\beta+}/I_{ann}$. The mean value obtained for $I_K/I_{\beta+}$ was 2.1 ± 0.2.

The high-energy part of the γ-spectrum of Nd^{140} + Pr^{140} was measured by means of a 4 x 4 cm NaI(Tl) crystal. Inasmuch as the $Pr^{140} \rightarrow Ce^{140}$ transition energy exceeds 3 Mev, one could expect to observe in the spectrum of the equilibrium Nd^{140} source many γ-lines of La^{140}. Actually, however, we observed only a line with an energy of ~1600 kev, presumably, corresponding to the well-known 1596 kev

level in Ce^{140}. For determining the absolute intensity of this line we carried out parallel calibration measurements under identical conditions with an Na^{22} source for which the intensity ratio between the β^+-radiation and the 1280 kev γ-rays is known ($I_{\beta+}/I_{\gamma-1280} = 0.89$).[11]

Typical γ-spectra obtained for the Nd^{140} + Pr^{140} and Na^{22} sources are reproduced in Fig.4. In processing these results we introduced an appropriate correction for the difference between the efficiencies of the crystal in detecting 1596 and 1280 kev γ-rays[12] and also took into account the difference in the absorption of these γ-rays in the lead absorbers shielding the source. The average result for 12 series of measurements carried out with different sources and different absorbers (5, 10 and 15 mm thick) for the intensity ratio of the 1596 kev line and the annihilation radiation line proved to be

$$\frac{I_{\gamma\text{-}1600}}{I_{\gamma\text{-}510}} = (4.0 \pm 0.5)\cdot 10^{-3}.$$

For the intensities of the 1600 kev γ-radiation and the β^+-radiation we obtained the following ratio:

$$\frac{I_{\gamma\text{-}1600}}{I_{\beta^+}} = (8.0 \pm 1.0)\cdot 10^{-3}.$$

It may be noted that the conversion coefficient for the 1596 kev γ-rays computed on the basis of our data and the experimental data of Dzhelepov et al[5] does not agree with the theoretical value of α_{K+L} for this line. This transition, as was fairly reliably established, is pure E2; hence for it α_{K+L} should be of the order of $8\cdot 10^{-4}$, i.e., approximately half the value following from our experimental data:

$$\alpha_{K+L} = \left(\frac{I_{e^-\,K+L}}{I_{\gamma\text{-}1596}}\right) = \frac{1.4\cdot 10^{-5}}{8\cdot 10^{-3}} = 1.7\cdot 10^{-3}\,*$$

The intensity of the other (not observed by us) higher energy lines (the spectrum was investigated in the energy range to 3 Mev) does not, according to our evaluation, exceed 10% the intensity of the 1596 kev line. Observation in this energy region was hampered by the fact that the sources utilized had a relatively low intensity (of the order of 5-10 microcurie), while the background of the scintillation spectrometer even in detecting high-energy pulses was rather strong.

In the energy range below 500 kev it is difficult to carry out measurements in view of the intensity of the Compton component of the annihilation radiation. It can only be stated that if low energy lines do exist, their intensity must be low. Thus the intensity of the 340 kev line, known from the γ-spectrum of La^{140}, does not exceed, according to our evaluation, 2% the intensity of the β^+-radiation.

3. Thus, we obtained the following ratios for the intensities of the x-, β^+- and γ-radiations from the equilibrium Nd^{140} + Pr^{140} source:

$$I_L : I_K : I_{\beta^+} : I_{\gamma\text{-}510} : I_{\gamma\text{-}1596} = 0.27 : 2.1 : 1.0 : 2.0 : 8\cdot 10^{-3}.$$

---

*The experimental value of the conversion coefficient determined for this transition on the basis of analysis of the decay scheme of La^{140} agrees with its theoretical value.[12]

On the basis of these ratios one can attempt to draw certain inferences regarding the decay scheme for Nd^{140} and Pr^{140} and evaluate the energy of the $Nd^{140} \rightarrow Pr^{140}$ transition.

Thus, for example, using the value deduced for the $I_K/I_{\beta+}$ ratio (2.1) and the data of Browne et al[2] on the ratio between the intensities of the x-radiations from neodymium and praseodymium $\left(\frac{K_{\alpha_1\alpha_2} + K_{\beta_1}(\mathrm{Nd})}{K_{\alpha_1\alpha_2} + K_{\beta_1}(\mathrm{Pr})} = 2.1\right)$, one can calculate the percentages of the various decay modes of Nd^{140} and Pr^{140}. Thus, denoting the number of K captures in Pr^{140} by x, we have the following distribution for the L, K and β^+-radiations from these isotopes:

	L	K	β^+
Nd^{140}	$1-2.1\,x$	$2.1\,x$	—
Pr^{140}	$0.134\,x$	x	$1-1.134\,x$

We made use of the ratio between the number of L and K captures (taking into account the captures from the L_{II} shell) in the praseodymium nucleus (Z = 59), that should obtain[13] for allowed high energy transitions. This ratio is 0.134.

More precise calculations taking into account screening and finite nuclear size have been carried out by Brysk & Rose[14] and Zyryanova[15]; these calculations give the same value for the ratio within 2%. Taking our experimental value for the $I_K/I_{\beta+}$ ratio (2.1) and the value of the mean fluorescence yield ω_K for Nd and Pr (0.89), we obtain $x = 0.41$. Using this value we find the following distribution among the decay modes of Nd^{140} and Pr^{140}:

	L	K	β^+
Nd^{140}	14%	86%	—
Pr^{140}	5%	41%	54%

The distribution deduced for Pr^{140} is consistent with the electron capture-positron decay branching ratio expected for this isotope. Thus, we assume that the positron spectrum end-point energy is 2.380 Mev (this value was obtained by averaging the values given by the authors listed in Table 1 and agrees with the probably most accurate to date evaluation of E_{ep} for Pr^{140} carried out recently by Dzhelepov et al[5] for allowed transitions, a class to which the $Pr^{140} \rightarrow Ce^{140}$ transition belongs). Assuming this value for the end-point energy, the K/β^+ ratio should be 0.81, according to the formulas of Zyrayanova.[15] From our experimental data we have $K/\beta^+ = 0.76$.

The above intensity distribution is not in conflict with the measured values of the relative intensities of the L and K x-radiations of $Nd^{140} + Pr^{140}$. Thus, from Ref.9 it follows that $(L/K)_{Nd^{140}} = 0.16$. From the measured integral ratio $I_L/I_K = 0.13$, it follows that

$$(L/K)_\Sigma = \left(\frac{I_L}{I_K}\right)_\Sigma \left(\frac{\omega_K}{\omega_L}\right)_\Sigma - (n_{KL})_\Sigma = \frac{0.13 \cdot 0.89}{0.11} - 0.87 = 0.18 \pm 0.40,$$

whence

$$(L/K)_{Nd^{140}} = \frac{(L/K)_\Sigma\,(1 + p + (L/K)_{Pr^{140}}) - p\,(L/K)_{Pr^{140}}}{1 + (L/K)_{Pr^{140}} + p\,(L/K)_{Pr^{140}} - p\,(L/K)_{Pr^{140}}},$$

where p is the fraction of decays in Pr^{140} accounted for by electron capture ($p = 0.46$), and $(L/K)_{Nd^{140}}$ may be taken equal to 0.13. Then for $(L/K)_{Pr^{140}}$ we obtain a value of 0.20 ± 0.40, which is in agreement within the indicated uncertainty with the value given above.

Actually one can calculate the distribution between the decay modes on the basis of our values for $I_K/I_{\beta+}$ and I_L/I_K alone, i.e., without invoking the data

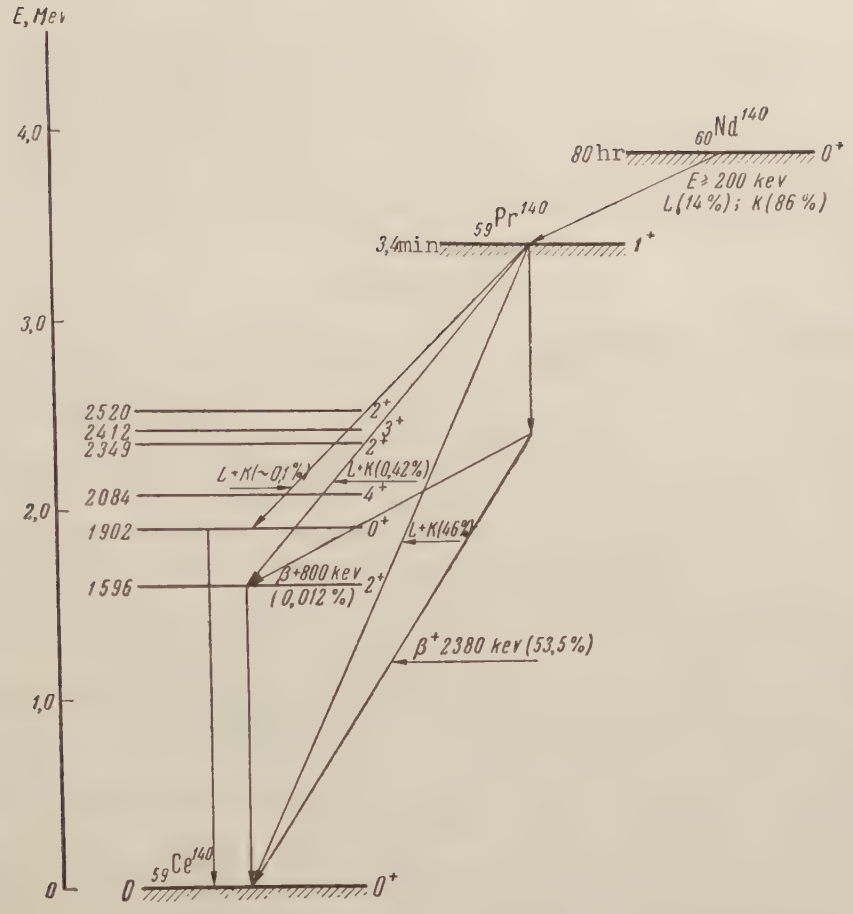

Fig.5. Decay scheme for Nd^{140} and Pr^{140}.

of Browne et al on the ratio of the intensities of the different K components of the radiation from Nd^{140} + Pr^{140}. The distribution deduced in this manner is close to that given above (somewhat higher values are obtained for the fraction of L capture in Nd^{140} and for the K/β^+ ratio for Pr^{140}).

However, the L/K ratio obtained from the ratio I_L/I_K in this case, as was shown above, comprises an appreciable uncertainty; hence we feel it is more expedient to depend on the first procedure, particularly since the error in the data of Browne et al[2] can hardly be large.

It appears from the deduced value of L/K for Nd^{140} that the energy of the $Nd^{140} \rightarrow Pr^{140}$ transition must be appreciable. Thus, for example, it follows from the formulas of Marshak[16] that the energy is not less than 200 kev. We recall that from Levy's empirical formula for atomic masses the energy of the $Nd^{140} \rightarrow Pr^{140}$ transition is 330 kev, while the value taken from Cameron's tables[3] exceeds 1 Mev. True, these formulas yield agreement within 250 kev with experimental energies only in about 85% of all cases and so that the agreement cannot be taken as full confirmation of the above deduced value for the $Nd^{140} \rightarrow Pr^{140}$ transition energy.

The measured intensity of the 1596 kev γ-rays also helps refine the decay scheme for Pr^{140}. Thus if we use the above cited value of 0.76 for $(K/\beta^+)_{Pr^{140}}$, we obtain a value of $(4.3 \pm 0.5) \cdot 10^{-3}$ γ-rays per disintegration of Pr^{140} for the intensity of the 1596 kev γ-line, i.e., we find that the transitions to this excited level occur in only 0.5% the total number of disintegrations of Pr^{140}.

Since these transitions are also allowed (it is known that the 1596 kev level and the ground state of Ce^{140} have spins 2+ and 0+, respectively) and since their energy must be of the order of 3400 = 1600 + 1800 kev, it is obvious that primarily electronic decay is involved. Thus according to the tables of Zyranova (Ref.15) for $E_{\beta^+_{ep}}$ = 1800 kev, the K/β^+ ratio for allowed transitions is of the order of 30. The ratio between the numbers of L and K captures in transitions to the 1596 kev excited level should be close to the theoretical value (for a high energy conversion transition) of 0.13. All these considerations were taken into account in elaborating the decay scheme shown in Fig.5.

References

1. G.Wilkinson & H.Hicks, Phys.Rev., 75, 1687 (1949).
2. C.Browne, J.Rasmussen, J.Surls & D.Martin, Ibid., 85, 146 (1952).
3. G.Gorodinskii, A.Murin, V.Pokrovskii & B.Preobrazhenskii, Doklady AN SSSR, 111, 405 (1957). (Trans.Soviet Physics - Doklady.)
4. J.Ya.Gromov, B.S.Dzhelepov, A.S.Dmitriev & B.K.Preobrazhenskii, Izv.AN SSSR, Ser.fiz., 22, 153 (1958). (Trans.Bulletin 22, 151.)
5. B.Dzhelepov, I.Uchevatkin & N.S.Shestopalova, Transactions of the June Conference on Neutron-Deficient Isotopes, Dubna, 1959.
6. O.I.Grigor'ev, B.S.Kuznetsov, N.S.Shimanskaya & I.A.Yutlandov, Izv.AN SSSR, Ser.fiz., 22, 850 (1958). (Trans.Bulletin 22, 845.)
7. A.Bisi & L.Zappa, Nuovo cimento, 12, 211 (1954).
8. S.Allen, Handbook of Chemistry and Physics, Cleveland, Ohio, 1952; K. Siegbahn (editor), Beta- and Gamma-Ray Spectroscopy, N.Y., 1955.
9. P.Axel, R.S.I., 25, 391 (1954).
10. R.Maeder, R.Muller & V.Wintersteiger, Helv.phys.acta, 27, 3 (1954).
11. W.Kreger, Phys.Rev., 96, 1554 (1954).
12. A.A.Bashilov, B.S.Dzhelepov, N.D.Novosil'tseva & L.S.Chernivskaya, Izv. AN SSSR, Ser.fiz., 22, 179 (1958). (Trans.Bulletin, 22, 176.)
13. M.Rose & I.Jackson, Phys.Rev., 76, 1540 (1949).
14. H.Brysk & M.Rose, Revs.Mod.Phys., 30, 1169 (1958).
15. L.N.Zyryanova, Unikal'nye perekhody (Unique transitions) (Monograph in press.)
16. R.Marshak, Phys.Rev., 61, 431 (1942).
17. H.Levy, Phys.Rev., 106, 1265 (1957).
18. D.Cameron, Tables, 1958.

POSSIBILITY OF UTILIZING THE (n,2n) REACTION IN NUCLEAR SPECTROSCOPY

- V.V.Komarov, A.B.Kurepin & A.M.Popova

As is known, the angular distribution of the products from stripping and pick-up reactions is distinguished by pronounced structure which makes it possible to obtain information on the relative spins and parities of the initial and final states of the nuclei involved. In treatments based on different formalisms there have been obtained identical results as regards the angular distributions of the products of stripping and pick-up reactions.[1] Thus stripping and pick-up reactions have come to occupy an important place in the techniques of nuclear spectroscopy.

At the same time, it has become clear that coulomb scattering of the products of these reactions leads to significant deviations from the results given by theories not taking into account the particle charges, particularly in the region of reactions on heavy nuclei.

Below we consider the (n,2n) reaction as a pick-up reaction. Earlier, we showed[2,3] that in the energy distribution of the products of reactions involving the ejection of several particles including two neutrons there are present narrow peaks due to the interaction of these neutrons in the final singlet state. Taking into account strong interaction of neutrons with a low relative intensity one can speak of a pick-up mechanism, i.e., of simultaneous ejection of two interacting neutrons as a result of direct interaction of the incident neutron with the nucleus.

Thus using the (n,2n) reaction, instead of the (p,d) or (n,d) reaction, one can hope to obtain data on the nuclear energy levels from the shapes of the angular distribution curves in the region of medium and heavy nuclei and also in the range of low energies where coulomb effects in usual pick-up reactions are significant and make it impossible to utilize ordinary pick-up reactions for making level assignments.*

The differential cross section for the (n,2n) reaction on the assumption of simultaneous ejection of both neutrons with a relative energy between E_{nn} and $E_{nn}+dE_{nn}$ as a result of direct interaction, calculated in the Born approximation or in the framework of the Butler-Gerjuoy theory[4] is of the form

$$\frac{d\sigma}{dE_{nn}\,d\Omega_1 d\Omega_2}=\frac{1}{16\,\pi^2\hbar^2}\cdot\frac{\mu_{n0}M_n\mu_{2n}}{\mu_n^2}\frac{k_{2n}k_{nn}}{k_{n_0}}\cdot[B(Q)]^2\cdot\left(\frac{V_0A}{Z}\right)^2\times$$

$$\times\left(|E_b|+\frac{\hbar^2}{2\mu_n}Z^2\right)^{-2}[j'(za)-gl(\varkappa a)je(za)]^2\frac{3\theta}{a}, \qquad (1)$$

where

$$\mu_{n0}=\frac{M_nN_i}{M_i+M_n};\quad \mu_n=\frac{M_nM_f}{M_f+M_n};\quad \mu_{2n}=\frac{2M_nM_f}{M_f+2M_n};$$

M_i is the mass of the initial and M_f the mass of the final nucleus; k_{n0}, k_{2n} and k_{nn} are the wave functions of the incident neutron, the center of mass of the two outgoing neutrons and of their mutual motion;

$$\frac{\hbar^2k_{nn}^2}{M_n}=E-\frac{\hbar^2k_{2n}^2}{2\mu_{2n}};\ \mathbf{Z}=\mathbf{Z}_{2n}-\left(\frac{M_f}{M_f+M_n}\right)\mathbf{K}_{n0};\ \mathbf{Q}=\frac{\mathbf{K}_{2n}}{2}-\mathbf{K}_{n0};$$

E is the energy in the center of mass system after the collision and E_b is the binding energy of the neutron in the initial nucleus; $d\Omega_1$ and $d\Omega_2$ are the elements of solid angle for the vectors $\mathbf{k}_1$ and $\mathbf{k}_2$; θ^2 is the dimensionless reduced width;

---

*This fact was brought to the attention of the authors by V.G.Neudachnii.

l is the orbital momentum of the picked-up neutron; a is the interaction range;

$$g_l(\varkappa a) = \frac{1}{rh_l^{(1)}(i\varkappa r)} \cdot \frac{d}{dr}\left(rh_l^{(1)}(i\varkappa r)\right)|_{r=a}$$

is the logarithmic derivative at the nuclear boundary expressed in terms of Hankel's spherical functions of the first type;

$$\varkappa = (2\mu_n |E_b|)^{1/2}/\hbar;$$

the function $j_l(za)$ is introduced as was done in Ref.5.

The interaction in the final state of the two outgoing neutrons is taken into account in the matrix element integral

$$\int V_{nn} e^{i\vec{Q}\vec{\rho}} \varphi_{2n}(\vec{\rho})\, d\vec{\rho}.$$

Here $\vec{\rho}$ is the vector between the neutrons in the final state; V_{nn} is the interaction potential of the neutrons in the final state; this is taken in the form of a potential well of depth V_0 and radius $\varrho_0 = 2.65$ f. The radial part of the two neutron wave function φ_{2n} was chosen in the same way as in Ref.6.

The calculated integral enters into Eq.(1) in the form

$$B = \int_0^{\rho_0} \frac{\sin Q\rho}{Q} \sin k\rho\, d\rho.$$

The energy distribution described by Eq.(1) has a narrow peak in the $E_{nn} =$ = 0 to 160 kev region, due to interaction of the two neutrons in the final singlet state. The value of k is only weakly dependent on the mutual energy of the two neutrons and equals $11.04 \cdot 10^{12}$ cm^{-1}. Below we give the values of A^2 (in units of 10^{-22} cm^2) for different values of the relative neutron energy

E_{nn}, Mev	0.02	0.04	0.06	0.08	0.10	0.12	0.14	0.16
A^2 =	298	237	159	139	114	97	84	60

We obtain the angular distribution of the center of mass of the two neutrons emitted at an angle ϑ in the center of mass system of the nucleus by integrating the energy distribution over the narrow range E_{nn} = 0 to 160 kev for each ϑ.

By comparing the absolute values of the cross section for the transitions to different levels of the final nucleus, one can determine the relative values of the reduced width.

To illustrate the application of the described method of calculation we plotted the angular distributions for the center of mass of the two outgoing neutrons from the (n,2n) reaction on Be^9 at an incident neutron energy of 14 Mev for the 2.9 Mev state of the final nucleus, Be^8.

Fig.1,a shows the angular distributions for $l = 1$. This case corresponds to experiment inasmuch as the neutron is probably picked up from the p shell of Be^9. It will be evident from the figure that the angular distribution is strongly dependent on the interaction range a. Inasmuch as the final state of the two neutrons is not bound, the angular distribution maximum differs somewhat from Butler's curve (dashed curve in Fig.1,a) for emission of the bineutron in the bound state. The angular distributions for $l = 0$ and 2 are shown in Fig.1,b; it will be evident that they differ appreciably from the distributions of Fig.1,a. Comparison of curves a and b shows that the momentum of the picked-up neutron can be determined from the experimental angular distributions by comparing these with the calculated distributions, in the same way as when the usual Butler curves are employed.

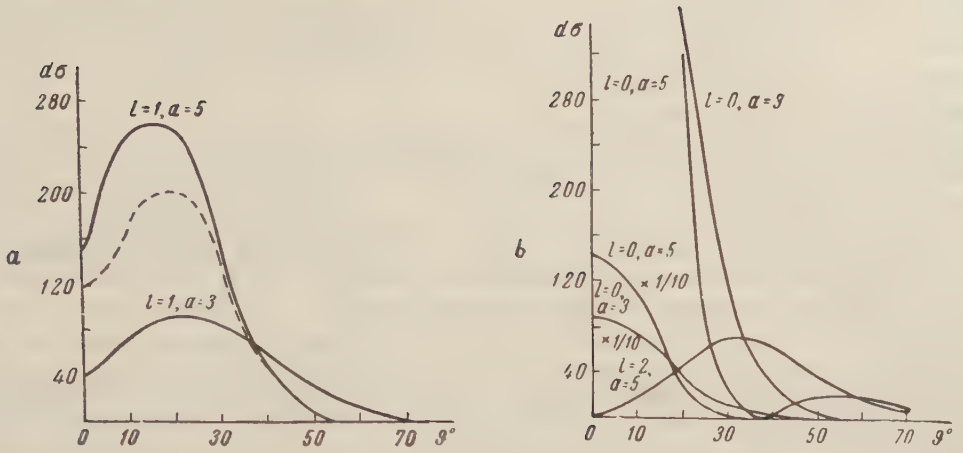

Fig.1. Angular distributions of the center of mass of the two interacting neutrons from the $Be^9(n,2n)Be^8$ reaction leading to the 2.9 Mev level of Be^8 calculated for an incident neutron energy of 14 Mev: a) $l = 1$; the dashed curve is calculated according to Butler's theory[1]; b) $l = 0$ and 2.

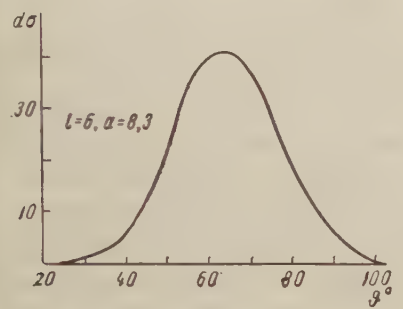

Fig.2. Angular distribution (in arbitrary units) of the center of mass of the two interacting neutrons from the $Pb^{208}(n,2n)Pb^{207}$ reaction leading to the 1.63 Mev level of Pb^{207} at an incident neutron energy of 14 Mev.

Taking into account the interaction of the two neutrons in the final state weakly distorts the shape of the ordinary Butler curve (Fig.1,a) particularly in the range of large angles. Hence the angular dependence for the $Pb^{208}(n,2n)Pb^{207}$ reaction leading to the 1.63 Mev state of Pb^{207} was calculated using the part of our formula analogous to Butler's. The interaction range was taken equal to $1.4 \cdot 10^{-13} A^{1/3}$ cm. The angular momentum $l = 6$ in this case is determined uniquely inasmuch as the levels of Pb^{208} and Pb^{207} have been thoroughly studied and their spins are known to be 0+ and 13/2+, respectively. The neighboring levels (0.89 and 2.34 Mev) are fairly distant from the investigated level of Pb^{207} and the angular distributions for them are determined by orbital momenta of different parity.

The calculated distribution curve is shown in Fig.2. It will be seen that the peak lies at a fairly large angle, which is convenient for experimental measurement. The value of the cross section at the peak is one order of magnitude smaller than the cross section at the peak of the angular distribution for $l = 1$.

No special investigations were carried out with a view to bringing out the noted distinctive features of the angular distributions from the (n,2n) reaction. It is almost impossible in experiments to obtain the distributions of the joint momentum vector of the two neutrons except for some individual cases as, for example, the $Be^9(n,2n)Be^8$ reaction. One can, however, investigate the energy distributions of the outgoing neutrons. The peak in such distributions, due to interaction of the two neutrons at low relative energies, for an infinitely heavy nucleus must lie at an energy E_n equal to half the maximum energy of the neutron from the (n,2n) reaction, while for a finite nucleus it should lie at an energy equal to $\frac{1}{2} \cdot \frac{M_i}{M_f}$ the maximum value.

It must be emphasized that there is the possibility of erroneous determination of the energy states of nuclei from the peaks in the energy distributions of inelastically scattered neutrons, inasmuch as these peaks can be due to the (n,2n) process with simultaneous emission of two neutrons in one direction, rather than to the (n,n') process.

In the spectra of inelastically scattered neutrons, there are present neutrons formed as a result of the investigated process in the (n,2n) reaction, statistical processes in the (n,2n) reaction, the cascade process in the (n,2n) reaction, the (n,n') process and, finally, accompanying some reactions, for example, the (n,pn) reaction. It is possible that most of the neutrons in the spectra are due to the enumerated competing mechanisms. Nevertheless, the effect of simultaneous direct emission of two neutrons in one direction can be recorded inasmuch as in this case the neutrons will be concentrated in a narrow (of the order of a few hundred kilovolts) energy region, corresponding to a certain condition of the final nucleus.

The experimental problem consists in recording the angular dependence for the given narrow range of the neutron energy spectrum, corresponding to the investigated state of the nucleus A - 1 for the reaction A(n,2n)A - 1. In this case one can expect to obtain typical angular dependences similar to those shown in Figs.1 & 2, dependences that can be used for determining the spins of the excited levels (or of a group of close levels if the experimental technique employed does not have the requisite resolution).

The experimental difficulties are worth overcoming since solution of the problem could make it possible to elucidate the mechanism of the (n,2n) reaction and to determine the assignments for medium and heavy nuclei, where ordinary pick-up reactions are inapplicable, and also to obtain more accurate assignments for light nuclei. Of particular interest is determination of the spins of radioactive nuclei not susceptible of investigation by other methods, and investigation of the second excited levels of even-even nuclei with a view to obtaining an answer to the question of their splitting into a number of states with different momenta.

Scientific-Research Institute for Nuclear Physics,
Moscow State University

References

1. A.G.Sitenko, Uspekhi fiz.nauk, 67, 377 (1959). (Trans.Soviet Physics - Uspekhi.)

2. V.V.Komarov & A.M.Popova, Zhur.eksp.i teor.fiz., 38, No.1 (1960). (Trans.Soviet Physics - JETP.)

3. V.V.Komarov & A.M.Popova, Ibid., 38, 1559 (1960). (Trans.Ibid.)

4. E.Gerjuoy, Phys.Rev., 91, 645 (1953).

5. A.B.Kurepin & V.G.Neudachin, Zhur.eksp.i teor.fiz., 36, 1725 (1959). (Trans.Soviet Physics - JETP.)

6. V.V.Komarov & A.M.Popova, Ibid., 36, 1574 (1959). (Trans.Ibid.)

ENERGY STATES OF Be^8 IN THE DISINTEGRATION OF C^{12} INTO THREE α-PARTICLES UNDER BOMBARDMENT WITH PROTONS AND NEUTRONS

- S.S.Vasil'ev, V.V.Komarov & A.M.Popova

We investigated the $C^{12} \rightarrow 3\alpha$ disintegration reaction under the influence of 8.5 to 19 Mev neutrons[1] and 15 to 30 Mev protons[2] for the purpose of elucidating the mechanism of this reaction.

Inasmuch as in this disintegration there is the possibility of formation of a compound Be^8 nucleus in the chain

$$C^{12} \rightarrow Be^8 + \alpha \rightarrow 3\alpha,$$

as well as resonance interaction of two α-particles in the final state[3], it is of interest to search for evidence of these effects and to attempt to determine whether there exists the broad level centered at 11.7 Mev in Be^8 as well as other levels located between 3 and 11 Mev, the existence of which is still under question[4].

The $C^{12}(n,n'3\alpha)$ disintegration was observed in the form of three-pronged stars, and the $C^{12}(p,p'3\alpha)$ decay in the form of five-pronged stars in photographic emulsions irradiated with neutrons and protons of different energies obtained from the 72 cm cyclotron and the 120 cm phasotron of the Scientific Research Institute of Nuclear Physics at Moscow State University.

Analysis of the stars yielded information on the energies and spatial distributions of the particles involved in the disintegrations and also on the excitation energies of the intermediate nuclei including Be^8. The analysis of emulsion stars is familiar and will not be described here. The technique of nucleon bombardment on the phasotron is described in Ref.5.

The energy distribution in the C^{13} center of mass system of α-particles from the $C^{12}(n,n'3\alpha)$ reaction for one grouping of incident neutron energy is shown in Fig.1,a; the energy distributions in the N^{13} center of mass system of α-particles from the $C^{12}(p,p'3\alpha)$ disintegration for four groupings of incident proton energy are shown in Fig.1,b.

We note that with increase of the incident nucleon energy from 14 to 30 Mev, the peak in the energy distributions does not shift to any extent but remains at ~3 Mev. If the reaction occurred with simultaneous emission of four particles without interaction of the products in the final state, the shift of the peaks should be ~3 Mev and the experimental histograms would agree with the curves calculated on the assumption of four-particle disintegration (dash-dot curves). The agreement of these curves with the histograms is appreciably poorer than the agreement of the curves (dashed curves) calculated on the assumption of strong interaction of the α-particles formed in disintegration to the level in Be^8 with an energy of 2.9 Mev and a width of 3 Mev. This and the fact that the distribution peak is not shifted with increasing energy indicate interaction of the α-particles in the final state and are evidence for a high probability of formation of Be^8 in an excited 2.9 Mev state. The dashed curve was calculated on the basis of the Chew-Brueckner-Hart theorem[6] by means of the formula

$$\frac{d\sigma}{dE_\alpha} \sim \rho(E_\alpha)\,\Psi_0(E_\alpha),$$

where $\rho(E_\alpha)$ is the density of states, and $\Psi_0(E_\alpha)$ is a function of the relative motion of the scattering α-particles.

Figs.2,a & b show the Be excitation energies calculated for each pair of α-particles in the observed stars. As usual, for each star there were calculated

Fig.1. Energy distributions of α-particles (in the C^{13} center of mass system) from the $C^{12}(n,n'3\alpha)$ reaction for an incident proton energy 14-19 Mev (a) and of α-particles (in the N^{13} center of mass system) from the $C^{12}(p,p'3\alpha)$ reaction for incident proton energies of 15-20 (I), 21-23 (II), 24-26 (III) and 27-30 Mev (IV). The dashed curve was calculated on the assumption of resonance interaction of the α-particles at E_p = 3 Mev, and Γ = = 3 Mev for simultaneous disintegration into four particles; the dash-dot curve was calculated for four-particle disintegration but without the assumption of resonance interaction.

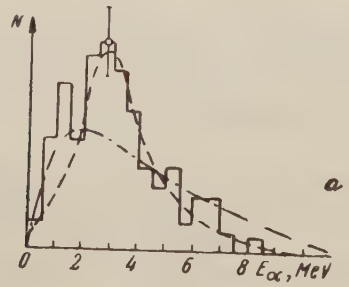

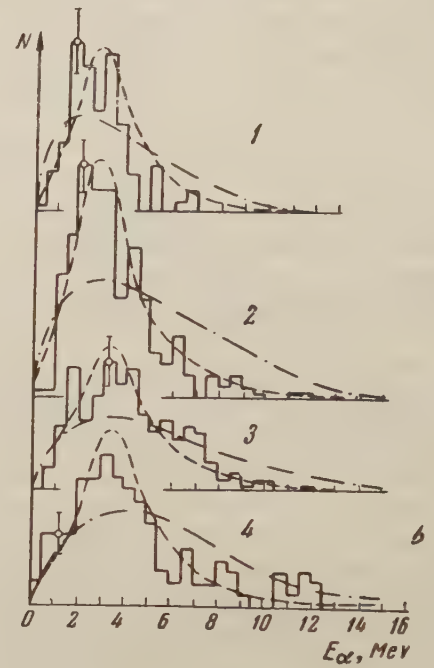

three excitation energies inasmuch as it is not known which two of the three α-particles formed in the break-up of Be^8. In Fig.2,a we have collected all the values calculated for the $C^{12}(n,n'3\alpha)$ events at incident neutron energies from 14 to 19 Mev; in Fig.2,b we give all the values calculated from the $C^{12}(p,p'3\alpha)$ disintegrations at proton energies from 15 to 30 Mev. Against the background of the statistical distribution of spurious excitation energy values there rise two peaks corresponding to the energies of the well-known levels in Be^8: the ground state and the first excited state at ~3 Mev. In addition, there appear groupings at 4-5, 8-9 and 11-12 Mev above the statistical curve (dashed line) plotted on the assumption of simultaneous disintegration due to inelastic scattering of the nucleons from C^{12}.

If we accept that the disintegration proceeds via the 0 and 2.9 Mev levels of Be^8 and that these levels, which have been observed by many investigators, actually exist, one can reduce the statistical background of spurious values in the upper histogram of Fig.2,b by eliminating the second and third values for each star in which the first value is equal to 0.0 ± 0.5 or 3.0 ± 1.0 Mev. The results of such elimination are shown in the lower histogram of Fig.2,b. It will be seen that this elimination of the spurious values does not bring out any levels above 4 Mev. It should be recalled, however, that such detection of weakly evinced higher levels is hampered by the large number of spurious values associated with the diversity of disintegration modes.

The general appearance of the experimental histogram reproduced in Fig.2,a is in agreement with the data of Frye, Rosen & Stewart[7] and other investigators.

If one compares the large number of experimental data on the energy states of Be^8, it becomes clear that so far there has been reliably established the existence of only one excited level, namely that at 2.9 Mev, for excitation ener-

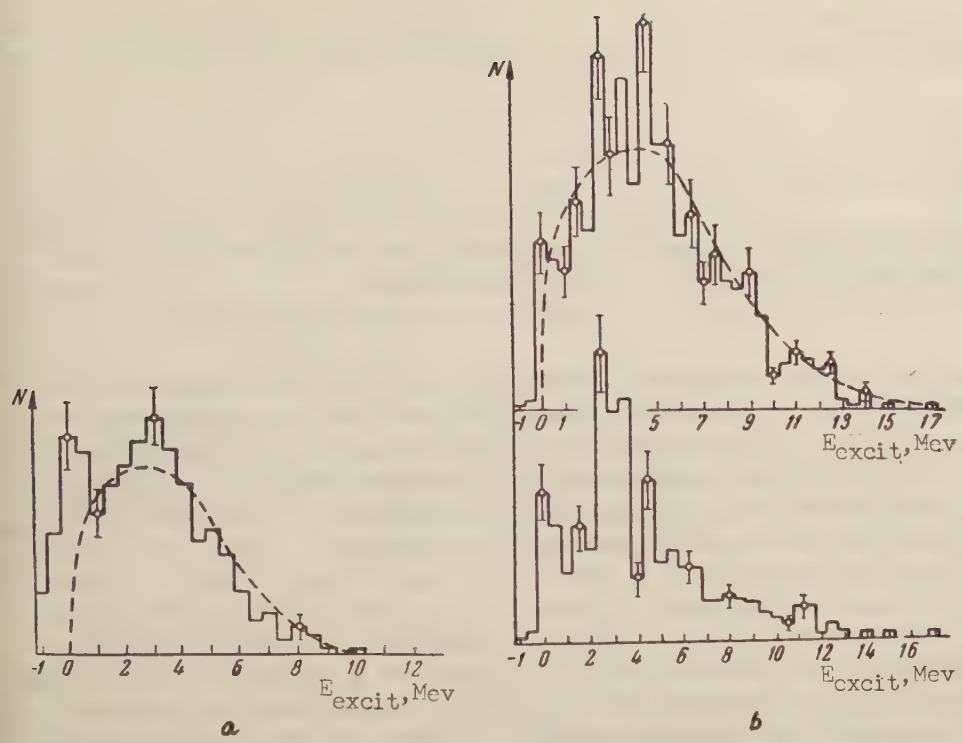

Fig.2. Excitation energies of Be^8 formed in the $C^{12}(n,n'3\alpha)$ disintegration at E_n = 14-19 Mev (a) and in the $C^{12}(p,p'3\alpha)$ disintegration at E_p = 15-30 Mev (b). The dashed curves were calculated on the assumption of simultaneous disintegration.

gies from 0 to 15 Mev. The manifestation of levels in Be^8 in many-particle disintegrations, for example, the $C^{12}(p,p'3\alpha)$ and $C^{12}(\gamma,3\alpha)$ reactions[9] indicates that this nucleus may have levels at 9 and 11-12 Mev; the latter values are usually attributed to a broad level centered at 11.7 Mev. Our data indicate that if the evidence for such 8-9 and 11-12 Mev states is valid, it corresponds not to a single broad state but to a number of discrete levels. Despite the adequately high energy of the incident neutrons, the 11.7 Mev level was evinced very weakly as compared with the first excited level. In stars formed by 26 to 30 Mev protons the probability for disintegration via this level amounts to 1/10 the number of disintegrations to the first excited level. This can be explained if we recall that the threshold energy for the $C^{12} \rightarrow 3\alpha$ process is nearly 8 Mev.

In conclusion, we note that our data (Fig.1) indicate that the disintegration of C^{12} into three α-particles may occur in the form of simultaneous disintegration with strong resonance interaction of the particles in the final state. In this case the lifetime of the Be^8 nucleus in the intermediate state should be close to the nuclear lifetime.

Scientific Research Institute of Nuclear Physics,
Moscow State University

References

1. S.S.Vasil'ev, V.V.Komarov & A.M.Popova, Zhur.eksp.i teor.fiz., 33, 1321 (1957). (Trans.Soviet Physics - JETP.)
2. S.S.Vasil'ev, V.V.Komarov, G.V.Koshelyaev & A.M.Popova, Ibid., 37, 1460 (1959). (Trans.Ibid.)
3. V.V.Komarov & A.M.Popova, Transactions of the Tenth Conference on Nuclear Spectroscopy, M.-L., 1960; Zhur.eksp.i teor.fiz., 38, 1559 (1960). (Trans.Soviet Physics - JETP.)
4. F.Ajzenberg-Selove & T.Lauritsen, Nucl.Phys., 12, 1 (1959).
5. S.S.Vasil'ev, V.V.Komarov, G.V.Koshelyaev & A.M.Popova, PTE, No.1 (1961). (Trans.Instruments & Experimental Techniques).
6. K.Brueckner, Phys.Rev., 82, 598 (1951).
7. G.M.Frye, L.Rosen & L.Stewart, Ibid., 99, 1375 (1955).

8. J.Need, Ibid., 99, 1356 (1955).
9. H.Glätti, E.Loepfe & P.Stoll, Helv.phys.acta, 28, 366 (1955).

* * * * * * *

INVESTIGATION OF THE ENERGY DISTRIBUTIONS OF THE PRODUCTS OF NUCLEAR REACTIONS INVOLVING EMISSION OF SEVERAL PARTICLES

- V.V.Komarov & A.M.Popova

The energy spectra of the products of reactions involving the emission of several particles at medium incident particle energies as a rule have a complex shape that cannot be explained on the assumption of either direct disintegration of the target nucleus or formation of compound nuclei in the process of disintegration. Many spectra are characterized by peaks, the height and shape of which depends on the direction of emission of the observed product.

One can, however, explain the shape of these spectra if one takes into account interaction of the reaction products in the final state. The interaction of reaction products at high energies was first considered by Migdal[1] in 1950, and subsequently by a number of other authors[2,3]. Below we propose a method for investigating the energy distributions of the products of reactions at medium energies, involving the emission of several particles. The interaction between the particles with small relative momentum is taken into account preciesly; the parameters of this reaction are taken from the results of experiments on scattering of the investigated particles; the interaction between the pair of particles with small relative momentum and the remaining particles is considered in the Born approximation. Strictly speaking, use of the Born approximation for such energies is not fully justified. However, this approximation has been successfully used in this energy region for explaining the angular and energy distributions in stripping reactions[4], which in some respects are similar to the process in question. Hence it may be assumed that in the given case use of the Born approximation in treating the interaction between the particle pair with small relative momentum with a third particle will give angular and energy distributions close to the true ones. Of greatest interest is investigation of the energy distribution of the products of reactions with emission of three particles when there may occur interaction in the final state between each pair of particles. Then for simultaneously taking into account the interaction of all the pairs of particles with small relative momentum, the wave function $\Psi(t)$ must satisfy the Shrödinger equation for the given problem

$$i\hbar \frac{\partial \Psi(t)}{\partial t} = (T + V_{12} + V_{23} + V_{31})\,\Psi(t),$$

$$V_{ij} = U_{ij} + \alpha_{ij} v_{ij},$$

where v_{ij} is the interaction between the particles in the final state, and the coefficients α_{ij} are smooth functions of the momenta such that

$$\alpha_{ij} = 1 \quad \text{for} \quad |\mathbf{p}_i - \mathbf{p}_j| \leqslant B$$
$$\alpha_{ij} = 0 \quad \text{for} \quad |\mathbf{p}_i - \mathbf{p}_j| \gg B$$

(B is the magnitude of the relative momentum of the two particles, corresponding to the interaction energy of these particles). It is most convenient to choose

the coefficients α_{ij} in the form

$$\alpha_{ij} = e^{-[a\ p_i - p_j]^2}.$$

Obviously, the interaction between the particles can be neglected if their relative momentum appreciably exceeds B. Then the entire range of possible particle energies can be subdivided into four regions:

a) where the interaction of particles 1 and 3 in the final state is significant ($\alpha_{13} = 1,\ \alpha_{12} = \alpha_{23} = 0$);

b) where interaction of particles 1 and 2 in the final state is significant ($\alpha_{12} = 1,\ \alpha_{13} = \alpha_{23} = 0$);

c) where interaction of particles 2 and 3 in the final state is significant ($\alpha_{23} = 1,\ \alpha_{12} = \alpha_{31} = 0$);

d) where pair interaction can be neglected (the relative momentum of any pair of particles differs appreciably from B) ($\alpha_{12} = \alpha_{23} = \alpha_{31} = 0$).

In the Born approximation the transition matrix element taking into account the interaction of each pair of particles in the final state will have the form

$$H \approx \langle \Psi_{123} A [(1-\alpha_{12}) V_{12} + (1-\alpha_{23}) V_{23} + (1-\alpha_{31}) V_{31}] \Phi_{123} \rangle,$$

where Ψ_{123} and Φ_{123} are the wave functions of the final and initial states; Ψ_{123} is determined for each energy region of the investigated particle (a, b, c or d above) depending on the magnitude of the relative momentum of the particles.

By this procedure we investigated the energy distributions of He^3 from the d + t $\rightarrow$ He^3 + n + n reaction at angles of 25 and 75° in the center of mass system for a deuteron energy of ~12 Mev. In the calculations we took into account the potential scattering of two neutrons on the singlet state.[5] The neutron-neutron interaction constant was taken equal to 70 kev. In Fig.1 we show the experimental energy distribution for He^3 obtained by Brolley et al[6] and the curves calculated taking into account the neutron interaction in the final state and ignoring this interaction. It will be evident that taking into account the scattering of the neutrons formed in the reaction explains the position and shape of the peaks in the He^3 spectra. Owing to the large uncertainty in the experimental data it was impossible in this case to find the neutron-neutron interaction from comparison of the experimental and theoretical curves.

Using the proposed method, we also calculated the energy distributions for the protons from the p + d $\rightarrow$ p + p + n reaction at angles of 0 and 180° in the center of mass system with respect to the direction of the incident protons for a total reaction energy of 4 Mev; the corresponding experimental distribution was obtained by Vlasov et al[7] (Figs.2 & 3).

The neutron spectrum for 0° was calculated by Heckrotte & McGregor[8] taking into account the interaction of two protons in the final state (Fig.2). As will be evident from the figure, this explains only the position of the peak at the high energy edge of the spectrum.

In the calculation we took into account the potential scattering of each pair of nucleons produced in the reaction[9]; the calculated curves are shown in Figs.2 & 3.

The calculated spectrum of neutrons emitted at 0° has two peaks, as does the experimental distribution. The position and shape of the peaks at a neutron energy of ~0.7 Mev, as our calculations showed, is due to interaction of the neutron with a proton in the final state. The peak in the neutron spectrum near the high energy boundary is due to interaction of two protons with small relative momentum. The cross section for the p + d reaction in the region of the maximum at $E_n \approx 0.7$ Mev is greater than the cross section in the region of the maximum near

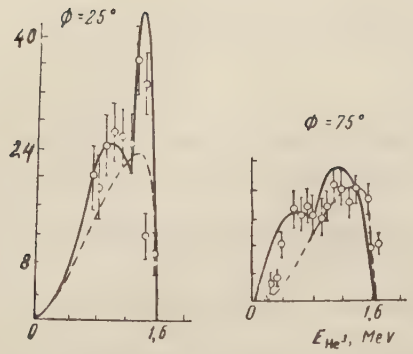

Fig.1. Energy distributions of He^3 from the d + t → He^3 + n + n reaction in the center of mass system. Points - experimental data of Brolley et al[6]; solid line - curve calculated taking into account interaction of the neutrons in the final state; dashed line - curve calculated without taking this interaction into account.

the high energy edge of the neutron spectrum, which can be explained by the higher probability for the process of pick-up by the incident neutron of a proton from the deuteron and their emission forward. The shape of the spectrum for neutrons emitted at an angle of 180° relative to the direction of the incident protons, as our calculations showed, is determined primarily by interaction of protons with small relative momentum, which corresponds to the most probable process of pick up of a proton by the incident proton with emission of the two protons forward and of a neutron backward. The ratio of the areas under the experimental points $\frac{d\sigma}{d\Omega}(180°) \Big/ \frac{d\sigma}{d\Omega}(0°) = 1.8 \pm 0.3$, while the ratio of the areas under the respective theoretical curves $\frac{d\sigma}{d\Omega}(180°) \Big/ \frac{d\sigma}{d\Omega}(0°) =$ = 1.75. This demonstrates that our method of calculation can be used for describing the angular distribution of the products of reactions involving the emission of several particles.

In view of isotopic invariance it may safely be assumed that the spectrum of protons emitted at 0° relative to the direction of the incident neutrons in the

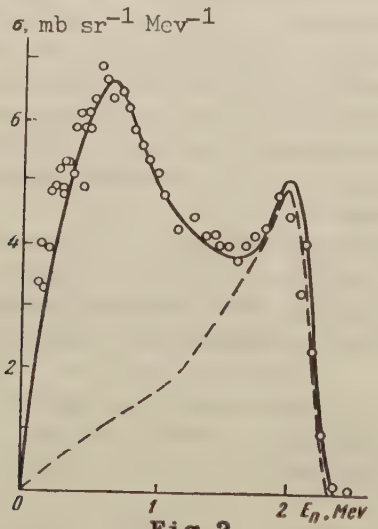

Fig.2

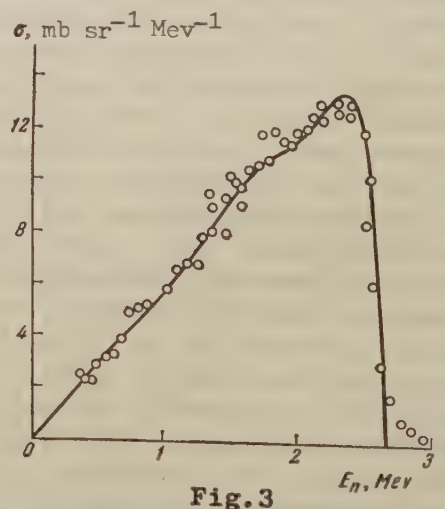

Fig.3

Fig.2. Spectrum of neutrons produced at 0° in the center of mass system by the p + d → p + p + n reaction for a total reaction energy ~4 Mev. Points - experimental data of Vlasov et al[7]; solid line - curve calculated by our method; dashed line - curve calculated by Heckrotte & McGregor[8].

Fig.3. Spectrum of neutrons produced at 180° in the center of mass system by the p + d → p + p + n reaction (Q ≈ 4 Mev). Points - experimental data of Vlasov et al[7]; curve calculated by our method.

center of mass system from the n + d → n + n + p reaction at neutron energies of ~10 Mev will also have two peaks, like the corresponding spectrum of neutrons from the p + d → p + p + n reaction. The first peak at a proton energy of ~0.7 Mev should correspond to interaction of a neutron with the proton with small relative momentum; the second peak near the nigh energy edge of the spectrum should correspond to the interaction of two neutrons with small relative momentum. Of great interest, however, is experimental investigation of the spectrum of protons emitted at 0^{o} from the n + d → n + n' + p reaction, inasmuch as theoretical treatment of this case by our method makes it possible to obtain the neutron-neutron scattering length.

By means of the method described here and in Refs.5, 9 & 10, one can analyze the products from such reactions as d + d, d + t, d + α, t + t and others for the purpose of elucidating the role of interaction of the reaction products and the possibility of existence of excited states in some light nuclei, for example, He^{4}, He^{5} and Li^{5}, which are evinced as resonance interaction in the final state of the products of reactions involving emission of several particles.

Scientific Research Institute of Nuclear Physics
Moscow State University

References

1. A.B.Migdal, Zhur.eksp.i teor.fiz., 28, 3 (1955). (Trans.Soviet Physics - JETP.)
2. K.Brueckner, Phys.Rev., 82, 595 (1951).
3. K.M.Watson, Ibid., 88, 1163 (1952).
4. A.G.Sitenko, Uspekhi fiz.nauk, 66, 577 (1958). (Trans.Sov.Physics - Uspekhi).
5. V.V.Komarov & A.M.Popova, Zhur.eksp.i teor.fiz., 38, 253 (1960). (Trans. Soviet Physics - JETP.)
6. J.E.Brolley, W.S.Hall, Jr, L.Rosen & L.Stewart, Phys.Rev., 109, 1277 (1958).
7. A.N.Vlasov, S.P.Kalinin, B.V.Rybakov & V.A.Sidorov, Zhur.eksp.i teor. fiz., 38, 1773 (1960). (Trans.Sov.Physics - JETP.)
8. W.Heckrotte & M.McGregor, Phys.Rev., 11, 593 (1958).
9. V.V.Komarov & A.M.Popova, Zhur.eksp.i teor.fiz., 38, 1559 (1960). (Trans. Soviet Physics - JETP.)
10. V.V.Komarov & A.M.Popova, Ibid., 36, 1574 (1959). (Trans.Ibid.)

DOUBLE-FOCUSING MAGNETIC SPECTROMETER

- N.G. Afanas'ev

Introduction

For the solution of many problems in nuclear physics it is essential to have available a spectrometer which in addition to high resolution has high luminosity. A significant increase in luminosity can be attained in instruments with double focusing.

Double focusing can be realized in spectrometers with a uniform field by utilizing the fringing field at the magnet boundaries for focusing.[1] A significant advantage of such instruments is the possibility of utilizing the method of nuclear resonance for measurement and stabilization of the magnetic field.

Three spectrometers of this type have been described in the literature.[2-4] The first two of these[2,3] have rectilinear boundaries of the magnet and hence cannot provide good focusing in a large solid angle. In contrast, the spectrometer described by Crewe[4] has curvilinear boundaries which are designed to insure ideal horizontal focusing. However, Crewe utilized a very special method of designing the boundaries, which does not allow much freedom for satisfying the requirement of vertical focusing.

In the present contribution we propose a different method of attaining ideal horizontal focusing, a method which provides for the possibility of improving the vertical focusing.

Moreover, hitherto all design calculations for spectrometers were carried out without taking into account the extent of the fringing fields. In our design we employ magnetic shields at the entrance and exit of the particle beam for reducing the effective action region of the fringing field and mainly for precise determination of the field. Below we give formulas for calculating the vertical and horizontal focusing taking into account the fringing field.

1. Method of obtaining ideal horizontal focusing

We shall start by considering an ideal magnet, i.e., we shall assume that outside the physical boundaries of the magnet the field is zero, while inside the magnet it is rigorously constant: $H = H_0$.

First, we consider a magnet with rectilinear boundaries. In a magnet of this type (Fig.1) double focusing of the particles is realized by appropriate choice of the angles of entrance ε_1 and exit ε_2 of the principal (central trajectory) particle ($\alpha = 0$), i.e., particles emitted from the source S within the angular ranges $-\alpha_0 < \alpha < +\alpha_0$ in the median plane of the magnet (we call this the horizontal plane) and $-\beta_0 < \beta < +\beta_0$ in the vertical plane are collected - focused - at a single point D (neglecting aberration). Obviously, the requirements as regards horizontal focusing must be more exacting than as regards vertical, inasmuch as the former determines the resolution of the instrument.

A magnet with rectilinear boundaries can have only first order focusing in the horizontal and vertical planes. To improve the resolution it is expedient to improve the horizontal focusing by going over to curvilinear boundaries.

We note that for an arbitrary entrance boundary one can shape the exit boundary so that the magnet will have ideal horizontal focusing (Fig.1). The equation for the exit boundary can readily be derived from the condition that the tangents to the trajectories of the particles (with arbitrary α) at the point of exit from the magnet K' must pass through one and the same point D:

$$l_2' = \{(C-B)^2 + \mathscr{E}^2 - R^2 + v^2 - 2v[-(C-B)\sin(\zeta-\alpha) + \mathscr{E}\cos(\zeta-\alpha)]\}^{1/2} \qquad (1)$$

and

$$\beta' = \operatorname{arc\,tg}\frac{R}{l_2'} + \operatorname{arc\,sin}\frac{E - v\cos(\zeta-\alpha)}{(l_2'^2 + R^2)^{1/2}} - \operatorname{arctg}\frac{R}{l_2}. \qquad (2)$$

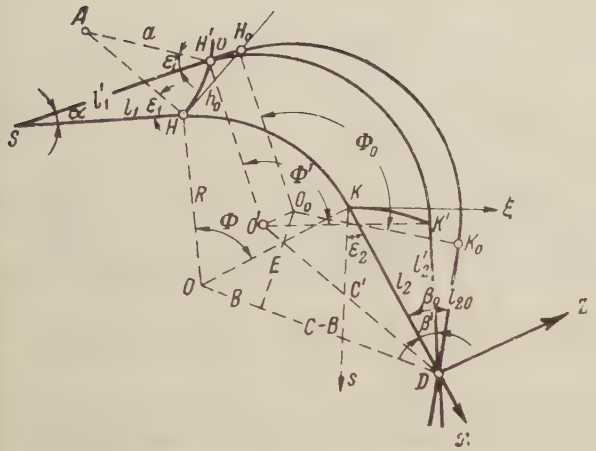

Fig.1. Determination of the exit boundary of the magnet insuring ideal horizontal focusing.

Here C and ζ are constants; B and $\mathscr{E}$ are functions only of α, determined by the initial magnet with rectilinear boundaries, and $v(\alpha)$ is the deviation of the exit boundary from the rectilinear boundary. The point D must, obviously, be the first order focus of the initial magnet with rectilinear boundaries.

An exit boundary shaped according to this equation will insure ideal focusing of the particles in the range of the entire "capture" angle ($-\alpha_0 < \alpha < +\alpha_0$) of the magnet with an arbitrary entrance boundary.

2. Improvement of vertical focusing

This arbitrariness as regards the entrance boundary can be utilized for improving the vertical focusing in the entire capture angle of the magnet. The simplest way of realizing this is to require that the magnet have first order vertical focusing not only for $\alpha = 0$, (which is assured by rectilinear boundaries) but for angles $\alpha = \pm\alpha_0$.

We will attain this aim if our magnet, producing a horizontal image of the source at point D, will produce a vertical image at the same point. In other words, the magnet parameters l_1', ε_1', l_2', ε_2' and Φ' must satisfy the familiar conditions for double focusing[5].

The specified quantities l_2' and $\Phi' = \Phi + \alpha + \beta'$ can be expanded in a series in powers of the small parameter v, and in many cases the expansion can be limited to the first terms. Thus the value of v for the angle $\alpha = +\alpha_0$ must satisfy the equation

$$\frac{1}{l_{20}} + c_1 v = \frac{1}{2}\left[\operatorname{tg}(\Phi_0 + \beta_1 v - \psi') - \frac{1}{\Phi_0 + \beta_1 v - \operatorname{ctg}\eta'}\right], \qquad (3)$$

where ψ' and η' are auxiliary functions:

$$\operatorname{tg}\psi' = \operatorname{tg}\varepsilon_1' + \frac{R}{l_1\dfrac{\cos\varepsilon_1}{\cos(\varepsilon_1+\alpha_0)} - v}, \qquad (4)$$

$$\operatorname{tg}\eta' = \operatorname{tg}\varepsilon_1' - \frac{R}{l_1\dfrac{\cos\varepsilon_1}{\cos(\varepsilon_1+\alpha_0)} - v}; \qquad (5)$$

in Eq. (3)

$$c_1 = \frac{E\cos(\zeta-\alpha_0) - (C-B)\sin(\zeta-\alpha_0)}{l_{20}^3}, \qquad (6)$$

and

$$\beta_1 = \frac{[ER - l_{20}(C-B)]\cos(\zeta-\alpha_0) - [(C-B)R + El_{20}]\sin(\zeta-\alpha_0)}{l_{20}(R^2 + l_{20}^2)}, \qquad (7)$$

and, in addition, we have introduced the notation $l'_{2\,(v=0)} = l_{20}$ and $\Phi'_{(v=0)} = \Phi_0$.

The entrance angle ε'_1 is still an arbitrary function of v, and thus we still have a certain freedom of choice as regards the entrance boundary. Eq.(3) can be satisfied by a circular entrance boundary. In this case

$$\varepsilon'_1 = \varepsilon_1 + \alpha_0 - 2\operatorname{arc\,tg}\frac{v\cos(\varepsilon_1+\alpha_0)}{l_1\dfrac{\sin\alpha_0}{\cos(\varepsilon_1+\alpha_0)} - v\sin(\varepsilon_1+\alpha_0)}; \qquad (8)$$

hence Eq.(3) can be solved, and the value of $v(\alpha_0)$ satisfying this equation determines the radius a of the entrance boundary for the angular range $0 \leqslant \alpha \leqslant +\alpha_0$. The radius a^* of the entrance boundary for the angular range $-\alpha_0 \leqslant \alpha \leqslant 0$ is determined in an analogous fashion. Thus the entrance boundary of a magnet having ideal horizontal and improved vertical focusing consists of two circular arcs, joining at the point of entrance of the principal particle ($\alpha = 0$). If instead of circular arcs we use higher order curves for the entrance boundary, we could in principle obtain double focusing at a larger number of points and in fact theoretically for all angles $-\alpha_0 < \alpha < +\alpha_0$.

The exit boundary of the magnet is a complex curve defined by Eqs.(1) and (2).

If we give up the requirement of ideal horizontal focusing, the exit boundary can be realized in the form of a circular arc, or more accurately speaking, one circle for $\alpha > 0$ and another for $\alpha < 0$. In many cases this modification does not substantially reduce the resolution inasmuch as the resultant aberrations do not exceed the dimensions of the image of targets of the size commonly employed.

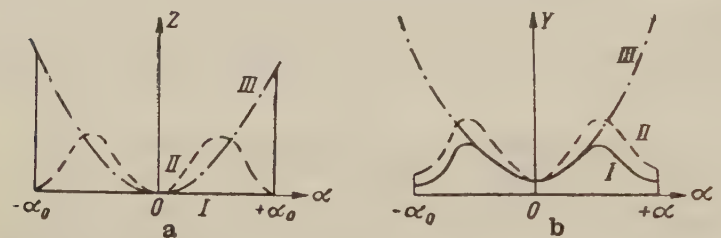

Fig.2. Aberrations (a - horizontal, b - vertical) of magnets with different types of focusing: I - magnet with ideal horizontal and improved vertical focusing, II - magnet with circular exit boundary, III - magnet with second order focusing.

Spectrometers with large capture angles constructed on this principle usually have smaller horizontal aberrations than spectrometers with second or even higher order focusing. This is explained by the fact that the maximum aberration in them is attained for $\alpha \approx \alpha_0/2$, while for $\alpha = 0$ and $\pm\alpha_0$ the aberration is zero; this is shown in Fig.2,a, where for comparison we also show the aberration of a spectrometer with second order focusing (curve III) in which the aberration attains a maximum at $\alpha = \pm\alpha_0$.

The corresponding curves for vertical aberrations in the same spectrometer are shown in Fig.2,b.

3. Determination of the field distribution in a magnet with a shield

For reducing the effective action region of the fringing field and mainly for precise definition of the field at the entrance of the particle beam into the spectrometer and at the exit from the spectrometer one can make use of magnetic shields. In the presence of a shield, the fringing field penetrates into the depth of the shield to a distance of the order of the gap between the magnet and the shield, and hence in measuring the field distribution one can assume the magnet pole to be infinite and rectilinear. Moreover, in cases important in practice, when the distance between the magnet and the shield is small (of the order of the magnet gap) the thickness of the shield is not particularly important.

We shall consider two limiting cases, namely, the case of an infinitely thick shield and the case of an infinitely thin shield. Obviously, the distribution for a shield of finite thickness will lie between the two limiting cases.

In both cases the solution can be obtained by the method of conformal transformation. For determining the particle trajectory in the field of a real magnet it is useful to consider an ideal magnet, equivalent to the real magnet as regards the angle of deflection of the particles in the horizontal plane (Fig.3). The boundary of this ideal magnet (it is located at a distance ξ from the physical boundary) is called the effective boundary. According to Reuterswärd[6], the value of ξ is given by

$$\xi = \int_{-\infty}^{0} h_y(X)\,dX - \int_{0}^{+\infty} [1 - h_y(X)]\,dX \ , \qquad (9)$$

where $h_y = \frac{H_y(X)}{H_0}$, H_0 is the intensity of the magnetic field in the uniform region of the magnet, and $H_y(X)$ is the vertical component of the field.

For a magnet with an infinitely thick shield

$$\xi = \frac{D}{2} - \frac{D}{\pi} \arcsin \frac{1}{\left[1 + \frac{4l^2}{D^2}\right]^{1/2}} + \frac{l}{\pi} \ln \left[1 + \frac{D^2}{4l^2}\right], \qquad (10)$$

where D is the distance between the magnet and the shield, and l is equal to half the magnet gap.

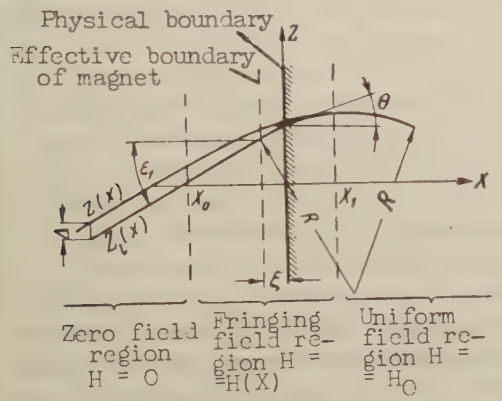

Fig.3. Particle trajectories in an ideal $(Z_i(X))$ and a real $(Z(X))$ magnet.

Values of ξ / l

D/l	Infinitely thick shield	Infinitely thin shield
1	0,42	0,49
3/2	0,59	0,68
2	0,72	0,83

For a magnet with an infinitely thin shield a somewhat cumbersome expression is obtained for ξ. The results of numerical calculations of ξ for shields of both types are given in the accompanying table. It will be evident from the table that for the small values of D/l encountered in practice, the value of ξ changes little with increase in the thickness of the shield.

The calculated field distribution will be realized with good accuracy if the length a_{sh} of the shield and its width b_{sh} satisfy the condition $a_{sh}, b_{sh} \gg l$. The thickness of the shield should be chosen on the basis of the condition that the average induction at the boundary (of length L), along which the halves of the shield facing the two poles of the magnet join,

$$B_{av} = \frac{\psi}{l c_{sh}} \qquad (11)$$

not exceeds H_0. Here ψ is the flux to the shield, which is calculated by summing the elementary values. In this case the shield will attain saturation simultaneously with the magnet pole piece.

4. Influence of fringing fields on horizontal and vertical focusing

Let us first consider the trajectory of particles emitted from the source in the horizontal plane.

In our case of a magnet with shields, the magnet field in the region close to the boundary (Fig.4) may be described to a good approximation by

$$h_y(x) = \frac{1}{2c}(x + c). \tag{12}$$

The value of c is readily determined if the above mentioned conformal transformation has already been performed. For this distribution of the fringing field the equation of motion is readily integrated. If we consider the case when the trajectories inside the real and ideal magnets coincide, outside the magnet the real trajectory proves to be parallel to the ideal and located at a distance

$$\Delta(\alpha) = \frac{1}{6}\frac{c^2}{R\cos^3\varepsilon_1} \tag{13}$$

from it (in the direction of the Z axis).

From the values of $\Delta(\alpha = 0)$ and $\Delta(\alpha = -\alpha_0)$ one can easily determine the new positions of the source and detector and also the horizontal aberrations connected with replacement of the ideal field by the real field. In the case of magnets with shields, the Δ proved to be very small and the aberrations even smaller.

Now let us consider the motion of a particle emitted from the source at an angle β to the median plane of the magnet with an arbitrary horizontal emergence angle $-\alpha_0 < \alpha < +\alpha_0$. For analyzing the vertical motion it is convenient to introduce (Fig.4) the curvilinear coordinates λ and ζ.[1] Coordinate λ is scaled along the trajectory of a particle with an arbitrary emergence angle α and angle $\beta = 0$, while the ζ axis is directed perpendicular to λ in the horizontal plane. Thus, the λ and ζ axes are always located in the horizontal plane. The Y axis remains unchanged.

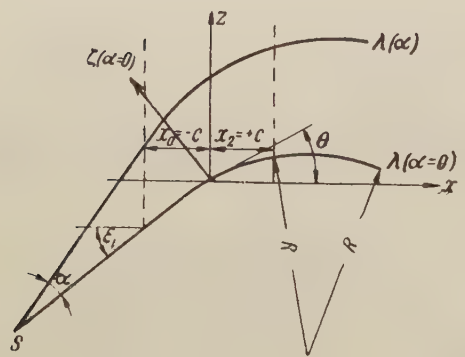

Fig.4. Trajectory of a particle moving in the horizontal plane.

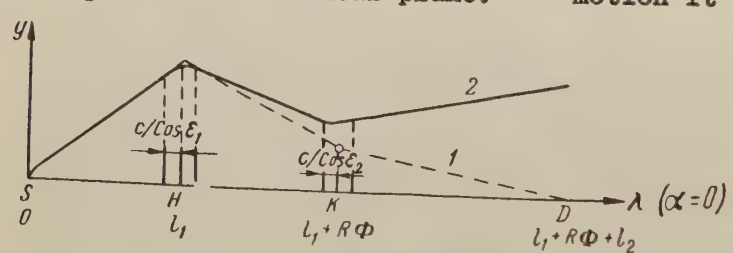

Fig.5. Trajectory of particles moving in the vertical plane without taking into account the influence of fringing fields (1) and taking this influence into account (2).

According to Cotte[1], the vertical trajectory of a particle with arbitrary emergence angles α and β is described accurately to within first order terms by the equation

$$\frac{d^2y}{d\lambda^2} = \frac{y}{R}\left(\frac{\partial h_y}{\partial \zeta}\right)_0, \tag{14}$$

where $\left(\frac{\partial h_y}{\partial \zeta}\right)_0$ is the gradient of the magnetic field at the given point of the trajectory of the particle with emergence angles α and $\beta = 0$. Expansion in terms of powers of $(\lambda - \lambda_0)$ gives

$$\left(\frac{\partial h_y}{\partial \zeta}\right)_0 = -\frac{\sin \varepsilon_1'}{2c}\left[1 - \frac{\cos \varepsilon_1'}{4cR \operatorname{tg} \varepsilon_1'}(\lambda - \lambda_0)^2\right]. \tag{15}$$

Integrating (14) we obtain

$$y_1 - y_0 = -y_0 c \frac{\operatorname{tg} \varepsilon_1'}{R \cos \varepsilon_1'} + y_0' \frac{2c}{\cos \varepsilon_1'}, \tag{16}$$

$$y_1' - y_0' = y_0\left[-\frac{\operatorname{tg} \varepsilon_1'}{R} + \frac{c(1 + \sin^2 \varepsilon_1')}{3R^2 \cos^3 \varepsilon_1'}\right] + y_0'\left(-c \frac{\operatorname{tg} \varepsilon_1'}{R \cos \varepsilon_1'}\right), \tag{17}$$

where y_0, y_0' and y_1, y_1' are the values of y and $y' = \frac{dy}{d\lambda}$ at the points of entrance and exit of the particles into and from the region of action of the fringing field.

The values of y_2 and y_2', which characterize the trajectory at the point of its approach to the region of action of the fringing field at the entrance boundary (Fig.5), are given by

$$y_2 = y_1 + \left(\Phi' - \frac{c}{R \cos \varepsilon_1'} - \frac{c}{R \cos \varepsilon_2'}\right) R y_1' \tag{18}$$

and

$$y_2' = y_1', \tag{19}$$

inasmuch as the radius of curvature of the particle trajectory is equal to R with accuracy to second order terms.

The corresponding equations for the exit boundary are

$$y_b - y_2 = -y_2 c \frac{\operatorname{tg} \varepsilon_2'}{R \cos \varepsilon_2'} + y_2' \frac{2c}{\cos \varepsilon_1'} \tag{20}$$

and

$$y_b' - y_2' = y_2\left[-\frac{\operatorname{tg} \varepsilon_2'}{R} + \frac{c(1 + \sin^2 \varepsilon_2')}{3R^2 \cos^3 \varepsilon_2'}\right] + y_2'\left(-c \frac{\operatorname{tg} \varepsilon_2'}{R \cos \varepsilon_2'}\right). \tag{21}$$

If in these equations we set $c = 0$ and $\alpha = 0$ (ideal magnet), we obtain the familiar formulas given by Gross[5] for vertical focusing.

It should be noted that, in contrast to the case of horizontal focusing, taking into account the extent of the fringing field has a substantial effect on the vertical focusing.

Thus by means of Eqs.(16)-(21) one can carry out an accurate calculation of the vertical focusing taking into account the influence of fringing fields.

Conclusions

Using the described procedure, we designed a number of magnetic spectrometers of the type diagramed in Fig.6. One such spectrometer has already been realized in the form of an experimental model, and tests have shown that the experimental parameters are in excellent agreement with the calculated values. This spectrometer will be described in a separate report.

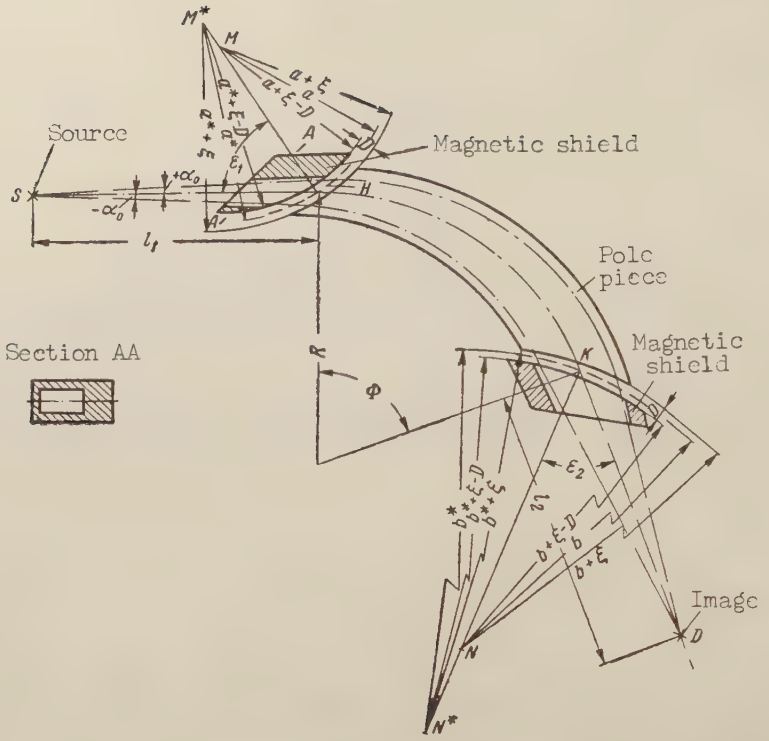

Fig.6. Diagram of spectrometer with shields.

Khar'kov Physical-Technical Institute,
Academy of Sciences of the Ukrainian SSR

References

1. M.Cotte, Ann.phys., 10, 333 (1938).
2. A.Lovatti & H.Tyren, J.Sci.Inst., 33, 151 (1956).
3. M.G.Meshcheryakov, V.P.Zrelov, B.S.Neganov, I.K.Vzorov & A.F.Shabudin, Proc.CERN Symposium, 2, 346 (1956).
4. A.V.Crewe, Rev.Sci.Inst., 29, 880 (1958).
5. W.G.Gross, Rev.Sci.Inst., 22, 717 (1951).
6. C.Reuterswärd, Arkiv.Math., Astr.Fysik, 3, 53 (1952).

RECORDING PHOTOMULTIPLIER PULSES BY MEANS OF A TAPE RECORDER AND AN AUTOMATIC RECORDING VOLTMETER

- A.N.Silant'ev

The equipment described below is intended for detecting and recording the spectrum of pulses from a photomultiplier on recorder tape or an automatic voltmeter chart.

The pulses are recorded on magnetic tape in case of measurement of the radiation from radioactive substances with a short period, when it is not feasible to use a multiple channel pulse height analyzer. The circuit was developed to operate in conjunction with a "Melodiya" tape recorder. The permissible load is determined by the characteristics of the recorder head.

The pulses are recorded on the chart of the automatic recording voltmeter in the case of measurement of the radiation from radioactive substances with a low level of activity and in working with coincidence circuits.

The pulse stretching assembly consists of three stretching stages and two control stages. The pulses for the tape recorder are taken off the output of the first stretching stage.

The converter assembly consists of an amplifier, a gating stage and a control unit.

The pulses from the photomultiplier are applied through an amplifier with an amplification factor of from 1 to 10 to the input of the stretching unit. A diagram of this unit is shown in Fig.1. The pulse stretching circuit consists of three stages. The first stage converts the incoming pulse to a pulse of 100 μsec duration. This stage operates as follows. The pulse from the PM, through a cathode follower and diode, charges a 200 pf capacitor. The same pulse also trips the trigger. The duration of the trigger pulse is 100 μsec. The trailing edge of this pulse unblocks the tube shunting the 200 pf capacitor. Thus, at the output of this stage there is attained a pulse of 100 μsec duration with an amplitude proportional to the amplitude of the input signal. The trigger threshold is set for a pulse height equal to 1/3 the minimum pulse it is desired to detect.

From the first stage the pulse is applied via a cathode follower to the recorder head for recording on magnetic tape and is also fed into the next stage of the stretching circuit. The pulses enter the next stage through a relay which cuts off these stages during the time of shaping of the pulse. In the second stage the pulse charges a 1000 pf capacitor. From the second stage the pulse through a cathode follower and a diode goes to the third stage. Here the pulse charges a 0.1 μf capacitor. The trigger actuating the second and third stages is tripped either by an external pulse or by the pulse from the first stage. The trigger pulse through a cathode follower charges a 1 μf capacitor and fires the bantam pentode 6P15P. This tube continues to conduct until all the charge leaks off the capacitor. This time can be varied by regulating the bias voltage on the grid of the 6P15P tube. A negative pulse from the plate of the 6P15P tube is applied through a divider to the grids of the tubes shunting the 1000 pf and 0.1 μf capacitors. Thus the circuit passes pulses only when a pulse is applied to the starting trigger. The starting pulse can be applied from a single channel pulse height analyzer with a wide gate. This allows of recording pulses with amplitudes in the desired interval. The pulse from the output of the circuit is applied through a divider to the input of the automatic recording voltmeter. The load at the circuit output should not exceed 60 pulses/min.

In playback of pulses recorded on magnetic tape there are obtained pulses with a very long rise time. Such pulses cannot be analyzed by means of conventional analyzers. Hence, for playback the pulses from the tape recorder are

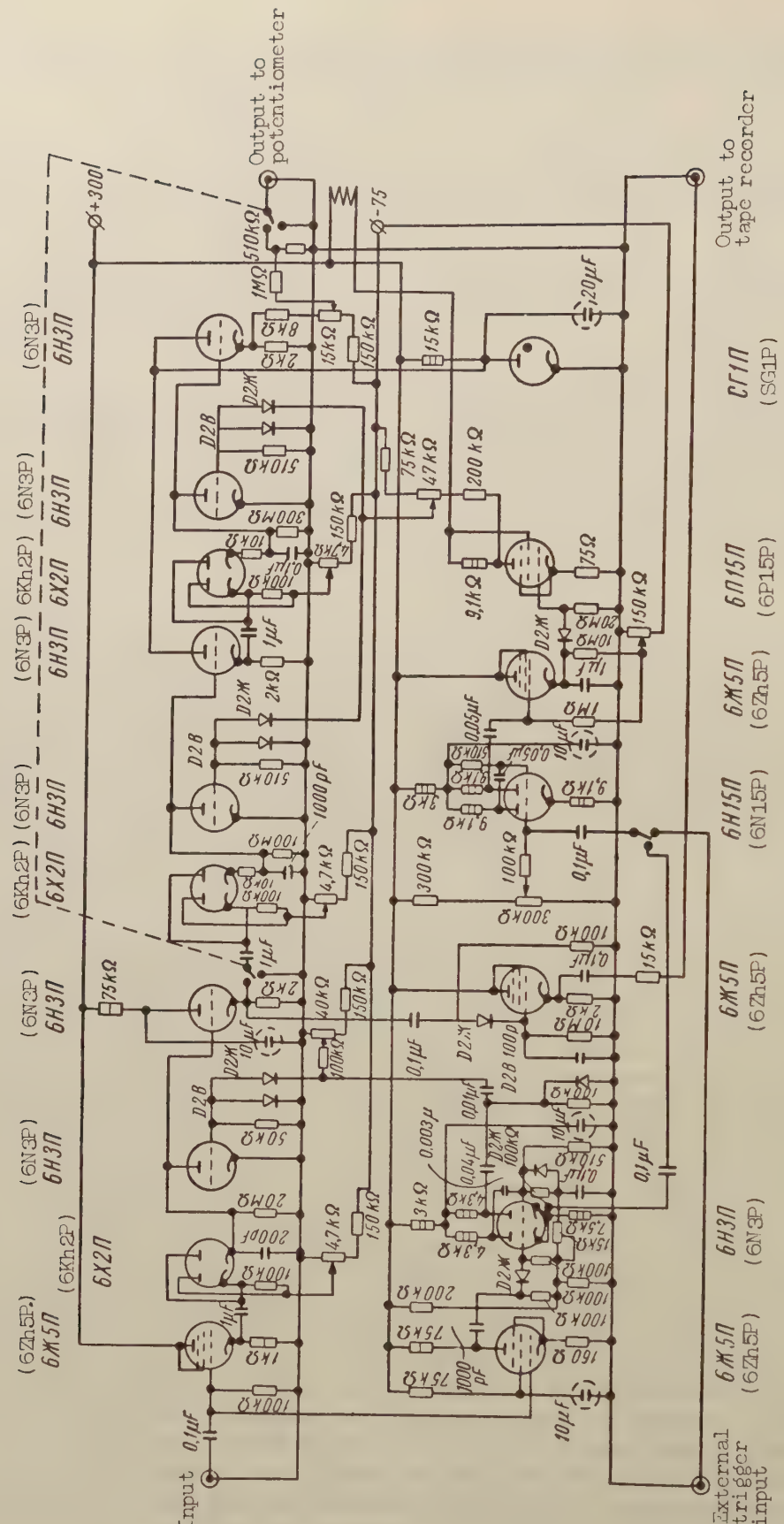

Fig.1. Circuit of pulse stretching unit.

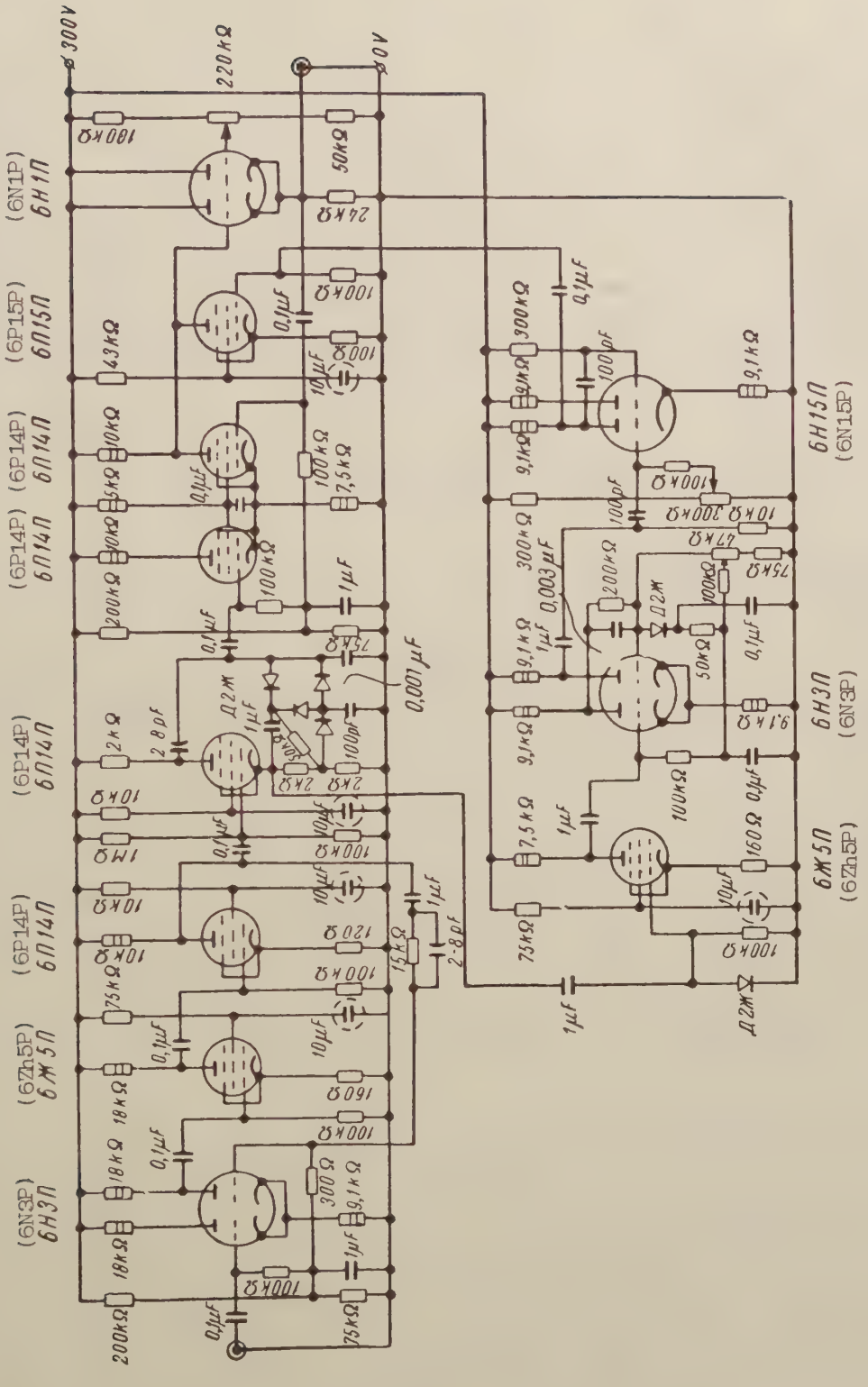

Fig.2. Circuit of pulse converter.

amplified and enter the converter unit, which is diagramed in Fig.2. In the converter unit the input pulse is fed into the shaping circuit; at the output from this stage there is obtained a pulse with a flat top and a duration equal to half the width of the input pulse. Parallel to this stage the input pulse is differentiated and after amplification applied to the trigger. The trigger is tripped at the instant when the input pulse passes through its maximum value. For greater stability the circuit incorporates two triggers, the first of which is a Schmitt type trigger. The differentiated pulse from the first trigger trips the second one. The duration of the pulse from the second trigger is equal to the duration of the signal at the output of the circuit.

Next, the pulse goes through a gating circuit, which is opened by the pulse from the trigger. Since the pulse from the trigger begins when the input pulse has already attained its maximum amplitude and ends before the pulse at the output of the stretching circuit has begun to drop off, there is obtained at the output of the gating circuit a square pulse with an amplitude proportional to the amplitude of the input signal and a length equal to the duration of the trigger pulse.

Since the pulses at the tape recorder output have an appreciable length, the load on the recorder in recording should not exceed 100 pulses/sec.

The described circuit allows of simultaneous recording of the pulses by means of the tape recorder and the automatic recording potentiometer.

"V.G.Khlopin" Radium Institute,
Academy of Sciences of the USSR

References

A.F.Ioffe, Primenenie magnitnoi zapisi (Applications of magnetic recording), M.-L., 1959.

CONCERNING THE MEAN CHARGE OF IONS PASSING THROUGH MATTER

- I.S.Dmitriev, V.S.Nikolaev, L.N.Fateeva & Ya.A.Teplova

Introduction

Determination of the equilibrium charge distribution and the cross section for electron loss and attachment by multicharged ions is important in connection with a number of different practical and theoretical problems. In particular, in some nuclear spectroscopy studies use is made of the mean ion energy loss, which depends on the mean charge. The mean ion charge is determined from the equilibrium charge distribution arrived at as a result of loss and attachment of electrons by the ions moving through the medium. The mean charge $\bar{i}$ of multicharged atoms differs substantially from the nuclear charge Z.[1,2]

In the present report we give the result of experimental investigations of the equilibrium charge distribution of the ions of light elements with Z from 2 to 18 and Kr ions in helium, nitrogen, argon, krypton and celluloid film, together with some results of measurements of the charge exchange cross section of these atoms in gases.

Experimental procedure

The source of fast multicharged ions was a 72 cm cyclotron.[3] The ion beam extracted from the accelerator was focused at a distance of about 8 meters from the cyclotron. Near the focus the beam was defined by two slits 1 (Fig.1) with a width up to 1 cm. To obtain ions with different charges a thin celluloid film 2 of thickness ~2 $\mu g/cm^2$ was inserted in the path of the beam near the first slit. As a result of loss and attachment of electrons during passage through the celluloid film there were formed from the initial ions with charge i ions with charges $i \pm 1$, $i \pm 2$, etc. The ions with a given charge were deflected by the analyzing magnet H_1 into the charge exchange chamber K, into which a uniform flow of the investigated gas was maintained. The ends of the chamber were delimited by channels 3 with cross section 2 x 5 and a length of about 30 mm; these constricting channels allowed of maintaining a pressure differential of up to 1 to 60 between the exchange chamber and the neighboring volumes. For measurements of the equilibrium charge distribution in the gases another channel (4) of cross section 7 x x 0.7 mm and length 310 mm was installed in the chamber along the path of the beam. The average pressure in this channel was maintained at the level necessary for attainment of equilibrium charge distribution in the beam. For determining the equilibrium charge distribution in passage of the ions through celluloid film channel 4 was replaced by one or two celluloid films 5 with a thickness of 2-5 $\mu g/cm^2$.

For investigating the charge distribution of the ions after their passage through the charge exchange chamber we used a second analyzing magnet (H_2). The ions were detected by proportional counters (6).

Each measurement was repeated 2 or 3 times. In most cases the difference between the results of individual measurements was small and the measurement error was assumed to be equal to the statistical uncertainty. The error in measuring the relative quantity Φ_i of ions with charge i in most cases was equal to $A/\sqrt{\Phi_i}\%$, where for ions with $Z \leqslant 10$ the coefficient $A \approx 0.4$, while for ions with $Z > 10$, $A \approx 1$. The mean charge $\bar{i}$ was determined with an accuracy of 1%.

The ion velocity before the target 2 was determined from the strength of the field produced by the focusing magnet, which was calibrated with reference to protons, deuterons and α-particles of different energies accelerated in the cyclotron. For these measurements we changed the field of the first analyzing

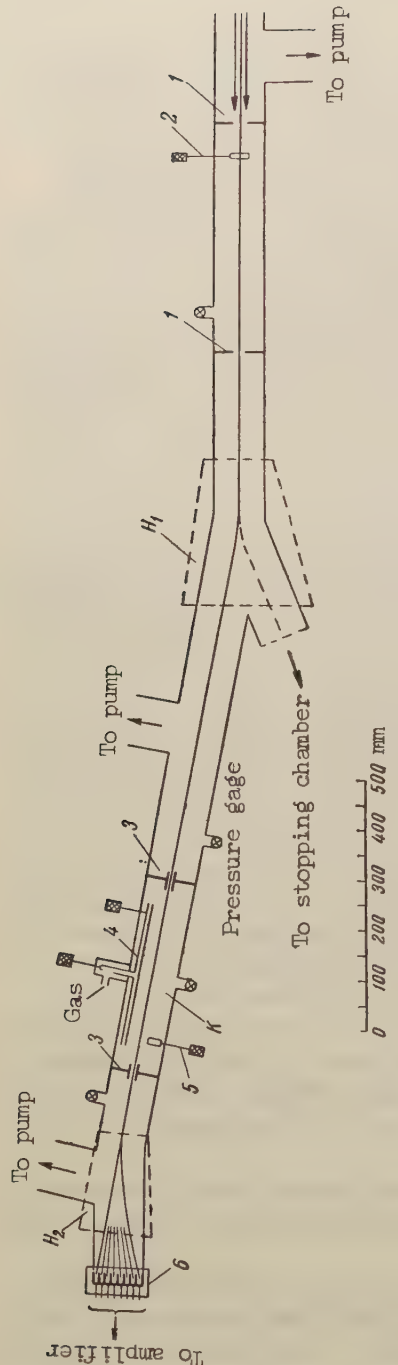

Fig.1. Diagram of the experiment.

magnet H_1 and thus directed the beam into the stopping chamber, described in Ref.2. The velocities of these particles were determined from their ranges in air and in nuclear emulsions, making use of the range-energy curves given in Refs.4 and 5. The uncertainty in determining the particle velocities did not exceed 2%. In the final result we took account of the decrease in the velocity of the particles incident to passing through the celluloid film or gas layer.

Measurement results

Measurements of the equilibrium charge distribution for ions with $Z \leqslant 10$ were carried out in the velocity range from $2.6 \cdot 10^{-18}$ to $12 \cdot 10^{-8}$ cm/sec in helium, nitrogen, argon, krypton and the celluloid film. The measurements for B, N and Ne ions in argon and Li, B and Ne ions in celluloid agreed within the limits of the experimental error with the results of our earlier investigation[1]. As indicated in this earlier investigation, the charge distribution for ions with Z from 3 to 10 is nearly Gaussian. For every ion the charge distribution width σ in the indicated velocity interval and in the investigated substances is approximately the same. The mean values of σ for Li, B, N and Ne ions are approximately, 0.56, 0.68, 0.78 and 0.85, respectively. The variation of the degree of ionization $\bar{i}/Z$ with the ion velocity differs in different media. In Fig.2 this velocity dependence is given for Li and N ions in helium, nitrogen, argon, krypton and celluloid. In the $\bar{i}/Z \approx 0.2$-0.6 region the degree of ionization in the investigated gases can be approximated by a function (different for each gas) of the parameter $v \cdot Z^{-\alpha}$, where $\alpha \approx 0.45$. It is logical to expect a monotonic Z dependence of $\bar{i}/Z$ within any period of the Mendeleev table of elements. There is, however, no a priori justification in extending this dependence to a wider range of Z values. In connection with this we felt it would be of particular interest to investigate the regularities in the equilibrium distributions in a wider range of variation of Z. To this end we carried out measurements of the equilibrium charge distribution of ions with $Z > 10$ in helium, nitrogen, argon, krypton and celluloid film at ion velocities of $2.6 \cdot 10^8$ and $4.1 \cdot 10^8$ cm/sec.

The measurements showed that with increase of Z the mean charge $\bar{i}$ at a given ion velocity increases in all the investigated substances. The character of the Z dependences of $\bar{i}/Z$, however, differs in the gases as compared with the solids (celluloid).

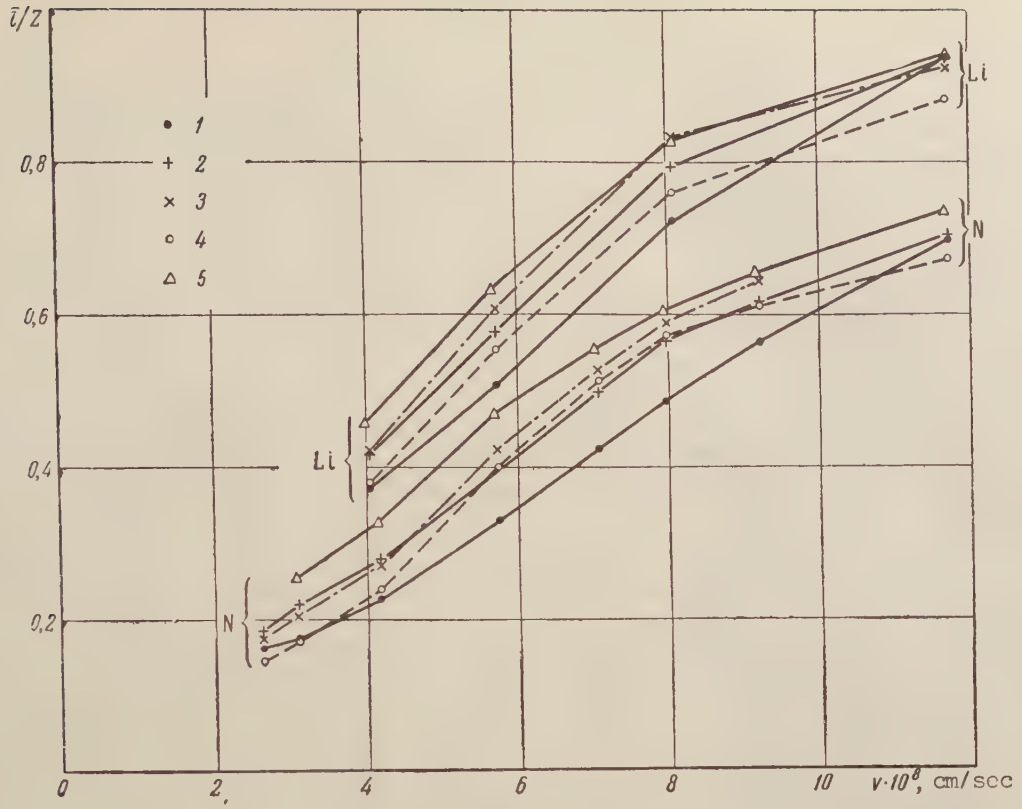

Fig.2. Variation of the degree of ionization of Li and N ions in 1) helium, 2) nitrogen, 3) argon, 4) krypton, 5) celluloid film as a function of the ion velocity.

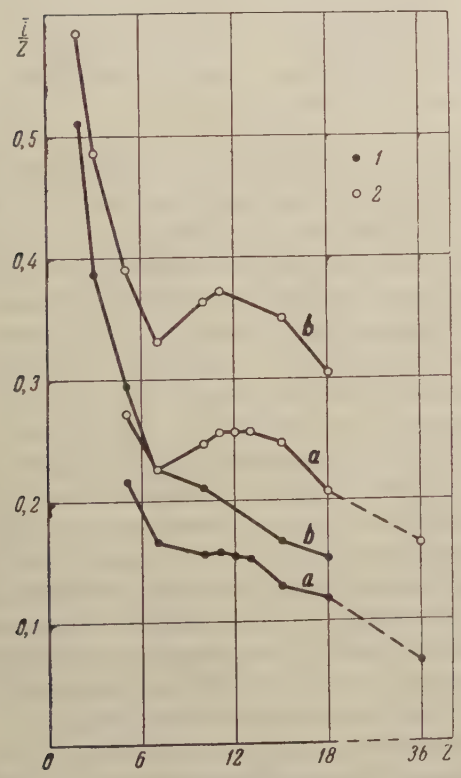

Fig.3. Z dependence of the degree of ionization $\bar{i}/Z$ in 1) helium and 2) celluloid film at ion velocities a) $v = 2.6 \cdot 10^8$ and b) $4.1 \cdot 10^8$ cm/sec.

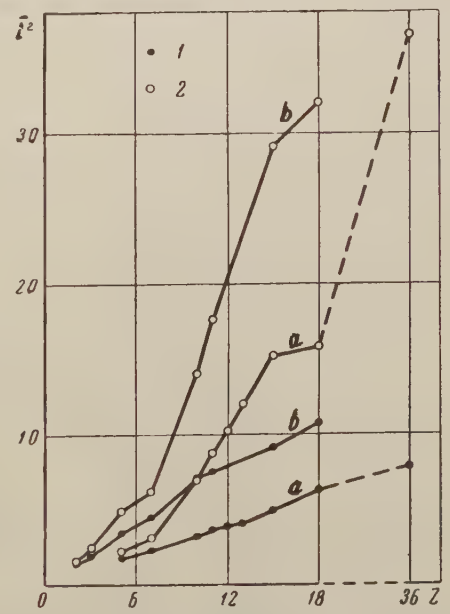

Fig.4. Z dependence of the mean square ion charge $\bar{i}^2$ in 1) nitrogen and 2) celluloid film at ion velocities a) $v = 2.6 \cdot 10^8$ and b) $4.1 \cdot 10^8$ cm/sec.

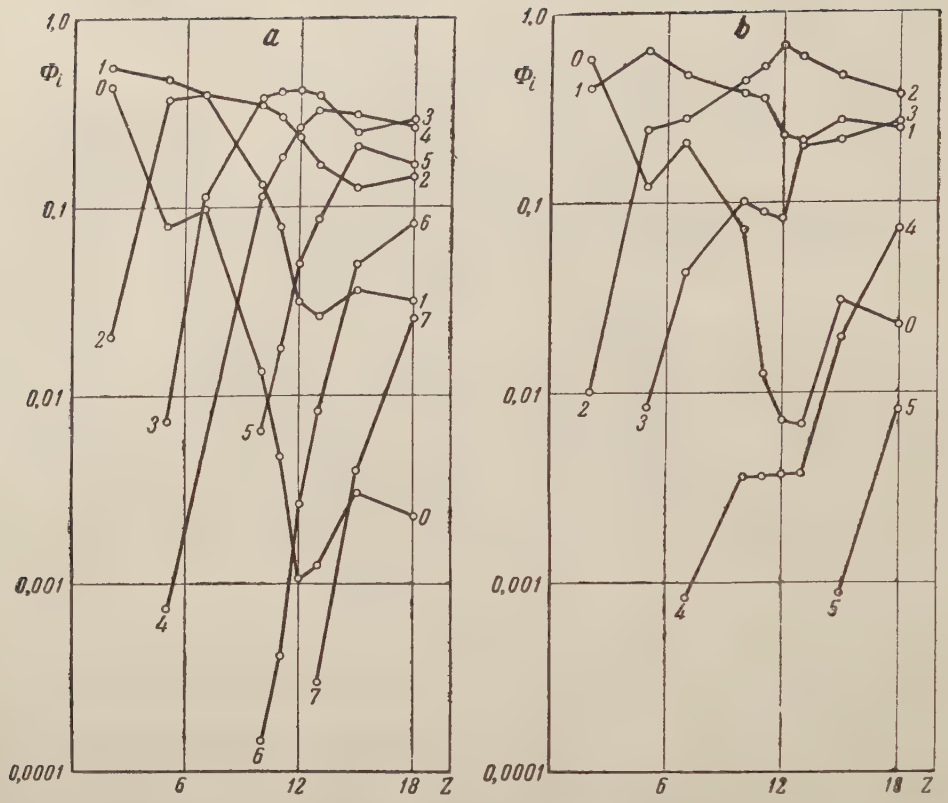

Fig.5. Z dependence of Φ_i: a) in celluloid film, b) in helium. The figures at the curves give the corresponding value of i; $v = 2.6 \cdot 10^8$ cm/sec.

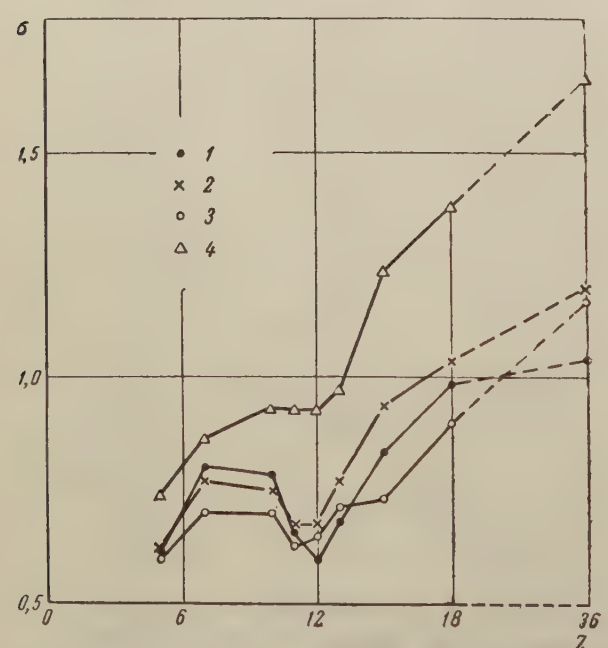

Fig.6. Z dependence of the equilibrium charge distribution width $\sigma = \sqrt{\bar{i}^2 - \bar{i}^2}$ in 1) helium, 2) nitrogen, 3) krypton and 4) celluloid film; $v = 2.6 \cdot 10^8$ cm/sec.

The Z dependences of $\bar{i}/Z$ in helium and celluloid at ion velocities of $2.6 \cdot 10^8$ and $4.1 \cdot 10^8$ cm/sec are shown in Fig.3. In gases the degree of ionization $\bar{i}/Z$ decreases monotonically with increase of Z. However, in the $Z \approx 11$-13 region the rate of decrease of $\bar{i}/Z$ with increase of Z slows down. In the solid (celluloid film) in this Z region there is observed a slight increase of $\bar{i}/Z$. These regularities are also evinced in the variation of the mean square charge $\bar{i}^2 = \Sigma i^2 i$, which is used for calculation of the mean energy loss.[2] Fig.4 shows the variation of $\bar{i}^2$ with Z in nitrogen and in celluloid film at $v = 2.6 \cdot 10^8$ and $4.1 \cdot 10^8$ cm/sec. In connection with this if we represent $\bar{i}/Z$ in the given gas in the form of a function of $v \cdot Z^{-\alpha}$, α will no longer be a constant; for $Z \approx 10$-12, $\alpha \approx 0$, while for $Z \approx 13$-18, $\alpha \approx 0.6$.

Even sharper deviations in the $Z \approx 11$-13 region are observed for the

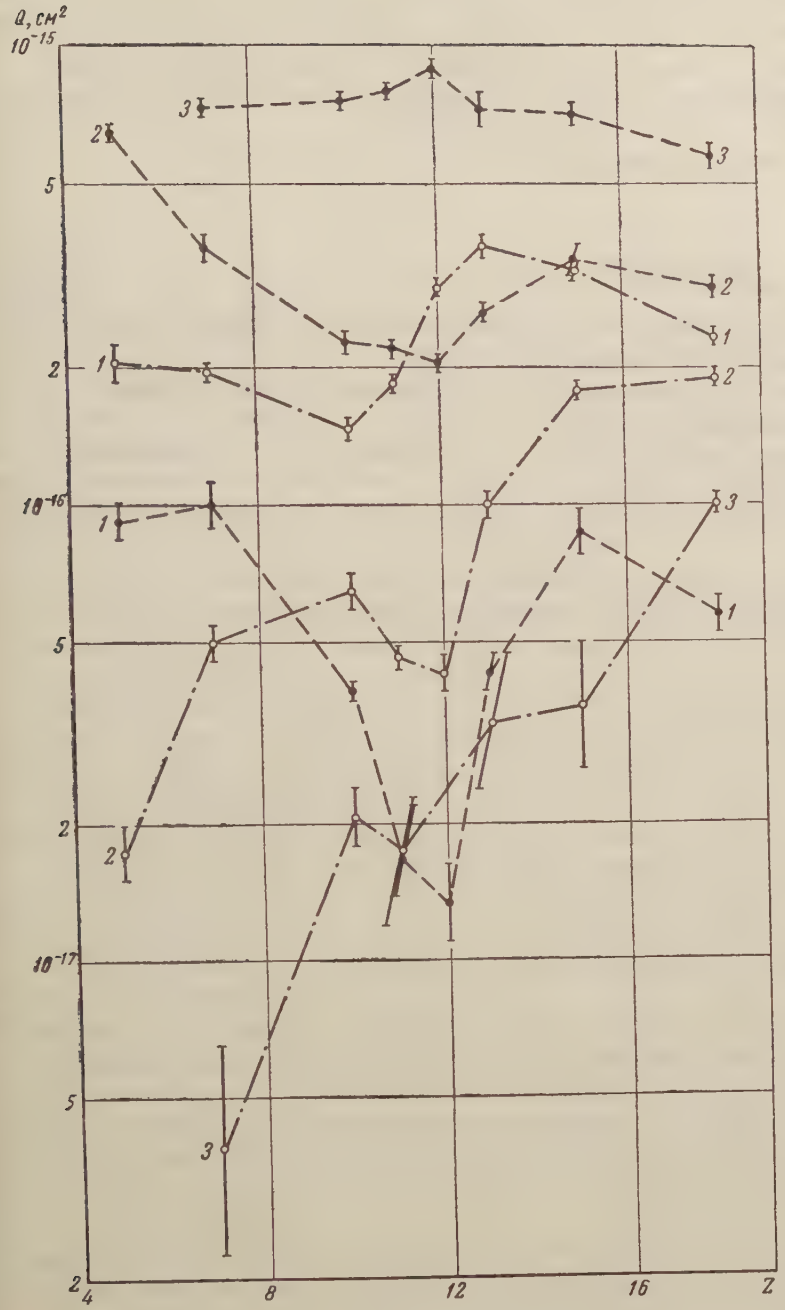

Fig.7. Variation of the electron loss (o) and attachment (•) as a function of the nuclear charge Z of the ion in nitrogen at an ion velocity of $2.6 \cdot 10^8$ cm/sec The figures at the curves indicate the values of the ion charge i.

values of Φ_i, the relative number of ions in the beam with the given charge i. In all media the curves for Φ_0 and Φ_1 exhibit a pronounced minimum in the vicinity of Z = 12. With increase of i these dips in the Z = 12 region become weaker (see, for example, Fig.5). The minima in the Φ_0 and Φ_1 curves and the slowing down of the rate of growth of Φ_3 and Φ_4 in gases with increase of Z in the vicinity of Z = 12 indicates a decrease of the distribution width σ. As will be evident from Fig.6, the value of σ for Mg ions (Z = 12) has a minimum value. For Z > 10 the distribution width in solids begins to increase substantially as compared with the width in gases. This difference attains 40 and 50% for A and Kr ions, respectively.

The deviation from smooth variation of $\bar{i}$ and Φ_i with Z in the Z = 11-13 region is due to the fact that the third electron shell begins to fill in this Z region. It should be noted that in gases the deviation is evinced most strongly in the value of the distribution width σ, while in solids it is evinced in the value of the mean charge $\bar{i}$ and, consequently, in the magnitude of the average energy loss.

The equilibrium charge distribution in an ion beam depends on the electron loss and attachment cross sections, Q_n and Q_3, respectively. Measurements of these cross sections showed that the Z dependences of Q_n and Q_3 are not monotonic (Fig.7). The electron loss and attachment cross sections have a minimum in the Z = 10-12 region, and the depth of the minimum depends on the ion charge i. The minimum of Q_n can be explained by the fact that in this region the electron binding energy attains a maximum value, while the minimum of Q_3 can be attributed to the fact that in this region the ionic dimensions are minimal and the binding energy of

the attached electron attains the lowest value.

The results obtained indicate the importance of taking into account the influence of the periodic structure of the electron shells of ions on the values of $\overline{i}$ and $\overline{i^2}$ that are used in calculating the mean energy losses of ions in matter.

Scientific-Research Institute of Nuclear Physics,
Moscow State University

References

1. V.S.Nikolaev, I.S.Dmitriev, L.N.Fateeva & Ya.A.Teplova,, Zhur.eksp.i toer.fiz., 33, 1325 (1957). (Trans.Soviet Physics - JETP.)

2. Ya.A.Teplova, V.S.Nikolaev, I.S.Dmitriev & L.N.Fateeva, Izv.AN SSSR, Ser.fiz., 23, 894 (1959). (Trans.Bulletin, 23, 883.)

3. V.S.Nikolaev, I.S.Dmitriev, Ya.A.Teplova & L.N.Fateeva, in "Uskoriteli" (Accelerators - Collected articles), M., 1960.

4. E.Segre (editor), Experimental and Nuclear Physics, N.Y., 1953. (Cited in Russian trans.)

5. M.Boghardt & L.Vigneron, in "Fotograficheskii metod v yadernoi fizike" (The photographic method in nuclear physics - Collected articles), M. 1952.

Bulletin of the Academy of Sciences of the USSR - Physical Series
Vol.24, No.9 - Sept.1960

Transactions of the Tenth All-Union Conference on Nuclear Spectroscopy
(Continued from Vol.24, Nos.3 & 7;
to be continued in Vol.24, No.12 & Vol.25, No.1)

TABLE OF CONTENTS

	Page Orig.	Trans.
Present state of beta-decay theory - V.A.Lyubimov	1021	1031
Investigation of the fine structure of alpha-radiation from U^{234} and U235 - S.A.Baranov, A.G.Zelenkov & V.M.Kulakov	1035	1045
The Auger effect - M.A.Listengarten	1041	1050
Influence of magnetic fields on resonance absorption of gamma-rays - V.A.Lyubimov & A.I.Alikhanov	1076	1084
New iridium and platinum isotopes: Ir^{184} and Pt^{187} - V.I.Baranov, K.Ya.Gromov, B.S.Dzhelepov, Zyong Chong Bai, T.V.Malysheva, V.A.Morozov, B.A.Khotin & V.G.Chumin	1079	1086
On the existence of isomeric states of Te^{119} - N.G.Zaitseva, M.Ya.Kuznetsova, I.Yu.Levenberg, V.N.Pokrovskii & V.A.Khalkin	1083	1090
Operation of an ionization alpha-spectrometer under heavy loads - A.A.Vorob'ev & V.A.Korolev	1086	1093
Investigation of alpha-decay of U^{235} by means of an ionization alpha-spectrometer - A.A.Vorob'ev, A.P.Komar & V.A.Korolev	1092	1099
Decay scheme for Eu^{147} - Yu.A.Aleksandrov, Yu.A.Nemilov, M.K. Nikitin & Sh.Piskorzh	1099	1105
Concerning the $Yb^{164} \rightarrow Tm^{164} \rightarrow Er^{164}$ decay chain - B.Dalkhsuren, I.Yu.Levenberg, A.N.Murin, Yu.V.Norseev, V.P.Pokrovskii & I.A.Yutlandov	1105	1109
Investigation of new neutron-deficient platinum isotopes - T.V.Malysheva, B.A.Khotin, A.K.Lavrukhina, L.N.Kryukova & V.V.Murav'eva	1109	1113
Neutron-deficient isotopes of rare earth elements of the cerium group (Spallation products of europium bombarded with 660 Mev protons) - A.K.Lavrukhina, G.M.Kolesov & Tan Syao-en	1113	1117
Investigation of the neutron-deficient isotopes of osmium - Yu.A.Surkov, G.M.Chernov, A.K.Lavrukhina & Z.V.Khromchenko	1119	1123
Beta-gamma angular correlation in the decay of La^{140} and Ce^{141} - V.P.Rudakov	1124	1128
Conversion electron spectrum of the dysprosium fraction from the spallation products of tantalum - A.A.Abdurazakov, K. Ya.Gromov, B.S.Dzhelepov & G.Ya.Umarov	1126	1130
Disintegration of Nd^{140} and Pr^{140} - E.I.Biryukov, O.I.Grigor'ev, B.S.Kuznetsov & N.S.Shimanskaya	1135	1138
Possibility of utilizing the (n,2n) reaction in nuclear spectroscopy - V.V.Komarov, A.B.Kurepin & A.M.Popova	1145	1147
Energy states of Be^{8} in the disintegration of C^{12} into three alpha-particles under bombardment with protons and neutrons - S.S.Vasil'ev. V.V.Komarov & A.M.Popova	1149	1151
Investigation of the energy distributions of the products of nuclear reactions involving emission of several particles - V.V.Komarov & A.M.Popova	1153	1154

Double-focusing magnetic spectrometer - N.G.Afanas'ev 1157 1158
Recording photomultiplier pulses by means of a tape recorder and an automatic recording voltmeter - A.N.Silant'ev 1165 1165
Concerning the mean charge of ions passing through matter - I.S.Dmitriev, V.S.Nikolaev, L.N.Fateeva & Ya.A.Teplova 1169 1169

Translated in 1961 by
Columbia Technical Translations
5 Vermont Ave., White Plains, N.Y.

Number 10 Volume 24 1960

BULLETIN

of the

ACADEMY OF SCIENCES OF THE USSR

— PHYSICAL SERIES —

(Izvestiya Akademii Nauk SSSR)
(Seriya fizicheskaya)

Reproduction rights reserved
by
Columbia Technical Translations
5 Vermont Avenue
White Plains, New York

Single Issues
$20

Annual Subscription
$215

Transactions

of the

Third Conference on Ferroelectricity

(Moscow, 25-30 April 1960)

(To be continued in Vol.24, No.11)

Lithoprinted in U.S.A.
EDWARDS BROTHERS, INC.
Ann Arbor, Michigan

CONTRIBUTION TO THE STATISTICAL THEORY OF FERRO- AND ANTIFERROELECTRICS

- V.I.Klyachkin

With a view to obviating the shortcomings of model theories[1-4] which utilize the inadequate formalism of Boltzmann's gas statistics for investigating crystals, we attempt in the present contribution to study the physical attributes of phase transitions in ferroelectrics by means of the statistical method of Bogolyubov[5]. We shall treat these transitions as effects of statistical ordering in ionic displacement space. In our opinion Bogolyubov's method of partial functions based on the dynamical principles of Gibbs' statistics should make it possible to circumvent the difficulties inherent in the model approach and provide a means for relating the familiar thermodynamic equations of the general theory of phase transition with the structure of crystals.

We start with the following physical picture of the thermal motion of ions in a crystal in the temperature region near the phase transition point, and we shall restrict our consideration to ferroelectrics with the perovskite structure (the most thoroughly studied representative of this group is barium titanate). The states corresponding to temperatures above and below θ differ as regards the type of stable crystal structure: in the $T > \theta$ region the structure is cubic, while in the $T < \theta$ region the structure is tetragonal, sometimes (for antiferroelectrics) with superstructure.

In the cubic region the ions execute harmonic (or anharmonic) oscillations about the lattice sites in a potential field having cubic symmetry. As is known from the theory of lattices, the system can be represented in the form of a conjunction of independent harmonic oscillators with a set of intrinsic frequencies ν_i (for anharmonic oscillations the different oscillators are energetically coupled). The vibration spectrum of the system is wholly determined by the character of the bonds between the ions comprising this structure. In the $T < \theta$ region, where the structure becomes tetragonal, the vibration spectrum of the system changes owing to alteration of the intrinsic frequencies ν_i. In the region of the phase transition, i.e., at $T \approx \theta$, however, the structure becomes "loose" and unstable; this means that individual ions acquire the possibility of shifting from their equilibrium positions. In this "loose" structure the equilibrium centers about which the ions oscillate are no longer characterized by the regularity of the normal cubic or tetragonal structure.

Using the initial stable cubic structure at $T > \theta$ as the point of departure, we can describe the thermal motion in the $T \approx \theta$ region if we assume that each ion is displaced a certain distance $\vec{\rho}$ from the initial site of the cubic lattice and oscillates with a certain frequency about the new displaced center.

Inasmuch as our problem does not include investigation of the spectrum of oscillations of the ions relative to the displaced positions of equilibrium, we will not introduce normal coordinates, the use of which is expedient and justified in constructing a dynamic theory based on analytic solution of the equations of motion. For developing the statistical theory under consideration, introduction of normal coordinates is not necessary inasmuch as all the mean values of interest to us are obviously invariant under canonical transformation of the coordinates. Moreover, from the standpoint of procedure it is of interest to derive equations that will allow of determining the mean values without recourse to the condition that the ionic displacements are small relative to the lattice constants. It is not clear to what extent this condition, which is fundamental to the introduction of normal coordinates, will be fulfilled in the region of the phase transition, where the structure is "loose" and unstable.

Our problem will be investigation of the process of statistical ordering of the ionic displacements and the resultant appearance of a new type of crystal

structure in the region below the Curie point.

Where ferroelectrics of the perovskite type are concerned this ordering means that at $T < \theta$ the displaced centers of oscillation of the ions will acquire an order corresponding to the tetragonal structure.

Bearing in mind the above considerations let us consider the distribution of ionic displacement from the standpoint of the statistical method of Bogolyubov. We note that inasmuch as displacement of an ion from the initial position is equivalent to the appearance of a dipole with moment $\vec{\mu} = z^* e \vec{\rho}$ ($z^* e$ is the effective charge), we can speak of the transition to the tetragonal state as an effect of statistical ordering of the dipoles. As a result of this ordering, obviously, the average projection of the dipole moment $\vec{\mu}$ on any crystallographic axis and, consequently, the average projection of the ionic displacement $\langle \vec{\rho} \rangle$ will be nonzero. In contrast to the familiar case of a Langevin dipole gas, where the averaging is carried out only over different directions of the rigid dipole, here the averaging must also be carried out over its magnitude, i.e., over all three coordinates of the displaced ion.

This treatment gives us the right, in using the formalism of classical statistics for calculating the average values, to choose as our configuration space the space of the ionic displacements $\vec{\rho}$ (or, what is the same thing, the space of the dipole moments $\vec{\mu}$ connected with the ionic displacements).

We now introduce into our chosen configuration space, following Bogolyubov[5,6], the sequence of distribution functions $F_1(\vec{\rho})$, $F_2(\vec{\rho}_1, \vec{\rho}_2) \ldots F_s(\vec{\rho}_1 \ldots \vec{\rho}_s)$. These functions describe the probabilities that ions 1,2,3,...s will be displaced vector distances $\vec{\rho}_1, \vec{\rho}_2 \ldots \vec{\rho}_s$ from their initial equilibrium positions.

Now following the usual procedure, we can construct a set of integro-differential equations relating the successive distribution functions:

$$DF_s = LF_{s+1} \ldots, \tag{1}$$

where the D and L are differential and integral operators, respectively.

If we are interested in the mean value of the ionic displacement in some direction $\langle x_\alpha \rangle$, in order to calculate it we must know the first order distribution function $F_1(\vec{\rho})$, related by Eq.(1) with the function $F_2(\vec{\rho}_1, \vec{\rho}_2)$. Making use of the procedure developed in Ref.6 for solving this problem, one can obtain the initial equations and establish the conditions for determining the Curie temperature for ferro- and antiferroelectrics.

Below we give the results of investigation of the physical properties of the ferro- and antiferroelectric states based on analysis of one particular form of the equations deduced in Ref.6, corresponding to the case of one ordering crystallographic sublattice of the total number of five comprised in the perovskite structure. To do this one must first determine the potential energy of the ion in the displaced position by solving Eq.(3) of Ref.6. One must expand the ionic pair interaction energy $U^{pq}_{ikjl}(\vec{\rho}, \vec{\rho}')$ in a series in relative displacement of the ion pairs (ikp) and (jeq), where i and j are the numbers of the ions in the given chemical sublattice, k and l are the indices of the chemical sublattice, and p and q are the indices of the superstructure sublattices into which the chemical lattice is subdivided. Carrying out the expansion to fourth order terms, we obtain (taking into account the external electric field E_α):

$$W^p_k = W_\Gamma + W_{A\Gamma} = \sum_\alpha \xi^k_\alpha x^2_\alpha - 2 \sum_\alpha \sum_q \left[\xi^{kp,kq}_\alpha \langle x_\alpha \rangle^q_k + \frac{1}{2} q_k E_\alpha \right] x_\alpha + \sum_\alpha \sum_\beta \varepsilon^k_{\alpha\beta} x^2_\alpha x^2_\beta \ldots, \tag{2}$$

wherein

$$F_k^p(\vec{\rho}) = \lambda_k^p \exp - \frac{W_k^p(\vec{\rho})}{kT}\ ;\ (\lambda_k^p)^{-1} = \frac{1}{V_k}\int \exp - \frac{W_k^p(\vec{\rho})}{kT}\, d\vec{\rho}. \qquad (2a)$$

The coefficients ξ_α^k, $\xi_\alpha^{kp,kq}$ and $\varepsilon_{\alpha\beta}^k$ are structural sums determined, respectively, through the second and fourth, derivatives of the energy U_{ikjl}^{pq} with respect to the coordinates of the displaced ion.

Now we can determine the mean values of the displacements $\langle x_\alpha \rangle$, $\langle x_\alpha^2 \rangle$, etc., using an expansion in powers of the anharmonic term in the energy $W_k^p(\vec{\rho})$.

We will not give the specific expressions for the mean values of these quantities, but will give only the principal results of calculations.

1. Using the expressions for the Curie points of ferro- and antiferroelectrics (see Eq.(10) in Ref.6) and determining $\langle x_\alpha^2 \rangle$, we obtain the following dynamic criterion for the existence of ferro- and antiferroelectricity:

$$\xi_{\alpha s}^{kk} > \xi_\alpha^k;\quad \xi_{\alpha a}^{kk} > \xi_\alpha^k;\quad \xi_\alpha^k > 0, \qquad (3)$$

where the $\xi_{\alpha s}^{kk}$ and $\xi_{\alpha a}^{kk}$ are the elastic coefficients for the ferro- and antiferroelectric configuration of a shifting sublattice of type k (see Eq.(10a) in Ref.6), and the ξ_α^k are the corresponding elastic coefficients of the same lattice associated with the effects of interaction with all the other lattices in the structure. Obviously, inequalities (3) are fulfilled on condition of strong compensation of the positive and negative contributions to the magnitude of ξ_α^k.

2. Calculation of the mean displacement $\langle x_\alpha \rangle$ leads to the following expressions (for $E_\alpha = 0$):

$$\left.\begin{aligned} \langle x_\alpha \rangle^2 &= A_s(\theta_s - T) \\ \langle x_\alpha \rangle^2 &= A_a(\theta_a - T). \end{aligned}\right\} \qquad (4)$$

for a ferro- or antiferroelectric (second order phase transition).

3. The dielectric susceptibility, connected with the ionic displacements for each configuration determined in the usual manner proved to be identical with that given by the thermodynamic equations of Ginzburg[7] and Kittel[8]:

$$\varkappa_{i_\alpha}^k = C_k/(T - \theta_s);\ T > \theta_s;\ \varkappa_{i_\alpha}^k = \frac{1}{2} C_k/(\theta_s - T);\ T < \theta_s \qquad (5)$$

for a ferroelectric, and

$$\varkappa_{i_\alpha}^k = [a_k + b_k(T - \theta_a)]^{-1};\ T > \theta_a;\ \varkappa_{i\alpha}^k = [a_k + 2b_k(\theta_a - T)]^{-1};\ T < \theta_a \qquad (6)$$

for an antiferroelectric.

4. Investigation of the heat capacity discontinuity showed that in the given approximation there obtains the equality

$$\Delta C_{V_s} = \Delta C_{V_a}. \qquad (7)$$

5. Investigation of the relative stability of the ferro- and antiferroelectric configurations gives reason to infer that

$$\Phi_s > \Phi_a \quad \text{for} \quad \theta_a > \theta_s$$

and

$$\Phi_s < \Phi_a \quad \text{for} \quad \theta_a < \theta_s,$$

(Φ is the thermodynamic potential), i.e., the state with the higher Curie temperature is more advantageous.

The structural coefficients entering into Eqs.(3)-(8) can be determined if one knows the law governing the pair interaction of the two ions in the displaced position as a function of the relative displacements.

More detailed results of numerical calculations for the specific case of $BaTiO_3$ are given in Ref.9, where on the basis of comparison with experiments we established the shortcomings of the approximation involving one displaced lattice and show that use of the concept of two or more shifting sublattices one can obtain quantitative agreement between theory and experiment for barium titanate.

I desire to express my gratitude to G.A.Smolenskii for constant interest in the work.

References

1. J.C.Slater, Phys.Rev., 78, 748 (1950).
2. A.F.Devonshire, Phil.Mag., 40, 1040 (1949).
3. V.Tikagi, Proc.Int.Conf.of Theor.Phys., 824, Tokyo (1954).
4. G.A.Smolenskii & V.Kh.Kozlovskii, Zhur.tekh.fiz., 33, 445 (1953).
5. N.N.Bogolyubov, Problemy dinamicheskoi teorii v staticheskoi fizike (Problems of dynamic theory in static physics), M.-L., 1946.
6. V.I.Klyachkin, Fizika tverdogo tela, 1, 1874 (1959). (Trans.Soviet Physics - Solid State.)
7. V.L.Ginzburg, Zhur.eksp.i teor.fiz., 15, 739 (1945).
8. C.Kittel, Phys.Rev., 82, 729 (1951).
9. V.I.Klyachkin, Fizika tverdogo tela, 3, No.1 (1961). (Trans.Soviet Physics - Solid State.)

CONTRIBUTION TO THE THERMODYNAMIC THEORY OF FERROELECTRICITY

- V.L.Indenbom

Using the results of Landau's[1] theory of second order phase transitions, Ginzburg[2] investigated ferroelectric phase transitions by expansion of the thermodynamic potential in even powers of the components of the polarization vector $\vec{P}$:

$$\Phi(\vec{P}) = \Phi_0 + \alpha_{ij} P_i P_j + \beta_{ijkl} P_i P_j P_k P_l + \ldots \qquad (1)$$

It is found that a crystal may undergo either second or first order transitions, depending on the temperature variation of the coefficient in expansion (1).

It must be noted, however, that an expansion of type (1) appears in the theory of Landau only after there are excluded from consideration all the variants for which the symmetry of the crystal forbids second order phase transitions. If we are interested in all possible types of ferroelectric phase transitions, we cannot reject these variants and limit the consideration to expansion (1). Moreover, as was noted earlier by the writer[3], the fundamental assumption of the thermodynamic theory of ferroelectricity to the effect that the polarization is an auxiliary parameter describing phase transitions, cannot be applied to many ferroelectric phase transitions, among them all transitions involving a change in the number of atoms per unit cell.

Let us consider in detail the two types of ferroelectric phase transitions not covered by the usual theory.

1. Ferroelectric phase transitions for which the polarization is a parameter

First, let us particularize Landau's theory for the case when components of the polarization vector P_i serve as parameters determining the change in the crystal symmetry in the transition. Particular cases in Landau's theory can arise only when the components of P_i transform through each other as a result of a symmetry operation for the given crystal class (i.e., transform according to the multidimensional irreducible representation of point group symmetry). These cases are exemplified by cubic crystals (P_x, P_y and P_z transform in the general three dimensional representation) and uniaxial crystals P_x and P_y transform in the general two dimensional representation). Ferroelectric transitions in biaxial crystals and transitions in uniaxial crystals with appearance of polarization along the axis do not give rise to any complications.

For the symmetry of the crystal to allow a second order ferroelectric phase transition the following two conditions must be satisfied:

1) the state of the crystal at the transition point must be stable; hence the expansion of the thermodynamic potential Φ in terms of P_i must not contain third order invariants (composed of the components P_x, P_y and P_z for cubic or of the components P_x and P_y for uniaxial crystals);

2) the transition must result in a uniform and not in a laminar crystal; hence in the expansion of Φ there must not be present invariants of the type

$$\left(P_i \frac{\partial P_j}{\partial x_k} - P_j \frac{\partial P_i}{\partial x_k}\right).$$

For the sake of simplicity we will compose invariants of types 1) and 2) of all three components of the polarization vector. Then we need specifically investigate only cases when the symmetry of the paraelectric phase does not result in vanishing of all the components of two tensors of the third rank: a) symmetrical with regard to all indices, and b) antisymmetrical with regard to one pair

of indices. Below we list the invariants for all nonpyroelectric classes.

Invariant $P_xP_yP_z$ is allowed by classes D_2, D_{2d}, S_4, T and T_d. In class D_2 (biaxial crystals!) this invariant does not give rise to complications inasmuch as the transition is determined by one of the components of the polarization vector (for example, Rochelle salt). In class D_{2d} appearance of polarization in the basal plane gives rise to secondary polarization along the principal axis. In a second order transition P_x and P_y increase with decrease in temperature in proportion to $\sqrt{\theta - T}$, while P_z increases in proportion to $(\theta - T)$ (θ is the Curie point). The end of the spontaneous polarization vector with decreasing temperature will describe a parabola tangent to the basal plane. If the polarization appears along the principal axis (for example, KH_2PO_4) the invariant $P_xP_yP_z$ determines the behavior of the dielectric constant in the basal plane. Analogous effects should be observed in crystals of class S_4, which allows of invariants $P_xP_yP_z$ and $P_z(P_x^2 - P_y^2)$.

In classes T and T_d invariant $P_xP_yP_z$, as was noted earlier by the writer[4], forbids second order ferroelectric phase transitions. Owing to the asymmetry of the thermodynamic potential, a first order phase transition may have a number of distinctive characteristics as compared with the first order phase transition in barium titanate. Unfortunately, the only known example (boracite - class T_d) has not been adequately studied.

Invariant $P_x(3P_y^2 - P_x^2)$ is allowed by classes D_3, D_{3h} and C_{3h}. The last class (depending on choice of axes in the basal plane) also allows invariant $P_y(3P_x^2 - P_y^2)$. As a result in classes D_3, D_{3h} and C_{3h} second order ferroelectric phase transitions may occur only in case of appearance of polarization along the principal axis.

Invariant $\left(P_x\frac{\partial P_y}{\partial z} - P_y\frac{\partial P_x}{\partial z}\right)$ is allowed by classes D_3, D_4 and D_6. Hence in these classes second order ferroelectric phase transitions should be accompanied by the appearance of polarization along the principal axis. Upon the appearance of polarization in the basal plane, the crystal (inside the domains) may break up into layers parallel to the base.

Invariant $\vec{P}\cdot\mathrm{rot}\vec{P}$ is allowed by cubic classes T and O. As a result, in these classes second order phase transitions are forbidden, while first order ferroelectric phase transitions, accompanied by weak distortion of the lattice, may result in stratification of the crystal inside the domains.

Thus, among uniaxial nonpyroelectric crystals only crystals of classes C_{4h}, D_{4h}, S_6, D_{3d}, C_{6h} and D_{6h} and among cubic crystals only crystals of classes of T_h and O_h are satisfactorily described by expansion (1). For all other uniaxial and cubic crystals there must also be taken into account the above listed invariants. Having supplemented expansion (1) with these invariants, we obtain a complete set of all possible ferroelectric transitions for which polarization is a parameter.

2. Ferroelectric phase transitions for which polarization is not a transition parameter

From the fact that ferroelectric phase transitions lead to the appearance of spontaneous polarization it does not necessarily follow that the polarization is a parameter describing the transition. By way of example, we can cite the following second order phase transitions not involving a change in the number of atoms in the unit cell allowed by Landau's theory:

$$C_{3h}(E_u) \rightleftarrows C_1;\ D_{3h}(E'') \rightleftarrows C_2;\ D_{3h}(E'') \rightleftarrows C_s;\ T_d(F_1) \rightleftarrows C_3;\ C_{6h}(E_{1u}) \rightleftarrows C_2.$$

In the parentheses we give the representation in which the parameter describing the given transition is transformed and which describes the character of the change in symmetry of the crystal. The first four examples are ferromagnetic transitions. Here the parameter is the magnetization (in classes C_{3h} and D_{3h} - magnetization in the basal plane). Electric polarization appears as a secondary effect. With change in temperature the magnetization increases in proportion to $\sqrt{\theta - T}$, and the electric polarization increases in proportion to $(\theta - T)$. In the last example the polarization P_z appears as a third order effect with respect to asymmetry as a parameter and increases in proportion to $(\theta - T)^{3/2}$ (in contrast to the case of the transition $C_{6h}(A_u) \rightleftarrows C_6$, when $P_z \sim \sqrt{\theta - T}$).

If the pyroelectric phase appears as the result of a phase transition involving change in the number of atoms per unit cell, such a ferroelectric transition obviously cannot be described by means of the polarization vector since in this case it is clear that no vector or tensor quantity can serve as a transition parameter.[3] Consequently, in this case spontaneous polarization can only be a second (or higher) order effect.

By way of illustrative example, we can cite the second order ferroelectric transitions from phases with symmetry C_{4h}^6, investigated by Lyubarskii[5]. In addition to ordinary transitions connected with the appearance of polarization along the principal axis $(C_{4h}^6 \rightleftarrows C_4^6)$ and in the basal plane $(C_{4h}^6 \rightleftarrows C_s^4)$, the crystal symmetry also allows of $C_{4h}^6 \rightleftarrows C_4^2$ phase transitions with doubling of the volume of the unit cell. In this case, as can readily be shown, the polarization P_z is determined by a quadratic combination of parameters describing the transition and increases in proportion to $(\theta - T)$, and not in proportion to $\sqrt{\theta - T}$.

In all cases when the polarization is not a parameter of the ferroelectric transition, the transition occurs not to a higher subgroup of the initial space group allowing spontaneous polarization*, but to a subgroup of lower symmetry. Apparently more than half of all known ferroelectric transitions belong in this class, which is not encompassed by the ordinary theory of ferroelectricity. For describing such transitions one can use the theory developed earlier by the writer[3] if the number of atoms per unit cell remains the same. Otherwise for describing the transition one must have recourse to the concept of space groups.

Note added in proof:

At the conference, in the discussion following presentation of this report, there were cited a number of examples of temperature variation of the spontaneous polarization in apparent agreement with the developed theory. However, in our opinion the presented experimental data are in need of further checking and refinement. The writer is deeply grateful to V.A.Koptsikii for offering to undertake the appropriate experiments.

Institute of Crystallography,
Academy of Sciences of the USSR

---

*The condition for transition to a higher subgroup allowing spontaneous polarization is a consequence of the initial assumption of thermodynamic theory of ferroelectricity[2] to the effect that polarization is an auxiliary parameter describing the transition. The (and only this) consequence of the usual theory is sometimes utilized for constructing tables of "possible ferroelectric transitions".

References

1. L.D.Landau & E.M.Lifshits, Statisticheskaya fizika p.428, Pub.M.-L., 1951. (Trans.Statistical Physics.)

2. V.L.Ginzburg, Usp.fiz.nauk, 38, 490 (1949).

3. V.L.Indenbom, Kristallografiya, 5, 115 (1960). (Trans.Soviet Physics - Crystallography.)

4. L.D.Landau & E.M.Lifshits, Elektrodinamika sploshnykh sred (Electrodynamics of continuous media), p.121, M., 1957.

5. G.Ya.Lyubarskii, Teoriya grupp i ee primenenie v fizike, (Group theory and its applications in physics), p.122, M., 1958.

THERMODYNAMICS OF SOLID SOLUTIONS WITH FERROELECTRIC PROPERTIES

- V.G.Granovskii

Owing to the expanding engineering use of solid solutions with ferroelectric properties there is a growing interest in their theoretical investigation. In view of the success of the thermodynamic theory of single component ferroelectrics (such as $BaTiO_3$) an attempt was made to extend the results of this theory to solid solution ferroelectrics typified by barium titanate with isomorphic substances. In an earlier contribution[1] the writer deduced the solution-composition dependence of some of the coefficients in the expansion of the thermodynamic potential in powers of the polarization

$$\Phi = \Phi_0 + \alpha P^2 + \frac{1}{2}\beta P^4 + \frac{1}{3}\gamma P^6 + \ldots \qquad (1)$$

Considering a series of solid solutions having the same base material (for example, $BaTiO_3$), in the case of a first order phase transition the following expressions were obtained[1] for α and β (the temperature dependence of β was not taken into account):

$$\alpha = \alpha_{\theta_0}[1 + \xi a x(\eta a x + x - 2)] + \alpha'_{\theta_0}[T - \theta_0(1 - ax)], \qquad (2)$$

$$\beta = \beta_0 \sqrt{1 + \xi a x(\eta a x + x - 2)}, \qquad (3)$$

where a is a constant characterizing the chemical composition of the solid solution, x is the concentration, ξ and η are parameters which are constant for any given series of solid solutions, and $\theta_0 = \theta_{x=0}$ and $\beta_0 = \beta_{x=0}$. It is assumed here and below that transition from one phase to another occurs only when the first phase loses its stability.[2]

Making use of Eqs.(2) and (3), let us investigate the dependence of the shape of the hysteresis loop on the composition of the solid solution. The temperature intervals defined by Kholodenko[2] for barium titanate, taking into account the geometric shape of the hysteresis loop, as well as the coercive field strengths within these intervals, can be found by means of Eq.(2) for any solid solution. The temperature interval $T_{12} < T < 0.2(4\theta + T_{12})$ (T_{12} is the temperature of transition from the nonferroelectric to ferroelectric phase), within which, in contrast to the ordinary hysteresis loop, a unique relation obtains between the electric field and polarization for small values of polarization, and the temperature interval $\theta < T < 0.8\ (2.25\theta - T_{12})$ within which a "double" hysteresis loop obtains, are equally dependent on the composition of the solid solution. The width of these intervals, considering that $T_{12} = \theta - \frac{\alpha_\theta}{\alpha'_\theta}$ (Ref.2), is $0.8\ \frac{\alpha_{\theta_0}}{\alpha'_{\theta_0}}[1 + \xi a x(\eta a x + x - 2)]$, while the temperature interval $0.2(4\theta + T_{12}) < T < \theta$, wherein the hysteresis loop has an inflection point, is equal to $0.2\ \frac{\alpha_{\theta_0}}{\alpha'_{\theta_0}}[1 + \xi a x(\eta a x + x - 2)]$. For $a > 0$ as the concentration is increased to $x_m = \frac{1}{1+\eta a}$ the width of all the above intervals decreases, but none of them goes to zero (at least in the case of $BaTiO_3$ solid solutions). In the case of a second order transition, however, these intervals are equal to zero, since $\alpha_{\theta_0} = 0$. Consequently, as the concentration approaches x_m and, accordingly, the intervals become narrower, the characteristics peculiar to second order phase transitions become more clearly evinced. This fact was noted earlier on the basis of experimental considerations.[3] The decrease of the temperature interval $\theta - T_{12}$, wherein temperature hysteresis is possible, points to the same conclusion.

The expression for the coercive field in the first two temperature intervals has been deduced by Kholodenko[2], and may be written in the form

$$E_c = -2\sqrt{\frac{3}{5}}\,\frac{(-\beta)^{5/2}}{\gamma^{3/2}}\left(\frac{6}{25}-\frac{\alpha\gamma}{\beta^2}\right) =$$

$$= 4\sqrt{-\frac{0{,}6\,\alpha_{\theta_0}}{\beta_0}}\,[1+\xi ax(\eta ax+x-2)]^{\frac{1}{4}}\,\{0.04\alpha_{\theta_0}[1+\xi ax(\eta ax+x-2)]+\alpha'_{\theta_0}[T-\theta_0(1-ax)]\}, \quad (4)$$

and for the third interval in the form

$$E_c = \sqrt{-\frac{2\beta}{\gamma}}\,\alpha'_\theta(T-\theta) = 2\alpha'_{\theta 0}\sqrt{-\frac{2\alpha_{\theta_0}}{\beta_0}}\,[1+\xi ax(\eta ax+x-2)]^{\frac{1}{4}}\times$$

$$\times[T-\theta_0(1-ax)] = E_{c0}[1+\xi ax(\eta ax+x-2)]^{\frac{1}{4}}\left(1+\frac{\theta_0 ax}{T-\theta_0}\right), \quad (5)$$

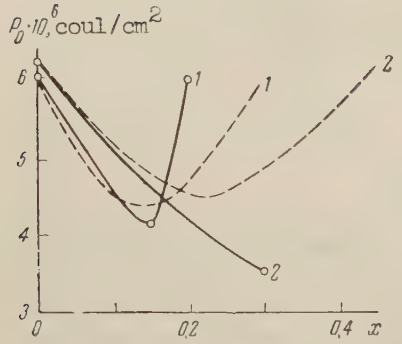

where E_{c0} is the coercive field for $x = 0$. However, we are most interested in the way in which the shape of the hysteresis loop depends on the composition of the solid solution for temperatures $T < T_{12}$ in the case of a first order phase transition (for temperatures $T < \theta$ in the case of a second order phase transition the shape of the hysteresis loop will be the same). It turns out that the coercive field in this case can be calculated approximately by means of Eq.(5). From (4) and (5) one may conclude that in any temperature intervals equidistant from θ, as the concentration approaches x_m the coercive field will diminish, reaching a minimum when $x = x_m$.

For a more complete description of the hysteresis loop one can obtain the variation of the spontaneous polarization with the composition of the solid solution. In the assumed approximation (β independent of temperature) the spontaneous polarization can be written in the form (recalling that $\beta^2 = 4\alpha_\theta\gamma$ - Ref.4):

$$P^2 = \frac{-\beta+\sqrt{\beta^2-4\alpha\gamma}}{2\gamma} = \frac{\sqrt{\alpha_\theta}+\sqrt{\alpha'_\theta(\theta-T)}}{\sqrt{\gamma}} = P_\theta^2\left[1+\sqrt{\frac{\alpha'_\theta}{\alpha_\theta}\,(\theta-T)}\right], \quad (6)$$

where $P_\theta^2 = -\frac{2\alpha_\theta}{\beta}$ is the spontaneous polarization at the phase transition temperature. It is evident from this that as the concentration increases to x_m with $a > 0$, the quantity P^2 diminishes. It is therefore possible to follow the variation in shape of the hysteresis loop with change in the composition of the solid solution. As an example, the x dependences of P for $Ba(Ti,Zr)O_3$ and $(Ba,Sr)TiO_3$ are shown in the accompanying figure (dashed curves 1 and 2, respectively). The corresponding experimental curves (solid curves) taken from the work of Smolenskii et al[5,6] are also given for comparison.

One of the parameters that characterize the degree of nonlinearity of ferroelectrics is the slope of the reversible dielectric constant curve. Kholodenko[4] obtained the variation of the polarization with the applied electric field. Using this relation, the expression for the slope of the reversible characteristic can be written in the following form (retaining only significant terms):

$$\left(\frac{\partial\varepsilon}{\partial E}\right)_T = -\frac{7\beta P^2+10\alpha}{16P(\beta P^2+2\alpha)^3} = -\frac{\sqrt{-\beta}\,[2\sqrt{\alpha_\theta}+7\sqrt{\alpha'_\theta(\theta-T)}]}{64\sqrt{2}\,[\alpha_\theta\alpha'_\theta(\theta-T)]^{3/2}}. \quad (7)$$

It is clear from Eq.(7) that with increasing electric field strength the dielectric constant ε decreases. With approach to the Curie point θ the slope of the reversible characteristic increases. The composition dependence of $\left(\frac{\partial \varepsilon}{\partial E}\right)_T$ can be investigated by utilizing Eqs.(2) and (3). In the case of a positive solid solution constant, as the concentration approaches x_m the slope of the reversible characteristic at identical distances from θ increases and attains a maximum at $x = x_m$. In the case of a negative solid solution constant, on the other hand, the curvature of the reversible characteristic decreases as the concentration increases to x_m.

Consequently, for $a > 0$ a solid solution with concentration x_m has a number of extremum properties (for the given series of solid solutions): minimum coercive field, minimum spontaneous polarization, maximum dielectric constant, maximum slope of the reversible characteristic, plus a number of extremum electroelastic properties.[1] At the same time increase of a with $a > 0$, as easily seen from Eq.(1), increases the absolute maximum (or reduces the minimum) values of the above physical quantities.

Quantitative verification of the above equations is hindered by the great scatter in the experimental data published by different authors. Nevertheless, a preliminary evaluation of the dielectric properties of solid solutions does seem feasible.

It should be noted that in the case of a second order phase transition it is still impossible to draw any definite inferences concerning the composition dependence of the dielectric properties of solid solutions, inasmuch as the composition dependence of the coefficient β remains unknown.

I desire to express my deep gratitude to A.L.Khodakov for his guidance in the work.

Rostov-on-the-Don State University

References

1. V.G.Granovskii, Sbornik nauchnykh rabot RGU (Collected Scientific reports, Rostov State University), 1961.
2. L.P.Kholodenko, Kristallografiya, 1, 393 (1956).
3. S.Triebwasser, Phys.Rev., 114, 63 (1959).
4. L.P.Kholodenko, Zhur.eksp.i teor.fiz., 31, 1035 (1956). (Trans.Soviet Physics - JETP.)
5. G.A.Smolenskii, N.P.Tarutin & N.P.Grudtsin, Zhur.tekh.fiz. (J.Tech.Phys.), 24, 1534 (1954).
6. G.A.Smolenskii & K.I.Rozgachev, Zhur.tekh.fiz., 24, 1751 (1954).

INTERNAL FIELDS IN SOME FERRO- AND ANTIFERROELECTRIC MODEL STRUCTURES BASED ON $BaTiO_3$

- N.N.Krainik

The electrostatic forces acting on the ions of the crystal lattice are one of the most important factors determining the relative stability of the ferro- and antiferroelectric state. In order to explain the appearance of ferro- and antiferroelectricity in the specific cases of solid solutions the base material of which is an antiferroelectric material, it is useful to consider the variation of the internal field as a function of the parameters of the ions comprising the crystal lattice of antiferro- and ferroelectric substances of the perovskite type. The stronger the internal fields, the more stable, other conditions being equal, will be the structure exhibiting spontaneous polarization.

Takagi[1] carried out a comparison of the coefficients entering into the expression for the electrostatic forces acting on the ions in a ferroelectric structure of the $BaTiO_3$ type and one type of antiferroelectric structure as a function of the electronic polarizabilities α of the ions. Venevtsev et al[2] published the results of calculations of the internal field in ferroelectric materials for different values of the polarizability α and the unit cell volume V. Earlier the writer[3] carried out a comparison of the internal fields (calculated by the method of Kinase[4]) acting in two typical models of antiferroelectric structure, on the one hand, and in the ferroelectric structure of the $BaTiO_3$ type on the other hand, for different values of α and V. In the considered antiferroelectric model structures the fields acting on the corner ions (the ions A in compound ABO_3 with the perovskite structure) are zero inasmuch as these ions lie midway between layers of antiparallel dipoles. In actual antiferroelectric crystals there is observed an appreciable displacement of the corner ions, and, consequently, the internal fields acting on these ions are nonzero. It is of interest to consider an antiferroelectric model structure in which the fields acting on the corner ions are not zero. Moreover, examination of several different models should help determine whether there is a general regularity governing the dependence of the relative stability of the ferro- and antiferroelectric states as a function of the ion parameters.

In the present work we calculated the coefficients entering into the expression for the internal field in the antiferroelectric structure shown schematically in Fig.1 and compared their values with the corresponding coefficients in the expression for the fields in the ferroelectric structure of the $BaTiO_3$ type. The spontaneous polarization is produced by the corner ions A and the oxygen ions O_{III} (Fig.2). The fields acting on ions B, O_I and O_{II} are zero.

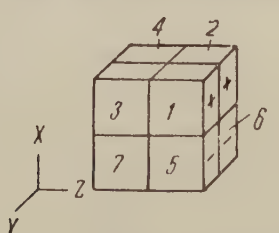

Fig.1

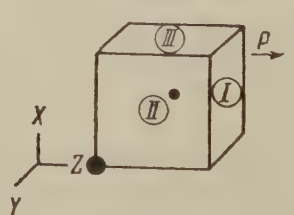

Fig.2

Fig.1. Diagram of unit cell consisting of eight initial unit cells with the perovskite structure for which the internal fields were calculated. The signs + and - correspond to positive and negative direction of the spontaneous polarization produced by ions A and O_{III}.

Fig.2. Initial unit cell of the perovskite structure: • - ion B, ● - ion A, I - ion O_I, II - ion O_{II}, III - ion O_{III}.

The field strength as a function of the polarizability of the ions and the volume of the unit cell were calculated by the method of Kinase[4], using Kinase's values for the structure coefficients for a cubic lattice with undisplaced ions. As the initial parameters we took the polarizabilities used by Slater[5] for $BaTiO_3$ and assumed the unit cell volume to be $64 \cdot 10^{-24}$ cm^3. In each case we varied some one parameter, keeping the other parameters constant. In order to utilize the structure coefficients for a cubical lattice, the edges of the initial unit cell were doubled so that the new unit cell contained 8 "molecules".

For purposes of calculation the crystal lattice was regarded as consisting of point charges and point dipole moments located at the positions occupied by ions. It was assumed that the charges of the corner and central cations and anions were related as (+1):(+2):(-1). Admittedly, these assumptions are rough, and hence the results can be regarded as only semiquantitative. However, we deemed the accuracy to be sufficient for finding the tendency in the variation of the relative stability of the ferro- and antiferroelectric structure as a function of the ion parameters.

The equations for the internal fields acting on the corner ions (E'_A) and on the O_{III} oxygen ions ($E'_{O_{III}}$) are of the form

$$E'_A = \frac{1}{\varepsilon_0}\,\frac{1}{8}\,[(q+p)(v_0+v)+(4m+4h)(x_{02}+x_2)], \qquad (1)$$

$$E'_{O_{III}} = \frac{1}{\varepsilon_0}\,\frac{1}{8}\,[(q+p)(x_{02}+x_2)+8(p-q)x_{02}+(4m+4h)(v_0+v)],$$

where q, p, m and h are the structure coefficients

$$S_z(00\,{}^1/_2),\ -S_z({}^1/_2\,{}^1/_2\,0),\ S_z(0\,{}^1/_4\,{}^1/_4) \text{ and } -S_z({}^1/_2\,{}^1/_4\,{}^1/_4);$$

v and x_2 are the electronic polarizations of ions A and O_{III}; v_0 and x_{02} are the ionic polarizations of ions A and O_{III}, which are taken equal to the product of the ionic charges by their displacement from the position in the initial cubic lattice:

$$\varepsilon_0 = 10^{-9}/(36\pi)\ \mathrm{F\ m^{-1}}.$$

The solution of (1) is of the form

$$v = \gamma_{vv} \cdot v_0 + \gamma_{vx_2} \cdot x_{02},$$
$$x_2 = \gamma_{x_2 v} \cdot v_0 + \gamma_{x_2 x_2} \cdot x_{02}. \qquad (2)$$

The results of comparison of the values of γ_{ij} for the ferro- and antiferroelectric structures with variation of the polarizability of the oxygen and variation in the size of the unit cell are summarized in the accompanying table. It will be evident from the table that the relative stability of the given antiferroelectric structure as compared with the ferroelectric structure increases with decrease in the polarizability of the oxygen and with increase in the volume of the unit cell. These results are in qualitative agreement with the data of Refs.1 and 3.

Thus comparison of the relative stability of three different antiferroelectric structures and the ferroelectric structure of the $BaTiO_3$ type, as evaluated from the strength of the internal fields, showed the same quantitative dependence of the stability on the polarizability of the oxygen ion and the volume of the unit cell. Hence it may be assumed that the deduced dependences are also valid for real antiferroelectric structures.

Ratios (in percent) of the difference between the coefficients γ for the ferro- and antiferroelectric structures with the value of the coefficient in the ferroelectric structure:

$$k_{ij}=\frac{\gamma_{ij_{ferr.}}-\gamma_{ij_{antif.}}}{\gamma_{ij_{ferr.}}}$$

Parameters	k_{vv},	k_{vx_z},	k_{x_zv}	$k_{x_zx_z}$
Initial parameters used in Ref.5 $\alpha_A^0, \alpha_0^0, V^0$	+25.2	+48.9	—2.2	5.6
$\alpha_0=0.5\alpha_0^0$; $\alpha_A=\alpha_A^0$; $V=V^0$	+14.7	+37.8	—5.0	+3.9
$V=3.75^3$Å$^3=0.822V^0$;	+33	+55.3	+10.6	+19.3
$\alpha_A=\alpha_A^0$; $\alpha_0=\alpha_0^0$				

According to Tessman et al[6], the polarizability of oxygen in simple oxides rises with increase in the volume occupied by the ion. In the perovskite structure, however, the presence of oxygen octahedra is an important distinctive feature which is responsible, when certain conditions are occupied, for the appearance of ferro- and antiferroelectricity. Hence it may be assumed that the polarizability of the oxygen will be determined primarily by the conditions of packing of the ions in the octahedron and will depend more on the B—O than on the distance A—O.

Let us consider the size of the oxygen ion as evaluated from the distance B—O, assuming the oxygen ion to be compressible and the radii of the B cations to be constant and equal to the tabular values. This assumption is reasonably justified inasmuch as in compounds in which the degree of covalence of the chemical bonds does not exceed 50%, the ionic radii of the cations vary much less than the radii of the anions (see, for example, Batsanov[7]).

In compounds with the perovskite structure, in which an antiferroelectric phase appears, the structure factor $t<1$* and the size of the B ion exceeds the size of the octahedral "hole". Consequently, the oxygen ions are "compressed" to a greater degree in the B—O direction than in the A—O direction; the degree of "compression" will increase and the "size" of the oxygen ion will decrease with decrease in the size of the corner ion A and increase in the size of the central ion B (i.e., with decrease of t). Comparison of the sizes of the oxygen ion evaluated from the distance B—O for a number of compounds with the perovskite structure substantiated the above reasoning in the case when the cation B has the electronic configuration of a noble gas.

It may be assumed that with decrease in the dimensions of the oxygen ion, as evaluated from the distance B—O, its polarizability will decrease. This, as follows from comparison of the internal fields, increases the stability of the antiferroelectric state as compared with the ferroelectric state. This assumption helps explain why the antiferroelectric state in crystals with the perovskite structure appears when $t<1$, and also helps understand one of the reasons for the appearance upon increase of t of a ferroelectric phase in solid solutions of the antiferroelectric materials $PbZrO_3$ and Pb_2MgWO_6.

I desire to express my gratitude to G.A.Smolenskii for valuable discussions.

Institute of Semiconductors,
Academy of Sciences of the USSR

---

*According to Goldschmidt et al[8], $t=\frac{R_A+R_0}{(R_B+R_0)\sqrt{2}}$, where R_A, R_B and R_0 are the ionic radii.

References

1. Y.Takagi, Proc.Internat.Confer.on Theor.Phys., Tokyo, 824 (1954).
2. Yu.N.Venevtsev, G.S.Zhdanov, S.P.Solov'ev & Yu.A.Zubov, Kristallografiya, 3, 473 (1958). (Trans.Soviet Physics - Crystallography.)
3. N.N.Krainik, Fizika tverdogo tela, 2, 993 (1960). (Trans.Soviet Physics - Solid State).
4. W.Kinase, Progr.Theor.Phys., 13, 529 (1950).
5. J.C.Slater, Phys.Rev., 78, 748 (1950).
6. J.R.Tessman, A.H.Kahn & W.Shockley, Ibid., 92, 890 (1953).
7. S.S.Batsanov, Zhur.fiz.khim., 30, 2640 (1956).
8. V.M.Goldschmidt, T.Barth & G.Lunde, Skrifter Norske Videnskaps Acad., Oslo, J.Mat.Natur.Klasse, 7, 21 (1925).

METHOD OF CALCULATING THE INTERNAL ELECTRIC FIELDS IN COMPLEX DIPOLE STRUCTURES AND APPLICATION OF THE METHOD TO $CaTiO_3$

- S.P.Solov'ev, Yu.N.Venevtsev, G.S.Zhdanov & V.V.Ivanova

Introduction

An important problem in the physics of crystals with special electric and magnetic properties, in particular ferro- and antiferroelectric crystals, is that of determining the internal fields at different points in the unit cell. A number of authors[1-9] have published calculations of the internal electric fields in some ferroelectric materials with the perovskite structure; generally these calculations have been based on specific models of the ferroelectric crystals. There have also been published[6,10] the results of calculations of the internal field for simple antiparallel dipole configurations. In all these investigations the directions of the fields were assumed to be known, although this is actually not true in the case of more complex dipole configurations.

At present we have no data on the distribution of internal fields in actual structures, although such data are of great interest in connection with the ferro- and antiferroelectric properties of compounds with such structures. In this report we give a general method for calculating the internal fields in complex structures in which in general there may obtain both parallel and antiparallel displacements of the ions in arbitrary directions. We applied the method to calculating the fields in $CaTiO_3$.

Method

The proposed method is a generalization of the method used for calculating the field in ABO_3 type ferroelectric crystals and takes into account the specific model structure of the compound under consideration. We assume that the crystal lattice of the compound consists of point charges (equivalent to the effective ionic charges) on which there are superposed point dipole moments of unknown magnitude and direction, induced by the internal fields. The values of the effective charges and the electronic polarizabilities α of the ions are assumed to be known; we also assume that the charges and dipoles are situated in the displaced positions of the atoms in the lattice.

Under the above assumptions, the electric field at any point in the lattice may be described as the sum of the external field (which hereinafter we shall assume to be zero) and the fields produced by all the charges and all the dipoles forming an infinite lattice. Since the unit cells of many compounds, including antiferroelectric compounds, contain a rather large number of atoms, the number of unknowns will also be large. However, taking into account the symmetry of the lattice, the number of unknowns can be substantially reduced.

Each space group is characterized by a certain assortment of general and special complexes, in each of which the atoms are equivalent and thus can be obtained as a result of "multiplication" of one atom by the symmetry elements. Hence it is sufficient to determine the field at any atom of each complex; and then one can attribute to the other atoms of the given complex a field of the same magnitude but directed in accord with the rules of symmetry.

Thus if each unit cell contains m atoms grouped in n different complexes $(n < m)$ and we use l_j to denote the multiplicity of the j-th complex, we can write the following set of linear equations with $3n$ unknowns for the projections of the electronic dipole moments p_j on the coordinate axes x, y and z:

$$\frac{1}{v}\sum_{j=1}^{n} p_{jx}\sum_{l=1}^{l_j}\{\delta_{ij}-(h_{xx})_{ijl}\}-\frac{1}{v}\sum_{j=1}^{n} p_{jy}\sum_{l=1}^{l_j}(h_{xy})_{jjl}-\frac{1}{v}\sum_{j=1}^{n} p_{jz}\sum_{l=1}^{l_j}(h_{xz})_{ijl}=\frac{1}{v^{2/3}}\sum_{j=1}^{n} e_j\sum_{l=1}^{l_j}(f_x)_{ijl};$$

$$-\frac{1}{v}\sum_{j=1}^{n} p_{jx}\sum_{l=1}^{l_j}(h_{yx})_{ijl}+\frac{1}{v}\sum_{j=1}^{n} p_{jy}\sum_{l=1}^{l_j}\{\delta_{ij}-(h_{yy})_{ijl}\}-\frac{1}{v}\sum_{l=1}^{n} p_{jz}\sum_{i=1}^{l_j}(h_{yz})_{ijl}=\frac{1}{v^{2/3}}\sum_{j=1}^{n} e_j\sum_{l=1}^{l_j}(f_y)_{ijl}; \quad (1)$$

$$-\frac{1}{v}\sum_{j=1}^{n} p_{jx}\sum_{l=1}^{l_j}(h_{zx})_{ijl}-\frac{1}{v}\sum_{j=1}^{n} p_{jy}\sum_{l=1}^{l_j}(h_{zy})_{ijl}+\frac{1}{v}\sum_{j=1}^{n} p_{jz}\sum_{l=1}^{l_j}\{\delta_{ij}-(h_{zz})_{ijl}\}=\frac{1}{v^{2/3}}\sum_{j=1}^{n} e_j\sum_{l=1}^{l_j}(f_z)_{ijl}.$$

Here v is the volume of a unit cell,

$$\delta_{ij}=\begin{cases} 0 & \text{for } i\neq j \\ v/\alpha_i & \text{for } i=j, \end{cases}$$

and the f_{ij} and h_{ij} with appropriate indices are structural sums, which are numerically equal to the fields produced, respectively, by infinite simple lattices of unit charges and unit dipoles extending in the directions of the axes x, y and z.

The problem of calculating the fields actually resolves into two independent problems, one of which is constructing and solving the set of equations, and the other is calculating the necessary structural sums. At present, thanks to the availability of high speed computers, the problem of solving a set of equations even with a large number of unknowns presents no particular difficulties. Then the computer can be programmed to compute the structural sums. In particular, all the sums f and h in Eqs.(1) can readily be calculated for lattices of any symmetry by the method of Ewald[11].

Calculation of the internal field in $CaTiO_3$

According to the data of Kay & Baily[12], $CaTiO_3$ at room temperature has a rhombic lattice with parameters a = 5.3670 ± 0.0001 Å, b = 7.6438 ± 0.0001 Å, and c = 5.4439 ± 0.0001 Å. The unit cell, pictured in the accompanying figure, contains 20 atoms (m = 20), but only 4 complexes: I - 4 Ca in position 4(c) II - 4 Ti in position 4(a) III - 4 O_I in position 4(c) and IV - 8 O_{II} in position 8(d). The symmetry of position 4(a) is $\bar{1}$, that of position 4(c) is m, and that of position 8(d) is 1. The atomic displacements allowed by symmetry are indicated in the figure by arrows and have the following values:

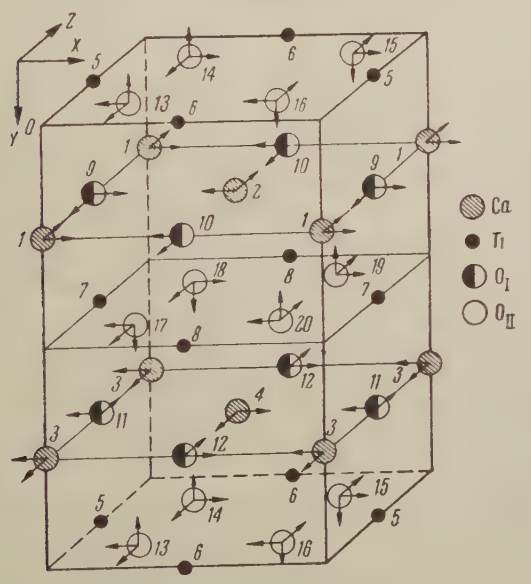

Unit cell of $CaTiO_3$.

$$|\delta x|_{Ca}=0; \quad |\delta z|_{Ca}=0.030c=0.16 \text{ Å};$$
$$|\delta x|_{O_I}=0.037a=0.20\text{Å}; \quad |\delta z|_{O_I}=0.018c=0.10\text{Å};$$
$$|\delta x|_{O_{II}}=0.018a=0.10\text{Å}; \quad |\delta y|_{O_{II}}=0.026b=0.20 \text{ Å};$$
$$|\delta z|_{O_{II}}=0.018c=0.10 \text{ Å}.$$

A distinctive feature of the structure of $CaTiO_3$ is that the TiO_6 octahedra are virtually not distorted and only slightly rotated relative to each other; the Ca ions are displaced antiparallel.

In view of the symmetry of the particular positions $4(a)$ and $4(c)$, the field acting on the Ti ions as well as the components of the field acting in the y direction on the Ca and O_I ions are zero. Hence the five corresponding equations can be eliminated from the set (1), as a result of which the total number $3n$ of unknowns is reduced from 12 to 7.

In view of the fact that the precise values of the polarizability and effective charges of the ions in $CaTiO_3$ are not known, we carried out six parallel calculations using different reasonable values of the polarizabilities and charges. The structural sums f and h were calculated by the method of Ewald for the actual rhombohedral $CaTiO_3$ lattice. The calculations were performed on a "Strela" computer in the Computing Center of Moscow State University.

Results and Discussion

The proposed method of calculating internal fields can be applied to any compounds, both with centrosymmetric and with noncentrosymmetric structure, in particular, to models of real ferroelectric structures. The computational difficulties are rather easily overcome by modern computational techniques and should be no obstacle to systematic calculation of the fields in various actual structures.

The results of calculation of the fields in $CaTiO_3$ indicate that the field distribution in this compound is weakly dependent on the polarizability of the Ca ions but is strongly dependent on the values of the effective ionic charges, to the extent of change of the sign of the fields acting on the oxygen ions, although generally the qualitative picture remains the same. The fields acting on the Ca ions vary very little. In all six cases analyzed the fields were found to be substantially smaller than in the case of ABO_3 type ferroelectrics; moreover as follows from the symmetry of the structure, the field acting on the Ti ions is zero, whereas in the case of $BaTiO_3$ and $PbTiO_3$ fields of maximum strength act on the Ti ions[8,9].

The substantial difference between the field pattern in $CaTiO_3$ and that in related ABO_3 type ferroelectrics is due to the fact that in the latter the BO_6 octahedra are strongly distorted, whereas in $CaTiO_3$ they are nearly ideal. One can also observe the correlation between the dielectric anomaly and the distortion of the BO_6 octahedra in the case of such ABO_3 type compounds as $PbZrO_3$, $PbHfO_3$ and $NaNbO_3$.

Analysis of the structures and dielectric properties of a number of ABO_3 type compounds with the perovskite structure makes it possible to explain the presence or absence in them of antiferroelectricity from the standpoint of "crumpling" of the structure, a consequence of distortion of the valence angles of the B—O bonds occurring with decrease of temperature. It may be assumed that a necessary condition for an antiferroelectric phase transition is "crumpling" in the B—O direction. A sufficient condition, apparently, is a certain critical (for each compound) degree of such "crumpling" sufficient to cause distortion of the BO_6 octahedra and leading to displacement of the "squeezed" B ions. The stronger internal fields arising as a result of distortion of the octahedra will favor displacement of the B ions, and from the geometry of the BO_6 octahedra in the "crumpled" structure it follows that the displacements of the B ions must necessarily be antiparallel.

I take this opportunity to thank N.P.Trifonov, staff member of the Moscow State University Computing Center, for solving the set of equations on the "Strela" computer.

"L.Ya.Karpov" Physical-Chemical Institute

References

1. G.I.Skanavi, Zhur.eksp.i teor.fiz., 17, 399 (1947).
2. J.C.Slater, Phys.Rev., 78, 748 (1950).
3. W.Kaenzig, Helv.Phys.Acta, 24, 175 (1951).
4. V.Kh.Kozlovskii, Zhur.tekh.fiz., 21, 1388 (1951).
5. R.Hagedorn, Z.f.Physik, 133, 394 (1952).
6. W.Kinase, Progr.Theoret.Phys., 13, No.5, 529 (1955).
7. S.Triebwasser, J.Phys.Chem.Solids, 3, 1/2, 53 (1957).
8. Yu.N.Venevtsev, G.S.Zhdanov, S.P.Solov'ev & Yu.A.Zubov, Kristallografiya, 3, No.4, 373 (1958). (Trans.Soviet Physics - Crystallography.)
9. Yu.N.Venevtsev, S.P.Solov'ev, G.S.Zhdanov & V.V.Ivanova, Ibid., 4, No.6, 855 (1959). (Trans.Ibid.)
10. M.H.Cohen, Phys.Rev., 84, 369 (1951).
11. P.P.Ewald, Ann.d.Physik (4), 64, 253 (1921).
12. H.F.Kay & P.C.Baily, Acta Crystallogr., 10, 219 (1957).

INVESTIGATION OF SOME FERROELECTRICS BY THE METHOD OF NUCLEAR MAGNETIC RESONANCE

- A.G.Lundin, K.S.Aleksandrov, G.M.Mikhailov & S.P.Gabuda

There are, in our opinion, two promising directions for investigation of ferroelectrics by the nuclear magnetic resonance method:[1]

1. Study of the absorption spectra for different orientations of a single crystal in an external magnetic field. Such studies afford the possibility of determining, for crystals of known structure, the position of the hydrogen atoms in the lattice (see Ref.2, for example). If the structure is not known, the orientation of the proton-proton vectors and the separation between protons can be determined. The possibilities for research in this direction are discussed in Ref.3.

2. The study of polycrystalline specimens. This involves the experimental investigation of a single parameter: the second moment S_2 of the absorption line and its change incident to phase transitions.

The second moment of the absorption line, having the contour $f(H - H_0)$, where H is the external magnetic field, is defined by the following expression:[1]

$$S_2 = \int_{-\infty}^{\infty} (H - H_0)^2 f(H - H_0)\, dH \Big/ \int_{-\infty}^{\infty} f(H - H_0)\, dH.$$

The values of the second moment are generally measured with an accuracy approaching 5-10%. This quantity is a characteristic of the relative position and mobility of the resonating nuclei in the crystal lattice and is determined by means of the Van Vleck[4] formula:

$$S_2 = \frac{6}{5} I(I+1)\, g^2 \mu_0^2 N^{-1} \sum_{j>k} r_{jk}^{-6},$$

where I is the spin of the resonating nucleus, g is the splitting factor, μ_0 is the nuclear magneton, N is the total number of nuclei in the crystal, and r_{jk} is the length of the vector joining nuclei j and k.

Investigations in this direction were first carried out by Newman[5], who failed to find the expected change of the second moments with phase transitions in

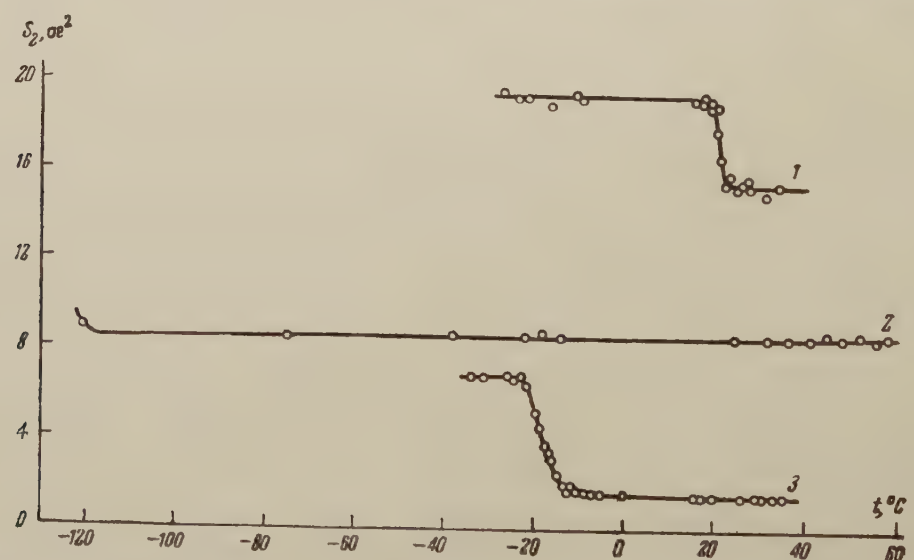

Fig.1. Temperature dependence of the second moment of the absorption line in some ferroelectrics: 1) Rochelle salt; 2) tri-glycine sulfate; 3) potassium ferrocyanide.

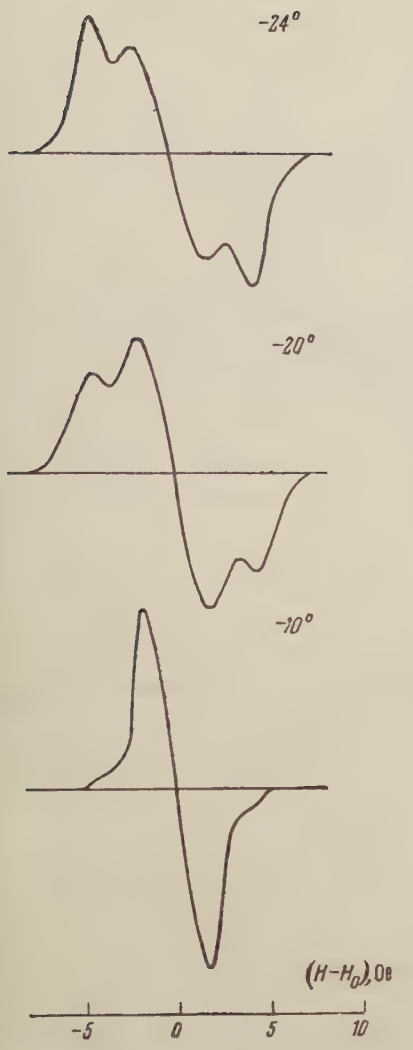

Fig.2. Variation of the derivative of the proton magnetic resonance line of potassium ferrocyanide in the phase transition region.

the dihydrogen phosphates of potassium and ammonium. Using the nuclear magnetic resonance method, Lösche[6] investigated Rochelle salt in the region of the upper Curie point and found a jump of the second moment from 15 to 19 oe^2.

Recently, Blink[7] reported that he detected small variations in line width in the region of the phase transitions in the antiferroelectrics $Ag_2H_3IO_6$ and $(NH_4)_2H_3IO_6$.

We investigated polycrystalline samples of Rochelle salt, tri-glycine sulfate and potassium ferrocyanide in the temperature region of the phase transitions in these substances. To enhance the signal level, we compressed the samples, which had a volume of about 2 cm^3, at a pressure of ~100 kg/cm^2. The equipment employed is described in Ref. 8. We obtained the following results.

Rochelle salt $KNaC_4H_4O_6 \cdot 4H_2O$. At +23°C (Fig. 1, 1) the second moment undergoes a jump of 4 oe^2, which agrees with the data of Lösche[6]. No change in the region of the lower Curie point was detected.

The large magnitude of the second moment indicates that the protons of the water of hydration and the tartrate group are not in any intensive vibrational-rotational motion. Analysis of the spectra also indicates that the variation of the second moment is not due to the protons bound in the water molecules. This variation can apparently be explained by displacement of one of the protons of the tartrate group, which is consistent with neutron diffraction data[9] for Rochelle salt. The invariance of the second moment in the region of the lower Curie point suggests that phase transitions in Rochelle salt differ in character and that the disappearance of spontaneous polarization at -18°C is not connected with a significant change in the mobility and position of the protons.

Tri-glycine sulfate $(NH_3CH_2COO)_3 \cdot H_2SO_4$. As can be seen from curve 2 in Fig.1, the second moment remains constant at ~8 oe^2 in a wide temperature range. Structural investigations[10] show that proton-proton separations in the NH_3 and CH_2 groups are about 1.4 Å, which should lead to a value of the second moment of the order 30-40 oe^2 for a stationary structure. This means that the NH_3 and CH_2 groups in the tri-glycine sulfate crystal at room temperature are in a state of intensive rotational motion. The type of mobility of these groups does not change incident to transition through the Curie point. Thus the experimental data are not inconsistent with the hypothesis advanced by Pepinsky[10] to the effect that ferroelectric transition is due to a displacement along the hydrogen bond of one of the protons not belonging to the rotating groups. The isolated condition of these groups leads to their contribution to the second moment being insignificant, so that no change in the moment with temperature is evinced.

Potassium ferrocyanide $K_4Fe(CN)_6 \cdot 3H_2O$. The ferroelectric phase transition in this substance at -22°C was discovered by Waku[11] in 1959. Investigations[12] show that potassium ferrocyanide contains separate water molecules. For station-

ary water molecules the second moment should be ~20 oe^2. The spectrum of potassium ferrocyanide attains this width only at liquid oxygen temperature. The line width decreases with increasing temperature, which attests to the presence of vibrational-rotational motion of the water molecules. At -22°C there is still another jump of the second moment from 7 to 1.8 oe^2, which can be explained by the appearance of additional degrees of freedom of the water molecules. Fig.2 shows the variation in shape of the derivative of the resonance line upon cooling through the Curie point. Curve 3 in Fig.1 illustrates the change of line width incident to the phase transition.

It is interesting to note that Kobeko and Kurchatov[13] postulated such behavior of the water of hydration to explain the ferroelectric properties of Rochelle salt. Further investigations will show to what extent the ferroelectric properties of potassium ferrocyanide may be due to the influence of the H_2O molecules.

Institute of Physics,
Siberian Branch of the
Academy of Sciences of the USSR

References

1. E.Endryu, Yadernyi magnitnyi rezonans (Nuclear magnetic resonance), M., 1957.
2. K.S.Aleksandrov, A.G.Lundin & G.M.Mikhailov, Kristallografiya, 5, No.1, 84 (1960). (Trans.Soviet Physics - Crystallography.)
3. D.W.McCall & E.W.Hamming, Acta Crystallography., 12, 81 (1959).
4. J.H.Van Vleck, Phys.Rev., 74, 1168 (1948).
5. R.Newman, J.Chem.Phys., 18, 669 (1950).
6. A.Lösche, Exp.Techn.Phys., 3, 18 (1956).
7. R.Blink, J.Chem.Phys., 31, 849 (1959).
8. A.G.Lundin & G.M.Mikhailov, PTE, No.2, 90 (1960). (Trans.Instruments & Experimental Techniques.)
9. G.Shirane, F.Jona & R.Pepinsky, Proc.Inst.Radio Engrs., 43, 1738 (1955).
10. S.Hoshino, Y.Okaya & R.Pepinsky, Phys.Rev., 115, 323 (1959).
11. S.Waku, a.a., J.Phys.Soc.Japan, 14, 973 (1959).
12. Structural Reports, 11, 421 (1948).
13. P.P.Kobeko & I.V.Kurchatov, Zhur.russk.fiz-khim.ob-va, (Jour. of the Russian Physical-Chemical Society), 62, 251 (1930).

X-RAY DIFFRACTION STUDIES OF SOME NEW FERROELECTRICS WITH LAMINAR STRUCTURE

- I.G. Ismailzade

Introduction

Auriwillius[1] investigated the crystal structure of niobates and tantalates of the types $ABi_2Nb_2O_9$, $ABi_2Ta_2O_9$ (A = Ca, Sr, Pb or Ba), and of Bi_3NbTiO_9 and $Bi_4Ti_3O_{12}$. He showed that at room temperature the unit cells of $CaBi_2Nb_2O_9$, $CaBi_2Ta_2O_9$, Bi_2NbTiO_9 and $PbBi_2Nb_2O_9$ have rhombic symmetry and consist of $(Bi_2O_2)^{2+}$ layers and a perovskite layer perpendicular to [001].

Recently Smolenskii and his co-workers[2] discovered that $PbBi_2Nb_2O_9$ is a ferroelectric with $T_C \approx 520^o$. Subsequent investigations[3] by these authors revealed ferroelectric properties in $ABi_2Nb_2O_9$, $ABi_2Ta_2O_9$ (A = Ca, Sr, Ba), Bi_3NbTiO_9, $Bi_4Ti_3O_{12}$ and $PbBi_2Ta_2O_9$. Thus there was discovered a new group of ferroelectrics of the oxygen octahedron type.

The present work was devoted to investigation of the structure of polycrystalline specimens of $CaBi_2Nb_2O_9$, $CaBi_2Ta_2O_9$, $PbBi_2Nb_2O_9$ and Bi_3NbTiO_9.

Experimental Procedure

Using Cu Kα radiation, we recorded the x-ray diffraction patterns of our polycrystalline specimens by the photographic method (D ≈ 143 mm, asymmetric positioning of the film) and the ionization method (on an URS-50I diffractometer). The temperature dependence of the lattice parameters was investigated on the URS-50I with the aid of a simple attachment, designed in collaboration with V.I.Tutushkin, which provided for heating the specimen up to 750°. The temperature was

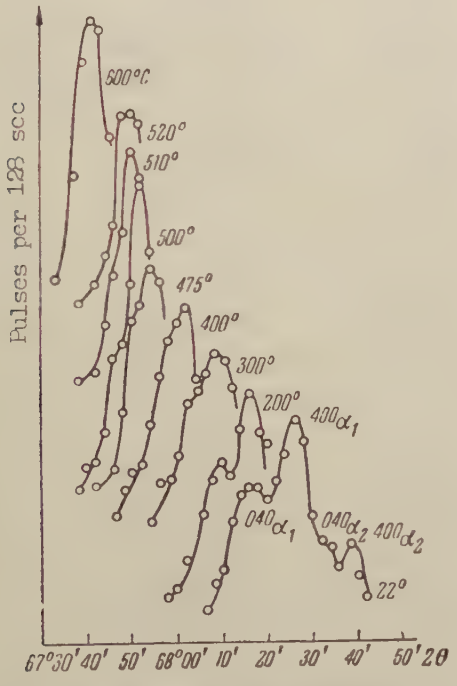

Fig.1. Temperature dependence of the positions of the 040_{α_1} and 400_{α_1} maxima for $PbBi_2Nb_2O_9$.

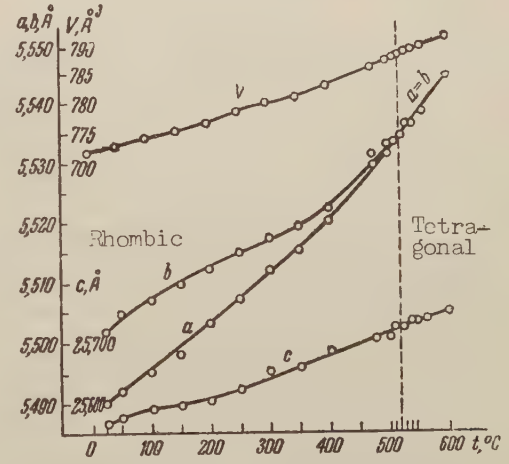

Fig.2. Temperature dependence of the lattice parameters of $PbBi_2Nb_2O_9$.

monitored by a chromel-alumel thermocouple, the hot junction of which was in direct contact with the heated surface of the specimen. We kept track of the variation in structure by recording the $040_{\alpha_1} - 400_{\alpha_1}$, $137_{\alpha_1} - 317_{\alpha_1}$, 00,10 and 00,20 reflection maxima (the x-ray photons were counted for periods of 128 sec at

Table 1

Temperature dependences of the lattice parameters of $CaBi_2Nb_2O_9$, $CaTi_2Ta_2O_9$ and Bi_3NbTiO_9

Parameter	20°C	100°	150°	200°	250°	300°	350°	400°	450°	500°	525°	550°	575°	600°	650°	700°
							$CaBi_2Nb_2O_9$									
a, Å	5,442	—	5,453	—	5,458	—	5,465	—	5,480	5,485	—	$5,488_3$	$5,495_5$	—	$5,502_5$	5,504
b, Å	$5,482_5$	—	5,484	—	5,487	—	5,491	—	$5,496_7$	$5,501_3$	—	$5,502_5$	$5,503_7$	—	$5,502_5$	5,504
c, Å	24,920	—	24,955	—	24,990	—	25,035	—	25,070	25,080	—	25,090	25,105	—	25,125	25,140
b/*a*	1,0075	—	1,0056	—	$1,005_8$	—	1,0047	—	1,0036	1,0029	—	1,0025	1,0015	—	1,000	1,000
V, Å³	743,5	—	746,0	—	748,5	—	751,0	—	755,0	756,8		758,0	759,3	—	760,7	761,6
							$CaBi_2Ta_2O_9$									
a, Å	5,435	5,438	—	5,444	—	5,452	—	5,464	—	5,470	—	5,473	—	5,479	5,484	—
b, Å	$5,468_5$	5,471	—	$5,475_6$	—	5,479	—	$5,482_6$	—	$5,483_7$	—	5,484	—	5,479	5,484	—
c, Å	24,970	24,980	—	25,015	—	25,040	—	25,060	—	25,070	—	25,083	—	25,085	25,105	—
b/*a*	1,006	1,006	—	$1,005_8$	—	1,005	—	$1,003_5$	—	$1,002_5$	—	$1,002_4$	—	1,000	1,000	—
V, Å³	742,0	743,2	—	745,6	—	748,0	—	750,6	—	751,9	—	752,8	—	730,0	755,0	—
							Bi_3NbTiO_9									
a, Å	$5,409_4$	5,418	—	$5,425_6$	—	5,434	—	5,442	5,447	$5,452_7$	5,458	$5,463_4$	5,469	$5,474_3$	5,488	5,490
b, Å	5,453	5,458	—	$5,465_7$	—	5,471	—	5,477	5,480	$5,482_4$	5,485	$5,487_8$	5,488	$5,490_5$	5,488	5,490
c, Å	25,160	25,195	—	25,230	—	$25,25_2$	—	$25,28_6$	25,297	25,309	25,315	25,320	25,325	25,332	25,344	25,350
b/*a*	1,008	1,0075	—	$1,007_3$	—	1,0068	—	1,0065	1,0060	1,0054	1,0050	1,0044	1,0034	1,0029	1,000	1,000
V, Å³	742,0	745,0	—	748,0	—	750,0	—	753,6	755,1	756,4	757,8	758,9	760,0	761,2	763,2	764,0

2-3' angular intervals). The values of the lattice parameters were then calculated from the positions of the maxima.

The temperature dependence of the 040_{α_1}—400_{α_1} maxima positions for $PbBi_2Nb_2O_9$ is shown in Fig.1. Similar results were obtained for the other three compounds.

The temperature dependence of the lattice parameters of $PbBi_2Nb_2O_9$ is given in Fig.2; the corresponding data for $CaBi_2Nb_2O_9$, $CaBi_2Ta_2O_9$ and Bi_3NbTiO_9 are listed in Table 1.

Discussion

The presence at room temperature of 040_{α_1}—400_{α_1} and 137_{α_1}—317_{α_1} maxima showed that the structure of the investigated compounds is rhombic. With increasing temperature these maxima shift to the side of smaller angles and gradually converge. In the case of $PbBi_2Nb_2O_9$, for example, at 475° the 040_{α_1} and 400_{α_1} maxima are well separated and distinct; at 500-510° they almost merge, and at 520° and higher there is evident only a single 400 reflection peak. Thus at 520° and above the symmetry is tetragonal. With increasing temperature, a increases more rapidly than b so that b/a decreases; c grows relatively slowly. Below the Curie point for all the investigated compounds there are observed the systematic extinctions:

hkl for $h+k,\ k+l,\ l+h = 2n+1$,
$hk0$ for $h+k = 2n+1$,
$h0l$ for $h+l = 2n+1$,
$0kl$ for $k+l = 2n+1$,
$h00$ for $h = 2n+1$,
$00l$ for $l = 2n+1$,

corresponding to space groups $D_{2h}^{23} = Fmmm$, $D_2^7 = F222$ and $C_{2v}^{18} = Fmm2$. Of these only $C_{2v}^{18} = Fmm2$ is polar. The presence of ferroelectricity in all four investigated compounds[2,3] restricts the choice to C_{2v}^{18}.

In the paraelectric (tetragonal) phase one can choose a smaller unit cell with $a' = b' = \frac{1}{\sqrt{2}}a$. Then the systematic extinctions of the reflections with the above indices will correspond to space groups $D_4^9 = I42$, $D_{2d}^9 = I\bar{4}m2$, $C_{4v}^9 = I4mm$ and $D_{4h}^{17} = I4/mmm$. The first two groups are noncentrosymmetric and nonpolar, C_{4v}^9 is polar and D_{4h}^{17} is centrosymmetric and nonpolar. The most probable group is $D_{4h}^{17} = I4/mmm$.

Thus in these compounds the change in lattice symmetry incident to the ferroelectric phase transition is described by C_{2v}^{18} (rhombic) $\rightleftarrows D_{4h}^{17}$ (tetragonal). Below the Curie temperature $\frac{b}{a} > 1$, while above the Curie point $\frac{b}{a} = 1$; this indicates that the spontaneous polarization vector is in the (001) plane and probably in the [010] direction. In the last case the symmetry group may be $Fm2m$, inasmuch as in C_{2v} the polar direction is that of axis 2.

In the unit cell of $CaBi_2Nb_2O_9$, $CaBi_2Ta_2O_9$, $PbBi_2Nb_2O_9$ and $Bi_IBi_{II}(NbTi)O_9$ $z = 4$. If one disregards the insignificant ionic displacements responsible for the appearance of spontaneous polarization, in $C_{2v}^{18} = Fm2m$ the ion coordinates will be the following:

$$\left(000;\ 0\tfrac{1}{2}\tfrac{1}{2};\ \tfrac{1}{2}0\tfrac{1}{2};\ \tfrac{1}{2}\tfrac{1}{2}0\right) + 4\,\mathrm{Ca\,(Pb, Bi_I)\ in\ 4}(a)\mathrm{:}\ 00z\ \text{with}\ z = \tfrac{1}{2};$$

$8\,\mathrm{Bi}\,(\mathrm{Bi_{II}})$ in $8\,(c)$: $0yz,\ 0\bar{y}\bar{z}$ with $y = \frac{1}{2}$, $z = 0{,}200$;

$8\,\mathrm{Nb}\,(\mathrm{Ta, Nb, Ti})$ in $8\,(c)$: $0yz,\ 0\bar{y}\bar{z}$ with $y = \frac{1}{2}$, $z = 0{,}422$;

$4\,O^{2-}$ in $4\,(a)$: $00z$, $z = 0$;

$8\,O^{2-}$ in $8\,(c)$: $0yz,\ 0\bar{y}\bar{z}$ with $y = \frac{1}{2}$, $z = 0{,}156$;

$24O^{2-}$ in three groups in positions $8\,(b)$: $\frac{1}{4}\ \frac{1}{4}\ z,\ \frac{1}{4}\ \frac{3}{4}\ z$ with $z_{\mathrm{I}} = \frac{1}{4}$,

$z_{\mathrm{II}} = 0{,}079,\ z_{\mathrm{III}} = -0{,}079.$

In evaluating the structural parameters Z_{Nb}, $Z_{O^{2-}}$, Z_{Bi} and Z_{Ta}, we assumed the following spacings: $Nb^{5+}—O^{2-}$ = 2.02 Å, $Ti^{4+}—O^{2-}$ = 2.02 Å, and $Bi^{3+}—O^{2-}$ = 2.56 Å.

The unit cell of $PbBi_2Nb_2O_9$ is shown in Fig.3. The cell consists of a perovskite layer ($PbNb_2O_7$), normal to [001] and lying between two Bi—O layers parallel to it. In the perovskite layers the oxygen octahedra are joined at their vertices which is characteristic of ferroelectrics of the oxygen octahedron type. The other investigated compounds have an analogous structure. In the perovskite layer of $BiBi_2(NbTi)O_9$, i.e., in Bi_3NbTiO_9, the Nb and Ti ions are distributed in a statistically chaotic manner.

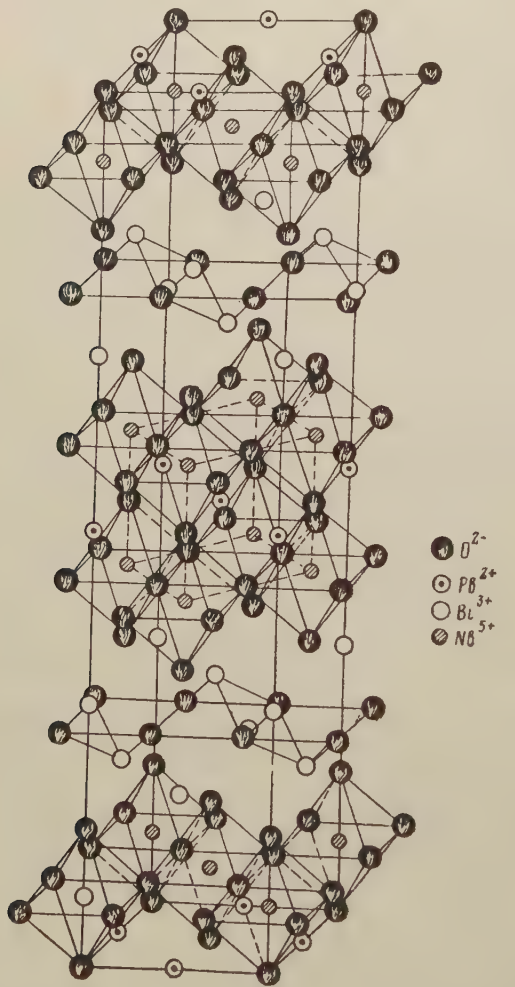

Fig. 3. Unit cell of rhombic $PbBi_2Nb_2O_9$.

We calculated the structure factor t, taking into account the coordination correction, and obtained:

$CaBi_2Nb_2O_9$ t = 0.94	$CaBi_2Ta_2O_9$ 0.94
$PbBi_2Nb_2O_9$ 1.02	$BiBi_2(NbTi)O_9$ 1.00

It will be evident that the geometric condition (t = 0.94) for the first two compounds is unfavorable for the appearance of ferroelectricity. Probably spontaneous polarization in these compounds is due partially to the covalent character of the $Nb^{5+}—O^{2-}$ and $Ta^{5+}—O^{2-}$ bonds. Possibly the appearance of spontaneous polarization is also connected with the Bi—O layers.

It will be evident from Table 1 and Fig.2 that the phase transition in the investigated compounds is realized with gradual variation of the unit cell volume v, i.e., the phase transition is a second

Table 2

Compound	Curie point, T_C °C	
	According to dielectric data	According to structural data
$CaBi_2Nb_2O_9$	500	575-650
$CaBi_2Ta_2O_9$	500	550-600
$BiBi_2(NbTi)O_9$	440	600-650

order transition. This smooth variation of v also apparently indicates that these compounds have a phase transition region rather than a transition point. This is substantiated by the smearing out of the ϵ peak in the temperature dependence of ϵ observed for $PbBi_2Nb_2O_9$ by Smolenskii et al[2].

Owing to the high conductivity of $CaBi_2Nb_2O_9$, $CaBi_2Ta_2O_9$ and $BiBi_2(NbTi)O_9$ at high temperatures it proved impossible to determine the phase transition region in these compounds from the temperature dependence of the dielectric constant. In contrast, it proved feasible to determine this region from our structural data (Table 2).

V.I.Khodzhaeva and M.Kh.Annagiev participated in the experimental part of this work. I desire to express my deep gratitude to G.A.Smolenskii for providing the specimens and for valuable advice.

Institute of Petrochemical Processes,
Academy of Sciences of the Azerbaidzhan SSR

References

1. B.Auriwillius, Arkiv.Kemi, 1, (5), 479 (1950).
2. G.A.Smolenskii, V.A.Isupov & A.I.Agranovskaya, Fizika tverdogo tela, 1, 169 (1959). (Trans.Soviet Physics - Solid State.)
3. G.A.Smolenskii, V.A.Isupov & A.I.Agranovskaya, Program of the Third Conference on Ferroelectricity, p.45, M., 1960.

PREPARATION AND FERROELECTRIC PROPERTIES OF DEUTERATED TRI-GLYCINE SULFATE CRYSTALS

- V.P.Konstantinova, I.M.Sil'vestrova, L.A.Shuvalov & V.A.Yurin

Study of the properties of deuterated tri-glycine sulfate (DTGS) crystals is of theoretical as well as practical interest, first, from the standpoint of comparing their properties with those of ordinary tri-glycine sulfate (TGS) and, second, in connection with the various applications envisaged for TGS crystals and the possibility of replacing them by DTGS crystals.

We used the following procedure for preparing DTGS single crystals. Single crystals of ordinary TGS were dissolved in heavy water (D_2O). The solution was boiled for more complete deuteration and then large single crystals of DTGS weighing up to 100 g were grown from the solution. The crystals were grown by lowering the temperature from 65° to 50°C. Measurement of the dielectric constant ϵ_{22} showed that the Curie temperature of crystals produced in this manner is 58.9°. We succeeded in obtaining a still higher Curie point (T_C = 60.1°C) by modifying the above procedure. In synthesizing DTGS in this case, we first recrystallized the starting glycine in heavy water. The synthesis itself was effected from solutions of glycine and sulfuric acid in heavy water. This deuteration technique had the effect of raising the Curie point some 10-11°.*

In shape DTGS crystals are identical with TGS crystals. DTGS crystals do not differ in symmetry from TGS crystals, i.e., they belong to the monoclinic system. The bisector of the angle between the optical axes coincides with the polar *b* axis (Y axis). Hence it is impossible to observe the domain structure by polarized light. Consequently, to observe the domain structure in DTGS crystals we used the method of etching plates cut normal to the *b* axis. This method was used earlier[1,2] to observe domains in TGS crystals.

Characteristic domain shapes in the (010) plane are ellipses, sometimes with pointed ends (Fig.1,a), sections of straight lines parallel to the (001) face (Fig. 1,b) or an alternation of these shapes (Fig.1,c). The variation of domain walls under the influence of an electric field is considered in Ref.3. Here we can only point out that the twinned regions in DTGS crystals, as in TGS crystals, are bounded either by planes parallel to the (001) plane or by cylindrical surfaces. The major axis of the elliptical cross section of these cylinders through the (010) plane is parallel to the (001) plane.

As indicated above, the polar direction in DTGS crystals is the Y axis. Therefore we felt that it would be of interest to investigate the temperature dependence of the dielectric constant ϵ_{22} in this direction. The results of measurements carried out on an impedance bridge in weak electric fields are shown in Fig. 2, from which it can be seen that the Curie point of DTGS, which lies at 58.9°C, is considerably higher than the Curie point of TGS, which varies, according to different authors, from 47° to 49.6° C. The temperature dependence of ϵ also exhibits the hysteresis characteristic of ferroelectrics. Fig.2 clearly shows the increase of ϵ in the region of the Curie point and the shift of the Curie point to the side of lower temperatures after the sample has been kept above the Curie point for some time (curve 2). Curves 3 and 4 were recorded while the sample was exposed to a dc biasing field that caused the values of ϵ to decrease in the region of the Curie point and the point to shift to the side of higher temperatures.

Fig.3 shows the variation of ϵ_{22} with the applied alternating field, as the field was increased (1) and decreased (2). It will be seen that ϵ_{22} attains its maximum value at $E_\sim$ = 420 v/cm when the field is increased, and at $E_\sim$ = 240 v/cm

---

*The measurement results given below pertain to crystals with T_C = 58.9°.

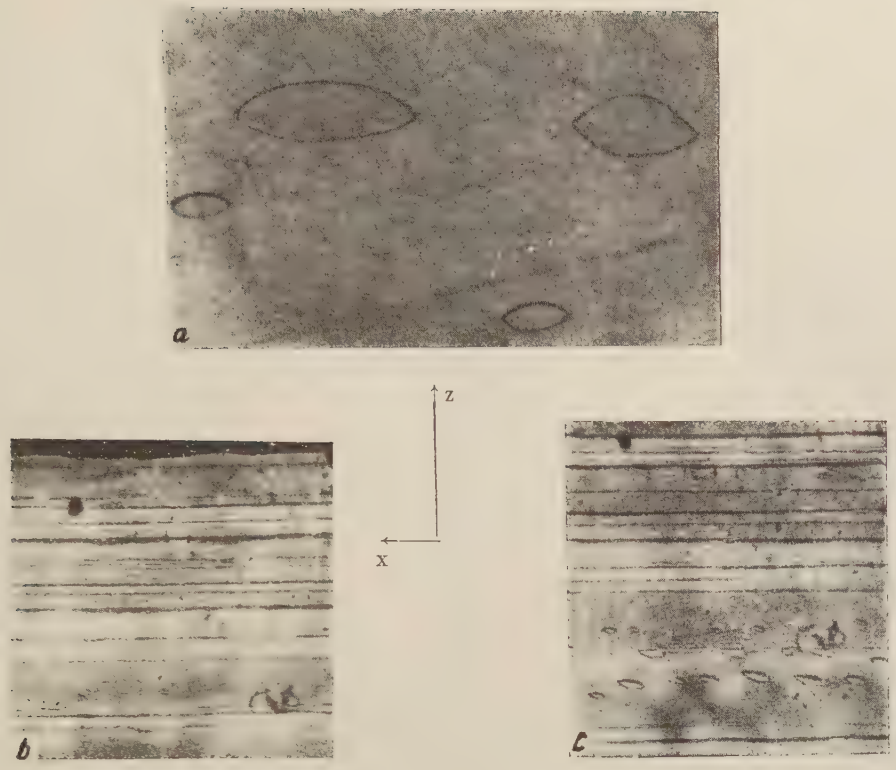

Fig.1. Shape of domains in DTGS crystal: a) elliptical walls, b) walls parallel to the (001) plane; c) mixed walls. Magnification 60 X.

when the field is decreased. The nonlinearity of DTGS, which can be characterized by the ratio $\epsilon_{max}/\epsilon_{init}$, amounts to 38 000/32 = 1200 for curve 1 and 37 000/38 = = 1000 for curve 2. For TGS crystals[2] these ratios equal 1300 and 1000, respectively, but the field strengths at which ϵ_{max} is attained (200 and 100 v/cm, respectively) are considerably lower (than for DTGS).

Fig.4 shows the dc field dependence of ϵ_{22} measured in a weak alternating field. We started measurements after preliminary protracted poling of the specimen in a dc field of 1200 v/cm; the sequence of measurements is indicated by the numbers in Fig.4.

Fig.5 shows curves characterizing the temperature dependences of the spontaneous polarization P_s and coercive field E_c for DTGS crystals. The shape of these curves is analogous to that of the corresponding curves for TGS crystals[2], from which DTGS crystals differ in having somewhat larger values of P_s and E_c. We submit the following comparative data on P_s and E_c for TGS and DTGS crystals, determined from the hysteresis loops at room temperature:

Crystal	P_s, μcoul/cm^2	E_c, v/cm
TGS	2.2-2.6	150-400
DTGS	2.8-3.0	500-800

The hysteresis loops of DTGS, from which the values of P_s and E_c were determined, differ little in shape from those of TGS.

We studied polarization reversal of our DTGS crystals under periodic bipolar rectangular 10 microsecond pulses of uniform amplitude (cf.Ref.4). The maximum switching current i_{max} and the switching time τ_{max} corresponding to i_{max} were

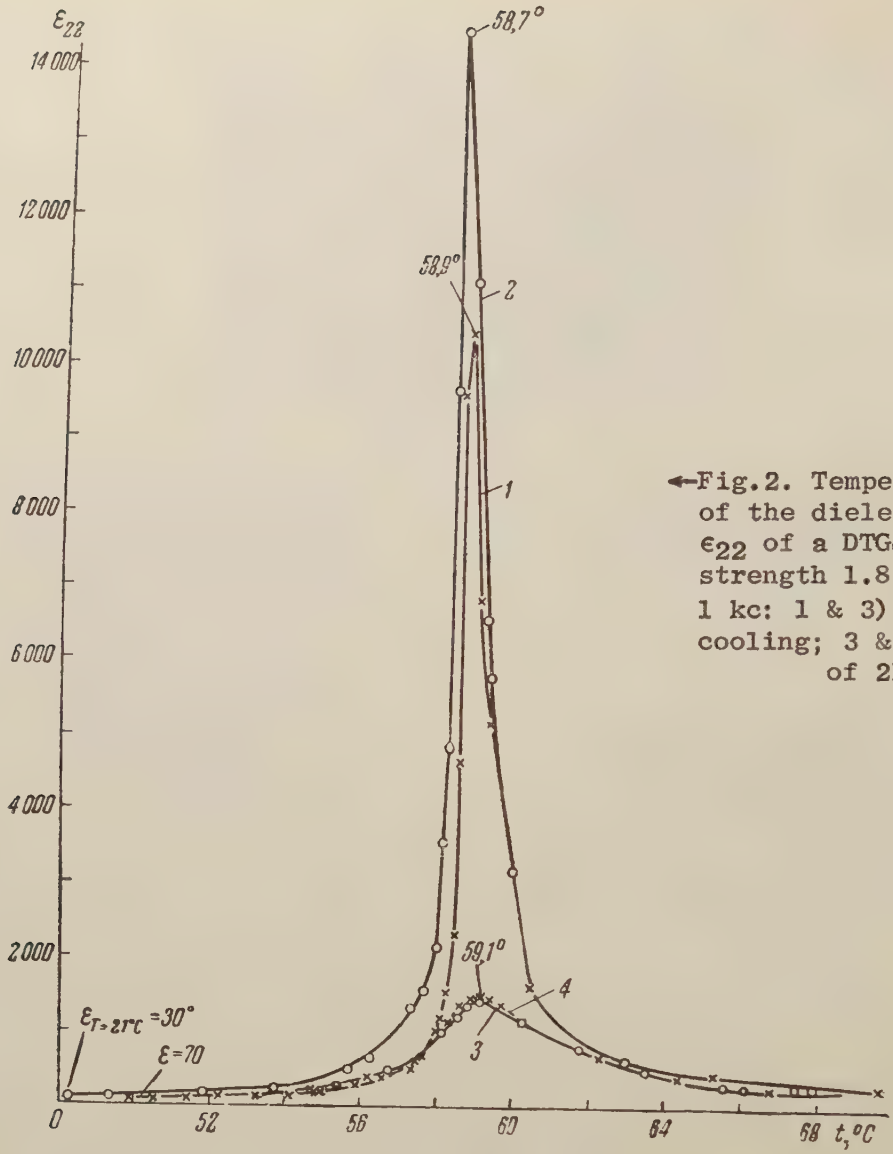

←Fig.2. Temperature dependence of the dielectric constant ϵ_{22} of a DTGS crystal. Field strength 1.8 v/cm, frequency 1 kc: 1 & 3) heating, 2 & 4) cooling; 3 & 4) in a dc field of 2170 v/cm.

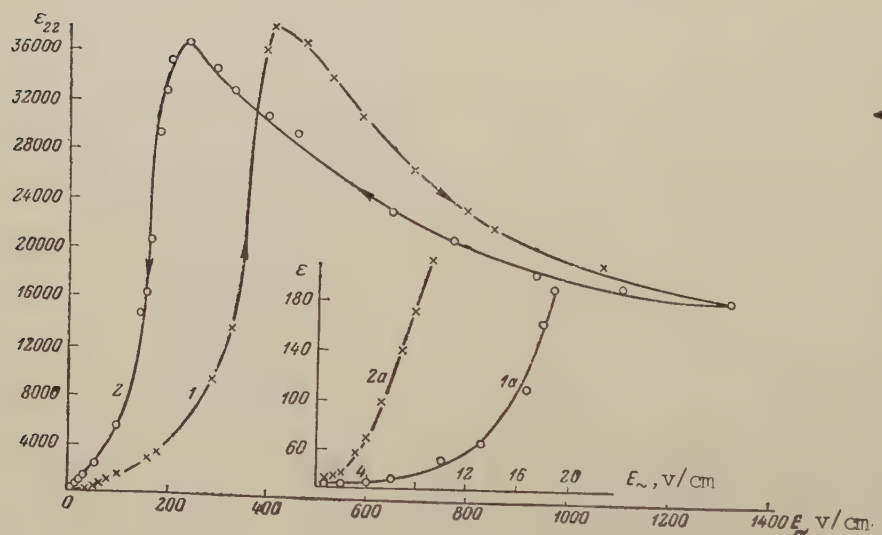

←Fig.3. Alternating field dependence of ϵ_{22} of a DTGS crystal at 42°C: 1) increasing voltage, 2) decreasing voltage; 1a & 2a) initial sections of the curves enlarged.

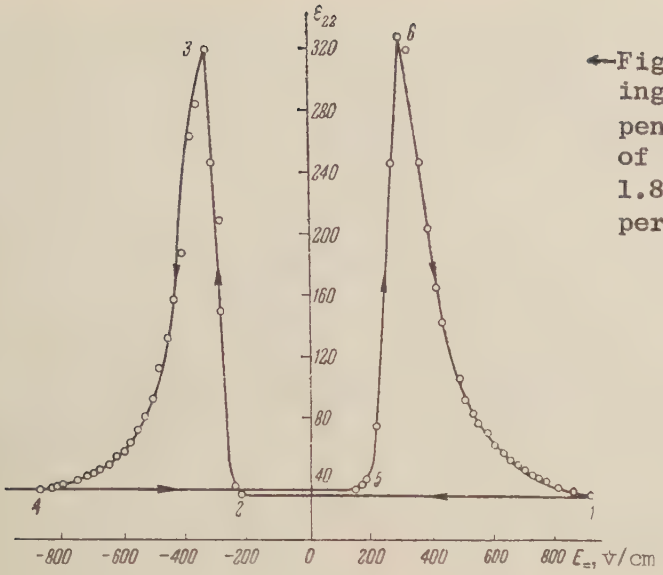

←Fig.4. Dc biasing field dependence of ϵ_{22} of DTGS; ac field 1.8 v/cm; temperature 36.8°.

determined from the trace on an oscillograph.

The specimens were 1 x 1 mm plates 0.15 to 0.25 mm thick cut normal to the polar axis of the crystal. After grinding and washing of the plates, we applied silver electrodes in the form of crossed strips ($\leqslant$ 0.5 mm wide) by vacuum evaporation. We chose this electrode size so that we could disregard the effect of heating of the specimen incident to switching.[5]

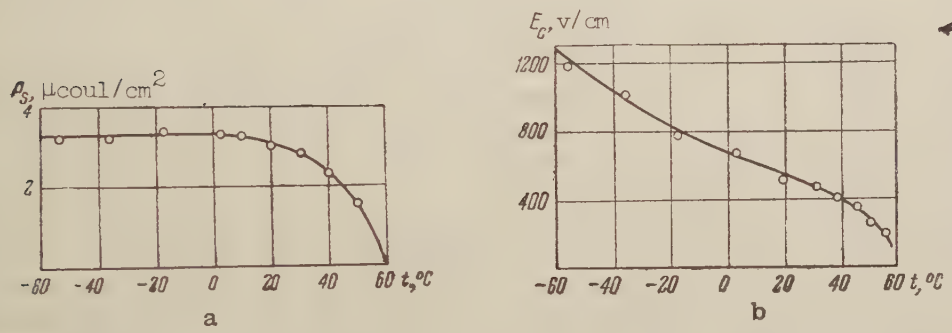

←Fig.5. Temperature dependence of the spontaneous polarization P_S (a) and coercive field E_C (b) for DTGS crystals. Frequency 50 cps; specimen thickness 1 mm; electrode area 1 cm^2.

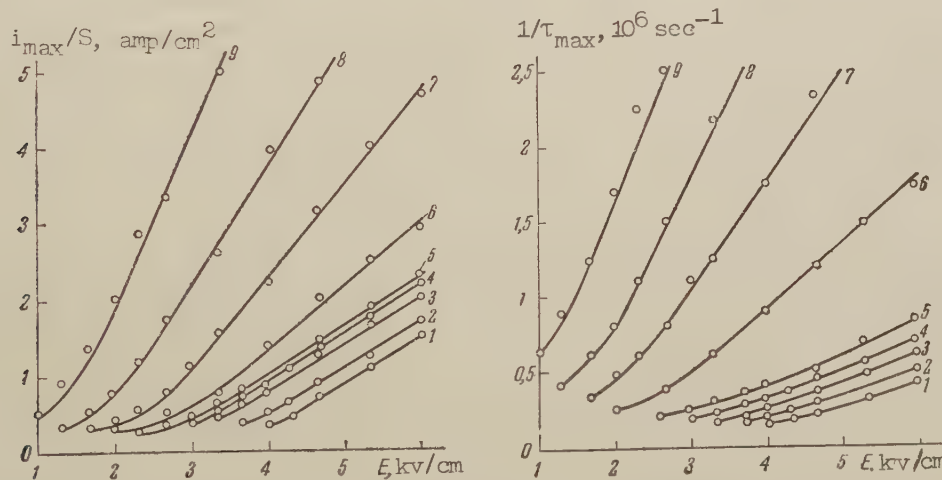

Fig.6. Pulse field dependence of i_{max}/S and $1/\tau_{max}$ at different temperatures for DTGS crystals: 1) 9.0°, 2) 11.0°, 3) 15.0°, 4) 20.3°, 5) 30.3°, 6) 45.0°, 7) 50.0°, 8) 55.0°, 9) 57.0°. Specimen thickness 0.15 mm; f = 300 cps.

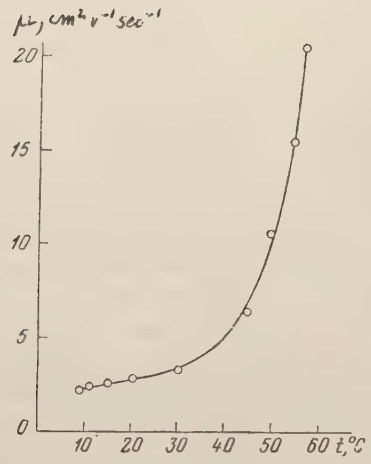

Fig.7. Temperature dependence of wall mobility for DTGS crystals at pulse repetition rate of 300 cps.

Our measurements showed that in DTGS crystals the characteristic dependences of polarization reversal on temperature, field, frequency, and other variables are qualitatively similar to the same dependences for TGS crystals. The deviations of experimental data from the simplest theoretical scheme[6,7] that are observed in TGS crystals (asymmetry of currents and switching time under non-equispaced pulases, sharp increase of the threshold field for reversal by single pulses, etc. - see Refs 4, 5 and 8) also occurs in DTGS crystals.

Fig.6 shows typical $i_{max}/S = f(E)$ (S is the electrode area; E is the pulse field) and $1/\tau_{max} = f(E)$ curves recorded at different temperatures (we note that the upper parts of the curves often deviate from a straight line). Fig.7 shows the temperature dependence of the mobility μ calculated by the formula

$$\mu = \frac{d}{\tau_{max}\,(E - E_\alpha)},$$

where d is the plate thickness and E_α is the activation field. In accord with the character of the temperature dependence of μ, the rate of increase of i_{max}, $1/\tau_{max}$ and reversal conductivity rises with approach to the Curie point; at the same time the activation field falls off. Unlike TGS crystals, however, DTGS crystals exhibit a strong temperature dependence of i_{max} and $1/\tau_{max}$ only above 40°C, while at room temperatures the dependence is relatively weak, which is quite natural considering the difference in Curie points.

Comparison of the pulse polarization reversal characteristics of TGS and DTGS crystals, for example, at t = 20°C and a pulse repetition rate of 300 pps, shows that in conformity with the greater elastance of DTGS crystals, their activation field E_α is ~1.5 times higher than that of TGS crystals and their mobility ~2 times lower; their polarization reversal conductivity σ_p, in spite of a greater value of P_s, also is ~1.5 times lower. If we assume that μ does not depend on the thickness in either case (or depends on it proportionally), it follows that, inasmuch as E_α is higher for DTGS than for TGS and μ is lower, the values of i_{max} and $1/\tau_{max}$ are always higher for TGS plates at any field strength than for DTGS plates of the same thickness and in the same field. It is obvious, however, that using thinner plates of DTGS than TGS, it is possible to obtain the same values of i_{max} and i/τ_{max} at a given temperature for the same pulse voltage.

If therefore we take into consideration that DTGS crystals have a wider useful temperature range than TGS crystals and that the temperature dependence of their characteristics in the region of room temperatures is substantially weaker, we conclude that in spite of their higher elastivity DTGS crystals can be employed in the same cases as TGS crystals.

We desire to thank I.S.Zheludev for valuable discussions and E.M.Akulenok, K.A.Pluzhnikov and L.N.Kurkovska for help in carrying out the experiments.

Institute of Crystallography,
Academy of Sciences of the USSR

References

1. Bell Lab.Record, 25, 7, 271 (1957).
2. V.P.Konstantinova, I.M.Sil'vestrova & V.A.Yurin, Kristallografiya, 4, 125 (1959). (Trans.Soviet Physics - Crystallography.)
3. V.P.Donstantinova, Izv.AN SSSR, 24, No.11 (1960). (Trans.Bulletin, 24, No.11).
4. L.A.Shuvalov, Kristallographiya, 5, 409 (1960). (Trans.Soviet Physics - Crystallography.)
5. L.A.Shuvalov, Izv.AN SSSR, Ser.fiz., 24, No.11 (1960). (Trans.Bulletin, 24, No.11.)
6. W.Merz, Phys.Rev., 95, 500 (1954).
7. C.Pulvari & W.Kuebber, J.Appl.Phys., 29, No.9, 63 (1958).
8. L.A.Shuvalov, Kristallografiya, 5, 282 (1960). (Trans.Sov.Phys. - Crystallography.)

ON THE FERROELECTRIC PROPERTIES OF $NaNO_2$

- A.S.Sonin, I.S.Zheludev & G.F.Dobrzhanskii

For some years two of the present authors have been developing a principle to aid in the search for new ferroelectrics, based on the changes of symmetry incident to phase transitions associated with the appearance of spontaneous polarization. The regularity in the variation of point symmetry with ferroelectric phase transitions that one of the authors discovered in collaboration with Shuvalov[1,2], has made it possible to formulate a crystallophysical* criterion for seeking new ferroelectrics[3]; this can be summarized as follows: a dielectric may have ferroelectric properties if its point symmetry group below the phase transition temperature is a higher subgroup of the point symmetry group above the phase transition temperature and the $\infty \cdot m$ symmetry group describing spontaneous polarization. Ref.3 lists six inorganic compounds whose changes comply with the crystallophysical criterion; in other words, these compounds ($RbNO_3$, $CsNO_3$, $NaNO_2$, AgCN, Cu_2S and $Mg_3B_7O_{13}Cl$) are potential ferroelectrics.

To refine the principle formulated to aid in the search for new ferroelectrics, we investigated the change in space symmetry with ferroelectric phase transitions. It turned out that the variation of space symmetry associated with the appearance of spontaneous polarization, also complies strictly with certain regularities[4]. This has afforded the possibility of refining the crystallophysical criterion and selecting further compounds that may have ferroelectric properties.

The refined crystallophysical criterion can be formulated as follows: a dielectric will in all probability have ferroelectric properties if its space symmetry below the phase transition temperature is generally a higher subgroup of the space symmetry group above the phase transition temperature and the $(\infty \cdot m)T$ symmetry group describing the vector field of the spontaneous polarization. Whether this criterion is not only necessary but also sufficient remains an open question for the time being. This question can only be answered after more experimental work has been done on compounds with the indicated symmetry changes. The crystallophysical criterion has, however, already made it possible to reduce the number of compounds in which it is reasonable to look for ferroelectric properties. Thus, in only two of the above mentioned six substances (namely, AgCN and $NaNO_2$) do the actually established changes in space symmetry with phase transitions allow the presence of spontaneous polarization below the phase transition temperature.

Silver cyanide undergoes a polymorphous transition at ~190°. Below the phase transition temperature AgCN crystallizes in space group $C_{3v}^5 = R3m$ (point group $3 \cdot m$ in Shubnikov's system of designations); above this temperature it crystallizes in space group $O_h^5 = Fm3m$ (point group $\bar{6}/4$)[5,6]. Such a change of symmetry incident to the phase transition can occur if spontaneous polarization in the [111] direction appears in the initial high-temperature cubic phase of AgCN. The electrical properties of this compound will be studied in the near future.

Sodium nitrite also has a phase transition at ~160°.[7] Below the phase transition temperature $NaNO_2$ belongs to space group $C_{2v}^{20} = Imm$ (point group $2 \cdot m$) with lattice parameters a = 3.55 Å, b = 5.38 Å, and c = 5.56 Å and has two formula units per unit cell. Above the phase transition temperature the space group is $D_{2h}^{25} = Immm$ (point group $m \cdot 2 : m$) with cell parameters a = 3.69 A, b = 5.68 A, and c = 5.33 A at 205°.[7] This symmetry change is compatible with the appearance of spontaneous polarization in the initial high-temperature phase in the [001] direction.

---

*In Ref.3 this criterion was unfortunately termed "crystallographic".

The other four substances, while they meet the crystallophysical criterion as regards their point symmetry groups, in fact evince a change of space symmetry that does not comply with the refined crystallophysical criterion. The nitrates of rubidium and cesium at ~164° undergo polymorphous transitions from space group $O_h^1 = Pm3m$ (point group $\bar{6}/4$ to space group $C_{3v}^2 = H3m$ (point group $3 \cdot m$). If spontaneous polarization in the [111] direction appeared in the high-temperature phases of these compounds (only in this case will the transition be to $3 \cdot m$) the space symmetry groups of the low-temperature phases would be $C_{3v}^5 = R3m$.[4] Consequently, the phase transitions in rubidium and cesium nitrate cannot be ferroelectric.

Nor can we, by the same token, regard the changes of symmetry of Cu_2S and $Mg_3B_7O_{13}Cl$ as being due to the appearance of spontaneous polarization. At 103° Cu_2S undergoes a polymorphous transition with a change of space symmetry from $D_{6h}^4 = C6/mmc$ (point group $m \cdot 6 : m$) to space group $C_{2v}^{15} = Abm$ (point group $2 \cdot m$).[8] But a phase transition with the appearance of spontaneous polarization in the $11\bar{2}0$ direction (only in this case the point group would be $2 \cdot m$) should lead to space group $C_{2v}^{16} = Ama$.[4] $Mg_3B_7O_{13}Cl$ at 265° changes from space group $T_d^5 = F\bar{4}3c$ (point group $3/4$) to space group $C_{2v}^5 = Pca$ (point group $2 \cdot m$).[4] But the appearance of spontaneous polarization in the [100] direction should lead to space group $C_{2v}^{21} = Iba$.[4] We investigated the electrical properties of rubidium nitrate and boracite and, in accordance with what was said above, they showed no evidence of ferroelectricity.

Early in 1958 I.V.Garvilova at our request grew single crystals of sodium nitrite from solution. These single crystals, however, had very high conductivity and proved unsuitable for dielectric measurements. In 1958 Sawada[9] and his collaborators, independently of us, discovered ferroelectricity in $NaNO_2$ crystals grown from a melt.

The sodium nitrite crystals that we used in the measurements described below were grown from a melt by a variant of the Obreimov-Shubnikov technique.[10] The raw material for the crystallization was chemically pure grade sodium nitrite with T_{melt} = 271°. The crystals were grown in cylindrical glass ampoules 16 mm in diameter with a 45° conical bottom. To reduce the adhesion we coated the inner surface of the ampoule with a thin layer of aquadag and dried it carefully. To make efficient use of the volume of the ampoule, the substance was introduced into it not in the form of a powder but in the form of a compressed (800 kg/cm^2 pressure) plug fitting the ampoule. Before the start of crystallization, the furnace was heated to 10-15° above the melting point of sodium nitrite. The loaded and sealed ampoule was suspended at the end of the feed cable and initially positioned in the furnace so that the lower part of the ampoule was 3-5 mm above the crystallization zone. The ampoule was lowered into the furnace at the rate of 2 mm per hour. The crystal was annealed in the same furnace while slowly lowering the temperature.

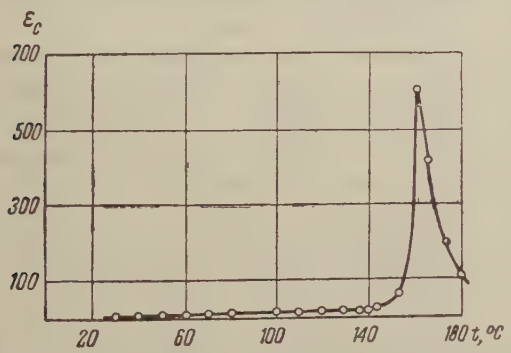

Fig.1.Temperature dependence of the dielectric constant ϵ_c of $NaNO_2$.

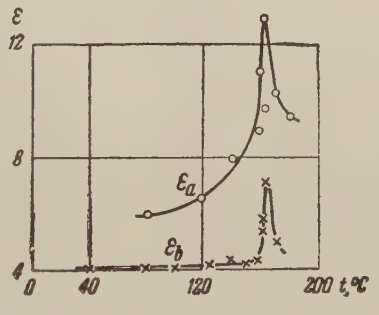

Fig.2. Temperature dependence of the dielectric constants ϵ_a and ϵ_b of $NaNO_2$.

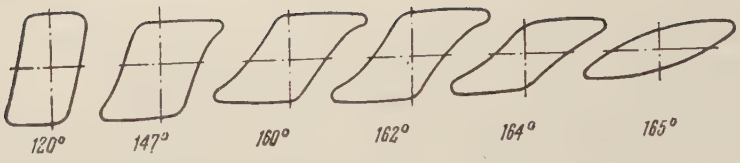

Fig.3. Shape of $NaNO_2$ hysteresis loops.

The single crystals had the shape of the ampoule. They were 40-50 mm long, 16 mm in diameter, and slightly yellowish in color. They cleaved readily along the (101) planes. The orientation of the cleaved chips was determined from Laue diffraction patterns.

Unlike the authors of Ref. 3, we mounted the crystal in accordance with international practice: the c axis along a second order axis of the crystal and the dimension along the b axis was greater than along the a axis.

Silver electrodes were applied to the $NaNO_2$ plates by vacuum evaporation. Measurements in the range from room temperature to 100° were carried out in a Vobzer thermostat with water and in the range from 100° C to 200° in a thermostat with silicone liquid No.5. The values of the dielectric constant were measured at a frequency of 500 kc. Figs.1 and 2 show the temperature dependence of the dielectric constants along the three crystallographic axes. It will be seen that the dielectric constant along the ferroelectric c axis has a very pronounced peak rising to ~600 at the phase transition temperature (165°). The dielectric constants along the a and b axes also have noticeable peaks, the maximum values being ~13 and ~7, respectively.

The dielectric hysteresis loops were investigated at 50 cps with the aid of a circuit that provided for compensation of the conduction.[11] In the range from room temperature to 120° no hysteresis loops are observed even at a field strength of 10 kv/cm, above which breakdown occurs. From 120° to 147°C "unsaturated" hysteresis loops are observed. The form of the loop at 165° (shown in Fig.3) testifies to the high conductivity of the crystal. The spontaneous polarization and coercive field were calculated from the hysteresis loops.

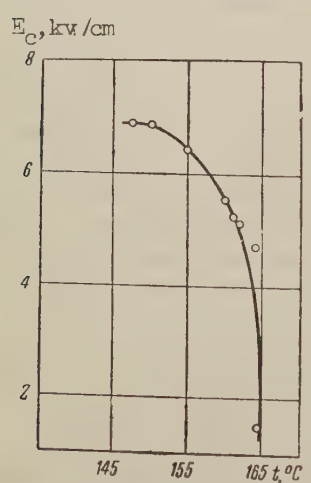

Fig.4. Temperature dependence of the coercive field in $NaNO_2$.

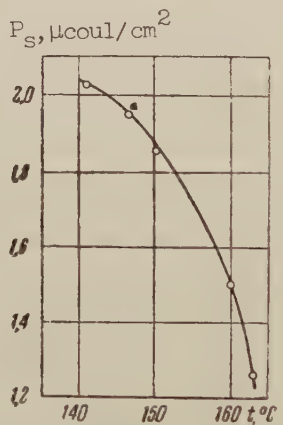

Fig.5. Temperature dependence of the spontaneous polarization in $NaNO_2$.

The temperature dependences of P_s and E_c are shown in Figs. 4 and 5. At 147° the spontaneous polarization is equal to 2 μcoul/cm^2, and the coercive field is equal to 7 kv/cm. The form of the hysteresis loop as well as the temperature dependence of the coercive field testifies to the high elastivity of $NaNO_2$ in the range from room temperature to 147°; the spontaneous polarization and coercive field fall off sharply as the Curie point is approached. The samples used in our measurements had a smaller value of P_s and greater value of E_c than those reported by Sawada[9]. This is explained by the difference in crystal growing conditions and also the high hygroscopicity of sodium nitrite.

We thank V.I.Pakhomov and G.M.Lobanova for orienting the samples, I.Fenina for help in the experiments, and L.A.Shuvalov and I.S.Rez for discussing the results.

Institute of Crystallography,
Academy of Science of the USSR

References

1. I.S.Zheludev & L.A.Shuvalov, Kristallografiya (Crystallography), 1, 681 (1956).
2. I.S.Zheludev & L.A.Shuvalov, Izv.AN SSSR, Ser.fiz., 21, 264 (1957). (Trans. Bulletin 21, 266.)
3. I.S.Zheludev & A.S.Sonin, Ibid., 22, 1441 (1958). (Trans.Bulletin, 22, 1435.)
4. A.S.Sonin & I.S.Zheludev, Kristallografiya, 4, 487 (1959). (Trans.Soviet Physics - Crystallography.)
5. C.F.Ziegler, Phys.Rev., 38, 1040 (1931).
6. G.B.Carpenter, Acta Crystl, 5, 132 (1952).
7. B.Strijk & C.H.MacGillavry, Rec.trav.chim., 62, 703 (1943).
8. N.V.Belov & V.A.Butuzov, Doklady AN SSSR, 54, 721 (1946).
9. S.Sawada, S.Nomura, S.Fujii & I.Yoshida, Phys.Rev.Letters, 1, 320 (1958).
10. L.M.Belyaev, B.V.Vitovskii & G.F.Dobrzhanskii, in "Rost kristallov" (Growth of Crystals - collected articles), p.253, Pub. 1957.
11. H.Diamant, K.Drenck & R.Pepinsky, Rev.Sci.Inst., 28, 30 (1957).

CONCERNING LIGHT DETECTORS UTILIZING THE PYROELECTRIC EFFECT

- I.M. Sil'vestrova

As has been reported by a number of authors[1-3], one can utilize the pyroelectric effect to realize detectors for radiation in the visible and infrared regions. We investigated the possibility of using tri-glycine sulfate crystals as light detectors. As was shown by Chynoweth[1], in working with pyroelectric crystals, one can observe the voltage either across the crystal or across a resistor connected in series with the illuminated crystal. The pyroelectric current is given by the following formula

$$i = \frac{dP}{dt} = \gamma \frac{dT}{dt},$$

where P is the polarization of the specimen, $\gamma = dP/dT$ is the pyroelectric constant of the specimen and dT/dt is the rate of change of the specimen temperature.

Inasmuch as ferroelectric crystals are characterized by a high value of the pyroelectric constant, on the one hand, and exhibit a relatively strong dependence of the polarization on the temperature and applied dc field, on the other hand, in attempting to realize a light detector it is of interest to investigate the variation of the pyroelectric voltage as a function of all these parameters. For the purposes of our investigation we used the simple method of orienting the crystal relative to the incident light shown in Fig.1.

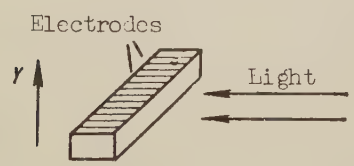

Fig.1. Orientation of the crystal relative to the incident light.

The crystal plates were cut perpendicular to the polar axis and measured 6 x 3.5 x 1.5 and 6 x 3 x 1 mm. The electrodes, applied to two opposite faces of the plate, were made of silver foil. The light source was a 6 v, 30 watt incandescent bulb mounted on the optical bench at a distance of 1 meter from the crystal. The image of the filament was first focused (glass optics) on the circular apertures in the rotating disk; the spacing between the holes was equal to their diameter. The interrupted light beam was then focused on the crystal. The pulse frequency could be varied from 200 to 5000 pulses/sec.

The electric circuit used in our experiments is shown in Fig.2. The voltage from the crystal plate was applied to the input of the amplifier. The amplifier circuit was designed to amplify the electric signal without significantly amplifying the noise from the crystal. The use of negative feedback largely compensated the influence of the long leads. This made it feasible to locate the crystal at a considerable distance from the amplifier, that is, this enabled us to mount the crystal in a thermostat and to carry out measurements with strong polarizing fields applied to the crystal. The noise level at the input to the 28IM vacuum-tube voltmeter did not exceed $15 \cdot 10^{-6}$ v. The pyroelectric voltages were read directly off the 28IM meter.

The results of measurement of the temperature dependence of the pyroelectric voltage are shown in Fig.3 (these measurements and those described below were carried out at a light pulse frequency of 1720 pulses/sec). It will be evident that the sensitivity of the detector rises substantially in the neighborhood of 40°, and then falls off beginning with a temperature of 46-47°. In the course of these experiments the specimen was always in a polarized state, i.e., a dc field of 6000 v/cm was applied to the crystal during the measurements. If the crystal is prepolarized, but no dc field is applied during the time of measurement, the sensitivity beings to fall off at 45.5° and drops to zero at 48.5°. If, however, a dc field is applied at this point, the sensitivity increases with increasing field strength.

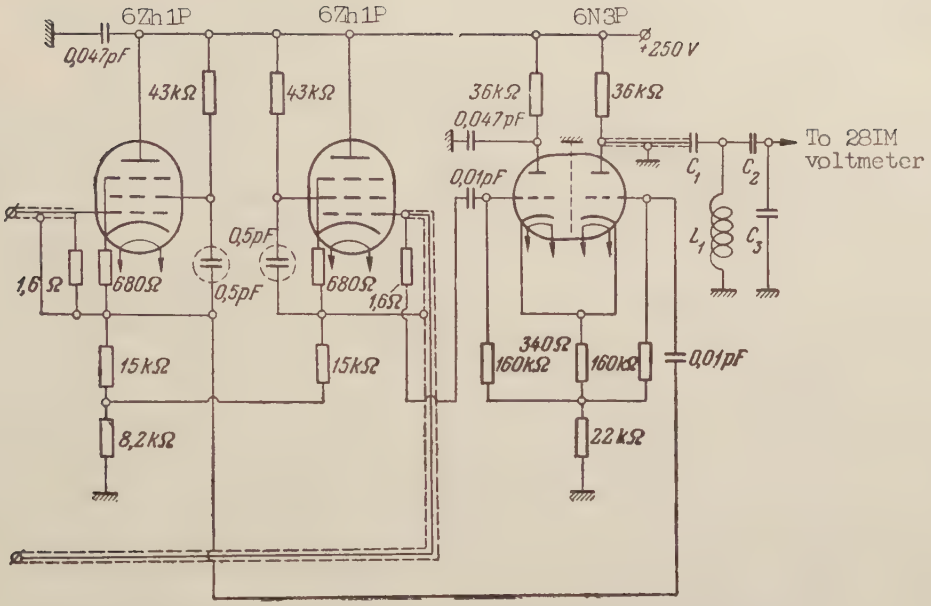

Fig.2. Electric circuit of the experimental set-up.

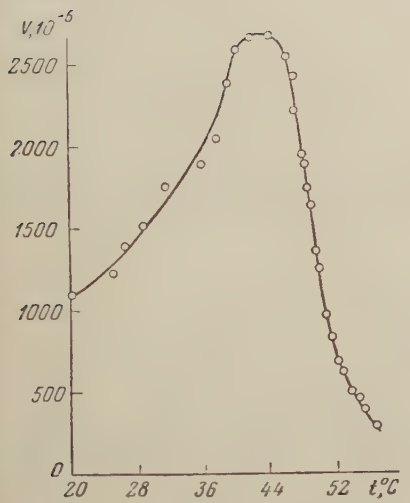

Fig.3. Variation of the pyroelectric voltage at the amplifier input with temperature.

The results of investigation of the influence of a dc field on the pyroelectric voltage at a number of different temperatures are shown in Fig. 4. The influence of a prepolarizing dc field on the pyroelectric voltage with the crystal at 20° is shown in Fig.5, from which it will be evident that the field dependence of the pyroelectric voltage exhibits hysteresis. The coercive field in the specimen, evaluated on the basis of these measurements, is 400 v/cm, which is in good agreement with the data of Savage & Miller[4].

On the basis of the experimental data it may be concluded that it is most expedient to use tri-glycine sulfate crystals as radiation detectors in the 40 to 45.5° temperature range, inasmuch as in this region the sensitivity is 2.5-2.7 times higher than the sensitivity at room temperature. Inasmuch as in this temperature region tri-glycine sulfate has a relatively high dielectric constant, this also simplifies the matter of matching the detector with the amplifier. If it is necessary to work in the temperature region close to 50°, a strong polarizing field should be applied to the crystal. Short term application of a field of opposite polarity of up to 180-200 v/cm does not significantly reduce the sensitivity of the detector.

I desire to express my gratitude to Yu.N.Sil'vestrov for supplying the amplifier circuit and V.P.Konstantinova for furnishing the crystal specimens.

Institute of Crystallography,
Academy of Sciences of the USSR

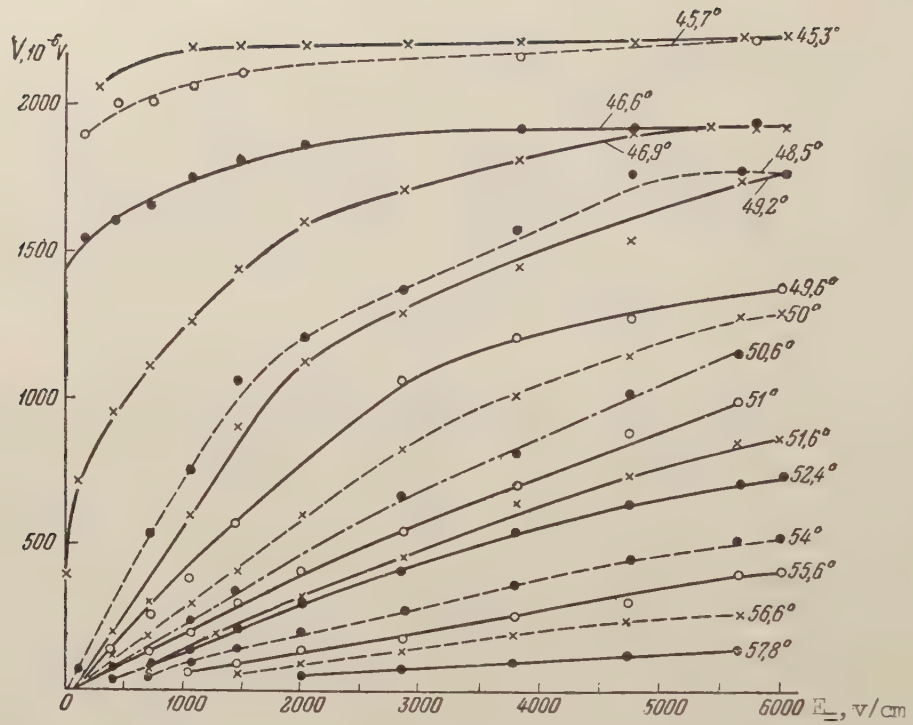

Fig.4. Variation of the pyroelectric voltage with the dc field at different temperatures.

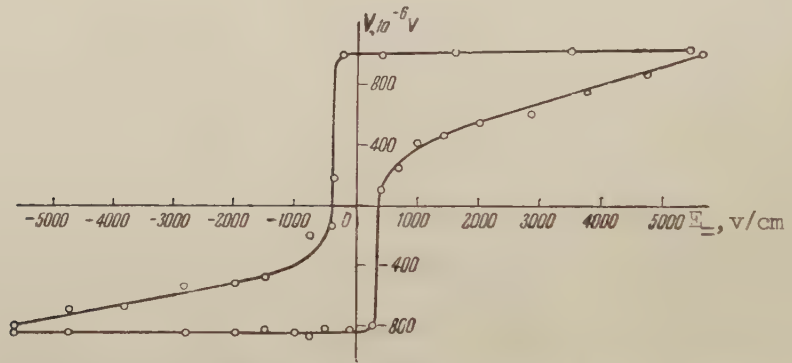

Fig.5. Variation of the pyroelectric voltage with the prepolarizing dc field at room temperature.

References

1. A.G.Chynoweth, J.Appl.Phys., 27, 78 (1956).
2. A.G.Chynoweth, Phys.Rev., 10, 707 (1956).
3. T.A.Perls, I.Diesel & W.I.Dobrov, J.Appl.Phys., 29, 1297 (1958).
4. A.Savage & R.C.Miller, J.Appl.Phys., 30, 1646 (1959).

DAMPING OF THE OSCILLATIONS OF PIEZOELECTRIC RESONATORS EMPLOYING FERROELECTRIC SINGLE CRYSTALS

- L.A.Shuvalov & Yu.S.Likhacheva

Introduction

It is well known that attenuation of mechanical oscillations and sound waves in ferromagnets is anomalously large as compared with attenuation in other metals, has a maximum at the Curie point and is strongly dependent on the magnetic field applied to the specimen. These anomalies have been studied in detail and are explained mainly by the effect of reorientation of the ferromagnetic domains (see, for example, Bozorth[1]).

The attenuation of mechanical oscillations and sound waves in ferroelectric materials is also characterized by similar anomalies. Among the few investigations in this field one can cite the work of Price[2] and the series of studies by Yakovlev and his co-workers[3-5] on attenuation of ultrasonic waves in Rochelle salt, the work of Takuro[6] and Hueter & Neuhaus[7] on ultrasonic absorption and internal friction in barium titanate ceramics, and the work of Matthias[8] who investigated attenuation in piezoelectric resonators of Rochelle salt.

Although there can be no doubt regarding the ferroelectric nature of the damping anomalies in ferroelectrics, there are discrepancies in different attempts to explain them, particularly as regards the role of domain processes, while the experimental data available to check theory are so far scanty. Hence additional experimental investigations are highly desirable. Moreover, investigation of attenuation, primarily in the case of single crystals, may be a fruitful method of investigating some of the fundamental manifestations of ferroelectricity, in particular, the domain structure and the influence on it of impurities, irradiation, aging and other factors, as well as the role of dislocations in the mechanism of domain reorientation. In addition, such investigations may be of practical interest from the standpoint of development of filters and acoustic systems.

Below we describe the results of some experiments on attenuation in piezoelectric resonators of Rochelle salt, both ordinary and γ-irradiated and also in piezoelectric resonators of tri-glycine sulfate.

1. Measurement Procedure

For investigating attenuation in piezoelectric resonators of ferroelectric single crystals we chose the procedure based on direct measurement of the damping of the natural mechanical oscillations of the resonator, inasmuch as this procedure has a number of advantages over other techniques.

A block diagram of the experimental set-up is shown in Fig.1. The temperature of the specimen was controlled thermostatically and there were applied to it pulses with a duty frequency equal to the frequency of the series resonance of the specimen. The frequency was measured by comparison with the frequency of a high precision oscillator by observing the Lissajous figures. The frequency of the series resonance was assumed to be the natural frequency of the resonator (we disregarded the minor error involved in this assumption). The onset of resonance was observed on the screen of the I0-4 oscillograph to which the specimen was connected via a low value resistor ($R_2 \approx 30$ ohm) and amplifier. In the intervals between pulses there occurred free attenuation of the mechanical oscillations. As a result there appeared a stationary pattern on the oscillograph screen (Fig.2); from photographs of this pattern (or visually) we determined the logarithmic attenuation decrement δ taking into account the time markers and the natural frequency of the resonator. When desired a dc biasing field $E_=$ (monitored by a

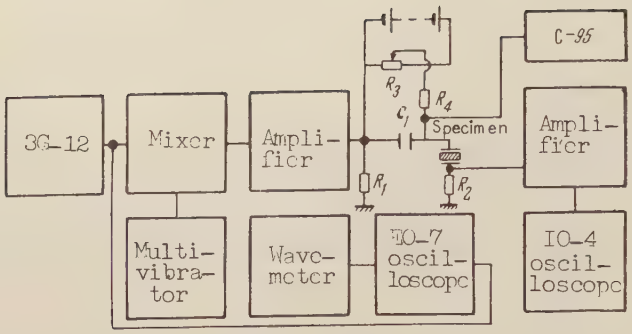

Fig.1. Block diagram of set-up for measuring attenuation in piezoelectric resonators.

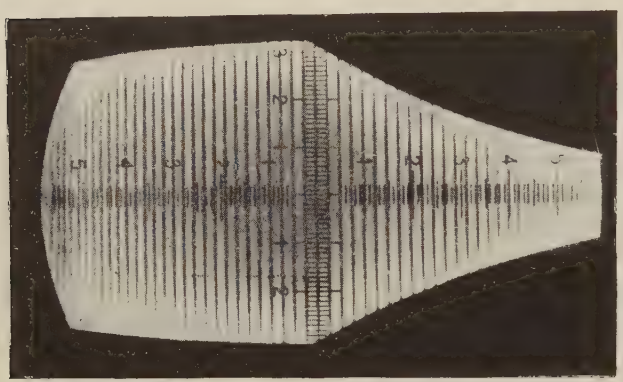

Fig.2. Typical attenuation pattern observed on oscillograph screen (pattern obtained for 45° X cut Rochelle salt crystal with $E_{=} = 0$ and $t = 36.8°$; $\delta = 0.0059$.

voltmeter) could be applied to the specimen through the capacitor C_1. Owing to the fact that ferroelectric materials may have an appreciable ΔE effect ($E_{=}$ dependence of the elasticity), it was necessary to re-establish the resonance frequency for each value of $E_{=}$.

Inasmuch as a resonator is an electromechanical transducer, its attenuation (particularly in the case of ferroelectrics) depends on the conditions on the electric side. In order to obtain conditions close to those for short circuited operation, the total resistance in the resonator circuit $R_1 + R_2$ was made small compared with the minimum equivalent resistance of the resonator. Moreover we determined the variation of δ with $R_1 + R_2$; extrapolation of the curve to $R_1 + R_2 = 0$ showed that the fact that $R_1 + R_2$ has a finite value produces only a small change in the value of δ (~3%).

Strictly speaking, for a ferroelectric piezoelectric resonator* one can give the values of the resonance (or natural) frequency, the elasticity modulus and other parameters not in general but only for a given oscillation amplitude inasmuch as at large amplitudes there becomes evident, particularly near the Curie point, nonlinearity of its elastic properties, which leads, as was noted earlier by one of the authors of Ref.9, to tilting of the resonance curve and the appearance on it of hysteresis amplitude jumps and, consequently, to ambiguity (multiple values) of the resonance frequency.** Moreover, it must be borne in mind that at high oscillations amplitudes there occurs significant nonuniform heating of the resonator; the presence of a temperature gradient (and, consequently, an elasticity gradient, which becomes very steep near the Curie point) also introduces a degree of nonlinearity and complicates the situation further. In order to be able to neglect these effects, which become significant in the in-

---

*Here and below we use the term "ferroelectric piezoelectric resonator" in order to emphasize the diverse specific properties of piezoelectric resonators employing a ferroelectric crystal, the vibrations of which are connected with a "ferroelectric" (anomalous) elasticity constant. It is obvious that not every piezoelectric resonator with a ferroelectric crystal will be a ferroelectric piezoelectric resonator in this sense.

**The existence in a ferroelectric resonator of two stable amplitudes at one and the same frequency can in principle be utilized for realizing bistable elements for logic and other switching circuits.

vestigated 45° X-cut specimens of Rochelle salt at exciting field values of the order of 10-30 v/cm (the difference between the on and off resonance frequencies attains several hundred cps), and be able to regard the resonator as linear in the experiments, the amplitude of the exciting field was not allowed to exceed 0.5 v/cm.

Direct determination of the oscillation amplitude of the resonator is difficult; hence the measurements were carried out not at a constant oscillation amplitude A (which would be more desirable in view of the dependence of the damping on the oscillation amplitude) but at a constant amplitude of the current through the resonator, i.e., with $V_{R_2} = \text{const}$. The oscillation amplitude of the resonator with $E_{=} = 0$ did not remain constant with change in temperature but decreased upon approach to the Curie point owing to growth of the piezoelectric coefficient e_{ij}. Inasmuch as at the chosen values of V_{R_1}, $\partial\delta/\partial A > 0$, normalization of the experimental conditions led in general to some smoothing out of the maximum in the $\delta = f(t)$ curve (t is the temperature). Owing to a maximum of the piezoelectric coefficient d_{ij} at the Curie point, normalization of the experimental conditions when V_{R_1} is kept constant (these were the conditions of Matthias' experiments[8]) leads to the opposite result. As control experiments showed, the difference between the values of δ in zero dc biasing field for the two different normalizations even at the Curie point does not exceed ~15%. At large values of $E_{=}$ the difference between the temperature dependences should be even smaller.

In order to be able to neglect the error due to deviation of the actual attenuation curve from an exponential one[10], the number of oscillation periods taken for determining δ was large (from 10 to 300 depending on the magnitude of δ).

2. Specimens

The specimens in the form of rectangular bars (approximate dimension 20 x 4 x 2 mm) were cut from single crystals grown by the usual technique. Silver electrodes (tinsel or sputtered) were applied to the main (largest) faces.

The specimens were mounted either on rigid leads attached by conducting cement to the centers of the main faces or they were clamped between weak spring knife contacts along the nodal line. Control measurements showed that the form of mounting and method of applying the electrodes had no significant influence on the value of δ. The mounted specimens were placed in the envelope of a bantam type tube, the opening of which was then capped.

3. Experimental Results

The results of measurements of $\delta = f(t)$ with $E_{=} = \text{const}$ and $\delta = f(E_{=})$ with $t = \text{const}$ on 45° X, 45° Y and 45° Z cut Rochelle salt specimens are shown in Figs. 3 and 4.

It will be evident from Fig.3, first, that for 45° X cut bars at $E_{=} = 0$ in the ferroelectric region far from the Curie point δ is 2-3 times higher than for 45° Y and 45° Z cut bars. Second, for 45° X cut bars at $E_{=} = 0$, δ depends strongly on the temperature and at the Curie point* has a sharp peak, while in the case of 45° Y and 45° Z cut bars δ is virtually independent and does not peak near the Curie point. Above the Curie point δ in 45° X cut bars falls off rapidly and beginning with 35-37° becomes weakly temperature dependent, the value of δ remaining one order of magnitude higher than for 45° Y and 45° Z cut bars. The δ vs t curve for a 45° X cut specimen in zero biasing field plotted on the basis of the

---

*As preliminary measurements showed, all the singularities in the behavior of δ in the region of the upper Curie point also obtain in the region of the lower Curie point.

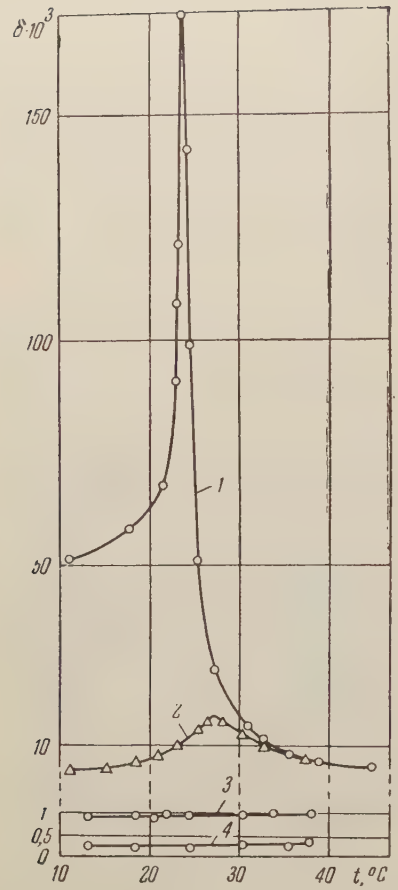

Fig.3. Variation of δ with temperature for 45° X cut bar with $E_{=}$ = 0 (1) and $E_{=}$ = 2000 v/cm (2), 45° Y cut (3) and 45° Z cut (4) Rochelle salt crystal.

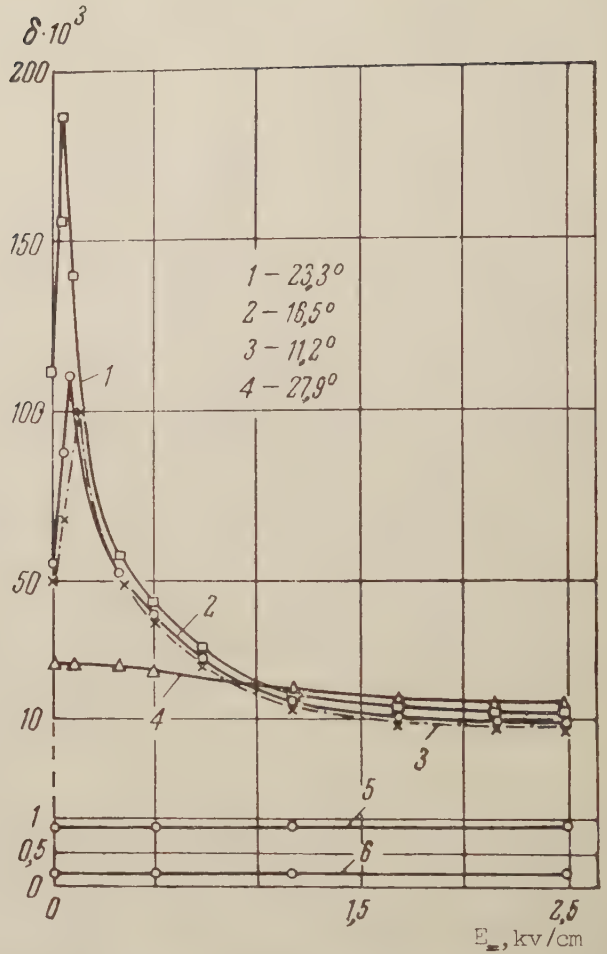

Fig.4. Variation of δ with $E_{=}$ for 45° X cut bars at different temperatures (1-4) and 45° Y and 45° Z (6) cut specimens of Rochelle salt. Only the parts corresponding to decrease of $E_{=}$ are shown for curves 1-4.

data of Matthias[8] is very close to our curve, except that the maximum at the Curie point is broader and higher.

The influence of a dc biasing field on δ differs for 45° X cut as compared with 45° Y and Z cut bars. Whereas in the case of the latter, δ does not depend on $E_{=}$, in the case of 45° X cuts in the ferroelectric region near it, δ depends strongly and in a rather complicated manner on $E_{=}$ (Fig.4). With increase of $E_{=}$ δ at first increases, then after passing through a maximum falls off, at first rapidly and then more slowly, leveling off at $E_{=}$ = 1200-1500 v/cm. The influence of $E_{=}$ on δ is most pronounced in the region of the Curie point; it is weaker elsewhere but still evident to some 10° beyond the ferroelectric region. The point of maximum δ on the $\delta = f(E_{=})$ curve with increase in temperature and approach to the Curie point is shifted to the left, and beginning with approximately the Curie temperature is centered at $E_{=}$ = 0.

The temperature dependence of δ in 45° X cut bars in the range of large $E_{=}$ is smoothed out (curve 2 in Fig.3); however, the maximum, although appreciably lower, persists (since the Curie point upon application of a biasing field is

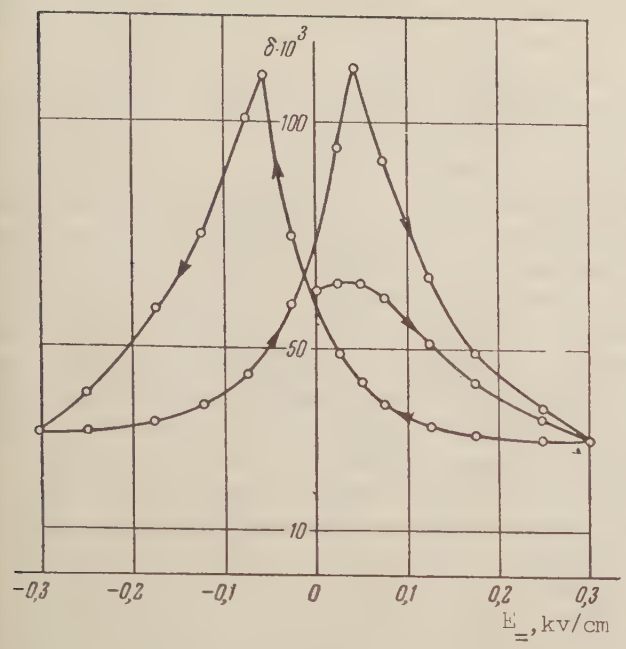

Fig.5. "Butterfly" hysteresis loop characterizing the variation of δ with $E_{=}$ for a 45° X cut Rochelle salt bar at t = 17.0°. The successive variations of $E_{=}$ are indicated by the arrows.

shifted to the right, the peak of curve 2 in Fig.3 lies to the right of the peak in curve 1). This curve is very close to the corresponding curve plotted on the basis of Matthias' data, but lies somewhat higher.

The attenuation of 45° X cut resonators at temperatures below the Curie point in the region of dc biasing fields that strongly affect δ proved to be a non-unique function of $E_{=}$, the form of which depends on the previous variation of $E_{=}$. As is shown in Fig.5, with initial increase of $E_{=}$, δ goes through a relatively low flat maximum, while with reverse variation (decrease) of $E_{=}$, the $\delta = f(E_{=})$ curve lies lower, while the maximum of δ is shifted into the region of fields of opposite (negative) sign and becomes higher and sharper, i.e., coincides with the maximum of $\partial\delta/\partial E_{=}$. The δ peak in the second half-cycle of the variation of $E_{=}$ also becomes high and sharp so that there is obtained the characteristic, approximately symmetrical hysteresis curve: a butterfly type curve with the two branches intersecting at $E_{=} \approx 0$. Subsequent cycles of $E_{=}$ do not produce any significant change in the shape of the curve or any noticeable shift of δ_{max} relative to the $E_{=}$ axis.

In further experiments we found that if the ferroelectric resonator of Rochelle salt is subjected to intense γ-irradiation there results a significant decrease of δ for $E_{=} = 0$, a weakening of its dependence on temperature and a marked change in the character of the $\delta = f(E_{=})$ curve (Fig.6). With increase of the γ-radiation dose, together with the general decrease of δ, the maxima in the $\delta = f(E_{=})$ curve

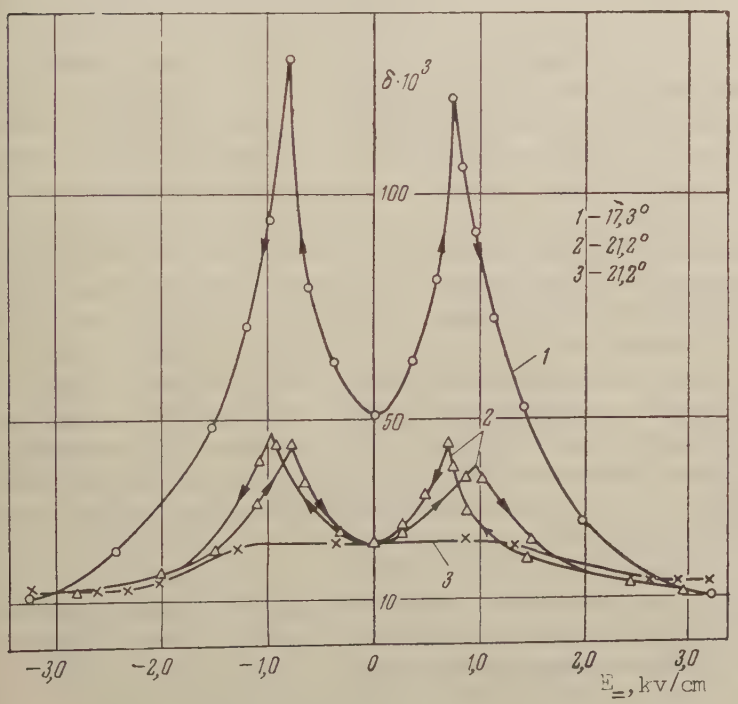

←Fig.6. Variation of δ with $E_{=}$ for resonators of X cut Rochelle salt subjected to different doses of γ-radiation (1 & 2 - $3 \cdot 10^5$ r; 3 - $11 \cdot 10^5$ r). The successive variation of the biasing field is shown by the arrows. Curve 1 is plotted only for increase of $E_{=}$; curve 2 for a complete cycle of variation of $E_{=}$.

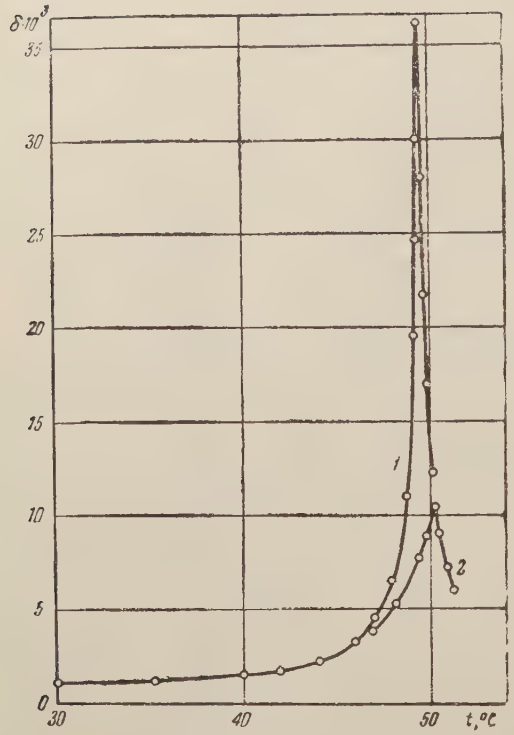

Fig.7. Variation of δ with temperature for Y cut bars of triglycine sulfate with the long side parallel to the Z axis: 1) $E_{=} = 0$, 2) $E_{=} = 300$ v/cm.

become lower and shift away from the $E_{=} = 0$ axis. After a dose of the order of 10^6 r the maxima virtually disappear and δ becomes almost independent of $E_{=}$.*

Preliminary investigations of ferroelectric resonators of tri-glycine sulfate (TGS) showed that Y cut bars of TGS in the ferroelectric region are characterized by substantially smaller attenuation than 45° X cut bars of Rochelle salt; the $E_{=}$ dependence of δ for them is also substantially weaker (Fig.7). The temperature dependence of δ at $E_{=} = 0$ for Y cut TGS bars has an even sharper maximum in the region of the Curie point; this peak with decreasing temperature is shifted to the left relative to its position on the rising temperature curve. The application of stronger biasing fields lowers this maximum but does not suppress it entirely.

4. Discussion

The experimental results can be explained by taking into account the role of domain structure and its behavior in the investigated crystals.

Among 45° cut Rochelle salt resonators operating in the compression-elongation in length mode only resonators of 45° X cut bars are ferroelectric resonators (see first footnote), inasmuch as the anomalous constant S_{44} enters into their effective elastic constant and their oscillations can be accompanied by periodic hysteresis reorientation of the domains (this also applies to X cut plates oscillating in the circuit mode). Hence only for these resonators are there evinced anomalies in the temperature and $E_{=}$ dependences of δ; for these resonators the values of δ at $E_{=} = 0$ in the ferroelectric region are very large. Also ferroelectric as we understand the term are the investigated TGS resonators in the form of bars with the largest face perpendicular to the polar Y axis.

The strong temperature dependence of δ and the sharp peak of δ in the region of the Curie point with $E_{=} = 0$ exhibited by ferroelectric resonators (Figs.3 & 7) can be explained by the strong dependence of the domain mobility on the temperature and the tendency of the mobility to become infinite with approach to the Curie point. This also explains why δ_{max} and the minimum value of the resonance frequency for 45° X cut bars coincide in the temperature scale. The great height of the δ peak with $E_{=} = 0$ obtained from the data of Matthias[8] agrees with the difference in the normalization conditions (see section 1), while the somewhat smaller values on the $\delta = f(t)$ curve for large $E_{=}$ can be explained by individual peculiarities of the crystals and possibly by the type of mounting.

---

*These measurements were carried out on X cut plates oscillating in the circuit mode. Inasmuch as the resonators were not of highest quality, the absolute values of δ (particularly δ_{min}) are only approximate.

Upon increase of the biasing field $E_{=}$ on a ferroelectric resonator (in the direction of the polar axis) increase of $E_{=}$ at first favors reorientation of the domains during oscillation (Figs.4 & 5); hence δ grows, attaining a maximum at $E_{=} \approx E_{coerc}$ with a maximum value of $\partial P/\partial E$, when reorientation of the domains in weak alternating fields occurs most easily at the given temperature. Clearly, with approach to the Curie point, together with decrease of E_{coerc}, the positions of the δ peaks shift towards $E_{=} = 0$. With further increase of $E_{=}$ as the crystal approaches the single-domain state the domain mechanism comes to play an every more minor role (the damping decreases), and, finally, becomes completely insignificant (δ stops being dependent on $E_{=}$ and is only weakly dependent on t). We note that at the same field values the ΔE effect disappears. The fact that these fields are several times greater than the saturation field can be explained, following Matthias[8], by recalling that mechanical stresses in the oscillating resonator also give rise to local fields which again produce domains. Moreover, there may persist individual "persistent" domains even in fields substantially greater than the saturation field. The difference between the initial $\delta = f(E_{=})$ curve and the subsequent loops (Fig.5) can be explained in the same way as the difference between the "virgin" branch of the field dependence of the polarization and subsequent P vs E curves (see, for example, Gurevich et al[11]); hypothesizing that the specimen "remembers" application of the initial biasing field, one can readily explain the displacement of δ_{max} with decrease of the field in the $E_{=} < 0$ region and the butterfly shape of the curve. The persistence of the δ peak at the Curie point in the range of strong biasing fields, when domain losses are absent, can be explained by the thermodynamic theory of phase transitions (see Yakovlev & Velichkina[5]).

We note that the $E_{=}$ and t dependences of δ are similar to the dependences of the reversible dielectric constant ϵ (and also the susceptibility) on $E_{=}$ and t. This appears to be natural inasmuch as both quantities, although different in their manifestations, are determined largely by processes of domain reorientation. In particular, just as for ϵ, for δ of 45° X cut bars of Rochelle salt above the Curie point, there is fulfilled the Curie-Weiss law; however, for reliable determination of the Curie constant more accurate measurements are necessary.

The relation between attenuation and the behavior of the domain structure is clearly evinced in the case of ferroelectric resonators subjected to γ-irradiation. As Zheludev & Yurin[12,13] showed, as a result of γ-irradiation the hysteresis loop of Rochelle salt changes from a single to a double loop; the critical field E_{cr} at which the process of domain reorientation begins increases with increase of the radiation dose. Hence δ for $E_{=} < E_{cr}$ decreases; with increase of the radiation dose the positions of the δ maxima on the $\delta = f(E_{=})$ curve move further apart and the curve for a complete cycle of variation of $E_{=}$ contains two characteristic butterfly type loops with maxima corresponding to the coercive fields of the two loops (Fig.6). When the crystal is subjected to still greater doses of radiation the hysteresis loops completely degenerate: the domains become rigidly fixed and can no longer reorient. Consequently, δ no longer varies with $E_{=}$. It may be assumed that similar changes in δ of ferroelectric resonators will obtain in all cases of "fixation" of the domains whether due to irradiation, introduction of impurities or aging[14]. Hence observation of the variation of δ may prove to be a sensitive method for investigating such effects and changes in domain structure.

It may be assumed that the smaller values of δ and the weaker $E_{=}$ dependence of δ exhibited by ferroelectric resonators of TGS, as compared with 45° X cut Rochelle salt resonators, are explained by the fact that the losses due to domain reorientation in TGS crystals are substantially smaller owing to the crystallographic difference between the domain structure of TGS crystals and Rochelle salt crystals (in the former there is no rearrangement of the lattice incident to re-

orientation of the domains[15], while in the latter such rearrangement occurs[16]). It may be asserted that for crystals having the same domain symmetry (here $2 = C_2$), but differing in that in the paraelectric phase one crystal has a piezoelectric effect (Rochelle salt - class $2:2 = D_2$), while the other does not (TGS - class $2:m = C_{2h}$)*, there generally obtains a substantial difference in attenuation, the characteristics of pulse polarization reversal and other properties dependent on the character of the domain structure.

We desire to express our gratitude to K.A.Pluzhnikov for assistance in carrying out the measurements, I.S.Zheludev, M.I.Yaroslavskii and V.A.Yurin for helpful discussions and E.G.Bronnikova and A.I.Yaroslavskii for assistance in preparing the specimens and perfecting the experimental technique.

Institute of Crystallography,
Academy of Sciences of the USSR

References

1. R.M.Bozorth, Ferromagnetism, N.Y., 1951. (Cited in Russian trans.)
2. W.J.Price, Phys.Rev., 75, 946 (1949).
3. I.A.Yakovlev, T.S.Velichkina & K.N.Baranskii, Zhur.eksp.i teor.fiz., 32, 935 (1957). (Trans.Soviet Physics - JETP.)
4. I.A.Yakovlev, T.S.Velichkina & K.N.Baranskii, Ibid., 33, 1075 (1957). (Trans.Ibid.)
5. I.A.Yakovlev & T.S.Velichkina, Uspekhi fiz.nauk, 63, 411 (1957).
6. I.Takuro, J.Phys.Soc.Japan, 13, 809 (1958).
7. T.Hueter & D.Neuhaus, J.Acoust.Soc.Amer., 27, 292 (1955).
8. B.Matthias, Helv.Phys.Acta., 16, 99 (1940).
9. V.A.Krasil'nikov, L.A.Shuvalov & A.S.Sheip, Doklady na soveshchanii po voprosam fizicheskoi i izmeritel'noi akustika (Report presented at the Conference on Problems of Physical and Measurement Acoustics), Leningrad, Jan.1951.
10. R.L.Zaidel'man, Zavodsk labor., 25, 1233 (1959). (Trans.Industrial Laboratory).
11. V.M.Gurevich, I.S.Zheludev & I.S.Rez, Kristallografiya 5, No.5 (1960). (Trans.Soviet Physics - Crystallography.)
12. I.S.Zheludev & V.A.Yurin, Izv.AN SSSR, Ser.fiz., 20, 211 (1956). (Trans. Bulletin, 20, 193.)
13. V.A.Yurin, Ibid., 21, 329 (1957). (Trans.Bulletin, 21, 336.)
14. V.A.Yurin, Ibid., 24, No.11 (1960). (Trans.Bulletin, 24, No.11.)
15. L.A.Shuvalov, K.S.Aleksandrov & I.S.Zheludev, Kristallografiya, 4, 130 (1959). (Trans.Sov.Phys. - Crystallography.)
16. I.S.Zheludev & L.A.Shuvalov, Trudy (Proceedings), Institute of Crystallography), 12, 59 (1956).

---

*This is why resonators of TGS below the Curie point with $E_{=} = 0$ are excited only with natural unipolarity, while above the Curie point they are no longer excited.

OSCILLATIONS OF DIELECTRIC PENDULUMS AND POLARIZATION OF FERROELECTRICS

- I.S.Zheludev

In an earlier contribution[1], we described natural and forced oscillations of dielectric pendulums. We noted the difficulties of explaining the observed effects and advanced the hypothesis that the oscillation amplitude is a function of the polarization of the dielectric. In the present report we give the results of experiments undertaken for the purpose of quantitative interpretation of this functional relationship. The experimental procedure was the same as that employed in the earlier study[1].

Fig.1 shows the ac field dependence of the amplitude of the forced oscillations of the pendulum in the case when the active element is an X cut disk of Rochelle salt. The data were recorded at 11° and a frequency of 99 cps, equal to the natural frequency of the mechanical system (the pendulum). The experimental points used in plotting the dependence are indicated in the figure. Concurrent with recording the oscillation amplitude by the optical method, we photographed the dielectric hysteresis loop of the oscillating pendulums by the conventional procedure with a constant gain of the oscillograph amplifier. The loops corresponding to some ac crest field values are also shown in Fig.1.

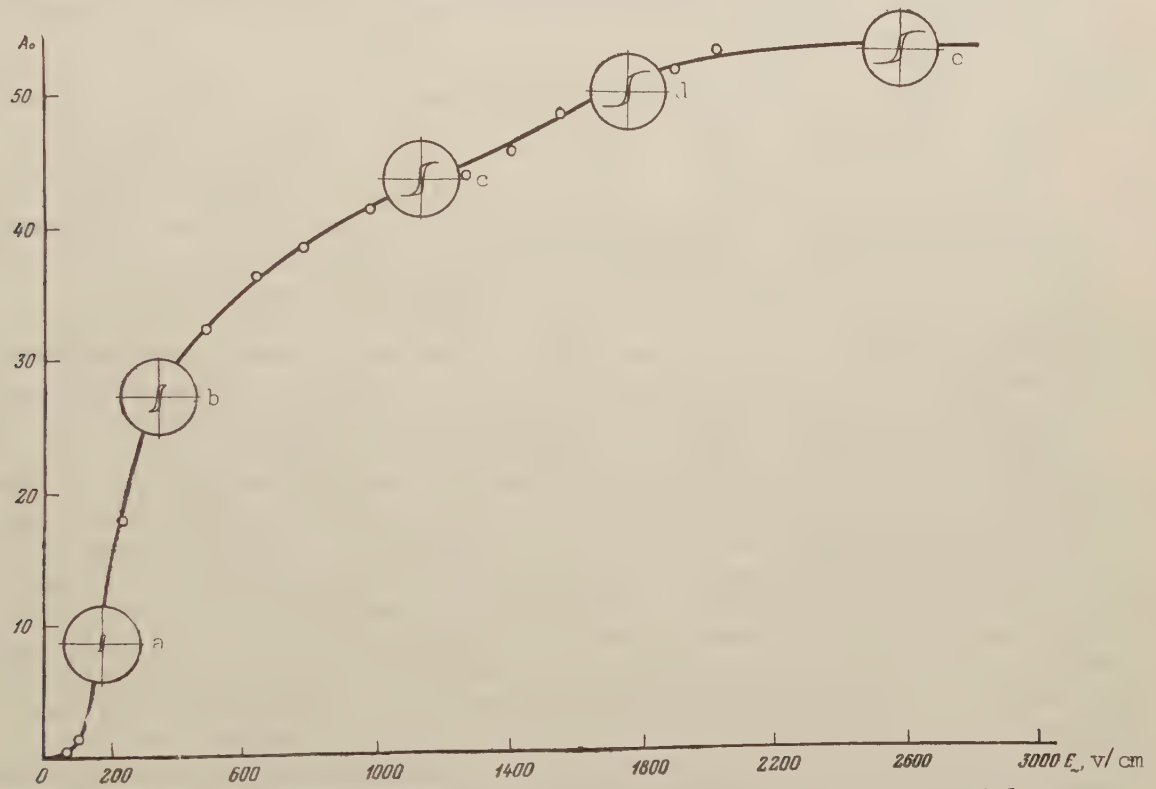

Fig.1. Variation of the amplitude of forced oscillations of a pendulum containing Rochelle salt as a function of the ac field $E_{\sim}$

It will be evident from Fig.1 that the greater the total polarization of the specimen, the greater the oscillation amplitude (loops a--d) and that the greatest increase of polarization (fields close to the coercive field) is associated with the most appreciable change in the oscillation amplitude (loops a & b, and a & c), while a small change in the polarization (saturation field) is accompanied by a small change in oscillation amplitude (loops d & e). On the whole, the field dependence of the amplitude A_0 shown in Fig.1 corresponds to the usual $E_{\sim}$ dependence of polarization P for ferroelectrics. (We must emphasize, however, that in our

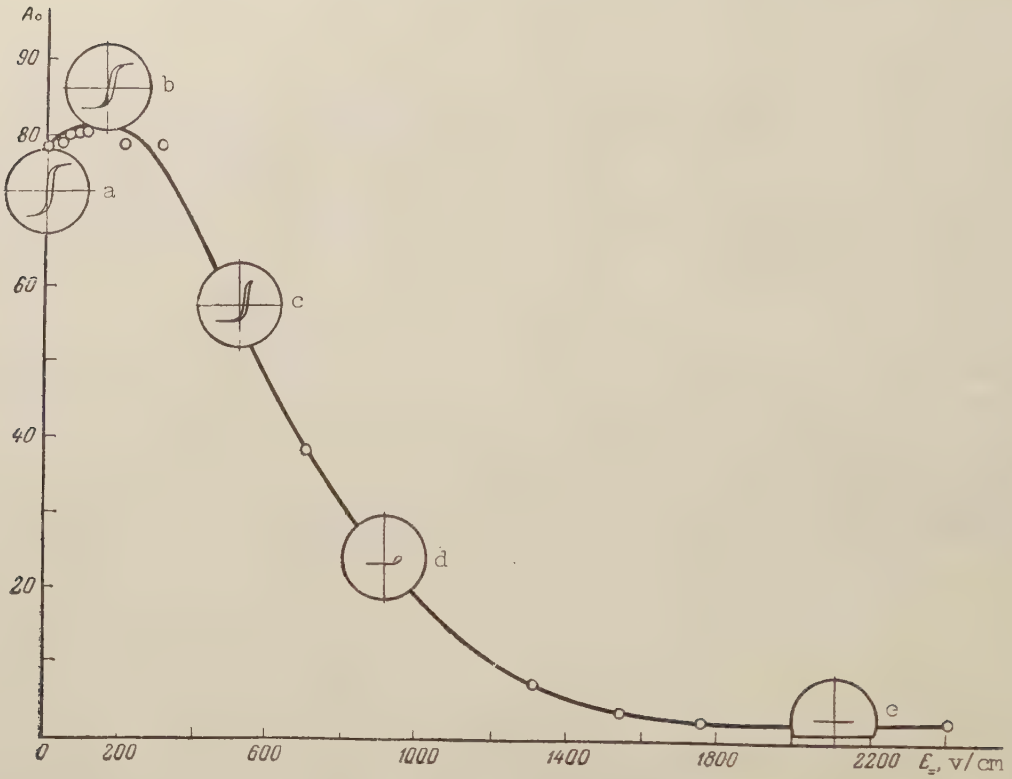

Fig.2. Variation of the amplitude of forced oscillations of a pendulum containing Rochelle salt with the dc polarizing field $E_{=}$. The ac field $E_{\sim}$ is the same for all points and equals 1050 v/cm.

experiments we did not check the quantitative relationship between the polarization and oscillation amplitude, so that the indicated correspondence is only qualitative in character.)

As is known, there exists a direct relation between the shape of the hysteresis loops and the degree of polarization reversal of the domains in ferroelectrics (Refs.2 & 3). Invoking this fact, we note that the greatest change in oscillation amplitude of the pendulum is correlated with an appreciable change in the number of domains beginning to participate in the polarization with increase in the amplitude of the applied field (compare loops a and b), while small changes in oscillation amplitude correspond to cases in which the increase of the field does not lead to a substantial increase in the number of domains undergoing switching. It may even be inferred that whenever increase of the field does not lead to an increase in the number of switching domains (fields stronger than the saturation field), the oscillation amplitude does not change (compare loops d and e). (This argument is based on the assumption that the major part of the polarization in ferroelectrics is due to polarization reversal of the domains.)

Examination of Fig.2 substantiates our conclusion regarding the correlation between the oscillation amplitude and the polarization of the specimen (and its domain structure). The curve in this figure, which was recorded at the same temperature and frequency (11° and 99 cps), shows the dc field dependence of the oscillation amplitude of a pendulum containing Rochelle salt with a constant amplitude of the "exciting" ac field ($E_{\sim}$ = 1050 v/cm). In addition to the experimental points, we show tracings of the dielectric hysteresis loops corresponding to different values of the dc (polarizing) field.

It will be evident from Fig.2 that as the polarization of the specimen due to the applied dc field decreases, i.e., as the domain structure is "clamped", the oscillation amplitude of the pendulum drops (loops b and d), and the oscillations virtually cease upon complete "clamping" of the domain structure (loop e). We cannot at present advance a convincing explanation for the increase of the oscillation amplitude of pendulums in weak dc fields, which we also observed earlier (see Ref.1). The present and earlier experimental results were obtained for pendulums in which the electrodes were applied directly to the surface of the dielectric. The measurement conditions therefore corresponded to a constant field intensity in the samples. Moreover, all the above experiments were carried out in air. We were curious to find out what effect placing the pendulum in vacuum would have upon the oscillations and whether the pendulum would oscillate when the dielectric is mounted in an empty capacitor so that there is an airless gap between the specimen and the capacitor plates (inductive dc conditions). To this end we set up a pendulum containing barium titanate inside a capacitor, arranged so that there was a ~1 mm gap between each side of the specimen (devoid of metallic coverings) and the capacitor plates. The entire assembly was placed in a glass envelope which was evacuated to 10^{-4} mm Hg and sealed off. It was found that in this case also when an ac field is applied to the capacitor plates the pendulum executes forced oscillations at a field frequency equal to the natural frequency of the mechanical system, and that the regularities characterizing the behavior of such a pendulum are similar to those observed earlier and described above.

I am grateful to S.V.Rozhkov and A.Yu.Kurkovskii for assistance in the experiments.

Institute of Crystallography
Academy of Sciences of the USSR

References

1. I.S.Zheludev, Kristallografiya, 4, 571 (1959). (Trans.Soviet Physics - Crystallography.)
2. I.S.Zheludev & R.Ya.Sit'ko, Ibid., 1, 689 (1956).
3. N.A.Romanyuk & I.S.Zheludev, Ibid., 5 (1960). (Trans.Crystallography.)

DIELECTRIC AND CALORIMETRIC INVESTIGATION OF AMMONIUM SULFATE AND AMMONIUM FLUOBERYLLATE CRYSTALS

- V.A.Koptsik, B.A.Strukov, A.A.Sklyankin & M.E.Levina

It is known that $(NH_4)_2SO_4$ and $(NH_4)_2BeF_4$ have phase transitions at -50° and -970°C, respectively.[1-3]

In the low-temperature phase both crystals are ferroelectric; the polar axis is the c axis in ammonium sulfate and the b axis in ammonium fluoberyllate. The character of the anomalies associated with the phase transitions differs in these crystals, which indicates that their phase transitions involve essentially different mechanisms. Their crystal symmetry changes incident to the phase transition: ammonium sulfate changes from class $Pnam$ (D_{2h}^{16}) to class $Pna2_1$ (C_{2v}^{9}) and ammonium fluoberyllate changes from $Abam$ (D_{2h}^{18}) to $Ab2_1a$ (C_{2v}^{17}) (we use the usual convention for the crystallographic axes: $c < a < b$).[4]

Preparation of Samples and Measurement Procedure

Large single crystals of ammonium sulfate were grown from an aqueous solution of the chemically pure reagent by the method of lowering the temperature. The growth cycle was 4 weeks. There were obtained crystals measuring 80 x 40 x 15 mm.

The ammonium fluoberyllate was synthesized by the Lebeau procedure[5]. Single crystals measuring about 20 x 7 x 2 mm were grown from a water solution by the method of evaporation at constant temperature. For control purposes both the initial reagent and the crystals were subjected to chemical analysis.

Dielectric measurements were carried out on c-cut $(NH_4)_2SO_4$ and b-cut $(NH_4)_2BeF_4$ crystals. For the calorimetric measurements we used samples of the initial fine-crystalline powder employed for growing the crystals.

In the dielectric measurements we gave particular attention to close temperature control near the phase transition points. The thermostating set-up employed insured stabilized temperature points at 0.1° intervals with an accuracy of ±0.005° (Ref.6). The crystals were kept in a dry air atmosphere. The temperature in the controlled space was monitored by a triple copper-constantan thermocouple. The dielectric constant ϵ and the loss tangent δ were measured at a frequency of 50 kc in a ~3 v/cm field by means of a precision logarithmic bridge.

A vacuum adiabatic calorimeter[7] was used for the specific heat determinations. The accuracy in determining individual equilibrium values of the specific heat was evaluated to be 0.5-1%. The reliability of the procedure was checked by measuring the temperature dependence of the specific heat of a standard substance, namely, benzoic acid C_6H_5COOH.

Dielectric Measurements

The ϵ and tan δ measurements were made after attainment of thermal equilibrium; the usual holding time at each constant temperature was 25 to 40 min.

Fig.1 shows the temperature dependences of ϵ and tan δ for a c-cut ammonium sulfate crystal, obtained in the process of cooling (about 1-2° below the transition point the crystal fractures along the cleavage planes). From room temperature to the phase transition point, ϵ and tan δ exhibit slow linear variation. At -48.2°C a sharp rise of ϵ and tan δ is observed: ϵ rises from 17.2 to 50 in a temperature interval by only 0.2° and then falls off abruptly to about 20. In heating of the cracked specimen, the peak value of ϵ is observed at 48.7°C, i.e., at a point approximately 0.5° higher than in cooling.

Fig.2 shows the temperature dependences of ϵ and tan δ for a b-cut ammonium fluoberyllate crystal. In contrast to $(NH_4)_2SO_4$, the rise of ϵ on approaching

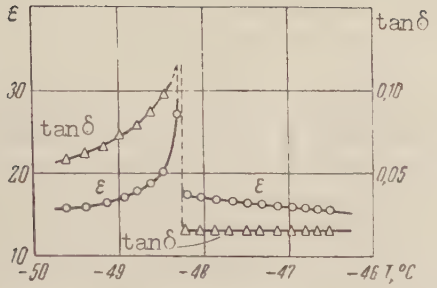

Fig.1. Temperature dependence of ϵ and tan δ for c-cut $(NH_4)_2SO_4$ crystal.

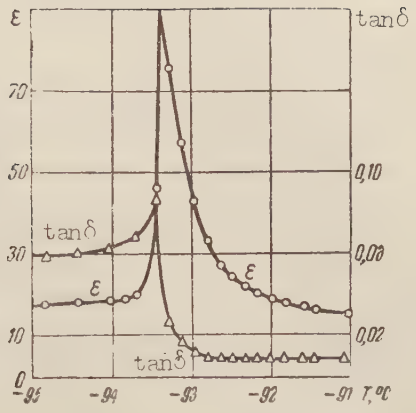

Fig.2. Temperature dependence of ϵ and tan δ for b-cut $(NH_4)_2BeF_4$ crystal.⟶

the transition point from the side of higher temperatures occurs in conformity with the Curie-Weiss law, i.e., the temperature variation of $1/\epsilon$ is linear. Tan δ rises sharply at the transition temperature and attains its maximum value at a point corresponding to the most precipitate drop of ϵ.

While the temperature dependences of tan δ are similar for ammonium sulfate and ammonium fluoberyllate, the T dependences ϵ differ substantially.

We also carried out detailed investigations of the temperature dependence of polarization in the phase transition region of different field strengths. The results will be published elsewhere.

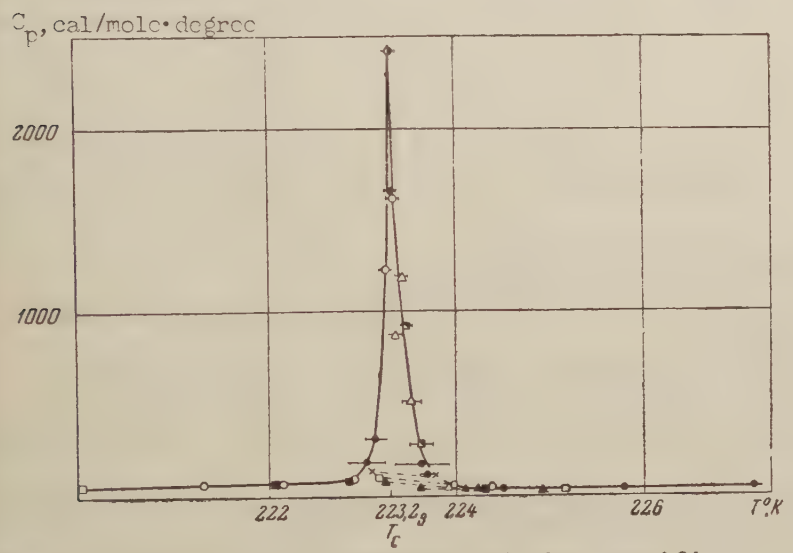

Fig.3. Temperature dependence of the specific heat C_p for $(NH_4)_2SO_4$.

Calorimetric Measurements

Fig.3 shows the temperature dependence of the specific heat C_p for $(NH_4)_2SO_4$. Points identified by the same symbol pertain to a single series of successive temperature increments. The measurements in the phase transition region were made at 0.08-0.20° intervals. The specific heat at the phase transition point rises to 2427 cal/mole·degree, in contrast to 50 cal/mole·degree in the region of the normal temperature variation. Further increase of temperature leads to a sharp drop of C_p to 40 cal/mole·degree.

During the course of our experiments we discovered that cooling a specimen initially at $T > T_C$ is not always accompanied by transition to the ferroelectric phase. In the case of not very severe cooling, the specific heat may not rise sharply in conformity with the normal temperature dependence of C_p, but instead changes insignificantly, i.e., retains a value close to that of the high temperature phase (dashed lines in Fig.3). We obtained supercooling of the order of

0.4-0.5°, which is in good agreement with the dielectric data. The mean value of the integral transition energy was found to be 490 cal/mole.

The temperature dependence of the specific heat for ammonium fluoberyllate is shown in Fig.4. The curve exhibits a characteristic λ peak; no supercooling effect was observed. The procedure employed for determining the specific heat enabled us to obtain equilibrium values of C_p at each temperature (the holding time after each heating was 50-60 min). It is therefore not surprising that our data differ from the results of Hochino et al[4].

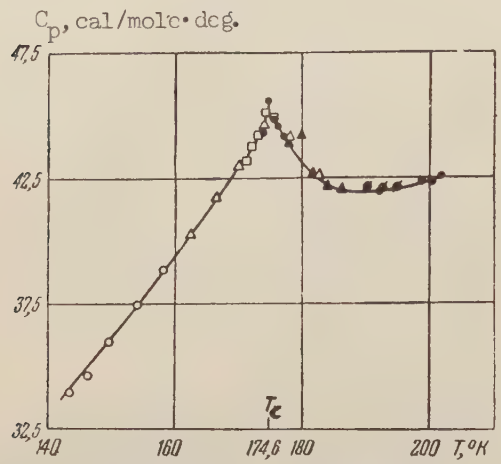

Fig.4. Temperature dependence of C_p for $(NH_4)_2SO_4$.

It will be evident from Figs.1-4 that the transition temperatures obtained from calorimetric measurements (-49.9° and -98.6°C) and from dielectric measurements (-47.6° and 93.4°C) differ somewhat. The calorimetric data are more reliable inasmuch as the temperature was measured by means of a high grade platinum resistance thermometer. We attribute the disagreement to inadequate accuracy in calibrating the thermocouples used in the dielectric measurements.

We desire to thank A.N.Izrailenko and A.F.Solov'ev, who participated in the experiments.

Moscow State University &
VNIIFTRI

References

1. R.Guillien, Ann.de Phys., 17, 334 (1942).
2. R.Pepinsky & F.Jona, Phys.Rev., 105, 344 (1957).
3. V.A.Koptsik, K.A.Minaeva & B.A.Strukov, Izv.AN SSR, Ser.fiz., 22, 1537 (1958). (Trans.Bulletin, 22, 1529.)
4. S.Hoshino, K.Vedam, F.Jona & R.Pepinsky, Phys.Rev., 112, 405 (1958).
5. Leveau, Ann.Chim., 16, 440 (1899).
6. V.A.Koptsik, B.A.Strukov & L.A.Ermakova, PTE, No.1 (1961). (Trans. Instr. & Experimental Techniques.)
7. P.G.Strelkov, E.S.Itakevich, V.N.Kostryukov, G.G.Mirskaya & B.N.Samoilov, Zhur.fiz.khim. (Jour.Phys.Chem.), 28, 459 (1954).

INVESTIGATION OF THE OPTICAL PROPERTIES OF SOME FERROELECTRIC CRYSTALS

- V.A.Koptsik, B.A.Strukov & I.K.Nevedomskaya

Introduction

The possibility of optical observation of polymorphous phase transitions in crystals is based on differences in the shape and orientation of the optical indicatrix in the two crystal modifications. As is known, isotropic, uniaxial and biaxial crystals differ optically. The optical indicatrices of such crystals are a sphere, an ellipsoid of revolution and a triaxial ellipsoid, respectively.

Polymorphous transformations are optically "indistinguishable", if the optical symmetry of the crystals (the symmetry of the optical indicatrix) does not change. However, continuous observation of the temperature variation of the birefringence affords the possibility of distinguishing polymorphous transitions on the basis of the abrupt change in magnitude of the refractive indices at the phase transition point. It is obvious that the optical indicatrix at this point changes size without changing its orientation relative to the symmetry elements of the crystal.

We investigated the temperature dependences of the birefringence for ferroelectric cuts of ammonium sulfate $(NH_4)_2SO_4$ and ammonium fluoberyllate $(NH_4)_2BeF_4$ crystals.

Optically, $(NH_4)_2SO_4$ and $(NH_4)_2BeF_4$ crystals are biaxial. Phase transitions in $(NH_4)_2SO_4$ at -50°C and in $(NH_4)_2BeF_4$ at -100°C and associated anomalies of the specific heat and dielectric constant have been noted by various authors[1-4]. Structural investigation[5] has shown that phase transition in these crystals leads to a change in symmetry of the type $m\cdot 2 : m \rightarrow 2\cdot m$ (in the designation of A.V.Shubnikov); the c-axis becomes the ferroelectric axis in ammonium sulfate, and the b-axis in ammonium fluoberyllate. It is easy to see that the optical symmetry of the crystals does not change incident to the transitions, which precludes optical observation of the domain structure.

Measurement Procedure

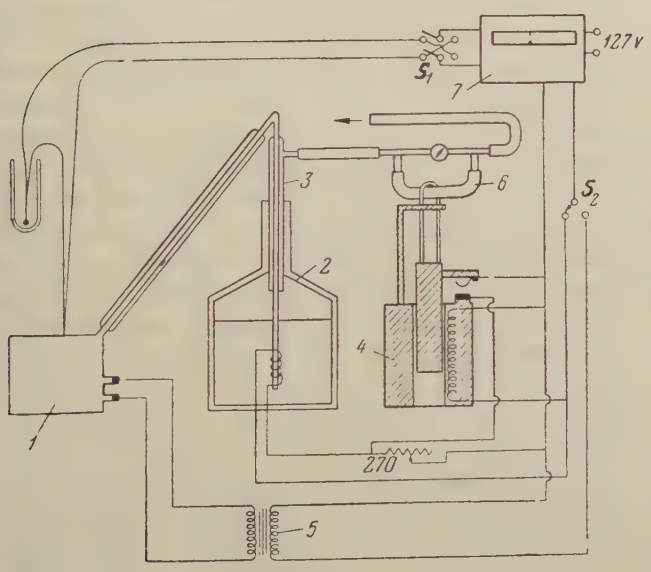

←Fig.1. Equipment for investigating optical properties of crystals in a wide range of temperatures: 1) thermostatic microscope stage, 2) Dewar with liquid nitrogen, 3) siphon for transfer of liquid nitrogen, 4) electromagnet regulating dry nitrogen outflow from the Dewar, 5) transformer for stage heater, 6) tube for blowing dry nitrogen at the microscope lens, 7) ERM-47 electronic regulator; S_1 and S_2 are the "heating" and "cooling" control switches.

In addition to a polarizing microscope, our equipment for crystallooptical studies comprised the following components (Fig.1): 1) a thermostatic microscope stage with heater, specimen holder and Lazo lens, 2) an arrangement for supplying a coolant

(liquid nitrogen) to the microscope stage, consisting of a Dewar, a siphon with heater, an ERM-47 electronic regulator and an electromagnetic squeeze valve that pinched the dry nitrogen outlet hose, and 3) a device for heating the stage, consisting of a heater, an LATR-1 autotransformer and a step-down transformer.

The equipment was built and assembled according to drawings kindly lent us by the designers of this universal microscope stage, Tsurinov & Vol'nova[6]. It allows of providing any desired rate of heating and cooling of the specimen, and insures maintenance of stable temperatures. The specimen holder mechanism provides for translation and rotation of the specimen on the microscope stage. The birefringence was measured by means of a rotary Berek compensator. The birefringence value was calculated by the formula $\Delta n = C/d$, where d is the plate thickness, C is the optical path difference, and Δn is the difference between the principal refractive indices in the plane normal to the direction of observation. The plate thickness was selected so that bright interference colors in the second or third orders would be observed.

Results

The temperature dependence of the birefringence for a c-cut $(NH_4)_2SO_4$ crystal is shown in Fig.2.

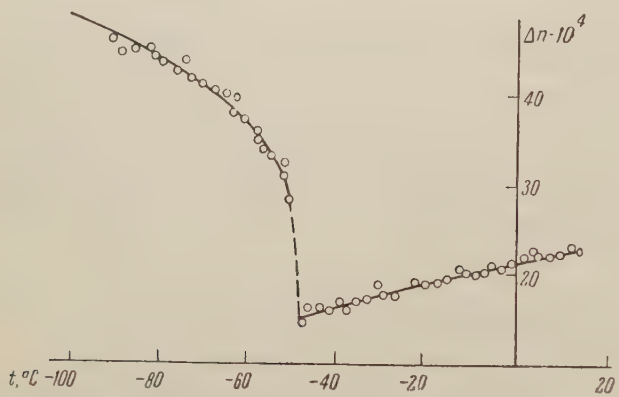

Fig.2. Temperature dependence of birefringence or c-cut $(NH_4)_2SO_4$ crystal.

The birefringence decreases slightly down to the phase transition temperature; at the phase transition point it rises sharply and then more slowly as the temperature of the specimen is further reduced. Variation of the path difference owing to the thermal expansion of the specimen results in only a minor correction to the observed value of this difference (parameter C changes at the transition point from 5.97 to 5.93 Å).

The abrupt change in the value of Δn at the transition point makes it feasible to observe the course of the phase transition in ammonium sulfate crystals. Usually the color change starts at the corners of the specimen. The color fields slowly converge toward the center and the entire specimen assumes a uniform tone. We assume that the process of "color change" reflects the propagation of the "front" of the transition from the paraelectric to the ferroelectric phase through the crystal plate. Below the transition point the crystal fractures along the cleavage planes. We succeeded in following the dynamics of the process of crack formation. The boundary between the two phases is the place where considerable internal stresses develop in crystals, and these internal stresses give rise to the fractures along the cleavage planes.

Fig.3 shows the temperature dependence of the birefringence Δn for a b-cut $(NH_4)_2BeF_4$ crystal in the range from +20° to -130°C. At about -90°C the birefringence goes through a clearly pronounced maximum, which we cannot ascribe to the change in the geometrical size of the specimen owing to thermal expansion anymore than we could in the case of $(NH_4)_2SO_4$ (at the transition point parameter increases from 10.43 to 10.47 Å; see Ref.7).

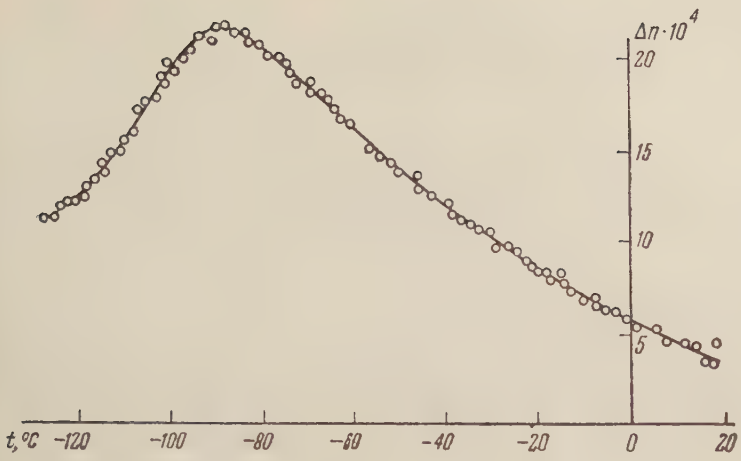

←Fig.3. Temperature dependence of birefringence for *b*-cut $(NH_4)_2BeF_4$ crystal.

As was to be expected, the domain structure is not brought out even in a strong transverse electric field.

Our optical observations confirm the dielectric and calorimetric data indicating that the transition in ammonium sulfate is of first order, while that in ammonium fluoberyllate is of second order or of first but very close to second order.

Moscow State University &
VNIIFTRI

References

1. R.Guillien, Ann.de Phys., 17, 334 (1942).
2. R.Pepinsky & F.Jona, Phys.Rev., 105, 344 (1957).
3. V.A.Koptsik, K.A.Minaeva & B.A.Strukov, Izv.AN SSSR, Ser.fiz., 22, 1537, (1958). (Trans.Bulletin, 22, 1529.)
4. V.A.Koptsik, B.A.Strukov, A.A.Sklyankin & M.E.Levina, Present issue of the Bulletin, p.1230.
5. V.Ikaya, K.Vedam & R.Pepinsky, Acta Cryst., 11, 307 (1958).
6. G.G.Tsurinov & V.A.Vol'nova, Zavod.labor. (Industrial Laboratory), 10, 1532 (1952).
7. S.Hoshino, K.Vedam, F.Jona & R.Pepinsky, Phys.Rev., 112, 405 (1958).

SOME PHYSICAL PROPERTIES OF FERROELECTRIC $BaTiO_3$-$PbTiO_3$, $BaTiO_3$-$BaSnO_3$ AND $BaTiO_3$-$PbTiO_3$-$BaSnO_3$ SINGLE CRYSTALS

- S.V.Bogdanov, G.M.Kovalenko & A.M.Cherepanov

Polycrystalline solid solutions in the binary systems $BaTiO_3$-$PbTiO_3$ and $BaTiO_3$-$BaSnO_3$ and the ternary system $BaTiO_3$-$PbTiO_3$-$BaSnO_3$ have been studied in considerable detail.[1-13] The purpose of the present work was to study some physical properties of single crystals of the same composition.

Growing the Single Crystals

Single crystals of the above solid solutions containing up to 15 mole percent $PbTiO_3$ and 10 mole percent $BaSnO_3$ were grown from solutions in molten KF by slow cooling of the solution from 1000-1200° to 400°C. The same procedure was employed for growing single crystals from a solution with the initial composition 85% $BaTiO_3$ + 10% $PbTiO_3$ + 5% $BaSnO_3$. The single crystals were grown both from previously synthesized $BaTiO_3$, $PnTiO_3$ and $BaSnO_3$ and from the usual synthesis components (in both cases we added Fe_2O_3 to some batches but not to others). The single crystals were obtained mainly in the form of triangular plates with a hypotenuse of up to ~5 mm. The composition of the $BaTiO_3$-$PbTiO_3$ single crystals was more or less identical with the composition of the initial mixture. In the $BaTiO_3$-$BaSnO_3$ system, however, owing to the difficulty of entry of $BaSnO_3$ into the solid solution, this was rarely the case, i.e., the composition deviated from that of the initial batch. These inferences regarding the composition of the single crystals and the degree of entry of the second component into the solid solution are based on determination of their Curie points, which are known for polycrystalline specimens of roughly equal composition. In this connection we bore in mind that each mole percent of $PbTiO_3$ raises the Curie temperature by ~3.8°, while each mole percent of $BaSnO_3$ lowers it by ~5.4°. The Curie temperature of single crystals grown from the 85% $BaTiO_3$ + 10% $PbTiO_3$ + 5% $BaSnO_3$ mixture was found to be 133.5-135°, which corresponds to the Curie temperature of polycrystalline specimens of the same composition.

Physical Properties of the Single Crystals

Variation of the dielectric constant with field strength, temperature and composition

Before firing on the silver electrodes the crystals were carefully checked over and only good plane-parallel plates free of cracks and inclusions were accepted for measurement.

Fig.1 shows the ac field dependence of the dielectric constant ϵ of single crystals of $BaTiO_3$ under the simultaneous influence of a dc bias field. Measurements in zero dc field were carried out twice. As can be seen, the peak value of ϵ for the second series of measurements is higher and is shifted to the side of lower fields. This effect must be ascribed to "aging": ordering of the domain structure under the influence of the ac field during the first series of measurements.

Fig.1 also shows the ac field dependence of ϵ in the presence of 250, 600 and 750 v/cm dc fields. With increase of the dc field, the maximum of ϵ, as is to be expected, decreases and shifts to the side of higher values of the ac field. It is worthy of note that in a relatively wide range of ac field values the variation of the capacitance with the ac field is linear; increase of the dc field leads to a shift of the point of departure from linearity to the side of stronger ac fields.

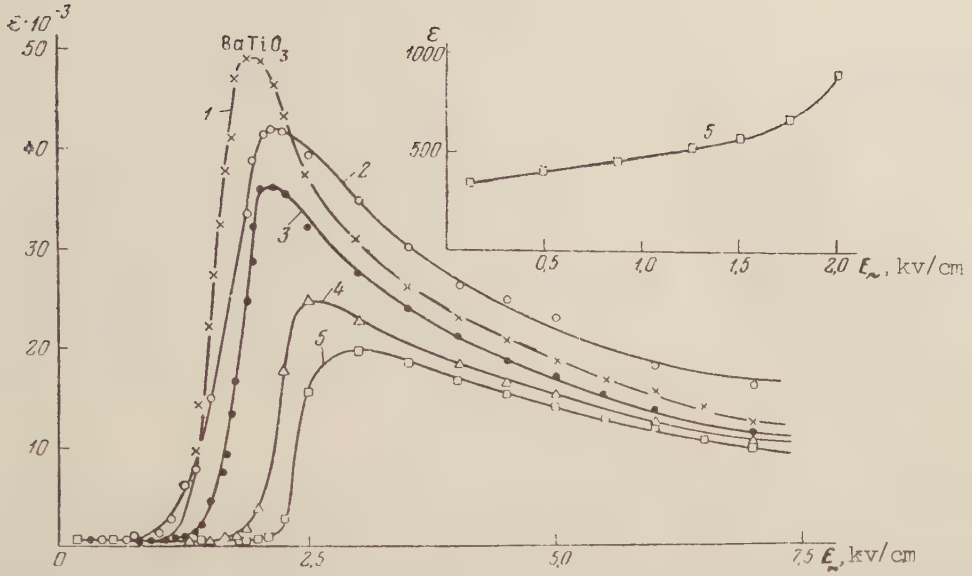

Fig.1. Ac field dependence of the dielectric constant for single crystals of $BaTiO_3$: 1 & 2) second and first cycles with $E_{=} = 0$, 3) $E_{=} = 250$ v/cm, 4) $E_{=} = 600$ v/cm, 5) $E_{=} = 750$ v/cm.

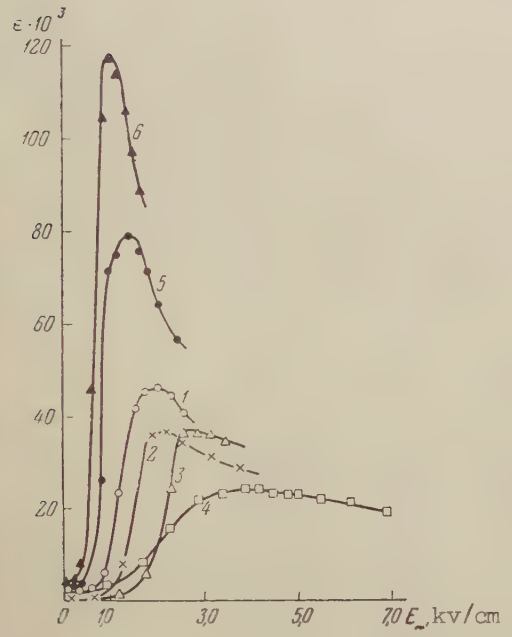

Fig.2. Variation of the ac field dependence of the dielectric constant with the crystal composition: 1) pure $BaTiO_3$, 2) 5% $PbTiO_3$, 3) 10% $PbTiO_3$, 5) 5% $BaSnO_3$, 6) 10% $BaSnO_3$.

The section of linear variation of the capacitance with the ac field in a 750 v/cm dc field is shown separately in the figure to an enlarged scale.

Fig.2 shows the ac field dependence of ϵ for single crystals of different composition. The measurements were carried out at room temperature (~20°C). It will be evident from the figure that with increasing $BaSnO_3$ content, the dielectric constant increases as compared with its value for $BaTiO_3$, and its maximum is observed at lower field intensities. Increasing the content of $PbTiO_3$, on the other hand, reduces the dielectric constant; its maximum shifts to the side of stronger fields and is gradually smeared out.

We investigated the temperature dependence of ϵ for all the crystals at different values of the ac field: in weak fields, in fields corresponding to the sharp rise of ϵ and in fields corresponding to ϵ_{max} (see the $\epsilon = f(E_{\sim})$ curves in Fig.2). Inasmuch as these dependences are virtually identical for all the investigated single crystals, we show (Fig.3) the temperature dependences only for 95% $BaTiO_3$ + 5% $PbTiO_3$.

As can be seen from Fig.3, the temperature dependence of ϵ in strong fields differs radically from that in weak fields. Whereas in weak fields ϵ has a pronounced peak at the Curie temperature, in strong fields ϵ is considerably greater and is only weakly dependent on the temperature in a comparatively wide range. Only near the Curie point is a sharp drop of ϵ

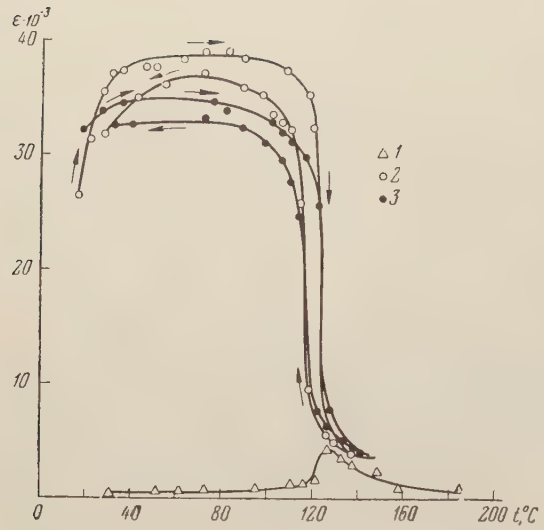

Fig.3. Temperature dependence of the dielectric constant at different ac field strengths for the 95% $BaTiO_3$ + 5% $PbTiO_3$ system: 1) $E_{=}$ = 50 v/cm, 2) 1550 v/cm, 3) 1900 v/cm.

observed. The entire shape of the $\epsilon = f(T)$ curve is analogous to that of the same dependence for Rochelle salt in strong fields.

It is interesting to note that in strong fields the temperature hysteresis of ϵ is very pronounced, the values of ϵ with decreasing temperature being significantly lower with rising temperature, in contrast to the case of temperature hysteresis in weak fields.

We also note that the temperature dependence of ϵ in fields corresponding to the sharp rise of ϵ (Fig.3, $E_{\sim}$ = 1550 v/cm) is stronger and its maximum value is greater than in fields corresponding to ϵ_{max} (Fig.3, $E_{\sim} \approx$ 2000 v/cm).

Dielectric Hysteresis

Dielectric hysteresis loops were recorded for all the specimens. By means of a special attachment to the oscillograph the loops were recorded directly, natural size, on photographic paper. From the loops we calculated the spontaneous and residual polarization, coercive field and rectangularity coefficients of the hysteresis loops. All the loops were recorded using the familiar Sawyer-Tower circuit, with some minor modifications introduced for the purpose of avoiding possible errors due to phase shift.

Variation of P_s, P_o, E_c and rectangularity coefficient with composition of the single crystals

Composition of single crystals, %			Dielectric hysteresis loop characteristics			
Base	Impurity		$P_s \cdot 10^6$ coul/cm²	$P_o \cdot 10^6$, coul/cm²	E_c, kv/cm	$\frac{P_o}{P_{max}}$
$BaTiO_3$	$PbTiO_3$	$BaSnO_3$				
100	—	—	18,3 (5,0)	16,2 (4,2)	0,8 (2,3)	0,83 (0,50)
95	5	—	26,0 (10,0)	22,3 (9,0)	1,5 (2,8)	0,80 (0,76)
90	10	—	13,7 (5,4)	11,5 (5,0)	3,2 (7,4)	0,65 (0,77)
85	15	—	12,7 (9,2)	9,2 (9,0)	4,6 (8,4)	0,66 0,80
95	—	5	12,4 (6,6)	9,5 (6,0)	1,5 (2,0)	0,60 (0,83)
90	—	10	8,0 (5,7)	6,3 (3,3)	1,2 (0,9)	0,55 (0,35)
85	10	5	14,4 (7,0)	13,0 (6,2)	3,0 (3,0)	0,70 (0,60)

The results are given in the accompanying table. The figures in parentheses pertain to polycrystalline specimens of the same composition. Comparison of the tabular data shows that the regularities characterizing the variation of P_s, P_o, E_c and the rectangularity coefficient with the mole percent of $PbTiO_3$ and $BaSnO_3$ added to the $BaTiO_3$ base material are the same as for the analogous polycrystalline specimens.

In the case of ternary system $BaTiO_3$-$PbTiO_3$-$BaSnO_3$ the crystals were imperfect, and their characteristics were close to those of single crystals of $BaTiO_3$.

Introduction of Fe_2O_3 into the crystal-growing batch in all cases enhanced the characteristics of the single crystals. For example, for 90% $BaTiO_3$ + 10% $PbTiO_3$ without Fe_2O_3 the value of P_s was $13.7 \cdot 10^{-6}$ μcoul/cm^2, while with 0.2% Fe_2O_3 impurity it was $14.6 \cdot 10^{-6}$ μcoul/cm^2 - an increment of ~6%.

Thus we have established that the nature of the variation of the investigated quantities with the composition of single crystals is similar to that for polycrystalline specimens of analogous composition; however, such characteristics as the dielectric constant, spontaneous polarization and residual polarization are considerably higher and the coercive force considerably smaller for single crystals than for polycrystalline specimens.

References

1. F.H.Jonker & J.H.van Santen, Chem.Weekblad, 43, 672 (1947).
2. G.A.Smolenskii, Zhur.tekh.fiz., 20, 137 (1950).
3. G.Shirane & K.Suzuki, Journ.Phys.Soc.Japan, 6, 274 (1951).
4. K.Suzuki, Ibid., 6, 340 (1951).
5. N.A.Roi, Akust.zhur., 2, 62 (1956). (Trans.Soviet Physics - Acoustics.)
6. I.E.Myl'nikova, Izv.AN SSSR, Ser.fiz., 21, 423 (1957). (Trans.Bulletin, 21, 423.)
7. G.A.Smolenskii, M.A.Karamyshev & K.I.Rozgochev, Doklady AN SSSR, 79, 53 (1951).
8. R.H.Dugan & D.F.Kane, Journ.Amer.Cer.Soc., 35, 318 (1952).
9. G.A.Smolenskii & V.A.Isupov, Doklady AN SSSR, 96, 53 (1954).
10. G.A.Smolenskii & V.A.Isupov, Zhur.tekh.fiz., 24, 1375 (1954).
11. G.A.Smolenskii, Zhur.neorg.khimii (J.Inorg.Chem.) 1, 1402 (1956).
12. V.A.Bokov, Zhur.tekh.fiz., 27, 1784 (1957). (Trans.Soviet Physics - Technical Physics.)
13. S.V.Bogdanov, G.M.Kovalenko, R.Ya.Razbash & A.M.Cherepanov, Izv.AN SSSR, Ser.fiz., 22, 1500 (1958). (Trans.Bulletin, 22, 1493.)

$BaTiO_3$-$BaSnO_3$ SOLID SOLUTION SINGLE CRYSTALS

- A.L.Khodakov & M.L.Sholokhovich

The growth of single crystals of $BaTiO_3$-$BaSnO_3$ solid solutions from different fused media presents serious difficulties. While a continuous series of single crystals of (Ba,Sr)TiO_3, (Ba,Pb)TiO_3, and (Sr,Pb)TiO_3 can be produced with comparative ease[1-4], it is considerably harder to obtain Ba(Ti,Sn)O_3 crystals. Success in growing these crystals is determined to a considerable extent by the state of the initial components employed, the length of the high-temperature holding time of the melts, the provision of equilibrium crystallization conditions

The initial components chosen for our experiments were mixtures of polycrystalline $BaTiO_3$ and SnO_2 presintered at 1200°C. We added 5, 10 and 15%* tin dioxide relative to the $BaTiO_3$. If the initial mixture contained more than 10% SnO_2 the latter could not be completely dissolved even by heating the melt up to 1450°C. The partially dissolved excess SnO_2 would precipitate when the melt cooled. About 10% SnO_2 is apparently the limiting quantity that can replace titanium dioxide in barium titanate with subsequent formation of a solid solution. In this series of experiments we succeeded in producing crystals of isomorphous mixtures containing up to 7% of $BaSnO_3$.

However, when the initial batch was a mixture of presintered (to 1200°) $BaCO_3$, TiO_2 and SnO_2 taken in the stoichiometric proportions requisite to formation of solid solutions of barium titanate and stannate, or a mixture of polycrystalline barium titanante to which barium carbonate and tin dioxide that had not been roasted were added, we succeeded in producing crystals containing up to 13% of $BaSnO_3$. We noted incidentally that using unsintered $BaCO_3$ and SnO_2 as the components of the initial mixtures, facilitates the solution of the mixture in molten KF and the process of formation of crystals with high $BaSnO_3$ content.

In order to obtain plate-like crystals we added small amounts (up to 0.2 percent by weight) of Fe_2O_3 to the mixture in a number of experiments, just as Remeika did when producing tabular $BaTiO_3$ crystals[5]. We avoided adding greater amounts of Fe_2O_3 to prevent its influencing the ferroelectric properties of the resulting crystals[6,7]. In the ensuing experiments it developed that adding the indicated amounts of Fe_2O_3 did not, under our experimental conditions, have any effect on the shape of the crystals formed. Thin plate-like crystals with an edge length of up to 11-12 mm formed every time, regardless of the absence or presence of Fe_2O_3, provided the cooling rate of the melt was 11-15 degree per hr. Slower cooling of the melts, however, even when they contained Fe_2O_3, resulted in cube-shaped crystals. An analogous influence of the cooling rate on the shape of the growing crystals was observed by Timofeeva[8] for $BaTiO_3$ crystallizing from a solution in $BaCl_2$, and by ourselves for $PbTiO_3$ crystals.

We also carried out crystal-growing experiments using as the initial component a ceramic similar in composition to that proposed by Verbitska[9] and known in the literature as Varikond VK-2. The composition of this ceramic is

$$(94\%\ BaTiO_3 + 6\%\ SnO_2) + (0.5\%\ Cr_2O_3 + 0.5\%\ B_2O_3).$$

In separating the crystals from the flux, we detected an appreciable concentration of Cr^{3+} ions in the wash water, which would indicate that little or no chromium remained in the crystals. In some experiments of this series we succeeded in obtaining crystals corresponding as regards their dielectric characteristics to a solid solution of $BaTiO_3$ with approximately 7% $BaSnO_3$. It is natural that

---

*Except as noted, all percentages here and below are molar.

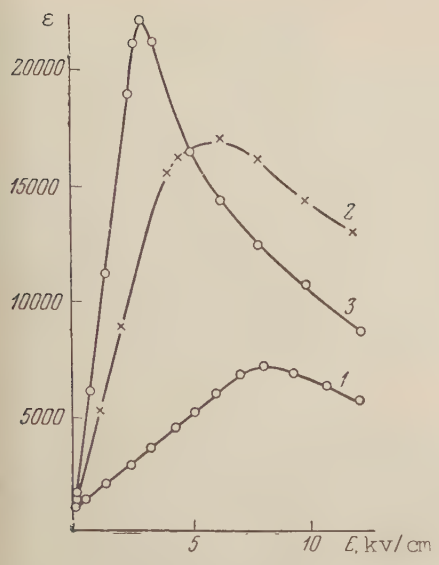

Fig.1. Ac field (50 cps) dependence of ε for $BaTiO_3$-$BaSnO_3$ crystals: 1) $BaTiO_3$; 2) 3% $BaSnO_3$; 3) 8% $BaSnO_3$.

the properties of the resulting crystals, in spite of the close similarity of their composition to that of the initial ceramic, are not entirely comparable to the properties of the latter, inasmuch as the properties of the ceramic are obviously affected by the presence of some titanium dioxide, which is displaced from the $BaTiO_3$ by the SnO_2 in the process of formation of the $BaTiO_3$-$BaSnO_3$ solid solution as well as by the Cr_2O_3 and B_2O_3 impurities.

Although growth of the crystals was rather slow and the cooling rate was from 10 to 15 degrees per hr, the stresses developing in the process of cooling had a substantial effect on their dielectric properties. As a result, the maximum of the dielectric constant for a number of crystals did not occur at the phase transition temperature characteristic of the given compound. To eliminate these anomalies the crystals were heated for 2 hours at 1200°C and then cooled at the rate of 15 degrees per hr. It was not necessary to heat treat crystals containing more than 8% $BaSnO_3$.

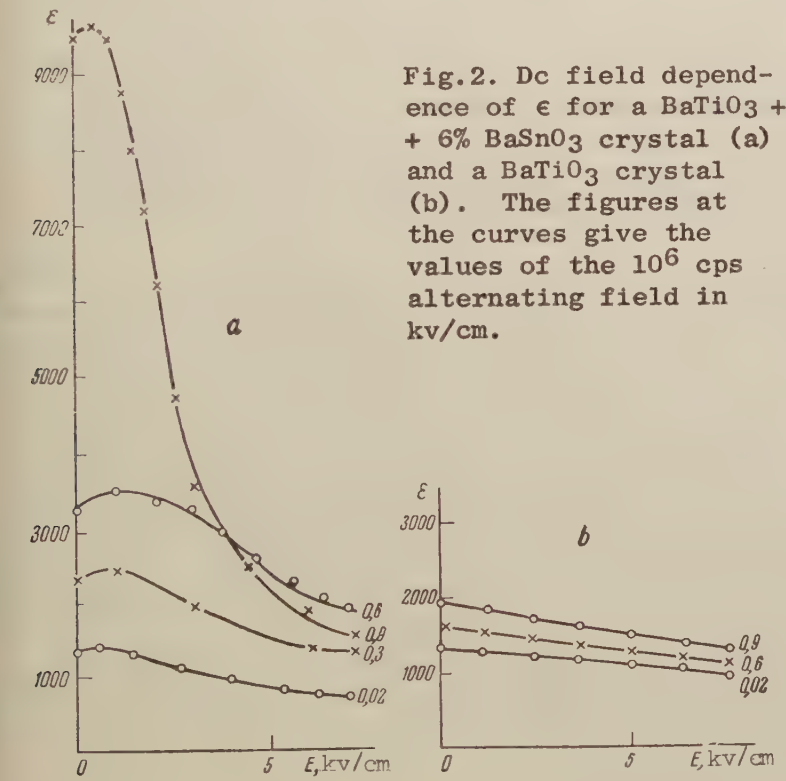

Fig.2. Dc field dependence of ε for a $BaTiO_3$ + + 6% $BaSnO_3$ crystal (a) and a $BaTiO_3$ crystal (b). The figures at the curves give the values of the 10^6 cps alternating field in kv/cm.

Although each crystal batch exhibits an appreciable scatter of the dielectric parameters, the curves shown in Figs.1-3 are fairly representative. The scatter of dielectric properties is most likely due to some difference in the number of 180° and 90° domains, which is particularly characteristic of crystals grown under less than optimum equilibrium conditions. Heat treatment partially "stabilizes" the dielectric parameters. It will be evident from Fig.1 that the ac field dependence of the dielectric constant is considerably more pronounced for $BaTiO_3$-$BaSnO_3$ crystals as compared with $BaTiO_3$ crystals. The dc biasing field dependence of the reversible dielectric constant is also more clearly evident for $BaTiO_3$-$BaSnO_3$ crystals. Practical utilization of ferroelectrics demands that their dielectric constant vary with the ac field and the simultaneous action of a biasing dc field. These dependences are shown in Fig.2.

The hysteresis loops of the crystals have the usual shape. At the Curie point they become straight lines. Instantaneous parameters at different points

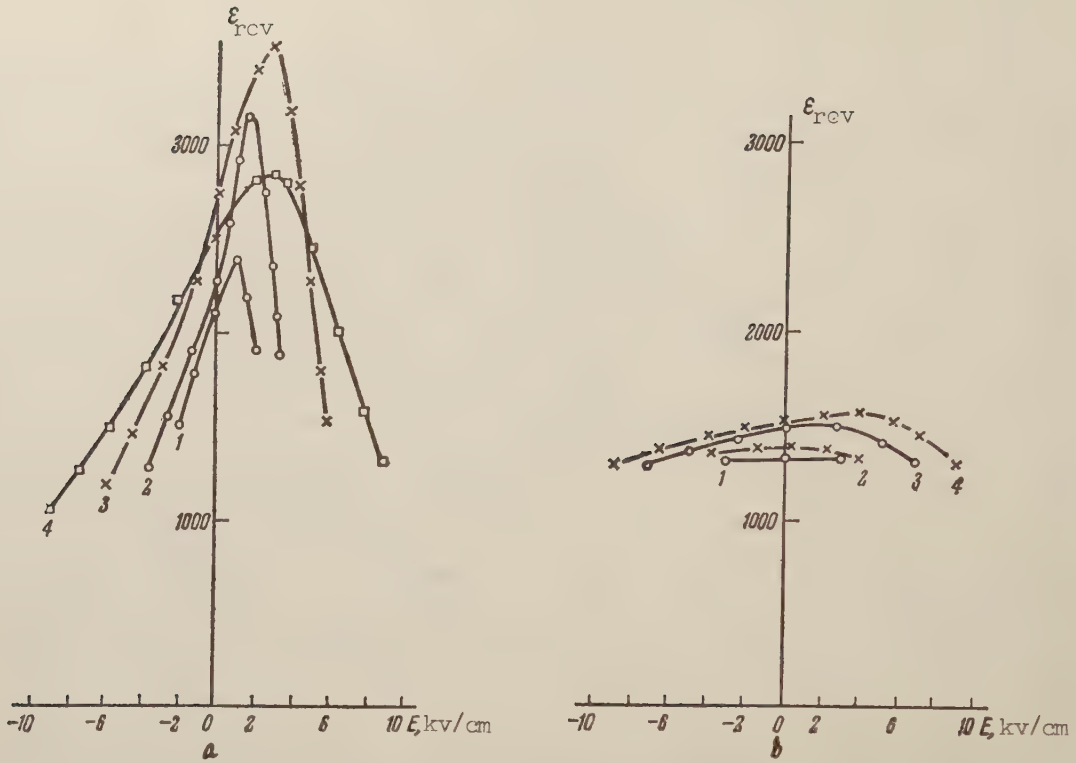

Fig.3. Values of the reversible dielectric constant at different points of the hysteresis loop for $BaTiO_3$-$BaSnO_3$ crystals containing 8% $BaSnO_3$ (a) and for $BaTiO_3$ crystals (b). Crest field values: 1) E_o = 3 kv/cm; 2) E_o = 4 kv/cm; 3) E_o = 7 kv/cm; 4) E_o = 9 kv/cm.

of the hysteresis loop were determined on a two-frequency bridge[10]. An ac voltage with a frequency of 50 kc was applied to the specimen simultaneously with a weak (15 v/cm) high-frequency (10^5 kc) ac field. By compensating for the high-frequency current in the bridge diagonal, it was possible to determine the reversible dielectric constant[11] at different points of the hysteresis loop. An oscillograph was used as the compensation indicator. The curves obtained by means of this apparatus are shown in Fig.3,a. Already at 100 v/cm the value of the reversible dielectric constant for crystals containing 8% of $BaSnO_3$ varies appreciably at different points of the hysteresis loops. For higher voltages the peak value of the reversible dielectric constant increases by a factor exceeding three. For barium titanate (Fig.3,b) the instantaneous values of reversible dielectric constant vary considerably less.

The conductivity of all the crystals was less than 10^{-11} mho/cm; only at temperatures above 150°C does it rise to 10^{-8} mho/cm. The dielectric loss of the crystals at a frequency of 10^6 cps does not exceed 1-2%.

Conclusions

1) Single crystals of $BaTiO_3$-$BaSnO_3$ solid solutions with a high $BaSnO_3$ constant can be grown from KF-$BaTiO_3$-$BaSnO_3$ melts. Such crystals can be grown more easily if the initial substances employed are $BaCO_3$ and SnO_2 not subjected to preliminary roasting.

There were obtained single crystals of $BaTiO_3$-$BaSnO_3$ solid solutions containing up to 13% $BaSnO_3$.

2) The formation of plate-like $BaTiO_3$-$BaSnO_3$ single crystals is determined by the conditions of cooling and the melt concentration, and does not depend on the presence of Fe_2O_3 impurity in the melt.

3) The resulting crystals, in particular those containing 8% $BaSnO_3$, have nonlinear properties that are considerably more pronounced than those of $BaTiO_3$ crystals. The values of the instantaneous dielectric constant of solid solution crystals containing 8% $BaSnO_3$ differ at different points of the hysteresis loop by more than a factor of 3.

Rostov-on-the-Don State University

References

1. A.L.Khodakov, M.L.Sholokhovich, E.G.Fesenko & O.P.Kramarov, Doklady AN SSSR, 108, 825 (1956). (Trans.Doklady.)

2. ,.L.Sholokhovich, E.G.Fesenko, O.P.Kramarov & A.L.Khodakov, Ibid., 111, 1025 (1956). (Trans.Ibid.)

3. M.L.Sholokhovich, Zhur.neor.khimii (J.Inorg.Chem.), 3, 1214 (1958).

4. N.S.Novosil'tsev, A.L.Khodakov, M.L.Sholokhovich, E.G.Fesenko & O.P.Kramarov, Kristallografiya, 4, 101 (1959). (Trans.Soviet Physics - Crystallography.)

5. J.Remeika, J.Amer.Ceram.Soc., 76, 940 (1954).

6. N.Atsno, S.Kyozo & O.Maskazu, J.Phys.Soc.Japan, 11, 180 (1956).

7. E.G.Fesenko & O.I.Prokopalo, Krsitallografiya, 1, 703 (1956).

8. V.A.Timofeeva, In "Rost kristallov" (Growth of crystals), 2, 95 (1957).

9. T.N.Verbitskaya & D.M.Aleksandrova, Izv.AN SSSR, Ser.fiz., 22, 1534 (1958). (Trans.Bulletin, 22, 1525.)

10. M.Drougard, H.Funk & D.Young, J.Appl.Phys., 25, 1166 (1954).

11. A.L.Khodakov, Izv.AN SSSR, Ser.fiz., 22, 1527 (1958). (Trans.Bulletin, 22, 1519.)

PREPARATION AND STRUCTURE OF CRYSTALS OF SOME LEAD-CONTAINING FERROELECTRIC SUBSTANCES AND THEIR SOLID SOLUTIONS

- M. L. Sholokhovich & E. G. Fesenko

Many ferroelectric salts containing Pb^{2+} cations are substances that melt incongruently. Consequently, their preparation in the form of single crystals must be effected from a solution in melts of other substances that do not interact chemically with them.

In the present work we give the results of investigating the possibility of preparing $PbTiO_3$-$PbZrO_3$ solid solution single crystals, $PbNb_2O_6$ crystals and $PbTiO_3$-$PbNb_2O_6$ solid solutions from solutions of these substances in melts of $PbO + B_2O_3$. Earlier[1-4] we proposed a technique for preparing single crystals of $PbTiO_3$ from its solutions in molten $PbO + B_2O_3$.

Fig.1 shows the [50% PbO + 50% B_2O_3]-$PbTiO_3$-$PbZrO_3$ crystallization surface that we investigated up to 1000°C for the purpose of determining the possibility of preparing single crystals of $PbTiO_3$-$PbZrO_3$ solid solutions. It was found that in the investigated section the crystallization surface of the system comprises three phases: a vitreous phase occupying a minutely small part of the crystallization surface, a phase of limited $PbTiO_3$-$PbZrO_3$ solutions with a maximum of 13.9% $PbZrO_3$, and a phase of the ternary compound $PbO \cdot B_2O_3 \cdot ZrO_2$. Crystals of Pb(Ti,Zr)O solid solutions can be separated from the other phase by dissolving the latter in HNO_3.

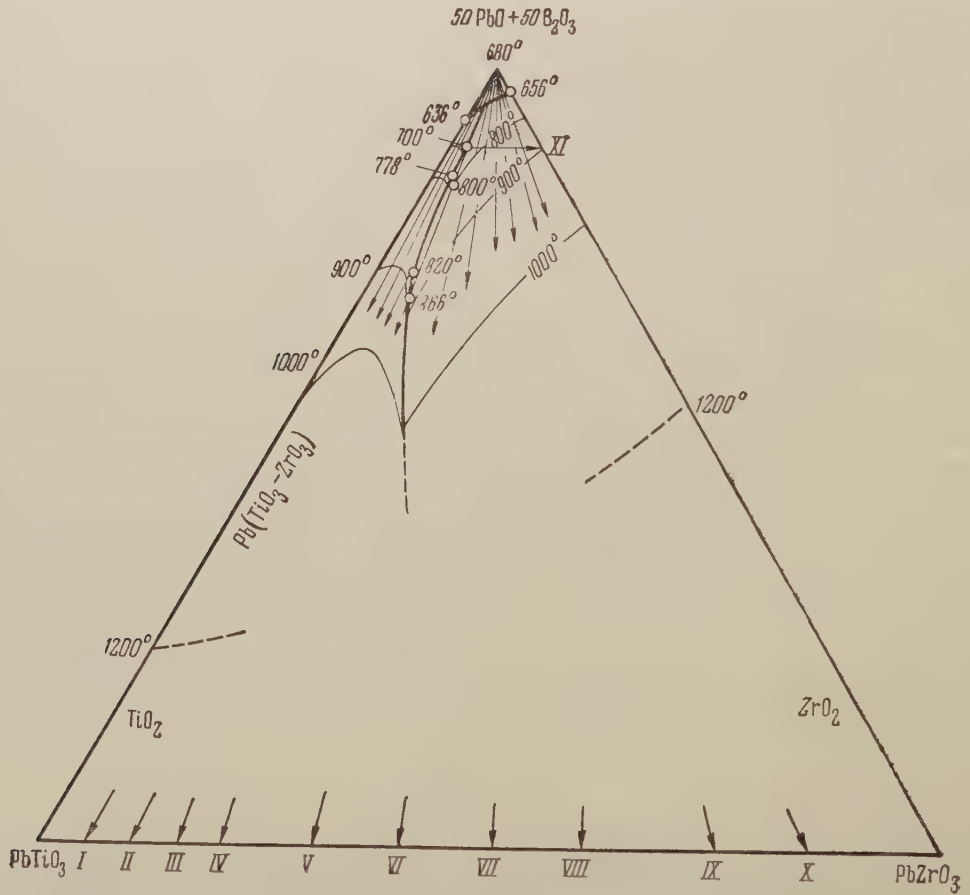

Fig.1. Diagram of the [50% PbO + 50% B_2O_3]-$PbTiO_3$-$PbZrO_3$ crystallization surface.

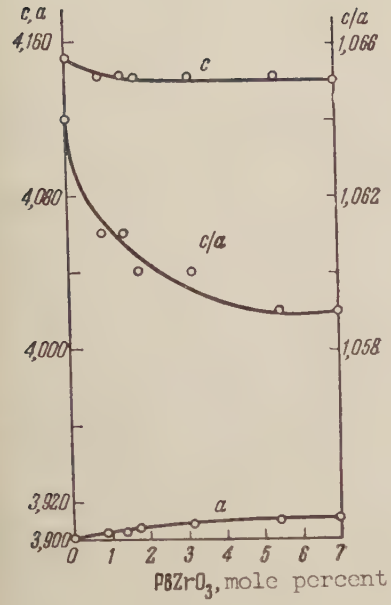

Fig.2. Variation of the lattice parameters of $Pb(Ti,Zr)O_3$ crystals with the composition.

From some melts of the investigated cross section we gew single crystals of $Pb(Ti,Zr)O_3$ solid solutions containing 0.9, 1.4, 1.7, 3.2, 5.4, 7.0 and 13.9% $PbZrO_3$. The crystals were grown from melts of PbO and B_2O_3 in molar proportions, to which was added 2.5% of the desired mixture of $PbTiO_3$ and $PbZrO_3$. In all cases, however, the composition of the resulting crystals differed somewhat from that of the mixtures employed for crystallization. The initial components of the mixtures were the appropriate calculated quantities of PbO, TiO_2 and ZrO_2.

The crystals had a golden yellow hue and were transparent. The shape of the crystals varied with the conditions of crystallization; for the most part hexahedral plates and cubes were obtained.

X-ray diffraction studies of the crystals showed that their structure was of the tetragonal perovskite type. The structural type, symmetry and parameters were determined from powder patterns. The variation of the parameters with the $PbZrO_3$ concentration is shown in Fig.2. These data agree with those for the corresponding polycrystalline solid solutions[5].

The index of refraction, determined by the method of immersion in Se-S, was found to be 2.72 for all the investigated crystals. Curie temperatures were determined by means of a polarizing microscope.

We established the possibility of preparing single crystals of lead metaniobate from its solutions in PbO + B_2O_3 melts.

Fig.3 shows the primary crystallization surface of the $PbO-B_2O_3-Nb_2O_5$ system, investigated up to 1100°. Of the six binary compounds* known for the $PbO-Nb_2O_5$ system[6], only three compounds appear in the investigated part of the ternary system. The major part of the system is occupied by the freely crystallizing lead metaniobate phase. The two other phases, which penetrate from the $PbO-Nb_2O_5$ side and appear in the region of high PbO concentrations and at high temperatures,

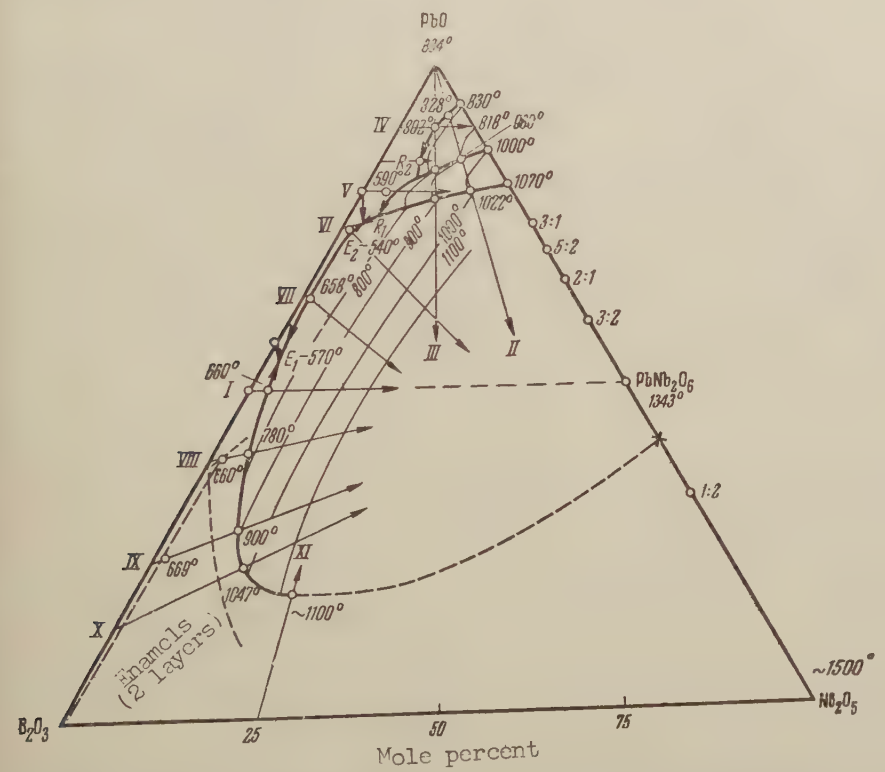

Fig.3.Crystallization surface of the $PbO-B_2O_3-Nb_2O_5$ system.

---

*The poles of these compounds are indicated in Fig.3 on the $PbO-Nb_2O_5$ side.

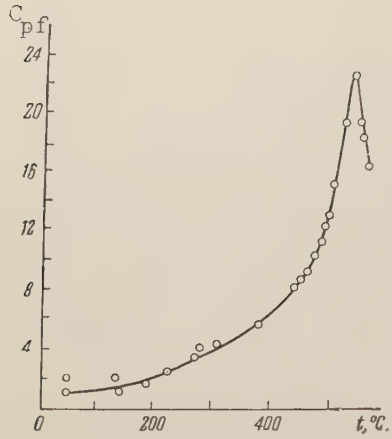

Fig.4. Temperature dependence of the capacitance for specimens of single crystals of $PbNb_2O_6$ roasted at 1300°C.

upon cooling of the melts decompose at point R_1 corresponding to 660° and at point R_2 (730°). Thus only lead metaniobate and lead-boron glasses crystallize upon final solidification of the melts. In contrast to $PbNb_2O_6$, the lead-boron glasses are easily soluble in HNO_3, making quantitative analysis of the solid phases feasible. From a melt of PbO and B_2O_3 taken in molar ratio, to which was added 24% [50% PbO + 50% Nb_2O_5], there were obtained $PbNb_2O_6$ crystals. The crystals grew in the temperature range from 1100° to 660° with the melt cooled at the rate of 20 degree per hr. They were transparent hexahedral light-yellow plates up to ~100 μ thick and to 5 mm in cross section.

The crystals prepared under these conditions did not evince ferroelectric properties; however, after roasting at 1300°C for 3.5 hours, they became characteristic ferroelectrics. The dielectric properties of the crystal were investigated by A.L. Khodakovii; the pertinent data are given in Fig.4.

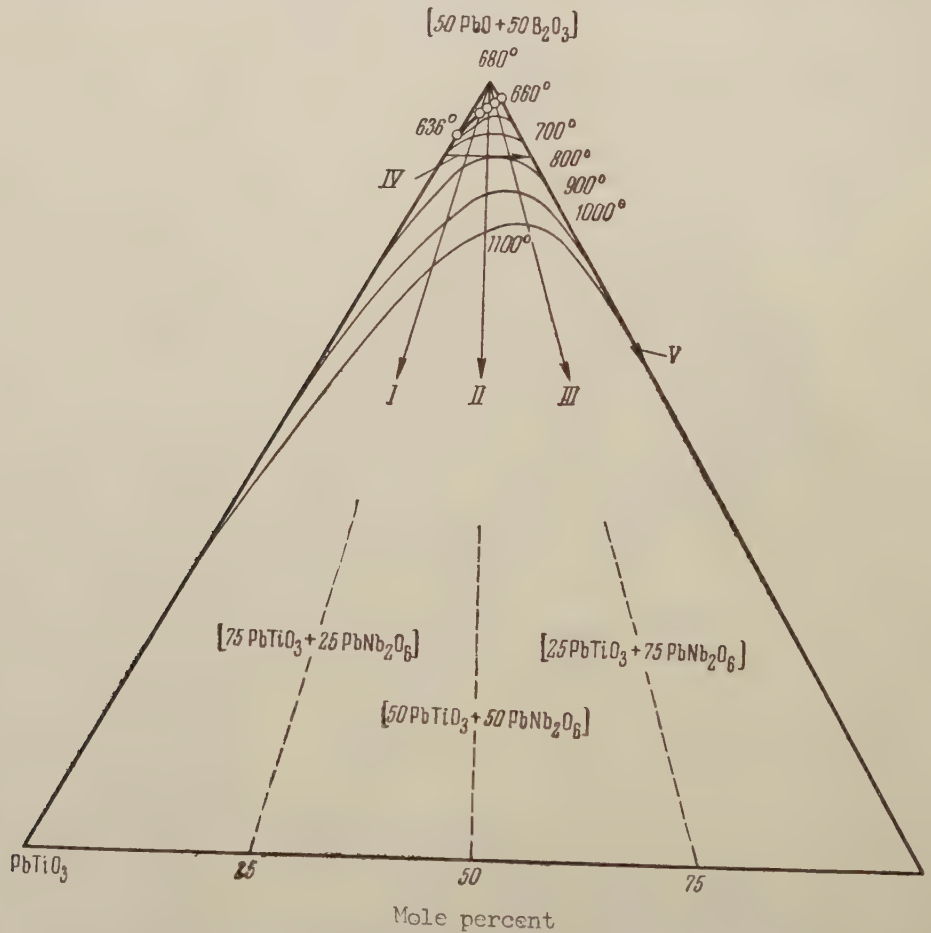

Fig.5. Fusibility diagram for [50% PbO + 50% B_2O_3]-$PbTiO_3$-$PbNb_2O_6$.

The fusibility diagram of the [50% PbO + 50% B_2O_3]-$PbNb_2O_6$-$PbTiO_3$ system (Fig.5), which was investigated up to 1000°C is instructive. The character of the isotherms indicates that a continuous series of solid solutions of nonferroelectric $PbNb_2O_6$ and $PbTiO_3$ can crystallize from these melts at low temperatures.

The crystals obtained from melts of this system at temperatures from 1000° to 600°C were transparent orange plates measuring up to 2-3 mm. Optical observations did not reveal any domain structure in nonannealed crystals.

X-ray diffraction studies of the resulting crystals and of the same crystals heated to 1300°C established that in a wide range of concentrations from pure $PbNb_2O_6$ up to 90% or more $PbTiO_3$, there exists a continuous series of solid solutions with a structure different from perovskite. Roasting changes the structural type of the crystals. It is probable that roasting is accompanied by transition from the modification found in Ref.7 (rhombohedral $PbNb_2O_6$) to that described in Refs.8 and 9 (rhombic $PbNb_2O_6$). Examination of the diffraction patterns for nonannealed crystals shows a monotonic variation of the parameters of rhombohedral $PbNb_2O_6$ with increasing $PbTiO_3$ concentration.

The authors are grateful to A.L.Khodakov for his interest in the work and discussion of the results.

Physical-Mathematical Scientific Research Institute,
Rostov-on-the-Don University

References

1. M.L.Sholokhovich, E.G.Fesenko, L.P.Kramarov & A.L.Khodakov, Doklady AN SSSR, 3, 1025 (1956). (Trans.Doklady.)
2. M.L.Sholokhovich, Zhur.neorg.khimii (J.Inorg.Chem.), 3, 1213 (1958).
3. E.G.Fesenko, O.P.Kramarov, A.L.Khodakov & M.L.Sholokhovich, Izv.AN SSSR, Ser.fiz., 21, 305 (1957). (Trans.Bulletin, 21, 314.)
4. E.G.Fesenko & R.V.Kolesova, Krsitallografiya, 4, 60 (1959). (Trans.Soviet Physics - Crystallography.)
5. G.Shirane, K.Suzuki & A.Takeda, J.Physic.Soc.of Japan, 7, 11 (1952).
6. Robert Roth, J.Research National Bureau of Standards, 62, No.1, 2925 (1959).
7. M.H.Francombe, Acta Cristallogr., 9, No.8, 683 (1956).
8. G.Goodman, J.Amer.Ceram.Soc., 36, 368 (1953).
9. M.H.Francombe & B.Lewis, Acta Cristallogr., 11, 696 (1958).

SEMICONDUCTOR PROPERTIES OF $BaTiO_3$

- S.V.Bogdanov & V.A.Rassushin

To judge from the literature on ferroelectricity, in recent years more and more attention has been given to the electric properties of barium titanate. It may be inferred from the work of Soviet and foreign investigators[1-6] that barium titanate has purely n-type conductivity.

In 1949 Busch, Flury & Merz[7] investigated the temperature dependence of the conductivity of barium titanate single crystals and came to the conclusion that $BaTiO_3$ is a semiconductor and that the activation energy calculated from the slope of the $\sigma = f(1/T)$ curves is 1.75 ev. Later measurements of optical absorption carried out by Yatsenko[8] yielded a value of 3.1 Mev for the width of the forbidden band.

So far there has been no satisfactory explanation for the divergence between the data obtained from optical measurements and measurements of the temperature dependence of the conductivity. It may be assumed that the 1.75 ev slope value is the result of the presence of impurities that give rise to additional levels in the forbidden band. One may judge of the character of these levels, for example, from the sign of the thermoelectromotive force. The first data on the type of conductivity of barium titanate are given in the work of Remeika[9]. According to Remeika, the conductivity of $BaTiO_3$ single crystals determined from the sign of the thermo-emf is electronic; moreover, Remeika is of the opinion that the decrease in conductivity accompanying introduction of iron impurity is the result of compensation of the intrinsic donor levels in $BaTiO_3$ by iron acceptor levels. More detailed information on the influence of iron will be found in the work of Nishioka et al[10].

Saburi[11], in addition to determining the sign of the thermo-emf, attempted to measure the Hall constant for "semiconductor" barium titanate. The sign of the Hall constant inferred from his experiments indicates that the current carriers in "semiconductor" $BaTiO_3$ are electrons.

From the above brief review it may be inferred that barium titanate is a semiconductor with a 3.1 ev wide forbidden band and n-type conductivity. In view of this we felt it would be of interest to determine the effect of some impurities not only on the ferroelectric but also on the electric properties of barium titanate, or as Saburi puts it, on the "semiconductor" properties of $BaTiO_3$.

Below we give some data on the variation of $\log \rho$ with $1/T$ for $BaTiO_3$ single crystals deliberately doped with lanthanum and vanadium. The single crystals were grown by the Remeika technique. The impurities were introduced into the initial batch in the form of La_2O_3 and V_2O_5 in amounts of 0.01, 0.05 and 0.1 mole percent in excess of stoichiometry. Whereas in the case of pure $BaTiO_3$ most of the single crystals obtained are in the form of triangular plates, as a result of doping, the number of plate-like crystals decreases. Most of our crystals were of granular form. In the case of V_2O_5 doping the crystals were bright yellow in color; in the case of La_2O_3, the color of the crystals varied from rose to violet; the violet crystals, however, were in the form of very small grains unsuitable for measurements.

Unfortunately, we were not able to determine the precise impurity concentrations in the crystals. However, the fact that the impurities entered the structure of the crystal is shown by indirect data, as, for example, the shift of the Curie point with increase in the impurity content in the initial batch. We observed a shift of the Curie point both for barium titanate doped with vanadium and barium titanate doped with lanthanum. For example, in the case of La, the shift of the Curie point is clearly evinced even in the case of ceramic specimens with a high impurity content.

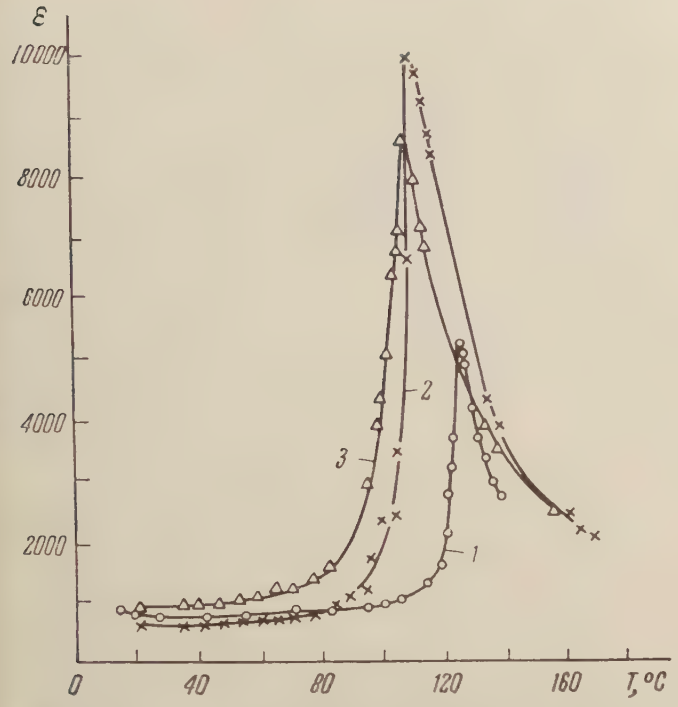

Fig.1. Variation of the dielectric constant ϵ with temperature for barium titanate single crystals with lanthanum impurity: 1) crystal of the initial "pure" $BaTiO_3$, 2) sample A, 3) sample B.

Fig.1 shows the variation of the dielectric constant ϵ with temperature for single crystals doped with La, as well as the curve for the initial "pure" $BaTiO_3$. It will be evident from the curves that sample A contains less La than sample B.

We recorded the temperature variation of the resistivity of our single crystals. Some of the results for the crystals doped with vanadium are shown in Fig.2. Here curve 1 pertains to the sample with the lowest vanadium concentration; curve 2 to the sample with the highest vanadium concentration. It will be seen that the slopes of the plots are nearly equal. The resistivity of the specimens at room temperature is $1.37 \cdot 10^{12}$ ohm·cm.

The resistivity data for the specimens doped with lanthanum are shown in Fig.3. Curve 1 pertains to sample B with the higher impurity concentration. It will be evident from the figure that the log ρ vs 1/T plot has an anomalous section similar to that described by Saburi for barium titanate ceramic doped with rare earth elements. The fact that there is such an anomalous section may serve as proof that the impurity entered into the structure of the single crystal. However, we did not succeed in obtaining a substantial decrease of ρ. The slopes of the two linear sections are almost the same. For curve 1 the equivalent energy is 2.44 ev; for curve 2 the corresponding value is 2.34 ev.

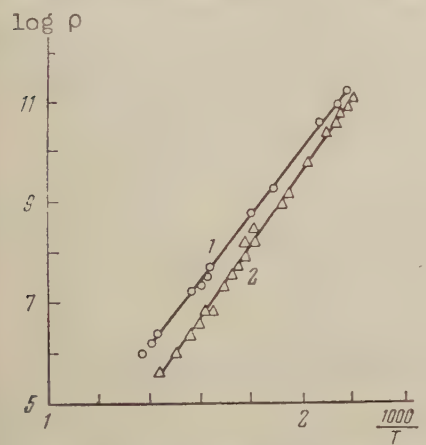

Fig.2. Variation of the resistivity with temperature for $BaTiO_3$ single crystals doped with vanadium: 1) lowest impurity concentration; 2) highest impurity concentration.

Similar results were obtained for a large number of different crystals; moreover the reproducibility of repeat measurements on the same crystal was good.

To explain the anomalous temperature variation of ρ it must be noted that this section of the log ρ vs 1/T curve lies in the region of the phase transition. This phase transition is accompanied by rearrangement of the band structure of the crystal, which is clearly evident from the work of Yatsenko & Rabkin[12] on the luminescence spectra of rare earths in barium titanate. Below the phase transition point the impurity levels are split, which leads to increase of the conductivity; above the phase transition, the splitting vanishes and the conductivity decreases.

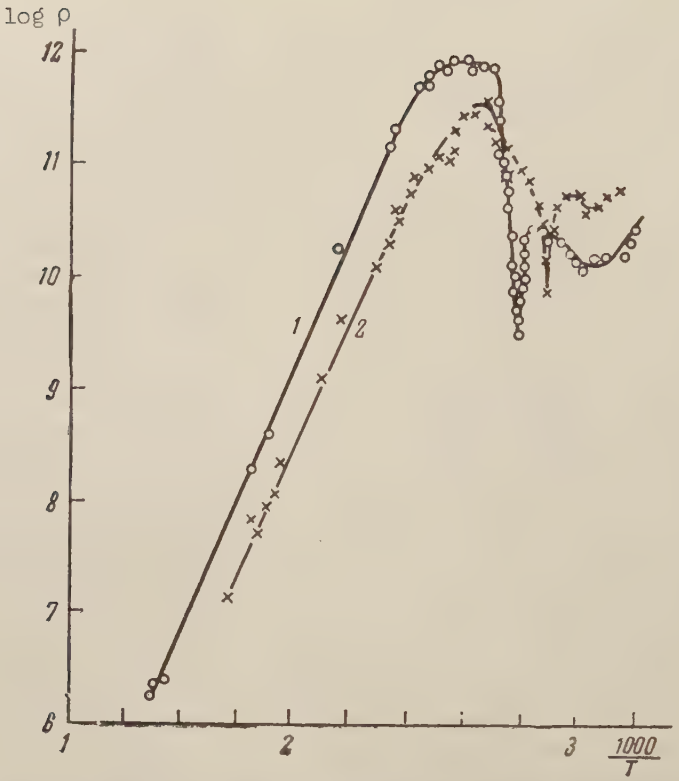

Fig.3. Variation of the resistivity with temperature for $BaTiO_3$ single crystals doped with lanthanum: 1) sample A, 2) sample B (see Fig.1).

References

1. M.D.Mashkovich, Thesis GIEKI (State Electrical Ceramics Research Institute), M., 1954.

2. E.V.Sinyakov & B.K.Chernyi, Zhur.tekh.fiz. (Journal Technical Physics) 22, 265 (1954).

3. I.Inuishi & S.Uematsu, J.Phys.Soc.Japan, 13, 761 (1958).

4. E.K.Weise & I.A.Lesk, J. of Chem.Physics, 21, 801 (1953).

5. N.S.Kostyukov, Dissertation, Moscow Power Institute, M., 1959.

6. G.Harman, Phys.Rev., 106, 1358 (1957).

7. G.Busch, H.Flury & W.Merz, Helv.Phys.Acta, 21, 212 (1948).

8. A.F.Yatsenko, Izv.AN SSSR, Ser.fiz., 22, 1456 (1958). (Trans.Bulletin, 22, 1450.)

9. J.P.Remeika, J.of Amer.Chem.Soc., 76, 940 (1954).

10. A.Nishioka, K.Sekikawa & M.Owaki, J.Phys.Soc.Japan, 11, 180 (1956).

11. O.Saburi, Ibid., 14, 1159 (1959).

12. A.F.Yatsenko & L.Rabkin, Izv.AN SSSR, Ser.fiz., 24, 11 (1960). (Trans. Bulletin, 24, No.11.)

GROWING FERROELECTRIC SINGLE CRYSTALS FROM MELTS

- O.P.Kramarov

The procedure developed earlier[1] for preparing ferroelectric single crystals by zone recrystallization of ceramic samples enabled us to obtain fairly large single crystals of $BaTiO_3$ and other ferroelectric substances with the perovskite structure. However, the crystals obtained contained a large number of imperfections in the form of gaseous inclusions and mosaic structure. Attempts to obtain crystals free of defects by this procedure failed to yield positive results.

Accordingly, on the basis of the same principle, we developed new universal equipment for growing single crystals by the zone melting technique and the Verneuil technique.

We decided to use Silit for the heater element of the universal furnace. Tests of Silit heaters have shown that they successfully withstand prolonged operation in air at temperatures to 1600-1650° and can be operated for short periods at 1650-1700° (the indicated temperatures are those of the heater element itself and not of the furnace). Thus the available temperatures are high enough for melting many ferroelectric materials.

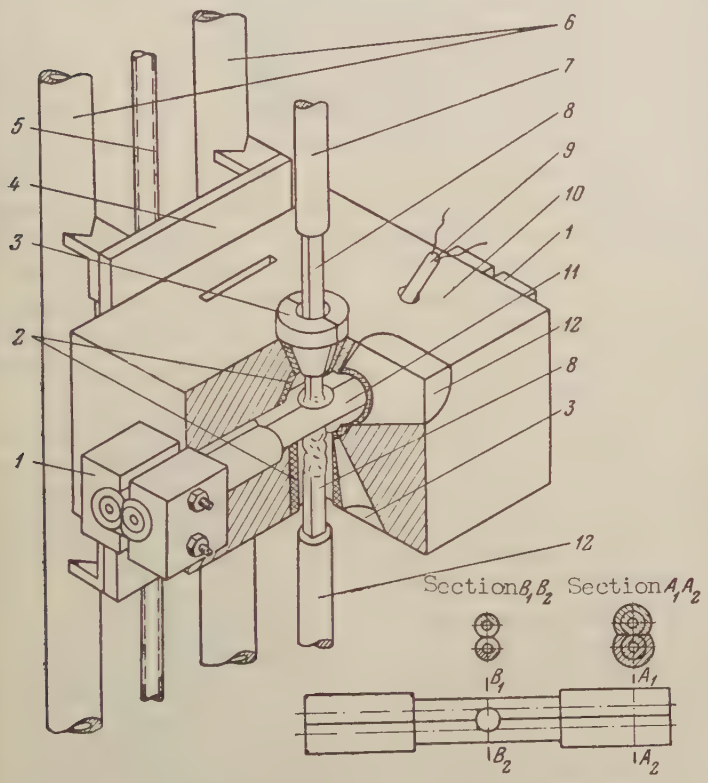

Fig.1. Design of furnace. Insert below - shape of the Silit rods.

We tested a number of different designs of the furnace and the heating elements. The best results were obtained with the furnace diagramed in Fig.1. The heating element 11 consists of two sections of ordinary 8 mm diameter Silit rod. The sections are shaped as shown in the insert in Fig.1. The thin cylindrical parts are in direct contact, and in the center there is an opening for passage of the specimen 8. The thicker parts of the rods have flats on one side and are held in contact by the aluminum clamps 1. The heater is housed in the foam fire clay block 10, which has a cross-shaped space for the rod assembly and the specimen. This space is coated on the inside with a high alumina lining. Two openings 12 are provided for observation of the hot zone. These openings are covered on the outside with mica windows to reduce the flow of cold air through the furnace. From above the working space is closed with an alumina ceramic plug 3. The entire furnace is mounted on the base 4 which can be moved up and down along the guide rails 9 by means of the lead screw 5. The thermal regulator is controlled by a platinum-platinorhodium thermocouple 9, the hot junction of which is in contact with the heater rods at some distance from the hottest point. The specimen 8 is mounted in Silit holders 7 and 12. The upper holder 7 can be rotated at the rate of 2 rpm to provide stirring action in the melting zone.

After mounting the specimen in the furnace, the temperature is slowly raised to the melting point of the specimen. Initially the temperature is monitored by

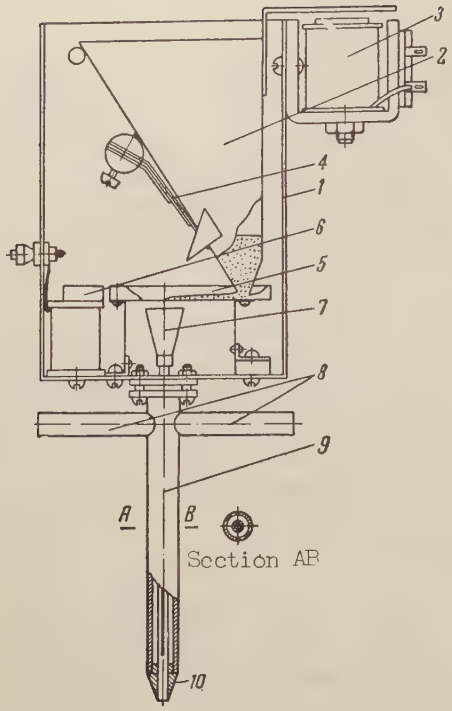

Fig.2. Powder feed mechanism: 1) housing, 2) hopper, 3) hopper electromagnet, 4) hopper spring, 5) vibrating conveyor, 6) conveyor electromagnet, 7) funnel, 8) inlet and outlet connections for cooling water, 9) water cooled jacket, 10) tube carrying powder into the furnace.

means of the thermocouple 9 (Fig.1) and then maintained at the desired level by the thermal regulator. When the feed mechanism is set into operation, the melting zone moves over the specimen. If desired, rotation of the upper holder is started.

For working by the Verneuil technique the upper holder is replaced by a powder feed device. The rotation mechanism is transferred to below the furnace and into its holder is inserted a receiver plug with (or without) a seed.

The powder feed device is diagramed in Fig.2. The use of a vibrating conveyor and hopper provides for satisfactory control of the powder supply rate. We call attention to the tendency of very fine barium titanate powders to conglomerate and cake; hence for more uniform feed it is desirable to use powders with a grain size of 20-30 μμ. This grain size insures a free-flowing powder.

In the process of developing the equipment we carried out preliminary experiments on zone melting of samples of solid solutions of $BaTiO_3$ + + 5% $SrTiO_3$ and fusing of barium titanate powder. The results were generally satisfactory. It was found that the molten material is well retained between the solid phase particles and that the specimen does not darken, which indicates a sufficient supply of oxygen in the working space of the furnace.

Preliminary tests showed the presence of large single crystal blocks in specimens that had passed through the furnace and almost complete absence of gaseous inclusions. Dielectric measurements showed increased nonlinearity of the specimens as compared with the initial ceramic.

In working by the Verneuil technique there were obtained fused globules of $BaTiO_3$. The experiments were carried out without inoculation. The structure of the resulting specimens was coarse crystalline with a minor amount of pores. It should be noted that in working by the Verneuil technique the furnace has to be maintained at the maximum temperature in order to insure fusing of the powdered material which is fed into the furnace cold. This leads to appreciable overheating of the rods so that their service life is reduced to 5-6 hours. The service life in working by the Verneuil technique is also shortened because a certain amount of $BaTiO_3$ powder inevitably comes in contact with the Silit rods.

I desire to express my gratitude to A.L.Khodakov for guidance and assistance in the work.

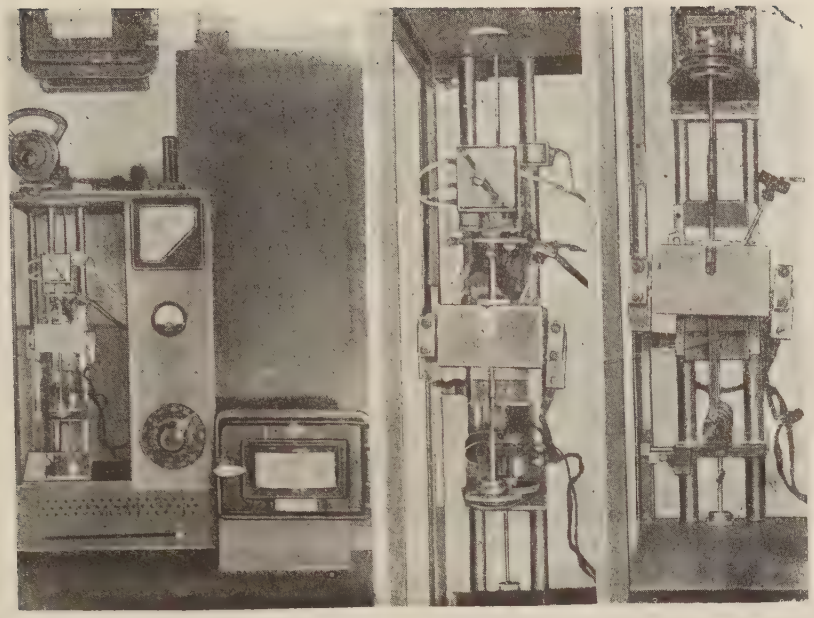

a b c

Fig.3. Equipment for preparing ferroelectric single crystals: a) general view of the equipment, b) furnace with device for working by the Verneuil technique, c) furnace with device for zone melting.

Fig.4.

Physical-Mathematical Scientific Research Institute
Rostov-on-the-Don State University

Reference

1. O.P.Kramarov, Kristallografiya, AN SSSR, 4, 109 (1959). (Trans.Soviet Physics - Crystallography.)

CONCERNING THE ELECTRIC CONDUCTIVITY OF BARIUM TITANATE AND SOME BARIUM TITANATE BASE SOLID SOLUTIONS

- E.V. Sinyakov & B.K. Chernyi

Investigations of the temperature dependence of the conductivity of alkaline earth metal titanates with the perovskite structure show that the activation energy in the region of intrinsic conductivity is only weakly dependent on the bivalent cation.[1,2] Table 1 lists the values of the activation energy U for the alkaline earth metal titanates according to the data of Ref.1 and our measurements for $BaZrO_3$ and $SrZrO_3$.

Table 1

Substance	U, ev	Substance	U, ev
$BaTiO_3$	1,83	$BeTiO_3$	1,88
$CaTiO_3$	1,82	$BaZrO_3$	2,50
$SrTiO_3$	1,70	$SrZrO_3$	2,40

Table 2

Concentration $BaZrO_2$ wt.,%	U, cv	Concentration $BaSnO_2$ wt.,%	U, cv
0	1,81	0	1,70
10	1,89	10	1,85
20	1,96	40	2,28
30	2,21	60	2,28
40	2,43		
60—100	2,40		

On the other hand; the presence of a tetravalent cation has a significant influence on the activation energy of alkaline earth perovskites. Thus, for example, in the case of $Ba(Ti,Zr)O_3$ and $Ba(Ti,Sn)O_3$ solid solutions, the activation energy increases with increase of the $BaZrO_3$ and $BaSnO_3$ concentration. The values of the activation energy in these series of solid solutions according to the data of Novosil'tsev & Khodakov[3], are shown in Table 2.*

Thus, in view of the cited data on the activation energy for alkaline earth perovskites it may be inferred that the conduction band in barium titanate is formed of Ti ion levels.

Of interest in this connection are the results of Blokhin[4] on the K absorption spectra of titanium in barium titanate. It follows from Blokhin's results that the conductivity of barium titanate is due to the tunnel effect in the $3d$ bands and to passage of electrons over the potential barriers. On the basis of this scheme it would follow that in the temperature region where the activation energy is 1.75-1.80 ev the conductivity should be primarily of the n-type rather than of the p-type. Our measurements of the thermo-emf coefficient[5], as well as the measurements of other authors[2], show, however, that the thermo-emf coefficient in the temperature region where the activation energy is 1.75-1.80 ev corresponds to hole type conductivity. Consequently, the scheme proposed by Blokhin[4] does not fully correspond to the actual conductivity mechanism in barium titanate.

It follows from the proposed scheme, however, that the $3d$ band is only partially filled and this means that in the $2p$ band of the oxygen ions there are unoccupied levels, which may be responsible for the inferred hole conductivity of barium titanate.

In investigating optical polarization of barium titanate Van Santen & Boer[6] calculated the energy of the electron transitions from the oxygen ions to the titanium ions. They found that the transition energy is 2 ev. Inasmuch as the optical transition energy is greater than the thermal activation energy, it may be inferred that the activation energy of 1.75-1.80 ev, calculated from the temperature dependence of the conductivity of barium titanate, represents the width of the forbidden band between the normal band (which we take to be the $2p$ band of

---

*The activation energy was calculated by means of the formula $\sigma = Ae^{-\frac{U}{kT}}$.

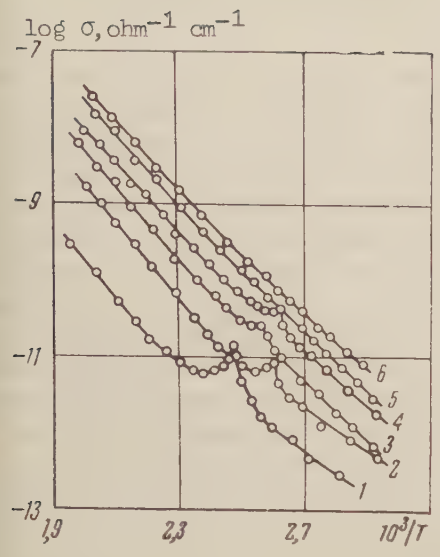

Fig.1. Variation of log σ with 1/T for different impurity concentrations in barium titanate (the curves are identified in Table 3).

the oxygen ions) and the $3d$ levels of the Ti ions. In this case the mobility of the holes in the normal band will be greater than the electron mobility in the $3d$ band since the latter is divided by potential barriers. This explains why hole type conductivity is observed in barium titanate. Probably a similar conductivity mechanism obtains in $CaTiO_3$ and $SrTiO_3$ because in them the sign of the thermo-emf coefficient corresponds to hole type conductivity, while the magnitude of the thermo-emf is almost the same as in $BaTiO_3$.[2]

Measurements carried out in the work of Ref. 5 and in the present study show that the conductivity σ of barium titanate with approach to the Curie point increases, attains a certain maximum value and then decreases, i.e., in the region of the Curie temperature there is observed an anomalous jump in the conductivity. The $\log \sigma = f(1/T)$ curves recorded for barium titanate and barium titanate doped with small amounts of impurities are shown in Fig.1. The impurities were introduced for the purpose of lowering the Curie temperature, i.e., to see whether the change in conductivity follows the phase transition point. The data on the impurity concentration, the resultant Curie temperature and the resistivity are listed in Table 3.

It will be evident from Fig.1 that the variation in conductivity is correlated with change in the Curie temperature of the investigated specimens. An increment in conductivity at the Curie point is observed in the region of impurity conductivity and decreases with increase of the latter. Thus the higher the impurity conductivity the less significant is the effect of addition of charges into the conduction band as regards its behavior in the region of the Curie temperature.[7] At an appreciable value of the impurity conductivity no noticeable increase in electric conductivity at the Curie point is observed. Also, no increase in electric conductivity is observed for compositions which have a Curie region rather than a Curie point. The jump-like increase in electric conductivity is observed both in heating and in cooling the barium titanate specimens. Consequently, the effect of increase in electric conductivity in the region of the phase transition is primarily a result of rearrangement of the lattice and lowering of the conduction band.[7]

Table 3

Curve No. in Fig.1	Impurity concentration, wt., %	θ, °C	ρ, ohm·cm at $t = 185°$	ρ, ohm·cm at $t = 84°$
1	0	130	$4{,}50 \cdot 10^{10}$	$3{,}17 \cdot 10^{10}$
2	0,3 CoO & 1,0 B_2O_3	113	$7{,}80 \cdot 10^{9}$	$7{,}95 \cdot 10^{11}$
3	0,1 CoO	116	$1{,}25 \cdot 10^{9}$	$4{,}57 \cdot 10^{11}$
4	0,3 CoO	110	$6{,}10 \cdot 10^{8}$	$1{,}82 \cdot 10^{11}$
5	1,0 $CoTiO_3$	124	$3{,}35 \cdot 10^{8}$	$1{,}15 \cdot 10^{11}$
6	2,0 $CoTiO_3$	122	$1{,}75 \cdot 10^{8}$	$3{,}46 \cdot 10^{10}$

Conductivity of $(Ba,Ni)(Ti,Zr)O_3$ and $(Ba,Co)(Ti,Zr)O_3$ solid solutions

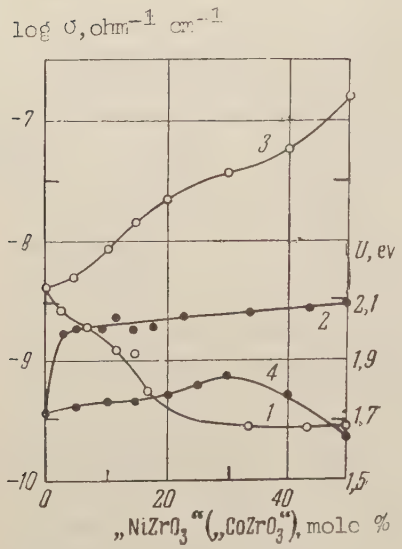

Fig.2. Variation of the conductivity at t = 181°C (1,3) and the activation energy (2,4) with the composition of the solid solution: 1 & 2 - $(Ba,Ni)(Ti,Zr)O_3$ and 3 & 4 - $(Ba,Co)(Ti,Zr)O_3$.

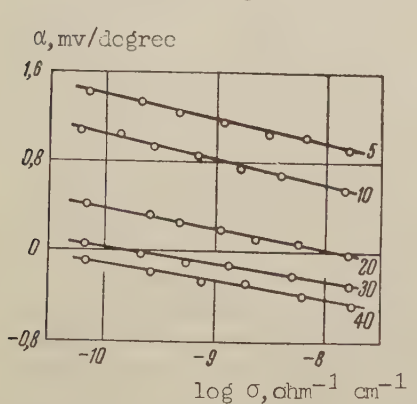

Fig.3. Variation of the thermo-emf coefficient with log σ for the $(Ba,Co)(Ti,Zr)O_3$ system. The figures at the curves indicate the $CoZrO_3$ concentration in mole percent.

The electric conductivity of the $(Ba,Ni)(Ti,Zr)O_3$ and $(Ba,Co)(Ti,Zr)O_3$ system was investigated in the temperature range from 50 to 260° in a field of 0.55 kv/cm. The activation energy U_1 for the $(Ba,Ni)(Ti,Zr)O_3$ system, calculated from the maximum slope of the $\log \sigma = f(1/T)$ plot at first increases sharply with increase of the $NiO \cdot ZrO_2$ concentration and then continues to rise slowly (Fig.2). The conductivity of this system decreases with increase of the $NiO \cdot ZrO_2$ concentration.

In the $(Ba,Co)(Ti,Zr)O_3$ system the activation energy U_1 increases with increase of the $CoO \cdot ZrO_2$ concentration up to 30% and then begins to decrease; the electric conductivity, on the other hand, monotonically increases, the rate of increase becoming particularly noticeable beginning with 30% $CoO \cdot ZrO_2$ (Fig.2).

X-ray diffraction studies of the $(Ba,Ni)(Ti,Zr)O_3$ and $(Ba,Co)(Ti,Zr)O_3$ systems carried out earlier[8,9] and in the present work by means of a URS-50I diffraction camera showed that in the $(Ba,Ni)(Ti,Zr)O_3$ system the zirconium ions enter into the $BaTiO_3$ lattice in the entire investigated concentration range (from 0 to 50 mole percent). When the $NiO \cdot ZrO_2$ concentration attains 15% there appear in the diffraction patterns lines corresponding to the structure of $NiTiO_3$.

In the $(Ba,Co)(Ti,Zr)O_3$ system there form solid solutions up to a $CoO \cdot ZrO_2$ concentration of 30%; above this concentration there appear lines characteristic of $CoO \cdot ZrO_2$.

Thus in the region of formation of solid solutions in the $(Ba,Ni)(Ti,Zr)O_3$ system decrease of the electric conductivity is connected with replacement of the Ba ions by Ni ions, while in the $(Ba,Co)(Ti,Zr)O_3$ system replacement of the Ba ions by Co ions leads to increase of the conductivity. The radii of the Ni and Co ions ($r_{Ni^{2+}} = 0.78$ A, and $r_{Co^{2+}} = 0.82$ Å) differ little; hence this contrary influence of Ni and Co ions on the conductivity of the investigated compositions (in the region of formation of solid solutions) is probably connected with filling of the electron shells of these ions (the $3d^8$ shell in Ni^{2+} and the $3d^7$ shell in Co^{2+}).

The thermo-emf was measured on the same specimens as the electric conductivity. The measurements showed that the thermo-emf coefficient of barium titanate changes sign at 184°C (temperature of the hot junction). Below this temperature barium titanate has n-type conductivity; above this temperature p-type. The $\log \sigma = f(1/T)$ plot exhibits a break in the temperature region corresponding to the change in sign of the thermo-emf.

In $(Ba,Ni)(Ti,Zr)O_3$ and $(Ba,Co)(Ti,Zr)O_3$ solid solutions with increase of the $NiO \cdot ZrO_2$ and $CoO \cdot ZrO_2$ concentration to 15% the sign of the thermo-emf corresponds to n-type conductivity in the entire investigated temperature interval. In compositions containing 15% or more $NiO \cdot ZrO_2$ and $CoO \cdot ZrO_2$ the thermo-emf coefficients decrease and change sign. With increase of the "impurity" concentration the point at which the thermo-emf changes sign shifts to the side of lower temperatures. For 50% $BaTiO_3$ + 50% $CoZrO_2$ the sign of the thermo-emf in the entire investigated temperature range corresponds to hole type conductivity. This is apparently connected with the presence in this material of a large amount of undissolved $CoO \cdot ZrO_2$, inasmuch as the sign of its thermo-emf in a wide temperature range corresponds to hole type conductivity.

For barium titanate and $(Ba,Ni)(Ti,Zr)O_3$ and $(Ba,Co)(Ti,Zr)O_3$ solid solutions there obtains the relationship $\alpha = A - C \log \sigma$ (Fig.3), characteristic of impurity semiconductors[10] (α is the thermo-emf coefficient, σ is the conductivity, and A and C are constants). It is interesting to note that the value of the constant C, obtained in the present work for $(Ba,Co)(Ti,Zr)O_3$ specimens is close to the theoretical value ($2 \cdot 10^{-4}$). For barium titanate and $(Ba,Ni)(Ti,Zr)O_3$ solid solutions the experimental value of the constant C is 3-4 times greater than the theoretical value.

References

1. E.V.Sinyakov, Thesis, Dnepropetrovsk Univ., 1948.
2. Pigon Krzusztof, Roszn.chem., 28, 4 (1954).
3. N.S.Novosil'tsev & A.L.Khodakov, Zhur.tekh.fiz., 26, 310 (1956). (Trans. Soviet Physics - Technical Physics.)
4. M.A.Blokhin, Doklady AN SSSR, 95, 965 (1954).
5. E.V.Sinyakov & B.K.Chernyi, Fizika dielektrikov (Transactions of the All-Union Conference on the Physics of Dielectrics, Dnepropetrovsk, 1956.) M.1958.
6. J.H.Van Santen & F.Boer, Nature, 163, 957 (1949).
7. M.A.Blokhin, Doklady AN SSSR, 95, 1165 (1954).
8. E.V.Sinyakov & B.K.Chernyi, Fizika tverdogo tela, 1, 352 (1959). (Trans. Soviet Physics - Solid State.)
9. B.K.Chernyi, Fizika dielektrikov (Transactions of the Second All-Union Conf. on the Physics of Dielectrics, Dnepropetrovsk, 1956.) M. 1960.
10. A.F.Ioffe, Fizika poluprovodnikov (Physics of semiconductors), M., 1957.

POSSIBILITY OF CONTROLLING THE CONDUCTIVITY OF LEAD METANIOBATE BY DOPING

- V.M.Gurevich & I.S.Rez

It is known that ferroelectrics with $PbNb_2O_6$ as the base material that are characterized by a high Curie temperature T_C have a tendency to lose their piezoelectric activity at temperatures that are sometimes substantially lower than T_C. The most probable reason for this loss in piezoelectric activity is increase of the conductivity at temperatures above 250-300°.

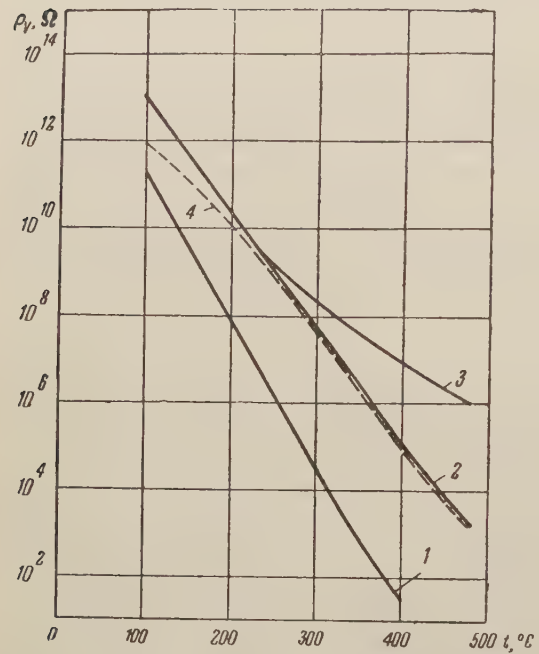

Fig.1. Temperature dependences of different $PbNb_2O_6$ specimens: 1 & 2) $PbNb_2O_6$ synthesized from different materials, 3 & 4) $PbNb_2O_6$ composition corresponding to curve 2 but doped with La^{3+} and Li^+, respectively.

One of the means for reducing the conductivity is introduction of small amounts of impurities. In our experiments we used high purity $PbNb_2O_6$ with $T_C \approx 560$-580°; this, as might have been expected, did not exhibit piezoelectricity. We investigated the effect of Li^+, K^+ and La^{3+} introduced in amounts from 0.01 to 0.4 atomic percent relative to the replaced ions. It may be assumed that the La^{3+} and K^+ replaced Pb^{2+} (the ionic radii are, respectively, 1.14, 1.33 and 1.2 Å), and that the Li^+ replaced Nb^{5+}? (ionic radii 0.68 and 0.69 Å, respectively). Inasmuch as the nature of the bonds in $PbNb_2O_6$ is not known, we provisionally, by analogy with covalent semiconductors, assume that La^{3+} is a donor and K^+ and Li^+ are acceptors. The influence of La^{3+} and Li^+ on the conductivity of $PbNb_2O_6$ is shown in the accompanying figure. The introduction of K^+ had no effect on the conductivity; this could be explained by the fact that owing to conditions of preparation one of the initial oxides, namely, Nb_2O_5, already contained some K^+ impurity.

It must be noted that lead metaniobate specimens synthesized from different initial materials differ appreciably as regards their conductivity, apparently due to minor differences in impurity content. This again substantiates the possibility of controlling the conductivity by doping. On the basis of the accepted classification for the utilized impurities it may be inferred that the conductivity in the investigated $PbNb_2O_6$ is of the p-type. Preliminary measurements of the sign of the thermo-emf in control $PbNb_2O_6$ specimens (i.e., without the addition of La^{3+}, K^+ or Li^+) substantiated this inference.

The recommendations made on the basis of the present study were utilized in the work of Smazhevskaya & Podol'ner[1] in preparing piezoelectrically active $PbNb_2O_6$ base specimens with a high Curie temperature, and, according to preliminary data, yielded positive results.

We are grateful to R.M.Lerman for determining the optimum sintering conditions.

Reference

1. E.G.Smazhevskaya & N.A.Podol'ner, Izv.AN SSSR, Ser.fiz., 24, No.11 (1960). (Trans.Bulletin, 24, No.11.)

SOME PHYSICAL PROPERTIES OF VACUUM ANNEALED POLYCRYSTALLINE BARIUM TITANATE

- A.V.Chebkasov

In the course of developing the technology* for high quality $BaTiO_3$ ferroelectric ceramics it was found that sintering in an oxygen-poor medium (closed capsule or well sealed furnace) leads to darkening of the specimens. At the same time the electric conductivity and dielectric loss of such specimens increase.

Similar effects were observed earlier[1,2] for rutile, which as a result of roasting in a reducing medium becomes an n-type semiconductor.

Determination of the nature of the processes evinced externally by blackening of $BaTiO_3$ ceramic is of undoubted interest and involves extensive investigation of the physical characteristics of the material. Yet so far there have been very few studies of the influence of heat treatment in a reducing medium on the properties of oxygen-containing ferroelectric ceramics. (See, for example, Refs. 3 & 4.)

On the other hand, comprehensive investigation of blackened $BaTiO_3$ and similar substances can help determine the range of application of such semiconductor ceramics with controllable properties.

In the present report we give the results of investigation of some of the physical properties of polycrystalline $BaTiO_3$ subjected to repeated heating under vacuum.

The specimens were prepared by the usual ceramic procedure of analytic reagent grade $BaCO_3$ and TiO_2. The synthesis temperature was 1200°. The ceramics were sintered in a Silit furnace with a holding time of 2 hours at a maximum temperature of 1380°.

For vacuum heating there was constructed a special small portable furnace with an enclosed molybdenum heater, which was installed under a vacuum bell. In this furnace it was feasible to roast pellets up to 2.5 x 2.5 x 0.5 cm at temperatures up to 1200°.

For roasting specimens at temperatures higher than 1200° and in using longer holding times we employed a TVV-2 vacuum furnace with the same vacuum (10^{-4} mm Hg). Different batches of specimens differed as regards the vacuum roasting temperature - from 800 to 1280° - and holding time at maximum temperature - from 0.5 to 24 hours.

The color of vacuum roasted specimens varies from bluish-grey to grey-black and depends primarily on the roasting temperature. The darkening is a volume effect; the color is uniform throughout the thickness of the specimen. Noticeable darkening begins at temperatures of the order of 760-780°.

Inasmuch as the result of sintering in a reducing medium, in particular under vacuum, polycrystalline $BaTiO_3$ changes its properties and acquires a characteristic dark color, hereinafter for the sake of brevity we will refer to it as "black barium titanate" by analogy with the use of the term "blue" for partially reduced titanium dioxide.

Investigation of the temperature dependence of the dielectric constant, the data of x-ray diffraction studies and the results of dilatometric measurements show that black $BaTiO_3$ is also basically a ferroelectric ceramic. In addition, however, it acquires a number of properties characteristic of semiconductors, in particular, a substantially higher electric conductivity than ordinary "yellow" $BaTiO_3$.

The electric properties of black $BaTiO_3$ were investigated in dc fields from 1 to 400 v/cm. Our measurements showed that with increase of the temperature and

---

*The research program was carried out under N.S.Novosil'tsev and A.L.Khodakov in the laboratory of Rostov University.

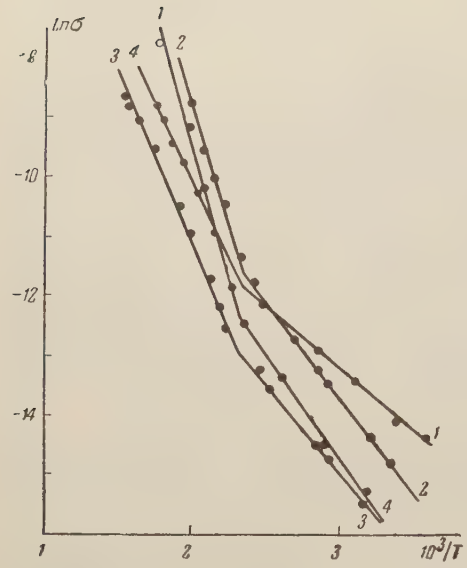

Fig.1. Temperature dependence of the conductivity σ of $BaTiO_3$ specimens subjected to different vacuum heat treatments: 1 - sample No.9 (T = 1100°, t = 2 hr), 2 - sample No.3 (T = 1150°, t = = 2 hr), 3 - sample No.13 (T = 1180°, t = 5 hr), 4 - sample No.14 (T = 1180°, t = = 24 hr).

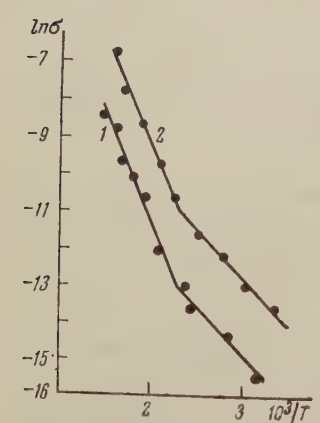

Fig.2. Temperature dependence of the conductivity σ of sample No.13 before (1) and after (2) repeat vacuum heating.

duration of vacuum annealing the conductivity σ increases. Thus at room temperatures specimens blackened at T = 1100-1200° have a conductivity of 10^{-5}-10^{-6} mho/cm, which is some 10^5-10^6 times higher than the conductivity of ordinary (not vacuum roasted) $BaTiO_3$. The conductivity of samples vacuum roasted at T = 800° is only 10^{-9} mho/cm.

The holding time in vacuum at a given temperature also affects the conductivity but to a much lower degree. For example, the conductivity of a sample roasted at T = 1200° for 5 hours was $0.3 \cdot 10^{-5}$ mho/cm, whereas that of a sample roasted at the same temperature for 24 hours was $2.5 \cdot 10^{-5}$ mho/cm, i.e., one order of magnitude higher.

With increase of the temperature the conductivity of black $BaTiO_3$ increases exponentially. For all specimens a break is observed in the ln $\sigma = f(1/T)$ plot at about 160°, indicating a change in the nature of the conduction mechanism (Fig.1). Above the break the slope of the ln $\sigma = f(1/T)$ line for all the specimens is nearly the same. The activation energy calculated from the slope of the plots above the break points is 0.9-1 ev, and increases only slightly with increasing vacuum roasting temperature. A somewhat greater scatter in the values of the activation energy calculated from the slopes of the lower part of the ln $\sigma = f(1/T)$ plots (0.3-0.6) is presumably connected with contamination of the specimens by chance impurities in the process of roasting.

The above results pertain to specimens blackened by vacuum roasting two years ago. Repeat roasting of these specimens resulted in increase of their conductivity by about one order of magnitude with no noticeable change in the activation energy. Thus apparently with the passage of time the resistance of black $BaTiO_3$ increases, i.e., the specimens age (Fig.2).

In order to determine the nature of the current carriers in black $BaTiO_3$ we determined the sign and magnitude of the thermo-emf of the ceramic specimens taken in pairs with applied metallic electrodes. The results indicate that in the temperature range from 20 to 400° black $BaTiO_3$ is electronegative and is, consequently, an n-type semiconductor.

The thermal conductivity of specimens with different degrees of blackening was determined at room temperature by the procedure developed by A.F. and A.V.Ioffe[5]. It was established that with increase of the roasting temperature the heat conduction coefficient $\varkappa$ decreases (Fig.3). Whereas for an ordinary unblackened specimen, $\varkappa = 1.1 \cdot 10^{-2}$ cal/cm·sec·degree, as the result of successive roastings at increasing temperatures the value of $\varkappa$ falls off to $0.6 \cdot 10^{-2}$ cal/cm·sec·degree.

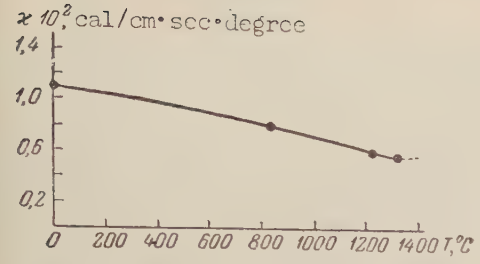

Fig.3. Variation of the heat conduction coefficient with the vacuum roasting temperature.

Roasting of a specimen in air (oxidizing medium) for a period of 6 hours at 1150° led to increase of its thermal conductivity to a value close to that obtained for the same specimen prior to blackening. At the same time, heating in air re-established all the other properties of the specimens, including its color: it became virtually undistinguishable from ordinary $BaTiO_3$ ceramic.

Conclusions

The experimental data indicate that the semiconductor properties of $BaTiO_3$ subjected to vacuum roasting, like the properties of "blue" titanium dioxide, are due to partial reduction leading to the formation of oxygen vacancies localized at the lattice sites. These vacancies play the role of a donor impurity so that the material exhibits n-type impurity conductivity.

The degree of reduction is so small (in any case less than 0.1%) that the specimen exhibits no detectable loss in weight as a result of roasting. For reliable interpretation of the decrease in thermal conductivity in the process of reduction it is necessary to carry out additional research and in particular to investigate the temperature dependence of the thermal conductivity.

References

1. B.I.Boltaks, F.I.Vasenina & A.E.Salunina, Zhur.tekh.fiz., 21, 532 (1951).
2. F.A.Grant, Revs.Mod.Phys., 31, 646 (1959).
3. E.K.Weise & I.A.Lesk, J.Chem.Phys., 21, 5 (1953).
4. G.Goshida, S.Nomura & S.Sawada, J.Phys.Soc.Japan, 13, 1550 (1958).
5. A.V.Ioffe & A.F.Ioffe, Zhur.tekh.fiz., 22, 2005 (1952).

INFLUENCE OF COMPRESSION ON POLARIZATION PROCESSES IN FERROCERAMICS

- V.Z.Borodin

There have been a number of studies[1-3] of unilateral pressure - compression - on the dielectric properties of ferroelectric ceramics. It was found that in the case of compression in the direction of the applied electric field the change in the properties of the ceramic in strong fields amounts essentially to decrease of the spontaneous polarization.[1] Experimental investigation of the deformation under compression shows that the fraction of domains switched 90° is small and is of the same order of magnitude as the fraction of domains switched by a strong electric field (approximately 13% under a compressive stress σ of 309 kg/cm^2).[2] Izhak[3] observed decrease of the dielectric constant ϵ with increase of the compressive strength in the direction of the field (longitudinal compression) and increase of ϵ with increasing stress in the perpendicular direction (transverse compression); in the former case the maximum of ϵ in the ϵ vs E curve is shifted to the side of stronger fields, while in the latter case the shift is to the side of weaker fields. In the last case in strong fields there is observed some weakening of the σ dependence of ϵ.

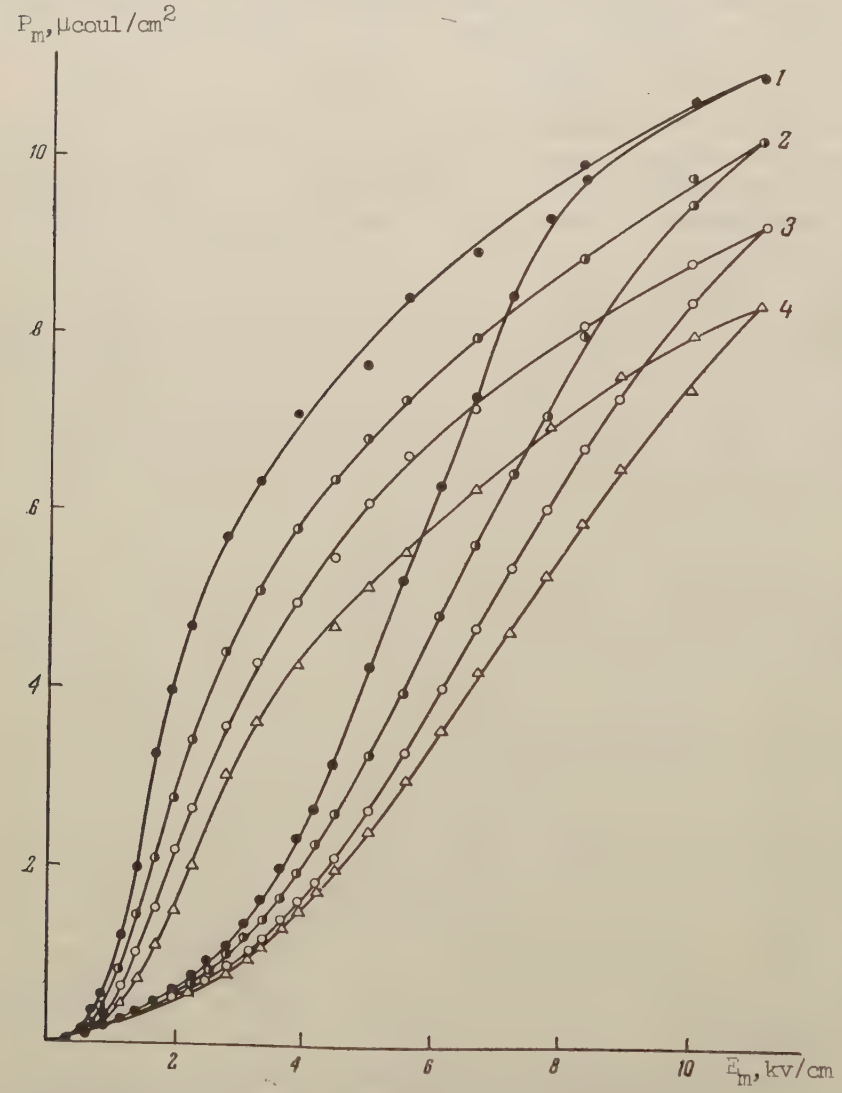

Fig.1. Polarization curves with longitudinal compression: 1 - σ = 0, 2 - σ = 120 kg/cm^2, 3 - σ = 250 kg/cm^2, 4 - σ = 370 kg/cm^2.

In the present work the influence of compression on polarization processes was investigated by the oscillographic technique. We plotted the polarization curves ($P_m = f(E_m)$) for different values of σ on the basis of the peaks of the hysteresis loops. The curves were recorded both for increasing amplitude of the field E_m (forward variation) and for decreasing field amplitude (reverse variation). In switching the electric field was increased by the same value at equal time intervals (10 min), which enabled us to judge of the time variation of the polarization under the influence of an applied field for two consecutive measurements of P_m. We also recorded the $P_m = f(\sigma)$ curves for different values of E_m. We investigated the behavior

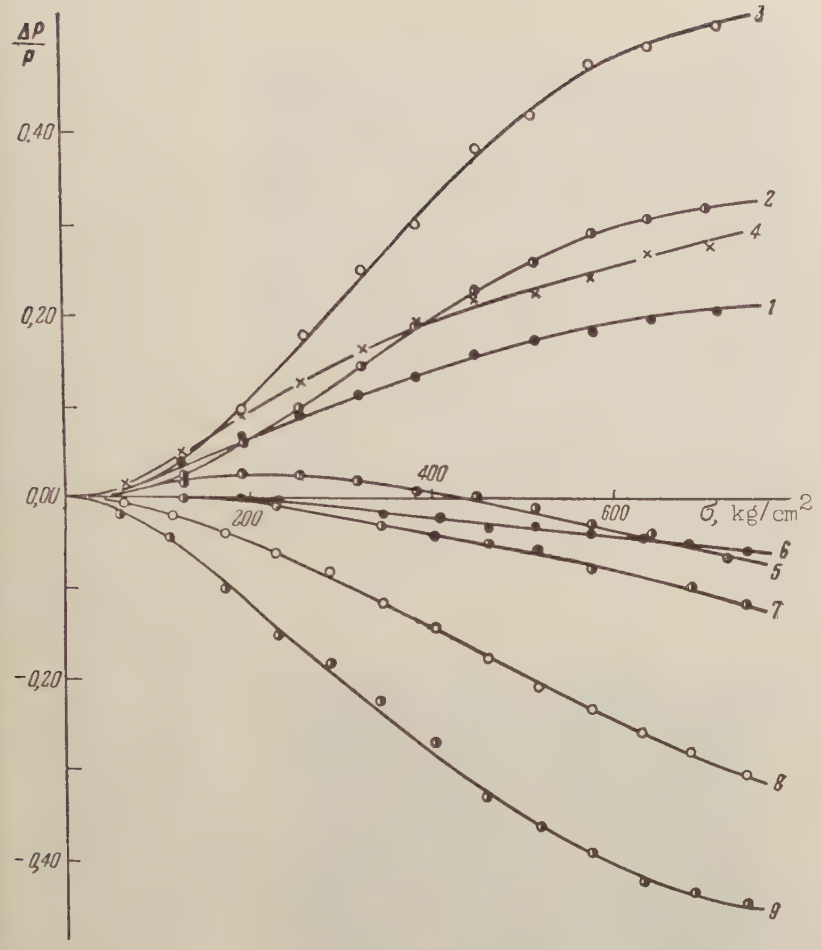

Fig.2. Variation of total polarization with compressive stress: 1) E_m = 0.3 kv/cm, 2,5,7 & 9) E_m = 1.4 kv/cm, 3) E_m = 2.2 kv/cm, 4 & 8) E_m = 3.0 kv/cm, 6) E_m = 0.7 kv/cm. 1-5 - transverse compression, 6-9 - longitudinal compression. Curves 5 & 9 were recorded after the specimen had been subjected to a 10 kv/cm field for a prolonged period.

of the differential dielectric constant ϵ_d as a function of the applied field and the degree of compression by observing the so-called "current loops" which characterize the variation of the instantaneous current flowing through the capacitor with the instantaneous strength of the applied field.[4]

We investigated ceramic specimens of $BaTiO_3$, $BaTiO_3$-$BaSnO_3$ solid solutions and Varikond, a new ceramic material with enhanced nonlinear characteristics. Below we give the data obtained for $BaTiO_3$; similar regularities were observed for the other materials.

The polarization curves in the case of longitudinal compression are shown in Fig.1. As will be evident from the figure, with increase of σ the total polarization decreases, the $P_m = f(E_m)$ curves become less steep, and the point of inflection corresponding to the maximum of ϵ_d is shifted into the region of higher fields. With increase of σ saturation is attained at higher field values. As for the time variation in the process of attainment of polarization, investigation of this effect showed that there is a maximum of the relative change in polarization with time in a certain field region corresponding to transition from the Rayleigh field dependence of P to the usual hysteresis loops. With increase of σ this maximum is smeared out somewhat and shifted to the side of higher field values. The σ dependence of P_m with increase of the field at first becomes stronger and then gradually weakens. Ceramic specimens poled beforehand in a strong electric field yield a stronger σ dependence of P_m (Fig.2). Thus whereas prior to treatment with a strong field the relative change in polarization $\frac{1}{\sigma} \cdot \frac{\Delta P_m}{P_m}$ averages $1.4 \cdot 10^{-4}$ cm^2/kg, after treatment with a 10 kv/cm field, the relative change increases to $6.4 \cdot 10^{-4}$ cm^2/kg, and the σ dependence of P_m becomes nonlinear. Compression results in decrease of ϵ_d and the ϵ_d maximum is smoothed out; the greatest variation in ϵ_d is observed close to the ϵ_d maximum. In relatively weak fields ($E < 3$ kv/cm) for non-poled specimens there is observed some change in the character of the E dependence of ϵ_d (Fig.3).

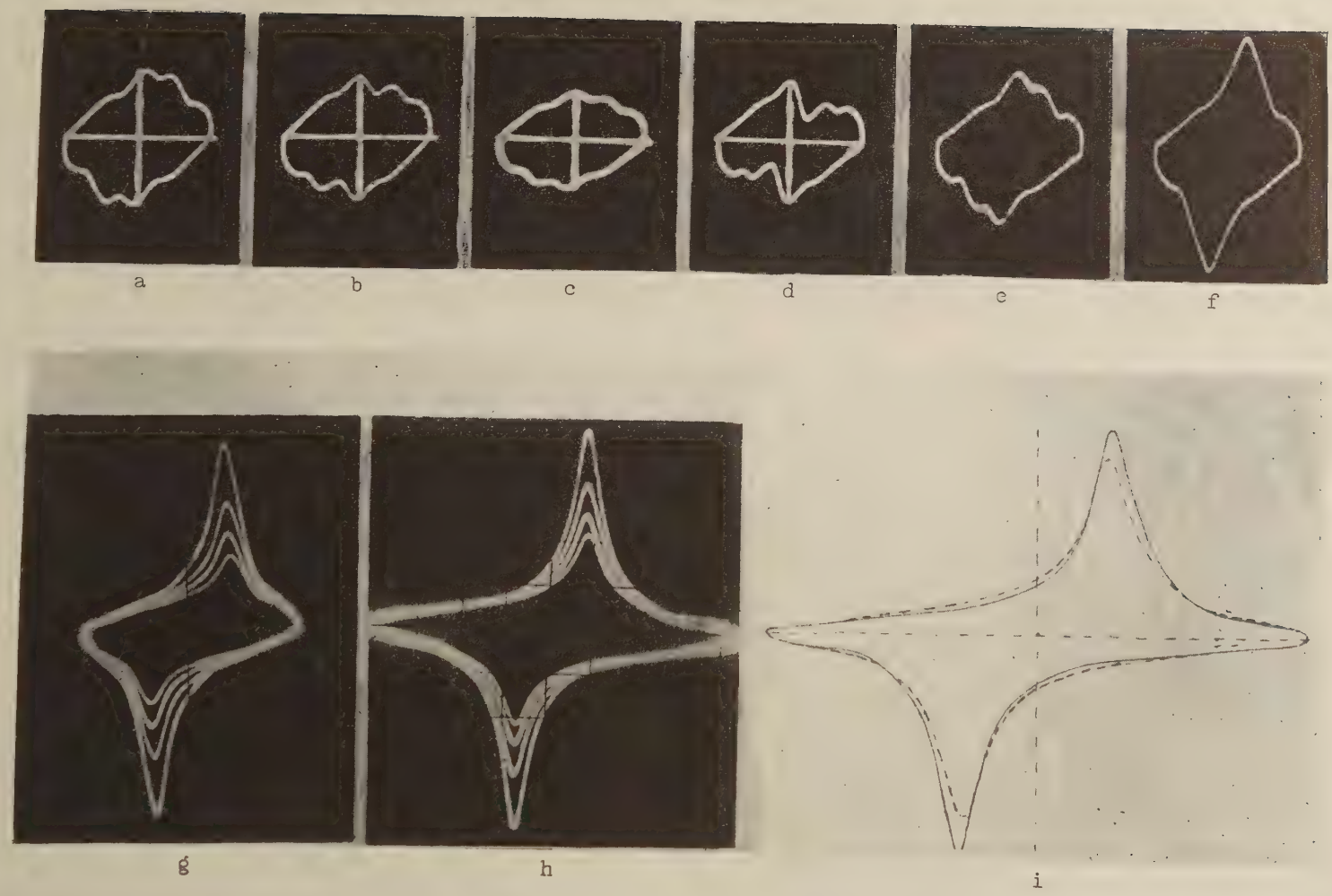

Fig.3. Current loops. Longitudinal compression: a - $\sigma = 0$, b - $\sigma = 70$ kg/cm^2, c - $\sigma = 460$ kg/cm^2, $E_m = 4$ kv/cm; family of loops obtained at different values of σ(0 to 690 kg/cm^2): g - $E_m = 4$ kv/cm (after poling of the specimen in a 10 kv/cm field), h - $E_m = 10$ kv/cm. Transverse compression: d - $\sigma = 0$, e - $\sigma = 70$ kg/cm^2, f - $\sigma = 180$ kg/cm^2, $E_m = 3$ kv/cm; i - after specimen was subjected to a 10 kv/cm field (solid curve for $\sigma = 0$; dashed curve for $\sigma =$ = 180 kg/cm^2).

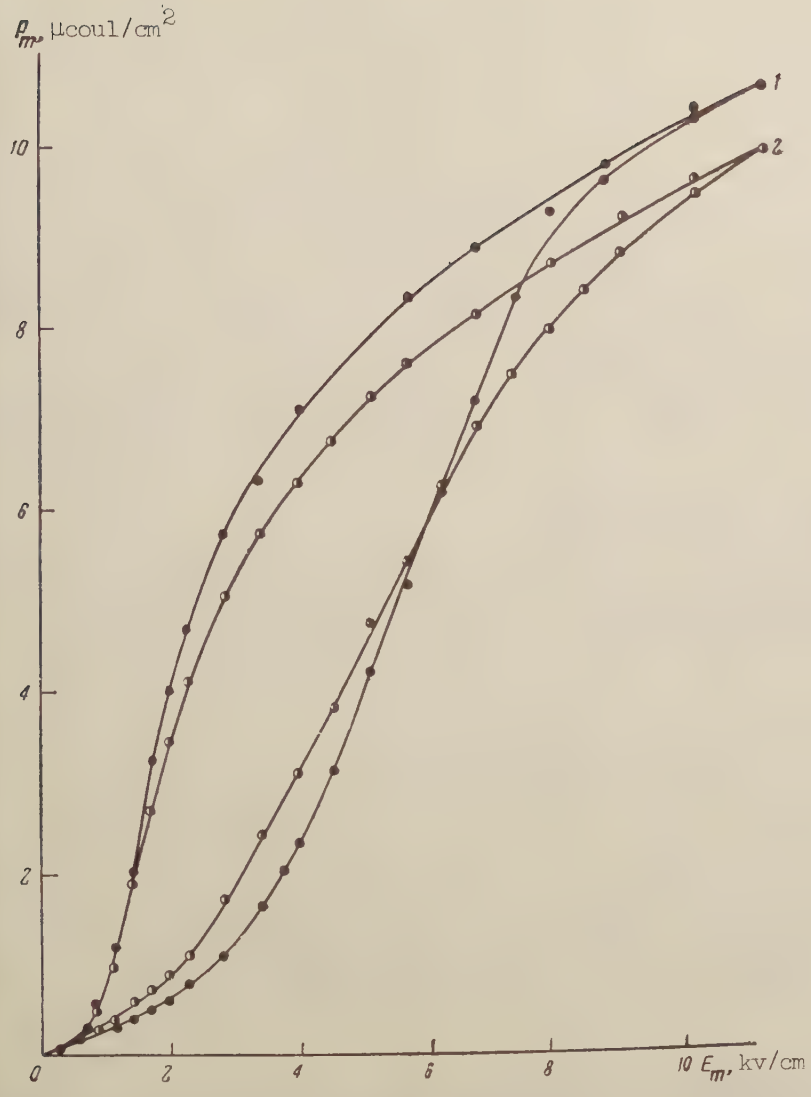

Fig.4. Polarization curves with transverse compression: 1 - $\sigma = 0$, 2 - $\sigma = 420$ kg/cm^2.

Fig.4 gives two curves for polarization in the direction perpendicular to the compression axis (for $\sigma = 0$ and 420 kg/cm^2). It will be seen that for the specimen under compression the P_m vs E_m curve in weak fields lies above the $\sigma = 0$ curve, but then with increase of the field approaches the $\sigma = 0$ curve, intersects it and at high fields, lies below it. On the other hand, the curve recorded in a decreasing field consistently lies below the initial, $\sigma = 0$ curve.

In the transverse compression case, the σ dependence of P_m depends on the order of application of the field and stress. If at first one applies a strong field and then compresses the specimen, the polarization curves coincide with the initial, $\sigma = 0$ curve, up to $\sigma = 400$ kg/cm^2, and then with further increase of σ the polarization gradually begins to fall off. In the case of transverse compression the maximum of the relative change in polarization with time is shifted to the side of weaker fields. The curves characterizing the variation in polarization as a function of the pressure at different values of E_m are consistent with the polarization curves (Fig.2). In ceramics not subjected to the action of a strong field beforehand, the polarization increases with increase of σ; the σ dependence of P_m becomes stronger with increase of E_m in the range of fields weaker than the field corresponding to the maximum relative change with time. In stronger fields, the σ dependence of P_m weakens with increase of E_m and changes in character: there appears a smeared out maximum in the P_m vs σ curve, and with further increase of σ the initial increase of P_m is replaced by consistent decrease of the polarization. In ceramic specimens treated beforehand in a strong field, the polarization, as a rule, slowly decreases with increase of σ in all fields except very weak fields ($E < 0.2$ kv/cm), where the relative change in polarization is almost independent of preliminary poling. Transverse compression facilitates compliance of the ceramic specimen under the influence of an electric field and therefore greatly alters the character of the field dependence of ϵ_d; as a result of transverse compression the magnitude of ϵ_d increases appreciably (Fig.3). In ceramics subjected to treatment with a strong field beforehand there is observed

with increase of pressure smoothing out of the maximum of ϵ_d and shift of this maximum to the side of weaker fields. Measurements carried out on aged (2 weeks) specimens showed a stronger dependence of P_m on σ than exhibited by specimens heated beforehand (relative change $\frac{1}{\sigma} \cdot \frac{\Delta P_m}{P_m} = 11 \cdot 10^{-4}$ cm^2/kg).

It follows from thermodynamic theory that if a crystal is compressed in the direction of the spontaneous polarization vector P_0 at a certain critical value of the stress σ_{cr}, the state of the crystal becomes unstable, and it abruptly goes over into a new state with the direction of P_0 differing from the initial one by 90°. On the other hand, it has been shown in a number of investigations[2,5-7] that the process of polarization in ceramic barium titanate is almost wholly realized by 180° domain rotation. The value of the external electric field at which 180° switching of the polarization vector in each individual domain occurs is determined by the condition $E \cos \vartheta_i = E_{cr}$, where the critical field E_{cr} depends on the temperature, the dimensions of the domain, the presence of internal stresses and electric fields, etc., and ϑ_i is the angle between the direction of the applied field and the spontaneous polarization vector.

Using the relations between the parameters of a ceramic and a corresponding single crystal given by Bogdanov et al[7] and Kholodenko & Shirobokov[8], introducing the function $f(E_{cr})$ characterizing the distribution of domains in values of the critical field and neglecting 90° rotation[9], we obtain the following field dependence of P (polarization curves) for domains characterized by the same value of σ_{cr}:

for $\sigma = 0$

$$P = 0.5 P_0 \int_0^E \left[1 - \left(\frac{E_{cr}}{E}\right)^2\right] f(E_{cr})\, dE_{cr}; \tag{1}$$

for $\sigma \neq 0$ (polarization along the compression axis)

$$P_1 = 0.5 P_0 \left(\frac{\sigma_{cr}}{\sigma}\right)^2 \int_0^e \left[1 - \left(\frac{E_{cr}}{e}\right)^2\right] f(E_{cr})\, dE_{cr};\ e = \left(\frac{\sigma_{cr}}{\sigma}\right) E; \tag{2}$$

for $\sigma \neq 0$ (polarization perpendicular to the compression axis)

$$P_2 = 2P - P_1. \tag{3}$$

As will readily be evident from Eqs.(1) and (2) the general form of the E dependence of P in the case of longitudinal compression persists but with a change in scale: the $P = f(E)$ curve is "stretched out" in the horizontal direction (along the E axis) and "compressed" in the vertical direction. Physically this means decrease of the polarization and ϵ_d with increase of the compressive strength and shift of the ϵ_d maximum to the side of stronger fields, i.e., in this case there obtains qualitative agreement with the experimental data. In the case of transverse compression the polarization should increase with increase of σ for any E and the greatest relative changes in polarization should occur in the weakest fields. At saturation the polarization curves for different σ should be parallel.

As was shown above, however, the experimental data in a number of cases yield qualitatively different results. These divergences as well as the effects not described by the theoretically deduced regularities can be satisfactorily described if we assume that in a ceramic specimen, owing to the presence of internal electric fields and mechanical stresses, there is a group of domains that are nearly unstable and are incapable of going over into a new state under the influence of external factors (field, compression). After treatment of the specimen with a strong field part of these domains will be in a metastable state and will leave this state under the influence of longitudinal compression: the σ dependence of P in this case will be stronger than for a nonpoled ceramic. In the case of transverse compres-

sion in a ceramic not treated with a strong field there are rotated 90° the easily oriented domains that switch under the influence of a strong field; hence in this case the σ dependence of P is weakened after treatment with a strong field. Moreover, strong inhomogeneous stresses appearing incident to compression apparently lead to decrease of the polarization and ϵ_d, enhancing the σ dependence of P in longitudinal compression and weakening this dependence (or changing its character) in transverse compression. Fragmentation of the domains leads to opposite effects[10], enhancing the σ dependence of P in weak fields in the case of transverse compression and weakening this dependence in the case of longitudinal compression; this presumably explains the stronger σ dependence of P as a result of transverse compression in the case of aged specimens.

I desire to express my deep gratitude to A.L.Khodakov for guidance in the work and for valuable discussion of the results and to V.D.Komarov for preparing the specimens.

References

1. E.V.Sinyakov & I.A.Izhak, Doklady AN SSSR, 100, 243 (1955).
2. E.C.Subbarao, M.C.McQuarrie & W.S.Buessem, J.Appl.Phys., 28, 1194 (1957).
3. I.A.Izhak, Thesis, Kharkov State University, 1956.
4. A.L.Khodakov, Zhur.tekh.fiz., 24, 51 (1956). (Trans.Soviet Physics - Technical Physics.)
5. J.Boer, Chem.Weekbl., 59, 137 (1958).
6. D.Berlincourt & H.Jaffe, Phys.Rev., 111, 143 (1958).
7. S.V.Bogdanov, B.M.Vul & A.M.Timonin, Izv.AN SSSR, Ser.fiz., 21, 374 (1957). (Trans.Bulletin, 21, 377.)
8. L.P.Kholodenko & M.Ya.Shirobokov, Zhur.tekh.fiz., 27, 929 (1957). (Trans. Soviet Physics - Tech.Physics.)
9. V.Z.Borodin, Izv.vyssh.uch.zav., Elektromekhanika (Bulletin of Higher Schools, Electromechanics), 2, 140 (1960).
10. W.Koch, Z.Naturwissenschaften, 13, 303 (1955).

SOME PHYSICAL PROPERTIES OF FERROELECTRIC LEAD FERRONIOBATE AND FERROTANTALATE

- V.A.Isupov, A.I.Agranovskaya & N.P.Khuchua

There are now known to exist numerous ferroelectric compounds with the perovskite structure, forming in multiple component oxide systems[1-4], for example, $Pb_3[MgNb_2]O_9$, $Pb_2[ScNb]O_6$, $Pb_2[MgW]O_6$ and $Pb_3[Fe_2W]O_9$. A characteristic of such ferroelectrics is simultaneous presence in the oxygen octahedra of di- and penta-, tri- and penta-, di- and hexa-, and tri- and hexavalent ions. The diversity of di- and trivalent ions that may be situated in the oxygen octahedra offers extensive possibilities for investigation of the influence of different ionic characteristics (ionic size, electronic polarizability, structure of electron shells, etc.) on the ferroelectric state. In connection with this, study of the physical properties of the new ferroelectrics is of considerable interest. Actually, however, they have scarcely been studied. In particular, little is known regarding the properties of Pb_2FeNbO_6 (Ref.3) and Pb_2FeTaO_6 (Ref.4). Lead ferroniobate has a Curie temperature close to that of barium titanate and hence it is of particular interest to compare its properties with those of $BaTiO_3$. Lead ferroniobate and ferrotantalate, owing to the presence of iron in the octahedral positions, must have a more or less appreciable magnetic susceptibility in conjunction with a high dielectric constant.

The present investigation was concerned with the physical properties of these two compounds.

For synthesizing the specimens we used analytic reagent grade Fe_2O_3 and PbO, and niobium and tantalum pentoxides prepared by oxidation of metallic Nb (99.4%) and Ta (99%). The specimens were prepared by the conventional ceramic technique. For synthesis the mixtures were fired for 3 hours at 750-800°. The final ceramic sintering was carried out either in air or in an atmosphere of PbO vapor at 1050-1100° with a holding time of 20 to 60 min. Only specimens for which the loss in weight owing to volatilization of PbO did not exceed 1% were chosen for subsequent study. The surface porosity of the sintered ferroniobate and ferrotantalate specimens did not exceed 8-10%.

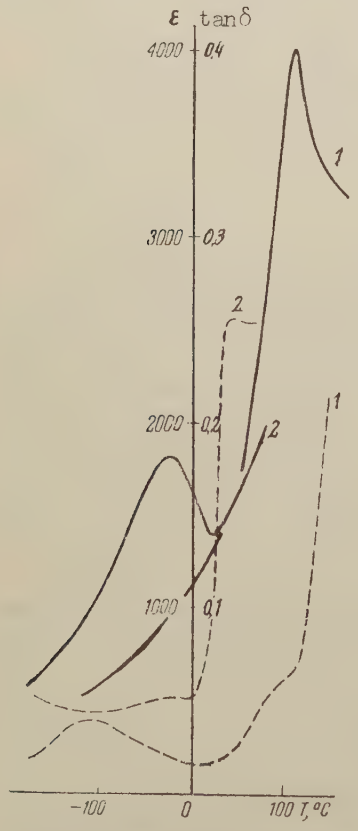

Fig.1. Temperature dependences of the dielectric constant (solid curves) and loss tangent (dashed curves) of lead ferroniobate (1) and lead ferrotantalate (2) at a frequency of 1 kc.

X-ray diffraction studies of powdered specimens in a 57.3 mm diameter camera showed that both the investigated compounds have the perovskite structure with lattice parameters equal to 4.00 Å (the calculations were carried out on the assumption that the lattice was cubic).

The temperature dependences of ϵ and tan δ at a frequency of 1 kc in weak fields are shown in Fig.1. It will be evident that in the case of lead ferroniobate ϵ has a maximum at 110°, while for lead ferrotantalate the maximum of ϵ occurs at -25°. These maxima correspond to ferroelectric phase transitions in the respective compounds.

Measurements of the dielectric constant of lead ferroniobate at frequencies of 450 and 4500 kc showed that the temperature at which the maximum of ϵ occurs does not depend on the measurement frequency. In this respect Pb_2FeNbO_6 differs from such ferroelectric compounds as $Pb_3NiNb_2O_9$ and $Pb_3MgNb_2O_9$, in which the loca-

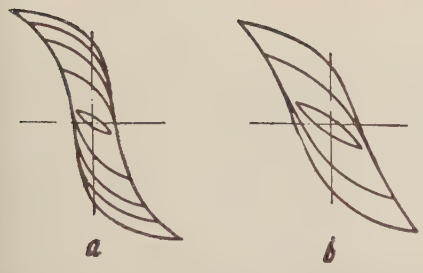

Fig.2. Dielectric hysteresis loops recorded at -163° for lead ferroniobate in fields of 8.5, 17, 25.5, 29.7 and 34 kv/cm (a) and lead ferrotantalate in fields of 10, 20 and 30 kv/cm (b).

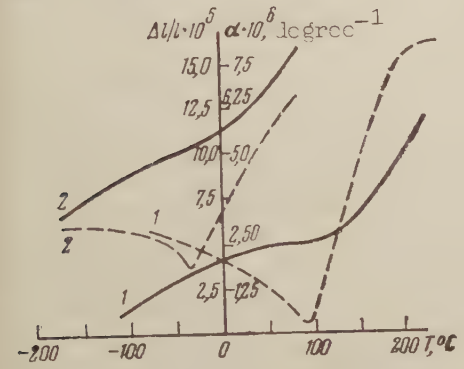

Fig.3. Temperature dependences of the elongation per unit length $\Delta l/l$ (solid curves) and linear expansion coefficient α (dashed curves) of polycrystalline lead ferroniobate (1) and lead ferrotantalate (2).

tion of the ϵ peak is frequency dependent.[1,5]

The dielectric polarization of lead ferroniobate and ferrotantalate below the Curie point is a nonlinear function of the electric field (Fig.2). At -136° the values of the spontaneous polarization of lead ferroniobate and ferrotantalate are 5.3 and 2.4 μcoul/cm^2, the total polarization 6.2 and 2.9 μcoul/cm^2, and the coercive force 10 and 17 kv/cm, respectively.

There are inflections in the $\Delta l/l = f(T)$ curves at temperatures close to those of the ϵ maxima; consequently these are obviously associated with the ferroelectric phase transitions (Fig.3). These temperatures also correspond to minima in the linear expansion coefficient curves. The character of the temperature dependence of the elongation per unit length indicates that the sign of the spontaneous volume deformation and, accordingly, the volume electrostriction of both the investigated ferroelectrics is positive.

For investigating the piezoelectric properties of lead ferroniobate the specimens were first polarized by holding in a 27 kv/cm field for 2.5 hours. The resonance and antiresonance frequencies of the radial oscillations monotonically decrease with heating and approach to the Curie point, and at the Curie point go through a sharp minimum. The piezoelectric coefficient d_{31} at room temperature equals $-1.7 \cdot 10^6$ cgse units, which nearly agrees with the value of d_{31} for polycrystalline barium titanate. Near the Curie point the piezoelectric coefficient passes through a maximum. The values of the piezoelectric characteristics d_{31}/ϵ and $(d_{31} \cdot E)^2$ of lead ferroniobate are close to the corresponding values for barium titanate.

At room temperature the conductivity of lead ferroniobate is of the order of 10^{-8} mho/cm and hence appreciably higher (4-5 orders of magnitude) than the conductivity of barium titanate. The characteristic break in the linear $\log \rho = f(1/T)$ plots occurs at 212°. The activation energy calculated for the 20 to 212° interval from the slope of the $\log \rho = f(1/T)$ line is 0.76 ev; the activation energy for the 212 to 350° interval is 2.3 ev. The sign of the thermo-emf for lead ferroniobate specimens proved to be positive in the entire temperature range from 20 to 350°

In view of the values of the activation energy it may be assumed that at temperatures below 212° the conductivity is primarily of the impurity type, while at higher temperatures, intrinsic conductivity predominates.

Apparently in the region of intrinsic conductivity the hole mobility is greater than the electron mobility. Possibly the intrinsic conductivity is realized owing to partial transition of trivalent iron ions to the divalent state, leading to motion of the electrons over the iron ions (conduction band) and holes over the oxygen ions (valence band). In view of the fact that the oxygen ions are characterized by close packing, the holes should readily migrate from one oxygen ion to another. The migration of electrons over the iron ions located in the oxygen

octahedra is hampered by the niobium ions, which are also located in the octahedral positions. Hence the mobility of the holes is greater than the mobility of the electrons.

The magnetic susceptibility of a polycrystalline specimen of lead ferroniobate at room temperature was found to be $120 \cdot 10^{-6}$. With increase of temperature the magnetic susceptibility decreases. The temperature dependence of $1/\chi$ is linear in a wide temperature range. In the case of a paramagnet $1/\chi$ should be zero at $0^{\circ}K$. Extrapolation of the $1/\chi = f(T)$ plot for a lead ferroniobate specimen showed that $1/\chi$ is not zero at $0^{\circ}K$, but is positive, which is characteristic of antiferromagnets. We could not, however, exclude the possibility of there being present in the specimen some ferromagnetic or antiferromagnetic impurity. In view of this, the nature of the high magnetic susceptibility of polycrystalline lead ferroniobate remains unclear.

If lead ferroniobate at room temperature were ferro- or antiferromagnetic, one could expect the application of a strong magnetic field to produce a significant change in the dielectric constant of the specimen. Investigation of the dielectric constant as a function of the applied magnetic field (the magnetic field in one case was applied parallel to the electric field and in another case perpendicular to the electric field) showed, however, that within the limits of the experimental error ϵ does not depend on the strength of the applied magnetic field up to 30 000 oersted.

Thus our experiments have substantiated the existence of the compounds Pb_2FeNbO_6 and Pb_2FeTaO_6 with the perovskite structure and ferroelectric properties. The spontaneous polarization of polycrystalline specimens of these compounds is apparently lower than that of barium titanate. Like barium titanate, lead ferroniobate and lead ferrotantalate have positive volume electrostriction. In contrast to $BaTiO_3$, these compounds do not have low temperature phase transitions (at least down to -190°). The piezoelectric coefficient d_{31} of polycrystalline specimens of lead ferroniobate has approximately the same value as the coefficient of barium titanate; the electric conductivity of lead ferroniobate is substantially higher than that of $BaTiO_3$. Lead ferroniobate specimens exhibit a high magnetic susceptibility.

We take this opportunity to thank G.A.Smolenskii for his interest in the work and discussion of the results.

References

1. G.A.Smolenskii & A.I.Agranovskaya, Zhur.tekh.fiz., 28, No.7 (1958). (Trans.Soviet Physics - Technical Physics.)

2. G.A.Smolenskii, V.A.Isupov & A.I.Agranovskaya, Fizika tverdogo tela, 1, 170 (1959). (Trans.Soviet Physics - Solid State.)

3. G.A.Smolenskii, A.I.Agranovskaya, S.N.Popov & V.A.Isupov, Zhur.tekh.fiz., 28, No.10 (1958). (Trans.Soviet Physics - Technical Physics.)

4. G.A.Smolenskii, A.I.Agranovskaya & V.A.Isupov, Fizika tverdogo tela, 1, 990 (1959). (Trans.Soviet Physics - Solid State.)

5. I.E.Myl'nikova & V.A.Bokov, Kristallografiya, 4, No.3, 433 (1959). (Trans.Crystallography.)

PHYSICAL-CHEMICAL INVESTIGATION OF THE FORMATION OF COMPLEX FERROELECTRICS WITH THE PEROVSKITE STRUCTURE

- A.I.Agranovskaya

In Refs.1-3 Smolenskii and the writer considered in general terms the possibility of obtaining compounds of complex composition with the perovskite structure in which there are present in the same sublattices ions of different valence. We gave some variants of the general chemical formulas for which one can expect formation of compounds of complex composition and listed the ions that can occupy the A and B positions in ABO_3 compounds with the perovskite structure.

In the present report we give the results of synthesis of a number of compounds of complex composition and consider the mechanism of formation of such compounds in the specific cases of $PbNi_{1/3}Nb_{2/3}O_3$, $PbFe_{1/2}Nb_{1/2}O_3$, $PbFe_{2/3}W_{1/3}O_3$, and Pb_2MgWO_6. The first three compounds are ferroelectric (Refs.2-5); the fourth is antiferroelectric[5].

Experimental Data

Synthesis. By way of raw materials we used reagent grade pure barium, strontium, calcium and potassium carbonates and bismuth and lead oxides, and chemically pure sodium, magnesium and cobalts carbonates, titanium dioxide, lanthanum, nickel, and zinc oxides, and aluminum and tungsten hydroxides. Tantalum pentoxide was prepared by heating electronic grade tantalum containing 3% niobium; niobium pentoxide was prepared by heating metallic niobium containing 99% niobium and 0.5% tantalum. The grain size of the initial materials was 3-5 microns.

Synthesis of the specimens was realized by reaction in the solid phase. In Table 1 we list the general chemical formulas and synthesized compositions, the conditions of heat treatment, the dielectric characteristics of the sintered materials and the results of x-ray phase analyses.

The x-ray diffraction patterns were recorded by the powder technique in an RPK 57.3 mm diameter camera (asymmetric film loading) using Fe filtered Co $K\alpha$ x-radiation. As will be evident from Table 1 phases with the perovskite structure were obtained for all the investigated forms of the general chemical formulas. For some compositions in which there are simultaneously introduced into the octahedral position di- and pentavalent, as well as tri- and pentavalent ions, when $A = Pb^{2+}$, there is observed the appearance of a phase with the pyrochlore structure. In the process of synthesis these specimens lost an appreciable quantity of lead oxide owing to evaporation. It was impossible to reduce the loss of PbO even by roasting in an atmosphere of lead oxide vapor. The PbO content of the specimens was monitored by weighing before and after roasting.*

In the x-ray diffraction patterns for the compounds of complex composition with the perovskite structure, aside from the lines of Ba_2MgWO_6 and Pb_2MgWO_6, there were not observed any lines indicating ordered arrangement of the ions of different valence located in the oxygen octahedra. Galassa et al[7] in investigating complex Ba^{2+} and Sr^{2+} niobates and tantalates also did not observe ordering.

For a number of compounds we determined the specific gravity by means of a pycnometer both for polycrystalline specimens and for single crystals grown by Myl'nikova. The results are listed in Table 2. Comparison of the pycnometric density with that deduced from the x-ray patterns substantiates the proposed formulas

---

*In these cases a more successful procedure was growing single crystals from molten lead oxide; I.E.Myl'nikova[6] by this procedure succeeded in obtaining a number of compounds with the perovskite structure that it was impossible to obtain by reaction in the solid phase.

Table 1

Synthesis composition	Roasting temp. °C: Initial synth.	Roasting temp. °C: Final sint.	ε at 20°C	tan δ at 20°	a, KX	Structure of phase obtained
$[(A_1^{1+})_{1/2}(A_2^{3+})_{1/2}]B^{4+}O_3$						
$Na_{1/2}Bi_{1/2}TiO_3$	1000	1100			3,88	Perovskite
$K_{1/2}Bi_{1/2}TiO_3$	1000	1080			3,94	Perovskite
$Na_{1/2}La_{1/2}TiO_3$	1100	1230			3,86	Perovskite
$K_{1/2}La_{1/2}TiO_3$	1100	1220				Perovskite (poorly formed)
$A^{2+}[(B_1^{2+})_{1/3}(B_2^{5+})_{2/3}]O_3$						
$BaNi_{1/3}Nb_{2/3}O_3$	$1100_{(2)}$	$1250_{(0,5)}$	22	0,002	4,06	Perovskite
$SrNi_{1/3}Nb_{2/3}O_3$	$1100_{(2)}$	$1300_{(1)}$	21	<0,001	3,98	Perovskite
$CaNi_{1/3}Nb_{2/3}O_3$	$1100_{(2)}$	$1300_{(1)}$	21	<0,001	3,88	Perovskite?
$BaZn_{1/3}Nb_{2/3}O_3$	$800_{(1)}$	$950_{(1)}$	—	—	4,06	Perovskite
$PbNi_{1/3}Nb_{2/3}O_3$	$850_{(4)}$	$1150_{(0,5)}$	Ferroelectric $\theta = -120°$		4,02	Perovskite + + traces pyrochlore
$PbMg_{1/3}Nb_{2/3}O_3$	$850_{(4)}$	$1180_{(0,5)}$	Ferroelectric $\theta = -12°$		4,04	Perovskite
$PbNi_{1/3}Ta_{2/3}O_3$	$800_{(2)}$	$1080_{(1)}$	19	0,003		Pyrochlore + + NiO + + traces perovskite
$PbMg_{1/3}Ta_{2/3}O_3$	$800_{(2)}$	$1100_{(1)}$	40	0,005		Pyrochlore + + perovskite
$PbMn_{1/3}Nb_{2/3}O_3$	$800_{(1)}$	$1100_{(1)}$	500	>1		Pyrochlore + + perovskite
$PbCo_{1/3}Nb_{2/3}O_3$	$800_{(1)}$	$1100_{(1)}$	350	>1		Pyrochlore + + traces perovskite
$PbCu_{1/3}Nb_{2/3}O_3$	$700_{(1)}$	$900_{(1)}$				Pyrochlore
$A_1^{2+}[(B_1^{3+})_{1/2}(B_2^{5+})_{1/2}]O_3$						
$BaAl_{1/2}Nb_{1/2}O_3$	$1300_{(1)}$	$1450_{(1)}$	23	0,14		No reaction
$BaAl_{1/2}Ta_{1/2}O_3$	$1350_{(1)}$	$1480_{(1)}$	90	0,54		
$BaSc_{1/2}Nb_{1/2}O_3$	$1250_{(1)}$	$1350_{(1)}$	27	0,13	4,10	Perovskite
$BaSc_{1/2}Ta_{1/2}O_3$	$1250_{(1)}$	$1500_{(1)}$	8	—	4,11	"
$BaYb_{1/2}Nb_{1/2}O_3$	$1300_{(1)}$	$1500_{(1)}$	104	0,0012	4,17	"
$BaYb_{1/2}Ta_{1/2}O_3$	$1350_{(1)}$	$1500_{(1)}$	11	—	4,16	"
$BaFe_{1/2}Nb_{1/2}O_3$	$1000_{(2)}$	$1250_{(1)}$	—	>0,5	4,07	"
$BaFe_{1/2}Ta_{1/2}O_3$	$1000_{(2)}$	$1250_{(1)}$	—	>1	4,07	"
$PbAl_{1/2}Nb_{1/2}O_3$	$1000_{(1)}$	$1120_{(1)}$	48	0,02		Pyrochlore
$PbAl_{1/2}Ta_{1/2}O_3$	$1050_{(1)}$	$1150_{(1)}$	51	0,03		"
$PbSc_{1/2}Nb_{1/2}O_3$	$800_{(2)}$	$1270_{(1)}$	Ferroelectric $\theta = 90°$		4,07	Perovskite + + traces pyrochlore
$PbSc_{1/2}Ta_{1/2}O_3$	$800_{(2)}$	$1270_{(1)}$	Ferroelectric $\theta = 26°$		4,07	Perovskite + + traces pyrochlore
$PbYb_{1/2}Nb_{1/2}O_3$	$800_{(2)}$	$900_{(2)}$	Antiferroelectric, $\theta = 280°$		4,15	Perovskite + + traces pyrochlore
$PbYb_{1/2}Ta_{1/2}O_3$	$800_{(2)}$	$900_{(2)}$	13	0,012	4,13	Perovskite + + pyrochlore
$PbFe_{1/2}Nb_{1/2}O_3$	$800_{(2)}$	$1150_{(0,5)}$	Ferroelectric $\theta = 115°$		4,00	Perovskite

Table 1 continued

Synthesis composition	Roasting temp. °C: Initial synth.	Roasting temp. °C: Final sint.	ε at 20°C	tan δ at 20°	a, KX	Structure of phase obtained
$PbFe_{1/2}Ta_{1/2}O_3$	800(2)	1150(0,5)	Ferroelectric θ = −30°		4,00	Perovskite + + traces pyrochlore
$PbGa_{1/2}Nb_{1/2}O_3$	800(2)	950(1)	25	0,012		Pyrochlore
$A_1^{2+}[(B_1^{2+})_{1/2}(B_2^{6+})_{1/2}]O_3$ $BaMg_{1/2}W_{1/2}O_3$	1100(1)	1260(1)	—	—	4,045×2	Perovskite (super-structure)
$BaNi_{1/2}W_{1/2}O_3$	1100(1)	1320(1)	3	0,02	4,01	Perovskite
$PbCa_{1/2}W_{1/2}O_3$	700(4)					Perovskite (poorly formed)
$PbMg_{1/2}W_{1/2}O_3$	700(4)	1000(1)	Antiferroelectric, θ = 40°		4,0	Perovskite (distortions? super-structure?)
$A_1^{2+}[(B_1^{3+})_{2/3}(B_2^{6+})_{1/3}]O_3$ $PbFe_{2/3}W_{1/3}O_3$	700(4)	880(1)	Ferroelectric θ = −90°		3,97	Perovskite
$A_1^{3+}[(B_1^{2+})_{1/2}(B_2^{4+})_{1/2}]O_3$ $LaMg_{1/2}Ti_{1/2}O_3$	1350(1)	1500(1)	—	—	3,95	Perovskite

Table 2

Composition	Density: Pycnometric: Poly-cryst.	Density: Pycnometric: Single cryst.	Density: x-ray diffr.
$PbNi_{1/3}Nb_{2/3}O_3$	8,33	8,55	8,572
$PbMg_{1/3}Nb_{2/3}O_3$	7,82	8,12	8,18
$PbFe_{1/2}Nb_{1/2}O_3$	8,39	—	8,54
Pb_2MgWO_6	9,19	—	9,39
$PbFe_{2/3}W_{1/3}O_3$	9,17	—	9,38

for the compounds. Steward & Rooksby[8] determined the density of Ba_2CaWO_6 and also obtained satisfactory agreement with the theoretical value. They determined the atomic coordinates in this compound and showed that the Ca^{2+} and W^{6+} ions occupy the centers of the octahedra.

The results of chemical analysis of a polycrystalline specimen and a single crystal of $PbNi_{1/3}Nb_{2/3}O_3$ agree with the proposed formula (Table 3). The analysis of the single crystal was carried out by N.N.Parfenova.

Table 3

Composition	Percent by weight: PbO: Calc.	PbO: Analysis	Nb_2O_5: Calc.	Nb_2O_5: Analysis	NiO: Calc.	NiO: Analysis
$PbNi_{1/3}Nb_{2/3}O_3$, ceramic	66,29	66,25	26,32	26,46	7,39	7,22
$PbNi_{1/3}Nb_{2/3}O_3$, single crystal	66,29	64,1	26,32	26,6	7,39	8,2

Table 4

Composition	500°C	600°C	700°C	800°C	900°C	1000°C	1100°C	1150°C	1180°C	1200°C
$Pb_3NiNb_2O_9$	Mixture of oxides	Pyrochlore + PbO + NiO	Pyrochlore + NiO	Pyrochlore + NiO	Pyrochl. + perovskite	Perovskite + pyrochl.	Perovsk.+ trace pyrochlore	Perovskite + faint trace pyrochlore		--
$3PbO \cdot NiO$	--	--	Mixture PbO & NiO		--	--	--	--	--	--
$NiO \cdot Nb_2O_5$	--	--	--	--	--	--	--	--	--	Columbite
$3PbO \cdot Nb_2O_5$	--	Phase X	Rhombic pyrochl.	Pseudotetrahedral pyrochlore		--	--	--	--	--
$2PbO \cdot Nb_2O_5$	--	Phase X	Pyrochlore (rhombohedral), = 10.675 A, $\alpha = 88^\circ 44'$							
Pb_2FeNbO_6	Mixture of oxides	Pyrochlore + ?		Pyrochl. + perov.	Perovskite					Perovskite + ?
$2PbO \cdot Fe_2O_3$	--	Mixture of oxides	Perovskite	Perovskite	Fuses with decomposition at 920° (Ref.11)		--	--	--	--
$Fe_2O_3 \cdot Nb_2O_5$	--	--	--	--	Mixture of oxides	--	--	--	--	Columbite
Pb_2MgWO_6	Scheelite+?	Perovskite + traces scheelite		Perovsk. +?	Perovskite		--	--	--	--
$PbO \cdot WO_3$	--	--	Scheelite		Scheelite (Ref.12)		--	--	--	--
$Pb_3F_2WO_9$	Pyrochlore + ?	Pyrochl. + perovsk.		Perov. + traces pyro.	Perovskite	Fuses & decomposes	--	--	--	--

The polycrystalline specimens for determination of the specific gravity and for chemical analysis were prepared by firing three times with intermediate grinding. After the final sintering no traces of the second phase (pyrochlore) could be detected.

Mechanism of Formation of Compounds of Complex Composition with the Perovskite Structure

Hitherto there has been no published information regarding the mechanism of formation of compounds of complex composition with the perovskite structure in reactions in the solid phase. Hence we undertook to investigate this mechanism as exemplified by the formation of $PbNi_{1/3}Nb_{2/3}O_3$, $PbFe_{1/2}Nb_{1/2}O_3$, $PbFe_{2/3}W_{1/3}O_3$ and Pb_2MgWO_6, which represent the most interesting variants of complex introduction of ions. To this end we investigated the phase composition of the sinter products at different stages of synthesis. The roasting was carried out at different temperatures with a holding time of 2 hours at the maximum temperature and subsequent cooling with the furnace. We also tried quenching the specimens from the high temperature. This led to the same results. We also carried out x-ray phase analyses of the sinter products of some two component compositions. The results obtained are shown in Table 4, from which it will be evident that in the case of $PbNi_{1/3}Nb_{2/3}O_3$ and $PbFe_{1/2}Nb_{1/2}O_3$ the first phase that appears in the course of the solid state reaction has the structure of pyrochlore. With increase of the sintering temperature there appears and increases in concentration a phase with the perovskite structure; at the same time the lines in the diffraction patterns corresponding to the phase with the pyrochlore structure weaken and finally disappear. The set of lines in the diffraction patterns for sinter products obtained at 700-800°, corresponding to the phase with the pyrochlore structure, is similar to the set of lines in diffraction patterns for lead pyroniobate[9]. At higher roasting temperatures this phase yields a diffraction pattern more similar to the pattern for cadmium pyroniobate.[10]

In the lead magnesium-tungstate composition roasted at 500° there forms a phase the diffraction pattern for which is similar to the pattern for $PbWO_4$, which has the structure of scheelite ($CaWO_4$). However, the reaction product is poorly crystallized and this inference must be regarded as only tentative.

In the case of lead ferrotungstate, at the first stages of reaction there also appears a phase the structure of which is similar to the structure of pyrochlore. So far it is not clear what the composition of this phase may be, but we tentatively assume that the chemical composition of this phase is characterized by $Pb_2Fe_{2/3}W_{4/3}O_7$.

The formation of lead niobates also occurs via a number of intermediate stages. Thus when the mixtures $3PbO + Nb_2O_5$ and $2PbO + Nb_2O_5$ are roasted at 600° there forms the same so far unidentified phase, which we provisionally designate as phase X. When roasted at 700° both mixtures yield diffraction patterns agreeing with the diffraction patterns for lead pyroniobate with the structure of pyrochlore[9]. Increase of the sintering temperature does not change the appearance of the patterns for $2PbO + Nb_2O_5$. In the case of $3PbO + Nb_2O_5$ mixture a diffraction pattern corresponding to the compound $3PbO \cdot Nb_2O_5$ is obtained only after firing at 800°.

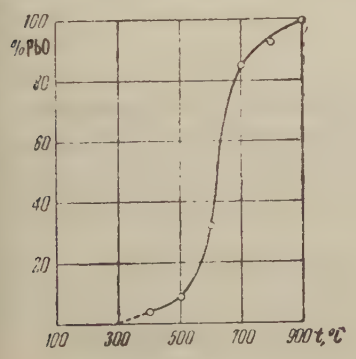

←Content of bound PbO in $PbNi_{1/3}Nb_{2/3}O_3$ sinter as a function of the firing temperature.

In addition to x-ray phase analyses, we also carried out chemical phase analyses. This enabled us to follow the variation in the amount of bound PbO in $PbNi_{1/3}Nb_{2/3}O_3$ sinter as a function of the roasting temperature with a 2 hour holding time. The results are shown in the accompanying figure. The free lead oxide was extracted by 5 minute treatment with 1:5 acetic acid, which does not dissolve NiO and Nb_2O_5, and then precipitated in the form of the sulfate. Fully synthesized $PbNi_{1/3}Nb_{2/3}O_3$ as the result of the acetic acid treatment lost ~0.5% in weight. It will be evident from the figure that intense binding of lead oxide occurs at temperatures of 600-700°. Increase of the holding time at these temperatures to 10 hours does not lead to increase in the amount of bound PbO. In the case of sinters obtained at 600° free PbO is also evinced in the diffraction patterns. Thus it will be evident that the results of chemical phase analysis are not in conflict with the results of x-ray diffraction studies.

Conclusions

1. We synthesized compounds of complex composition characterized by the chemical formulas:

$$[(A_1^{1+})_{1/2}(A_2^{3+})_{1/2}]B^{4+}O_3,\quad A^{2+}[(B_1^{2+})_{1/3}(B_2^{5+})_{2/3}]O_3,\quad A_1^{2+}[(B_1^{3+})_{1/2}\times(B_2^{5+})_{1/2}]O_3,$$

$$A_1^{2+}[(B_1^{2+})_{1/2}(B_2^{6+})_{1/2}]O_3,\quad A_1^{2+}[(B_1^{3+})_{2/3}(B_2^{6+})_{1/3}]O_3,\quad A_1^{3+}[(B_1^{2+})_{1/2}\times(B_2^{4+})_{1/2}]O_3.$$

2. X-ray diffraction studies showed that for all the variants of these general chemical formulas there can be obtained compounds with the perovskite structure.

3. We determined the lattice parameters and showed that, except for the compounds Ba_2MgWO_6 and Pb_2MgWO_6, there is no ordering of the ions in the sublattices, i.e., the superstructure lines do not appear in the Debye patterns.

4. We investigated the mechanism of formation of $PbNi_{1/3}Nb_{2/3}O_3$, $PbFe_{1/2}Nb_{1/2}O_3$, $PbFe_{2/3}W_{1/3}O_3$ and Pb_2MgWO_6. We established that in the case of the first three compositions there at first forms a phase with the structure of pyrochlore, then a second phase with the structure of perovskite. In the case of many lead compounds it is impossible to carry these reactions in the solid phase to completion and obtain the corresponding perovskite type phase. In the case of Pb_2MgWO_6 there apparently first forms a phase with the structure of scheelite.

5. In the process of synthesis of $3PbO\cdot Nb_2O_5$ and $2PbO\cdot Nb_2O_5$ there also form intermediate compounds.

I desire to express my deep gratitude to G.A.Smolenskii for his constant interest in the work.

Institute of Semiconductors,
Academy of Sciences of the USSR

References

1. G.A.Smolenskii & A.I.Agranovskaya, Izuchenie vozmozhnosti ispol'zovaniya redkozemel'nykh okislov dlya izgotovleniya radiotekhnicheskikh izdelii. Otchet Instituta khimii silikatov AN SSSR (Investigation of the possibility of utilizing rare earth oxides for preparing electronic components. Report of the Institute for the Chemistry of Silicates, USSR Ac.of Sci.) 1954.

2. G.A.Smolenskii & A.I.Agranovskaya, Zhur.tekh.fiz., 28, 1491 (1958). (Trans.Soviet Physics - Technical Physics.)

3. G.A.Smolenskii & A.I.Agranovskaya, Fizika tverdogo tela, 1, 1562 (1959). (Trans.Soviet Physics - Solid State.)

4. G.A.Smolenskii, A.I.Agranovskaya, S.N.Popov & V.A.Isupov, Zhur.tekh.fiz., 28, 2152 (1958). (Trans.Soviet Physics - Technical Physics.)

5. G.A.Smolenskii, A.I.Agranovskaya & V.A.Isupov, Fizika tverdogo tela, 1, 999 (1959). (Trans.Sov.Phys. - Solid State.)

6. I.E.Myl'nikova & V.A.Bokov, Program of the Third Conference on Ferroelectricity, M., 1960.

7. F.Galasso, L.Katz & R.Ward, J.Amer.Chem.Soc., 81, 820 (1959).

8. S.G.Steward & H.P.Rooksby, Acta Crystallogr., 4, 503 (1951).

9. R.S.Roth, J.Research Nat.Bur.Standards, 62, No.1, 27 (1959).

10. A.Bystroem, Arkiv.Kemi.Mineral., Geol., 18A, No.21 (1944).

11. A.Cocco, Ann.Chimica, 45, 737 (1955).

12. V.I.Mikheev, Rentgenograficheskii opredelitel' mineralov (X-ray diffraction guide to minerals), M., 1957.

ELECTRIC PROPERTIES OF SOME SOLID SOLUTIONS OF DIVALENT METAL NIOBATES AND TANTALATES

- P.S.Mikhailov & B.A.Rotenberg

Investigations[1,2] of the properties of lead metaniobate and two-component solid solutions of rare earth metal niobates with replacement of the niobium by tantalum showed that increase in the tantalum content leads to weakening of the ferroelectric properties and appearance of relaxation characteristics. We felt it would be of interest to determine in greater detail the regularities obtaining in the three component solutions $(Pb,Ba,Sr)Nb_2O_6$ and $(Pb,Ba,Ca)Nb_2O_6$ in the case of replacement of the niobium by tantalum.[3]

For purposes of the present investigation we chose the compositions $(Pb_{0.5},Ba_{0.1},Sr_{0.4})(Nb_{1-x},Ta_x)_2O_6$ (Hereinafter NBST) and $(Pb_{0.6},Ba_{0.2},Ca_{0.2})(Nb_{1-x},Ta_x)_2O_6$ (hereinafter NBCT). The specimens were synthesized of chemically pure grade barium, strontium and calcium carbonates and lead oxide, and of niobium and tantalum pentoxides prepared by oxidation of $\geqslant 99\%$ pure Nb and Ta. The synthesis was carried out by the usual ceramic technique, the mixtures with a high tantalum content being sintered in a protective atmosphere. We carried out measurements only on thoroughly sintered specimens; the quality of the sintering was checked by measuring the dielectric loss before and after moistening.

The dielectric constant ϵ and tan δ of the specimens were measured at 1 and 100 kc by the bridge procedure. The temperature dependences of ϵ and tan δ at 1 kc for the NBST and NBCT systems are shown in Figs.1 and 2. It will be evident that compositions with up to 10 mole percent Ta have a clearly pronounced dielectric constant peak; in compositions with $x = 0.3$ there appears a second maximum in the ϵ vs t curve. With further increase of the Ta content, the first maximum disappears, while the second becomes increasingly promonent. For compositions with $x \geqslant 0.4$ the ϵ vs t curves have the appearance characteristic of materials with relaxational polarization[4]. All specimens are characterized by some increase of the dielectric loss at negative temperatures, which is typical of solid solutions of $PbNb_2O_6$ with rare earth metal niobates[3]. Measurements of the temperature dependence of the dielectric constant at $f = 100$ kc showed that in these specimens there are actually observed relaxation type effects. With increase of the frequency the ϵ maximum is shifted to the side of higher temperatures. Fig.3 shows the variation of θ_m, the temperature of the ϵ peak, at different frequencies with the concentration of Ta ions. It will be evident that for compositions with $x \leqslant 0.3$ the temperature of the ϵ peak is shifted somewhat with change in frequency, the magnitude of the shift increasing with increase of the Ta content. The temperature of the second ϵ maximum is strongly dependent on the frequency, but in this case the magnitude of the shift of θ_m changes little with increase of the Ta content.

Inasmuch as the investigated compositions are in general complex multiple component systems, it is not impossible that there may form in them phases with a structure differing from the known structure for $(Pb,Ba,Sr)Nb_2O_6$ solid solutions[5].

X-ray diffraction phase analysis, carried out at our request by V.G.Prokhvatilov, showed that $(Pb_{0.5},Ba_{0.1},Sr_{0.4})Nb_2O_6$ and $(Pb_{0.6},Ba_{0.2},Ca_{0.2})Nb_2O_6$ are isostructural with $(Pb_{0.5},Ba_{0.1},Sr_{0.4})Ta_2O_6$ and $(Pb_{0.6},Ba_{0.2},Ca_{0.2})Ta_2O_6$, and have the structure of orthorhombic lead metaniobate. In view of this and the fact that the ionic radii of Nb^{5+} and Ta^{5+} are nearly equal, it was impossible to determine reliably whether the investigated compositions are true solid solutions or heterogeneous mixtures of the corresponding niobates and tantalates. The diffraction patterns, however, showed no evidences of phases with a different structure that could be responsible for the appearance of relaxation properties.

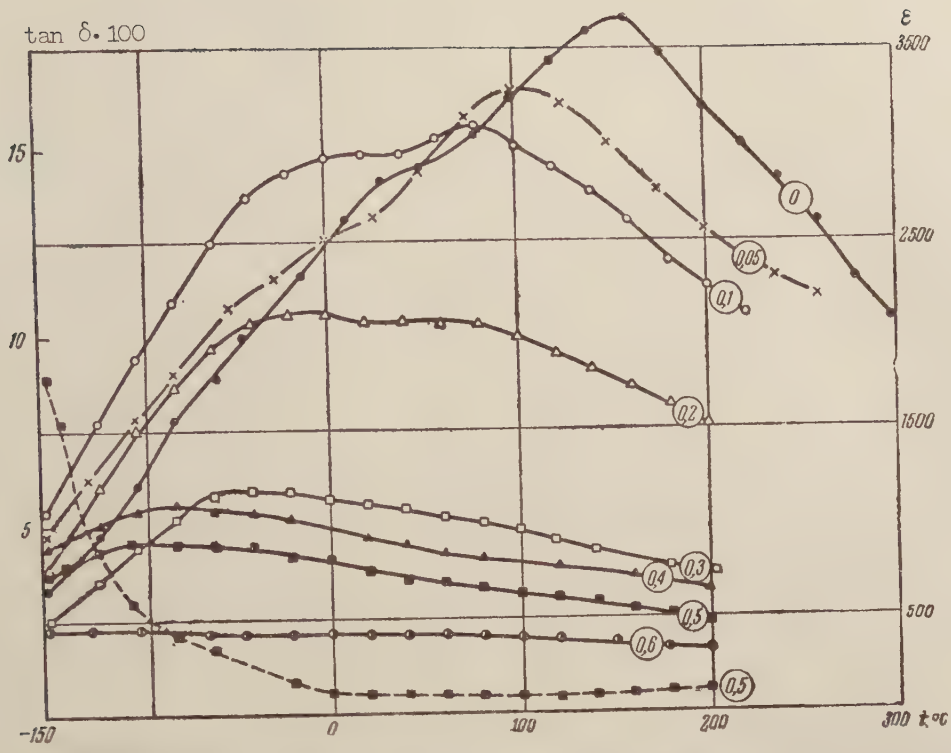

Fig.1. Temperature dependences of ϵ (solid lines) and tan δ (dashed lines; x = 0.5) at 1 kc for NBST specimens. The figures at the curve indicate the relative tantalate content.

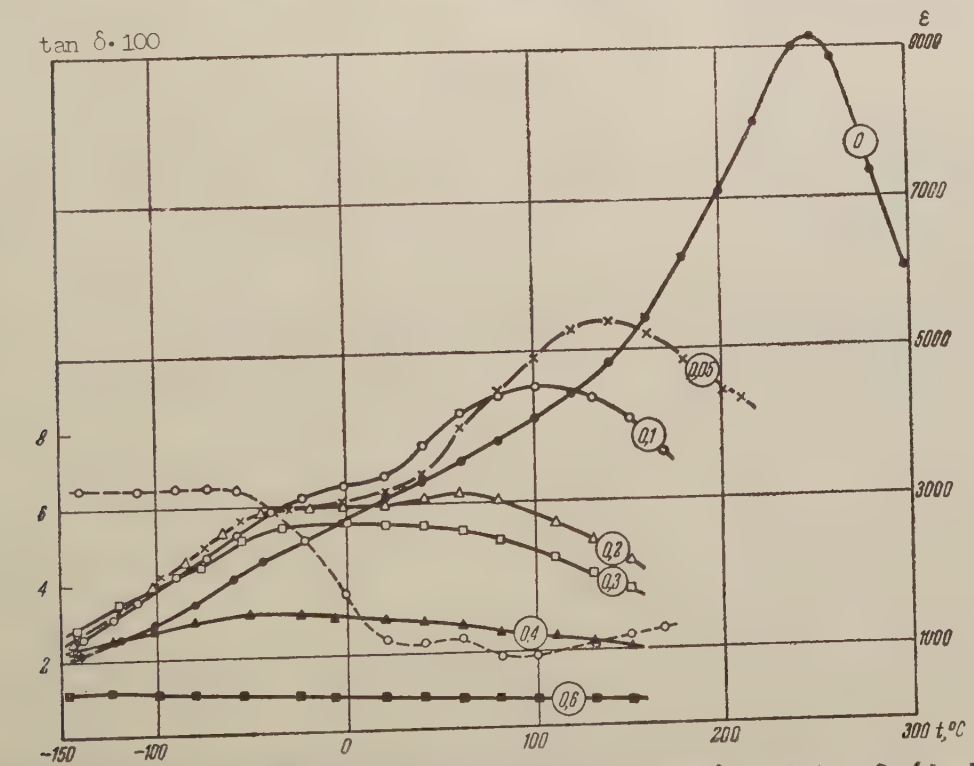

Fig.2. Temperature dependences of ϵ (solid lines) and tan δ (dashed lines; x = 0.1) at 1 kc for NBCT specimens. The figures at the curve indicate the relative tantalate content.

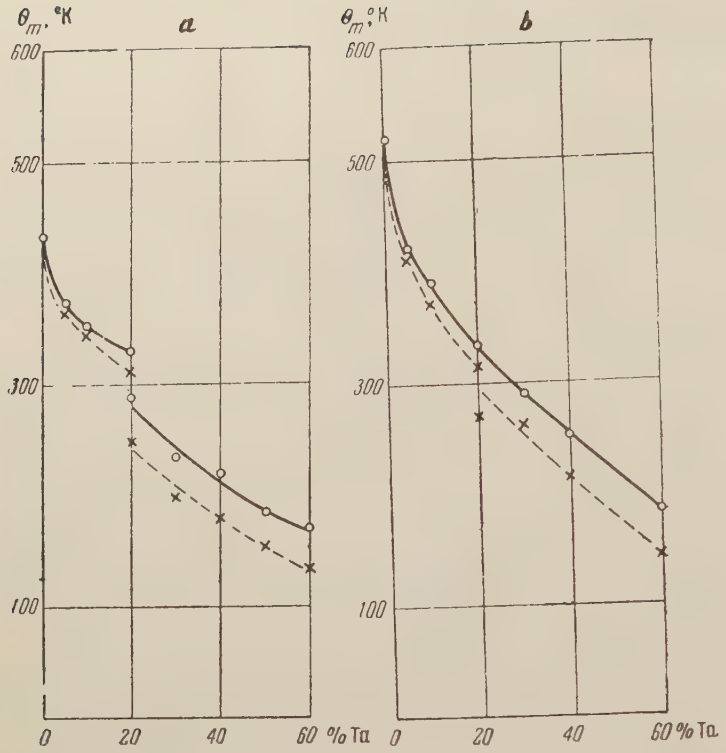

Fig.3. Variation of θ_m, the temperature of the ϵ peak, with the Ta concentration for the NBST (a) and NBCT (b) systems at f = 1 kc (dashed lines), and f = 100 kc (solid lines).

Hysteresis loops were not observed at liquid nitrogen temperature for the compositions with pronounced relaxation properties. It should be noted that hysteresis loops at this temperature were also not observed in the case of compositions with $x \leqslant 0.3$ for which loops were observed at room temperature; true, this can be due to appreciable increase of the coercive field at low temperatures.

Thus increase of the tantalum content in the three-component solid solutions of lead and rare earth metal metaniobates leads at first to weakening of the ferroelectric properties and then to the appearance of relaxation properties. At a tantalum content less than 20 mole percent both ferroelectric and relaxation properties are observed.

References

1. M.H.Frankombe & B.Lewis, Acta Crystallogr., 2, 696 (1958).
2. G.A.Smolenskii, V.A.Isupov & A.I.Agranovskaya, Fizika tverdogo tela, 1, 992 (1959). (Trans.Soviet Physics - Solid State.)
3. G.A.Smolenskii, V.A.Isupov & A.I.Agranovskaya, Ibid., 1, 442 (1959). (Trans.Ibid.)
4. G.I.Skanavi, Ya.M.Ksendzov, V.A.Trigubenko & V.G.Prokhvatilov, Zhur.eksp. i teor.fiz., 33, 320 (1957). (Trans.Soviet Physics - JETP.)
5. I.G.Ismailzade, Kristallografiya, 4, 658 (1959). (Trans.Soviet Physics - Crystallography.)

CONCERNING WAYS AND MEANS OF OBTAINING MATERIALS WITH A SMOOTHED OUT TEMPERATURE DEPENDENCE OF THE DIELECTRIC CONSTANT

- N.A.Andreeva, O.A.Grushevskaya & V.I.Zhukovskii

Preparation of ceramic materials with a high dielectric constant that is little dependent on the temperature presents a difficult problem. This stems from the fact that in many binary and more complex systems possessing ferroelectric properties substitutional solid solutions generally form in a wide concentration range.

Consequently, so far it has proved impossible to solve the problem of smoothing out the temperature dependence of the dielectric constant of ceramic materials by mixing several ferroelectrics with different Curie points. To date there have been only a few studies devoted to materials with a weak temperature dependence of the dielectric constant.

In most attempts to develop such materials the base substance was barium titanate to which there were added varying amounts of $Bi_2O_3 + TiO_2$, $Bi_2O_3 + SnO_2$, etc. By introduction of $Bi_4Ti_3O_{12}$ into barium titanate, Coffeen[1,2] and Popper et al[3] succeeded in obtaining materials with a dielectric constant of about 2000 and a relatively weak temperature dependence of ϵ in the range of positive temperatures. In the range of negative temperatures, however, the dielectric constant falls off sharply. The cited authors offer no explanation for the observed effects.

Skanavi and his co-workers[4] obtained ceramics based on strontium and bismuth tantalates with a favorable temperature dependence of the dielectric constant. These authors explain the high value of ϵ by the relaxation character of the polarization and indicate that similar properties may be exhibited by barium titanate doped with bismuth oxide and titanium dioxide.

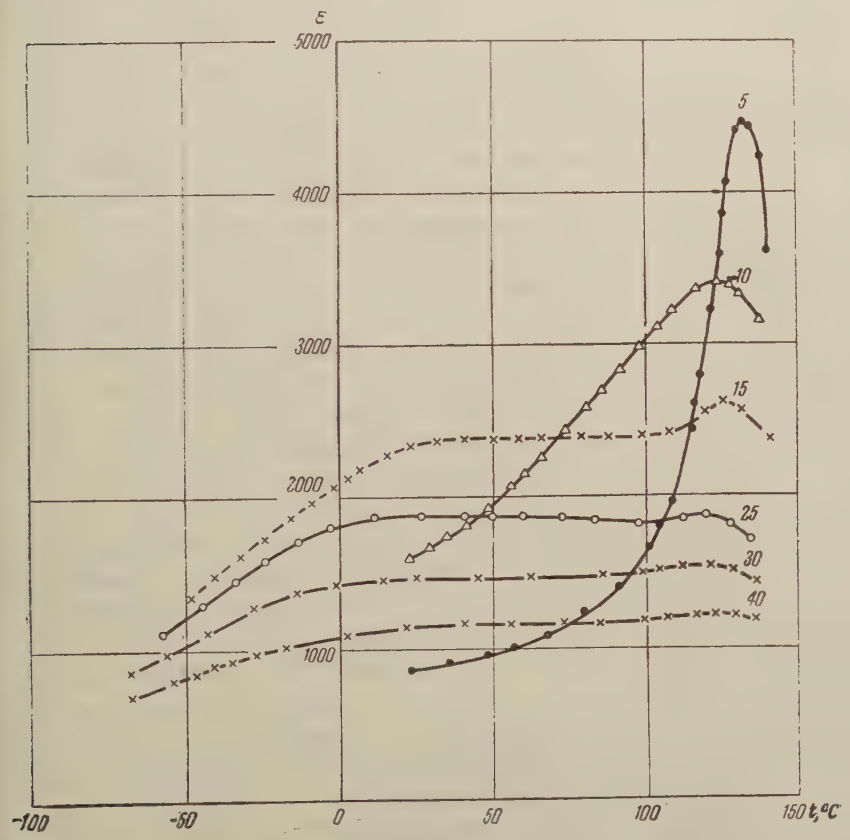

Fig.1. Temperature dependences of ϵ for specimens of the $BaTiO_3$-$Bi_4Ti_3O_{12}$ system. The figures at the curve indicate the $Bi_4Ti_3O_{12}$ content in percent by weight.

Smolenskii et al[5] found that the indicated materials possess not only relaxational but also ferroelectric properties.

Guided by the above, for the purpose of smoothing out the temperature dependence of the dielectric constant, we decided to try doping $BaTiO_3$ with the oxides of bismuth, titanium and zirconium in different proportions and combinations. So far we have investigated the $BaTiO_3$-$Bi_4Ti_3O_{12}$ system in greatest detail.

By way of raw materials we used barium titanate

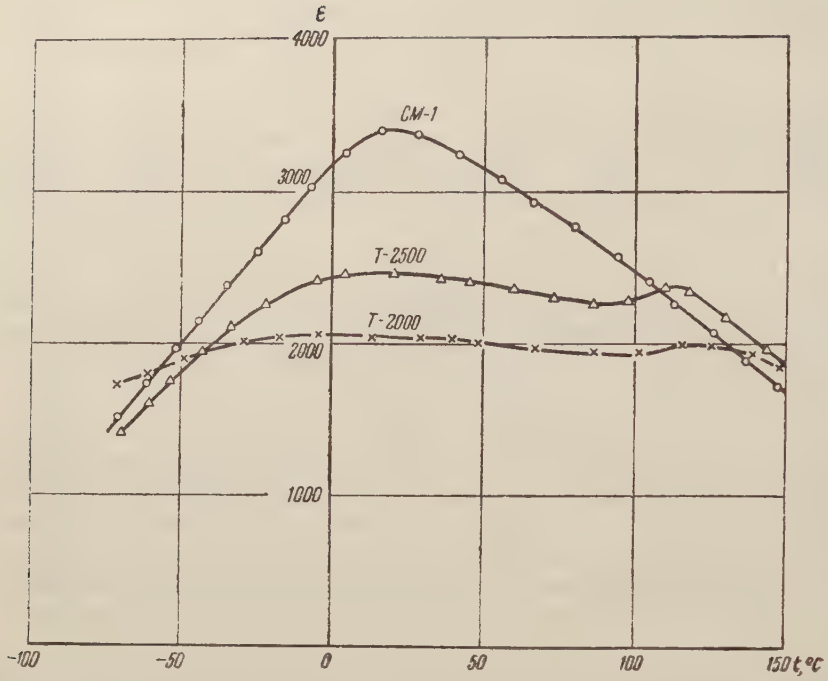

Fig.2. Temperature dependences of ε for some synthesized materials.

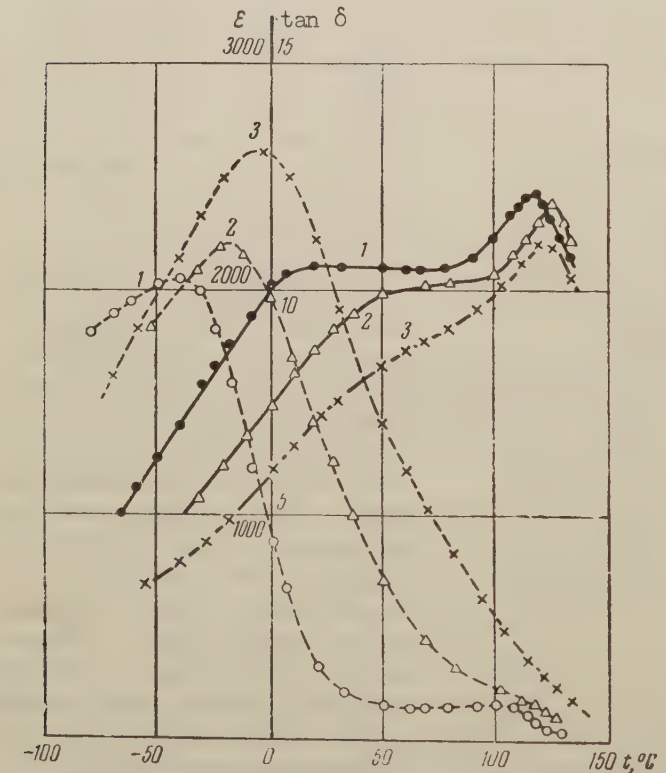

Fig.3. Temperature dependences of ε (solid lines) and tan δ (dashed lines) of 85% $BaTiO_3$ + 15% $Bi_4Ti_3O_{12}$ ceramic at different frequencies: 1) 10^3 cps, 2) 10^5 cps, 3) 10^6 cps.

sinter prepared by the usual ceramic technology, bismuth oxides and capacitor grade titanium dioxide. The batches were prepared by mixing the components in a vibrating mill for two hours. The measurements were carried out on sintered specimens.

The capacitance and tan δ were measured by the bridge procedure at a frequency of 1 kc, and in a number of cases at other frequencies. The temperature dependences of the dielectric constant obtained for a number of specimens are shown in Fig.1. It will be evident that $Bi_4Ti_3O_{12}$ as an additive greatly smoothes out the temperature dependence of the dielectric constant but does not affect the position of the ε peak (Curie point) of the base material, i.e., barium titanate.

Qualitatively similar effects were observed in tests on specimens of the $BaTiO_3$-Bi_2O_3-ZrO_2 system. The temperature dependences of the dielectric constant for three materials are shown in Fig.2. Material T-2500 is representative of the $BaTiO_2$-Bi_2O_3-TiO_2 system; ceramic T-2000 is based on the $BaTiO_2$-Bi_2O_3-ZrO_2 system. For purposes of comparison we give the temperature dependence of ε for technical ceramic CM-1. It should be noted that the new materials have a relatively high electric strength (greater than 9 kv/mm in a nonuniform field) and a low sintering temperature (1100-1250°).

The temperature dependences of ε and tan δ at different frequencies for one of the specimens of the $BaTiO_3$-$Bi_4Ti_3O_{12}$ system are shown in Fig.3. It will be seen that for this specimen there is observed a change in the height and temperature position of the tan δ maximum with frequency, which indicates the presence of relaxation properties. On the other

hand, the material exhibits a maximum of the dielectric constant (a characteristic of ferroelectrics) at t = 120°, the position of which virtually does not vary with frequency, and dielectric hysteresis. The dielectric hysteresis loops disappear at temperatures above 120°. The ϵ vs temperature curves have two maxima; it is evident that the first, low temperature maximum is relaxational, while the second high temperature maximum is ferroelectric in character. The cited data are also consistent with the temperature dependence of tan δ at different frequencies. In the tan δ vs temperature curves recorded at 10^3 cps there is observed a relaxation maximum at -40° and at the same time a variation of tan δ in the vicinity of the Curie point characteristic of ferroelectrics. With increase of the frequency the relaxation maximum is shifted to the side of higher temperatures, while the inflection in the curve in the vicinity of the Curie point is smoothed out. Curves of qualitatively similar character are obtained for specimens with different proportions of the components.

Data of x-ray diffraction studies, carried out at our request by V.G.Prokhvatilov and E.I.Gindina, showed that in specimens of the $BaTiO_3$-Bi_2O_3-TiO_2 and $BaTiO_3$-Bi_2O_3-ZrO_2 systems there are present a phase with the structure of barium titanate, but with somewhat altered lattice parameters, and a second phase, which, it must be assumed, is responsible for the relaxation properties of the material. It must be emphasized that the diffraction patterns did not disclose the presence of solid solutions in the investigated systems. Apparently, solid solutions can form (if at all) only in a very narrow range of concentrations.

On the basis of the experimental data it may be asserted that in materials of the $BaTiO_3$-Bi_2O_3-TiO_2 and $BaTiO_3$-Bi_2O_3-ZrO_2 systems there are present phases with ferroelectric and relaxation properties. The composition of the latter phase has not yet been established. The data obtained do not substantiate the inferences of Skanavi et al[4] regarding the absence of ferroelectric properties in barium titanate based materials with more than 15 mole percent $Bi_2O_3 \cdot 2TiO_2$. It must be noted that Skanavi et al carried out their measurements at temperatures to 100° and hence did not observe the maximum of ϵ, characteristic for $BaTiO_3$.

Conclusions

1. On the basis of the $BaTiO_3$-Bi_2O_3-TiO_2 and $BaTiO_3$-Bi_2O_3-ZrO_2 systems one can formulate ceramic materials with a smoothed out temperature dependence of the dielectric constant.

2. It was established by x-ray diffraction studies that in specimens of the above systems there are present barium titanate with altered lattice parameters (not strictly cubic) and a second phase.

3. The smoothed out temperature dependence of the dielectric constant is due to the presence in the material of two phases - a ferroelectric phase and a relaxational phase - which did not form solid solutions in a wide concentration range.

4. For a number of specimens of the above systems there was established the presence of two maxima of the dielectric constant. The experimental data indicate that the low temperature maximum is relaxational and the high temperature maximum ferroelectric in character.

References

1. W.W.Coffeen, J.Am.Ceram.Soc., 39, 154 (1956).
2. W.W.Coffeen, J.Am.Ceram.Soc., 37, 480 (1954).
3. P.Popper, S.N.Ruddlesden & T.A.Ingles, Trans.Brit.Cer.Soc., 56, 356 (1957).
4. G.I.Skanavi, Ya.M.Ksendzov, V.A.Trigubenko & V.G.Prokhvatilov, Zhur.eksp. i teor.fiz., 33, 320 (1957). (Trans.Soviet Physics - JETP.)
5. G.A.Smolenskii, V.A.Isupov & A.I.Agranovskaya, Fizika tverdogo tela, 1, 992 (1959). (Trans.Soviet Physics - Solid State.)

SOLID SOLUTIONS IN THE TERNARY FERROELECTRIC SYSTEM $Ba(Ti,Zr,Sn)O_3$

- M.M.Nekrasov & Yu.M.Poplavko

Ferroelectric solid solutions of the $Ba(Ti,Zr)O_3$ and $Ba(Ti,Sn)O_3$ systems are of considerable practical interest as materials for nonlinear ceramic capacitors. The properties of these solid solutions have been studied by a number of investigators[1-7]. It has been established that with increase of the second component (barium zirconate or barium stannate), the "ferroelectric compliance" is enhanced, i.e., the dielectric constant increases and its dependence on the applied dc or ac electric field becomes stronger. The Curie point (cubic to tetragonal transitional point) of the solid solutions is lowered, while the temperatures of the transitions from tetragonal to orthorhombic and from orthorhombic to rhombohedral symmetry are increased, until finally all three transitions coincide. At a barium zirconate concentration above 18% or barium stannate concentration above 12% the structure becomes rhombohedral. At the same time the mobility of the domains[8] and the orientation polarization[3] increase substantially, and consequently, the nonlinearity is enhanced.

In $Ba(Ti,Sn)O_3$ solid solutions the rhombohedral structure appears at temperatures below room temperature, while in $Ba(Ti,Zr)O_3$ solid solution the rhombohedral structure forms at higher temperatures, which is a positive feature of the latter system. At the same time $Ba(Ti,Sn)O_3$ solid solutions have a higher "ferroelectric compliance", and their reversible nonlinearity N_r attains 1.3 cm/kv, as compared with $N_r = -0.5$ cm/kv for $Ba(Ti,Zr)O_3$.

For some compositions of solid solutions in the $Ba(Ti,Zr,Sn)O_3$ system one can obtain the rhombohedral phase at temperatures substantially above room temperature and thus combine pronounced nonlinearity with a comparatively low dielectric loss.

Ceramic specimens of $Ba(Ti,Zr,Sn)O_3$ solid solutions of different composition were prepared in the form of disks 10 to 25 mm in diameter and 0.5 to 2 mm thick by the usual ceramic technology of chemically pure barium carbonate and titanium, zirconium and tin oxides. The barium titanate, zirconate and stannate were synthesized beforehand at a temperature of 1200°. The final sintering was carried out in a Silit furnace at a temperature of 1400-1430° with a holding time sufficient to insure minimal porosity. Chemical analyses showed that the true composition of the sintered specimens agreed with the calculated composition based on proportioning of the batch.

We investigated the dielectric properties of $Ba(Ti,Zr,Sn)O_3$ solid solutions of different compositions as indicated by the points on the concentration triangles shown in Fig.1,a. The temperature dependences of the dielectric constant and loss tangent were measured on a "Tesla" bridge and a Q-meter. The effects of barium zirconate and barium titanate on the temperature shift of the phase transitions are additive (Fig.1,b). Near the merging of the phase transitions it was impossible to distinguish the maximum of the dielectric constant, so that the variation in structure as a function of the temperature and concentration of the components is shown only approximately in Fig.1,b. The merging of the phase transitions is characterized in Fig.1,b by the spatial line of intersection of the three surfaces. Projection of this line on the plane of the concentration triangle gives the composition of the corresponding solid solutions. Solid solutions near the line of merging of the phase transitions have appreciable nonlinearity together with a relatively low dielectric loss.

We investigated the variation of the dielectric constant and loss tangent as a function of the applied ac and dc fields for a number of synthesized solid solutions. The resultant family of curves (Fig.2) characterizes both the effective and the reversible nonlinearity. Inasmuch as the quality of a nonlinear capacitor depends not only on the reversible nonlinearity $N_r = (1/\epsilon)(d\epsilon/dE_=)$ but also on the

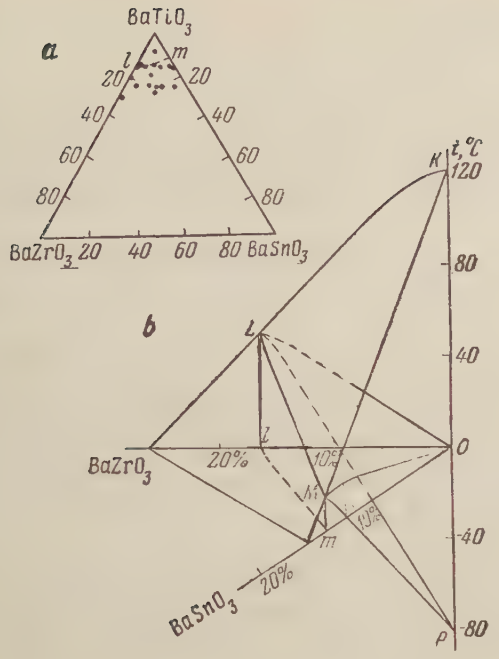

Fig.1

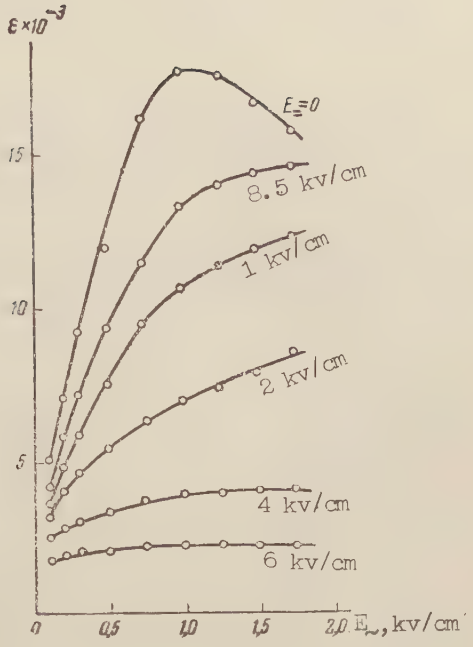

Fig.2

Fig.1. a - Concentration triangle for the $Ba(Ti,Zr,Sn)O_3$ system. The points indicate the investigated compositions; the dashed line indicates the composition in which the phase transitions coincide. b - Variation of the temperature of the phase transition as a function of the component concentration in the $Ba(Ti,Zr,Sn)O_3$ system. The horizontal plane represents part of the concentration triangle. KLM is the surface separating cubic and tetragonal structure; below the line LM the structure is cubic and rhombohedral; OLM is the surface separating the tetragonal and orthorhombic structures; PLM is the surface separating the orthorhombic and rhombohedral structures. These three surfaces intersect along the line LM; the projection of this line (l_m) on the concentration triangle characterizes the composition for which the phase transitions merge.

Fig.2. Variation of the dielectric constants of $Ba(Ti_{0.85},Zr_{0.73},Sn_{0.02})O_3$ specimens with the ac field at different values of the dc biasing field.

dielectric loss, it is convenient to characterize it by the coefficient $K = N_{r\ max}/\tan\delta$.

Among the investigated solid solutions, the highest value of K (12) was obtained for $Ba(Ti_{0.85},Zr_{0.11},Sn_{0.04})O_3$, for which $N_r = 0.9$ cm/kv with $\epsilon_{max}/\epsilon_{min} = 20$; $\tan\delta = 0.03$ in weak fields and 0.15 at its maximum.

References

1. G.A.Smolenskii & V.A.Isupov, Zhur.tekh.fiz., 24, 1375 (1954).
2. G.A.Smolenskii, K.P.Tarutin & N.P.Grudtsin, Ibid., 24, 1584 (1954).
3. V.A.Bokov, Ibid., 27, 1785 (1957). (Trans.Soviet Physics - Tech.Physics).
4. V.A.Bokov, Ibid., 28, 77 (1958), (Trans.Ibid.); Izv.AN SSSR, Ser.fiz., 21, 382 (1957), (Trans.Bulletin, 21, 386).
5. N.S.Novosil'tsev & A.L.Khodakov, Zhur.tekh.fiz., 26, 310 (1956). (Trans. Soviet Physics - Technical Physics.)
6. E.V.Sinyakov, E.A.Stafiichuk & L.S.Sinegubova, Zhur.eksp.i teor.fiz., 21, 1936 (1951).
7. T.N.Verbitskaya, Doklady AN SSSR, 100, 29 (1955).
8. W.Merz, Phys.Rev., 95, 690 (1954).

PRELIMINARY REPORT ON A FERROELECTRIC CERAMIC WITH A DIELECTRIC CONSTANT OF 80 000 - 100 000

- T.N.Verbitskaya, L.M.Aleksandrova & L.S.Sinitsi

In the course of developing ceramics with pronounced nonlinear properties we obtained a number of materials the peak dielectric constant (ϵ_{max}) of which in a narrow but definite range of field values (E_{max}) attains an exceptionally high value.[1,2]

Our research led to the development of a new material, designated VK-50, wi ϵ_{max} = 80 000-100 000, i.e., a value of ϵ_{max} appreciably higher than that exhibited by other known ferroelectric ceramics.

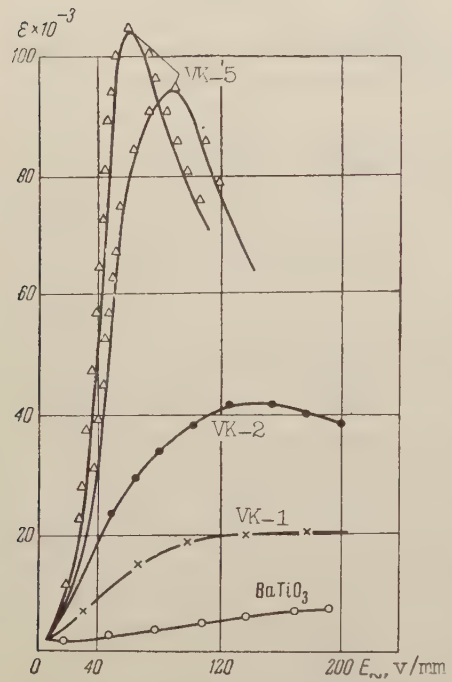

Fig.1. $\epsilon = f(E_{\sim})$ for $BaTiO_3$, VK-1, VK-2 and VK-5 at room temperature.

Below we give a comparison of the principal nonlinearity parameters (ϵ_{init}, ϵ_{max} and E_{max}) of the developed ceramics with the corresponding parameters of barium titanate. The initial value of the dielectric constant ϵ_{init} and the Curie temperature were determined in a weak field at a voltage of 5 v/mm.

In investigating the temperature dependence of the dielectric constant in a weak field it was established that the $\epsilon_{init} = f(t^{o})$ curves for all three ceramics - VK-1, VK-2 and VK-5 - differ littl from each other. On the other hand, as regards the principal characteristic, $\epsilon = f(E_{\sim})$, which characterizes the nonlinearity, the three ceramics differ appreciably. It will be evident from Fig.1 that the degree of nonlinearity increases substantially in going successively from barium titanate to VK-1, VK-2 and, finally, VK-5. Inasmuch as the initial values of the dielectric constant of the three VK materials are almost the same, the nonlinearity coefficient $K_{\sim} = \epsilon_{max}/\epsilon_{init}$, depends primarily on the peak dielectric constant ϵ_{max}. For VK-5 ceramic, $K_{\sim}$ = 40-50.

VK-5 exhibits pronounced nonlinear characteristics in a wide temperature range. With cooling from room temperature to approximately -150° the nonlinearity coefficient increases from 40-50 to 320-360.

Ceramic	Curie point, °C	ϵ_{init}	ϵ_{max}	E_{max}, v/mm
$BaTiO_3$	120	1700-1800	6000-8000	600-800
VK-1	75	2300-2500	16000-20000	150-200
VK-2	75	2000-2300	35000-45000	100-150
VK-5	75	2000-3000	80000-100000	80-100

Increase of $K_{\sim}$, due primarily to decrease of ϵ_{init} in the range of negativ temperature, is exhibited not only by VK-5 but also by VK-2 and barium titanate. With reduction of the temperature from +20° to -150° $K_{\sim}$ of barium titanate increases from 4 to 25, while $K_{\sim}$ of VK-2 ceramic increases from 8 to 200. With increase of temperature above room temperature, the nonlinearity coefficient decreases and near the Curie point becomes close to unity.

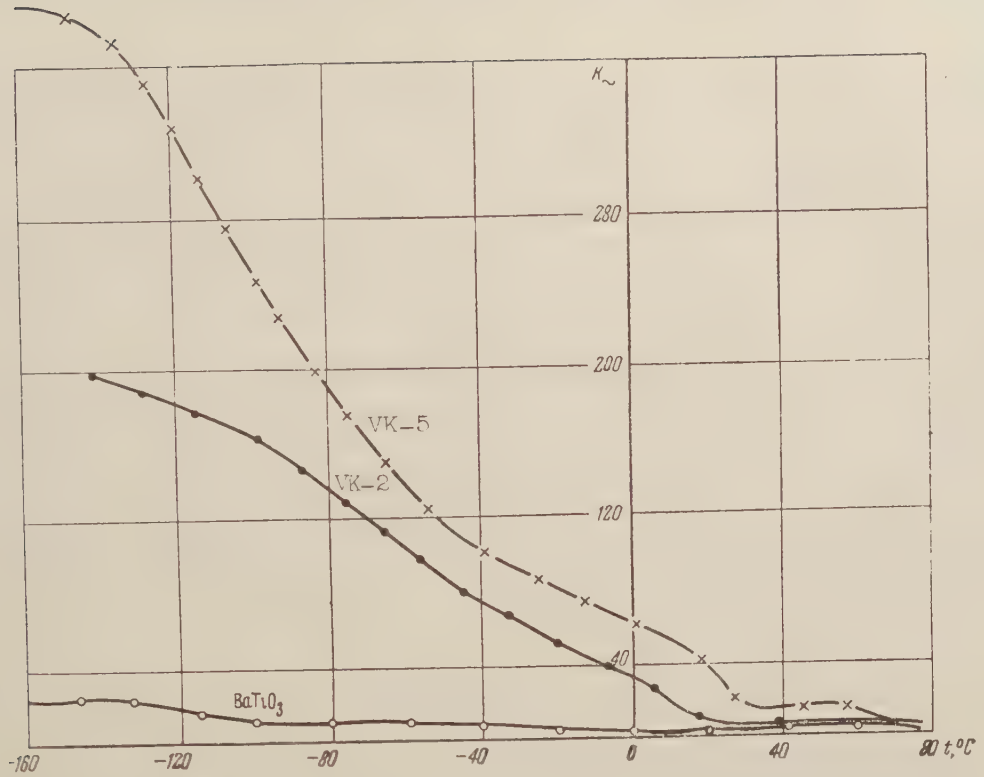

Fig.2. Temperature dependence of the nonlinearity coefficient $K_{\sim}$ of $BaTiO_3$, VK-2 and VK-5.

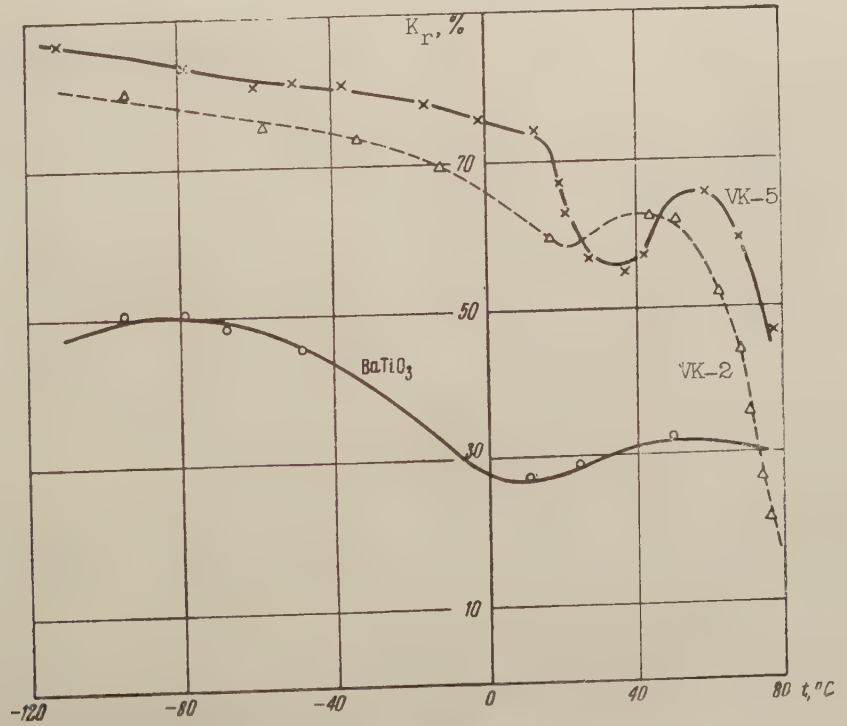

Fig.3. Temperature dependence of the hysteresis loop rectangularity coefficient of $BaTiO_3$, VK-2 and VK-5.

The peak dielectric constant field E_{max} increases somewhat with cooling to below room temperature and decreases somewhat with heating above room temperature. Accordingly, in determining K_ν at different temperatures we used the corresponding values of E_{max}.

In investigating the temperature dependence of ϵ in different fields we observed four maxima of the dielectric constant. The four temperature maxima of ϵ (located at +65, +20, -5 and -40°C) are evinced most clearly at a field strength of 60-100 v/mm; under these conditions ϵ attains a value of about 80 000.* This characteristic of VK-5 ceramic makes it possible to insure exceptionally high values of ϵ in a wide temperature range through appropriate selection of the polarizing field. Whereas for VK-2 ceramic, in a field of 100-110 v/mm, ϵ has a value of about 40 000 in the temperature interval from +20 to -30°, for VK-5 under the same conditions the value of ϵ exceeds 80 000.

We also determined the hysteresis loop rectangularity coefficient K_r (the ratio of the charge at saturation to the charge at zero field) for barium titanate and the VK-2 and VK-5 ceramics. We found that there is a definite correlation between the nonlinearity and rectangularity coefficients: the higher K_ν, the higher K_r (Figs.2 & 3). Even for VK-5 ceramic, however, K_r at room temperature does not exceed 60-65%, but it does arise to 85% at very low temperatures.

After further tests and development of the technology, VK-5 ceramic will be recommended for the production of varikonds and fabrication of miniature ceramic capacitors.

References

1. T.N.Verbitskaya, Doklady AN SSSR, 100, 29 (1955).

2. T.N.Verbitskaya & L.M.Aleksandrova, Izv.AN SSSR, Ser.fiz., 22, 1534 (1958) (Trans.Bulletin, 22, 1525.)

3. H.Rabenhorst & J.Melichercik, An. der Phys., 1, 261 (1958).

---

*The existence of four maxima in the case of VK-5 is in agreement with the results of Rabenhorst & Melichercik[3] who report observing four maxima for barium titanate.

RESULTS OF THERMAL ANALYSIS OF DOPED BARIUM TITANATE

- V.I.Zhukovskii, M.P.Dorokhova, N.E.Zaremba, D.G.Dykman & G.V.Bois

Engineering materials and components of barium titanate usually contain certain additives designed to impart the requisite electric properties to the ceramic. The stability and reproducibility of the characteristics of such materials depend to a great extent on the technology of their preparation and primarily on the conditions of sintering. In view of this, we felt it would be desirable to investigate the influence of the various additives commonly used in practice (ZrO_2, Bi_2O_3, TiO_2, $CaCO_3$, $MgCO_3$, $BaCO_3$ and others) on the process of sintering barium titanate.

The principal method of investigation was thermal analysis carried out on UKTA-58 equipment. This equipment provides for automatic recording of the thermal curves and the variation in weight and volume of the specimens during heating, holding at heat, and cooling. The rate of variation of temperature was 300°/hr; the holding time at the given temperature was 30 min or 1 hour. Inasmuch as the research was undertaken for practical purposes, we used technical grade raw materials and prepared the specimens by the conventional ceramic technology. The barium titanate was synthesized beforehand at 1260°.

The thermogram for barium titanate without additives is shown in Fig.1. The first exothermic effect - the break at 300° - is connected with burning out of the plasticizer; the second exothermal effect - at 1300° - is due to completion of the process of formation of barium titanate. The endothermic effect at 870° is explained by polymorphous transformation of $BaCO_3$, a small amount of which was present in the initial material.

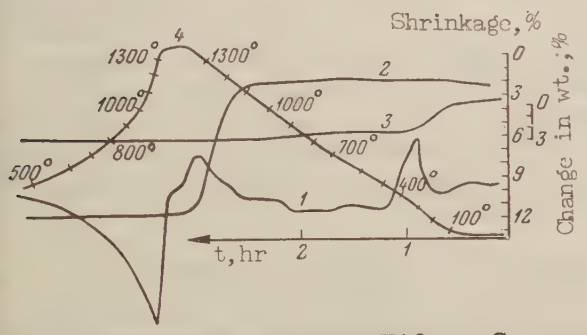

Fig.1. Thermogram for $BaTiO_3$. Curves: 1) thermal effects, 2) shrinkage, 3) variation in weight, 4) temperature rise and cooling.

The addition of rare earth carbonates and bismuth oxide in amounts up to several percent did not alter the character of the thermograms. At the same time introduction of TiO_2 and ZrO_2 results in the appearance of two new thermal effects in the 1250 to 1290° interval: an endothermic effect in heating and an exothermic effect in cooling (Fig.2). The thermal effects occurring as a result of addition of TiO_2 should presumably be associated with the formation of a eutectic solution of $BaTiO_3$ with the more acid titanates and its crystallization.

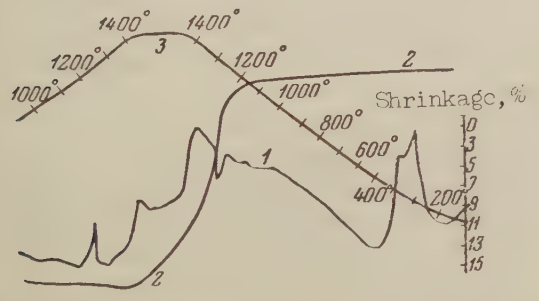

Fig.2. Thermogram for 95% $BaTiO_3$ + + 5% ZrO_2. Curves: 1) thermal effect, 2) shrinkage, 3) temperature rise and cooling.

According to the phase diagram for the $BaO-TiO_2$ system given by Rase & Roy[1] and the data of Keler & Karpenko[2], in the range of impurity concentrations under consideration there should form a eutectic solution of $BaTiO_3$ + $BaTi_2O_5$ with the formation of the said compounds upon crystallization. The inference regarding the eutectic character of the thermal effects is in good agreement with the shrinkage curve: the first thermal effect coincides with the beginning of rapid decrease in volume (eutectic point); the second with increase in volume (crystallization).

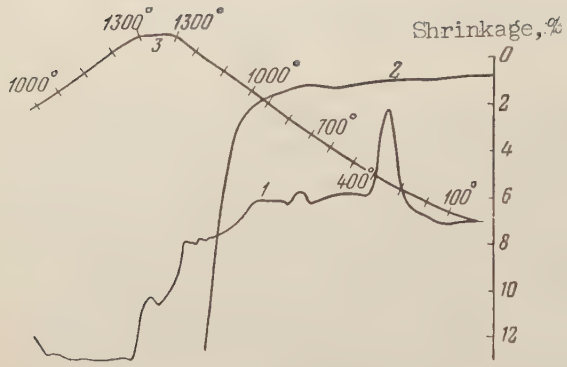

Fig.3. Thermogram for 90% $BaTiO_3$ + + 5% ZrO_2 + 5% Bi_2O_3. Curves: 1) thermal effects, 2) shrinkage, 3) temperature rise and cooling.

X-ray diffraction studies of the $BaTiO_3$-ZrO_2 system with up to 20 per cent by weight ZrO_2, carried out by E.I.Gindin, showed the presence of a solid solution with the perovskite structure.

From the fact that $BaTiO_3$-$BaZrO_3$ solid solution does exist, it follows that there must form an excess of titanium dioxide. Apparently, this is responsible for the thermal effects such as those observed in the $BaTiO_3$-TiO_2 system. It is impossible on the basis of the available data to determine what compounds form the eutectic solution. It may be regarded as definitely established, however, that at some point in the sintering of barium titanate doped with appreciable quantities of TiO_2 and ZrO_2 there forms a liquid phase; this should be taken into account in specifying the sintering procedure. It may be noted that the thermal effects associated with the presence of ZrO_2 persist in the presence of $MgCO_3$, $CaCO_3$, $BaCO_3$ and other similar additives.

Thus it may be inferred that the addition of ZrO_2 determines the character of the sintering process not only in the case of barium titanate but also in the case of other technical ceramics. The introduction of Bi_2O_3 leads to disappearance of the thermal effects (Fig.3). Apparently, in this case there forms a low melting point phase, which is substantiated by the decrease of the sintering temperature for the material.

Conclusions

1. In thermographic investigation of barium titanate with the addition of rare earth carbonates, zirconium dioxide and titanium dioxide, there were observed two opposed thermal effects during heating and cooling, due to the presence of the last two compounds.

2. The presence of the observed thermal effects is associated with the formation of a eutectic solution and its subsequent crystallization.

3. The introduction of Bi_2O_3 suppresses the thermal effects.

References

1. D.E.Rase & Roy, J.Amer.Ceram.Soc., 38, No.3, 102 (1955).

2. E.K.Keler & N.B.Karpenko, Zhur.neorg.khim., No.4, 1125 (1959). (Trans. Russian Journal of Inorg.Chem.)

TECHNOLOGY AND PROPERTIES OF SOME CERAMIC FERROELECTRICS

- P.L.Strelets, I.A.Serova, N.D.Yatsenko & P.L.Markus

Piezoelectric ceramics of barium titanate are now extensively used in various fields of electronic engineering. Although these materials have a number of advantages over crystalline piezoelectrics, they also have a number of shortcomings: a phase transition at 8-10°, a relatively low Curie temperature, substantial loss in high fields, etc. These shortcomings of barium titanate stimulated a number of searches for superior piezoelectric ceramics.

Of particular interest in this field from our standpoint are the researches of Schofield & Brown[1], who investigated a solid solution of barium and calcium titanates doped with cobalt oxide, Smolenskii et al[2,3], who investigated lead metaniobate solid solutions, and Jaffe et al[4] who studied the PZT system. It must be noted that the data on the physical parameters of most of the new piezoelectric ceramics published by the cited authors were obtained for experimental specimens prepared under laboratory conditions and involving rather complicated synthesis procedures.

It is a familiar fact that conversion from laboratory methods of synthesis to industrial procedures often requires additional research. The present work was concerned with investigation and development of conditions of synthesis of the following ferroelectrics:

$$95\%\ BaTiO_3 + 5\%\ CaTiO_3 + 0.75\%\ CoCO_3,$$

$$40\%\ BaNb_2O_6 + 60\%\ PbNb_2O_6,$$

and

$$55\%\ PbZrO_3 + 45\%\ PbTiO_3.$$

In general, the process of industrial preparation of the new ceramics is based on the technology employed for barium titanate ceramics. However, specific adaptations of the technology had to be made for each of the new piezoelectric ceramics; in each case the modifications were dictated by the particular chemical composition of the ceramic.

The 95% $BaTiO_3$-5% $CaTiO_3$-0.75% $CoCO_3$ solid solution was synthesized not from previously prepared barium titanate and calcium titanate, but directly from the corresponding oxides and salts mixed in the appropriate proportions by weight. The synthesis was carried out at a temperature of 1300°, the holding time being 1/2 to 1 hour. The final sintering temperature was between 1440 and 1460°; the firing time varied from 2 to 3 hours depending on the weight of the charge.

In specifying the sintering time it must be borne in mind that with increase of the temperature and particular with increase of the firing time, the volatilization of the cobalt oxide increases sharply, which leads to deterioration of the piezoelectric and dielectric properties of the product.

A positive attribute of this composition is that it has a low chemical activity with respect to the kiln blocks, which are commonly made of clay, chamotte or alumina.

The final ceramic components were polarized at a temperature close to the Curie point (118°) at a field strength of 0.8 kv/mm either in air or in the silicone liquid "Kaloriya 2".

As regards many operations the industrial process of preparing the 40% $BaNb_2O_6$-60% $PbNb_2O_6$ solid solution is simpler than the technology of barium titanate. This solid solution was also synthesized directly from the corresponding salts and oxides; these were taken in appropriate proportions by weight, mixed and sintered at 1000°. Separate preliminary synthesis of the components is not expedient

Table 1

Batch No.	Impurity content, %	tan δ, %	ε	$d_{31} \cdot 10^8$ cgse units	$C \cdot 10^{-5}$, cm*	$E_Y \cdot 10^{-12}$ dyne/cm²	$\frac{d_{31}}{\varepsilon} \cdot 10^9$, cgse units	$E_Y \cdot d_{31}^2 \times 10^{-12}$ cgse units
9	SiO_2 — 0,22; TiO_2 — 0,98; K — 8,0; Fe_2O_3 — 0,1; F — 0,4; Al < 0,1; Na — 0,1; S — 0,02	Reaction did not occur						
15	SiO_2 — 0,085; TiO_2 — 1,07; K — 1,0; Fe_2O_3 — 0,13; F — 0,15; Al < 0,1; S — 0,17	2,2	1140	0,52	3,84	0,8	0,46	0,17
27	SiO_2 < 0,26; TiO_2 — 0,8; F — 0,1; K — 0,39; Fe_2O_3 — 0,4; Al — 0,42	1,0	2100	2,75	4,19	0,96	1,3	6,85
30	TiO_2 — 0,87; Fe_2O_3 — 0,44; K — 4,75; F — 0,12	1,8	1200	0,35	4,0	0,86	0,29	0,1
417	Ta_2O_3 — 0,03; SiO_2 < 0,002; TiO_2 — 0,01; Fe_2O_3 — 0,025	1,1	1350	2,2	4,05	0,91	1,63	4,9
533	Ta_2O_3 — 0,17; SiO_2 — 0,11; TiO_2 — 0,01; Fe_2O_3 — 0,025	1,8	1460	2,45	4,05	0,95	1,68	5,4
1041	Ta_2O_5 — 0,075; SiO_2 — 0,51; TiO_2 — 0,005; Fe_2O_3 — 0,005	0,8	1910	1,3	4,1	0,9	1,1	3,8

*The capacitance was measured at audio frequencies.

since it obviously requires more operations and does not yield any improvement in the properties of the final product.

The chemical composition of the niobium oxide used in preparing this ceramic has a significant influence on the piezoelectric and dielectric properties of the fabricated components. Technical niobium pentoxide is obtained by processing a metallic ore of complex composition, containing, in addition to the base material, many different impurities: TiO_2, ZrO_2, Ta_2O_5, K, Na, Fe_2O_3, Al_2O_3, SiO_2 and F.

In Table 1 we list the properties of ceramic specimens prepared from eight different experimental batches of niobium pentoxide, containing different amounts of impurities. Examination of the data shows that K, Na, F, Fe, Si and Al impurities severely impair the piezoelectric and dielectric properties of the final ceramic. On the other hand, it must be noted that comparatively pure Ni_2O_5 ($\leqslant 0.3\%$ impurities) also does not insure a product with the most desirable characteristics. Thus, there is apparently a certain proportion of impurities for which the resultant piezoceramic components have optimum properties. At present, however, we do not have sufficient data to make specific recommendations on the subject.

By way of plasticizer one can use either a water solution of polyvinyl alcohol or paraffin. Long components and those of complex geometric shape are best formed of mixtures plasticized with paraffin.

The ceramic components were sintered at 1260-1280°. So low a sintering temperature is a great advantage of this material as compared with other ferroelectric ceramics. The fact that lead metaniobate undergoes little or no thermal dissociation at 1000-1300° makes it possible to carry out the firing in air (rather than in a special atmosphere), which is also a positive feature. It was established by tests that the vaporization of lead oxide in the case of final sintering at 1280° does not exceed 1.5%. The sintering time may vary from 5 to 20 min, depending on the cross section of the ceramic component and the size of

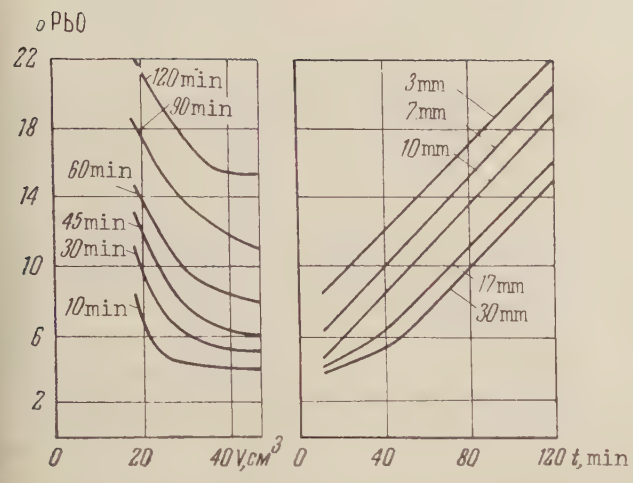

Fig.1. Variation of the volatilization of lead oxide with the thickness and volume of the specimen and the time of final sintering.

Table 2

Ceramic	Curie point, °C
$BaTiO_3$	120
95% $BaTiO_3$ — 5% $CaTiO_3$—0,75% $CoCO_3$	118
40% $BaNb_2O_6$— 60% $PbNb_2O_6$	290
55% $PbZrO_3$—45% $PbTiO_3$	390

the furnace charge.

In view of the fact that the 40% $BaNb_2O_6$ + 60% $PbNb_2O_6$ solid solution has a high Curie temperature and a high value of the coercive force, this ceramic must be polarized under "harder" conditions. We carried out polarization of this ceramic at 17-180° and 3-5 kv/mm.

The 55% $PbZrO_3$ + 45% $PbTiO_3$ solid solution merits particular attention; there are good reasons to assume that its characteristics are superior to many other similar materials.

Superficially, the technology of this ceramic differs little from that of synthesis of barium titanate. Although basically the technological operations are simple for the most part, one must note the difficulties that arise in synthesizing this material under industrial conditions. These difficulties are connected primarily with the appreciable volatility of lead oxide at temperatures above 1000°. Hence, unless appropriate measures are taken, the stoichiometric proportions observed in formulating the initial batch will not obtain in the final product.

As our tests showed, the amount of lead oxide volatilized depends on the temperature, the holding time, and the thickness and volume of the fired components. The variation of the amount of lead oxide volatilized as a function of the above factors is shown in Fig.1. Examination of the curves shows that the amount of lead oxide vaporized increases with increase of the sintering temperature and holding time; other conditions being equal, the amount of lead oxide volatilized decreases with increase in the cross section and volume of the specimens.

On the basis of these experimental data one can calculate for any specific conditions how much excess lead oxide must be added prior to final sintering in order to obtain components with the desired composition. This matter of allowing for the volatilization of lead oxide is the principal difference between the technology of piezoelectric ceramics of this type and the technology of barium titanate ceramics.

Using the developed, modified procedures we prepared specimens of the enumerated compositions, determined their Curie points and measured their dielectric and piezoelectric properties in the temperature range from -50 to +50°. The values of the Curie points are listed in Table 2 together with the value for barium titanate.

In Fig.2 we show the temperature dependences of the principal parameters of barium titanate and the synthesized piezoelectric materials, namely, the dielectric constant, the piezoelectric coefficient d_{31}, and the temperature shift

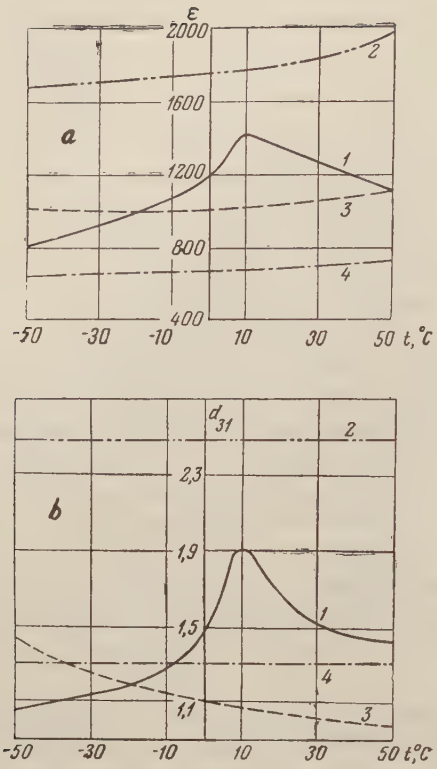

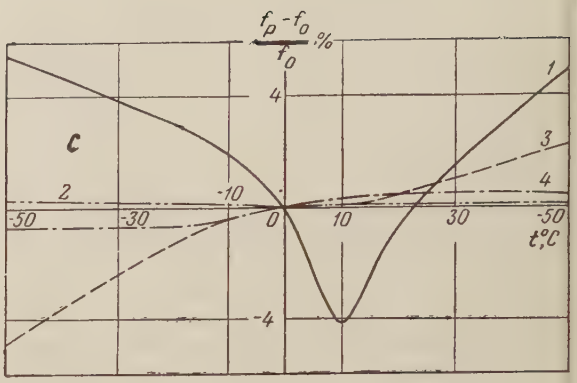

Fig.2. Temperature dependences of the parameters ϵ_1 (a), d_{31} (b) and $(f_p - f_o)/f_o$ (c) for different ceramics: 1) $BaTiO_3$, 2) 40% $BaNb_2O_6$ + + 60% $PbNb_2O_6$, 3) 95% $BaTiO_3$ + 5% $CaTiO_3$ + 0.75% $CoCO_3$, 4) 55% $PbZrO_3$ + 45% $PbTiO_3$.

of the resonance frequency from the value at 0°. It will be evident from the curves that the new caramics are in many respects superior to barium titanate.

References

1. Schofield & Brown, Can.J.Phys., 35, 378 (1959).
2. G.A.Smolenskii, V.A.Isupov & A.I.Agranovskaya, Fizika tverdogo tela, 1, 3, 442 (1959). (Trans.Soviet Physics - Solid State.)
3. V.A.Isupov & V.I.Kosyakov, Zhur.tekhn.fiz., 28, 10, 2175 (1958). (Trans. Soviet Physics - Technical Physics.)
4. B.Jaffe, B.S.Roth & S.Marzullo, J.Appl.Phys., 25, 6, 809 (1954).

RAPID PROCEDURE FOR PREPARING AND INVESTIGATING FERROELECTRIC CERAMICS

- O.P.Kramarov

Research in the field of synthesis and investigation of ferroelectric ceramics generally involves the preparation of a large number of specimens. Also it is necessary to determine by trial and error the optimum sintering temperature for each synthesized composition. All this involves a great expenditure of time inasmuch as the roasting cycle for each specimen requires a minimum of 8-10 hours.

Vekshinskii[1] developed a new procedure for metallographic investigation of alloys using specimens of varying composition. Use of a similar procedure could greatly accelerate exploratory research in the field of ferroelectric materials.

We tested a number of different methods for preparing ceramic specimens of varying composition.

The best results were obtained by means of the equipment diagramed in Fig.1. The wedge-shaped hoppers 2 and 4 are rigidly mounted in the frame 6 which also carriedsseveral sifting-scattering screens 5. The bottom opening of hopper 2 is covered with a screen of appropriate mesh. The bottom opening of hopper 4 is open. Into this hopper there can be inserted interchangeable inserts 3 of the same shape as the interior of the hopper but somewhat shorter. The bottom openings of the inserts are also covered with screens. Hopper 2 and insert 3 are filled with the raw materials or mixtures A and B of which the specimen is to be prepared. Insert3, which has the larger bottom area, is commonly charged with the less freely flowing powder. The opening areas are designed so that the emptying of the hopper and insert will occur simultaneously.

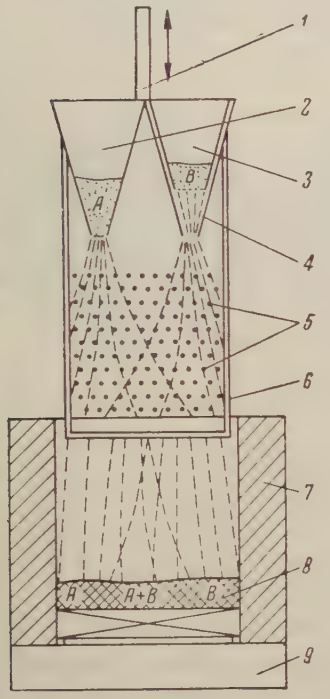

Fig.1

The entire assembly - hoppers, frame and screens - is jiggled vertically by means of an electromagnetic vibrator (not shown) connected to the top end of rod 1. The powders dropping from the hoppers are scattered by the screens and distributed over the bottom 9 of the square cross section die mold 7. Thus there is obtained a specimen 8 of varying composition. After deposition of a layer of the requisite thickness (to obtain a specimen 2-3 mm thick after compression), the specimen is compressed in the mold and then roasted in a conventional furnace at 1000-1100° to give it the requisite mechanical strength. Then the specimen is transferred to the special gradient furnace, the design of which is shown in Fig.2.

As a result of roasting in such a furnace there is obtained a specimen in which the composition varies in one direction and the sintering temperature varies in the other. Thus, the plane of the specimen essentially represents the system of coordinates: composition vs sintering temperature. Hence applying an appropriate square matrix of electrodes, one can on the same specimen investigate the dielectric properties of a number of different compositions depending on the sintering temperature.

For measuring the basic parameters of such specimens it is convenient to use complex equipment consisting of a thermal dielectrograph with an appropriate galvanometer and a nonlinearity tester. The first instrument allows of obtaining on a photographic plate curves characterizing the temperature variation of the dielectric constant. The nonlinearity tester allows of observing on the screen of an oscillograph the variation of the impedance of the specimen at a frequency of 20 kc

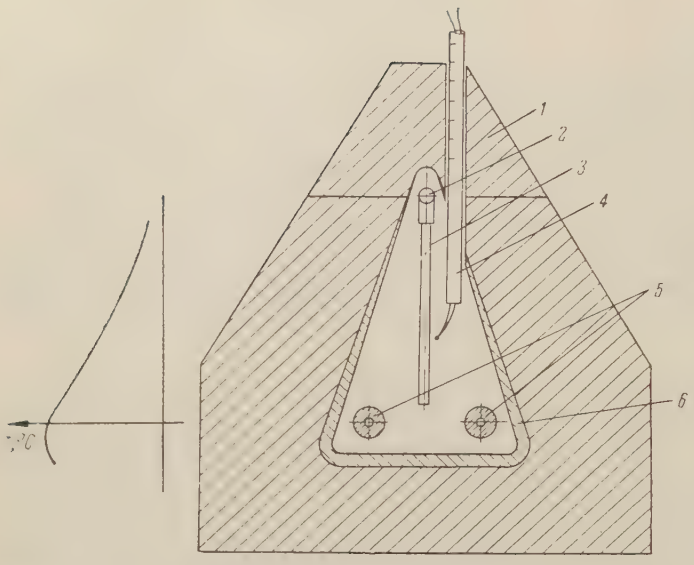

Fig.2. Gradient furnace: 1) foam fireclay insulation, 2) porcelain rod for suspending specimens, 3) specimen, 4) thermocouple, 5) Silit rod heaters, 6) high alumina lining. The diagram at the left gives the temperature distribution inside the furnace.

as a function of the instantaneou value of the 50 cps biasing field.

With the given procedure for preparing specimens of varying composition the distribution of components along the specimen remains unknown. This distribution can be determined either by spectroscopic analysis or in the following manner. There is prepared a specimen of $BaTiO_3$-$SrTiO_3$ (or some other thoroughly studied system). Then the Curie points are determined in steps across the specimen and from these the compo nent concentrations are inferred. In determining the corresponding concentrations in unknown composi tions, it is assumed that for the given design of the hoppers and scattering screens the distribution remains constant. For more detailed study of the composition region of greatest interest one can prepare a new specimen using the limit mixtures instead of pur initial components.

Use of a gradient furnace is in itself worthwhile even in the case of specimens of uniform composition. The design of the furnace in this case can be somewhat different[2,3].

Thus, use of a gradient furnace enabled us to detect anomalies in ceramic specimens sintered in the 1170 to 1210° range. In these experiments, long, narrow $BaTiO_3$ specimens were placed in the gradient furnace so that individual zones of the specimens were roasted at temperatures ranging from 800 to 150 As a result of such roasting there always appears in a relatively narrow region (50-60°) appreciable expansion of the specimen, whereas the rest of the specimen exhibit normal shrinkage, the degree of which increases with increase of the temperature. A photograph of one such specimen is reproduced in Fig.3. An expanded region always appears regardless of the initial materials and the preliminary (synthesis) roasting temperature. These particular experiments were carried out on specimens prepared of "paint pigment" and "capacitor" grade TiO_2 and different lots of $BaCO_3$. An expanded region appears in all specimens regardless of deviations from stoichiometry and variation in the preliminary roasting temperature.

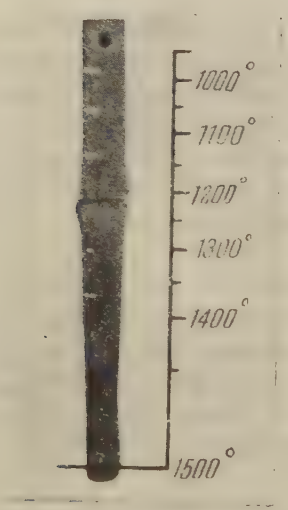

Fig.3. Barium titanate specimen sintered in a gradient furnace; the scale at the left gives the sintering temperature.

Microanalysis of the structure of the specimens showed an entirely different character of the individual crystallites in the temperature regions above and below the temperature of expansion. Micrograms of the surface structure in zones roasted at different temperatures are reproduced in Fig.4. (In order to illustrate the varia-

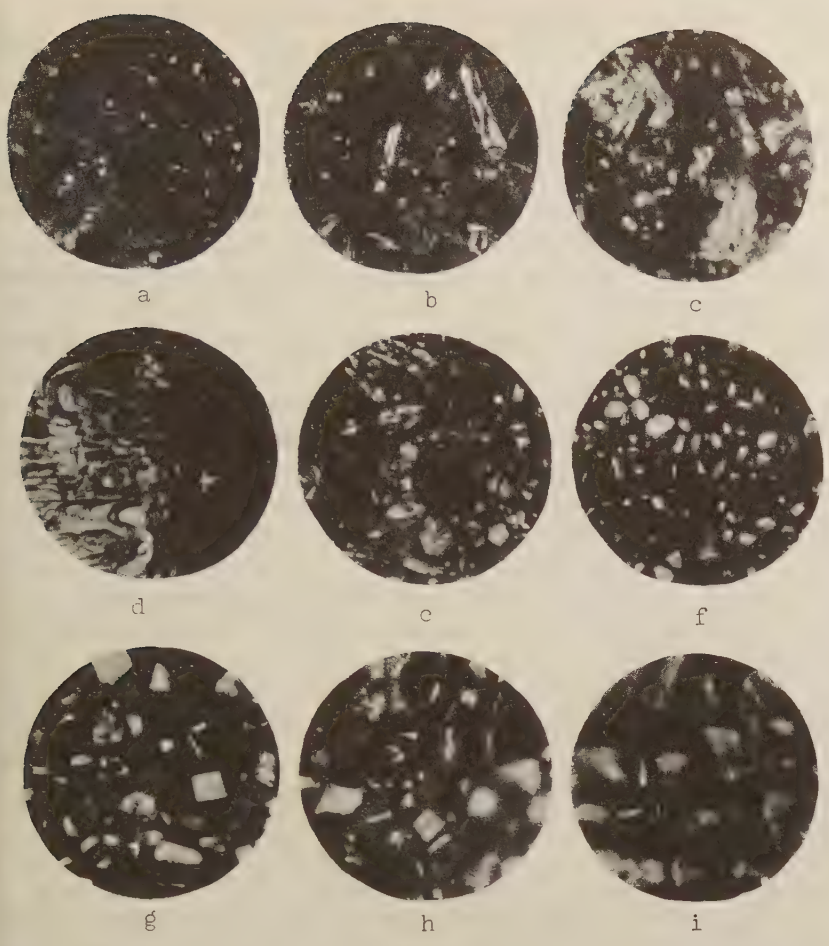

Fig.4. Micrograms of the surface structure of specimen sections sintered at different temperatures: a) $t = t_{ex} - 60^{o}$, b) $t_{ex} - 10^{o}$, c) $t_{ex} - 5^{o}$, d) t_{ex}, e) $t_{ex} + 10^{o}$, f) $t_{ex} + 30^{o}$, g) $t_{ex} + 50^{o}$, h) $t_{ex} + 90^{o}$, i) $t_{ex} + 110^{o}$. t_{ex} = temperature of maximum expansion.

tion in structure more clearly, we have used photographs of typical structures obtained in different specimens.) Inasmuch as the temperature at which maximum expansion occurs fluctuates somewhat from specimen to specimen*, the temperatures in the caption are indicated relative to the maximum expansion temperature.

As will be evident from the photographs, in the vicinity of the expansion region the structure of the specimen varies markedly with the sintering temperature. Up to temperatures 50-60° below the expansion point, the structure of the specimen remains unchanged, i.e., identical with that formed during the initial roasting. With increase of the sintering temperature there begin to appear crystalline formations of acicular habit (Fig.4,b). With a few degrees increase of roasting temperature these formations begin to branch out, forming distinct intrusions (Fig.4,c). At the point of maximum expansion there sometimes forms a close-packed interlocking acicular structure (Fig.4,d). A few degrees above the zone of maximum expansion the acicular structure breaks up and transforms into individual, for the most part regularly, faceted crystals (Fig.4,e). Then the acicular structure disappears entirely. The small crystals increase in size, while retaining their regular faces (Fig.4,f). When examined by polarized light many of these crystallites show domain structure. With further increase of the temperature (Fig.4,g-i) the regular faceting of the grains breaks down; they become rounded and tend to merge.

The temperature dependences of the dielectric constant of $BaTiO_3$ specimens taken from the expansion region are shown in Fig.5.

Preliminary x-ray diffraction studies disclosed no singularities of the crystal lattice in the expansion zone.

---

*Possibly this scatter is due to errors in determining the temperature distribution along the specimen.

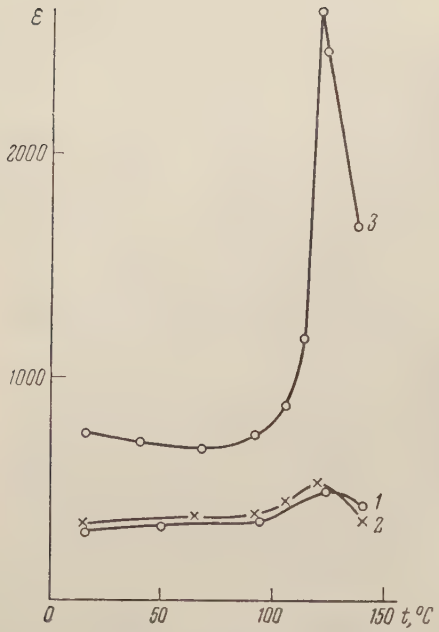

Fig.5. Temperature dependences of the dielectric constant of $BaTiO_3$ specimens taken from different regions: 1) 1150-1160° zone, 2) 1160-1180° (maximum expansion) zone, 3) 1180-1200° zone.

At present it is difficult to suggest an explanation of the observed effect. Similar expansion of metal specimens prepared by powder metallurgy techniques has been observed by a number of authors[4]. In this case, also, the reason for the anomalous behavior is not known. For ceramic it may be assumed that at low temperatures there occurs nonequilibrium growth of crystallites, leading to the formation of dendrites which "bulg the specimen.

The process of expansion proceeds rather rapidly (for some specimens expansion takes place within 15-20 min). This factor must be taken into account in producing ferroelectric ceramics. In order to reduce rejects due to cracking and excessive porosity the furnace temperature should be raised rapidly through the 1170-1210° range, wherein expansion occurs.

I desire to express my deep gratitude to A.L.Khodakov for assistance and guidance in the work.

Physical-Mathematical Scientific Research Institu
at
Rostov-on-the-Don State University

References

1. S.A.Vekshinskii, Novyi metod metallografii cheskogo issledovaniya splavov (New method of metallographic investigation of alloys), M., 1944.

2. O.P.Kramarov, Kristallografiya 4, 109 (1959). (Trans.Soviet Physics - Crystallography.)

3. V.Satava & K.Stransky, Silikaty, 3, 343 (1959).

4. G.A.Gich, in "Uspekhi fiziki metallov" (Advances in the physics of metals Vol.1, p.120, M., 1956.

HIGH-TEMPERATURE PIEZOELECTRIC ACCELEROMETER SENSING ELEMENTS

- M.M.Kachkacheva, A.A.Dryabchuk, L.Z.Rusakov & E.G.Smazhevskaya

In the past few years we have designed a number of piezoelectric accelerometers with sensing elements of barium titanate ceramic.[1] Using these transducers, it was possible to extend the working range to the side of higher frequencies and reduce the dimensions and weight of the sensing unit as compared with transducers of other types. Depending on the purpose and requirements involved, the units can be designed ranging from 5 to 50 g in weight with a sensitivity from 1 to 15 mv/G and capable of measuring accelerations of up to 300 G at frequencies to 10 kc. The lower bounds of the measurable accelerations and frequencies are determined by the parameters of the indicator equipment.

It must be noted, however, that measurements by means of these units are limited to temperatures of the order of 70-80°, i.e., to under temperatures close to the phase transition point of barium titanate ceramic, temperatures at which the ceramic begins to depolarize with resultant decrease in sensitivity.

In connection with the increasing need for measuring vibrations at higher temperatures, we felt it would be desirable to increase the upper bound of the useful temperature interval. The possibility of extending the temperature range of piezoelectric transducers is determined primarily by the parameters of the piezoelectric ceramic. Accordingly, there were prepared and investigated solid solutions of barium, calcium and lead titanates $(Ba,Ca,Pb)TiO_3$ (Ref.2) and solid solutions of lead and barium metaniobates $(Pb,Ba)Nb_2O_6$ (Ref.3) with different proportions of the components, inasmuch as these solid solutions are characterized by higher transition points.

There were prepared and tested piezoelectric transducers with sensing elements made of $(Ba_{0.797},Ca_{0.083},Pb_{0.12})TiO_3$ solid solution, which has a Curie temperature of 140-160°. These acceleration pickups can operate at temperatures of up to 110-130° without loss in sensitivity. However, the piezoelectric coefficients of this composition are small compared with the piezoelectric coefficients of barium titanate ceramic; hence the sensitivity of these units proved to be about half that of units with elements of $BaTiO_3$.

After successful development of lead and barium metaniobate piezoceramic materials with a Curie temperature of 270° and a piezoelectric coefficient $d_{31} \approx$ $\approx 2.0 \cdot 10^{-6}$ cgse units, there were prepared piezoelectric pickups with sensitive elements made of this material.

As in the earlier pickup units, the sensitive element was made in the form of a ring. The ring is polarized so that it operates in shear. To this end temporary electrodes are first applied to the upper and lower faces of the ring and the ring is polarized along this axis. After polarization, the temporary electrodes are removed and permanent working electrodes are applied to the inner and outer surfaces. Under the influence of shear strains there appear on these electrodes charges with a proportionality factor equal to the piezoelectric coefficient d_{15}. No other mechanical stresses can give rise to charges on the working electrodes and, consequently, the sensitivity of the pickup to transverse vibrations is virtually nil.

A general view of the high-temperature acceleration pickup is shown in Fig.1; its design is diagramed in Fig.2. The piezoelectric element is housed in a duraluminum case. The sensitive element, which is made of $(Pb_{0.6},Ba_{0.4})Nb_2O_6$ ceramic, is mounted in the case so that under the influence of vibrations directed along the axis of the unit there appears on the electrodes a voltage proportional to the shear deformation. The ceramic ring is mounted in the case by means of epoxy cement. The brass weight, which serves as the inertial mass, is also cemented into the ring.

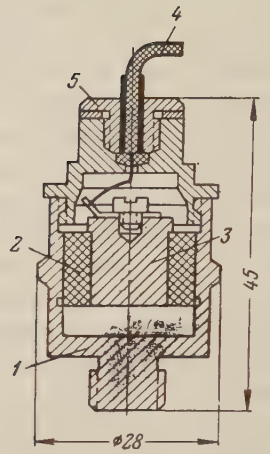

Fig.2

Fig.1. High-temperature piezoelectric pickup.
Fig.2. Design of the high-temperature piezoelectric pickup: 1) base, 2) piezoceramic ring, 3) brass weight, 4) lead, 5) cover.

The assembled pickup, owing to its unitary construction, is capable of withstanding overloads of up to 300 G. The sensitivity of the unit, which has a weight of only 50 g, is 10 mv/G. The sensitivity to transverse vibration is much lower (5-6% of the axial sensitivity). Units of the same basic design can be prepared with greater sensitivity but with some increase in weight, or with less weight but some sacrifice of sensitivity.

The frequency and temperature dependences of the sensitivity of the high-temperature pickup units with sensing elements of $(Pb_{0.6},Ba_{0.4})Nb_2O_6$ ceramic are shown in Figs.3 & 4. For purposes of comparison in the same figures we give the comparative data for piezoelectric units with sensing elements of $(Ba_{0.797},Ca_{0.08}Pb_{0.12})TiO_3$ and $BaTiO_3$. The design dimensions and weights of all the units are the same. In determining the sensitivity, the output voltage was measured by means of an instrument with an input resistance of 15 megohm, hence the frequency characteristics are given from a frequency of 50 cps. It will be evident from Fig.3 that the frequency characteristics of the sensitivity and the absolute sensitivity of the high temperature $(Pb_{0.6},Ba_{0.4})Nb_2O_6$ pickup unit are virtually the same as those of pickups with a sensing element of barium titanate ceramic. The absolute sensitivity of the unit with a sensing element of the ternary system ceramic is only about half the sensitivity of the high-temperature units.

As will be evident from Fig.4, the pickups with sensing elements of $BaTiO_3$

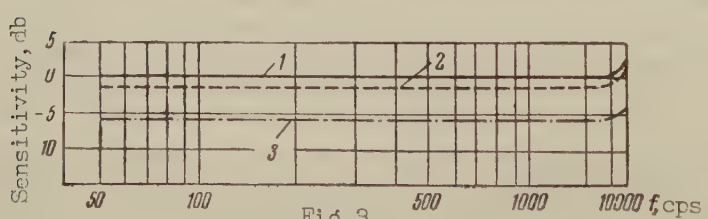

Fig.3

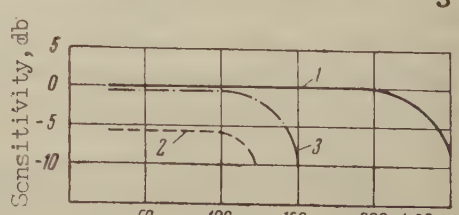

Fig.4

Fig.3. Frequency characteristics of the pickup units with sensing elements of 1 - $(Pb_{0.6},Ba_{0.4})Nb_2O_6$, 2 - $BaTiO_3$, and 3 - $(Ba_{0.797},Ca_{0.083},Pb_{0.12})TiO_3$.
Fig.4. Temperature characteristics of the sensitivity of pickup units with sensing elements of 1 - $(Pb_{0.6},Ba_{0.4})Nb_2O_6$, 2 - $BaTiO_3$, and 3 - $(Ba_{0.797},Ca_{0.083},Pb_{0.12})TiO_3$.

and $(Ba_{0.797},Ca_{0.083},Pb_{0.12})TiO_3$ can operate satisfactorily only up to a temperature of 80 and 110°, respectively. In contrast, the sensitivity of the transducer with the $(Pb_{0.6},Ba_{0.4})Nb_2O_6$ element does not decrease up to 200°. With further increase of the temperature, the sensitivity gradually falls off and at a temperature of 220-230° decreases by 15-20% relative to the sensitivity at 20-30°. In the course of testing, the high-temperature units were held for 3 days at 200°, after which their sensitivity and frequency characteristics were rechecked. The repeat tests showed no significant change in the absolute value of the sensitivity and the frequency characteristics.

References

1. L.Z.Rysakov & M.M.Kachkacheva, Trudy nauchno-tekhnicheskoi konferentsii po vibrostendam i vibroizmereniyam (Transactions of the scientific-technical conference on vibrotesters and vibration measurement), Part II, p.17, L., 1960.

2. W.Mason & R.Wick, Ferroelectrics and Dielectric Amplifiers, Proc.IRE, 11, 1606 (1954).

3. G.A.Smolenskii, V.A.Isupov & A.I.Agranovskaya, Doklady AN SSSR, 108, 232 (1956). (Trans.Doklady.)

Bulletin of the Academy of Sciences of the USSR - Physical Series
Vol. 24, No. 10 - October 1960

Transactions of the Third Conference on Ferroelectricity
(to be continued in Vol. 24, No. 11)

TABLE OF CONTENTS

	Page Orig.	Trans.
Contribution to the statistical theory of ferro- and antiferroelectrics - V.I.Klyachkin	1176	1179
Contribution to the thermodynamic theory of ferroelectricity - V.L.Indenbom	1180	1183
Thermodynamics of solid solutions with ferroelectric properties - V.G.Granovskii	1184	1187
Internal fields in some ferro- and antiferroelectric model structures based on $BaTiO_3$ - N.N.Krainik	1187	1190
Method of calculating the internal electric fields in complex dipole structures and application of the method to $CaTiO_3$ - S.P.Solov'ev, Yu.N.Venevtsev, G.S.Zhdanov & V.V.Ivanova	1191	1194
Investigation of some ferroelectrics by the method of nuclear magnetic resonance - A.G.Lundin, K.S.Aleksandrov, G.M. Mikhailov & S.P.Gabuda	1195	1198
X-ray diffraction studies of some new ferroelectrics with laminar structure - I.G.Ismailzade	1198	1201
Preparation and ferroelectric properties of deuterated triglycine sulfate crystals - V.P.Konstantinova, I.M.Sil'vestrova, L.A.Shuvalov & V.A.Yurin	1203	1206
On the ferroelectric properties of $NaNO_2$ - A.S.Sonin, I.S. Zheludev & G.F.Dobrzhanskii	1209	1212
Concerning light detectors utilizing the pyroelectric effect - I.M.Sil'vestrova	1213	1216
Damping of the oscillations of piezoelectric resonators employing ferroelectric single crystals - L.A.Shuvalov & Yu.S. Likhacheva	1216	1219
Oscillations of dielectric pendulums and polarization of ferroelectrics - I.S.Zheludev	1225	1227
Dielectric and calorimetric investigation of ammonium sulfate and ammonium fluoberyllate crystals - V.A.Koptsik, B.A.Strukov, A.A.Sklyankin & M.E.Levina	1228	1230
Investigation of the optical properties of some ferroelectric crystals - V.A.Koptsik, B.A.Strukov & I.K.Nevedomskaya	1231	1233
Some physical properties of ferroelectric $BaTiO_3$-$PbTiO_3$, $BaTiO_3$-$BaSnO_3$ and $BaTiO_3$-$PbTiO_3$-$BaSnO_3$ single crystals - S.V.Bogdanov, G.M.Kovalenko & A.M.Cherepanov	1234	1236
$BaTiO_3$-$BaSnO_3$ solid solution single crystals - A.L.Khodakov & M.L.Sholokhovich	1238	1240
Preparation and structure of crystals of some lead-containing ferroelectric substances and their solid solutions - M.L. Sholokhovich & E.G.Fesenko	1242	1244
Semiconductor properties of $BaTiO_3$ - S.V.Bogdanov & V.A.Rassushin	1247	1248
Growing ferroelectric single crystals from melts - O.P.Kramarov	1251	1251
Concerning the electric conductivity of barium titanate and some barium titanate base solid solutions - E.V.Sinyakov & B.K. Chernyi	1255	1254

Possibility of controlling the conductivity of lead metaniobate by doping - V.M.Gurevich & I.S.Rez	1259	1258
Some physical properties of vacuum annealed polycrystalline barium titanate - A.V.Chebkasov	1261	1259
Influence of compression on polarization processes in ferro-ceramics - V.Z.Borodin	1264	1262
Some physical properties of ferroelectric lead ferroniobate and ferrotantalate - V.A.Isupov, A.I.Agranovskaya & N.P. Khuchua	1271	1268
Physical-chemical investigation of the formation of complex ferroelectrics with the perovskite structure - A.I.Agranovskaya	1275	1271
Electric properties of some solid solutions of divalent metal niobates and tantalates - P.S.Mikhailov & B.A.Rotenberg	1282	1278
Concerning ways and means of obtaining materials with a smoothed out temperature dependence of the dielectric constant - N.A. Andreeva, O.A.Grushevskaya & V.I.Zhukovskii	1285	1281
Solid solutions in the ternary ferroelectric system $Ba(Ti,Zr,Sn)O_3$ - M.M.Nekrasov & Yu.M.Poplavko	1289	1284
Preliminary report on a ferroelectric ceramic with a dielectric constant of 80 000-100 000 - T.N.Verbitskaya, L.M.Aleksandrova & L.S.Sinitsina	1291	1286
Results of thermal analysis of doped barium titanate - V.I. Zhukovskii, M.P.Dorokhova, N.E.Zaremba, D.G.Dykman & G.V.Bois	1294	1289
Technology and properties of some ceramic ferroelectrics - P.L. Strelets, I.A.Serova, N.D.Yatsenko & P.L.Markus	1296	1291
Rapid procedure for preparing and investigating ferroelectric ceramics - O.P.Kramarov	1300	1295
High-temperature piezoelectric accelerometer sensing elements - M.M.Kachkacheva, A.A.Dryabchuk, L.Z.Rusakov & E.G.Smazhev-skaya	1304	1299

Translated in 1961 by
Columbia Technical Translations
5 Vermont Ave., White Plains, N.Y.

Transactions

of the

Third Conference on Ferroelectricity

(Moscow, January 25-30, 1960)

(Concluded from Vol.24, No.10)

TEMPERATURE DEPENDENCE OF THE INFRARED ABSORPTION SPECTRA OF $BaTiO_3$, $PbTiO_3$ AND $PbZrO_3$

- A.F.Yatsenko

Some authors associate the ferroelectric effects occurring in barium titanate with the specific temperature behavior of one of the optical modes of the lattice vibrations of the material.

Of the three optical frequencies characteristic of the perovskite lattice, only two have been observed[1,2], namely, the frequencies associated with the valence (stretching) and deformation (bending) vibrations of the $Ti(O/2)_6$ octahedron; the third frequency, associated with the external translational vibrations (motion of the cation relative to the TiO_3 group), is located somewhere in the far infrared and so far has not been observed owing to great experimental difficulties. This frequency was not detected in the Raman spectrum, apparently owing to the almost cubic symmetry of the $BaTiO_3$ lattice, and has not been found so far among the electronic-vibrational transitions in $BaTiO_3$ activated with rare earths.[3]

Anderson[4] assumes that with approach to the Curie temperature, the frequency of one of the limit vibrations decreases and goes to zero at the Curie point. Ginzburg[5] also infers temperature drift of the frequency of the external translational vibrations of the Ba ions relative to the oxygen octahedra.

In view of this, investigation of the temperature behavior of the absorption bands of ferroelectrics with the perovskite lattice is of particular interest.

In our earlier study[6] of the temperature variation of the absorption spectrum of $BaTiO_3$ it was noted that the deformation vibration band does not exhibit any characteristic "ferroelectric" anomalies and hence our attention was concentrated on investigating the temperature behavior of the valence vibration band. As a rule the valence vibration band of perovskite type ferroelectrics is noticeably broadened and exhibits fine structure. In Fig.1 we show for comparison the absorption bands of the ferro- and antiferroelectric materials $BaTiO_3$, $PbTiO_3$, $PbZrO_3$ and WO_3 and nonferroelectric $SrSnO_3$, characterized by relatively narrow and symmetrical bands.

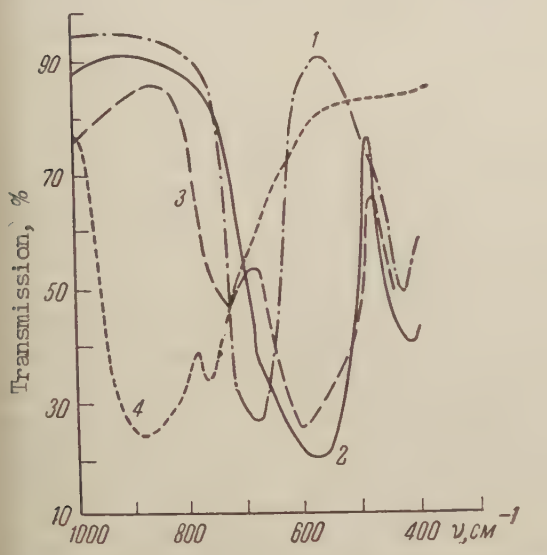

Fig.1. Absorption bands associated with the valence (stretching) and deformation (bending) vibrations of the $Ti(O/2)_6$ octahedron in different dielectrics: 1) $SrSnO_3$, 2) $BaTiO_3$, 3) $PbTiO_3$, 4) WO_3. Effective specimen thickness 1-1.5 μ.

In Ref.6 we described the temperature behavior of the valence band of $BaTiO_3$ and indicated that its fine structure undergoes substantial changes. The barely noticeable shoulder at room temperature, with increase of the temperature, transforms to a discrete narrow valence vibration band, which disappears above the Curie point. The low frequency satellites of the valence bands of $PbTiO_3$ and $PbZrO_3$ (Fig.2) behave in a similar fashion. The spectra of the last, in addition, comprise a "lead" satellite (on the high frequency side of the valence vibration band), which is observed in all perovskites containing lead. This satellite decreases in intensity with increase of the temperature but with no anomalies at the Curie point.

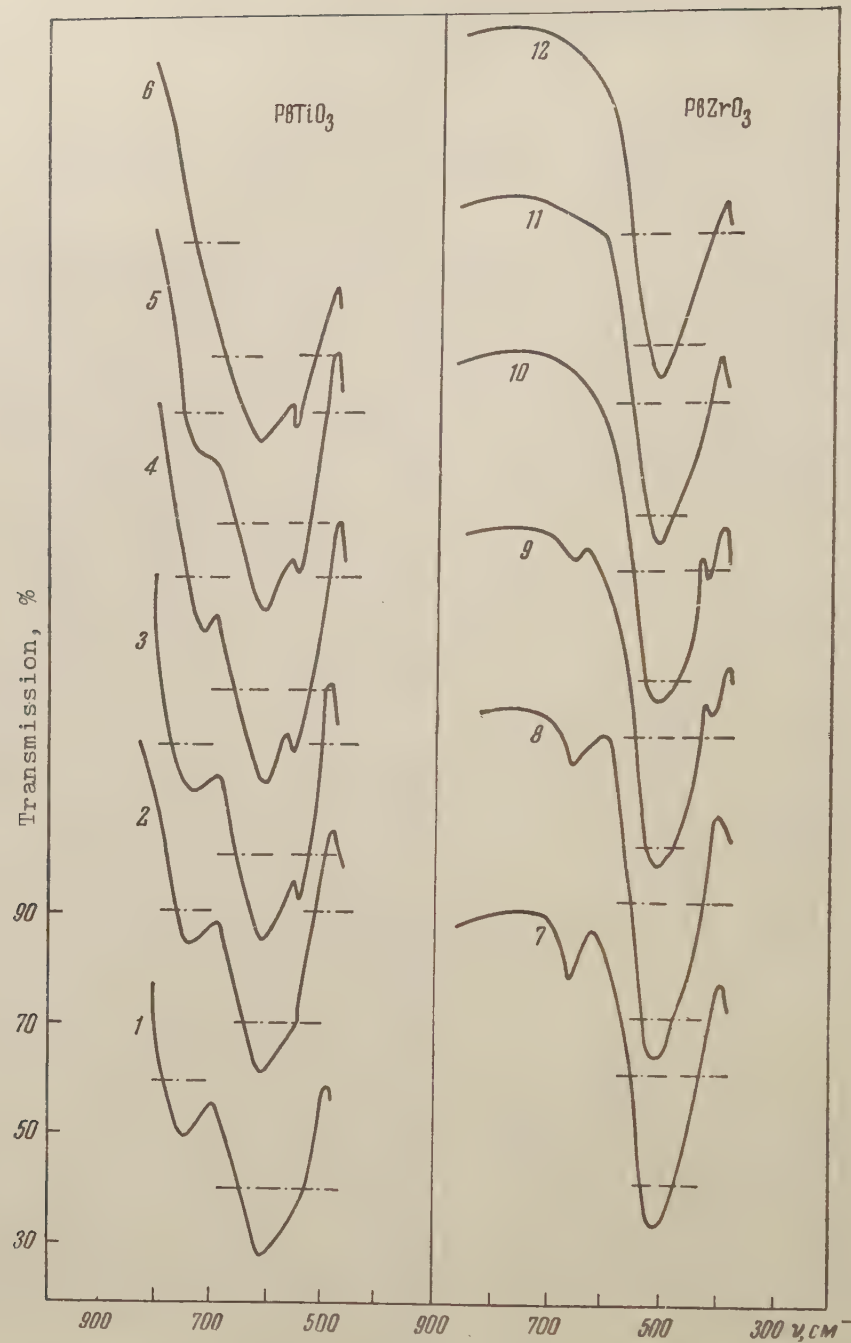

Fig.2. Temperature dependence of the absorption in the valence vibration band of $PbTiO_3$ and $PbZrO_3$: 1) 18°, 2) 100°, 3) 150°, 4) 220°, 5) 270°, 6) 400°, 7) 18°, 8) 100°, 9) 175°, 10) 200°, 11) 250°, 12) 300°C. The dash-dot lines on each spectrum indicate the 60 and 40% transmission levels.

When the normal vibrations of a lattice consisting of rigid ions are regarded as harmonic, the dipole moment of the crystal proves to be a linear function of the lattice displacements. Different lattice waves do not interact with each other, but the electromagnetic waves interact independently with each individual lattice wave and can be absorbed when the usual conditions as regards frequency, wave number and polarization are satisfied. In this approximation the infrared

spectrum should consist of narrow lines. Experiment shows, however, that the spectra comprise broad bands often accompanied by side peaks on one or both sides.

Born & Huang[7] were the first to show that the finite width of the bands is due to third order terms of the potential $V = \frac{1}{2}\sum c_{ij}q_iq_j + \sum c_{ijk}q_iq_jq_k + \sum c_{ijkl}q_iq_jq_kq_l$, which provide a coupling channel between the normal vibrations, while second order terms of the dipole moment $M = \alpha_0 q_0 + \sum \beta_{ij}q_iq_j + \sum \gamma_{ijk}q_iq_jq_k + \cdots$ are responsible for the intensity of the satellites. Burstein et al[8], analyzing the data for different ionic crystals, came to the conclusion that the intensity of the side peaks and the width of the main band increase with increasing deviation of the elastic constants from the Cauchy relation and increase of the electronic polarizabilities, i.e., increase in the same measure as the deformability of the electron shells. To us this parallelism appears very strange. Recently, Szigetti[9] showed that one cannot consider high order terms of the electric moment independently of high order terms of the potential, and thus was able to explain the above mentioned parallelism in the properties of the absorption bands and the deformability of the electron shells.

From the character of the ionic displacements in different normal vibrations of the $BaTiO_3$ lattice[1,2] it follows that what is significant from the standpoint of the valence vibrations of the $Ti(O/2)_6$ octahedron is nonlinearity of the dipole moment, which is responsible for broadening of this band and the appearance of side absorption peaks. Thus the temperature behavior of the satellites is direct evidence of temperature dependence of the deformability of the electron shells.

Aside from the above, no other manifestations of ferroelectricity were observed, at least where the two vibration modes of the octahedron are concerned. There are good experimental reasons to infer that the third absorption band, associated with external translation vibrations of the Ba ions relative to the oxygen octahedra, also will not exhibit anomalous temperature behavior (for example, frequency drift). In view of this it would be highly interesting to obtain direct experimental data on the temperature behavior of this band.

I take this opportunity to thank S.P.Rubtsova who participated in the spectroscopic measurements.

Rostov-on-the-Don State University

References

1. J.T.Last, Phys.Rev., 105, 1740 (1957).
2. A.F.Yatsenko, Izv.AN SSSR, Ser.fiz., 22, 1456 (1958). (Trans.Bulletin, 22, 1450.)
3. A.F.Yatsenko & L.M.Rabkin, Present issue of the Bulletin, p.1313.
4. P.Anderson, Fizika dielektrikov (Transactions of the Second All-Union Conference on the Physics of Dielectrics, 1958). Pub.M.1960.
5. V.L.Ginzburg, Fiz.tv.tela, 2, 2031 (1960). (Trans.Sov.Phys. - Solid State.)
6. A.F.Yatsenko, Fizika dielektrikov (Transactions of the 2nd All-Union Conference on the Physics of Dielectrics, 1958), M.1960.
7. M.Born & Kun Huang, Dynamical Theory of Crystal Lattices, Oxford,1954. (Cited in Russian trans.)
8. E.Burstein, J.J.Oberly & E.K.Plyler, Proc.Indian Acad.Sci., 28, 338 (1948).
9. B.Szigetti, Proc.Roy.Soc. A252, 217 (1959).

SOME ELECTRIC PROPERTIES OF BARIUM TITANATE DOPED WITH RARE EARTH ELEMENTS

- A.F.Yatsenko & T.P.Popova

A number of authors[1-3] have recently reported that barium titanate containing small amounts of oxides of the rare earth elements (RE) exhibits interesting electrical properties. These may be due to the fact that the RE activator atoms have incomplete inner (4*f*) shells. To investigate the influence of RE impurities on the electric properties of $BaTiO_3$ we prepared a series of specimens containing from 0.1 to 3 mole percent of the following oxides: Sm_2O_3, Pr_2O_3, Nd_2O_3, Yt_2O_3, Tb_2O_3, Dy_2O_3, Er_2O_3, Lu_2O_3, Tm_2O_3, Yb_2O_3 and Gd_2O_3 (see table).

Some characteristics of RE doped $BaTiO_3$

RE (oxide)	Impurity content, %	ε_o	ε_θ	$\varepsilon_\theta/\varepsilon_o$	tan δ	θ, °C	Activation energy, ev
Sm	0,1	2575	5770	2,24	0,175	130	0,24
	0,3	1900	6120	3,22	0,078	130	0,74
	1	2850	5700	2	0,09	98	0,7
	3	5020	6350	1,27	0,78	41	0,78
Pr	0,1	1500	7850	5,24	0,09	122	0,84
	0,3	2300	6750	2,9	0,099	119	0,8
	1	3100	4500	1,45	0,098	100	0,7
	3	3650	3950	1,08	0,072	45	0,6
Yb	0,1	1670	3900	2,33	—	124	0,3
	0,3	1900	3800	2	—	124	0,77
	1	1500	3450	2,3	—	96	0,6

The specimens were prepared by the usual ceramic procedure; the preliminary roasting temperature was 1280°; the final sintering was carried out at 1380° for a period of 1-2 hours. It must be noted that generally barium titanate specimens with RE impurities sinter poorly and even increasing the final sintering temperature does not always result in complete sintering. Introduction of RE into previously prepared $BaTiO_3$ is even more difficult.

In most cases small amounts of RE stabilize the tetragonal phase. Thus we were unable to obtain hexagonal barium titanate even from melts when the material contained 0.5% Pr or Sm, and only in the case of 0.3% Gd and 0.1% Yb did we observe partial transition to the hexagonal phase.

We recorded the temperature dependences of the dielectric constant and the loss tangent at V = 50 v and f = 1 kc for all the specimens.

The values of the dielectric constant at room temperature, ϵ_o, and at the Curie point, ϵ_θ, tan δ, the Curie temperature θ and the ratio $\epsilon_\theta/\epsilon_o$ are listed in the table. As will be evident from the table a significant shift of the Curie point occurs in specimens containing Sm_2O_3, PrO_2 and Yb_2O_3; thus the addition of 1 mole percent of these RE oxides reduces the Curie point by approximately 25-30°. The fact that the luminescence spectrum consists of discrete lines[4], the smooth variation of the lattice parameters and the regular shift of the Curie point, all indicate that in these cases there form solid solutions.

Most of the investigated compositions exhibit a high dielectric constant, but at the same time some of them are characterized by high dielectric loss. With increase of RE content the $\epsilon_\theta/\epsilon_o$ ratio decreases (see table), and the ϵ peak broadens and becomes lower (Fig.1). The introduction of RE impurities affects the temperature variation of the resisitivity. The resistance of the specimens was measured by means of TO-1 and F-57 meggers. To minimize surface effects the speci

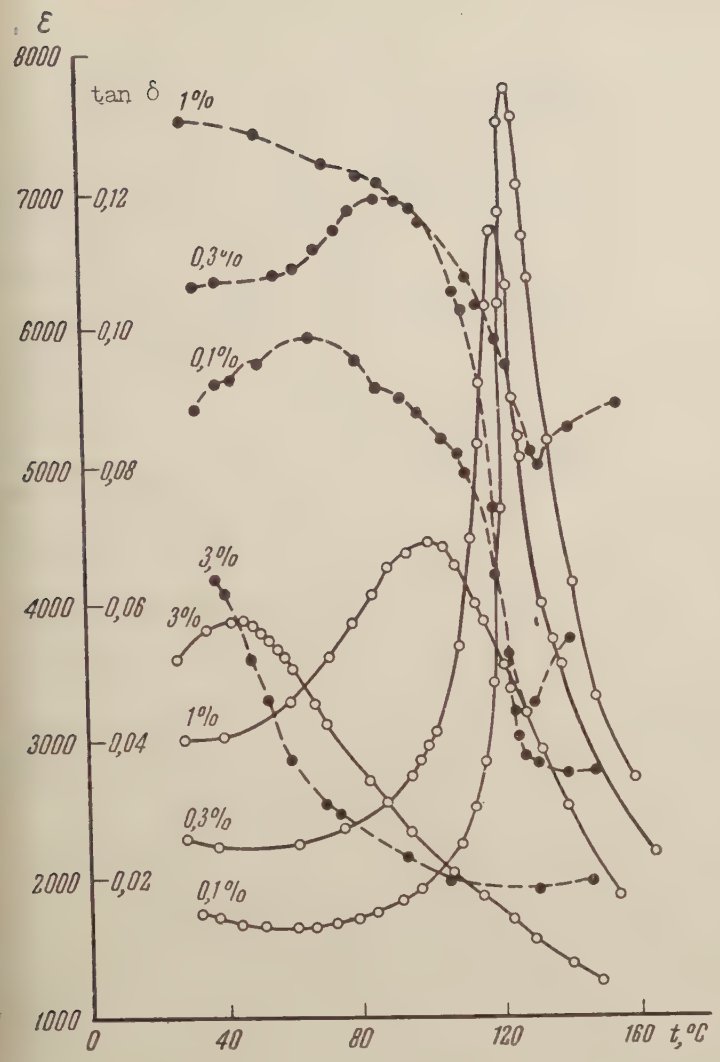

Fig.1. Temperature dependences of ε and tan δ for $BaTiO_3$ specimens with different Pr impurity concentrations.

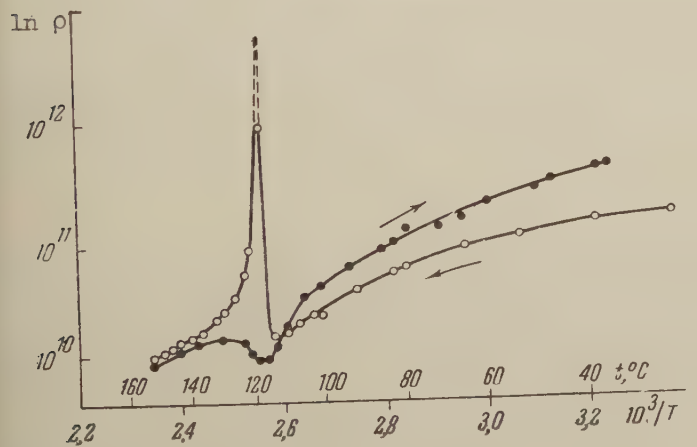

←Fig.2. Temperature dependence of the resistivity for a specimen containing 0.1% Sm (heating and cooling curves).

mens prior to measurement were heated for a long time and coated with oil while in the hot state.

The investigated specimens differ as regards temperature variation of the resistivity. Specimens containing small amounts of RE oxide (1-3%) yield a temperature vs resistivity curve similar to that for pure $BaTiO_3$: the resistance falls off exponentially with temperature (the activation energies are given in the last column of the table). Specimens containing 0.1% Sm_2O_3, 0.1% Er_2O_3, 0.1% Tb_2O_3 and 0.1% Nd_2O_3 in heating exhibit a sharp increase in resistance at the Curie point. In cooling there is a minimum in the temperature vs resistance curve (Fig. 2). A small resistance peak at the Curie point is observed for specimens containing 0.3% Tb, 0.3% Nd, 0.3% Er and 0.3% Tm.

Upon more careful investigation we found that at the resistance "maximum" at the Curie point the current flowing through the specimen not only falls off to zero, but also changes direction. Apparently the observed effect is a result of a radical change of polarization; the effect is most clearly evinced in barium titanate specimens containing 0.1 mole percent Sm_2O_3, Nd_2O_3, Er_2O_3 and Tb_2O_3. For specimens with appreciably larger and smaller amounts of RE impurity, as in the case of pure $BaTiO_3$, no peak appears in the resistance vs temperature curves. The phenomenon of sharp increase in resistance at the Curie point may be of practical value.

Physical-Mathematical Faculty,
Rostov-on-the-Don State University

References

1. G.G.Harman, Phys.Rev., 106, 1358 (1957).
2. O.Saburi, J.Phys.Soc.Japan, 14, 1159 (1959).
3. S.V.Bogdanov & V.A.Rassushin, Izv.AN SSSR, Ser.fiz., 24, 1247 (1960). (Trans.Bulletin, 24, 1248.)
4. A.F.Yatsenko & L.M.Rabkin, Present issue of the Bulletin, p.1313.

PROBING THE LATTICE FIELD OF $BaTiO_3$ WITH RARE EARTH IONS

- A.F.Yatsenko & L.M.Rabkin

Investigation of the crystal lattice field acting on the individual ions is of importance for clarifying the nature of ferroelectricity. Venevtsev, Zhdanov & Solov'ev[1,2] calculated these fields by different methods. In the present work an attempt was made to probe these fields experimentally. Our procedure can also be used to find the vibrational frequencies of the lattice through observation of the electronic-vibrational transitions; furthermore, it can serve as a means for monitoring reactions in the solid state and solving other research problems.

In our experiments we used small amounts (<0.5 mole percent) of rare earth elements (RE), which were introduced into the host lattice to serve as "voltmeter" probes. Essentially we utilized the ability of RE to yield line luminescence spectra even in the solid state. This is connected with the fact that RE have incomplete $4f$ shells, which are screened from external influences by the $5s^25p^6$ electrons. Consequently, the "extra" energy of the $4f$ electrons in the field of the crystal lattice is appreciably lower than the energy of spin-orbit interaction, which means that the lattice field may be regarded as a small perturbation. The strength of the lattice field is evinced not only in the magnitude of the level splitting, but also in lowering of all the terms and, consequently, in a general "red" shift of the entire spectrum. The extent to which the degeneracy of the levels is removed is determined by the symmetry of the crystal field. The symmetry also affects the intensity of the spectrum: when the RE ion is in an inversion center, dipole transitions are forbidden and hence the spectrum of the ion is very weak; in the absence of an inversion center forced dipole transitions are allowed, which leads to greater intensity of the spectrum.

Incorporation of impurity ions into the lattice gives rise to local distortions, which together with the RE ions form distinctive luminescence centers. Before one can use such RE ions as probes of the crystal field, however, one must clarify the structure of the luminescence centers. The location and general appearance of the luminescence spectrum of RE ions in $BaTiO_3$ indicate that the luminescence is due to triply charged RE ions. When the RE^{3+} ions replace Ti^{4+} or Ba^{2+} ions, one may expect a hole or electron, respectively, to appear at the luminescence center. Centers of somewhat different structure will be formed when two RE^{3+} ions replace the nearest Ba^{2+} and Ti^{4+} ions. In all three cases we should have point symmetry C_{4v} or C_{3v}. The sharp luminescence spectra actually observed indicate, however, that the RE ions occupy sites with point symmetry O_h. It must therefore be assumed that the RE^{3+} ions replaced Ti ions without local distortion of the point symmetry.

In $SrTiO_3$ and above the Curie point in $BaTiO_3$ the RE ions occupy positions with point symmetry O_h; hence the static potential $V(r, \theta, \varphi)$ must satisfy the operator equation $\widetilde{O}_h V(r, \theta, \varphi) = V(r, \theta, \varphi)$, where $\widetilde{O}_h$ is the operator of all the symmetry elements of group O_h. Whence, representing the potential $V(r, \theta, \varphi)$ in the form of a harmonic expansion, we obtain

$$V(r, \theta, \varphi) = A_4^0\Big[\sum_k r_k^4 Y_4^0(\theta_k\varphi_k) + 5\sum_k r_k^4 Y_4^4(\theta_k\varphi_k)\Big] + V(\omega t),$$

where $V(\omega t)$ is the dynamic part of the potential due to thermal vibrations of the lattice. We have omitted sixth order terms inasmuch as their contribution to the potential is several orders of magnitude smaller than that of fourth order terms.[3] Thus, for determining $V(r, \theta, \varphi)$, aside from the symmetry, one must know one constant, namely, A_4^0 which can be determined either by direct calculations or by comparing matrix elements of the $\langle SLJM|V|S'L'J'M'\rangle$ type with the observed spectrum. Inasmuch as both methods involve great computational difficulties, the results will be reported in a separate communication.

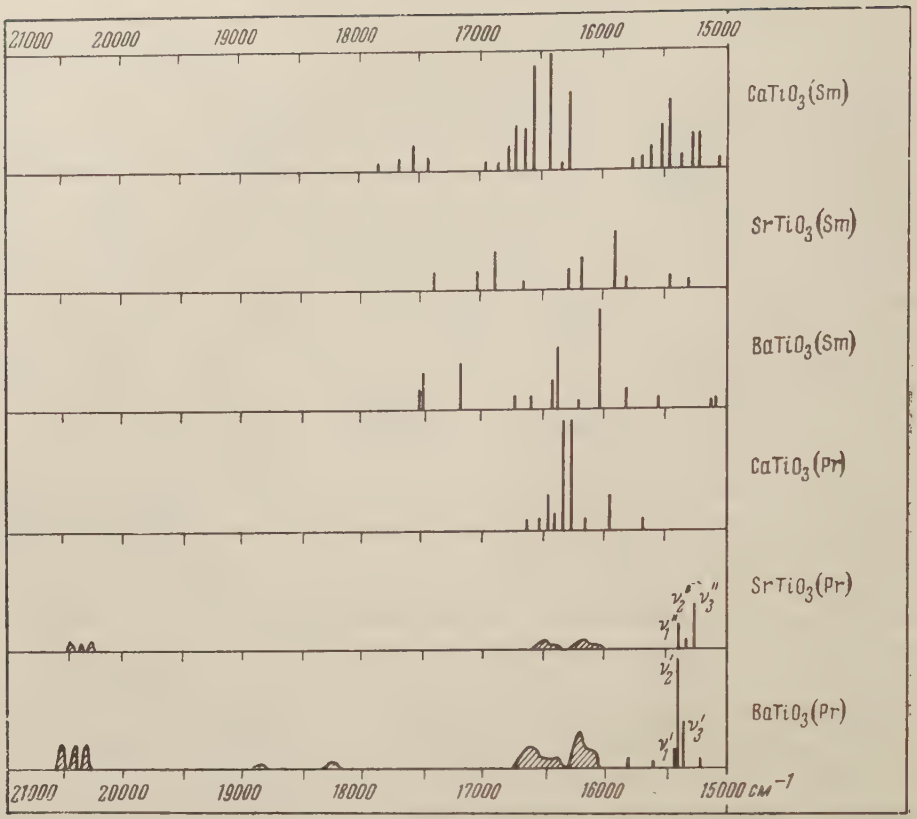

Fig.1. Luminescence spectra of Ba, Sr and Ca titanates activated by Pr and Sm.

In going through the Curie point the symmetry is lowered from O_h to C_{4v} and the inversion centers vanish. In connection with this there appear in the expression for the potential second and odd power terms. The second power terms are responsible for increase of the splitting, while the odd power terms lead to increase in the general intensity of the spectrum and, particularly, the intensity of individual transitions.

As will be evident from Fig.1, the luminescence spectra of $BaTiO_3$(RE) and $SrTiO_3$(RE) are generally similar; there are, however, substantial differences as regards the total intensity and the positions of a number of lines. On the whole the luminescence of $BaTiO_3$(RE) is several times stronger than that of $SrTiO_3$(RE). The ν_2' = 15 390 cm^{-1} line, which is the most intense line in the spectrum of $BaTiO_3$(Pr) is much weaker in the spectrum of $SrTiO_3$(Pr) (ν_2'' = 15 340 cm^{-1}); this is particularly clearly evident if one compares the intensity of this line with the intensities of the neighboring ν_1 and ν_3 lines.

Moreover, in going from $BaTiO_3$)Pr) to $SrTiO_3$(Pr) there is observed a shift of the spectrum to the long wavelength side, which is especially noticeable in the case of the ν_1, ν_2 and ν_3 lines. Similar differences are observed for $BaTiO_3$(Sm) and $SrTiO_3$(Sm). The spectrum of $SrTiO_3$(Sm) is shifted to the long wavelength side and the splitting of the lines is substantially greater than in the spectrum of $BaTiO_3$(Sm).

The variation of the luminescence spectra incident to transition through the Curie point is obviously of particular interest. Observations of the temperature behavior of the luminescence of $BaTiO_3$(Pr) showed that the intensity ratio of the

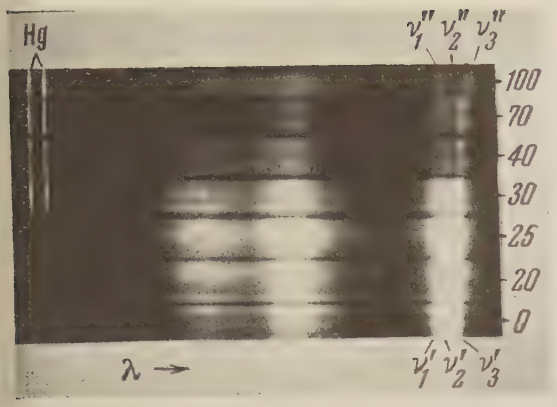

Fig.2. Luminescence spectra of Pr^{3+} in $(Ba,Sr)TiO_3$ solid solutions. The scale at the right gives the $SrTiO_3$ concentration in mole percent.

ν_2 and ν_1 lines, which characterizes the symmetry of the electron cloud, decreases smoothly in going through the Curie point and becomes less than unity (O_h symmetry) only at 150-160°. It must be noted that observation of the luminescence spectra at 100-150° is hampered owing to vibrational broadening of the lines and temperature quenching of the luminescence, which precludes observation of the change in Stark splitting at 127° (observed at the third phase transition by Osima et al[4]). The transition through the Curie point can be realized at room temperature by working with a series of solid solutions in the $(Ba,Sr)TiO_3(Pr)$ system. In order to insure uniform conditions of excitation and recording of the luminescence spectra we arranged our specimens in a row in order of increasing $SrTiO_3$ concentration and recorded their luminescence simultaneously.

In the series of spectra shown in Fig.2 one can readily follow the shift of the lines to the long wavelength side with increasing $SrTiO_3$ concentration. Also clearly evident is the decrease in the total luminescence intensity beginning with specimens whose Curie point lies below room temperature, and particularly the decrease in the intensity of the $\nu_2' = 15\ 390\ cm^{-1}$ line.

So far we have been unable to observe the luminescence of RE in $PbTiO_3$: this compound decomposes at the relatively high temperatures necessary for diffusion of the RE ions into the crystal lattice.

Pr and Sm introduced into $CaTiO_3$ yielded a very intense luminescence with a large number of lines in the visible region.

We made an attempt to follow the formation of $(Ba,Ca)TiO_3$ solid solutions by observing the luminescence. To this end, mixtures with different proportions of $BaTiO_3$ and $CaTiO_3$ were activated by Sm. In the $CaTiO_3$ concentration range from 25 to 75% there is observed a bright luminescence, the spectrum of which corresponds to that of Sm in $CaTiO_3$, which indicates the presence of unreacted $CaTiO_3$.

It may be inferred from the observed spectra that the RE ion replaces a lattice ion located in a field of cubic symmetry, i.e., replaces either Ti or Ba. For unique determination of the location of the replacing ion one must precisely evaluate the ratio of the coefficients A_6^0/A_4^0, which should be different for different coordination numbers. Nevertheless, on the basis of a number of other considerations, namely, the fact that there exists $BaPrO_3$ with the perovskite structure[5], the strong Pr concentration dependence of the Curie temperature[6], and the relative size and charges of Pr and Ti ions, it may be concluded that the Pr ions replace Ti ions.

In view of the O_h symmetry position of the RE ions in $SrTiO_3$, the intensity of the spectrum is very low and is presumably due more to the dynamic part of the potential $V(\omega t)$ than to quadrupole and magnetic radiations. In the system of (Ba, Sr)TiO_3 solid solutions the spectrum remains rather weak for all nonferroelectric compositions; for ferroelectric compositions the intensity of the spectrum increases markedly.

The small lowering of point symmetry from O_h to C_{4v} in transition through the Curie point has almost no effect on the Stark splitting of the levels, but exerts a strong influence on the intensity of some of the lines associated with forced

dipole transitions in the absence of an inversion center. The line most sensitive to the vanishing of inversion centers proved to be the $\nu_2' = 15\ 390\ cm^{-1}$ line ($^1D_2 - {}^3H_4$ transition).

Both the position of the spectrum and the magnitude of the splitting indicate that the crystal field in $SrTiO_3$ is somewhat stronger than in $BaTiO_3$, and that this field varies continuously and more or less linearly in the system of $(Ba,Sr)TiO_3$ solid solutions. The same inferences may be drawn from the spectrum of Sm in $BaTiO_3$ and $SrTiO_3$.

Observations of the temperature behavior of the spectrum of Pr in $BaTiO_3$ and investigation of the $(Ba,Sr)TiO_3$ solid solution system showed that internal dipole transitions (ν_2' line) are allowed not only below the Curie point but also up to 15-20° above the Curie point; this indicates that the electron cloud remains polarized above the Curie point and retains O_h symmetry only statistically.

It has been reported[7] that the spectrum of Pr is more sensitive to changes in the crystal field than the spectrum of Sm. In our case, however, the spectrum of Sm seems to undergo greater changes in going from $BaTiO_3$ to $SrTiO_3$ than the spectrum of Pr.

The substantially greater intensity of the spectrum of RE in $CaTiO_3$ indicates that in this case there may occur dipole transitions with a very great oscillator strength, owing to the highly asymmetrical position of the RE ion in $CaTiO_3$.

Conclusions

1. The rare earth probe procedure makes it possible to determine the potential function of the crystal lattice field (magnitude and symmetry).

2. The fact that there is evinced a sharp luminescence spectrum indicates that there form substitutional $Ba(RE,Ti)O_3$ solid solutions.

3. Even our qualitative observations of the spectra have enabled us to compare the lattice fields in $BaTiO_3$, $SrTiO_3$ and $CaTiO_3$ and to follow the changes occurring incident to the phase transition. In particular, we established that above the Curie point the electron cloud of the central ion in the oxygen octahedron remains strongly polarized.

4. Use of the rare earth probe technique may prove useful in the solution of a number of technological problems: for example, investigation of the formation of $(Ba,Ca)TiO_3$ solid solutions and other reactions in the solid state. Use of this technique in conjunction with x-ray diffraction studies and other procedures should greatly facilitate interpretation of crystal structures.

Physical-Mathematical Faculty,
Rostov-on-the-Don State University

References

1. Yu.N.Venevtsev, G.S.Zhdanov, S.P.Solov'ev & V.V.Ivanova, Kristallografiya, 4, 255 (1959). (Trans.Soviet Physics - Crystallography.)

2. G.S.Zhdanov, S.P.Solov'ev & Yu.N.Venevtsev, Ibid., 2, 639 (1957). (Trans. Ibid.)

3. N.V.Afanas'eva, Optika i spektroskopiya, 3, 629 (1958); Thesis, Leningrad Polytechnic Institute, 1953.

4. K.Osima, S.Hauakawa, H.Nagano & M.Nagusa, J.Chem.Phys., 24, No.4, 903 (1956).

5. J.Naray-Szabo, Bull.Univ.Tech.Sci., Budapest, 1, 30 (1947).

6. A.F.Yatsenko & T.P.Popova, Present issue of the Bulletin, p.1310.

7. M.A.El'yashevich, Spektry redkikh zemel' (Spectra of the rare earths), M. 1953.

PREPARATION AND SOME FERROELECTRIC PROPERTIES OF LITHIUM HYDROSELENITE

- V.P.Konstantinova, I.M.Sil'vestrova, L.A.Shuvalov & V.A.Yurin

Lithium hydroselenite $LiHSeO_3 \cdot H_2SeO_3$ (hereinafter LHS) crystallizes in the monoclinic system, with space group P_n. As a ferroelectric it was first described by Pepinsky & Vedam[1]. The spontaneous polarization at room temperature, according to these authors, is 15 μcoul/cm^2, the coercive field 1400 v/cm.

We synthesized LHS in an aqueous solution of selenious acid and lithium hydroxide in stoichiometric proportions:

$$2H_2SeO_3 + LiOH = LiHSeO_3 \cdot H_2SeO_3 + H_2O.$$

A number of difficulties were encountered in attempting the synthesis. One of these stemmed from the instability of selenious acid and its compounds at temperatures above 50°. A large amount of heat is evolved when the solutions are mixed, leading to heating of the mixture and precipitation from it of amorphous red selenium. Hence synthesis must be carried out with continuous stirring and cooling of the solution. In the process of recrystallization of LHS, evaporation of the solvent is carried out at room temperature. The presence of SO_2 or SO_3 in the ambient air also has a deleterious effect on the stability of LHS solutions.

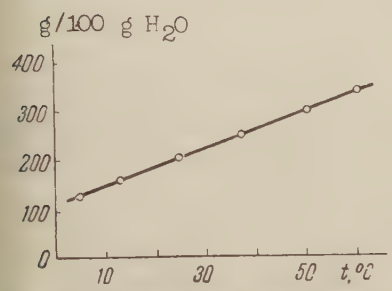

Fig.1. Temperature dependence of the solubility of LHS.

The temperature dependence of the solubility of LHS (Fig.1) shows that LHS crystals can be grown by the method of reducing the temperature in conventional laboratory crystallization pans.[2]

LHS solutions are highly viscous and capable of high degrees of supersaturation. At low supersaturations from a point seed there grow thin plates with the width along the b axis and the length along the c axis. The surface of such plates is distorted and covered with a large number of growth hillocks. Upon supercooling of a saturated solution by 5-6° these rounded faces disappear and there appear the (110) faces of regular rhombic prisms. In crystallizers of 700 cm^3 capacity we succeeded in growing crystals of up to 100 g in three days (Fig.2). To the other difficulties encountered in growing LHS crystals, one might add the tendency of the crystals to crack along the cleavage plane during growth. We were able to obviate this difficulty by additional purification of the initial material and growing the crystals at high degrees of supersaturation.

According to our measurements, the melting point of LHS is 110.5°. The specific gravity (pycnometric measurement) is 3.185 g/cm^3. Measurement of the angles between the faces, using the values of the lattice constants given by Pepinsky & Vedam[1] enabled us to establish that the most highly developed faces are the four (110) faces of the rhombic prism and the two pinacoids $(\bar{1}01)$ and $(10\bar{1})$.

As noted above, LHS is monoclinic; the monoclinicity angle is 105°. The crystals are characterized by perfect cleavage. We assumed the following orientation of the crystallographic axes. As the b axis we take the perpendicular to the cleavage plane. The a and c axes are assumed to lie in the cleavage plane at an angle of 105° to each other and are parallel to the natural edges of the crystal (Fig.3). The cleavage plane coincides with the only symmetry element, namely, the symmetry plane.

The principal difficulty in investigating LHS crystals was determination of the polar direction. Pepinsky & Vedam[1] state that the polar direction lies close to the $[40\bar{1}]$ direction, which according to our choice of axes is located at an angle

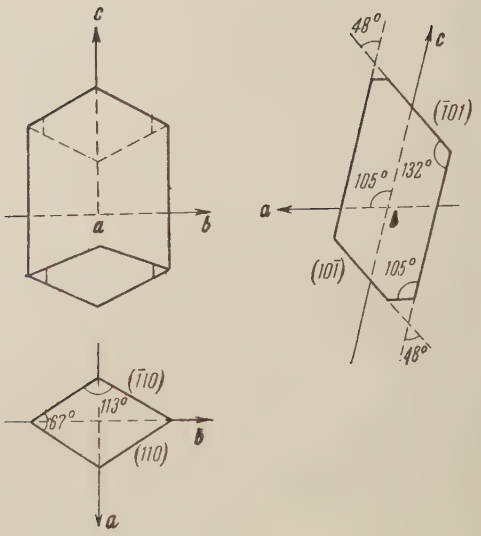

Fig.2. Typical LHS crystal (weight 100 g).

Fig.3. Orientation of the crystallographic axes in an LHS crystal and location of the principal faces. The figure at the right is a cross section of the crystal in the cleavage plane.

Measured parameter	+35°	+15°	0°	−10°	−42°	−54°	−72°	−90°	−105°	−115°
ε'_{33}	19,4	21–25,5	—	31,5	43,5–45	44,5–44,7	39,9	33,4	—	—
P_s, μcoul/cm^2	0	0	0,16	6,45	7,6–9,6	9,45–9,7	10,2–10,5	10–13	9,0	5,0
E_c, v/cm	Fluctuates in the range from 1700 to 2700									

of -65° to the c axis.* In connection with the fact that the polar direction is not given precisely in the work of Pepinsky & Vedam, we investigated the variations of the dielectric constant ε'_{33}, the spontaneous polarization P_s and the coercive field E_c as functions of the direction in the crystal. For these measurements we cut plates the normals to the principal faces of which lay in the cleavage plane in different directions. The results of these measurements are given in the accompanying table.

The variation of ε'_{33} and P_s with the direction in the cleavage plane is shown in Fig.4, from which it will be evident that the maximum values of ε'_{33} and P_s are observed in different directions: -50° to the c axis for ε'_{33} and -90° to the c axis for P_s. Neither of these directions agrees with the $[40\bar{1}]$ direction reported by Pepinsky & Vedam. Further and more accurate investigations are necessary for precise determination of the polar direction in LHS crystals.

In Fig.4 we also reproduce the hysteresis loops observed in different directions in the LHS crystal. The most symmetrical and rectangular loops were observed in cuts parallel to the $(\bar{1}01)$ face, the normal to which is located in the cleavage plane at an angle of -42° to the c axis. In the direction corresponding to the maximum value of P_s there are frequently observed distorted, in particular "double" hysteresis loops. These distortions are presumably caused by impurities absorbed by the crystal in the process of growth.

The value of the dielectric constant ε_{22} in the direction perpendicular to the cleavage plane proved to be 11.8, which agrees with the data of Pepinsky &

---

*The erroneous assertion in Ref.1 that the polar direction must lie along a perpendicular to the (001) plane is presumably a misprint.

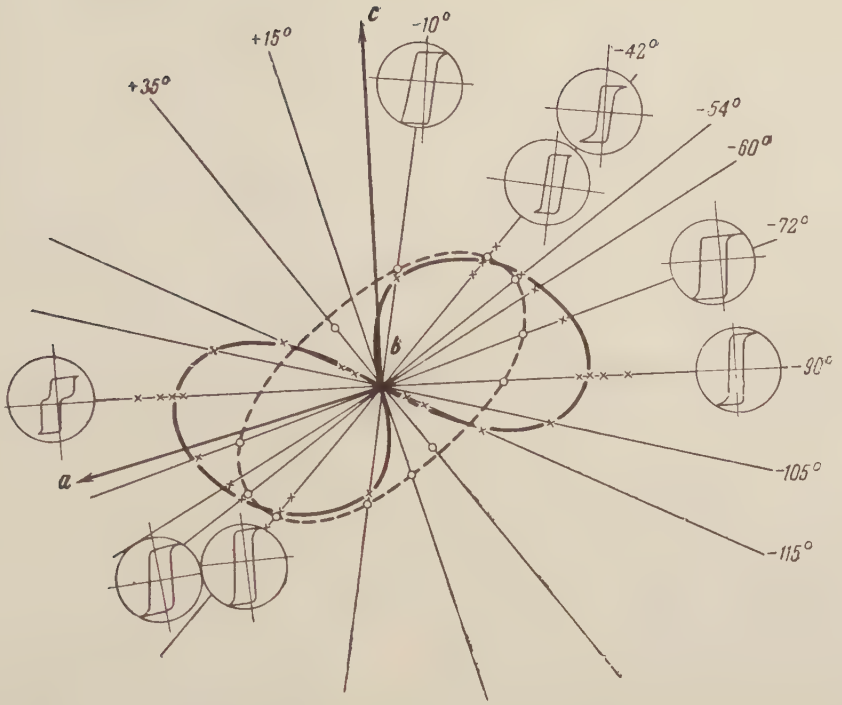

Fig.4. Variation of the dielectric constant ε'_{33} (dashed line) and spontaneous polarization P_S (solid lines) with the direction in the cleavage plane (ac plane), and corresponding hysteresis loops.

Vedam.

We investigated the temperature dependences of the dielectric constant, the spontaneous polarization and the coercive field, and also the variation of the dielectric constant with the strength of alternating fields of different frequencies on plates with the normals forming an angle of -42° with the c axis (direction close to the direction of maximum ε'_{33}). These dependences are plotted in Figs.5,6 & 7.

It will be evident from Fig.5 that the dielectric constant increases with increasing temperature. Presumably the rise of the dielectric constant at elevated temperatures approaching the melting point should be attributed to increase in conductivity. The temperature dependence of the dielectric constant obtained in our experiments is similar to the dependence recorded by Pepinsky & Vedam[1], but our values of the constant are somewhat higher.

It follows from Fig.6 that the spontaneous polarization of LHS increases continuously with temperature; in contrast to the case of many other ferroelectrics, the increase of spontaneous polarization is accompanied by a decrease rather than an increase of the coercive field.

It will be seen from Fig.7 that the maximum value of the dielectric constant with increase of the ac field (curve 1) is attained at $E_{\sim} = 3600$ v/cm. In repeat measurements, carried out after the passage of sufficient time for cooling of the specimen, ε_{max} was attained at $E_{\sim} \approx 2000$ v/cm. This is undoubtedly due to "aging" of the specimen by the alternating field during the first series of measurements.

Switching (polarization reversal) of LHS crystals by bipolar square pulses was investigated by the same procedure as that used in investigating switching of tri-glycine sulfate[2] and deuterated tri-glycine sulfate crystals[3]. In view of the fact that we had to use longer pulses, the set-up described in Ref.4 had

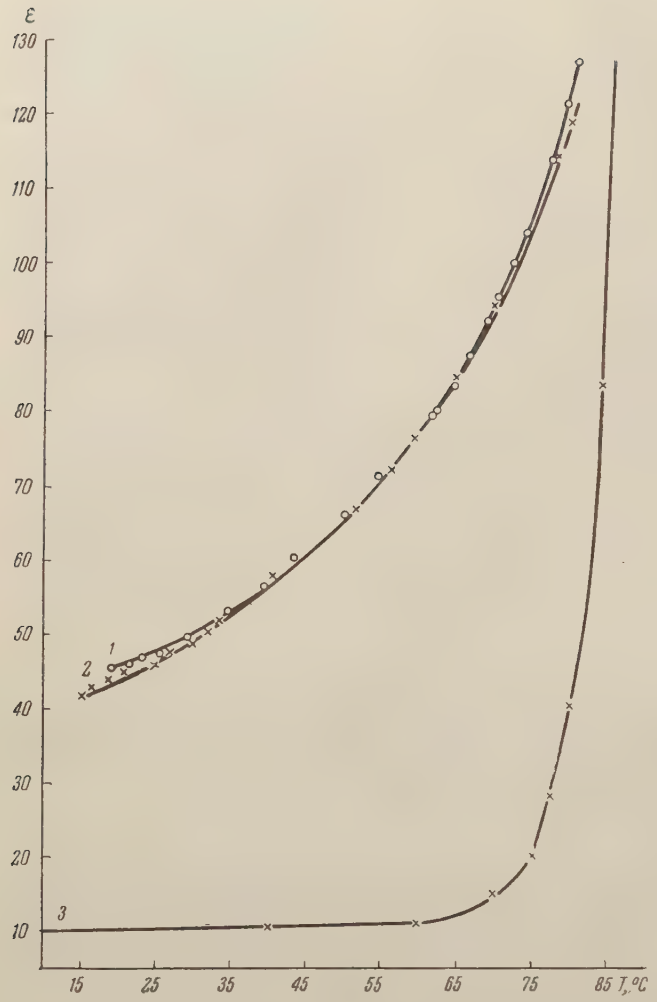

Fig.5. Temperature dependences of the dielectric constant of LHS in different directions: 1 - normal to the crystal plate at an angle of -42° to the *c* axis in the cleavage plane (field 1.8 v/cm, frequency 1 kc); 2 - same plate (field 5 v/cm, frequency 10 kc); 3 - normal to the plate perpendicular to the cleavage plane (field 5 v/cm, frequency 1 kc).

than for plates of the same thickness with the

Even at relatively elevated temperatures* completely only with relatively long pulses (30-200 μsec) having amplitudes to 130 v (to 7 kv/cm). In almost all cases the switching pulse rise time τ_{max} proved to be substantially shorter than the pulse decay time τ_d (by a factor of 6-15). This shows that in weak fields the nucleation time in LHS is appreciably greater

to be modified somewhat. For producing the pulses we used a GIS-2 generator with a power amplifier, having a somewhat higher output resistance (~300 ohm).

As in the tri-glycine sulfate experiments, the specimens were prepared in the form of thin plates (0.15-0.25 mm thick) with cross-shaped electrodes. It was found, however, that electrodes of vacuum evaporated silver rapidly lose their metallic conductivity. Hence we used electrodes of silver foil, which retained their conductivity for an appreciable period. Moreover, in view of the poisoning effect of selenium oxide vapor the specimens were sealed into vacuum tube envelopes.

Inasmuch as LHS crystals have a high dielectric loss, it was particularly important to have a small switching volume in order to avoid overheating.[4] Thus, plates 4-5 mm^2 in area and 0.23 mm thick with fully metallized top and bottom surfaces in being switched at room temperature at a frequency of 5-10 kc overheated, broke down and melted within a fraction of a second; hence in most experiments the electrode area did not exceed 0.2 mm^2.

Most of the investigated crystal plates in being switched by bipolar pulses exhibited appreciable unipolarity. The values of the maximum switching current density i_{max}/S and the reciprocal of the switching time $1/\tau_s$ proved to be greater for plates with the normal at an angle of -42° to the *c* axis normal at an angle of -90°.

---

*In switching at elevated temperatures the silver foil electrodes rapidly lost metallic conductivity.

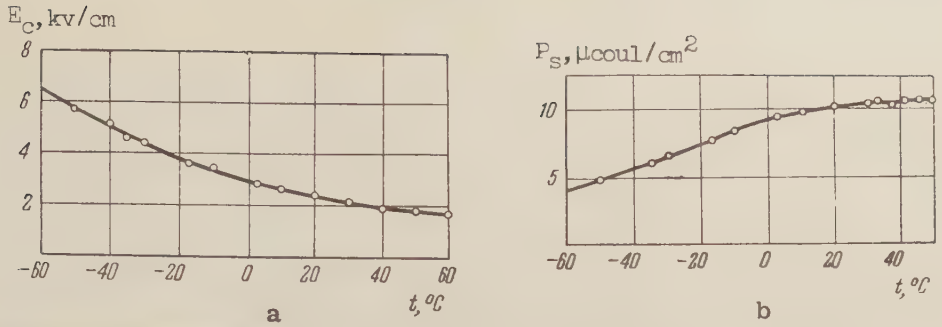

Fig.6. Temperature dependences of the coercive field E_c and spontaneous polarization P_s. Normal to the plate at an angle of -42° to the c axis in the cleavage plane.

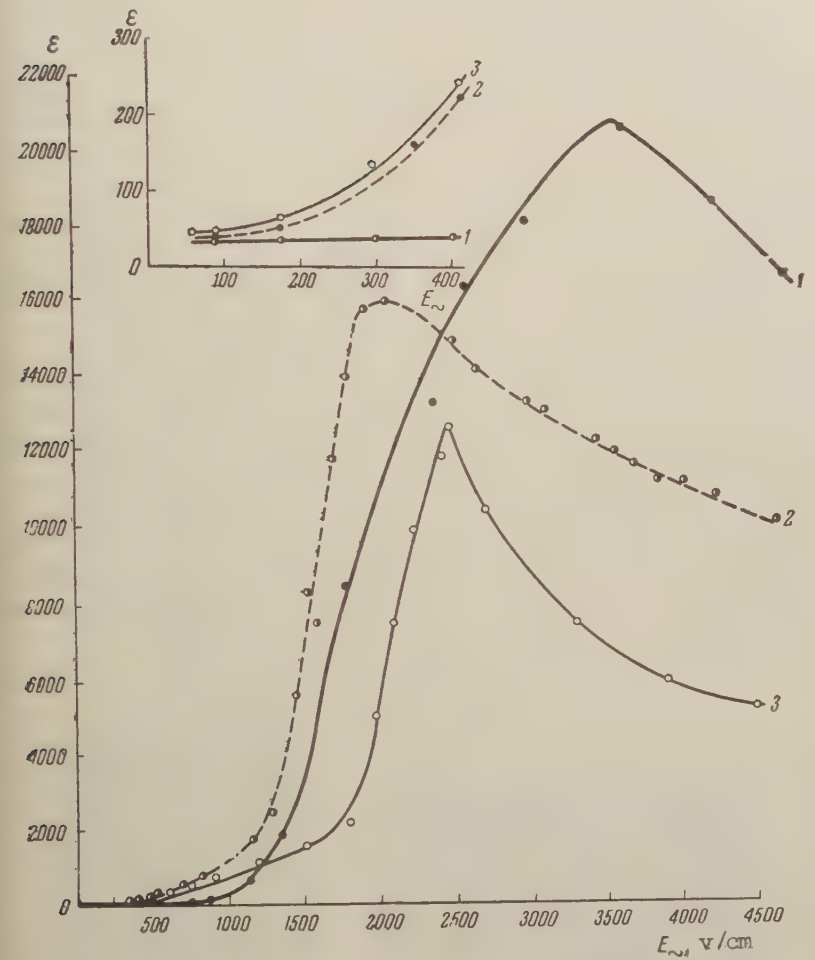

Fig.7. Field dependences of the dielectric constant of LHS. Normal to the crystal plate at -42° to the c axis in the cleavage plane; temperature 20°. 1 - frequency 100 cp; 2 - repeat measurement under the same conditions; 3 - frequency 1 kc. The insert above shows the initial sections of the curves to an enlarged scale.

than the domain wall motion time*.

The values of the activation field determined from the intersection of the linear parts of the $i_{max}/S = f(E)$ and $1/\tau_{max} = f(E)$ curves, recorded at 150 pps, with the horizontal axis varied at room temperature in the range from 3.8 to 4.5 kv/cm, and at 80° in the range from 2.7 to 3.3 kv/cm. The wall mobility μ, determined from the slope of the approximately linear section of the $1/\tau_{max} = f(E)$ curve was less than 1 $cm^2 \cdot v^{-1} \cdot sec^{-1}$ at 20° and of the order of 4 $cm^2 \cdot v^{-1} \cdot sec^{-1}$ at 80°. The switching conductivity σ_s, determined in a similar manner, was found to be less than $1 \cdot 10^{-3}$ $ohm^{-1} \cdot cm^{-1}$ at 20°, and of the order $4 \cdot 10^{-3}$ $ohm^{-1} \cdot cm^{-1}$ at 80°. The above data are preliminary in nature and hence must be regarded as only approximate.

We take this opportunity to thank V.A.Frolova,

---

*This result disagrees with the latest data of Fatuzzo & Merz[5], whose report we read only in preparing the present article for publication, and is not consistent with the concepts developed by these authors.

L.N.Kurkovskaya and K.A.Pluzhnikov for assistance in carrying out the investigation and I.S.Zheludev for valuable suggestions.

References

1. R.Pepinsky & K.Vedam, Phys.Rev., 114, 1217 (1959).
2. I.S.Zheludev, Report presented at the Third Conference on Ferroelectricity, M., 1960.
3. V.P.Konstantinova, I.M.Sil'vestrova, L.A.Shuvalov & V.A.Yurin, Izv.AN SSSR, Ser.fiz., 24, 1203 (1960). (Trans.Bulletin, Vol.24, 1206.)
4. L.A.Shuvalov, Present issue of the Bulletin, p. 1407.
5. E.Fatuzzo & W.J.Merz, Phys.Rev., 116, 61 (1959).

DOMAIN WALLS AND ETCH PIT NETWORKS IN DEUTERATED TRI-GLYCINE SULFATE CRYSTALS

- V.P.Konstantinova

Surface etching is widely employed for investigating different properties of crystals: for studying twinning, for bringing out the faces of disoriented blocks and slip planes and for determining the distribution and motion of dislocations. For example, Hooton & Merz[1] and Pearson & Feldmann[2] employed the etching technique for studying twinning and other effects in ferroelectric $BaTiO_3$ crystals.

In earlier studies[3,4] we used the method of surface etching of plates cut parallel to the (010) and (100) faces to investigate the orientation and structure of domain walls in tri-glycine sulfate (TGS) crystals. Pearson & Feldmann[2] and Meleshina, Zheludev & Rez[5] give the results of comparative investigation of the domain structure of GAS and TGS crystals by two procedures, namely, the charged powder procedure and the etching technique. In our opinion, the etching technique can not only give a clearer picture of twin walls, but can also yield more detailed information on the structure of individual single domain regions.

The present contribution is devoted to the question of the correlation between the domain walls in ferroelectric crystals of deuterated tri-glycine sulfate (DTGS) and the defect network in such crystals, and to the question of the variation of this network with movement of the domain walls under the influence of an applied electric field.

As noted in an earlier report[6], the domain structure of DTGS can readily be observed by means of a metallographic microscope on the etched surface of plates split along the cleavage plane or cut out by means of a moist thread, perpendicular to the polar Y axis (b axis). The etching was carried out by laying the crystals face down on a smooth cloth soaked with water or an unsaturated water solution of DTGS. Plates that are ground beforehand etch more rapidly, and the etching process simultaneously brings out the twin (domain) boundaries and etch figures that are different on the twin components with opposite directions of spontaneous polarization. The twin component with the negative end of the polar Y axis etches more rapidly than the component with the positive end of the polar axis. Etching of plates obtained by splitting the crystal along the cleavage plane and of plates polished beforehand proceeds more slowly. In this case there are first revealed domain walls and then etch pits on the side with negative Y and last etch pits on the side with positive Y.

In earlier reports there were reproduced micrographs of the domain structure of TGS[3,4] and the similar domain structure of DTGS[6].

It was found[3] that individual domains in TGS and DTGS crystals may occupy the

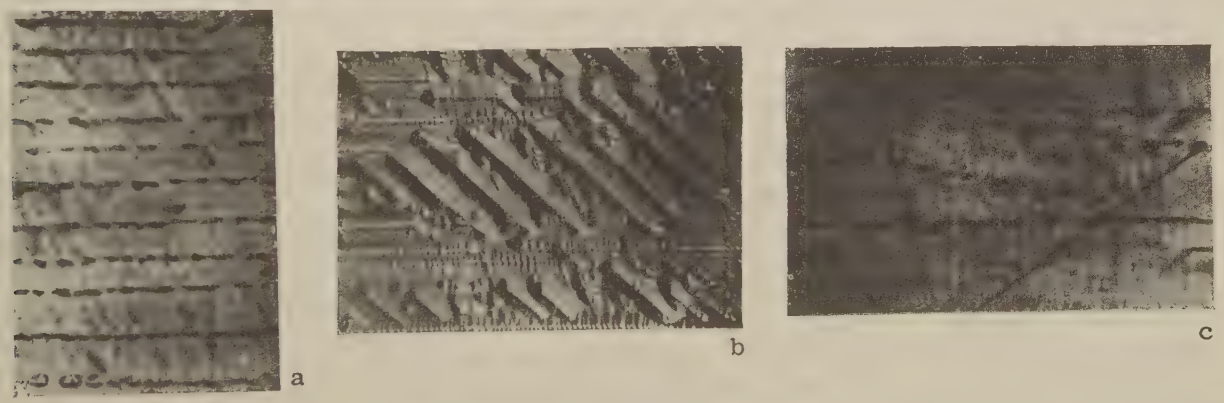

Fig.1. Ordered arrangement of etch pits on the surface of a Y cut DTGS crystal plate: a - parallel rows (50 X), b - system of parallel rows (50 X), c - system of parallel rows (150 X).

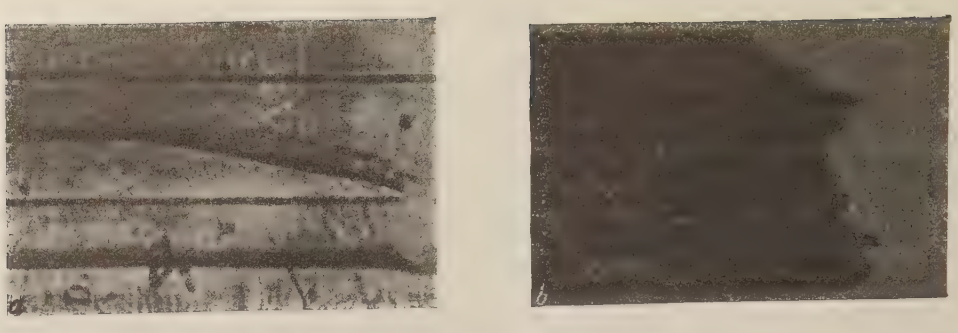

Fig.2. Shape of twin walls in Y cut DTGS crystal plates: a - partially polarized specimen (150 X), b - nonpolarized crystal grown by the block technique (4 X).

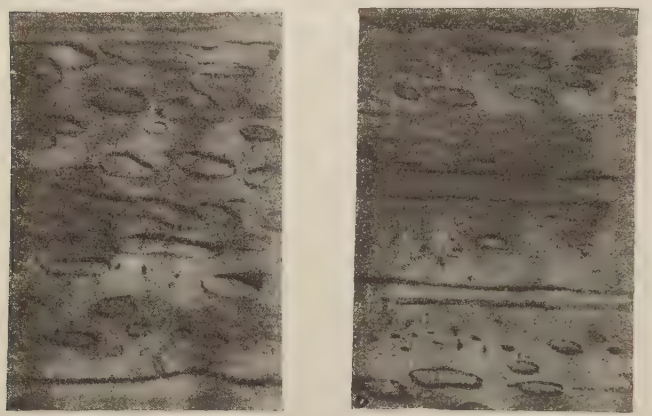

Fig.3. Domain walls on different sections of a Y cut DTGS crystal before application of an electric field.

entire growth pyramid of a face. In the case of large crystals the volume corresponding to a domain may amount to several cubic centimeters. Hence it is of interest to investigate the structure of an etched surface of a single domain region, i.e., to study the arrangement of etch pits on an etched single domain surface.

In addition to a random distribution of etch pits, we frequently observed clear regular patterns. Micrographs of etched Y cut DTGS crystal plates (Fig.1,a) show that the etch pits are arranged in parallel rows. In some cases there appears not just one system of parallel rows, but several (Figs.1,b & c) oriented at definite angles to each other. At present we are trying to determine whether these etch pits are the points of emergence of dislocations or due to some other crystal defects. It is interesting to note that these pits are highly mobile both under the influence of variation in temperature and under the action of an electric field. The angles between the rows of pits are not arbitrary; similar angles are observed in domain wall patterns (Figs.2,a & b).

Upon application of a sufficiently strong dc field to a metallized polydomain Y cut DTGS plate the plate is "monodomainized" and the domain walls disappear. In the case of partial switching of the specimen and subsequent etching one can follow the displacement of the domain walls under the influence of the applied electric field.

We carried out a number of experiments designed to bring out the wall motion. Micrographs of two sections of the etched surface of a non-poled Y cut DTGS plate are reproduced in Fig.3. Then silver foil electrodes were applied to this plate and it was subjected to the action of a 900 v/cm electric field for 20 hours. After removal of the field the plate was etched again and the etched surfaces rephotographed (Fig.4). It will be seen in Fig.4,a that the original characteristic elliptical domain walls have been replaced by rectilinear walls. These walls are parallel to the (001) face. The ends of the domain strips are also bounded by straight lines oriented at an angle of ~10° to the (001) planes. Angles of the same magnitude were observed earlier between the rows of etch pits on single domain plates (Fig.1). There also appear on the surface of the plate domains in the form

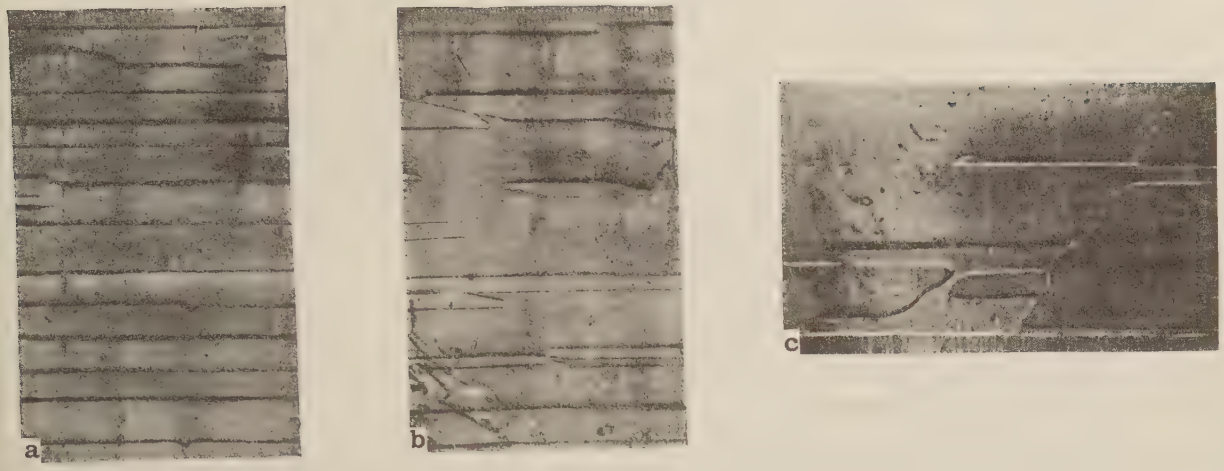

Fig.4. Domain walls on different sections of a Y cut DTGS crystal plate after removal of a 900 v/cm electric field. a - rectilinear domain walls; the domain walls move in steps; the field was applied for a period of 20 hours. b - rhombic twin; field applied for 20 hours. c - regular rows of etch pits marking trails of domain walls; field applied for a period of 30 hours. d - chaotic distribution of etch pits; field applied for 4 days.

of parallelograms with an acute angle of 10° (Fig.4,b).

Repeat application of an electric field leads to further "monodomainization": the domain walls move, leaving a trail of a series or row of etch pits (Fig.4,c), which in some cases fully repeats the domain wall pattern. Finally, application of a stronger field for a period of 2 days or more breaks up the ordered arrangement of the domain pits (Fig.4,d).

At present it is premature to draw any definitive deductions. One can only assert that there exists a network of defects in DTGS crystals. The distribution of these defects is intimately connected with the arrangement of the domain walls in the crystal. The shape of the domain walls is determined by how these domains appear or disappear during crystal growth, under the influence of an applied field or spontaneously.

In a recent note, Chynoweth[7] reports the existence in a TGS crystal of very fine, stable ("persistent") domains pointed at both ends and lying along the ferroelectric direction. Possibly what Chynoweth actually observed was not "persistent" domains, but series of etch pits of the type observed by us.

I desire to express my gratitude to E.M.Akulenko and V.A.Frolova for assistance in growing the crystals and carrying out the experiments.

Institute of Crystallography,
Academy of Sciences of the USSR

References

1. J.A.Hooton & W.J.Merz, Phys.Rev., 98, 409 (1955).
2. G.L.Pearson & W.L.Feldmann, J.Phys.Chem.Solids, 9, 28 (1958).

3. V.P.Konstantinova, I.M.Sil'vestrova & V.A.Yurin, Kristallografiya, 4, 125 (1959). (Trans.Soviet Physics - Crystallography.)

4. V.P.Konstantinova, I.M.Sil'vestrova & K.S.Aleksandrov, Fizika dielektrikov (Transactions of the Second All-Union Conference on the Physics of Dielectrics, 1958), M., 1960.

5. V.A.Meleshina, I.S.Zheludev & I.S.Rez, Kristallografiya, 5, 322 (1960). (Trans.Soviet Physics - Crystallography.)

6. V.P.Konstantinova, I.M.Sil'vestrova, L.A.Shuvalov & V.A.Yurin, Izv.AN SSSR, Ser.fiz., 24, 1203. (Trans.Bulletin, 24, 1206.)

7. A.G.Chynoweth, Phys.Rev.Letters, 4, 147 (1960).

SOME ELECTRIC CHARACTERISTICS OF AMMONIUM DI-H-PHOSPHATE SINGLE CRYSTALS

- I. Ya. Eisner

As is known[1-3], investigation of the temperature dependence of the dielectric constant of ammonium di-H-phosphate (ADP) single crystals has been limited on the low temperature side by the critical temperature -125° at which the crystals fracture. Hence investigation of ADP single crystals in the region of low temperatures is particularly intriguing.

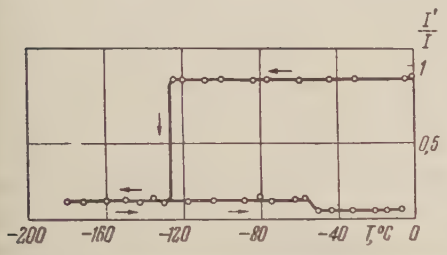

Fig.1. Temperature dependence of the transparency of an X cut ADP single crystal during cooling and heating.

1. Some information on the changes occurring in ADP crystals at the critical temperature can be obtained by investigating the transparency. To this end we placed an X cut ADP single crystal plate between a photocell and a white light source and followed the variation of the photocell current in the process of cooling the crystal from 0 to -180°. It was found that at the critical temperature (-125°) the transparency of the specimen, as indicated by the ratio of the photocell currents I'/I, falls off abruptly from 0.85 to 0.05, as shown in Fig.1 (I is the current with the photocell directly illuminated by the source, and I' is the current with the light passing through the ADP specimen). This abrupt decrease in transparency can be explained by phase transition of the ADP crystal at -125°. With transition from the tetragonal to the orthorhombic modification[4] there develop severe stresses in the crystal and these produce numerous microcracks which sharply reduce the transparency of the crystal. Further gradual cooling of the crystal to -180° does not result in any further change in transparency. In the course of reverse temperature variation, i.e., slow warming from -180° to 0° there is observed a minor additional decrease in transparency at a temperature close to -50°.

2. We measured the variation of the dielectric constant and loss tangent at a frequency of 50 cps in fields from 3000 to 10 000 v/cm in the directions of the X (or Y) and Z axes in specimens cut from "pure" ADP single crystals.

We found that metallizing the crystal plates with 0.004 mm thick gold foil results in favorable conditions for carrying out electric measurements in the range of low temperatures. Despite the development of microcracks, metallized X and Z cut specimens remain in one piece throughout the cooling-heating cycle and are suitable for repeat measurements.

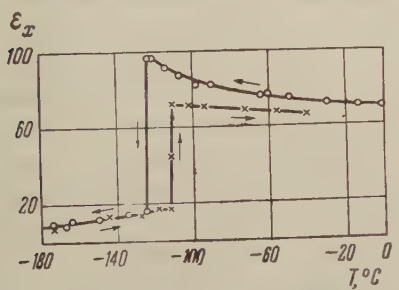

Fig.2. Temperature dependence of the dielectric constant of an X cut ADP crystal plate during cooling and heating.

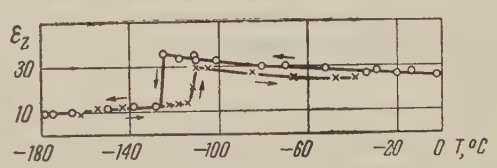

Fig.3. Temperature dependence of the dielectric constant of a Z cut ADP crystal plate during cooling and heating.

The results obtained by us (Figs.2 & 3) in the temperature range from 0 to -125° are in good agreement with the results of earlier investigators[1-3]. With decrease in temperature the dielectric constants ϵ_x and ϵ_z monotonically increase,

attaining values of 97 and 35, respectively, just above the critical temperature and then simultaneously at -125° abruptly fall to 15 and 12, respectively. Cooling of the specimens down to -180° is accompanied by further slow decrease of both dielectric constants to a value of about 9-10.

Subsequent slow warming results in growth of the dielectric constant, but the maximum of the dielectric constant is attained at a temperature somewhat higher than the critical point. The observed temperature hysteresis, which, incidentally, is characteristic of higher order phase transitions, is in agreement with the specific heat hysteresis observed in an ADP single crystal by Stephenson & Zettlemoyer[5]. Further heating of the specimens to -50° is accompanied by monotonic decrease of the dielectric constant.

Debye patterns recorded for the specimens before cooling to the critical temperature and then again for the same specimens cooled to -180° and warmed do not show any significant differences.*

Thus in going from low to high temperatures, X cut ADP crystals in passing through the critical point undergo a phase transition from the orthorhombic to the tetragonal modification. Consequently, the critical temperature (-125°) is the Curie point.

Measurements of the loss tangents of X cut plates show a rapid decrease of tan δ from 0.2 at room temperature to 0.001-0.0001 at temperatures below 0°C. This is presumably connected with rapid decrease of the electric conductivity due to impurities that are inevitably present even in "pure" ADP crystals. But if one follows the temperature variation of tan δ during heating of an X cut specimen from -180° to 0° there is observed a value of the order of 0.0001 for tan δ in the interval from -180° to -50° and then a rather rapid rise. This increase of tan δ is probably due to further disturbance of the crystal structure in the process of warming.

3. We also investigated the dielectric constant and loss tangent of ADP single crystals grown from solutions containing $(NH_4)_2S_2O_8$ and $(NH_4)_2Cr_2O_7$ in different concentrations from 1 to 6%.

These impurities noticeably alter the habit of the ADP crystals and modify their piezoelectric properties[6], but we did not observe any effect on the temperature of the phase transition. The difference between the values of ϵ_x at the Curie point for "pure" and doped ADP crystals does not exceed a few units. On the other hand, introduction of impurities results in a significant change of tan δ. Thus, for example, the room temperature value of tan δ for specimens from an ADP solution with only 1% $(NH_4)_2S_2O_8$ increases by a factor of 3 compared with the value for "pure" ADP. (Tan δ = 0.2 for pure crystals and 0.6 for doped crystals.) The observed increase of tan δ for doped ADP crystals can be attributed to increase of the conductivity owing to the presence of impurity ions.

References

1. G.Busch, Helv.Phys.Acta, 11, 359 (1938).
2. P.Baertschi, B.Matthias, W.Merz & P.Scherrer, Helv.Phys.Acta, 18, 238 (1945).
3. W.P.Mason, Phys.Rev., 69, 173 (1946).
4. W.P.Mason & B.T.Matthias, Phys.Rev., 88, 477 (1952).
5. C.C.Stephenson & J.Zettlemoyer, J.Am.Chem.Soc., 66, 1405 (1944).
6. F.M.Alemaikin, Thesis, L'vov State University, 1954.

---

*The x-ray diffraction studies were carried out by I.V.Kavich in the Crystallography Department of L'vov State University.

OBTAINING A STABLE SINGLE-DOMAIN STATE OF FERROELECTRICS

- V.A.Yurin

Earlier it was reported[1-4] that γ-irradiation of Rochelle salt crystals produces substantial alterations of their ferroelectric properties. When an X cut Rochelle salt specimen is subjected to a certain dose of γ-radiation, its hysteresis loop transforms from the usual normal loop to a double one. Further increase of the radiation dose leads to complete disappearance of the hysteresis loop without (and this is significant) any substantial changes in the domain structure pattern.[2] Somewhat analogous changes in the ferroelectric properties of Rochelle salt are produced by the introduction of copper ions in the process of growing the crystals.[5-7] Subsequently, we also investigated the effect of γ-radiation on the ferroelectric properties of another ferroelectric, namely, tri-glycine sulfate: with increase of the radiation dose the properties of this material vary in the same way as those of Rochelle salt.[8] A tendency to analogous variation of the ferroelectric properties has been reported for a barium titanate single crystal subjected to irradiation in a pile.[9] All these effects are of a highly complex nature, and their interpretation and explanation require comprehensive and extensive investigation. The present work was a continuation of the research reported on in Refs.1-6 and was devoted primarily to investigation of the effect of different external influences (annealing and electric fields) on the anomalous properties and domain structure of ferroelectrics.

For the present experiments we chose Rochelle salt containing Cu ions (~0.01 percent by weight), since this has been found to be more susceptible to external influences than irradiated salt.

For X cut plates of such crystals there are observed clear (in some cases asymmetrical) double hysteresis loops (Fig.1,a & e). The critical field E_{cr} (the field corresponding to the center of the loop components) of such double loops attains 1-2 kv/cm and depends on the impurity concentration, on the temperature and, as will be shown below, on the previous history of the specimen. The domain structure (as revealed by a polarizing microscope) has the same appearance as that in ordinary Rochelle salt crystals. However, the behavior of the domain structure under the influence of electric fields differs in copper containing crystals from the behavior in ordinary crystals. Reorientation or switching of the domains in crystals with copper impurity begins in an applied field $E = E_{cr}$ of the double hysteresis loop. The specimen becomes a single domain specimen in a field corresponding to the saturation field E_{sat} of the double loop. The field values are appreciably higher than those at which switching of the domains begins and goes to completion in ordinary Rochelle salt crystals.

Annealing of the specimens at 40-45° for 15-20 hours or holding them in alternating field $E \gg E_{sat}$ for 8-10 days at room temperature transforms the double hysteresis loop into a normal one (Fig.1, process a—b). However, if an annealed specimen is held for a prolonged period at a temperature between the Curie points in the absence of external influences continuously "disturbing" the domains (for example, alternating fields), there is re-established the state for which there is observed the initial double hysteresis loop. The rate of re-establishment of the double hysteresis loop depends on the temperature at which the specimen is held: the time decreases with reduction of the temperature. Fig.2 shows two typical curves characterizing the variation of Ecr with the holding time at different temperatures. Analysis shows that these curves are closely approximated by the analytic expression

$$E_{cr}(t) = E_0(1 - e^{-\frac{t}{\tau}}),$$

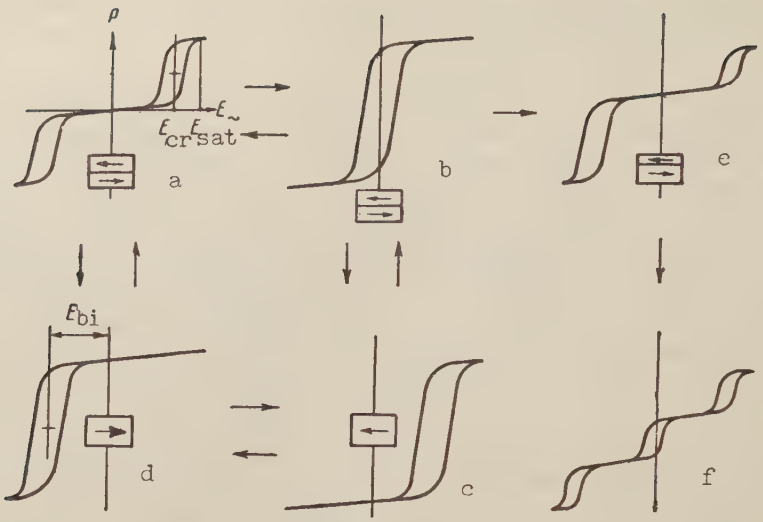

Fig.1. Transformation of hysteresis loops of Rochelle salt containing Cu. a—b and c—b: heating of the specimen at 35-45°. The other transformations occur at temperatures between the Curie points. a—b: holding the specimen in an alternating field $E_{\sim} \gg E_{cr}$. b—a: holding in zero external field. b—c: holding in a dc field $E_{=} > E_{sat}$ (in this case $E_{=} < 0$). c—b: same but with $E_{\sim} \gg E_{bi}$. a—d: same but with $E_{=} > E_{sat}$. d—c: same but with $E_{=} \gg E_{bi}$. b—e: same but with $E_{=} < E_{sat}$. d—a: same but with $E_{=} = E_{bi}$. e—f: same but with $E_{=} = E_{cr}$. The rectangles with arrows symbolically indicate the domain structure established in the specimen after removal of the external fields. The hysteresis loops were recorded oscillographically at a frequency of 50 cps in zero dc field.

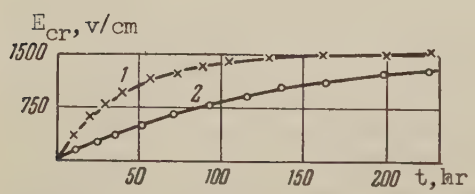

Fig.2. Variation of the critical field E_{cr} of the double hysteresis loop with the holding time at different temperatures (process b—a in Fig.1): 1 - at 18°, 2 - at 5°C.

where E_0 is determined primarily by the copper concentration in the crystal and the temperature. Assuming the relaxation time τ of the process of re-establishment of the double hysteresis loop to be described by $\tau = \tau_0 e^{\frac{U}{kT}}$ (on the assumption that the variation of E_{cr} is connected with diffusion processes in the crystal) and having plotted the variation of ln τ vs 1/T, one can from the slope of this plot determine the activation energy of the process. We obtained a value of 1.08 ev for the activation energy.

We continuously observed the domain structure of the specimen through transparent electrodes in the process of re-establishment of the double hysteresis loop. We observed no noticeable changes in the shape and dimensions of the domains. However, with increase of E_{cr} we noted an increase of the angle between the positions of extinction for neighboring domains, which indicates increase of the spontaneous deformation y_z^0. Our preliminary measurements showed that at room temperature the difference between the domain extinction angles in some specimens before and after re-establishment of the double hysteresis loop is about 0.4°.

It may be concluded on the basis of the described experimental results that the introduction of Cu ions into a Rochelle salt crystal brings it to a new state in which the domain structure acquires substantial stability as regards external

lectric fields. The stability is evinced in that for domain switching in such rystals a substantially stronger field is required than for switching in ordinry Rochelle salt crystals. This stable state persists in the crystal indefinitey and breaks down (and then reversibly) only as a result of very prolonged aplication of such external influences as a strong alternating field or annealing t a temperature above the upper Curie point.

It is important to note that the specimens after annealing were held in their atural polydomain state, as a result of which this state acquired stability. Our urther studies showed that if the specimens after annealing are held at the same emperature but in the single domain rather than the polydomain state (the single domain state can be obtained by applying a dc field $E_{=} > E_{sat}$ of the normal hysteresis loop to the specimen), this state also becomes stable. Observations by means of the polarizing microscope showed that specimens after removal of the dc field do not fragment into domains even after aging in a strong alternating field for several hours. The hysteresis loop in this case transforms from the normal loop not to a double loop but to a shifted or biased loop (Fig.1, process b—c). The direction of the shift is opposite to the direction of the polarizing dc field and consequently of the direction of the spontaneous polarization vector P_0. If the specimen after annealing is held in a field of opposite polarity, after removal of the field the loop is biased in the opposite direction (Fig.1,d). To disturb the stability of the single domain state (Fig.1, process c—b) one must apply external influences for an appreciable time, just as for disrupting the stability of the polydomain state. The degree of stability of the single domain state can be evaluated from the magnitude of the bias field E_{bi} (the bias field is the value of the field corresponding to the center of the biased hysteresis loop - Fig.1,d) and its dependence on the time the "disturbing" influence (annealing or $E_{\sim} \gg E_{bi}$) is applied. It is more convenient to determine E_{bi} not from the loop oscillogram but by measuring the value of external dc field that must be applied to the specimen in order to bring the center of the hysteresis loop back to the zero coordinate on the oscillograph screen, i.e., the value of the external field necessary to compensate the "internal bias" in the specimen. The variation of this field as a function of the holding time in a polarizing field leading to formation of the biased loop is characterized by curves similar to those shown in Fig.2.

Further investigations showed that low temperature annealing is not necessary for obtaining a stable single domain state in the specimens. If a specimen with a double hysteresis loop is held for a long time in a dc field $E_{=} > E_{sat}$ (for example, a positive field) at some temperature between the Curie points, the double hysteresis loop gradually transforms into a biased loop, and consequently, the specimen goes over from the stable polydomain state to the stable single domain state. The transformation of the hysteresis loop is realized by gradual displacement of the "right" loop to the left until it joins the "left" loop (Fig.1, process a—d). In like manner one can transform a stable single domain state with negative direction of the polarization vector to a stable single domain state with positive direction of P_0 (Fig.1, process c—d). To accomplish this the specimen must be held in a negative dc field $E_{=} > E_{bi}$ (in the presence of which the specimen becomes a single domain one with P_0 in the negative direction). In the course of this process the "internal bias" changes sign, passing through zero in the process.

The variation of E_{bi} with the holding time in a dc field $E_{=}$ = 5 kv/cm in the course of processes d→c and c→d is shown in Fig.3. Curves 1 and 2 are closely characterized by the following analytic expressions:

$$E_{bi}(t) = E_0 (1 - 2e^{-\frac{t}{\tau}})$$

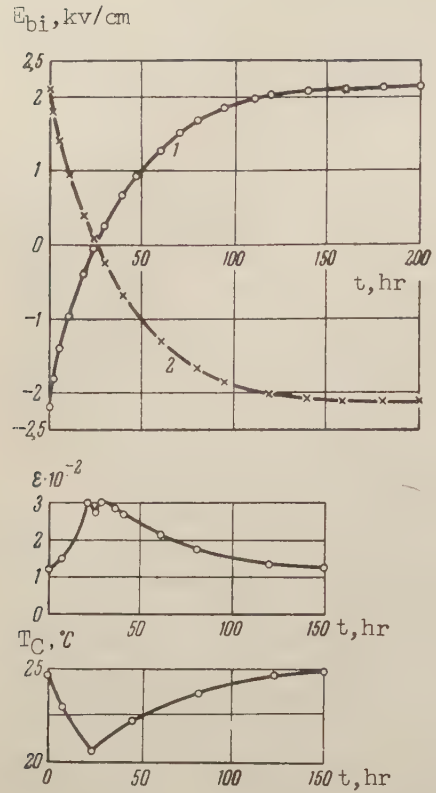

Fig.3. Time variation of the bias field E_{bi}, the dielectric constant ϵ and the Curie temperature T_C of Rochelle salt containing Cu in the course of processes d—c and c—d (see Fig.1). Temperature 18°. The $E_{=}$ = 5 kv/cm field was removed during the measurements.

and

$$E_{bi}(t) = E_0 (2e^{-\frac{t}{\tau}} - 1)$$

The time variations of the dielectric constant ϵ and the Curie points T_C observed in the course of these processes are also shown in Fig.3.

It follows from the above described experimental results that in a crystal of Rochelle salt containing copper ions one can "fix" any desired domain pattern from 50% twins to the single domain state. To this end one need only apply the appropriate external influence to form the desired domain structure and hold the specimen under these conditions for an adequate time. This inference is substantiated by the results of our further experiments on transformations of the hysteresis loop. Thus for obtaining an unsymmetrical loop one must hold the annealed specimen in a dc field $E_{=} < E_{sat}$ (Fig.1, process b—e) in the presence of which the volume occupied by domains with opposed polarizations are not equal. The ratio of the areas of the "right" and "left" hysteresis loops in this case will be determined by the ratio of the domain volumes.

In order to transform a biased loop into a double loop (i.e., to transfer the specimen from the stable single domain state to a stable polydomain state), one must first "force" the specimen to fragment into domains. To accomplish this one need only apply to the specimen a dc field $E_{=} = E_{bi}$ compensating the "internal bias" (upon application of the dc field, domains appear in the field of view of the polarizing microscope) and hold the specimen for an appropriate time in this compensating field. By cutting off the dc field from time to time and applying an alternating field (for observation of the loops) one can follow the "splitting" of the bias loop and its gradual transformation into a double loop (Fig.1, process d—a). One can readily split either of the components forming the double loop. Splitting of the "left" loop is illustrated in Fig.1 (process e—f).

From the experiments with Rochelle salt containing copper it was concluded that in the process of γ-irradiation of Rochelle salt or tri-glycine sulfate specimens there must be "fixed" the domain pattern that obtains in the specimen prior to irradiation. Thus in the case of tri-glycine sulfate specimens strongly polarized in a dc field prior to irradiation, after irradiation there was observed not a double but a biased hysteresis loop.[8]

After most of the above described experimental work was completed, we received the journal containing Chynoweth's[10] exhaustive study of "Radiation Damage Effects in Tri-glycine Sulfate." Chynoweth's results are in good agreement with what was found earlier for Rochelle salt irradiated with γ- and x-rays[1-4] and with the results of the present investigation.

A detailed discussion of our results will be published at a later date, hence here we shall restrict ourselves to a few remarks.

The character of the curves shown in Figs.2 and 3 gives reason to infer that he transformations of the hysteresis loops for crystals containing impurities re due to diffusion processes. Apparently, as a result of directed diffusion he impurity ions come to occupy positions in the crystal lattice that make for reater stability of the direction of the spontaneous dipole moments of the unit ell.

There is evident a clear analogy between the above described effects and the erminvar effect, as well as the magnetic diffusive aftereffect, observed in some erromagnets containing impurities. This analogy is strengthened by the fact that he above hypothesis regarding diffusion of the impurity and stabilization of the ipole moments is in good agreement with the explanations proposed[11-13] for the erminvar effect and the magnetic aftereffect.

In further investigations of the effects due to impurities one must bear in ind the great similarity between these effects and "aging" of ferroelectrics.[14-16]

The possibility of obtaining stable single domain states of ferroelectrics hould facilitate utilizing the piezoelectric effect in the class of ferroelec- ric materials that exhibit piezoelectricity only in the polarized state. It is ot impossible that a suitable piezoelectric state can be realized in many ferro- lectric materials by means of an appropriate impurity or form of radiation.

I desire to thank I.S.Zheludev for guidance in the work and V.P.Konstantin- va and I.Ya.Eisner for making available the crystals.

Institute of Crystallography,
Academy of Sciences of the USSR

References

1. I.S.Zheludev, M.A.Proskurnin, V.A.Yurin & A.S.Baberkin, Doklady AN SSSR, 103, 207 (1955).

2. I.S.Zheludev & V.A.Yurin, Izv.AN SSSR, Ser.fiz., 20, 211 (1956). (Trans. Bulletin, 20, 193.)

3. V.A.Yurin, Ibid., 21, 329 (1957). (Trans.Bulletin, 21, 336.)

4. V.A.Yurin, Kristallografiya, 1, 734 (1956).

5. V.P.Konstantinova & V.A.Yurin, Ibid., 2, 294 (1957). (Trans.Soviet Physics - Crystallography.)

6. V.A.Yurin & I.S.Zeludev, Ibid., 4, 253 (1959). (Trans.Ibid.)

7. I.Ya.Eisner, Izv.AN SSSR, Ser.fiz., 21, 334 (1957). (Trans.Bulletin, 21, 341.)

8. V.A.Yurin, A.S.Baberkin, E.N.Kornienko & I.V.Gavrilova, Present issue of the Bulletin, p.1334.

9. V.A.Yurin, Soobshchenie na II Soveshchanii po varikondam (Report presented at the Second Conference on Varikonds)., L., 1959.

10. A.G.Chynoweth, Phys.Rev., 113, 159 (1959).

11. J.Snoek, Physica, 8, 711 (1941).

12. L.Neel, J.de Phys. et radium, 15, 225 (1954).

13. J.Broz, S.Krupicka & B.Zitka, Chekhosl.fiz.zhurn. (Czech.Physics Journal), 9, 314 (1959).

14. V.L.Indenbom & M.A.Chernysheva, Izv.AN SSSR, Ser.fiz., 22, 1469 (1958). (Trans. Bulletin, 22, 1461.)

15. Z.Pajak & Stankowsky, Proc.Phys.Soc., 72, 1144 (1958).

16. E.Sawaguchi & M.Charters, J.Am.Ceram.Soc., 42, No.4, 157 (1959).

EFFECT OF GAMMA-RADIATION ON THE FERROELECTRIC PROPERTIES OF TRI-GLYCINE SULFATE

- V.A.Yurin, A.S.Baberkin, E.N.Kornienko & I.V.Gavrilova

It is known that γ-radiation produces substantial changes in the ferroelectric properties of Rochelle salt crystals.[1-3] A certain dose of γ-radiation causes the hysteresis loop of X cut Rochelle salt plates to change from the normal shape to a double loop. Further increase of the radiation dose leads to complete disappearance of the loop.

After our early work with Rochelle salt, we investigated the influence of γ-radiation on the ferroelectric properties of another ferroelectric, namely, triglycine sulfate (TGS). In this work particular attention was given to obtaining a single domain state, the possibility of obtaining which in ferroelectric materials was established earlier in the case of Rochelle salt.[4]

The investigations were carried out by the following procedure. Y cut specimens of TGS of different shape and size, after application of silver electrodes by vacuum evaporation, were placed in a holder which was then mounted near a Co^{60} source. The dosage rate was 235 r/sec. The holder was connected by means of a shielded cable with a set-up for oscillographic observation of the hysteresis loop which enabled us to observe the loops in the process of irradiation.

The experimental results for TGS hysteresis loops may be summarized as follows.

1. If the irradiation is carried out at a temperature below the Curie point of TGS ($t_{ir} < T_C$), then with increase of the dose received by the specimen, its hysteresis loop gradually transforms from the normal loop to a double one (Figs. a & b), the critical field E_{cr} (for the meaning of E_{cr} and other fields see Ref. 4 - the preceding article) of which increases approximately in proportion to the radiation dose. At the same time the coercive field E_c of both parts of the double loop gradually increases (for observation of the loops an appropriate alternating field was applied for brief periods at 20-30 min intervals). The increase of E_{cr} at first is not accompanied by any noticeable change of the maximum polarization P_{max}, but beginning with a dose of $5 \cdot 10^6$ r, P_{max} begins to decrease rapidly.

2. If in the process of irradiation there is applied to the specimen an alternating field $E_{\sim} > E_{sat}$ of the normal loop, no noticeable changes in the shape and size of the loop are observed; however, after removal of $E_{\sim}$ a double loop soon appears. The rate of this process decreases with decreasing temperature much as in the case of Rochelle salt containing copper[4].

3. If the specimen is irradiated at $t_{ir} > T_C$, then after cessation of irradiation and cooling to room temperature there are observed double loops with a small value of E_{cr}, which under the influence of an alternating field rapidly transform into a normal loop. If the cooling is carried out in the presence of an alternating field, then even after an appreciable dose of radiation the loops remain normal. In this case also, however, after removal of $E_{\sim}$ at room temperature there soon form double loops.

4. If the irradiation is carried out at $t_{ir} < T_C$ and in the presence of a dc field $E_{=} > E_{sat}$ of the normal loop (i.e., with the specimen in the single domain state), then after removal of $E_{=}$, instead of a double loop, there is observed a biased loop (Fig.c), the bias field E_{bi} of which is also approximately proportional to the radiation dose. The direction of displacement of the loop is opposite to the direction of $E_{=}$, i.e., the sign of the radiation induced "internal biasing" in the specimen is the same as the sign of the applied external field $E_{=}$. Reversing the polarity of $E_{=}$ changes the direction of the loop shift to the opposite.

5. If the irradiation is carried out under the conditions outlined in sections 2 and 3 above (we recall that such irradiation does not produce any change

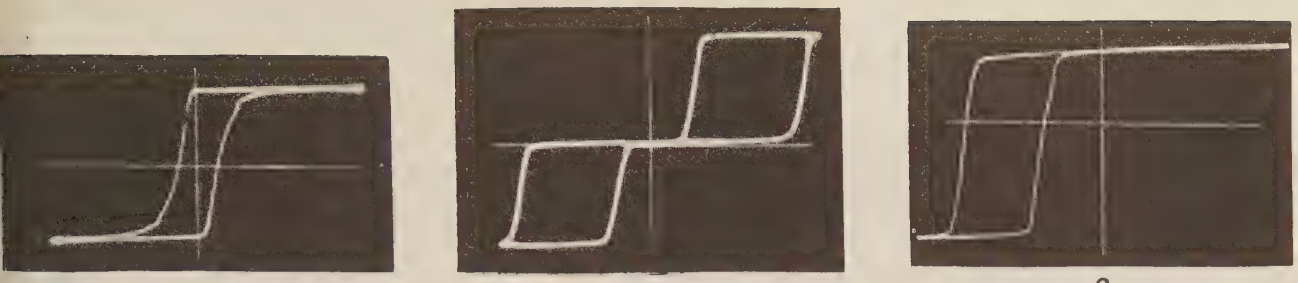

a b c

Hysteresis loops of tri-glycine sulfate: a - normal loop prior to irradiation, b - double loop after a radiation dose of $2 \cdot 10^6$ r, c - after a dose of $2 \cdot 10^6$ r but with the irradiation carried out in the presence of a positive dc field $+E_{=} > E_{sat}$. Measurement conditions: peak ac field 2 kv/cm, $f = 50$ cps, $t = 20^{\circ}$.

of the normal loop prior to removal of $E_{\sim}$), but after removal of $E_{\sim}$ and cessation of radiation the specimen is held in a dc field $E_{=} > E_{sat}$, instead of a double loop there forms a biased hysteresis loop.

6. Some of the larger specimens after irradiation were subjected to repeated grinding; after removal of each successive surface layer, we immediately applied electrodes and recorded the hysteresis loops. No noticeable changes in the form of the hysteresis loop (double or biased) were observed. We note that in the process of irradiation the specimens acquired a uniform greenish-yellow color.

7. When irradiated specimens are stored for a long period at room temperature in a state of "rest" (i.e., no external fields), the "damaged" hysteresis loops become more stable. After such stabilization in order to transform the "damaged" loop back to a normal loop one must either expose the specimen for a prolonged period to an alternating field or anneal it for a considerable time at a temperature well above the Curie point.

Conclusions

1. Under the influence of γ-radiation there is formed in tri-glycine sulfate crystals either a stable polydomain state (evinced by a double hysteresis loop) or a stable single domain state (manifested by a biased hysteresis loop), i.e., there is "fixed" in the specimen the domain structure that obtains in the process of irradiation and holding at $t < T_C$ after irradiation. The fact that a double loop corresponds to a polydomain structure and a biased loop to the single domain state in ferroelectrics was established earlier[2-4].

2. The stability of the domain structure is due to the formation in the crystal of "internal bias fields"; the signs of the "internal biases" in neighboring antiparallel domains in a polydomain specimen are opposed, while in a single domain crystal the sign of the "internal bias" is the same for the entire specimen. Under irradiation these biases do not form instantaneously but in the course of relaxation processes, probably diffusive processes, as a result of which the products of radiolysis are located in the lattice at points with minimum energy. These points are apparently connected with the presence of spontaneous polarization (and its direction) in the crystal. The corresponding phenomenon in ferromagnetic materials is directed ordering, which is responsible for uniaxial magnetic anisotropy, the appearance of which serves to explain the Perminvar effect and magnetic aftereffects.[5]

3. The above described experimental results are in good agreement with the

results obtained in studies of the effects of x-rays[6] and ultraviolet radiation[7] on tri-glycine sulfate crystals.

We are grateful to I.S.Zheludev, M.A.Proskurnin and I.S.Rez for their interest in the work.

Institute of Crystallography,
Academy of Sciences of the USSR

References

1. I.S.Zheludev, M.A.Proskurnin, V.A.Yurin & A.S.Baberkin, Doklady AN SSSR, 103, 207 (1955).

2. I.S.Zheludev & V.A.Yurin, Izv.AN SSSR, Ser.fiz., 20, 211 (1956). (Trans. Bulletin, 20, 193.)

3. V.A.Yurin, Ibid., 21, 329 (1958). (Trans.Bulletin, 21, 336.)

4. V.A.Yurin, Present issue of the Bulletin, p. 1329.

5. L.Neel, J.phys.et radium, 15, 225 (1954).

6. A.G.Chynoweth, Phys.Rev., 113, 159 (1959).

7. I.M.Sil'vestrova & N.A.Romanyuk, Kristallografiya, 5, 147 (1959). (Trans. Soviet Physics - Crystallography.)

VARIATION OF THE ELASTIC CONSTANT s'_{33} OF TRI-GLYCINE SULFATE CRYSTALS AS A FUNCTION OF THE DC FIELD IN THE REGION OF THE CURIE POINT

- I.M.Sil'vestrova

It is known[1,2] that both the electromechanical coupling coefficient for contraction-elongation in length of Y cut bars of tri-glycine sulfate (with the length parallel to the crystallographic c axis) and the elastic constant s'_{33} in the same direction have the highest values as compared with the values of these parameters in all the other directions in the XZ plane. We felt it would be of interest to investigate the influence of dc fields on the magnitude of s'_{33} in the vicinity of the Curie point.

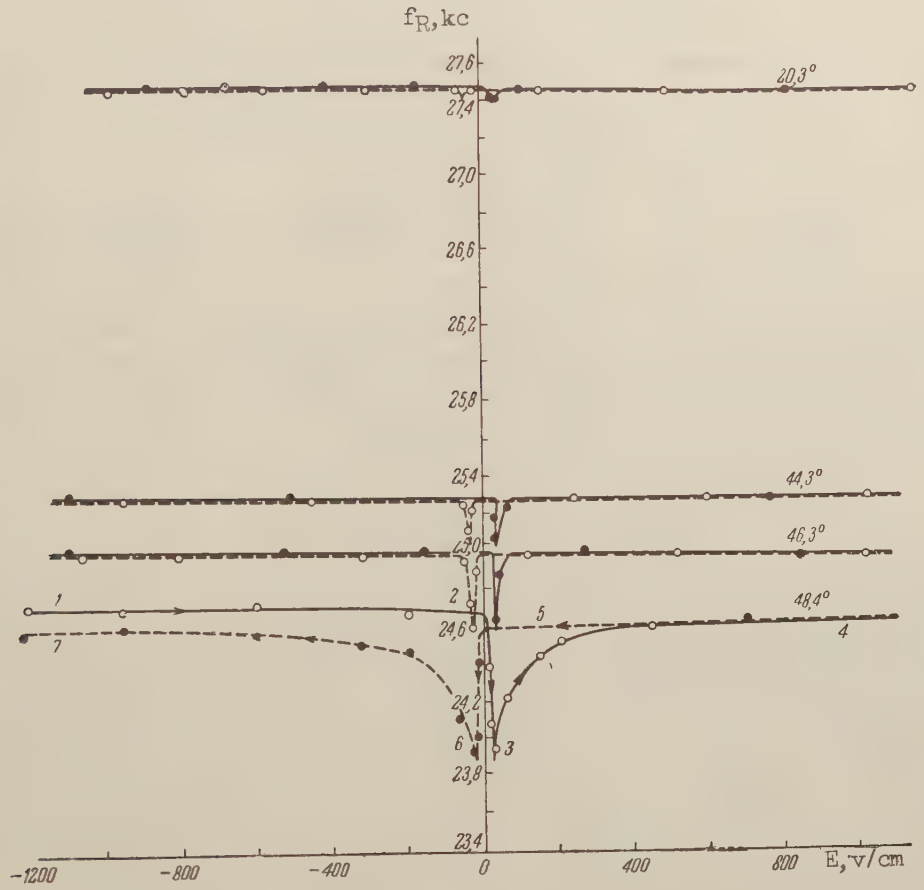

Fig.1. Variation of the resonance frequency of a tri-glycine sulfate bar as a function of the dc polarizing field at different temperatures below the Curie point.

The measurements were carried out by the usual procedure of recording the resonance and antiresonance frequencies of the vibrating bar. The specimen dimensions were 48.73 x 3.5 x 1.5 mm. Silver foil electrodes were applied to the faces normal to the Y axis. The results of measurements of variation of the resonance frequency as a function of the polarization reversing dc field at different temperatures below the Curie point are shown in Fig.1. In all cases prior to the beginning of measurements the specimen was held in a polarizing dc field E_p = 1000 v/cm for 1 hour. The field variation sequence followed in all the measurements is indicated by the figures 1 through 7 at the curve for T = 48.4°C. It will be seen that at the instant of polarization reversal the crystal becomes "softer",

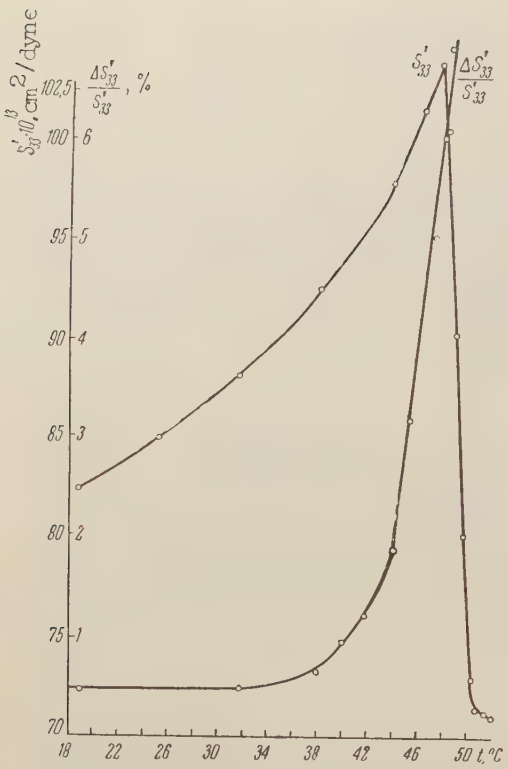

Fig.2

i.e., s'_{33} increases, while f_R decreases; with increase of the temperature and approach to the Curie point the increment

$$\Delta s'_{33} =$$

$$= s'_{33}(\text{at } E_p = E_{\text{switching}}) - s'_{33}(\text{at } E_p = 1000 \text{ v/cm})$$

grows. For the investigated specimens Δf_R varied from 50 cps at 20° to 950 cps at 48°, while $\Delta s'_{33}$ varied from $0.36\cdot10^{-13}$ to $6.12\cdot10^{-13}$ cm^2/dyne.

The temperature dependence of s'_{33} for the case when the dc polarizing field (1000 v/cm) was not cut off during the time of measurement is shown by curve 1 in Fig.2. It will be seen

←Fig.2. Variation of s'_{33} and $\Delta s'_{33}/s'_{33}$ as a function of temperature for the same specimen. Initial polarizing field E_p = 1000 v/cm.

Fig.3. Variation of the resonance and antiresonance frequency of the same specimen as a function of the dc switching field at different temperatures. ↓

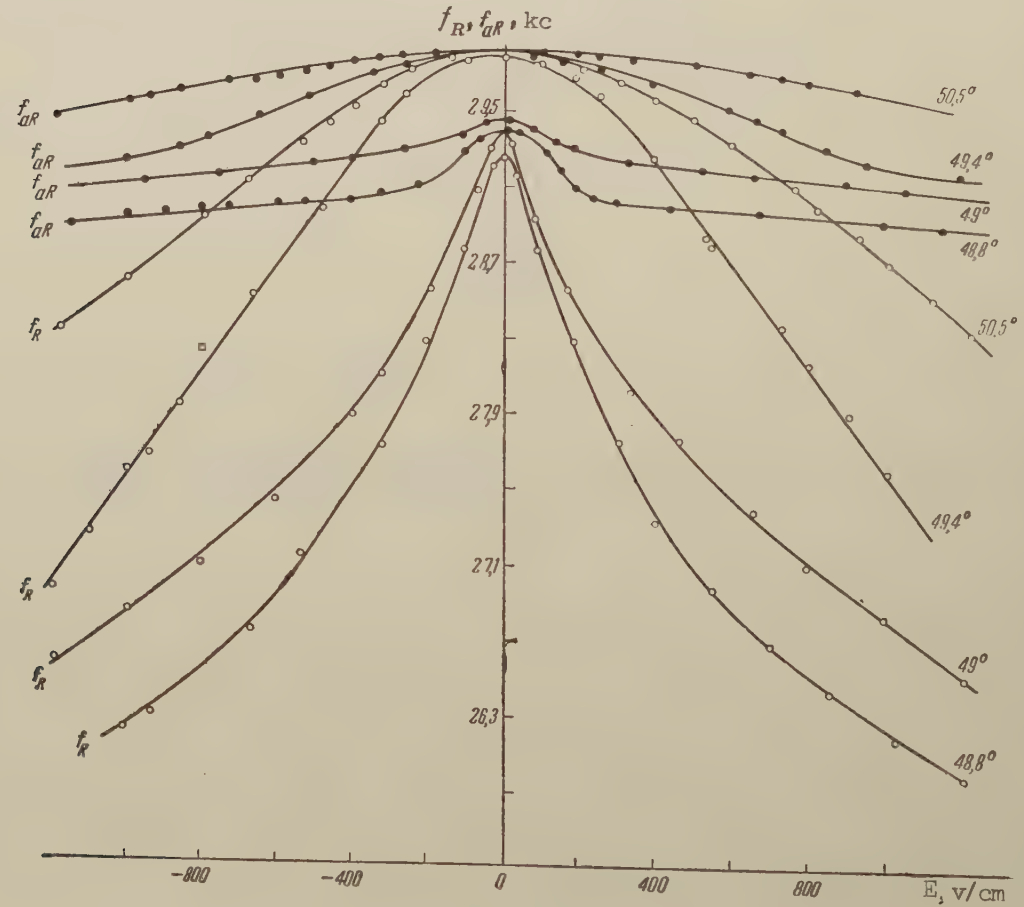

Fig.3

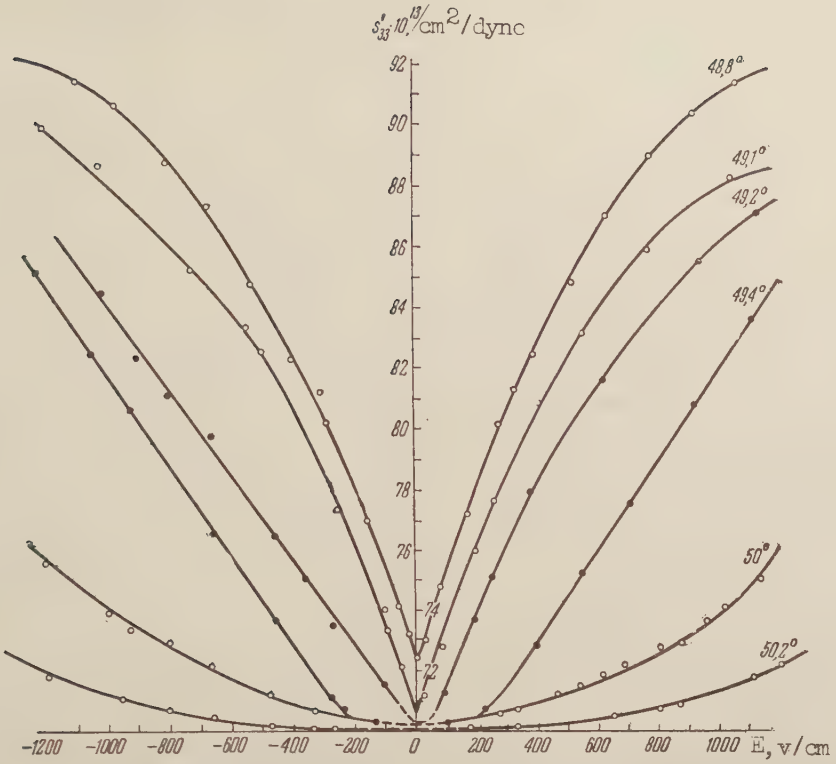

Fig.4. Variation of the elastic constant s'_{33} of the same specimen as a function of the dc field at different temperatures.

that s'_{33} increases rather rapidly with rising temperature, attains a maximum value at 48° and then falls off abruptly at higher temperatures. We note that the peak temperature, 48°, lies below the Curie point for the given crystal, which at E_p = = 0 is 49.1° and for E_p = 1000 v/cm is 50.3° (as determined from measurements of the dielectric constant).

Curve 2 in Fig.2 shows the variation of $\Delta s'_{33}/s'_{33}$ as a function of temperature: $\Delta s'_{33}/s'_{33}$ begins to rise at 35-36°, increases rapidly in the 44 to 46° interval, attaining a value of 6-7% at about 46°.

It should, however, be noted that at temperatures above 48° there is evinced a strong and inverse dependence of s'_{33} on the polarizing field. At temperatures close to 48° and in weak dc fields there is observed a high value of f_R and, accordingly, a low value of s'_{33}, while in strong dc fields the crystal becomes "softer" and exhibits a low value of f_R (and a high value of s'_{33}). This effect is observed only in the temperature region from 48 to 50.5°. However, reliable experimental results can be obtained only beginning with 48.5-48.8° (Fig.3). The changes of s'_{33} as a function of the applied dc field in this region are very large and attain 30%. For example, at a temperature of 48.8°, s'_{33} with E = 0 equals $72\cdot 10^{-13}$ cm^2/dyne, while with E = 1000 v/cm s'_{33} equals $92\cdot 10^{-13}$ cm^2/dyne (Fig.4).

In order to help this effect we recorded the variation of the antiresonance frequency f_{aR} of the vibrating bar as a function of the dc field at the same temperatures. The resultant curves are shown in Fig.3. Using these data we calculated the values of the electromechanical coupling coefficient K shown in Fig.5. It will be seen that the electromechanical coupling coefficient K increases with increase of the dc field. It is known that the magnitude of the effective piezoelectric coefficient d'_{33} is proportional to K, i.e., that

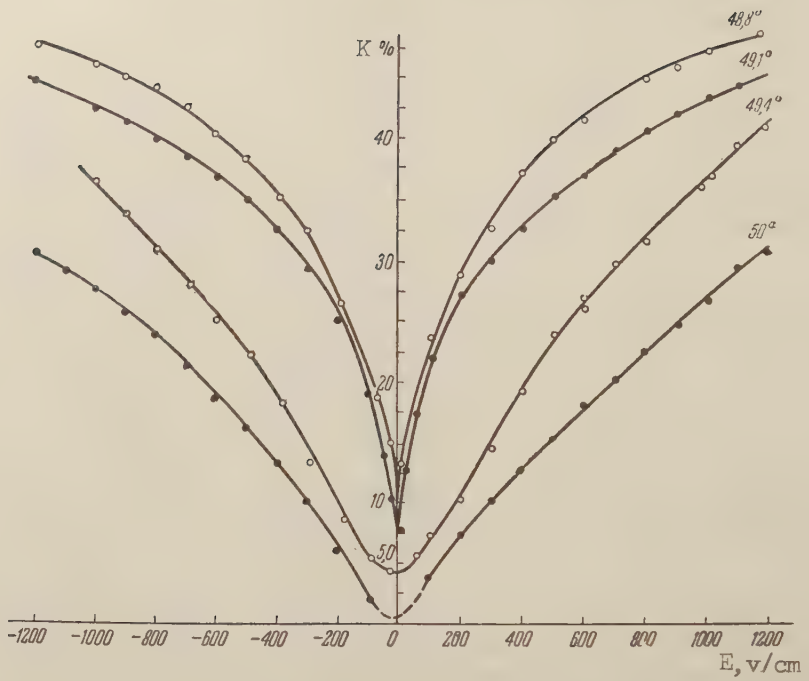

Fig.5. Variation of the electromechanical coupling coefficient K of the same specimens as a function of the dc field at different temperatures.

$$d'_{33} = K\left(\frac{\varepsilon_{22}}{4\pi} s'_{33}\right)^{1/2},$$

where ε_{22} is the dielectric constant.

Thus it may be inferred that the greater the applied dc field, the higher the degree of noncentral symmetry of the crystal. However, with rise of temperature it becomes increasingly difficult to disturb the noncentral symmetrical structure which the crystal would have at the given temperature in the absence of an external influence (field). It will be evident from Figs.2 & 4 that in the almost central symmetrical state s'_{33} already has a low value, i.e., about $70 \cdot 10^{-13}$ $cm^2/dyne$.

I desire to express my gratitude to I.V.Gavrilova for supplying the specimens and to L.A.Shuvalov for discussion of the results.

Institute of Crystallography,
Academy of Sciences of the USSR

References

1. K.Husimi & K.Kataoka, J.Phys.Soc.Japan, 14, 105 (1959).

2. V.P.Konstantinova, I.M.Sil'vestrova & K.S.Aleksandrov, Kristallografiya, 4, 69 (1959). (Trans.Soviet Physics - Crystallography.)

FERROELECTRIC PROPERTIES OF TRI-GLYCINE SULFATE SINGLE CRYSTALS IN THE 0.01 TO 50 cps FREQUENCY RANGE

- V.M.Gurevich & I.S.Zheludev

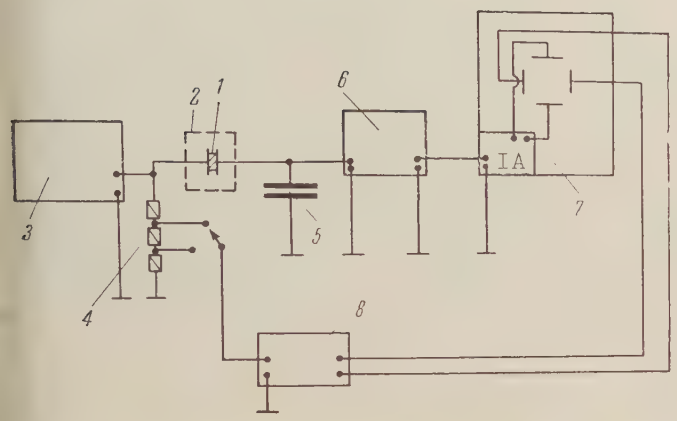

Fig.1. Diagram of the equipment for investigating hysteresis loops in the frequency range from 0.01 to 100 cps: 1) crystal, 2) thermostat maintaining temperature to within ±0.01°, 3) NGPK-2 audiofrequency oscillator, 4) variable voltage divider, 5) standard capacitor, 6) EMU-3 voltmeter ($R_{in} \geqslant 10^{13}$ ohm), 7) ENO-1 dc oscillograph (IA - internal dc amplifier in vertical channel - R_{in} = 520 kilohm), 8) external dc amplifier.

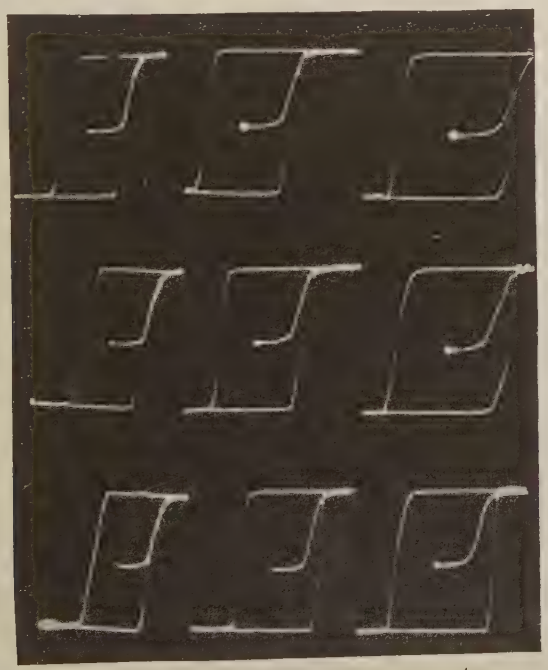

In an earlier report[1] we described the results of our investigation of tri-glycine sulfate (TGS) single crystals at infralow frequencies, mainly at 0.01 cps. The results of the present study, which was carried out with improved equipment with photographic recording of the hysteresis loops, give reason to assert that the anomalies observed earlier at 0.01 cps are also evinced in the frequency range from 0.01 to 50 cps and hence are not peculiar to infralow frequencies.

A diagram of the experimental set-up is shown in Fig.1. The present equipment differs from that used earlier[1] by incorporation of a dc oscillograph with an external dc amplifier in the horizontal deflection channel. The present circuit differs from those used earlier for recording the quasistatic hysteresis loops of $BaTiO_3$ crystals[2] and $(Ba,Sr)TiO_3$ ceramic[3], not only as regards the frequency range available (these frequencies have not been used hitherto for investigating ferroelectric hysteresis) but also in the use of a sinusoidal voltage instead of a step voltage, while retaining a low input impedance of the oscillator (~1 kilohm) and the use of an oscillographic indicator instead of the usually employed electronic recorders characterized by appreciable lag.

Photographs of hysteresis loops obtained on the new set-up (Fig.2) fully substantiate the inferences drawn in Ref.1 regarding the dependence of the coercive field E_c in TGS crystals on the frequency f and applied field E. The quantitative dependences are shown in Fig.3. It

←Fig.2. Influence of frequency and field strength on the hysteresis loops of TGS at infralow frequencies (the indicated fields are crest values).

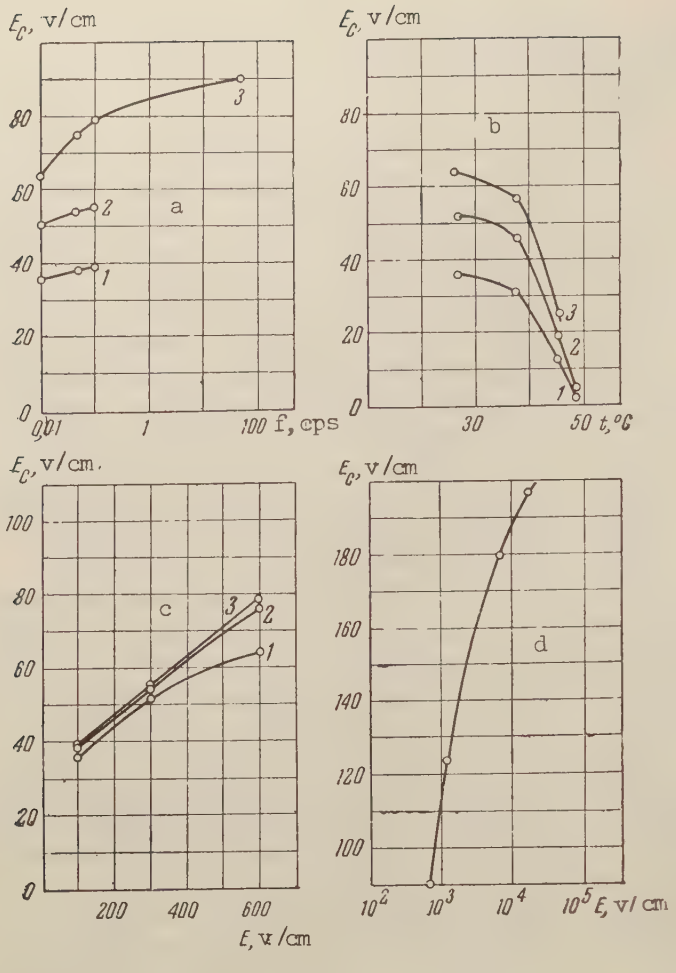

←Fig.3. Variation of the coercive field E_c with frequency, applied field and temperature: a) 1 - E = = 100 v/cm, 2 - E = 300 v/cm, 3 - E = 600 v/cm; b) 1 - E = 100 v/cm, 2 - E = 300 v/cm, 3 - E = 600 v/cm; c) 1 - f = 0.01 cps, 2 - f = 0.05 cps, 3 - f = 0.1 cps; t = 27.4°; d) f = 50 cps, t = 29.5°; a & b) t = = 27.4°, f = 0.01 cps.

must be noted that a significant dependence of E_c on E is also observed at frequencies of 10 and 50 cps, i.e., is not a feature peculiar only to the infralow frequency range (0.01 to 0.1 cps) investigated earlier[1]. Broadening of the hysteresis loops leads to increase of the hysteresis loss (Fig.4,a), but this loss is always lower than the loss at 50 cps for the same field value (Fig.4,b).

In considering the observed effect one must note that a broadening of the hysteresis loops with increase in the frequency and amplitude of the applied electric field would be observed if the oscillator had an input impedance comparable with the switching impedance R_{sw} of the crystal in a field with the given frequency and amplitude. The switching impedance is given approximately by

$$R_{sw} \approx \frac{V_c \Delta\tau}{\Delta P_s s},$$

where V_c is the coercive voltage in volts, $\Delta\tau$ is the switching time (time for reversal of the polarization from $+P_s$ to $-P_s$ in sec, $\Delta P_s = |+P_s| + |-P_s|$ in coul/cm^2, and s is the area of the crystal in cm^2. Other conditions being equal, $\Delta\tau \sim (1/fE_c)$, i.e., $R_{sw} \sim (1/f)$ (the frequency dependence of E_c in this case can be neglected inasmuch as it is insignificant). Calculations showed that at a field strength of 100 v/cm R_{sw} of a TGS crystal at a frequency

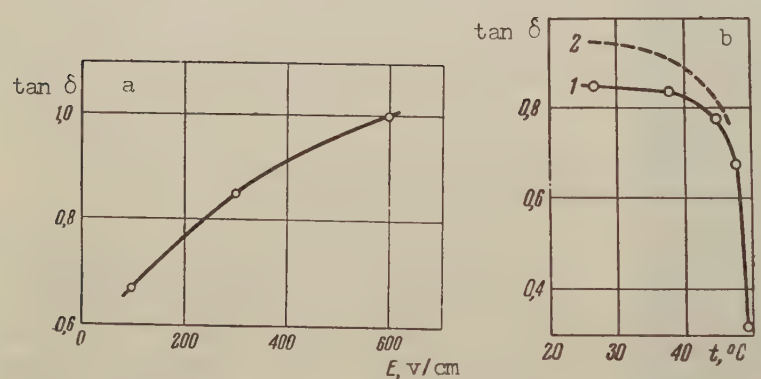

Fig.4. Variation of the hysteresis loss with field strength and temperature (the values of tan δ were calculated from the hysteresis loops): a) f = 0.05 cps, t = 27.4°; b) 1 - f = 0.05 cps, E = 300 v/cm, t = 27.4°; 2 - f = 50 cps, E = = 300 v/cm, t = 27.4°.

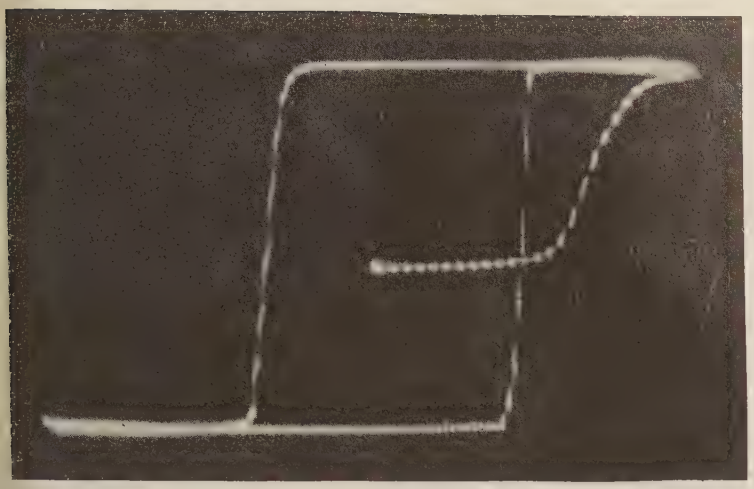

Fig.5. Hysteresis loop including the virgin curve.

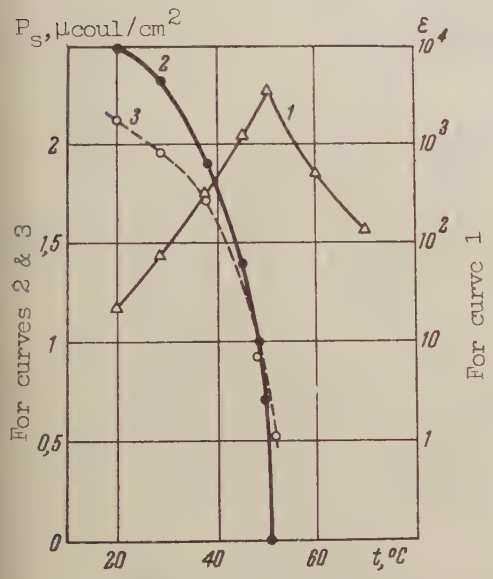

Fig.6. Temperature dependences of the dielectric constant ε (1) measured at a frequency of 10^6 cps and the polarization P_S calculated from the hysteresis loops recorded at a frequency of 0.05 cps (2 & 3): 2 - our data, 3 - data of Konstantinova et al[6].

of 0.01 cps is $4.3 \cdot 10^6$ ohm, at a frequency of 0.05 cps - $1.51 \cdot 10^6$ ohm, and at a frequency of 0.1 cps - $8.5 \cdot 10^5$ ohm. All these values are much greater than the input impedance of the oscillator ($\sim 10^3$ ohm) so that the input impedance obviously could not affect the measurement results.

In Ref.1 we explained the dependence of E_c on f and E by the "time of action of the field", reducible to the variation of E_c as a function of $dE/d\tau$. Hysteresis loops recorded for virgin specimens (i.e., specimens not subjected to an electric field) as a rule have the appearance shown in Fig.5. In this case the crystal is first brought from the twinned state to a single domain state and then from the single domain state of one sign goes over into the single domain of opposite sign.

As will be evident from the figure, the process of polarization from the initial virgin state requires a stronger field than the process of polarization reversal (switching). The ease or difficulty of switching must, in turn, depend on the degree of monodomainization of the crystal: if after switching there still remain in the crystal nuclei of opposite sign, the switching must occur more easily, i.e., at lower fields, than if all nuclei are destroyed. Apparently, the greater the amplitude of the field, the higher the degree of monodomainization of the crystal attained and the more difficult the process of switching. This effect is presumably the reason why increase of the field amplitude leads to a more noticeable increase of E_c than increase of the frequency. This will be evident in Fig.2. This interpretation is also supported by the "rocking" effect observed in the work of Ref.1.

Determinations of the temperature dependence of P_s, determined from the hysteresis loops recorded at 0.05 cps and measurements of the temperature dependence of the dielectric constant ε show that our TGS crystal did not differ in any significant way from the crystals investigated by other authors (Fig.6).

Next we turn to change in the shape of the hysteresis loop with variation in frequency f and field strength E with $E > E_S$ (E_S is the saturation field). (Variation in the shape of the hysteresis loop with $E < E_S$ was already considered and explained in Ref.1; here one must only add that for equal E the values of the

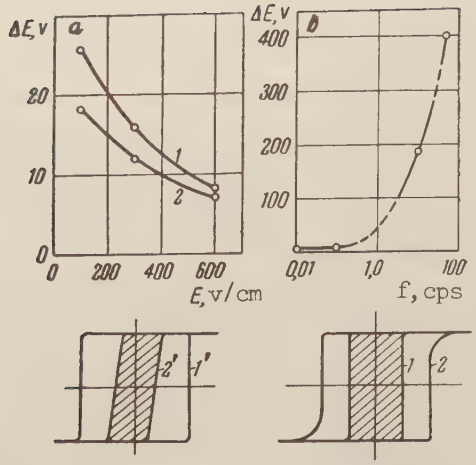

Fig.7. Influence of field strength (a) and frequency (b) on the shape of the hysteresis loops; $\Delta E = E_s - E_c$: a) $E_1' > E_2'$: 1 - f = 0.1 cps, 2 - f = 0.01 cps, t = 38°; b) for frequencies from 0.01 to 10 cps E = = 600 v/cm; for 50 cps E = 665 v/cm: 1 - infralow frequency, 2 - 50 cps, t = 38°.

polarization in the infralow frequency region are always higher and the values of E_c always lower than at 50 cps.) As was noted above (Fig.2), with increase of f and E the hysteresis loops broaden. Moreover, with variation of f and E the rectangularity of the hysteresis loops changes (Fig.7). Fig.7,a shows the variation in the shape of the hysteresis loop as a function of the field strength in the range of infralow frequencies. The loop recorded at a lower field value (2') is less rectangular than the loop recorded at a higher field strength (1'). This can be explained as follows: reduction of E leads to decrease of E_c, i.e. polarization switching occurs in this case at a lower field value and, consequently, over a longer time[4]. Fig.7,b shows the variation in the shape of the hysteresis loops as a function of the frequency at the same field value. Here above a frequency of 0.1 cps the rectangularity of the loop begins to deteriorate owing to growth of ΔE. The reason for this is still unclear. Thus optimum rectangularity of the hysteresis loop of the investigated TGS crystal is observed at a frequency of about 0.1 cps.

Turning back to Fig.5 we note that the illustrated "maturation" of the crystal is completed in one cycle apparently only at not excessively high frequencies (hundredths or tenths of a cycle per second). At 50 cps such "maturation" does not occur at all in some sections of the crystal.[5] From the hysteresis loop recorded at infralow frequency with registration of the virgin curve (Figs.2 & 5), one can determine the unipolarity of the crystal with an accuracy to within 1% or possibly better.

We desire to express our gratitude to I.V.Gavrilova and M.F.Koldobskaya for furnishing the crystal specimens and to I.S.Rez for his interest in the work and discussion of the results.

Institute of Crystallography,
Academy of Sciences of the USSR

References

1. V.M.Gurevich, I.S.Zheludev & I.S.Rez, Kristallografiya, 5, 802 (1960). (Trans.Soviet Physics - Crystallography.)
2. H.H.Wieder, J.Appl.Phys., 27, 413 (1956).
3. F.Brown, J.Am.Cer.Soc., 42, 350 (1959).
4. W.J.Merz, Phys.Rev., 95, 690 (1954).
5. V.A.Meleshina, I.S.Zheludev, I.S.Rez, I.V.Gavrilova & M.F.Koldobskaya, Report presented at the Third Conference on Ferroelectricity, Moscow, Jan.1960.
6. V.P.Konstantinova, I.M.Sil'vestrova & V.Yurin, Kristallografiya, 4, 125 (1959). (Trans.Soviet Physics - Crystallography.)

EFFECT OF ULTRASOUND ON SOME PHYSICAL PROPERTIES OF ROCHELLE SALT CRYSTALS

- T.Kh.Chormonov

Some physical properties of Rochelle salt crystals and many other ferroelectric materials may be significantly altered under the influence of even weak external factors. The influence of such a relatively strong factor as ultrasonic vibrations may be even more pronounced. Under the influence of ultrasonic vibrations, as a result of complex physical-mechanical processes, the surface of the crystal is hardened to an appreciable degree. However, the nature of such hardening has yet scarcely been studied.

The purpose of the present work was to determine the influence of ultrasound on some of the physical properties of Rochelle salt crystals.

Growth of Rochelle Salt Crystals Under the Influence of Ultrasound

The Rochelle salt crystals were grown in individual thermostatically controlled crystallizers by the planetary technique. The temperature was maintained at the desired level within $\pm 0.05^{\circ}$. By way of crystallizers we used chemically pure Pyrex crystallization pans equiped with a special stirrer. In the process of crystal growth the crystallization medium was sealed off from the atmosphere.

The ultrasonic vibrations were produced by a magnetostrictive transducer with a frequency of 21.5 kc and a specific power of 2 watt/cm^2. The crystallizer was located almost on the surface of the vibrator.

The process of crystallization of the Rochelle salt crystals was controlled by varying the intensity of the ultrasonic vibrations acting on the growing crystal. Ultrasound tends to enhance the mobility of the ions. With increase in the intensity of the ultrasound, however, the homogeneity of the crystals deteriorates. For growing homogeneous crystals one must have a grow low rate of crystallization and a very low level of ultrasonic vibration.

Microhardness of Sonicized Rochelle Salt Crystals

The microhardness of the Rochelle salt crystals was determined by means of a PMT-3 tester using loads from 20 to 200 g. Five indentations were made in each "sonicized" crystal, the hardness computed for each and the result averaged. The results obtained indicate that the mechanical properties of sonicized crystals of Rochelle salt differ substantially from the properties of ordinary crystals. Thus sonicized crystals have an average microhardness of the order of 77 kg/mm^2, while the microhardness of ordinary crystals is 58 kg/mm^2.

Under the influence of ultrasound the structure of Rochelle salt crystals becomes finer grained and the crystals are strengthened and hardened. The degree of hardening depends on the intensity and duration of application of the ultrasonic vibrations.

Influence of Ultrasound on the Dielectric Constant and Loss Tangent of Rochelle Salt Crystals

The dielectric constant ϵ and loss tangent tan δ of the sonicized Rochelle salt crystals were measured by means of an SG-IM electrometer and a KV-1 type Q-meter.

We investigated the temperature dependence of the dielectric constant of Rochelle salt crystals treated with ultrasonic vibrations during growth. The results are given by curve 1 in Fig.1; for comparison we give the corresponding dependence for ordinary Rochelle salt (curve 2). It will be evident that the

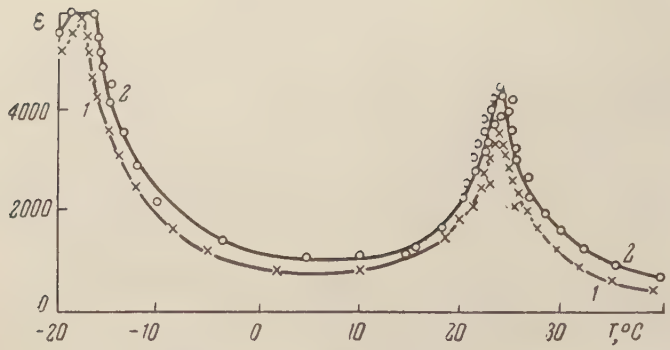

Fig.1. Temperature dependence of the dielectric constant of Rochelle salt crystals: 1) sonicized, 2) ordinary.

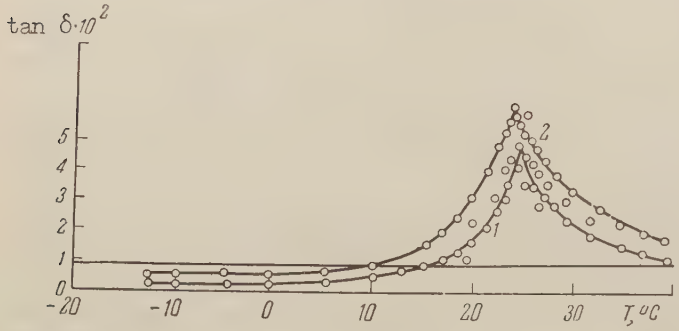

Fig.2. Temperature dependence of tan δ of Rochelle salt crystals: 1) sonicized, 2) ordinary.

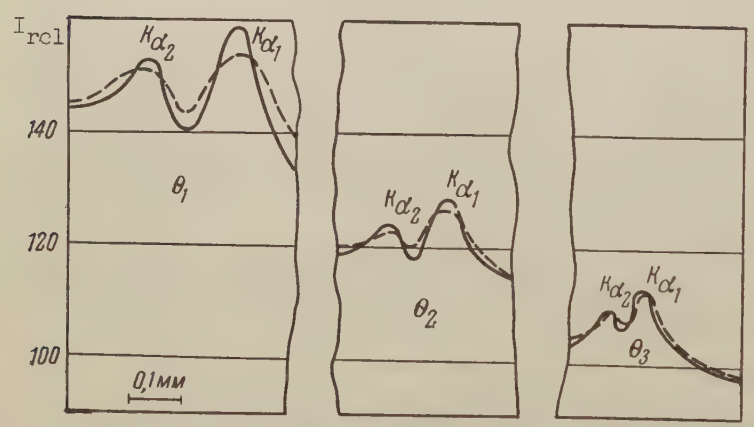

Fig.3. Change in the intensity and width of the x-ray diffraction lines for Rochelle salt crystals under the influence of ultrasound. Solid lines - ordinary crystal; dashed lines - sonicized crystal.

dielectric constant of sonicized crystals differs from the dielectric constant of ordinary Rochelle salt at all temperatures.

We also determined the temperature dependence of the dielectric loss in X cut specimens of sonicized Rochelle salt crystals; the results are shown in Fig.2 (curve 1) where we also give the dependence for ordinary Rochelle salt. It will be evident that as a result of the ultrasonic treatment the dielectric loss is substantially reduced. Apparently, under the influence of ultrasound the domain structure of the crystals becomes finer, which leads to decrease of their dielectric constant and loss tangent.

Influence of Ultrasound on the Diffusion Width and Intensity of X-ray Interference Lines

Investigation of the diffusion width and weakening in intensity of the x-ray interference lines of Rochelle salt crystals was carried out by the method of back recording using a BSV-4 x-ray tube with a Cu anode. In our experiments we used a camera with a new specially designed cassette by means of which one can obtain six x-ray diffraction patterns with symmetrically arranged interference lines on one semicylindrical film without reloading the cassette. We note that this improved cassette gives better results than the usual cassette supplied with the KROS-1 camera.

The results of studies of the widths and weakening in intensity of the x-ray interference lines of sonicized and ordinary crystals of Rochelle salt are shown in Fig.3. It will be evident that treatment with ultrasound leads to a finer structure of the crystal, which gives rise to an appreciable increase in the diffusion width of the interference lines with large glancing angles.

The intensity of the interference lines with large glancing angles for sonicized specimens is weakened as compared with the intensity of the corresponding

lines for ordinary Rochelle salt crystals. This weakening in intensity can also be explained by reduction in the size of the domains in crystals subjected to ultrasonic vibration.

Kazakh Polytechnic Institute

* * * * * * *

ELECTROLUMINESCENCE OF BARIUM TITANATE AT AUDIO FREQUENCIES

– E.V.Stauer

In 1956 Harman[1] reported observing weak yellowish luminescence from barium single crystals under the influence of a radio frequency field. Subsequently, electroluminescence resulting from high frequency excitation was observed in $BaTiO_3$ ceramic as well as in $SrTiO_3$, TiO_2, $KNbO_3$, $CaTiO_3$ and $PbZrO_3$.[2-4]

Investigation of the correlation between the behavior of the luminescence of such materials and their ferroelectric properties may be of help in understanding the nature of these materials and in particular the structure of their surface layers.[5]

In present work we found that when an electric field of audio frequency is applied to a ceramic barium titanate specimen, beginning with a certain threshold value of the field it begins to emit yellowish or rosy light that can be seen in the dark. The emission is observed for specimens with electrodes of silver, aquadag, graphite and transparent SnO_2. Specimens containing minor amounts of Fe, Ni, Nb, Zr and Pb impurities yield a less bright electroluminescence.

With increase in temperature the intensity of the luminescence attains a maximum near the Curie point. During cooling the luminescence maximum is shifted to the side of lower temperatures, an effect that is analogous to the shifts observed for the maxima of the dielectric constant[6] and x-irradiation induced photo-emf[7].

With increase of the frequency from 20 cps to 20 kc the luminescence intensity increases; it is difficult, however, to determine the character of this increase owing to rapid heating of the specimens at elevated frequencies.

In the case of some specimens, particularly at higher temperatures, one can detect electroluminescence under the influence of a dc field by means of a photomultiplier. The applied voltage, however, must be at least one order of magnitude higher than the threshold ac voltage producing electroluminescence.

The increase of the intensity of electroluminescence of barium titanate with increase of the applied field is characterized by the empirical formula

$$L = AV^b,$$

where A and b are constants for any given frequency and temperature (b varies between 3 and 4).

Upon application of a biasing dc field to a specimen under ac excitation, the brightness of the emission decreases; this is analogous to the decrease of the dielectric constant under the same conditions observed by Sinyakov et al[8]. With increase of the biasing field up to a certain value the luminescence brightness decreases and then tends to level off (Fig.1).

The luminescence intensity decreases when the specimen is subjected to compression in the direction of the electric field. When the pressure is removed there is observed a burst of light after which the luminescence returns to the initial level. The dielectric constant exhibits a similar behavior under compression.[9]

Fig.1. Variation in the intensity of the electroluminescence of barium titanate with the biasing dc field (alternating voltage 350 v, f = 2 kc).

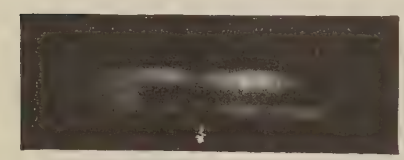

Fig.2. Electroluminescence of barium titanate specimen. Magnification 4X.

The electroluminescence intensity of specimens depends on their previous history. The emission does not remain constant in time. The brightest luminescence is observed at the instant of application of the field; thereafter it falls off at first rapidly and then more slowly. Under a microscope one can see that the emission is brightest in the surface layer in the immediate proximity of the electrode and decreases in intensity into the depth of the specimen (Fig.2).

Oscillographic observations show that under excitation by a sinusoidal voltage there appear luminescence peaks during each half cycle, and that the peak luminescence occurs somewhat in advance of the crest field (Fig.3,a). With excitation of the barium titanate specimen by a trapezoidal voltage the luminescence is emitted only during the intervals of rise and fall of the field (Fig.3,b). If the photomultiplier is set up to receive light from the region of only one electrode, it becomes apparent that the electroluminescence peak at each electrode appears only during the interval when a positive voltage is applied to the given electrode (Fig.3,c). At very high voltages, however, there may also be observed a weak electroluminescence peak during the negative half-cycle.

The mechanism responsible for the electroluminescence of barium titanate is not yet fully understood. However, by analogy with what is known for more thoroughly studied[10] ZnS one can advance the following tentative explanation.

Upon application of a negative voltage to the electrode fixed to the specimen, under the influence of the high electric field induced in the surface layer[11,12], there occurs either field emission from the cathode or release of electrons from shallow traps. The released electrons, accelerated in the field, produce electron-hole pairs by impact ionization. This

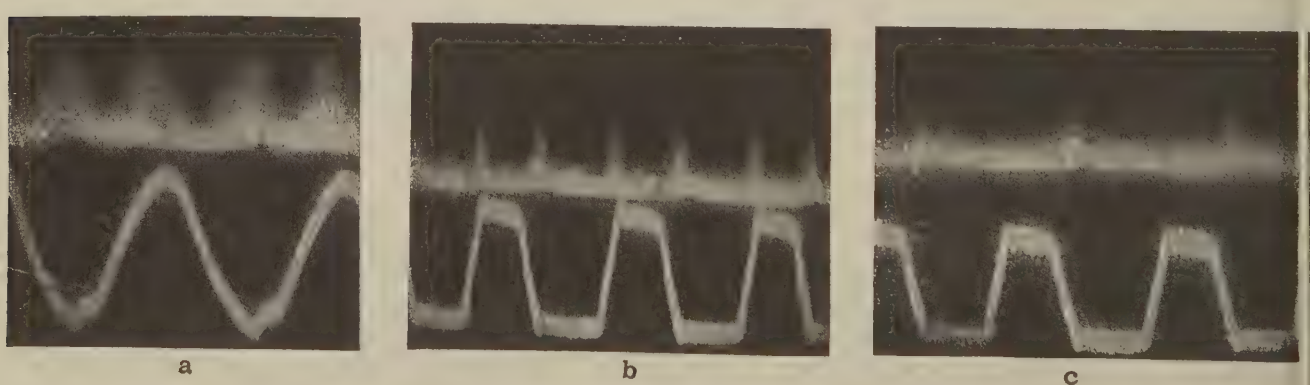

Fig.3. Brightness waves: fluctuation of the electroluminescence of barium titanate
a - sinusoidal voltage, f = 20 kc; b & c - trapezoidal voltage pulses, f = 2 kc;
b - emission observed from the regions of both electrodes, c - emission observed only from the region of one electrode (positive half cycle below).

process continues until the field attains its maximum value. Then, when a positive voltage is applied to the electrode, the electrons, earlier displaced into the low field region, return to the holes and recombining with them, possibly through impurity levels, produce the observed luminescence in the surface layer adjacent to the electrode.

Correlation between the electroluminescence and ferroelectric properties of barium titanate is evinced primarily in that with variation of the dielectric constant under the influence of various external factors (temperature, pressure, biasing field, etc.) there occurs a change of the current flowing through the specimen and consequently a change in the intensity of the emitted luminescence. Thus the electroluminescence is correlated with the ferroelectric properties of the materials.

I desire to express my gratitude to F.I.Kolomoitsev for guidance in the work, and to E.A.Stafiichuk for providing the specimens.

Dnepropetrovsk State University

References

1. G.G.Harman, Bull.Am.Phys.Soc., 1, 112 (1956).
2. G.G.Harman & R.L.Raybold, Phys.Rev., 104, 1498 (1956).
3. G.G.Harman, Rev.Sci.Inst., 28, 127 (1957).
4. G.G.Harman, Phys.Rev., 111, 27 (1958).
5. Nat.Bur.Stand.Techn.News Bull., 42, 206 (1958).
6. E.V.Sinyakov & A.S.Nikonenko, Nauchn.zap.(Scientific notes), Dnepropetrovsk State University, 45, 29 (1956).
7. F.F.Kodzhesiprov, Thesis, Dnepropetrovsk State University, 1958.
8. E.V.Sinyakov, E.A.Stafiichuk & L.S.Sinegubova, Zhur.eksp.i teor.fiz., 21, 1396 (1951).
9. I.A.Izhak, Thesis, Dnepropetrovsk State University, 1956.
10. D.R.Frankl, Phys.Rev., 111, 1540 (1958).
11. W.Kanzig, Phys.Rev., 98, 549 (1955).
12. A.G.Chynoweth, Phys.Rev., 102, 705 (1956).

DIELECTRIC CONSTANTS OF PIEZOCERAMIC ELEMENTS OF BARIUM TITANATE

- S.V.Bogdanov

1. The dielectric constant of polarized barium titanate specimens (piezoelectric transducers and the like) should differ from the dielectric constant of the unpolarized ceramic. This difference may be due to a) the piezoelectric reaction and/or b) orientation of the domains incident to polarization.

Let us consider these effects separately.

Piezoelectric reaction. Every piezoelectric element is essentially an electromechanical transducer, i.e., is characterized by a certain relationship between its electric and mechanical parameters. This relationship can be described by the following equations[1]:

$$\begin{aligned} D_n &= \varepsilon^{\sigma}_{mn} E_m - 4\pi d_{nkl} \cdot \sigma_{kl}, \\ \xi_{ij} &= s^{E}_{ijkl} \sigma_{kl} - d_{mij} E_m; \end{aligned} \tag{1}$$

where the D_n and E_m are the components of the electric induction and electric field, σ_{kl} and ξ_{ij} are the components of the mechanical stress and strain, s^{E}_{ijkl} are the components of the compliance coefficient with E = 0, $\varepsilon^{\sigma}_{mn}$ are the components of the dielectric constant in the absence of mechanical stress, and d_{mkl} are the components of the piezoelectric coefficient.

It follows from Eq.(1) that the dielectric constant $\varepsilon^{\sigma}_{mn}$ of a "free" crystal must be larger than the dielectric constant ε^{ξ}_{mn} of a "compressed" crystal. In particular for $BaTiO_3$ one can obtain the following relationships:

$$\varepsilon^{\sigma}_{33} - \varepsilon^{\xi}_{33} = 4\pi \left[\frac{d^2_{33}}{s^{E}_{33}} + \frac{2d^2_{31}}{s^{E}_{11} + s^{E}_{12}} - \frac{4d_{33} d_{31} \cdot s^{E}_{13}}{s^{E}_{33} (s^{E}_{11} + s^{E}_{12})} \right], \tag{2}$$

$$\varepsilon^{\sigma}_{11} - \varepsilon^{\xi}_{11} = 4\pi \frac{d^2_{15}}{s^{E}_{44}}. \tag{3}$$

Inasmuch as unpolarized ceramic does not have an integral piezoelectric effect, it is natural to assume that its dielectric constant must approach the constant ε^{ξ} of polarized ceramic measured at the same frequency. Thus it may be assumed that $\varepsilon^{\sigma} > \varepsilon_{k1}$ and $\varepsilon^{\xi} \approx \varepsilon_{k2}$, where ε_{ki} is the dielectric constant of the unpolarized ceramic measured at frequencies f_1 and f_2 corresponding to the values of ε^{σ} and ε^{ξ}.

Orientation effect. Inasmuch as the dielectric constants ε^{*}_{11} and ε^{*}_{33} of a single domain single crystal are not equal to each other ($\varepsilon^{*}_{11} > \varepsilon^{*}_{33}$), ordering of the domain structure owing to polarization should result in a change of the permittivity of the entire specimen[2]. Thus, whereas prior to polarization

$$\varepsilon_k = \frac{1}{3} (2\varepsilon^{*}_{11} + \varepsilon^{*}_{33}),$$

after polarization

$$\begin{aligned} \varepsilon_{11} = \varepsilon_{22} &= \frac{1}{6} [(4 + \cos\theta + \cos^2\theta)\varepsilon^{*}_{11} + (2 - \cos\theta - \cos^2\theta)\varepsilon^{*}_{33}], \\ \varepsilon_{33} &= \frac{1}{3} [(2 - \cos\theta - \cos^2\theta)\, \varepsilon^{*}_{11} + (1 + \cos\theta + \cos^2\theta)\, \varepsilon^{*}_{33}] \end{aligned} \tag{4}$$

(θ is the maximum angle between the direction of the polarizing field and the direction of the residual polarization of individual domains).

As will be evident from Eq.(4), for $\theta < 90^{\circ}$ we will have $\varepsilon_{33} < \varepsilon_k < \varepsilon_{11}$ and only for $\theta = 90^{\circ}$ will $\varepsilon_{33} = \varepsilon_k = \varepsilon_{11}$.

The change in permittivity produced by ordering of the domain structure will be superposed on the change due to the piezoelectric reaction. The purpose of the present work was to evaluate the relative contributions of these processes

Table 1

Specimen lot	ε_k at 50 cps	ε_k at 11 Mc	$\varepsilon_{33}^{\sigma}$	ε_{33}^{ξ}	d_{33}, cgsc units	$\frac{1}{2}(d_{33}+d_{31})$, cgsc units
I	1660	1460	1770	1290	$5,4\cdot10^{-6}$	$-1,9\cdot10^{-6}$
II	1510	1330	1640	1200	$5,2\cdot10^{-6}$	$-1,9\cdot10^{-6}$

and to compare the theoretical values of (2) and (3) with those given by experiment.

2. Our measurements were carried out on two lots of $BaTiO_3$ specimens differing somewhat as regards conditions of preparation; each lot consisted of 30 specimens, which were in the form of cubes 10 mm on edge. The values of the dielectric constant before and after polarization were measured at 50 cps and 11 Mc, i.e., at frequencies lying substantially below and above the resonance frequency, which for our specimens was about 250 kc. Thus it may be assumed that the dielectric constant of polarized specimens measured at 50 cps is ε^{σ} while the constant measured at 11 Mc is ε^{ξ}. We also measured the piezoelectric coefficients d_{33} and d_{31} of the polarized specimens. The measurements of both the piezoelectric coefficients and the dielectric constants were carried out 10 to 15 days after polarization, i.e., when it could be assumed that the piezoelectric properties of the specimens had become stabilized. The results of these measurements are shown in Table 1 (averaged values for each lot of specimens).

Analysis of the tabulated data shows the following:

1. The dielectric constant of unpolarized ceramic depends on the frequency: it decreases with increasing frequency.

2. As might be expected, the dielectric constant $\varepsilon_{33}^{\sigma}$ of a free crystals is larger than ε_{k1}.

3. The dielectric constant ε_{33}^{ξ} of a compressed crystal is smaller than ε_{k2}.

As noted above, the piezoelectric reaction could lead only to increase of $\varepsilon_{33}^{\sigma}$ over ε_{k1}, so that ε_{33}^{ξ} should remain approximately equal to ε_{k2}. Hence decrease of ε_{33}^{ξ} compared to ε_{k2} can naturally be attributed to the orientation effect.

It follows from Eq.(4) that if the decrease of ε_{33}^{ξ} as compared with ε_{k2} is actually due to the orientation effect, there must be observed an increase of ε_{11}^{ξ} compared with ε_{k2} and ε_{33}^{ξ}. From Eq.(4) one can also evaluate the expected difference, namely,

$$\varepsilon_{11}^{\xi} - \varepsilon_{33}^{\xi} = 1.5\,(\varepsilon_{k2} - \varepsilon_{33}^{\xi}). \qquad (5)$$

Thus for our specimens one could expect $\varepsilon_{11}^{\xi} - \varepsilon_{33}^{\xi}$ to be ~225, i.e., ε_{11}^{ξ} to be some 18% greater than ε_{33}^{ξ}.

To check this we removed the original electrodes from the No.3 faces of all the specimens of lots 1 and 2 and applied new electrodes by vacuum sputtering onto faces No.1 of 25 specimens of each batch and anew on faces No.3 on 5 specimens (for the purpose of checking the quality of the electrodes). Then we again measured the dielectric constant of these specimens at 50 cps and 11 Mc. The results of these measurements (averaged value for each lot) are compared with the preceding measurements in Table 2.

Table 2

Specimen lot	$\varepsilon_{33}^{\sigma}$	$\varepsilon_{11}^{\sigma}$	ε_{33}^{ξ}	ε_{11}^{ξ}	Control $\varepsilon_{33}^{\sigma}$	Control ε_{33}^{ξ}
I	1770	1710	1290	1270	1730	1290
II	1640	1560	1200	1170	1620	1210

As will be evident from Table 2, the dielectric constant ε_{11}^{ξ} proved to approximately equal to ε_{33}^{ξ}. At the same time from

the values obtained for the control specimens it will be apparent that the application of new electrodes has virtually no effect on their properties. Thus the observed decrease of ε_{33}^{ξ} relative to ε_{k2} cannot be explained by the orientation effect.

To explain the phenomenon we suggest that the domains in the unpolarized ceramic cannot be regarded as completely piezoelectrically compressed, whereas in polarized specimens, which vibrate as a whole, the effect of piezoelectric compression is manifested more fully.

If, however, we take this view, there arises the question of how to explain the decrease of ε_k of unpolarized ceramics with increase of the frequency: Is this a consequence only of the piezoelectric reaction or a result of dielectric relaxation? In our opinion one can decide between these mechanisms on the basis of the magnitude of the difference $(\varepsilon_{nn}^{\sigma} - \varepsilon_{nn}^{\xi})$. If the decrease of the dielectric constant of unpolarized ceramic with increasing frequency is due to the piezoelectric effect, this decrease must enter wholly into the observed difference $(\varepsilon_{nn}^{\sigma} - \varepsilon_{nn}^{\xi})_{exp}$, which in this case should approach the expected theoretical difference given by Eq.(2). If, on the other hand, the decrease of ε_k is due to dielectric relaxation, then for evaluation of the piezoelectric reaction from the total difference $(\varepsilon_{nn}^{\sigma} - \varepsilon_{nn}^{\xi})_{exp}$ one must subtract the change $(\varepsilon_{k1} - \varepsilon_{k2})$ not due to the piezoelectric factor. For evaluating $(\varepsilon_{33}^{\sigma} - \varepsilon_{33}^{\xi})_{theo}$ and $(\varepsilon_{11}^{\sigma} - \varepsilon_{11}^{\xi})_{theo}$ we used the measured values of the piezoelectric coefficients d_{33} and d_{31}, the empirical relation $d_{15} \approx d_{33} - d_{31}$ and the values of s_{ij}^{E} for barium titanate ceramic given by Berlincourt & Jaffe[3]. The results of our calculations are summarized in Table 3. It must be borne in mind that the calculated value of $(\varepsilon_{11}^{\sigma} - \varepsilon_{11}^{\xi})_{theo}$ is not as accurate as might be desired owing to the uncertainties in the measurements of d_{15} and s_{44}^{E}.

Table 3

Specimen lot	$(\varepsilon_{33}^{\sigma} - \varepsilon_{33}^{\xi})_{theo}$ acc. to Eq.(2)	$(\varepsilon_{33}^{\sigma} - \varepsilon_{33}^{\xi})_{exp}$	$(\varepsilon_{33}^{\sigma} - \varepsilon_{33}^{\xi})_{exp} - (\varepsilon_{k1} - \varepsilon_{k2})$	$(\varepsilon_{11}^{\sigma} - \varepsilon_{11}^{\xi})_{theo}$ acc. to Eq.(3)	$(\varepsilon_{11}^{\sigma} - \varepsilon_{11}^{\xi})_{exp}$	$(\varepsilon_{11}^{\sigma} - \varepsilon_{11}^{\xi})_{exp} - (\varepsilon_{k1} - \varepsilon_{k2})$
I	290	480	280	287	440	240
II	270	440	260	268	390	210

As will be evident from Table 3, the calculated values of $(\varepsilon_{33}^{\sigma} - \varepsilon_{33}^{\xi})_{theo}$ are in good agreement with $[(\varepsilon_{33}^{\sigma} - \varepsilon_{33}^{\xi})_{exp} - (\varepsilon_{k1} - \varepsilon_{k2})]$, which indicates that the decrease of ε_k with increase of frequency occurs primarily due to dielectric relaxation. In further support of this inference one can adduce the following argument: inasmuch as the linear dimensions of the individual domains in the ceramic specimen do not exceed 10^{-3} cm, for them the effect of piezoelectric compression should be observed only at frequencies substantially exceeding 10^{8} cps.

3. The following conclusions may be drawn on the basis of the cited data:

a) the individual domains comprising the microcrystals in unpolarized barium titanate ceramics cannot be regarded as fully piezoelectrically compressed (at frequencies under 10^{8} cps),

b) the decrease of the dielectric constant of unpolarized ceramic with increasing frequency is a result of dielectric relaxation.

"P.M.Lebedev" Physical Institute
Academy of Sciences of the USSR

References

1. W.P.Mason, Piezoelectric Crystals and Their Application to Ultrasonics, N.Y., 1950 (Cited in Russian trans.).
2. S.V.Bogdanov, B.M.Vul & A.M.Timonin, Izv.AN SSSR, Ser.fiz., 21, 374 (1956). (Trans.Bulletin, 21, 377.)
3. D.Berlincourt & H.Jaffe, Phys.Rev., 111, 143 (1958).

* * * * * * *

DIELECTRIC PROPERTIES OF POLARIZED CERAMICS IN STRONG ALTERNATING ELECTRIC FIELDS

- V.I.Zaitseva, R.E.Pasynkov, V.I.Pozern & A.M.El'gard

A number of uses of piezoelectric ceramics require a knowledge of the dielectric properties of these materials in strong electric fields in the audio and ultrasonic frequency range. Yet these properties have not been studied sufficiently, and considerable difficulties are encountered when experiments are performed in strong fields owing to dielectric-loss heating of the sample. Baerwald & Berlincourt[1] give only data relating to the dielectric loss in the polarized $BaTiO_3$ ceramic in fields to 4 kv/cm at a frequency of 1 kc. We know of no published data on the variation of the dielectric constant of polarized ceramic with the field strength. This paper presents some results of a study of the field dependence of the dielectric constant and the loss tangent of polarized ceramic.

Theory

Let us consider the behavior of a single-domain single crystal of $BaTiO_3$ in strong alternating fields. The deduced qualitative relations, as shall become plain in what follows, can be applied with some degree of approximation to polarized ceramics.

Following Kholodenko[2], who analyzed the phenomenon of hysteresis in a single domain crystal, we begin by expanding the thermodynamic potential Φ of the system in a series in powers of the polarization components P_i to sixth order terms. We then make use of the numerical values of the expansion coefficients $\beta_1, \gamma_1, \beta_2$ and γ_2 and their temperature dependence in accordance with Meyerhofer[3], who assumed that $BaTiO_3$ undergoes a first order transition at the Curie point. In solving the equations of state

$$\frac{\partial \Phi}{\partial P_i} = E_i \qquad (1)$$

(the E_i are components of the electric field) and in determining the regions where the stability condition

$$\frac{\partial^2 \Phi}{\partial P_i^2} > 0 \qquad (2)$$

holds, we take into account the components of induced polarization P_{ui} up to P_{ui}^5 for Eq.(1) and to P_{ui}^4 for Eq.(2). Still following Kholodenko, we introduce, for the convenience of qualitative evaluation, the dimensionless parameters

$$p_i = \frac{P_i}{\sqrt{-\frac{\beta_1}{\gamma_1}}} \quad \text{and} \quad e_i = \frac{E_i}{\sqrt{-\frac{\beta_1^5}{\gamma_1^3}}}.$$

The dimensionless induced polarization p_{u2} for the region of tetragonal symmetry is sought in the form of a series:

$$p_{uz}(e_z) = \sum_{u=0}^{5} a_n e_z^n, \tag{3}$$

where the coefficients a_n are expressed in terms of the dimensionless spontaneous polarization p_{0i} and the coefficients α_1, β_1 and γ_1; that is, they are functions of the temperature. Setting $e = e_0 \sin \omega t$ and inserting this into (3), we obtain

$$p_{uz}(t) = \sum_{n=1}^{5} p_{uz}^n (a_n e) \sin (n\omega t - \varphi_n), \tag{4}$$

where p_{uz}^n is the amplitude of the n-th harmonic.

From Eq.(4) one can find both the total dielectric constant ε and that part of it which is associated with measurement of a particular current harmonic:

$$\varepsilon_{zz\,\mathrm{tot}} \approx 4\pi \frac{P_{uz}}{E_z}; \qquad \varepsilon_{zz}^n = 4\pi \frac{P_{uz}^n}{E_z}.$$

The most interesting of these is $\varepsilon_{zz}^{1'}$, the dielectric constant determined from the first harmonic of the current; this quantity is measured by means of the most accurate resonance and bridge techniques and has practical significance in the design of circuits using capacitors of ferroelectric ceramics, intended for operation in strong fields.

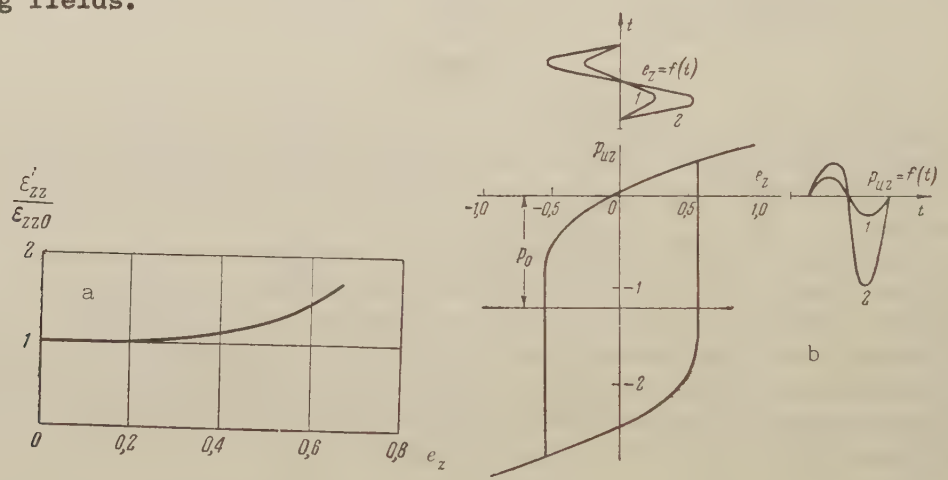

Fig.1. Theoretical e_z dependences of ε_{zz}^1 (a) and P_{uz} (b) for a single-domain single crystal (T = 20°). In a $\frac{E_z}{E_c} = 1$ for $e_z \approx 0.5$.

The theoretical curve characterizing the relative change in ε_{zz}^1 as a function of the electric field e_z is given in Fig.1,a. The increase of ε_{zz}^1 with e_z can be understood in view of the following. The hysteresis loop obtained from Eq.(1) is shown in Fig.1,b. Under the influence of an alternating field the induced polarization will change, as shown in the figure, namely: the polarization rises only slightly as the field increases in amplitude during the positive half-cycle, whereas during the negative half-cycle the growth is sharper. Such field dependence of

the induced polarization leads to nonlinear growth of the first harmonic of the polarization and, consequently, to nonlinear increase of the dielectric constant calculated from the first harmonic of the current. In view of the fact that the shapes of the hysteresis loops of a single domain crystal and of polarized ceramic are qualitatively similar, one can apply to the latter the reasoning presented above, and, consequently, expect a qualitative agreement of the theoretical curve (Fig.1,a) with the experimental data for polarized ceramics.

The analysis presented here is valid for values of E_z that do not exceed the magnitude of the coercive field. If, however, one hypothesizes the existence of a region with $E_z > E_c$, i.e., field values for which irreversible depolarization of the specimen does not occur, then from an analysis of Fig.1,b one can deduce the appearance of a maximum in the $\varepsilon^1_{zz} = f(e_z)$ curve (see Ref.4 regarding the possible existence of such high fields).

It should be noted that theoretical interpretation of the variation of the dielectric loss with field strength is considerably more complicated and will not be attempted here.

Experimental Procedure and Results

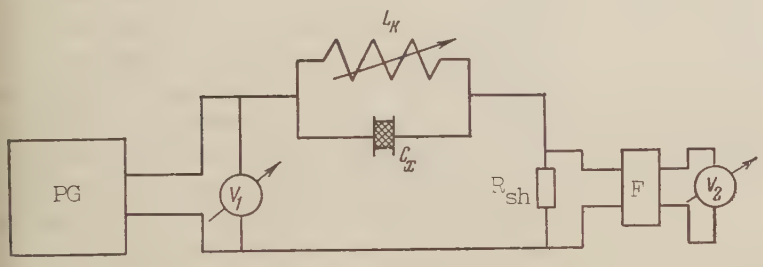

Fig.2. Experimental arrangement for measuring the dielectric constant and loss tangent.

The variations of the dielectric constant ε and the loss tangent tan δ were determined by the resonance technique using both parallel and series circuits. The experimental set-up is diagramed in Fig.2. The measuring circuit was tuned to resonance by means of the variometer L_K. Resonance was indicated by minimum current in the circuit loop, as shown by the voltmeter or oscilloscope V_2, connected through the filter F across the shunt R_{sh}. The filter was tuned to the frequency of the first harmonic of the current, so that the measured quantities corresponded to this harmonic. The dielectric constant and the loss tangent were calculated from the capacitance and the equivalent loss resistance of the specimen, determined, respectively, from the condition for resonance and from the ratio of the voltage to the current in the circuit at resonance.

To avoid heating of the specimen as a result of dielectric losses the measurements in strong fields were carried out under pulsed operation with a small duty cycle. The tests showed that with a pulse duration of 10 to 20 millisec and an interval of 1 to 5 sec between pulses the specimens did not heat up to any noticeable degree. The pulses of desired amplitude and frequency were supplied by a pulse generator - PG in Fig.2.

The voltage and current were measured at 10 kc by means of an ENO-1 oscilloscope, which also served for observation of the shape of the current and voltage pulses. The temperature of the specimen (the measurements were performed at room temperature) was checked by a thermocouple. The error in the measurement of capacitance and loss tangent did not exceed ±5% and ±20%, respectively. Three specimens were prepared of each batch of ceramic: the specimen thickness was 1.55 mm. The obtained results for each series of three specimens were averaged (the scatter did not exceed the estimated experimental error).

The specimens were polarized by the following procedure. The specimens, preheated to their Curie temperature, were held in a dc field of 0.8 kv/mm for an

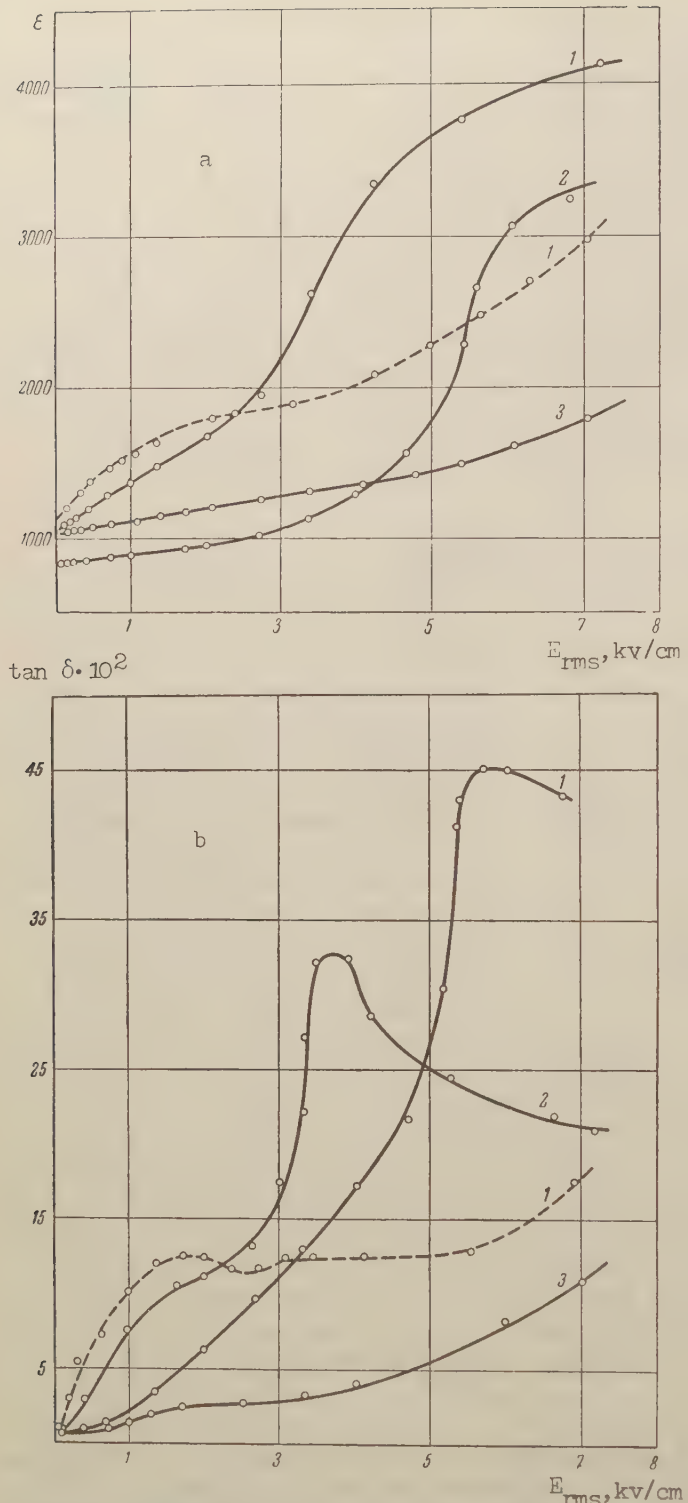

Fig.3. Variation of the dielectric constant (a) and the loss tangent tan δ (b) with electric field strength for polarized ceramics of different compositions: 1) $BaTiO_3$ (the dashed curve is for unpolarized ceramic); 2) 94% $BaTiO_3$ + 6% $CaTiO_3$, 3) 95% $BaTiO_3$ + 5% $CaTiO_3$ + 0.75% $CoCO_3$.

hour at the maximum temperature, then gradually cooled in the same field to room temperature. The dielectric measurements were performed three days after polarization.

The field dependences of ε^1_{zz} and tan δ were measured for samples of three compositions: $BaTiO_3$, 94% $BaTiO_3$ + 6% $CaTiO_3$, and 95% $BaTiO_3$ + + 5% $CaTiO_3$ + 0.75% $CoCO_3$.

As will be evident from Fig.3, ε^1_{zz} grows with increasing field strength; furthermore, in a certain field interval characteristic for each composition, there occurs a sharper rise of the constant. Correspondingly, in that same field interval, there also occurs a rapid growth of tan δ (tan δ rises to a maximum in $BaTiO_3$). This accelerated growth occurs, as might be expected, when the crest value of the applied field approaches the value of the static coercive field for the ceramic. The values of the static coercive field for the ceramic specimens under consideration are 4.5 kv/cm for $BaTiO_3$, 7.0 kv/cm for 94% $BaTiO_3$ + 6% $CaTiO_3$ and 8.5 kv/cm for 95% $BaTiO_3$ + 5% $CaTiO_3$ + + 0.75% $CoCO_3$.[5,6]

In addition to polarized specimens of $BaTiO_3$, we tested unpolarized samples. Fig.3 shows that as the field increases, ε^1_{zz} and tan δ of the unpolarized ceramic are at first greater than for the polarized ceramic; but later, in fields nearing the magnitude of the static coercive field, ε^1_{zz} and tan δ of the polarized ceramic begin to increase more rapidly, so that in strong fields they reach higher values. The same regularity obtains for the other two compositions.

The noted difference in behavior can be explained if we recall that in weak fields, the polarized ceramic, being characterized by a higher elastivity, exhibits a lower dielectric constant and a smaller loss tangent. On the other hand, in strong fields, close to the

magnitude of the static coercive field, the reaction of the domains in the polarzed ceramic is enhanced to a greater degree with the result that ε_{zz}^{1} and tan δ increase. It should be noted that in strong alternating fields with a crest value close to the static coercive field, the possible reorientation of domains is reversible so that the initial residual polarization is practically fully restored upon removal of the voltage. Studies of the depolarization of $BaTiO_3$ specimens performed by measuring the piezoelectric coefficients in strong alternating fields[4], as well as in a weak field after the action of a strong field, showed that at room temperature the polarization persists up to fields equal in value to, or even slightly greater than, the static coercive field.

It should be noted that the field dependences of the dielectric constant of polarized ceramics obtained for the field range, where irreversible reorientation of domains (depolarization) does not occur, are in qualitative agreement with the above deductions from theory.

References

1. H.G.Baerwald & D.A.Berlincourt, J.Acoust.Soc.Am., 25, 703 (1953).
2. L.P.Kholodenko, Izv.AN SSSR, Ser.fiz., 21, 368 (1957). (Trans.Bulletin 21, 372.)
3. D.Meyerhofer, Phys.Rev., 112, 413 (1958).
4. G.A.Velyukhanova, R.E.Pasynkov, V.I.Pozern & A.M.El'gard, Present issue of the Bulletin, p. 1358.
5. A.L.Gray & J.M.Herbert, Acoustica, 6, 265 (1956).
6. D.Schofield & R.E.Brown, Canad.J.Phys., 35, 369 (1957).

PIEZOELECTRIC PROPERTIES OF POLARIZED CERAMICS IN STRONG ALTERNATING FIELDS

- G.A.Velyukhanova, R.E.Pasynkov, V.I.Pozern & A.M.El'ga

Theory

In determining the theoretical variation of the piezoelectric coefficients d_{33} and d_{31} as a function of the field E_z applied in the direction of the ferroelectric axis, we begin with the same assumptions as in our derivation[1] (see preceding article) of the field dependence of the dielectric constant ε_{zz}.

Using the familiar expression for the thermodynamic potential Φ of a single-domain crystal wherein the elastic energy and that part of it due to electric fields are taken into account[2,3], we obtain the equations of state for the regions of tetragonal symmetry:

$$E_z = \frac{\partial \Phi}{\partial P_z}, \tag{1a}$$

$$u_{33} = -\frac{\partial \Phi}{\partial \sigma_{33}} = \nu_{33} P_z^2, \tag{1b}$$

$$u_{11} = -\frac{\partial \Phi}{\partial \sigma_{11}} = \nu_{31} P_z^2, \tag{1c}$$

where the σ_{ik} and u_{ik} are components of the stress and strain tensors, respectively, P_z is the component of polarization in the direction of the ferroelectric axis, and ν_{33} and ν_{31} are electrostriction coefficients[2,3].

Equation (1a) was solved by Kholodenko[4] in the form $P_z = f(E_z)$ and in Ref.1 as $P_{uz} = f(E_z)$ for the case of induced polarization. Separating that part of the strain u_{uik} which arises upon application of an electric field, we obtain:

$$u_{u33} = \nu_{33}(2P_{0z}P_{uz} + P_{uz}^2); \tag{2a}$$

$$u_{u11} = \nu_{31}(2P_{0z}P_{uz} + P_{uz}^2). \tag{2b}$$

At this point, as in Refs.1 and 4, it is convenient to introduce the dimensionless variables p_{uz}, p_{0z} and e_z; then, invoking the theoretical e_z dependence of p_{uz}, deduced in Ref.1, inserting it into Eqs.(2a) and (2b), and discarding terms in e_z^6 and higher, we obtain the set (2) in the form

$$u_{uik} = \nu_{ik} \sum_{n=0}^{5} b_n e_z^n. \tag{2'}$$

Setting $e_z = e_0 \sin \omega t$, we express (2') in the form of an expansion in harmonics:

$$u_{uik}(t) = \nu_{ik} \sum_{n=0}^{5} c_n (e_z^n b_n) \sin(n\omega t + \varphi_n), \tag{3}$$

where the c_n are known functions of the thermodynamic potential expansion coefficients and powers of the field e_z.

Of greatest interest, in our opinion, is study of the first harmonic in the expression for u_{uik}, since it is this quantity which determines the efficiency of a piezoelectric transducer at the frequency of mechanical resonance. In addition this quantity lends itself to comparison with experimental data. For the first harmonic $u_{ik}^{(1)}$ we have

$$u_{33}^{(1)}(t) = \nu_{33} c_1 \sin \omega t;$$

$$u_{11}^{(1)}(t) = \nu_{31} c_1 \sin \omega t.$$

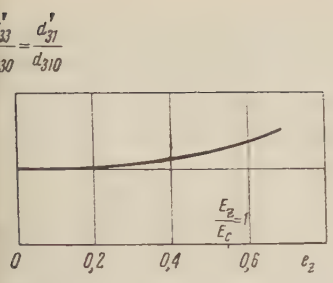

←Fig.1. Calculated field dependence of $\frac{d_{33}^{(1)}}{d_{33_0}}=\frac{d_{31}^{(1)}}{d_{31_0}}$ the interval from 0 to 2) for T = 20°. The ordinate scale equals 1.

The piezoelectric coefficients determined for the first harmonic are described by the formulas

$$d_{33}^{(1)}=\frac{\nu_{33}c_1}{E_z} \quad \text{and} \quad d_{31}^{(1)}=\frac{\nu_{31}c_1}{E_z}. \tag{4}$$

The field dependence of $d_{ik}^{(1)}$ was calculated for two values of temperature in relative units: $\frac{d_{33}^{(1)}}{d_{330}}=\frac{d_{31}^{(1)}}{d_{310}}=f(e_z)$, where d_{330} and d_{310} are the piezoelectric coefficients measured in very weak fields (Fig.1). The dependence obtained can be explained on the basis of the following considerations. If we limit ourselves to fields at which P_{uz} is still small compared to P_{0z} (in practice it suffices to take $P_{uz}=\frac{1}{3}P_{0z}$), then in Eqs.(2a) and (2b) we can, with no sacrifice in accuracy, neglect the second terms on the right and rewrite these equations as

$$\begin{aligned} u_{u33}&=2\nu_{33}P_0P_u(E_z);\\ u_{u31}&=2\nu_{31}P_{z0}P_{uz}(E_z). \end{aligned} \tag{5}$$

It can be seen that $u_{uik}(E_z)$ is determined by the field dependence of P_{uz}, and hence

$$d_{33}^{(1)}(E_z)=\frac{2\nu_{33}P_{0z}}{4\pi}\varepsilon_{zz}^{(1)}(E_z) \quad \text{and} \quad d_{31}^{(1)}(E_z)=\frac{2\nu_{31}P_{0z}}{4\pi}\varepsilon_{zz}^{(1)}(E_z).$$

Consequently, ε and d_{ik} have the same e_z dependences, i.e.,

$$\frac{\varepsilon_{zz}^{(1)}}{\varepsilon_{zz0}}\approx\frac{d_{33}^{(1)}}{d_{330}}=\frac{d_{31}^{(1)}}{d_{310}}=f(e_z).$$

Experimental Results

The field dependences of the piezoelectric coefficients $\frac{d_{33}^{(1)}}{d_{330}}$ and $\frac{d_{31}^{(1)}}{d_{310}}$ were determined using cylindrical specimens, polarized radially and tangentially and prepared of three different compositions:

$BaTiO_3$, 95% $BaTiO_3$ + 5% $CaTiO_3$, and $BaTiO_3$ + 0.75% $CoCO_3$.

The experimental procedure was the following (Fig.2). An 8 kc sinusoidal voltage was applied in single pulses of 5 millisec duration to the specimen, mounted in air. The natural resonance frequency of the specimens was 15 kc. The sound pressure developed by the specimen, proportional to the product $d_{ik}E_z$ when operating off resonance in air, was recorded by means of a broadband sound detector placed at some distance from the specimen. The signal from the narrow-band filter tuned to 8 kc was measured by means of an oscilloscope. The temperature of the sample, which virtually did not rise even upon application of an 8 kv/cm field, was monitored by a thermocouple. During the experiments the specimen was kept in a tempera-

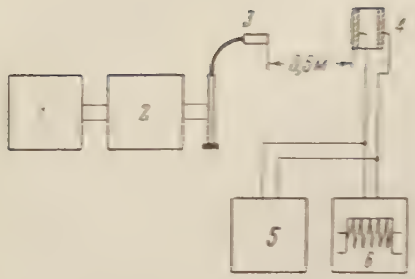

Fig.2. Experimental arrangement for investigating the field dependence of the piezoelectric coefficients: 1) oscilloscope, 2) filter, 3) microphone, 4) specimen, 5) oscilloscope, 6) oscillator.

ture chamber equipped with a "window" transparent to sound; the chamber temperature could be varied from -20° to + 40°. Considering that a relative effect was measured, the accuracy of the measurements, and the reproducibility of the results were entirely satisfactory.

The field dependences of $\frac{d_{ik}^{(1)}}{d_{ik0}}$ determined for the three above mentioned compositions at three different temperatures are shown in Fig.3. Examination of the curves leads to the following conclusions.

1. The ratio $\frac{d_{ik}^{(1)}}{d_{ik0}}$ increases with increasing field strength up to ~4.5 kv/cm for all three compositions at all temperatures.

2. In fields higher than 4.5 kv/cm $\frac{d_{ik}^{(1)}}{d_{ik0}}$ decreases noticeably for $BaTiO_3$ (but remains larger than unity); it decreases less rapidly for the 95% $BaTiO_3$ + 5% $CaTiO_3$ ceramic, and it continues to grow for the material with the highest elastivity, i.e., $BaTiO_3$ + 0.75% $CoCO_3$.

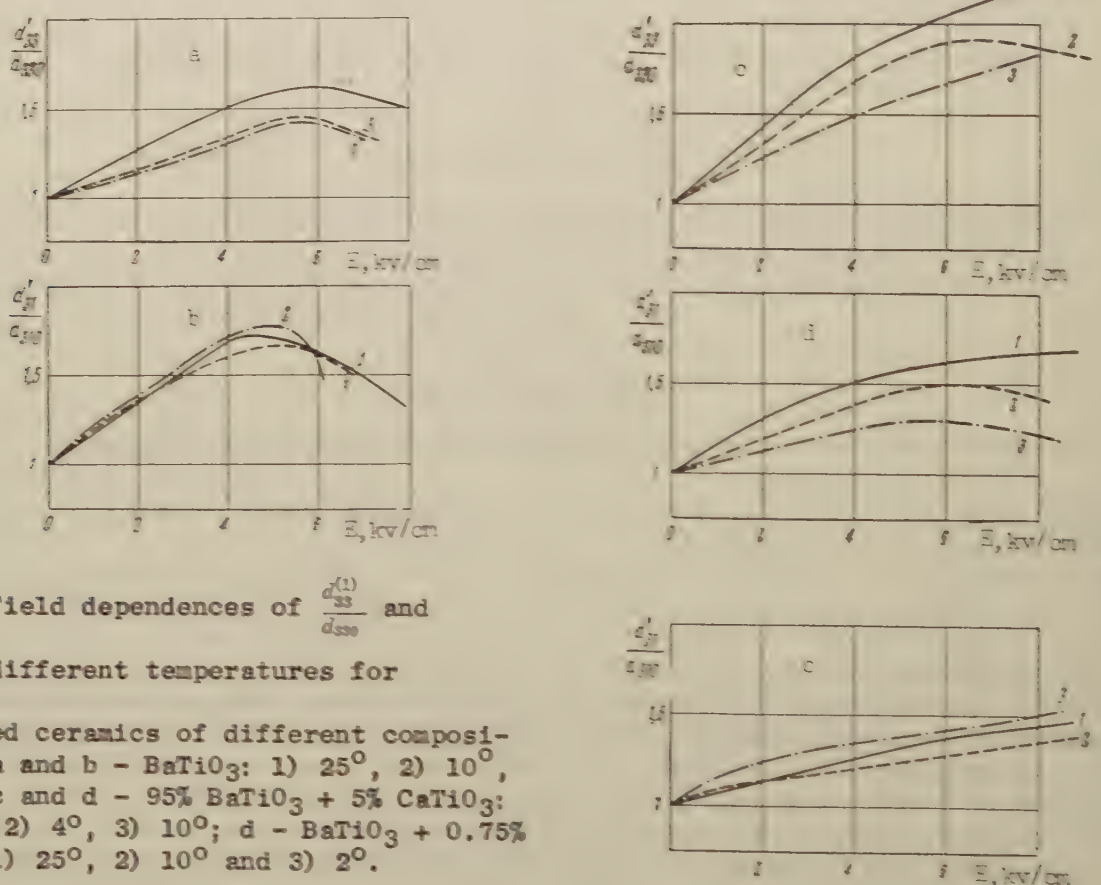

Fig.3. Field dependences of $\frac{d_{33}^{(1)}}{d_{330}}$ and $\frac{d_{31}^{(1)}}{d_{310}}$ at different temperatures for polarized ceramics of different composition. a and b - $BaTiO_3$: 1) 25°, 2) 10°, 3) 4°; c and d - 95% $BaTiO_3$ + 5% $CaTiO_3$: 1) 25°, 2) 4°, 3) 10°; d - $BaTiO_3$ + 0.75% $CoCO_3$: 1) 25°, 2) 10° and 3) 2°.

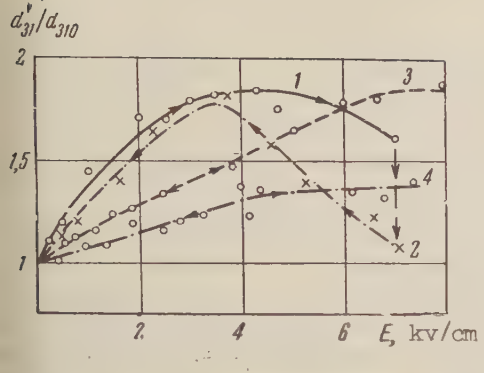

Fig.4. Field dependences of $\frac{d^{(1)}_{31}}{d_{310}}$ in increasing and decreasing fields (holding time in maximum, 8 kv/cm field 30 min): 1 & 2 - forward and reverse runs for $BaTiO_3$, 3 - forward and reverse runs for 95% $BaTiO_3$ + 5% $CaTiO_3$, 4 - forward and reverse runs for $BaTiO_3$ + 0.75% $CoCO_3$.

3. There is a qualitative agreement between the behavior of $d^{(1)}_{33}$ and $d^{(1)}_{31}$.

4. In studying the field dependence of $\frac{d^{(1)}_{ik}}{d_{ik0}}$ forward and reverse runs were made with $E_\sim$ increasing and decreasing, respectively, with the specimen held in the maximum, 8 kv/cm, field for 30 min before decreasing the applied field. This procedure resulted in coincident curves for 95% $BaTiO_3$ + 5% $CaTiO_3$ and $BaTiO_3$+0.75% $CoCO_3$, and somewhat divergent curves for $BaTiO_3$. For $BaTiO_3$, moreover, when the field is held steady for 30 minutes at the maximum value of 8 kv/cm the piezoelectric coefficient returns to its original value d_{ik0}. Thus, for $BaTiO_3$ there is a certain ambiguity as regards the values of $d^{(1)}_{ik}$, i.e., there is a difference between the values in increasing and decreasing fields in the field region above E_c, that is not connected with irreversible changes of d_{ik0} and, apparently, P_{0z}.

On the whole, there is qualitative correspondence between the theoretical variation of $d^{(1)}_{ik}(E_z)$ and the curves for $\varepsilon^{(1)}(E_z)$ in the range of fields $E_z < E_c$. This correspondence is most pronounced for the material with the highest elastivity: $BaTiO_3$+0.75% $CoCO_3$. The values of the coercive field E_c for the three compositions are 4.5 kv/cm for $BaTiO_3$, 7 kv/cm for $Ba(Ca)TiO_3$, and 8.5 kv/cm for $Ba(Ca,Co)TiO_3$.[5,6]

A study of the behavior of the higher harmonics, $d^{(2)}_{ik}(E_z)$, $d^{(3)}_{ik}(E_z)$, etc. would be of interest as would be comparison of the variation of $d_{ik}(E_\sim)$ with the hysteresis loops obtained at audio frequencies under pulsed operation with different holding times in the maximum (high) field).

References

1. V.I.Zaitseva, R.E.Parynkov, V.I.Pozern & A.M.El'gard, Present issue of the Bulletin, p.1353.

2. L.P.Kholodenko, Zhur.eksp.i teor.fiz., 31, 251 (1956). (Trans.Soviet Physics - JETP.)

3. G.A.Smolenskii & R.E.Pasynkov, Zhur.eksp.i teor.fiz., 24, 69 (1953).

4. L.P.Kholodenko, Izv.AN SSSR, Ser.fiz., 21, 368 (1957). (Trans.Bulletin, 21, 372.)

5. A.Gray & J.Herbert, Acustica, 6, 265 (1956).

6. D.Schofield & R.Brown, Canad.J.Phys., 35, 369 (1957).

PIEZOELECTRIC HYSTERESIS IN POLYCRYSTALLINE BARIUM TITANATE

- I.P.Kozlobaev

The magnitude of the induced polarization P_i in polycrystalline barium titanate caused by an applied stress σ_{zz}, according to the theory of ferroelectric phenomena[1,2] is given by $P_i = P_z - P_{0z} = \frac{\gamma_1 \sigma_{zz}}{2\beta_1 P_{0r}}$, where P_z is the total polarization, P_{0z} the spontaneous polarization, and β_1 and γ_1 are pressure and temperature dependent coefficients in the expansion of the thermodynamic potential.

At temperatures not close to the Curie point, where $P_{0z} \gg P_i$, the piezoelectric polarization is proportional to the applied stress, the piezoelectric effect assumes its usual linear form, and the mean piezoelectric coefficient is described by $\bar{d}_{33} = \frac{P_z - P_{0z}}{\sigma_{zz}} = \frac{\gamma_1}{2\beta_1 P_{0z}}$. In this range of pressures $\frac{\gamma_1 \sigma_{zz}}{\beta_1 P_{0z}^2} \ll 1$; experimental data[3] obtained for values of σ_{zz} up to 100 kg/cm^2, show that the magnitudes of the piezoelectric effect and of the dielectric constant in the temperature interval from 5 to 90°, are virtually independent of pressure. Setting $\frac{\gamma_1 \sigma_{zz}}{\beta_1 P_{0z}^2} \approx 1$, i.e., $\sigma_{zz} = \frac{\beta_1 P_{0z}^2}{\gamma_1}$, we find that in this temperature interval (and far from the Curie point) stresses must have a noticeable influence on the polarization P_z and, consequently, on the piezoelectric effect, since $\bar{d}_{33} = \frac{P_z - P_{0z}}{\sigma_{zz}}$. In order to evaluate σ_{zz} we shall make use of the known values of β_1, γ_1 and P_{0z}.

In electrostatic units we have $P_{0z} = 4.5 \cdot 10^4$, $\beta_1 = 1.7 \cdot 10^{-12}$ and $\gamma_1 = 2.7 \cdot 10^{-12}$ for single crystals below the Curie point. Inserting these values in the above equation, we obtain $\sigma_{zz} = 1.3 \cdot 10^9$ dyne/cm^2 = 1300 kg/cm^2. At temperatures closer to the Curie point, the change in polarization must become evident at lower stresses. To verify this experiments were set up to study the piezoelectric effect under high pressures.

A hydrostatic press at our disposal allowed of applying uniform deforming stresses from 100 to 7000 kg/cm^2. Since for the investigated specimens the ultimate compressive strength under temporary loads lies in the range of 4000 to 5000 kg/cm^2, the loads were limited to stresses of 3000 to 3500 kg/cm^2 in most of the experiments. The piezoelectric charges were measured by means of a ballistic galvanometer both during application of the load and during its removal.

Whereas the values of the mean piezoelectric coefficient $\bar{d}_{33}$ were of the same magnitude but of opposite sign during application and removal at stresses lower than 100 kg/cm^2, at stresses from 100 to 1100 kg/cm^2 the values of the coefficient differed not only in sign but also in magnitude. At stresses above 1000 kg/cm^2 application and removal once again give values of $\bar{d}_{33}$ equal in magnitude and opposite in sign. The curves for one specimen are shown in Fig.1. The effective piezoelectric coefficient $\bar{d}_{33}$ has its maximum value at a load of about 500 kg/cm^2. From 3000 kg/cm^2 and up to crushing loads d_{33} retains a certain constant value, which does not depend on the stress either during compression or "decompression". If the mean value of the piezoelectric coefficient is measured while slowly decreasing the deforming pressure, the values obtained during loading and unloading coincide within the limits of experimental error ($\leqslant 10\%$).

The results obtained give reason to infer that an external stress, by altering the deformation of the cells, changes the magnitude of the polarization. This change of P_z can be represented as a change in the orientation of the polarized

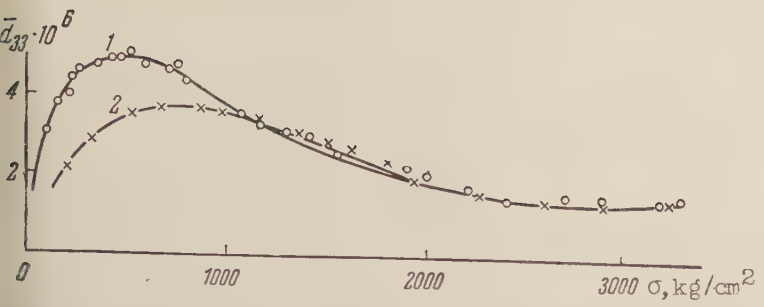

ig.1. Stress dependence of the piezoelectric coefficient $\bar{d}_{33}$: 1) compression, 2) decompression.

regions (domains). The resultant disorientation of domains reduces the effective values of the piezoelectric coefficient. Under low pressures, the number of domains in which the polarization vector changes direction is obviously small; that is why we obtain experimentally a linear increase of the charge on the faces of the specimen with increase of pressure. At pressures of the order of 300 kg/cm^2 this growth becomes slower, which can be explained by increase of the number of domains in which he polarization changes direction. In the high pressure range (above 1000 kg/cm^2) he piezoelectric charge decreases with increasing pressure and there occurs gener-l disorientation of the domains, which stops only at pressures approaching the upture point.

The direction of spontaneous polarization in a polarized sample of barium itanate corresponds to the direction of the polarizing field applied; we denote his as the Z axis. If a uniform compressive stress is applied along the X or Y xis, the resultant strains will cause distension along the Z axis, thereby increasing the spontaneous polarization. If upon compression along the Y-axis the pontaneous polarization diminished, releasing a portion of the bound charges to ppear on the electrodes connected to the sample, with the same sign as the charge f the polarizing field, then upon expansion with an increase in polarization, the bound surface charges will not be sufficient for compensation and charge of opposite sign will appear on the electrodes. This is confirmed by the results shown in Fig.2, obtained in measuring the pressure dependence of the piezoelectric coefficients $\bar{d}_{31}$ and $\bar{d}_{32}$. These coefficients attain their maximum values at loads of 150 to 200 kg/cm^2; at loads of 400 to 450 kg/cm^2 for $\bar{d}_{31}$ and for 475 to 525 kg/cm^2 for $\bar{d}_{32}$ the coefficients change sign. At these pressures the strains produced

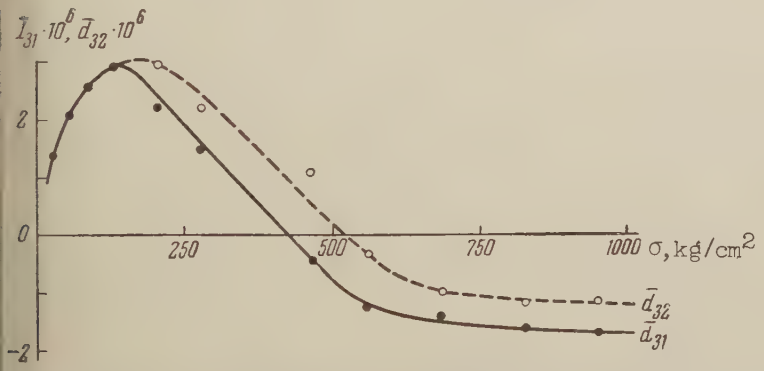

ig.2. Load dependence of the piezoelectric coefficients $\bar{d}_{31}$ and $\bar{d}_{32}$.

by the external load, significantly change the magnitude of P_z and a charge of opposite sign appears on the electrodes. The charge increases with increasing pressure (P_z increases), and levels off only at loads of about 1000 kg/cm^2. It may be assumed that at pressures of the order of 10^9 dynes/cm^2 the external deforming forces are balanced by internal elastic stresses, and P_z assumes a constant value. If the deforming force is decreased, the reverse variation of the coefficient does not correspond to the initial increasing load variation. The forward and reverse run values of $\bar{d}_{31}$ for one of the specimens are shown in Fig.3. It is apparent that the observed phenomenon is analogous to hysteresis. In the reverse run the change in sign occurs at a higher load than in the forward run.

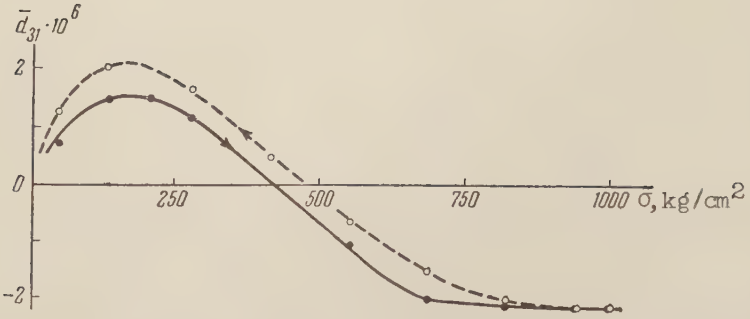

Fig.3. Load dependence of the piezoelectric coefficient $\bar{d}_{31}$ during application and removal of the stress.

An analogous phenomenon was observed for the dielectric constant.[4] For a second cycle of measurements the width of the loop decreases, while for a third cycle the forward and reverse curves coincide within limits of the experimental error. However, if the measurement cycle is repeated after allowing the specimen to "rest" 25-30 min, there are again obtained curves similar to those shown in Fig.3. Analogous hysteresis is observed for the piezoelectric coefficient $\bar{d}_{32}$.

Voronezh State University

References

1. V.L.Ginzburg, Uspekhi fiz. nauk, 38, 490 (1949).
2. M.Ya.Shirobokov, L.P.Kholodenko, Zhur.eksp.i teor.fiz., 21, 1239 (1951).
3. I.P.Kozlobaev, Izv.AN SSSR, Ser.fiz., 20, 195 (1956). (Trans.Bulletin, 20, 177.)
4. I.P.Kozlobaev, Doklady AN SSSR, 104, 387 (1955).

CONCERNING THE PIEZOELECTRIC EFFECT IN VARIKONDS

- B.A.Strukov & N.D.Gavrilova

Variation of capacitance with the applied dc field is a property of nonlinear ielectric elements (Varikonds) that finds application in a number of electronic evices. The steepness of the reversible characteristics of Varikonds makes it easible to realize wide variation of the resonant frequency of circuits incorporting Varikond capacitors.

Applying a dc field to a Varikond induces a considerable electric moment, the bsolute magnitude of which can be evaluated from the hysteresis loops. This means hat the nonlinear capacitor becomes a more or less active piezoelectric transducer. he frequency dependence of the impedance of such a "forced" transducer should evince maxima corresponding to the different natural oscillation modes of the specimen nd their harmonics.

Whenever the natural frequency of a circuit in which the capacitance element s a Varikond coincides with one of the natural frequencies of the Varikond, we hould observe a sharp dip of the Q-factor inasmuch as in this case the impedance f the Varikond becomes equal to the resistance due to its internal and radiation osses. This effect is extremely undesirable particularly in equipment designed o operate in a wide frequency range.

Fig.1 shows the frequency characteristic of the admittance of a VK-2 specimen n the form of a rectangular bar measuring 18.4 x 4.2 x 3.0 mm.

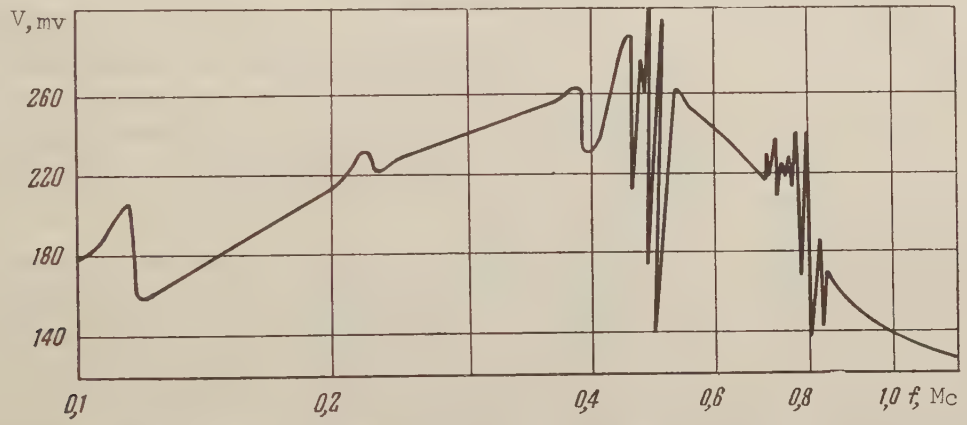

ig.1. Frequency characteristic of the admittance of a VK-2 Varikond bar measuring 18.4 x 4.2 x 3.0 mm.

Three resonance groups are clearly discernable at 100, 500 and 800 kc. On the basis of the specimen's geometrical dimensions, we can unambiguously identify the resonances near 100 kc with oscillations in length, those at 500 kc with oscillations in width, and those at 800 kc with oscillations in thickness.

The results of quantitative investigation of the piezoactivity of the bar for oscillations in length are shown in Fig.2, where the horizontal scale is laid off in values of the voltage applied to the specimen, while the ordinates are values of the electromechanical coupling coefficient k_{31}, calculated from the resonance and antiresonance frequencies. Curve k_{31} (V) corresponds to a symmetrical loop for voltage variation from +1000 v to -1000 v and back ("negative" values of k_{31} correspond to negative fields), attaining a saturation value of 11.5% at 10°C. The electric field strength at which piezoactivity vanishes corresponds in magnitude to the coercive field found from the hysteresis loops. When sufficiently high fields are applied, piezoactivity is also evinced considerably above the Curie point. In investigating the frequency dependence of tan δ by means of a Q-meter, we observed

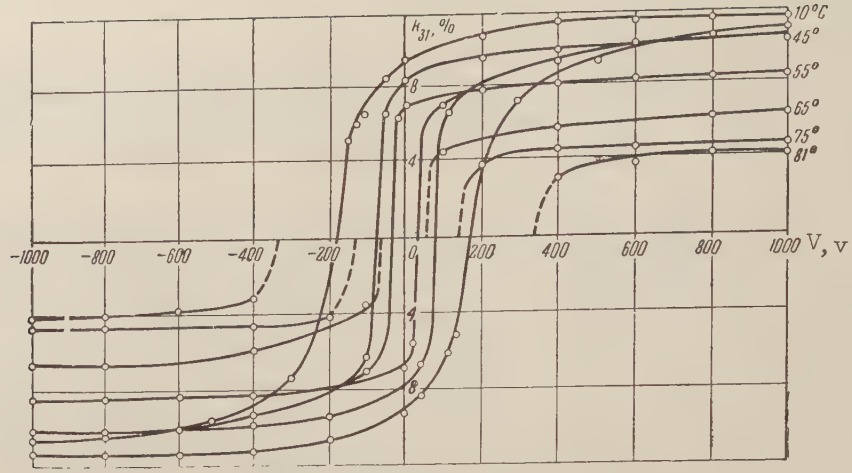

Fig.2. Variation of the electromechanical coupling coefficient k_{31} with the biasing field and temperature.

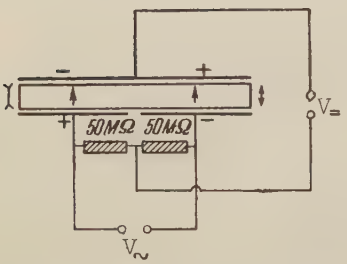

Fig.3. Method of connecting the specimens so as to reduce losses at frequencies corresponding to thickness resonances.

abrupt changes in tan δ at frequencies corresponding to the piezoelectric resonance peaks. The reason for this was explained above.

It is obvious that oscillations in thickness constitute the most serious problem inasmuch as oscillations in length and width can be eliminated from the working range by adjusting the geometric dimensions of the specimen. The thickness of the specimens, however, cannot be changed without affecting their operating characteristics.

To suppress thickness resonances we used the connecting arrangement shown in Fig.3. With this electrode arrangement the polarizing field acts on the whole specimen so that polarization is homogeneous throughout the volume. The deformation of the specimen incident to application of an ac voltage to the split electrodes is such that one half of the specimen is compressed while the other half expands, i.e., oscillations of the two individual sections occur in counterphase. In principle, if the natural frequencies of both halves coincide, total suppression of oscillation should be possible, i.e., the oscillation amplitude will differ little from the static value. Losses are reduced by a factor of ten, and tan δ near the thickness resonances does not exceed 10%.

It is obvious that this electrode arrangement does not affect the nonlinearity. Thus, let us characterize the nonlinearity by the coefficient

$$N = \frac{C_0}{C_U},$$

where C_0 and C_U are the values of the capacitance in the absence and in the presence of a bias field, respectively. Upon separation into two sections the capacity of the plate will be reduced by a factor of four, i.e.,

$$C_0' = \frac{C_0}{4}.$$

Upon application of a bias field,

$$C'_U = \frac{C_U}{4},$$

so that we will have

$$\frac{C'_0}{C'_U} = \frac{C_0}{C_U} = N.$$

Hence parasitic piezoelectric thickness resonances can be eliminated from the working frequency band by appropriate choice of the geometric parameters and use of the proposed electrode arrangement.

Physics Faculty,
Moscow State University

NONLINEAR PROPERTIES OF FERROELECTRICS AT MICROWAVE FREQUENCIES

- V.M.Petrov

In order to understand the nature of ferroelectricity it is instructive to investigate the frequency range of the nonlinear properties of ferroelectrics. This is also important from the standpoint of practical utilization of ferroelectrics at high and superhigh frequencies.

Since it is difficult to avoid heating of the specimens, ferroelectrics, so far as we know, have only been studied in weak microwave fields. A number of authors have investigated the variation of the dielectric constant ϵ of barium titanate and some $BaTiO_3$-base solid solutions as a function of the dc biasing field $E_{=}$. Earlier we measured the $E_{=}$ dependences of ϵ and tan δ at 3000 Mc for single-crystal and ceramic barium titanate[1] as well as for different Varikonds[2]. It was demonstrated that the influence of the biasing field at 3000 Mc is qualitatively analogous to its influence at low frequencies, i.e., both ϵ and tan δ decrease in the presence of $E_{=}$. The only difference is that at 3000 Mc the values of ϵ is approximately half that at radiofrequencies, while tan δ is some 10-20 larger.

The fact that ϵ measured at microwave frequencies depends on the dc field does not in itself betoken significant nonlinearity of ferroelectrics at superhigh frequencies. In Fousek's work[3] the $E_{=}$ dependences of ϵ at 1000 Mc are mistakenly called "nonlinear properties of $BaTiO_3$ at 1000 Mc". Cassedy[4] also confuses these two essentially different questions when, by analogy with semiconductor diodes, he calculates a parametric ferroelectric microwave amplifier on the basis of curves of ϵ versus $E_{=}$. A dielectric is nonlinear at a given frequency only if its dielectric constant varies with the instantaneous value of the ac field. This condition is equivalent to ϵ varying with the amplitude of the field of the given frequency, inasmuch as $\epsilon = f(E_{\sim})$ is an even function.

In the present work we studied the $E_{\sim}$ dependences of ϵ of barium titanate and Varikonds at 3000 Mc. We used the coaxial measuring line procedure of Ivanov & Petrov[5]. Our specimens were small: $d < \lambda/2\sqrt{\varepsilon}$ and $r_1 < \lambda/14\sqrt{\varepsilon}$, where d is the thickness and r_1 is the radius of the specimen. Calculations[6] show that in this case the microwave field is homogeneous throughout the specimen to within 5%. The values of ϵ were found from measured capacitance by means of the formulas for nonquasistatic plane capacitors[6].

We succeeded in avoiding excessive heating of the specimens by using a pulse field with a low duty factor (1:12500) and small specimens ($d \approx 0.5$ mm, $r_1 \approx 0.2$ mm). The maximum temperature differential between the center of the specimen and its faces, which were in thermal contact with massive metallic electrodes, was

$$\Delta T = \frac{\varepsilon \tan\delta \cdot f E_{\sim}^2 \tau}{3.6 \cdot 10^{12} c\rho \left(1 - e^{-1/F\tau_0}\right)}, \qquad (1)$$

where τ and F are the pulse duration and repetition frequency, f is the frequency of the microwave field, c is the specific heat and ρ is the density of the ferroelectric material, $\tau_0 = c\rho d^2/8\lambda_0$ is the time to attainment of thermal equilibrium at the center of the specimen, and λ_0 is the heat conduction coefficient of the dielectric. In our case, for $\epsilon = 1000$, tan $\delta = 0.25$ and $E_{\sim} \approx 5$ kv/cm, the maximum temperature differential, according to (1), was about 7°; the capacitor plates were at room temperature (20°C).

A block diagram of the set-up is given in Fig.1. The oscillator 1 had a pulse power of 80 kw, a pulse duration of 1 μsec and a repetition frequency of 80 pps. For decoupling the oscillator and controlling the power we used two dissipative waveguide attenuators with graphite-cement vanes. A third coaxial attenuator was used for decoupling the IMM-10 power meter 3 from the slotted line.

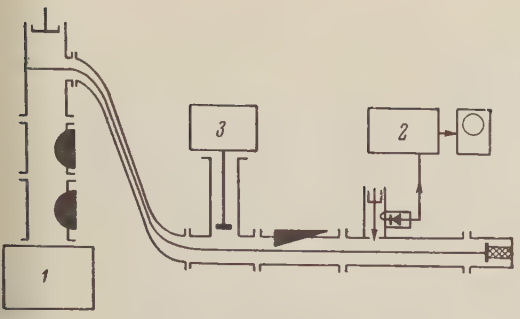

Fig.1. Diagram of set-up for measuring the $E_\sim$ dependence of ϵ at 3000 Mc.

By way of standing-wave indicator we employed a 103-I pulse amplifier 2 and an I0-3 slave sweep oscillograph.

The microwave field amplitude at the specimen was determined by measuring the pulse power P passing through the slotted line with a matched load in place of the measurement capacitor. The power incident on the capacitor and reflected from it will also equal P inasmuch as the oscillator is decoupled from the load by the dissipative attenuators. The field amplitude at the specimen was calculated by the formula

$$E_\sim = \frac{2}{md}\sqrt{2Z_0P}\sin 2\pi l/\lambda = \frac{2}{md}\sqrt{2Z_0P/(1+\omega^2Z_0^2C^2)}; \qquad (2)$$

here the coefficient m, which equals $(1-\alpha C_1)J_0(x_1\sqrt{\epsilon})\,J_0(x_2)/J_0(x_1)$ (in the notation of Ref.6), takes into account the field distribution over the radius of the capacitor (in the quasistatic case $m = 1$), Z_0 = 50 ohm is the characteristic impedance, l is the distance of the standing wave minimum from the load, and C is the capacitance of the capacitor.

Measurements of the $E_\sim$ dependence of ϵ for $BaTiO_3$ ceramic showed that up to $E_\sim$ = 10 kv/cm the dielectric constant is invariant and does not depend on the field amplitude. For further measurements we chose the most nonlinear $BaTiO_3$-base ferroelectrics: Varikonds of the VK-2 type, whose dielectric constant at 50 cps increases by a factor of 20-30 with increase of $E_\sim$ from 0 to 0.8 kv/cm. Curve 1 of Fig.2 shows the dependence obtained. The dielectric constant increases only slightly with increase of the crest value of the microwave field from 0 to 3 kv/cm. With further increase of the field amplitude ϵ begins to grow rapidly. There is a considerable spread of values for different specimens (hatched area in Fig.2). The larger the specimen, the sharper the rise of its dielectric constant. This in itself suggested that the observed field dependences were due not to nonlinearity of the material but rather to a temperature effect. VK-2 Varikonds are very sensitive to temperature change near 20°C (see insert curve in Fig.2). Increase of $E_\sim$ causes the inner layers of the specimen to heat; therefore ϵ also increases. Rise of ϵ in turn increases ΔT, (see Eq.(1)), etc. This is why the curves of ϵ vs E are so steep in the vicinity of $E_\sim \approx 5$ kv/cm.

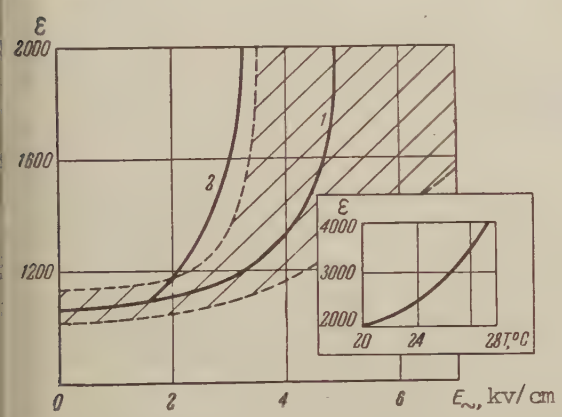

Fig.2. Variation of the dielectric constant of VK-2 material with the field amplitude at 3000 Mc: 1) pulse repetition rate 80 pps, 2) 240 pps. Insert: variation of ϵ with temperature at 0.5 Mc.

Fig.3 shows the $E_\sim$ dependences of ϵ for VK-4 Varikonds, which have more stable temperature characteristics. The inserts in the figure show the temperature dependences of ϵ of the same materials at radio frequencies. The dielectric constant of specimens of 2SZ material (curves 1) rises upon heating; it also increases with increasing $E_\sim$. Although the nonlinear properties of this material at low frequencies are approximately the same as those of VK-2 (ϵ at $E_\sim$ = 1 kv/cm is 30 times the initial "zero field" value), the $E_\sim$ dependence ϵ at microwave frequencies is weaker than in the case of VK-2. This is

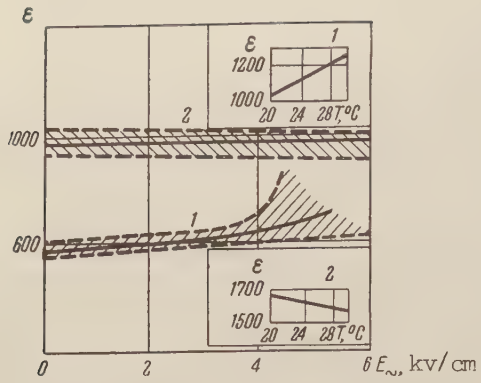

Fig.3. Variation of the dielectric constant of VK-4 Varikonds with the field amplitude at 3000 Mc: 1) 2SZ material, 2) 0.5SZ and 0.5SH materials. The shaded area represents the experimental scatter. Inserts: temperature dependences at 0.5 Mc.

due to the weaker temperature dependence of ϵ in the 2SZ ceramic.

The dielectric constant of the 0.5SZ and 0.5SH materials drops slightly upon heating (curve 2) in insert to Fig.2). Accordingly, no rise of ϵ with an increase of the field up to $E_{\sim} = 7$ kv/cm was observed for specimens of this material. The nonlinear properties of these Varikonds at 50 cps can be summed up as follows: the ratio of the maximum dielectric constant (at $E_{\sim} = 1$ kv/cm) to its initial value is 16 for the 0.5SZ material and 20 for the 0.5SH.

Consequently, barium titanate and the most nonlinear $BaTiO_3$-base solid solutions (Varikonds) exhibit no appreciable nonlinearity at 3000 Mc up to field strengths of the order 7 kv/cm. This deduction agrees with the results of a number of radiofrequency investigations. Thus, Obukhov[7] demonstrated that the nonlinearity of $Ba(Ti,Sn)O_3$ solid solutions similar in composition to the tested Varikonds vanishes at frequencies near 1 Mc. The high nonlinearity of Varikonds in relatively weak (~1 kv/cm) low-frequency fields is apparently due primarily to domain polarization per se. As is known, the domain polarization switching time is about 10^{-6} sec, so that at microwave frequencies the domain walls do not have time to keep up with the field variation even in strong fields. The high value of the initial dielectric constant is due to the high degree of polarization of the individual domains, i.e., to induced polarization. The $E_{=}$ dependence of ϵ in weak ac fields, which is due to domain orientation by the biasing field, persists at microwave frequencies inasmuch as the anisotropy of ϵ in the direction of polarization and in the perpendicular direction obtains up to optical frequencies.

Consequently, for use in fields up to 7 kv/cm microwave parametric amplifiers frequency multipliers and other devices that utilize the variation of ϵ with the instantaneous field value should not be fabricated of barium titanate and Varikonds. However, the latter can be employed to realize frequency and amplitude modulation of microwave signals and in the design of phase shifters and other microwave components in which the frequency of the control voltage does not exceed a few megacycles. The existence of nonlinearity of the induced polarization near the Curie temperature in actual fields is of course not excluded; in this case it is possible in principle to employ ferroelectrics as nonlinear microwave elements.

I wish to thank I.V.Ivanov for valuable advice with regard to the experiments and T.N.Verbitskaya for providing the Varikond specimens and data on their nonlinear properties at low frequencies.

Physics Faculty,
Moscow Sate University

References

1. V.M.Petrov, Fiz. tv. tela, 2, 997 (1960). (Trans.Soviet Physics - Solid tate.)

2. L.M.Aleksandrova, T.N.Verbitskaya, I.V.Ivanov & V.M.Petrov, Voprosy adioelektroniki (Questions of radio electronics), Series III, No.3 (1960).

3. J.Fousek, Czech.Phys.Jour., 8, 254 (1958).

4. E.S.Cassedy, Proc.IRE, 47, 1374 (1959).

5. I.V.Ivanov & V.M.Petrov, Izv.AN SSSR, Ser.fiz., 22, 1524 (1958). (Trans. ulletin, 22, 1516.)

6. V.M.Petrov, PTE, No.4, 118 (1960). (Trans.Instruments & Experimental echniques.)

7. A.A.Obukhov, Izv.AN SSSR, Ser.fiz., 22, 1531 (1958). (Trans.Bulletin, 2, 1523); Fiz.tv.tela, 1, 1730 (1959). (Trans.Soviet Physics - Solid State).

FERROELECTRIC FILMS WITH A RECTANGULAR HYSTERESIS LOOP

- M.S.Lur'e, E.I.Vasil'eva & I.V.Ignat'eva

In recent years many investigators have been concerned with the development of polycrystalline ferroelectrics with rectangular hysteresis loops.[1,2] Smolensk suggested that the rectangularity coefficient of polycrystalline ferroelectrics c be increased by reducing the unit cell anisotropy. On the basis of geometrical considerations, Ksendov demonstrated that when the dielectric constant has the sa or nearly the same value along different crys- tallographic axes, the integral dynamic polar- ization curve for chaotically scattered domai acquires a more rectangular character. In th connection of particular interest are ferro- electric materials with a nearly cubic (for example, rhombohedral) structure.

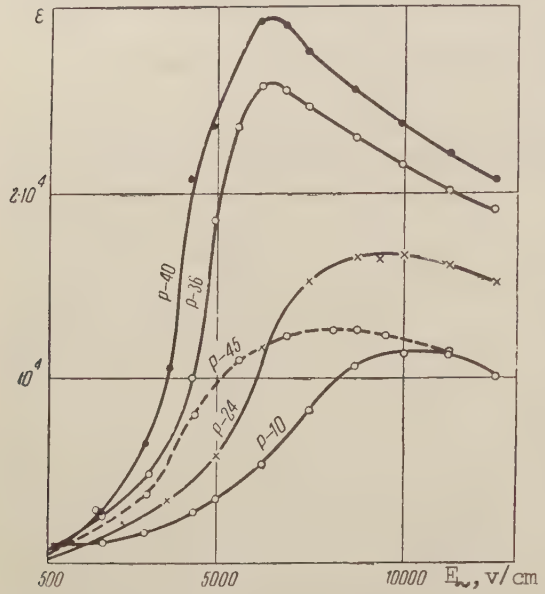

Fig.1. Ac field dependence of the dielectric constant for $Pb(Ti,Zr)O_3$ solid solution specimens of different composition.

In view of the available experimental data, we assume that the character of the chemical bonds in the crystal lattice also plays an important role where the shape of the hysteresis loop is concerned. It is known for example, that the increase of homopolarity incident to replacement of Ba^{2+} by Pb^{2+} ions in solid solutions of the $(Ba,Pb)TiO_3$ system, increases the rectangularity of the dielectric hysteresis loop in spite of increase in the anisotropy of the unit cell.

Pursuant to the above assumption we thoug it would be worthwhile to investigate the pro- perties of some solid solutions in the Pb(Ti, $Zr,Sn)O_3$ system. Our specimens were discs pre pared from a mixture of the oxides by the con- ventional procedure of sintering in an atmos- phere containing lead oxide vapor. By care- ful control of the synthesis conditions we succeeded in reducing the loss in weigh due to evaporation of lead to 0.1-0.5%. Silver electrodes were fired onto the sintered discs. Fig.1 shows the ac field dependences of the dielectric constant for some $Pb(Ti,Zr)O_3$ system specimens. It will be evident from the curves that the nonlinearity increases with increasing $PbTiO_3$ concentration and goes through a maximum in the vicinity of morphotropic transition from the rhombohedral to the tetragonal phase (according to the data of Ref.3 the transition occurs at a 45% content of $PbTiO_3$).

The oscillograms reproduced in Fig.2 show a considerable increase in rectangu larity of the hysteresis loops with increasing $PbTiO_3$ concentration. The para- meters of the specimens remain stable in a wide temperature range (Fig.3). Sub-

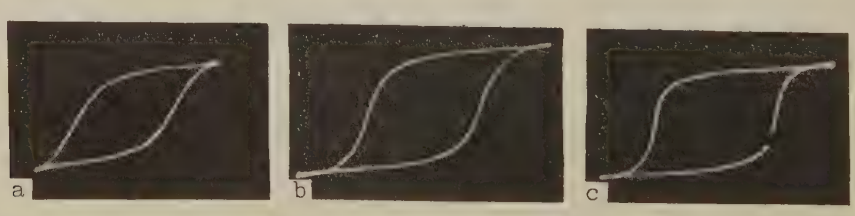

Fig.2. Hysteresis loops for specimens of the $Pb(Ti,Zr)O_3$ system: a) 24% $PbTiO_3$ + + 76% $PbZrO_3$; b) 30% $PbTiO_3$ + 70% $PbZrO_3$; c) 40% $PbTiO_3$ + 60% $PbZrO_3$.

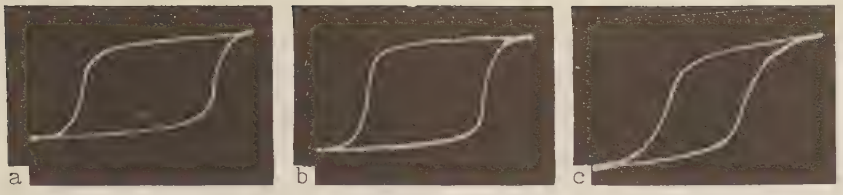

Fig.3. Temperature dependence of the hysteresis loops for specimens of 40% $PbTiO_3$ + + 60% $PbZrO_3$: a) 20°; b) 150°; c) 200°C.

stitution of "$PbSnO_3$" for $PbZrO_3$ leads to some increase of polarization and a minor decrease of the coercive field. The rectangularity coefficient remains virtually unchanged.

Thus, in the $Pb(Ti,Zr,Zn)O_3$ system there is a very wide range of concentrations characterized by nearly rectangular hysteresis loops. The principal characteristics of some of the investigated compositions are given in the table.

Specimen	Composition, mole %			$P_s \cdot 10^6$, Coul/cm^2	E_c, v/cm	K_r
	$PbZrO_3$	$PbTiO_3$	«$PbSnO_3$»			
P-10	90	10	—	8,4	8350	0,65
P-24	76	24	—	10,4	6950	0,78
P-36	64	36	—	12,2	6350	0,83
P-36—10	54	36	10	15	5850	0,85
P-40	60	40	—	13	6650	0,85
P-45	55	45	—	14	6900	0,83

Polycrystalline films ~2 μ thick with the indicated compositions were prepared by deposition of the appropriate oxides onto a platinum foil or platinized ceramic backing by hydrolysis from a solution of the corresponding tetrachlorides, and then sintered in a lead oxide vapor atmosphere. The base served as one electrode; the other electrode was applied to the films by vacuum evaporation. Sintering conditions were determined experimentally to obtain maximum agreement between the fundamental parameters of film and ordinary specimens. We succeeded in obtaining exact coincidence of Curie temperatures for ordinary and film specimens of identical composition. The other parameters, however, differed to some extent. This is not surprising if we recall that at the surface of ferroelectrics there exists an anomalous layer associated with the presence of a space charge compensating the contact potential difference at the interface of the two phases. The presence of such a layer has been reported by a number of authors[4-7] who also noted that owing to the high value of the internal field, the surface layer must be in a strongly polarized state and have a small value of ϵ as compared with the value for the inner volume. Hence for film thicknesses commensurate with that of the surface layer, the parameters of the specimens will inevitably differ sharply from those of bulk material.

Figs.4 show oscillograms of the hysteresis loops and Fig.5, the nonlinearity characteristic of film specimens, measured, as in the case of the bulk specimens, at a frequency of 50 cps. Noteworthy is the abnormally high value of the saturation field. The value of the peak dielectric constant ϵ_{max} is much lower than that for bulk specimens of analogous composition.

To elucidate the influence of the surface layer on the electric characteristics we carried out a series of experiments using different materials for the "second" electrode. In all cases the "first" electrode was the platinum foil

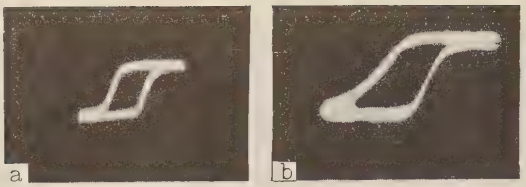

Fig.4. Hysteresis loops of ferroelectric films: a) Pt-Ag electrodes; b) Pt-In electrodes.

backing. To eliminate errors due to possible variation of different individual specimens, each electrode material was deposited at three separate points on the same specimen; each electrode spot was 0.6 mm in diameter. Deposition was effected by vacuum evaporation at the lowest possible temperature of the specimen in order to minimize diffusion of the electrode materi into the film.

Fig.6 shows the ac field dependences o the dielectric constant for one of the speo mens with different electrodes; the data were recorded at a frequency of 500 cps. It will be evident from the curves that the value of the dielectric constant and saturation field differ greatly for different electrode materials.

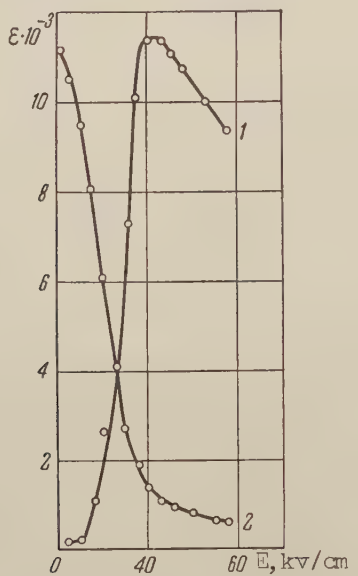

Fig.5

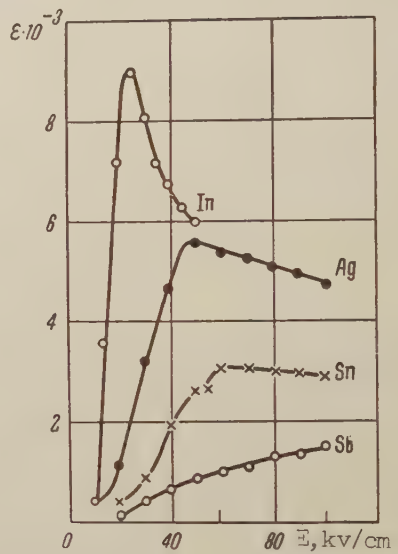

Fig.6

Fig.5. Ac and dc field dependences of the dielectric constant of ferroelectric films: 1) $\epsilon = f(E_{\sim})$, $E_{=} = 0$; 2) $\epsilon = f(E_{=})$, $E_{\sim} = 40$ kv/cm.
Fig.6. Variation of the nonlinearity of ferroelectric films with the second electrode material.

A characteristic feature of film specimens with different electrodes is the marked asymmetry of the hysteresis loops; this is particularly noticeable in the range of fields weaker than the saturation field (Fig.4,b). Such asymmetric loop were obtained for indium, tin and antimony electrodes, but were not for gold. In the case of silver electrodes a weak asymmetry was observed for some specimens bu not for others. This asymmetry may be due to the presence of an internal field i the volume of the ferroelectric; such a field may arise owing to disparity betwee the space charges at the different electrodes and/or owing rectification at the ferroelectric-metal interface. This point of view is consistent with our earlier observations[7] and the work of Saburi[8], who detected uncompensated polarization in unpolarized polycrystalline specimens and the presence of rectification on the boundary between conducting barium titanate and silver. The influence of the

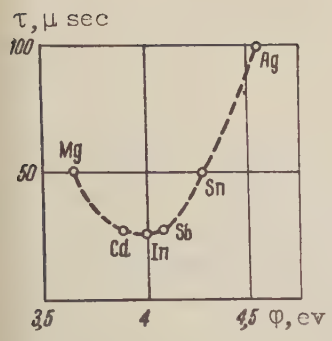

Fig.7. Variation of the switching time of ferroelectric films as a function of electrode material.

anomalous layer in the contact region is also clearly evident in measurements of the switching time of ferroelectric films (Fig.7).

It should be noted that the curves reproduced in the above figures differ somewhat for different specimens and are therefore qualitative rather than quantitative in character. This variation in individual specimen characteristics is connected with the difficulty of insuring stoichiometric composition and identical impurity concentration in preparing film specimens. Nevertheless, we believe that the present data may be of interest, particularly insofar as it indicates the possibility of controlling the properties of ferroelectric films by varying the state of the surface layer.

References

1. S.V.Bogdanov, G.M.Kovalenko, R.Ya.Razbash & A.I.Cherepanov, Izv.AN SSSR, Ser.fiz., 22, 1500 (1958). (Trans.Bulletin, 22, 1493.)
2. M.S.Lur'e, Doklady AN SSSR, 128, 73 (1959). (Trans.Doklady.)
3. B.Jaffe, R.S.Roth & S.Marzullo, J.Res.Nat.Bur.Standards, 55, 239 (1955).
4. W.Känzig, Phys.Rev., 98, 549 (1955).
5. A.G.Chynoweth, Phys.Rev., 102, 705 (1956).
6. W.R.Büssem & E.C.Subbarao, Naturwissenschaften, 44, 509 (1957).
7. M.S.Lur'e & I.V.Ignat'eva, in Fiz. tverdogo tela (Collected articles on Solid State Physics), I, 190,M. 1959.
8. O.Saburi, J.Phys.Soc.Japan, 14, 1159 (1959).

ELECTRIC CONDUCTIVITY OF $BaTiO_3$ BASE SOLID SOLUTIONS OF MANGANESE, COBALT AND NICKEL NIOBATES AND TANTALATES

- E.A.Stafiichuk & E.V.Sinyakov

We investigated the dielectric properties of polycrystalline specimens of $BaTiO_3$-base solid solutions of manganese, cobalt and nickel niobates and tantalates in ac fields and observed a number of interesting properties[1]. In the present report we give the results for the temperature and concentration dependences of the electric conductivity and thermo-emf of the indicated solid solutions and compare the effects of Mn^{2+}, Co^{2+} and Ni^{2+} ions on the conductivity of $BaTiO_3$.

The specimen preparation procedure was described in Ref.1. The specimens for the conductivity measurements were discs 15 mm in diameter and 2-3 mm thick. Platinum electrodes with guard rings were applied to the solid solution specimens by cathode sputtering. The temperature dependence of the conductivity was measured on a string electrometer set-up in the range from 50° to 200°C in ~20 v/mm fields. A special electrometric arrangement was employed to measure the thermo-emf of the same specimens. In this case silver electrodes were fired on.

Table 1 gives the results of investigating $\sigma = f(T)$ for the compositions employed as the second components of the $BaTiO_3$ solid solutions. These data indicate that AB_2O_6 and "$A_2B_2O_7$" compositions (where A stands for Mn, Co or Ni and B for Nb or Ta) have a rather high resistivity ρ (as a rule, ρ is higher for compositions of the AB_2O_6 type than for "$A_2B_2O_7$"). The plots of $\log \sigma = f(1/T)$ for AB_2O_6 compositions are straight lines without a break.

Compositions of the "$A_2B_2O_7$" type exhibit breaks in the $\log \sigma = f(1/T)$ plots. In going from Mn to Ni we note an increase of the break temperature, of the activation energy U (calculated by the formula $\sigma = \sigma_0 e^{\frac{-u}{2kT}}$) and the resistivity. It should be noted that "$Co_2Nb_2O_7$", "$Co_2Ta_2O_7$" and "$Mn_2Ta_2O_7$" exhibit the same kind of breaks as V_2O_5 and ZnO and that the activation energy of "$Co_2Ta_2O_7$" and of "$Mn_2Ta_2O_7$" increases by a factor of two in going through the break point, i.e., doubles above the break temperature.

Table 1

Compound	U, ev	ρ at 149° ohm·cm	Compound	U_1, ev	U_2, ev	Break temp., °C	ρ at 149° ohm·cm
$MnTa_2O_6$	1,84	$1,03 \cdot 10^{11}$	«$Mn_2Ta_2O_7$»	0,54	1,02	115	$6 \cdot 10^6$
$CoTa_2O_6$	1,7	$3,57 \cdot 10^{11}$	«$Co_2Ta_2O_7$»	0,62	1,16	127	$2 \cdot 10^7$
$NiTa_2O_6$	1,68	$3 \cdot 10^{10}$	«$Ni_2Ta_2O_7$»	1,92	1,56	153	$4 \cdot 10^{10}$
$MnNb_2O_6$	1,08	$2,49 \cdot 10^9$	«$Mn_2Nb_2O_7$»	1,38	—	—	$1,6 \cdot 10^7$
$CoNb_2O_6$	1,56	$2,99 \cdot 10^{10}$	«$Co_2Nb_2O_7$»	1,46	1,76	113	$5,2 \cdot 10^7$
$NiNb_2O_6$	1,74	$7,7 \cdot 10^{11}$	«$Ni_2Nb_2O_7$»	1,62	1,19	150	$6,2 \cdot 10^{11}$

Careful x-ray diffraction studies showed that $AO + B_2O_5$ mixtures form AB_2O_6 compounds of the columbite type, while $2AO + B_2O_5$ compositions do not form chemical compounds but result in a mixture of AB_2O_6 compound and AO oxide. This explains the differences between the resistivities of the indicated compositions and the presence of breaks in the $\log \sigma = f(1/T)$ plots for "$A_2B_2O_7$".

As was noted in Ref.1, introducing Mn, Co and Ni niobates and tantalates into $BaTiO_3$ leads to formation of solid solutions. Measurements of the temperature and concentration dependences of the conductivity of the indicated solid solutions showed that the resistivity of solid solutions of the $BaTiO_3$-AB_2O_6 type is considerably higher than that of $BaTiO_3$-"$A_2B_2O_7$" systems (see Table 2), which can be associated with differences between the types of solid solutions formed in

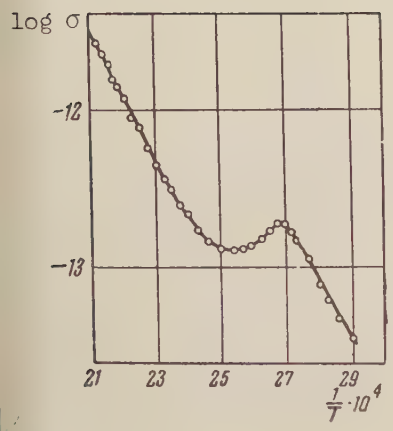

Fig.1. Log $\sigma = f(1/T)$ for 99% $BaTiO_3$-1% $MnNb_2O_6$ solid solution.

systems and the fact that the concentration of transition metal ions is higher in solid solutions of the second type.

As is known, a number of authors[2,3] have observed a conductivity anomaly in $BaTiO_3$ at the Curie point. In our investigations jumps of the conductivity at the Curie point were observed for a number of $BaTiO_3$ solid solutions with 0.5 to 1 mole percent manganese niobate or tantalate (Fig.1). For other concentrations the Curie points of $BaTiO_3$-"$A_2B_2O_7$" solid solutions lie outside the temperature range of our measurements, while $BaTiO_3$-"AB_2O_6" solid solutions with "impurity" concentrations greater than 1 mole percent are nonferroelectric. As a rule, jumps of conductivity are not observed for solid solutions of Mn and Co compounds.

It is probable that the marked rise of σ at the Curie point for manganese-containing solid solutions is due to the fact that the Mn^{2+} ion has a weaker effect on the ferroelectric properties of $BaTiO_3$ than the other ions (for example, Co^{2+} and Ni^{2+})[1,4]. At the Curie point, where rearrangement of the crystal lattice occurs, there obtain in Mn-containing solid solutions the most favorable conditions for increase in the number of current carriers owing to "loosening" of the lattice as well as to freeing bound charges on the domain walls. With increasing content of the second, Mn-containing components (beginning with 2%), the conductivity of the solid solution increases and the activation energy decreases, dropping to a value of ~1.0 ev.

Some nickel compounds, on the contrary, act to increase the resistivity of the solid solutions. This has been noted earlier by other authors[3,4]. Ni^{2+}-containing solid solutions also have the highest activation energies (see Table 2).

Comparison of the properties of solid solutions of niobates and tantalates of the metals under consideration shows that niobium-containing solid solutions as a rule have a higher resistivity than those containing tantalum.

The indicated regularities in the variation of the resistivity and activation energy of solid solutions as a function of the introduced A and B ions are in good agreement with the ionization potentials of these cations.

To elucidate the reason for the appearance of breaks in the $\log \sigma = f(1/T)$ straight line plots we investigated the temperature dependence of the thermo-emf. The results for some systems are given in Fig.2.

Comparison of the $\sigma = f(T)$ and $\alpha = f(T)$ plots showed that the breaks in the log σ vs 1/T straight lines correspond, as a rule, either to a change in sign or a maximum (or minimum) of the thermo-emf. Thus, for example, for the specimen containing 1% $NiTa_2O_6$ breaks were observed at 145° and 90° and the thermo-emf changes its sign twice (at 135° and 75°); in "$Co_2Ta_2O_7$"-containing solid solutions the thermo-emf does not change sign and the log σ vs 1/T plots evince no breaks (Fig. 2,b). Comparison of the values of the conductivity and thermo-emf of specimens of different composition shows that the relation $\alpha = C - B \log \sigma$ (valid for semiconductors) is satisfied.

From analysis of the $\sigma = f(T)$ plots follows still another important deduction: in the investigated temperature range the sign of the thermo-emf of Ni^{2+}-containing solid solutions is negative, while for compositions with Mn^{2+} and Co^{2+} it is positive. If we recall that normally in $BaTiO_3$ n-type conductivity persists up to about 180°C, we are led to infer that the character of the conductivity of $BaTiO_3$ is affected little by Ni-containing additives, but is significantly altered

Table 2

Impurity	Mole %	U_1, ev	U_2, ev	ρ at 161° ohm·cm	ρ at 80° ohm·cm	Break. temp., °C	Impurity	Mole %	U_1, ev	U_2, ev	ρ at 150° ohm·cm	ρ at 70° ohm·cm	Break temp., °C
$NiNb_2O_6$	1	2,6	1,2	$8\cdot10^{11}$	$4,3\cdot10^{11}$	138; 78	$NiTa_2O_6$	1	1,78	0,7	$1,96\cdot10^{11}$	—	145; 98
	2	1,74	0,84	$4\cdot10^{11}$	$1,2\cdot10^{13}$	127		2	1,78	0,84	$2,6\cdot10^{12}$	$2,8\cdot10^{13}$	145
	3	1,44	0,14	$1,5\cdot10^{13}$	$5,6\cdot10^{13}$	127		—	—	—	—	—	—
	5	1,6	0,8	$3,6\cdot10^{14}$	$1,1\cdot10^{15}$	138		—	—	—	—	—	—
$CoNb_2O_6$	1	1,6	0,52	$1,6\cdot10^{11}$	$8,9\cdot10^{11}$	181	$CoTa_2O_6$	1	0,7	0,54	$5,4\cdot10^{10}$	$2,5\cdot10^{11}$	132
	2	1,16	0,42	$1,3\cdot10^{11}$	$5,1\cdot10^{11}$	147		2	0,8	0,64	$1,2\cdot10^{11}$	$8,9\cdot10^{11}$	150
	3	0,78	—	$2,9\cdot10^{10}$	$3,3\cdot10^{11}$	—		3	0,88	0,6	$1,4\cdot10^{10}$	$1,7\cdot10^{11}$	90
	5	0,76	0,54	$1,8\cdot10^{10}$	$8,5\cdot10^{10}$	144		5	1,0	0,8	$5,2\cdot10^{10}$	$7,3\cdot10^{11}$	123
$MnNb_2O_6$	0,5	2,0	0,4	$7,5\cdot10^{12}$	$2,10^{13}$	Jmp. 109	$MnTa_2O_6$	—	—	—	—	—	—
	1	1,68	1,2	$2,1\cdot10^{12}$	$1,6\cdot10^{13}$	Jmp. 97		1	1,12	—	$1,3\cdot10^{11}$	$6,10^{11}$	Jmp. 95
	2	1,02	—	$3,7\cdot10^{11}$	$8,4\cdot10^{12}$	—		2	1,05	0,84	$9,5\cdot10^{9}$	$1,9\cdot10^{11}$	113
	3	1,04	—	$2,9\cdot10^{10}$	$5,6\cdot10^{11}$	—		3	1,0	—	$6,6\cdot10^{9}$	$1,7\cdot10^{11}$	—
	5	1,04	0,96	$2,3\cdot10^{10}$	$6,1\cdot10^{11}$	145		—	—	—	—	—	—
	7	1,12	1,04	$5,1\cdot10^{9}$	$1,3\cdot10^{11}$	140		7	1,04	—	$9,7\cdot10^{8}$	$2,5\cdot10^{10}$	—
«$Ni_2Nb_2O_7$»	1	1,82	0,6	$3,1\cdot10^{11}$	$1,1\cdot10^{13}$	124	«$Ni_2Ta_2O_7$»	1	2,18	0,88	$3,5\cdot10^{10}$	$2,7\cdot10^{11}$	147
	2	1,9	0,7	$3\cdot10^{11}$	$5,2\cdot10^{12}$	147		2	1,84	1,0	$1,2\cdot10^{10}$	$5,2\cdot10^{11}$	134
	3	1,52	1,02	$3,28\cdot10^{11}$	$3,9\cdot10^{13}$	91		3	1,5	1,2	$3,6\cdot10^{10}$	$1,2\cdot10^{11}$	130
	5	1,4	1,14	$1,98\cdot10^{11}$	$1,45\cdot10^{13}$	80		5	1,2	—	$2,5\cdot10^{10}$	$1,5\cdot10^{12}$	—
«$Co_2Nb_2O_7$»	1	1,2	0,86	$8,2\cdot10^{9}$	$9,4\cdot10^{10}$	185	«$Co_2Ta_2O_7$»	1	0,78	—	$2\cdot10^{10}$	$2\cdot10^{11}$	—
	2	0,78	—	$1,9\cdot10^{9}$	$1\cdot10^{10}$	—		2	0,82	—	$2,2\cdot10^{8}$	$2,8\cdot10^{9}$	—
	3	0,92	—	$2,3\cdot10^{8}$	$3,6\cdot10^{9}$	—		3	0,96	—	$2,2\cdot10^{8}$	$3,7\cdot10^{9}$	—
	5	1,28	—	$2\cdot10^{8}$	$1,6\cdot10^{9}$	—		5	1,2	—	$1,1\cdot10^{9}$	$4,3\cdot10^{10}$	—
«$Mn_2Nb_2O_7$»	0,5	1,3	1,2	$3,8\cdot10^{10}$	$4,1\cdot10^{12}$	Jmp. 109	«$Mn_2Ta_2O_7$»	0,5	1,5	—	$1\cdot10^{11}$	$6\cdot10^{11}$	Jmp. 104
	1	0,98	0,98	$1\cdot10^{10}$	$1,2\cdot10^{11}$	119		1	1,04	0,82	$2,9\cdot10^{11}$	$6\cdot10^{10}$	132
	2	1,12	—	$9,8\cdot10^{8}$	$1,6\cdot10^{10}$	—		2	0,96	—	$2,6\cdot10^{8}$	$5,8\cdot10^{9}$	—
	3	1,04	0,88	$3,8\cdot10^{8}$	$6,4\cdot10^{9}$	130		3	0,96	—	$6,2\cdot10^{8}$	$1,2\cdot10^{9}$	—
	5	0,98	—	$1,3\cdot10^{8}$	$2,6\cdot10^{9}$	—		5	0,92	—	$1,5\cdot10^{7}$	$2,6\cdot10^{8}$	—
	7	1,0	—	$6\cdot10^{7}$	$1,2\cdot10^{9}$	—		—	—	—	—	—	—

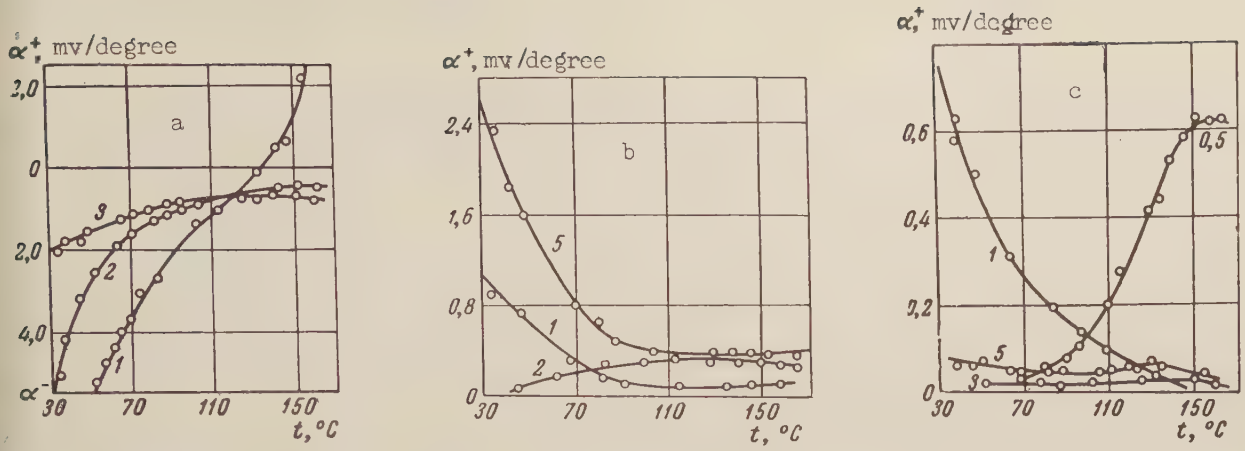

Fig.2. Temperature dependences of the thermo-emf of solid solutions: a) $BaTiO_3$-"$Ni_2Ta_2O_7$"; b) $BaTiO_3$-"$Co_2Ta_2O_7$"; c) $BaTiO_3$-"$Mn_2Ta_2O_7$". The figures at the curves indicate the impurity (second component) content in mole percent.

by additives containing Mn and Co; the last result in transition to p-type conductivity at a lower temperature.

It is evident from the foregoing that the conductivity of the investigated Mn, Co and Ni niobate and tantalate solid solutions is determined to a considerable extent by the properties of the divalent substituting cation.

It is at present impossible to construct energy diagrams for the investigated solid solutions partly because of their complexity but mainly because the energy diagram for pure $BaTiO_3$ has not yet been definitively established.

References

1. E.V.Sinyakov & E.A.Stafiichuk, Fiz.tv.tela, 2, 73 (1960). (Trans.Soviet Physics - Solid State.)

2. E.V.Sinyakov & B.K.Chernyi, Fizika dielektrikov (Transactions of the All-Union Conference on the Physics of Dielectrics), M. 1958.

3. S.Namura & S.Sawada, J.Phys.Soc.Japan, 5, 227 (1952).

4. Sakudo Tunetaro, J.Phys.Soc.Japan, 12, 1050 (1957).

PROPERTIES OF SOME $BaTiO_3$-"$A_2B_2O_7$" TYPE SOLID SOLUTIONS IN STRONG ELECTRIC FIELDS

- E.V.Sinyakov & E.A.Stafiichuk

In recent years a good deal of attention has been devoted to the study of niobates and tantalates of divalent metals and their solid solutions based on different ferroelectrics. We felt it would be interesting to study the electric properties of $BaTiO_3$ solid solutions with the niobates and tantalates of transition metals of the iron group.

Mn, Fe, Co and Ni are particularly interesting where such studies are concerned: their ionic radii are close, while the number of electrons in their subshell increases in the series. Consequently, investigation of $BaTiO_3$-base solid solutions of like compounds of these metals should disclose the effect of the degree of filling of the electron shells of introduced ions on the properties of solid solutions.

For this study we synthesized compositions of the $AO-B_2O_5$ and $2AO-B_2O_5$ types where A stands for Mn, Co or Ni and B for Nb or Ta, and their $BaTiO_3$-base solid solutions. The preparation procedure and the results of investigation of the specimens in weak high-frequency fields were described in Ref.1.

Careful x-ray diffraction studies showed that compositions of the $AO-B_2O_5$ type form AB_2O_6 compounds, while $2AO-B_2O_5$ compositions represent mixtures of the metacompound with the oxide of the divalent metal; provisionally, we designate compositions of the latter type "pyrocompositions".

On the basis of x-ray diffraction data and the variation of the Curie temperature with the second-component concentration, we assume that in $BaTiO_2$-"$A_2B_2O_7$" systems in the investigated range of concentrations there are formed solid solutions in which the Mn^{2+}, Co^{2+} and Ni^{2+} cations occupy Ba^{2+} positions. Some other authors[2,3] have also inferred that transition metal ions may replace the Ba^{2+} ion in $BaTiO_3$ and Sr^{2+} ions in $SrTiO_3$.

Inasmuch as the radii of the A cations and the degree of filling of their electron shells differ from the corresponding values for Ba^{2+}, the presence of A ions in the barium sublattice must result in great distortion of the unit cells as well as in decrease of the degree of covalence of the Ti—O bonds.[4,5] These factors result in some change in tetragonality of the cells, which is substantiated by x-ray diffraction analysis. The decrease in the degree of tetragonality of the cells and the merging of the phase transitions at a certain second-component concentration must have a definite effect on the electric properties of the solid solutions in strong electric fields.

The nonlinear properties of the specimens were measured at 50 cps by means of the equipment described in Ref.6 at temperatures that were about equally distant from the Curie points of the different compositions. We made 18 x 24 cm photographic prints of the hysteresis loops, which enabled us to determine the specimen parameters with good accuracy.

The results of investigating the nonlinear properties of different solid solutions are shown in Figs.1 and 2 and in the table, where E_m denotes the field corresponding to the maximum of the dielectric constant and ε_m denotes the corresponding maximum value of the constant. It will be evident from the curves and the table that for all the systems with increase of the second-component concentration up to 3 mole percent there is observed decrease of E_m together with a consistent growth of ε_m.

Mn, Co and Ni "pyroniobate" ("pyrotantalate") solid solutions exhibit clear dependence of E_m and ε_m on the degree of filling of the $3d$ subshell of the divalent cation (see the Table and Fig.2). The lowest values of E_m are observed for nickel tantalate and niobate solid solutions.

Nonlinear Properties of $BaTiO_3$-$AOAB_2O_6$ Solid Solutions

Second component	1 mole %				2 mole %			3 mole %		
	θ, °C	E_m, kv/cm	ε_m	c/a	θ, °C	E_m, kv/cm	ε_m	θ, °C	E_m, kv/cm	ε_m
«$Mn_2Nb_2O_7$»	90	7	10800	$1,007_4$	35	3,3	16000	—25	12	5100
«$Co_2Nb_2O_7$»	82	5	12000	$1,005_4$	22	2,2	20800	—70	8,6	7340
«$Ni_2Nb_2O_7$»	73	4,3	9750	$1,003_7$	1	1,09	32400	—95	6,86	9500
«$Mn_2Ta_2O_7$»	82	7,6	8100	$1,006_4$	44	2,98	11000	8	—	—
«$Co_2Ta_2O_7$»	85	6,18	12800	$1,004_9$	7	1,95	16400	—76	9,23	5200
«$Ni_2Ta_2O_7$»	66	3,2	14900	$1,004_5$	—7	1,45	28000	—108	4,14	8040

It should be noted that the most pronounced nonlinear properties for all the investigated solid solution systems are evinced at 2 mole percent second-component concentration. The nonlinear properties are enhanced up to this concentration and wane with further increase of the second-component concentration.

The usual regularities in the variation of the hysteresis loop parameters as a function of temperature, common to other solid solutions[7], are observed for the investigated solid solutions. In all the pyrotantalate (pyroniobate) solid solutions, up to a concentration of 3 mole percent, the coercive field E_c decreases consistently with increase in the number of electrons in the $3d$ subshell of the divalent cation. The minimum value of E_c for all systems is obtained for 2 mole

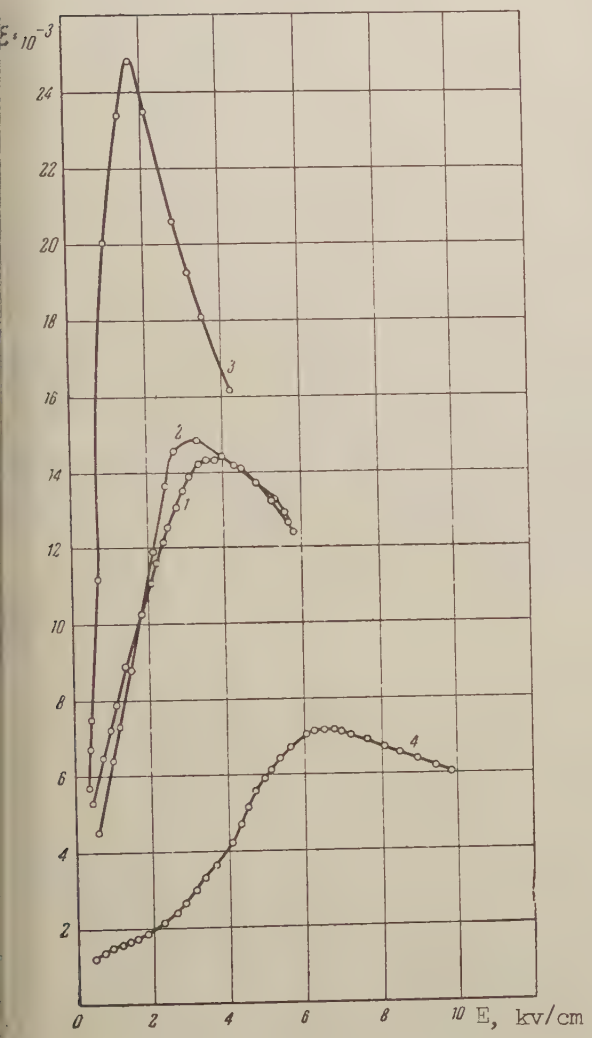

Fig.1

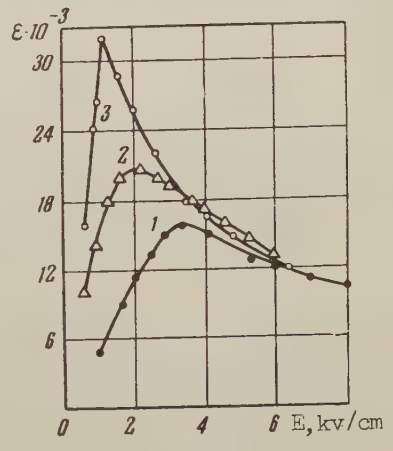

Fig.2

Fig.1. Field dependences of ε for the $BaTiO_3$-"$Ni_2Ta_2O_7$" system at different temperatures and with different "$Ni_2Ta_2O_7$" concentrations: 1) 22°C, 0 mole %; 2) 22°C, 1 mole %; 3) 40°C, 2 mole %; 4) 185°C, 3 mole %.

Fig.2. Field dependences of ε for solid solutions with 2 mole percent: 1) "$Mn_2Nb_2O_7$", 2) "$Co_2Nb_2O_7$", 3) "$Ni_2Nb_2O_7$".

percent of the second component; upon further increase of the concentration, E_c rises sharply. We calculated the rectangularity coefficients K for all the hysteresis loops and found that the composition characterized by the highest rectangularity coefficients is that containing 1 mole percent "$Co_2Ta_2O_7$" (for which $K = 93\%$ and $K_2 = 76\%$ at room temperature). It should also be noted that as a rule the saturation field has lower values for nickel-containing compositions than for those containing manganese or cobalt.

The results of investigating the properties of solid solutions in high field agree quite well with the data from x-ray diffraction studies and measurements carried out at high frequencies.

As noted above, replacement of barium ions by divalent transitions metal cat ions leads to a decrease in the degree of tetragonality of the unit cells and an appreciable shift of the Curie point to the side of lower temperatures.

The most pronounced nonlinear properties and lowest values of E_m are observe in just those compositions for which the degree of tetragonality at equal second-component concentrations is lowest, i.e., for compositions containing nickel ions The nonlinear properties increase, together with the decrease in the degree of tetragonality, with increase of the second-component concentration up to 2 mole percent. Moreover, the appreciable increase of nonlinearity at 2 percent second-component concentration is associated with increasing mobility of the domain wall in connection with merging of the two phase transitions.[7]

Beginning with 3 mole percent second-component concentration, as a rule, the values of ε_m on the ε vs temperature curves decrease for all the compositions, th nonlinear properties deteriorate and the coercive field rises appreciably. All this is probably due to the fact that the amount of nonferroelectric phase, which forms interlayers that screen the regions of spontaneous polarization, increases with increase of the second component concentration above ~3 mole percent.

Thus, the above data indicate that in spite of having radii that differ very little from each other, Mn^{2+}, Co^{2+} and Ni^{2+} ions have a substantially different (as regards magnitude) effect on the properties of $BaTiO_3$-base solid solutions. This difference is obviously connected with the different degrees of filling of the $3d$ subshells of these ions.

References

1. E.V.Sinyakov & E.A.Stafiichuk, Fiz.tv.tela, 2, 73 (1960). (Trans.Soviet Physics - Solid State.)

2. B.Lewis, Proc.Phys.Soc., 73, 17 (1959).

3. H.W.Gandy, Phys.Rev., 113, 795 (1959).

4. I.N.Belyaev, Izv.AN SSSR, Ser.fiz., 22, 1463 (1958). (Trans.Bulletin, 22, 1430.)

5. A.von Hippel, Dielectrics and their Applications. (Cited in Russian translation.)

6. E.V.Sinyakov, B.K.Chernyi & F.F.Kodzhespirov, Nauch.zap. (Scientific Notes), Dnepropetrovsk State Univer., 45, No.5, 35 (1956).

7. V.A.Bokov, Zhur.tekh.fiz., 27, 1784 (1957). (Trans.Soviet Physics - Technical Physics.)

IELECTRIC PROPERTIES AND STRUCTURE OF $PbTiO_3$-$SrTiO_3$-"$Bi_{2/3}TiO_3$" SOLID SOLUTIONS

- V.Ya.Fritsberg, E.Zh.Freidenfel'd & Ya.Ya.Kruchan

One of the sides of the $PbTiO_3$-$SrTiO_3$-"$Bi_{2/3}TiO_3$" concentration trangle, namely, the binary system $PbTiO_3$-$SrTiO_3$, has been investigated by Smolenskii[1-3] and other authors[4,5]. It was found that solid solutions with typical ferroelectric properties form in a wide concentration range and that the Curie point consistently shifts to the side of higher temperatures with increase of the $PbTiO_3$ concentration. The second side of the concentration triangle, representing the $SrTiO_3$-"$Bi_{2/3}TiO_3$" system, was investigated in detail by Skanavi et al[6]. These authors established that in this system there exists a region of solid solutions with a cubic lattice of the perovskite type, extending to 35 mole percent bismuth titanate concentration. Investigation of the dielectric properties brought out the relaxational nature of the polarization (the temperature maxima of ϵ and tan δ shift with frequency). Further, x-ray diffraction studies showed that if the sintering temperature is not too high and there does not occur dissociation of the oxides, there forms an omission type solid solution with vacant sites in the strontium part of the lattice. These authors attribute the observed relaxation effects to ionic relaxation due to the defect structure. At room temperature the dielectric constant retains a high value (about 1000), while tan δ is less than 0.01, which is of interest from the standpoint of practical utilization of these materials. Skanavi et al[6] did not observe dielectric hysteresis loops, variation of ϵ with the field strength or other properties characteristic of ferroelectrics.

In view of the above it may be assumed that by investigating an appropriate series of compositions in the $PbTiO_3$-$SrTiO_3$-"$Bi_{2/3}TiO_3$" system one can follow the transition from typical ferroelectrics to compositions with relaxation polarization. Study of this transition was the purpose of the present work. In view of the closeness of the ionic radii of Pb^{2+}, Sr^{2+} and Bi^{3+}, we hypothesized the existence of a certain definite region of solid solutions, wherein the expected regularities could be observed in relatively pure form.

The specimens were prepared by the usual ceramic technology of "pure grade" PbO, Bi_2O_3, TiO_2 and $SrCO_3$. Synthesis of high quality specimens in our case presented certain difficulties owing to the fact that Bi_2O_3 at sintering temperatures of 1100-1350° tends to fuse, while PbO tends to vaporize. As a rule the synthesis was carried out in an atmosphere of lead oxide vapor; the losses in the process of synthesis were monitored by weighing. Tests showed that by careful choice of the synthesis conditions one can reduce the losses of PbO and Bi_2O_3 to a minimum and obtain specimens with negligible porosity. The composition of the specimens was checked by chemical analysis. The data given in the present report pertain to materials in which the content of the various oxides deviated from the specified values by no more than 1.5% by weight. The water absorption of the specimens did not exceed 1%.

We carried out measurements of ϵ and tan δ in a wide range of frequencies and temperatures by means of conventional bridge and resonance equipment. A standard Sawyer-Tower circuit was used to study the ferroelectric properties at a frequency of 50 cps. The x-ray diffraction studies were carried out on a URS-50I diffractometer. We used the point counting procedure for determining the lattice parameters, the accuracy in determining which is estimated to be ±0.002 kX.

Specifically, we investigated two cross sections of the ternary systems (Fig. 1) in each of which the ratio of $SrTiO_3$ to $PbTiO_3$ was constant (7:3 in specimens of cross section A and 4:6 in specimens of section B), while the "$Bi_{2/3}TiO_3$" concentration increased in steps. Thus in effect we doped the "pure" ferroelectric $PbTiO_3$-$SrTiO_3$ with increasing quantities of "$Bi_{2/3}TiO_3$". In addition, we investi-

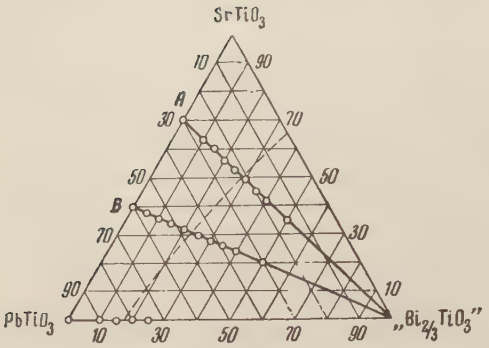

Fig.1. Investigated compositions and region of solid solutions in the $PbTiO_3$-$SrTiO_3$-"$Bi_{2/3}TiO_3$" system. The data on the boundary of solid solutions along the $SrTiO_3$-"$Bi_{2/3}TiO_3$" line are taken from the work of Skanavi et al[6].

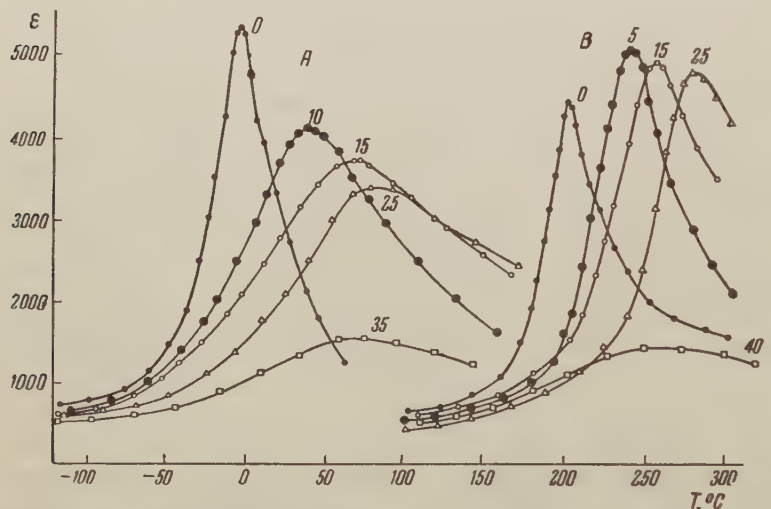

Fig.2. Temperature dependence of the dielectric constant ϵ for some compositions of sections A and B. The figures at the curves give the "$Bi_{2/3}TiO_3$" concentration in mole percent; f = = 0.5 Mc.

gated the structure of some compositions along the $PbTiO_3$-"$Bi_{2/3}TiO_3$" line.

On the basis of the x-ray diffraction data it may be asserted that in the given system there does exist a region of solid solutions (outlined in Fig.1). X-ray studies also showed that at room temperature the crystal lattice of A specimens with low "$Bi_{2/3}TiO_3$" concentration is pseudo cubic. The lattice constant a of the initi 0.7 $SrTiO_3$-0.3 $PbTiO_3$ composition is 3.906 kX. With increase of the "$Bi_{2/3}TiO_3$" concentration in section A specimens, some of the reflection spots (particularly 200 and 310) become wider and finally split into doublets, characteristic of a tetragonal lattice. Thus for the A section composition containing 15 mole percent "$Bi_{2/3}TiO_3$" a = = 3.908 and c = 3.927 kX.

The lattice of B compositions at room temperature is tetragonal. The constant a fluctuates about a mean value of 3.908 kX, while c consistently increases with increase of the "$Bi_{2/3}TiO_3$" concentration from 3.971 kX for the initial 0.4 $SrTiO_3$-0.6 $PbTiO_3$ composition to 3.98 kX for the composition containing 20 mole percent "$Bi_{2/3}TiO_3$".

With increase of the "$Bi_{2/3}TiO_3$" content, simultaneously with increase in the degree of tetragonality of the lattice, there is observed a shift of the phase transition to the side of higher temperatures (Fig.2); the phase transition in B compositions is associated with a sharp ϵ peak, characteristic of a "pure" ferroelectric, while for compositions of section A the ϵ peak is gradually smeared out. This presumably indicates that the phase transition extends over a wider temperature range.

Section B compositions in the region of solid solutions exhibit all the basic properties of ferroelectrics. Thus, for example, typical dielectric hysteresis loops are readily observed at room temperature. Although it is impossibl to obtain a saturation curve (up to breakdown fields), nevertheless the so-called normal curve, passing through the vertices of the family of hysteresis loops, has two distinctive inflection points, which, as is known, is characteristic of ferro electrics.

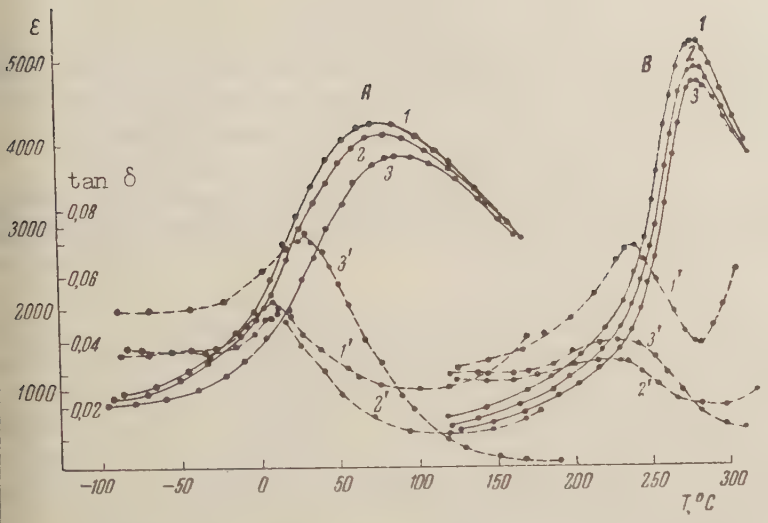

Fig.3. Temperature dependence of the dielectric constant and loss tangent at different frequencies for compositions of sections A and B containing 25 mole percent "$Bi_{2/3}TiO_3$": 1 & 1') 50 cps, 2 & 2') 1000 cps, 3 & 38) 0.5 Mc.

The dielectric properties of section A compositions are more complicated. Fig.3 shows typical ε and tan δ vs temperature curves recorded at different frequencies for section A and B compositions containing equal amounts of "$Bi_{2/3}TiO_3$". Clearly evident is the greater temperature extent of the phase transition in the section A composition as compared with the B composition and the presence of a relaxation shift of the ε and tan δ peaks in the curve for the section A specimen. Nevertheless, for section A specimens also one can readily observe a dielectric hysteresis loop which, incidentally, disappears only at temperatures some tens of degrees above the temperature of the ε peak, which is also evidence of the extended temperature range of the phase transition. As in the case of section B specimens, for section A specimens one cannot obtain saturation of the polarization curve (loop) by increasing the field strength (again breakdown occurs first). Here again both inflection points on the normal curve are clearly in evidence, so there can be no doubt regarding the existence of ferroelectricity in section A solid solutions.

Conclusions

X-ray diffraction studies show that there exists a definite region of solid solutions in the $PbTiO_3$-$SrTiO_3$-"$Bi_{2/3}TiO_3$" system. The variation of the properties of these solid solutions as a function of composition is characterized by the following regularities.

1. With increase of the "$Bi_{2/3}TiO_3$" content in specimens with a constant ratio of $PbTiO_3$ to $SrTiO_3$ the tetragonality of the crystal lattice increases and the phase transition is displaced to the side of higher temperatures.

2. In compositions in which $PbTiO_3$ predominates over $SrTiO_3$ the ferroelectric properties of the initial composition persists despite introduction and increase in the amount of "$Bi_{2/3}TiO_3$".

3. In system cross sections wherein the content of $SrTiO_3$ predominates over $PbTiO_3$ introduction of "$Bi_{2/3}TiO_3$", in addition to shift of the phase transition to the side of higher temperatures, leads to broadening of the temperature region of the phase transition and to the appearance of relaxation polarization.

The increase in the degree of tetragonality of the lattice as the result of introduction of "$Bi_{2/3}TiO_3$" can be explained by the high polarizability of the bismuth ion.

The observed relaxation effect can hardly be attributed to defects in the Pb, Sr or Bi sublattice due to formation of omission type solid solutions, inasmuch as, for example, the number of defects in compositions of sections A and B with the same "$Bi_{2/3}TiO_3$" content should be the same; yet whereas in section A specimens relaxation effects are clearly evident, in section B specimens they are virtually absent. In view of the fact that all the investigated compositions exhibit a typical ferroelectric hysteresis loop, it is more logical to associate the relaxation with the domain orientation mechanism operating under conditions of an extended phase transition region.

We desire to thank G.A.Smolenskii for suggesting the topic and guidance in the work and I.E.Myl'nikova for valuable advice on the problems involved in synthesizing the specimens.

Latvian State University &
Riga Polytechnic Institute

References

1. G.A.Smolenskii & K.I.Rozgachev, Zhur.tekh.fiz., 24, 1751 (1954).
2. G.A.Smolenskii, Ibid., 23, 3 (1952).
3. G.A.Smolenskii, Ibid., 20, 137 (1950).
4. S.Nomura & S.Sawada, J.Phys.Soc.Japan, 10, 108 (1955).
5. A.G.Bogdanov & R.A.Khomutetskaya, Izv.AN SSSR, Ser.fiz., 21, 433 (1957). (Trans.Bulletin, 21, 432.)
6. G.I.Skanavi, Ya.M.Ksendzov, V.A.Tregubenko & V.G.Prokhvatilov, Zhur.tekh. fiz., 33, 320 (1957). (Trans.Soviet Physics - Technical Physics.)

INVESTIGATION OF THE EFFECT OF ISOMORPHOUS REPLACEMENT OF Ti IONS ON PHASE TRANSITIONS IN $BaTiO_3$

- V.D.Komarov & E.G.Fesenko

In 1948 Vul & Goldman[1] investigated the dielectric properties of the nonferroelectric modification of $BaTiO_3$. At that time, its structure was considered to be rhombohedral. Burbank & Evans[2] prepared a single crystal of nonferroelectric $BaTiO_3$ and showed that its structure is hexagonal with $a = 5.735$ Å and $c = 14.05$ Å.

For a long time, the conditions of formation of the hexagonal modification remained unclarified. It was assumed that it is formed when the initial components are pure, while the ferroelectric modification results when technical grade materials are used.

In our Institute, the nonferroelectric modification has been obtained in the process of crystallization of $BaTiO_3$ from melts in Na_2CO_3 and K_2CO_3, using iron crucibles.[3] In addition to the nonferroelectric modification, there were also always formed in the same crucible ferroelectric crystals with the peak value of ϵ shifted to the side of lower temperature. These results can be explained by assuming that the Fe ions from the crucible material in the process of crystallization enter into the crystal and stabilize the hexagonal modification.

Investigations of the $BaTiO_3$-$BaFeO_3$ system confirmed[4,5] this assumption. In this system, in contrast to all previously investigated perovskite solid solutions, the hexagonal modification appears even at a low concentration of $BaFeO_3$ (about 2%). In this case, the hexagonal to perovskite transition temperature is lower than that given by the BaO-TiO_2 phase diagram (1460°). In subsequent experiments the iron was introduced in the form of Fe_2O_3; essentially the same results were obtained.

The characteristic structural feature of the hexagonal modification is the Ti_2O_9 group, which consists of two oxygen octahedra with a common face, surrounding the titanium ions. In this structure the Ti ions are closer than in the case of neighboring perovskite octahedra. According to crystal chemistry, this indicates a less stable structure. Replacement of the tetravalent Ti ion by a trivalent Fe ion probably increases the stability of the hexagonal modification, for in this case, the electric forces between the Ba cations can be weaker.

The above described effects of replacement of Ti by Fe ions stimulated our interest in other elements of the iron group (Co and Ni) and, subsequently, other trivalent ions.

In order to investigate the influence of these elements, appropriately doped polycrystalline samples were prepared and subjected to x-ray diffraction analysis and dielectric measurements.

Sample Preparation. The samples were prepared by thoroughly mixing (for 4 hours) oxides of the introduced elements with powdered $BaTiO_3$, which was synthesized beforehand at 1280°. The samples were sintered, first at 1430°, then ground and sintered again at 1380°. The inter-sintering grinding served to insure uniform distribution of the oxide and to prevent recrystallization.

Effect of Co^{2+} and Ni^{2+}. The examination of these samples revealed that when the Ni^{2+} content exceeds 2 mole percent (and the Co^{2+} content - 8 mole percent) the hexagonal modification is stabilized after sintering at 1380°. The data obtained on the influence of Co and Ni are in qualitative agreement with the data for the $BaTiO_3$-$BaFeO_3$ system. With increase of the Co (or Ni) content the Curie point at first is lowered and, accordingly, the c/a ratio and the peak value of ϵ decrease (this was also reported by Sakudo[6]). When the Co (or Ni) content is increased further, the ferroelectric properties vanish owing to transition of the material to the hexagonal modification.

Effect of Cr and Mn. The effects observed when the Ti ions are replaced by Cr^{3+} and Mn^{4+} are almost the same as in the case of Co^{2+} or Ni^{2+}. The difference is that here the Curie point drop and the corresponding decrease of the c/a ratio are not observed. The stabilization of the hexagonal modification was observed when the Cr and Mn content exceeded 2 mole percent. It is noteworthy that the Cr and Mn ions produce essentially the same effect, although their valences and ionic radii are different (Cr^{3+}, Mn^{4+}; $R_{Cr^{3+}} = 0.64$, $R_{Mn^{4+}} = 0.52$).

Effect of Lanthanides. In order to investigate the influence of the ionic radii of elements isomorphically replacing the Ti ions, we used rare earths, since they are chemically similar while their ionic radii vary from 1.04 for La to 0.80 for Lu. The elements La, Ce, Pr, Nd, Sm, Gd, Tb, Er, Yb and Lu were introduced into $BaTiO_3$, replacing the titanium. From their x-ray diffraction patterns, we learned that the hexagonal modification is not formed (at sintering temperatures up to 1500°) in the samples containing the elements to the left of Gd, while in the samples containing Tb, Er, and Yb, the hexagonal modification is formed. In the ϵ vs T curves for samples containing La, Ne and Ce, we observed the appearance of diffuse ϵ maxima below the Curie temperature. X-ray diffraction patterns revealed that with increase of the rare earth concentration the tetragonality decreases ($c/a \rightarrow 1$). Inasmuch as the stable equilibrium position for ions with radii larger than unity is the position with coordination number 12 (in the cubo-octahedral of the perovskite cell), the La, Ce and Nd ions occupy not the octahedral but the cubo-octahedral vacancies, as in the cases of Ce ions in loparite and in $CeAlO_3$ and of the La ions in $LaCrO_3$ in $LaAlO_3$. This is probably the reason for the different effect of the La, Ce and Nd ions on $BaTiO_3$, as compared with that of the other ions considered above. At present we are investigating the nature of the diffuse ϵ-peaks.

Effect of Mo^{6+}, W^{6+}, Ne^{5+}, Sb^{5+} and V^{5+}. All the trivalent ions investigated stabilize the hexagonal modification when replacing the Ti. This can be explained by the fact that when these ions replace Ti in the Ti_2O_9 group, the stability of the hexagonal modification increases. When the Ti ions are replaced by ions of higher valence, the stability of the hexagonal modification (at least in some cases) must decrease, i.e., the transition from the perovskite to the hexagonal modification is hindered. For this reason, we investigated the influence of the Mo^{6+}, W^{6+}, Nb^{5+}, Sb^{5+} and V^{5+} ions (in quantities up to 10 mole percent). In all cases, the hexagonal modification was not observed despite the high sintering temperature (1500°) employed.

Altogether, we tested more than 20 elements of various radii and valences. It was established that when the titanium in $BaTiO_3$ is replaced by ions whose valence is less than four, the transition temperature from the perovskite to the hexagonal modification goes down and the stability of the hexagonal modification increases. If, on the other hand, the Ti is replaced by ions of valence higher than four, the hexagonal modification is not formed.

We desire to thank S.N.Belyaev and O.S.Prokopalo for valuable discussions.

Physical-Mathematical Scientific Research Institute at
Rostov-on-the-Don State University

References

1. B.M.Vul & I.M.Gol'dman, Doklady AN SSSR, 60, 41 (1948).
2. R.D.Burbank & H.T.Evans, Acta Cryst., 1, 330 (1948).
3. I.N.Belyaev, N.C.Novosil'tsev, A.L.Khodakov & E.G.Fesenko, Doklady AN SSSR, 78, No.5, 875 (1951).

4. E.G.Fesenko & O.I.Prokopalo, Krystallografiya (Crystallography), 1, No.6, 703 (1956).
5. O.I.Prokopalo & E.G.Fesenko, Izv.AN SSSR, Ser.fiz., 22, 1488 (1958). (Trans.Bulletin 22, 1483.)
6. T.Sakudo, J.Phys.Soc.Japan, 12, 1050 (1957).

* * * * * * *

SOME RESULTS OF AN INVESTIGATION OF THE $PbO-Nb_2O_5-Nd_2O_3$ SYSTEM

- E.G.Smazhevskaya & N.A.Podol'ner

One of the most promising ferroelectric materials for preparation of piezoceramic components capable of operating at elevated temperatures is lead metaniobate (Curie point - 570°C). The properties of lead metaniobate have been investigated by a number of authors.[1-9]

However, the metastability of the ferroelectric phase of $PbNb_2O_6$ at temperatures below 1250° and its appreciable "ferroelectric rigidity" preclude use of this material for electromechanical transducers.

With a view to exploring the possibilities of stabilizing the ferroelectric phase and reducing the "ferroelastance" of $PbNb_2O_6$ without substiantially lowering the Curie point, we investigated a number of systems consisting of lead metaniobate and different metal oxides: Al_2O_3, ZrO_2, TiO_2, La_2O_3, Sm_2O_3, WO_3, Ge_2O_3, Er_2O_3, Y_2O_3, Dy_2O_3 and Nd_2O_3. The oxide concentrations in each system were 0.5 and 1 mole percent.

In view of the fact that a noticeable piezoelectric effect was detected in specimens containing neodymium trioxide, we decided to investigate this system in more detail.

In order to determine the optimum neodymium trioxide concentration in $PbNb_2O_6$ there were prepared and tested specimens containing 0.5, 1, 3, 4, 5, 7 and 10 mole percent Nd_2O_3. For preparing the specimens appropriate amounts of PbO, Nb_2O_5 and Nd_2O_3 were thoroughly mixed, briquetted and roasted at temperatures to 1000°. The synthesized material was ground and the resultant powder compressed into disks 14-15 mm in diameter and 2-3 mm thick. The disk specimens were sintered under different conditions, the final temperature usually being of the order of 1250°. After sintering the specimens were metallized and then polarized under appropriate conditions.

Tests showed that specimens containing 0.5, 1 and 3 mole percent Nd_2O_3 in $PbNb_2O_6$ have an insignificant piezoelectric effect, while those containing 7 and 10 mole percent exhibit no piezoelectric effect at all; the highest values of the piezoelectric constant d_{31} were obtained for specimens containing 4 and 5 mole percent Nd_2O_3. The properties of polarized specimens of 4% Nd_2O_3 + 96% $PbNb_2O_6$ are characterized by the following figures:

$d_{31}\cdot10^6$, cgse units	ϵ	tan δ	ρ_v, ohm·cm	K_r
0.6	480	1.1	$1.8\cdot10^{12}$	0.12

In investigating the temperature dependences of the dielectric constant ϵ, the piezoelectric constant d_{31} and the dielectric loss tangent tan δ (Figs.1 & 2) for the 4% Nd_2O_3 + 96% $PbNb_2O_6$ specimens it was found that these parameters are susceptible of measurement only up to a temperature of 200-250°. With further increase of the temperature there was observed an avalanche-like increase of the dielectric loss and a sharp increase of the conductivity; the volume resistivity in the 200-300° temperature interval decreased by 3-5 orders of magnitude.

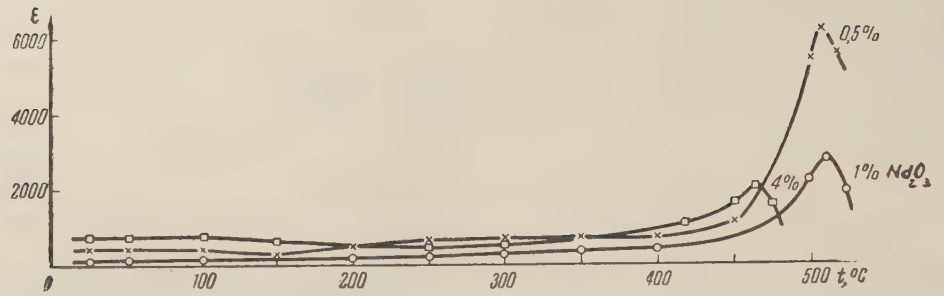

Fig.1. Temperature dependence of the dielectric constant ε for lead metaniobate compositions with different amounts of Nd_2O_3 (mole percent). The measurements were carried out on unpolarized specimens.

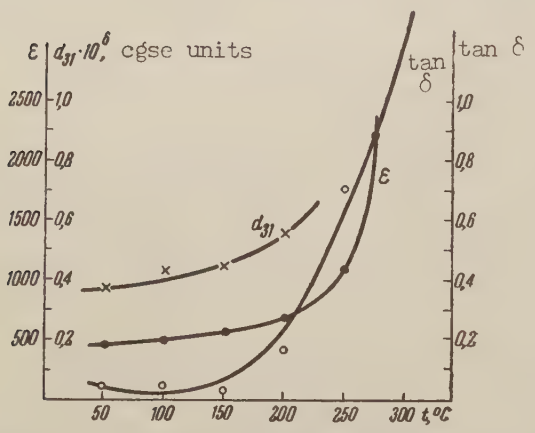

Fig.2. Temperature dependences of d_{31}, tan δ and ε for 4% Nd_2O_3 + 96% $PbNb_2O_6$. The measurements were carried out on polarized specimens.

It is reported in the literature[10-12] that the conductivity of barium titanate and lead metaniobate has been successfully reduced by doping these materials with lanthanum (La^{3+}) and lithium (Li^+) and also by sintering the specimens in oxygen. In view of the fact that some lanthanum was present as an impurity in our Nd_2O_3, we carried out experiments on introduction of Li^+ into the $PbO-Nb_2O_5-Nd_2O_3$ system and sintering in oxygen. Judging from the preliminary results, doping with lithium and sintering in oxygen do slow down the increase in conductivity at temperatures above 200°; ρ_v in the 200-250° temperature range decreases only one or two orders of magnitude.

Preliminary x-ray diffraction studies of $PbO-Nb_2O_5$ and $PbO-Nb_2O_5-Nd_2O_3$, carried out at our request by E.M.Mikhailova, showed the following.

1. In a number of cases there were obtained multiphase specimens, the main phase of which was the compound $3PbO\cdot 2Nb_2O_5$, although the batch was formulaed for obtaining $PbO\cdot Nb_2O_5$. The compound $3PbO\cdot 2Nb_2O_5$ has a face-centered cubic lattice. In addition to $3PbO\cdot 2Nb_2O_5$, there were present in the multiphase specimens the non-ferroelectric rhombohedral phase $PbO\cdot Nb_2O_5$, and free oxide, Nb_2O_5.

2. Upon introduction of neodymium trioxide into lead metaniobate, i.e., in synthesis of the system $PbO-Nb_2O_5-Nd_2O_3$, there apparently forms a limited solid solution with a face-centered cubic lattice. The presence of Nd_2O_3 in the system improves the phase composition in that it reduces the amount of nonferroelectric phase.

3. In some cases after sintering of the specimens the structure changed: the face-centered cubic lattice transformed to a rhombic one, i.e., the compound $3PbO\cdot 2Nb_2O_5$ was converted to $2PbO\cdot Nb_2O_5$.

Accordingly, it was hypothesized that in the $PbO-Nb_2O_5-Nd_2O_3$ system, in addition to lead metaniobate, there may form compounds of the $PbO\cdot Nd_2O_3$ and $Nd_2O_3\cdot Nb_2O_5$ type. To check this, mixtures of $PbO + Nd_2O_3$ and $Nd_2O_3 + Nb_2O_5$ were subjected to thermographic analysis. (The thermographic analyses were carried out at our request by I.A.Gai at the State Electric Ceramic Research Institute.)

In the case of $Nd_2O_3 + Nb_2O_5$ there were not detected any thermal effects in the differential temperature curve or volume effects in the shrinkage curve indi-

cating the formation of a compound. In the case of PbO + Nd_2O_3 the character of the shrinkage curve indicates that a chemical compound forms in the temperature range from 715 to 800° (Fig.3). On the basis of the thermographic data, we synthesized the compound PbO·Nd_2O_3 at a temperature of about 1000°. The resultant powder (specific gravity ~7.6 g/cm^3) had the following chemical composition:

Components	Theoretical composition,%	Actual composition, %
PbO	40.0	37.6
Nd_2O_3	60.0	61.9

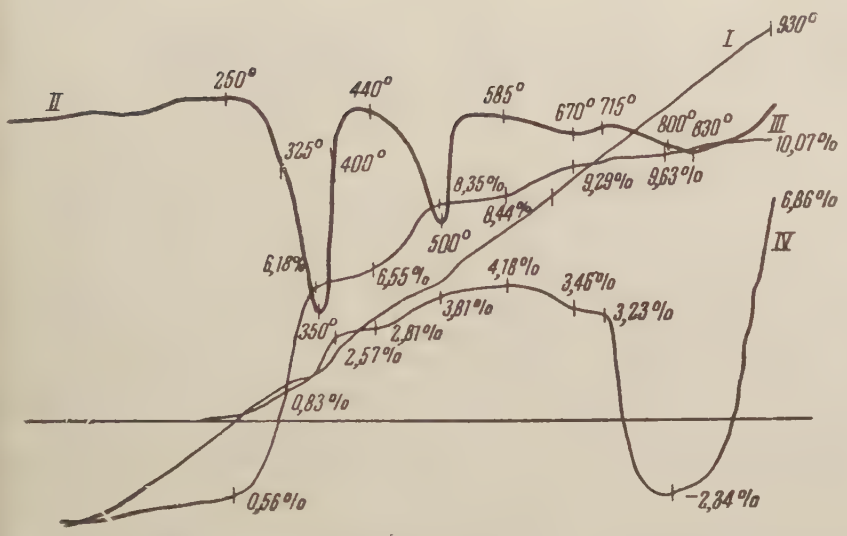

Fig.3. Thermogram for PbO + Nd_2O_3: I - temperature of standard specimen, II - differential temperature, III - variation in the weight of the specimen, IV - variation in the dimensions of the specimen.

The powder was grey-lilac in color; it dissolved readily in water, alcohol, acetone, benzene, metaxylene, carbon tetrachloride and silicone liquid No.5.

Polycrystalline specimens of PbO·Nd_2O_3 were prepared by sintering at 1050°; we tested the specimens after poling in a 7 kv/mm field, but failed to detect any noticeable piezoelectric effect, and could not measure the dielectric constant.

Conclusions

1. We prepared and investigated specimens of the PbO-Nb_2O_5-Nd_2O_3 system containing from 0.5 to 10 mole percent Nd_2O_3.

It was established that polycrystalline specimens containing 4-5 mole percent Nd_2O_3 have a piezoelectric constant $d_{31} \approx 0.6 \cdot 10^{-6}$ cgse units, a dielectric constant of the order of 500 and a Curie point above 450°.

2. There apparently forms in the PbO-Nb_2O_5-Nd_2O_3 system a limited solid solution with a face-centered cubic lattice, characteristic of the compound 3PbO·2Nb_2O_5.

3. We synthesized the compound PbO·Nd_2O_3, which as regards its properties is similar to the corresponding compound of cerium.

References

1. G.A.Smolenskii, Izv.AN SSSR, Ser.fiz., 21, 233 (1957). (Trans.Bulletin, 21, 235.)

2. V.A.Isupov & V.I.Kosyakov, Zhur.tekh.fiz., 28, 10, 2175 (1958). (Trans. Soviet Physics - Technical Physics.)

3. G.A.Smolenskii, V.A.Isupov & A.I.Agranovskaya, Fiz.tv.tela, 1, 442 (1959). (Trans.Soviet Physics - Solid State.)

4. G.A.Smolenskii, V.A.Isupov & A.I.Agranovskaya, Ibid., 1, 10 (1959). (Trans. Ibid.)

5. R.S.Roth, Acta Cryst., 10, N 6, 437 (1957).

6. R.S.Roth, J.Research Natl.Bur.Standards, 62, 27 (1959).
7. M.H.Francombe & B.Lewis, J.Acta Cryst., 11, 696 (1958).
8. G.Goodman, J.Am.Ceram.Soc., 36, No.11, 368 (1953).
9. K.E.Nelson & R.L.Cook Ibid., 42, No.3, 138 (1959).
10. V.M.Gurevich & I.S.Rez, Voprosy radioelektroniki (Questions of radioelectronics) Series III, No.4 (1960).
11. H.Sauer & S.Flashen, in "Symposium on Radio Components", Washington, 1956.
12. G.Harman, Phys.Rev., 106, 1358 (1957).

* * * * * * *

CONCERNING THE INFLUENCE OF LOW CONCENTRATIONS OF VARIOUS ELEMENTS ON THE PROPERTIES OF $(Pb_{0.57}, Ba_{0.43})Nb_2O_6$ SOLID SOLUTIONS

- E.G.Smazhevskaya & V.I.Rivkin

As a result of research on the preparation and properties of polycrystalline lead and barium metaniobate solid solutions it was established that, all other technological factors being the same, the piezoelectric characteristics of the solid solution specimens vary appreciably depending on the quality of the technical grade niobium pentoxide employed in their preparation. Thus, for example, for $(Pb_{0.6}Ba_{0.4})Nb_2O_6$ the values of the dielectric constant ϵ fluctuated from 700 to 2000, and the values of the piezoelectric coefficient d_{31} from 0.5 to $3.0 \cdot 10^{-6}$ cgse units. Chemical analyses of 11 different lots of technical niobium pentoxide showed that the impurity concentrations varied in the following ranges (element equivalent by weight): Ti^{4+} from 0.06 to 0.6%, Si^{4+} from 0.06 to 0.12%, Fe^{3+} from 0.08 to 0.4%, F^- from 0.1 to 0.25%, Ta^{5+} from 0.15 to 0.9%, Na^+ from 0.03 to 0.3% and K^+ from 0.13 to 1.8%.

In view of the above, it was hypothesized that the properties of $(Pb,Ba)Nb_2O_6$ piezoelectric ceramics may depend to a great extent on the concentrations of different elements contained in technical Nb_2O_5. The purpose of the present work was to investigate the influence of each of these elements separately on the piezoelectric properties of $(Pb,Ba)Nb_2O_6$ solid solutions.

For purposes of the investigation we chose the $(Pb_{0.57},Ba_{0.43})Nb_2O_6$ solid solution which is characterized by optimum piezoelectric properties and has a Curie temperature of ~250°. For preparation of the specimens we used reagent grade $BaCO_3$ and PbO and chemically pure Nb_2O_5 (total impurities $\leqslant$ 0.4%). The various elements encountered in technical grade niobium pentoxide were introduced into the chemically pure Nb_2O_5 in the form of oxides or salts in the concentrations indicated in the accompanying table (the percentages are referred to Nb_2O_5).

The maximum concentrations of the introduced elements did not in general exceed the amount of the element present in technical grade Nb_2O_5. After mixing and briquetting, all the compositions were synthesized simultaneously by heating for one hour at 1000°. Then lots of compressed specimens including representatives of all compositions (including a control composition free of introduced impurities) were sintered at different final temperatures ranging from 1260 to 1320°. After grinding to the same thickness (1.5 mm) and applying electrodes, the specimens were poled under the following conditions: field strength 1.3 kv/mm, heating for 2 hours to 180° and holding for 1 hour at this temperature, cooling for 1.5 hours with gradual increase of the field to 2.5 kv/mm. Three days after polarization we measured the principal dielectric and piezoelectric characteristics, namely, ϵ, tan δ, d_{31} and k_r.

Variation of the properties of $(Pb_{0.57},Ba_{0.43})Nb_2O_6$ solid solution with the concentration of different elements artificially introduced into the chemically pure niobium pentoxide
(The listed values are averages for three specimens)

Comp. no.	Introduced element	Impurity conc., % wt.	ε at 800 cps and 20±5°C	tan δ, 800 cps and 20±5°C	$d_{31} \cdot 10^6$, cgse units at 20±5°C	k_r	Sintering temp., °C
1	Control experiments		1170	0,60	1,9	0,28	
2	Ti^{4+} (in TiO_2)	0,05	1140	0,50	1,74	0,24	
3		0,1	1140	0,45	1,74	0,25	
4		0,5	1350	0,40	1,87	0,26	
5		1,0	1450	0,38	1,40	0,20	
6	Ta^{5+} (in Ta_2O_5)	0,05	1100	0,42	1,71	0,25	
7		0,1	1070	0,46	0,61	0,25	
8		0,5	970	0,61	1,47	0,23	
9		1,0	1000	0,46	1,51	0,24	1320
10	Na^{+} (в Na_2CO_3)	0,01	1240	0,60	2,20	0,32	
11		0,05	1250	0,63	2,29	0,32	
12		0,1	1230	0,73	2,10	0,30	
13		0,5	1250	1,07	1,60	0,24	
14	K^{+} (in K_2CO_3)	0,05	1250	0,73	2,16	0,30	
15		0,1	1350	0,95	2,35	0,32	
16		0,5	1280	1,19	1,86	0,27	
17		1,0	750	1,40	1,20	0,21	
18	Control experiments		1040	0,70	1,38	0,25	
19	Fe^{3+} (in Fe_2O_3)	0,05	1000	0,45	1,33	0,24	
20		0,1	1100	0,45	1,51	0,26	
21		0,3	1180	0,50	1,72	0,28	
22		0,5	1280	0,50	1,46	0,23	
23	Si^{4+} (in SiO_2)	0,01	930	0,50	1,27	0,23	
24		0,05	790	0,60	1,11	0,21	1300
25		0,1	880	0,60	1,26	0,24	
26		0,2	730	0,70	1,13	0,22	
27	F^{-} (in BaF_2)	0,05	1100	0,70	1,40	0,24	
28		0,1	1100	0,50	1,43	0,25	
29		0,5	1070	0,52	1,42	0,24	

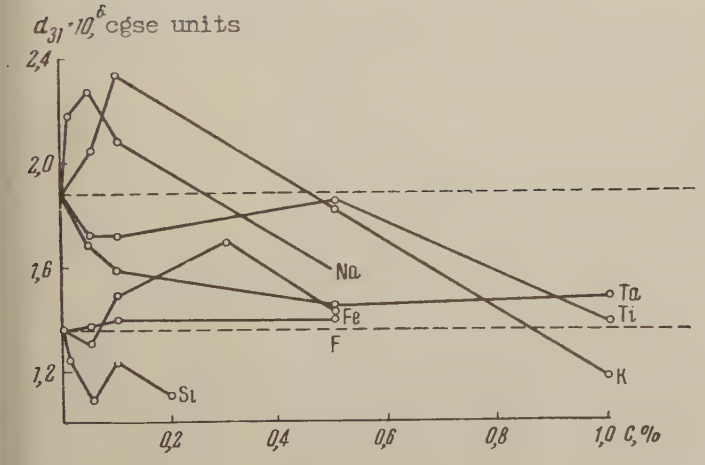

Fig.1. Variation of the piezoelectric coefficient d_{31} of $(Pb_{0.57},Ba_{0.43})Nb_2O_6$ piezoceramic specimens as a function of the concentration of artificially introduced elements. The upper group of curves pertain to specimens sintered at 1320°; the lower group to specimens sintered at 1300°.

It was found that the values of ϵ, d_{31} and k_r of specimens of the same composition depended to some extent on the final sintering temperature. There was, however, observed a consistent characteristic variation of the dielectric and piezoelectric parameters as a function of the concentra-

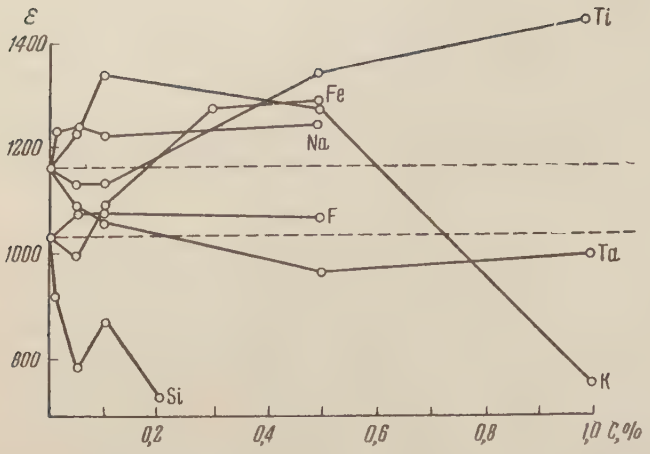

Fig.2. Variation of the dielectric constant ε of $(Pb_{0.57},Ba_{0.43})Nb_2O_6$ piezoceramic specimens as a function of the concentration of artificially introduced elements. The upper group of curves pertain to specimens sintered at 1320°; the lower group to specimens sintered at 1300°.

tion of the impurity elements; except for some increase with increasing Na^+ and K^+ concentration, tan δ virtually did not change (see table and Figs.1 & 2).

On the basis of our experimental results we arrived at the following conclusions. The piezoelectric properties of polycrystalline $(Pb_{0.57}, Ba_{0.43})Nb_2O_6$ solid solution depend to a great extent on the presence and concentration of certain elements that are naturally present in technical grade niobium pentoxide.

Si^{4+} and Ta^{5+} within the range of investigated concentrations significantly reduce ε, d_{31} and k_r. Introduction of Ti^{4+} and Fe^{3+} leads to increase of ε. Up to a Ti^{4+} concentration of 0.5% the piezoelectric coefficient d_{31} remains virtually constant, but then with further increase of the Ti^{4+} concentration it falls off rapidly. With increase of the Fe^{3+} concentration to 0.3% d_{31} increases on the average by 20%. Introduction of F^- in concentrations up to 0.5% has virtually no effect on ε, d_{31} and k_r.

The presence of Na^+ and K^+ ions in Nb_2O_5 in amounts exceeding 0.5% is highly undesirable inasmuch as this results in a sharp decrease of d_{31} and k_r, and to significant increase of tan δ. On the other hand, the introduction of minor (up to 0.1%) amounts of Na^+ and K^+ is beneficial in that it increases d_{31} (on the average by 25%) and k_r (on the average by 15%).

It is impossible to assure reproducibility of the piezoelectric properties of specimens in preparing these of different lots of technical grade Nb_2O_5, even when these differ almost insignificantly as regards chemical composition.

It must be noted that if one used spectroscopically pure niobium pentoxide or if one simultaneously introduced several elements in different combinations and proportions, the above described impurity dependences of the dielectric and piezoelectric properties of $(Pb,Ba)Nb_2O_6$ ceramic might prove to be significantly different; hence it is highly desirable to undertake further comprehensive studies utilizing x-ray diffraction, spectrographic and other research techniques.

SOME ANOMALOUS PROPERTIES OF CHEMICALLY PURE BARIUM TITANATE CERAMIC

- A.A.Anan'eva, M.A.Ugryumova & B.V.Strizhkov

The present work was devoted to investigation of the properties of very pure barium titanate ceramic. Since impurities commonly present in technical grade barium titanate may influence its physical and electrical properties, it is of interest to study the properties of pure barium titanate ceramic. Employing the procedure developed by Clabaugh et al[1] for synthesizing barium titanate powder, we prepared barium titanate ceramic of high purity, studied its properties and then compared them with the properties of commercial ceramic.

The initial materials were titanium tetrachloride, chemically pure barium chloride and chemically pure oxalic acid. The reaction resulting in the formation of barium titanyl oxalate tetrahydrate is described by

$$BaCl_2 \cdot 2H_2O + TiCl_4 + 2H_2C_2O_4 \cdot 2H_2O \rightarrow BaTiO(C_2O_4)_2 \cdot 4H_2O + 6HCl + H_2O.$$

Upon heating, the barium titanyl oxalate is decomposed and barium titanate is formed:

$$BaTiO(C_2O_4)_2 \cdot 4H_2O \rightarrow BaTiO_3 + 2CO_2 + 4H_2O.$$

Thermograms of the process indicated that the decomposition goes to completion and barium titanate forms at a temperature of 790°C.

This process yields highly pure barium titanate. Spectroscopic analysis showed that the barium titanate powder obtained is free of impurities.

It is known that four different titanates may form in the $BaO-TiO_2$ system and that only barium metatitanate in the tetragonal modification has ferroelectric properties. Chemical analysis of the barium titanate powder showed that the molar ratio of barium oxide to titanium dioxide is unity, which corresponds to the composition of barium metatitanate. X-ray diffraction patterns indicated that the above-described synthesis procedure yields only chemically pure barium metatitanate with tetragonal structure at room temperature.

We investigated the variation of the dielectric constant ϵ of pure barium titanate with the sintering temperature of the ceramic. Specimens prepared from barium titanate powder, obtained by the procedure described above, were sintered at various temperatures from 900° to 1450°. Above 1450° barium metatitanate transforms to the nonferroelectric hexagonal modification[2,3]; in view of this 1450° was the highest sintering temperature used. The holding time at heat was the same in all cases: 30 min. The dielectric constants were measured at room temperature on a VM-2 bridge.

As will be evident from Fig.1, in the range of sintering temperatures from 1170° to 1290°, ϵ of the chemically pure ceramic attains anomalously high values with a maximum of 6000 at 1240°. At sintering temperatures above 1300° a stable value of 2300 is obtained. Fig.1 also shows the sintering temperature dependence of ϵ for specimens of ordinary technical barium titanate ceramic. It will be seen that no anomalous increase of ϵ is observed for technical ceramic in the interval from 1170° to 1290°, and that the usual stable value of ϵ = = 1200 is substantially lower than the corresponding value for chemically pure ceramic (2300) for sintering temperatures above 1300°.

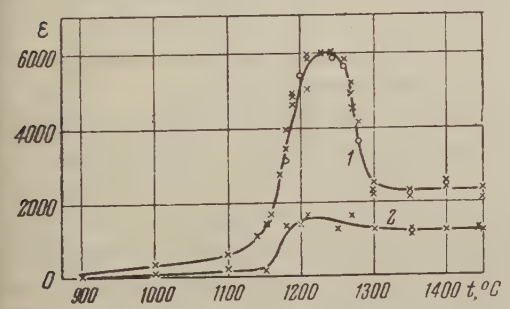

Fig.1. Variation of the dielectric constant ϵ with sintering temperature for specimens of barium titanate ceramic: 1) chemically pure, and 2) technical grade.

We also investigated the influence of the holding time at different sintering temperatures on the dielectric constant of the pure ceramic.

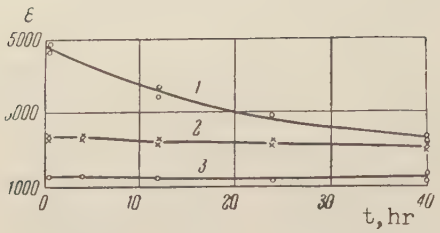

Fig.2. Variation of the dielectric constant with duration of sintering: 1) chemically pure $BaTiO_3$ sintered at 1270°, 2) chemically pure $BaTiO_3$ sintered at 1350°, 3) technical $BaTiO_3$ sintered at 1350°.

It is interesting to note that for temperatures from 1170° to 1290° the values of ε of chemically pure ceramic vary with the sintering time. Thus, for example, as shown in Fig.2, with increase of the holding time at 1270° the value of ε at room temperature decreases; for a duration of 40 hours it drops almost to the value of ε for specimens sintered at 1300° to 1450°. On the other hand, with increase of the sintering time at 1350° there occurs only an insignificant decrease of ε (approximately by a factor of 1.1). The dielectric constant of ordinary ceramic does not vary with the sintering time at 1350° (curve 3 in Fig.2).

The specimens sintered at temperatures of 1240°, 1270° and 1350° had tetragonal structure at room temperature. However, the degree of tetragonality in these specimens has not yet been determined. Probably it varies with the sintering temperature, which may partially explain the observed dependence of ε on sintering temperature.

In investigating the effect of sintering temperature on the properties of chemically pure barium titanate specimens, we also determined, by the usual procedures, their apparent density, surface porosity, and water absorption. The apparent density was determined not only in distilled water, but also in carbon tetrachloride. The variation of these quantities is shown in Fig.3. Pronounced variations in density, porosity and water absorption are observed for sintering temperatures up to 1240°. At a sintering temperature of 1240° the density reaches its maximum value of 5.94 g/cm^3 and remains at this level with further increase of the sintering temperature. The surface porosity and water absorption drop close to zero at the same sintering temperature. In the case of porous specimens the two different methods of measuring density result in values that differ by about 10%. This is explained by the different penetrating abilities of H_2O and CCl_4. Complete agreement of the density determinations is obtained for specimens with maximum density.

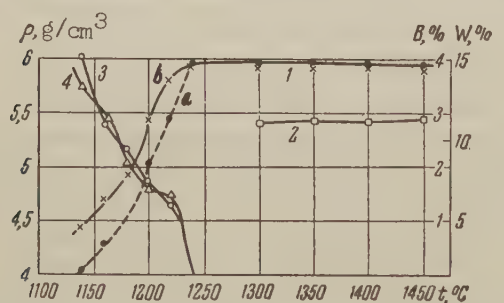

Fig.3. Variation of specimen density ρ, porosity B and water absorbing capacity W with sintering temperature: 1) ρ of chemically pure ceramic measured in distilled water (a) and in carbon tetrachloride (b); 2) ρ of technical ceramic; 3) B of chemically pure ceramic; 4) W of chemically pure ceramic.

The maximum value of the density of chemically pure barium titanate (5.94 g/cm^3) is close to the x-ray density of 6.017 g/cm^3 (Refs.4 & 5), differing from the latter by only 1.5%. The maximum density of ordinary technical grade ceramic, 5.4 g/cm^3, differs from the x-ray density by 10% and is considerably lower than the maximum density of chemically pure ceramic.

The sintering temperature of the specimens affects the character of the ceramic structure. The variation of grain size with the sintering temperature can be seen in Fig.4. The structure with the finest grain is obtained at a sintering temperature of 1240°. With increase in temperature from 1240° to 1300° the grain size increases appreciably. Further increases of the sintering temperature does not result in any noticeable change in grain size.

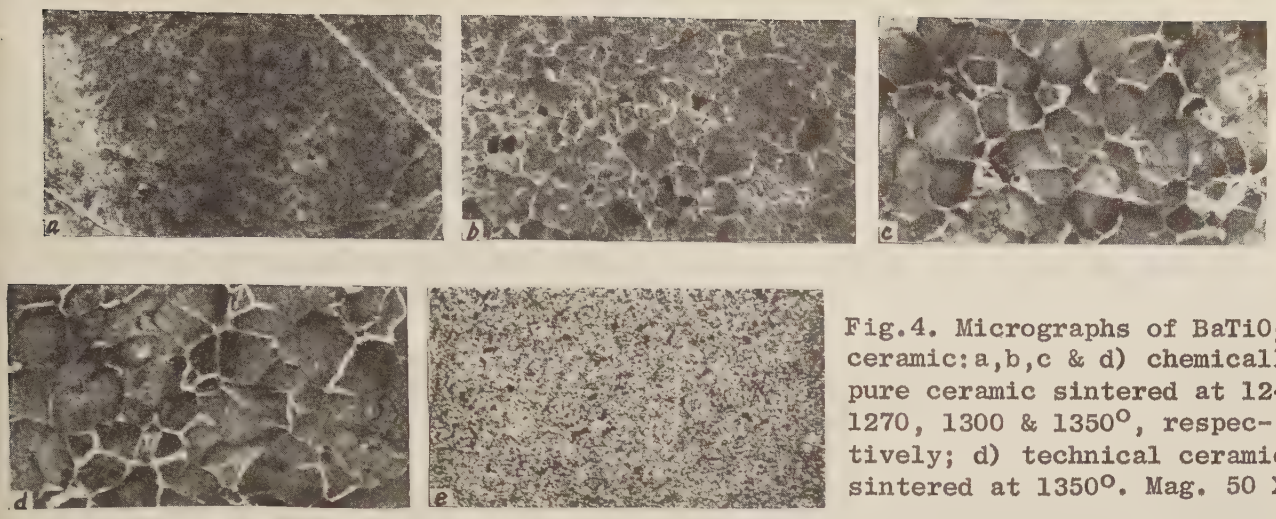

Fig.4. Micrographs of $BaTiO_3$ ceramic: a,b,c & d) chemically pure ceramic sintered at 1240, 1270, 1300 & 1350°, respectively; d) technical ceramic sintered at 1350°. Mag. 50 X.

As pointed out, the value of ϵ at room temperature for polycrystalline chemically pure barium titanate changes considerably with increase of the sintering temperature. It is entirely possible that the grain size of the ceramic specimens affects the value of ϵ. Specimens of chemically pure barium titanate sintered at 1240° have the maximum value of ϵ (6000) and also exhibit the finest grain structure. With an increase of sintering temperature, the grain size increases while the value of ϵ decreases.

Fig.4 also includes a photograph of a microsection of technical grade barium titanate ceramic sintered at 1350°. The technical ceramic has a large number of pores, uniformly distributed among the comparatively fine grains. The large number of pores in technical ceramic, as compared to chemically pure ceramic, reduces the relative density of the material.

References

1. W.S.Clabaugh, E.M.Swiggard & R.Gildirist, J.Research Nat.Bur.Standards, 56, 289 (1955).
2. R.D.Burbank & U.T.Evans, Acta Cryst. 1, 330 (1948).
3. W.Trzebiatowski & M.Drys, Roczn.Chem. 28, 21 (1954).
4. D.Berlincourt & H.H.A.Krueger, Phys.Rev., 105, 56 (1957).
5. H.D.Megaw, Ferroelectricity in Crystals, London, 1957.

DIELECTRIC AND PIEZOELECTRIC PROPERTIES OF CHEMICALLY PURE BARIUM TITANATE CERAMIC

- A.A.Anan'eva, B.V.Strizhkov & M.A.Ugryumova

The electrical and physical properties of barium titanate depend to a large extent on heat treatment of the material, as Novosil'tsev and Khodakov[1] demonstrated for barium titanate single crystals and as we[2] showed for polycrystalline specimens of chemically pure barium titanate. As a result of preliminary heating, the crystal structure of barium titanate at room temperature changes in single crystals; it does not change in polycrystalline barium titanate, but the structure of ceramic specimens varies appreciably.

The present work was devoted to the study of the dielectric, elastic, and piezoelectric properties of chemically pure barium titanate ceramic.

Dielectric Properties

The temperature dependences of the dielectric constant ϵ and of the dielectric loss tangent tan δ were measured for specimens of chemically pure barium titanate ceramic* sintered at 1180°, 1240°, 1270° and 1400°C, as well as for specimens of technical grade ceramic fired at 1380°.

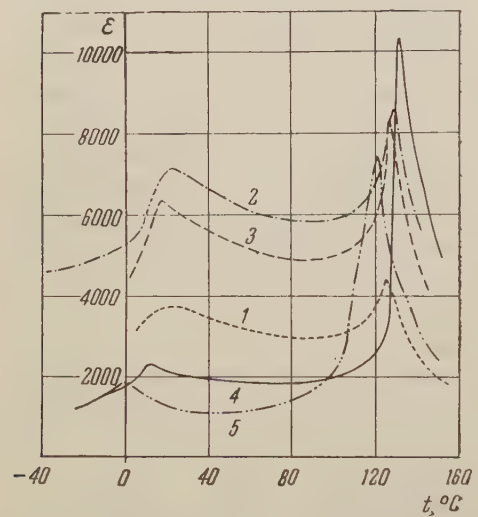

Fig.1. Temperature dependence of ϵ for specimens of barium titanate ceramic: 1,2,3 & 4) chemically pure ceramic sintered at 1180°, 1240°, 1270° and 1400°, respectively; 5) technical ceramic sintered at 1380°.

The temperature dependence of the dielectric constant of barium titanate ceramic is strongly affected by the sintering temperature, as will be evident from Fig.1. Only chemically pure barium titanate ceramic sintered at 1400° has a temperature dependence of ϵ similar to that of technical ceramic. In all other cases anomalous values of ϵ are evinced in the entire temperature range from 20° to 130°C with a minor increase at the Curie points.

Table 1 gives the values of the dielectric constants ϵ_k^1 and ϵ_k^2 at the first (high temperature) and second (low temperature) transition points, as well as the minimum values of the dielectric constant ϵ_o.

It is interesting to note that in comparison with technical ceramic both phase transitions in chemically pure ceramic are shifted to the side of higher temperatures. The shift of the high temperature transition (9°) is most noticeable for specimens sintered at 1400°, whereas the shift of the low-temperature transition is greatest for specimens sintered at temperatures between 1180° and 1270°.

The temperature dependence of tan δ for specimens sintered at 1180° to 1270°, differs substantially from the dependence for specimens sintered at 1400°. In the first case a decrease in tan δ with temperature is observed, while in the second case tan δ increases. The last is similar to the temperature dependence of tan δ for technical ceramic.

It will be evident from Table 2 that specimens sintered at temperatures from 1180° to 1270°, in addition to anomalously high values of ϵ, have rather high

---

*The procedure for preparing ceramic specimens of chemically pure barium titanate is described in Refs.2 and 3.

Table 1

Sintering temp., °C	ε_k^1	ε_k^2	ε_0	$\frac{\varepsilon_k^1}{\varepsilon_0}$	$\frac{\varepsilon_k^2}{\varepsilon_0}$	Temp. of 1st phase transition, °C	Temp. of 2nd phase transition, °C
1180	4500	3750	3100	1,45	1,21	126	25
1240	8600	7300	5900	1,45	1,23	130	23
1270	8300	6400	5000	1,66	1,28	127	20
1400	10300	2400	1750	5,95	1,37	132	12
Technical ceramic, 1380°	7400	1900	1200	6,16	1,58	123	0

Table 2

Sintering temp., °C	tan δ at 20°	tan δ at 80°
1180	0,059	0,03
1240	0,081	0,056
1270	0,055	0,033
1400	0,01	0,028
Technical ceramic, 1380°	0,02	0,08

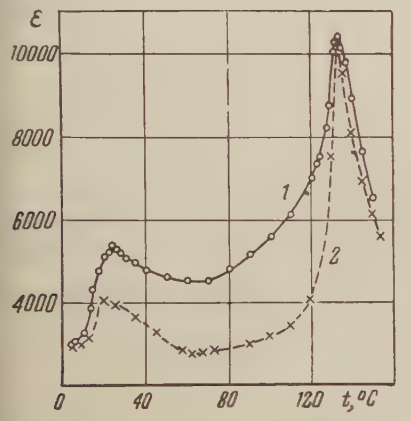

Fig.2. Temperature dependence of the dielectric constant for polarized (1) and unpolarized (2) specimens of coarse-grained chemically pure barium titanate ceramic.

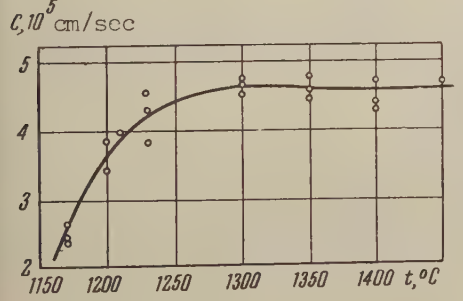

←Fig.3. Velocity of sound C in specimens of chemically pure barium titanate ceramic vs sintering temperature.

values of tan δ at room temperature. Presumbaly this can be explained to a degree by the fact that in these ceramics the second (low temperature) phase transition occurs at about room temperature. In contrast, specimens sintered at 1400° exhibit low values of tan δ in the range of room temperatures.

We also determined the temperature variations of ε and tan δ for a specimen roasted at 1270° for a period of 40 hours. The dependences are similar to those for specimens sintered at 1400° for 30 min.

It is interesting to note that a substantial increase of ε (by a factor of ≤1.6) occurs as a result of polarization of the specimens. The increase in ε is most noticeable in specimens which were sintered for a long period of time or were sintered briefly at high temperatures, i.e., for coarse-grained ceramic (Fig.2). For coarse-grained chemically pure ceramic there is also a large difference as regards the values of tan δ between polarized and unpolarized specimens.

Elastic and piezoelectric properties

The velocity of sound C in specimens of chemically pure barium titanate ceramic sintered at temperatures ranging from 1160° to 1450° was determined on the basis of the radial oscillations of poled discs.

As Fig.3 shows, chemically pure ceramic sintered at temperatures under 1250° has low values of C. Thus for specimens sintered at 1170°, the velocity of sound is 1.8 times lower than for specimens sintered at temperatures above 1300°. For chemically pure ceramic specimens sintered at temperatures ranging from 1300° to 1450°, the velocity of sound remains virtually constant at an average value of $4.6 \cdot 10^5$ cm/sec. Consequently, for specimens sintered at these temperatures for a period

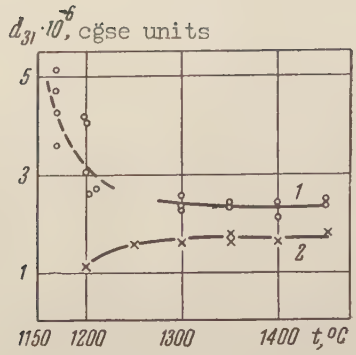

Fig.4. Piezoelectric coefficient d_{31} of chemically pure barium titanate ceramic vs sintering temperature.

of 30 minutes and having a density of 5.9 g/cm^3, Young's modulus is equal to $1.25 \cdot 10^{12}$ dynes/cm^2. According to published data[4], Young's modulus for technical ceramic is $1.05 \cdot 10^{12}$ dynes/cm^2 at a density of 5.3 g/cm^3.

Measurements of the piezoelectric coefficient d_{31} were carried out dynamically on thin discs vibrating in the radial mode. The value of d_{31} for specimens sintered for a period of 30 min at temperatures ranging from 1300 to 1450° remains practically constant at $2.4 \cdot 10^{-6}$ cgse units.

As may be seen in Fig.4, the value of d_{31} for ceramic made of chemically pure barium titanate is 1.5 times higher than the value for technical barium titanate ceramic. Chemically pure specimens sintered at temperatures below 1250° yielded very high values of d_{31}. Thus for example, for a specimen sintered at 1170° d_{31} attained a value of the order of $5 \cdot 10^{-6}$ cgse units. However, these high values of d_{31} should be not regarded as truly representative, particularly since the piezoelectric coefficient of specimens not kept under controlled temperature conditions decreases with time. This can be explained by the fact that such specimens may remain for an extended period at or near their transition temperature (room temperature), and hence undergo spontaneous polymorphous transformations accompanied by depolarization. It may be that specimens with a Curie point in the room temperature range can find practical applications only under conditions providing for continuous polarization.

References

1. N.S.Novosil'tsev & A.L.Khodakov, Doklady AN SSSR, 35, 1263 (1952).

2. A.A.Anan'eva, M.A.Ugryumova & B.V.Strizhkov, Present issue of the Bulletin, p.1395.

3. W.S.Clabaugh, E.M.Swiggard & R.Gildirist, J.Research Nat.Bur.Standards, 56, 289 (1955).

4. W.P.Mason, Piezoelectric Crystals and their Application to Ultrasonics, N.Y.1950. (Cited in Russian translation.)

EFFECT OF DOPING WITH CHROMIC OXIDE ON SOME DIELECTRIC AND PIEZOELECTRIC PROPERTIES OF BARIUM TITANATE

- L.N.Kamysheva

It follows from the work of Meisinger[1] that the presence of 1% chromic oxide in barium titanate increases the dielectric loss. On the other hand, it is known[2] that small amounts of chromic oxide reduce the loss tangent in $BaTiO_3$ and other materials used for the preparation of capacitor ceramics.

The present work was undertaken to determine the influence of Cr_2O_3 not only on the dielectric but also on the piezoelectric properties of barium titanate. We investigated polycrystalline specimens of $BaTiO_3$ prepared by the usual ceramic technology of reagent grade and chemically pure initial materials with 0.1 to 8 mole percent Cr_2O_3 deliberately added.

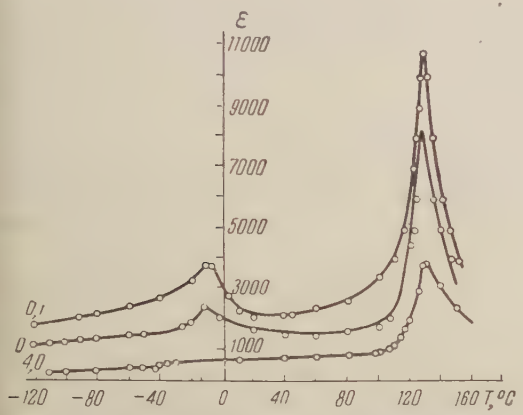

Fig.1. Temperature dependence of the dielectric constant of barium titanate doped with different amounts of Cr_2O_3 (indicated in mole percent at the curves), recorded in weak fields at a frequency of 1 kc.

The temperature dependences of the dielectric constants for some compositions are shown in Fig.1. It will be seen that only 0.1% Cr_2O_3 increases the dielectric constant at the ϵ peak to about 11 000. Higher concentrations of Cr_2O_3 reduce ϵ at the Curie point (Fig.2) as well as at all other temperatures.

As will be evident from Figs.3 & 4, low Cr_2O_3 concentrations (but not 0.1 mole percent!) reduce the loss tangent. Whereas for pure $BaTiO_3$ $\tan\delta \approx 1.7\cdot10^{-2}$, upon the introduction of 0.3-0.5% Cr_2O_3 $\tan\delta$ drops to $3\text{-}7\cdot10^{-3}$ and then beginning with 1% Cr_2O_3 increases appreciably.

We determined the temperature dependence of the piezoelectric coefficient d_{31} and also measured the coefficient d_{33} by the static procedure (Figs.5 & 6). As will be evident from the curves the piezoelectric coefficients d_{31} and d_{33} are slightly higher than the corresponding values for pure $BaTiO_3$ only in the case of 0.1% chromic oxide, i.e., only with the amount of doping resulting in some increase of ϵ at its peak and room temperatures.

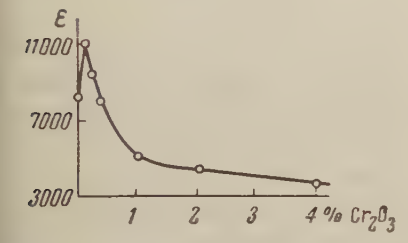

Fig.2. Variation of the dielectric constant of barium titanate at the Curie point with the introduced Cr_2O_3 concentration.

It must be noted that the introduction of chromic oxide into barium titanate impairs sintering of the ceramic, increases the porosity and causes the specimens to darken, probably, owing to reduction of the titanium or chromium in the process of roasting.

On the basis of the data for the loss tangent, the dielectric constant and the piezoelectric coefficients it may be inferred that only compositions with 0.3 to 0.5 mole percent Cr_2O_3 are of practical interest, inasmuch as their dielectric and piezoelectric properties are similar to those of pure $BaTiO_3$, while the loss is only about half that in pure $BaTiO_3$.

We calculated the values of the spontaneous polarization P_s from the hysteresis loops recorded at room temperature with a field amplitude of 17 kv/cm (Fig.7), and obtained the following values:

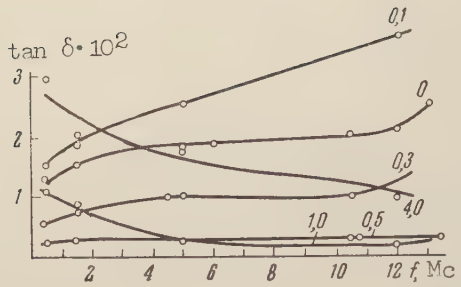

Fig.3

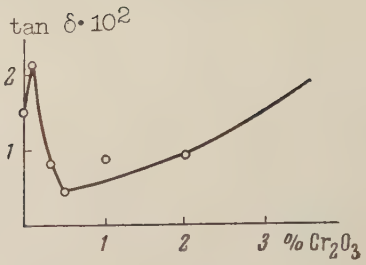

Fig.4

Fig.3. Frequency dependence of tan δ for barium titanate doped with different amounts (indicated in mole percent at the curves) of Cr_2O_3 in weak fields.
Fig.4. Variation of tan δ of barium titanate with the introduced Cr_2O_3 concentration; f = 1.5 Mc, T = 20°.

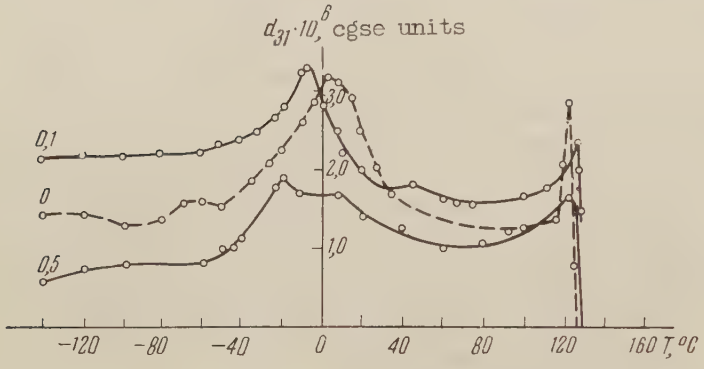

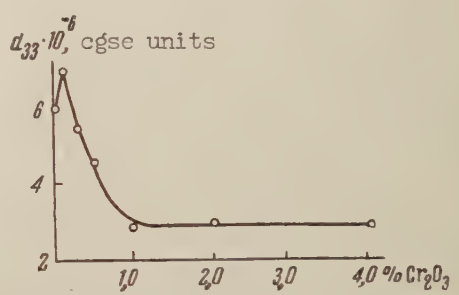

Fig.6. Variation of d_{33} at 20° with the Cr_2O_3 concentration.

Fig.5. Temperature dependence of the piezoelectric coefficient d_{31} of barium titanate doped with different amounts (indicated in mole percent by the figures at the curves) of Cr_2O_3

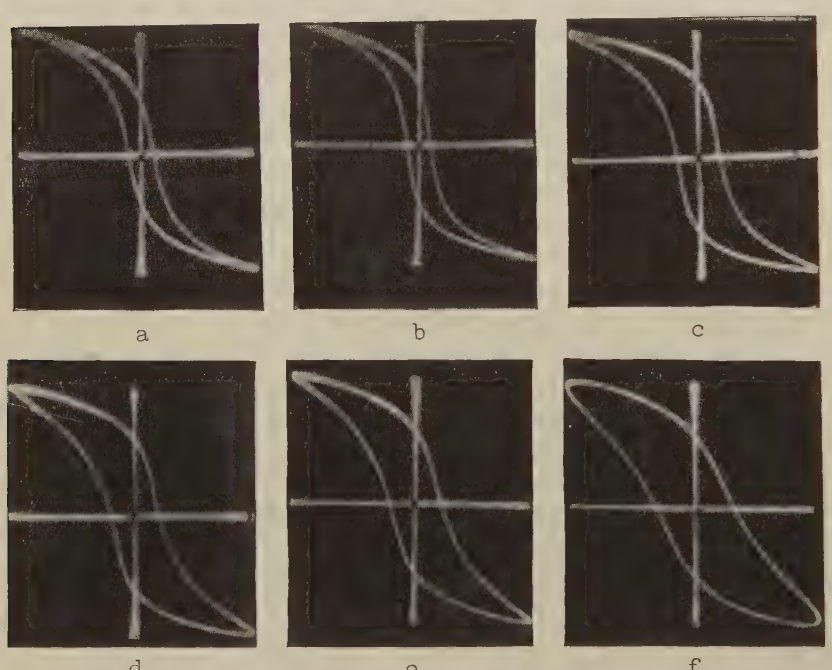

←Fig.7. Hysteresis loops recorded at room temperature for barium titanate specimens doped with different amounts of Cr_2O_3: a) 0, b) 0.1, c) 1.0, d) 2.0, e) 4.0, f) 8.0 mole percent.

Cr_2O_3 content in mole percent	0	0.1	0.3	0.5	1.0	2.0	4.0	8.0
$P_s \cdot 10^6$, coul/cm^2	9.23	10.80	10.50	9.16	4.53	4.84	5.64	7.12

Introduction of up to 0.1% chromic oxide into barium titanate increases P_s somewhat; this increase of P_s may explain the observed increase of ϵ, d_{31} and d_{33} over the values for pure $BaTiO_3$ (bearing in mind that the polarizability of the trivalent Cr ion is somewhat greater than the polarizability of the tetravalent Ti ion).

While definitive deductions must await completion of x-ray diffraction studies, which are now in progress, recalling that the radius of the trivalent Cr ion is equal to the radius of the tetravalent Ti ion and taking into account the fact that the coordination number of Cr is generally 6, it can tentatively be assumed that substitutional solid solutions may form in the $BaTiO_3$-Cr_2O_3 system only in a very restricted range of Cr_2O_3 concentrations. The introduction of more than 1 or 2% chromic oxide noticeably impairs the ferroelectric properties of the system and probably results in alteration of the structure of barium titanate itself.

I desire to express my deep gratitude to I.P.Kozlobaev for guidance in the work.

Voronezh State University

References

1. J.Meisinger, Z.Angew, Phys., 8, No.9, 422 (1956).

2. T.N.Verbitskaya, Fizika dielektrikov (Transactions of the Second All-Union Conference on the Physics of Dielectrics, M., 1958), Pub.USSR Ac. of Sci., 1960.

INVESTIGATION OF THE EFFECT OF DOPING WITH CHROMIUM AND BISMUTH OXIDES ON THE DIELECTRIC AND PIEZOELECTRIC PROPERTIES OF POLYCRYSTALLINE BARIUM TITANATE

- V.I.Moskalev & S.S.Ordan'yan

The aim of the present work was search for new piezoelectric materials with an enhanced temperature stability by doping barium titanate with bismuth and chromium oxides.

For synthesis of the specimens we used technical grade materials except for the bismuth and chromium oxides which were chemically pure and reagent grade pure, respectively. The specimens were prepared by the usual ceramic technology with the impurity oxides introduced into the initial batch. The preliminary firing of the barium titanate with the added bismuth and chromium oxides was carried out at 1220-1340° for 2 hours; the final sintering - at 1280 to 1340° with a holding time of 2-3 hours.

All the specimens had virtually zero surface porosity. They were polarized by the "hot" procedure in air at temperatures close to the Curie point. Depending on the composition, a polarizing field of from 8 to 15 kv/cm was applied for a period of from 15 to 60 min.

The dielectric constants and loss tangents were measured on a Tesla bridge with f = 1 kc and E = 40 v/cm. The values of the piezoelectric coefficient were determined by the method of resonance and antiresonance. For determination of the loss in high fields the specimens were ground down on one side to a thickness of 0.3 mm. These measurements were carried out at a frequency of 10 kc on a Tesla bridge.

In order to reduce the influence of heating of the specimen to a minimum we employed continuous air cooling and cut off the voltage on the specimen for some time after each measurement.

The results obtained for barium titanate doped with chromic oxide are shown in Table 1. (The chromium was introduced in the form of $Cr_2O_3 \cdot 3TiO_2$ on the assumption, by analogy with $Bi_2O_3 \cdot 3TiO_2$, that this compound exists.)

Table 1

Composition, wt.%	T_C, °C	ε at T_C	ε at 20°C	Second transition temp., °C	$d_{31} \cdot 10^6$ cgsc units at 20°C
$BaTiO_3$	120	8000	1550	15	1,9
99,4% $BaTiO_3$—0,6% $Cr_2O_3 \cdot 3TiO_2$	120	8000	1100	10	1,3
98,3% $BaTiO_3$—1,7% $Cr_2O_3 \cdot 3TiO_2$	125	6000	800	0	0,9
96,5% $BaTiO_3$—3,5% $Cr_2O_3 \cdot 3TiO_2$	125	2200	450	—30	—

As will be evident from the table, the temperature of the second (low temperature) phase transition monotonically decreases with increase of the chromic oxide concentration; apparently solid solutions form in this range of concentrations.

Skanavi et al[1] and Baldwin[2] investigated the dielectric properties of solid solutions in the barium titanate-bismuth titanate system. Our results in general agree with the data reported by these authors.

Investigation of the piezoelectric properties of solid solutions in the $BaTiO_3$-$Bi_2O_3 \cdot 3TiO_2$ and $BaTiO_3$-$Bi_2O_3 \cdot 3TiO_2$-$Cr_2O_3 \cdot 3TiO_2$ systems in the region of low bismuth and chromium titanate concentrations showed that the introduction of Bi ions or Bi and Cr ions simultaneously into barium titanate leads to an appreciable improvement of the temperature stability of the piezoelectric parameters.

The temperature dependences of the dielectric constant ϵ for the compositions (all indicated percentages are by weight):

I. 95% $BaTiO_3$ + 5% $Bi_2O_3 \cdot 2TiO_2$*
II. 96.4% $BaTiO_3$ + 0.6% $Cr_2O_3 \cdot 3TiO_2$ + 3% $Bi_2O_3 \cdot 3TiO_2$, and
III. 94.4% $BaTiO_3$ + 0.6% $Cr_2O_3 \cdot 3TiO_2$ + 5% $Bi_2O_3 \cdot 2TiO_2$

show no evidence of a low temperature phase transition (no second ϵ peak) down to -80°. The dielectric constant ($\epsilon \approx 900$) varies very little (5-10%) in the temperature range from -80 to +50°C. The temperature dependences of tan δ (in weak fields) are nearly straight lines lying at ~3% in the range from -80 to +100°.

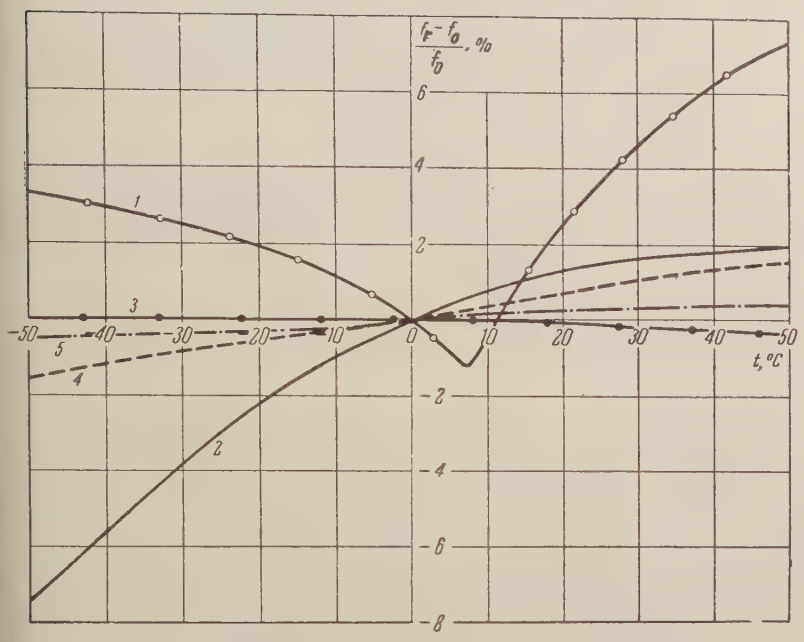

←Fig.1. Variation of the resonance frequency deviation with temperature for specimens of different compositions: 1) $BaTiO_3$, 2) 94% $BaTiO_3$ + 6% $CaTiO_3$, 3) 95% $BaTiO_3$ + 5% $Bi_2O_3 \cdot 2TiO_2$, 4) 96.4% $BaTiO_3$ + + 0.6% $Cr_2O_3 \cdot 3TiO_2$ + 3% $Bi_2O_3 \cdot 3TiO_2$, 5) 94.4% $BaTiO_3$ + 0.6% $Cr_2O_3 \cdot 3TiO_2$ + + 5% $Bi_2O_3 \cdot 2TiO_2$.

The temperature dependences of the piezoelectric parameters for compositions I, II, III, "pure" technical $BaTiO_3$, and 94% $BaTiO_3$ + 6% $CaTiO_3$ solid solution are shown in Figs.1 & 2. Compositions I, II and III exhibit an extremely weak temperature dependence of the resonance frequency. The frequency deviation in the temperature range from -50 to +50° does not exceed 3-5% for the worst composition (II), while for the other two it amounts to only a small fraction of a percent (as in the case of niobates). A shortcoming of these compositions is the low value of the parameter d_{31}/ϵ (characterizing the sensitivity), which

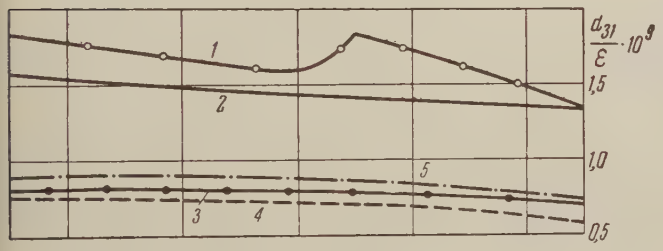

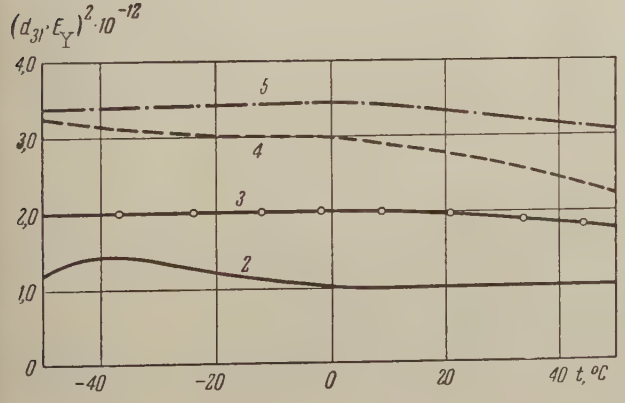

←Fig.2. Temperature dependences of the piezoelectric parameters $(d_{31} \cdot E_Y)^2$ and d_{31}/ϵ for specimens of different compositions (curve-composition designations same as in Fig.1).

---

*Tests show that it makes virtually no difference whether the bismuth oxide is introduced in the form of $Bi_2O_3 \cdot 2TiO_2$ or in the form of $Bi_2O_3 \cdot 3TiO_2$.

is explained by the relatively low value of the piezoelectric coefficient ((0.7-0.8)·10^{-6} cgse units). On the other hand, a positive feature of these compositions as compared with 94% $BaTiO_3$ + 6% $CaTiO_3$ stabilized ceramic is the high value of the parameter $(d_{31} \cdot E_Y)^2$, characterizing the specific acoustic power, which is 2-3 times higher than for the calcium-containing ceramic. The high value of the parameter $(d_{31} \cdot E_Y)^2$ is due to increase of Young's modulus as a result of introduction of the additives which leads to increase of the apparent density of the ceramic (to ~5.8 g/cm^3 from 5.5 g/cm^3 for $BaTiO_3$).

It follows from a comparison of the ac field dependences of tan δ for $BaTiO_3$ and the compositions I, II and III (Fig.3) that doping with bismuth oxide results in decrease of the loss in strong fields. On the other hand, comparison of the curves for compositions I and III shows that the introduction of chromic oxide in small amounts leads to increase of the loss in strong fields.

Tests on the specimens showed that the addition of bismuth oxide to barium titanate results in increase of the mechanical strength. Thus whereas for $BaTiO_3$ ceramic the ultimate compressive strength is ~3000 kg/cm^2, for composition I the ultimate strength is ~5000 kg/cm^2; the bending strength increases from 600 to 800 kg/cm^2.

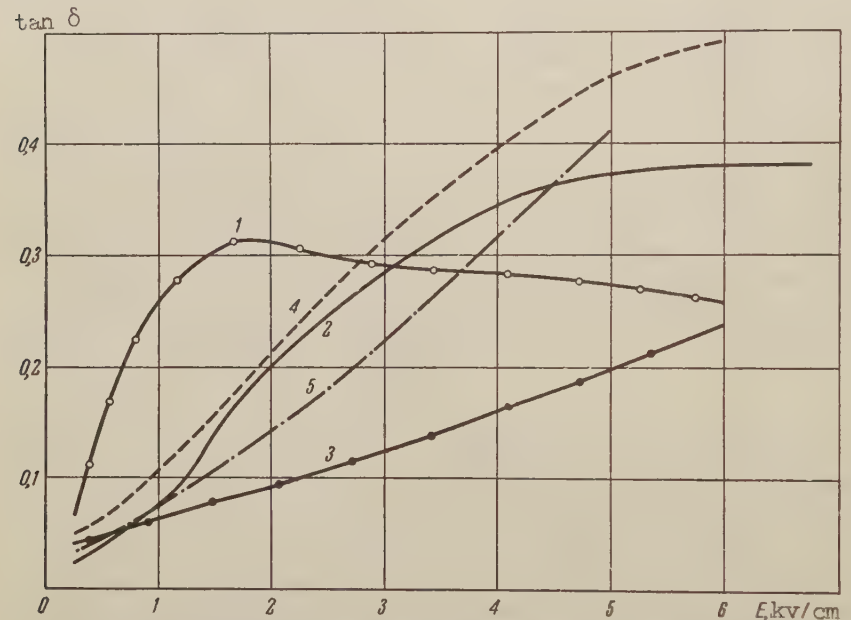

Fig.3. Variation of tan δ with $E_\sim$ for different specimens (curve designations as in Fig.1).

Conclusions

The investigation showed that doping of barium titanate with bismuth oxide (or bismuth and chromium oxides simultaneously) results in a significant improvement of the temperature stability of the dielectric piezoelectric parameters, particularly ε, f_{res} and $(d_{31} \cdot E_Y)^2$. The value of the last parameter, despite some decrease of the piezoelectric coefficient is still 2-3 times higher than for 94% $BaTiO_3$ + 6% $CaTiO_3$ ceramic. Moreover, the introduction of small amounts of bismuth oxide substantially reduces tan δ in strong fields.

Thus it is probably expedient to use the investigated compositions for the fabrication of electromechanical transducers, particlarly for use in equipment where forced cooling is impossible and good temperature stability of the piezoelectric parameters is essential.

References

1. G.I.Skanavi, Ya.M.Ksendzov, V.A.Trigubenko & V.G.Prokhvatilov, Zhur.eksp. i teor.fiz., 33, 320 (1957). (Trans.Sov.Phys. - JETP.)

2. W.J.Baldwin, Ceramic Ind., 71, No.2, 88 (1958).

SOME FEATURES OF PULSE SWITCHING OF FERROELECTRIC CRYSTALS

- L.A.Shuvalov

Considerable interest has been evinced recently in investigation of the processes involved in polarization reversal or switching of ferroelectrics in view of the fact that these processes are fundamental to a number of possible practical applications.

Below we describe some experimentally observed features of pulse switching of ordinary tri-glycine sulfate (TGS) and deuterated tri-glycine sulfate (DTGS) crystals that are not explicable in the framework of the simple theory proposed by Pulvari & Kuebler[1].* Presumably similar effects obtain to a certain degree in other ferroelectric crystals as well.

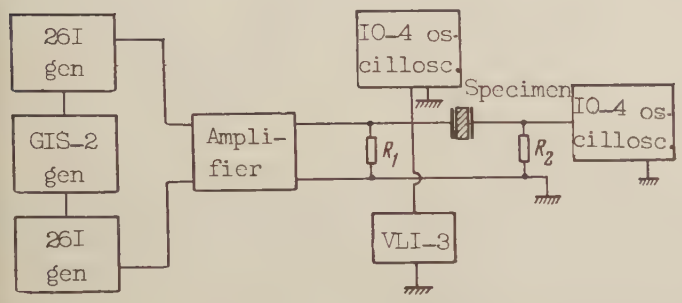

Fig.1. Block diagram of the set-up for studying pulse switching.

The measurements were carried out by means of the set-up diagramed in Fig.1. This allowed of applying bipolar square voltage pulses produced by the two 26I generators and amplified by the two channel amplifier with a low output resistance (R_1 = 50 ohm) to the crystal specimen. The set-up had provision for independent control of the pulse parameters and wide variation (by means of a GIS-2 generator used as a long delay line) of the delay between pulses of opposite polarity. The voltage applied to the crystal was measured by a VLI-3 crest voltmeter, while its waveform was monitored by means of an I0-4 oscilloscope. The switching current and time were determined from the trace on the screen of a second I0-4 oscillograph shunted by a low voltage resistor ($R_2 \approx$ 10-70 ohm).

Most of the measurements were carried out on specimens in the form of 1 x 1 cm plates 0.15 to 0.30 mm thick cut normal to the ferroelectric axis of the crystal. Cross-shaped silver electrodes were applied by vacuum evaporation.

1. Whereas when equispaced bipolar pulses are applied to the crystal, the switching currents and times corresponding to pulses of opposite polarity are the same (in the absence of unipolarity of the crystal), upon the application of unequally spaced pulses the switching current and times become asymmetrical[5]. If the sequence of pulses of one polarity is shifted relative to the other, there occurs an increasingly rapid growth of i_{max} and $1/\tau_{max}$ for the pulses the separation between which is decreased and a slowing down decrease of i_{max} and $1/\tau_{max}$ for the pulses the separation between which is increased. An opposite shift of the pulse sequences results in a similar change of i_{max} and $1/\tau_{max}$ for the corresponding pulses, i.e., there is obtained a symmetrical picture.

This indicates that in the intervals between pulses of opposite polarity there occur processes associated with change of the conditions of nucleation and domain wall mobility that slow down the subsequent polarization reversal and that become evident only with an appreciable difference in the intervals between pulses.

II. According to the simple theory and experimental data of Pulvari & Kuebler (Refs.1,6) the $i_{max}/S = f(E)$ (S is the electrode area) and $1/\tau_{max} = \varphi(E)$ curves

---

*The results of measurements of $i_{max} = f(E,t)$ and $1/\tau_{max} = \varphi(E,t)$ for TGS and DTGS crystals (i_{max} is the maximum switching current and τ_{max} is the switching pulse rise time) are described in Refs.2,3 & 4.

for TGS and DTGS crystals (as well as for other ferroelectrics) coincide when plotted to an appropriate scale. However, our measurements[3,4] carried out at different temperatures with pulses of less than 20 microsec duration show that with increase of the field the $i_{max}/S = f(E)$ curve deviates upward from the $1/\tau_{max} = \varphi(E)$ curve, which leads to apparent increase in the value of the spontaneous polarization calculated by means of the formula[1] $P_s = 0.825\ i_{max}\tau_{max}/S$.

This divergence between the field dependences of i_{max}/S and $1/\tau_{max}$ can apparently be explained, on the one hand, by incomplete switching of the interelectrode volume in weak fields and increase of the switching volume with increase of the field strength; on the other hand, the divergence between the curves may be caused by variation with field of the relationship between τ_{max} and τ_s, the total switching time, i.e., by variation in the shape of the switching pulse (the shape of the $i = f(t)$ curve which in the theory of Pulvari & Kuebler is assumed to be constant). It is found that the ratio τ_{max}/τ_s actually increases with increase of the field strength, which is apparently connected with change in the relationship between the processes of nucleation and domain growth and propagation.[7] Nevertheless, the product $i_{max}\tau_s$ increases with increase of the field strength, although to a lesser degree than the product $i_{max}\tau_{max}$. Thus, the divergence between the curves is apparently due to both causes.

We note further that the $1/\tau_{max} = f(E)$ and $1/\tau_s = \varphi(E)$ curves plotted to an appropriate scale will also diverge: the former curve with increase of the field will deviate upward from the latter, i.e., the equality $\tau_s = k\tau_{max}$, where k is a constant equal to 2.6-2.7 (according to Pulvari & Kuebler), is not satisfied. According to our measurements, in fields up to 6 kv/cm k varies from 4.5 to 2.6, remaining greater than 3 in fields weaker than 5 kv/cm.

III. In view of the hysteresis character of the field dependence of P_s in ferroelectrics the process of polarization reversal in these materials is always accompanied by substantial evolution of heat and, consequently, heating of the specimen. Under conditions of periodic pulse switching there is established within a short time a certain stationary temperature distribution owing to thermal lag. The strength of the heat source constituted by the switching volume and, consequently, the temperature rise to not depend on the separation between pulses of opposite polarity or on the pulse duration (assuming the pulse duration to be greater than τ_s), so that in the first approximation they are proportional to the pulse repetition rate and the pulse voltage.

This heating effect must necessarily alter the field and frequency dependences of the switching characteristics, i.e., it must cause increase of i_{max} and $1/\tau_{max}$ (and $1/\tau_s$), and with increase of the frequency (or field) lead to overheating of the crystal and a pronounced change in the character of the field and frequency dependences. Thus with a considerable switching volume the monotonically rising i_{max} vs frequency f (or field E) curve, at a certain value of the frequency (or field), depending on the initial temperature and the geometry of the interelectrode volume, begins to bend over and may even begin to drop back towards the horizontal axis; under the same conditions the specimen with a substantially smaller electrode volume continues to exhibit a monotonic increase of i_{max} (Fig.2,a).

That this radical change in the frequency dependence of i_{max} is due to heating is substantiated by the following simple experiment. If one junction of a differential thermocouple is mounted in contact with the center of the electrode cross and the other junction is placed in the temperature control chamber at some distance from the specimen, the temperature difference Δt registered by the thermocouple may be taken as a measure of the heating of the specimen.*

---

*While preparing the report for publication we became acquainted with the work of Campbell[8] in which the heating of a barium titanate single crystal was measured by a similar procedure, although for a different purpose.

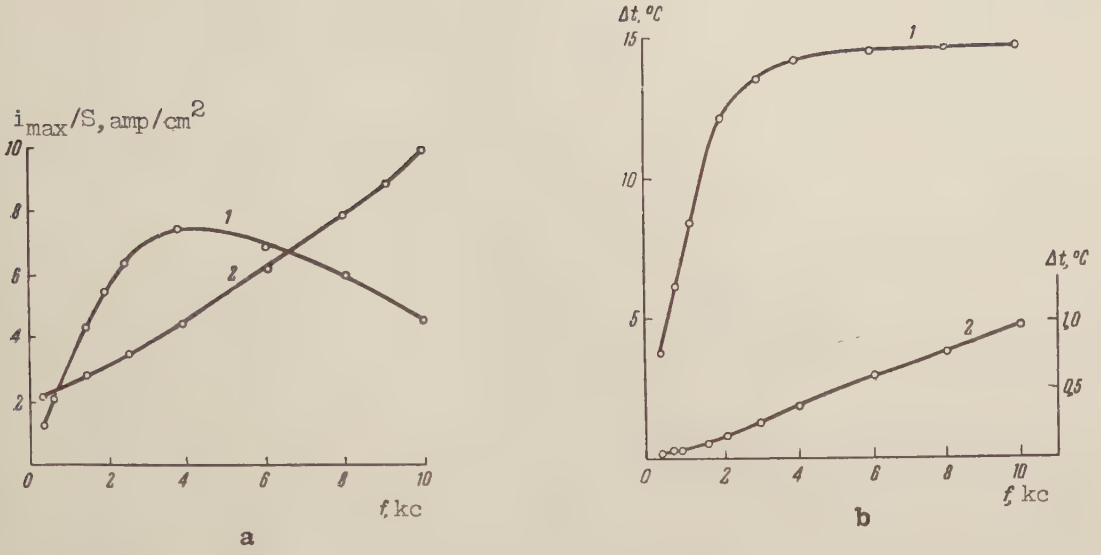

Fig.2. Variation of the current density i_{max}/S and heating Δt (initial temperature $t = 20^{\circ}$) with the pulse repetition rate for TGS specimens with different interelectrode volumes: 1) 2.1 x 2.1 x 0.28 mm, 2) 0.5 x 0.4 x 0.19 mm.

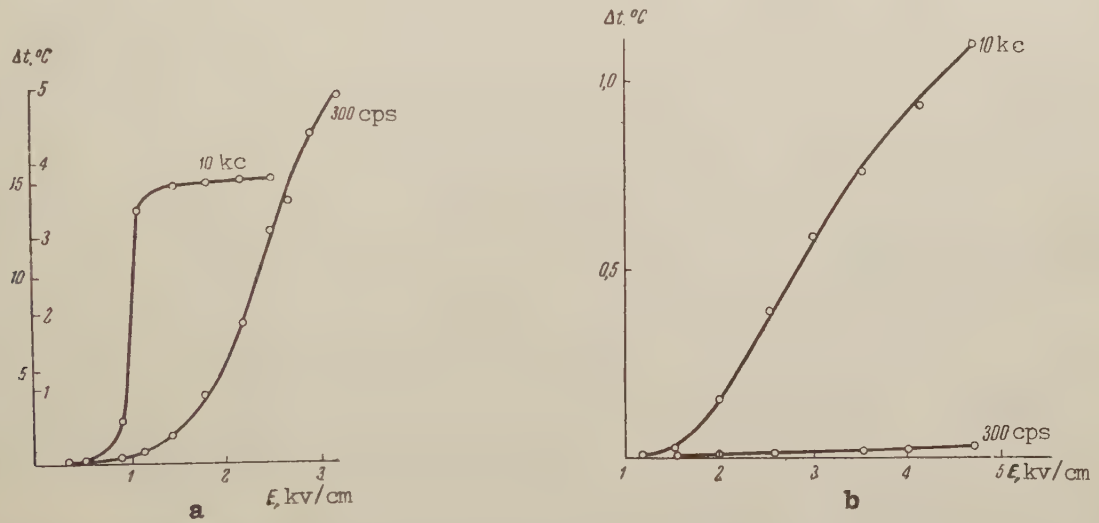

Fig.3. Heating of TGS specimens at different frequencies as a function of the field. Interelectrode volume dimensions: a) 2.1 x 2.1 x 0.28 mm, b) 0.5 x 0.4 x 0.19 mm. Initial (ambient) temperature 20°.

The Δt vs f curve recorded by this procedure is shown in Fig.2,b; it will be seen that this curve also changes slope at about the same frequency as the $i_{max} = \varphi(f)$ curve, but instead of dipping downward, tends to saturation. Thus the appearance of the curves shown in Fig.2 can be explained on the assumption that there occurs heating of the switching volume with resultant impairment of the polarization and decrease of the switching current; this in turn leads to decrease of the heating and to partial restoration of the polarization reversal. As a result there is established a slowly varying dynamic equilibrium: the Δt vs f curve continues almost parallel to the horizontal axis, while the i_{max} vs f curve goes through a

maximum and then slopes downward. The change in the character of the $i_{max} = f(E)$ and $\Delta t = \varphi(E)$ curves (Fig.3,a) can be explained in analogous fashion.

Precise calculation of the specimen heating is somewhat complicated inasmuch as one must take into account the heat evolved in the switching volume, the heat expended on raising the temperature of this volume and the heat lost by transfer to the rest of the specimen and radiated out of the specimen through the side walls and the electrodes. Usually only the dependence of the heating on the size of the switching volume is considered (for example, see Ref.8). It can readily be seen, however, that even with a constant switching volume the heating can be reduced in practice by substantially increasing the surface and, consequently, the heat dissipation. If the heat flow through the side and end surfaces of the switching volume differs substantially (because of unequal linear dimensions or differences in thermal conductivity), a change of the switching volume by changing one or another of its linear dimensions will have a different effect on the heating. Thus, for example, it is obvious that in case one can neglect heat loss through the side surfaces of the switching volume (in case of a ferroelectric film for example) the heating will not depend on the size of the electrodes.

In the case of three dimensional decrease of the polarizing volume, however, the heating always decreases inasmuch as the amount of heat evolved decreases as l^3, while the heat transfer decreases as l^2. A typical example is shown in Fig.3 from which it will be seen that a crystal with an interelectrode volume of 2.1 x 2.1 x 0.28 mm subjected to pulses with a repetition frequency of 10 kc heats up immediately, while a crystal with a switching volume of 0.5 x 0.4 x 0.19 mm can be switched without significant heat rise definitely at a low repetition frequency, and that even at a frequency of 10 kc in fields to 5 kv/cm its heating is relatively minor. The pulse repetition frequency (or field amplitude) for which i_{max} and $1/\tau_{max}$ with increasing pulse repetition frequency cannot, apparently, be wholly explained by heating of the interelectrode volume: one must also take into account the possible influence of decrease in size of the switching volume and change in the separation between pulses of opposite polarity.

IV. Before concluding we must briefly mention other effects observed in the process of pulse polarization reversal, effects which can be partially explained by heating and partially by changes in the conditions of domain nucleation and domain wall mobility occurring in the intervals between pulses.

1. When periodic bipolar pulses are applied to a crystal, "steady" switching is not established immediately: actually i_{max} and $1/\tau_s$ gradually rise to a certain steady value and thereafter remain constant even with continuous switching for a period of up to 5-8 hours. The length of this "step-up" period depends on the frequency and amplitude of the pulses and on the preceding history of the specimen. For high field amplitudes (or small volumes) the steady state is attained in a fraction of a second.

2. The threshold field defined as the field for beginning of switching with increase of the pulse amplitude proves to be higher than the threshold field defined as the field of cessation of switching with decrease of the pulse amplitude. The difference between the two fields may be very appreciable: 200 to 500 v/cm.

3. The threshold field defined as the field for beginning of switching under periodic pulses of increasing amplitude increases after the crystal has been allowed to rest for some time.

4. In the case of switching by single pulses, the threshold field is substantially higher and the $i_{max}/S = f(E)$ and $1/\tau_{max} = \varphi(E)$ curves lie appreciably lower than in the case of switching by periodic pulses.

All the above described effects make calculation of the switching characteristics of TGS and DTGS crystals rather difficult and hence hinder the use of such

crystals in switching circuits. It would, therefore, be highly desirable to investigate all these effects in detail.

I desire to thank V.A.Pluzhnikov for assistance in carrying out the experiments and I.S.Zheludev for stimulating discussions.

Institute of Crystallography,
Academy of Sciences of the USSR

References

1. C.Pulvari & W.Kuebler, J.Appl.Phys., 29, 63 (1958).
2. V.P.Konstantinova, I.M.Sil'vestrova, L.A.Shuvalov & V.A.Yurin, Izv.AN SSSR, Ser.fiz., 24, 1203 (1960). (Trans.Bulletin, 24, 1206.)
3. L.A.Shuvalov, Kristallografiya, 5, 409 (1960). (Trans.Soviet Physics - Crystallography.)
4. I.S.Zheludev, Report presented at the Third Conference on Ferroelectricity, 1960.
5. L.A.Shuvalov, Kristallografiya, 5, 282 (1960). (Trans.Soviet Physics - Crystallography.)
6. C.Pulvari & W.Kuebler, J.Appl.Phys., 29, 1742 (1958).
7. E.Fatuzzo & W.Merz, Angew.Chemie, 7, No.2, 76 (1959).
8. D.S.Campbell, J.Electronics Control, 13, 335 (1957).

SOME SPECIAL PROPERTIES OF FERROELECTRIC ELEMENTS AND FERROMAGNETIC TOROIDS WITH SQUARE HYSTERESIS LOOPS

- E.I.Mamonov & I.S.Zheludev

Ferroelectric and ferromagnetic materials with a hysteresis field dependence of the induced polarization or magnetization have a number of formally similar properties: hysteresis, switching characteristics, the presence of spontaneous polarization or magnetization, the character of the variation of these quantities with temperature, etc. At the same time, owing to the basically different nature of ferroelectricity and magnetism, these effects in the two types of materials differ substantially from each other.

In the present article we shall consider the qualitative aspects of certain processes occurring in ferroelectric and ferromagnetic materials that are of practical importance from the standpoint of their application in switching circuits.

Switching Characteristics

Fig.1. Oscillogram of hysteresis loop with time markers, typical for ferroelectric and ferromagnetic elements used in switching circuits (the strength of the applied sinusoidal field is approximately twice the coercive field).

The effect fundamental to the utilization of ferroelectric and ferromagnetic materials in switching circuits is hysteresis[1-4]. Fig.1 shows an oscillogram of a hysteresis loop with time markers, the distribution of which over different sections of the loop allows of evaluating the rate of transition from one extreme state of polarization or magnetization to the opposite.[3] Upon the application of a sufficiently strong constant field, ferroelectric (ferromagnetic) elements are polarized (magnetized) to saturation in the direction of the applied field and after removal of the field retain their residual polarization (magnetization) even when the driving circuit electrodes are short circuited. This effect is utilized for storage of information in binary form: one of the saturated states corresponds to "zero"; the other to "one".

The switching rate is determined by the transition time of the polarization (magnetization) processes over the vertical sections of the loop. It should be noted that over these sections, where the transition has a "trigger" character, the duration of the process is much shorter than over the "horizontal" sections of the loop.

The switching rate is a significant parameter in one of the most important engineering applications of ferroelectrics and ferromagnets, namely, storage of information. In this application the ferroelectric or ferromagnetic elements are controlled - driven - by pulses. The waveforms of the switching signals for elements of both types are similar (Fig.2). The duration of switching is usually measured by means of an oscillograph (Fig.2, a), the switching time τ_s being reckoned to the 10% level of maximum signal amplitude (Fig.2,b). The driving pulse width is usually made somewhat greater than τ_s in order to insure a sufficiently long driving pulse at the given field amplitude for complete switching of the element. The initial overshoot (Fig.2) is due to the leading edge of the driving pulse and not to the switching process. The switching signal when the driving pulse is of the same polarity as the preceding pulse proves to be appreciably shorter than the switching signal (Fig.2,b dashed line). The amplitude of this signal, which is essentially a noise signal, is proportional to the slope (dP/dt or dB/dt) of the corresponding sections of the

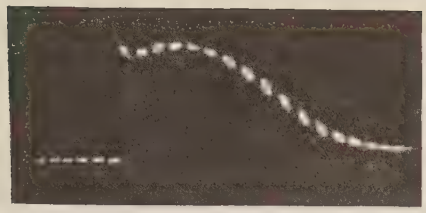

a

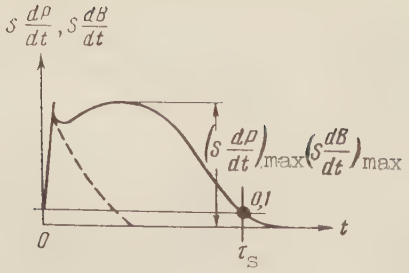

b

Fig.2. Shape of signals arising as a result of pulse switching in circuits with ferroelectric and ferromagnetic elements (for fields corresponding to the full saturation or limit cycle).

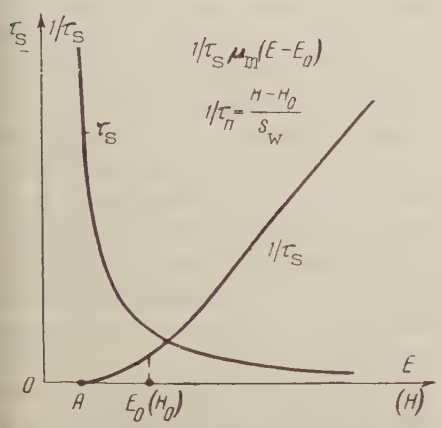

Fig.3. Applied field dependences of the switching time τ_S and reciprocal time $1/\tau_S$ for ferroelectric and ferromagnetic materials with a square hysteresis loop.

loops. By effectively reducing the time constant of the circuit under these conditions, the ferroelectric or ferromagnetic element acts so that there occurs differentiation of the driving pulses. Consequently, the amplitude of the noise signals will increase with decrease in the rise (decay) time of the driving pulses. Moreover, both the useful signal and the noise signal are proportional to the area S of the electrodes of the ferroelectric capacitor or the cross section of the ferromagnetic toroid.

The character of the variation of the switching time with the applied field is also similar for elements of both types. Typical field (E or H) dependences of the switching time τ_S and reciprocal time $1/\tau_S$ are shown in Fig.3.

In weak fields insufficient for switching over the limit cycle (i.e., in fields equal to or weaker than the coercive fields) the variation of $1/\tau_S$ as a function of the field is nonlinear. For fields exceeding E_0 (or H_0) (which for the case of ferroelectrics is called the critical or limit field[1], and for the case of magnetic media the threshold field[2]), the variation of $1/\tau_S$ as a function of the field is linear and is described by the relationships

$$1/\tau_S = \mu_m (E - E_0) \qquad (1)$$

for ferroelectric elements[1], and

$$1/\tau_S = \frac{1}{S_W}(H - H_0) \qquad (2)$$

for ferromagnetic elements; here μ_m is the domain mobility coefficient and S_W is the switching coefficient. Both these coefficients depend on the physical nature of the material and on the composition and structure of the given switching element.

It is interesting to note that with increase of the time constant of the switching circuit with a ferroelectric or ferromagnetic element the switching speed decreases (the slope of the $1/\tau_S$ curve increases). Point A in Fig.3 corresponds to the field strength below which no switching occurs. It may be hypothesized that the nonlinear section of the $1/\tau_S$ vs H curve is due to nonuniform

Material	P_o, μcoul/cm^2	B_o, kgauss	E_c, kv/cm	H_c, oe	W_{sp}, 10^{-3} joule/cm^3 per switching event	Vol, 10^{-5} cm^3	Linear dimensions, mm	OD, (P_{cfs}, σ_s, 6)	ID, (P_{cfs}, σ_s, 6)	Height, (P_{cfs}, σ_t, 6)	$W_{abs} \cdot 10^{-6}$, w sec per switching event	T_C, °C	μ_m, at 20°, $\sqrt{\text{sec}^{-1}}$, calc. acc. to Merz[1]	$S_w \cdot 10^{-6}$ at 20°, oe sec
Barium titanate	26		0,75		39	1,2	0,2×0,2×0,3				0,47	120	~0,6	
Tri-glycine sulfate	2,3		0,22		1,0	1,2	0,2×0,2×0,3				0,01	~47 (60 for DTGS)	~0,3	
Guanidine aluminum sulfate hexahydrate	0,35		1,0—3,0		0,7—2,1	1,2	0,2×0,2×0,3				0,008—0,03	(300)		
Ferrite K-28		2,6		1,5	0,06	650		2,1	3,0	0,9	0,39	290		0,66
toroids VT-2		2,6		0,8	0,03	2200		3,1	2,0	1,3	0,66	275		0,71
VT-5		2,7		0,15	0,006	1570		3,0	2,0	1,0	0,1	240		0,65
Perminvar (ribbon toroid)		10		0,3	0,05							500		

distribution of the driving field in the magnetic medium: the nearer internal layers of the toroid are under the influence of a stronger field and switch earlier or under weaker pulses. Moreover, for different components of the magnetic induction the switching rates may differ for a given field. It must be noted that other interpretations of the effect, based on the concept of domain processes, have been proposed. The section 0-A of the $1/\tau_s = f(E)$ curves for ferroelectrics may be associated with conditions under which the applied field does not produce switching. The nonlinear part of the curve can be related with the presence of polarization components acting at different rates. Over this section of the cycle the predominant role is played by domain nucleation, while over the linear section domain growth and penetration processes predominate. The domain growth rate may be compared with the velocity of sound in the given medium. On the basis of this one can make quantitative estimates of the switching speed.

There also exists the view according to which for some ferroelectrics (barium titanate) there is no critical field below which switching, no matter how slow, does not occur[1]. From the standpoint of practical application of ferroelectrics (as well as ferromagnetic elements) this, of course, is undesirable, it is essential to have a fairly sharp separation, marked by the threshold or critical field, between the field regions where switching does occur and where it does not.

It will be evident from the curves of Fig.3 that with increase of the driving field the switching time decreases. It would seem that this should make it possible to calculate the maximum attainable switching frequency: $f_{max} = 1/2\tau_{min}$. In practice, however, this frequency is rarely attainable owing to the fact that because of heating the switching parameters are impaired, thus setting a lower limit to the maximum switching frequency.

Losses

The unfavorable effects of heating due to losses and other factors will, other conditions being equal, be evinced sooner for materials with a lower Curie point. In practice (for example, in ferrite memory devices) forced cooling is essential in most cases. We note that on the assumption of the same thermal conductivity the conditions of heat loss for ferroelectrics are better (owing to heat transfer through the metal electrodes) than for ferrites. Of the various losses encountered in switching devices, the greatest fraction is accounted for by hysteresis loss, which is proportional to the area of the hysteresis loop. Moreover, ferroelectric elements have loss components due to conductivity, the piezoelectric effect and electrostriction, while ferrite elements have losses due to eddy currents and magnetostriction. Some loss can also be attributed to relaxation processes. Evaluation of the magnitude of the losses, the degree of their interaction and their influence on the switching mechanism is of great practical interest.

Some significant parameters and the approximate values of the specific and absolute hysteresis losses of a number of ferroelectric elements and ferromagnetic toroids calculated for a single switching event are given in the accompanying table (for frequencies of 50 to 100 cps). The specific losses for ferroelectrics ($W_{sp} \approx 2P_oE_c$) and for magnetic toroids ($W_{sp} \approx (1/2\pi)B_o H_c$) are given in joules per cm^3.

At present, researchers are working on problems of preparation and utilization of film elements wherein the absolute losses are low enough to permit operation at relatively high switching rates.

The specific losses in magnetic toroids are lower than in ferroelectric elements; in practice, however, ferroelectric elements can be made much smaller than toroids[4] so that the absolute losses prove to be lower than the losses in toroids. On the other hand, the ferromagnetic materials listed in the accompanying table have higher Curie temperatures than the listed ferroelecrrics. Ferroelectric elements generally require driving pulses of lower power than magnetic elements, while yielding an appreciably stronger readout signal.

The switching mechanism and associated effects in ferroelectrics have been studied less than those in ferromagnetic materials. The technology for obtaining ferroelectric elements with the desired special characteristics is also lagging behind the corresponding technology for ferromagnetic toroids. This is the reason for the relatively slow adoption of ferroelectric materials for switching purposes, despite their advantages over ferrite cores. Particularly important is the search for ferroelectric crystals with a sufficiently high Curie temperature that could be used for switching elements with stable characteristics in a wide range of frequencies, temperatures, etc. It is also of interest to elucidate the reasons for some of the shortcomings of certain ferroelectrics (for example, the so-called "forming time" to establishment of the full switching cycle).

Institute of Crystallography,
Academy of Sciences of the USSR

References

1. W.J.Merz, J.Appl.Phys., 27, 938 (1956).
2. D.R.Brown et al, J.AIEE, 631, Jan. (1955).
3. E.I.Mamonov, Inventor's Certificate No.124029, 12, Nov., 1957.
4. E.I.Mamonov & I.S.Zheludev, Doklad na Vsesoyuznom soveshchanii po vychislitel'noi matematike i tekhnike (Report presented at the All-Union Conference on Computation Mathematics and Engineering, Moscow State University, 16-21 November 1959.

PRINCIPLES AND APPLICATION OF FERROELECTRIC MATRICES FOR INFORMATION STORAGE IN COMPUTERS

- E.I.Mamonov

Ferroelectric matrices can be constructed either in the form of continuous plates with a grid of orthogonal strip electrodes on opposite sides of the plate or in the form of an array of individual miniature ferroelectric capacitors. The former construction is preferable from the standpoint of ease of assembly and the possibility of utilizing printed circuit techniques (Fig.1). The electrodes are applied to the plates by vacuum evaporation of an appropriate metal through templets prepared of metal foil by photochemical etching. The leads from the matrix plate are attached not by soldering but by means of a conducting cement consisting of a polymer, a metallic powder and a solvent. The basic parameters of the plate and templet are chosen such that the width of the slots in the templet (and consequently the width of the electrode strips) will be greater than the thickness of the plate. This serves to reduce edge effects in the elementary capacitors formed by the crossovers of the orthogonal electrodes.

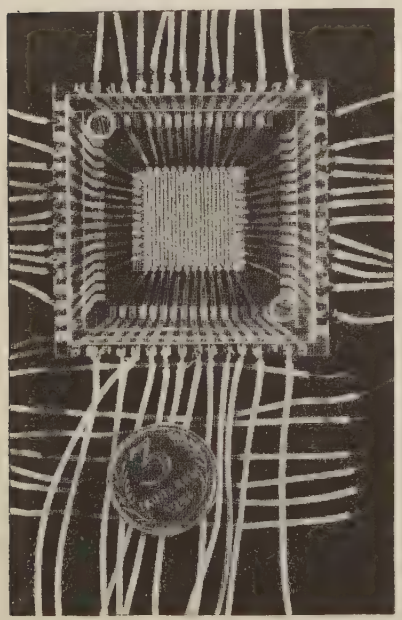

Fig.1. Experimental ferroelectric matrix.

For experimental purposes[1] we prepared matrices with a storage capacity of from 81 to 1024 binary bits; these consisted of 10 x 10 and 20 x 20 mm ferroelectric plates prepared of tri-glycine sulfate single crystals.*

Information storage in ferroelectrics is based on the hysteresis dependence of their polarization (or bound charge) on the applied electric field; one of the residual polarization states is taken as "zero"; the other as "one". Control of the information storage (recording, readout and restoration of the information after reading) is realized by pulses. In all types of circuits writing and restoration of the information is based on the addition of electric fields applied to pairs of mutually orthogonal electrodes. The total field E_m (for example, $\pm\frac{1}{k}E_m$ and $\pm(1-\frac{1}{k})E_m$, where usually $3 \geqslant k > 1$) must be sufficient for complete switching of the ferroelectric element over the limit cycle. In view of the fact that the charge stored in a ferroelectric element is bound and cannot be detected statically in the external circuit, the detection and recognition of information in readout must be carried out in the process of pulse switching, in most cases with loss of the stored information. In the process of reading (Fig.2) there are switched only the elements holding "one" (Fig.2,b), while from the unswitched cells with code "zero" there are obtained shorter pulses (Fig.2,c) due to differentiation in the geometric (static) crossover electrode capacitance.[2,3] This circumstance allows of increasing the useful signal-to-noise ratio[1,4] by gating with a suitable delay (Fig.2,d).

The most suitable principle of operation for two coordinate storage systems is that in which parallel readings may be carried out by applying pulses of arbitrarily high voltage to one matrix electrode, the electrode along which all the

---

*There were also prepared 40 x 40 mm matrices of tri-glycine sulfate single crystals.

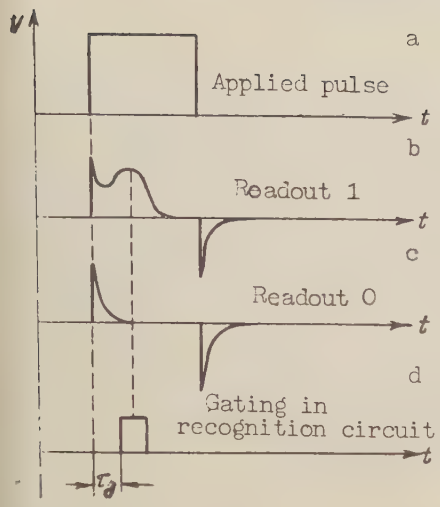

Fig.2. Time diagram of reading and recognition of stored information.

digits of the word are located.[1,4]

Three dimensional systems, which can have a much higher storage capacity, may be based on two principles: 1. An extension of the two-dimensional type where each digit of a given word is written on the crossovers along the single matrix electrode, and different groups of words are written along different matrices comprising the three-dimensional system, the third coordinate in this case being the matrix numbers. 2. A purely three-dimensional type, where each digit of a given word is located in different matrices.

The first principle provides for higher reliability and speed[1,5], and easier adjustment of the operating point, taking into account the scatter of the parameters of the individual matrices and crossover electrodes. The presence of signals from partially excited (not addressed) crossovers in the second case may substantially impair the signal-to-noise ratio in reading and thus constitutes a serious restriction on the information storage capacity.* For square matrices with n x n electrodes the parasitic signal in the best case is proportional to $C_o(n - 1)$, where C_o is the geometric capacitance of a crossover[2].

Institute of Crystallography,
Academy of Sciences of the USSR

References

1. E.I.Mamonov & I.S.Zheludev, Doklad na Vsesoyuznoi soveshchanii po vychislitel'noi tekhnike i matematike (Report presented at the All-Union Conference on Computation Mathematics and Engineering), Moscow State University, November, 1959.
2. C.Pulvari, Trans. IRE, CT-3, 1, 3 (1956).
3. E.I.Mamonov, Doklad na II Konferentsii po segnetoelektrichestvu (Report presented at the Second Conference on Ferroelectricity), Rostov-on-the-Don, 1957.
4. E.I.Mamonov & Yu.M.Koval'skii, Present issue of the Bulletin, p.1418.
5. E.I.Mamonov & I.S.Zheludev, Present issue of the Bulletin, p.1412.

---

*This holds despite the use of group noise-compensation procedures, which are convenient in transformer information recognition.

TRANSISTOR CIRCUITS FOR AUTOMATIC CONTROL OF WRITING, READING AND RESTORATION OF INFORMATION IN FERROELECTRIC MEMORY MATRICES

- E.I.Mamonov & Yu.M.Koval'skii

In employing ferroelectric information storage devices the simplest method of writing and reading information involves switching of the polarization of the ferroelectric. This is the method used in the two-dimensional ferroelectric matrix memory[1], the control system for which is described below (Fig.1). All the digits of each stored word (code number or command) are stored on the crossovers along one horizontal electrode. Corresponding bits in different words are located along the vertical electrodes. The required address is applied through the logical circuit I_1 to an address register consisting of flip-flops. In accord with this code, one of the address decoder selection lines in the register is excited and there is actuated (through a direct coupled input) one of the logical circuits I_2 or I_3. Thereupon writing or reading may be carried out according to the control program signals.

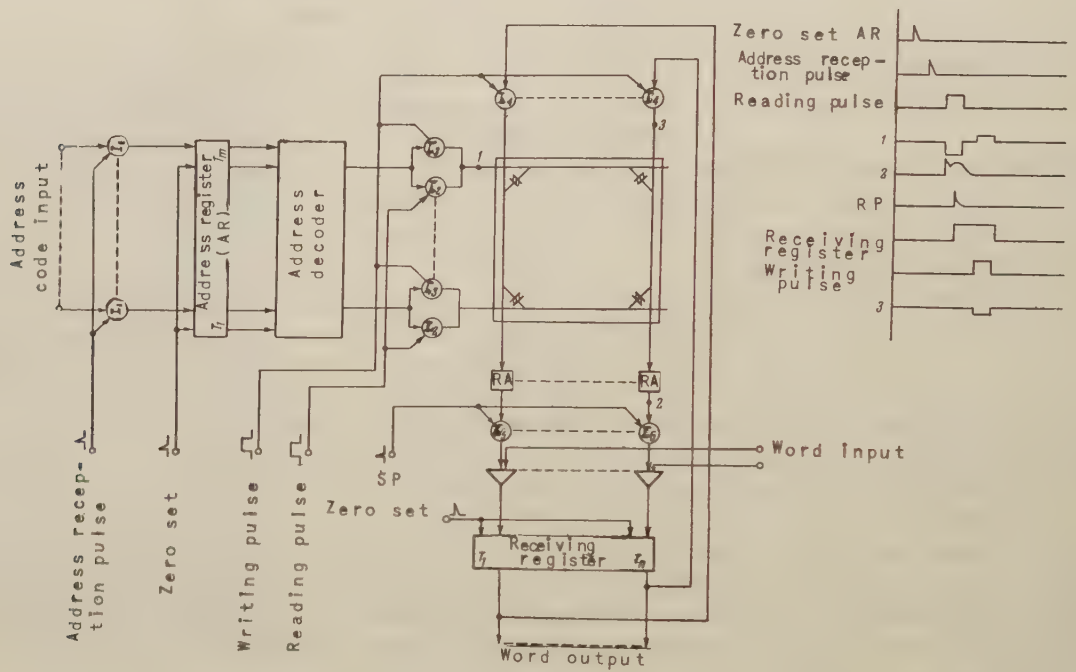

Fig.1. Block diagram of the two-dimensional ferroelectric matrix memory.

Recording is realized by applying to the ferroelectric capacitor electrodes pulses of opposite polarity and of amplitude equal to, for example, $E_m/2$ (E_m is the saturation field). The writing pulse passes through one I_3 circuit corresponding to the given address code and through circuit I_4 direct coupled to the individual flip-flop outputs of the buffer register, if the corresponding digit of the receiving register is in the 1 position. At the outputs of the I_3 and I_4 circuits there will appear pulses of opposite polarity; the amplitude of each pulse may be made equal to $E_m/2$. The pulse polarity is made such that the voltage across the memory element will be opposite to the voltage in reading. The crossovers where the writing pulses are applied to both electrodes (from I_3 and from I_4) are switched to position 1; the others remain in position 0.

A reading pulse applied to the circuits I_2 will pass only through one of them, selected in accordance with the address code (on the horizontal electrode

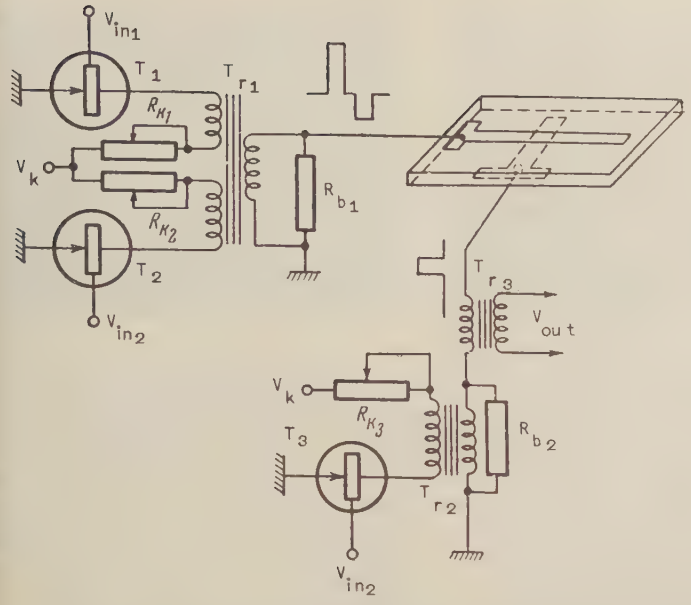

Fig.2. Writing, reading and recognition circuits with transformer coupling.

of the matrix). The reading pulse amplitude is greater than the ferroelectric switching voltage. Hence all crossovers on this electrode in position 1 will switch to the 0 position. The switching signal is applied through the reading amplifier RA to the input of the I_5 circuit to which the recognition pulse, shifted by a certain delay with respect to the start of the reading pulse, is also applied (RP in the time diagram in Fig.1). When a 1 is read this pulse will pass through the circuit I_5 to the corresponding place of the receiving register. When reading 0, switching does not occur; there will only be a noise pulse which terminates before the RP pulse arrives at circuit I_5, so that the recognition pulse does not pass through this gate. Thus the corresponding place in the receiving register remains in the 0 position.

The address register of $m = 5$ binary places and the receiving register of $n = 32$ binary places consists of static flip-flops employing P15 and P16 transistors. The address decoder is a two-stage unit employing D2V germanium diodes. Below we shall consider only the writing, reading and recognition circuits.

The schematic diagram of the writing, reading and recognition circuits is shown in Fig.2. In writing, the signal is applied to transistors T_2 and T_3. The resistance in the ferroelectric switching circuit in this case is low since it is determined by the resistance of the secondary windings of transformers Tr_1 and Tr_2 and the input resistance of the incoming information amplifier (through Tr_3).

Information is read by applying a reading pulse to transistor T_1. The switching current circuit consists of the secondary winding of transformer Tr_1, the capacitor electrode, the reading winding of Tr_3 and the resistance R_{b2} (since transistor T_3 is cut off and the resistance in the secondary of Tr_2 is high). The resistance of the external network in reading is determined mainly by the resistance R_{b2}. Inasmuch as in this circuit one can apply driving pulses of virtually unlimited amplitude, a very short reading time may be achieved.

Recognition of the information read is realized by means of transformer Tr_3, the secondary winding of which is connected to the input of the recognition amplifier.

The writing and reading signal amplitude can be controlled by the variable resistors R_{k1}, R_{k2} and R_{k3}, which are bypassed by capacitors (not shown in Fig. 2). Resistor R_{b1} is a ballast resistance to stabilize the writing and reading signal amplitudes with variation in the number of switching crossovers in a word.

The recognition amplifier with a resistance coupled emitter input is designed about a P16B transistor. The emitter circuit resistance $R_e \leqslant 55$ ohm. The transistor is cut off by a positive bias on the base. The voltage drop across R_e when the ferroelectric is switched is not sufficient to turn on the transistor. The recognition pulse (RP) is applied to a transformer in the base circuit; the amplitude of the signal in the secondary of the transformer is smaller than the

Fig.3. Oscillograms characterizing the operation of some of the control circuits: a) switching process in a static flip-flop (component of the address and receiving registers), b) signals in one of the lower order and one of the higher order positions of the address register, designed in the form of a binary counter with a through-carry network, c) output pulse from the writing or reading amplifier.

Fig.4. General view of the equipment with plug-in units.

bias and hence a single RP pulse does not cut in the transistor. If the ferroelectric switching current at the instant of arrival of the recognition pulse has not terminated, the RP pulse turns on the transistor and the amplifier output signal trips the flip-flop in the corresponding place in the receiving register (code 1 is read).

Oscillograms characterizing the operation of some of the elements and units described above are shown in Fig.3. A photograph of the experimental equipment designed to store 1024 32-digit words is reproduced in Fig.4.

Tests of the transistor control system showed that it can be used in conjunction with ferroelectric matrices for the construction of computer memories.

We desire to thank I.S.Zheludev for valuable assistance and advice and B.N. Perekatov for assistance in assembly and adjustment of individual units of the experimental equipment.

Institute of Crystallography,
Academy of Sciences of the USSR

Reference

1. E.I.Mamonov & I.S.Zheludev, Doklad na Vsesoyuznom soveshchanii po vychislietl'noi matematike i tekhnike (Report presented at the All-Union Conference on Computation Mathematics and Engineering), Moscow State University, 16-21 November 1959.

EQUIPMENT FOR EXPERIMENTAL INVESTIGATION OF FERROELECTRIC MATRICES WITH SEMIAUTOMATIC ADDRESS SELECTION

- E.I.Mamonov & V.G.Rzhanov

A common mode of operation of ferroelectric memory matrices consists of applying pulses of opposite polarity to appropriate electrodes in an orthogonal array. The resultant field strength produced by the pulses is made greater than the coercive field. In this mode of operation all the other memory cells, in addition to the selected one, are located along the excited electrodes and are acted on by pulses of opposite polarity (depolarizing) or identical polarity (repolarizing) according to the direction of the residual polarization in the cells. The amplitude of these pulses will be lower than the critical or threshold amplitude for switching over the limit hysteresis cycle.

For practical application of ferroelectrics as high speed memory elements it is important to determine the behavior of the ferroelectric cell under the influence of various combinations of switching pulses and partial amplitude pulses. The former are of sufficient amplitude to induce switching over the limit cycle; the latter may cause partial and undesirable changes in the residual polarization, the degree of which is of interest for specifying the operating conditions for such ferroelectric devices.

The equipment described below was developed for experimental studies of ferroelectric matrices and individual elements under conditions of pulse switching.

A block diagram of the equipment and the voltage-time diagrams characterizing its operation are given in Fig.1. The equipment consists of a synchronizing generator G, a control trigger T_1, a delay trigger T_2, an electronic delay line EDL, a one-shot multivibrator OSM for controlling the pulse sequence, two logical AND gates (I_1 - I_6), four pulse shaping Kipp oscillators KO_{1-4}, two OR gates and an output amplifier Amp. The one-shot multivabrators OSM and KO_{1-4} have provision for regulating the pulse duration and amplitude.

Peaked positive pulses (Fig.1) from the generator G are applied to the inputs of the gates I_1 and I_4. The pulses pass through the open gates I_1 and I_2 or I_3 (depending on the position of the trigger T_1) and go to the trigger of the shaping Kipp oscillators KO_1 and KO_2 which produce square pulses. Trigger T_2 is actuated by the first pulse from line 5 or 6. The switching pulse of T_2 is used to trigger the electronic delay line EDL. The delayed pulse from the delay line goes to the counting input of trigger T_1, which switches channels 5 & 6 and 12 & 13 and actuates the trigger of the one-shot multivibrator OSM. The duration of the pulse taken off the OSM (see Fig.1) should be less than two pulse repetition periods of the generator so that only one generator pulse can trigger the Kipp oscillator KO_3 or KO_4 (depending on the position of trigger T_1 and of the selector switch Sw).* Thus there is obtained at the output of gate OR_1 or OR_2 a series of positive square pulses, the amplitude of which is controlled by adjusting KO_{1-4}. Each pulse series consists of switching pulses from the Kipp oscillators KO_3 and KO_4 and N pulses from the Kipp oscillators KO_1 and KO_2. The amplitude of the latter pulses is usually made smaller than the amplitude of the switching pulses. The pulse series frequency is given by $f_{ser} = f_{gen}/2(N + 1)$, where f_{gen} is the frequency of the synchronizing pulses from the generator G, and N is the number of pulses in a series put out by the Kipp oscillators KO_1 and KO_2.

The output amplifier has one phase inverting input and combines the pulse series fed in through channels 18 and 19 into one output (Figs.1 & 2). The amplifier puts out square pulses with an amplitude of up to 200 v across a ballast load of 1 kilohm.

---

*This mode of operation is provided for by continuous regulation of the EDL delay time or/and the pulse duration from OSM.

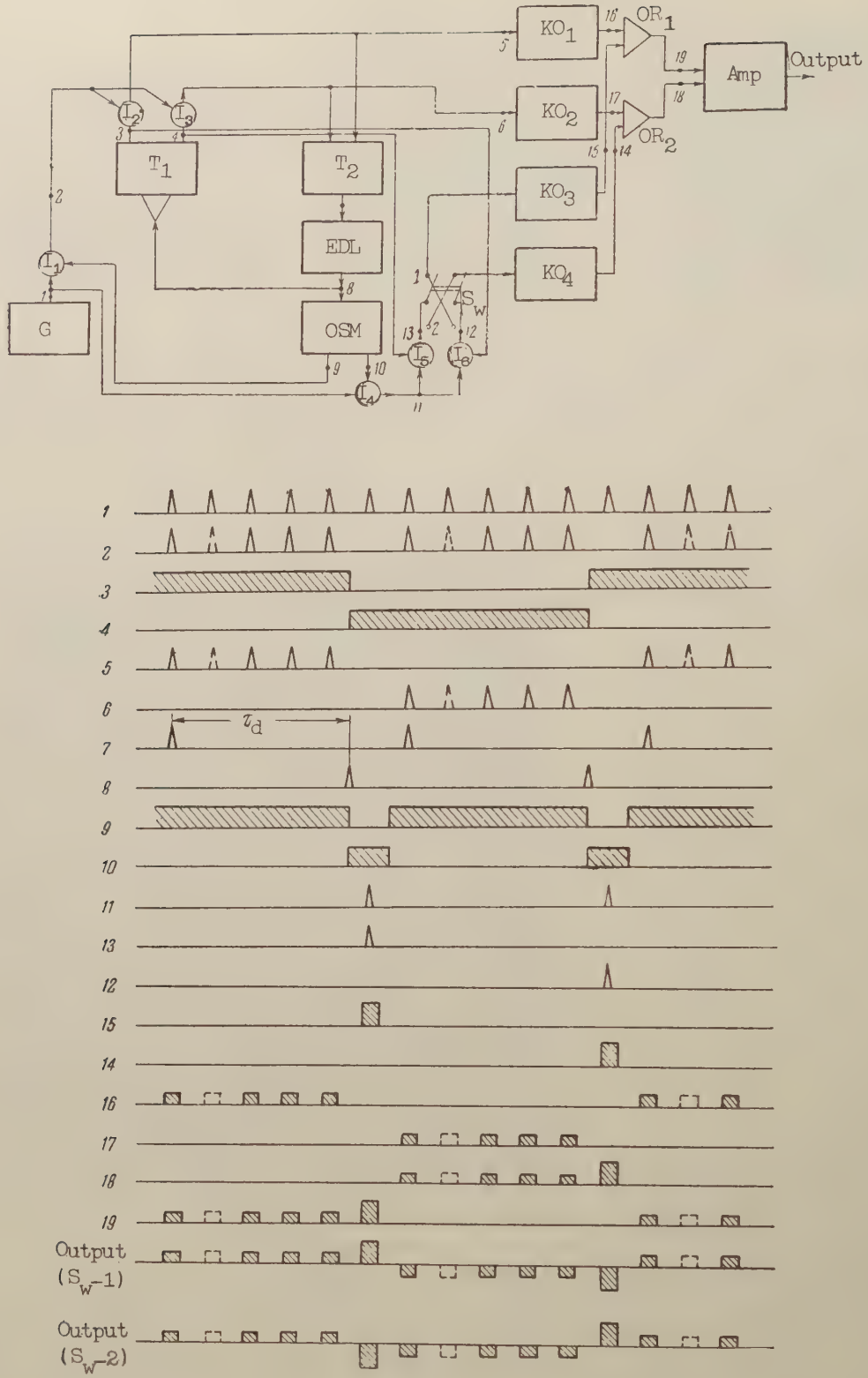

Fig.1. Block diagram of the equipment and voltage-time diagrams characterizing its operation.

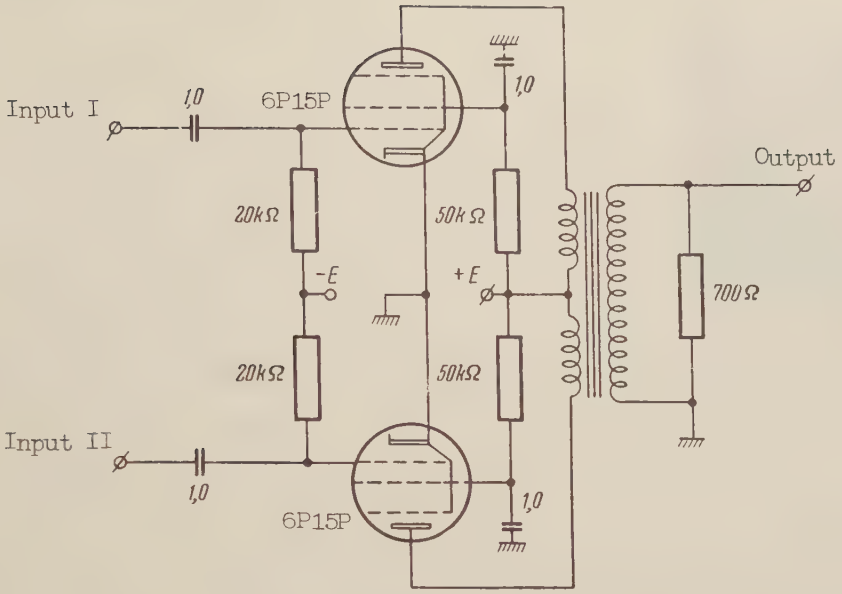

Fig.2. Output amplifier.

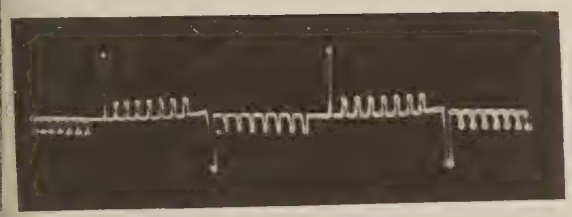

Fig.3. One type of pulse series put out by the amplifier.

The pulses (Fig.3) from the amplifier output are applied to a stepping relay selector. Two such stepping relay selectors provide for semiautomatic address selection over the X and Y coordinates of the ferroelectric matrix which has a storage capacity of up to 1024 binary digits.

Separate regulation of all the pulse magnitudes allows of obtaining the desired pulse amplitude-to-duration ratio at the output. The pulse series combinations are controlled by varying the delay τ_d and changing the position of the selector switch Sw.

The electronic delay line EDL consists of two one-shot multivibrators and has a range of delay times from 10 microsec to 10 millisec.

The individual circuits are designed in the form of standard blocks with 30-pin plug-in connectors. A general view of the instrument with a test ferroelectric matrix in place is shown in Fig.4.

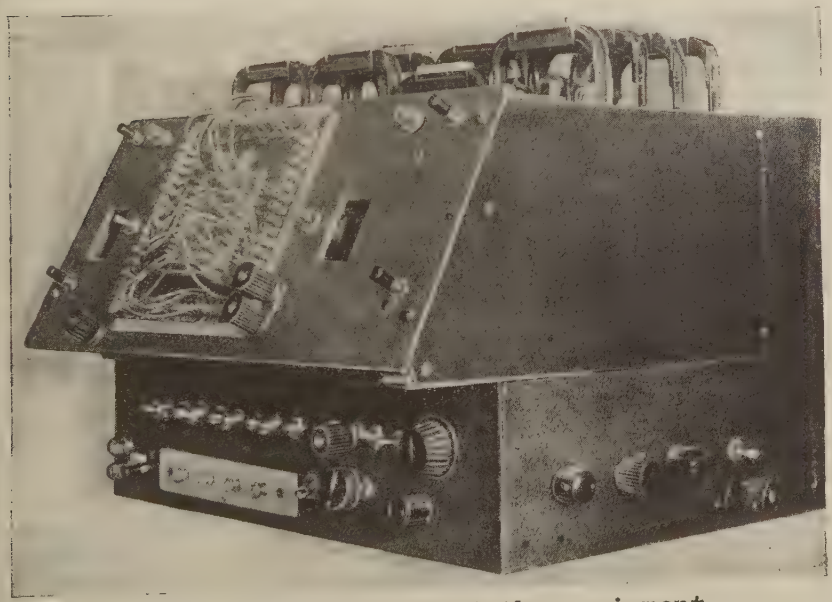

Fig.4. General view of the equipment.

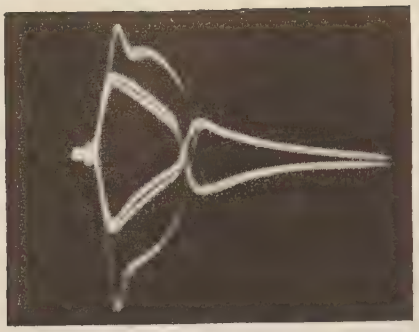

Fig.5. Oscillogram of signals at the matrix output.

The positions of the stepping relay selectors are indicated on dials that can be viewed through the windows in the front panel.

The following characteristics of ferroelectric elements and matrices can be determined by means of the described equipment:

a) the rate of switching processes and their dependence on the pulse amplitude, the pulse repetition rate, the thickness and other parameters of the matrix under different conditions;

b) values of the threshold switching field (Fig.5) under different conditions;

c) the stability of the stored information under the influence of depolarizing pulses of partial amplitude;

d) the ratio of the useful signal-to-noise and the degree of unipolarity of hysteresis;

e) the degree of uniformity of the various electric properties of the ferroelectric components;

f) the mutual influence of the switching elements;

g) other characteristics of the matrix such as fatigue, the time for attainment of the limit cycle, etc.

We desire to express our gratitude to I.S.Zheludev for valuable advice.

Institute of Crystallography,
Academy of Sciences of the USSR

SIMILAR AND DISSIMILAR FEATURES OF ANTISYMMETRY, MAGNETIC SYMMETRY AND COMPLETE SYMMETRY*

- I.S. Zheludev

Some years ago Shubnikov made an important contribution to the study of symmetry by introducing, in addition to the two forms of equality adopted in ordinary symmetry (congruent and mirror), two new forms of equality: congruent antiequality and mirror antiequality.[1] According to this generalization, the operations of congruent antiequality are used to superpose figures (or parts thereof) having a different coloration (color) by the usual rotations with subsequent change of the color to the "opposite". In turn, operations of mirror antiequality are employed to superpose figures (or parts thereof) by mirror rotations with subsequent "color inversion" (antisymmetry, black-white symmetry or ±-symmetry).

The total number of point groups obtained in this generalization proved to be 122. The 32 groups of ordinary symmetry are here considered to be "polar" groups, i.e., groups that describe the symmetry of figures having some given sign (polarity or color); 58 groups are groups of "mixed polarity", i.e., groups in which the figures may in part have "opposite" colors; finally, 32 groups are "grey" groups, i.e., groups describing figures having a neutral (grey) color or what is the same thing, devoid of color entirely.

Subsequently, Tavger & Zaitsev[2] made a generalization intended for describing the magnetic properties of crystals; this has come to be called "magnetic symmetry". The authors of this generalization utilize the indication of Landau and Lifshits to the effect that the operation of time inversion is not a symmetry operation for magnetic effects.[3] Analyses and treatments of magnetic symmetry are usually based on the fact that the operation of time inversion is not an independent symmetry operation for magnetic effects if only because magnetic moments (which can be likened to ring currents) change their direction to the opposite as a result of this operation. From this stems the contradiction between the generalization adopted in magnetic symmetry and the generalization adopted in antisymmetry. In the latter case the operation of "color inversion" of the figures is not an independent operation of antisymmetry (change of sign: operation $\underline{1}$); in the former case the operation of change of sign of the enantimorphism is not an operation of magnetic symmetry (change of the right-hand or, say, north magnetic pole to the left-hand or, say, south pole: operation R).**

Unfortunately, the generalization adopted in magnetic symmetry has not been consistently investigated to disclose its full consequences. It is impossible to determine from published treatments of magnetic symmetry precisely what meaning is attached to the transformations accomplished by the operations of antirotation and mirror antirotation in this generalization. The matter is further complicated by the fact that magnetic symmetry groups are frequently designated[4,5] by means of the same symbols that are used for designating groups of mixed polarity. Remarks that in magnetic symmetry these designations have a different meaning, without specifying this meaning clearly, hardly help clarify the matter[6,7].

The lack of clarity in defining the precise nature of the transformations adopted in magnetic symmetry leads to great difficulties and in some cases to misunderstandings in using the magnetic symmetry groups for describing the properties of crystals (including magnetic crystals).

---

*This report was presented at a seminar on the theory of ferroelectricity held April 18, 1960 in the Institute of Crystallography of the USSR Academy of Sciences.

**Operations $\underline{1}$ and R can enter into antisymmetry and magnetic symmetry, respectively, only in combination with the ordinary elements of symmetry.

The above shortcomings are not the only ones from which the generalization of magnetic symmetry suffers. From the standpoint of group theory the generalization adopted in magnetic symmetry gives nothing new compared with the generalization adopted in antisymmetry. This generalization only interprets the generalization of antisymmetry in the case of magnetic effects. At the same time, introduction of the term "magnetic symmetry" seems to be designed to emphasize the applicability of the principles of antisymmetry for describing magnetic effects. From this one might even draw the incorrect inference that inasmuch as the operation of time inversion does not change the sign of the charge, antisymmetry is inapplicable for description of electric and other similar properties of crystals.

As we noted above, the generalization that has come to be termed antisymmetry and the generalization that is called magnetic symmetry, being essentially the same generalization from the standpoint of group theory, emphasize the preeminence of one of two pairs of "opposite" quantities characterizing the properties of a figure or effect. In the antisymmetry generalization this preference is given to the sign (or color) of the figure, while in magnetic symmetry the preference is given to the sign of the enantiomorphism. In connection with this, the operation of "anti-identification" (the operation of color inversion of the figure, while retaining the sign of the enantimorphism; operation $\underline{1}$) is placed in correspondence with the operation of time inversion (operation of changing the sign of the enantiomorphism, while retaining the color of the figure; operation R or also operation $\underline{1}$). Each of these generalizations is in a sense one-sided.

Relation between the operations of antisymmetry and the operations of complete symmetry

Antisymmetry			Complete symmetry		
Operation	Transformation accomplished*	Designation of operation	Operation	Transformation accomplished	Designation of operation
Rotations	+→+ R→R	1;2;3;4...	Rotations	+→+ R→R	1;2;3;4...
Mirror rotations	+→+ R→L	$\bar{1};\bar{2};\bar{3};\bar{4}$...	Mirror rotations	+→+ R→L	$\bar{1};\bar{2};\bar{3};\bar{4}$...
Antirotations	+→- R→R	$\underline{1};\underline{2};\underline{3};\underline{4}$...	Antirotations	+→- R→L	$\underline{1};\underline{2};\underline{3};\underline{4}$...
Mirror antirotations	+→- R→L	$\underline{\bar{1}};\underline{\bar{2}};\underline{\bar{3}};\underline{\bar{4}}$...	Mirror antirotations	+→- R→R	$\underline{\bar{1}};\underline{\bar{2}};\underline{\bar{3}};\underline{\bar{4}}$...

*The symbols + and - designate "opposite" colors of parts of the figure, e.g., black and white. The letters R and L characterize the sign of the enantiomorphism of parts of the figure: right-hand and left-hand.

We felt it would be desirable to introduce a generalization which, although as compared with the generalizations of antisymmetry and magnetic symmetry is not new from the standpoint of group theory, would be free of the above mentioned one-sidedness. Such a generalization is the generalization introduced in the treatment of the symmetry of scalars, vectors and tensors.[8,9] In this generalization no preference is given to one of the pair of signs. The symmetry groups obtained in this generalization (there are also 32 + 58 = 90 such groups) we have called

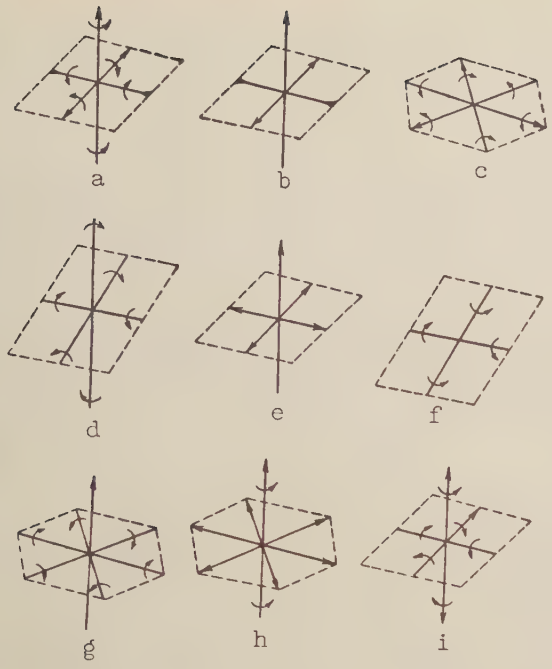

←Some groups of complete symmetry in vector and tensor interpretation:

a – $\underline{2}:2\ (L^2\ 2\ \underline{L}_2)$, e – $4\cdot m\cdot (L^4\ 4\ P)$,

b – $\underline{4}\cdot m\ (L^{2}_{\underline{4}}2\ \underline{L}_2\ 2\ P)$. f – $2\cdot \underline{m}\ (L^2\ 2\ \underline{P})$,

c – $\underline{6}:2\ (L^{3}_{6}3\ L^2 3 \underline{L}_2)$, g – $m\cdot 3:\underline{m}\ (L^{3}_{\underline{3}}3\ \underline{L}_2\ 3\ P\ \underline{P})$,

d – $m\cdot 2:\underline{m}\ (L^{2}_{2}3PC)$, h – $6:m\ (L^{6}_{\underline{6}}PC)$,

i – $4:2\ (L^4 4\ L^2)$.

Only the generating elements of symmetry are given in the symbols designating the groups (m - plane of symmetry, $\underline{m}$ - antiplane). In the parentheses we give the complete symmetry formulas (L designates the axis with the order given by the index; P - plane of symmetry, $\underline{P}$ - antiplane; C - center of symmetry; $\underline{C}$ - anticenter).

groups of complete symmetry. The principal point in this generalization is that operation $\underline{1}$ is an operation which with equal validity transforms the initial figure (or part thereof) into a figure having the opposite color (sign) and the opposite sign of enantiomorphism. (If, in a particular case, the figure has only one of these qualities, it is transformed into the opposite: plus to minus, right or left, etc.). Operation $\underline{1}$ defined in this way is equivalent to Landau's operation of combined inversion.[10] Thus the operation of combined inversion (transformation of a particle into the corresponding antiparticle in physics) is equivalent to operation $\underline{1}$, which corresponds in our terminology to transformation of the initial figure into the antifigure in symmetry. The new forms of equality following from this generalization we call anticongruent equality (equivalent to mirror antiequality in antisymmetry - see figure) and antimirror equality (equivalent to congruent antiequality). The relation between these different operations of complete symmetry and antisymmetry, the essence of the transformations involved and the designations of these operations are given in the accompanying table.

We note that the operations (antirotations and antimirror rotations) introduced in the complete symmetry generalization are actually the complete opposite to the operations in ordinary symmetry (rotations and mirror rotations) as regards the character of the transformations accomplished by them (this is the meaning of the prefix "anti-"). We also note that, for example, the operation of antimirror rotation in complete symmetry is equivalent to the operation of antirotation in antisymmetry only as regards the final result, but is not equivalent to the manner in which it is attained (in complete symmetry the transformation +→-, R→R is attained as a result of mirror rotation and change in the sign of the enantiomorphism and color, whereas in antisymmetry this transformation is realized as the result of simple rotation and "color inversion"; the analytic notations for these transformations are different). The same observation may be made regarding the equivalence of the operation of antirotation in complete symmetry and the operation of mirror antirotation in antisymmetry (see table).

To help clarify the meaning of the transformations accomplished by the operations of complete symmetry we show in the accompanying figure the geometric interpretation[11] (by means of vectors and tensors) of some of the crystallographic groups of complete symmetry. This interpretation allows of taking into account and discerning the direction of spontaneous polarization in crystals (polar-vector directions represented by a line with one arrow point at the end; see figures a, b, e and g), the directions of spontaneous magnetization (axial-vector directions represented by sections of a straight line with two like-directed circular arrows), etc.

Thus the generalization adopted in complete symmetry can be applied with equal success to the description of different effects (electric, magnetic, optical and the like) and, in particular, to description of the symmetry and distinctive properties of pyro-, ferro and antiferroelectric crystals.

Institute of Crystallography,
Academy of Sciences of the USSR

References

1. A.V.Shubnikov, Simmetriya i antisimmetriya konechnykh figur (Symmetry and antisymmetry of finite figures), M., 1951.

2. B.A.Tavger & V.N.Zaitsev, Zhur.eksp.i teor.fiz., 30, 564 (1956). (Trans. Soviet Physics - JETP.)

3. L.D.Landau & E.M.Lifshits, Elektrodinamika sploshnykh sred (Electrodynamics of continuous media), M., 1958.

4. B.A.Tavger, Kristallografiya, 3, 339 (1958). (Trans.Soviet Physics - Crystallography.)

5. L.A.Shuvalov, Ibid., 4, 399 (1959). (Trans.Ibid.)

6. B.A.Tavger, Uch.zap. (Scientific notes), Leningrad Pedagogical Inst., No.2 (1956).

7. B.A.Tavger, Kristallografiya, 3, 342 (1958). (Trans.Soviet Physics - Crystallography.)

8. I.S.Zheludev, Ibid., 5, 346 (1960). (Trans.Ibid.)

9. I.S.Zheludev, Ibid., 5, 508 (1960). (Trans.Ibid.)

10. L.D.Landau, Zhur.eksp.i teor.fiz., 32, No.2 (1957). (Trans.Soviet Physics - JETP.)

11. I.S.Zheludev, Kristallografiya, 2, 728 (1957). (Trans.Soviet Physics - Crystallography.)

ON THE USE OF LEAD AND BARIUM METANIOBATE SOLID SOLUTION PIEZOCERAMICS IN WIDE-BAND FILTERS

- E.G.Bronnikova, I.M.Larionov, N.D.Mileikovskaya, I.G.Smazhevskaya & I.A.Glozman

Until recently mainly quartz resonators have been used in the USSR and abroad for designing piezoelectric filters, while and in a number of cases specifically for wide wide-band filters there have been employed resonators of artificially grown dipotassium tartrate crystals (in the USSR) and ethylenediamine tartrate crystals (in Great Britain and the USA).

Now, progress in the search for and preparation of new ferroelectric materials with better time and temperature stability than barium titanate ceramics has made it possible to employ a new type of resonator, namely, piezoelectric resonators, in the design of filters.

The principal advantages of piezoelectric materials, provided they are stable, are the ease with which mechanically strong resonators of different configurations can be fabricated and the possibility of designing economical wide-band filters without the use of auxiliary elements.

There have been a number of papers[1-3] published abroad on the subject of designing piezoceramic resonators, piezoelectric transducers and filters. In the USA the Clevite Corporation has developed and is marketing under the brand designation PZT-6 a ceramic suitable for stable wide-band piezoceramic filters.

Among the stable piezoelectric materials available in the USSR the most thoroughly developed at present are solid solutions of lead and barium niobates[4] with different proportions of lead and barium; these are designated as KNBS 40/60, KNBS 45/55, etc. depending on the relative proportions of the two niobates. The electric characteristics of these materials and those of PZT-6 ceramic are listed in the accompanying table.

The temperature and time stabilities and the electromechanical coupling coefficients of KNBS type materials are lower than those of PZT-6 ceramic; however, the values are sufficiently high for many applications and in particular for intermediate frequency filters for radio receivers.

Such filters, depending on the class of receiver for which they are intended, must have a passband of 7 to 11 kc at a level of 3 db and a minimum damping in the attenuation band of 45 to 60 db with a rectangularity coefficient $k_r \approx 2$ referred to the 3 and 60 db levels. The allowable shift of the passband with change of temperature from 10 to 70° is ±1 kc.

The purpose of the present work was to develop filters with KNBS piezoceramic elements meeting these specifications.

Of the various known filter circuits the ladder network with L-sections appears to be the most expedient for use in conjunction with piezoceramic elements. Each section of such a filter consists of two resonators connected into a longitudinal and transverse arm as shown in Fig.1. One section allows of obtaining a symmetrical attenuation characteristic with damping peaks at the end frequencies. For obtaining a high damping factor in the attenuation band, the attenuation peaks should be located at frequencies appreciably removed from the edges of the passband, to which end the resonators in the longitudinal and transverse arms must differ somewhat from each other. In the case of piezoceramic resonators it is sufficient to have the unit parameters differ by only a factor of two; the required attenuation can be obtained by increasing the number of units. In view of the small

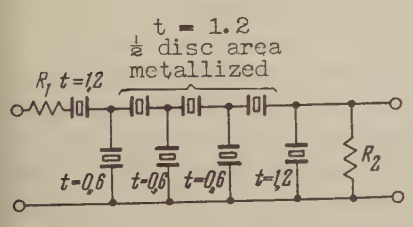

Fig.1. Diagram of 8-disk piezoceramic filter (t = = disk thickness).

Characteristics of disk resonators

Electric characteristics	PZT-6	KNBS 40/60	Parameters	PZT-6	KNBS 40/60
Electromechanical coupling coefficient, radial mode, %	45	25	Resonant frequency, kc	430	450
			Dynamic capacitance, pF	71	33
Dielectric constant	1000	1200	Dynamic inductance, mH	1.92	4
Mechanical Q	400	400-800	Static capacitance, pF	399	410
Aging (as evinced by shift of resonance frequency)	Calculated; over ~10 yrs ~0.1%	Preliminary data for 6 mo. 0.3%	Resistance, ohm	14	20-40
			Q-factor	380	500-300
Temp. coef. (degree^{-1}) in 20 to 75° range	$< 8 \cdot 10^{-6}$	40-50· ·10^{-6}	Resonance interval, %	10	3.5

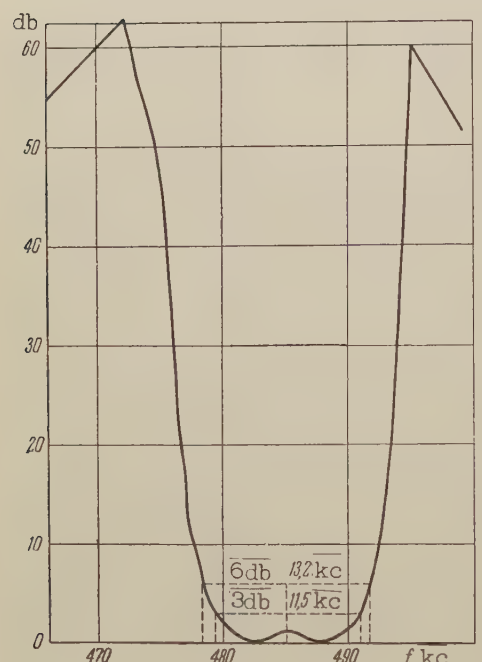

Fig.2. Operating characteristic of 8-disk piezoceramic filter.

size of piezoceramic resonators the overall dimensions of the filter still remain reasonable.

To solve the given design problem it proved expedient to use resonators oscillating at the radial mode, i.e., disks. Such disks have a single resonant frequency and at frequencies close to 465 kc (the intermediate frequency in most modern radio receivers) have a diameter smaller than 6 mm. Efficient filters can be assembled of disks of three thicknesses: 0.3, 0.6 and 1.2 mm, or of two thicknesses: 0.6 and 1.2 mm with electrodes applied either over the entire area or over half the area of the disk. The basic electric parameters of disk resonators of KNBS 40/60 (diameter 5.8 mm, thickness 0.6 mm) are given in the accompanying table. For comparison we also give the characterics of disk resonators of PZT-6 (diameter 5 mm, thickness 0.5 mm).

The experimental filters were designed in two models: in a flat and in a cylindrical case (Fig.3). Each filter consists of a stack of disks connected as indicated in the circuit diagram. The contacts between disks are realized by means of silvered copper springs, located between the disks. Insulation is provided by mica plates.

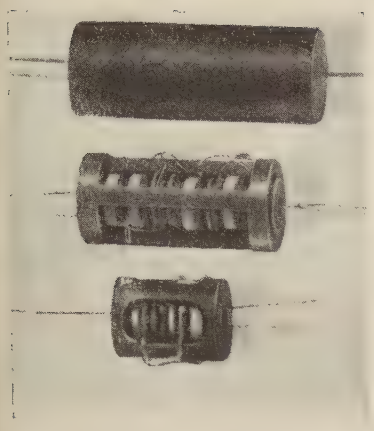

Fig.3. Prototype 8- and 4-disk piezoceramic filters.

By appropriate selection of the resonators on the basis of their resonance and antiresonance frequencies and resonance intervals we succeeded in designing four, seven, eight and ten-disk prototype filters with one and two end terminals.

Fig.2 shows the attenuation characteristic of an eight-disk filter meeting and technical specifications for intermediate-frequency filters for Class 1 receivers. The resistance characteristics of such a filter from the input and output sides are different, which is convenient for matching with transistor amplifier stages.

The attenuation characteristic of the four-disk filter falls off sharply after the maxima in the attenuation band, attaining 25 db. Such a filter can replace the intermediate frequency stage in the pocket type receivers now under development.

The volume of the eight-disk filter shown in Fig. 3 is 1.57 cm^3, the weight is 3.33 g; the volume of the four-disk filter is 0.560 cm^3, the weight 1.46 g.

We are also investigating piezoceramic resonators with other modes. The practical potentialities of such components depend entirely on success in developing a technology for preparation of elements with uniform parameters and on the extent of their aging, factors which at present have not been adequately investigated.

References

1. D.Elders & E.Gikov, Electronics Eng., 31, No.17, 59 (1958).
2. D.Curran & W.Gerber, Proc.Electronic Components Conference, Philadelphia, 1959.
3. A.Lundo, Electronics Ind., 18, 106 (1959).
4. G.A.Smolenskii, V.A.Isupov & A.I.Agranovskaya, Doklad.AN SSSR, 108, 232 (1956). (Trans.Doklady.)

Bulletin of the Academy of Sciences of the USSR - Physical Series
Vol. 24, No. 11 - November 1960

Transactions of the Third Conference on Ferroelectricity
(continued from Vol.24, No.11)

TABLE OF CONTENTS

	Page Orig.	Trans.
Temperature dependence of the infrared absorption spectra of $BaTiO_3$, $PbTiO_3$ and $PbZrO_3$ - A.F.Yatsenko	1308	1307
Some electric properties of barium titanate doped with rare earth elements - A.F.Yatsenko & T.P.Popova	1311	1310
Probing the crystal lattice field of $BaTiO_3$ with rare earth ions - A.F.Yatsenko & L.M.Rabkin	1314	1313
Preparation and some ferroelectric properties of lithium hydroselenite - V.P.Konstantinova, I.M.Sil'vestrova, L.A.Shuvalov & V.A.Yurin	1318	1317
Domain walls and etch pit networks in deuterated tri-glycine sulfate crystals - V.P.Konstantinova	1324	1323
Some electric characteristics of ammonium di-H-phosphate single crystals - I.Ya.Eisner	1326	1327
Obtaining a stable single-domain state of ferroelectrics - V.A.Yurin	1329	1329
Effect of gamma-radiation on the ferroelectric properties of tri-glycine sulfate - V.A.Yurin, A.S.Baberkin, E.N. Kornienko & I.V.Gavrilova	1334	1334
Variation of the elastic constant s'_{33} of tri-glycine sulfate crystal as a function of the dc field in the region of the Curie point - I.M.Sil'vestrova	1337	1337
Ferroelectric properties of tri-glycine sulfate single crystals in the 0.01 to 50 cps frequency range - V.M.Gurevich & I.S. Zheludev	1342	1341
Effect of ultrasound on some physical properties of Rochelle salt crystals - T.Kh.Chormonov	1347	1345
Electroluminescence of barium titanate at audio frequencies - E.V.Stauer	1350	1347
Dielectric constants of piezoceramic elements of barium titanate - S.V.Bogdanov	1353	1350

Dielectric properties of polarized ceramics in strong alternating electric fields - V.I.Zaitseva, R.E.Pasynkov, V.I.Pozern & A.M.El'gard	1357	1353
Piezoelectric properties of polarized ceramics in strong alternating fields - G.A.Velyukhanova, R.E.Pasynkov, V.I.Pozern & A.M.El'gard	1362	1358
Piezoelectric hysteresis in polycrystalline barium titanate - I.P.Kozlobaev	1366	1362
Concerning the piezoelectric effect in Varikonds - B.A. Strukov & N.D.Gavrilova	1369	1365
Nonlinear properties of ferroelectrics at microwave frequencies - V.M.Petrov	1372	1368
Ferroelectric films with a rectangular hysteresis loop - M.S.Lur'e, E.I.Vasil'eva & I.V.Ignat'eva	1376	1372
Electric conductivity of $BaTiO_3$ base solid solutions of manganese, cobalt and nickel niobates and tantalates - E.A.Stafiichuk & E.V.Sinyakov	1380	1376
Properties of some $BaTiO_3$-"$A_2B_2O_7$" type solid solutions in strong electric fields - E.V.Sinyakov & E.A.Stafiichuk	1384	1380
Dielectric properties and structure of $PbTiO_3$-$SrTiO_3$-"$Bi_{2/3}TiO_3$" solid solutions - V.Ya.Fritsberg, E.Zh.Freidenfel'd & Ya.Ya. Kruchan	1387	1383
Investigation of the effect of isomorphous replacement of Ti ions on phase transitions in $BaTiO_3$ - V.D.Komarov & E.G. Fesenko	1391	1387
Some results of an investigation of the PbO-Nb_2O_5-Nd_2O_3 system - E.G.Smazhevskaya & N.A.Podol'ner	1394	1389
Concerning the influence of low concentrations of various elements on the properties of $(Pb_{0.57}, Ba_{0.43})Nb_2O_6$ solid solutions - E.G.Smazhevskaya & V.I.Rivkin	1398	1392
Some anomalous properties of chemically pure barium titanate ceramic - A.A.Anan'eva, M.A.Ugryumova & B.V.Strizhkov	1401	1395
Dielectric and piezoelectric properties of chemically pure barium titanate ceramic - A.A.Anan'eva, B.V.Strizhkov & M.A.Ugryumova	1405	1398
Effect of doping with chromic oxide on some dielectric and piezoelectric properties of barium titanate - L.N.Kamysheva	1409	1401

Investigation of the effect of doping with chromium and bismuth oxides on the dielectric and piezoelectric properties of polycrystalline barium titanate - V.I.Moskalev & S.S.Ordan'yan 1412 1404

Some features of pulse switching of ferroelectric crystals - L.A.Shuvalov 1416 1407

Some special properties of ferroelectric elements and ferromagnetic toroids with square hysteresis loops - E.I.Mamonov & I.S.Zheludev 1421 1412

Principles and application of ferroelectric matrices for information storage in computers - E.I.Mamonov 1426 1416

Transistor circuits for automatic control of writing, reading and restoration of information in ferroelectric memory matrices - E.I.Mamonov & Yu.M.Koval'skii 1428 1418

Equipment for experimental investigation of ferroelectric matrices with semiautomatic address selection - E.I.Mamonov & V.G.Rzhanov 1432 1421

Similar and dissimilar features of antisymmetry, magnetic symmetry and complete symmetry - I.S.Zheludev 1436 1425

On the use of lead and barium metaniobate solid solution piezoceramics in wide-band filters - E.G.Bronnikova, I.M.Larionov, N.D.Mileikovskaya, E.G.Smazhevskaya & I.A.Glozman 1440 1429

Translated in 1961 by
Columbia Technical Translations,
5 Vermont Ave., White Plains, N.Y.

Transactions

of the

Tenth All-Union Conference on Nuclear Spectroscopy

(Moscow, 19-27 January 1960)

(Continued from Vol.24, Nos.3,7 & 9;
to be continued in Vol.25, No.1)

INVESTIGATION OF THE LEVEL DIAGRAM OF W^{182}

- V.S.Gvozdev, L.I.Rusinov & Yu.L.Khazov

With a view to making spin assignments for the high-lying levels of W^{182}, we measured the internal conversion coefficients (ICC) of a number of γ-transitions departing from these levels. Excited levels of W^{182} are formed in β-decay of 111-day Ta^{182}.

The internal conversion spectra were recorded on a $\pi\sqrt{2}$ β-spectrometer. The radioactive material was obtained by the $Ta^{181}(n,\gamma)Ta^{182}$ reaction. The sources were prepared of tantalum oxide, which was deposited on 4 μ thick aluminum foils.

To minimize the interference from 5-day Ta^{183}, which forms by the $Ta^{181}(n,\gamma)Ta^{182}(n,\gamma)Ta^{183}$ reaction, the measurements were started 40 days after neutron irradiation.

For investigating the internal conversion electron spectrum below 100 kev there was prepared a source having a superficial density of 0.5 mg/cm^2; for the 1000 to 1200 kev electron energy interval we used a 1.7 mg/cm^2 source and for the 820 to 960 kev interval a 13 mg/cm^2 source. The experimental conversion electron spectra are shown in Figs.1, 2 & 3.

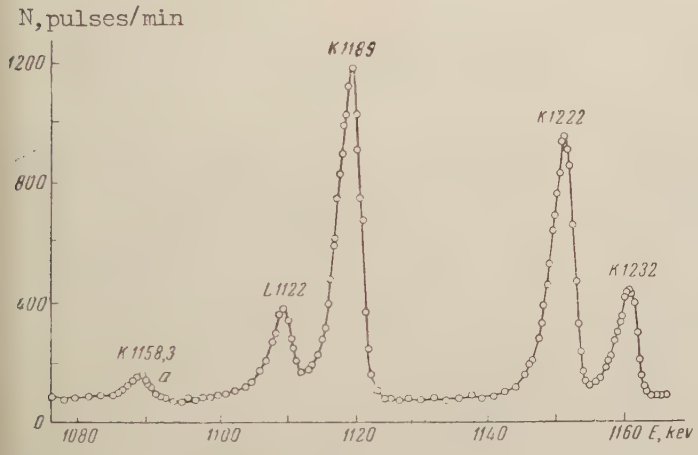

Fig.1. Conversion electron spectrum in the energy range from 1080 to 1170 kev.

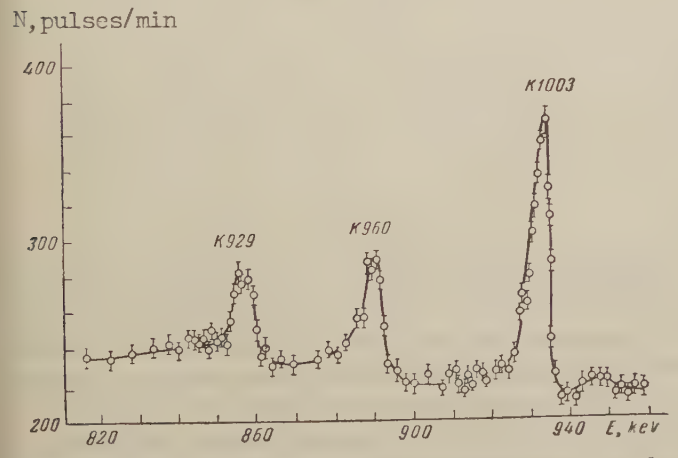

Fig.2. Conversion electron spectrum in the energy range from 820 to 960 kev.

In investigating the conversion electron spectrum there was detected a conversion line at 1088.8 kev (line *a* in Fig.1). For a γ-transition energy of ~1100 kev the value of the K/L ratio for all multipole orders is not less than 3.[1,2] The fact that there was not evinced in the conversion spectrum a second more intense line that could be identified as the K line of the same transition gives reason to infer that the *a* line is the K line of a γ-transition of 1158.3 kev energy (rather than an L line). According to Murray et al[3], a γ-transition of approximately this energy arrives at the 100.1 kev level of W^{182}. Consequently, the departure level of the 1158.3 kev transition is located at 1258.4 kev. Murray et al[3] placed this level at 1255 kev. The data of Fowler et al[4] are in agreement with our results.

Our experimental values for the K shell ICC for a number of γ-transitions in W^{182} and the theoretical values of the ICC for different multipole orders according to the tables of Sliv & Band[8] are listed in Table 1. The ICC were determined by comparing the intensities of the conversion electrons and γ-rays associated with the investigated transitions with the intensity of the conversion electrons

Table 1

Internal conversion coefficients and multipole order assignments for the transitions in W^{182}

γ-Transition energy, kev	Theoretical values of α_K						Electron energy	γ-ray intensity	Experimental value of α_K	Multipole order assignment
	E1	E2	E3	M1	M2	M3				
929	0,0018	0,0045	0,0094	0,0096	0,025	0,049	4,76	3±2	0,006 ±0,004	E2
960	0,00175	0,0042	0,0086	0,0087	0,0240	0,044	4,57	2,5±1,5	0,007 ±0,005	E3
1003	0,00146	0,00356	0,0075	0,00769	0,0188	0,0361	6,80	9±3	0,003 ±0,001	E2
1122	0,00123	0,0030	0,0062	0,0061	0,0142	0,0275	100	100	0,0039±0,0002	E2 (+M1)
1158,3	0,00116	0,00285	0,0059	0,0057	0,0133	0,026	5,0	7,1*	0,0027±0,0003	E2
1189	0,00112	0,00275	0,0056	0,0055	0,0128	0,024	64,2	56,8*	0,0043±0,0002	E3 or E1+M2
1222		0,0026					56,2	84±8		E2
1232	0,00104	0,00252	0,0052	0,0049	0,0112	0,0215	21,9	35±10	0,0024±0,0008	E2

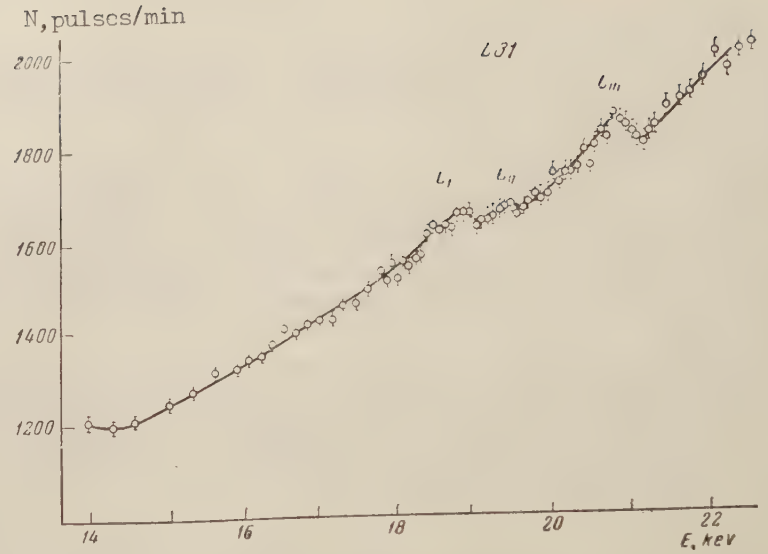

Fig.3. Conversion electron spectrum in the energy range from 14 to 23 kev.

and γ-rays of the 1222 kev transition. The multipole order of this γ-transition is E2 inasmuch as it is a $2^+ \rightarrow 0^+$ transition; for it we assumed the tabular value of 0.0026 for α_K.[1] The γ-ray intensities followed by an asterisk in Table 1 were taken from the work of Sumbaev[5]; the other intensities were taken from the report of Voinova, Dzhelepov & Zhukovskii[6].

With a view to more detailed investigation of the level scheme of W^{182} (Fig.4), in addition to the high energy γ-transitions, we also investigated the 31 kev transition. This transition occurs between excited levels with energies of 1289 and 1258.4 kev. The spectrum of the L shell conversion electrons associated with this transition is shown in Fig.3. The $(L_I + L_{II})/L_{III}$ ratio for this transition proved to be 2.1 ± 0.1. The theoretical values of the $(L_I + L_{II})/L_{III}$ ratio for E1, E2, E3, M1, M2 and M3 type transitions are 1.65, 0.88, 0.88, 89, 2.1 and 0.2, respectively.[2] Consequently, the 31 kev transition is M2.

It will be evident from the results listed in Table 1 that the 929 and 1158.3 kev transitions are both E2. On the basis of these data and the inferred multipole order of the 31 kev transition it must be concluded that the 1258.4 kev level has even rather than odd parity, as assumed by Murray et al[3]. The assignment for this level must be either 2^+ or 3^+. The 2^+ assignment is more probable inasmuch as the intensity of the 1258.4 kev cross-over transition to the ground state is not more than 2-3 times lower than the intensity of the 1158.3 kev transition.

Table 2

Comparison of the experimental and theoretical ratios of the reduced probabilities for γ-transitions from common levels

Common departure level, energy and spin & parity	γ-transition energy, kev	Spin & parity of final state	Experimental B(E2) ratio	Theoretical B(E2) ratios*			
				acc. to Davydov	acc. Alaga's rule		
					$K=0$	$K=1$	$K=2$
1222	893	4^+	$\leqslant 0{,}06$	0,2	2,58	1,145	0,07
2^+	1122	2^+	1,85	2,0	1,43	0,36	1,43
	1222	0^+	1,0	1,0	1,0	1,0	1,0
1332	1003	4^+	0,63	0,8	0	2,5	0,4
3^+	1232	2^+	1,0	1,0	0	1,0	1,0
1258,4	929	4^+	1,55	$I=2$ 0,1	1,8	3,23	0,049
				$I=3$ 0,8	0	2,5	0,4
2^+	1158,3	2^+	1,0	$I=2$ 1,0	1,0	1,0	1,0
				$I=3$ 1,0	0	1,0	1,0

*The reduced probability for the highest energy transition in each group is taken as unity.

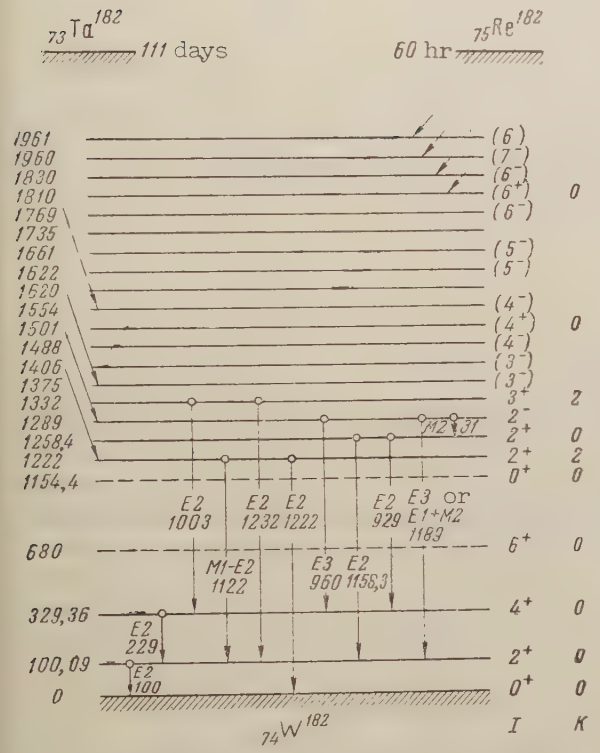

Fig.4. Level diagram for W^{182}.

From the internal conversion electron intensity ratios and the multipole orders of the γ-transitions listed in Table 1 one can calculate the ratio of the reduced probabilities B(E2) for the γ-transitions departing from common levels, namely, for the 929 and 1158.3 kev transitions departing from the 1258.4 kev level, the 1003 and 1232 kev transitions from the 1332 kev level, and the 1122 and 1222 kev transitions from the 1222 kev level. Since a transition of 893 kev energy from the 1222 kev level has not been observed, for it we give only the upper bound of the reduced probability ratio. In addition to the experimentally deduced reduced probability ratios, in Table 2 we also list the theoretical ratios calculated according to the data of Davydov & Filippov[7,8] and by means of Alaga's rule[9]. In Table 2 the reduced probability B(E2) for the highest energy γ-transition in each group is taken as unity.

As will be evident from Table 2, the experimental values of the B(E2) ratios for the 1122 and 1222 kev and the 1003 and 1232 kev transitions agree with the theoretical values calculated according to the data of Davydov & Filippov. For the 893 kev transition, however, there is a substantial divergence. This gives reason to question Davydov's inference that the 1222 kev level is a rotational level of a nonaxial nucleus.

Comparison of the experimental B(E2) ratios with the ratios for the same γ-transitions calculated according to Alaga's rule shows that best agreement of theory with experiment obtains if one assumes K = 2 for the 1222 and 1332 kev levels. From the standpoint of the unified model, excited nuclear states with energies $\gtrsim$1 Mev with $I = K = 2^+$ are interpreted as γ-vibrational states. In the case of W^{182} such an excited state is the level at 1222 kev ($I = 2^+$, $K = 2^+$).

The excited level at 1332 kev ($I = 3^+$, $K = 2^+$) should then be interpreted as the first rotational state of a band based on the 1222 kev level. The higher rotational states of this band should have spins 4^+, 5^+,....

Comparison of the experimental B(E2) ratios and the ratios calculated according to Davydov & Filippov for the 929 and 1158.3 kev γ-transitions indicates that the level at 1258.4 kev cannot be regarded as a rotational level of a nonaxial nucleus. Comparison of the experimental values with the results of calculations according to Alaga's rule gives reason to choose the assignments $I = 2$ and $K = 0$ for this level. On the basis of these values of I and K and the B(E2) ratios for the 929 and 1158.3 kev transitions, the 1258.4 kev level must be regarded as the first rotational level of a band based on a β-vibrational level with $I = 0^+$ and $K = 0^+$. The following excited levels of this band should have spins 4^+, 6^+,.... Gallagher & Rasmussen[10] indicate that in W^{182} there is an excited level with an energy of 1500.8 kev ($I = 4^+$). If we assume that this level is the next rotational level of the hypothesized band, one can calculate the energies of the levels with spins 0^+ and 6^+. Such calculations yielded values of 1154.4 and 1882.4 kev, respectively. No level with an energy of 1154,4 kev was detected either by Gallagher & Rasmussen[10] or in our work; this may be explained by the low probability for its formation in K capture in Re^{182} and β-decay of Ta^{182}, and also as a result of cascade γ-transitions in W^{182}.

Gallagher & Rasmussen[10] observed in W^{182} excited levels with energies of 1810.1 (6^+) and 1961.3 kev (spin 6). One of these levels (probably the former) may tentatively be identified as the 6^+ rotational level of the hypothesized band.

We take pleasure in acknowledging our gratitude to D.A.Varshalovich for valuable discussions.

Physical-Technical Institute,
Academy of Sciences of the USSR

References

1. L.A.Sliv & I.M.Band, Tablitsy koeffitsientov vnutrennei konversii gamma-izlucheniya Ch.I, K-obolochka (Tables of Internal Conversion Coefficients, Part I - K shell), M.-L., 1956.

2. L.A.Sliv & I.M.Band, Tablitsy koeffitsientov vnytrennei konversii gamma-izlucheniya Ch.II, L-obolochka (Tables of Internal Conversion Coefficients, Part II - L shell), M.-L., 1958.

3. J.Murray, F.Boehm, P.Marmier & J.DuMond, Phys.Rev., 97, 1007 (1955).

4. C.Fowler, H.Kruse, V.Keshishian, R.Klotz & G.Mellor, Ibid., 94, 1082 (1954

5. O.I.Sumbaev, Izv.AN SSSR, Ser.fiz., 21, 987 (1957). (Trans.Bulletin, 21, 989).

6. N.A.Voinova, B.S.Dzhelepov & N.N.Zhukovskii, Ibid., 23, 828 (1959). (Trans Bulletin, 23, 822.)

7. A.S.Davydov & G.F.Filippov, Zhur.eksp.i teor.fiz., 35, 440 (1958). (Trans. Soviet Physics - JETP.)

8. A.S.Davydov & G.F.Filippov. Ibid., 36, 1788 (1959). (Trans.Ibid.)

9. G.Alaga, K.Alder, A.Bohr & B.Motelson, Kgl.Danske Videnskab Selskab, Mat.-fys.Medd., 29, No.9 (1955).

10. C.J.Gallagher,Jr. & J.O.Rasmussen, Phys.Rev., 112, 1730 (1958).

INVESTIGATION OF $Bi^{212} \rightarrow Po^{212}$ DECAY BY MEANS OF α-γ AND γ-γ COINCIDENCES

- Yu.P.Gangrskii, G.M.Gusinskii & I.Kh.Lemberg

Polonium 212 (ThC') is of great interest from the standpoint of nuclear spectroscopy inasmuch as this nucleus has two protons and two neutrons outside the closed shells. Investigation of the levels of Po^{212}, however, presents great difficulties. This nucleus is α-active with a period of $3 \cdot 10^{-7}$ sec; consequently, for investigating it one cannot use a number of the usual techniques such as Coulomb excitation, resonance scattering and inelastic neutron scattering.

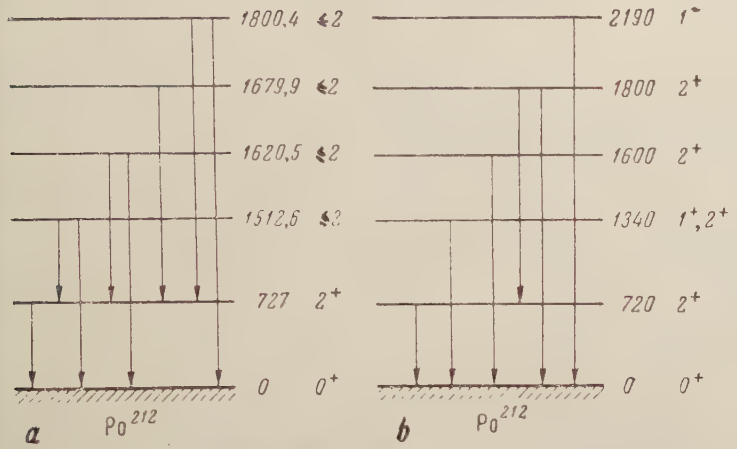

Fig.1. Level diagrams for Po^{212}: a) diagram given by Sergeev et al[1], b) diagram according to Burde & Rozner[2].

A natural source of information is β-decay of Bi^{212} (ThC), which goes both to the ground state and to a number of excited states of Po^{212}. In addition to β-decay, however, Bi^{212} also undergoes α-decay, converting to Tl^{208} which in turn decays to Pb^{208}; the γ- and β-spectra of Bi^{212} are very complex (over 20 γ-lines and more than 10 β-transitions), while the γ-lines associated with Po^{212} are of comparatively low intensity, inasmuch as the β-decay of Bi^{212} proceeds mainly to the ground state of Po^{212}. Consequently, despite the large number of investigations devoted to Bi^{212}, the level scheme for Po^{212} has not yet been definitively established. In recent reports devoted to the subject there are reproduced level schemes differing markedly from each other. Fig.1,a shows the level scheme for Po^{212} obtained by Sergeev et al[1] as the result of investigation of the conversion electron spectrum of Bi^{212}; Fig.1,b gives a diagram of the levels evinced, according to Burde & Rozner[2], in β-decay of Bi^{212}. It will be evident that there is good agreement only for two levels, namely, ~727 and 1800 kev. Some information can be gained from investigation of the long-range α-particles from Po^{212}. Rytz[3] observed three groups of long-range α-particles with energies of 9.488, 10.417 and 10.536 Mev. Inasmuch as the energy of the α-particles from the ground state of Po^{212} is 8.777 Mev, the above mentioned α-particle groups must be emitted from levels at 727, 1678 and 1800 kev.

Investigation of α-γ and γ-γ coincidences

In investigating the γ-spectrum of Bi^{212} we utilized the fact that the daughter isotope, Po^{212}, has a very short period - $3 \cdot 10^{-7}$ sec. The lowest energy of the α-particles emitted by Po^{212} is 8.78 Mev, so that its α-particles can readily be separated from the α-particles emitted by Bi^{212}, the energy of which does not exceed 6.09 Mev. Consequently, the γ-rays emitted from excited levels of Po^{212} will exhibit coincidences with α-particles from this nucleus. In our work we investigated the spectrum of Bi^{212} γ-rays coinciding in time with the 8.78 Mev α-particles. The resolving time of our coincidence circuit was $2 \cdot 10^{-6}$ sec, which is seven times longer than the lifetime of Po^{212}, so that the coincidence detecting efficiency was close to 100%. The α-particles were detected by a 2 mm thick CsI(Tl) crystal; the γ-rays by a 40 x 40 mm NaI(Tl) crystal. The α-γ coincidence spectrum recorded by means of a 52-channel pulse height analyzer is shown in Fig.2.

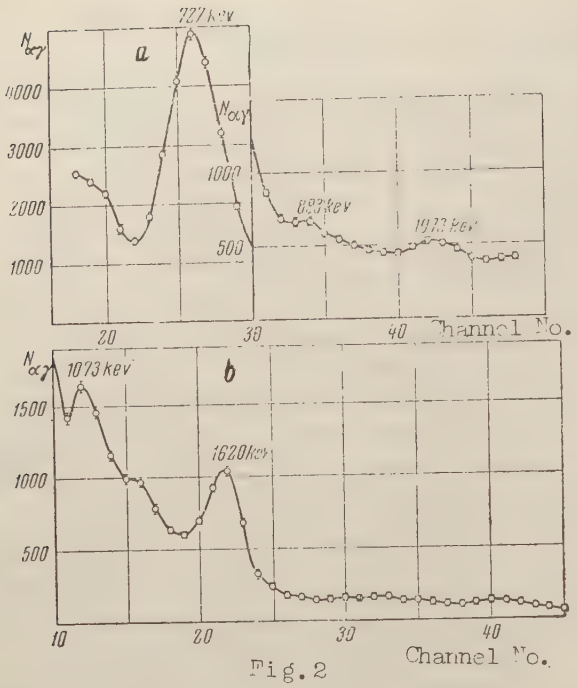

Fig.2

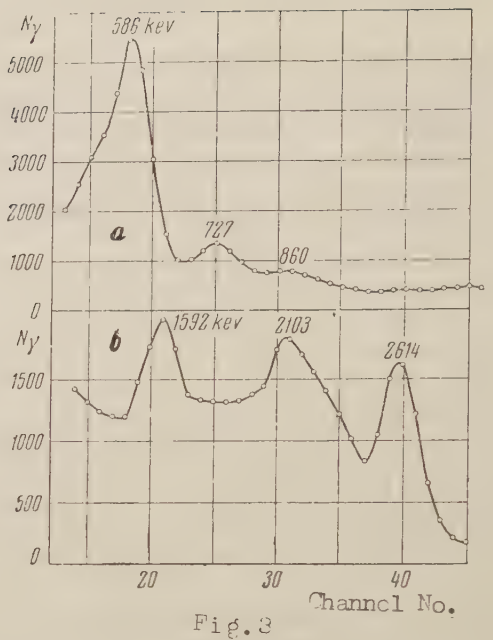

Fig.3

Fig.2. γ-Rays of Bi^{212} yielding coincidences with 8.78 Mev α-particles: a) 500 to 1200 kev region, b) 1200 to 2600 kev region.
Fig.3. Singles γ-spectrum of Bi^{212}: a) 500 to 1200 kev region, b) 1200 to 2600 kev region.

For comparison in Fig.3 we show the γ-spectrum of Bi^{212} recorded on a single scintillation spectrometer. It will be evident from Fig.2 that by means of the α-γ coincidence procedure one can clearly separate four lines of Po^{212} with energies of 727, 893, 1073 and 1620 kev from the background of the complex γ-spectrum of Bi^{212}.

We also investigated the spectrum of γ-rays in coincidence with the 727 kev gammas (Fig.4). In this spectrum there appear γ-lines with energies of 585, 727, 786, 860, 893, 952 and 1073 kev. Obviously, not all these lines belong to Po^{212} inasmuch as the 727 kev line on which the discriminator channel was set appears against the background of the rather intense 2614 kev line belonging to Pb^{208}. Consequently, some of the detected γ-transitions occur in Pb^{208}. To check this, the discriminator gate was set at 1200 kev. In the resultant spectrum (Fig. 5) there appear lines with energies of 586 and 860 kev which obviously belong to Pb^{208}. The other γ-lines do not appear in this spectrum; hence they may be attributed to Po^{212}. Knowing the efficiency of the NaI(Tl) crystal for detecting γ-rays of different energies, we could readily determine the intensity of the 786, 893, 952 and 1073 kev lines relative to the 727 kev line. These data are given in Table 1. We could also readily calcu-

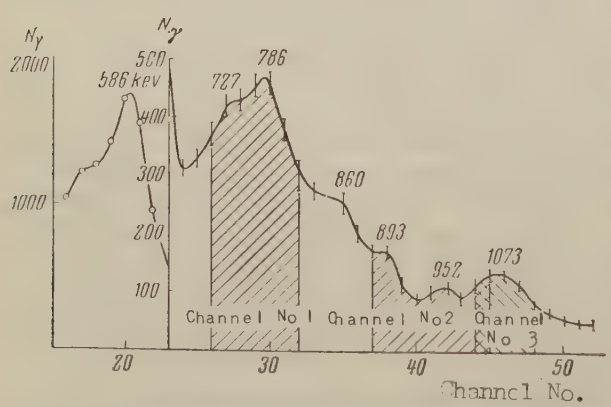

Fig.4. Spectrum of γ-rays yielding coincidences with the 727 kev γ-rays of Po^{212}.

Table 1

Energies and intensities of γ-rays corresponding to transitions in Po^{212}

γ-ray energy, kev	Intensity relative to 727 kev γ-rays, %	No. of γ-rays per 100 decays
727	100	10
786	10	1
893	2	0,2
952	1,5	0,15
1073	5	0,5
1620	20	2

Table 2

Intensities of Bi^{212} β-spectrum components

β-decay energy, kev	Arrival level, kev	Intensity, %	log ft
2250	0	87,8	7,3
1523	727	8,35	7,6
738	1513	1	7,4
630	1620	2,2	6,8
571	1679	0,15	7,9
450	1800	0,5	7,1

Table 3

Conversion coefficients and multipole orders of the transitions in Po^{212}

Transition energy, kev	Intensity per 100 decays: Conver. electr.	Intensity per 100 decays: γ-rays	α_K exp	α_K theo: E1	M1	E2	M2	Multipole order
727	0,1	10	0,01	0,0036	0,035	0,0096	0,084	*E2*
786	0,05	1,0	0,05	0,0030	0,034	0,009	0,08	*M1*
893	0,014	0,2	0,07	0,0025	0,020	0,0075	0,06	—
952	0,01	0,15	0,07	0,0020	0,018	0,0060	0,05	—
1073	0,006	0,5	0,01	0,0018	0,016	0,0056	0,038	*E2+M1*
1620	0,013	2,0	0,0065	0,0011	0,0057	0,0027	0,013	*M1*

late the number of γ-rays of given energy per decay, i.e., per α-particle, from the simple relationship

$$\frac{N_{\gamma_0}}{N_{\alpha_0}} = \frac{N_{\alpha\gamma}}{N_\alpha \varepsilon_\gamma},$$

where N_{γ_0} is the number of γ-rays of given energy emitted by Bi^{212}, N_{α_0} is the number of α-particles emitted by Po^{212}, N_α is the number of α-particles detected, $N_{\alpha\gamma}$ is the number of γ-rays of given energy detected in coincidences with the α-particles, and ε_γ is the efficiency in detecting the γ-rays of given energy. The values of $N_{\gamma_0}/N_{\alpha_0}$ for all the γ-rays are also listed in Table 1.

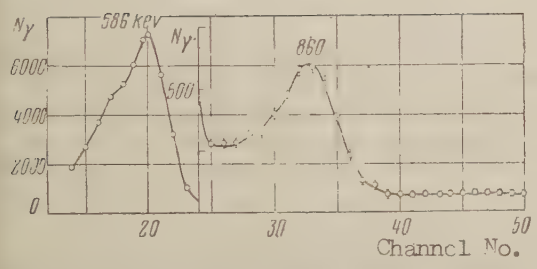

Fig.5. Spectrum of γ-rays yielding coincidences with ~1200 kev γ-rays.

Using these data one can readily construct the level diagram for Po^{212}: the 727 kev γ-rays, being the most intense and yielding coincidences with the other γ-rays, presumably correspond to the transition from the first level of Po^{212} to the ground state. The 786, 893, 952 and 1073 kev γ-rays correspond to transitions from levels at 1513, 1620, 1679 and 1800 to the first level at 727 kev; the 1620 kev line corresponds to a cross-over transition from the 1620 kev level to the ground state. The levels deduced in this manner are in complete agreement with the levels reported by Sergeev et al[1] (Fig.1,a), but do not correspond to the levels inferred from the work of Burde & Rozner[2] (Fig.1,b).

Knowing the number of γ-rays per decay one can readily determine the fraction of β-transitions to the corresponding levels of Po^{212}. These data are listed

in Table 2. All the log ft values are of the same order of magnitude and correspond to first forbidden β-transitions. Such transitions involve a change in parity and a change in spin not exceeding two units ($\Delta I \leq 2$, yes). It is known[1] that the ground state spin of Bi^{212} is 1-. Hence the assignment for the excited levels of Po^{212} may be 0^+, 1^+, 2^+ or 3^+.

The relative intensities of the lines in the conversion electron spectrum of Po^{212} are given in the work of Sergeev et al. Using these in conjunction with the relative intensities of the γ-rays determined in the present investigation, we could readily calculate the conversion coefficients for the transitions in Po^{212}. The values of the conversion coefficients found in this manner together with the theoretical values for different multipole orders as given in the tables of Sliv and Band[5] are listed in Table 3.

From a comparison of the experimental conversion coefficients with the theoretical ones, it is evident that the 727 kev transition is E2; the 1073 kev transition is a mixture of E2 and M1 and the 786 and 1620 kev transitions are both M1. The values of α_K for the 893 and 952 kev transitions involve a great uncertainty inasmuch as the corresponding γ-rays are the least intense in the spectrum. Consequently, one cannot safely make multipole order assignments for these transitions on the basis of the experimental α_K values.

Investigation of γ-γ angular correlation

With a view to determining the level spins and transition multipolarities we investigated the angular correlation of the 786—727 and 1073—727 kev cascade γ-rays. The experimental set-up consisted of two scintillation counters with 40 x x 40 NaI(Tl) crystals coupled to FEU-11 photomultipliers connected to a fast-slow coincidence circuit with a resolving time of $2 \cdot 10^{-8}$ sec. The side surfaces of the crystals were covered with 1 cm lead in order to shield the crystals from scattered γ-rays. The front faces of the crystals were located at a distance of 70 mm from the source. The angular resolution of the counters (half-width of the annihilation line with a Zn^{65} source) was 25°.

In investigating the 786—727 kev cascade, the position of the discriminator channel (channel No.1) was the same for both counters (Fig.4). It will be evident from Fig.4 that about half the spectrum is occupied by the integral 727—786 kev peak, while the other half is taken up by the background from the 860, 893, 952, 1073 and 2614 kev γ-lines. Under these conditions, the contribution from these higher energy γ-rays distorts the angular correlation of the γ-rays of interest to us.

In order to allow for this contribution we used a third discriminator, the channel of which (channel 2) was set so that it would receive sections of the photopeaks or Compton distributions of the background γ-lines. Inasmuch as their intensities in both channels were approximately equal, the difference between the number of coincidences in channels Nos.1 and 2 represented the sought effect.

In investigating the 1073—727 kev cascade, the channel of one discriminator was set on the 727 kev line (channel No.1), while the other was set on the 1073 kev γ-line (channel No.3). It will be evident from Fig.4 that the 1073 kev γ-line appears against a background equal to the effect.

Hence, as in the preceding case, the channel of the third discriminator was set to the right of the 1073 kev peak and the sought effect determined as the difference between the number of coincidences in these channels.

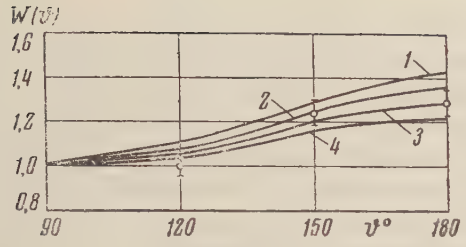

Fig.6

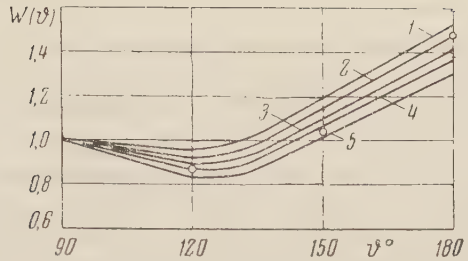

Fig.7

Fig.6. γ-γ angular correlation; 786—727 kev cascade. The curves are plotted for 2—2—0 type transitions: 1) $\delta = 0$, 2) $\delta = -0.05$, 3) $\delta = -0.1$, 4) $\delta = -0.125$.

Fig.7. γ-γ angular correlation; 1073—727 kev cascade. The curves are plotted for 2—2—0 type transitions: 1) $\delta = 2$, 2) $\delta = 2.5$, 3) $\delta = 3$, 4) $\delta = 3.5$, 5) $\delta = 5$.

The results of the γ-γ angular correlation measurements are shown in Figs. 6 & 7. It follows from the value of the conversion coefficients for the 727 kev transition and the systematics of the first levels of even-even nuclei that the assignment for the 727 kev level is 2+. It follows from the probabilities for β-transitions to the 1513 and 1800 kev levels that the spins of these levels can have the values 0+, 1+, 2+ and 3+. It is known that long-range α-particles are emitted from the 1800 kev level; consequently, in view of conservation of total angular momentum and parity in α-decay one can eliminate the second and last possibilities so there remain only the assignments 0+ and 2+.

For purposes of comparison with the experimental results there were calculated, according to the data of Biedenharm & Rose[6], the theoretical γ-γ angular correlation functions

$$W(\vartheta) = 1 + \alpha_2\beta_2 a_2 \cdot P_2(\cos\vartheta) + \alpha_4\beta_4 a_4 P_4(\cos\vartheta),$$

where the $P_{2,4}(\cos\vartheta)$ are Legendre polynomials, $a_{2,4}$ are the polynomial coefficients, and $\alpha_{2,4}$ and $\beta_{2,4}$ are correction coefficients for the angular resolution of both counters. The coefficients $\alpha_{2,4}$ and $\beta_{2,4}$ were calculated by the method described by Alkhazov et al[7]. The $W(\vartheta)$ functions were calculated for the spin sequences 0—2—0, 1—2—0, 2—2—0 and 3—2—0. In the first case both transitions are E2, while in the other cases the first transition may be E2, M1 or a mixture of E2 + M1. In these cases the functions were calculated for pure E2 and M1 transitions and for a mixture. As will be evident from Figs.6 & 7, comparison of the calculated $W(\vartheta)$ functions with the experimental data shows that the spin sequence consistent with the 786—727 kev cascade is 2—2—0. The 786 kev transition is mixed with an E2 to M1 intensity ratio characterized by $\delta^2 = 0.01 \pm 0.005$, and $\delta < 0$. The spin sequence corresponding to the 1073—727 cascade is 2—2—0 with the mixture being characterized by $\delta^2 = 10 \pm 6$ and $\delta > 0$. The experimental data for both cascades cannot be reconciled with spin sequences 1—2—0 or 3—2—0 for any values of δ. Thus as a result of our investigation of the γ-γ angular correlation it may be concluded that the assignment for the 1512 and 1800 kev levels is 2+. The cascade transition from the 1512 kev level is mainly M1 ($E2 \leqslant 1\%$), while the transition from the 1800 kev level is mainly E2 ($M1 \approx 10\%$).

Level lifetimes

The lifetimes of the levels from which α-particles are emitted can be evaluated on the basis of the data on the long-range α-particles. The number of γ-rays or α-particles emitted from a given level is inversely proportional to the partial lifetime of the level with respect to the given type of decay, i.e., $N_\gamma/N_\alpha = \tau_\alpha/\tau_\gamma$, where N_γ is the number of γ-rays and N_α is the number of α-particles emitted, and τ_γ and τ_α are the partial γ-decay and α-decay lifetimes of the level. Usually, $N_\gamma \gg N_\alpha$, hence $\tau_\gamma \ll \tau_\alpha$, and the lifetime of the level as a whole is determined by τ_γ. The values of τ_α can be found from the α-spectrum systematics. For transitions between the ground states of even-even nuclei the variation of τ_α with the α-decay energy E_α is a smooth function, inasmuch as in this case the spin does not change and there are no factors speeding up or retarding the decay. In our case long-range α-particles are emitted from excited levels of Po^{212} and the change in spin is 2. Rasmussen[8], however, systematized transitions with $\Delta I = 2$ and showed that in this case the probability for α-decay is close to the probability for α-decay between ground states, i.e., without change of spin. Hence, for determining τ_α one can use the values of E_α for transitions between the ground states of even-even nuclei. We found the values of τ_α from the rectilinear plot of $\log \tau_\alpha = (a/\sqrt{E_\alpha}) + b$. The calculated values of τ_α and τ_γ are given in Table 4. For the α-particle groups emitted from the 1512 and 1620 kev levels there are given the upper bounds for the intensity (1.7 α-particles per 10^6 decays); hence for these levels we list only the upper bounds of their lifetimes.

The measured lifetimes may be compared with the lifetimes calculated according to the single-particle model. The values of τ_γ calculated for different transition multipolarities are listed in Table 5.

Table 4

Lifetimes τ of the excited states of Po^{212}

Level, kev	E_α, Mev	N_α	τ_α, sec	τ_γ, sec
727	9,700	$35 \cdot 10^{-6}$	$7 \cdot 10^{-9}$	$2{,}5 \cdot 10^{-12}$
1512	10,480	$<1{,}7 \cdot 10^{-6}$	$6 \cdot 10^{-10}$	$<10^{-13}$
1620	10,590	$<1{,}7 \cdot 10^{-6}$	$2 \cdot 10^{-10}$	$<10^{-14}$
1679	10,650	$20 \cdot 10^{-6}$	10^{-10}	$1{,}3 \cdot 10^{-12}$
1800	10,780	$170 \cdot 10^{-6}$	$6 \cdot 10^{-11}$	$2 \cdot 10^{-12}$

Table 5

Calculated values of τ_γ for different multipole orders

Energy, kev		τ_γ, sec		
Level	Trans.	*E1*	*M1*	*E*
727	727	$5 \cdot 10^{-16}$	$1{,}4 \cdot 10^{-13}$	$5{,}5 \cdot 10^{-11}$
1512	786	$4 \cdot 10^{-16}$	$0{,}7 \cdot 10^{-13}$	$3{,}7 \cdot 10^{-11}$
1620	893	$2{,}5 \cdot 10^{-16}$	$0{,}5 \cdot 10^{-13}$	$2 \cdot 10^{-11}$
	1620	$0{,}5 \cdot 10^{-16}$	$0{,}8 \cdot 10^{-14}$	$1{,}1 \cdot 10^{-12}$
1679	952	$2 \cdot 10^{-16}$	$0{,}4 \cdot 10^{-13}$	$1{,}4 \cdot 10^{-11}$
1800	1073	$1{,}5 \cdot 10^{-16}$	$0{,}3 \cdot 10^{-13}$	$8 \cdot 10^{-12}$

It was found from the γ-γ angular correlation data and the values of the conversion coefficient that the 727 kev transition is E2. From a comparison of experimental and theoretical values of τ_γ it will be evident that this transition is speeded up by a factor of 20, which is characteristic of transitions from the first levels of even-even nuclei. The measured lifetimes of the 1679 and 1800 kev levels are in agreement with the theoretical lifetimes calculated on the assumption that the transitions from these levels to the first level are E2. For the 1512 and 1620 kev levels the upper bounds for the lifetimes are in agreement with the theoretical values arrived at on the assumption that from the 1512 kev level there occurs an M1 cascade transition and from the 1620 kev level an M1 cross-over transition.

Discussion

The assignments for the excited states of Po^{212} can be arrived at on the basis of four independent groups of data:

1) the log ft values for transitions to the excited levels of Po^{212},
2) the values of the conversion coefficients,
3) the results of γ-γ angular correlation measurements,
4) from the level lifetimes.

It follows from all four groups of data that the assignment for the first excited level (727 kev) is 2+. The spin of the second level (1513 kev) on the basis of the γ-γ angular correlation data appears to be 2+, and the cascade transition from this level to the ground state is mainly M1, which is substantiated by the values of the conversion coefficient and the lifetime of the level. The crossover transition from this level to the ground state was not detected in our experiments; its probability is less than 30% of the probability for the cascade transition. The assignment for the 1620 kev level is apparently 1+ inasmuch as from the value of the conversion coefficient for the transition from this level to the ground state it follows that this transition is M1. This spin value is also substantiated by the absence of long-range α-particles from this level. Above we noted that in view of conservation of total angular momentum and parity α-decay to the ground state of Pb^{208} (0+) can depart only from levels having even spin and even parity. The assignment for the 1679 kev level may be 0+ or 2+, inasmuch as from this level there are emitted long-range α-particles; the experimental lifetime substantiates these spin values. Lastly, the spin and parity of the 1800 kev level are 2+. This follows from the γ-γ angular correlation data, from the values of the conversion coefficient for the cascade transition leaving this level, and from the experimental lifetime of this state.

The $Bi^{212} \rightarrow Po^{212}$ decay scheme constructed on the basis of the above described data is shown in Fig. 8 with the inferred level spins and lifetimes. On the whole our data substantiate the level scheme for Po^{212} proposed by Sergeev et al[1], and are in conflict with the results of Burde & Rozner[2], who investigated β-γ coincidences, and the results of Chinaglia & Demichelis[9], who measured α-γ and γ-γ coincidences. The α-γ coincidence spectrum according to Chinaglia & Demichelis contains mainly the same lines as those observed in our work except for a 2200 kev line which we did not detect; Chinaglia & Demichelis carried out their γ-γ coincidence measurements by means of integral discriminators so that the contribution from background lines was very appreciable. Moreover, these authors used a radiothorium source which may have been contaminated. In view of this the level scheme for Po^{212} proposed by Chinaglia & Demichelis is open to question.

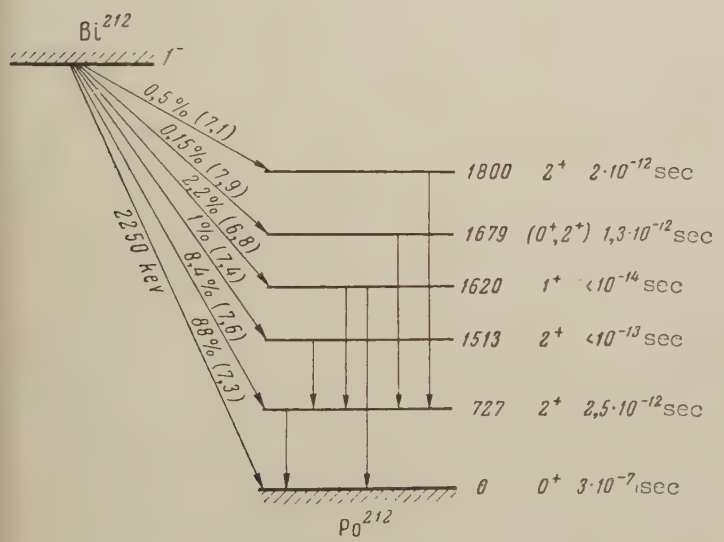

Fig.8. Decay scheme for Bi^{212}.

We desire to express our gratitude to A.P.Grinberg for assistance in calculating the theoretical correlation functions for different spins and different multipole order mixtures.

Physical-Technical Institute,
Academy of Sciences of the USSR

References

1. A.G.Sergeev, E.M.Krisyuk, G.D.Latyshev, Yu.Trofimov & A.Remennyi, Zhur. eksp.i teor.fiz., 33, 1140 (1957). (Trans.Soviet Physics - JETP.)
2. J.Burde & B.Rozner, Phys.Rev., 107, 531 (1957).
3. A.Rytz, J.rech.Centre nat.rech.scient., Labs. Bellevue, 25, 254 (1953).
4. J.Horton, Phys.Rev., 101, 717 (1956).
5. L.A.Sliv & I.M.Band, Tablitsy koeffitsientov vnytrennei konversii gamma-izlucheniya Ch.I, K-obolochka (Tables on Internal Conversion Coefficients, Part I - K shell),M.-L., 1956.
6. L.C.Biedenharn & M.E.Rose, Revs.Mod.Phys., 25, 729 (1953).
7. D.A.Alkhazov, I.Kh.Lemberg & A.P.Grinberg, Izv.AN SSSR, Ser.fiz., 17, 487 (1953).
8. J.O.Rasmussen, Phys.Rev., 113, 1593 (1959).
9. B.Chinaglia & F.Demichelis, Nuovo cimento, 8, 365 (1958).

RELATIVE INTENSITIES OF Lu^{170} AND Lu^{172} CONVERSION ELECTRONS

- V.V.Tuchkevich, V.A.Romanov & M.G.Iodko

Investigation of the levels of Yb^{170} and Yb^{172} is of considerable interest in view of the possibility of gaining information concerning excited levels above 1 Mev in even-even nuclei. The radiations from Lu^{170} and Lu^{172} have been investigated by several authors[1-8], who studied the internal conversion electron spectra and also the γ-spectra with a scintillation spectrometer. The transition energies obtained were used by Romanov et al[4] to construct the decay scheme for Lu^{172}.

We measured the relative intensities of the conversion lines on a double-focusing spectrometer with a resolution of 0.25-0.35% and a solid angle of 0.1-0.2% 4π. Our source, which measured 5 x 1 mm, was the lutetium fraction separated from a tantalum target bombarded with 660 Mev protons.

1. Lu^{172}. Using the relative intensities of the Lu^{172} conversion lines obtained in our measurements and the relative γ-ray intensities reported by Dillman et al[2], one can calculate the internal conversion coefficients for a number of transitions and make multipole order assignments. Of course, the internal conversion coefficients evaluated in this manner must be treated with caution because the relative intensities of the γ-rays were measured on a scintillation spectrometer, an instrument with poor resolution, while the spectrum of lutetium is very complicated.

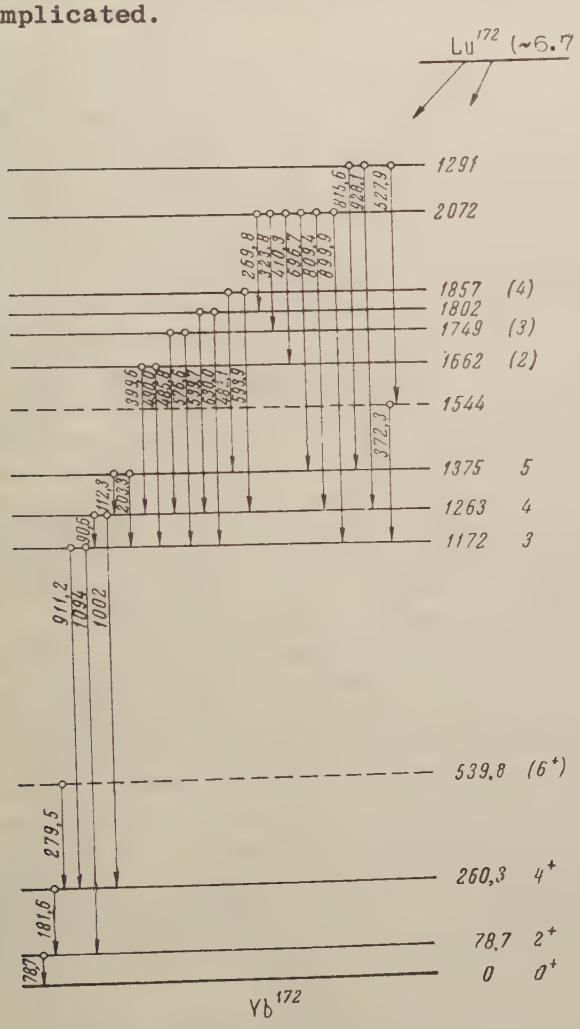

Fig.1. Decay scheme for Lu^{172}.

Table 1 gives the energies and relative intensities of the Lu^{172} conversion lines, the energies and relative intensities of the γ-rays taken from Dillman et al[2], and the calculated internal conversion coefficients. The error in determining the relative intensities is estimated to be ~10% for the strong conversion lines, and appreciably greater for the weak lines. The uncertainty in the energies of conversion lines for transitions up to 1 Mev energy is ~0.1%; for transitions with energies >1 Mev the uncertainty attains 0.3-0.5%. The relative intensities are normalized to the L shell conversion coefficient α_L of the 181.6 kev transition. The value of α_L in this case was found by interpolation of data in the tables of Sliv and Band[9].

The level diagram for Yb^{172}, including some additions to and minor modifications of the scheme elaborated by Romanov et al[4], is given in Fig.1. Owing to the fact that the multipole orders of most of the transitions can be determined accurately, it is very difficult to analyze the level scheme. Nevertheless, it seems to us that an attempt should be made, because even a very rough analysis can bring out the existence of discrepancies between the level diagram and theoretical results and show which experimental data stand in need of checking and refinement.

Table 1

Transition energies, conversion line intensities and conversion coefficients for transitions in Yb^{172}

E, kev	I_K*	I_L	I_M	Energy from Ref. 2, kev	Intensity acc. Ref. 2 in our units	α_K	I^{**}_{tot}
78,7	1300±100	2700±60	700±100	79±2	1557	0,81	4830
90,6	500±30	600	140±10	—	—	—	1550
112,3		100	25±5	113±3	750	—	~130
181,6	195±5	100	24,5±0,5	181±5	806	0,24	1100
203,3	36,5±0,8	11,1±0,3	5,8±0,3	203±5	528	6,9(—2)	310
269,8	13,3±0,4	2,3±0,2	<1,7	—	—	—	—
279,5	4,5	1,1	—	—	—	—	~74
318,8	1,3	—	—	—	—	—	—
323,8	8,6±0,5	1,7±0,1	0,8	325	—	—	—
372,3	6,3±0,1	1,2	—	370±5	556	1,1(—2)	(560)
377,4	1,2	—	—	—	—	—	—
399,6	1,9±0,2	—	—	—	—	—	—
410,3	4,9±0,3	1,3	—	—	—	—	—
482,1	1,2±0,1	0,7	—	—	—	—	~380
485,8	1,2±0,15	—	—	—	—	—	30—220
490,0	3,5±0,4	—	—	—	—	—	100—230
527,9	4,5±0,2	1,4±0,2	—	525±10	528	8,5(—3)	(530)
539,7	1,7	0,3	—	—	—	—	60÷360
576,6	0,5	—	—	—	—	—	20÷120
594,0	0,74	—	—	—	—	—	~200
626,4	1,6±0,2	0,4	—	—	—	—	—
630,0	0,65	<0,58	—	—	—	—	30÷200
696,7	3,6±0,3	0,8+0,1	0,38	—	—	—	—
809,4	6,2±0,2	1,2±0,1	0,47	820±7	258	2,4(—2)	(260)
815,6	0,71	—	—	—	—	—	—
899,9	10,1±0,2	1,5+0,2	0,36	900±5	722	1,4(—2)	(720)
911,2	3,0±0,1	0,54	0,2	—	—	—	155—1960
928,1	1,2	—	—	—	—	—	—
986,3	0,4	<0,2	—	—	—	—	—
1002	0,9±0,2	<1,0	—	—	—	—	62—760
1094	7,2±0,2	1,4±0,1	—	1090±10	1446	5,0(—3)	590—6580
1113	0,54	<0,40	—	—	—	—	—

*The indicated uncertainties characterize the reproducibility of the results in different series of measurements.

**The intensities in parentheses are taken from Dillman et al[2].

The first two levels of the first rotational band of Yb^{172} - 78.7 kev (2+) and 260.3 kev (4+) - are well known. The energy ratio $E_{4+}/E_{2+} = 3.31$ is consistent with the ratios observed for nuclei in this Z region. The 6+ level should be located at ~550 kev, i.e., the transition from this state to the 4+ state should have an energy of ~290 kev. The Lu^{172} spectrum does include a 279.5 kev γ-transition. The ratio $(K/L)_{exp} \approx 4$ is somewhat larger than the theoretical ratio for an E2 transition (2.9); however, the error in determining K/L can be quite large because the transition is comparatively weak. If the 279.5 kev transition does occur between levels of the first rotational band, the energy of the inferred 6+ level must be 539.8 kev, and $E_{6+}/E_{2+} = 6.88$.

The second rotational band is based on the level at 1172 kev. The experimental ratio of the energies of the first levels in this band is 2.44. Inasmuch as there are cross-over transitions between these levels, the energy ratio can be established quite accurately. The theoretical values of the ratios as calculated by means of the formula

$$E = E^{(0)} + E^{(1)}[I(I+1)] + E^{(2)}[I(I+1)]^2$$

for different K (2.32 for K = 2, 2.23 for K = 3, and 2.19 for K = 4), indicate that the most probable quantum number for this band is K = 3. A 911 kev and a 1094 kev transition are observed from the 1172 kev level to levels of the rotational band based on the ground state.

It is difficult to establish the multipole orders of the transitions. For the 911 kev transition we know only that $(K/L)_{exp} = 5.6$, and in this energy region the ratio K/L is insensitive to a change in multipole order.

For the 1094 kev transition α_K calculated on the basis of our data and those of Dillman et al is $5 \cdot 10^{-3}$. The following theoretical values of α_K for transitions of this energy were obtained by interpolation of the tables of Sliv & Band[9]: $1.1 \cdot 10^{-3}$(E1), $2.6 \cdot 10^{-3}$ (E2), $5.4 \cdot 10^{-3}$ (E3), $4.9 \cdot 10^{-3}$ (M1), $1.2 \cdot 10^{-2}$ (M2), $2.3 \cdot 10^{-2}$ (M3). Thus the values of α_K do not exclude E2, E3, M1, M1 + E2 and E1 + M2. This does not conflict with the inference that K = 3 for the second rotational band; in this case the transitions should be either M1 + E2 or E1 + M2. The K = 2 assignment for the second rotational band is also excluded because there is a transition from the 1172 kev level to the 260.3 kev level but no transition of detectable intensity to the ground state. For K = 2 the transition intensity to the ground state should be appreciable, since the ratio of the reduced transition probabilities is

$$\frac{B(E\ 2.22 \rightarrow 40)}{B(E\ 2.22 \rightarrow 00)} \approx 0.07.$$

On the other hand, for K = 3, the intensity of the transitions to the ground state should be low.

The spins of the 1263 and 1375 kev levels are clearly 4 and 5, respectively, and the parity is the same as that of the 1172 kev level. The 90.6 kev transition is of the M1 + E2 type; in the work of Ref.3 we evaluated the mixture as 30% M1 + + 70% E2. In addition to the 90.6 kev transition from the 1263 kev level, there is a rather weak 1002 kev transition from this level to the 4+ level of the ground state rotational band, which is not in conflict with the inferred spin values. From the 1375 level there depart transitions of 112.3 and 203.3 kev and possibly a 1113 kev transition (this 1113 kev value is some 2 kev less than the value given by the difference between the level energies). The 203.3 kev transition is E2; the 112.3 kev transition is obviously mixed M1 + E2. In our experiments there were superposed on the conversion lines associated with this transition some stronger lines from the decay of other isotopes. Therefore in this case it is expedient to use the data of Mihelich, Harmatz and Handley[6]. From the $(L_I + L_{II})/L_{III}$ ratio given by these authors it follows that this transition is mainly E2 and that the admixture - if any - of M1 is minor.

It may be assumed that the 1662, 1749 and 1857 kev levels form a third rotational band. No direct transitions between levels of this rotational band are observed; consequently, it is impossible to establish unambiguously the value of K for this band from the experimental ratio of the level energies (equal to 2.26). The possible values are K = 2 and K = 3. Tentatively assuming these values, we can evaluate the relative intensities of the transitions from the levels of this rotational band to the levels of the second rotational band. Two transitions of relatively low intensity are observed from the 1662 kev level: 399.6 and 490.0 kev. We were unable to detect any of the L lines associated with these transitions. The multipole orders of the transitions are unknown. Table 2 lists the theoretical values of the intensity ratios calculated according to Alaga et al[10] and the experimental ratios assuming different multipole orders. For K = 2 and I = 2, the intensity ratio agrees with the theoretical value for a reasonable mixture of multipole orders (~70% E1 + 30% M2). For quantum numbers K = 3 and I = 3, we obtain a factor of 2 divergence between the experimental and calculated intensity ratios.

Table 2

Comparison of the experimental and theoretical intensity ratios of the γ-transitions from the 1662 kev level.

Quantum numbers	$\left(\frac{I_{\gamma_{899,6}}}{I_{\gamma_{490,0}}}\right)_{\text{theo}}$	$\left(\frac{I_{\gamma_{899,6}}}{I_{\gamma_{490,0}}}\right)_{\text{exp}}$
$K=2;\ I=2$	$\frac{I_{\gamma_1}M2}{I_{\gamma_2}M2}=0.36$	$\frac{I_{\gamma_1}M2}{I_{\gamma_2}M2}=0.29$
$K=3;\ I=3$	$\frac{I_{\gamma_1}E1}{I_{\gamma_2}E1}=0.18$	$\frac{I_{\gamma_1}E1}{I_{\gamma_2}E1}=0.34$
$K=4;\ I=4$	$\frac{I_{\gamma_1}E1}{I_{\gamma_2}E1}=0.14$	

Table 3

Comparison of the experimental and theoretical intensity ratios of the γ-transitions from the 1749 kev level.

Quantum numbers	$\left(\frac{I_{\gamma_{485,8}}}{I_{\gamma_{576,6}}}\right)_{\text{theo}}$	$\left(\frac{I_{\gamma_{485,8}}}{I_{\gamma_{576,6}}}\right)_{\text{exp}}$
$K=3;\ I=4$	$\frac{I_{\gamma_1}E1}{I_{\gamma_2}E1}=1.39$	$\frac{I_{\gamma_1}E1}{I_{\gamma_2}E1}=1.79$
$K=2;\ I=3$	$\frac{I_{\gamma_1}E1}{I_{\gamma_2}E1}=1.81$	

Table 4

Comparison of the experimental and theoretical intensity ratios of the γ-transitions from the 1857 kev level.

Quantum numbers	$\left(\frac{I_{\gamma_{462,1}}}{I_{\gamma_{593,9}}}\right)_{\text{theo}}$	$\left(\frac{I_{\gamma_{492,1}}}{I_{\gamma_{593,9}}}\right)_{\text{exp}}$
$K=2;\ I=4$	$\frac{I_{\gamma_1}E1}{I_{\gamma_2}E1}=1.28$	$\frac{I_{\gamma_1}E1}{I_{\gamma_2}E1}=1.05$
$K=3;\ I=5$	$\frac{I_{\gamma_1}E1}{I_{\gamma_1}E1}=0.58$	

There are transitions of 485.8 and 576.6 kev energy from the 1749 kev level. Assuming that this level is a member of the third rotational band, we can calculate the relative intensities of the transitions.

It will be evident from Tables 2,3 & 4 that in all cases the relative intensities of transitions from the levels of this rotational band agree with theory best for K = 2.

K and I are not known for the 1802 kev level. There are six transitions from the 2072 kev level to the levels of the second and third rotational bands. The values of α_K for the 899.9 and 809.4 kev transitions are known. However, inasmuch as the uncertainties in determining the α_K are appreciable, one cannot make unambiguous multipole order assignments. These transitions could be E3, M1, M2, E1 + M2 or M2 + E3. It is obvious that in this case calculations of the relative intensities cannot give much information because not even the approximate values of K and I are known for these levels.

We have not yet considered two relatively strong transitions in Lu^{172}. The energies of these transitions are 372.3 and 527.9 kev. According to Dillman et al[2], these transitions are in coincidence and of approximately equal intensity. The sum of the transition energies is 900.2 kev, which is almost equal to the 899.9 kev energy of the cross-over transition. It may be assumed that these transitions lead from the 2072 kev level to the 1172 kev state. The intermediate level lies at either 1544 kev or 1700 kev. The multipole orders of the transitions can be determined by comparing the experimental and theoretical internal conversion coefficients. For the 372.3 kev transition the most probable multipolarity is E1, but E2 is not excluded. For the 527.9 kev the most probable assignments are also E1 and E2. The experimental K/L ratio in this case corresponds to E2.

The last column of Table 1 gives the total relative intensities of the transitions, calculated on the basis of the relative intensities of the conversion lines and the known multipole orders. When the multipolarity of a transition has not been accurately established, we list the limits within which the total intensity may vary. Analysis of the total intensity values leads to the inference that, given the decay scheme pictured in Fig.1, K capture leads mainly to the 2072, 1857, 1802 and 1263 kev levels, i.e., levels that evidently have high spins. In

our units the number of transitions to the 1172 kev level is ~4000. The intensity of the K conversion lines is $\geqslant$ 2100. Thus the net number of vacancies formed in the K shell is ~6000 in our units. Inasmuch as the Auger yield in this Z region is small, the number of vacancies in the given case characterizes the intensity of the x-rays associated with the transitions to the 1172 kev level and with conversion on the K shell. According to Dillman et al[2], the intensity ratio $I_x/I_{\gamma 79}$ = = 1000:56. According to our data

$$I_{\gamma 78.7} = \frac{I_{L78.7}}{\alpha_{L78.7}} = 516.$$

Thus, in our units, the intensity of the K x-rays emitted in the decay of Lu^{172} is 10750. Analysis of the intensity values shows that K capture leads mainly to excited levels of Yb^{172} with energies exceeding 1 Mev, which is not in conflict with the possible Lu^{172} ground state assignments of 3- and 4- (or even 4- and 5-, as inferred by Peker[12] in considering the spins of neighboring odd-A nuclei).

2. Lu^{170}. Investigation of the levels of Yb^{170} dates back several years. Mihelich & Church[7] and Day[8] studied the decay of 129-day Tm^{170} and found that the first excited level has an energy of 84.2 kev. Study of the decay of Lu^{170} ($T \approx 2$ days) provides more detailed information on the Yb^{170} level scheme. Possible values of the spin and parity of Lu^{170} are 0+ and 7+ (or 1^- and 8^- according to Peker[12]). The energy difference between the parent and daughter nuclei is >3 Mev.

Mihelich, Harmatz and Handley[6] observed two transitions in Lu^{170}, associated with the ground state rotational band. Dillman et al[2] list four transitions. Bobrov et al[1] and Kel'man et al[5] observed many transitions with a period of 1.5-2 days, but because of the small difference between the half lives of Lu^{169} and Lu^{170}, both of which were present in their sources, found it difficult to establish to which isotope the transitions belonged. After publication of the recent report by Harmatz, Handley and Mihelich[11] listing a large number of transitions in Lu^{169}

Table 5

Energies of transitions in Yb^{170} and conversion line intensities

Transition energy, kev*	I_K**	I_L	Total intensity	Multipolarity	Transition energy, kev*	I_K**	I_L	Total intensity	Multipolarity
84,2	1400±200	7600	14300	*E*2	511,7	1,4	—	—	—
184,5	14,9	—	—	—	543,9	<7	—	—	—
193,3	100	59	760	*E*2	(560,9	1,2	—	—	—
222,7	11±2	~3	—	—	571,8	2,4	—	—	—
279,4	—	~4	—	—	756,2	~0,3	—	—	—
282,9	8,5±0,3	1,8	—	—	837,1	~2,1	—	—	—
286,5	3,3±0,4	—	—	—	938,1	3,7±0,1	—	—	—
382,1	~3,5	<1,8	—	—	983,2	<5	—	—	—
(386,3	1,4	—	—	—	997,9	~2	—	—	—
388,7	2,7	<1,3	—	—	(1103)	1,3±0,1	—	—	—
396,1	4,6	~2	—	—	1139	2,3±0,1	—	~1000	—
416,8)	1,5	—	—	—	1224	2,1±0,3	—	~1000	—
419,6)	—	~1,8	—	—	1281	2,0±0,1	—	—	—
455,2	~3	~1,2	—	—	1454	14,0±0,3	1,8	1500÷18000	—
487,3	1,7	—	—	—	1484	8,4±0,2	1,5	1000÷13000	—
					1568	1,8	—	200÷3000	—

*The transitions whose energy values are given in parentheses are regarded as doubtful.

**The uncertainties characterize the reproducibility of the results in different series of measurements.

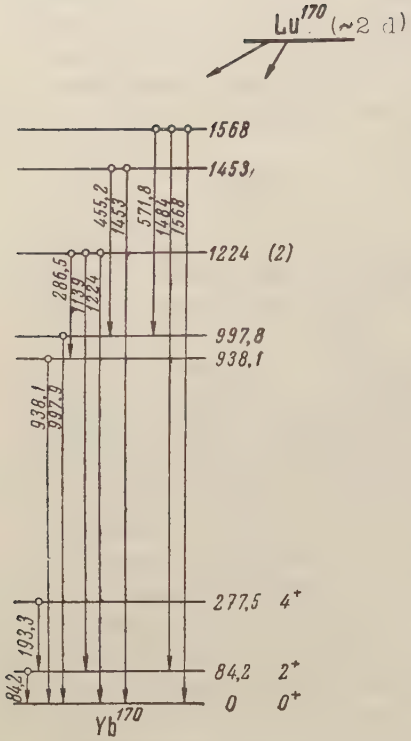

Fig.2. Possible version of the decay scheme for Lu^{170}.

and completion of our supplementary measurements of the conversion electron spectra of neutron-deficient isotopes of lutetium, it became feasible to identify with fair certainty the transitions involved in the decay of Lu^{170}. The conversion electron spectrum was recorded under the same conditions as the spectrum of Lu^{172}. The transition energies and the relative intensities of the strongest conversion lines in the Lu^{170} spectrum are given in Table 5. The existence of the transitions for which the energies are given in parentheses is open to question. In addition to the lines listed in Table 5, the conversion electron spectra of the neutron-deficient isotopes of lutetium comprise a large number of weaker lines with short periods. Identification of these lines is not feasible at present. Since the Lu^{170} spectrum is observed against a background of radiations from longer lived isotopes, the accuracy with which the relative intensities of the lines are determined is poor (no better than 20%).

One possible decay scheme for Lu^{170} constructed on the basis of the determined transition energies is shown in Fig.2. The 84.2 and 193.3 kev transitions are transitions between the levels of the rotational band based on the ground state. Both the transitions are E2. The total intensities of these transitions can easily be calculated in our units (the intensity of the K line of the 193.3 kev γ-transition is taken as 100); they are listed in the fourth column of Table 5. The 1454 and 1484 kev transitions are of particular interest. In general, internal conversion coefficients in this energy region are small. Nevertheless, the intensities of the conversion lines corresponding to these transitions are comparatively high, indicating that these transitions are of great intensity. Transitions of multipolarity $l \leqslant 3$ must feed either the ground state or the first excited state. On the basis of the proposed scheme (Fig.2) we evaluated the relative intensities of the transitions departing from the 1224 and 1568 kev levels to the levels of the ground state rotational band. Inasmuch as the multipole orders of the transitions are not known, the relative γ-ray intensities were calculated by assuming different multipole orders up to $l = 3$. For the 1139 and 1224 kev transitions from the 1224 kev level the experimental intensity ratio is 0.95. The theoretical intensity ratios calculated assuming different values of K and I for the 1224 kev state are 0.41 for K = 1 and I = 1, 1.01 for K = 2 and I = 2, and 1.29 for K = 3 and I = 3. It will be evident that the value calculated for K = I = 2 is in good agreement with the experimental intensity ratio. For the 1484 and 1568 kev transitions from the 1568 level the experimental value of the intensity ratio is appreciably higher than the theoretical values calculated for all values of K and I from 1 through 3. The reason for this may be that the 1484 kev transition is a mixture of multipole orders.

We desire to express our gratitude to V.M.Kel'man for his constant interest in the work, to B.S.Dzhelepov and L.K.Peker for valuable suggestions in discussing the results and to G.L.Vlasenko and V.P.Belov for assistance in carrying out the measurements.

References

1. Yu.G.Bobrov, K.Ya.Gromov, B.S.Dzhelepov & B.K.Preobrazhenskii, Izv.AN SSSR, Ser.fiz., 21, 940 (1957). (Trans.Bulletin, 21, 942.)

2. L.T.Dillman, R.W.Henry, N.B.Gove & R.A.Becker, Phys.Rev., 113, 635 (1959).

3. M.G.Iodko, V.V.Tuchkevich, V.A.Romanov & O.M.Kresin, Zhur.eksp.i teor. fiz., 38, 1027 (1960). (Trans.Soviet Physics - JETP.)

4. V.A.Romanov, L.K.Peker, V.V.Tuchkevich & M.G.Iodko, Materialy vtorogo soveshchaniya po neitronodefitsitnym izotopam v OIYAI. Lyutetsievaya fraktsiya (Transactions of the Second Conference on Neutron-Dificient Isotopes at the Joint Institute for Nuclear Research. Lutetium Fraction), Dubna, 1959.

5. V.M.Kel'man, R.Ya.Metskhvarishvili, B.K.Preobrazhenskii, V.A.Romanov & V.V.Tuchkevich, Zhur.eksp.i teor.fiz., 35, 1309 (1958). (Trans.Soviet Physics - JETP.)

6. J.W.Mihelich, B.Harmatz & T.Handley, Phys.Rev., 108, 989 (1957).

7. J.W.Mihelich & E.L.Church, Phys.Rev., 85, 690 (1952).

8. P.P.Day, Phys.Rev., 102, 1572 (1956).

9. L.A.Sliv & I.M.Band, Tablitsy koeffitsientov vnutrennei konversii gamma-izlucheniya. Ch.I & II (Tables of internal conversion coefficients, Parts I & II), M.L. 1956 & 1958.

10. G.Alaga, K.Alder, A.Bohr & B.Mottelson, Kgl.Danske Viedenskab.Selskab, Mat.-fys.Medd., 29, No.9 (1955).

11. B.Harmatz, T.H.Hansley & J.W.Mihelich, Phys.Rev., 114, 1082 (1959).

12. L.K.Peker, Transactions of the Second Conference on Neutron-Deficient Isotopes at the Joint Institute for Nuclear Research. Lutetion Fraction, Dubna, 1959.

RELATIVE INTENSITIES OF Lu^{169} AND Lu^{171} CONVERSION ELECTRONS

- M.G. Iodko, V.A. Romanov & V.V. Tuchkevich

The conversion electron spectrum of Lu^{169} was studied with a double-focusing β-spectrometer. The relative half-width of the lines was 0.25-0.35%. We used two sources, which were prepared by bombarding a tantalum target with 660 Mev protons from the Joint Institute for Nuclear Research synchrocyclotron. The rare earth elements formed by spallation of the Ta were separated by ion-exchange. The extracted lutetium fraction was deposited on aluminum foils. A series of measurements was carried out for each source; this enabled us to attribute the observed lines to the appropriate Lu isotopes on the basis of their periods. Since the periods of Lu^{169} and Lu^{170} are nearly equal (1.5 days and 2 days), it is difficult to distinguish between the lines of these isotopes.

The energies of the γ-rays emitted by Lu^{169} were determined earlier by Kel'man et al.[1] Harmatz, Handley and Mihelich[2] recently studied the spectra of Lu^{169} and Lu^{171} using sources composed of separated isotopes. Thus, in addition to the known transitions in Lu^{169}, using the results of Harmatz et al[2], we assigned to Lu^{169} the transitions with energies in good agreement with their data.

The decay scheme for Lu^{169}, constructed on the basis of the transition energies reported by Harmatz et al[2] and Peker[3], is shown in Fig.1.

Table 1 gives the relative intensities of the conversion lines in the spectrum of Lu^{169}. In evaluating the relative intensities, the intensity of the K line of the 290 kev Y-transition was taken as 100. In the medium and high-energy regions of the spectrum (E > 200 kev) our relative line intensities agree well with the data of Harmatz et al[2]. In the low-energy region, we obtained values approximately twice as large as theirs. A rotational band with K = 1/2 is clearly evinced in the Lu^{169} spectrum. The levels of this band have spins and parities $1/2^-$, $3/2^-$, $5/2^-$, $7/2^-$ and $9/2^-$ and energies 24.23, 87.0, 99.2, 244 and 264.4 kev, respectively.

Between the $3/2^-$ and $1/2^-$ levels there is a 62.75 kev M1 + E2 transition. From our data we obtained $(L_I + L_{II})/L_{III} = 1.4$ for this transition; this ratio indicates that the admixture of E2 is ~27%. Iodko et al[4] found the same percentage of E2 in the mixed 66.7 kev transition in Lu^{171} between the rotational band levels with the same spins and parities ($3/2^-$ and $1/2^-$). According to Harmatz et al[2], the admixture of E2 in the 62.75 kev transition is ~34%. It may be that our value for the admixture of E2 is an underestimate, because the lines we in-

Table 1

Relative intensities of the Lu^{169} conversion lines

E,kcv	K	L	M	E,kcv		L		E,kcv	K		M
24,2	—	9000	—	227,9	—	12	—	563	9	—	—
62,6	—	11300	—	243	—	22	9	590,8	—	4	—
87,3	18100	—	—	258	112	—	—	634,6	15	—	—
91,8	3800	—	—	290,9	100	20	7,4	646,9	3,5	—	—
110,9	—	1000	250	369,1	102	—	—	655,4	1,4	—	—
144,5	—	186	105	378,3	205	30	11	707,4	>3,6	—	—
156,8	830	530	—	403,9	12	—	—	820,9	8	—	—
164,9	1100	790	130	456,5	57	9	—	879,3	6,7	—	—
166,5	130	—	—	470,4	—	6	—	960,6	55	8,7	—
191,5	1700	350	—	479,5	16	4	—	1061	28	—	—
198,6	200	—	—	491,7	—	9	—	1072	24	—	—
				548	17	3	—	1079,5	6,4	—	—

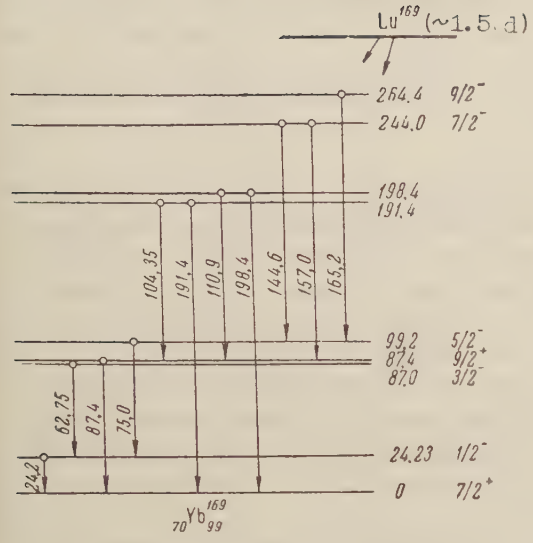

Fig.1. Decay scheme for Lu^{169}.

vestigated appeared against a fairly strong background formed by the lines of other, longer-lived isotopes.

We observed no 75.0 kev transition between the $5/2^-$ level and the ground level of the rotational band. According to Harmatz et al[2], who observed the L_{II} and L_{III} lines of this transition, its multipole order is E2. We determined the K/L and $L_I:L_{II}:L_{III}$ ratio for the 156 kev ($7/2^-$ to $3/2^-$) and 164 kev ($9/2^-$ to $5/2^-$) γ-transitions within the rotational band. This enabled us to determine the multipole orders of these transitions by comparing these ratios with the corresponding ratios of theoretical conversion coefficients for different multipole orders as given in the tables of Sliv & Band[5] (Table 2).

The experimental conversion coefficient ratios correspond to the theoretical ratios for E2 transitions. In the work of Harmatz et al[2] the 156 and 164 kev transitions were also identified as E2 transitions. The 144.6 kev transition goes from the $7/2^-$ to the $5/2^-$ level. We could observe only the L and M lines of this transition. There is a 24.23 kev transition from the first level of the K = 1/2 rotational band to the ground state of Yb^{169}. Harmatz et al[2] give E3 for the multipole order of this transition. The ratio $L_{II}/L_{III} = 1.0 \pm 0.2$, deduced from our data, does not contradict this assignment (for an E3 transition $(L_{II}/L_{III})_{theo} = 0.88$). The total intensity of the 24.23 kev transition is ~12 000 in our units (the intensity of the K line of the 290 kev transition is taken as 100). The total intensity of the transitions to the 24.23 kev level is 25 000. This factor of two discrepancy may be explained by appreciable stopping of low-energy electrons in the source material.

The ground state of Yb^{169}, $7/2^+$ according to Harmatz et al[2], and the 87.4 kev ($9/2^+$) level may form a second rotational band. The $11/2^+$ level of this rotational band should have an energy of 194.2 kev. In our experiment, we observed 191.4 and 198.4 kev transitions. If the 191.4 kev level has spin $11/2^+$, then the

Table 2

Determination of the multipole orders of the 156 and 164 kev transitions in Yb^{169}

E, kev	Experiment		Theory								Multipole order assignment
			E2		E1		E3		M1		
	K/L	$(L_I+L_{II})/L_{III}$	K/L	$(L_I+L_{II})/L_{III}$	K/L	$(L_I+L_{II})/L_{III}$	K/L	$(L_I+L_{II})/L_{III}$	K/L	$(L_I+L_{II})/L_{III}$	
156	$1,55 \pm 0,05$	$1,63 \pm 0,09$	1,42	1,65	6,35	5,71	0,28	1,58	6,42	90,76	E2
164	1,44	1,74	1,58	1,74	6,4	5,83	0,32	1,66	6,42	92,61	E2

191.4 kev transition must have multipolarity E2. On the basis of our data, however, one can assert that this transition is not pure E2: $(K/L)_{exp} = 4.75 \pm 0.17$ and $(L_I:L_{II}:L_{III})_{exp} = 7.25 : 2.33 : 1$. The corresponding theoretical ratios for an 191.4 kev E2 transition are $(K/L)_{theo} = 1.9$ and $(L_I:L_{II}:L_{III})_{theo} = 0.70 : 1.42 : 1$. Possibly this transition is mixed M1 + E2, in which case, according to our data, the admixture of E2 does not exceed 25%. Consequently, the assignment for the 191.4 kev level cannot be $11/2^+$.

From the 198.4 kev level there depart two transitions of 110.9 and 198.4 kev energy to levels with $9/2^+$ and $7/2^+$. If we assume that the 198.4 kev level has spin $11/2^+$, then the 198.4 kev transition would have a multipole order of E2. Unfortunately, it is impossible to determine the multipole order of this transition directly from our data because we detected only the K line.

The 110.9 kev transition is 96% M1 + 4% E2, as calculated using the ratio $L_I:L_{II}:L_{III}$ taken from Harmatz et al[2]. If we assume that the 198.4 kev transition is E2, then the intensity ratio of the 198.4 kev and 110.9 kev transitions, calculated according to Alaga et al[6], is $(I_{\gamma 110.9}/I_{\gamma 198.4})_{theo} = 0.26$, while the experimental ratio proves to be 0.07.

The experimental ratio of the level energies is

$$\frac{E_{K\,198.4}}{E_{K\,87.3}} = 2.27.$$

The simplified formula $E_K(I) = E_K^{(0)} + E_K^{(1)}[I(I+1)]$, using different ground state spin values, gives the following level energy ratios:

I_0	E_{K_2}/E_{K_1}
3/2	2.4
5/2	2.29
7/2	2.22
9/2	2.18

Comparison shows poor agreement of the experimental and theoretical values of the intensity and energy ratios for the transitions from these levels. Consequently, it still remains to be determined whether these levels belong to the same rotational band.

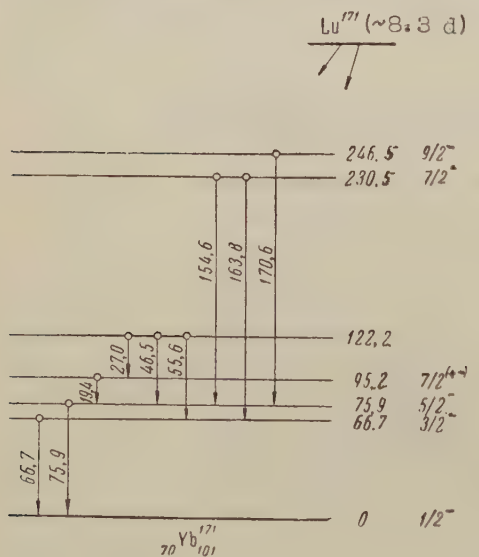

Fig.2. Decay scheme for Lu^{171}.

In addition to the Lu^{169} spectrum, we also investigated the spectra of the other Lu isotopes in our sources, including the spectrum of Lu^{171}. The 8.3 day period of Lu^{171} (Fig.2) is long enough to distinguish its radiations from those of shorter-lived Lu^{169} and Lu^{170}. Nevertheless, identification was hampered by the fact that our sources contained Lu^{172}, which has a half-life of 6.7 days. Substantial distortions of the apparent period may arise owing to superposition of the lines of different isotopes. In this respect the results of Harmatz's work with separated isotopes were helpful. Our values for the transition energies and relative intensities are listed in Table 3. Table 4 gives the intensity ratios of the L subshell conversion electrons for some transitions. Up to 300 kev our transition energy values differ little from the energies found

Table 3

Yb^{171} transition energies and relative conversion electron intensities

E, kev	K	L	M	E, kev	K	L	M
55,63	—	5500	—	712,6	10	2,7	1,4
66,8	—	14600	—	739,4	100	16	3
72,38	—	3600	—	767,2	8,5	—	—
75,97	2800	41000	8700	780,6	9	—	—
85,55	3800	—	—	839,3	26	5,5	—
91,28	1500	—	—	853,9	9	—	—
498,4	5	—	—	986,0	2	—	—
517,7	9	4	—	1020	2,5	—	—
626,2	11	2	—	1029	1,4	—	—
666,8	29	5	3	1037	2,6	—	—
688,8	6,5	—	—	1042,9	0,6	—	—
				1102,8	1,2	—	—

by Harmatz et al[2]; in the higher energy region the energy difference attains 2 kev.

Losses in the source itself and in the foils separating the counters from the spectrometer chamber are significant where low energy electrons are concerned. In our case the minimum energy of the electrons penetrating into the counters was around 6 kev. In order to reduce this threshold the electrons were accelerated by a 5 kev bias potential between the source and the first aperture. This enabled us to investigate the L lines of the 19.4 kev γ-transition. Determination of the relative intensities of these L-lines was difficult since they could not be compared directly with the K line of the 739.5 kev transition, taken as 100 in our relative intensity scale. Therefore, the relative intensities were evaluated indirectly. The K line of the 78.9 kev transition is located near the L lines of the 19.4 kev transition. Harmatz et al[2] and Iodko et al[4] have determined that the multipole order of this transition is E2. Using the K/L ratio for this multipolarity and the relative intensities of the L lines of the 78.9 kev γ-transition, we found the intensity of the K line in our units. Once the intensity ratios of the K line of the 78.9 kev transition and the L lines of the 19.4 kev transition are found, it is simple to evaluate the ratio of the L line intensities. Unfortunately, the L_{III} line of the 19.4 kev transition falls on the L_I line of the 20.75 kev transition in Yb^{169} and hence cannot be resolved with satisfactory accuracy. Harmatz et al[2] indicate that the 19.4 kev transition is E1. The L_I/L_{II} ratio which we obtained is compatible with this finding; it is also not inconsistent with the assignment 91.5% M1 + 8.5% E2.

With regard to the location of this level in the decay scheme, at present we can say only that judging from its intensity this transition goes either directly to the ground state of Yb^{171} or to a low-lying level. The ground state of Yb^{171} has spin and parity $1/2^-$, according to both Harmatz et al[2] and Elebek et al[7]. The assignments for the 66.7 and 75.9 kev levels are given by these authors and by Gromov et al[8]. Together with the ground state these levels form a K = 1/2 rotational band. The higher lying levels of this band should have energies of 231.6 kev $(7/2^-)$ and 248.1 kev $(9/2^-)$. Transitions corresponding to de-excitation of these levels have been observed by Harmatz et al[2]. The transition from the first excited level of this rotational band to the ground state $(3/2^- \rightarrow 1/2^-)$ has an energy of 66.7 kev and multipole order M1 + E2. Iodko et al[4] established that the admixture of E2 is 32%.

As noted above, Lu^{169} has a K = 1/2 rotational band analogous to the band in Lu^{171}.

Table 4

$L_I:L_{II}:L_{III}$ ratios for some transitions in Tb^{171}

E, kcv	$L_I : L_{II} : L_{III}$
19,4	$1 : 1{,}15 : (\approx 1{,}3)$
66,68	$(0{,}45 \pm 0{,}04) : (0{,}99 \pm 0{,}02) : 1$
72,38	$2{,}67 : 0{,}87 : 1$
75,83	$L_{II} : L_{III} = 0{,}97 : 1$

The values characterizing the moments of inertia of the bands are $(3\hbar^2/J)_{169}$ = = 70.1 kev and $(3\hbar^2/J)_{171}$ = 72.2 kev; the values of the coefficients a_{169} and a_{171} are 0.79 and 0.85, respectively.

The transitions from the $3/2^-$ and $1/2^-$ states have about the same energies and multipole order mixtures.

We desire to thank V.M.Kel'man for his unflagging interest in the work, B.S. Dzhelepov and L.K.Peker for valuable suggestions in discussing the results, and G.L.Vlasenko and V.P.Belova for their help in the experiments.

Physical-Technical Institute,
Academy of Sciences of the USSR

References

1. V.M.Kel'man, R.Ya.Metskhvarishvili, B.K.Preobrazhenskii, V.A.Romanov & V.V.Tuchkevich, Zhur.eksp.i teor.fiz., 35, 1309 (1958). (Trans.Soviet Physics - JETP.)

2. B.Harmatz, T.H.Handley & J.W.Mihelich, Phys.Rev., 114, 1082 (1959).

3. L.K.Peker, O skheme raspada Lu^{169}. Materialy vtorogo soveshchaniya po neitronodefitsitnym izotopam (On the decay scheme of Lu^{169}. Transactions of the Second Conference on Neutron-Deficient Isotopes), Dubna, 1959.

4. M.G.Iodko, V.V.Tuchkevich, V.A.Romanov & O.M.Kresin, Zhur.eksp.i teor. fiz., 38, 1027 (1960). (Trans.Soviet Physics - JETP.)

5. L.A.Sliv & I.M.Band, Tablitsy koeffitsientov vnutrennei konversii gamma-izlucheniya. Ch.I. K-obolochka. Ch.II. L-obolochka (Tables of internal conversion coefficients, Part I - K-shell, Part II - L-shell), M.-L. 1956 & 1958.

6. G.Alaga, K.Alder, A.Bohr & B.Mottelson, Klg.Danske Videnskab.Selskab, Mat.-fys. Medd., 29, 9 (1955).

7. B.Elbek, K.O.Nielsen & M.C.Olesen, Phys.Rev., 108, 406 (1957).

8. K.Ya.Gromov, B.S.Dzhelepov, A.G.Dmitrieva & B.K.Preobrazhenskii, Izv.AN SSSR, Ser.fiz., 21, 1573 (1957). Trans.Bulletin, 21, 1562.)

CASCADE EXCITATION OF THE SECOND ROTATIONAL LEVELS IN SEPARATED TUNGSTEN ISOTOPES

- D.S.Andreev, K.I.Erokhina & I.Kh.Lemberg

Until recently, in experiments on Coulomb excitation of strongly deformed even-even nuclei investigators succeeded in exciting only the first rotational levels (with spin and parity 2+). Coulomb excitation of second rotational levels (4+) was not achieved.

Only protons or α-particles with energies considerably lower than the potential barrier were used in the Coulomb excitation experiments. Under these conditions the probability for exciting a nuclear level in any individual collision is very low, and, consequently, the Coulomb excitation cross section can be calculated accurately even in the first approximation of perturbation theory. Calculations made in this manner indicate that in the case of strongly deformed even-even nuclei, the cross section for Coulomb excitation of second levels with spin 4+ (E4 transition) is several orders of magnitude smaller than the cross section for excitation of 2+ levels (E2 transition).

This situation is due to the selection rules for the low multipole order transitions characteristic of Coulomb excitation, and to the fact that the Coulomb cross section falls off sharply with increase in the energy ΔE of the excited state, since with growth of ΔE the lifetime becomes increasingly shorter than the effective flight time of the particle in the vicinity of the target nucleus, and the process becomes increasingly adiabatic. At the same time, the energy of second rotational levels is about 3.3 times greater than ΔE of the first rotational levels.

The excitation probability for nuclear levels increases sharply with increase of the energy and of the atomic number of the bombarding particles. As the excitation probability increases, the probability of second-order processes increases as well. Whereas in the first approximation, direct excitation of the 4+ state can be achieved only by inducing a direct E4 transition, in the second approximation of perturbation theory, this state can be excited by means of two successive E2 transitions. Qualitatively this process can be represented as follows: owing to the high excitation probability, the 2+ state is excited by the bombarding particle while moving over the first part of its trajectory; then during the remaining part of the trajectory the nucleus is raised to the 4+ state by a second E2 transition.

For investigating the two-step Coulomb excitation process we used quadruply charged 27.8 Mev Ne^{20} and 36 Mev N ions. The targets were prepared of four specimens of metallic tungsten enriched in W^{182}, W^{183}, W^{184} and W^{186}. The isotope contents of the targets are listed in the table. The specimen enriched in W^{183} was used for control experiments.

The γ-rays emitted by the bombarded targets were detected by means of a scintillation spectrometer with an NaI(Tl) crystal coupled to a photomultiplier. The photomultiplier pulses, after amplification, were recorded by a 63-channel pulse height analyzer (type AMA-2, designed at the Leningrad Electrotechnical Institute). The energy scale was calibrated with reference to a Hg^{203} γ-ray source (E = 279 kev) before and after the measurements.

Figs.1 and 2 give the spectra obtained in bombarding targets enriched in W^{182} and W^{184} with 27.8 Mev Ne ions, while Fig.3 shows the spectrum obtained in bombarding a target enriched in W^{186} with 36 Mev nitrogen ions. The peaks evident in the spectra correspond to lines at 0.23 Mev (W^{182}), 0.25 Mev (W^{184}) and 0.275 Mev (W^{186}). Control experiments showed that there are no background lines of these energies when carbon or oxygen are bombarded with nitrogen and neon ions. The presence of any other light elements in our targets is unlikely, and there are virtually no nuclear reactions on other, heavier contaminating elements. Earlier[2] we showed

Isotope content of tungsten specimens (%)

Specimen	W^{180}	W^{182}	W^{183}	W^{184}	W^{186}
W^{182}	3,8	87,6	3,6	3,2	1,8
W^{183}	0,1	3,6	90,1	4,0	2,2
W^{184}	0,1	1,1	3,6	91,3	4,0
W^{186}	0,5	0,2	0,6	2,7	96,0

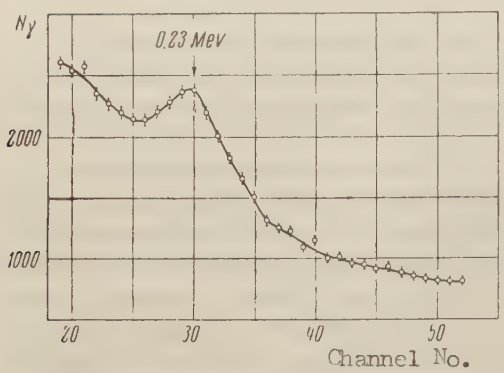

Fig.1. Experimental γ-spectrum obtained in bombarding W^{182} with quadruply charged 27.8 Mev Ne^{20} ions.

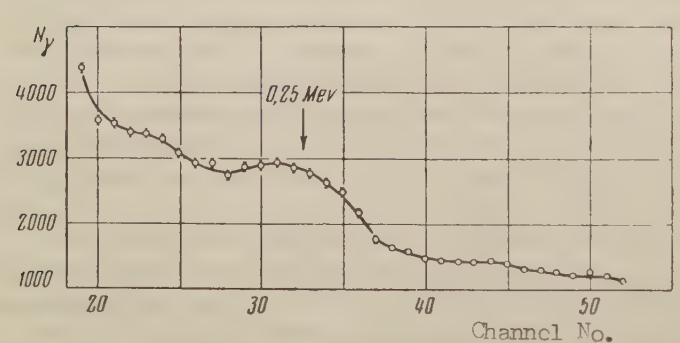

Fig.2. Experimental γ-spectrum obtained in bombarding W^{184} with 27.8 Mev Ne^{20} ions.

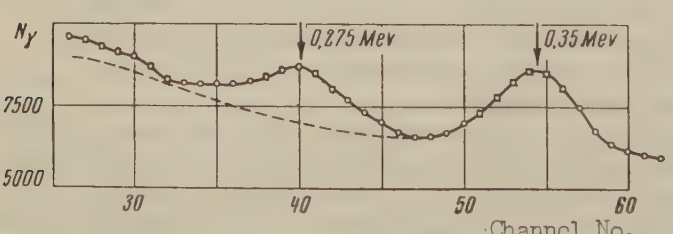

Fig.3. Experimental γ-spectrum obtained in bombarding W^{186} with 36 Mev N^{14} ions.

that in bombardment of carbon with N ions 350 kev γ-rays are emitted as a result of the N + C reaction.

A peak corresponding to this line appears in the γ-spectrum reproduced in Fig.3. This peak is due to formation of a thin carbon film on all cyclotron-bombarded targets. The shape of the 350 kev line was studied in a special experiment in which we recorded the γ-ray spectrum from a natural lead target bombarded with 36 Mev N ions. This γ-spectrum is given by the dashed curve in Fig.3.

In the control experiment, the γ-ray spectrum from a W^{183} enriched target under bombardment with 27.8 Mev neon ions was studied. In the range from 200 to 320 kev, there was observed one peak at E_γ = 295 kev, corresponding to Coulomb excitation of a nuclear level of this energy in W^{183}. The yield of the 295 kev γ-rays is low, and in view of the small content of W^{183} in the targets enriched in even isotopes, we felt justified in neglecting it.

In the work of Murray et al[2] on β-decay of Ta^{182} to W^{182} the energy of the γ-rays emitted in the cascade transition from the second rotational level of W^{182} to the ground state was measured precisely with a crystal spectrometer and found to be 229.27 kev. Analogous γ-rays emitted in the decay of Ta^{184} have, according to Butement and Poe[3], an energy of 240 kev. One must, however, note the relatively low accuracy of the energy determination in the latter work, inasmuch as the measurements were performed by means of a scintillation spectrometer in the presence of considerable background due to other γ-radiation emitted in β-decay of Ta^{184}. $Ta^{186}\rightarrow W^{186}$ decay was studied by Poe[4], but the line corresponding to the transition from the 4+ state to the 2+ state was not detected. In studies of the radiations emitted in the K-capture transitions $Re^{182}\rightarrow W^{182}$, $Re^{184}\rightarrow W^{184}$ and $Re^{186}\rightarrow W^{186}$, no lines corresponding to $4+\rightarrow 2+$ transitions were detected either. In order to evaluate the probable energy of the $4+\rightarrow 2+$ transition in W^{184} and W^{186}, one can use the energy of the first level and the known ratio between the energies of the first and second

rotational levels. The calculated values are 257 kev and 291 kev, respectively, for W^{184} and W^{186}. Actually, owing to the interaction between rotational and vibrational motions, these values should be somewhat lower. According to our data, the values of E for the 4+→2+ transitions in W^{182}, W^{184} and W^{186} are 0.230, 0.250 and 0.275 Mev, respectively (see Figs.1, 2 & 3). Thus, in our experimental investigation of two-step Coulomb excitation of even tungsten isotopes, we have demonstrated excitation of the 4+ level in every one of the investigated isotopes.

The fact that the observed lines do correspond to 4+→2+ transitions is proved a) by the agreement between the energies of the lines and the energy values calculated on the basis of the known energy ratios for rotational levels, and b) by the fact that the same lines were observed in bombardment of the tungsten targets with neon as well as with nitrogen ions.

Calculations on the assumption of Coulomb excitation of the 4+ state by E4 transitions, using the single-particle reduced transition probability value, yield an intensity value for the γ-rays emitted in 4+→2+ transitions some 10^3-10^4 times lower than that actually observed.

There is another possible explanation for the observed lines. It may be that second levels with spin 2+ (2'+ levels), are excited, so that the experimentally observed γ-rays are associated not with 4+→2+ transitions but with 2'+→4+→2+ cascade transitions. To check this possibility we evaluated the additional contribution to the 4+→2+ transition γ-ray yield that would result from excitation of the 2'+ level. For the calculations we used the data obtained in the work of Ref.5. The evaluations showed that the contribution from possible excitation of 2'+ levels is negligibly small. This results from the circumstances, first, that Coulomb excitation of high-lying levels by means of heavy ions diminishes sharply with an increase in the atomic number of the bombarded element, and, second, that transitions from the 2'+ level mainly feed the 2+ and 0+ levels.

Hence, it may safely be asserted that the observed 230, 250 and 275 kev γ-rays arise as a result of two-step Coulomb excitation of energy levels at 330, 360 and 400 kev in W^{182}, W^{184} and W^{186}, respectively. This is the first experimental proof of the existence of a second rotational level with E = 400 kev in W^{186}.

The two-step (double E2) Coulomb excitation was also observed by Newton and Stephens[6]. They investigated the Coulomb excitation of tungsten bombarded with 40 to 80 Mev oxygen ions, and observed a broad peak at E_γ = 250 kev, corresponding to the superposition of lines emitted in 4+→2+ transitions in W^{182}, W^{184} and W^{186}.

The results of our investigation, carried out with separated isotopes and using neon and nitrogen ions, agree with the data of Newton and Stephens and to a certain extent, complement their data.

Physical-Technical Institute,
Academy of Sciences of the USSR

References

1. D.G.Alkhazov, A.P.Grinberg, G.M.Gusinskii & I.Kh.Lemberg, Izv.AN SSSR, Ser.fiz., 23, 1465 (1959). (Trans.Bulletin 23, 1451.)
2. J.Murray, F.Boehm, P.Marmier & J.DuMond, Phys.Rev., 97, 1007 (1955).
3. F.Butement & A.Poe, Phil.Mag., 46, 482 (1955).
4. A.Poe, Phil.Mag., 46, 1165 (1955).
5. D.G.Alkhazov, A.P.Grinberg, G.M.Gusinskii, K.I.Erokhina & I.Kh.Lemberg, Zhur.eksp.i teor.fiz., 35, 1325 (1958). (Trans.Soviet Physics - JETP.)
6. J.O.Newton, F.S.Stephens, Phys.Rev.Letters, 1, 63 (1959).

COULOMB EXCITATION OF THE FIRST LEVELS OF EVEN ISOTOPES OF CHROMIUM, SELENIUM AND NEODYMIUM

- D.S.Andreev, A.P.Grinberg, G.M.Gusinskii, K.I.Erokhina & I.Kh.Lemberg

At the Ninth All-Union Conference on Nuclear Spectroscopy we reported the results of our investigation of Coulomb excitation of a number of even-even nuclei under bombardment with heavy ions.

In the present report we give the new results obtained in investigating Coulomb excitation of even isotopes of chromium, neodymium and selenium, using cyclotron accelerated 16.3 and 36.0 Mev nitrogen and 23.2 Mev neon ions.

The experimental set-up and procedure have been described earlier.[1,2] The results of the present investigation are summarized in the accompanying table, wherein ΔE is the energy of the excited level, $B(E2)\uparrow$ is the experimental value of the reduced transition probability, $B(E2)\uparrow^*$ is the reduced transition probability according to the data in the literature, F is the ratio of the experimental value of $B(E2)$ to $B(E2)_{spt}$ (the value of the reduced probability given by the formula for single-particle transitions), and τ is the lifetime of the level (the values of ΔE are given in Mev; the reduced probabilities in 10^{-48} e^2 cm^4 units). The values of τ were calculated by means of the following equation:

$$\tau = \frac{375}{4\pi} \cdot \left(\frac{\hbar c}{\Delta E}\right)^5 \frac{\hbar}{B(E2)\uparrow} = \frac{4.0939 \cdot 10^{-13}}{(\Delta E)^5 \cdot B(E2)\uparrow} \text{ sec},$$

which is valid for all even-even nuclei in which the spin and parity of the first excited states are always 2+.

The values of $B(E2)_{spt}$ were calculated by the formula

$$B(E2)_{spt} = \frac{5}{4\pi} e^2 \left(\frac{3}{5} R_0^2\right)^2 = 3 \cdot 10^{-5} A^{4/3},$$

and the nuclear radius R_0 being taken equal to $1.2 \cdot 10^{-13}$ $A^{1/3}$ cm. In the table we also indicate the levels (nucleus, ΔE and $B(E2)$ that served as the reference in each of the experiments.

Experimental Results

Chromium. For our experiments we had available targets of chromium oxide, Cr_2O_3, enriched with Cr^{52} and Cr^{54}, and a target of natural chromium prepared by vacuum evaporation. The energies of the first excited states of all three even chromium isotopes are known from studies of inelastic proton scattering.[10]

In the experiments on Coulomb excitation of Cr^{54} the target was chromium oxide; the projectiles were 23.2 Mev Ne^{20} ions. The value of $B(E2)$ obtained in these experiments differs little from the value obtained earlier[1] in bombardment with nitrogen ions.

It is impossible to investigate Coulomb excitation of Cr^{52} using a chromium oxide target, inasmuch as in this case there appears in the spectrum a strong γ-peak at 1.37 Mev due to nuclear reactions.[11] The peak corresponding to a 1.37 Mev γ-line was also observed in bombarding a target of natural chromium with 36 Mev nitrogen ions. The area of the peak in this case, however, is much smaller, and consequently, the integral peak can be resolved into two peaks (Fig.1). The energy of the first level of Cr^{52} according to the data of Van Patter et al[10] is 1.432 ± 0.005 Mev. In our experiments we obtained $\Delta E = 1.45$ Mev.

In the table we give the value of $B(E2)$ calculated on the assumption that $\Delta E = 1.45$ Mev. If one takes $\Delta E = 1.43$ Mev, the resultant value of the reduced transition probability is approximately 15% lower.

Reduced probabilities for Coulomb excitation and lifetimes of the first excited states of even isotopes of chromium, selenium and neodymium

Nucleus	ΔE, Mev	Bombarding particles and their energy in Mev	Reference levels: Nucleus	Reference levels: ΔE, Mev	Reference levels: $B(E2)\cdot10^{48}$, e^2	Reference levels: Ref.	$B(E2)\uparrow\cdot10^{48}$, $e^2\cdot cm^4$	$B(E2)\uparrow^{**}\cdot10^{48}$, e^2cm^4 [Ref]	$\tau\cdot10^{11}$, sec	F
Cr^{50}	0,78	$Ne^{20}(23,2)$	Mo^{100}	0,53	0,614	[3]	0,15		0,9	27
Cr^{52}	1,45	$N^{14}(36,0)$	Ni^{58}	1,45	0,080	[1]	0,062		1,2	10
Cr^{54}	0,84	$N^{14}(16,3)$, $Ne^{20}(23,2)$	Ti^{48}	0,99	0,070	[4]	0,057		1,7	9
Se^{78}	0,560	$N^{14}(36,0)$, $Ne^{20}(23,2)$					0,42	0,43 [7] 0,45 [8]	1,8	44
Se^{78}	0,615	$N^{14}(36,0)$, $Ne^{20}(23,2)$	Mo^{100}	0,53	0,614	[3]	0,36	0,36 [7]	1,3	36
Se^{80}	0,650	$N^{14}(36,0)$	Ti^{48}	0,99	0,070	[4]	0,23	0,23 [7]	1,5	22
Se^{82}	0,660	$N^{14}(36,0)$					0,19		1,7	18
Nd^{144}	0,695	$N^{14}(36,0)$	$Zr^{92,94}$	0,92	0,079	[3]	0,23		1,1	10
Nd^{146}	0,455	$N^{14}(36,0)$	$Zr^{92,94}$	0,92	0,079	[3]	0,25	0,25 [9]	8,4	11
Nd^{148}	0,300	$N^{14}(36,0)$	Rh^{103}	0,30	0,21	[5]	0,57	0,69 [9]	30	24
Nd^{150}	0,130	$N^{14}(36,0)$	Ta^{181}	0,136	2,04	[6]	1,92	2,3 [9]	575	80

The operation of separating the peaks naturally increases the error in determining the area. As a result the possible error in the value of $B(E2)$ for the first excited level of Cr^{52} is ±35%, according to our evaluation.

Coulomb excitation of Cr^{50} was investigated using 23.2 Mev Ne^{20} ions. The target was natural chromium. The content of Cr^{50} in natural chromium is only 4.31%. The situation is further complicated by the presence of Cr^{54}, the abundance of which in natural chromium is 2.38%. As a result there was obtained a common peak in the spectrum (Fig.2). In calculating the value of $B(E2)$ for Cr^{50} we subtracted from the area under this peak the fraction due to excitation of Cr^{54}. This fraction was calculated on the basis of the previously determined value of $B(E2)$ for Cr^{54}. Inasmuch as this fraction is relatively small (~15% of the total area under the peak), the additional error involved in determining the value of $B(E2)$ for Cr^{50} is minor.

Selenium. Our original results for Coulomb excitation of selenium, obtained in experiments with nitrogen ions bombarding targets enriched with different Se isotopes, are described in Ref.1. In the present experiments the measurements were repeated by using 23.2 Mev Ne^{20} ions. The values of $B(E2)$ obtained were the same as in the earlier experiments. We note the good agreement of our values for $B(E2)$ with those obtained by Temmer & Heydenburg[7] in experiments with 7 Mev α-particles. It must be pointed out, however, that Temmer & Heydenburg obtained a value of 880 kev for the first excited level of Se^{82}, whereas according to our data ΔE = 660 ± 10 kev. A close value for ΔE (670 ± 10 kev) was obtained by Stelson & McGowan[8], who, however, do not give a value for $B(E2)$. Possibly Temmer & Heydenburg observed a γ-line due to the nuclear reaction $Se^{82}(\alpha,2n)Kr^{84}$. The energy of the first level of krypton 84, according to Johnson & O'Kelley[12] is 880 kev.

The lifetime of the first excited state of Se^{76} was measured in the work of Belyagin[13] who investigated resonance scattering of As^{76} γ-rays from selenium. According to Belyagin's data, $\tau = (1.3 \pm 0.2)\cdot10^{-11}$ sec. This value agrees within the limits of the experimental error with our value of $(1.8 \pm 0.4)\cdot10^{-11}$ sec.

It must be noted, however, that recently Pruett[14] published a different value for the lifetime of the first excited state of Se^{76};

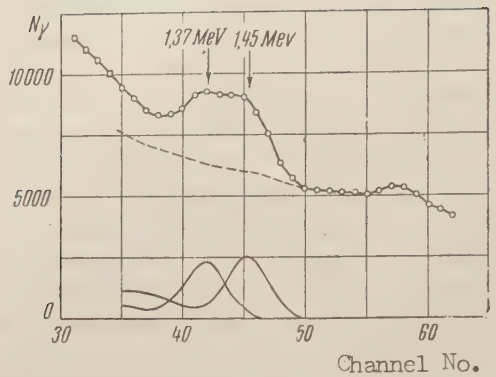

Fig.1. Experimental γ-ray spectrum obtained in bombarding natural chromium with 36.0 Mev N ions.

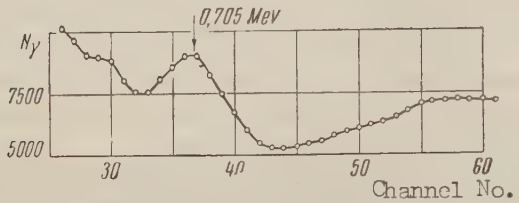

Fig.3. Experimental γ-spectrum obtained in bombarding a target of natural neodymium with 36.0 Mev N ions.

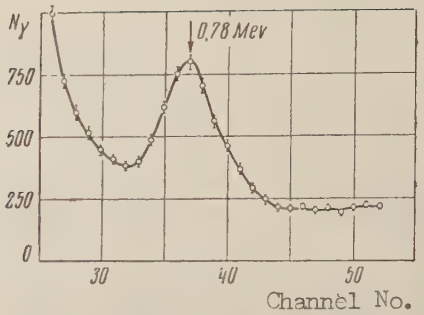

Fig.2. Experimental γ-spectrum obtained in bombarding natural chromium with quadruply charged 23.2 Mev Ne^{20} ions.

this was also obtained in experiments on resonance scattering. Pruett gives $\tau = (2.6 \pm 0.3) \cdot 10^{-11}$ sec.

It will be evident that there is an appreciable divergence between the lifetime values obtained in resonance scattering experiments. In contrast, the values of $B(E2)$ obtained by different authors in investigating Coulomb excitation of the first level of Se^{76} are in good agreement. This can be explained by the fact that the state in question is abundantly excited, while background effects are very weak compared with the intensity of the observed line. Hence it may be inferred that the lifetime values obtained from Coulomb scattering experiments are more reliable.

Neodymium. Coulomb excitation of neodymium was investigated by Simmons et al[15] and Temmer & Heydenburg[9], who bombarded appropriately enriched targets with 3.3 Mev protons and 6 Mev α-particles, respectively. In these studies there were successfully excited the first levels of Nd^{146}, Nd^{148} and Nd^{150}, i.e., of the isotopes in which the excitation energy of the first level is relatively low.

In our experiments we also obtained results for Nd^{144}. This was facilitated by the use of a target of natural metallic neodymium (Nd^{144} content 23.87%). By way of projectiles we used 36 Mev nitrogen ions. The energy of the first excited level of Nd^{144} (ΔE = 0.695 Mev) is known from the work of Engelder[16] and Kreger & Cook[17]. In our experiments we obtained $\Delta E = 705 \pm 10$ kev (Fig.3). In calculating the value of $B(E2)$ we used ΔE = 0.695 Mev. The satisfactory agreement of our values of $B(E2)$ for Nd^{146}, Nd^{148} and Nd^{150} with the results of other authors gives reason to assert that the error in calculating $B(E2)$ for Nd^{144} does not exceed 25%. The presence of a relatively strong background in the E_γ = 1.5 Mev region, due to contamination of the target, prevented us from detecting Coulomb excitation of the first level of Nd^{142} (ΔE = 1.57 Mev).

Conclusions

The results obtained in the present study of Coulomb excitation of the even isotopes of chromium, selenium and neodymium supplement the available data on the first levels of even-even nuclei, and justify the following observations.

It has been inferred by Knapp[4] and other authors that the values of τ determined from experiments on Coulomb excitation are consistently higher than the lifetime values determined on the basis of resonance scattering of γ-rays. As we noted previously[1], however, this is not actually the case. Thus the value of the lifetime for the first level of Se^{76} deduced from our experiments is in good agreement with the value of τ obtained in investigations[13,14] of resonance scattering of As^{76} γ-rays by selenium.

The character of the variation of the energy and reduced transition probabilities for the first excited levels of nuclei of different isotopes of the same element as a function of the number of neutrons in the nucleus is well known. With deviation of the number of neutrons from the magic number, the value of ΔE decreases, while the value of $B(E2)$ increases. This behavior of ΔE and $B(E2)$ is clearly evinced for the isotopes of selenium and neodymium.

The Cr^{52} nucleus (Z = 24) has 28 neutrons, i.e., a closed neutron shell. Accordingly, the energy of the first excited level of Cr^{52} (ΔE = 1.45 Mev) is substantially greater than the energy of the first levels of Cr^{50} and Cr^{54} (ΔE = 0.780 and 0.840 Mev, respectively). Noteworthy, however, is the fact that the value of $B(E2)$ for the first level of Cr^{52} is almost identical with the value of the reduced transition probability for the first level of Cr^{54}.

Physical-Technical Institute,
Academy of Sciences of the USSR

References

1. D.S.Andreev, A.P.Grinberg, K.I.Erokhina & I.Kh.Lemberg, Nucl.Phys., (1960). (In press.)
2. D.G.Alkhazov, D.S.Andreev, A.P.Grinberg, K.I.Erokhina & I.Kh.Lemberg, Izv. AN SSSR, Ser.fiz., 25, No.1 (1961). (Trans.Bulletin, 25, No.1.)
3. P.N.Stelson & F.K.McGowan, Phys.Rev., 110, 498 (1958).
4. V.Knapp, Proc.Phys.Soc., 71, 194 (1958).
5. K.Alder, A.Bohr, T.Huus, B.Mottelson & A.Winther, Revs.Mod.Phys., 28, 432 (1956).
6. F.K.McGowan & P.H.Stelson, Phys.Rev., 109, 901 (1958).
7. G.M.Temmer & N.P.Heydenburg, Phys.Rev., 104, 967 (1956).
8. P.H.Stelson & F.K.McGowan, Bull.Amer.Phys.Soc., Ser.II, 4, 282 (1959).
9. G.M.Temmer & N.P.Heydenburg, Phys.Rev., 100, 150 (1955).
10. D.M.Van Patter, W.C.Porter, M.A.Rothman & C.E.Mandeville, Bull.Amer.Phys. Soc., Ser.II, 3, 38 (1958).
11. D.G.Alkhazov, A.P.Grinberg, G.M.Gusinskii & I.Kh.Lemberg, Izv.AN SSSR, Ser.fiz., 23, 1465 (1959). (Trans.Bulletin, 23, 1451.)
12. N.R.Johnson & G.D.O'Kelley, Nucl.Sci.Abstrs., 11, No.6B (1957).
13. N.N.Delyagin, Tezisy dokladov X ezhegodnogo soveshchaniya po yadernoi spektroskopii (Program of the Tenth Annual Conference on Nuclear Spectroscopy), M.-L., 1960.
14. J.R.Pruett, Bull.Amer.Phys.Soc., Ser.II, 4, 57 (1959).
15. B.E.Simmons, P.M.Van Patter, K.F.Famularo & R.V.Stuard, Phys.Rev., 97, 89 (1955).
16. T.Engelder, Phys.Rev., 90, 259 (1953).
17. W.E.Breger & C.S.Cook, Phys.Rev., 96, 885 & 1276 (1954).

COULOMB EXCITATION OF Ne^{21}

- D.S.Andreev, K.I.Erokhina & I.Kh.Lemberg

Investigation of Coulomb excitation of nuclear levels using gas targets is complicated by the difficulties associated with exact determination of the absolute yields. Heydenburg, Pieper & Anderson[1,2] studied Coulomb excitation of isotopes of krypton and xenon. However, they obtained only relative γ-ray yields. These data are insufficient for the determination of the level lifetimes.

The use of cyclotron accelerated ions of the gaseous element being studied as bombarding particles allows of circumventing the difficulties associated with the use of gas targets. This method was used by us[3] to investigate the Coulomb excitation of Ne^{20} and Ne^{22}. In these experiments natural neon was fed into the ion source of the cyclotron.

The abundance of Ne^{21} in natural neon is only 0.26%. Consequently, the Ne^{21} ion current in the extracted beam was so small that accurate measurements of the Ne^{21} Coulomb excitation was impossible.

Below we give the results obtained in investigating Coulomb excitation of the first level of Ne^{21}. Neon enriched with Ne^{21} was placed in the ion source. The current of quadruply charged Ne^{21} ions with E = 24.2 Mev to the target was $\sim 5 \cdot 10^{-11}$ amp.

At a given frequency of the generator the resonance value of the magnetic field intensity is proportional to the ratio M/Z, where M is the mass of the accelerated ion and Z is its charge in electron charge units. For quadruply ionized Ne^{21} M/Z = 5.25. In principle, in supplying neon to the ion source, in view of possible contamination, one can expect simultaneous acceleration of ions of carbon, nitrogen and oxygen isotopes. The value of M/Z in the present case is most closely approached by triply ionized O^{16}. For triply charged O^{16} M/Z = 5.33 and the resonance value of the cyclotron magnetic field is 1.6% greater than the field value necessary for the acceleration of quadruply charged Ne^{21} ions.

It was found, however, that as a result of a 1% change of the cyclotron field from the value corresponding to acceleration of Ne^{21} ions, the current intensity at the target decreased by more than a factor of 20. From this it follows that the proportion of triply ionized O^{16} in the extracted beam was not more than 5%.

By way of targets we used graphite, aluminum and molybdenum. The γ-rays produced by bombardment of the targets by Ne^{21} ions were detected by means of a γ-spectrometer with a NaI(Tl) crystal. In all cases the recorded spectra composed a peak corresponding to 0.35 Mev gammas. By way of illustration the γ-spectrum obtained in bombarding the aluminum target with Ne^{21} ions is reproduced in the accompanying figure.

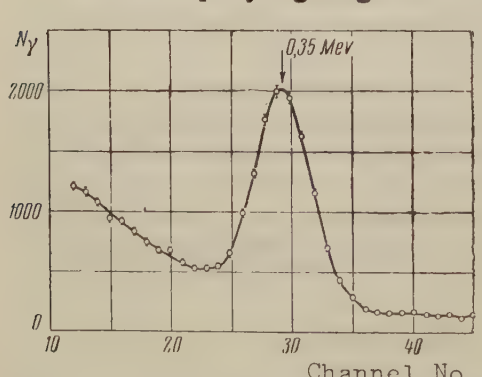

Gamma-spectrum obtained in bombarding aluminum with 24.2 Mev quadruply charged Ne^{21} ions.

According to the data of Serdyukova et al[4], Ahnlund[5] and French & Thomson[6], who studied the nuclear reactions $O^{18}(\alpha,n)Ne^{21}$, $Ne^{20}(d,p)Ne^{21}$ and $Na^{23}(d,\alpha)Ne^{21}$, Ne^{21} has an excited level at 0.35 Mev. It is natural to assume that the γ-line observed in our experiments corresponds to excitation of this level in Ne^{21}.

Working with Ne^{20} ions we observed[7] a low intensity γ-line occurring as a result of nuclear reaction of Ne^{20} ions with carbon. In principle, one cannot exclude the possibility that the 0.35 Mev γ-line observed in the present experiments is also due to a nuclear reaction with carbon. In this case, however, the yield of 0.35 Mev γ-rays in bombarding aluminum

should have been roughly 100 times lower than in bombarding carbon (our observations showed that a carbon film formed on all the targets, apparently as a result of decomposition under ion bombardment of oil vapor deposited on the target surface). It was found, however, that the 0.35 Mev γ-ray yields in bombardment of aluminum and graphite are comparable. This proves that the 0.35 Mev γ-line is not a result of nuclear reaction on carbon but is due to Coulomb excitation of Ne^{21}.

The mean value of the reduced probability $B(E2)$ for transition of Ne^{21} from the ground state to the 0.35 Mev excited state according to the data of our experiments with C, Al and Mo is $0.025 \cdot 10^{-48}$ e^2 cm^4.

According to the data of Ahnlund[5], the assignment for the first excited state of Ne^{21} is 3/2+ or 5/2+; according to Hubbs & Grosof[8] the ground state spin of Ne^{21} is 3/2+. Using these spin values, one can calculate the reduced probability $B(E2)\downarrow$ for transition from the 0.35 Mev state to the ground state: $(2J_0+1)\cdot B(E2)\uparrow = (2J_f+1)\cdot B(E2)\downarrow$. We obtain $B(E2)\downarrow = 0.025 \cdot 10^{-48}$ e^2 cm^4 or $0.017 \cdot 10^{-48}$ e^2 cm^4, depending on which value of J_f is adopted.

From the values of $B(E2)\downarrow$ making use of the formula

$$\tau(E2) = 0.819 \cdot 10^{-13} \frac{1}{(\Delta E)^5 B(E2)\downarrow},$$

one can calculate the value of the partial lifetime of the first excited state of Ne^{21}:

$$\tau(E2) = (6.3 \text{ or } 9.2) \cdot 10^{-10} \text{ sec.}$$

Thus, the following values of $B(E2)\uparrow$ for the first levels of all three neon isotopes (in units of e^2 10^{-48} cm^4) were obtained: Ne^{20} - 0.047; Ne^{21} - 0.025; Ne^{22} - 0.039. The weak dependence of $B(E2)$ on the number of neutrons is striking.

We take this opportunity to thank A.B.Girshin who assured the uninterrupted operation of the cyclotron.

Physical-Technical Institute,
Academy of Sciences of the USSR

References

1. N.P.Heydenburg, G.F.Pieper & C.E.Anderson, Phys.Rev., 108, 106 (1957).
2. G.F.Pieper, C.E.Anderson & N.P.Heydenburg, Bull.Amer.Phys.Soc., 3, 38 (1958).
3. D.G.Alkhazov, A.P.Grinberg, I.Kh.Lemberg & V.V.Rozhdestvenskii, Zhur.eksp. i teor.fiz., 36, 322 (1959). (Trans.Soviet Physics - JETP.)
4. I.A.Serdyukova, A.G.Khabakhpashev & E.M.Tsenter, Izv.AN SSSR, Ser.fiz., 21, 1017 (1957). (Trans.Bulletin, 21, 1018.)
5. K.Ahnlund, Arkiv fys., 7, 155 (1954).
6. A.P.French & D.M.Thomson, Proc.Phys.Soc., A,64,203 (1951).
7. D.G.Alkhazov, A.P.Grinberg, G.M.Gusinskii & I.Kh.Lemberg, Izv.AN SSSR, Ser.fiz., 23, 1465 (1959). (Trans.Bulletin, 23, 1451.)
8. J.Hubbs & G.Grosof, Phys.Rev., 104, 715 (1956).

DETERMINATION OF THE L FLUORESCENCE COEFFICIENTS OF Ga^{71}, Cu^{65} AND V^{51}

- A.A.Konstantinov, T.E.Sazonova & V.V.Perepelkin

The L x-ray fluorescence coefficients, or ratios of the number of L x-rays to the number of vacancies in the L shell, have been determined experimentally only for elements with Z = 36 (Ref.1) and Z > 40 (Refs.2-6). Knowledge of the L fluorescence coefficients for elements with Z < 36 is essential not only for refinement of the present theory of the Auger effect but also for the solution of a number of specific physical problems involving radioactive nuclides. Unfortunately, experimental determination of the L fluorescence yields of elements with Z < 36 is hampered by the fact that these x-rays are strongly absorbed in air.

For determining the L fluorescence coefficients of Ga^{71} (Ge^{71}), Cu^{65} (Zn^{65}), and V^{51} (Cr^{51}) we used a 4π proportional counter and employed the method of three fillings of the counter developed by Konstantinov[7] for determining the activity of electron capture nuclides from the K x-rays.

A 4π proportional counter is the most suitable instrument for measuring the L fluorescence coefficients of daughter elements of electron capture isotopes with Z < 36 because of the high sensitivity of this instrument in detecting soft low intensity x-radiation. Moreover, in the case of a 4π proportional counter the source is located inside the counter so that the only material in the path of the L x-rays is the thin (85-170 $\mu g/cm^2$) celluloid film with which the source is covered in order to absorb the Auger electrons. At one particular gas filling (pressure) of the 4π proportional counter one can detect only L x-rays and the background, while at a different pressure there are detected L and K x-rays and the background.

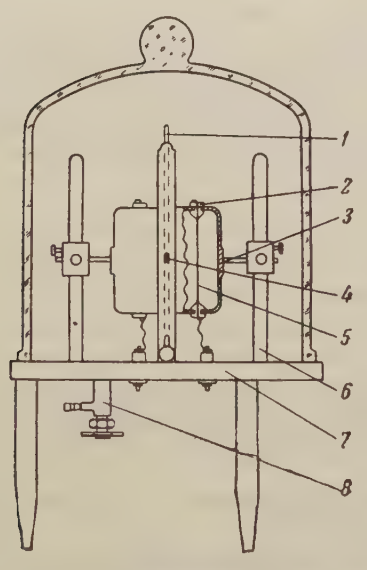

Fig.1. Diagram of the 4π proportional counter: 1) frame with aluminum foil, 2) polystyrene lead-in seals, 3) counter housing, 4) source, 5) counter filament, 6) supporting stand, 7) brass base plate, 8) valve.

Essentially the 4π proportional counter (Fig.1) consists of two 2π counters with the source between them. The source is vacuum evaporated on an aluminized celluloid film and then covered on the activity side with a similar celluloid film so that the emission from both sides is the same. The film is made thick enough to stop all K series Auger electrons.

When the 4π counter is filled with pure methane at 20 cm Hg, in the case of Zn^{65} and Ge^{71} there are detected only the L x-rays and a background (Fig.2). In the case of a Cr^{51} (V^{51}) source even with the 4π counter filled with pure methane, in addition to the L x-rays, there are detected the K x-rays (Figs.3 & 4). The L x-rays of V^{51} (Cr^{51}) are completely absorbed in the methane filling the counter when the methane pressure is 20 cm Hg; hence the number of L x-rays detected by each half of the 4π counter can be determined from the area under the L x-ray peak with the background subtracted (see the solid-line and dashed-line peaks in Figs.3 and 4).

In order to determine the total number of L x-rays emitted in the 2π angle by the source one must take into account the absorption of these x-rays in the celluloid film covering the source. The absorption in the film was determined experimentally. To this end the source was covered with an additional celluloid film and the absorption of L x-ray in the first film was determined from the absorption in the second

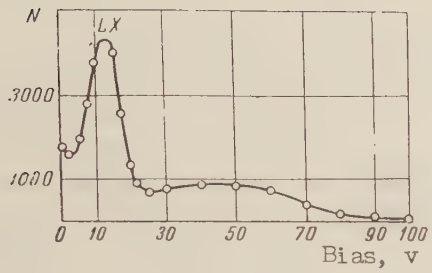

Fig.2

Fig.3

Fig.2. L x-ray peak of Ga^{71} (Ge^{71}) with the 4π counter filled with methane at a pressure of 20 cm Hg.

Fig.3. L and K x-ray peaks of V^{51} (Cr^{51}) with the 4π counter filled with methane at a pressure of 20 cm Hg. Source covered with an 85 μg/cm² celluloid film.

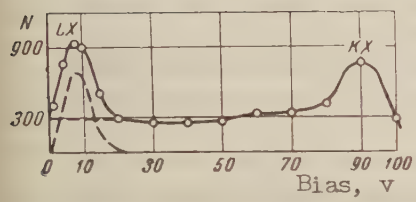

Fig.4. L and K x-ray peaks of V^{51} (Cr^{51}) with the 4π counter filled with methane at a pressure of 20 cm Hg. Source covered with a 155 μg/cm² celluloid film.

film by means of the two equations:

$$N_1 = \frac{N_0}{2}\int_1^\infty e^{-\mu h_1 z} z^{-2}\, dz; \qquad (1)$$

$$N_2 = \frac{N_0}{2}\int_1^\infty e^{-\mu h_2 z} z^{-2}\, dz, \qquad (2)$$

where N_1 is the number of L x-rays passing through the first film, N_0 is the total number of L x-rays emitted in the 4π solid angle, μ is the absorption coefficient for L x-rays in the film, h_1 is the thickness of the first film, $z = 1/\cos\theta$ (Fig.5), N_2 is the number of L x-rays passing through the two films, and h_2 is the total thickness of the two films.

The values of the integrals (1) and (2) as a function of μh have been tabulated by Gold[8].

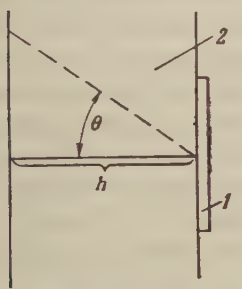

Fig.5. Experimental arrangement of source (1) and film (2).

The L x-rays of Ga^{71} (Ge^{71}) are not absorbed completely in the methane filling the counter even at a pressure of 60 cm Hg. Hence for determining the number of Ga^{71} L x-rays passing through the film we used Konstantinov's[7] method of three fillings (10, 20 and 40 cm Hg methane pressure). It was assumed that the counter background does not vary with changes in the methane pressure. This is undoubtedly true for Ga^{71} (Ge^{71}), inasmuch as Ge^{71} is a pure electron capture isotope. The L x-rays of Cu^{65} (Zn^{65}) and of Ga^{71} (Ge^{71}) are not absorbed completely in the methane filling the counter even at a pressure of 60 cm Hg. However, it is impossible to determine the number of Cu^{65} L x-rays passing through the counter by the method of three fillings inasmuch as with a Cu^{65} (Zn^{65}) source the counter background varies as a function of the methane pressure. This occurs because Zn^{65} is not a pure electron capture isotope and the accompanying radiation (positrons and conversion electrons) increases the background, which varies with the methane pressure. The number of Cu^{65} L x-rays passing through the film was determined from measurements at two fillings of the 4π counter with methane at 40 and 60 cm Hg. From the number of L x-rays absorbed by the methane at these two pressures we calculated the absorption coefficient for the L x-rays in methane,

L fluorescence coefficients of Ga^{71}, Cu^{65} and V^{51}

Isotope	N_1	N_2	N_0	Activity of source, curie	Number of L shell vacancies	ω_L, %
*Ga^{71}	26 500	18 100	75 800	$4 \cdot 10^{-6}$	$112 \cdot 10^5$	0,68
**Ga^{71}	16 400	11 800	40 700	$2,4 \cdot 10^{-6}$	$68 \cdot 10^5$	0,60
Cu^{65}	72 000	28 700	227 000	$1,4 \cdot 10^{-5}$	$10 \cdot 10^5$	0,56
*V^{51}	5 950	3 000	20 200	$2,5 \cdot 10^{-6}$	$93 \cdot 10^5$	0,22
**V^{51}	9 400	—	33 500	$3,6 \cdot 10^{-6}$	$135 \cdot 10^5$	0,25

Note: The * and ** pertain to two different sources.

and then from the calculated absorption coefficient determined the number of Cu^{65} L x-rays passing through the film. It may be noted that the experimental and theoretically calculated absorption coefficients for the L x-rays in methane agree within the limits of the experimental error.

In order to determine the L fluorescence coefficients, in addition to the total number of L x-rays emitted by the given source, one must know the number of vacancies in the L shell formed as a result of electron capture from the K and L shells during the radioactive decay. In the presence of conversion electrons one must also take into account the formation of L shell vacancies owing to internal conversion.

Inasmuch as Ge^{71} is a pure electron capture isotopes, while the number of conversion electrons in Cr^{51} and Zn^{65} is insignificant (less than 1% per decay), for these elements one can neglect the formation of addition vacancies in the L shell owing to internal conversion.

The number of L shell vacancies forming as a result of decay of an electron capture isotope can readily be determined from the activity of the source, inasmuch as it is known that for every L capture there forms one L shell vacancy for all elements, while for every K capture event the number of L shell vacancies formed differs in different elements; the specific numbers for the investigated nuclides are 1.33 for Ga^{71} (Ge^{71}), 1.39 for Cu^{65} (Zn^{65}) and 1.60 for V^{51} (Cr^{51}).

To insure distinct L x-ray peaks standing well above the background the Ge^{71}, Zn^{65} and Cr^{51} sources were prepared with an activity of $\sim 10^{-5}$ curie. Measurement of the activity of such strong sources directly in the 4π counter is impossible owing to overloading of the counter; hence the activities were determined through comparison with sources of lower activity ($\sim 10^{-7}$ curie), the activity of which could be measured directly in the 4π counter by the method of three fillings[7]. The comparison of the activities was carried out with reference to the K x-rays by means of an end window counter or a 4π counter.

The values of the L fluorescence coefficients obtained in our experiments for Ga^{71} (Ge^{71}), Cu^{65} (Zn^{65}) and V^{51} (Cr^{51}) are listed in the accompanying table.

We evaluate the error in determining the values of ω_L as 12-16%. As will be evident from the table, the values of ω_L for the two Ga^{71} (Ge^{71}) and the two Cr^{51} (V^{51}) sources (* and **) agree within the limits of the experimental error. For the second Cr source (**) the absorption of L x-rays in the film was determined from the absorption coefficient μ that was found in the measurements with the first Cr^{51} (V^{51}) source (*).

"D.I.Mendeleev" All-Union Scientific Research Institute of Metrology

References

1. P.Auger, J.Phys.et radium, 6, 205 (1925).
2. H.Lay, Z.Phys., 91, 533 (1934).
3. H.Küstner & E.Arends, Ann.Phys., 22, 433 (1935).
4. R.J.Stephenson, Phys.Rev., 51, 637 (1948).
5. B.B.Kinsey, Canad.J.Res., A.26, 404 (1948).
6. R.W.Fink & B.Robinson, Phys.Rev., 98, 1293 (1955).
7. A.A.Konstantinov, PTE, No.1, 67 (1959). (Trans.Instruments & Experimental Techniques.)
8. E.Gold, Proc.Roy.Soc., A82, 62 (1909).

INVESTIGATION OF THE DECAY OF Te^{118} AND Te^{119} AND THE LEVEL SCHEME OF Sb^{119}

- A.A.Sorokin, A.Bedesku, M.V.Klimentovskaya, L.N.Kryukova, K.P.Mitrofanov, V.V.Murav'eva, V.N.Rybakov, G.Chandra & V.S.Shpinel'

Introduction

The tellurium isotopes Te^{118} and Te^{119} were discovered in 1948 by Lindner & Perlman[1]. These authors also determined some of the characteristics of the decay of these isotopes. Thus, Te^{118} converts by electron capture with a period of 6 days to 3.5 min Sb^{118}. The latter decays to stable Sn^{118}, emitting positrons in the process. The positron energy was found to be 3.1 ± 2 Mev by absorption in beryllium.

Te^{119} has a period of 4.5 days and, also, by electron capture transforms to Sb^{119}. The decay of Te^{119} is accompanied by 1.5 Mev γ-rays. As a result of electron capture in Sb^{119} there is excited a 24 kev level of Sn^{119}, which by a strongly converted γ-transition de-excites to the ground state of Sn^{119}.

Zaitseva et al[2] in their recent study, in addition to 4.5 day Te^{119}, observed an activity with a period of 12 ± 1 hr also leading to the formation of Sb^{119}. This means that Te^{119} forms an isomeric pair. This is not surprising inasmuch as Te^{119} (67 neutrons) is located in the same island of isomerism as the tellurium isotopes with mass numbers 121 through 133. It is also reported[3] that the decay of the 12 hour isomer is accompanied by emission of 660 kev γ-rays.

In the present work we investigated the decay of Te^{118} and Te^{119} and constructed a tentative level diagram for Sb^{119}.

Sources

The neutron-deficient isotopes of tellurium were obtained by bombardment of a KI target with 660 Mev protons in the internal beam of the Joint Institute for Nuclear Research synchrocyclotron. The irradiation time was 1-1.5 hours. The tellurium fraction was separated chemically (see appendix) from the target some 1-2 days after bombardment. The final product was metallic tellurium powder. The specific activity of the specimen owing to the necessity of adding a carrier was not high and amounted to only 5 mC/g. The sources for β-spectrometry were prepared by deposition of the tellurium from a suspension in alcohol with a small amount of BF adhesive onto 1.6 mg/cm^2 aluminum foils.

Equipment

The γ-spectrum and the γ-γ coincidence spectra were measured by means of scintillation spectrometers[4]. The γ-ray detectors were 40 x 40 NaI crystals coupled to FEU-13 photomultipliers. The half-width of the Cs^{137} 660 kev line was 10%. The resolving time of the coincidence circuit was $2\tau = 2 \cdot 10^{-7}$ sec. The spectra were recorded on a 100-channel pulse height analyzer (type AI-100). The electron spectra were measured on a two-lens β-spectrometer of the BML type, equipped with a helical aperture. Depending on the specific measurements, the resolution of the spectrometer varied from 1.5 to 3.5%, the corresponding transmission factors being 2 and 5%, respectively.[5]

Some sections of the conversion electron spectrum were investigated on a spiral spectrometer[6] with a resolution of ~1%. In measuring β-γ coincidences, for the purpose of discriminating the partial β-spectra, we used a set-up consisting of a two-lens β-spectrometer and a scintillation γ-spectrometer, connected in coincidence.[7]

Measurements and results

Te^{118}. The Kurie plot of the positron spectrum obtained by means of the BML β-spectrometer is shown in Fig.1. As will be evident from the figure, the spectrum consists primarily of one component with end-point energy 2700 ± 50 kev. The period determined from this spectrum proved to be 6.1 ± 0.1 days. This value allows of attributing the activity to Te^{118} or to Sb^{118} in equilibrium with it. However, further experiments carried out with the daughter Sb isotopes separated from the given tellurium specimen showed that this β^+-spectrum should be attributed to Sb^{118}. This inference is in agreement with the results of Lindner & Perlman[1].

In investigating the γ-spectrum and the conversion electron spectrum (see below) we did not detect any γ-transitions corresponding to the above 6 day period. From this it may be concluded that the decay of both Te^{118} and Sb^{118} goes mainly to the ground states of the daughter nuclei. From the more accurate value for the Sb^{118} positron end-point energy obtained in our experiments, we find log ft = = 4.5, which corresponds to an allowed transition. Inasmuch as the ground state of the even-even Sn^{118} nucleus is 0+, it must be inferred that the assignment for the initial state of Sb^{118} is 0+ or 1+.

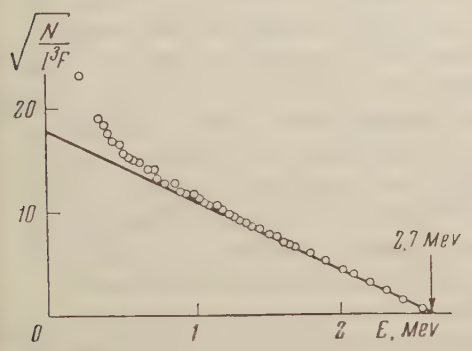

Fig.1. Kurie plot for the β^+-spectrum of the tellurium fraction measured on the BML β-spectrometer with an 8 mm diameter, 3 mg/cm² source.

McGinnis & Kundu[8] who investigated the decay of 3.5 min Sb^{118} report observing a γ-transition of 1.22 Mev energy and give a value of 0.05 for the γ/β^+ intensity ratio. From Coulomb excitation experiments it is known that Sn^{118} has a level with this energy and spin and parity 2+. If this level is actually excited with the indicated intensity, the 0+ assignment for 3.5 min Sb^{118} is excluded.

Sb^{118} is reported to have another isomer with a period of 5.1 hours. In our measurements with separated daughter Sb isotopes this period was not observed, which is in agreement with the data of Lindner & Perlman[1].

Te^{119} (T = 4.75 days). The γ-spectrum of the tellurium fraction recorded four days after bombardment by means of a scintillation spectrometer is shown in Fig.2. As repeat measurements carried out over a period of a month showed, the intensity of the spectrum in the region above 700 kev (Fig.2,b) falls off with a period of 4.75 ± 0.2 days. An equal decay period was noted for the peak at 270 kev and the main part of the ~150 kev peak, which is formed by superposition of two close γ-lines with different periods. The peak at 510 kev is due to annihilation of the positron radiation from Sb^{118} and falls off in intensity with a period of 6 days. After decay of the relatively short-lived activity there remained in the γ-spectrum the radiation corresponding to the long-lived tellurium isotopes: 154-day Te^{121} (E_γ = 2.3, 506 and 575 kev) and 104-day Te^{123} (E_γ = 159 kev) (Fig.2,a, dashed curve).

In accord with the determined period (4.75 days), the observed γ-radiation can be attributed to the decay of Te^{119}. Measurement on the antimony fraction separated from the source showed the presence of strong x-radiation, the intensity of which fell off with a period of 40 hours, which is in good agreement with the value of T = 38 hours known for Sb^{119}. Inasmuch as in the γ-spectrum of Sb^{119} there should be observed virtually only characteristic x-radiation, it must be inferred that all the observed γ-transitions with T = 4.75 days must be transitions between levels of Sb^{119}. This was substantiated by experiments on the

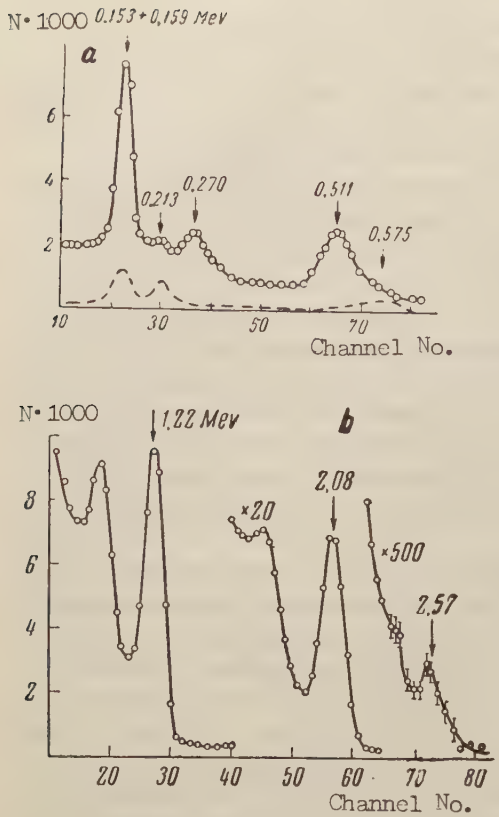

Fig.2. γ-Spectrum of the tellurium fraction, measured on a scintillation spectrometer four days after irradiation: a) 100 to 600 kev region, b) 600 to 3000 kev region. The dashed curve represents the contribution from long-lived isotopes.

weakening of x-γ coincidences for the 153, 271 and 700 kev transitions in characteristic filters (Cd, Ag, and Rh). In addition, for the 153 and 271 kev transitions we measured (spiral spectrometer) the energy differences between their K and L conversion peaks. The values obtained substantiate the inference that these γ-transitions occur in a nucleus with Z = 51, i.e., in antimony.

All the γ-transitions in Sb^{119} could not be resolved in the γ-spectrum obtained on the scintillation spectrometer. Additional information on these transitions was obtained by recording the conversion electron spectrum and the γ-γ coincidence spectrum. The conversion electron spectrum, measured on the BML spectrometer, is shown in Fig.3. The line identifications shown in the figure were made on the basis of the known data on the radiations from Te^{121}, Te^{123} and Te^{125} and for the peaks for which there is no information in the literature on the basis of the determined periods corresponding to these peaks. We determined the K/(L + M) ratios for the 153 and 271 kev transitions. For purposes of comparison of the experimental ratios with the theoretical values we extrapolated the theoretical of K/(L + M) ratios from the tables of Sliv & Band[10,11] and Rose[12]. Despite some uncertainty in the latter data (Rose's tables were calculated without taking screening into account), the results of comparison indicate that the 153 and 271 kev transitions are primarily of the dipole type. In addition, from comparison of the intensity of the peaks corresponding to the 153, 271 and 1220 kev transitions in the γ-ray and conversion electron spectra with the corresponding intensities of the peaks for the 213 kev transition in Te^{121}, for which the K shell conversion coefficient is known, we evaluated the values of α_K for these γ-transitions in Sb^{119}. The experimental values of α_K proved to be close to the tabulated values for M1 transitions. In view of the appreciable uncertainty in the experimental values, one cannot exclude the possibility of a certain admixture of E2.

E_γ, kev	I_γ, %	α_K	K/(L + M)	Multipole order
152,7 ± 0,3	55 ± 10	0,12 ± 0,03	6,3 ± 1	*M*1 or *M*1 + *E*2
271,0 ± 0,5	35 ± 8	0,04 ± 0,005	6,2 ± 0,5	*M*1 or *M*1 + *E*2
760 ± 10				
800 (?)				
920 ± 10				
950 ± 10	~15			
980 ± 20	} 60			
1100 ± 10	~15			
1220 ± 5	100	0,001 ± 0,0002		*M*1 or *E*2
1370	⩽1			
2080 ± 20	6 ± 0,5			
2350	⩽0,2			
2570 ± 50	~0,2			

The data on the γ-transitions in Sb^{119} obtained from analysis of the singles γ-spectrum, the conversion electron spectrum and partially the γ-γ coincidence spectra

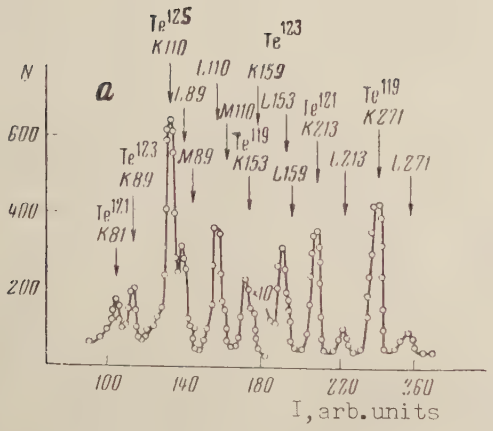

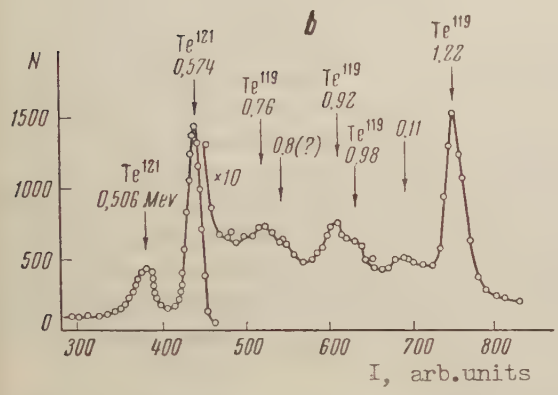

Fig.3. Conversion electron spectra: a) 30 to 300 kev region; 5 mm diameter 0.2 mg/cm^2 source; resolution ~2 %; b) 300 to 1300 kev region, 8 mm diameter 3 mg/cm^2 source; resolution 3.5 %.

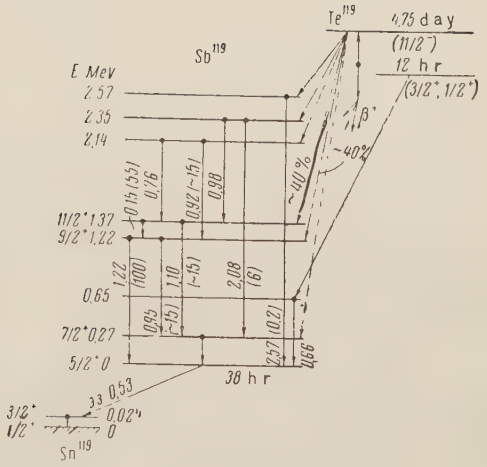

Fig.4. Decay scheme for Te^{119}. The figures in parentheses at the transition lines are the relative intensities of the transitions.

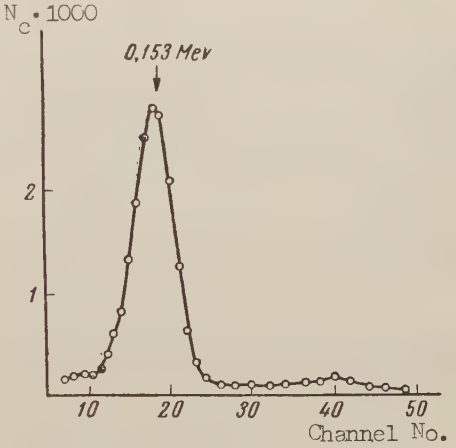

Fig.5. Spectrum of γ-rays in the 50 to 300 kev interval yielding coincidences with the 1220 kev γ-rays.

are summarized in the accompanying table.

The results of γ-γ coincidence measurements enabled us to construct a tentative diagram of the levels of Sb^{119} excited in the decay of 4.75 day Te^{119}. This diagram is shown in Fig.4. The most intense cascade is the 153-1220 kev cascade (Fig.5). The high intensity of this cascade and of the 153 and 1220 kev transitions makes it imperative to introduce a level at 1370 kev. Inasmuch as the intensity of the 1220 kev transition is greater than the intensity of the 153 kev transition (see table), it must be inferred that the 1220 kev transition departs from a level at 1220 kev and feeds the ground state. The 2080 kev γ-rays yield coincidences with the 127 kev γ-rays (Fig.6) but do not yield coincidences with γ-rays of other energies. It must therefore be inferred that there is a level at 2350 kev.

In addition, there were observed 271-950, 271-1100 (Fig.7) and 153-950 kev (Fig.8) cascades. It was also found that there are no 1100-950 and 271-1220 kev cascades, but there are coincidences between the 153 and 271 kev γ-rays. These facts can be explained if we introduce a level with 271 kev energy and assume

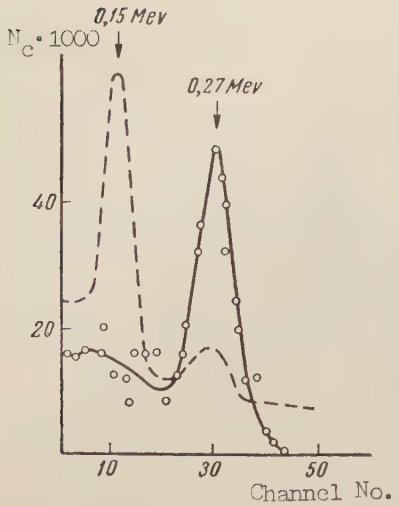

Fig.6

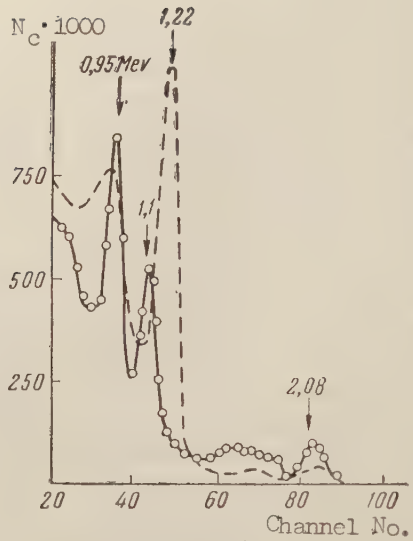

Fig.7

Fig.6. Spectrum of γ-rays yielding coincidences with the 2080 kev γ-rays. Dashed curve - singles γ-spectrum.

Fig.7. Spectrum of γ-rays yielding coincidences with the 270 kev γ-rays. Dashed line - singles spectrum. On the basis of these measurements one can determine the relative intensities of the 950 and 1100 kev γ-transitions not resolved in the singles spectrum.

that the 950 and 1100 kev transitions arrive at this level from levels at 1220 and 1370 kev, respectively. In the high energy part of the spectrum of γ-rays yielding coincidences with the 1270 kev gammas (Fig.9) there are evident peaks at 920, 1000 and 1200 kev. On the basis of this and the existence of a 2570 kev transition we introduced levels at 2140 and 2570 kev. It is not impossible that the level diagram for Sb^{119} in the 2 to 2.5 Mev region is more complicated than shown in Fig.4.

Angular correlation of the 153-1220 kev cascade was investigated on the set-up described in Ref.13. The correlation function obtained, after introduction of the appropriate corrections for the angular resolution of the detectors may be represented in the form

$$W(\theta) = 1 - (0.06 \pm 0.01)\ P_2(\cos\theta) + (0.01 \pm 0.01)\ P_4(\cos\ \theta).$$

Certain inferences regarding the spins and parities of the Sb^{119} levels can be drawn on the basis of the experimental data. The ground state of this nucleus is apparently 5/2+ (Ref.10). On the basis of the multipole orders of the 153 and 1220 kev transitions (see table) the 1370 kev level may be assigned spin values in the range from $1/2^+$ to $11/2^+$. The low intensity of the 1370 kev cross-over transition (if it exists at all) would indicate that its multipolarity is higher than E2. In this case the 1370 kev level can only be $11/2^+$. The measured correlation function for the 153-1220 kev cascade satisfies the sequences

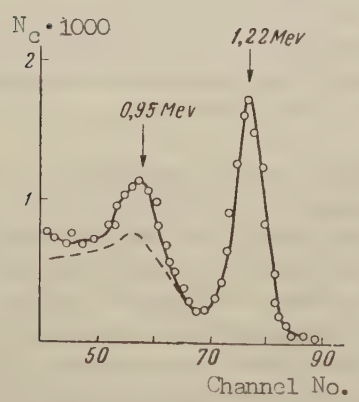

Fig.8. Spectrum of γ-rays yielding coincidences with the 153 kev γ-rays. After subtraction from the spectrum of the Compton distribution from the 1220 kev γ-rays there remains a peak corresponding to a γ-transition of 950 kev energy.

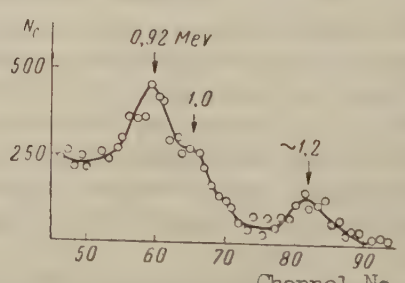

Fig.9. Spectrum of γ-rays yielding coincidences with 1220 kev γ-rays.

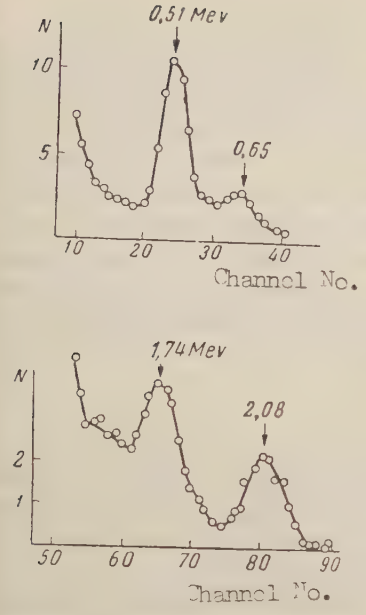

Fig.10. Sections of the scintillation γ-spectrum of the Te fraction measured 2 days after irradiation. There are evident γ-peaks at 650 and 1740 kev which may be attributed to the Te^{119} isomer with T = = 12 hours.

11/2 (Q) 7/2 (D) 5/2 or 11/2 (D) 9/2 (Q) 5/2, the admixture of quadrupole radiation to the dipole radiation in the first case being $\leqslant 10^{-3}$, and in the second case $\leqslant 3 \cdot 10^{-4}$. Inasmuch as according to the measured value of the ratio K/(L + M), the 153 kev transition is mainly M1, one must prefer the second alternative and choose the 9/2+ assignment for the 1220 kev level. According to the inferred multipole order of the 271 kev transition (M1 or M1 + E2), the assignment for the 271 kev level may be 3/2+, 5/2+ or 7/2+. In view of the fact that the transitions to this level from the 9/2 (1220 kev) and 11/2 (1370 kev) levels have an appreciable intensity the most probable assignment is 7/2+.

In β-γ coincidence experiments we were able to distinguish β^+ components with end-point energies of about 1.7, 0.9 and 0.4 Mev yielding coincidences with the γ-rays of Te^{119}. The β^+/EC ratio amounts to several percent. The data of these measurements require further checking and refinement; it may be concluded, however, that the disintegration energy of Te^{119} lies in the range from 3 to 4 Mev.

Te^{119} (T = 12 hours). In the γ-spectrum of the source investigated soon after separation of the tellurium fraction there were observed γ-transitions with energies of 650 ± 10 and 1740 ± 20 kev (Fig.10). Their intensities fell off with a period of the order of 10-15 hours. In view of the results obtained in the work of Zaitseva et al[2] these transitions can be attributed to the Te^{119} isomer with T = 12 hours. We determined the intensity ratio of these γ-rays and obtained $I_{1740}/I_{650} \approx 4\%$. These transitions were not observed in the decay of 4.75 day Te^{119}. This can be explained on the assumption that the spins of the Te^{119} isomers differ greatly from each other and hence in their decay to Sb^{119} entirely different sets of levels are excited in the antimony nucleus. On the basis of these data it may be inferred that there is a level at 650 kev in Sb^{119}. Location of the 1740 kev level in the decay scheme must await further experimentation.

Isomerism of Te^{119}. Inasmuch as Te^{119} is located in the $81 \geqslant N \geqslant 65$ island of isomerism, where there occurs competition between the $h_{11/2}$, $d_{3/2}$ and $s_{1/2}$ states, it may be inferred that one of the Te^{119} isomers has spin $11/2^-$, while the other is characterized by $3/2^+$ or $1/2^+$ by analogy with the other odd isotopes of tellurium (Te^{121} through Te^{133}).

The intensity balance drawn up for the γ-transitions in Sb^{119} indicates that in the decay of 4.75 day Te^{119} there are excited with the greatest abundance the levels with energies 1220 and 1370 and tentative assignments $9/2^+$ and $11/2^+$. Evaluation of the log ft values for the β-transitions to these levels leads to 7 ± 0.4. It may be concluded from the γ-transition intensity balance that the intensity of the β-transition to the 270 kev level is low (<10%) and that for this level log ft > 8. There apparently do not occur β-transitions to these levels from the Te^{119} state with T = 12 hours. It may therefore be concluded that the state of Te^{119} with T = 4.75 is the excited isomeric state with spin $11/2^-$.

In this case the β-transitions to the 1370 and 1220 kev levels must be first forbidden transitions ($\Delta I = 0$, yes) while the transition to the 270 kev level should be unique ($\Delta I = 2$, yes). This is not inconsistent with the above evaluations of log ft for these transitions. This being the case, the state of Te^{119}

with T = 12 hours must be the ground state. According to the Mayer single-particle model, it must have spin and parity $1/2^+$ or $3/2^+$. Definitive inferences on these points must await further detailed investigation of the decay of Te^{119}.

The isomeric transition between the isomeric states has not been detected. Apparently the partial lifetime with respect to β-decay in this case is appreciably shorter than the lifetime for the isomeric transition to the ground state.

We desire to express our gratitude to V.N.Mekhedov for making available the radioactive sources and for his interest in the work and L.Vasina, B.A.Komisarova and Chzhen Tszunshuan, students in the Physics Department of Moscow State University, for their assistance in carrying out the measurements and processing the experimental results.

References

1. M.Lindner & E.Perlman, Phys.Rev., 73, 1124 (1948).

2. N.T.Zaitseva, M.Ya.Kuznetsova, I.Yu.Levenberg & V.A.Khalkin, Program of the Ninth All-Union Conference on Nuclear Spectroscopy, M.-L., 1959.

3. N.T.Zaitseva, M.Ya.Kuznetsova, I.Yu.Levenberg, V.N.Pokrovskii & V.A. Khalkin, Program of the Tenth All-Union Conference on Nuclear Spectroscopy, M.-L., 1960.

4. N.N.Delyagin & A.A.Sorokin, Zhur.eksp.i teor.fiz., 38, 1106 (1960). (Trans. Soviet Physics - JETP.)

5. K.P.Mitrofanov & V.S.Shpinel', Izv.AN SSSR, Ser.fiz., 21, 1607 (1957). (Trans.Bulletin,21, 1595.)

6. A.V.Gnedich, L.N.Kryukova, V.V.Murav'eva & V.I.Shumshurov, PTE, No.6, 41 (1958). (Trans.Instruments & Experimental Techniques.)

7. N.N.Delyagin, A.A.Sorokin, N.V.Forafontov & V.S.Shpinel', Izv.AN SSSR, Ser.fiz., 20, 913 (1956). (Trans.Bulletin, 20, 828.)

8. C.L.McGinnis & D.N.Kundu, Bull.Amer.Phys.Soc., Ser.II, 3, 63 (1958).

9. D.Strominger, J.M.Hollander & G.T.Seaborg, Table of Isotopes, Revs.Mod. Phys., 30, 585 (1958).

10. L.A.Sliv & I.M.Band, Tablitsy koeffitsientov vnytrennei konversii gamma-luchei, Ch.I. (Tables of Internal Conversion Coefficients, Part I - K shell), M. -L., 1956.

11. L.A.Sliv & I.M.Band, Ibid., Part II - L shell), M.-L., 1958.

12. M.E.Rose, Tables of Internal Conversion Coefficients, Amsterdam, 1958.

13. M.V.Klimentovskaya & P.I.Shavrin, Zhur.eksp.i teor.fiz., 36, 5, 1360 (1958) (Trans.Soviet Physics - JETP.)

14. M.Ya.Kuznetsova, V.N.Mekhedov, V.N.Rybakov & V.A.Khalkin, Atomnaya energiya 4, 583 (1958). (Trans.Soviet Journal of Atomic Energy.)

Appendix

Separation procedure

The proton bombarded potassium iodide (6-8 g) was dissolved in 30 ml 1 N HCl; it contained approximately 5-10 mg tellurium, 10 mg each As, Sn and Sb and traces of Ca, Ni, Se, Cu, V and Cr. The sulfides were precipitated by means of H_2S, filtered out with a No.4 glass filter and washed with 0.3 N HCl. After elimination of the soluble sulfides by means of concentrated HCl, the arsenic and tellurium sulfides were dissolved in a mixture of hydrochloric and nitric acids. Further operations for separating the radiochemically pure tellurium were carried out by the procedure described earlier[14]. As the source for the measurements we used metallic tellurium, precipitated by means of SO_2.

For separation of the daughter products (antimony isotopes), the metallic tellurium was dissolved in 8 M HCl containing Br_2; then 10 mg Sb (V) were added to the solution and the antimony was extracted with diisopropyl ether. The ether layer, washed with an equal amount of 8 M HCl, served as the source for the measurements.

* * * * * * *

INVESTIGATION OF THE PROBABILITIES FOR RADIATIVE TRANSITIONS BETWEEN THE ROTATIONAL LEVELS OF Er^{166} AND Tm^{169}

- E.E.Berlovich, V.V.Il'in, A.I.Kislyakov, M.K.Nikitin & T.Bedike

The ytterbium fraction chromatographically separated from the other rare earth elements formed in a tantalum target bombarded with 660 Mev protons contains two long-lived ytterbium isotopes: Yb^{166} and Yb^{169}. Yb^{166}, which has a period of 58 hours, converts by electron capture to Tm^{166}, which in turn, with a period of 7.7 hours, transforms to stable Er^{166}. Yb^{169}, which has a period of 30.6 days, disintegrates to stable Tm^{169}. Both even-even Er^{166} and odd-odd Tm^{169} belong in the group of strongly deformed nuclei and have a clearly evinced rotational level structure. The Tm^{169} nucleus, in addition to the ground state band with K = 1/2 (K is the projection of the total angular momentum on the nuclear deformation axis) apparently has one or two bands with K = 7/2.

The purpose of the present work was to investigate the lifetimes of the first excited level (81 kev) of Er^{166} and three levels (118, 139 and 473 kev) of Tm^{169}. We employed the method of a twinned magnetic spectrometer by means of which one can carry out measurements of e—e, β—e, A—e and A—A coincidences (here e denotes internal conversion electrons, β - decay electrons and A - Auger electrons). The twin magnetic coincidence spectrometer[1] consists of a combination of two magnetic spectrometers of the sector type with improved focusing[2] with independently controlled magnetic fields and a coincidence circuit with a variable delay line. The transmission factor of each arm of the spectrometer is 1% of 4π; the resolution in the pulse scale is better than 2%. The electrons are detected by means of POPOP scintillators with a decay time of $2 \cdot 10^{-9}$ sec.

Er^{166}

The radiations emitted in the process of electron capture in Tm^{166} have been investigated by a number of authors[3-7], so that the decay scheme for Tm^{166} has been established in considerable detail[8]. The most intense lines in both the γ-ray spectrum and the conversion electron spectrum are the lines associated with E2 type transitions of 184 and 81 kev energy between the 4^+, 2^+ and 0^+ levels of the ground state rotational band (K = 0) (see insert in Fig.1).

During the first days after separation of the ytterbium fraction the intensity of the conversion lines of the 81 kev transition in Er^{166} is at least an order of magnitude greater than the intensity of the strongest lines of the transitions in Tm^{169}. Moreover, under our conditions the M line of the 81 kev transition in Er^{166} was well resolved from the close K line of the 130 kev transition in Tm^{169}, and the K line of the 184 kev transition was clearly separated from the close K line of the 177 kev transition in Tm^{169}. In Fig.2, which shows the conversion electron spectrum of the ytterbium fraction recorded after decay of the 58-hour Yb^{166}, the locations of the M line of the 81 kev transition and the K line of the 184 kev transition are indicated by arrows.

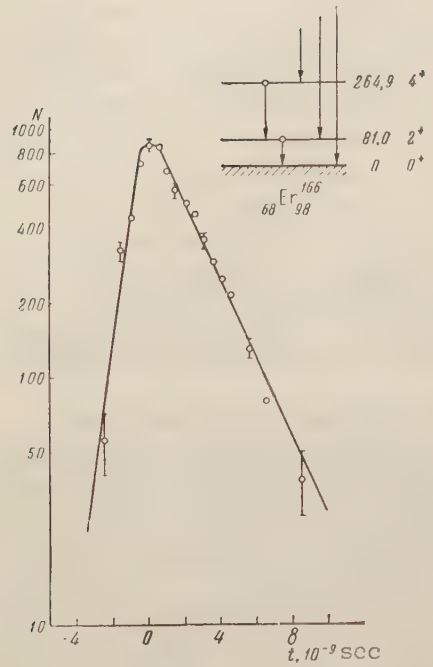

Fig.1

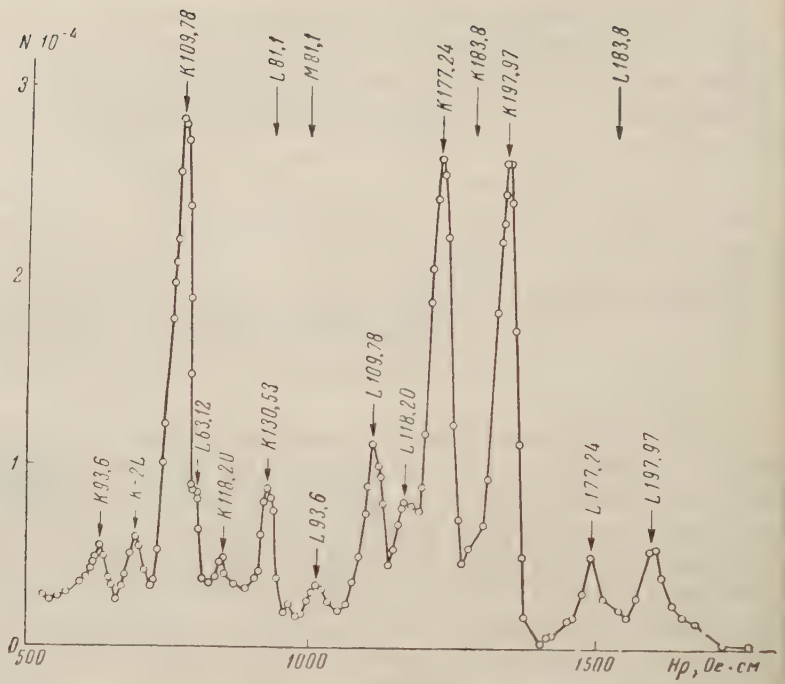

Fig.2

Fig.1. Decay curve for the 81 kev state of Er^{166} ($T_{1/2} = 2.0 \pm 0.2) \cdot 10^{-9}$ sec).
Fig.2. Spectrum of conversion electrons emitted by Yb^{169}.

The ytterbium activity, separated chromatographically in the form of the lactate, was applied in a narrow strip on a collodion film, the thickness of which is characterized by the appearance of interference colors. The film was lightly metallized by vacuum evaporation.

Fig.1 shows the decay curve in semilogarithmic coordinates for the first excited (2+) state of Er^{166}, obtained by measuring the number of coincidences between the K electrons of the 184 kev transition (left arm of the spectrometer) and the M electrons of the 81 kev transition (right arm of the spectrometer).

We obtained a value of $(2.0 \pm 0.2) \cdot 10^{-9}$ sec for the half-life of this state. This value agrees with the result obtained earlier in our laboratory[9] in investigating $Ho^{166} \rightarrow Er^{166}$ decay on a twin scintillation spectrometer, and, accordingly, leads to the same value of the internal quadrupole moment of Er^{166} ($Q_o = 6.8 \cdot 10^{-24}$ cm^2).

Tm^{169}

The $Yb^{169} \rightarrow Tm^{169}$ conversion scheme, established as a result of numerous investigations of the electromagnetic and conversion radiations[10-15], is shown in Fig.3.

Investigation of the lifetimes of the excited states of Tm^{169} is of particular interest in view of the fact that this nucleus has a ground state rotational band with K = 1/2. Rotational bands of this type represent an exceptional case in which the coupling between the spin of the odd nucleon and the nuclear deformation axis is disturbed. This leads, in particular, to a more complex sequence of level energies in the band than obtains in other cases, namely,[16]

$$E_I = \frac{\hbar^2}{2J} I\left[(I+1) + a(-1)^{I+1/2}\left(I+\frac{1}{2}\right)\right], \qquad (1)$$

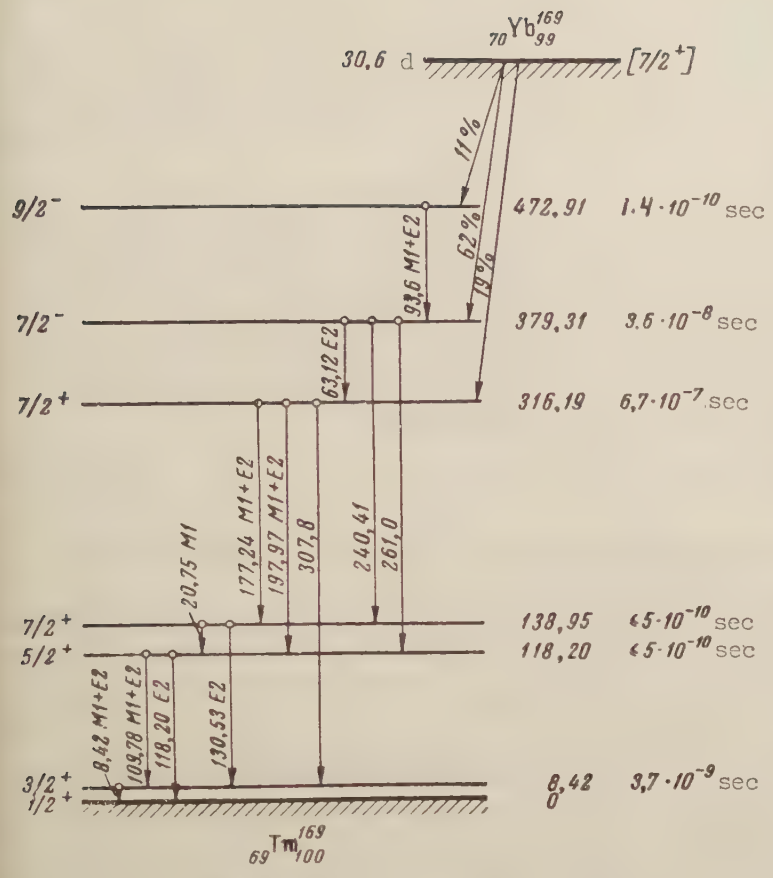

Fig.3. Decay scheme for Tb^{169}.

where a is a factor characterizing the degree of disturbance or weakening of the said coupling. The values of the parameters entering into Eq.(1) can be determined from the experimental values of the level energies: for example, from the data of Baranov et al[14]

$$a = -0.763 \text{ and } \frac{\hbar^2}{2J} = 12.457 \text{ kev.}$$

Further, at energies only 200-300 kev higher than the energy of the upper level (7/2+) of the ground state rotational band, there are located levels with other states of internal motion, levels which have high spin values (7/2 and 9/2) and are intensively populated in electron capture of Yb^{169}, the spin of which is, apparently, 7/2. This leads to the appearance of strongly forbidden (owing to the large ΔK), but at the same time intense transitions from the higher lying levels to the levels of the lower band, which are not directly populated in electron capture of Yb^{169}. Owing to this K-forbiddance and the relatively low values of the energies of the transitions to the levels of the ground state band, the lifetimes of the levels from which these transitions depart are very considerable.

A. Transitions between the levels of the ground state rotational band. The lifetime of the first excited level in Tm^{169} (8.42 kev, 3/2+) was measured by Beekhuis & De Waard[17], who accelerated the M shell conversion electrons by means of a high potential and investigated coincidences between the accelerated electrons and γ-rays. They obtained for this level $T_{1/2} = (3.7 \pm 0.5)\cdot 10^{-9}$ sec, which after taking into account conversion on the M and N shells yields a value of $(3.0 \pm 0.4)\cdot 10^{-7}$ sec for the radiation period T_γ, which is in satisfactory agreement with the result of calculations carried out by these authors for the probability for an M1 transition inside a band with K = 1/2 by means of the equations given for this case by Mottelson & Nilsson[18]:

$$T_N = 3.6\cdot 10^{-7} \text{ sec.}$$

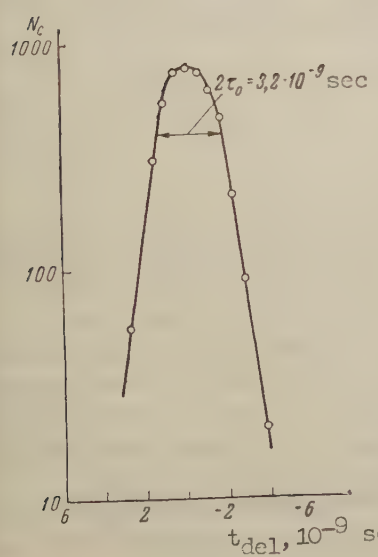

←Fig.4. Variation of the number of coincidences between the M electrons of the 110 kev transition and the K electrons of the 198 kev transition in Tm^{169} as a function of the delay time ($T_{1/2} \leqslant 5\cdot 10^{-10}$ sec).

To determine the lifetime of the second excited level (118 kev, $5/2^+$), we investigated the coincidences between the conversion electrons of the 198 and 110 kev transitions. The Yb^{169} conversion electron spectrum as recorded by one of the arms of the twin magnetic spectrometer is shown in Fig.2. For the coincidence measurements the right arm of the spectrometer was set on the K198 line, the left arm on the K110 line. The coincidence curve, shown in semilogarithmic coordinates in Fig.4, proved to be symmetrical.

The upper bound of the period of the 118 kev level determined from the slope of the left hand branch of the curve is $T_{1/2} \leqslant 5 \cdot 10^{-10}$ sec. The lifetime of this level is determined primarily by the 110 kev mixed M1 + E2 transition, inasmuch as the relative intensity of the 118 kev pure E2 transition is only ~10% (Ref.13).

The admixture of E2 in the 110 kev transition, according to Kel'man et al[19], is only 2.5%. Hence, tentatively treating it as pure M1, assuming the values of $\alpha_{110} = 2.39$ and $\alpha_{118} = 1.46$ for the total conversion coefficients of the 110 and 118 transitions, respectively, and utilizing the relationship

$$T_{\gamma\,110} = [(1 + \alpha_{110}) + 0.1\,(1 + \alpha_{118})]\,T_{1/2},$$

we obtain for the upper bound of the radiative period $T_{\gamma 110} \leqslant 1.8 \cdot 10^{-9}$ sec (110 kev M1 type transition).

One can readily calculate what the unified nuclear model predicts for this case. The probability for an M1 type transition is given by the expression[16]

$$\lambda\,(M1) = \frac{16\pi}{9} \cdot \frac{1}{\hbar} \cdot \left(\frac{\Delta E}{\hbar c}\right)^3 \cdot B\,(M1), \tag{2}$$

where $B\,(M1)$ is the reduced probability, which for transitions inside a band with K = 1/2 is of the form[18]

$$B\,(M1) = \frac{3}{64\pi}\left(\frac{e\hbar}{2Mc}\right)^2 \frac{2I+1}{I+1} G_0^2\,[1 + (-1)^{I-1/2} b_0]^2, \tag{3}$$

the parameters G_0 and b_0 are given by

$$G_0 = 3\mu - \frac{1}{2} g_s + g_l\,(1 - a) - g_R\,(2 - a); \tag{3a}$$

$$b_0 = -\frac{1}{2G_0}\left[3\mu + \frac{1}{2} g_s - g_l\,(1 - a) - g_R\,(1 + a)\right]. \tag{3b}$$

The experimental value of the parameter a was given above. The value of the magnetic moment of the Tm^{169} nucleus, determined by Lindenberg & Stendel[20], is $\mu = (-0.20 \pm 0.05)$ nuclear magnetons.

The spin and orbital g factors for the odd-Z Tm^{169} nucleus may be taken equal to the corresponding g factors for an odd proton:

$$g_s = 5.58 \text{ and } g_l = 1,$$

and the value of the g factor for the collective rotation may be taken as

$$g_R = \frac{Z}{A} = 0.41.$$

Making use of the above equations, we readily obtain

$$T_\gamma\,(M1) = \frac{\ln 2}{\lambda_\gamma} = 2.7 \cdot 10^{-11} \text{ sec},$$

which is not in conflict with the above experimentally deduced upper bound for the radiative period of a 110 kev M1 transition.

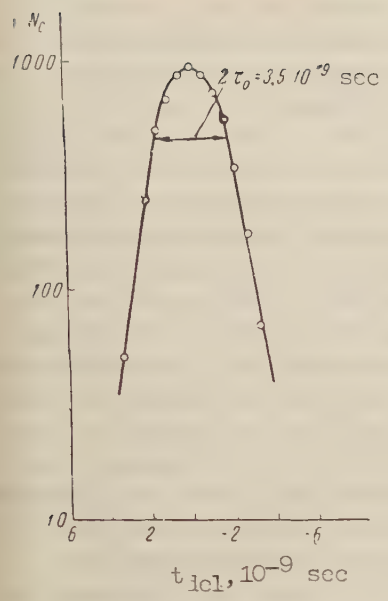

←Fig.5. Variation of the number of coincidences between the K electrons of the 130 kev transition and the K electrons of the 177 kev transition in Tm^{169} as a function of the delay time ($T_{1/2} \leqslant 5 \cdot 10^{-10}$ sec).

To determine the lifetime of the third excited level of Tm^{169} (139 kev, $7/2^+$), we investigated the coincidences between the K shell conversion electrons of the 177 and 131 kev transitions. The experimental results are shown in Fig.5. From these one can also only determine the upper bound for the period: $T_{1/2} \leqslant 5 \cdot 10^{-10}$ sec.

In view of the fact that the intensity of the 20.75 kev transition from the 139 kev $7/2^+$) level is very low, the lifetime of this level is determined mainly by the 131 kev pure E2 transition. Taking into account the value of the total conversion coefficient ($\alpha_{131} = 1$), we obtain for the radiative transition period $T_\gamma \leqslant 1 \cdot 10^{-9}$ sec.

Knowing the value of the parameter a and using the value of the deformation (0.28) obtained from Coulomb excitation experiments[21], by means of the formula for the probability of E2 type transitions in an odd nucleus inside a band with K = 1/2 with change of spin by two units, we find that the expected value for the radiative period is $3.7 \cdot 10^{-10}$ sec.

B. Lifetime of the 473 kev level. Determination of the lifetime of the highest-lying ($9/2^-$) of the levels of Tm^{169} excited in the Yb^{169}—Tm^{169} decay process is essential for establishing the nature of this level. It will be recalled that in strongly deformed nuclei with odd A there is usually an appreciable number of states of single-particle origin with lifetimes greater than 10^{-8} sec.[22] In particular, in Tm^{169} there are single-particle levels with periods of $6.7 \cdot 10^{-7}$ sec (316 kev) and $3.6 \cdot 10^{-8}$ sec (379 kev).

Hatch et al[13] identified the 473 kev level as the first excited level of a rotational band based on the 379 kev ($7/2^-$) single-particle level. The following arguments may be advanced in favor of this interpretation: first, the 94 kev transition from the $9/2^-$ level to the $7/2^-$ level is a mixed M1 + E2 transition (the admixture of E2 according to Kel'man et al[19] is 3.5%), which is characteristic of transitions between levels inside a rotational band in odd nuclei with a one unit change in spin; second, it follows from consideration of Nilsson's diagram[23] that above the $7/2^-$ level there is no single-particle orbit with negative parity closer than several hundred kiloelectronvolts. If the identification of the $9/2^-$ level as a rotational one is correct, its lifetime should be of the order of 10^{-10} sec.

The measurements of Mihelich et al[24], who investigated coincidences between K x-rays and γ-rays, led to a value of $T_{1/2} = 4 \cdot 10^{-7}$ sec for this level, which would preclude its being a member of a rotational band. Hence these authors identify this level as a single-particle one.

Further, Nathan & Marklund[25] measured the coincidences between the L conversion electrons of the 94 kev transition, detected by means of a magnetic spectrometer, and the K x-rays, detected by means of an NaI crystal. They obtained $T_{1/2} \leqslant 5 \cdot 10^{-8}$ sec. This result, while not conclusive, does not preclude identifying this level as a single-particle one.

Lastly, Hatch & Alburger[26] investigated coincidences between the L conversion electrons of the 94 kev transition, detected by a magnetic spectrometer, and the K capture x-rays. In contrast to the procedure of Nathan & Marklund, to

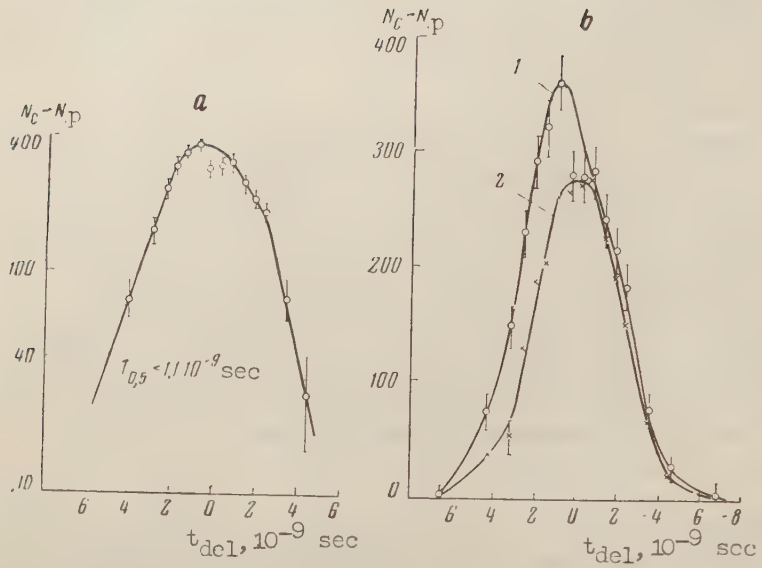

Fig.6. Variation of the number of coincidences between the K conversion electrons of the 94 kev transition in Tm^{169} and the Auger electrons as a function of the delay time: a) K 94—A coincidences, b) K 94—A (1) and A—A (2) coincidences.

improve the time resolution these authors detected the x-rays by means of an anthracene crystal. They obtained $T_{1/2} \leqslant \leqslant 3 \cdot 10^{-9}$ sec. This result is consistent with the level being a member of a rotational band.

In order to resolve the question, we undertook measurements of the lifetime of this level by the twin magnetic spectrometer procedure, which is free of the shortcomings of the techniques earlier employed and which combines good energy resolution with good time resolution.

For determining the lifetime of the 473 kev state we studied coincidences between the K shell conversion electrons of the 94 kev transition and K — - 2L Auger electrons, which compete in the process of electron capture with x-rays. Both peaks are clearly evinced in the spectrum shown in Fig.2. The energy of the conversion electrons is 34 kev; the energy of the Auger electrons is 39 kev. Although the Auger electron yield in the given Z region is of the order of 7%, the intensity of the K capture branch to the level in question amounts to only 10%, and a large number of the electrons comprising the Auger peak of interest accompanies numerous conversion electrons in the Tm^{169} nucleus (including the 93.6 kev transition); simple calculations (taking into account the transmission factor of the spectrometer, the branching ratio, the scintillation yield, and the resolving time of the coincidence circuit) show that both the absolute rate of the counted coincidences and the ratio of actual to chance coincidences are ample for carrying out decisive measurements.

The coincidence curve (Fig.6,a) proved to be almost symmetrical (width at half-height $2\tau \approx 5 \cdot 10^{-9}$ sec). From the slope of the left hand branch, which in case of a sufficiently long lifetime would have an exponential section, we find that the upper bound for the period is $1.1 \cdot 10^{-9}$ sec.

One can, however, determine not simply the upper bound but the value of the lifetime if one finds a "prompt" transition with the same electron energies. For a "prompt" curve one can use A—A coincidences. The Auger electrons yielding these coincidences accompany conversion in two of the investigated cascades (198——110 and 177—130 kev) for which, as was shown above, the period of the intermediate levels $T_{1/2} \leqslant 5 \cdot 10^{-10}$ sec. In this experiment both arms of the twin magnetic spectrometer were set on the K - 2L Auger line. In view of the fact that the Auger electrons accompanying both the conversion transitions forming the cascade enter into either of the spectrometer arms, the presence of a finite lifetime of the intermediate level leads only to a minor broadening of the coincidence curve but does not shift its centroid.

From two series of experiments (the results of one series are shown in Fig. 6,b) we obtained a mean value of $6.1 \cdot 10^{-10}$ sec for the displacement of the cen-

troids of the K 94—A and A—A coincidence curves.

However, for calculating the lifetime of the level from the observed shift of the curve centroids one must take into account the following effects:

1. In returning the left arm of the spectrometer from the K 94 line to the K - 2L Auger line the electron energy changes from 34.1 to 39.3 kev. Accordingly, there is a change in the electron transit time from the source to the detector (58 cm). The difference between the flight times in the two cases is $4 \cdot 10^{-10}$ sec, which leads to a shift of the coincidence curve by this amount to the right. This additional displacement must be subtracted from the experimental value.

2. There is a finite interval between the instant the electron impinges on the detector (phosphor) and the instant of appearance of the l-th electron on the photomultiplier cathode; this time is given by the familiar Post-Schiff formula:

$$\bar{t} = \frac{\tau_p l}{n}\left(1 + \frac{l+1}{2n} + \ldots\right), \qquad (4)$$

where τ_p is the fluorescence lifetime (decay time) of the phosphor, and n is the number of photoelectrons.

From the POPOP scintillator employed in our work $\tau_p = 2 \cdot 10^{-9}$ sec and the scintillation yield is equal to approximately 0.8 the yield of stilbene. This means that for electron energies of 34.1 and 39.3 kev with a photocathode efficiency of 10% the values of n are 7 and 8 electrons, respectively. It follows from the amplitude of the pulses measured at the output of the photomultiplier and the cut-off potential of the limiter tube that the lower bound for tripping of our circuit is not more than two photoelectrons. The mean time for appearance of a second photoelectron for incident electron energies of 34.1 and 39.3 kev are $7.2 \cdot 10^{-10}$ and $6.1 \cdot 10^{-10}$ sec, respectively. This means that as a result of retuning of the left arm of the spectrometer the centroid of the coincidence curve must be displaced $1.1 \cdot 10^{-10}$ sec.

3. The centroid shift obtained after introduction of the above corrections ($6.1 \cdot 10^{-10} - 4 \cdot 10^{-10} - 1.1 \cdot 10^{-10} = 1.1 \cdot 10^{-10}$) must be multiplied by two. This is due to the fact that in addition to e—A coincidences, corresponding to Auger electrons appearing in electron capture, there are also "prompt" coincidences of the same type, corresponding to Auger electrons accompanying the K shell conversion electrons of the 94 kev transition. The number of coincidences of both types is the same, which leads to reduction of the experimentally observed relative shift of the centroids by a factor of two. Thus after introduction of all the corrections we obtain $T_{1/2} = (1.4 \pm 0.7) \cdot 10^{-10}$ sec for the period of the 4173 kev level. The indicated uncertainty appreciably exceeds the deviation from the mean value in view of possible, unaccounted for systematic errors.

The radiation lifetime obtained by taking into account conversion for an M1 94 kev transition (the admixture of E2 is insignificant) proves to be 31 times greater than the lifetime calculated according to Weisskopf's single-particle formula.

It may therefore be asserted that the 473 kev ($9/2^-$) level is the first excited level of a third rotational band with K = 7/2 based on the 379 kev ($7/2^-$) level.

C. Transitions between levels of different rotational bands. The transitions between the levels of different rotational bands in Tm^{169} were investigated earlier in our laboratory by means of a twin scintillation spectrometer.[27] The results obtained in this investigation are summarized in the accompanying table.

Column 7 gives the radiation lifetimes obtained from experiment; column 8 - the lifetimes calculated by means of the Weisskopf single-particle formula; column 9 - the values of the F factor, which is defined as the ratio of the experimental to the single-particle probability for a radiative transition (or the inverse

Characteristics of the transitions between the levels of different rotational bands in Tm^{169}

Level energy, kev	$T_{\frac{1}{2}}$ exp, sec	Transition energy, kev	Transition	Rel. γ-ray intensity	α_{tot}	$\tau_{\gamma exp.}$, sec	τ_{Weiss}, sec	$F = \frac{\tau_{Weiss}}{\tau_{exp}}$
1	2	3	4	5	6	7	8	9
316	$(6,7 \pm 0,2) \cdot 10^{-7}$	177	*E2*	5,6	0,54	$2,9 \cdot 10^{-5}$	$8,3 \cdot 10^{-8}$	$2,9 \cdot 10^{-3}$
		177	*M1*	25	0,87	$6,4 \cdot 10^{-6}$	$5,8 \cdot 10^{-12}$	$0,9 \cdot 10^{-6}$
		198	*E2*	4,6	0,45	$3,5 \cdot 10^{-5}$	$4,8 \cdot 10^{-8}$	$1,4 \cdot 10^{-3}$
		198	*M1*	46	0,83	$3,5 \cdot 10^{-6}$	$4,1 \cdot 10^{-12}$	$1,2 \cdot 10^{-6}$
		308	*E2*	18	0,05	$9,0 \cdot 10^{-6}$	$5,2 \cdot 10^{-9}$	$0,58 \cdot 10^{-3}$
379	$(3,6 \pm 0,1) \cdot 10^{-8}$	63	*E1*	65	0,9	$1,1 \cdot 10^{-7}$	$1,2 \cdot 10^{-12}$	$1,1 \cdot 10^{-5}$
		240	*E1*	1	0,03	$6,4 \cdot 10^{-6}$	$2,2 \cdot 10^{-14}$	$0,34 \cdot 10^{-8}$
		260	*E1*	8	0,03	$7,8 \cdot 10^{-7}$	$1,8 \cdot 10^{-14}$	$2,3 \cdot 10^{-8}$

Note: τ_{Weiss} = lifetime calculated by means of the Weisskopf single-particle equation.

ratio of the lifetimes), and is a measure of the hindrance of the transition. It will be seen from the table that the E2 type transitions are retarded by 3 orders of magnitude, the M1 type transitions by 6 orders, E1 type transitions with energies of 240 and 260 kev by 8 orders and the transition of 63 kev energy by 5 orders.

The long lifetime of the 316 kev level has been explained by Koicki & Koicki[28] as being due to the fact that the transitions from it are forbidden by the K selection rules. Actually, all transitions from this level go to levels of the lowest band so that $\Delta K = 3$. The degree of forbiddenness, characterized by the number

$$\nu = \Delta K - L,$$

where L is the multipole order of the transition, is equal to two for M1 type transitions and to unity for E2 type transitions.

Thus for all transitions from the 316 kev level the hindrance per unit forbiddenness amounts to 3 orders of magnitude. It is interesting to note that this pertains to the E2 type transition as well, although in other cases electric quadrupole transitions in deformed nuclei are actually speeded up by 2 orders.

The magnitude of the hindrance per unit forbiddenness for the 240 and 260 kev E1 transitions from the 379 kev level is 4 orders. As for the 63 kev transition between the $7/2^-$ and $7/2^+$ levels, its hindrance is not connected with K forbiddenness but, as was shown in Ref.27, is connected with forbiddenness with respect to the asymptotic quantum numbers Λ, Σ and n_z, of which the first two are, respectively, the projection of the orbital and spin angular momenta on the deformation axis, and the third is the quantum number of the nucleon oscillations along this axis. The values of these three quantum numbers, which can be obtained with the aid of the formulas of Nilsson[23] and the value of the deformation (0.28) of the Tm^{169} nucleus, known from Coulomb excitation studies[21], are

$\Lambda=3, \quad \Sigma= {}^1/_2, \quad n_z=2$ for the 379 kev level, and

$\Lambda=4, \quad \Sigma=-{}^1/_2, \quad n_z=0$ for the 316 kev level.

By means of the asymptotic number selection rules deduced by Voikhanskii[29] one can establish that in the given case there is one degree of forbiddenness with

respect to each of these numbers. The transition probability per unit forbiddenness decreases therefore by a factor of 10-100, just as it does in most other cases[29].

The radiative lifetime calculated by means of Nilsson's[23] formulas for the probabilities for the single-particle transitions in deformed nuclei proved to be equal to $\tau_N = 2.3 \cdot 10^{-8}$ sec in the given case, which is in considerably better agreement with the experimental value: $\tau_N/\tau_\gamma = 0.21$.

All the data on the lifetimes of the levels of Tm^{169} are shown in Fig.3.

Physical-Technical Institute,
Academy of Sciences of the USSR

Note added in proof: After submission of the present report to the editor, we became acquainted with the work of Blaugrund[30]. This author measured the lifetimes of two levels of Tm^{169} by means of a new microwave technique and obtained $T_{1/2} = (6.2 \pm 1.0) \cdot 10^{-11}$ sec for the 118 kev level and $T_{1/2} = (2.9 \pm 0.7) \cdot 10^{-10}$ sec for the 139 kev level. These periods are not inconsistent with our data.

References

1. E.E.Berlovich, Izv.AN SSSR, Ser.fiz., 24, 336 (1960). (Trans.Bulletin, 24, 323.)
2. E.E.Berlovich, Ibid., 18, 589 (1954). (Trans.Bulletin, 18, 274.)
3. G.M.Gorodinskii, A.N.Murin, V.N.Pokrovskii & B.K.Preobrazhenskii, Ibid., 21, 1004 (1957). (Trans.Bulletin, 21, 1005.)
4. B.S.Dzhelepov, B.K.Preobrazhenskii & V.A.Sergienko, Materialy soveshchaniya v OIYaI po primeneniyu radiokhimicheskikh metodov izucheniya yadernykh reaktsii i β-γ-spektroskopii neitronodefitsitnykh yader (Transactions of the Conference Held at the Joint Institute for Nuclear Research on the Use of Radiochemical Methods in Investigating Nuclear Reactions and β-γ Spectroscopy of Neutron-Deficient Nuclei). Vol.III, p.12, Dubna, 1958.
5. V.I.Baranovskii, A.N.Murin & V.N.Pokrovskii, Ibid., p.22.
6. K.Ya.Gromov, B.S.Dzhelepov, A.G.Dmitriev, V.A.Morozov & A.V.Kalyamin, Ibid., p.32.
7. E.P.Grigor'ev, B.S.Dzhelepov & A.V.Zolotavin, Izv.AN SSSR, Ser.fiz., 23, 188 (1959). (Trans.Bulletin, 23, 180.)
8. B.S.Dzhelepov & L.K.Peker, Skhemy raspada radioaktivnykh yader (Decay schemes of radioactive nuclei), M.-L., 1958.
9. E.E.Berlovich, Izv.AN SSSR, Ser.fiz., 20, 1438 (1956). (Trans.Bulletin 20, 1315.)
10. S.Martin, E.Jensen, F.Hughes & R.Nichols, Phys.Rev., 82, 579 (1951).
11. S.Johansson, Phys.Rev., 100, 835 (1955).
12. J.Cork, M.Brice, D.Martin et al, Phys.Rev., 101, 1042 (1956).
13. E.Hatch, F.Boehm, P.Marmier & J.DuMond, Phys.Rev., 104, 745 (1956).
14. S.A.Baranov, R.M.Polevoi, Yu.F.Rodionov & G.V.Shishkin, Atomnaya energiya, 3, 456 (1957). (Trans.Soviet J.of Atomic Energy.)
15. K.Ya.Gromov, B.S.Dzhelepov & B.K.Preobrazhenskii, Izv.AN SSSR, Ser.fiz., 22, 775 (1958). (Trans.Bulletin, 22, 770.)
16. A.Bohr, Rotational States of Nuclei. Article in "Problemy sovremennoi fiziki" (Problems of Modern Physics, 1. Unified nuclear model), Moscow, 1956.
17. H.Beekhuis & DeWaard, Physica, 24, 767 (1958).
18. B.R.Mottelson & S.G.Nilsson, Z.Phys., 141, 217 (1955).

19. V.M.Kel'man, R.Ya.Metskhvarishvili, B.K.Preobrazhenskii, V.A.Romanov & V.V.Tuchkevich, Zhur.eksp.i teor.fiz., 37, 639 (1959). (Trans.Soviet Physics - JETP.)

20. K.Lindenberg & A.Stendel, Naturwissenschaften, 42, 41 (1955).

21. B.R.Mottelson & S.G.Nilsson, Classification of nucleon states in a deformed nucleus. Article in "Problemy sovremennoi fiziki, 1. Obobshchennaya model' radra" (Problems of Modern Physics, 1. Unified nuclear model), Moscow, 1956.

22. B.R.Mottelson & S.G.Nilsson, Mat.-fys. Skriftas Köngl.Dans.Vid.Selsk., 1, No.8, 1-105 (1959).

23. S.G.Nilsson, Kgl.Danske Videnskab Selskab. Mat.-fys.Medd., 29, No.16, 1-68 (1955).

24. J.W.Mihelich, T.J.Ward & K.P.Jacob, Phys.Rev., 103, 1285 (1956).

25. O.Nathan & I.Marklund, Nucl.Phys., 6, 102 (1958).

26. E.Hatch & D.Alburger, Phys.Rev., 110, 1116 (1958).

27. E.E.Berlovich, V.N.Klement'ev, V.G.Fleisher, O.V.Larionov, F.Sh.Murtazin & D.A.Apostolov, Zhur.eksp.i teor.fiz., 37, 1202 (1959). (Trans.Sov.Phys. - JETP.)

28. S.Koicki & A.Koicki, Bull.Inst.Nucl.Sci.Boris Kidrich, 6, 1 (1956).

29. M.E.Vokhanskii, Zhur.eksp.i teor.fiz., 33, 1004 (1957). (Trans.Soviet Physics - JETP.)

30. A.E.Blaugrund, Phys.Rev.Letters, 3, 226 (1959).

INTERACTION OF CARBON IONS WITH PHOTOGRAPHIC EMULSION NUCLEI

- L.I.Bolotin, A.P.Klyucharev, Yu.F.Kulygin, Yu.N.Ranyuk, E.I.Revutskii & N.Ya.Rutkevich

The present work was concerned with investigation of the interaction of carbon ions with the nuclei in photographic emulsions. Actually, emulsions contain a relatively small number of elements which may arbitrarily be subdivided into "light" - carbon, nitrogen and oxygen - and "heavy" - bromine and silver.

The 110 Mev carbon ion beam passed through a magnetic analyzer, was defined by an aperture, and allowed to fall on the photographic plate tilted at an angle of 25° to the beam axis. The exposure time was chosen so that the track density would be convenient for examination. There were observed in the emulsion events (stars) with the emission of charged particles: protons, α-particles and heavier fragments.

By virtue of the use of discriminative emulsions (NIKFI type D) we were able to distinguish between singly and double charged particles without difficulty. Owing to the complex composition of the emulsion one could not determine precisely with what type of nucleus the incident ions interacted. However, even without complete energy analysis of the star we could, from the range of the recoil nucleus, determine whether the collision occurred with a light or heavy nucleus.

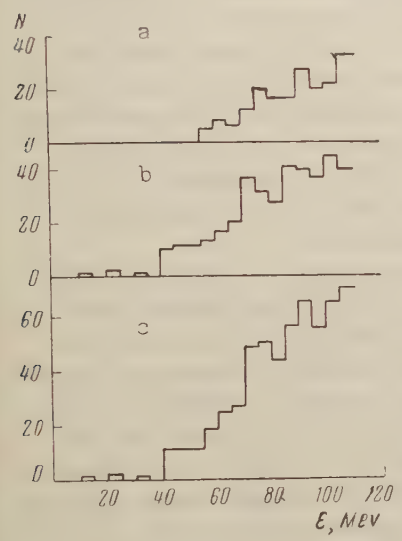

Fig.1. Variation in the number of stars formed as a function of the ion kinetic energy at the instant of collision: a) Ag and Br (203 events), b) C, N and O (391 events), c) all emulsion nuclei (total of 594 events).

Knowing the initial ion energy and having measured the range of the ion up to the collision, we could determine the kinetic energy of the C ion at the instant of the encounter. Histograms showing the variation in the number of stars formed with the kinetic energy of the ion at the instant of collision are shown in Fig.1.

The Coulomb barrier in the interaction of carbon ions with carbon, nitrogen and oxygen is 18-20 Mev, with bromine and silver - 40-50 Mev. From the data of Fig.1 it follows that the threshold for star formations lies substantially higher than the potential barrier for the light nuclei and approximately at the level of the barrier for heavy nuclei.

The characteristics of reactions produced by carbon ions on emulsion nuclei are listed in the accompanying table. Noteworthy is not only the great diversity of the reactions but the predominance of α-particles over protons in the products: thus of 1300 charged particles produced in the analyzed reactions only 300 particles may be identified as protons or other singly-charged particles.

The predominance of α-particles over protons in the reaction products can readily be understood if we recall that for the C^{12} nucleus the most advantageous fragmentation from the energy standpoint is break-up into three α-particles. The binding energy of the carbon nucleus with respect to break-up into three α-particles is 7.3 Mev, i.e., less than half the binding energy of the last neutron (18 Mev) and last proton (16 Mev) in the C nucleus. A substantially higher yield of α-particles as compared with the yield of protons was also observed in the work of Parfanovich et al[1] in bombarding emulsions with O and N ions.

Characteristics of reactions produced by carbon ions

Reaction products	Bombarded nuclei		Reaction products	Bombarded nuclei		Reaction products	Bombarded nuclei	
	C,N,O	Br, Ag		C,N,O	Br, Ag		C,N,O	Br, Ag
p	6	28	$2p$, 2α	5	1	p, f	2	1
$2p$	8	5	α	28	65	α, f	14	7
$3p$	1	—	2α	81	67	2α, f	15	6
α,p	33	49	3α	67	46	3α, f	10	4
p, 2α	44	20	4α	14	8	p, α, f	11	4
p, 3α	16	3	5α	2	—	p, 2α, f	6	1
p, 4α	1	1	6α	13	—	p, 3α, f	2	1
$2p$, α	13	4	7α	3	—	$2p$, α, f	2	—

Fig.2. Star formed in an encounter of a carbon ion with an oxygen nucleus.

Of particular interest are the six- and seven-pronged stars (Fig.2) formed by doubly-charged particles. Analysis of the kinematics of 20 such stars led to results in good agreement with the assumption that in each of them there occurred break-up of both the incident nucleus and the target nucleus into alpha fragments.

An appreciable fraction of the reactions occurred with the emission of fragments heavier than α-particles.

The observed reactions with the emission of protons, α-particles and possibly neutrons may be regarded as proceeding through a compound nucleus, while reactions as a result of which there are emitted only α-particles may be interpreted as events, involving direct interaction of the projectile with the target nucleus. This is substantiated by the observed α-particle distribution, which is predominantly forward.

The direct interaction process has recently been considered by Inopin[2] on the basis of the α-particle model. From the standpoint of this model Inopin regards the beryllium nucleus as a dumbbell composed of two α-particles and a weakly bound neutron moving about them; the carbon nucleus is modeled in the form of an equilateral triangle with the α-particles located at its vertices; in the oxygen nucleus the α-particles are assumed to be located at the vertices of a tetrahedron. In the first approximation, it is assumed that the radius of the target nucleus is appreciably greater than the mean dimensions of the incident particle and Coulomb repulsion is neglected, which is permissible for a sufficiently high initial energy of the incident particle as compared with the potential barrier.

Upon collision there may occur at the potential boundary of the target nucleus absorption by the nucleus of one α-particle in the case of Be, one or two particles in the case of C and one, two or three α-particles in the case of O; accordingly, there will be formed in the emulsion a one-, two- or three-pronged α-particle star.

For carbon calculations lead to equal cross sections for pick-off of one or two α-particles. Our experimental results are in agreement with this inference within the limits of the statistical error: the number of one-pronged α-stars (65) was nearly equal to the number of two-pronged stars (67) produced in the interaction of carbon ions with heavy nuclei.

Apparently, the α-particle model may prove useful in connection with investigation of nuclear reactions occurring in the interaction of heavy nuclei with α-correlated nuclei.

More detailed analysis of both direct interactions and reactions with the formation of a compound nucleus must await the accumulation of further experimental data.

Physical-Technical Institute,
Academy of Sciences of the Ukrainian SSR

References

1. D.M.Parfanovich, A.M.Semchinova & G.N.Flerov, Yadernye reaktsii pri malykh i srednikh energiyakh, Trudy Bses. Konferentsii (Transactions of the All-Union Conference on Nuclear Reactions at Low and Medium Energies), p.517, November, 1957.

2. E.V.Inopin, Ukr.fiz.zhur. (Ukrainian Physics Journal), No.5 (1960).

Bulletin of the Academy of Sciences of the USSR - Physical Series
Vol. 24, No.12 - December 1960

Transactions of the Tenth All-Union Conference on Nuclear Spectroscopy
(Continued from Vol.24, Nos.3, 7 & 9; to be continued in Vol.25, No.1)

TABLE OF CONTENTS

	Page Orig.	Trans.
Investigation of the level diagram of W^{182} - V.S.Gvozdev, L.I.Rusinov & Yu.L.Khazov	1444	1439
Investigation of $Bi^{212} \rightarrow Po^{212}$ decay by means of α-γ and γ-γ coincidences - Yu.P.Gangrskii, G.M.Gusinskii & I.Kh.Lemberg	1449	1443
Relative intensities of Lu^{170} and Lu^{172} conversion electrons - V.V.Tuchkevich, V.A.Romanov & M.G.Iodko	1457	1451
Relative intensities of Lu^{169} and Lu^{171} conversion electrons - M.G.Iodko, V.A.Romanov & V.V.Tuchkevich	1465	1458
Cascade excitation of the second rotational levels in separated tungsten isotopes - D.S.Andreev, K.I.Erokhina & I.Kh.Lemberg	1470	1463
Coulomb excitation of the first levels of even isotopes of chromium, selenium and neodymium - D.S.Andreev, A.P.Grinberg, G.M.Gusinskii, K.I.Erokhina & I.Kh.Lemberg	1474	1466
Coulomb excitation of Ne^{21} - D.S.Andreev, K.I.Erokhina & I.Kh.Lemberg	1478	1470
Determination of the L fluorescence coefficients of Ga^{71}, Cu^{65} and V^{51} - A.A.Konstantinov, T.E.Sazonova & V.V.Perepelkin	1480	1472
Investigation of the decay of Te^{118} and Te^{119} and the level scheme of Sb^{119} - A.A.Sorokin, A.Bedesku, M.V.Klimentovskaya, L.N.Kryukova, K.P.Mitrofanov, V.V.Murav'eva, V.N.Rybakov, G.Chandra & V.S.Shpinel'	1484	1476
Investigation of the probabilities for radiative transitions between the rotational levels of Er^{166} and Tm^{169} - E.E.Berlovich, V.V.Il'in, A.I.Kislyakov, M.K.Nikitin & T.Bedike	1492	1483
Interaction of carbon ions with photographic emulsion nuclei - L.I.Bolotin, A.P.Klyucharev, Yu.F.Kulygin, Yu.N.Ranyuk, E.I.Revutskii & N.Ya.Rutkevich	1502	1493

Translated in 1961 by
Columbia Technical Translations
5 Vermont Ave., White Plains, N.Y.

SUMMARY OF THE CONTENTS

of

VOLUME XXIV

of the

BULLETIN OF THE ACADEMY OF SCIENCES OF THE USSR

- Physical Series -

SUBJECT SUMMARY - VOLUME 24

TRANSACTIONS OF THE SECOND ALL-UNION CONFERENCE ON THE PHYSICS OF DIELECTRICS

	Page (Trans.)
Number 1	
Gregorii Ivanovich Skanavi (1910-1959)	2
Dielectric relaxation in liquid alcohols, alkyl halides and solutions - Robert H.Cole	3
On the dielectric dispersion of some aliphatic alcohols - M.Magat & C.Brot	9
Dielectric constant of dielectric liquids in strong electric fields - A.Piekara	17
Dielectric relaxation and molecular size and shape - C.P.Smyth	24
Field and current density distribution inhomogeneities in CdS single crystals - K.W.Böer	35
Some theoretical considerations concerning inhomogeneous field distribution in electric breakdown - K.W.Böer	41
Influence of field emission on the distribution of strong fields in solids - É.I.Adirovich	47
Currents in alkali-halide crystals due to electron emission from the cathode in strong electric fields - E.A.Konorova	56
Temperature and voltage dependences of the current in KBr single crystals in prebreakdown fields - E.A.Afanas'eva, V.S.Vinogradov & E.A.Konorova	63
Regularities of pulse breakdown of solid dielectrics - A.A.Vorob'ev & G.A.Vorob'ev	75
Breakdown voltage of thick insulating layers in a nonuniform field - F.Obenaus	84
Characteristics of the motion of fast current carriers in polar crystals - Yu.I.Gorkun & K.B.Tolpygo	91
New form of polar crystal model - A.E.Glauberman	97
Some electroluminescent properties of zinc oxide doped with bismuth oxide - É.G.Pettsol'd	100
Number 2	
Investigation of relaxation polarization and the phase composition of dielectrics in the system $SrTiO_3$--$Bi_2O_3 \cdot \eta TiO_2$ (η = 2,3) - A.M.Kashtanova, N.N.Kurtseva & G.I.Skanavi	109
On the relaxation time and distribution function of quasidipoles in ionic crystals with a defect structure - G.I.Skanavi	117
Relaxation polarization of the $SrTiO_3 \cdot \eta MnO$ system - E.V.Sinyakov & A.M.Solok	125
Correlation between the dielectric loss and the structure of ionic crystals - N.P.Bogoroditskii, B.A.Kulik & I.D.Fridberg	130
Investigation of high-frequency dielectric loss in solid dielectrics - K.A.Vodop'yanov & G.I.Galibina	134
Thermal expansion, dielectric constant and loss of alkali halide crystals - V.V.Panchenko	141
Relaxation polarization and losses in alkali halide single crystals - V.N.Lozovskii	151

On the relaxation polarization of crystals with the structure of rutile and perovskite - I.Ts.Lyast 160
Application of the theory of vibrations of a crystal lattice with deformable ions to treatment of the physical properties of binary cubic crystals - K.B.Tolpygo 167
Contribution to the theory of the permittivity of an anisotropic medium polarized at a finite rate - R.A.Suris & B.N.Finkel'shtein 178
Towards a theory of incompletely polar crystals - K.B.Tolpygo 182
On the kinetics of ion conductivity and electric polarization in condensed substances - Yu.L.Khait 191
Possibility of thermal polarization of electrons in zinc sulfide crystal phosphors - F.I.Vergunas & P.E.Ramazanov 203
Absorption spectra of defects in ionic lattices - O.Stasiw 209
Dielectric and optical properties of some zinc sulfides - E.V.Stauer & V.P.Izotov 213
On the nature of stimulated luminescence in KCl crystals - N.P.Kalabukhov 217
Influence of the electric field strength on the photoconductivity of liquid organic systems - P.K.Mitskevich & V.G.Bobyl' 219
Investigation of the photoconductivity of ether solutions - Yu.A.Kopylov 223
Piezoelectric effect in electrets - A.N.Gubkin & V.S.Sorokin 232
Effect of slow-neutron irradiation on the dielectric properties of polycrystalline titanates - L.K.Vodop'yanov & G.I.Skanavi 238

TRANSACTIONS OF THE TENTH ALL-UNION CONFERENCE ON NUCLEAR SPECTROSCOPY

Number 3

Alpha-radiation from U^{233} - B.S.Dzhelepov, R.B.Ivanov, V.G.Nedovesov & Yu.T.Puzynovich 247
Radioactive decay of Th^{231} - S.A.Baranov, R.M.Polevoi, Yu.F.Rodionov, G.V.Shishkin & V.M.Shubko 249
Conversion electrons and gamma-rays from Tm^{165} - K.Ya.Gromov, B.S. Dzhelepov, A.G.Dmitriev, V.A.Morozov & K.I.Yakovlev 260
Regarding the 75-min ytterbium activity - A.A.Abdurazakov, K.Ya.Gromov, B.S.Dzhelepov, Yu.V.Norseev, G.Ya.Umarov & V.G.Chumin 266
Investigation of the positron spectra of neutron-deficient isotopes - N.A.Bonch-Osmolovskaya, B.S.Dzhelepov & O.E.Kraft 270
Beta-decay of La^{140} - V.S.Dzhelepov, B.A.Emel'yanov, K.P.Kupriyanova & Yu.N.Podkopaev 275
Investigation of the gamma-radiation of Ag^{110m} in the energy range from 0.2 to 2.0 Mev - N.A.Voinova, B.S.Dzhelepov & N.N.Zhukovskii 278
Gamma-spectrum of $Eu^{152,154}$ in the 245 to 500 and 1450 to 2000 kev energy intervals - B.S.Dzhelepov & Yu.V.Khol'nov 288
Resonance fluorescence in Ce^{140} excited by La^{140} gamma-rays - B.S.Dzhelepov & M.A.Dolgoborodova 292
Gamma-spectrum of W^{187} - B.S.Dzhelepov, V.L.Rumyantsev, Yu.V.Khol'nov & G.E.Shchukin 299
Determination of the number of disintegration events in electron-capture materials by means of a 4π scintillation counter - V.I.Baranovskii & G.M.Gorodinskii 301
Comparison of the theory of nonaxial nuclei with experiment - E.P.Grigor'ev & M.P.Avotina 311

On some applications of the coincidence technique in nuclear spectroscopy - É.E.Berlovich 323
Ionization chamber in a magnetic field - G.E.Kocharov & M.A.Yamshchikov 336
Investigation of pulses arising on the grid of an ionization chamber - G.A.Korolev & G.E.Kocharov 342
Rotational levels in deformed odd-odd nuclei - L.K.Peker 350
Contribution to the interpretation of the high-lying levels of $_{74}W^{182}$ - L.K.Peker 354
Magnetic moments of deformed nuclei with K = 1/2 - L.K.Peker & D.A.Varshalovich 357
Variation of the gain of photomultipliers with the pulse height and time intervals between pulses - A.G.Berkovskii & V.G.Pol'skii 361

Number 7

Formation of Eu^{145} in spallation of tantalum - A.A.Bashilov, O.V.Larionov, M.K.Nikitin & V.B.Smirnov 791
Magnetic gamma-spectrometer with high resolution - L.V.Groshev, A.M.Demidov, V.N.Lutsenko & A.F.Malov 794
Conversion electron spectrum of neutron-deficient lutetium isotopes in the 1000 and 3500 kev region - B.S.Dzhelepov, I.F.Uchevatkin & S.A.Shestopalova 805
Conversion electron spectrum of Lu^{167} + Yb^{167} - A.S.Basina, B.S. Dzhelepov & V.A.Chikhladze 810
Conversion electron spectrum of the dysprosium fraction from spallation of tantalum - A.S.Basina, K.Ya.Gromov & B.S.Dzhelepov 813
On the 106 kev transition in Tm^{167} - A.S.Basina & V.A.Morozov 819
The (n,2n) and (γ,n) reactions on Au^{197} - M.A.Bak, K.A.Petrzhak & Chen' Tya-mei 820
Rotational energy of even-even and odd nuclei - A.S.Davydov 822
Gamma-radiation from the $Cl^{35}(n,\gamma)Cl^{36}$ reaction - L.V.Groshev, A.M.Davydov & V.N.Lutsenko 834
Gamma-spectra of the isotopes in the lanthanum fraction from spallation of tantalum - E.P.Grigor'ev, S.L.Sakharov & V.O.Sergeev 844
Determination of the periods of Dy^{159}, Ho^{160m}, Tm^{166} and Lu^{173} - E.P.Grigor'ev, O.V.Larionov, M.K.Nikitin, S.L.Sakharov & V.O.Sergeev 846
Gamma-spectra of the tantalum activity formed by proton bombardment of tantalum - E.P.Grigor'ev, O.V.Larionov, M.K.Nikitin, S.L. Sakharov & V.O.Sergeev 850
Measurement of the mean lifetime of Lu^{175} in the 113.8 kev excited state - V.P.Bozhko, I.I.Zalyubovskii & A.I.Tutubalin 852
Gamma-radiation from Zr^{95} + Nb^{95} - N.A.Voinova, B.S.Dzhelepov & N.N.Zhukovskii 854
Gamma-radiation from Tb^{160} - N.A.Voinova, B.S.Dzhelepov, N.N. Zhukovskii & Yu.V.Khol'nov 856
Determination of level spins and parities from inelastic scattering and the pick-up reaction on Be^{9} - O.F.Nemets, L.S.Saltykov, M.V. Sokolov & Yu.V.Tsekhmistrenko 861
Spins and parities of C^{13} levels - N.I.Zaika, O.F.Nemets & M.A. Tserineo 865
Assignments for the levels of Ti^{47-50} and Sr^{89} - N.I.Zaika & O.F.Nemets 868
Spin of the 1.38 Mev level of Mg^{24} - O.F.Nemets & G.A.Prokopets 872

Spins and parities of Ca^{41} levels - N.I.Zaika, O.F.Nemets & V.S.Prokopenko 875
Angular distribution of protons inelastically scattered from Cr and Ni isotopes - N.V.Pasechnik, N.N.Pucherov & V.I.Chirko 876
Investigation of the levels of Cl^{35} - Yu.P.Antuf'ev, A.K.Val'ter, V.Yu.Gonchar, E.G.Kopanets, A.N.L'vov & S.P.Tsytko 878
Elastic scattering of protons by Ne^{20} - A.K.Val'ter, A.S.Deineko, P.V.Sorokin & A.Ya.Taranov 885
Elastic scattering of protons from nuclei - A.P.Klyucharev 888
Investigation of the levels of K^{41} by means of the $A^{40}(p,\gamma)K^{41}$ reaction - A.K.Val'ter, Yu.P.Antuf'ev, V.Yu.Gonchar, A.N.L'vov & S.P.Tsytko 892
Experimental and theoretical state-mixing coefficients and polarization of nucleons in deformed nuclei - D.A.Varshalovich 895
Internal bremsstrahlung accompanying β-decay of P^{32} - K.A.Korotkov & A.M.Chernikov 899
Excitation of collective nuclear levels in stripping reactions - A.M.Korolev 902
Beta-transitions in weakly deformed nuclei - B.D.Konstantinov & V.I.Ovcharenko 910
Magnetic and quadrupole moments of weakly deformed nuclei - Yu.L.Gurin, A.M.Korolev & B.D.Konstantinov 918
Double-focusing magnetic spectrometer - A.S.Deineko, A.I.Popov, P.V.Sorokin & A.Ya.Taranov 921
Preparation of isotope targets for nuclear studies - A.D.Bondar', A.S.Emlyaninov, A.P.Klyucharev, L.G.Lishenko, V.N.Medyanik, A.D.Nikolaichuk & O.E.Shalaeva 926
Determination of the ratio of K and L x-ray photons in the radiation from some neutron-deficient isotopes - V.D.Vitman, B.S.Dzhelepov, A.A.Pavlov, S.V.Semenov & S.A.Shestopalova 931

Number 9

Present state of beta-decay theory - V.A.Lyubimov 1031
Investigation of the fine structure of alpha-radiation from U^{234} and U^{235} - S.A.Baranov, A.G.Zelenkov & V.M.Kulakov 1045
The Auger effect - M.A.Listengarten 1050
Influence of magnetic fields on resonance absorption of gamma-rays - V.A.Lyubimov & A.I.Alikhanov 1084
New iridium and platinum isotopes: Ir^{184} and Pt^{187} - V.I.Baranov, K.Ya.Gromov, B.S.Dzhelepov, Zyong Chong Bai, T.V.Malysheva, V.A.Morozov, B.A.Khotin & V.G.Chumin 1086
On the existence of isomeric states of Te^{119} - N.G.Zaitseva, M.Ya. Kuznetsova, I.Yu.Levenberg, V.N.Pokrovskii & V.A.Khalkin 1090
Operation of an ionization alpha-spectrometer under heavy loads - A.A.Vorob'ev & V.A.Korolev 1093
Investigation of alpha-decay of U^{235} by means of an ionization alpha-spectrometer - A.A.Vorob'ev, A.P.Komar, & V.A.Korolev 1099
Decay scheme for Eu^{147} - Yu.A.Aleksandrov, Yu.A.Nemilov, M.K. Nikitin & Sh.Piskorzh 1105
Concerning the Yb^{164}--Tm^{164}--Er^{164} decay chain - B.Dalkhsuren, I.Yu.Levenberg, A.N.Murin, Yu.V.Norseev, V.P.Pokrovskii & I.A.Yutlandov 1109

Investigation of new neutron-deficient platinum isotopes - T.V.Malysheva, B.A.Khotin, A.K.Lavrukhina, L.N.Kryukova & V.V.Murav'eva 1113
Neutron-deficient isotopes of rare earth elements of the cerium group (Spallation products of europium bombarded with 660 Mev protons) - A.K.Lavrukhina, G.M.Kolesov & Tan Syao-en 1117
Investigation of the neutron-deficient isotopes of osmium - Yu.A.Surkov, G.M.Chernov, A.K.Lavrukhina & Z.V.Khromchenko 1123
Beta-gamma angular correlation in the decay of La^{140} and Ce^{141} - V.P.Rudakov 1128
Conversion electron spectrum of the dysprosium fraction from the spallation products of tantalum - A.A.Abdurazakov, K.Ya.Gromov, B.S.Dzhelepov & G.Ya.Umarov 1130
Disintegration of Nd^{140} and Pr^{140} - E.I.Biryukov, O.I.Grigor'ev, B.S.Kuznetsov & N.S.Shimanskaya 1138
Possibility of utilizing the (n,2n) reaction in nuclear spectroscopy - V.V.Komarov, A.B.Kurepin & A.M.Popova 1147
Energy states of Be^{8} in the disintegration of C^{12} into three alpha-particles under bombardment with protons and neutrons - S.S.Vasil'ev, V.V.Komarov & A.M.Popova 1151
Investigation of the energy distributions of the products of nuclear reactions involving emission of several particles - V.V.Komarov & A.M.Popova 1154
Double-focusing magnetic spectrometer - N.G.Afanas'ev 1158
Recording photomultiplier pulses by means of a tape recorder and an automatic recording voltmeter - A.N.Silant'ev 1165
Concerning the mean charge of ions passing through matter - I.S.Dmitriev, V.S.Nikolaev, L.N.Fateeva & Ya.A.Teplova 1169

Number 12

Investigation of the level diagram of W^{182} - V.S.Gvozdev, L.I. Rusinov & Yu.L.Khazov 1439
Investigation of $Bi^{212} \rightarrow Po^{212}$ decay by means of α-γ and γ-γ coincidences - Yu.P.Gangrskii, G.M.Gusinskii & I.Kh.Lemberg 1443
Relative intensities of Lu^{170} and Lu^{172} conversion electrons - V.V.Tuchkevich, V.A.Romanov & M.G.Iodko 1451
Relative intensities of Lu^{169} and Lu^{171} conversion electrons - M.G.Iodko, V.A.Romanov & V.V.Tuchkevich 1458
Cascade excitation of the second rotational levels in separated tungsten isotopes - D.S.Andreev, K.I.Erokhina & I.Kh.Lemberg 1463
Coulomb excitation of the first levels of even isotopes of chromium, selenium and neodymium - D.S.Andreev, A.P.Grinberg, G.M.Gusinskii, K.I.Erokhina & I.Kh.Lemberg 1466
Coulomb excitation of Ne^{21} - D.S.Andreev, K.I.Erokhina & I.Kh.Lemberg 1470
Determination of the L fluorescence coefficients of Ga^{71}, Cu^{65} and V^{51} - A.A.Konstantinov, T.E.Sazonova & V.V.Perepelkin 1472
Investigation of the decay of Te^{118} and Te^{119} and the level scheme of Sb^{119} - A.A.Sorokin, A.Bedesku, M.V.Klimentovskaya, L.N. Kryukova, K.P.Mitrofanov, V.V.Murav'eva, V.N.Rybakov, G.Chandra & V.S.Shpinel' 1476
Investigation of the probabilities for radiative transitions between the rotational levels of Er^{166} and Tm^{169} - É.E.Berlovich, V.V. Il'in, A.I.Kislyakov, M.K.Nikitin & T.Bedike 1483

Interaction of carbon ions with photographic emulsion nuclei - L.I.Bolotin, A.P.Klyucharev, Yu.F.Kulygin, Yu.N.Ranyuk, E.I.Revutskii & N.Ya.Rutkevich 1493

(Note: The transactions of the Tenth Conference on Nuclear Spectroscopy will be concluded in Vol.25, No.1).

TRANSACTIONS OF THE FOURTH ALL-UNION CONFERENCE ON X-RAY SPECTROSCOPY

Number 4

Selection of crystals for x-ray spectroscopy - J.Bačkovský 369
Nuclear x-ray generator for fluorescent analysis - K.I.Narbutt, R.L.Barinskii & I.S.Smirnova 372
Instrument for x-ray spectroscopic microanalysis - A.M.Solov'ev & V.N.Vertsner 378
Universal x-ray spectrograph for investigation of the chemical composition of microvolumes - N.P.Il'in 382
Development of the first automatic x-ray spectrograph in Czechoslovakia - R.Rotter & M.Klapuch 386
Reflection of x-rays from a bent crystal in the case of a microfocus source - S.A.Ditsman 390
Optimum correction of x-ray spectra for dispersive distortion - I.Ya.Nikiforov 394
On allowing for apparatus distortion and the width of dispersion type inner levels in emission spectra - Ya.E.Genkin & I.A. Rumyantsev 398
On specifying the energy of x-ray photons and the energy of electron levels - N.D.Borisov & V.V.Nemoshkalenko 406
Concerning the shape of energy bands in solids - M.A.Blokhin & V.P.Sachenko 410
Calculation of the charge of atoms in molecules from the K absorption spectra - R.L.Barinskii & E.G.Nadzhakov 419
Determination of the charge and type of bond of osmium in compounds from the L_{III} absorption spectra - E.G.Nadzhakov & R.L.Barinskii 425
On the origin of some satellites in x-ray spectra - Z.Gorak 432
Concerning interpretation of x-ray spectra - A.T.Shuvaev 434
Investigation of the correlation between the fine structure of x-ray absorption spectra and the characteristic electron energy losses - I.B.Borovskii & V.V.Shmidt 438
Note on the asymmetry index of the $K_{\alpha 1,2}$ lines of transition elements - N.Malkovskaya 442
Investigation of the fine structure of the K x-ray spectra of some sulfides - I.A.Ovsyannikova & I.B.Borovskii 444
Nature of the fine structure of the main K absorption edge of elements of the iron group - I.B.Borovskii & V.A.Batyrev 449
Influence of the nickel concentration on the structure of the electron energy spectrum of Fe-Cr alloys - N.D.Borisov, V.V. Nemoshkalenko & A.M.Fefer 451
Fine structure of the principal K absorption edge of transition metals of the iron group, their alloys and compounds - S.A.Nemnonov 455
Investigation of the principal K absorption edge of nickel in nickel-aluminum alloys - S.A.Nemnonov & M.F.Sorokina 462
Fluorescent L spectra of niobium in NbB_2, NbC, NbN and pure niobium - M.I.Korsunskii & Ya.E.Genkin 467

Relative intensities of the $L\beta_2$, $L\beta_{15}$ and $L\gamma_1$ lines in the L series spectra of substances with an unfilled N shell - M.I. Korsunskii & Ya.E.Genkin 470
Fluorescent L series of niobium bound in some compounds - M.I.Korsunskii & Ya.E.Genkin 475
High-temperature x-ray studies of Invar alloys - S.M.Karal'nik, L.G.Nikolaeva & N.N.Nefedov 477
Use of the method of external standards in fluorescent x-ray spectroscopic analysis - N.F.Losev 480

TRANSACTIONS OF THE EIGHTH CONFERENCE ON LUMINESCENCE
(Molecular luminescence)

Number 5

Opening address - V.L.Levshin 495
Internal conversion from the fluorescence to the phosphorescence level in naphthalene derivatives - V.L.Ermolaev, I.P.Kotlyar & K.K.Svitashev 499
Luminescence of matter with arbitrary absorption and emission bands in volumes of finite size - A.M.Samson 503
Secondary light absorption and emission processes - B.I.Stepanov & A.M.Samson 509
Probability method of calculating absorption and emission properties - P.A.Apanasevich 516
Spectroscopic investigation of vibrational energy transfer in collisions of complex molecules (Summary of report) - S.O. Mirumyants & B.S.Neporent 521
Investigation of the temperature dependence of the interaction between aromatic molecules in the vapor state - V.P.Klochkov 523
Temperature dependence of the fluorescence efficiency of complex molecule vapors - N.A.Borisevich & V.A.Tolkachev 527
Angular distribution of resonance radiation from vapors - P.A. Apanasevich & G.S.Kruglik 531
On agreement between the classical and quantum theories of the interaction of light with harmonic oscillators - V.P.Gribkovskii & B.I.Stepanov 535
Nonlinear optical effects in a system of particles with three energy levels - B.I.Stepanov & V.P.Gribovskii 540
Calculation of the probability of electronic-vibrational transitions for an anharmonic oscillator - K.K.Rebane & O.I.Sil'd 545
Electronic spectra of anthraquinone vapors - N.A.Borisevich & V.V. Gruzinskii 551
Luminescence of anthracene solid solutions - V.L.Broude & V.S.Medvedev 555
Luminescence of crystalline naphthalene containing minor impurities - M.T.Shpak & E.F.Sheka 559
Concerning the luminescence and photoconductivity of anthracene crystals - A.N.Faidysh 562
Effect of β-radiation on the photoluminescence of molecular crystals - Sh.D.Khan-Magometova, N.D.Zhevandrov & V.I.Gribkov 567
On the possible role of temperature quenching in scintillation of organic substances - I.M.Rozman 573
Effect of temperature on the electronic spectra or complex molecules in solutions - L.G.Pikulik 578

Influence of some fluorescence quenchers on the quantum efficiency of photochemical conversion of 9-methylanthracene and 9-methyl-10-methoxymethylanthracene - T.M.Vember & A.S.Cherkasov 583
Influence of temperature on the luminescence of halide solutions of heavy metals - M.U.Belyi & B.F.Rud'ko 588
Dielectric effects and the electronic spectra of polyatomic organic molecules in solutions - N.G.Bakhshiev 593
Influence of the solvent on the fluorescence spectra of acetyl-anthracenes - A.S.Cherkasov 597
Present views regarding the influence of the solvent on the spectra of complex organic molecules (Abstract) - I.A.Zhmyreva, V.V. Zelinskii, V.P.Kolobkov, A.S.Kochemirovskii & I.I.Reznikova 602
Principal processes of deactivation of excited states of complex organic molecules - V.A.Borgman, I.A.Zhmyreva, V.V.Zelinskii & V.P.Kolobkov 607
Influence of structure on the luminescence characteristics of complex organic molecules - V.V.Zelinskii & I.I.Reznikova 612
Optical properties of chlorophyll and pheophytin at low temperatures - L.A.Kravtsov 615
Luminescence efficiency of chlorophyll in different solvents - N.P.Ivanov 618
Aggregation of chlorophyll and chlorophyllide molecules - R.V.Efremova 621
Absorption and fluorescence spectra of perylene at low temperatures - R.I.Personov 624
Spectroscopy of some pyrene derivatives in frozen solutions - A.Ya.Khesina 629

Number 6

Ultimate lines of 3,4-benzopyrene dissolved in normal hydrocarbons at different temperatures - S.G.Bogomolov, F.D.Pemova & L.P. Kolosova 728
Luminescence of solutions of thioindigo and its di-derivatives at 77°K - R.N.Nurmukhametov, D.N.Shigorin & N.S.Dokunikhin 731
Temperature dependence of the fluorescence efficiency of some phthalimides in different solvents - L.G.Pikulik & A.N.Sevchenko 732
Concerning the relation between the absorption and luminescence spectra of complex molecules - M.N.Alentsev & L.A.Pakhomycheva 737
Influence of secondary impurities on the absorption and luminescence spectra of the primary impurity in molecular crystals - A.V.Solov'ev 740
Polarization of the luminescence of molecular crystals in different regions of the spectrum - V.I.Gribkov, N.D.Zhevandrov & Sh.D. Khan-Magometova 743
Mixed organic single crystals, their luminescence and scintillation properties - Yu.V.Naboikin, V.K.Dobrokhotova & V.V.Uglanova 747
Correspondence between the absorption and luminescence spectra of uranyl salt solutions - L.V.Volod'ko, A.N.Sevchenko & D.S.Umreiko 752
Influence of the adsorbent surface on the luminescence of uranyl ions - G.I.Kobyshev 755
Vitrification of polymers and phosphorescence - E.V.Anufrieva & A.D.Zaitseva 758
Luminescence of systems with hydrogen bonds - B.A.Zadorozhnyi & Yu.V.Naboikin 761

Reasons for elimination of internal nonradiative transitions in organic molecules incident to formation of intracomplex compounds with cations - E.A.Bozhevol'nov 765
Phosphorescence of certain solvents and their effect on the absorption spectra of organic phosphors - G.M.Kislyak 769
Correlation between the absorption and luminescence spectra of some organic compounds - E.F.Ryazanova, M.S.Fadeeva & T.S.Pavlina 771
Investigation of the luminescence of ionic forms of uranin and fluorescein - E.V.Grigoryan, L.T.Kantardzhyan & S.S.Chirkinyan 774
Concerning the electronic spectra of complex molecules - S.I.Kubarev 778
Luminescence spectra of halogen derivatives of anthraquinone in frozen solutions - D.N.Shigorin, N.A.Shcheglova & N.S.Dokunikhin 781

TRANSACTIONS OF THE NINTH ALL-UNION CONFERENCE ON CATHODE ELECTRONICS

Number 6

Influence of the electric field on the temperature threshold for the appearance of positive ions in surface ionization - E.Ya. Zandberg 639
Electron emission from a cold barium cathode, appearing after a current pulse in the ambient gas - N.V.Tatarinova & P.N.Chistyakov 644
Electron-optical contrast in observation of patch fields on emitters - G.V.Spivak, I.A.Pryamkova & N.N.Sedov 648
Kinetics of formation and some attributes of oxygen films adsorbed on tungsten - N.D.Morgulis & A.G.Naumovets 657
Variation of ion-electron emission as a function of certain parameters of the target and the bombarding ions - U.A.Arifov & R.R. Rakhimov 666
Secondary electron emission from sodium films bombarded with argon ions - U.A.Arifov & D.A.Tashkhanova 673
On the problem of measuring proton beam currents - P.Görlich, C.Keck, H.Krause, A.Krohs, H.-J.Pohl & F.Schlott 677
Investigation of collision of ions with metal surfaces - N.N.Petrov 682
Etching disintegration of semiconductor surfaces by ion bombardment - I.G.Sirotenko & G.V.Spivak 687
Contribution to the theory of scattering of ions from metal surfaces - V.N.Vapnik, L.G.Gurvich & N.V.Zinov'ev 692
Investigation of the interaction of fast deuterium ions with metals - V.M.Gusev, M.I.Guseva, V.P.Vlasenko & N.P.Elistratov 696
Concerning anisotropy of cathode sputtering of dielectrics - A.I.Krokhina & G.V.Spivak 701
Effect of polarization of the incident light on the emission of complex photocathodes - P.Görlich & H.Hora 705
Concerning neutralization of fast positive ions on metal surfaces - U.A.Arifov & Kh.Kh.Khadzhimukhamedov 711
On scattering of slow alkali metal ions from metal surfaces - U.A.Arifov, A.Kh.Ayukhanov & D.D.Gruich 716
Use of a dynamic type mass spectrometer for investigation of secondary processes - A.Kh.Ayukhanov & G.I.Iskhakov 720

TRANSACTIONS OF THE FIRST ALL-UNION CONFERENCE ON ELECTRONIC AND IONIC COLLISIONS

Number 8

Regarding the First All-Union Conference on Electronic and Ionic Collisions - L.A.Sena & G.F.Drukarev 941
Methods of calculating the cross sections for excitation of atoms by electrons - L.A.Vainshtein & I.I.Sobel'man 943
Partial excitation cross sections for hydrogen atoms - R.K.Peterkop 947
Excitation cross sections for some spectrum lines of krypton and xenon - L.M.Volkova, A.M.Devyatov & A.V.Kuralova 952
On the excitation functions of nitrogen and carbon dioxide molecules in encounters with electrons - I.P.Zapesochnyi & S.M.Kishko 955
Experimental investigation of the excitation functions of atomic spectrum lines - I.P.Bogdanova 958
Experimental determination of the cross sections for excitation of the 2^1S--n^1P lines of helium by electron impact - V.E.Yakhontova 962
Resonance charge exchange of alkali metal ions and atoms - A.M.Bukhteev & Yu.F.Bydin 966
Resonance charge exchange of positive alkali metal ions - D.V.Chkuaseli, U.D.Nikoleishvili & A.I.Guldamashvili 972
Dissociation of large molecules under electron impact - M.V.Gur'ev, M.V.Tikhomirov & N.N.Tunitskii 977
Modern methods for calculating atomic collision cross sections - G.F.Drukarev 981
Further investigation of resonance charge exchange of positive cesium ions - R.M.Kushnir & I.M.Buchma 989
Indirect evaluation of electron attachment cross sections - M.V.Konyukov 993
Energy transfer in molecular collisions - A.I.Osipov & E.V.Stupochenko 996
Theory of thermal dissociation of diatomic molecules - E.E.Nikitin & N.D.Sokolov 1000
Elementary processes involved in collisions between slow ions and molecules - V.L.Tal'roze 1006
Investigation of electron loss due to scattering by the residual gas in an accelerator chamber - A.G.Vlasov, A.A.Vorob'ev, A.N. Kislov & R.P.Meshcheryakov 1012
Procedure for measuring total particle collision cross sections in dense plasmas - L.V.Dubovoi & O.M.Shvets 1020
List of reports presented at the Conference, being published in other journals 1025

TRANSACTIONS OF THE THIRD CONFERENCE ON FERROELECTRICITY

Number 10

Contribution to the statistical theory of ferro- and antiferro-electrics - V.I.Klyachkin 1179
Contribution to the thermodynamic theory of ferroelectricity - V.L.Indenbom 1183
Thermodynamics of solid solutions with ferroelectric properties - V.G.Granovskii 1187

Internal fields in some ferro- and antiferroelectric model structures based on $BaTiO_3$ - N.N.Krainik 1190
Method of calculating the internal electric fields in complex dipole structures and application of the method to $CaTiO_3$ - S.P.Solov'ev, Yu.N.Venevtsev, G.S.Zhdanov & V.V.Ivanova 1194
Investigation of some ferroelectrics by the method of nuclear magnetic resonance - A.G.Lundin, K.S.Aleksandrov, G.M. Mikhailov & S.P.Gabuda 1198
X-ray diffraction studies of some new ferroelectrics with laminar structure - I.G.Ismailzade 1201
Preparation and ferroelectric properties of deuterated triglycine sulfate crystals - V.P.Konstantinova, I.M.Sil'vestrova, L.A. Shuvalov & V.A.Yurin 1206
On the ferroelectric properties of $NaNO_2$ - A.S.Sonin, I.S.Zheludev & G.F.Dobrzhanskii 1212
Concerning light detectors utilizing the pyroelectric effect - I.M.Sil'vestrova 1216
Damping of the oscillations of piezoelectric resonators employing ferroelectric single crystals - L.A.Shuvalov & Yu.S.Likhacheva 1219
Oscillations of dielectric pendulums and polarization of ferroelectrics - I.S.Zheludev 1227
Dielectric and calorimetric investigation of ammonium sulfate and ammonium fluoberyllate crystals - V.A.Koptsik, B.A.Strukov, A.A.Sklyankin & M.E.Levina 1230
Investigation of the optical properties of some ferroelectric crystals - V.A.Koptsik, B.A.Strukov & I.K.Nevedomskaya 1233
Some physical properties of ferroelectric $BaTiO_3$-$PbTiO_3$, $BaTiO_3$-$BaSnO_3$ and $BaTiO_3$-$PbTiO_3$-$BaSnO_3$ single crystals - S.V.Bogdanov, G.M.Kovalenko & A.M.Cherepanov 1236
$BaTiO_3$-$BaSnO_3$ solid solution single crystals - A.L.Khodakov & M.L.Sholokhovich 1240
Preparation and structure of crystals of some lead-containing ferroelectric substances and their solid solutions - M.L. Sholokhovich & E.G.Fesenko 1244
Semiconductor properties of $BaTiO_3$ - S.V.Bogdanov & V.A.Rassushin 1248
Growing ferroelectric single crystals from melts - O.P.Kramarov 1251
Concerning the electric conductivity of barium titanate and some barium titanate base solid solutions - E.V.Sinyakov & B.K.Chernyi 1254
Possibility of controlling the conductivity of lead metaniobate by doping - V.M.Gurevich & I.S.Rez 1258
Some physical properties of vacuum annealed polycrystalline barium titanate - A.V.Chebkasov 1259
Influence of compression on polarization processes in ferroceramics - V.Z.Borodin 1262
Some physical properties of ferroelectric lead ferroniobate and ferrotantalate - V.A.Isupov, A.I.Agranovskaya & N.P.Khuchua 1268
Physical-chemical investigation of the formation of complex ferroelectrics with the perovskite structure - A.I.Agranovskaya 1271
Electric properties of some solid solutions of divalent metal niobates and tantalates - P.S.Mikhailov & B.A.Rotenberg 1278
Concerning ways and means of obtaining materials with a smoothed out temperature dependence of the dielectric constant - N.A. Andreeva, O.A.Grushevskaya & V.I.Zhukovskii 1281

Solid solutions in the ternary ferroelectric system $Ba(Ti,Zr,Sn)O_3$ - M.M.Nekrasov & Yu.M.Poplavko 1284
Preliminary report on a ferroelectric ceramic with a dielectric constant of 80 000-100000 - T.N.Verbitskaya, L.M.Aleksandrova & L.S.Sinitsina 1286
Results of thermal analysis of doped barium titanate - V.I.Zhukovskii, M.P.Dorokhova, N.E.Zaremba, D.G.Dykman & G.V.Bois 1289
Technology and properties of some ceramic ferroelectrics - P.L. Strelets, I.A.Serova, N.D.Yatsenko & P.L.Markus 1291
Rapid procedure for preparing and investigating ferroelectric ceramics - O.P.Kramarov 1295
High-temperature piezoelectric accelerometer sensing elements - M.M.Kachkacheva, A.A.Dryabchuk, I.Z.Rusakov & E.G.Smazhevskaya 1299

Number 11

Temperature dependence of the infrared absorption spectra of $BaTiO_3$, $PbTiO_3$ and $PbZrO_3$ - A.F.Yatsenko 1307
Some electric properties of barium titanate doped with rare earth elements - A.F.Yatsenko & T.P.Popova 1310
Probing the crystal lattice field of $BaTiO_3$ with rare earth ions - A.F.Yatsenko & L.M.Rabkin 1313
Preparation and some ferroelectric properties of lithium hydroselenite - V.P.Konstantinova, I.M.Sil'vestrova, L.A.Shuvalov & V.A.Yurin 1317
Domain walls and etch pit networks in deuterated tri-glycine sulfate crystals - V.P.Konstantinova 1323
Some electric characteristics of ammonium di-H-phosphate single crystals - I.Ya.Eisner 1327
Obtaining a stable single-domain state of ferroelectrics - V.A.Yurin 1329
Effect of gamma-radiation on the ferroelectric properties of tri-glycine sulfate - V.A.Yurin, A.S.Baberkin, E.N.Kornienko & I.V.Gavrilova 1334
Variation of the elastic constant s'_{33} of tri-glycine sulfate crystals as a function of the dc field in the region of the Curie point - I.M.Sil'vestrova 1337
Ferroelectric properties of tri-glycine sulfate single crystals in the 0.01 to 50 cps frequency range - V.M.Gurevich & I.S.Zheludev 1341
Effect of ultrasound on some physical properties of Rochelle salt crystals - T.Kh.Chormonov 1345
Electroluminescence of barium titanate at audio frequencies - E.V.Stauer 1347
Dielectric constants of piezoceramic elements of barium titanate - S.V.Bogdanov 1350
Dielectric properties of polarized ceramics in strong alternating electric fields - V.I.Zaitseva, R.E.Pasynkov, V.I.Pozern & A.M.El'gard 1353
Piezoelectric properties of polarized ceramics in strong alternating fields - G.A.Velyukhanova, R.E.Pasynkov, V.I.Pozern & A.M.El'gard 1358
Piezoelectric hysteresis in polycrystalline barium titanate - I.P. Kozlobaev 1362
Concerning the piezoelectric effect in Varikonds - B.A.Strukov & N.D. Gavrilova 1365
Nonlinear properties of ferroelectrics at microwave frequencies - V.M.Petrov 1368

Ferroelectric films with a rectangular hysteresis loop - M.S.Lur'e, E.I.Vasil'eva & I.V.Ignat'eva 1372
Electric conductivity of $BaTiO_3$ base solid solutions of manganese, cobalt and nickel niobates and tantalates - E.A.Stafiichuk & E.V.Sinyakov 1376
Properties of some $BaTiO_3$-"$A_2B_2O_7$" type solid solutions in strong electric fields - E.V.Sinyakov & E.A.Stafiichuk 1380
Dielectric properties and structure of $PbTiO_3$-$SrTiO_3$-"$Bi_{2/3}TiO_3$" solid solutions - V.Ya.Fritsberg, E.Zh.Freidenfel'd & Ya.Ya. Kruchan 1383
Investigation of the effect of isomorphous replacement of Ti ions on phase transitions in $BaTiO_3$ - V.D.Komarov & E.G.Fesenko 1387
Some results of an investigation of the PbO-Nb_2O_5-Nd_2O_3 system - E.G.Smazhevskaya & N.A.Podol'ner 1389
Concerning the influence of low concentrations of various elements on the properties of $(Pb_{0.57},Ba_{0.43})Nb_2O_6$ solid solution - E.G. Smazhevskaya & V.I.Rivkin 1392
Some anomalous properties of chemically pure barium titanate ceramic - A.A.Anan'eva, M.A.Ugryumova & B.V.Strizhkov 1395
Dielectric and piezoelectric properties of chemically pure barium titanate ceramic - A.A.Anan'eva, B.V.Strizhkov & M.A.Ugryumova 1398
Effect of doping with chromic oxide on some dielectric and piezoelectric properties of barium titanate - L.N.Kamysheva 1401
Investigation of the effect of doping with chromium and bismuth oxides on the dielectric and piezoelectric properties of polycrystalline barium titanate - V.I.Moskalev & S.S.Ordan'yan 1404
Some features of pulse switching of ferroelectric crystals - L.A. Shuvalov 1407
Some special properties of ferroelectric elements and ferromagnetic toroids with square hysteresis loops - E.I.Mamonov & I.S.Zheludev 1412
Principles and application of ferroelectric matrices for information storage in computers - E.I.Mamonov 1416
Transistor circuits for automatic control of writing, reading and restoration of information in ferroelectric memory matrices - E.I.Mamonov & Yu.M.Koval'skii 1418
Equipment for experimental investigation of ferroelectric matrices with semiautomatic address selection - E.I.Mamonov & V.G.Rzhanov 1421
Similar and dissimilar features of antisymmetry, magnetic symmetry and complete symmetry - I.S.Zheludev 1425
On the use of lead and barium metaniobate solid solution piezoceramics in wide-band filters - E.G.Bronnikova, I.M.Larionov, N.D. Mileikovskaya, E.G.Smazhevskaya & I.A.Glozman 1429

RESUME OF THE CONFERENCE TRANSACTIONS PUBLISHED IN VOLUME 24

of the

BULLETIN OF THE USSR ACADEMY OF SCIENCES

- Physical Series -

	Issue No.
Physics of Dielectrics (Second Conference on the Physics of Dielectrics)	1 & 2
Nuclear Spectroscopy (Tenth Conference on Nuclear Spectroscopy)	3,7,9 & 12
X-ray Spectroscopy (Fourth Conference on X-ray Spectroscopy)	4
Molecular Luminescence (Eighth Conference on Luminescence)	5 & 6
Cathode Electronics (Ninth Conference on Cathode Electronics)	6
Electronic and Ionic Collisions (First Conference on Electronic & Ionic Collisions)	8
Ferroelectricity (Third Conference on Ferro-electricity)	10 & 11

Columbia Technical Translations
5 Vermont Ave., White Plains, N.Y.